REPORT S2-R21-RW-4

Composite Pavement Systems: Appendices

SHRP2 RENEWAL RESEARCH

SHRP 2
STRATEGIC HIGHWAY RESEARCH PROGRAM
Accelerating solutions for highway safety, renewal, reliability, and capacity

TRANSPORTATION RESEARCH BOARD
OF THE NATIONAL ACADEMIES

TRANSPORTATION RESEARCH BOARD 2013 EXECUTIVE COMMITTEE*

OFFICERS

Chair: **Deborah H. Butler,** *Executive Vice President, Planning, and CIO, Norfolk Southern Corporation, Norfolk, Virginia*
Vice Chair: **Kirk T. Steudle,** *Director, Michigan Department of Transportation, Lansing*
Executive Director: **Robert E. Skinner, Jr.,** *Transportation Research Board*

MEMBERS

Victoria A. Arroyo, *Executive Director, Georgetown Climate Center, and Visiting Professor, Georgetown University Law Center, Washington, D.C.*
Scott E. Bennett, *Director, Arkansas State Highway and Transportation Department, Little Rock*
William A. V. Clark, *Professor of Geography (emeritus) and Professor of Statistics (emeritus), Department of Geography, University of California, Los Angeles*
James M. Crites, *Executive Vice President of Operations, Dallas–Fort Worth International Airport, Texas*
Malcolm Dougherty, *Director, California Department of Transportation, Sacramento*
John S. Halikowski, *Director, Arizona Department of Transportation, Phoenix*
Michael W. Hancock, *Secretary, Kentucky Transportation Cabinet, Frankfort*
Susan Hanson, *Distinguished University Professor Emerita, School of Geography, Clark University, Worcester, Massachusetts*
Steve Heminger, *Executive Director, Metropolitan Transportation Commission, Oakland*
Chris T. Hendrickson, *Duquesne Light Professor of Engineering, Carnegie Mellon University, Pittsburgh, Pennsylvania*
Jeffrey D. Holt, *Managing Director, Bank of Montreal Capital Markets, and Chairman, Utah Transportation Commission, Huntsville, Utah*
Gary P. LaGrange, *President and CEO, Port of New Orleans, Louisiana*
Michael P. Lewis, *Director, Rhode Island Department of Transportation, Providence*
Joan McDonald, *Commissioner, New York State Department of Transportation, Albany*
Donald A. Osterberg, *Senior Vice President, Safety and Security, Schneider National, Inc., Green Bay, Wisconsin*
Steve Palmer, *Vice President of Transportation, Lowe's Companies, Inc., Mooresville, North Carolina*
Sandra Rosenbloom, *Professor, University of Texas, Austin (Past Chair, 2012)*
Henry G. (Gerry) Schwartz, Jr., *Chairman (retired), Jacobs/Sverdrup Civil, Inc., St. Louis, Missouri*
Kumares C. Sinha, *Olson Distinguished Professor of Civil Engineering, Purdue University, West Lafayette, Indiana*
Daniel Sperling, *Professor of Civil Engineering and Environmental Science and Policy; Director, Institute of Transportation Studies, University of California, Davis*
Gary C. Thomas, *President and Executive Director, Dallas Area Rapid Transit, Dallas, Texas*
Paul Trombino III, *Director, Iowa Department of Transportation, Ames*
Phillip A. Washington, *General Manager, Regional Transportation District, Denver, Colorado*

EX OFFICIO MEMBERS

Rebecca M. Brewster, *President and COO, American Transportation Research Institute, Marietta, Georgia*
Anne S. Ferro, *Administrator, Federal Motor Carrier Safety Administration, U.S. Department of Transportation*
John T. Gray II, *Senior Vice President, Policy and Economics, Association of American Railroads, Washington, D.C.*
Michael P. Huerta, *Administrator, Federal Aviation Administration, U.S. Department of Transportation*
Paul N. Jaenichen, Sr., *Acting Administrator, Maritime Administration, U.S. Department of Transportation*
Michael P. Melaniphy, *President and CEO, American Public Transportation Association, Washington, D.C.*
Victor M. Mendez, *Administrator, Federal Highway Administration, U.S. Department of Transportation*
Robert J. Papp *(Adm., U.S. Coast Guard), Commandant, U.S. Coast Guard, U.S. Department of Homeland Security*
Lucy Phillips Priddy, *Research Civil Engineer, U.S. Army Corps of Engineers, Vicksburg, Mississippi, and Chair, TRB Young Members Council*
Cynthia L. Quarterman, *Administrator, Pipeline and Hazardous Materials Safety Administration, U.S. Department of Transportation*
Peter M. Rogoff, *Administrator, Federal Transit Administration, U.S. Department of Transportation*
Craig A. Rutland, *U.S. Air Force Pavement Engineer, Air Force Civil Engineer Center, Tyndall Air Force Base, Florida*
David L. Strickland, *Administrator, National Highway Traffic Safety Administration, U.S. Department of Transportation*
Joseph C. Szabo, *Administrator, Federal Railroad Administration, U.S. Department of Transportation*
Polly Trottenberg, *Under Secretary for Policy, U.S. Department of Transportation*
Robert L. Van Antwerp *(Lt. General, U.S. Army), Chief of Engineers and Commanding General, U.S. Army Corps of Engineers, Washington, D.C.*
Barry R. Wallerstein, *Executive Officer, South Coast Air Quality Management District, Diamond Bar, California*
Gregory D. Winfree, *Administrator, Research and Innovative Technology Administration, U.S. Department of Transportation*
Frederick G. (Bud) Wright, *Executive Director, American Association of State Highway and Transportation Officials, Washington, D.C.*

---

*Membership as of November 2013.

The Second
STRATEGIC HIGHWAY RESEARCH PROGRAM

SHRP 2 REPORT S2-R21-RW-4

Composite Pavement Systems: Appendices

Shreenath Rao
Applied Research Associates, Inc., Littleton, Colorado

Michael Darter
Applied Research Associates, Inc., Tucson, Arizona

Derek Tompkins, Mary Vancura, and Lev Khazanovich
University of Minnesota, Minneapolis

Jim Signore
University of California, Berkeley

Erdem Coleri, Rongzong Wu, and John Harvey
University of California, Davis

Julie Vandenbossche
University of Pittsburgh, Pennsylvania

TRANSPORTATION RESEARCH BOARD

WASHINGTON, D.C.
2014
www.TRB.org

The Second Strategic Highway Research Program

America's highway system is critical to meeting the mobility and economic needs of local communities, regions, and the nation. Developments in research and technology—such as advanced materials, communications technology, new data collection technologies, and human factors science—offer a new opportunity to improve the safety and reliability of this important national resource. Breakthrough resolution of significant transportation problems, however, requires concentrated resources over a short time frame. Reflecting this need, the second Strategic Highway Research Program (SHRP 2) has an intense, large-scale focus, integrates multiple fields of research and technology, and is fundamentally different from the broad, mission-oriented, discipline-based research programs that have been the mainstay of the highway research industry for half a century.

The need for SHRP 2 was identified in *TRB Special Report 260: Strategic Highway Research: Saving Lives, Reducing Congestion, Improving Quality of Life,* published in 2001 and based on a study sponsored by Congress through the Transportation Equity Act for the 21st Century (TEA-21). SHRP 2, modeled after the first Strategic Highway Research Program, is a focused, time-constrained, management-driven program designed to complement existing highway research programs. SHRP 2 focuses on applied research in four areas: Safety, to prevent or reduce the severity of highway crashes by understanding driver behavior; Renewal, to address the aging infrastructure through rapid design and construction methods that cause minimal disruptions and produce lasting facilities; Reliability, to reduce congestion through incident reduction, management, response, and mitigation; and Capacity, to integrate mobility, economic, environmental, and community needs in the planning and designing of new transportation capacity.

SHRP 2 was authorized in August 2005 as part of the Safe, Accountable, Flexible, Efficient Transportation Equity Act: A Legacy for Users (SAFETEA-LU). The program is managed by the Transportation Research Board (TRB) on behalf of the National Research Council (NRC). SHRP 2 is conducted under a memorandum of understanding among the American Association of State Highway and Transportation Officials (AASHTO), the Federal Highway Administration (FHWA), and the National Academy of Sciences, parent organization of TRB and NRC. The program provides for competitive, merit-based selection of research contractors; independent research project oversight; and dissemination of research results.

SHRP 2 Report S2-R21-RW-4

ISBN: 978-0-309-12959-6

© 2014 National Academy of Sciences. All rights reserved.

Copyright Information

Authors herein are responsible for the authenticity of their materials and for obtaining written permissions from publishers or persons who own the copyright to any previously published or copyrighted material used herein.

The second Strategic Highway Research Program grants permission to reproduce material in this publication for classroom and not-for-profit purposes. Permission is given with the understanding that none of the material will be used to imply TRB, AASHTO, or FHWA endorsement of a particular product, method, or practice. It is expected that those reproducing material in this document for educational and not-for-profit purposes will give appropriate acknowledgment of the source of any reprinted or reproduced material. For other uses of the material, request permission from SHRP 2.

Note: SHRP 2 report numbers convey the program, focus area, project number, and publication format. Report numbers ending in "w" are published as web documents only.

Notice

The project that is the subject of this report was a part of the second Strategic Highway Research Program, conducted by the Transportation Research Board with the approval of the Governing Board of the National Research Council.

The members of the technical committee selected to monitor this project and review this report were chosen for their special competencies and with regard for appropriate balance. The report was reviewed by the technical committee and accepted for publication according to procedures established and overseen by the Transportation Research Board and approved by the Governing Board of the National Research Council.

The opinions and conclusions expressed or implied in this report are those of the researchers who performed the research and are not necessarily those of the Transportation Research Board, the National Research Council, or the program sponsors.

The Transportation Research Board of the National Academies, the National Research Council, and the sponsors of the second Strategic Highway Research Program do not endorse products or manufacturers. Trade or manufacturers' names appear herein solely because they are considered essential to the object of the report.

SHRP 2 Reports

Available by subscription and through the TRB online bookstore:
www.TRB.org/bookstore

Contact the TRB Business Office:
202-334-3213

More information about SHRP 2:
www.TRB.org/SHRP2

THE NATIONAL ACADEMIES

Advisers to the Nation on Science, Engineering, and Medicine

The **National Academy of Sciences** is a private, nonprofit, self-perpetuating society of distinguished scholars engaged in scientific and engineering research, dedicated to the furtherance of science and technology and to their use for the general welfare. On the authority of the charter granted to it by Congress in 1863, the Academy has a mandate that requires it to advise the federal government on scientific and technical matters. Dr. Ralph J. Cicerone is president of the National Academy of Sciences.

The **National Academy of Engineering** was established in 1964, under the charter of the National Academy of Sciences, as a parallel organization of outstanding engineers. It is autonomous in its administration and in the selection of its members, sharing with the National Academy of Sciences the responsibility for advising the federal government. The National Academy of Engineering also sponsors engineering programs aimed at meeting national needs, encourages education and research, and recognizes the superior achievements of engineers. Dr. Charles M. Vest is president of the National Academy of Engineering.

The **Institute of Medicine** was established in 1970 by the National Academy of Sciences to secure the services of eminent members of appropriate professions in the examination of policy matters pertaining to the health of the public. The Institute acts under the responsibility given to the National Academy of Sciences by its congressional charter to be an adviser to the federal government and, on its own initiative, to identify issues of medical care, research, and education. Dr. Harvey V. Fineberg is president of the Institute of Medicine.

The **National Research Council** was organized by the National Academy of Sciences in 1916 to associate the broad community of science and technology with the Academy's purposes of furthering knowledge and advising the federal government. Functioning in accordance with general policies determined by the Academy, the Council has become the principal operating agency of both the National Academy of Sciences and the National Academy of Engineering in providing services to the government, the public, and the scientific and engineering communities. The Council is administered jointly by both Academies and the Institute of Medicine. Dr. Ralph J. Cicerone and Dr. Charles M. Vest are chair and vice chair, respectively, of the National Research Council.

The **Transportation Research Board** is one of six major divisions of the National Research Council. The mission of the Transportation Research Board is to provide leadership in transportation innovation and progress through research and information exchange, conducted within a setting that is objective, interdisciplinary, and multimodal. The Board's varied activities annually engage about 7,000 engineers, scientists, and other transportation researchers and practitioners from the public and private sectors and academia, all of whom contribute their expertise in the public interest. The program is supported by state transportation departments, federal agencies including the component administrations of the U.S. Department of Transportation, and other organizations and individuals interested in the development of transportation. **www.TRB.org**

www.national-academies.org

CONTENTS

1 APPENDIX A History and Background of HMA/PCC Composite Pavements
1 History
2 Research Studies
7 Recent Research
8 International Experience

10 APPENDIX B History and Background of PCC/PCC Composite Pavements
10 History
11 Background

15 APPENDIX C Highway Agency Survey
15 HMA/PCC Composite Pavement Agency Response Summary
19 PCC/PCC Composite Pavements Agency Response Summary

21 APPENDIX D Distress Mechanisms of HMA/PCC Composite Pavements
21 Performance Issues
21 Distress Mechanisms and Pavement Design

24 APPENDIX E Distress Mechanisms of PCC/PCC Composite Pavements
24 Distresses
26 Performance of PCC/PCC

29 APPENDIX F Construction of Test Sections at MnROAD
29 Introduction
29 Design and Specifications
29 HMA/PCC Composite Pavement Design Thickness
32 PCC/PCC Composite Pavement Design Thickness
33 Construction of the Test Sections
50 As-constructed Properties

54 APPENDIX G Construction of Test Sections at UCPRC
54 Introduction
54 Test Track Construction
63 Concrete Pavement Construction
68 HMA Construction
73 Initial Slab Response Monitoring

83 APPENDIX H Instrumentation and Analysis of Instrumented Data at MnROAD
83 Introduction
94 Characterization of Temperature and Moisture Gradients that Developed in Composite Sections at MnROAD
106 Establishing Built-in Temperature Gradient
113 Composite Pavement Curvature in Response to Environmental Loads

122 APPENDIX I HMA/PCC Rutting Model
122 Introduction
122 *MEPDG* Version 9-30A for Predicting Rut Depths—Enhancements

141 APPENDIX J Measurement and Analysis of PCC Slab Temperature Profiles at UCPRC
141 Objectives
144 Results Summary

147 APPENDIX K HVS Cracking Tests at UCPRC
147 Description of the HVS Testing Program for Cracking
154 HVS Test Results for Section 613HB
179 HVS Test Results for Section 614HB
205 Summary and Conclusions

207 APPENDIX L HVS Rutting Tests at UCPRC
207 Preliminary Analysis for the HVS Test Sections
208 HVS Test Criteria
214 HVS Test Data Summary
240 Asphalt Strain Gauge Results
244 Conclusions

245 APPENDIX M Joint Movement Monitoring at UCPRC
245 Introduction
245 Monitoring Program
247 Results Summary
268 Data Analysis and Observations
273 Summary of Findings

282 APPENDIX N Laboratory Testing of HMA Mixes at UCPRC
282 Experiment Design
283 Test Results

293 APPENDIX O HMA/PCC Bonding and Friction Literature
293 Introduction
293 Objective
294 Interface Modeling
294 Interface Testing Methods
296 Torsion Testing
296 Tension Testing
297 Other Test Methods
299 HMA on PCC Field or Laboratory Studies
300 HMA on HMA Field or Laboratory Studies

302 APPENDIX P CalME Model
302 Procedure for Rutting Performance Prediction and Calibration
305 Stiffness Model for Asphalt-Bound Materials
306 Fatigue Cracking Model
309 Reflection Cracking Model
312 Calibration of Incremental-Recursive Rutting Prediction Models in CalME Using HVS and MnROAD Experiments
315 Factor Levels for Sensitivity Study Variables
317 Results of the Sensitivity Study

320 APPENDIX Q Laboratory Testing of PCC Mixes
320 Introduction
320 SHRP 2 R21 Preliminary Laboratory Plan
320 Aggregates
328 Verifying Mix Designs

330 APPENDIX R *MEPDG* Modifications for PCC/PCC Pavements
330 *MEPDG* EICM Modifications for SHRP 2 R21

340 APPENDIX S Lattice 3D Model Background
340 Lattice Models
340 Lattice Model Formulation and Refinement for Fracture
342 Model Simulations of PCC/PCC Interface
343 Beam Simulation Results and Discussion

354 APPENDIX T Recycled Concrete Aggregates in PCC
354 History of RCA Use in PCC and Relevant Issues
361 Preliminary Testing of RCA Delivered for R21 MnROAD Use
361 Crushing Methods and Properties of RCA for R21 MnROAD Construction

369 APPENDIX U Freeze-Thaw Durability Testing of PCC Mixes
369 Introduction
369 RILEM and ASTM Freeze-Thaw Standards
371 Methodology
374 Results and Discussion
378 Conclusions

380 APPENDIX V Brushing and Exposed Aggregate Concrete
380 Introduction
380 Exposed Aggregate Concrete Brushing: Laboratory Experience
384 Exposed Aggregate Concrete Brushing: Field Experience

388 References

APPENDIX A

History and Background of HMA/PCC Composite Pavements

History

Composite pavements consisting of a hot-mix asphalt (HMA) wearing surface course placed over a portland cement concrete (PCC) layer (HMA/PCC) or an alternative cemented layer (lean concrete base [LCB], cement-treated base [CTB], or roller-compacted concrete [RCC]) have been used since the 1950s, whether as an intentionally designed facility or as part of overlay rehabilitation procedures under staged construction (Griffith 1963). Many thousands of miles of HMA overlays have been placed on PCC pavements considered unserviceable. Numerous cities have regularly used HMA/PCC composite pavements as their standard design. These pavements were constructed to facilitate access to utilities.

Major thrusts toward an engineered composite pavement began in the late 1950s, through the guidance of the Committee on Composite Pavement Design of the Highway Research Board. An important task of this committee was to develop a precise definition of "composite pavement" because by some definitions, any pavement consisting of varied layer materials could be considered a composite structure. The eventual definition decided upon by the committee, after variations in language and terminology among practitioners and researchers were considered, was

> A structure comprising multiple, structurally significant layers of different, sometimes heterogeneous composition. Two layers or more must employ dissimilar, manufactured binding agents. (Smith 1963)

Testing all types of composite pavements was impractical (Allen 1973), so the committee recommended studying the performance of composite pavements as a class and comparing it with that of conventional pavements; from this, designs could be developed that would be considered equivalent in design and performance to conventional pavements. The committee recommended

> To determine, through a series of experiments over different soils and in different environments, various designs for composite pavements that may be expected to exhibit the same performance as specified designs of conventional rigid and flexible pavements. When such information as to equivalent design is available, future choice of pavement type should be based on cost considerations. (Smith 1963)

As part of the movement toward a broader use of composite pavements, numerous design possibilities were suggested for study (Van Breemen 1963). Some examples of these options are listed below, along with their expected performance possibilities or characteristics.

- A simple design using HMA over jointed plain concrete (JPC) is expected to result in reflection cracking. It was hypothesized that adding reinforcing steel or fabric to the lower HMA layer along with using short-jointed PCC would reduce cracking through lesser joint movement and steel reinforcement. This design concept was used on some airfields in central and south Texas in the 1960s. However, the primary mode of failure was still reflection cracking. The shorter joint spacing and steel reinforcement kept the cracks in the HMA surface layer tighter, where a removal and replacement of the HMA wearing surface (layer above the reinforced layer) served the San Antonio International Airport well for many years.
- Using an LCB or low modulus PCC under the HMA layer was thought to perform well, in that the cracks would be of limited width because of the reduced cement content. This has been used by a number of highway agencies (e.g., in Louisiana, Kentucky, and Florida). Historically, random cracks still occur in the LCB and reflect to the surface. The time that reflection cracks appear at the surface and their severity depend on the thickness of the HMA layers and LCB layer.
- Another option is the placement of thicker HMA layers above the PCC or rigid layer. Thicker HMA layers are

beneficial in that they reduce temperature changes in the PCC and reduce the cracks in the PCC. This design strategy has proved to be effective in delaying and reducing the severity of reflection cracks.

- A promising technique was suggested that uses an untreated granular intermediate course to inhibit the cracks from propagating through to the surface layer. Risks were mentioned with using this technique for exhibiting premature fatigue cracking, especially if the surfacing is too thin or the granular aggregate material is not of high quality. Southwestern states have had satisfactory performance with this design strategy, and it reduces the occurrence of reflection cracks. An even more elaborate design that uses a bituminous stabilized or asphalt-treated base (ATB) between the granular course and surface course was suggested. The disadvantage of this method (use of a cushion layer between the PCC and HMA layers) is that the total pavement structure becomes very thick. In the 1960s, New Jersey successfully built many such composite pavements with an intermediate granular layer.
- Finally, using continuously reinforced concrete (CRC) under the HMA layer was thought to lead to good performance because of CRC's tight crack spacing.

Research Studies

Early full-scale test section research into the construction (Smith 1963) and evaluation (Ryell and Corkill 1973) of composite pavements with numerous layering options was conducted in Toronto, Ontario, Canada. The focus of the study was multifold, including addressing the following questions:

- Can a smooth-riding pavement be easily constructed by surfacing a PCC layer with HMA layers?
- What is the best combination of thicknesses of PCC layer and HMA surface for a high-class type of pavement designed to carry heavy traffic?
- Should the concrete layer be reinforced?
- How can reflection cracking be prevented or reduced?

Ontario Highway 401 Study (1959–1973)

Nine sections were built and instrumented with thermocouples, strain gauges, and crack width measuring "points." The soils, base materials, concrete, and HMA were all typical of that commonly used in Ontario, and the construction of the sections was comparable to conventional practice. Precautions were taken to ensure that the subgrade and base were of consistent quality under each section. The concrete mix was standard, with 569 lb/yd^3 and 28-day compressive strength of 3,500 psi. After 3 years under traffic, the pavement sections were assessed by looking at the tightness of the crack distribution as expressed by percentage of cracks greater than a given width. The best performing section was the 7-in. CRC-reinforced pavement with 0.44% welded wire and 1.5-in. HMA surface. This was closely followed by the "control section," which was an 8-in. conventional CRC pavement with 0.38% reinforcement and no HMA wearing course. The worst performing section was an 8-in. reinforced concrete (0.18% steel) with 89-ft contraction joints and 3.25-in. HMA. From an economic viewpoint, in general the unreinforced PCC pavements were performing adequately and were considerably cheaper than the reinforced PCC pavements. The author (Smith 1963) discussed how the performance of the unreinforced PCC layer could be improved through sawing or forming contraction joints at shorter intervals.

The pavements in the Ontario test site were evaluated again after 13 years by Ryell and Corkill (1973). The authors found that the cracks occurred less frequently but were widest in sections having unreinforced PCC or a reinforced PCC with formed joints. Cracks occurred most frequently and were narrowest on sections with PCC having the greatest percentage of reinforcing steel. Thicker PCC reduced cracking by a third in sections containing a heavier percentage of steel. Increasing the percentage of steel (from 108 to 140 lb per 100 ft^2) for a given thickness of PCC resulted in an 80% increase in the number of cracks and a slightly lower average crack width. Although the thickness of the HMA overlay varied from 1.5 to 4 in., it did not have any influence on the amount of cracking reflected. Wherever a crack was observed in the HMA, there was a crack directly below it—in the PCC layer. Although every section was affected by transverse cracking, little change occurred in either number or width of cracks after the first two winters. There was only one exception, in which the number of cracks had more than doubled after the first 2 years because of a breakdown of the macadam asphalt binder course.

The authors considered performance, initial cost, maintenance requirements, and rideability as rating factors and concluded:

> In a general sense, section A (3.25-in. HMA over an 8-in. plain [unreinforced] PCC with no joints) is considered to be the most satisfactory of the experimental sections. The present performance of that section, i.e., riding quality and skid resistance, is good, and its initial and estimated maintenance costs rank lowest of all the sections.

They further concluded:

> . . . it becomes apparent that the best composite pavement (section A), which has carried heavy traffic for 13 years and is still a good pavement, performs better than most other rigid or flexible pavements.

Superiority of the best composite section (A) over the control reinforced concrete section (I) is due to the superior skid resistance and lower initial cost of the composite section. On that basis, composite pavement offers potential advantages over conventional reinforced concrete pavement for heavily trafficked expressway pavements.

Additional conclusions by the authors regarding engineering aspects of the composite designs were

- The thicknesses of HMA layer were not adequate to bridge cracks or joints in the PCC layer.
- The HMA on a lightly reinforced PCC layer significantly reduced the number of transverse cracks in the PCC slab.
- The effect of the reinforcing mesh in the PCC slab was to increase the number and decrease the width of the cracks. In most sections, several very wide stepped cracks indicate failure of the mesh and loss of load transfer at the joints. Reinforcing mesh in the PCC layer appears to have no beneficial effect on the overall performance of the composite pavement. Note that this mesh was only 0.16% to 0.44%, in the range of jointed reinforced concrete pavement [JRCP], but far less than the 0.6+% normally used in continuously reinforced concrete pavement (CRCP).
- "Better performance may be achieved if the wide transverse cracks, present in each of the experimental sections, are prevented from occurring. That may be accomplished by the use of transverse crack inducers in the PCC layer at approximately 15-ft centers." The authors go on to suggest that the extra cost of this could be offset through use of lower-quality concrete in the PCC.

Analysis of the actual data results in the following additional or supportive conclusion on the thickness of the HMA surfacing and PCC thickness:

- The thicker the HMA surfacing and the PCC layer, the lower the maintenance requirements (Figure A.1 and Figure A.2) and the better the rideability. This is likely due to the increased structural capacity achieved from increasing thickness of layers.

Analysis of the actual data results in the following additional or supportive conclusions on transverse crack spacing:

- Longer crack spacing provides lower maintenance and better rideability. However, nearly all of these cracks deteriorate over time.
- The shorter the crack spacing (caused primarily by low amounts of reinforcement [0.16% to 0.44%] that result in shorter crack spacing) the wider and more deteriorated reflection cracks in the HMA surfacing.
- Neither of these options is desirable. The authors recommend the placement of joints at short distances (e.g., 15 ft) to control reflection cracking and width as a better alternative.

Analysis of the actual data results in the following additional or supportive conclusions on the thickness of the reinforcement in the PCC slab:

- The relatively light amount of longitudinal reinforcement (<0.44%) resulted in the reinforcement being ineffective in holding transverse cracks tightly together.

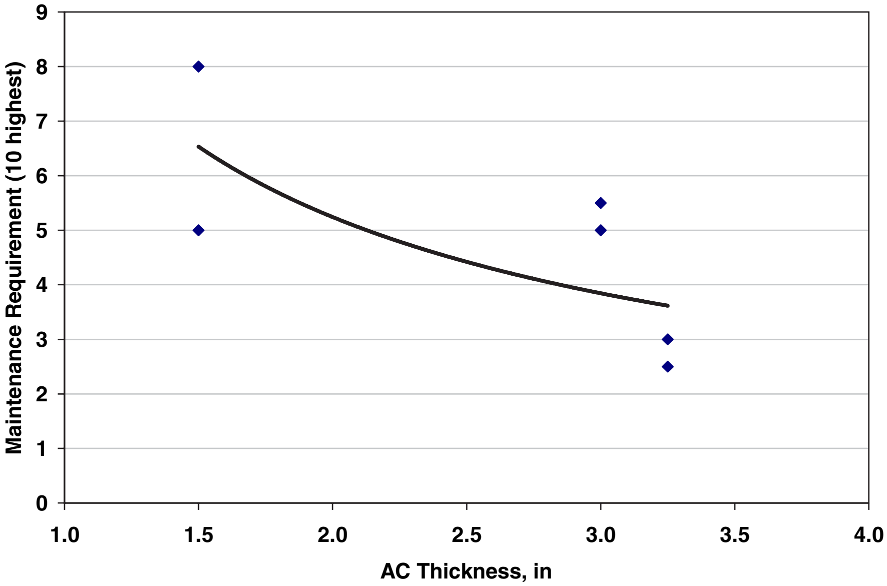

Figure A.1. Effect of HMA (AC) thickness on maintenance requirements (10 is highest maintenance requirement and 0 is none).

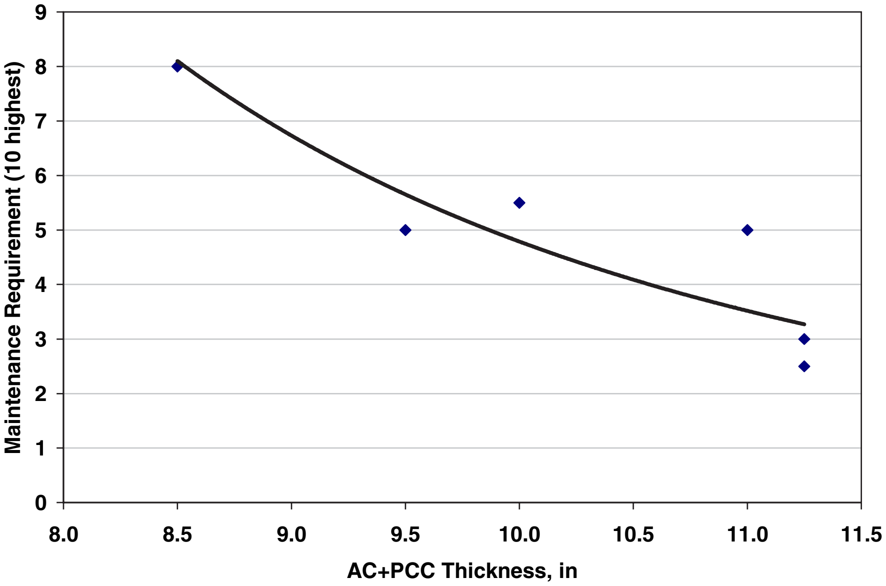

Figure A.2. Effect of HMA (AC) + PCC thickness on maintenance requirements (10 is highest maintenance requirement and 0 is none).

- The higher the percent reinforcement (within the 0.16% to 0.44% range), the more cracks developed, which were not held tightly, resulting in failure of the mesh and deterioration of the crack, requiring maintenance and creating roughness.
- It should not be concluded that use of more normal levels of reinforcement would cause additional reflection cracking because this has not been shown to be the case on many other projects with regular CRCP (e.g., percent reinforcement >0.6%).

New Jersey Composite Pavements

Another pioneering use of composite pavements was made in New Jersey on NJ-3 (Baker 1973). It was determined that a composite pavement would be better suited than a conventional PCC or HMA pavement for the following reasons:

- A portion of the terrain consisted of meadowlands with subsoils consisting of thin layers of silt, clay, and sand. The typical JRCP with 78-ft joint spacing was considered inappropriate because of the compressible nature of these soils and the potential for differential settlement, whereas bituminous pavements with a stable foundation performed very well with these soils.
- With high average annual daily traffic (AADT) with a large percentage of trucks, the section had to be of unusually sturdy construction to remain "trouble free" with minimal maintenance. Past experience with HMA wearing or surfacing mixtures showed they are capable of handling the traffic expected on NJ-3.

The pavement section consisted of the following design:

- 3.5-in. HMA (surface and binder);
- 5-in. dry bound macadam (2.5-in. stone choked with stone screenings);
- 3-in. dense graded crushed stone;
- 8-in. plain nondoweled PCC (NJ Class D mix) with 15-ft joint spacing;
- 6-in. crushed stone base; and
- Subgrade was meadowlands, varied layers of silt, clay, and sand.

The longitudinal joints between lanes did not include tie bars. The design is interesting in that it has essentially 8 in. of granular material between the JPC slab and the HMA surfacing to prevent reflection cracking. The design concept was as follows:

- Maintain the structural integrity of the pavement despite the unstable subgrade.
- Achieve a high load-carrying capacity.
- Achieve continuity of surface and minimize reflection cracking, thus reducing maintenance costs.

The section of highway had four lanes in the same direction with an HMA shoulder adjacent to the outside lane. Two-way traffic existed on the four lanes for a short period of time. The AADT in 1970 was 88,780 in two directions at the Hackensack River Bridge. Trucks were 14.6% of all traffic. The lane distribution of trucks and the estimated equivalent single-axle loads (ESALs) to December 1970 were as follows:

- Lane 1 (closest to outside shoulder): 19% (2.785 million ESALs);
- Lane 2 (closest to lane 1): 43% (6.426 million ESALs);
- Lane 3 (closest to lane 4): 32% (4.723 million ESALs); and
- Lane 4 (closest to inside shoulder): 6% (0.904 million ESALs).

The pavement was monitored from 1963 until 1971 for smoothness, deflections, and distresses as summarized below.

- Smoothness: The roughness index increased or decreased slightly on the various lanes over the 8-year period.
    - Lane 1: 103 to 115 in./mi;
    - Lane 2: 108 to 91 in./mi;
    - Lane 3: 102 to 101 in./mi; and
    - Lane 4: 110 to 128 in./mi.
- Rutting: Rut depth was measured at 50-ft intervals in both wheelpaths in lanes 1 and 4 using an 8-ft straightedge placed across one wheelpath to the bottom of the rut. Little increase in rutting occurred over the 8-year period.
- Condition survey: No reflection cracking was observed over the 15-ft spaced transverse joints or along the longitudinal joints. Little other random cracking was observed over the 8-year period.
- Deflections: The deflections (measured with a Benkelman Beam) were generally low, and there was only a slight increase in deflections over the 8-year period.

The authors concluded that the composite pavement functioned in accordance with design objectives and required no maintenance. A high load-carrying capability was achieved, as evidenced by low deflections. No localized differential settlement was observed, and no reflection cracking or other pavement cracking occurred. The ride quality of the pavement had not deteriorated to any significant degree.

New Jersey estimated the service life of the composite pavement using the American Association of State Highway and Transportation Officials (AASHTO) procedure for flexible pavements. A remaining service life of 30 years was estimated for a total structural life of 38 years. However, this does not consider the age hardening of the HMA surfacing. The cost of this composite pavement was 15% greater than the typical New Jersey JRCP section. The authors estimated that the increased expenditure produces approximately 23% greater service life.

Zero-Maintenance Pavements Study

The Federal Highway Administration (FHWA) sponsored multiple studies in the late 1970s and early 1980s to study and develop a new concept in design called "Zero-Maintenance Pavements." This project located and surveyed seven composite pavements (Table A.1), which included six constructed as composite pavements and one (I-94 in Michigan) constructed as an HMA overlay of an existing PCC pavement.

The NJ-3 pavement described above was included under the FHWA contract on "Zero-Maintenance" (Darter and

Table A.1. Summary of Information for Composite Pavement Projects Included in the "Zero-Maintenance Study" Field Survey

					Pavement Section				
Route	City, State	Date Opened	1974 AADT	Number of Lanes	Surface	Layer 2	Layer 3	Layer 4	Subgrade
I-94	Detroit, Michigan	1965	102,000	6	11-in. HMA	3-in. HMA exist.	9-in. PCC exist., 30-ft joint spacing	na	NA
Hwy 401	Toronto, Ontario	1959	63,000	4	3.25-in. HMA	8-in. PCC	6-in. Granular base	6 in. Granular base	Clay
Hwy 401	Toronto, Ontario	1959	63,000	4	3.25-in. HMA	8-in. PCC 100-ft joint spacing	6-in. Granular base	6 in. Granular base	Clay
QEW 10	Toronto, Ontario	1960	87,500	6	6-in. HMA	8.5-in. PCC	6-in. Granular base	na	NA
I-80	Ottawa, Illinois	1962	18,900	4	3-in. HMA	8-in. PCC	6-in. Granular base	na	A-6
NJ-3	New Jersey	1963	96,500	8	3.5-in. HMA	5-in. stone macadam	3-in. Granular base	8-in. PCC 15-ft joint spacing	6-in. Granular base, silt, clay, sand
I-5	Seattle, Washington	1966	43,500	6	4-in. HMA	6-in. PCC	2-in. Granular base	7-in. Granular base	Glacial till

Barenberg 1976) and was found to be providing excellent service at that time. Another section in New Jersey that included 6-in. JPC also performed well under lighter traffic. This section on NJ-20 did not require patching or other maintenance.

Several composite pavement projects were built in the state of Washington from the 1930s through the 1990s. One such project was constructed in 1955 on I-5 north of Seattle. This six-lane freeway project initially was evaluated for the Zero-Maintenance Study and had an AADT of 43,500. The design consisted of 4-in. HMA placed on a new 6-in. PCC slab. Over the years, the pavement exhibited good performance (three overlays over 50 years of service).

Transverse cracking was the major distress type observed on these composite pavements. The only project without any transverse cracking after 11 years of service and heavy traffic loading was the NJ-3 project with the 8-in. granular material between the HMA surface and the PCC slab. Darter and Barenberg (1976) concluded that the occurrence of transverse reflection cracks in composite pavements is not critical if the cracks remain tight. Three composite pavements (I-94, QEW 10, and I-5) exhibited cracking but did not receive any maintenance treatments because the cracks remained tightly closed. However, the two projects on Hwy 401 cracked and seriously spalled, resulting in maintenance. The I-80 project near Ottawa, Illinois, had major spalling and was scheduled to be overlaid. They state:

> The HMA surface thickness (for a given PCC slab) appears to be a very significant factor affecting crack spalling. A relatively thin HMA surface under heavy traffic is not capable of withstanding heavy traffic applications expected on high traffic volume pavements.

Rutting for all composite pavements surveyed was rated as only “minor” to “moderate,” even under very heavy traffic. The PCC slab seemed to have a definite effect on minimizing HMA surface rutting.

Premium Pavements Study

The FHWA changed the terminology from “zero maintenance” to “premium pavements” in the late 1970s, but the definition and design concept was the same. A follow-up study was completed by Von Quintus et al. (1980) that focused on flexible and composite pavement structures. In that study, the primary pavement structure recommended for use to satisfy the definition of premium pavements was a composite pavement consisting of an HMA wearing surface and CRC lower layer. That study reviewed composite pavements that had been built over a period of 10 to 20 years before the study but were still in service and providing good performance. Details from those projects were used in developing a preliminary design manual for both flexible and composite pavement types.

Many other agencies, including ones in Ohio, Kentucky, Florida, Oregon, Minnesota, New Mexico, and Texas, have constructed composite pavements consisting of HMA wearing surfaces with various types of PCC layers. A study was conducted by Globetrotter Engineering Corporation from 1983 to 1987 to review the performance of composite pavements. This study was a follow-on project to the FHWA-sponsored study on flexible and composite structures for premium pavements. One or more pavements from each of these agencies were included in the review for that project. The pavement condition at the time of the survey varied from poor to excellent. Only 1 of 11 projects was rated as poor. Most of the composite pavements were providing good to excellent performance. Longitudinal and transverse cracking were the primary types of distress observed on the projects visited. The following summarizes the reasons that five of those agencies decided to start constructing HMA/PCC composite pavements.

- Florida started using composite pavements in the 1970s as a result of the oil crisis and built an experimental composite pavement project in 1975 as part of a widening project along US-41, just north of Fort Myers. This experimental project consisted of varying HMA wearing surface types and thickness, econocrete base thickness, and different subgrade treatments. Composite pavements have been used in areas with heavy trucks and in areas with high water tables.
- Although the Kentucky Transportation Cabinet did not promote the use of composite pavements, the city of Louisville and other local areas have built composite pavement structures because they were perceived to be easier to maintain and are smoother. Two projects were surveyed in the premium composite pavement project: one project along the Algonquin Parkway (built in 1964) and one project defined as Breckinridge Lane (built in 1965). Both projects consisted of 1.5-in. HMA surface over an 8-in. JPC followed by a relatively thin aggregate subbase.
- Composite pavements in Ohio have been used for all classes of streets and highways in the Columbus area, and two segments along I-670 were used in the premium composite pavement project. These original composite pavements consisted of a 3-in. HMA surface, a 9-in. JPC, and a 6-in. aggregate subbase. One of these pavements was built in 1958 and the other one in 1961. Both segments performed without any rehabilitation or major maintenance for 24 and 27 years, respectively. The HMA wearing surface of both projects was covered with Ralumac, a rubberized slurry. Both segments have also carried heavy truck traffic.
- Similar to Louisville, Kentucky, state and local agencies in Oregon have used composite pavements because they were believed to be easy to maintain and cost effective. Two

projects were used in the premium pavement project within the Salem area: one within the North Albany interchange section of I-5 and the other segment along Highway 30. Both projects were built in 1973 and consisted of a 4-in. HMA surface over a 6-in. LCB. The only maintenance activity performed along both segments was to seal the cracks with rubberized asphalt in 1984.

- Texas started using new composite pavements in the late 1970s, because they were found to be easy to maintain. In addition, the HMA surface was believed to be an effective seal against moisture intrusion that can cause the erosion of soil along joints and cracks and reduce curling stresses in the PCC layer.

Recent Research

Various cities have used HMA/PCC composite pavements as their primary pavement design strategy for many years. One example is the city of New York, which has been using composite pavements since the 1990s. New York has found that reflection cracking is the primary distress that limits the performance of this design strategy. In an effort to reduce maintenance costs and extend the life of this pavement type, the city sponsored and built an experimental project that included HMA over JPC (new construction) with various treatments and techniques to retard and prevent the deterioration of reflection cracks in the HMA wearing surface. In summary, the reflection cracking treatment that was most economical and provided consistently good performance was the "saw and seal" method. Many other reflection cracking control treatments were used within the experimental project, but none of the test sections with specialized materials performed consistently better than the saw and seal method.

In studying heat island effects of asphalt rubber (AR) overlays, Belshe et al. (2006) cited the importance of minimizing the urban heat island effect and the part that AR plays in it. In using the darker AR open-graded friction course, there is an increased surface temperature during the daytime but reduced surface temperature at nighttime (explained by the porosity and lower thermal mass). Traffic is thought to have an aeration effect, and the relative coolness of the pavement is attributable to the high air void content and the lower thermal mass of the surface mix. Without the AR surfacing, the temperature of the PCC surface would be 3°F to 8°F higher. The authors believe this increased temperature would result in increased truck and warping/curling damage caused by greater slab stresses than would be experienced without the overlay. Although the insulating effect of overlays on PCC is not a new concept (this concept is considered in the *Mechanistic–Empirical Pavement Design Guide* [*MEPDG*]), the idea that the AR surface could provide such a benefit is crucial to the modeling of HMA/PCC composite pavements.

Arizona has developed a Quiet Pavement Program (Zareh et al. 2006), in which conventional HMA and PCC surfaces are overlaid by a 1-in. asphalt rubber friction course (ARFC). The ARFC was found to reduce noise by 3 to 5 dB compared with dense, fine-graded HMA, and by 6 to 12 dB compared with harshly cross-tined PCC pavement. Based on public pressure, it was decided to overlay approximately 7,000 lane-miles of PCC pavement with 1 in. of ARFC to reduce noise. The authors think this program has been very successful, although some transverse reflection cracks have occurred and future maintenance may be a problem.

There are several composite pavements in the LTPP GPS-2 experiment that consist of HMA surfacing over an LCB course and other lower quality PCC mixtures, including CTB layers. Some of the forensic work conducted for these projects included using test pits to measure in situ density and moisture content, as well as material sampling. HMA surfacing was removed to visually assess the transverse joint condition and measure the joint width periodically during the day and observe spalling, if any. Temperature gradient measurements on the pavement slabs were taken throughout the sampling day. Details of this research are still being compiled.

The Montana Department of Transportation made a decision in the mid-1990s to use the composite pavement strategy in upgrading many of their higher volume roadways. The construction process is to recycle the materials in place by using portland cement as the stabilizing material. The quality of the PCC layer varies and would be defined more as a semirigid pavement. However, the PCC layer can be similar to an LCB or RCC layer on some of the projects. Most of these projects were used to calibrate the *MEPDG* for Montana's future use in designing and constructing this type of pavement (Von Quintus and Moulthrop 2007). The local calibration process was challenging because most of the pavements that were built in the 1980s have yet to exhibit any fatigue cracking and have low levels of rutting and minimal material-related distresses (bleeding, stripping, raveling, and so forth).

Delatte (2004) presented a simplified design of RCC composite pavement with HMA surface. RCC pavements generally are not jointed but are allowed to crack naturally. He pointed out that RCC pavements in a variety of environments have shown very little crack faulting, even under heavy traffic loads. Therefore, crack faulting was ignored for design purposes, and the design method proposed was concerned only about fatigue cracking in the RCC layer. Various trucking terminals or distribution centers have used this design strategy because of lower initial construction costs and reduced maintenance costs over time. As an example, the United Parcel Service distribution center in Austin, Texas, built a composite pavement consisting of a 3-in. dense-graded HMA wearing surface over a 6-in. RCC base. This composite pavement was built in the late 1980s and was still providing good performance almost 25 years later.

Trevino et al. (2004) presented a listing of the various modes of failure that a thin HMA overlay over an existing CRC pavement may experience. These failure modes include

- Debonding: The bond between overlay and the underlying CRC may be lost because of insufficient bonding material, stripping of the asphalt from aggregate, and softening of asphalt binder caused by moisture.
- Stripping: Subbases under some old concrete pavements get saturated with subsurface water, and concrete slabs start to pump water through the joints and cracks. If the PCC has an HMA surface, the water under pressure can cause stripping and potholing of the overlays.
- Rutting: Rutting stems from the permanent deformation of the HMA overlay, usually caused by densification or lateral movement of the materials (i.e., shoving caused by traffic loads).
- Reflection cracking: Reflection cracking is defined as a crack that is initiated by discontinuity, such as a joint or punchout in the underlying PCC layers, which propagates through the HMA surface because of vertical or horizontal movement of the crack.
- Slippage cracking: Slippage cracks are crescent- or *U*-shaped cracks with the bottom of the *U* pointing in the direction of applied force. Cracks are mainly caused by poor bond between the surface and the next layer of the pavement structure or low strength of the surface mix. They generally are observed on paths where vehicles brake, accelerate, or turn.

Cho, Weissmann, and McCullough (1995) and Cho et al. (1998) stated that the HMA overlay on US-59 in Lufkin, Texas, exhibited reflection cracking and rutting on the pavement surface. Typical fatigue cracking was also apparent on the specific section that has a flexible (untreated granular) base layer between the HMA and PCC layers. It was assumed that these three types of distress represent the dominant HMA overlay failure mechanism. It was concluded that the transverse cracks occurred mainly by reflection action, whereas traffic had minor effect. These transverse cracks developed mostly during winter, with traffic loading affecting the rate of development. The longitudinal cracks developed randomly and connected with transverse cracks. Fatigue cracking increased continuously for the sections, but transverse cracks and longitudinal cracks had alternating periods of fast and slow development, reinforcing the conclusion that fatigue cracking is mainly a function of traffic loading.

Finally, the trend toward an integrated approach to pavement design has shown that the best facets of HMA and PCC materials could be used together (Christory et al. 2001). The competitive nature between the flexible and rigid design and construction communities has hampered the emergence of new designs and materials. The author suggests composite structures could be built that share the best qualities of both types of pavements to produce a more functional and economical structure that is generally more cost-effective in terms of service throughout its life. This "shared technique" suggests that this combination could provide long service life. The author emphasizes the need for improved bonding between the HMA and PCC layers throughout the life of the pavement, which can be better achieved through shot or water blasting. In turn, this will improve the performance of the surface HMA layer.

International Experience

Several countries in Europe, including the Netherlands, Italy, France, United Kingdom, Austria, and Belgium, have built a number of composite pavements. Many of these composites include relatively thin (2 to 3 in.) porous HMA over CRC. The thin porous HMA layer is intended to reduce noise, splash, and spray; provide good friction resistance and increased smoothness; and waterproof cracks in the CRC layer, which do not reflect through to the HMA layer. Its limitations include a significant decline in the noise-reducing effect over time as the pores in the HMA layer fill with materials, a relatively short life, and higher deicing salt requirements to prevent icing. Unsafe conditions can develop when icing cannot be prevented completely, as occurred in Austria. The following summarizes some of the uses in Europe:

- France uses lower-quality local aggregates in concrete pavements for which an HMA overlay is also to be placed during construction. This reduces overall pavement costs in areas where only poor aggregates exist. There is little freeze–thaw cycling in these areas. The French usually put SMA or a surface treatment on the surface to improve friction and smoothness, although the exposed aggregate surface is favored by many.
- The Netherlands has constructed about 10 projects with two-layer porous HMA surfacing over CRC. Transportation officials in the Netherlands believe that the porous HMA reduces noise by about 7 dB. These projects have performed well to date, and others are under construction.
- The United Kingdom recently constructed a major freeway as a composite pavement with porous HMA over CRC.
- Italy has constructed many miles of CRC with a porous HMA surfacing. The projects on the ring road around Rome carry very heavy traffic. The porous HMA is scheduled to be milled off about every 7 years and replaced because of clogging from fines and other problems. The total structural design life is 40 years. A cost comparison of the composite HMA/CRC versus conventional semirigid

> pavement that has an HMA surface over LCB or CTB follows, where R equals the ratio of the cost of composite versus conventional. Construction: $R = 1.3$, maintenance, $R = 0.3$; user costs, $R = 0.55$, total LCC, $R = 0.87$.

In recent years, France has made real progress with the HMA/CRC composite pavements. The pavement structure consists of a very thin layer of HMA surfacing (French designation BBTM) with maximum aggregate size of ¼ in. or ⅜ in. (6 or 10 mm), a CRC in the pavement body, and a layer of Class 3 asphalt-treated base (French designation GB3) beneath the CRC (Christory et al. 2001). The Road Directorate of the French Public Works Ministry published a structural data sheet for an experimental pavement with this structure (Christory et al. 2001). Based on field and laboratory test results, the CRC and underlying bituminous materials are considered bonded for 15 years and unbonded until the end of the pavement's theoretical service life. Shotblasting or hydroregeneration (water blasting) is carried out on the asphalt-treated base and the CRC layer before placing the upper layer.

APPENDIX B

History and Background of PCC/PCC Composite Pavements

History

The history of PCC/PCC in the United States dates to the first concrete pavement constructed in the United States, located in Bellefontaine, Ohio, in 1891, shown in Figure B.1.

This experimental pavement section featured a 4-in. structural layer with a water-to-cement (w/c) ratio 0.60 and a durable wearing course with w/c ratio 0.45. Both layers were mixed by hand and placed during the same time. The initial construction cost of the pavement was $9,000 and required only $1,400 in maintenance costs over its first 50 years (Snell and Snell 2002).

In addition, before the pavement in Bellefontaine, New York City and other smaller towns and cities had experimented with a different sort of composite sidewalk, one that featured an aggregate wearing course on a solid PCC base. These composite sidewalks and the success of the Bellefontaine pavement led to the continued development of PCC/PCC pavements in the early 1900s that could withstand the traffic loading of the day (horse-drawn wagons). Some of these early composite pavements are listed in the National Register of Historic Places (Cable and Frentress 2004).

From roughly 1950 to the mid-1970s, two-lift paving for concrete pavements was very common in many American states. However, this manner of two-lift paving was simply halving what would now be considered a full slab (although a slab with much longer joints and reinforcement) and paving each half-slab lift at a time. Before the second half-slab was paved, wire mesh reinforcement was placed on the first lift and dowel baskets were placed at the joints. These two-lift jointed reinforced concrete pavements (JRCP) began to disappear in the 1970s as state departments of transportation began to move toward what has become the standard jointed plain concrete pavement (JPCP) design (Cable and Frentress 2004).

In Europe, two-lift paving in the sense of constructing two layers with different properties for the sake of reducing noise, increasing skid resistance, lowering costs, and so forth, has been much more common than in the United States. Austria in particular has been active in regular two-lift paving for concrete pavements, and the standard concrete pavement in Austria is constructed according to two-lift specifications (Darter 1993; Hall et al. 2007).

Switzerland also has a number of JRCP designs featuring two-lift construction that have been implemented since the late 1950s. These two-lift JRCP pavements differ from their American counterparts in that the lifts are of different thicknesses and constituents. More information on the Swiss two-lift paving is available through the FHWA Concrete Pavement Evaluation System (COPES) database (ERES Consultants 1998).

Two-lift paving has been used for special projects in countries such as Belgium, the Netherlands, France, and Germany with regularity since the 1930s and is becoming more common as the techniques are refined. Germany has also used two-lift paving in airport pavements as a way of reclaiming recycled materials (Darter 1993). Overall, the desire for quieter, more economical roadways is motivating many countries to increase the frequency with which concrete pavements are constructed in two unique lifts. Future sections will discuss two wearing courses often associated with these PCC/PCC projects: exposed aggregate surfacing and porous concrete.

Much like their European counterparts, American pavement engineers have put a great deal of research, design, and construction effort into developing PCC/PCC. There were a limited number of experimental PCC/PCC projects in Iowa, Florida, and North Dakota during the late 1970s and 1980s. The Florida sections on US-41 in particular are discussed in the Structural Design section. Much of the interest in two-lift paving originated from collaborative initiatives between the FHWA, the AASHTO, and the NCHRP. These initiatives include

- The 1992 U.S. Tour of European Concrete Highways (TECH);
- The High Performance Concrete Pavement (HPCP) Test and Evaluation Project 30 (TE-30), also started in 1992; and

Figure B.1. The first PCC/PCC composite pavement in the United States in Bellefontaine, Ohio.

- The 2006 International Technology Scanning Program tour of long-life concrete pavements in Europe and Canada.

The HPCP project in particular was responsible for the development of experimental two-lift sections in the 1990s in Michigan and Kansas. These new two-lift experiments had as their larger research goals a desire to increase the service life of concrete pavements; lower life cycle costs; use innovative designs/materials; and improve construction practices. As a quick example of this new research (to be discussed later as well), the goal of the experimental sections along I-75 in Michigan was to compare the performance of a European two-lift JPCP design to a traditional Michigan Department of Transportation (DOT) JPCP design. A comparison of some properties from Michigan I-75 is included in Weinfurter et al. 1994.

The structural benefit of the European design is apparent from the figures provided. However, the additional cost of this innovative structure was a major focus of the research in Michigan. This and other research into PCC/PCC will be discussed in other sections.

Overall, PCC/PCC composite pavements are a historical curiosity for pavement engineering in that they have received a great deal of implementation without a corresponding amount of research. However, as more states and countries place a higher emphasis on innovative solutions to problems such as noise, environmental sustainability, and life-cycle economy, the interest in research on PCC/PCC has increased.

Background

The background discussion includes common structural designs of PCC/PCC composites, materials in PCC/PCC, construction of PCC/PCC, and performance of PCC/PCC.

Structural Design

Although the cross section of PCC/PCC has changed dramatically since 1891 and the placement of the two-lift concrete pavement in Bellefontaine, Ohio, a design procedure for PCC/PCC has remained within borders and has not been shared between countries/states until the past 20 years. Before that time, individual countries and state departments of transportation generally were left to experiment and trust design to engineering expertise and intuition. An exception is Austria, which was able to translate its large amount of PCC/PCC experience into a standard design for all concrete pavements in Austria.

The literature review on PCC/PCC design is essentially a review of bonded PCC overlay design developed since the 1960s. The two main methods are the Portland Cement Association (PCA) method for bonded PCC-on-PCC overlays and the 1993 AASHTO Design Guide. Neither of these significantly addresses PCC/PCC composite pavement critical design issues. In addition, the *Mechanistic–Empirical Pavement Design Guide* (*MEPDG*) procedure for bonded PCC overlays is relevant.

Other research reviewed presented a rational design procedure for new construction PCC/PCC. Kohn and Darter (1981) proposed a fatigue damage method that used finite element analysis to determine the critical stresses in the composite slab; in 1982, this work was expanded to tables and charts for use in the design of two-layer composite pavements. Larsen (1981) developed a design procedure based on that of Kohn and Darter for a pavement to compare to in-field PCC/PCC sections on US-41 in Florida. Packard (1981) also developed a structural design for monolithic and "non-monolithic" PCC/PCC with a lean concrete lower lift. Although all of these early PCC/PCC designs focus on variables such as slab dimensions, thicknesses, material properties, and drainage, the only consideration given to the PCC/PCC interface is setting the interface shear transfer to either 0% or 100% between layers. Later models that have yet to be incorporated into pavement design have looked more closely at the idea of a shear strength focus and "all or none" bond condition. These models are able to predict interface integrity because of the effects of temperature, shrinkage cracking, and traffic loading.

Thirty-three composite PCC/PCC test sections on US-41 near Fort Myers, Florida, constructed in 1977, were designed with 3-in. standard PCC in the top lift and 9-in. LCB in the lower lift. The sections were designed to observe performance and make comparisons between the different pavement constituents and design properties. The materials under investigation were three types of LCB and two subbases. The LCB lower lifts differed in terms of the amount of cement (8.5% by weight, 7.3%, and 5.5%), whereas the subbases were either 6-in. cement-treated subgrade (A-3) or 6-in. shell-stabilized subgrade (A-3).

The sections that did not fail within the first 2 years (because of experimental dowel placement or joint spacing) generally performed well, and the differences in performance between the different bases and subgrades were found to be minimal (ERES Consultants 1998). One cause for this homogeneity in performance, proposed in the 1998 Performance/Rehabilitation of Rigid Pavements FHWA report, is that these pavements were each thick enough to perform well despite their differences over a longer time period. Thus, as experimental test sections go, the US-41 PCC/PCC was too thick to rapidly yield performance data to composite pavement design methods. These sections are still in service and were included in the R21 database. As more PCC/PCC experimental sections are constructed, it is hoped these sections will yield data more conducive to a structural design for PCC/PCC.

Of recent interest to American pavement engineers is the use of an exposed aggregate surface course. This technique, typically used in conjunction with PCC/PCC, was first developed in Belgium in 1980. Austria first constructed exposed aggregate PCC/PCC in 1989 and has applied the technique regularly since that time (Darter 1993; Hall et al. 2007). This texture is becoming increasingly popular given European success in using exposed aggregate surfacing to reduce pavement noise and increase skid resistance (Figure B.2), and it is essentially the standard surfacing in European countries for concrete pavements.

Austrian PCC/PCC pavements are constructed so that both lifts are placed monolithically, which is to say simultaneously, using a specialized slipform paver. The following section on construction provides more information on the specialized construction equipment that allows monolithic, or so-called wet-on-wet, placement. The thicknesses observed during the 1992 U.S. TECH scanning tour were a 4-cm (1.6-in.) exposed aggregate surface course atop an 18-cm (7.1-in.) lower lift; the more recent scanning tour of long-life PCC pavements observed a 4-cm (1.6-in.) course atop a 21-cm (8.3-in.) lower lift. The top lift was a high-performance concrete containing a high-quality, smaller (0.3- to 0.43-in. or 8- to 11-mm maximum size) aggregate, whereas the lower lift was Austria's standard PCC mix containing local virgin or recycled aggregates (1.25 in. [32 mm] maximum size). The surface course, after being sprayed with a hydration retarder, allowed to cure for 24 to 72 hours, and brushed, yielded 1 to 2 mm of surface texture. Transverse joints are sawed to a depth of 75 mm (3 in.) within 8 to 24 hours after placement (Darter 1993).

Another new interesting paving technique involving PCC/PCC is the construction of so-called pervious or porous concrete pavements, shown in Figure B.3.

These pervious concretes typically are the top lift of the PCC/PCC, although, as noted in the 1992 U.S. TECH scanning tour of Europe, German experimental lane construction efforts completely remove deteriorated lanes and replace the concrete treated base with a porous concrete layer. Although rehabilitation is not the focus of the SHRP 2 R21 project, this use of porous concrete is a novel use of composite pavements and is illustrated in Figure B.4.

In new construction efforts, the porous concrete typically is placed in wet-on-wet construction as a surface course atop a conventional PCC lower lift. The Netherlands constructed sections of porous concrete over conventional concrete in the early 1990s that performed well for a few years but tended to ravel (Darter 1993). Although pervious PCC/PCC receives interest for its use in parking lots and is being considered by Japan as a replacement for all concrete systems, many researchers have noted the insufficient durability of this wearing course,

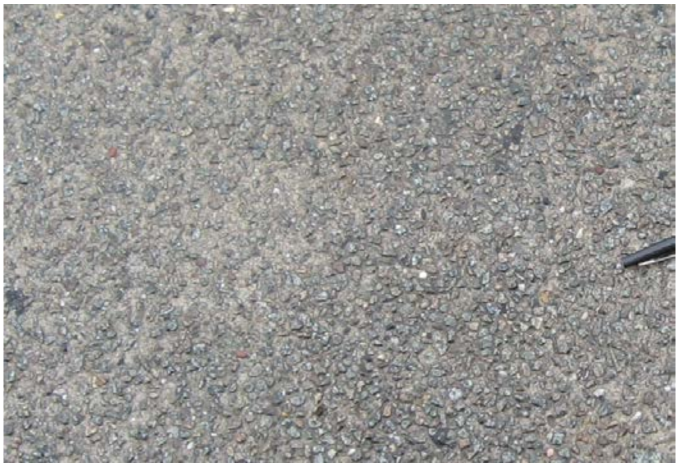

Figure B.2. An exposed aggregate PCC surface with pen cap at right for scale.

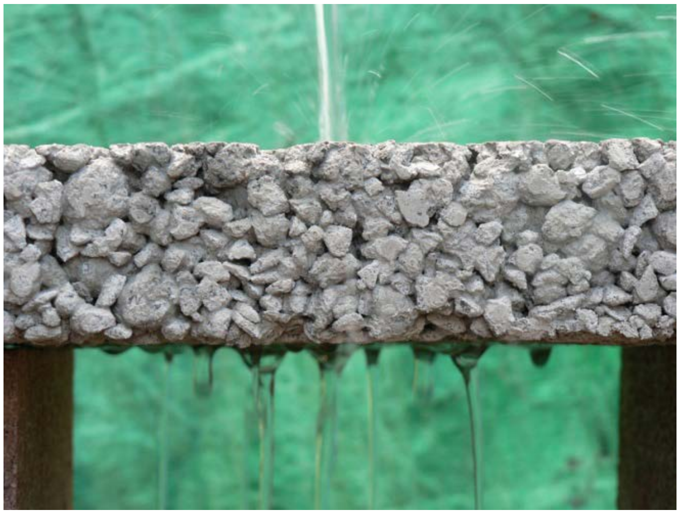

Photo courtesy of TecEco Inc.

Figure B.3. The porosity of pervious concrete is easily illustrated with a garden hose.

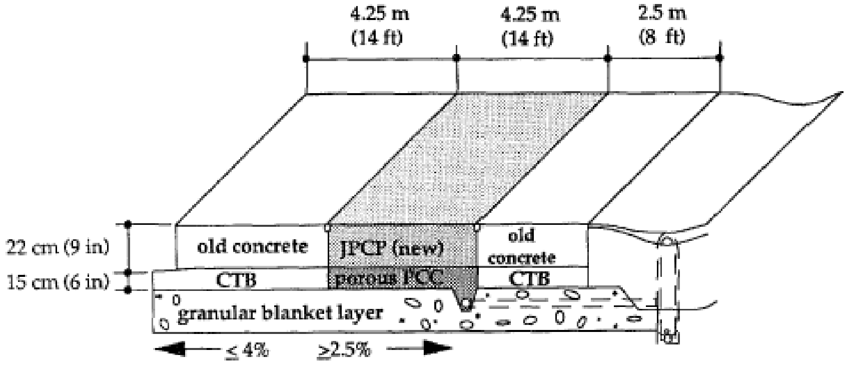

Source: Darter 1993.

Figure B.4. Porous PCC as a base layer for the rehabilitation of deteriorated lanes of JPCP.

both in its response to traffic loading and freeze–thaw cycling (Cable and Frentress 2004). Pervious pavements (both PCC and asphalt) also require regular maintenance given the tendency of the pores in the surface to become clogged with dirt and debris and require cleaning. In short, porous PCC/PCC as a highway solution for noise and safety will require additional research before it is widely adopted.

Materials

One of the more appealing features of composite pavements is the ability to use a wide variety of materials in the two lifts to improve the economics, safety, and noise reduction. The basic principle of composite PCC/PCC developed in Europe and incrementally being integrated into American practice is the idea that a concrete pavement need not be a high-performance concrete mix through the entire slab thickness to yield high performance in the field. Instead, the feature of the pavement that becomes the true performer is the design itself: situational needs—not a homogeneous, inflexible design—determine the nature of the pavement itself.

Thus, in a pavement that is required to have a highly durable wearing course that has both low noise and adequate skid resistance, an exposed aggregate PCC/PCC can be designed that puts a high-performance mix and high-quality aggregate into the first few inches of the pavement. The remainder of the pavement can then be specified to maximize structural performance while using more economical mix design and aggregates. This "high-performance design" allows the pavement to better match a given application and budget.

A large amount of interest in composite PCC/PCC is the potential for in-place recycling: that is, the process of replacing an existing pavement by removing the old structure onsite and immediately recycling that material into the new pavement.

The desire to use more innovative materials, such as recycled aggregates, led to the creation of three two-lift test sections on K-96 in Kansas. The K-96 test sections looked at three different factors of interest to Kansas DOT:

1. The use of recycled asphalt pavement (RAP) in the lower lift;
2. The use of a durable igneous rock with high alkali silica reactivity as aggregate in the upper lift instead of an abundant limestone in Kansas that has a tendency to polish and reduce skid resistance; and
3. The use of a lower w/c ratio in the upper lift to investigate if the differential volume changes between the two lifts would lead to debonding.

   More details on these sections are provided in Wojakowski 1998.

Researchers at Kansas DOT found that the replacement of 15% of total aggregates with RAP in a concrete mix did not affect the workability of the mix and resulted in a durable lower lift for a PCC/PCC. In addition, the researchers were able to counteract the alkali-silica reactivity of the hard igneous rock in the second two-lift section by the replacement of cement with a locally available pozzolanic product. The innovative use of the materials was a success, as tests for expansion indicated volume changes far below what would have been expected had alkali-silica reactivity occurred.

Finally, the low w/c ratio section showed no shrinkage cracking or evidence of debonding despite expectations of being difficult. It should be noted that all sections performed well in the long term, although a large number of transverse cracks were observed on the sections with the igneous rock in the upper lift by Kansas DOT in a 2002 annual report. The K-96 project is one of a growing field of research that is aware of PCC/PCC as a potential cost savings and increased performance opportunity through the use of innovative materials (Wojakowski 1998).

Construction

The difficulties of the construction of composite pavements for American contractors are collectively one of the main limitations to the application of PCC/PCC in the United States. European pavement engineers, on the other hand, have enough experience in PCC/PCC construction, and they have developed technologies over the past 30 years that better serve efficient, effective monolithic placement of a two-lift slab.

Although interest in PCC/PCC is slowly growing in the United States, an interest in developing newer, cheaper methods of two-lift construction has not followed. As pointed out by Cable and Frentress (2004), there are a number of factors for the hesitancy of contractors to bid on two-lift paving projects. These factors include the additional expense of a second cement plant, which introduces the need to double need for equipment, permits, fuel, and labor. In addition, there are the prohibitive costs of either one slipform paver that can pave both lifts monolithically or two slipform pavers that pave the lifts in succession. A slipform paver modified to place both lifts simultaneously is illustrated in Figure B.5.

One of the first results of the 1992 U.S. TECH scanning tour of European concrete highways was the later development of the PCC/PCC new construction on I-75 near Detroit. The overall goal of the project was to compare the performance of a standard Michigan DOT concrete pavement with its structural PCC/PCC equivalent of European design. This comparison in design is shown in FHWA 2006.

Although the research project had this comparison of design performance as its goal, the project was also a testing grounds for many two-lift techniques that until I-75 had not been attempted in the United States. Although the I-75 European PCC/PCC sections were placed without complication, this placement went slowly because the contractors were learning radical new techniques through the process of constructing the roadway. In constructing these sections, Michigan DOT and researchers from Michigan State University developed a number of recommendations for future two-lift paving. These recommendations include observations on appropriate sawing depths when forming joints, dowel bar spacing to save costs, minimal thicknesses of surface lifts, and improved techniques for brushing away cement in creating surface texture (Weinfurter et al. 1994; Smiley 1995; Smiley 1996; Buch et al. 2000). It is evident from the example of the experimental sections at I-75 that there is as much, if not more, to be learned in developing effective and economical construction techniques as there is from modeling and improved performance prediction.

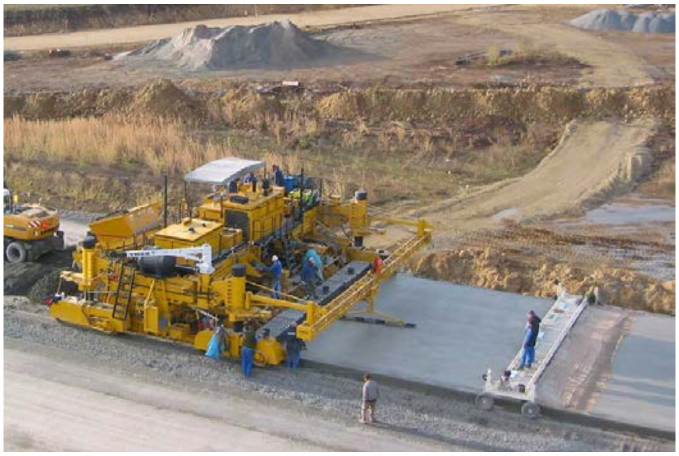

Figure B.5. Two-lift slipform paving in the Czech Republic.

Finally, another construction technology that may be applicable for a top or lower lift is roller compacted concrete (RCC). RCC is constructed by placing, with perhaps an asphalt paving machine, a very dry concrete mix and then compacting the concrete to ensure proper consolidation.

RCC is a desirable pavement in some situations given its ease and speed of placement, reduced costs relative to its conventional PCC counterpart, low resistance to shrinkage cracking, and very quick strength development. Although the method has seen application throughout North America, Norway, and Spain, it is still a lesser used technique in concrete pavements. In applications in Spain the technique has been found to be effective when joint formation takes place immediately after placement and joint spacings are restricted to 2.5 to 3.5 m. The technique is included in the literature review because it may be worth considering for PCC/PCC. The quality and strength of the RCC can be comparable to those of regular quality PCC.

APPENDIX C

Highway Agency Survey

Table C.1 shows the list of questions sent to various agencies during the initial request questionnaire. Based on the information provided during the initial request, follow-on questionnaires or phone surveys were conducted with some of these agencies to request additional information, particularly pertaining to composite pavement sections (design, construction, and performance details, location, age, etc.) constructed in their jurisdiction.

International agencies responding to the survey included Ontario, Montreal, Belgium, Germany, the Netherlands, Spain, and Sweden. U.S. agencies responding to the survey included Alabama, Alaska, Arizona, Arkansas, California, Colorado, Delaware, Georgia, Illinois, Kansas, Louisiana, Maine, Maryland, Massachusetts, Minnesota, Mississippi, Missouri, Montana, Nevada, New Mexico, New York, North Carolina, North Dakota, Ohio, Oklahoma, Oregon, Rhode Island, South Carolina, Texas, Utah, Vermont, Virginia, Washington, Wisconsin, and Wyoming.

HMA/PCC Composite Pavement Agency Response Summary

Question A1: *Has your agency constructed new HMA/PCC composite pavements or experimental (instrumented, accelerated loading, or otherwise) new HMA/PCC composite pavements in the past 20 years?*

NO—24 U.S. States (Alabama, Alaska, Arkansas, California, Colorado, Delaware, Georgia, Kansas, Maine, Maryland, Massachusetts, Minnesota, Mississippi, Missouri, Montana, Nevada, New Mexico, North Dakota, Oklahoma, Rhode Island, Texas, Utah, Vermont, Wyoming) and 1 international agency (Montreal).

YES—11 U.S. States (Arizona, Illinois, Louisiana, New York, North Carolina, Ohio, Oregon, South Carolina, Virginia, Washington, Wisconsin) and 6 international agencies (Ontario, Belgium, the Netherlands, Spain, Sweden, Germany).

- Arizona: 1 project of widening type-existing PCC pavement had 4 in. hot-mix asphalt (HMA). New widening was constructed of 14 in. PCC atop new HMA pavement. I-40 eastbound (EB) milepost (MP) 153.2–156.17 in 2003. Note: Arizona has been placing 1-in HMA-ARFC open graded HMA on top of the new existing PCC in the Phoenix metro area since 1998. The intent is to be used to provide a better quality ride, to improve skid number, and to use as noise mitigation. This program has been very successful and has been termed the Quiet Pavement Program.
- Illinois: Mainly on widening projects to add capacity. Also sometimes used on local roads, mainly in the Chicago area, to provide a more uniform surface appearance.
- Louisiana: We have new HMA over new soil cement base and new HMA over new cement stabilized base with instrumentation at our accelerated-loading facility (ALF) site.
- New York: Examples include Route 32 (Pearl Street) in Albany, and sections of I-690 and I-81 in Syracuse.
- North Carolina: Widened existing. Then placed ultra thin bonded wearing course across full section.
- Ohio: They were not recent.
- Oregon: No specific "new work" that anyone can recall, although we likely have constructed a widened section of HMA/PCC.
- South Carolina: Approximately 7 years ago, we widened Interstate 77 south of the Charlotte, N.C., area from four lanes to eight lanes by adding two new lanes and a barrier wall to the central median. The existing pavement was 10 in. of CRC constructed in 1968. We patched the existing pavement and constructed two new lanes of JPC. To avoid sympathy cracking, we did not tie the new lanes to the existing lanes, nor did we use any steel in the pavement. Then, we overlaid everything with approximately 4 inches of dense graded asphalt and one inch of permeable surface course. The project length was 6.4 miles.
- Ontario: Widening only—we do not design and construct new composite pavements.

Table C.1. Questions Included in the Initial Request Questionnaire Sent To Various Agencies

New HMA/PCC composite pavements
(A1) Has your agency constructed new HMA/PCC composite pavements or experimental (instrumented, accelerated loading, or otherwise) new HMA/PCC composite pavements in the past 20 years? (Note: this can include widening of existing JPC or CRC pavements where both existing pavement and new widened section are overlaid with new HMA).
(B1) If YES to (A1): Can we contact you (or someone at your agency) to get additional information on one or more of these projects for use in our research? If so, please provide name, email address, and phone number of person to contact within your agency for more information on these projects.
(C1) If YES to (A1): (1) What design procedure(s) have you used to design this/these pavement sections? (2) Have you developed specifications for construction of new HMA/PCC pavements? (3) Any additional comments on these projects (e.g., project experiences, construction techniques, quality management, performance, costs, etc.). (4) Has your agency published any reports on any aspects of this/these pavement sections?
(D1) If YES or NO to (A1): Is the construction of new HMA/PCC composite pavements of interest to your agency? Will the incorporation of design procedures to design new HMA/PCC composite pavements into the *MEPDG* be beneficial to your agency?
(E1) If YES or NO to (A1): What concerns or issues may restrict you or your agency from constructing new HMA/PCC composite pavements in your State?
New PCC/PCC composite pavements
(A2) Has your agency constructed new PCC/PCC composite pavements or experimental (instrumented, accelerated loading, or otherwise) new PCC/PCC composite pavements in the last 20 years?
(B2) If YES to (A2): Can we contact you (or someone at your agency) to get additional information on one or more of these projects for use in our research? If so, please provide name, email address, and phone number of person to contact within your agency for more information on these projects.
(C2) If YES to (A2): (1) What design procedure(s) have you used to design this/these pavement sections? (2) Have you developed specifications for construction of new PCC/PCC pavements? (3) Any additional comments on these projects (e.g., project experiences, construction techniques, quality management, performance, costs, etc.). (4) Has your agency published any reports on any aspects of this/these pavement sections?
(D2) If YES or NO to (A2): Is the construction of new PCC/PCC composite pavements of interest to your agency? Will the incorporation of design procedures to design new PCC/PCC composite pavements into the *MEPDG* be beneficial to your agency?
(E2) If YES or NO to (A2): What concerns or issues may restrict you or your agency from constructing new PCC/PCC composite pavements in your State?

- Belgium: In Belgium, a few worksites have recently (2002–2007) taken place where a new concrete pavement, in all cases CRC, was surfaced with asphalt layers (either porous asphalt, either thin bituminous layers). It was mostly in case of a rehabilitation of a part of a motorway (right lane and hard shoulder) in concrete with a resurfacing off the complete motorway (2 lanes plus hard shoulder) afterward.
- The Netherlands: In most cases because of noise production by traffic on the PCC surface. Sections near houses are covered with a stress absorbing HMA layer and a noise reducing top HMA layer. Or the PCC is reinforced and covered with only one (noise reducing) HMA layer. In the Netherlands, newly built motorways in CRC are systematically overlaid with a (double layered) porous asphalt for reasons of noise reduction.
- Spain: Composite pavements (HMA/PCC) are very used for pavements in streets in most of Spanish cities, e.g., in Madrid, but in these cases the PCC base is a lean concrete one, with a cement content about 140–180 kg/m^3, i.e., half of those used in highways and motorways.
- Sweden: We have built roads with cement stabilized gravel with compressive strength 10 MPa. We have followed up one of these roads for more than 10 years.
- Germany: In Germany several sections have been constructed in composite of HMA on a construction layer of cement concrete. Two of these are under closer observation: Autobahn A11 near Berlin (Split Mastix Asphalt on JCP) and Bundesstraße B56 between Cologne and Aachen (Split Mastix Asphalt on CRC).

Question B1: *If YES to (A1): Can we contact you (or someone at your agency) to get additional information on one or more of these projects for use in our research? If so, please provide name, email address, and phone number of person to contact within your agency for more information on these projects.*

All of the agencies who responded "Yes" to A1 provided follow-on contact information.

Question C1: *If YES to (A1):*

(1) What design procedure(s) have you used to design this/these pavement sections?
(2) Have you developed specifications for construction of new HMA/PCC pavements?
(3) Any additional comments on these projects (e.g., project experiences, construction techniques, quality management, performance, costs, etc.).
(4) Has your agency published any reports on any aspects of this/these pavement sections

- Arizona: 14 in. new PCC pavement based on the 1993 AASHTO Guide. HMA pavement to match existing adjacent HMA pavement. Arizona specs. for PCC and HMA were used. The same techniques for PCC and HMA were utilized.
- Illinois: Illinois has procedures for design of composite pavements. When adding lanes, often the design of the existing pavement is matched and then both new and old are overlaid. Below are links to design procedures for composite pavements that are in our design manuals. One is for state routes, and the other is for locals. www.dot.il.gov/desenv/BDE%20Manual/BDE/pdf/chap54.pdf, www.dot.il.gov/blr/manuals/Chapter%2037.pdf. Existing specs are used.
- Louisiana: 1986 AASHTO Design Guide was used for HMA/soil cement control section. Existing specs are used. The final report for the ALF experiment can be found on the Louisiana web site: www.ltrc.lsu.edu.
- New York: The methods for this construction are covered by the state's Technical Specification Sections 402 (Asphalt) and 503 (PCC). No postdesign reports have been published.
- North Carolina: Functional rather than structural overlay. Have special provisions. Improved ride quality, reduced noise. Covered poor surface finish on underlying concrete.
- Ohio: Our design procedure was more of a rule of thumb. A rigid design was done for the traffic and soils using AASHTO (81 or perhaps 86) and then 1 in. of concrete was subtracted and replaced with 3 in. of asphalt. Composite pavements have lost favor due to initial construction cost as well as higher future maintenance costs.
- Oregon: Our standard design procedure is AASHTO 1993. Most of our HMA/PCC pavements are the result of HMA overlays as a rehabilitation treatment over distressed CRC or JRC pavement, with the overlay design a result of the program DARWin for the calculation of a structural number. (Ohio is just beginning use of the *MEPDG.*) If a new HMA/PCC project was done for widening adjacent to one of these rehabilitation designs, it is likely that the "new work" section was designed by matching the existing pavement layer thicknesses. The design of HMA over rubberized PCC utilized mechanistic calculation of horizontal strains at the base of the HMA in concert with the concepts of a "perpetual pavement."
- South Carolina: The depth of the concrete layer was determined by the existing pavement and a desire not to create a "bathtub" section. We have many miles of existing high-volume nondoweled JPC of 10 in. or less that were overlaid after 20–30 years of service that are performing well after 15 or more years. Comparatively, no traffic, other than construction traffic, was ever allowed on the added lanes of I-77. Consequently, this section was selected based on our previous experience. This project is performing well, but the asphalt contractors convinced our agency that they could place 10 in. of HMA base overnight so the project could be made safe for traffic each morning. Consequently, the second phase of the I-77 widening was constructed using full-depth HMA base at a lower cost. The HMA section is also performing well.
- Virginia: AASHTO 1993. No, but since it was a widening project we treated it as standard construction and overlay. This project was completed last year. Not enough information available on performance.
- Washington: Unsure, but more than likely it was based on experience (DOT or other state practice) and not a specific design procedure.
- Wisconsin: We used AASHTO 1972 to the best of our abilities for this type of design. After 6 years, one had a psi of 2.19. The other had a pavement distress indeed (PDI) of 34 (we consider a PDI of 65 to be in need of remedial action or replacement).
- Ontario: Matching existing thickness of concrete pavement, then applying a premium two-lift hot mix overlay. Our biggest challenge is working with our Highway Design people to ensure that a widening can be full lane width rather than adding slivers of concrete pavement.
- Belgium: Most of the time overlays in HMA on older CRC on highways for comfort and noise solutions, not for structural reinforcement.
- The Netherlands: VENCON2.0 = Dutch design program. Specifications of our own for the PCC and supplier-specifications for the HMA layer(s). Projects are not older than 5 years, until now good performance. Some published reports but in Dutch and some papers in English.
- Germany: Standard designs currently valid in Germany are stipulated in the Guidelines for Standardization of Traffic-Bearing Superstructures (RStO 01). There we have our Standard Designs for Asphalt Concrete and for Jointed Cement Concrete. For composites of HMA/PCC and for CRC yet we do not have standards. The CRC pavement on Bundesstraße B56 between Cologne and Aachen was constructed on the

basis of the Belgium regulations (Standaardbestek 250 voor de wegenbouw—versie 2.0). Specifications for cement concrete pavements are written down in the Supplementary Technical Contractual Conditions and Guidelines on the Manufacture of Cement Concrete Carriageway Pavement (ZTV Beton—StB 01). Specifications for HMA pavements are written down in the Supplementary Technical Contractual Conditions and Guidelines on the Manufacture of Asphalt Concrete Carriageway Pavement (ZTV Asphalt—StB 01).

Question D1: *If YES or NO to (A1): Is the construction of new HMA/PCC composite pavements of interest to your agency? Will the incorporation of design procedures to design new HMA/PCC composite pavements into the* MEPDG *be beneficial to your agency?*

NO—11 U.S. States (Arkansas, Colorado, Georgia, Kansas, Maryland, Massachusetts, Missouri, Montana, Nevada, Rhode Island, Texas).

YES—13 U.S. States (Arizona, California, Minnesota, New Mexico, New York, North Carolina, Oregon, Utah, Vermont, Virginia, Washington, Wisconsin, Wyoming).

- Arizona: Our agency has done enough of this type of pavement. The incorporation of new HMA/PCC composite pavement into the *MEPDG* might be beneficial.
- New York: HMA/PCC pavements will allow us to preserve the underlying PCC for an extended service life.
- North Carolina: It may be helpful on occasion.
- Oregon: Yes, our pavement design staff is interested in the new work design of HMA over PCC. One thought we have discussed is using HMA as a sacrificial "wearing course" over PCC in and around the Portland metro area, due to studded tire wear ruts. The use of HMA would allow a "mill and fill" scenario rather than diamond grinding of PCC. If a satisfactory design method is created that would allow design of HMA and PCC as a composite structure, we would be interested if a cost savings could be shown. Our agency is just beginning to use the *MEPDG*, and we would be interested in an HMA/PCC composite design module.
- Virginia: In Virginia we believe this is a good competition to perpetual pavement. The more competition the better the product.
- Washington: There is some interest. The ability to design via the *MEPDG* would be beneficial.
- Wisconsin: I would say yes. Even though we've changed our texturing policy, we still find areas where an HMA/PCC pavement structure is warranted for noise. We might as well design it appropriately.
- Wyoming: Yes, it is valuable to have another pavement design alternative available.

MAYBE—7 U.S. States (Alabama, Delaware, Illinois, Louisiana, Ohio, Oklahoma, South Carolina).

- Alabama: Any interest in the construction of a new HMA/PCC composite pavement would depend upon the cost and overall serviceability of this type of pavement as compared to other alternative pavement types. The incorporation of design procedures into the *MEPDG* to facilitate the design of new HMA/PCC composite pavements would provide a rational methodology for the design and analysis of this type of pavement.
- Delaware: I would not recommend this unless reflection cracking can be controlled.
- Louisiana: Possibly. The use of a new HMA over new PCC or new PCC/PCC would be predicated on the life cycle cost of the system. Louisiana uses an Alternate Design/Alternate Bid system. Typically this consists of an HMA and PCC alternate or possibly two different HMA alternates. If the designs are estimated to be less than 20% different in costs, the designs are bid as alternates in an $A + B + C$ process, where A is the construction cost, B is the number of days to construct (or usage cost), and C is the LCC. If the outcome of R21 provides estimates or real data containing LCC, consideration could be given to designing this system as an alternate.
- Oklahoma: New HMA/PCC pavements are possible for the control of splash/spray/noise reduction, but in all reality, unlikely due to the additional cost involved and the competitive nature between the two industries.
- South Carolina: Although I believe this pavement type is promising, we would be more inclined to use roller-compacted concrete or high quality paver-laid cement stabilized aggregate base instead of PCC for cost reasons.

NO RESPONSE—4 U.S. States (Alaska, Maine, Mississippi, North Dakota).

Question E1: *If YES or NO to (A1): What concerns or issues may restrict you or your agency from constructing new HMA/PCC composite pavements in your State?*

The following factors (in descending order of frequency) were the key concerns and issues listed by various agencies:

1. Cost (11);
2. Reflecting cracking and HMA/PCC bond (11);
3. Industry acceptance and related issues (6);
4. Lack of experience with this type of construction (6);
5. Lack of long-term data (e.g., for local calibration and LCCA) (3);

6. Rehabilitation and characterization of underlying PCC (3);
7. Construction time and related issues (3); and
8. Surface durability (studded tire wear of HMA layer) (1).

PCC/PCC Composite Pavements Agency Response Summary

Question A2: *Has your agency constructed new PCC/PCC composite pavements or experimental (instrumented, accelerated loading, or otherwise) new PCC/PCC composite pavements in the last 20 years?*

NO—33 U.S. States (Alabama, Alaska, Arizona, Arkansas, California, Delaware, Georgia, Illinois, Louisiana, Maine, Maryland, Massachusetts, Minnesota, Mississippi, Missouri, Montana, Nevada, New Mexico, New York, North Carolina, North Dakota, Ohio, Oklahoma, Oregon, Rhode Island, South Carolina, Texas, Utah, Vermont, Virginia, Washington, Wisconsin, Wyoming) and 2 international agencies (Ontario, Spain).

YES—2 U.S. States (Colorado, Kansas) and 6 international agencies (Montreal, Belgium, Germany, the Netherlands, Sweden).

- Colorado: Colorado has constructed small repair sections about 1 to 2 inches thick due to hail and rain damage on fresh PCC.
- Montreal: No, but we plan to construct a 500-m two-lane test section this summer of a "wet-on-wet" concrete pavement (European style) for noise and skid resistance. The surface will be exposed aggregates.
- Belgium: Wet on wet CRC pavement with fine aggregate top layer. We have some recent experiences with that system, and I have written a paper about it for the Conference on Concrete Pavements that will be held in San Francisco this year.
- Germany: Since about 2 years, concrete pavement constructed in two layers, i.e., thin upper layer with exposed aggregate surface (minimum 500 mm thick upper layer [note the previously specified minimum thickness of 40 mm has now been changed to 50 mm] and up to 250 mm lower layer concrete, compacted fresh on fresh) is standard in Germany. Test sections have existed more than 10 years in Germany. In Austria this method started about 20 years ago.
- The Netherlands: In wet on wet systems (a structure that has been laid in two shifts with an exposed aggregate surface). Before 1982 we constructed like that, but these pavements are no longer representative for today's pavement structures. In 2000 we did a successful pilot with 90 mm noise reducing PCC on 180 mm "ordinary" PCC. In practice the noise production of the traffic still led to complaints. In 2007 this section got an experimental overlay of three different types of stress absorbing and noise reducing HMA layers.
- Sweden: We have not built so many concrete roads in Sweden during the last 30 years. Since 1990 we have only built 5 or 6 roads with jointed concrete pavement. All these roads are built with the concrete in two layers, depending on wear from studded tires. Normally we have used a concrete with compressive strength of 60 MPa (T 3.5) in both layers. The surface layer is 5 to 7 cm thick with a more wear resistant (and more expensive) aggregate. The two layers are cast wet on wet. At least on one road, the surface layer has a compressive strength of 80 MPa (T 4.5), where the bottom layer has a compressive strength of 60 MPa. The reason for this is that the maximum aggregate size is 8 mm (instead of 16 mm), depending on noise reduction, and smaller aggregate decreases the wear resistance, which was compensated with a higher concrete strength.

Question B2: *If YES to (A2): Can we contact you (or someone at your agency) to get additional information on one or more of these projects for use in our research? If so, please provide name, email address, and phone number of person to contact within your agency for more information on these projects.*

All of the agencies who responded "Yes" to A2 provided follow-on contact information.

Question C2: *If YES to (A2):*

(1) What design procedure(s) have you used to design this/these pavement sections?
(2) Have you developed specifications for construction of new PCC/PCC pavements?
(3) Any additional comments on these projects (e.g., project experiences, construction techniques, quality management, performance, costs, etc.).
(4) Has your agency published any reports on any aspects of this/these pavement sections?

- Colorado: No formal design was developed for these repair sections.
- Kansas: 1993 version of DARWin. Just used current specifications with modifications to the plans for sequencing of construction process.
- Montreal: AASHTO 1993. Specifications derived from Belgium specs.
- Belgium: Same design as for other pavements.
- Germany: The design is according to the German standard RStO (Richtlinien für die Standardisierung des Oberbaus von Verkehrsflächen; Guidelines for the Standard Design of Pavements for Trafficked Areas).

- The Netherlands: VENCON 2.0. Papers in Dutch and English and presented at the international concrete conference in Istanbul, 2004.

Question D2: *If YES or NO to (A2): Is the construction of new PCC/PCC composite pavements of interest to your agency? Will the incorporation of design procedures to design new PCC/PCC composite pavements into the MEPDG be beneficial to your agency?*

NO—12 U.S. States (Arkansas, California, Colorado, Massachusetts, Nevada, North Carolina, North Dakota, Ohio, Rhode Island, South Carolina, Texas, Vermont).

YES—13 U.S. States (Delaware, Georgia, Kansas, Maryland, New Mexico, New York, Oklahoma, Oregon, Utah, Virginia, Washington, Wisconsin, Wyoming).

- Georgia: Yes, we are proposing to do a two-lift construction PCC pavement in the near future.
- Maryland: As the price of asphalt increases, Maryland is reviewing when the first cost of HMA and PCC would be competitive. Incorporation of design procedures in the *MEPDG* may be beneficial.
- New York: New York sees this technology as beneficial, in that the lower (first) lift of PCC can be comprised of less costly (but not less quality) components, while the upper lift contains the more costly components. A perfect example is using low friction, high strength aggregates (such as native limestone) in the first lift and saving the high friction aggregate for the top course.
- Oklahoma: Yes, I think these designs have merit. I know they have been used in some European pavements with some success.
- Oregon: Yes, our pavement design staff would be interested in PCC overlay or the design concept that is used in Europe where PCC can be paved as two lifts; top lift of higher quality aggregate than the lower lift.
- Washington: Yes, we are interested in the European two-layer system for improving both surface durability (studded tire wear) and reducing pavement/tire noise.
- Wisconsin: I would like to have different tools in our arsenal (so to speak).
- Wyoming: Yes, have some areas where the locally available aggregates are limestone and prone to polishing. It would be more economical to construct only the top of the PCC pavement with polish resistant aggregate that may be hauled long distances.

MAYBE—6 U.S. States (Alabama, Illinois, Louisiana, Maryland, Minnesota, Missouri).

- Alabama: Any interest in the construction of a new PCC/PCC composite pavement would depend upon the cost and overall serviceability of this type of pavement as compared to other alternative pavement types. The incorporation of design procedures into the *MEPDG* to facilitate the design of new PCC/PCC composite pavements would provide a rational methodology for the design and analysis of this type of pavement.
- Louisiana: Possibly. The use of a new HMA over new PCC or new PCC/PCC would be predicated on the life cycle cost of the system. Louisiana uses an Alternate Design/Alternate Bid system. Typically this consists of an HMA and PCC alternate or possibly two different HMA alternates. If the designs are estimated to be less than 20% different in costs, the designs are bid as alternates in an $A + B + C$ process, where A is the construction cost, B is the number of days to construct (or usage cost), and C is the LCC. If the outcome of R21 provides estimates or real data containing LCC, consideration could be given to designing this system as an alternate.
- Maryland: Possibly, if it can be shown to be cost-effective.
- Missouri: It could be of interest to us, if it would result in more economical designs without a decrease in performance.

NO RESPONSE—4 U.S. States (Alaska, Arizona, Maine, Mississippi).

Question E2: *If YES or NO to (A2): What concerns or issues may restrict you or your agency from constructing new PCC/PCC composite pavements in your State?*

The following factors (in descending order of frequency) were the key concerns and issues listed by various agencies:

1. Cost (15);
2. Cracking and PCC/PCC bond (11);
3. Lack of experience with this type of construction and other construction issues (9);
4. Lack of long-term data (e.g., for local calibration and LCCA) (5);
5. Acceptance/resistance to new technology and related issues (2);
6. Specifications and guidelines (1); and
7. Surface durability (studded tire wear) (1).

APPENDIX D

Distress Mechanisms of HMA/PCC Composite Pavements

Performance Issues

Although a hot-mix asphalt/portland cement concrete (HMA/PCC) composite pavement provides shared advantages of different materials, some problems have been reported in the literature with regard to the performance of composite pavements. The following is a list of the common problems and issues in order of importance or priority that have been reported in the literature:

1. Reflection cracking: Reflection cracking is the most common problem reported in the literature for composite pavements. Various reflection cracking treatments have been used but without consistent success. The jointing or cracking of the base PCC slab is one factor that is critical to reflection cracking, with shorter spaced joints and cracks considered superior. The load transfer efficiency of these joints and cracks over time is also critical.
2. Construction defects: Construction defects that occur during placement are another common problem observed for this type of pavement. Construction defects include segregation in the HMA (both longitudinal and truck-to-truck segregation), inadequate densities along longitudinal construction joints, centerline streak down the center of the paver, and so forth. These defects can be related to placement or to the materials used. Segregation is probably the most common defect that has been exhibited on many HMA layers. Segregation will result in raveling and cracking of the HMA layer. Construction defects can only be reduced with an adequate quality control/quality assurance and inspection program.
3. Inadequate HMA layer thickness: Inadequate layer thickness affects two different aspects of HMA/PCC composite pavements—(1) structural thickness requirements to resist fatigue cracking of the PCC base and the insulation of the PCC layer, and (2) an HMA wearing surface that is too thin relative to the nominal maximum aggregate size. The first aspect relates to insufficient structure for the traffic, climate, and support conditions, whereas the second aspect relates to constructability problems and other construction-related issues/distresses.
4. Inadequate bond or loss of bond between the HMA wearing surface and PCC base layer: Another problem that has been reported on HMA/PCC composite pavements is the lack of interface friction or bond between the HMA surface and PCC base. Inadequate bond will result in fatigue cracking, potholes, and slippage cracks. Adequate bond can be ensured through proper placement of a tack coat and some texturing of the PCC surface.
5. Rutting of the HMA mixture: Rutting is a materials-related issue and has been reported on a limited basis. Rutting can be prevented easily through the mixture design and materials selection process. Thickness of the HMA layer will affect rutting potential.
6. Thermal cracking of the HMA wearing surface: Thermal cracking is a minor issue that is less likely to occur, assuming that adequate bond is retained between the different layers.

For HMA/PCC composite pavements to be long lasting and rapidly renewed, these issues must be overcome through appropriate selection and design of materials, structural design procedures, adequate specifications and guidelines, and quality inspection programs.

Distress Mechanisms and Pavement Design

Many agencies have designed HMA/PCC composite pavements as a PCC pavement using the AASHTO design procedure. Typically, in these cases the HMA surface layer is given some equivalent PCC thickness value. The thickness of the PCC pavement is determined based on traffic and other design factors included in the AASHTO procedure for the design of PCC pavements, whereas the thickness of the HMA layer is determined from experience to limit the time at which the reflection cracks begin to occur. Most of these earlier empirical-based methods, such as AASHTO, were not calibrated using field observations from this type of pavement design strategy. More fundamental procedures have been developed and used by a few agencies in the United States and Europe that are based on mechanistic-empirical (M-E) methods. All of these M-E based methods have a limited database from which they were developed. More important, most of the historical empirical and M-E based procedures assume that the HMA will be designed and placed such that minimum or negligible rutting will occur within those layers.

Zaghloul et al. (1994) concluded that the distress mechanisms of composite pavements are a combination of those of flexible and rigid pavements. When a heavy load is applied and repeated on a composite pavement, some permanent deformation develops in the HMA layer. Permanent deformation may, depending on the stress levels, also develop in asphalt-bound or unbound layers beneath the PCC slab. Permanent surface deflection in this case reflects the permanent deformation of the HMA layer only, whereas the total loaded deflection (elastic and plastic) reflects the permanent deformation of the HMA layer as well as any permanent deformation in the layers beneath the PCC slab. The permanent deformation in layers beneath PCC slab leads to formation of voids, which in turn lead to larger deflections, increased pavement roughness, and accelerated fatigue failure.

Field observations made by Von Quintus et al. (1980) matched the extensive review on distress mechanisms for composite pavements. They divided the major distress mechanisms into three basic categories: fracture, distortion, and disintegration. Among all the distresses, the most dominant distress modes are fatigue cracking, low-temperature cracking, reflection cracking, and rutting. Care should also be taken to avoid other secondary distress mechanisms, especially raveling and loss of bond between the HMA surface and underlying PCC layer.

Fatigue cracks normally initiate at the bottom of HMA (if the layer debonds) or PCC layer and propagate to the surface with continued traffic applications. The primary pavement response related to fatigue cracking is the maximum tensile stress at the bottom (or top) of the PCC layer. Low temperature or thermal cracking results when tensile stresses, caused by temperature variations or low temperatures, exceed the material's fracture strength. Reflection cracking is caused by horizontal or differential vertical movements between different layers at a discontinuity in the PCC layer. Slippage cracking is more common in airfield pavements than in highways because of the higher lateral loads of the turning aircraft; however, slippage cracks have been observed on some highway projects. These slippage cracks normally occur where the interface friction or bond has been lost in an area of turning or braking movements of loaded trucks. Rutting is related to several factors, including (1) the vertical compressive strain at the top of the subgrade, (2) the radial stress at the bottom of an unbound base course, and (3) the vertical compressive stress or strain in each pavement layer, but especially the HMA layers.

Von Quintus et al. (1980) selected four distress criteria for use in the structural design of composite pavement cross sections:

1. Fatigue cracking of the PCC layer;
2. Rutting, primarily in the HMA layers and limiting the vertical compressive strain at the top of the subgrade;
3. Low-temperature cracking, HMA layer; and
4. Roughness, as estimated by the present serviceability index (PSI).

Limit values for each of these distress criteria were selected based on a thorough review of the literature and past research from both laboratory and field studies. These limit values are listed in Table D.1. Based on these limit values, the maximum allowable critical pavement responses were established based on various performance models. These requirements are in turn used to determine the thickness requirements for various layers.

Key issues relating to distress mechanisms for HMA/PCC composite pavements are summarized below:

- Load-related area fatigue cracking of the HMA layer that initiates at the bottom of the HMA layer and propagates to the surface: Area fatigue cracking does not usually initiate at the bottom of the HMA layer because the HMA is almost always in compression, unless there is a loss of bond between the HMA and PCC layers. Fatigue cracking of the HMA layers is estimated by the tensile strain at the bottom the HMA.
- Load-related longitudinal cracking of the HMA layer that initiates at the surface of the HMA and propagates downward to the bottom of the HMA layer: Surface-initiated cracks for good quality composite pavements are rare because the tensile strains at the surface of the HMA layer are small, if they occur at all. Longitudinal cracking of

Table D.1. Design Criteria and Their Limit Values

Distress	Limit Value
Fatigue cracking in the wheel path	5%
Rut depth on HMA surface	0.4 in. (10 mm)
Transverse (low-temperature) crack spacing	30 ft (9 m)
Present service index (roughness requirement)	3.0

the HMA layers is estimated by the tensile strain at the top the HMA.

- Load-related fatigue midslab transverse cracking in the JPC layer: Fatigue damage occurs at the top and bottom of the PCC slab and combines to predict total transverse cracking in the slab. Fatigue cracking of the JPC slabs is estimated by the load-related tensile stress at the surface and bottom of the slab. These cracks are then propagated through the HMA layers using the reflection cracking model.
- Reflection cracking model: Reflection cracking is caused by horizontal or differential vertical movements between different layers at a discontinuity in the underlying PCC layer and are estimated by the thermal and load-related horizontal and vertical tensile and flexural strains in the HMA layer at the discontinuity.
- Load-related fatigue punchout development in the CRC layer: Punchouts in HMA/CRC composite pavements are similar to the bare CRC pavement except that the temperature gradient is considerably different because of the HMA layer. Punchouts in the CRC are estimated by the load-related tensile stress at the surface of the slab between two closely spaced transverse cracks. The punchout then propagates through the HMA layers.
- Rutting of the HMA layers and any unbound aggregate layer and subgrade: The magnitude of the rutting in the unbound aggregate base layers and subgrade normally is small under the PCC layer because the vertical compressive strains in those unbound layers are small. Rutting of the HMA layers is estimated by the load-related vertical strains in the HMA and unbound layers.
- Thermal cracking of the HMA layer: Thermal cracking or low-temperature cracking is a minor issue that is less likely to occur in HMA/PCC composite pavements, assuming that adequate bond is retained between the different layers. The thermal cracks are predicted based on tensile stress from temperature variations at the surface of the HMA layer.

APPENDIX E

Distress Mechanisms of PCC/PCC Composite Pavements

Distresses

Key failures in typical portland cement concrete (PCC) pavements should also be considered for PCC/PCC composite pavements. These failure mechanisms include

- Bottom-up cracking;
- Top-down cracking;
- Longitudinal cracking;
- Punchouts (for PCC/jointed plain concrete [JPC]); and
- Joint faulting.

These failure mechanisms are not expected to be a great concern in the case of PCC/PCC composite pavements as compared with conventional PCC pavements. A brief discussion of each follows.

Longitudinal Cracking

The RadiCAL project estimated that longitudinal cracking can be a concern for PCC pavements provided that a PCC pavement is very thin and nondoweled or significant shrinkage and built-in curling occurs in that pavement (Hiller 2007). Given that PCC/PCC pavements are sufficiently thick as a result of their layered structure, it is not anticipated that longitudinal cracking caused by insufficient thickness will be a concern for PCC/PCC. Experts on composite pavements in Europe concurred that for a slab consisting of heterogeneous layers, shrinkage and built-in curl and the resulting threat of longitudinal cracking are no more a threat to PCC/PCC than to a structurally similar single-layer PCC pavement. In addition, this failure was not observed during field surveys of PCC/PCC, nor was it observed on the European tour of PCC/PCC pavements.

Bottom-Up Cracking, Top-Down Cracking, and Punchouts

Fatigue failures caused by bottom-up and top-down cracking (in jointed plain concrete pavement [JPCP]) or punchouts (in continuously reinforced concrete pavement [CRCP]) are important modes of failure in single-layer concrete pavements. The main instigator of these modes of cracking is a combination of traffic loading and the "curled," deformed slab that results from built-in curling/warping and any combination of either temperature or moisture gradients through the slab. Once the slab is in a deformed convex/concave shape, traffic loading creates a cantilever effect that can result in bottom-up/top-down transverse cracking (or punchouts) in the pavement slab.

It is clear that curling is as prevalent in two-layered slabs as it is in single-layered slabs, and for this reason fatigue cracking is an important mode of failure for two-layered composite PCC pavement. After discussions with experts in Europe and from simulations using Lattice3D, however, it was evident that the built-in stresses in a given two-layered PCC slab are not exacerbated simply by the fact that the layers are heterogeneous. Provided that a two-layered system is constructed using wet-on-wet construction, the slab's performance in transverse cracking is not significantly different from that of a structurally equivalent one-layered slab. PCC/PCC pavements in the field performed quite well in resisting this failure—this may also be attributable to the care in construction that many PCC/PCC pavements are given. No transverse cracking was observed in the tour of European pavements, and very little transverse cracking has been reported, even in cases such as US-41 in Florida, in which the upper and lower lifts had very different strength properties and were composed of different materials (ERES Consultants 1998). That is not to say, however, that the effects of built-in curling and early-age behavior in two-layered slabs are not important factors in PCC/PCC composite pavements.

Joint Faulting

Although joint faulting is a concern for single-layer JPCP, it is not any more of a concern in PCC/JPC composite pavements than in JPCP. As in the case of the heterogeneous layered slab response to transverse cracking, the presence of heterogeneous layers in a slab does not exacerbate faulting relative to that of a structurally equivalent JPCP. In surveys of European PCC/PCC and in reported results from existing PCC, the only difficulty in the structural performance of a PCC/PCC pavement was that of the sections built on I-75 in Detroit. Those sections were reported to have suffered a significant loss in load transfer efficiency a few seasons after being opened to traffic (Buch et al. 2000). However, the loss in structural performance at the joint (and resistance to faulting) was not a result of the pavement system's having contained a two-layered PCC slab: rather, the low readings for load transfer efficiency (LTE) were attributed to possible measurement variability. In short, joint faulting in PCC/PCC is no more or less likely to occur than it is in single-layered PCC due to the classic causes of joint faulting: base, subbase, subgrade erodibility; subpar LTE; or oversaturation of the base near the joint, and the same models for JPC pavement faulting can be used for PCC/PCC composite pavements.

Debonding

Debonding is a particularly challenging issue that is aggravated by shrinkage and thermal gradients through the heterogeneous layers at early ages. With proper wet-on-wet construction techniques, debonding of the two PCC layers is not expected to be an issue. However, as the time between placing the two PCC lifts increases (>60 to 90 minutes), the lower PCC lift starts hydrating and the surface of the lower lift may no longer be "wet." In such situations, the bond between the two lifts can potentially be compromised.

Although debonding has always been a concern of PCC/PCC composite pavement design, past design focused on shear strength at the interface. Recent research has instead focused on improving tensile strength at the interface (normal to the interface surface) in limiting debonding in response to cracking. To account for debonding in PCC/PCC, the SHRP 2 R21 research considered nonuniform shrinkage, nonuniform thermal expansion/contraction (especially at early ages), nonlinear thermal gradients, nonuniform heat of hydration, and crack formation and propagation, as discussed in Volumes 1 and 2 of the final report and in the appendices.

Freeze–Thaw Durability and Performance Complications of RCA Use

Given that the use of recycled concrete aggregates (RCAs) as coarse aggregate replacement in the PCC mix of the lower lift can be expected for PCC/PCC composite pavements, durability is an important factor in the performance of PCC/PCC composite pavements. This is especially important given that a key difference between RCA and natural aggregate is the variability in the absorption capacity of different RCAs, due in part to the existing mortar surrounding the original aggregate (Figure E.1). More details on this are located in the corresponding chapters in Volumes 1 and 2 of the final report and in the appendices.

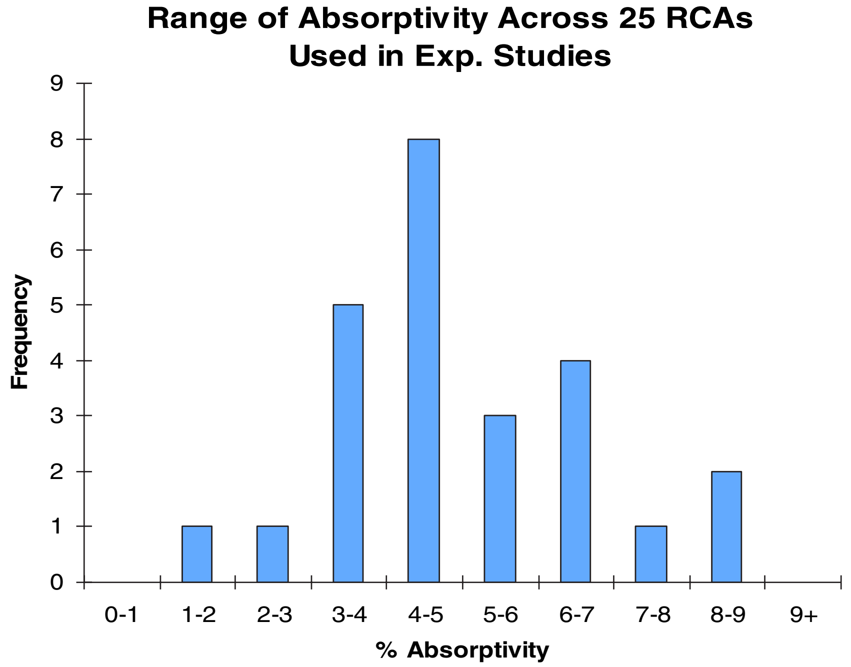

Note: Exp. = experimental.

Figure E.1. Range of absorptive capacities of RCA encountered across 17 research references.

Construction Defects

Construction defects that occur during placement are another problem in PCC/PCC composite pavements that can happen during paving of conventional JPCP or CRCP. Construction defects include vibration issues, such as inadequate consolidation of the PCC mix(es) around dowel bars or reinforcing steel; overmixing of the two PCC lifts; improper dowel bar placement; PCC mix issues (such as slump, gradation, temperature, and so forth); improper texturing or curing; and mechanical issues related to the paver. Construction defects can be reduced only with an adequate quality control/quality assurance and inspection program.

Performance of PCC/PCC

PCC/PCC failures were considered by the SHRP 2 R21 research in accordance with how these failures are modeled by the *MEPDG*. The following sections briefly reconsider typical PCC/PCC failures in terms of the *MEPDG* capabilities.

JPCP Transverse Cracking

The *MEPDG* considers two mechanisms of transverse cracking: bottom-up cracking and top-down cracking. When the truck axles are near the longitudinal edge of the slab, midway between the transverse joints, a critical tensile bending stress occurs at the bottom of the slab, as shown in Figure E.2.

This stress increases greatly when there is a high positive temperature gradient through the slab (on a hot sunny day, the top of the slab is warmer than the bottom of the slab). Repeated loadings of heavy axles under these conditions result in fatigue damage along the bottom edge of the slab, which eventually results in a transverse crack upward and across the surface of the pavement.

Repeated loadings by heavy trucks when the pavement is exposed to high negative temperature gradients (during nighttime, the top of the slab is cooler than the bottom of the slab) result in fatigue damage at the top of the slab, which eventually results in a transverse crack that is initiated on the surface of the pavement. The critical loading condition for top-down cracking involves a combination of axles that loads the opposite ends of a slab simultaneously. In the presence of a high negative temperature gradient, such load combinations cause a high tensile stress at the top of slab near the middle of the critical edge, as shown in Figure E.3. This type of loading is most often produced by the combination of steering and drive axles of truck tractors and other vehicles. Multiple trailers with a relatively short trailer-to-trailer axle spacing are other common sources of critical loadings for top-down cracking. The top-down stress becomes critical when a significant amount of permanent upward curl/warp is present.

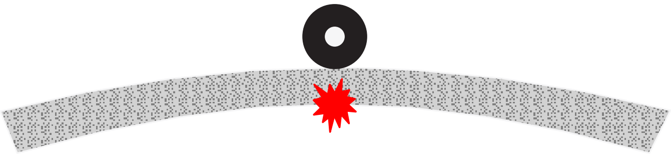

Figure E.2. Curling of PCC slab caused by nighttime negative temperature difference plus critical traffic loading position, resulting in high tensile stress at slab bottom.

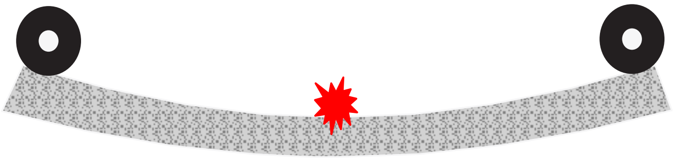

Figure E.3. Curling of PCC slab caused by nighttime negative temperature difference plus critical traffic loading position, resulting in high tensile stress at slab top.

Factors affecting *MEPDG* predictive models for JPCP transverse cracking include thicknesses of the top and the bottom PCC layers; moduli of elasticity, Poisson's ratios, and unit weights of the top and the bottom PCC layers; coefficient of thermal expansion (CTE) of the top PCC layer; shrinkage properties of the top PCC layer; flexural strength; base thickness, modulus of elasticity and unit weight; joint spacing; subgrade stiffness; lane-shoulder joint LTE; temperature distribution through the slab thickness; moisture distribution through the slab thickness; magnitude of effective permanent curl/warp; load configuration (for bottom-up cracking, axle type; for top-down cracking, wheelbase); axle weight; wheel tire pressure and aspect ratio; and axle position (distance from the critical slab edge).

Important points to consider regarding *MEPDG* predictive models of JPCP transverse cracking are

- The design procedure allows input of the various concrete properties, such as strength, modulus of elasticity, CTE, and shrinkage properties of the top and the bottom PCC layers separately.
- *MEPDG* transverse cracking models assume that both PCC layers have strength equal to the strength of the top PCC layer. Again, this assumption is not a significant drawback for design of the PCC overlay since the PCC mix designs of the overlay and the existing pavement are similar and the strength of the existing pavement is higher because of higher age. This may not be the case for two-layered composite PCC pavement if a less strong concrete mix is used for the bottom layer. For PCC/PCC composite pavements as part of SHRP 2 R21, the *MEPDG* was modified, which eliminated this assumption for bonded PCC overlay projects (which is used to model new PCC/PCC construction).

JPCP Faulting Model

Repeated heavy axle loads crossing transverse joints create the potential for joint faulting. Faulting can become severe and cause loss of ride quality and require premature rehabilitation if any of the following conditions occurs:

- Repeated heavy axle loads;
- Poor joint LTE;
- Presence of an erodible base, subbase, or subgrade beneath the joint; and
- Presence of free moisture under the joint.

Factors affecting *MEPDG* predictive models for JPCP faulting include thicknesses of the top and the bottom PCC layers; moduli of elasticity, Poisson's ratios, and unit weights of the top and the bottom PCC layers; CTE of the top PCC layer; shrinkage properties of the top PCC layer; base thickness, modulus of elasticity, and unit weight; joint spacing; subgrade stiffness; lane-shoulder joint LTE; temperature distribution through the slab thickness; moisture distribution through the slab thickness; magnitude of effective permanent curl/warp; load configuration; axle weight; axle position (distance from the critical slab edge); and base erodability.

The design procedure assumes that the CTE and shrinkage properties of the top and bottom PCC layers are the same. This assumption is not a significant drawback for design of bonded PCC overlays because it is advisable to match the properties of the existing PCC pavement and the overlays for the greatest possible effect to reduce the potential of debonding between the layers. For PCC/PCC composite pavements as part of SHRP 2 R21, the *MEPDG* was modified, which eliminated this assumption for bonded PCC overlay projects (which is used to model new PCC/PCC construction).

Debonding and Built-in Curling/Warping

Built-in curling is influenced by many factors, including material properties (PCC shrinkage, CTE, heat of hydration, and so forth), placement conditions, ambient temperature, ambient relative humidity, wind, sunshine, and curing techniques. Excessive built-in curling can increase the initial roughness of concrete pavements and may increase top-down cracking and faulting in JPCP. For composite pavements, excessive built-in curling may also cause premature debonding between the concrete layers. The *MEPDG* allows the user to evaluate the effect of built-in curling but does not provide recommendations for estimating the magnitude of the built-in temperature gradient.

Debonding between the PCC layers may lead to premature failure of the pavement. However, debonding is not currently predicted by the *MEPDG* for PCC overlays. Although early research into debonding of PCC overlays focused on shear strength at the interface, recent research focused on improving tensile strength at the interface (normal to the interface surface) in limiting debonding in response to cracking. The process of debonding includes crack initiation as a result of volume changes, thermal loads, and traffic loads; debonding occurring in the region of the crack; and peeling of the top-lift from the lower lift over time.

The main difficulties in dealing with built-in curling and debonding are nonuniform shrinkage, nonuniform thermal expansion/contraction (especially at early ages), nonlinear thermal gradients, nonuniform heat of hydration, and crack formation and propagation. Thus, a general research approach for modeling debonding is one that concerns shrinkage, creep, and crack propagation for cement-based materials. The drying of cement composites causes shrinkage that, when coupled with restraint, leads to stress production and possible cracking of the material. Exposed surfaces, from which moisture loss occurs, typically experience tension, whereas the other regions react to preserve equilibrium.

The mechanisms of drying shrinkage are commonly viewed from a materials science perspective, in which (at most) basic restraint conditions are assumed. However, in most practical situations, the various forms of restraint are present in combination and in varying degrees, depending on the interplay between material design, environmental exposure, curing conditions, structural dimensions, and structural boundary conditions. A model developed by Bolander et al. (2007) proposed to simulate shrinkage behavior of concrete (including shrinkage cracking) using rigid-body-spring elements that break according to simple rules.

The effect of surface drying is more complicated in the case of a two-lift PCC/PCC pavement, when differences in the properties of the lifts create different shrinkage effects in the layers. These effects create internal stresses, and when internal stresses reach critical levels, separation is initiated between the lifts of a PCC/PCC pavement. The model developed by Bolander et al. (2007) describes not only the processes of transport of moisture, differing rates in hydration, variable aggregates, and cement paste properties (including modulus of elasticity, creep, shrinkage, strength, and so forth), but also the possible separation between the lifts.

Because the model was developed for general modeling of fracture in concrete structures, including bonded overlays of bridges, it was adapted to PCC/PCC composite pavements. Figure E.4 depicts a basic idealized model for Bolander's work in debonding at different stages in the maturity of the concrete layer (on top).

Because the model can analyze separation between the concrete layers, it can model separation of the collective two-lift slab from the base layer in the pavement system. Further-

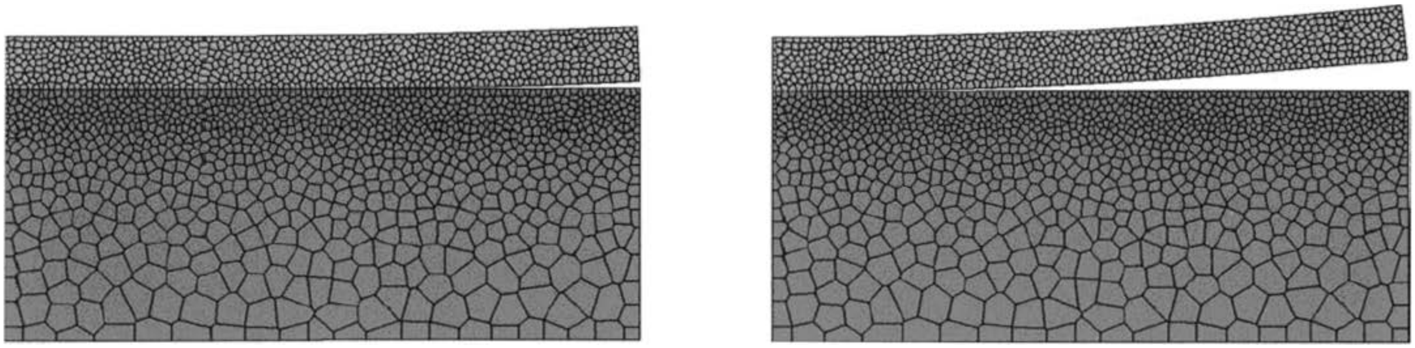

Source: Bolander and Berton 2004.

Figure E.4. Debonding along weak interface for (a) 20 days' exposure and (b) 50 days' exposure to drying environment.

more, the fracture model developed by Bolander et al. (2007) to describe the separation of layers can also be used to describe joint formation (as illustrated in Figure E.5). The SHRP 2 R21 work focused on the nature of fracture at the interface, which was judged the most critical factor in debonding. More detail on lattice modeling for debonding in a composite pavement can be found in the corresponding chapters in Volumes 1 and 2 of the final report and in the appendices.

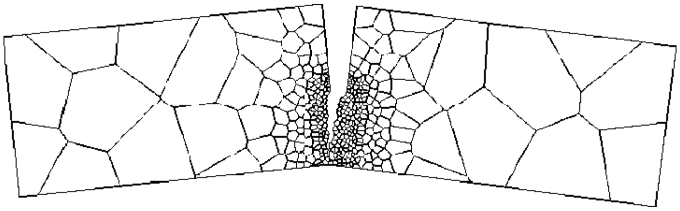

Source: Bolander and Sukumar 2005.

Figure E.5. Modeling of joint formation.

APPENDIX F

Construction of Test Sections at MnROAD

Introduction

In May 2010, three full-scale composite pavement test sections (one hot-mix asphalt/portland cement concrete [HMA/PCC] and two PCC/PCC) were constructed on I-94 at MnROAD to emulate best practices of constructing composite pavements. Before the construction of the mainline test sections, a 200-ft two-lane test strip of PCC/PCC composite pavement was constructed at the MnROAD facilities. Figure F.1 shows the location of the MnROAD test section relative to Minneapolis. An aerial view of a portion of the MnROAD facility is shown in Figure F.2.

Design and Specifications

The project consisted of recycling an existing concrete pavement in-place; the coarse aggregate (recycled concrete aggregate [RCA]) from the recycled pavement was used to construct the lower PCC layer for the HMA/PCC composite pavement section and the lower PCC layer for one of the PCC/PCC composite pavement sections. For HMA/PCC composite pavements, there were several candidate HMA materials that were considered, including porous HMA, rubber-asphalt porous friction course, Novachip, and stone matrix asphalt (SMA). The cost of placement of any specialized material on such a short roadway section prohibited the use of any of these surfaces. A typical Superpave HMA conforming to Minnesota Department of Transportation (MnDOT) specifications was specified. The relatively thin (3 in. [75 mm]) high-quality, dense-graded HMA layer was placed and bonded to the newly placed PCC layer after the PCC had hardened sufficiently. For the PCC/PCC composite pavements, various surface textures were considered to texture the surface PCC layer. Because of its potential with respect to durability, texture, and noise characteristics, an exposed aggregate concrete (EAC) texture was chosen. The EAC was constructed for both PCC/PCC test sections. However, the first 475 ft of the EAC was considered the "learning area," and the EAC texture was later diamond ground using conventional grinding in the passing lane and next-generation grinding in the driving lane.

The HMA/PCC section was designed to feature a 3-in. (75-mm), high-quality Superpave HMA layer over a 6-in. (150-mm) RCA PCC lower lift. The PCC/PCC sections constructed at MnROAD were designed to feature a 3-in., high-quality PCC layer over a 6-in., "low-cost" or RCA PCC lower layer. The term "lowcost" signifies that the PCC design was such that the lowest possible amount of cement and most inexpensive coarse aggregates were used by the contractor. The designs are summarized in Table F.1, Table F.2, and Figure F.3.

HMA/PCC Composite Pavement Design Thickness

During the initial design phase, the *MEPDG* was used to analyze performance and prepare a design for the composite pavement using the HMA overlay of jointed plain concrete pavement (JPCP) option. The *MEPDG* does not specifically provide for the design of a new HMA/PCC composite pavement; however, several inputs can be selected to match a newly constructed JPCP slab and HMA surfacing before opening to traffic.

- Dates of construction of each layer and opening to traffic: selected to match that of a new composite pavement (e.g., RCA placed May 2010, HMA placed June 2010 and opened to traffic in July 2010).
- Rehabilitation: select zero percent cracked slabs indicating no past fatigue damage.
- Strength and modulus of concrete: set at 28 days, thus the gain in strength until opening to traffic will be correct.
- Traffic opening: selected when the section was opened to traffic about July 2010.

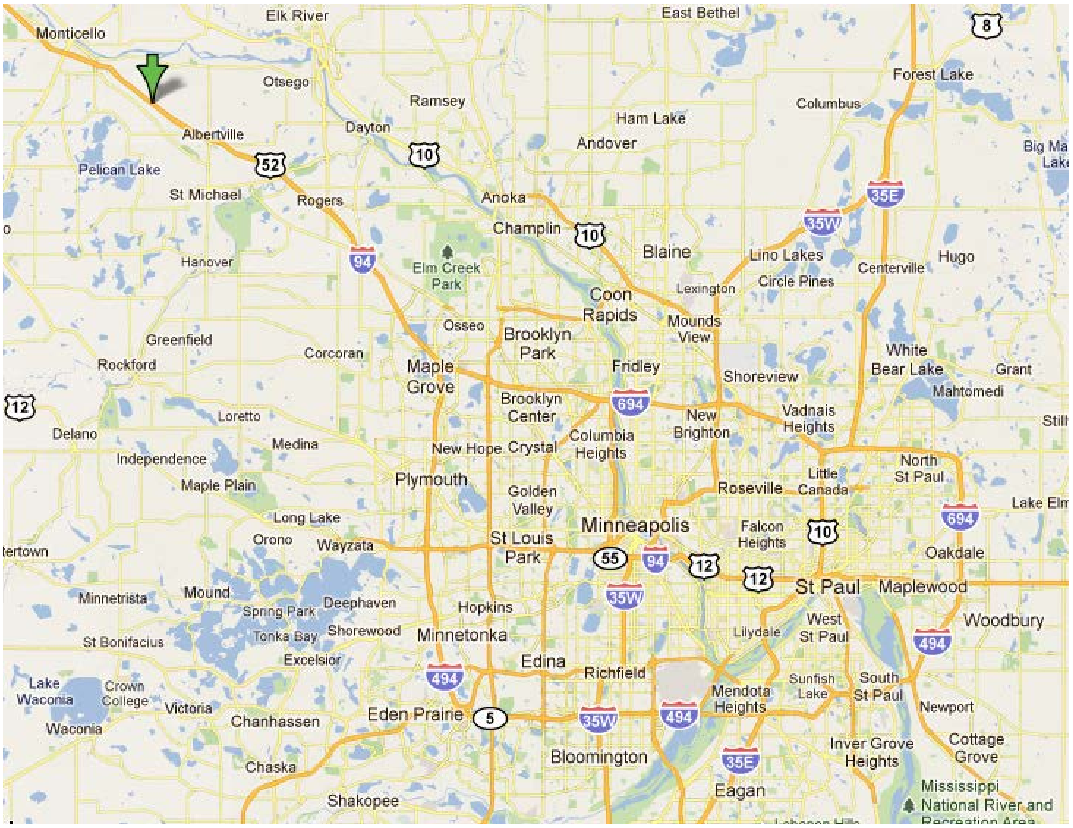
Monticello
Elk River
East Bethel
8
Otsego
Forest Lake
Ramsey
Columbus
Ham Lake
Albertville
Dayton
Andover
52
10
Pelican Lake
St Michael
Rogers
35E
Anoka
35W
Champlin
10
Blaine
Lino Lakes
Hugo
Hanover
94
Elm Creek Park
Centerville
Circle Pines
Lexington
Coon Rapids
Mounds View
Osseo
Brooklyn Park
White Bear Lake
Greenfield
Corcoran
Rockford
Maple Grove
Fridley
Shoreview
Grant
Mahtomedi
12
Loretto
Brooklyn Center
694
New Brighton
Vadnais Heights
Delano
Medina
Columbia Heights
Independence
New Hope
Crystal
North St Paul
Little Canada
Maple Plain
Plymouth
Golden Valley
Roseville
Long Lake
694
Orono
Wayzata
St Louis Park
Minneapolis
Falcon Heights
10
Oakdale
55
94
12
12
St Paul
Maplewood
Minnetrista
Mound
Deephaven
Hopkins
35W
Spring Park
West St Paul
Woodbury
Lilydale
Tonka Bay
Shorewood
Minnetonka
St Bonifacius
Excelsior
494
Edina
Richfield
Lake Waconia
Crown College
Sunfish Lake
South St Paul
Mendota Heights
Victoria
494
Newport
Waconia
Chanhassen
Eden Prairie
5
35W
Cottage Grove
Inver Grove Heights
Bloomington
Chaska
35E
Eagan
Mississippi National River and Recreation Area
Shakopee

Source: © 2012 Google.

Figure F.1. Location of the MnROAD composite pavement test sections on I-94 near Albertville, Minnesota, approximately 40 miles northwest of Minneapolis.

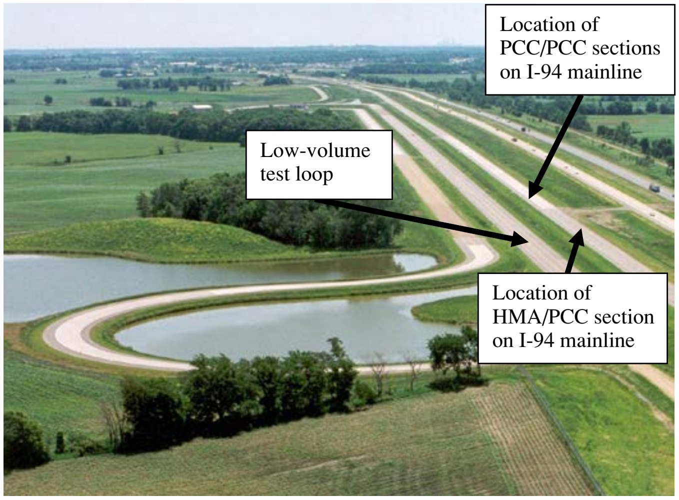
Location of PCC/PCC sections on I-94 mainline
Low-volume test loop
Location of HMA/PCC section on I-94 mainline

Figure F.2. Aerial view of MnROAD facility and location of HMA/PCC test section. Note that the mainline I-94 traffic is diverted to the center lanes during construction and testing.

The *MEPDG* models the HMA/jointed plain concrete (JPC) composite pavement layers in three ways simultaneously: (1) structural, (2) thermal, and (3) moisture. The following assumptions and procedures exist:

- The HMA/JPC is converted into an equivalent slab on a month-by-month basis because both HMA and PCC change over time due to temperature and moisture changes and strength gain.
- Traffic loading is applied through single, tandem, tridem, and quad axle loadings, and truck volume changes on an hourly, monthly, and annual growth basis.
- The unbound base course and clay subgrade are modeled as a resilient modulus, with the modulus changing monthly because of changes in degree of saturation and freeze–thaw temperatures.
- Hourly temperatures are computed throughout the HMA and JPC layers and converted into temperature gradients for use in stress calculation. Moisture gradient through the slab depends on the monthly relative humidity. Note that for new composite pavements with HMA surfaces, this calculation is not quite correct because the top of the concrete will now be saturated much of the time.

Table F.1. HMA/PCC Design for MnROAD Section

Section		**Cell 70 HMA/PCC (475 ft [145 m])**
HMA	Thickness	3 in. (75 mm) placed in two lifts
	Binder	PG 64-34
	Mix	Superpave wearing course designated SPWEB440F with 0.5 in. (12.5 mm) nominal maximum aggregate size (SP 12.5)
PCC	Thickness	6 in. (150 mm)
	Mix	Low portland cement (~360 lb/yd^3) plus 240 lb/yd^3 (40%) fly ash, Class C (FAC)
	Coarse aggregate	50% RCA, 50% MnDOT Class A Maximum aggregate size 1.25 in. (32 mm)
Base		8 in. (200 mm) Class 5 unbound
Subgrade		Clay
Joint spacing		15 ft (4.6 m)
Dowels		1.25 in. (32 mm) placed on baskets in driving lane at PCC middepth and nondoweled passing lane
Joints		Saw and seal HMA over PCC joints (except last six joints)

- Distress types predicted include the following: top-down and bottom-up fatigue concrete slab transverse cracking,
- rutting of the HMA surfacing,
- transverse reflection cracking of the HMA surfacing,
- top-down fatigue longitudinal cracking of the HMA surfacing in the wheelpath, and
- bottom-up fatigue cracking in the HMA surfacing and international roughness index (IRI).

Table F.3 shows the output from the *MEPDG* run over a 15-year period where the composite pavement was loaded with more than 8 million trucks (or more than 16 million equivalent single-axle loads [ESALs]). The only two distresses that are expected to show problems are

- Reflection cracking from the transverse joints. Note that most of the transverse joints were sawed and sealed, which may mitigate their deterioration into a maintenance requirement. Some joints were left unsealed, and they should break down and deteriorate.
- Transverse (bottom-up) fatigue cracking from the slab. This 75-mm (3-in.) HMA over 150-mm (6-in.) jointed RCA

Table F.2. PCC/PCC Designs for MnROAD Sections

Section		**PCC Over RCA PCC (Cell 71)**	**PCC Over Low-cost PCC (Cell 72)**
Upper PCC	Thickness	3 in.	3 in.
	Mix	High portland cement (~616 lb/yd^3) plus 109 lb/yd^3 (15%) FAC	High portland cement (~616 lb/yd^3) plus 109 lb/yd^3 (15%) FAC
	Coarse aggregate	Crushed granite (maximum size $\frac{3}{8}$ in.)	Crushed granite (maximum size $\frac{3}{8}$ in.)
Lower PCC	Thickness	6 in.	6 in.
	Mix	Low portland cement (~360 lb/yd^3) + 240 lb/yd^3 (40%) FAC	Low portland cement (~240 lb/yd^3) + 360 lb/yd^3 (60%) FAC
	Coarse aggregate	50% RCA, 50% MnDOT Class A Maximum aggregate size 1.25 in.	100% MnDOT Class A Maximum aggregate size 1.25 in.
Base		8 in., Class 5 unbound	8 in., Class 5 unbound
Subgrade		Clay	Clay
Joint spacing		15 ft	15 ft
Doweling		1.25 in. placed on baskets at total PCC middepth	1.25 in. placed on baskets at total PCC middepth
Surface texture		Conventional diamond grinding, next-generation diamond grinding	EAC, conventional diamond grinding, next-generation diamond grinding

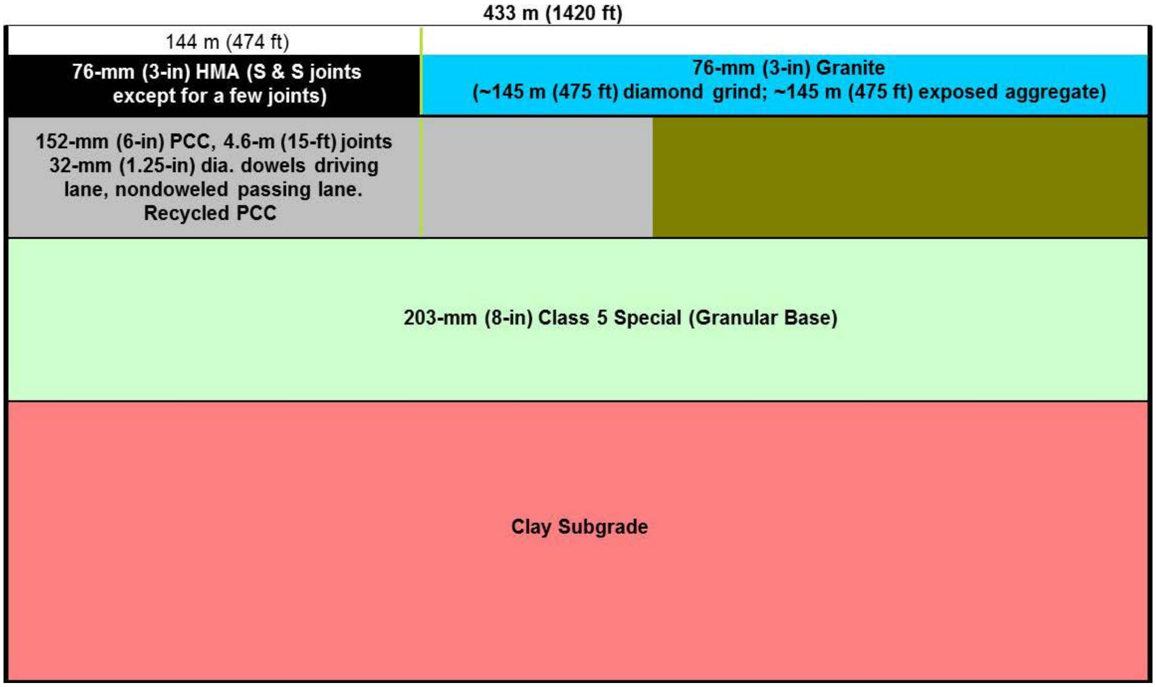
433 m (1420 ft)
144 m (474 ft)
76-mm (3-in) HMA (S & S joints except for a few joints)
76-mm (3-in) Granite
(~145 m (475 ft) diamond grind; ~145 m (475 ft) exposed aggregate)
152-mm (6-in) PCC, 4.6-m (15-ft) joints 32-mm (1.25-in) dia. dowels driving lane, nondoweled passing lane. Recycled PCC
203-mm (8-in) Class 5 Special (Granular Base)
Clay Subgrade

Figure F.3. Layout of test sections (Cell 70, HMA/PCC; Cell 71, PCC/RCA PCC; Cell 72, PCC/low-cost PCC) at MnROAD.

PCC pavement is not sufficient to last more than 15 years and 8 million heavy truck loadings and a thicker slab would be needed if this were regular MnDOT design over a 35-year period and not a research project. In fact, by increasing the PCC thickness from 150 mm (6 in.) to 200 mm (8 in.), the composite pavement design life would be extended to 30 years and 20 million trucks with no fatigue cracking of the PCC slabs.

PCC/PCC Composite Pavement Design Thickness

Although the upper PCC layer typically is constructed at thinner levels (as thin as 5 cm [2 in.]) in Europe, previous U.S. experience in two-layer construction cautions against upper PCC layers thinner than 2.75 in. Single-layer PCC pavements (JPCP) along the MnROAD mainline, including those as thin as 7.1 in., have yet to exhibit any major distress after 15 years of Interstate traffic. For this reason and to provide some comparative analysis with the HMA/PCC design, a 6-in. lower layer of concrete thickness was selected to provide an economic lower PCC layer, yet one that is not so thin as to risk structural failure.

Three-inch PCC for the upper PCC layer was chosen for comparative analysis with the HMA/PCC design. It was determined through analysis of conventional JPCP using *MEPDG* that the total thickness of 9 in. was more than adequate for the levels of traffic encountered on the MnROAD I-94 mainline section for many years into the future. Structural failure (cracking and faulting) were not expected within the 2 years of full R21 monitoring. The pavement is not

Table F.3. Predicted Performance of the MnROAD HMA/PCC Pavement Over Time Using the **MEPDG**

Age/ Trucks[a]	Transverse Slab Crack[b] (%)	Transverse Joint Reflection Cracks	Rutting (in.)	Top-down Longitudinal Crack (%)	Bottom-up HMA Fatigue Cracking (%)	IRI (in./mi)
0/0	0	0	0	0	0	63
5/2.5	1.1	All transverse joints	0.11	0	0	93
10/5	3.9	All transverse joints plus 3.9% slabs	0.15	0	0	100
15/8	8.1	All transverse joints plus 8% slabs	0.19	0	0	107

[a] Age in years and trucks in millions in design lane (multiply by 2 to obtain rigid ESALs).

[b] All bottom-up fatigue cracking.

expected to show structural deterioration for more than 5 to 10 years. Because of yet-unresolved issues with the use of *MEPDG* for the design of PCC/PCC composite pavements (specifically with the Enhanced Integrated Climatic Model [EICM] and *k*-value issues with using the "bonded PCC over PCC overlay" design procedure in the *MEPDG* for PCC/PCC composite pavements), the *MEPDG* was not directly used for designing the PCC/PCC composite pavement at MnROAD. As detailed in Volume 2 of the report, the *MEPDG* issues were eventually resolved, resulting in the SHRP 2 R21 version of the *MEPDG* (version 1.3000:R21).

Construction of the Test Sections

The construction project was awarded to C. S. McCrossan, Inc. of Maple Grove, Minnesota. WSB and Associates, Inc. was responsible for the administration of the construction contract and the inspections. Representatives and researchers from MnDOT, the University of Minnesota, Applied Research Associates, Inc., FHWA Mobile Concrete Lab, and the University of Pittsburgh were on site during all phases of construction to manage, monitor, and record various construction activities; sample and collect data; and instrument the test sections. Table F.4 shows a timeline of the major steps involved in the construction process.

Table F.4. Construction Timeline for Major Tasks

Major Task	Date
Salvage and recycling operations	April 12–16, 2010
Trimming and grading of subgrade	April 19–22, 2010
Aggregate base placement	April 23, 2010
Trimming base and preparing for PCC instrumentation placement	April 26–30, 2010
PCC placement and instrumentation (for HMA/PCC composite pavement), Cell 70	May 5, 2010
PCC placement and instrumentation (for PCC/PCC composite pavement), Cell 71	May 6, 2010
PCC placement and instrumentation (for PCC/PCC composite pavement), Cell 72	May 10, 2010
HMA placement and instrumentation, Cell 70 plus shoulders	May 20, 2010
Saw and seal bituminous joints	May 22, 2010
Conventional diamond grinding (passing lane), Cell 71 and a portion of Cell 72	May 25, 2010
Next-generation diamond grinding (driving lane), Cell 71 and a portion of Cell 72	May 27, 2010
Final sweeping of project	May 28, 2010
Open to traffic	July 7, 2010***

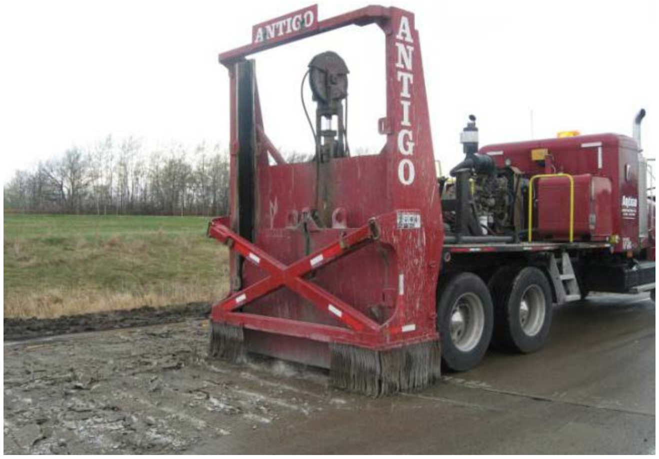

Figure F.4. Guillotine crusher breaking existing concrete for recycling into the PCC layer of the HMA/PCC composite pavement.

Recycling Operations

The recycling operations consisted of breaking (using an Antigo guillotine breaker), removing, transporting, crushing, washing, screening, and stockpiling the concrete pavement material from an existing MnROAD cell to be used as coarse aggregate in the recycled concrete mix. The concrete portions of the existing cells were broken with a guillotine crusher (Figure F.4 and Figure F.5), removed (Figure F.6), and transported to a crushing location (Figure F.7). The in-place bituminous shoulders were milled (Figure F.8) and used as reclaimed asphalt pavement for construction of the new HMA shoulders.

The crushing method and system determines some of the qualities of the RCA, such as mortar content and the gradation. An increase in the number of crushing processes reduces the

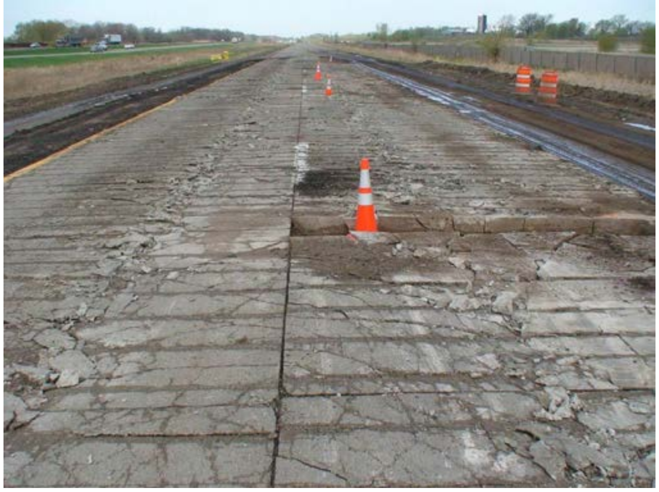

Figure F.5. Existing concrete pavement following breaking using the guillotine crusher.

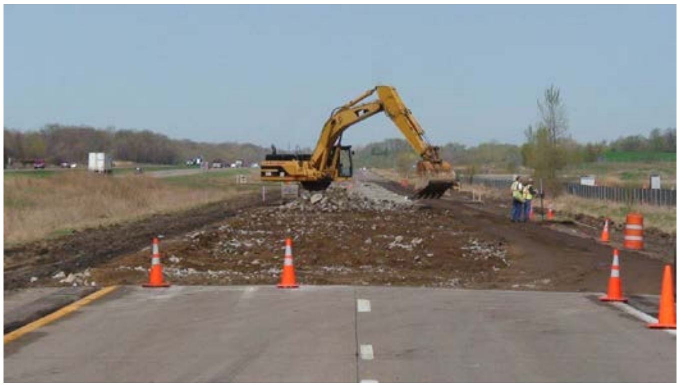

Figure F.6. Removal of existing concrete pavement for recycling.

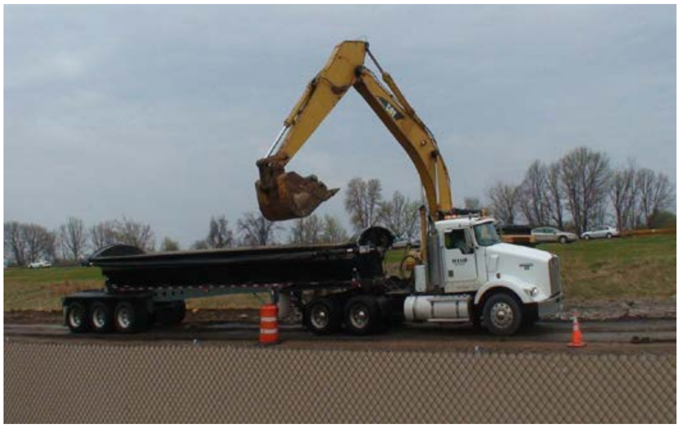

Figure F.7. Transportation of existing concrete pavement for recycling.

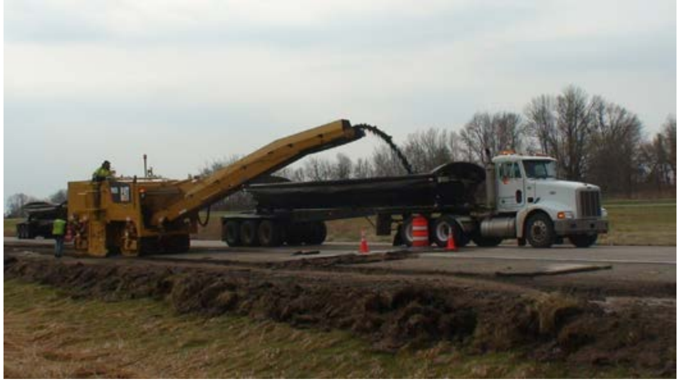

Figure F.8. Milling of existing HMA shoulder to be used as recycled asphalt pavement (RAP) in the construction of new HMA shoulders.

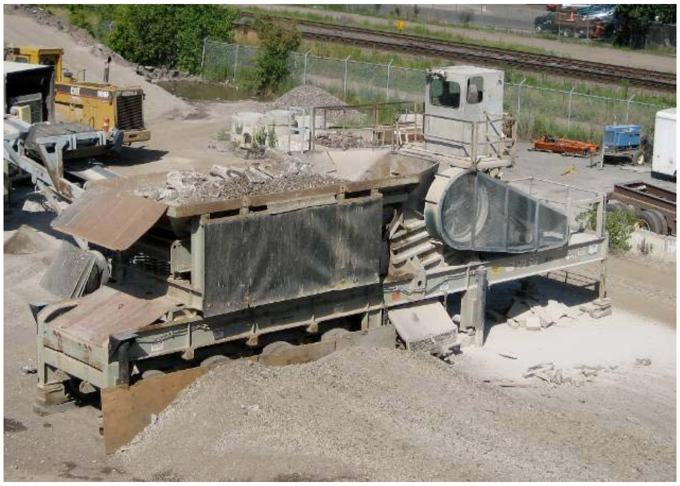

Figure F.9. The primary crusher was the jaw crusher operating at less than full capacity.

mortar content (Sanchez de Juan and Gutierrez 2009). As specified, all joint material, reinforcing members, and other inert materials (such as wood) were separated from the concrete sections before the existing concrete was crushed into coarse aggregate. For this project, the contractor used an industrial crushing operation that included a primary jaw crusher (Figure F.9) operating at less than full capacity and a secondary cone crusher (Figure F.10), then washed, screened, and stockpiled. The jaw crusher jaws were distanced to adjust the maximum aggregate size produced. The cone crusher was used as secondary crusher to further remove the mortar from the natural aggregates. A cone crusher squeezes material between an eccentrically gyrating spindle and a bowl below.

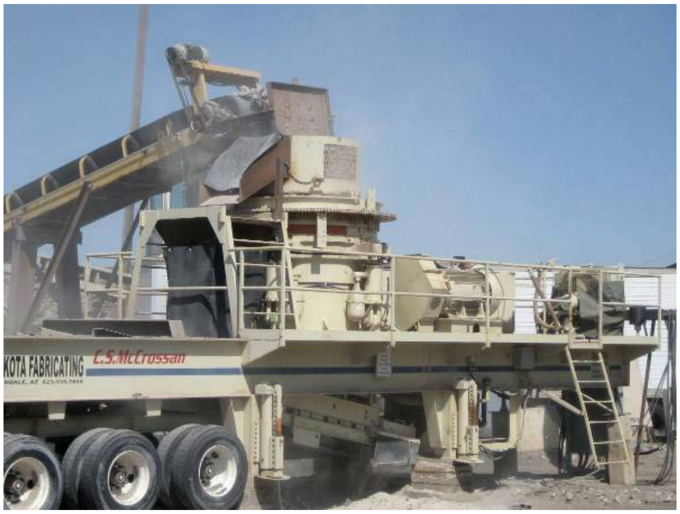

Figure F.10. Cone crusher was used as secondary crusher to further remove the mortar from the natural aggregates.

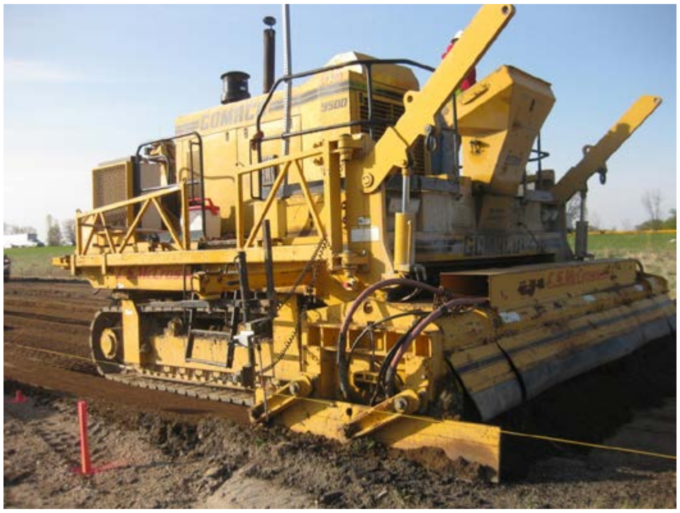

Figure F.11. Trimming the subgrade using a string line and trimmer.

As the pieces are broken, they fall to the lower, more closely spaced part of the crusher and are further crushed until small enough to fall through the bottom opening.

Laboratory tests on the recycled aggregate (AASHTO T84 and T85) revealed that the RCA absorption was 2.93%.

Subgrade Soil Grading and Compaction

A string line was set for trimming of the subgrade and the base. The subgrade was cut with a Gomaco 9500 trimming machine (Figure F.11) and compacted with a Dynapac CA262 steel drum roller (Figure F.12 and Figure F.13). Hand holes and conduits were set for the instrumentation cables (Figure F.14).

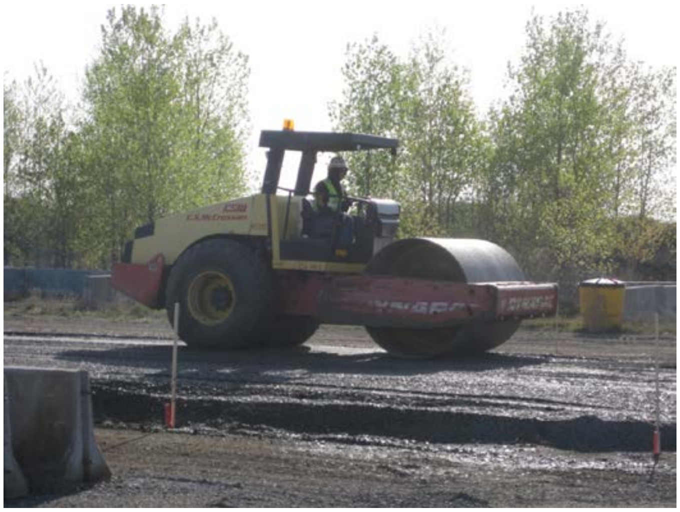

Figure F.12. Compacting the subgrade using a steel drum roller.

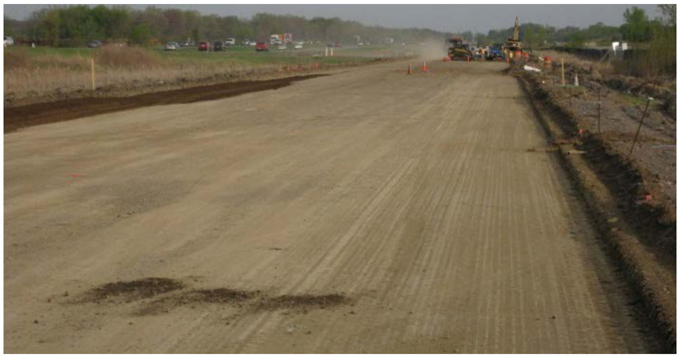

Figure F.13. Trimmed and compacted subgrade.

Testing was performed on the compacted subgrade using a dynamic cone penetrometer (DCP), lightweight deflectometer (LWD), and falling weight deflectometer (FWD). The Class 5 aggregate base was constructed in two 4-in. lifts.

PCC Mix Design

Numerous options were considered for PCC mixes to be used in the top and lower lifts of the PCC/PCC composite pavement. This involved a series of iterations on mix design followed by laboratory testing of the mixes. Three PCC mixes were used in the construction at MnROAD. These were designated as RCA, low-cost, and EAC, as detailed below. To gain some experience with paving the stiff "dry" PCC mix that was required for the lower PCC lift and to incorporate recycled aggregates in the

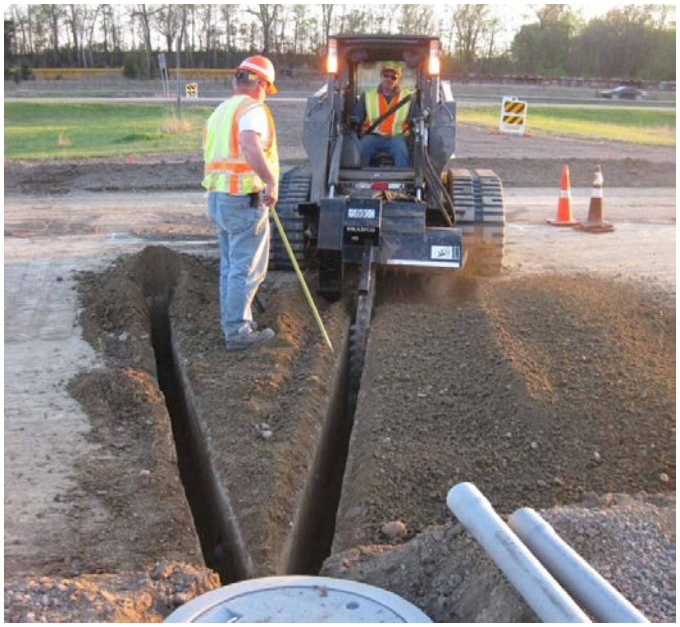

Figure F.14. Installing conduits to carry and protect the instrumentation cables.

HMA/PCC composite pavement, the RCA mix was also used as the lower PCC layer for the HMA/PCC composite pavement.

For this SHRP 2 R21 project, a "high-quality" PCC mix for the upper layer of PCC/PCC composite pavements is defined as a PCC mix containing increased cement content (relative to the American PCC paving standard of roughly 500 to 600 lb/yd^3 [297 to 357 kg/m^3]) and a high-quality, very durable aggregate (i.e., granite). Ideally, the aggregate in the upper lift must be gap-graded and of a maximum size no larger than 0.3 in. (8 mm). Although German and Austrian mix designs do not typically contain fly ash, it was used in mixes at MnROAD. In addition, the research team aimed for a PCC mix for the lower PCC that would contain reduced cement (relative to the standard described above), locally available natural fine aggregates, and a coarse RCA as a low-cost alternative coarse aggregate. All basic components of the lower-layer PCC were selected in light of a desire to reduce costs, investigate methods of sustainability, and investigate the reuse of materials into structural components. Each of the PCC mixes used is summarized below and in Table F.5.

RCA PCC Mix Design

Per the special provisions, the RCA comprised 50% of the total coarse aggregate in the PCC mix. In addition, aggregate fines less than 4.75 mm (no. 4) and coarse aggregates greater than 25.4 mm (1 in.) used in the PCC mix were specified to come from virgin aggregate sources. The special provisions also required the contractor to clean and wash the RCA. As much as 10% of the total recycled coarse aggregate could consist of bituminous particles. The cementitious fraction was specified to consist of as much as 60% supplementary cementitious materials (SCMs), including but not limited to fly ash. Fly ash replacement of 40% was approved and used in the final mix design. The main concern regarding this mix was the use of coarse RCA. As a result of these concerns, an extensive investigation into the use of RCA for structural PCC was conducted. This included laboratory work investigating aggregate absorption, gradation, freeze–thaw durability, aggregate washing/preparation, and methods of crushing.

Low-cost PCC Mix Design

Per the special provisions, the cementitious fraction was specified to consist of as much as 60% SCMs, including but not limited to fly ash. Fly ash replacement of 60% was approved and used in the final mix design for the low-cost PCC mix. The main concern regarding this mix had to do with setting time and early strength because of the high fly ash replacement

Table F.5. PCC Mix Design for PCC/PCC Construction at MnROAD

	Weight (per yd^3)		
	RCA PCC	**Low-cost PCC**	**Upper-layer PCC**
Materials			
Water	234 lb	173 lb	283 lb
Cement	360 lb	240 lb	616 lb
Fly ash	240 lb	360 lb	109 lb
Sand	1,200 lb	1,263 lb	843 lb
CA No. 1 (virgin aggregate, 1½ in. maximum aggregate size)	825 lb	787 lb	na
CA No. 2 (recycled aggregate)	920 lb	na	na
CA No. 3 (virgin aggregate, ¾ in. maximum aggregate size)	na	1,102 lb	na
⅜ in. Washed granite chips	na	na	843 lb
½ in. Washed granite chips	na	na	1,133 lb
Air entrainer	2–15 oz	2–15 oz	2–15 oz
Hydration stabilizer	na	na	0–5 oz
Water reducer	1–5 oz	1–5 oz	1–5 oz
Accelerator	0–30 oz	0–30 oz	na
Properties			
Water-cement ratio	0.39	0.29	0.39
Maximum slump	3 in.	3 in.	3 in.
Entrained air content	7%	7%	7%

percentage. However, it should be noted that although 60% is atypical, this level of cement replacement is possible and has been accomplished for other transportation concretes. Furthermore, a high percentage of cement has successfully been replaced using slag as the SCM in many construction projects throughout Europe.

Upper-layer PCC Mix Design

The upper-layer PCC mix included high cement content (616 lb/yd^3) in addition to 15% fly ash substitution. The mix incorporated polish-resistant, granite aggregates with a high cement content that would allow for an exposed aggregate surface texture. The mix included as needed hydration stabilizer for slump retention.

The portland cement used was a Holcim, St. Genevieve Type 1/2 cement. The fly ash was a Class F, Headwaters Coal Creek fly ash. The fine aggregate was an Elk River Concrete Sand. The coarse aggregate comprised No. 67 ¾-in. and No. 4 1½-in. Elk River gravel. The coarse aggregate for the top layer PCC comprised ⅜-in. and ½-in. washed granite chips from Martin Marietta. The water reducer, accelerator, and air entrainer were Sika products. The hydration stabilizer was a BASF product. The gravel aggregates and gradation of those aggregates were similar to conventional PCC pavements used by MnDOT for the MnROAD facility. The cement and fly ash information is summarized in Table F.6. The aggregate source and properties are summarized in Table F.7.

Table F.6. Cement and Fly Ash Source and Properties

	Cement	Fly Ash
Manufacturer	Holcim	Headwaters
Mill/Power plant	St. Genevieve @ Bloomsdale, MO (STGBLMO)	Coal Creek @ Underwood, ND (COCUNND)
Type/Class	1/2	C/F
Specific gravity	3.15	2.50

PCC Mix Gradation

The research team elected to use an exposed aggregate concrete (EAC) surfacing for the demonstration slab and mainline sections. Although EAC has been used successfully in Europe,

Table F.7. Aggregate Source and Properties

	Coarse Aggregate	Coarse Aggregate	Fine Aggregate
	RCA Mix[a]		
Pit Name	Aggregate Industries	McCrossan	Aggregate Industries
Town	Elk River	Maple Grove	Elk River
Size	No. 4 (1-½ in. maximum)	Recycled	Concrete sand
Specific gravity	2.75	2.49	2.63
Absorptivity	0.90%	2.93%	0.90%
	Low-Cost Mix[b]		
Pit name	Aggregate Industries	Aggregate Industries	Aggregate Industries
Town	Elk River	Elk River	Elk River
Size	No. 4 (1-½ in. maximum)	No. 67 (¾ in. maximum)	Concrete sand
Specific gravity	2.75	2.69	2.63
Absorptivity	0.90%	1.30%	0.90%
	EAC Mix[c]		
Pit name	Martin Marietta	Martin Marietta	Aggregate Industries
Town	St. Cloud	St. Cloud	Elk River
Size	½ in. washed chips	⅜ in. washed chips	Concrete sand
Specific gravity	2.72	2.72	2.63
Absorptivity	0.40%	0.40%	0.90%

[a] \$135/yd^3.
[b] \$140/yd^3.
[c] \$175/yd^3.

challenges were faced by the Kansas and Michigan DOTs in applying these techniques in the United States. A key issue regarding attaining a low-noise, high-durability EAC texture is the aggregate gradation of the PCC surface mix. Gradations for the PCC surface mix and the lower lift PCC mixes were chosen based on a combination of laboratory testing, communication with contractors and engineers and review of research reports from construction in Kansas and Michigan, and communication with engineers and contractors in Europe. To obtain a high-quality EAC texture, a gap-graded mix (small percentage between No. 4 and No. 16 sieve sizes) with maximum aggregate size less than 8 mm is desirable for the PCC surface mix. This results in closely spaced aggregates with a negative surface texture. However, limitations of construction funds and sources of aggregates close to MnROAD necessitated modifications to the original specifications. The modifications included use of maximum aggregate size of 9.5 mm and a denser gradation. The gradation ranges specified in the original and updated specifications along with the final approved gradation are shown in Table F.8 and in Figure F.15 through Figure F.18. Note the difference between Figure F.17 and Figure F.18 at the ⅜-in. sieve size and between No. 4 and No. 16 sieve sizes.

HMA Mix Design

The job mix formula (JMF) for the HMA mix proposed by the contractor and approved by the DOT included local granite and limestone sand and gravel. The target HMA amount was 5.4% with 4.0% air voids. Tests indicated a gyratory density of 2,386 kg/m^3 (149 lb/ft^3) at 90 design gyrations. One hundred percent of the aggregates pass the 19-mm (¾-in.) sieve, and 4.5% of the aggregates pass the No. 200 sieve. The aggregate source and properties are summarized in Table F.9, and the final approved gradation chart is shown in Figure F.19.

Paving Operations

The paving operations for the construction of HMA/PCC composite pavement at MnROAD are summarized below:

1. Place lower PCC layer. The lower PCC layer was paved on May 5, 2010 (Figure F.20) using the slipform paver GOMACO GHP2800. Paving began at 7:30 a.m. and ended at 12:15 p.m. The tie bars and dowel bars (with the use of dowel baskets) were placed in the lower layer of the concrete at the middepth (75 mm [3 in.]) of the PCC layer. Dowels were used only in the driving lane, whereas the passing lane was nondoweled as per plans. The pavement layers were instrumented with embedded thermocouples, moisture sensors, dynamic strain gauges, and vibrating wire strain gauges, as detailed in Appendix H. There were some issues present with the air content of the mix, and four loads were rejected. The slump was generally close to 1.5 to 1.75 in. (the low slump RCA concrete was chosen as a trial run for paving the PCC/PCC composite pavement the next day). Table F.10 shows the slump and air content test results for the PCC mixes.
2. Finish smooth. The surface was finished smooth to remove surface irregularities (Figure F.21).
3. Texture surface (longitudinal tined). The surface of the PCC layer was longitudinally tined to texture the surface and ensure a mechanical bond between the PCC and HMA layer (Figure F.22). Texturing the surface of the concrete has been shown to improve bond strength (Al-Qadi et al. 2008, Leng et al. 2008).
4. Spray on a curing compound. The surface of the PCC layer was sprayed with a curing compound to control the surface drying of the PCC and minimize early-age distresses (Figure F.23). The PCC was specified to be cured for 7 days or until the flexural strength of the concrete samples reached 550 psi, before the HMA layer was to be placed. There was some concern that the curing compound would reduce the bond between the HMA and PCC. Bonding will be examined over time through coring and nondestructive testing. It began raining the afternoon of the paving of the PCC layer. However, paving finished 15 minutes after the rain began, and the entire PCC placed was covered with polyethylene within 30 minutes after the end of paving.
5. Saw concrete joints. Unsealed single saw cuts for both transverse and longitudinal joints were cut in the PCC as soon as it gained adequate strength to perform the saw cutting operation without spalling the PCC. Both transverse and longitudinal joints were cut at a depth of *T*/3, where *T* indicates the thickness of the PCC (50 mm [2 in.] for the 150-mm [6-in.] PCC).
6. Pave HMA surface. The HMA surface was specified to be paved after 7 days or a concrete flexural strength of 550 psi. The paving of the HMA layer was performed on May 20, which is 15 days after the construction of the PCC layer at the discretion of the paving contractor, due to weather-related delays. A bituminous tack coat was sprayed on the concrete before the HMA paving to further help ensure adequate long-term bonding between the PCC and the HMA (Figure F.24). Applying a tack coat to the PCC surface has been shown in previous laboratory and field studies to improve bond strength (Donovan et al. 2000, Al-Qadi et al. 2008, Leng et al. 2008).
7. Saw and seal HMA over the PCC transverse joints. Bituminous transverse joints were cut with a single saw cut

Table F.8. Aggregate Gradation for PCC Mixes

Designation	37.5 mm (1½ in.)	31.5 mm (1¼ in.)	25.0 mm (1 in.)	19.0 mm (¾ in.)	16.0 mm (⅝ in.)	12.7 mm (½ in.)	9.5 mm (⅜ in.)	6.3 mm (¼ in.)	4.75 mm (No. 4)	2.36 mm (No. 8)	1.18 mm (No. 16)	.030 mm (No. 50)	.015 mm (No. 100)	.0075 mm (No. 200)
Working range limits	±5	±5	±5	±5	±5	±5	±5	±5	±5	±4	±4	±3	±2	1.6% maximum.
RCA PCC mix														
As-written specifications	100	97–87	87–77	76–66	70–60	63–53	55–45	na	41–31	30–20	23–13	14–4	10–1	7–1
Updated specifications	100	100	95–80	85–70	na	70–55	60–45	55–40	50–35	45–30	35–25	10–2	10–0	5–0
Final approved PCC blend	100	100	88	73	na	54	46		41	37	30	6	1	0.2
Low-cost PCC mix														
As-written specifications	100	97–87	87–77	76–66	70–60	63–53	55–45	na	41–31	30–20	23–13	14–4	10–1	7–1
Updated specifications	100	100	95–80	85–70	na	70–55	60–45	55–40	50–35	45–30	35–25	10–2	10–0	5–0
Final approved PCC blend	100	100	89	76	na	64	56	49	42	37	30	6	1	0.2
Upper-layer high-quality PCC mix														
As-written specifications	100	100	100	100	100	100	100	75–65	48–38	48–38	48–38	13–7	7–1	5–1
Updated specifications	100	100	100	100	100	100	100–95	75–65	55–45	40–30	35–25	13–7	7–1	5–0
Final approved PCC blend	100	100	100	100	100	100	98	69	48	33	29	11	2	0.4

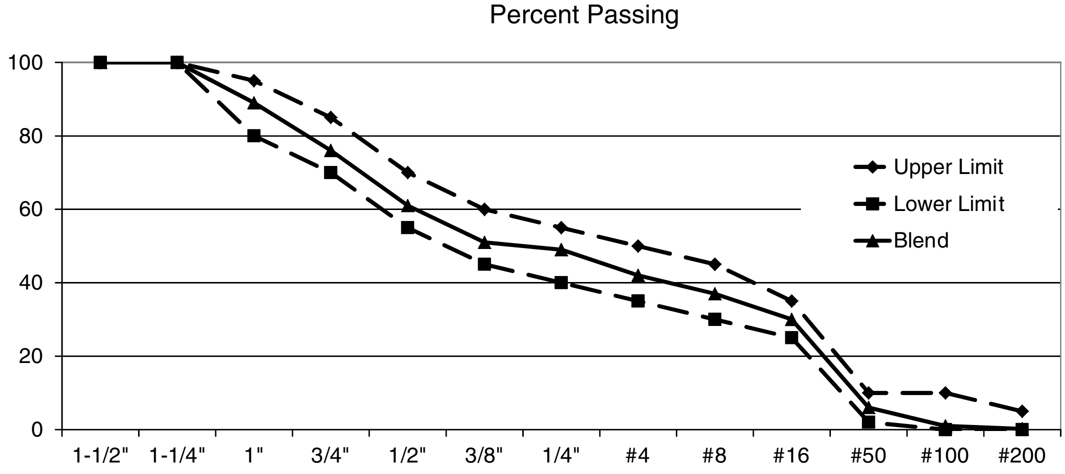

Figure F.15. Gradation limits and final approved blend gradation for RCA mix.

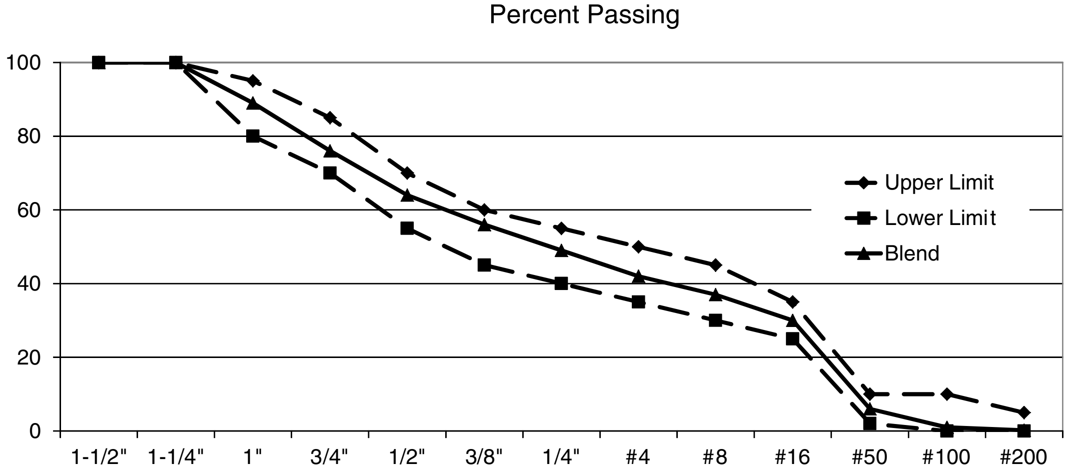

Figure F.16. Gradation limits and final approved blend gradation for low-cost mix.

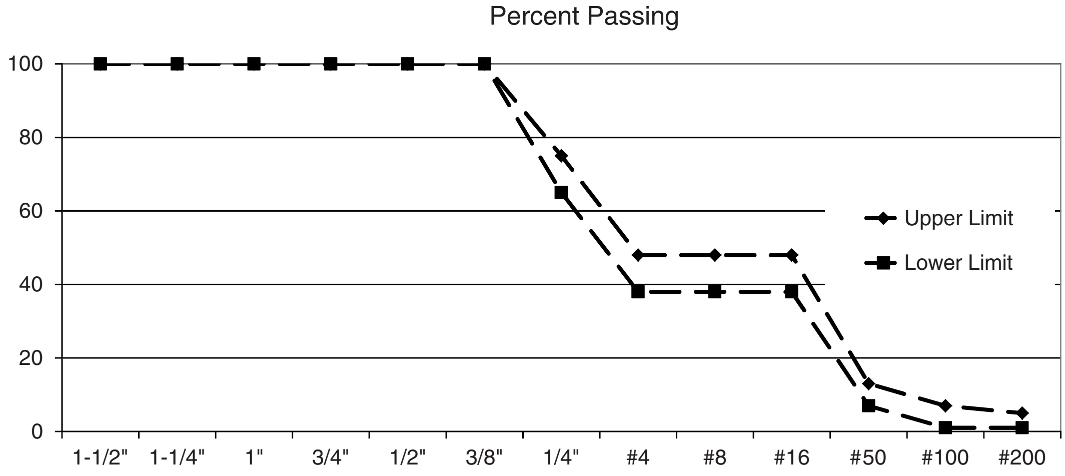

Figure F.17. Initially specified (based on research and communication with European consultants) gradation limits for the EAC mix.

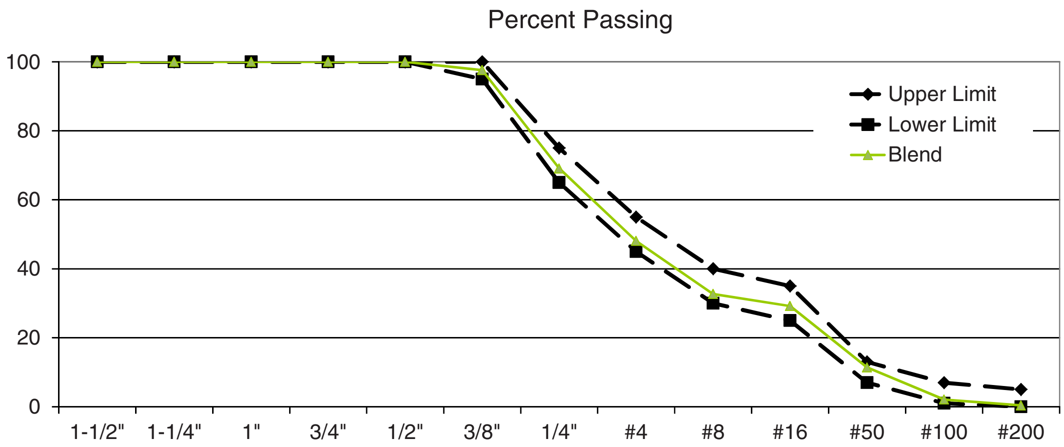

Figure F.18. Modified specification gradation limits (based on what could reasonably be achieved with the cost limitations) and final approved blend gradation for the EAC mix.

Table F.9. Aggregate Source and Properties for HMA Mix

Percent Used	Pit Name	Town	Material	Specific Gravity
20	Martin Marietta	St. Cloud	CA-50 (granite)	2.707
11	Kraemer	Burnsville	Lime sand (limestone)	2.716
44	Martin Marietta	St. Cloud	Washed sand (granite)	2.677
5	Kraemer	Burnsville	⅜ in. Chip (limestone)	2.664
20	Plant RAP	Maple Grove	na	2.646
			Mix	**2.680**

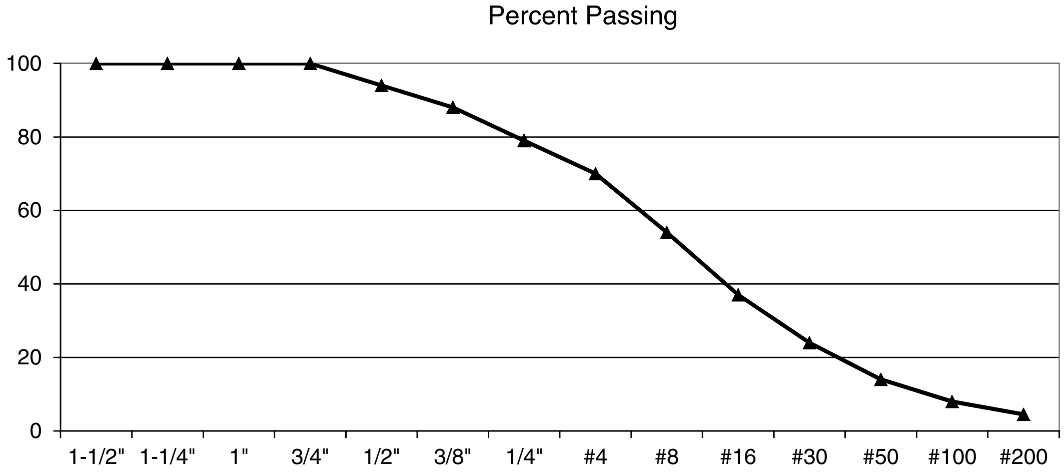

Figure F.19. Final approved JMF aggregate blend gradation for HMA mix.

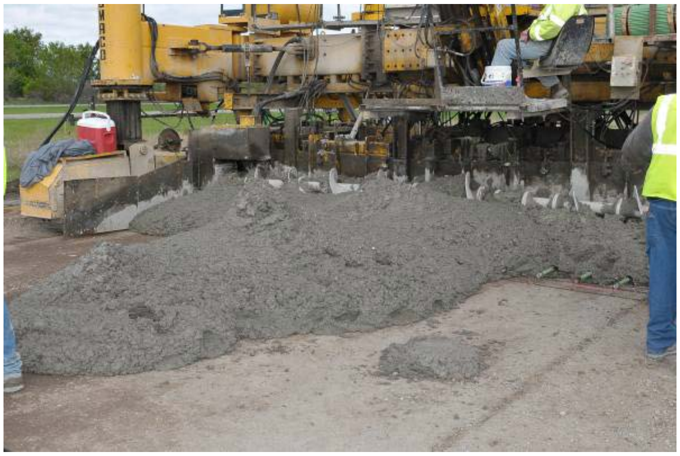

Figure F.20. Placement of PCC layer on the aggregate base.

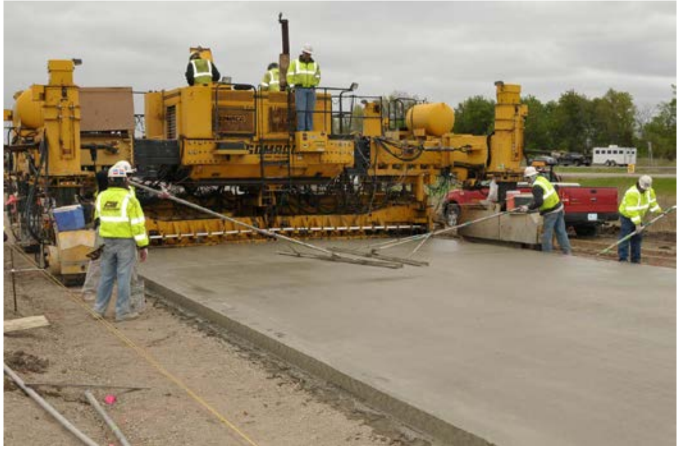

Figure F.21. Finishing the PCC surface to remove surface irregularities.

of 12.5 mm (0.5 in.) wide by 16 mm (⅝ in.) deep for the HMA layer (Figure F.24). The sawn bituminous joints were specified to be located within 12.5 mm (0.5 in.) of the concrete joints. The contractor ensured this by using stakes beyond the aggregate shoulders to mark the location of the joints in the PCC. Six joints were left unsealed for research purposes.

Paving operations for the PCC/PCC test sections began on April 28, 2010, with the construction of a 200-ft demonstration slab and concluded on May 10, 2010, with the completion of 950 feet of test sections along the mainline (I-94) test area. The two-lift paving used two GOMACO model GHP2800 pavers and a belt placer between the two pavers to place fresh mix for the upper lift (Figure F.25).

Many aspects of the paving were similar to those of a normal single-layer PCC pavement. As detailed in Table F.2, the pavement design included 1.25-in. dowels, placed at the middepth of the full slab using dowel baskets. Furthermore, the design included 30-in. long No. 4 tie bars spaced at 30 in. to reinforce longitudinal joints, which were inserted using a tie-bar inserter attachment on the first paver. One difference

Table F.10. Cell 70 Fresh Concrete Testing

Time (a.m.)	Slump (in.)	Air Content (%)
7:30	0.75	7.0
7:50	1.5	10.8
8:15	NA	10.6
9:07	3.25	8.5
9:43	1.5	6.8
10:55	1.75	6.8

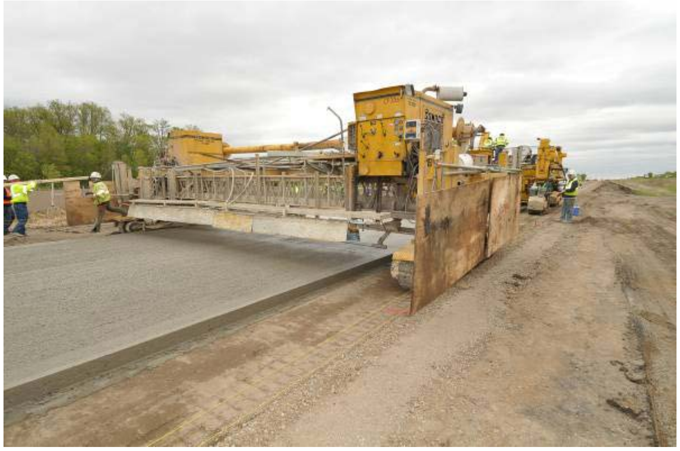

Figure F.22. Tining the PCC surface to provide texture for mechanical bonding between PCC and HMA layers.

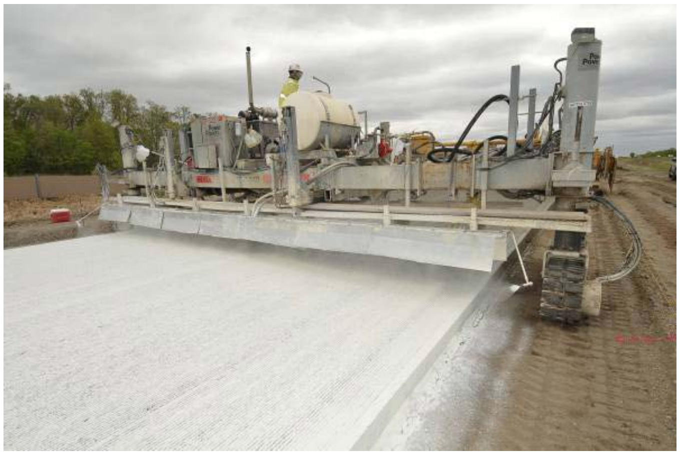

Figure F.23. Applying curing compound to the surface of the PCC to control surface drying of the PCC and minimize early-age distresses.

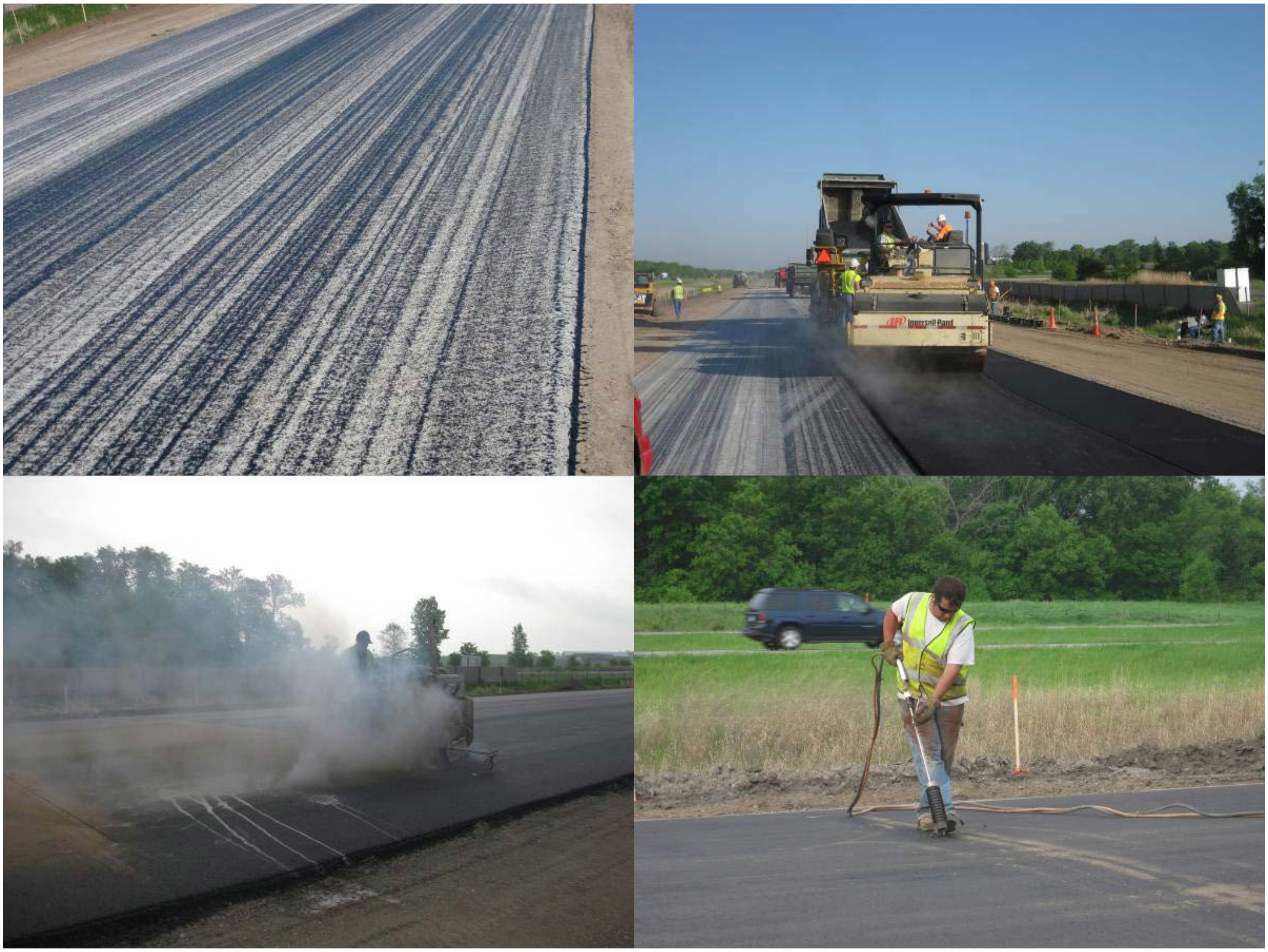

Figure F.24. Tack coat applied to PCC surface (top left) before HMA paving (top right). Sawing (bottom left) and sealing (bottom right) HMA layer; saw cuts in the HMA were matched to the saw cuts in the PCC below to within 12.5 mm (0.5 in.).

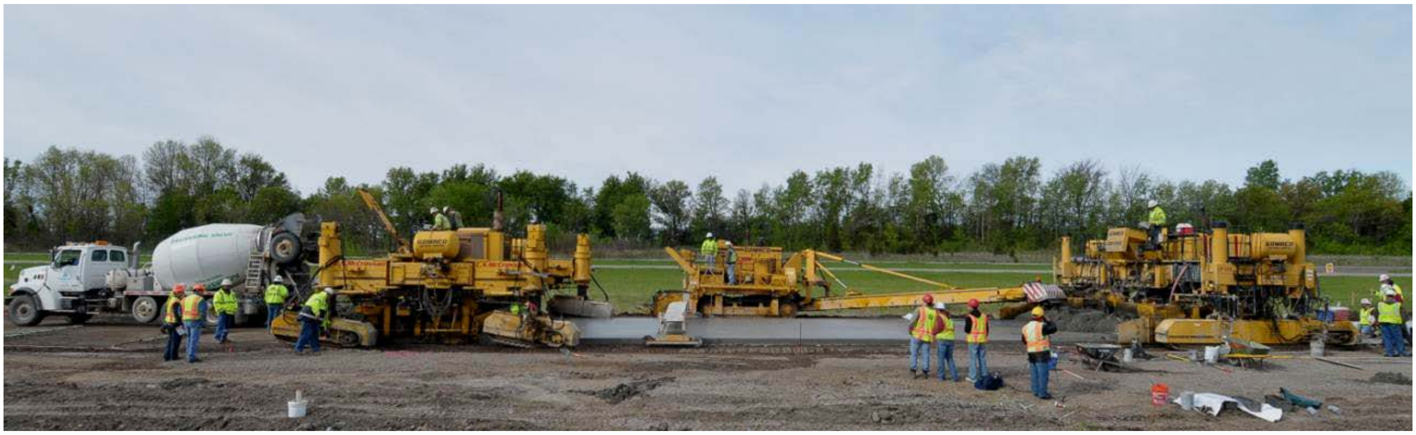

Figure F.25. Paving train constructing R21 test sections along I-94 at MnROAD. Pictured from left to right are the mixer truck, first paver, belt placer, and second paver.

in the use of two pavers in PCC/PCC versus single-layer PCC is that the upper lift paver was adjusted to "crown" the lower lift slab by 0.75 in. on each side; that is, the second paver paved a lift 1.5 in. wider than did the first paver in the train.

Unlike the paving trains encountered in Europe, which use low-frequency vibration on the second paver only, the paving train used for the MnROAD construction used vibrators in both pavers (the first paver set to 8,000 vpm, the second paver set to 4,000 vpm). Methods differ on this point due, in part, to the use of automated dowel bar inserters in Europe. Because of the use of dowel baskets for placing the dowel bars, vibrating the lower lift PCC was necessary to consolidate the PCC mix around the dowel bars. However, given the height of the dowel baskets (4.5 in.) and the small thickness of the lower PCC lift (6 in.), the vibrations were surficial. The vibration in the second paver was low and shallow to avoid overmixing the two PCC layers, particularly at the interface, and thus ensure the integrity of the individual layers.

The key complications with respect to the paving were those brought about by delays in the delivery of PCC for the two lifts. Although the construction specifications indicated that paving of the second lift was to occur no later than 90 minutes after the first lift (ideally no later than 60 minutes), on all three occasions of PCC/PCC paving (demonstration slab and two mainline sections), the paving was stalled for more than 90 minutes while the arrival of batched upper-lift PCC was awaited. During the construction of the demonstration slab, mix delivery delays led to 90- to 100-foot stretches of the placed lower lift being exposed to the environment for more than 120 minutes before the second lift was placed.

These delays resulted in a few problems that could be observed immediately on-site during paving. The most apparent was the setting up of concrete in the auger, the grout box, and on the profile pan of the paver. Frequent delays allowed the concrete to hydrate and attach to surfaces, normally assumed to be smooth, that physically form the slab. When paving resumed after long delays, concrete that had clung to these surfaces would "tear" at the freshly paved concrete, resulting in the need for additional finishing. Figure F.26 illustrates the tearing discussed above.

The delays in the delivery of the upper PCC compromised the pavement given that the weather during the demonstration slab paving was unseasonably warm, sunny, and windy. Temperatures were between 60°F and 69°F, the sun was strong with no clouds, and the wind was steady at 5 to 10 mph with occasional strong gusts. These conditions are especially critical when the slab in question is composed of the early batches of PCC that arrived for the demonstration slab, which were considerably dry (with measured slump on site of 0.75 to 1 in. from batch to batch). This early "dry" PCC was used for the 90 to 100 ft of lower lift placed at the beginning of the demonstration slab; it was more than 120 minutes before the upper lift was placed. Figure F.26 illustrates the most exaggerated of the shrinkage cracking encountered in these early slabs.

Another concern over delays included the integrity of the bond at the interface of the two lifts. An ultrasonic tomography testing device was used to assess the bond at the transverse joints and at midslab locations on the demonstration slab. Tomograms from two representative scans are shown in Figure F.27.

Ultrasonic reflection occurs only noticeably at the start of the base layer (measured as approximately 8 in.) in the tomogram at left in Figure F.27. However, in the tomogram at right,

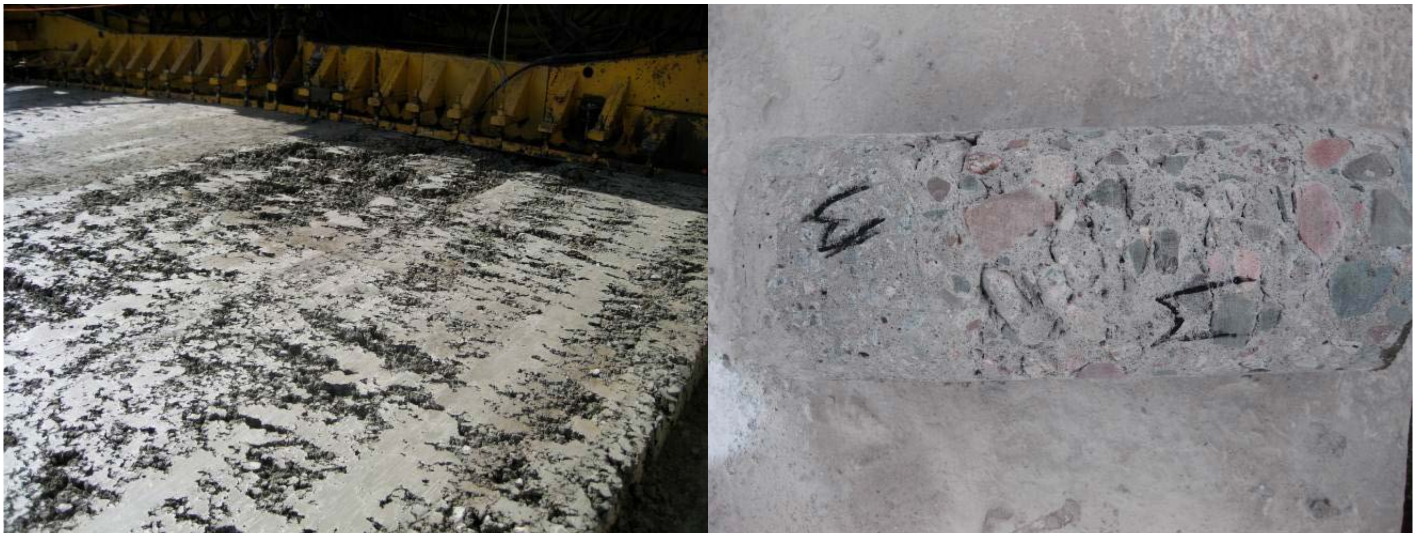

Figure F.26. At left, "torn" edges and surface caused by concrete setting on various parts of the paver; at right, coring showed poor mix consolidation in the lower PCC at select locations.

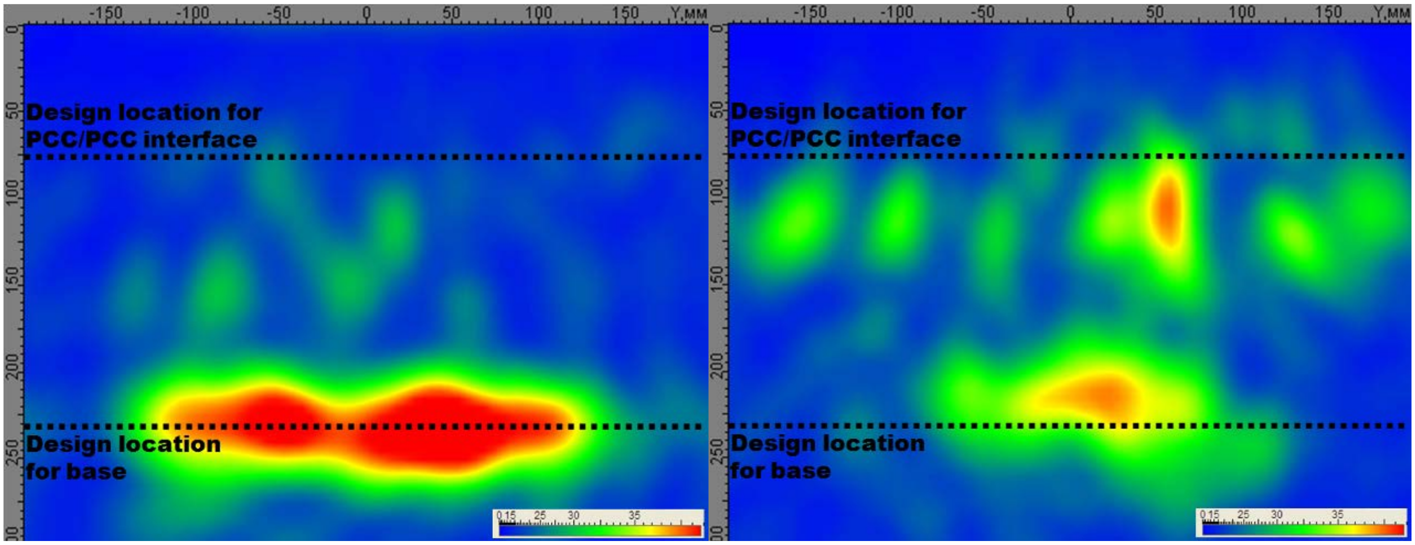

Figure F.27. At left, a typical tomogram from the PCC/PCC demonstration slab at MnROAD; at right, tomogram with ultrasonic reflection near the depth of the PCC/PCC interface.

significant ultrasonic reflections are measured at a depth of approximately 4 in., near the interface of the two PCC layers. This reflection near the interface may be indicative of a poorly developed bond between the two layers of PCC, or it may be indicative of other problems (such as tearing and voids) in the pavement. The scan at left is further evidence that the composite layers, from the view of the tomogram, are a unified layer, whereas the reflections in the scan at right suggests the possibility of internal distress. These conclusions were confirmed by cores taken from the demonstration slab.

Many lessons (regarding mix delivery, lower PCC slump, instrumentation installation, saw-cutting, and so forth) were learned from the construction of the demonstration slab that was incorporated during the construction of the mainline test sections. However, despite the problems encountered during the construction of the demonstration slab, a large portion of the PCC/PCC constructed (particularly the second 100 ft) was found (based on coring and trenching evidence) to meet the requirements of the design with good integrity of the individual PCC layers (no intermixing) and good bond between the PCC layers (Figure F.28).

Paving the mainline sections progressed at a rate of between 1 and 4 ft per minute, and the project contractor was confident that this rate would be greatly increased with a larger project and a consistent supply of PCC for paving. Although joint cuts, sawed to a depth of 3 in., did not necessarily propagate well on the demonstration slab because of construction delays and dry mixes, for the mainline sections all saw cuts were found to propagate as anticipated for a single-lift equivalent slab (the specifications were changed to saw cut one-third the total thickness or top layer thickness plus 0.5 in., whichever is greater, which in this case was a minimum of 3.5 in.).

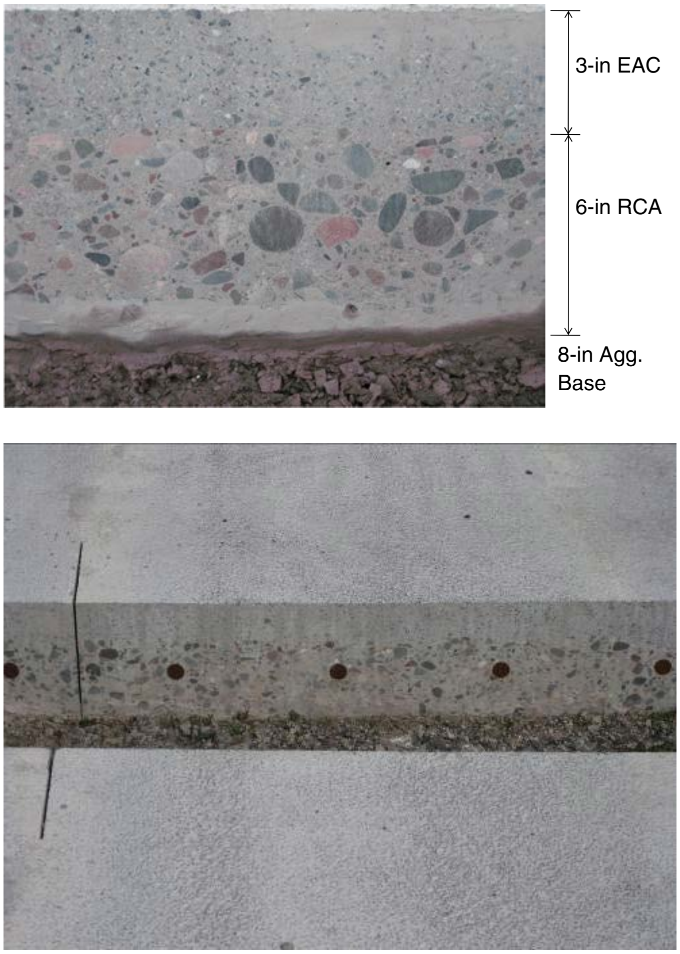

Figure F.28. Cross section of the PCC/PCC demonstration slab constructed at MnROAD showing very good integrity and bond between the two PCC layers.

Mix Design and Delivery

One of the more challenging aspects of the PCC/PCC sections constructed at MnROAD was the PCC itself. This challenge presented itself in two ways: (1) in the development of a mix design that uses alternative materials or meets low-cost specifications and (2) in terms of the logistics behind batching and delivering concrete to meet the demands of the paving operations.

The three PCC mixes used are summarized in Table F.5 and Table F.8 and Figure F.15 through Figure F.18. The most conventional of the three mixes is the PCC mix used for the upper lift, whereas the PCC used for the lower lifts presented challenges in its use of high fractions of fly ash or RCA. The specification for as much as 60% fly ash in the lower lift PCC was inspired by the high fraction of SCM replacement in the new St. Anthony Falls (I-35W) bridge in Minneapolis, which used as much as 81% SCM replacement in its mixes. The existence of a lower lift was also viewed as an opportunity to use lesser quality aggregates. To this extent, a thorough review of existing research on the use of RCA in PCC was performed. This review concluded that RCA was a viable coarse aggregate for the lower lift PCC provided the RCA came from a known source, fines were excluded, and the stockpile was properly maintained (i.e., kept saturated to eliminate variable absorption as a concern).

Both the use of high-fraction SCM replacement and RCA came with the challenges discussed above. These challenges were met with mixing preliminary batches of each mix in the laboratory (Figure F.29). As a result of these tests, adjustments to the mixes were made.

Although this preliminary work addressed some challenges, the two-lift paving at MnROAD revealed a larger problem for the concrete in terms of consistency from batch to batch.

Table F.11. Cell 71 and Cell 72 Fresh Concrete Testing

Time (a.m.)	Section	Mix	Slump (in.)	Air Content (%)
8:10	Cell 71	RCA	1.25	6.6
9:10	Cell 71	EAC	2.25	5.0
9:20	Cell 71	EAC	2.25	6.2
8:23	Cell 72	Low-cost	2.75	7.2
9:33	Cell 72	Low-cost	2.5	6.4
10:14	Cell 72	EAC	3.25	5.7
10:55	Cell 72	EAC	2.0	9.0
11:12	Cell 72	EAC	2.5	7.5

The challenge of providing a consistent batch from truck to truck was thought to be overcome after the demonstration slab. However, paving on the mainline again suffered from the consistency problem, particularly in the case of the lower PCC mixes, whose as-delivered slump varied between 0.25 and 2.75 in. (the target slump was 1 in.). Table F.11 shows the slump and air content test results for the PCC mixes of the trucks that were not rejected. Although the causes of this inconsistency remain uncertain, there are several possible explanations:

- The use of RCA requires close attention. The contractor had secured RCA of a known source and had washed the RCA of fines; however, the preparation of the RCA for batching (most notably, its degree of saturation) was not consistent. One explanation for the inconsistency from batch to batch, as evident in the variable slump, is the inadequate mainte-

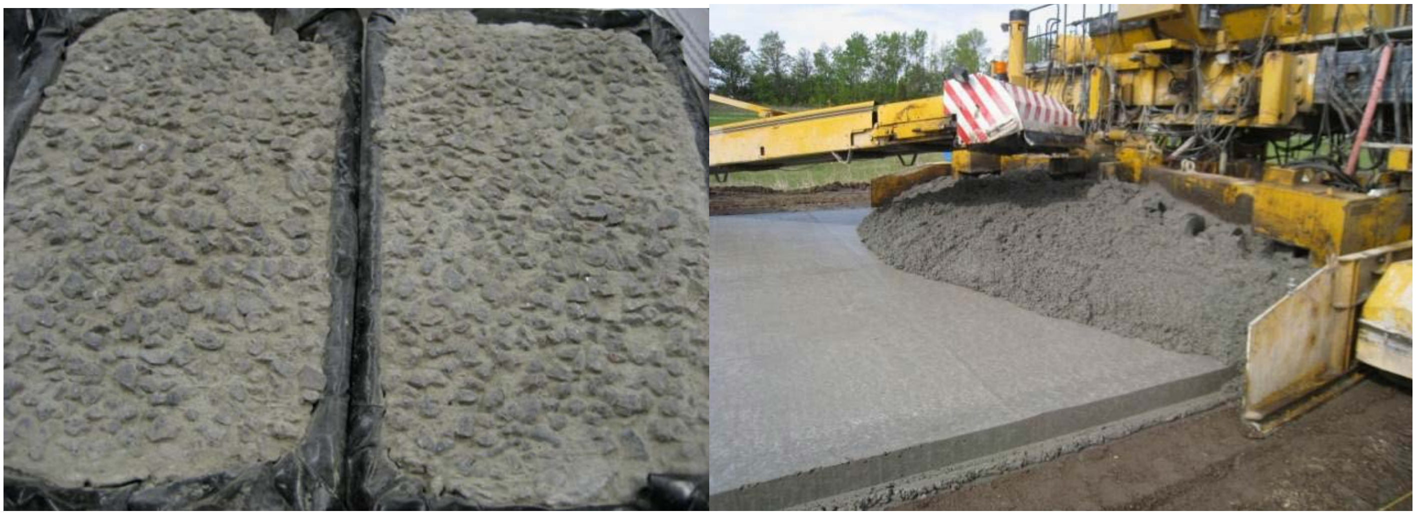

Figure F.29. At left, PCC specimens cast in preparation for the paving and brushing of the PCC/PCC demonstration slab. At right, top surface PCC mix being placed in front of the second paver on site at MnROAD.

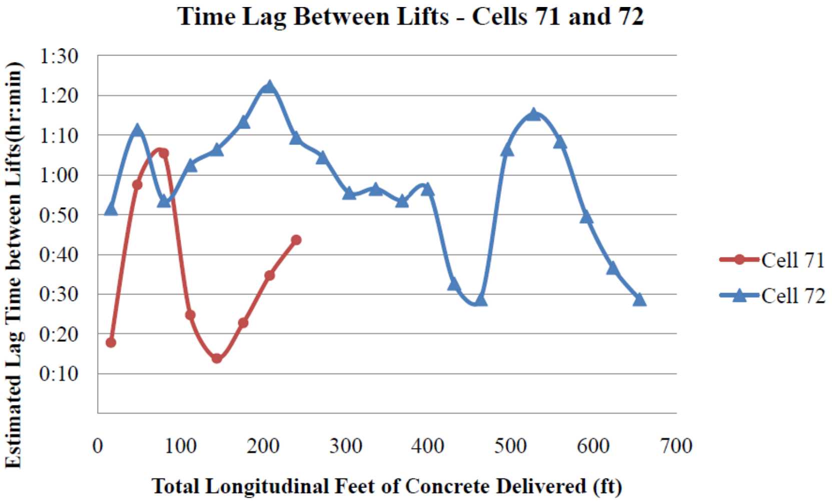

Source: Akkari and Izevbekhai 2011.

Figure F.30. Time lag between lower and upper PCC lifts.

nance of the RCA stockpile (Figure F.31). It is possible that portions of the stockpile had been allowed to dry.

- Another concern to emerge from the use of RCA was the underestimate of unprocessed recycled concrete required to achieve a coarse aggregate of a desired size. Early estimates missed the amount of recycled concrete required, which led to only 275 ft of PCC/PCC using the RCA mix being paved, instead of the originally planned 475 ft. Note that RCA was used in construction of the Cell 70 HMA/PCC test section and the PCC/PCC demonstration slabs and several truckloads had to be rejected (for a variety of reasons, including slump and entrained air).
- The ready-mix supplier used by the contractor did not frequently design concretes using a large fraction of fly ash. As a result, the ready-mix supplier's inexperience in fly ash led to the mix designs being inadequately composed to handle such large amounts of this SCM (in terms of water demands, admixtures, and so forth).
- A final challenge in meeting the mix design for the PCC/PCC pavements was the use of a local ready-mix supplier for the PCC/PCC concrete. Because of the small size and scope of the project, the contractor used a local ready-mix plant, instead of a mobile batching plant, and the use of one plant instead of two (as observed in Europe).

Thus, the observed delays in mix deliveries may have been attributable to the use of a ready-mix supplier that was inexperienced in certain mix designs and in delivering those designs in sufficiently large volumes. Although data are not available for the actual time lag between placing the two PCC lifts based on station location, in MnDOT's construction report for this project, Akkari and Izevbekhai (2011) estimated the time lag between lifts based on truck arrival time taken from the ready-mix supplier's batch tickets. The results are shown in Figure F.30. The figure shows a high amount of variability in the time lag, and although no portion of the paving had a time lag greater than the specified 90 minutes, several portions of the project exceeded the 60-minute mark. During the post-construction review, although the contractor maintained that one plant was enough to accommodate the three mixes for this project, the contractor also stated that a ready-mix plant was not sufficient to provide consistency in mix design and delivery. The contractor was confident that for a larger project, using the company's own mobile batching plant and staff (rather than subcontracting this work to a local ready-mix supplier), mix consistency/delivery would not complicate PCC/PCC paving.

Figure F.31 shows an RCA stockpile being processed and saturated at a concrete recycling facility. Figure F.32 shows the

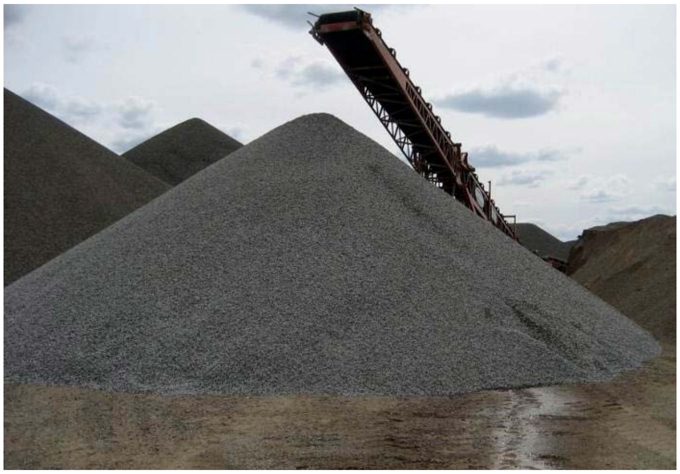

Figure F.31. RCA stockpile being processed and saturated at a concrete recycling facility.

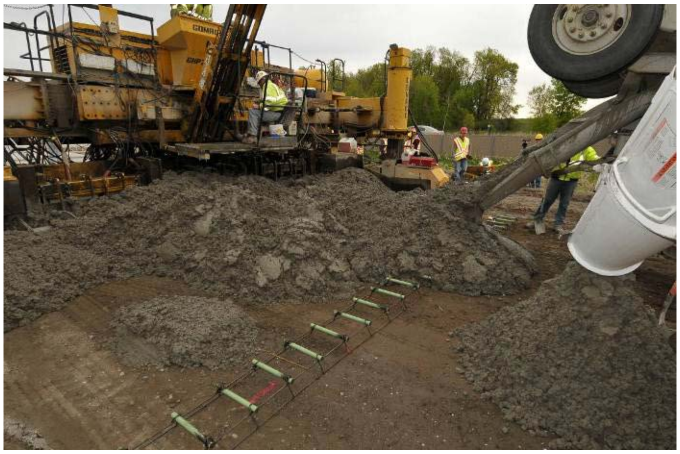

Figure F.32. Placement of the lower PCC mix.

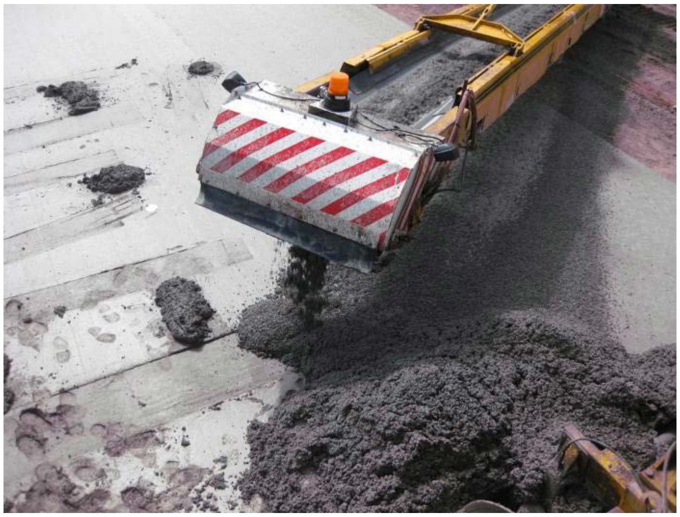

Figure F.33. Placement of the upper PCC mix on the lower PCC layer.

placement of the lower PCC mix (note the dryness and low slump of the mix, which was specified at 1 in.). Figure F.33 shows the placement of the upper PCC mix above the stiff lower PCC layer using a belt placer. The lower PCC layer was stiff enough to carry the impact and weight of the upper PCC layer while being placed (and the weight of an average size person as seen by the footprint impressions on the lower PCC). The footprints also show that the lower PCC layer was still "wet," which is necessary for a good bond between the two PCC layers.

Surface Texturing

The finishing platform used for the construction was a GOMACO model TC600 with Power Pavers Inc TC 2700T spray attachment. After paving, a curing/retarder compound (MBT Reveal from BASF Building Systems) was applied to the surface that acted as a moisture barrier (curing agent) and as a retarder of hydration in the PCC surface. During construction of the demonstration slabs, early applications of the surface treatment were delayed because of mechanical problems on the finishing platform, which provided insufficient pressure to the spray nozzles. The treatment (Figure F.34) was intended to be applied almost immediately after finishing of the placed second lift; however, because of frequent delays, the treatment was applied anywhere between 60 and 90 minutes after the completion of the paving of a given segment. For the construction of the mainline sections, the nozzle heights were adjusted and wind guards were attached to the side of the curing cart to apply the compound more uniformly.

For the demonstration slab and the first day of mainline paving, brushing was initiated anywhere between 5 and 8 hours after paving of a given section had been completed. The brush timing was based on limited laboratory tests, which did not mimic field conditions closely. To compensate for the lack of field experience, the surface was frequently tested at regular intervals, judging the brush readiness of the surface by the amount of cement and aggregate dislodged using a metal rod or handheld brush.

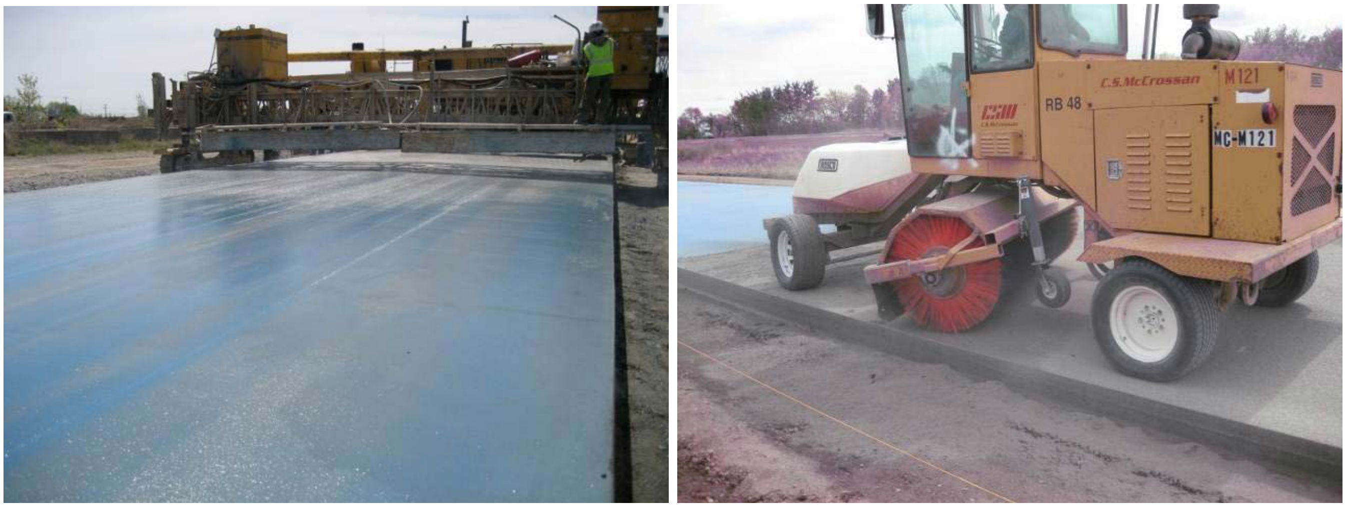

Figure F.34. Treated surface and finishing platform (left)*; equipment for EAC brushing* (right)*.*

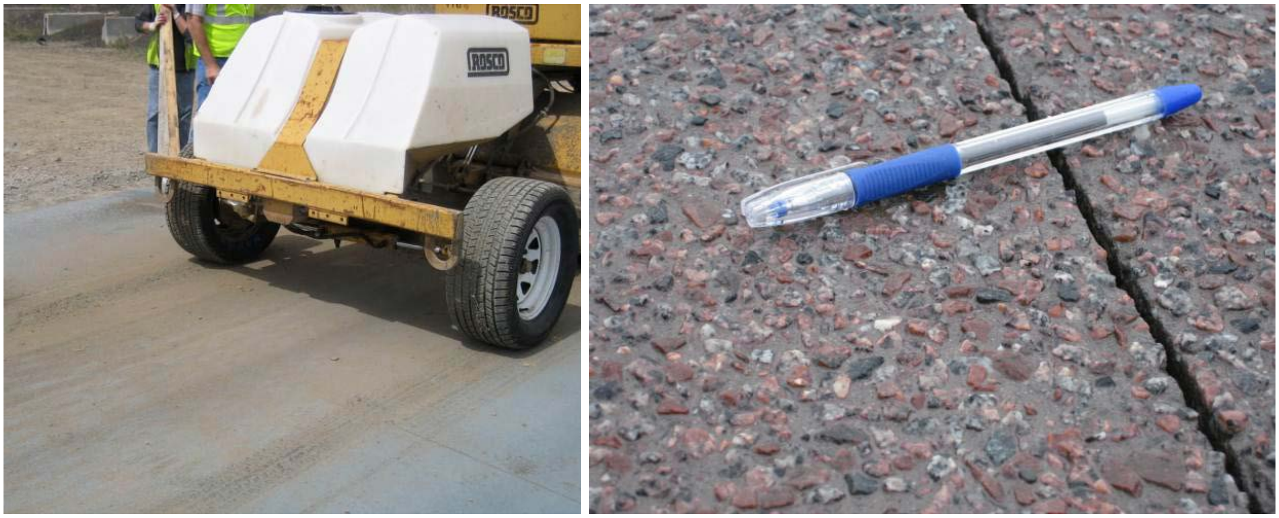

Figure F.35. Surface after first pass with brush (left); finished EAC surface after wash (right).

The brushing was accomplished using a small front-end loader with rotating wire brush attachment (Figure F.34). The brushing was complicated by the inability of the operator to know the depth of texturing with any kind of precision. Thus, the brushing was done in multiple passes to gauge the level of cement removal between the aggregates, which slowly revealed the EAC texture in pass after pass (Figure F.35). The extent of brushing was determined using a combination of a sand patch test and an aggregate peak counting test (Figure F.36). More detail on these techniques can be found in Weinfurter et al. 1994. Although it was not specified, the aggregate peak counting test was an informal quality control for the brushing that was adapted from Austrian methods. It aimed for a count of anywhere between 40 and 50 aggregate points per 25 cm^2 (3.88 in.^{2}), according to Haider et al. (2007). The sand patch test was conducted according to ASTM E965 at intervals as a quality control measure during brushing to ensure that the mean texture depth (MTD) was between 0.8 and 1.2 mm (0.03 to 0.05 in.), as specified. This target was based in part on German and Austrian specifications for texture depth (0.6 to 0.8 mm and 0.8 to 1.0 mm, respectively). The completed average MTD for the EAC surface was 0.76 mm (0.030 in.). Anywhere from two to five passes were needed to obtain the desired texture.

During the paving of the second PCC/PCC test section on the mainline, the construction encountered sudden onset of rain in the late afternoon. A vast portion of the finished, treated PCC/PCC paved was subjected to the rain before being covered with polyurethane sheeting. The delay in sheeting was due to delays in paving and then in the application of the surface treatment. For these reasons, the brush timing was uncertain, and brushing was not initiated until the morning of the next day, 20 hours after the second lift had been placed and after the joints had been sawed. Although an EAC texture was still obtained, because of the various factors (localized

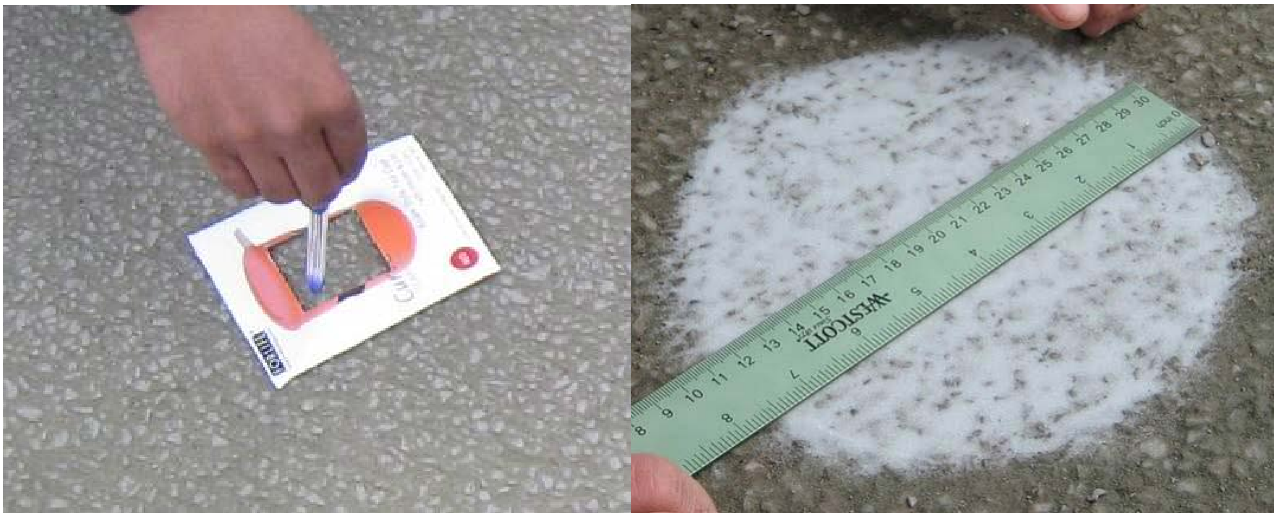

Figure F.36. Quality control tests for brushing: (left) 25 cm^2 test to count aggregate peaks, and (right) sand patch test to determine texture depth.

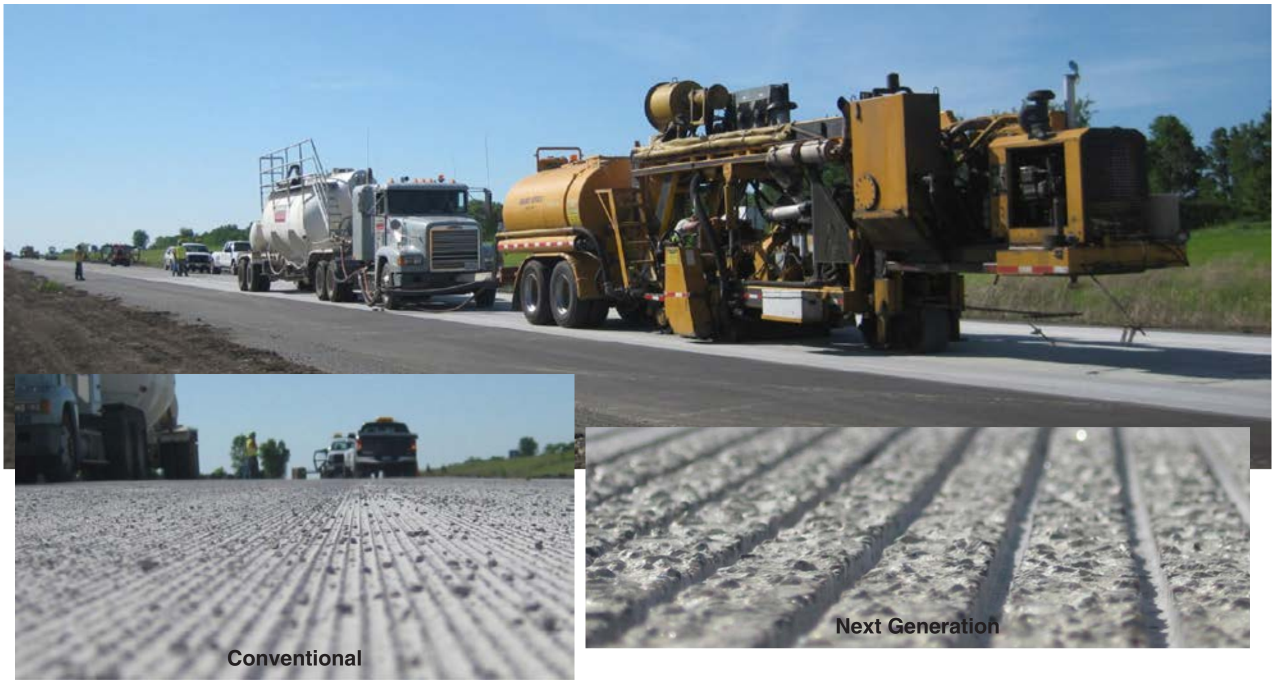

Figure F.37. The initial learning portion of the EAC texture was diamond ground using conventional grinding in the passing lane and next-generation grinding in the driving lane.

washing of some of the curing/retarding compound by rain, low temperatures, variability in application of the curing compound, and so forth) the final texture was less uniform with areas of good EAC texture and other areas of insufficient exposed aggregate. The situation was a reminder of the need to remain aware of the weather and sheet the PCC as soon after placement as possible should rain occur.

As shown in Figure F.37 and described earlier, the initial 475-ft portion of the PCC/PCC EAC texture (all of Cell 71 and a portion of Cell 72) was diamond-ground, resulting in a total of three surface textures for the PCC/PCC sections:

1. 475-ft passing and driving lane EAC;
2. 475-ft driving lane next-generation diamond grind; and
3. 475-ft passing lane conventional diamond grind.

As-constructed Properties

The FHWA Mobile Concrete Lab visited the R21 MnROAD construction site and collected PCC cores and material samples. The results, which are the average of two tests, are summarized in Table F.12. As-constructed material properties for the HMA mix are shown in Table F.13.

According to the Materials and Construction Optimization project (NCPTC 2008), for adequate protection of concrete in a freeze–thaw environment, spacing factor values less than 0.01 in. are desirable, although values less than 0.015 in. are commonly considered acceptable. The spacing factors of all the samples from this project were less than 0.015 in. In fact, the spacing factor of three of the four samples was less than 0.01 in. For specific surface, which indicates the size of the air bubbles, values greater than 600 in.$^{-1}$ are desirable. Three of the four samples that were tested had values higher than 600 in.$^{-1}$. Based on the test results for specific surface and spacing factor, the mixtures used in the composite pavements project have good air void distribution for protection against freeze–thaw damage.

Noise Measurements

Construction of the EAC finish was attempted because of its durability and because it channels water away from the wheelpath in multiple directions. However, the primary benefit of a properly constructed EAC surface is its noise mitigation potential. On-board sound intensity (OBSI) measurements of all of the finished composite pavement surfaces were collected to compare the sound intensity of the various surface finishes (Akkari and Izevbekhai 2011). The EAC and diamond-ground surfaces noise data were compared with those from the HMA/PCC composite pavement.

The OBSI test setup consists of a sedan outfitted with four GRAS sound intensity meters, a Brüel and Kjaer front-end four-channel frequency analyzer and a standard reference test tire. The microphones are suspended from the vehicle frame and positioned at 3 in. vertical displacement and 2 in. lateral displacement from the leading and trailing end of the standard reference tire and pavement contact. The microphones are anchored to a free rotating ring mounted on the right wheel that allows the microphone assembly to be fixed in position and direction without inhibiting the rotation of the tire. The OBSI equipment is shown mounted to the sedan wheel in Figure F.38.

Table F.12. As-constructed PCC Mix Properties (FHWA Mobile Concrete Lab)

Property	Cell 71 RCA Mix	Cell 71 Surface PCC Mix	Cell 72 Low-Cost Mix	Cell 72 Surface PCC Mix
Entrained air content, %	6.5	4.5	6.5	6.5
Unit weight, lb/ft^3	145.3	145.12	148.4	142.8
Flexural strength, psi (7 days)	527	606	468	790
Flexural strength, psi (14 days)	578	798	515	897
Flexural strength, psi (28 days)	665	891	548	816
Flexural strength, psi (90 days)	785	958	669	1,011
Compressive strength, psi (7 days)	3,599	5,314	3,618	5,289
Compressive strength, psi (14 days)	3,890	5,628	4,071	5,260
Compressive strength, psi (28 days)	4,305	5,855	5,062	5,663
Compressive strength, psi (90 days)	5,663	7,598	6,695	7,388
Modulus of elasticity, psi (7 days)	4.30×10^6	4.76×10^6	4.73×10^6	4.45×10^6
Modulus of elasticity, psi (14 days)	4.87×10^6	4.82×10^6	NA	4.44×10^6
Modulus of elasticity, psi (28 days)	4.83×10^6	4.95×10^6	5.11×10^6	4.83×10^6
Modulus of elasticity, psi (90 days)	5.42×10^6	5.46×10^6	5.77×10^6	5.04×10^6
Poisson's ratio (7 days)	0.22	0.26	0.21	0.25
Poisson's ratio (14 days)	0.25	0.24	NA	0.22
Poisson's ratio (28 days)	0.25	0.26	0.23	0.21
Poisson's ratio (90 days)	0.30	0.28	0.23	0.23
Split tensile strength, psi (28 days)	337	392	343	390
Coefficient of thermal expansion, /°C	10.4×10^{-6}	10.1×10^{-6}	9.7×10^{-6}	10.0×10^{-6}
Air void analyzer (AVA) spacing factor, in.	0.0088	0.0125	0.0088	0.0082
Air void analyzer (AVA) specific surface, (in.$^{-1}$)	580	639	628	710

Table F.13. As-constructed HMA Mix Properties

Property	Value
% Passing 12.5-mm (½-in.) sieve	93%
% Passing No. 200 sieve	4.4%
Asphalt concrete percent by weight	5.5%
Voids in mineral aggregate	15.8%
Bulk specific gravity	2.435
Maximum specific gravity	2.511
Percent fine aggregate angularity	46%
Density	151.7 lb/ft^3

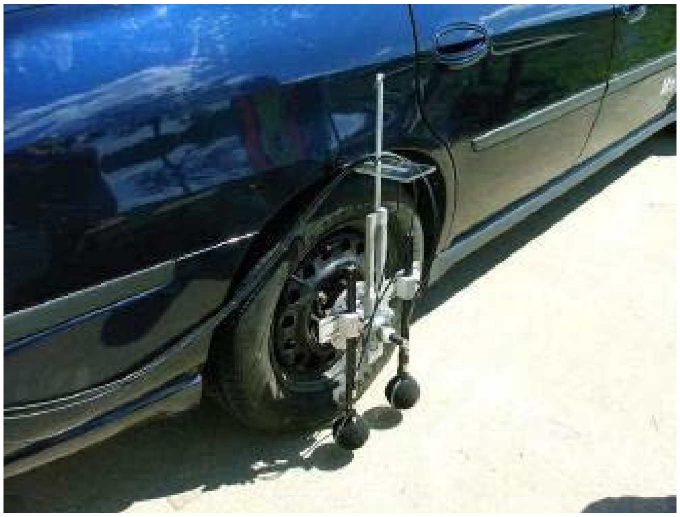

Figure F.38. OBSI device.

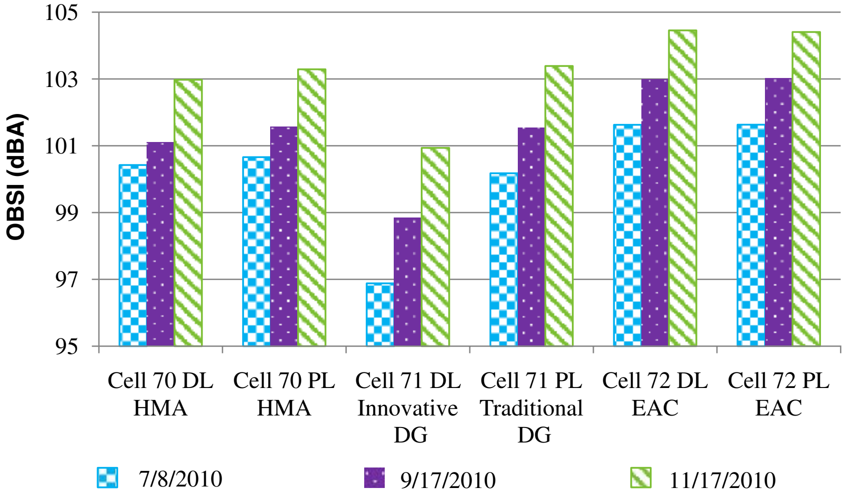

Figure F.39. OBSI for the HMA, innovative diamond-ground and traditional diamond-ground, and EAC finishes.

PULSE noise-and-vibration software is installed in a connected computer. The computer receives and analyzes the data, categorizing the response into component third-octave frequency output. Pavement noise response from the microphones is condensed into a third octave frequency sound intensity plot averaged for the leading edge and trailing edge. The OBSI parameter is the average of the logarithmic sum of the sound intensity at 12 frequencies (400, 500, 630, 800, 1,000, 1,250, 1,600, 2,000, 2,500, 3,150, 4,000, and 5,000 Hz). OBSI analysis is based on the AASHTO TP76-08 protocol. The results from OBSI testing done in 2010 are shown in Figure F.39.

Figure F.39 shows that the innovative diamond-ground (IG) finish (also called the Next Generation) has the lowest OBSI throughout the 3 months tested. The traditional diamond grind (TG) has an OBSI similar to that of the HMA surface. The EAC surface has the highest OBSI. There is not a considerable difference between the OBSI in the passing lane compared with that of the inside lane in Cell 70 or Cell 72. In a survey of exposed aggregate concrete pavements in Europe conducted by the National Concrete Pavement Technology Center, OBSI values were found to range from 101 to 106 dBA, which is similar to the results obtained for Cell 72. The one-third octave sound intensity spectrums used to calculate the OBSI values above are shown in Figure F.40 through Figure F.42; much similarity exists, except for the IG surface.

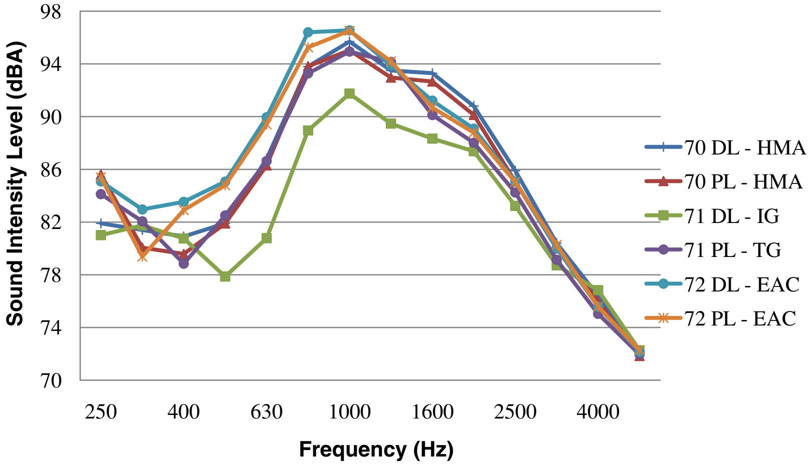

Figure F.40. One-third octave sound intensity spectrum for composite pavement surfaces on July 8, 2010.

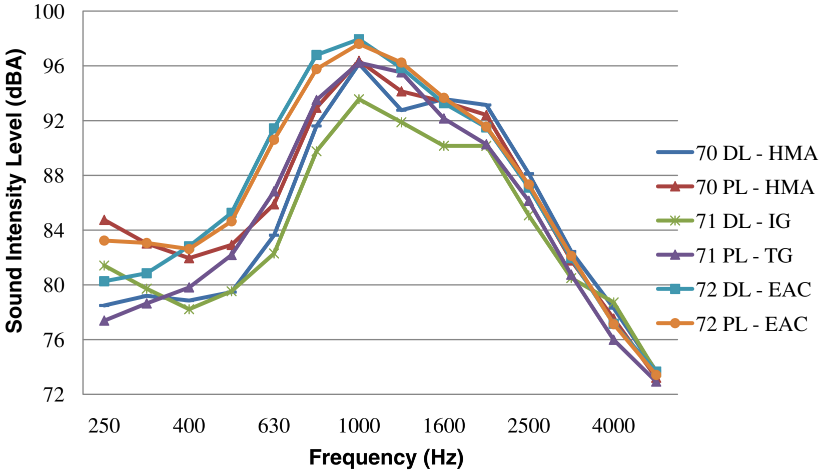

Figure F.41. One-third octave sound intensity spectrum for composite pavement surfaces on September 17, 2010.

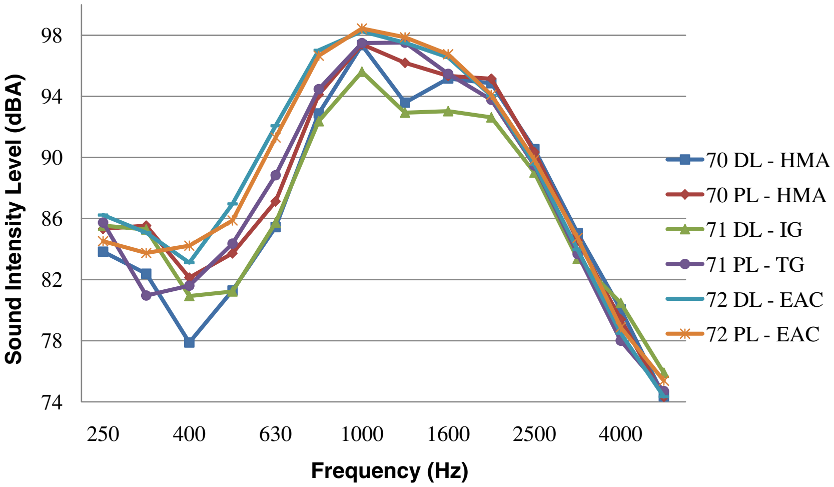

Figure F.42. One-third octave sound intensity spectrum for composite pavement surfaces on November 17, 2010.

APPENDIX G

Construction of Test Sections at UCPRC

Introduction

Construction of the University of California Pavement Research Center (UCPRC) SHRP 2 R21 composite pavement test track at the UC Davis Advanced Transportation Infrastructure Research Center (ATIRC) facility began in November 2008 and ended in October 2009. The design plans were developed to support the Heavy Vehicle Simulator (HVS) experimental design and testing plan to evaluate rutting and cracking performance and provide data for validation of performance models.

This appendix presents information regarding the construction of the test track, including subgrade preparation and base construction, instrumentation preparation and installation, concrete pavement construction, and hot-mix asphalt (HMA) placement. Also included are laboratory test results for the materials, and in-place characterization of the constructed pavement layers and overall pavement structure. Table G.1 shows a timeline of the major steps involved in the construction process.

Figure G.1 shows an aerial photograph of the ATIRC facility. ATIRC is located on the western portion of the UC Davis campus and possesses two right-angle test tracks; the outer track (paved with HMA in the figure) is for testing of construction and maintenance equipment and the inner for HVS pavement structural testing. The legs of the inner test track are 50 ft × 300 ft (north-south) and 50 ft × 350 ft (east-west) and are large enough to accommodate a significant number of HVS test sections. The test sections for the SHRP 2 R21 project were built along the north-south leg. The finished total test track size is 48 × 135 ft.

Figure G.2 and Figure G.3 show the pavement plan and cross section designs. The composite HMA/portland cement concrete (PCC) pavement consists of four lanes (A–D), comprising two HMA mixtures, with two HMA thicknesses, two PCC thicknesses, and PCC with and without dowels for load transfer. One of the asphalt mixes is dense-graded HMA with a polymer-modified binder (PG 64-28PM) and the other is gap-graded HMA with an asphalt-rubber binder (RHMA-G). Each of the three sections (1, 2, 3) in each lane consists of three slabs, each 15 ft in length, totaling 45 ft in length, to ensure that the HVS is properly supported and that the pavement trafficked by the HVS includes one complete slab and two PCC joints.

Test Track Construction

Subgrade Soil Grading and Compaction

Sierra Asphalt of Rancho Cordova, California, performed initial soil grading and compaction, in preparation for aggregate base placement. Typical grading plans are shown in Figure G.4 with a total material area of 250 yd^2 (225 m^2). Scarification was performed to 12 in. (300 mm) below natural subgrade. A Vibramax sheepsfoot roller made numerous passes over two 6-in. (150-mm) lifts to achieve density. At the southeast corner of the project, an unstable area existed, and the material was removed and replaced with drier native material and recompacted. The subgrade was compacted to meet the Caltrans Standard Specifications Section 19 for earthwork (subgrade) relative compaction of 95%. Based on the Caltrans CTM 216 procedure, the soil maximum dry density is 118 lb/ft^3 (1.9 g/cm^3) at an optimum moisture content of 12%. For clay soils, the CTM 216 procedure tends to produce maximum dry densities and optimum water contents between those of standard and modified Proctor compaction T99 and T180. Field measurements at 6-in. (150-mm) depth and at subgrade surface level gave results of 95% to just more than 100% of CTM 216 relative compaction. Figure G.5, Figure G.6, Figure G.7, and Figure G.8 are pictures of the subgrade soil grading and compaction process.

Laboratory tests were conducted by Construction Testing Services of Sacramento, California, and UCPRC staff to determine optimum moisture and maximum dry density

Table G.1. Construction Timeline for Major Tasks

Major Task	Date
Excavation and grading of subgrade	November 2008
Aggregate base placement	December 2008
Prime coat application to protect base in winter	December 2008
Instrumentation purchase and preparation	January to August 2009
Instrumentation placement on base (PCC instruments)	July and August 2009
PCC placement	August 2009
HMA placement and instrumentation	October 2009
Joint measurement instrumentation	February 2010 and ongoing

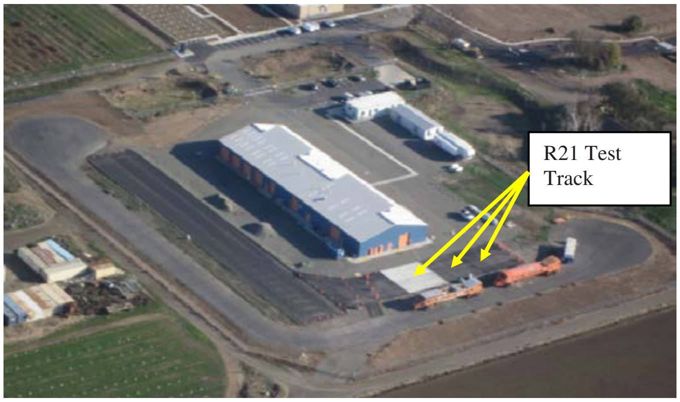

Figure G.1. Aerial photograph of ATIRC facility at UC Davis campus taken in December 2009.

parameters for the in situ subgrade soil. The Atterberg limits for the subgrade are: liquid limit 40, plastic limit 24, and plasticity index 16. The soil is classified as CL based on the Unified Soil Classification System.

Aggregate Base Placement and Compaction

Aggregate base placement followed subgrade preparation in November 2008. The material was placed by a Caterpillar G140 Motor Grader and rolled with a smooth drum roller. Total material placed and compacted was approximately 435 tons (395 metric tons) of Caltrans ¾-in. (19-mm) Class 2 aggregate base. The Class 2 aggregate base has a minimum *R*-value of 78, and the gradation specification is summarized in Table G.2.

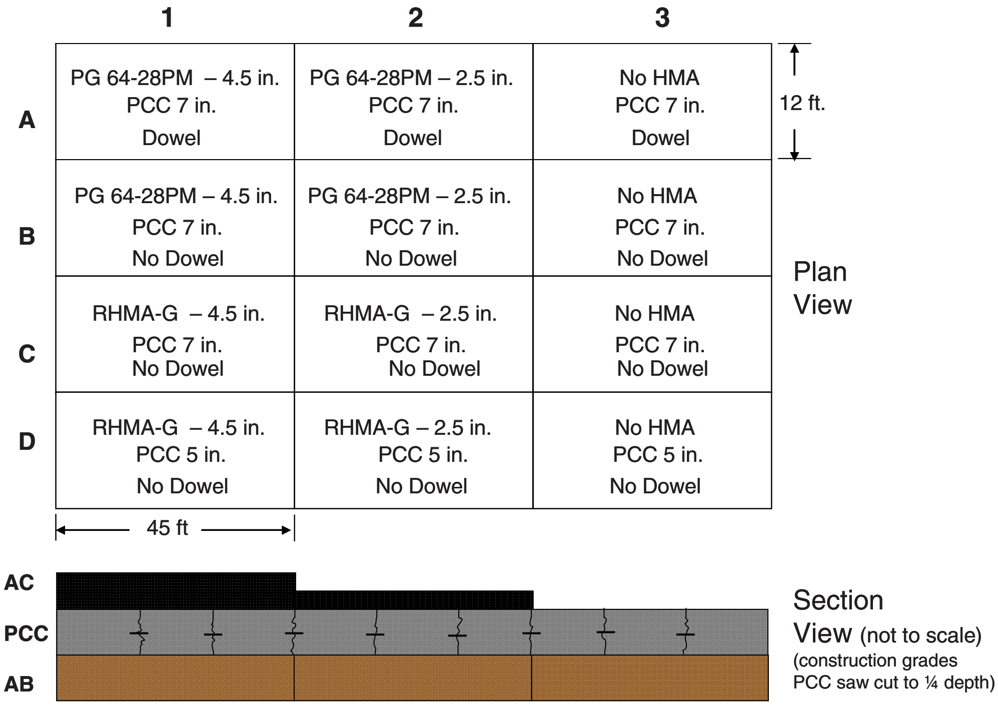

	1	2	3
A	PG 64-28PM – 4.5 in. PCC 7 in. Dowel	PG 64-28PM – 2.5 in. PCC 7 in. Dowel	No HMA PCC 7 in. Dowel
B	PG 64-28PM – 4.5 in. PCC 7 in. No Dowel	PG 64-28PM – 2.5 in. PCC 7 in. No Dowel	No HMA PCC 7 in. No Dowel
C	RHMA-G – 4.5 in. PCC 7 in. No Dowel	RHMA-G – 2.5 in. PCC 7 in. No Dowel	No HMA PCC 7 in. No Dowel
D	RHMA-G – 4.5 in. PCC 5 in. No Dowel	RHMA-G – 2.5 in. PCC 5 in. No Dowel	No HMA PCC 5 in. No Dowel

Figure G.2. Plan** (top) **and section view** (bottom) **of test section layout with approximate construction elevations.

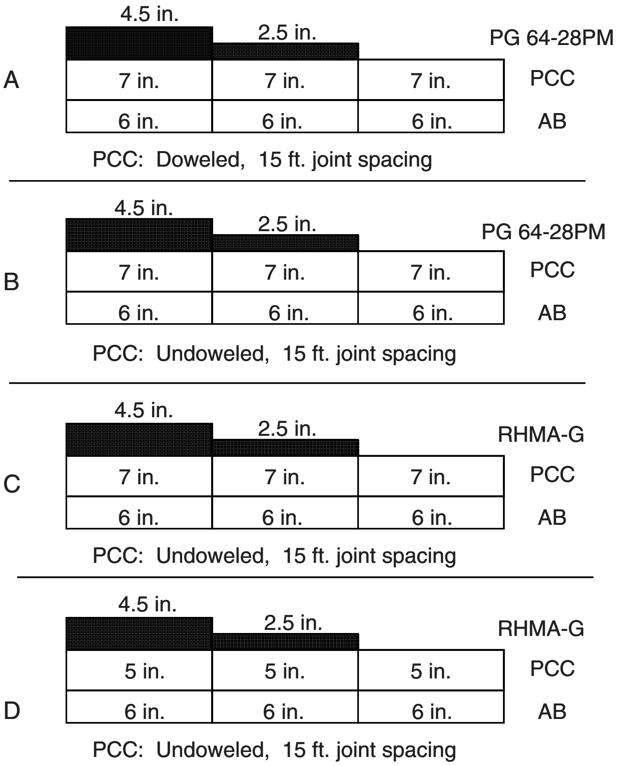
4.5 in.
2.5 in.
PG 64-28PM
A
7 in.
7 in.
7 in.
PCC
6 in.
6 in.
6 in.
AB
PCC: Doweled, 15 ft. joint spacing
4.5 in.
2.5 in.
PG 64-28PM
B
7 in.
7 in.
7 in.
PCC
6 in.
6 in.
6 in.
AB
PCC: Undoweled, 15 ft. joint spacing
4.5 in.
2.5 in.
RHMA-G
C
7 in.
7 in.
7 in.
PCC
6 in.
6 in.
6 in.
AB
PCC: Undoweled, 15 ft. joint spacing
4.5 in.
2.5 in.
RHMA-G
D
5 in.
5 in.
5 in.
PCC
6 in.
6 in.
6 in.
AB
PCC: Undoweled, 15 ft. joint spacing

(Note: Undoweled = Nondoweled.)

Figure G.3. Cross section diagram of PCC pavement sections.

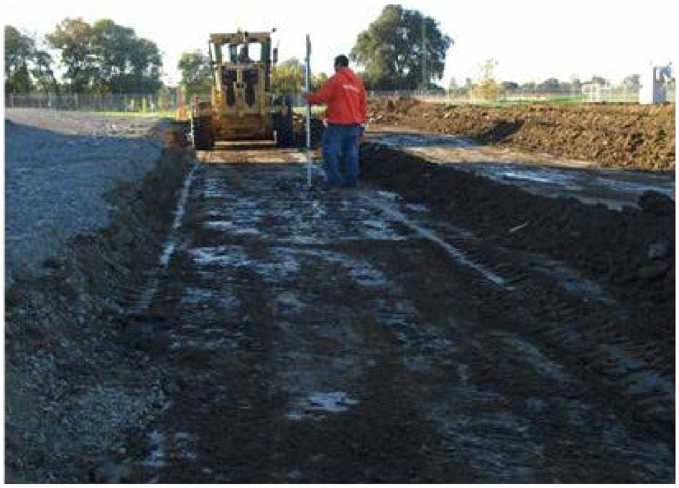

Figure G.5. Initial excavation of test track subgrade.

The aggregate base consisted completely of virgin aggregate, with no recycled PCC. Aggregate base lift thickness was nominally 6 in. (150 mm). Figure G.9 and Figure G.10 show grading and compaction of the aggregate base course. The aggregate base was compacted to meet the Caltrans specification of 95% density relative to CTM 216. For granular materials, CTM 216 maximum dry density is similar to that obtained using Modified Proctor Compaction T180. Maximum dry density of the aggregate base was measured at 140.1 lbf/ft^2 at an optimum moisture content of 5.7%.

The transverse cross-slope built into the subgrade and maintained in the aggregate base and PCC layers was 1.5%

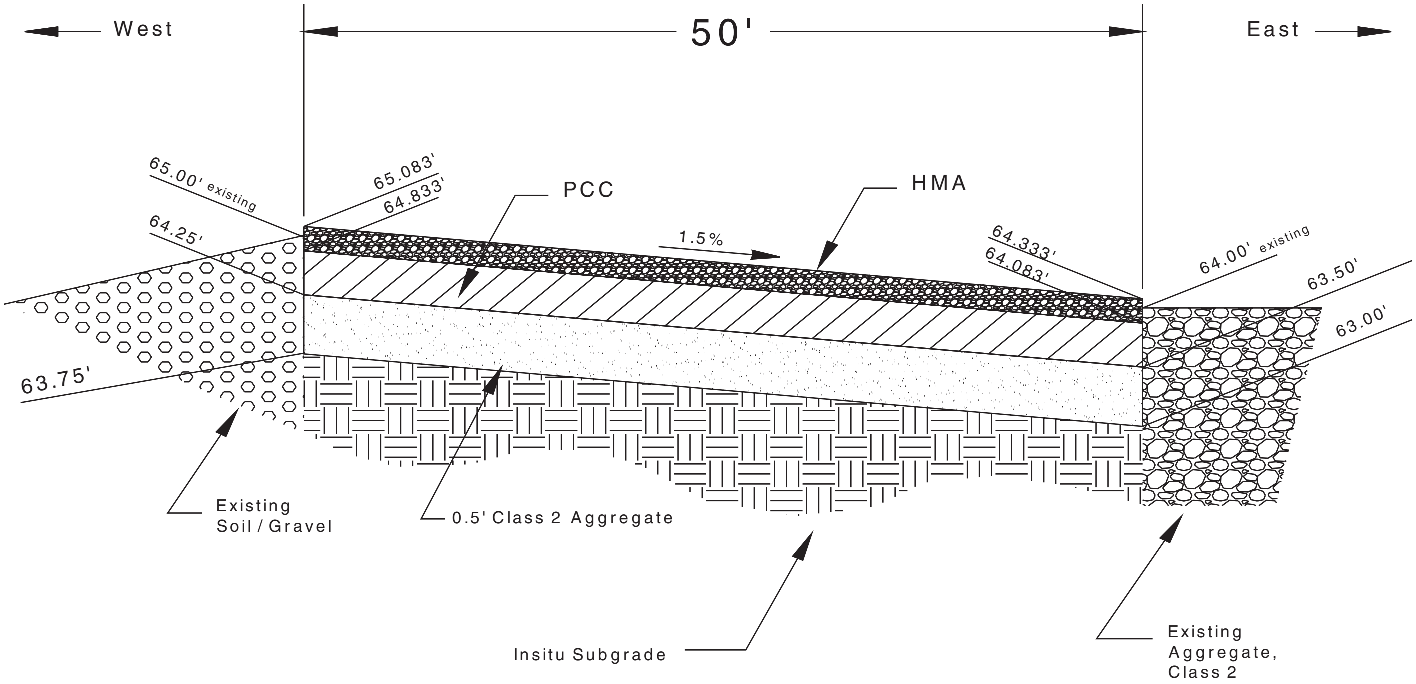
West
50'
East
65.00' existing
64.25'
63.75'
65.083'
64.833'
PCC
HMA
1.5%
64.333'
64.083'
64.00' existing
63.50'
63.00'
Existing Soil / Gravel
0.5' Class 2 Aggregate
Insitu Subgrade
Existing Aggregate, Class 2

Figure G.4. Typical transverse cross section of test track showing elevations and cross slopes.

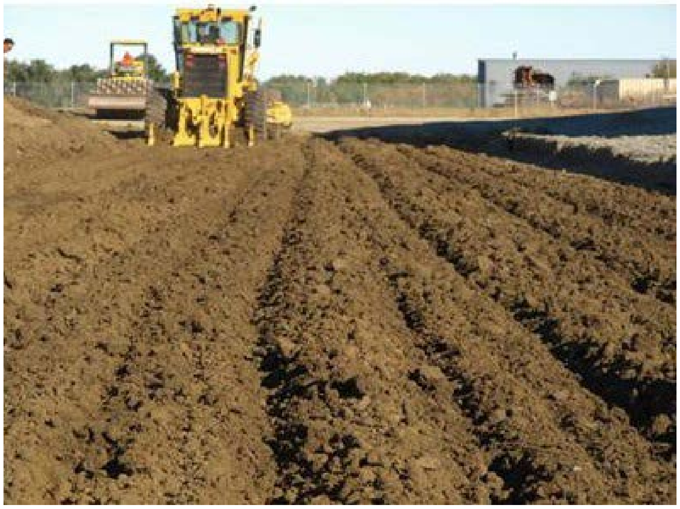

Figure G.6. Scarification and drying of test track subgrade before grading and compaction.

to a drainage line on the east side of the track. The drainage line consists of a perforated pipe placed in a gravel-filled trench at a level below the top of the subgrade and carries water to a pond approximately 150 ft (50 m) from the test track. The track also has an average longitudinal slope of 1.5% south to north.

Prime Coat Application

An SC-70 asphalt prime coat meeting Caltrans Specifications Section 93-1.01 was applied in December 2008 to the 250 yd^2 (225 m^2) aggregate base to minimize winter rain damage before PCC paving in 2009. The prime coat was supplied by the Telfer Company of Martinez, California. The application rate was 0.20 g/yd^2 (0.90 L/m^2). A second prime coat application occurred in June 2009 after it had deteriorated somewhat during the winter. Figure G.11, Figure G.12, and Figure G.13 show pictures of the prime coat application process.

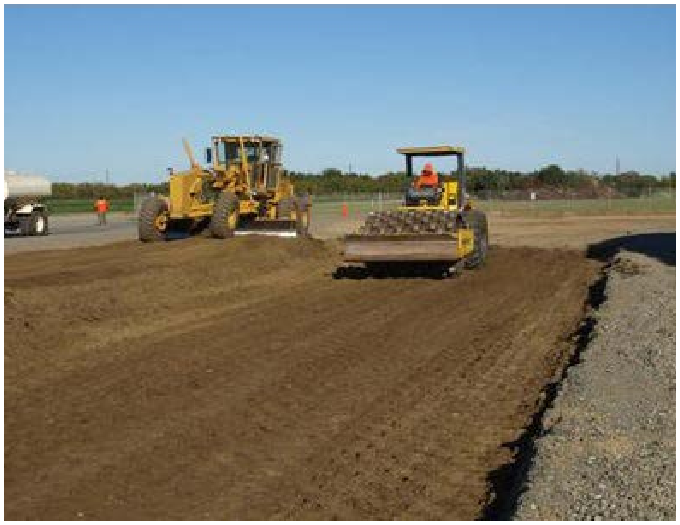

Figure G.7. Placement and compaction of test track subgrade.

Figure G.8. Initial leveling and rolling of test track subgrade.

Instrumentation Preparation and Installation

Overview

During winter 2008 and spring 2009, final decisions were made regarding the instrumentation plan. Conversations took place between MnROAD staff and UCPRC staff about best practice of sensor installation to provide the desired measurements, with some redundancy, within the budget. An effort was made to keep as much of the instrumentation in common with that used on the R21 project at MnROAD as possible. Figure G.14 shows a plan view of the final instrumentation layout for PCC instrumentation placed on top of the aggregate base. Refer to Figure G.2 for the pavement type in each cell. The letters in the figure correspond to the following: J = joint deflection measurement device (JDMD); H = horizontal

Table G.2. Class 2 Aggregate Base Gradation

	Percentage Passing	
Sieve Size	Operating Range	Contract Compliance
1 in.	100	100
¾ in.	90–100	87–100
No. 4	35–60	30–65
No. 30	10–30	5–35
No. 200	2–0	0–12

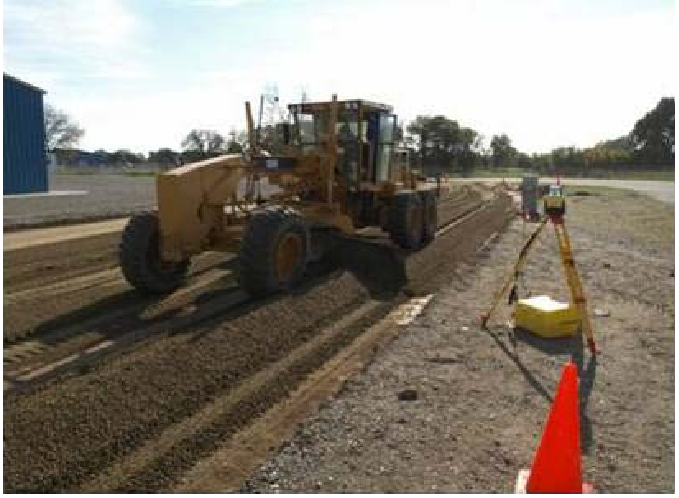

Figure G.9. Aggregate base grading.

joint deflection measurement device (HJDMD); T = thermocouple; D = dynamic strain gauge; S = static strain gauge; and M = moisture sensor. The numbers above each letter indicate the number of sensors placed at different heights above the aggregate base at each location.

As seen in Figure G.14, six different types of sensors were used in the PCC. Two of these sensor types are used on the PCC surface, J and H. The remaining sensor types (M, T, S, and D) are embedded within the PCC. The sensor types are described briefly below.

J: JOINT DEFLECTION MEASUREMENT DEVICE

JDMDs are devices designed to measure absolute vertical movement of PCC slab joints, from which the relative movement of the two slabs on each side of the joint can also be measured. They typically are placed at joint corners where maximum movement occurs under load. This device consists of a pair of linear voltage differential transducers (LVDTs) suspended on each side of the joint, both fixed to the subgrade soil, independent of the slabs. Figure G.15 shows a JDMD (red frame) used to measure vertical PCC joint movement. It can be seen in Figure G.15 that the rod to which the JDMD is attached passes through a hole cored in the slab, which is anchored approximately 5 ft below the surface of the slab. The specific LVDTs used for this project are model GHSDR750-500, with ±0.5-in. travel, and are manufactured by Macrosensors.

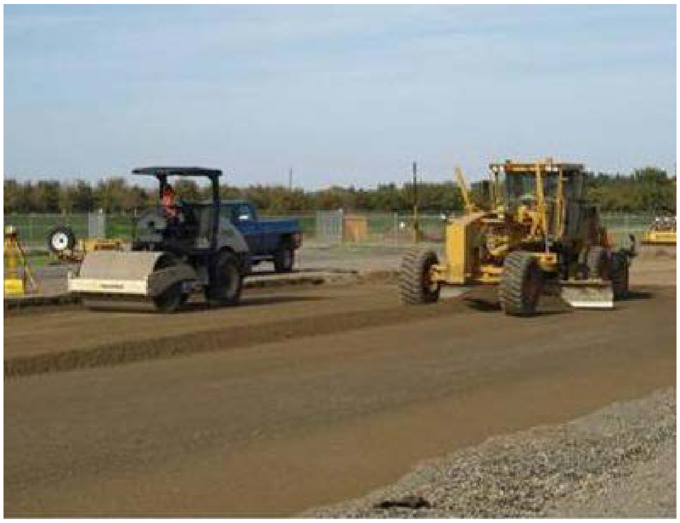

Figure G.10. Compaction and grading of test track aggregate base.

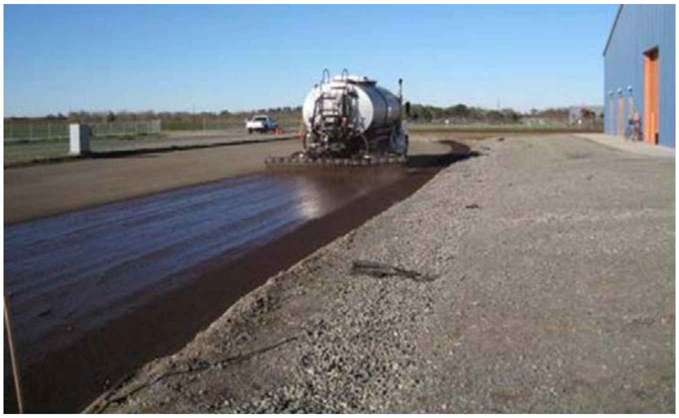

Figure G.11. Initial pass of prime coat application on eastern side of track.

H: HORIZONTAL JOINT DEFLECTION MEASUREMENT DEVICE

HJDMDs are similar to vertical JDMDs except they are used to measure relative horizontal joint movement caused by the opening and closing of PCC slab joints. They typically are placed at joint corners where maximum movement occurs under load. This device consists of a single LVDT fixed to the PCC slab on one side of the joint. A target affixed to the other

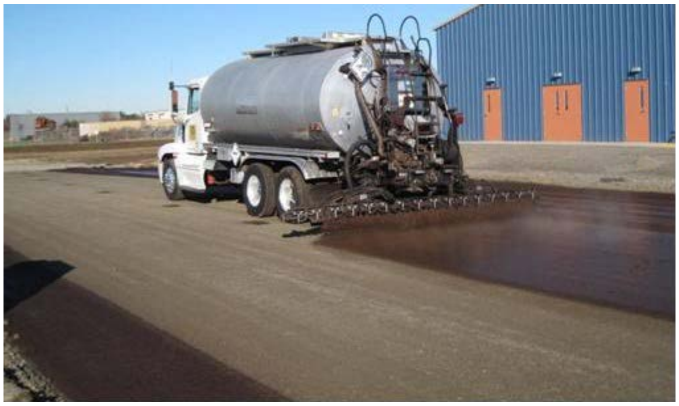

Figure G.12. Further pass of prime coat application truck.

Figure G.13. Completed application of prime coat.

slab contacts the LVDT plunger. Figure G.15 shows an HJDMD aluminum device in front of the red vertical JDMD. LVDTs used for this project are model GHSDR750-500, with a 0.5-in. travel, manufactured by Macrosensors.

T: THERMOCOUPLE

Thermocouples for measuring PCC temperature were placed in three locations in the PCC slabs: two slab corners and center slab. At each of these three locations, the sensors were placed at five uniformly spaced depths within the PCC slabs. The thermocouples used were T-type, model 8TX20PP from Omega Engineering.

To prepare the thermocouples for installation, the wires were cut to appropriate length and the ends of each thermocouple wire were stripped and soldered together at the tip.

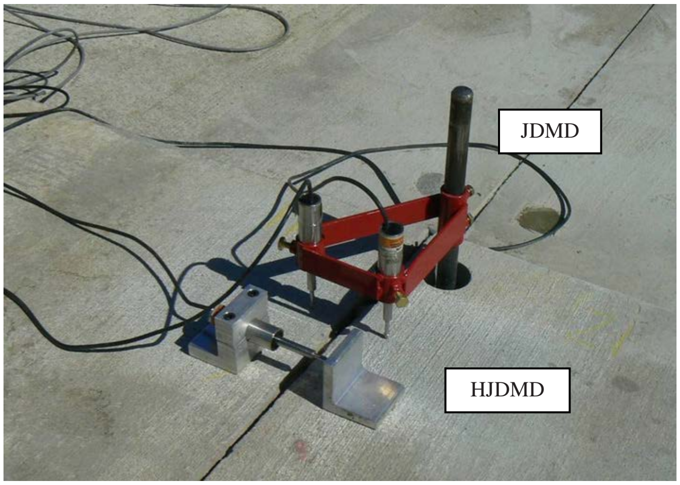

Figure G.15. JDMD and HJDMD used to measure vertical and horizontal PCC slab motion.

Each of the five sensor wires was attached to a precut, thin wooden dowel at the appropriate height with electrical tape. Table G.3 shows the vertical locations of these thermocouples within the PCC slabs as measured from the top of the aggregate base.

Figure G.16 shows the thermocouple wire, cut to length, soldered, and ready for placement onto the test track. Figure G.17 shows a picture of an installed thermocouple set. The wooden dowels holding the thermocouples are maintained in position vertically with wire fixtures. Fluted masonry nails (3.5 in. and 4 in.) were driven through small loops at the base of the fixture legs to hold the fixture assembly firmly to the aggregate base.

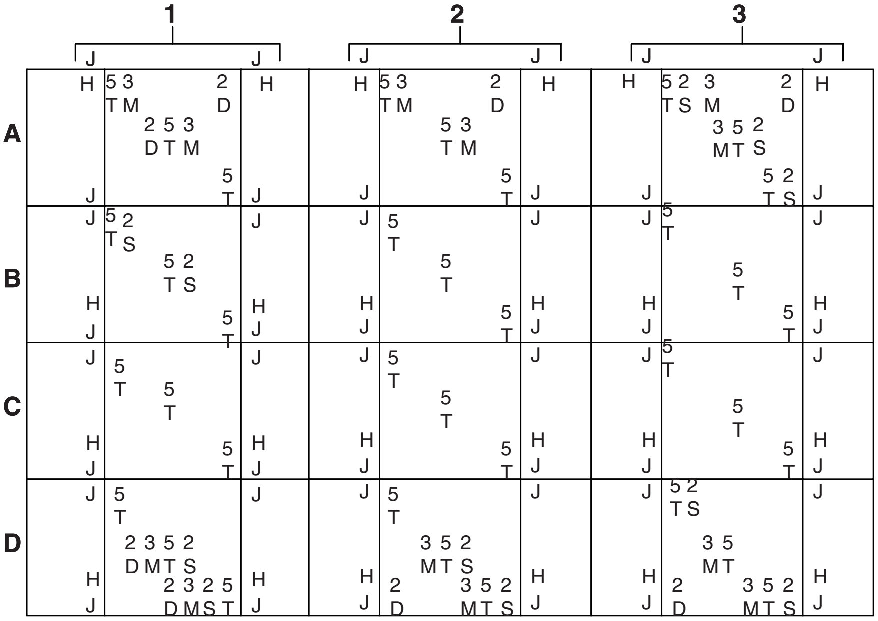
1
2
3
J J J J J J
A
B
C
D
H 5 3 2 H H 5 3 2 H H 5 2 3 2 H
T M D T M D T S M D
2 5 3 5 3 3 5 2
D T M T M M T S
5 5 5 2
J T J J T J J T S J
J 5 2 J J 5 J J 5 J
T S T T
5 2 5 5
T S T T
H H H H H H
5 5 5
J T J J T J J T J
J 5 J J 5 J J 5 J
T T T
5 5 5
T T T
H H H H H H
5 5 5
J T J J T J J T J
J 5 J J 5 J J 5 2 J
T T T S
2 3 5 2 3 5 2 3 5
D M T S M T S M T
H 2 3 2 5 H H 2 3 5 2 H H 2 3 5 2 H
J D M S T J J D M T S J J D M T S J

Figure G.14. Test track plan view showing sensor placement (refer to Figure G.2).

Table G.3. Nominal Thermocouple Depths as Measured from Bottom of Slabs

Slab Thickness (in.)	Thermocouple Distance Above Aggregate Base (in.)	Slab Thickness (in.)	Thermocouple Distance Above Aggregate Base (in.)
7	0.5	5	0.5
	2.0		1.5
	3.5		2.5
	5.0		3.5
	6.5		4.5

The thin metal rod extending from the top of the fixture is an orange identification flag to locate the sensors during concrete placement. Each of the five thermocouple sensor ends is outside the electrical tape for direct exposure to the PCC.

D: Dynamic Strain Gauge

Dynamic strain gauges were placed at slab corners and centers. Two gauges were placed for each location selected: nominally at 0.5 in. (13 mm) below and above the top and bottom of the slab, respectively, to measure strains occurring under the moving HVS wheel. The gauges used were from Tokyo Sokki, model PML-60-30L (30 m lead length) and PML-60-14L (14 m lead length). The gauges were placed parallel to the direction of traffic and parallel to the top and bottom surface of the PCC. Figure G.18 shows the dynamic strain gauges (light colored gauges at top of figure) affixed in position before PCC placement. Note the presence of static strain gauges (blue) and thermocouples (bottom left) in the figure.

Figure G.16. Thermocouple wire prepared for installation.

S: Static Strain Gauges

Static strain gauges were installed to measure slowly changing PCC strains at the top and bottom of the slab caused by creep, shrinkage, warping, and curling. Geokon 4200 vibrating wire strain gauges were selected. They were placed parallel to the direction of traffic loading and nominally 0.5 in. from the top and bottom of the PCC slab. Figure G.19 shows these gauges affixed to the aggregate base before PCC placement.

M: Moisture Sensors

Three moisture sensors were placed in the PCC. All sensors were placed parallel to the direction of traffic and parallel to the slab 1.0 in. from the bottom and top of the slab to provide relative measurement of top and bottom slab moisture. The sensors were donated by Decagon Devices of Pullman, Washington, and are 5TE. These sensors are designed primarily for

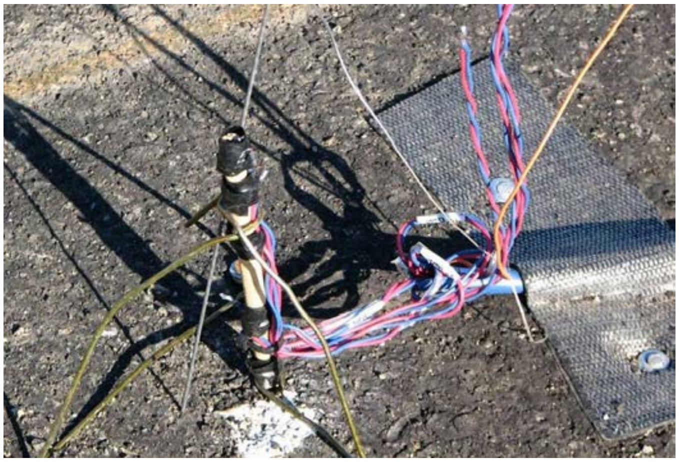

Figure G.17. Close up of thermocouple placement on wooden dowel with wire mounting fixture before PCC placement.

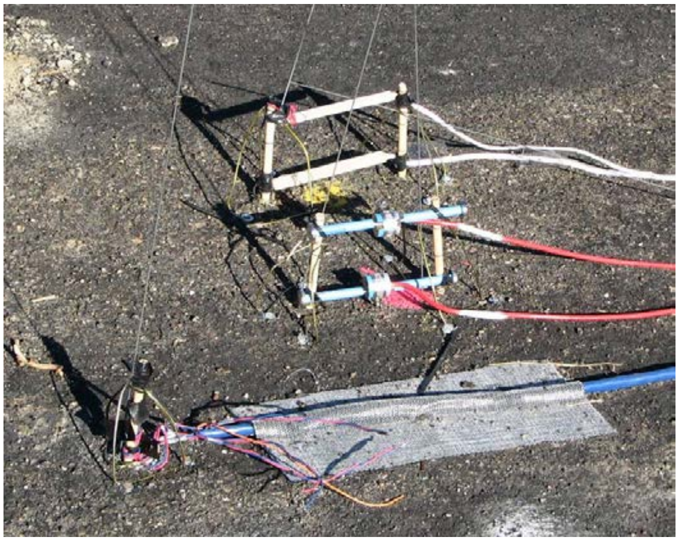

Figure G.18. Dynamic strain gauges (top of figure, white-colored gauge) affixed to aggregate base.

use in soil, and their application here in PCC is experimental. Figure G.20 shows the sensor held in place by a wire fixture.

Control and Data Acquisition

The data acquisition system consisted of two portions: (1) an HVS-based system for interfacing to JDMDs and dynamic strain gauges, and (2) a datalogger-based system for interfacing all other instrumentation.

HVS Data Acquisition System

JDMD data acquisition relied on the HVS data acquisition system (DAS) built by the Council for Scientific and Industrial Research (CSIR), South Africa. This system consists of a 64-channel National Instruments data acquisition (NI DAQ) board mounted in a PC and an electronics equipment chassis box containing a shielded connector block board which is connected to one NI DAQ board. As many as 15 JDMDs can be connected to the DAS. Figure G.21 shows a schematic of the data acquisition system.

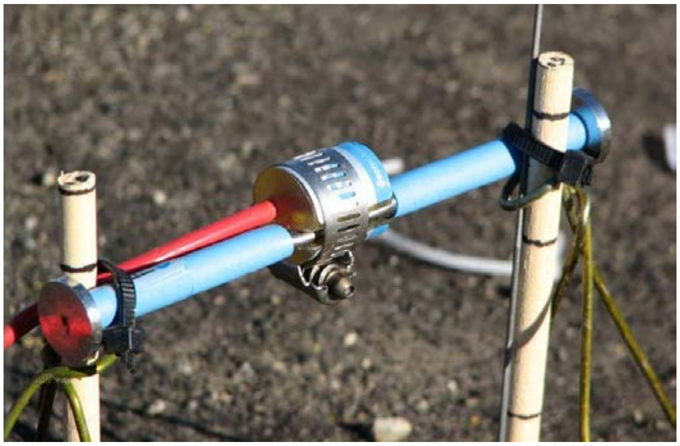

Figure G.19. Static strain gauge affixed to aggregate base with wire fixtures.

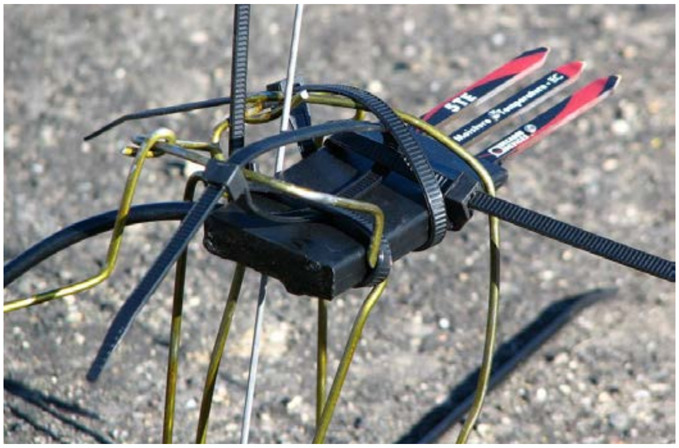

Figure G.20. Moisture sensor in place before PCC placement.

Two types of dynamic strain gauges were used. In the PCC slab were quarter-bridge Tokyo Sokki gauges, and in the asphalt concrete overlay were full-bridge CTL Group gauges. Both gauges were connected to a National Instruments strain gauge signal conditioner, with each gauge type connected through a separate eight-channel terminal block module. The strain gauge signal conditioner output signals were input to a second NI DAQ board mounted in the computer.

The DAS primarily was designed to collect data while the pavement was undergoing dynamic loading under the HVS test wheel. This was achieved with a clock connected to the motion of the HVS wheel. As the test wheel moved closer to an instrument, the clock triggered the first data point, and the acquisition system continued to record data until the wheel stopped moving or a maximum of 256 clock ticks were reached.

Datalogger-Based Data Acquisition System

The core of the datalogger-based DAS was the CR10X datalogger manufactured by Campbell Scientific. A schematic of the online DAS is presented in Figure G.22. The online system consisted of five CR10X dataloggers, two AM16/32 analog multiplexers, twelve AM25 thermocouple multiplexers, and one AVW200 vibrating wire spectrum analyzer, all of which were enclosed in a plastic outdoor garden tool box.

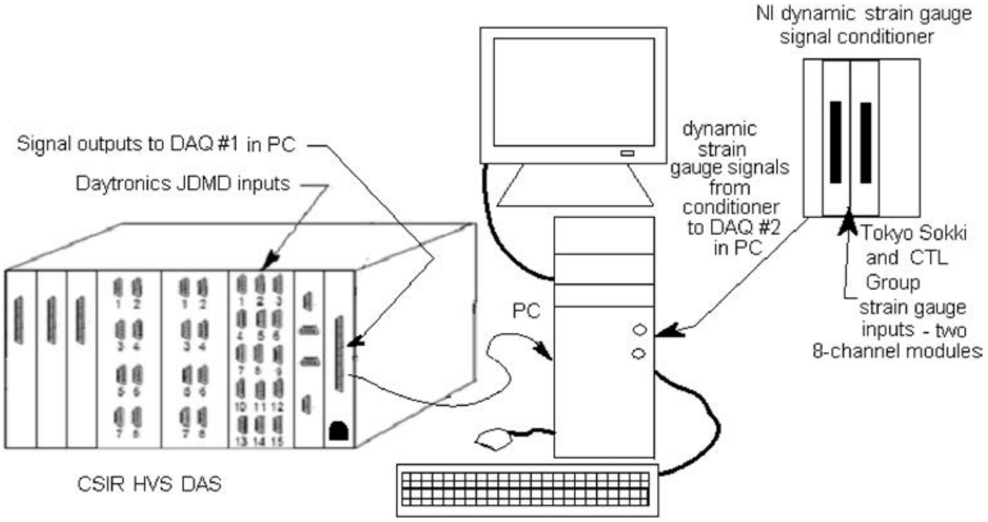
NI dynamic strain gauge signal conditioner
Signal outputs to DAQ #1 in PC
Daytronics JDMD inputs
dynamic strain gauge signals from conditioner to DAQ #2 in PC
Tokyo Sokki and CTL Group strain gauge inputs - two 8-channel modules
PC
CSIR HVS DAS

Figure G.21. HVS data acquisition system.

The system was used to periodically record data from thermocouples and Geokon vibrating wire static strain gauges embedded in the test sections' PCC slabs. The data recording period interval was 2 hours when the instrumentation was being used. The stored data could then be downloaded to a computer.

Sensor Layout and Connection

Cables for all instruments were cut to length, soldered, labeled, and assembled into harnesses by students directed by staff at ATIRC. After harness and sensor fabrication was completed, a grid was drawn on the test track to identify precisely the future dimensions of the PCC slabs. Paint dots with different colors for the different types of sensors were sprayed on the prime coat to indicate sensor location.

In August 2009, staff and student crews placed the harnesses and the instruments in their wire holders and fixed them to the prime-coated base in preparation for PCC paving. The cabling was placed either parallel or perpendicular to the expected pavement joints, and their locations were documented so that cracking patterns could be compared with cable locations. The cable ends were fixed in place at the appropriate sensor location by a combination of Bituthene (asphalt-impregnated tape) and 4-in. masonry nails. Figure G.23 shows this fastening process. The cables were then placed in their final positions and fastened down with the strap-and-nail assembly method. The control and DAS was positioned next to Cell A2 (see Figure G.14). Figure G.24 shows an overview of the test track with the cables affixed with the strap-and-nail method. Note the various color cables, indicating different sensor instruments.

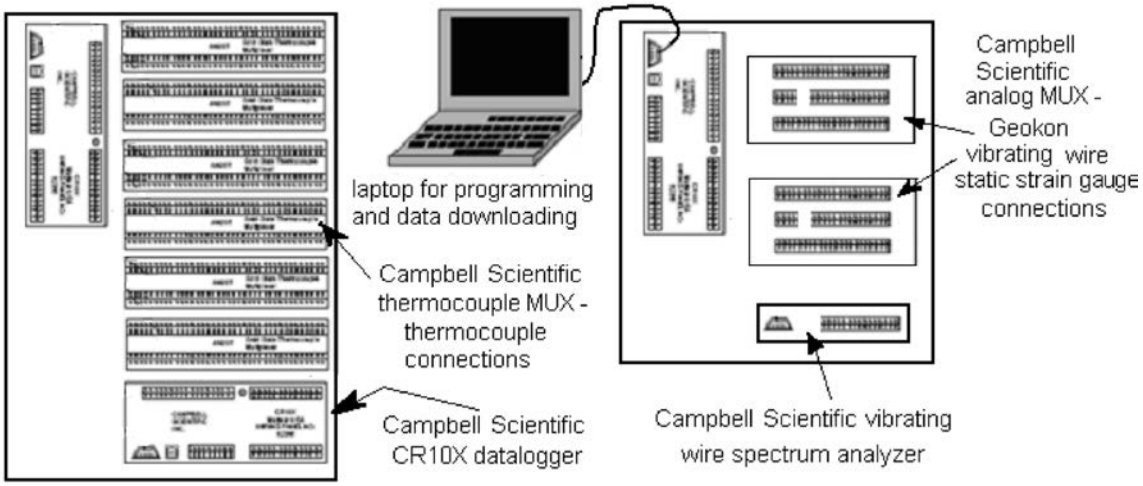
laptop for programming and data downloading
Campbell Scientific thermocouple MUX - thermocouple connections
Campbell Scientific CR10X datalogger
Campbell Scientific analog MUX - Geokon vibrating wire static strain gauge connections
Campbell Scientific vibrating wire spectrum analyzer

Figure G.22. Schematic of datalogger-based data acquisition system.

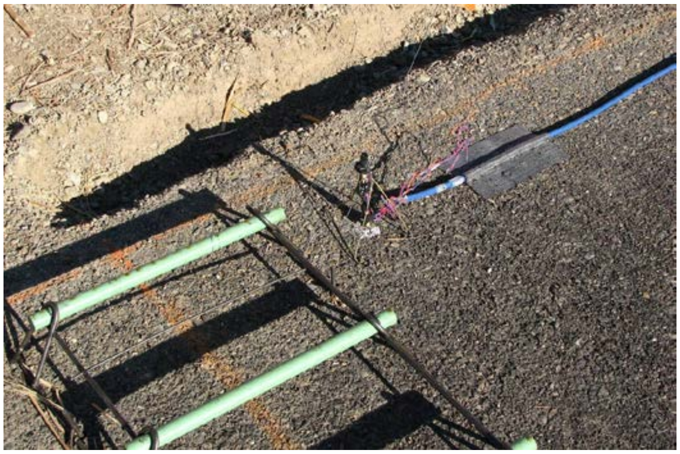

Figure G.23. Cable-fastening process showing a combination of Bituthene and nail methods.

A trench was dug at the west end of the track, and the cables were placed in a PVC pipe in the trench (which was later backfilled) to protect them during construction, as shown in Figure G.24.

Concrete Pavement Construction

Dowel Bars, Instrumentation, and Forms

Dowel bar assemblies were placed at the eight joints in Lane A. The dowel bar/basket assemblies were supplied free of charge by Dayton Superior Corporation through their Modesto, California factory. The dowels used were steel, 1 in. (25 mm) in diameter, and epoxy- and Tectyl-coated, and were soldered on one end to the basket assembly. Dowel bar spacing was 1 ft on center. Each assembly consisted of 12 dowel bars. The premade assemblies were supplied with 1-ft long hook-shaped fastening pins. The basket assemblies were attached to the aggregate base with fastening pins beaten into the base with sledge hammers to withstand the force of the pumped concrete.

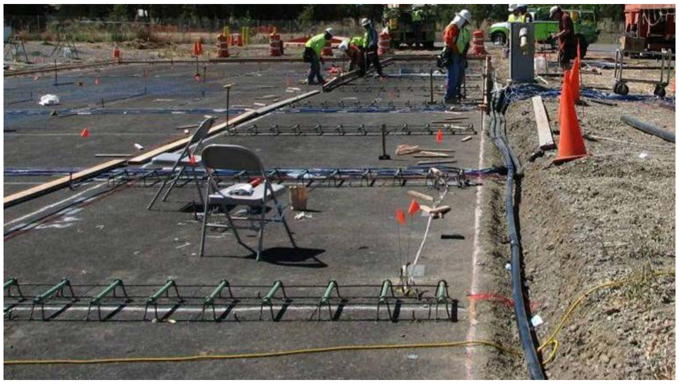

Figure G.24. Track overview showing sensor wires fixed to track.

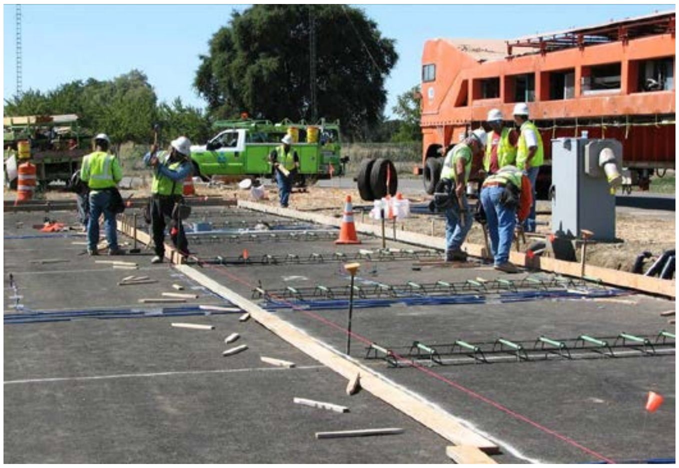

Figure G.25. PCC form construction.

All instrumentation (approximately 200 sensors) was verified for full functionality before PCC placement. The control and data acquisition box was completed, and cabling was attached and verified for correct placement. Each sensor was excited, and responses were measured at the box. Calibrations were performed to ensure that strain and temperature measurements were accurate.

PCC paving was performed by Teichert Construction of Sacramento, California. Teichert placed wooden forms on the test track on August 5 according to the grid placed on the aggregate base, which was checked by UCPRC staff. This is shown in Figure G.25.

Concrete Mix

PCC was supplied meeting Caltrans Standard Specification Section 90: Portland Cement Concrete Mix Design. The concrete was classified as a Type 3 concrete, having a cementitious material content of 564 lb/yd^3, which includes 85 lb of fly ash. No chemical admixtures were used in the concrete. Concrete was batched at the ready-mix plant and hauled approximately 20 miles to the test track site. Table G.4 presents the concrete mix design.

Concrete Placement and Finishing

PCC construction began on Friday, August 7, 2009, after a 1-day delay because of high winds and hot air temperatures. Lanes A and C were paved on the Friday. Lanes B and D were paved on the second and final construction day, Monday, August 10, 2009. Work began at 7 a.m. and was completed at approximately 3 p.m. on both days. On August 7, the weather was very clear

Table G.4. PCC Content Mix Design

Material	Absolute Volume (ft^3)	Weight (lb)	Percent of Mix (%)
Coarse aggregate	11.07	1,900	47
Fine aggregate	8.03	1,329	33
Portland cement type 2/5	2.44	479	12
Class F fly ash	0.65	85	2
Water	4.41	275	7
Air	0.41	0	0
Total	27	4,068	100
Slump	3–5 in.	na	na
Design air	1.5%	na	na
Design unit weight	150.7 lb/ft^3	na	na
Design wet-to-cement ratio	0.49	na	na

and sunny, with starting temperatures of 62°F and finishing temperatures of 80°F. Winds were out of the south and averaged 2 mph with occasional gusts to 5 mph. Humidity averaged 54%. On August 10, the weather was very clear and sunny with starting temperatures of 70°F and finishing temperatures of almost 100°F. Winds were from the south and averaged 2 mph with gusts to 6 mph. Humidity averaged 38%.

UCPRC staff and UC Davis construction inspectors were on site in addition to the contractor. Starting on August 7, on the south end of the project, concrete was placed on Lanes A and C by concrete pump. The 160-ft pump was obtained from Associated Concrete Pumping in Sacramento, California. It was deemed necessary to place the concrete by pump because of difficulties in using slipform paving on the short sections with heavy instrumentation. Figure G.26 and Figure G.27 show the pumping process. Wet concrete was placed by hand around and over each instrument and carefully rodded and vibrated. The concrete was placed just ahead of the pumping for the rest of the slab to minimize differential curing between the concrete around the instrument and the rest of the slab. Light vibration was applied around the instruments without touching them, using Minnich Manufacturing and Wacker Co. ¾-in. electric flex shaft vibrators ("stingers"). Figure G.28 shows this process, which resulted in zero damaged sensors. Construction flags were placed next to the wire holder at each instrument to indicate their position in the concrete to alert construction crew personnel. One person worked with the pumping crew to help keep them from stepping on the instruments under the fresh concrete before finishing. One sensor was stepped on and crushed during construction and could not be recovered. This sensor was a dynamic strain gauge located in Cell C1, 4.5-in. RHMA over 7-in. nondoweled PCC. A motorized screed was used for surface vibration, strike-off, and initial finishing, as shown in Figure G.29.

The surface was floated and textured by hand, as shown in Figure G.30. After evaporation of bleed water, two layers of white curing compound were sprayed on the surface at

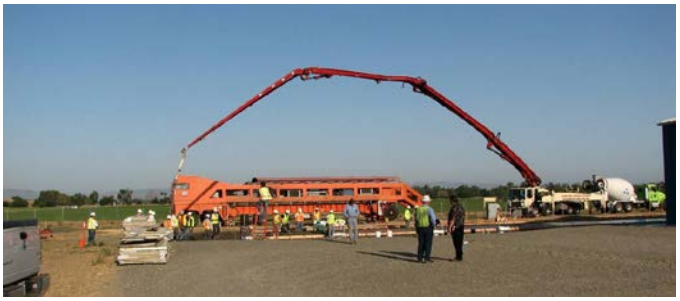

Figure G.26. View from east, concrete pump.

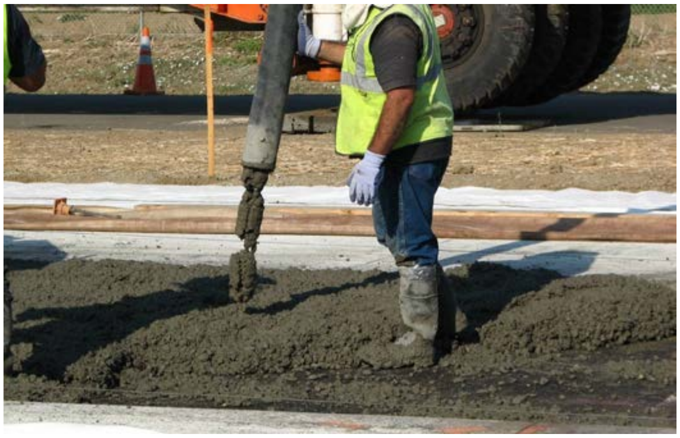

Figure G.27. Pumping concrete on Lane B on Day 2, between completed Lanes A and C.

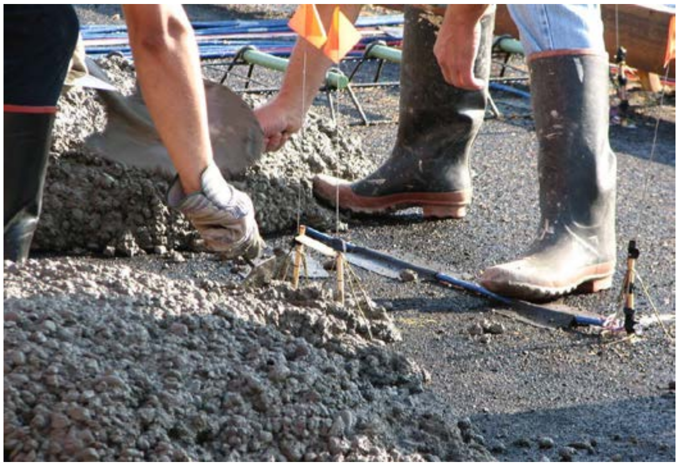

Figure G.28. Hand packing concrete around instrumentation.

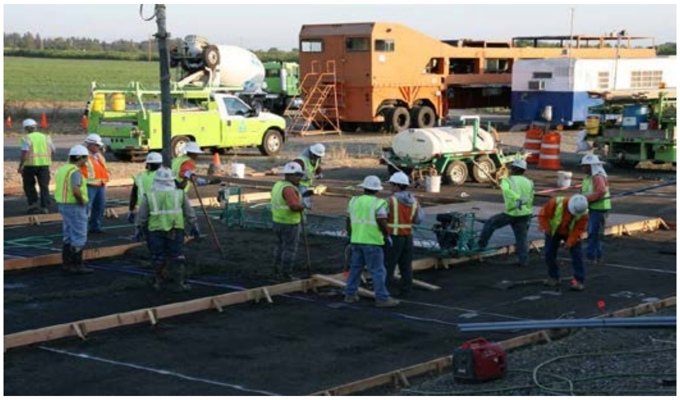

Figure G.29. Motorized screed on Lane C, Day 1 of PCC paving.

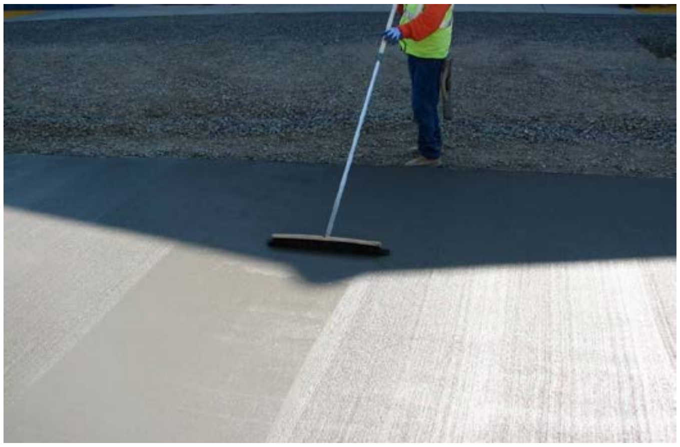

Figure G.30. Texturing the concrete surface.

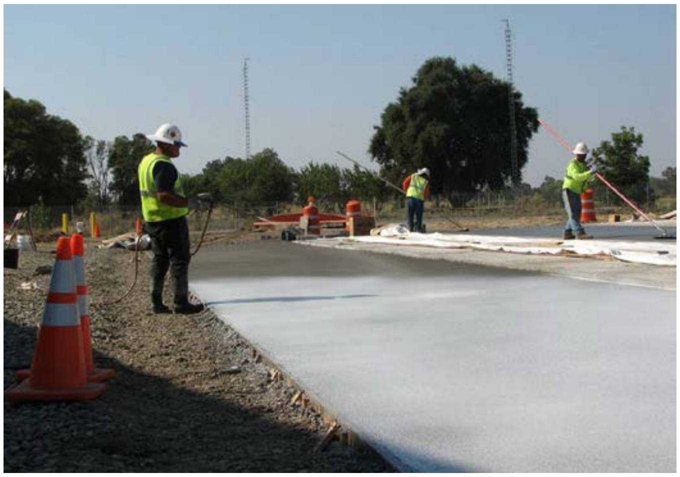

Figure G.31. Applying the first coat of curing compound on Lane D.

approximately 1 gallon per 100 ft^2, as shown in Figure G.31. Joints were cut within 5 hours of concrete placement using an early entry saw. Joints were cut to one quarter of the slab thickness. Figure G.32 shows the sawing process. The cut joints were sprayed again with curing compound where the curing compound had been removed during the cutting process.

Both curing compound and tarps were used to minimize the risk of early-age slab cracking caused by the hot, dry weather. When the curing compound was sufficiently dry to walk on, Burlene tarps (a proprietary product consisting of 10 oz/yd^2 burlap and 4 mil polyethylene sheeting sewn together) were soaked with water and placed on the concrete surface, burlap side down. The sheets were held down with lumber and buckets of aggregate. Figure G.33 shows the Burlene on Lanes A and C, which were paved on Friday, while Lane B was being paved on Monday.

Sixteen concrete mix trucks were required for the two construction days. Teichert removed the wood forms within 3 days

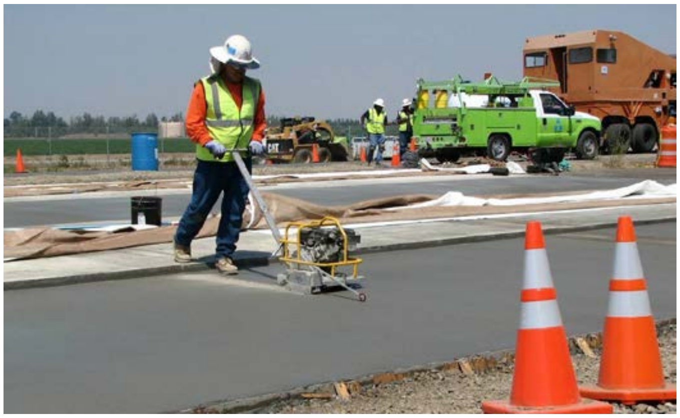

Figure G.32. Early entry saw cutting joints on Lane D.

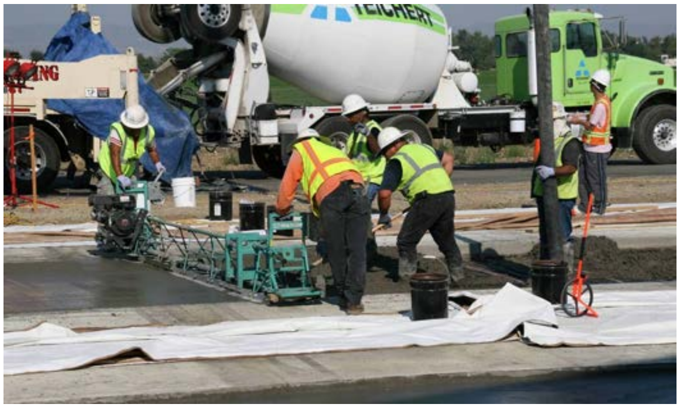

Figure G.33. Burlene in place on Lanes A and C, while Lane B is paved on Day 2 (Burlene has been temporarily pulled back to allow screed to pass).

of the second day of paving and cleaned the site. During both construction days, beams (6 in. square and 21 in. long) and cylinders (6 in. diameter and 12 in. tall) were made from concrete from almost all the delivery trucks. Beams and cylinders were produced according to AASHTO T23-08 (rodding), and curing compound was sprayed on the surface of each specimen. Wet Burlene tarps were placed to cover all specimens. A set of beams and cylinders was randomly selected for strength monitoring.

Two beams and two cylinders were connected to maturity meters to monitor curing progression. The Burlene tarps were removed 3 weeks after concrete placement, on August 24 and August 31, following the manufacturer's recommendations. Figure G.34 shows the high and low air temperatures and mean humidity during the first 3 weeks of the PCC curing period, in which the slabs were covered with wet Burlene tarps. Minimum temperatures fluctuated near 60°F and only once dropped below 50°F. No precipitation occurred during this period. The very high daily temperatures, typically at or above 90°F, necessitated semiweekly watering beneath the Burlene to facilitate curing. No concrete cracking other than contraction joint cracking was observed.

Concrete Strength, Expansion, and Slab Response Monitoring

Concrete Strength

Concrete strength was measured by beam and cylinder strength tests and by estimation from maturity measurements. Twenty-five beams and 20 cylinders were made using material sampled from most of the different concrete delivery trucks. Beams and cylinders were left at the side of the test track to cure for 3 days before being placed in the UCPRC moist

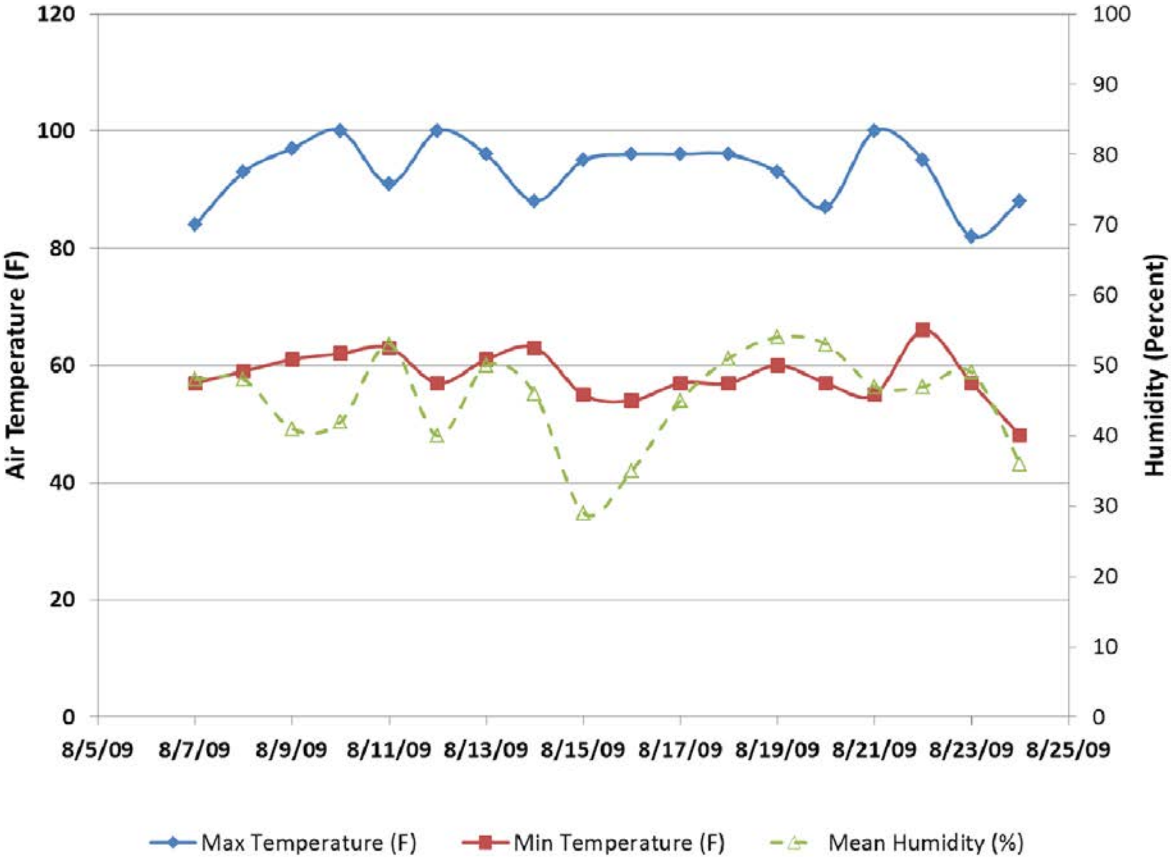

Figure G.34. Air temperature and humidity during first 3 weeks of the PCC curing period.

curing room at the Richmond Field Station. Maturity sensors were inserted into two beams and two cores to track their time-temperature relationship during the first 90 days after construction. For comparison, the thermocouples embedded in the test track were monitored and an equivalent maturity was calculated for the test track slabs. Table G.5 shows the results of unconfined compressive strength and split tensile strength testing on concrete cores that were cured in the UCPRC moist curing room for 7, 14, and 28 days. Maturity time-temperature factors were calculated and presented for each specimen tested based on initial field and subsequent curing room curing temperatures. Table G.6 presents the flexural strength of concrete beams measured from beam break tests for 7, 14, 28, and 90 days. Table G.7 presents the estimated slab compressive, indirect tensile, and flexural strength for PCC slabs for Day 1 and Day 2 construction. These field strength estimates were developed by computing field and laboratory maturity and using the field-to-laboratory maturity ratios to multiply laboratory measured strength data. Figure G.35 shows an example plot of Slab A1 (field) and laboratory maturity for PCC from Day 1 construction. Figure G.36 and Figure G.37 show plots of cylinder and beam break testing results, respectively.

Coefficient of Thermal Expansion

Coefficient of thermal expansion (CTE) tests were performed on three PCC cores taken from the test track from Slab C3 after a modified AASHTO TP-60 procedure. Table G.8 shows the results of CTE testing.

These results indicate that the CTE for this concrete is very low compared with the range of values measured in California by Kohler et al. Their results showed CTE values tested by UCPRC with an average, 16th percentile, and 84th percentile of 5.82, 5.37, 6.27 microstrain/°F, respectively, on CTE data from California long-term pavement performance sections. CTE testing was also performed previously on cores taken from LTPP sections by the FHWA, with values ranging from 3.7 to 7 microstrain/°F.

Table G.5. Unconfined Compressive Strength and Split Tensile Strength Test Results for Laboratory-Cured Concrete Cylinders

	Test Type	Curing Time (Days)	Curing Time (hr)	Maturity (Time × Temperature [°F])	Maturity (Time × Temperature [°C])	Compressive Strength (psi)	Compressive Strength (MPa)
Day 1							
D1T4C10	Compressive	7	168	7,936	4,409	3,657	25.2
D1T4C5	Compressive	14	336	14,024	7,791	4,349	30.0
D1T4C8	Compressive	28	672	27,369	15,205	5,305	36.6
D1T2SC2C1	Compressive	28	672	27,369	15,205	4,952	34.1
Day 2							
D2T3C6	Compressive	14	336	14,024	7,791	3,361	23.2
D2T3C4	Compressive	14	336	14,024	7,791	3,849	26.5
D2T5SB2C5	Compressive	14	336	14,024	7,791	3,606	24.9
D2T1SD3C1	Compressive	28	672	27,369	15,205	4,244	29.3
	Test Type	**Curing Time (Days)**	**Curing Time (hr)**	**Maturity (Time × Temp [°F])**	**Maturity (Time × Temp [°C])**	**Split Tensile Strength (psi)**	**Split Tensile Strength (Mpa)**
Day 1							
D1T8SA3C6	Split Tensile	7	168	7,936	4,409	655	4.5
D1T4C4	Split Tensile	7	168	7,936	4,409	711	4.9
D1T4SC1C3	Split Tensile	14	336	14,024	7,791	1,355	9.3
Day 2							
D2T3C5	Split Tensile	7	168	7,936	4,409	1,268	8.7
D2T3C2	Split Tensile	28	672	27,369	15,205	1,238	8.5
D2T3C3	Split Tensile	28	672	27,369	15,205	1,485	10.2
D2T3C8	Split Tensile	28	672	27,369	15,205	1,203	8.3

Table G.6. Flexural Strength Test Results for Laboratory-Cured Concrete Beams

Specimen Name	Curing Time (Days)	Curing Time (hr)	Maturity (Time × Temperature [°F])	Maturity (Time × Temperature [°C])	Flexural Strength (psi)	Flexural Strength (MPa)
Day 1						
D1T4B10	7	168	14,024	7,791	548	3.78
D1T4B3	14	336	14,024	7,791	655	4.52
SA3D1T8B6	28	672	27,369	15,205	384	2.65
SA2D1T6B5	28	672	27,369	15,205	612	4.22
D1T4B4	90	2,160	83,880	46,600	566	3.90
Day 2						
D2T3B10	7	168	7,936	4,409	452	3.12
SC2D1T2B1	7	168	14,024	7,791	473	3.26
D2T3B9	14	336	14,024	7,791	519	3.58
D2T3B8	14	336	14,024	7,791	609	4.20
D2T3B7	28	672	27,369	15,205	494	3.41
D2T1B1	90	2,160	83,880	46,600	647	4.46
D2T3B5	90	2,160	83,880	46,600	394	2.72

HMA Construction

HMA Materials

Two types of HMA, both meeting their respective Caltrans specifications, were placed on the test track at ATIRC on October 20, 2009. Work commenced at 7:30 a.m. and finished at 1 p.m. The weather was clear and sunny with starting temperatures around 54°F and finishing temperatures of 68°F. Winds were out of the north averaging 2 mph with gusts to 5 mph. Teichert Construction produced the mixes and performed the HMA construction. One mix, placed on Lanes A and B was a ¾-in. (19-mm) maximum aggregate dense gradation mix with polymer-modified PG 64-28 binder, referred to as PG 64-28PM. The other mix was a ½-in. (12.5-mm) maximum aggregate mix with gap graded and an asphalt rubber binder produced using the "wet process," referred to as RHMA-G. The mix designs are summarized in Table G.9.

Table G.7. Estimation of Slab Compressive and Flexural Strength from Maturity Data

Days of Slab Curing (hr)	Specimen Maturity (TTF) (°F)	Slab to Specimen Maturity Ratio	Slab Maturity (TTF) (°F)	Estimated Slab Compressive Strength (psi)	Estimated Slab Indirect Tensile Strength (psi)	Estimated Slab Flexural Strength (psi)
Day 1						
7	7,936	1.13	8,933	4,117	768	617
14	14,024	1.28	17,952	5,567	1,734	839
28	27,369	1.30	35,500	6,652	1,757	646
90	83,880	1.33	111,560	NA	NA	752
Day 2						
7	7,936	1.24	9,841	NA	1,572	574
14	14,024	1.29	18,091	4,651	NA	728
28	27,369	1.30	35,500	5,505	1,697	641
90	83,880	1.33	111,560	NA	NA	692

Note: NA = not available; TTF = Time Temperature Factor.

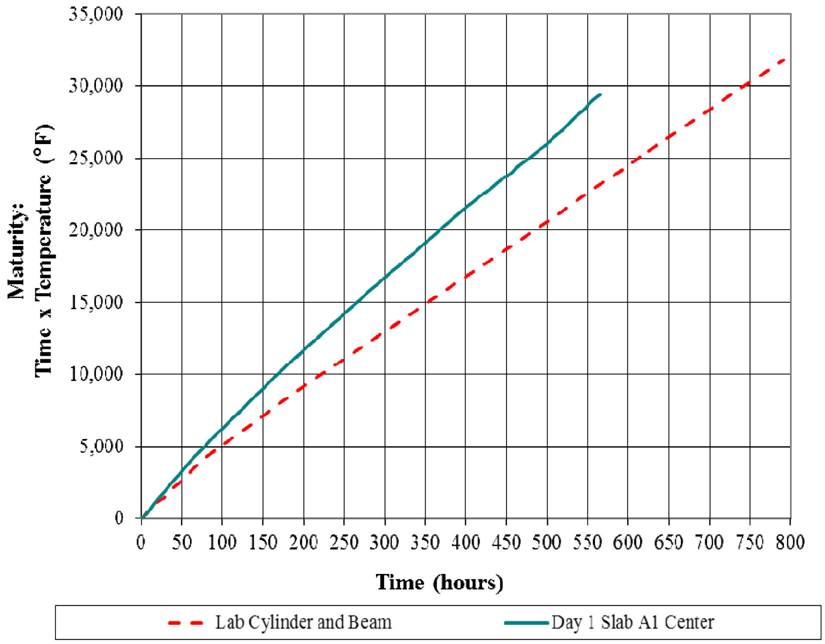

Figure G.35. Slab, lab cylinder, and beam maturity and strength versus time and Slab A1 maturity versus time.

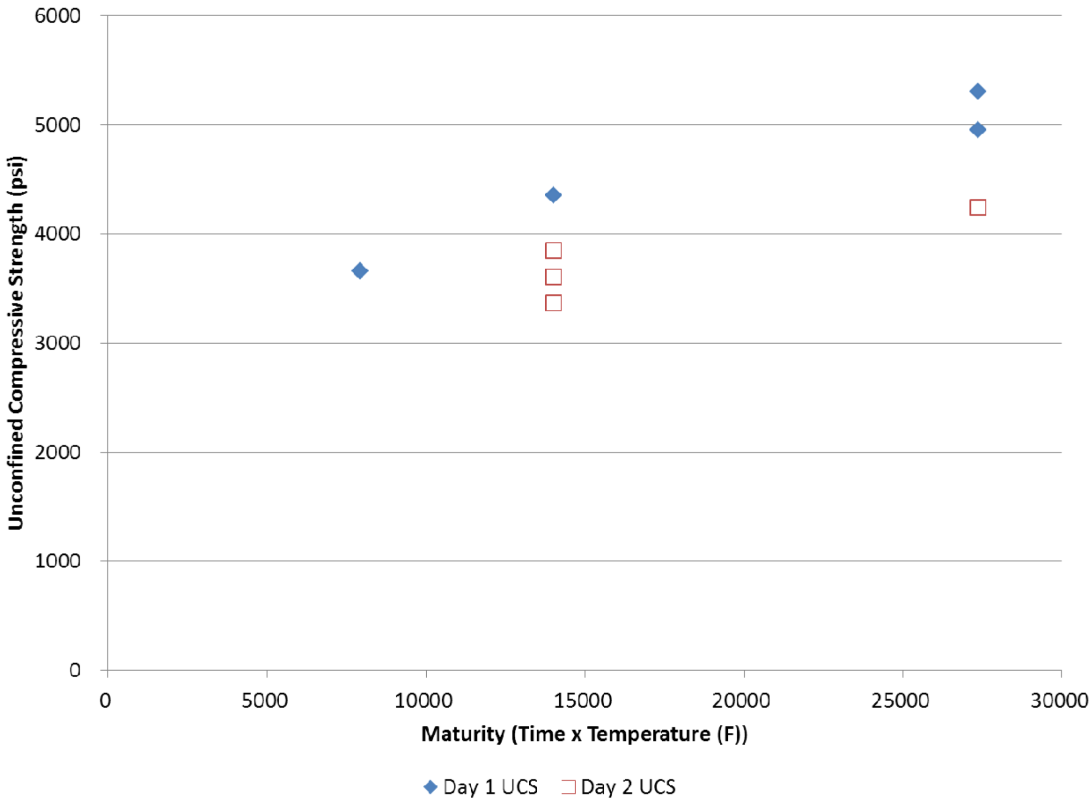

Figure G.36. Cylinder break unconfined compressive strength test results versus maturity.

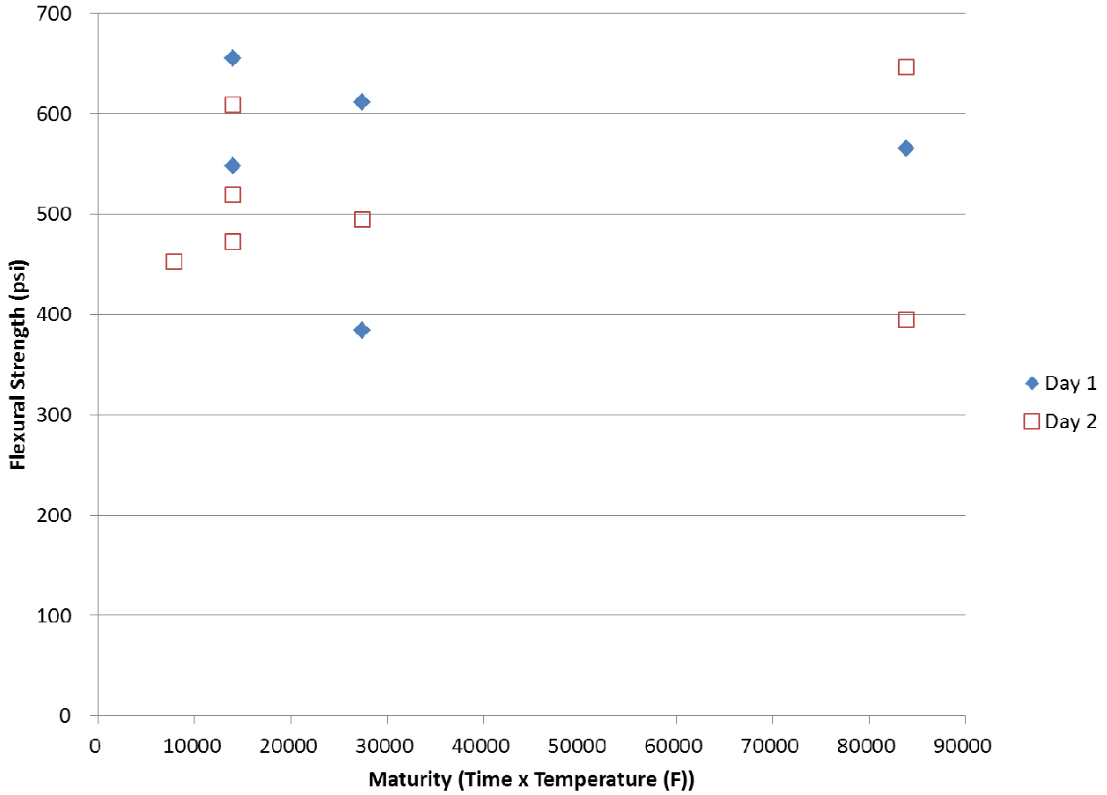

Figure G.37. Beam break flexural strengths versus maturity for lab samples.

Construction Process

The first lift of each mix type was placed over 90 ft of the track, and the top lift was placed over the first 45 ft of the track, as shown in Figure G.2.

HMA densities comparable to that typically found in the field were sought in the construction, with target values of approximately 7% air voids for the PG 64-28PM mix and 10% for the RHMA-G. With such short test sections, overcompaction could easily occur, and UCPRC staff and an outside testing laboratory monitored approximate densities using the nuclear gauge after each roller pass.

HMA construction began with the application of an anionic SS-1h emulsion tack coat over Sections 1 and 2 of Lanes A, B, C, and D (see Figure G.38); the emulsion tack coat was supplied by Paramount Petroleum of Elk Grove, California. The emulsion contained 61.5% solids by weight of emulsion. The asphalt within the emulsion had a penetration value of 51. The tack coat was applied with an oil pot and spray wand because of the small size of this project.

Once the tack coat had broken, 2.5 in. (65 mm) of the PG 64-28PM was placed and compacted on Lanes A and B, Sections 1 and 2. The paver used was a Terex-Cedar Rapids CR552

Table G.8. Coefficient of Thermal Expansion Test Results

Core ID	Average: CTE (microstrain/°C)	Average: CTE (microstrain/°F)
R21-CTE-C33-1	8.20	4.55
R21-CTE-C33-3	7.96	4.42
R21-CTE-C33-4	7.67	4.26

Table G.9. HMA Mix Designs

Polymer Modified Mix ¾ in. PG64-28PM			Rubber Gap Graded Mix ½ in. RHMA-G PG64-16		
Size	Target	Operating Range	Size	Target	Operating Range
1 in.	100	100	¾ in.	100	100
¾ in.	99	95–100	½ in.	98	92–100
⅜ in.	74	65–80	⅜ in.	84	78–90
No. 4	50	45–55	No. 4	34	27–41
No. 8	36	31–41	No. 8	21	16–26
No. 30	21	15–25	No. 200	3.5	1.5–5.5
No. 200	6.2	3–8			
Rice TMD: 2.57			Rice TMD: 2.49		
Optimum Binder: 5.0% (DWA)			Optimum Binder: 7.5% (DWA)		
T-308 Binder: 5.1% (DWA)			T-308 Binder: 7.4% (DWA)		

Note: TMD = theoretical maximum density; DWA = Dry Weight of Aggregate.

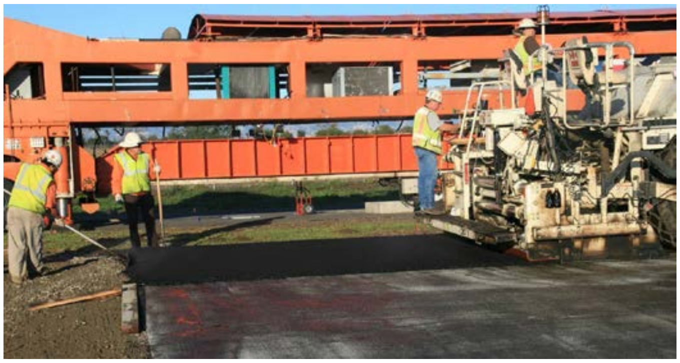

Figure G.38. Start of PG 64-28PM placement following application of tack coat.

with the 10-ft. standard paving screed extended to 12 ft. The compactor used was a Caterpillar model CB-534D XW with gross weight of 24,860 lb, a 79-in. drum, and operated at 2,520 cycles per minute at 0.01-in. vibration magnitude when in vibratory mode. Figure G.38 shows this process, and Figure G.39 shows the completed lifts for the PG 64-28PM. The paver was cleaned, and a 2.5-in. lift of the RHMA-G was placed and compacted on Lanes C and D, Sections 1 and 2. Figure G.40 shows this process, and Figure G.41 shows the completed lifts for the RHMA-G.

Nuclear density testing was performed by Construction Testing Services (CTS) of Sacramento, California. Testing results are shown in Table G.10. Air void contents were calculated from theoretical maximum density (TMD) tests (ASTM D 2041) performed by the UCPRC on loose mix collected during construction. The average lab TMD for the PG 64-28PM mix was 2.550, and for the RHMA-G mix it was 2.490.

During and following cooling of PG 64-28PM, asphalt strain gauges were installed on the first lift in Lanes A and B. These strain gauges, purchased from Construction Technology Laboratory (CTL, model ASG-152) and shown in Figure G.42, were located under and adjacent to the planned HVS wheelpath as part of a study of HMA movement under wheel load. Cables for the asphalt strain gauges were designed to withstand HMA placement temperatures and consisted of a Butyl rubber coating encapsulating Teflon-coated and braided shielding over the conducting wires. Precise locations of gauges were measured before placement of the second asphalt lift, as can be seen in Figure G.43. Figure G.44 shows the finished placement. The gauges were glued to the RHMA-G and PG 64-28PM with graded sand (No. 16) and SS-1h emulsion from tack coat truck mastic mixed in a 2:1 proportion by weight of sand to emulsion. After cooling of the RHMA-G, gauges were similarly placed on the first lift in Lanes C and D.

The same emulsified SS-1h tack coat was applied between lifts over Lanes A, B, C, and D, Section 1 only. Following tack coat placement and breaking, 2.0 in. (50 mm) of RHMA-G was placed and compacted on Lanes C and D. Figure G.45

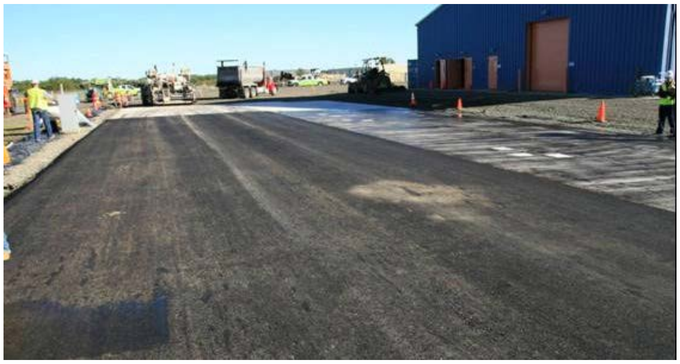

Figure G.39. Completed first lift of PG 64-28PM over Lanes A and B.

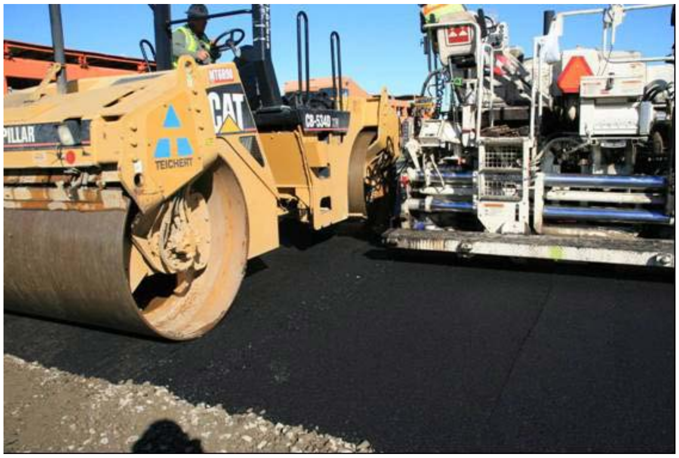

Figure G.40. Compaction and placement of RHMA-G in Lanes C and D.

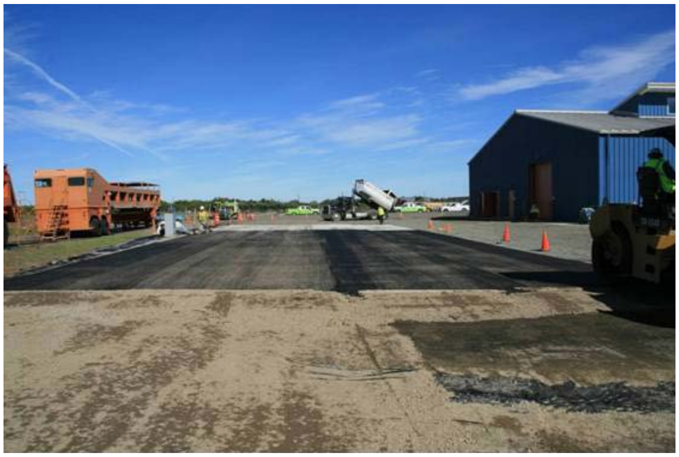

Figure G.41. Completed first lift of PG 64-28PM (left two lanes) and RHMA-G (right two lanes).

Table G.10. Nuclear Density Gauge Testing Results on HMA Lifts

Section	Description	Air Void Content (Rice) (%)
A1, A2, B1, B2, 2.5-in. PG 64-28PM	Bottom lift for 90 ft. Lanes A and B	7.8
A1, B1, 2.0-in. PG 64-28PM	Top lift for 45 ft. Lanes A and B	7.8
C1, C2, D1, D2 2.5-in. RHMA-G	Bottom lift for 90 ft. Lanes C and D	8.0
C1, D1 2.0-in. RHMA-G	Top lift for 45 ft. Lanes C and D	7.3

shows paving of RHMA-G in Lane D. Figure G.46 shows compaction of RHMA-G in Lane D. The paver was cleaned and 2.0 in. thick lift of PG 64-28PM was placed and compacted on Lanes C and D, Section 1 only. Figure G.46 shows this process. Figure G.47 shows the completed test track with two HMA thicknesses, two HMA materials, and the PCC section.

HMA Laboratory Specimen Preparation from Field Mix

UCPRC staff prepared laboratory-compacted HMA specimens from the field mix in parallel with the placement and compaction of the test track. Rolling wheel compaction was performed on PG 64-28PM and RHMA-G placed in ingot molds (trapezoidal shaped 19.5 in. × 21.5 in. × 3.5 in.). The ingots were later cut into 15- × 2.5- × 2.0-in. (380- × 62.5- × 50-mm) beams and 6- × 2-in. (150- × 50-mm) cores for flexural fatigue and repeated shear testing, respectively, to

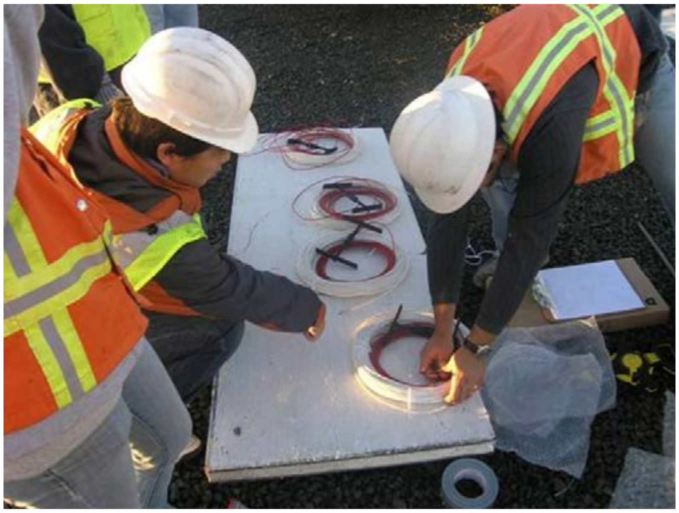

Figure G.42. CTL strain gauges, with 30 feet of coated cabling for thermal protection.

Figure G.43. Measurement of the positions of CTL strain gauges on first lift of PG 64-28PM, before placement of second lift.

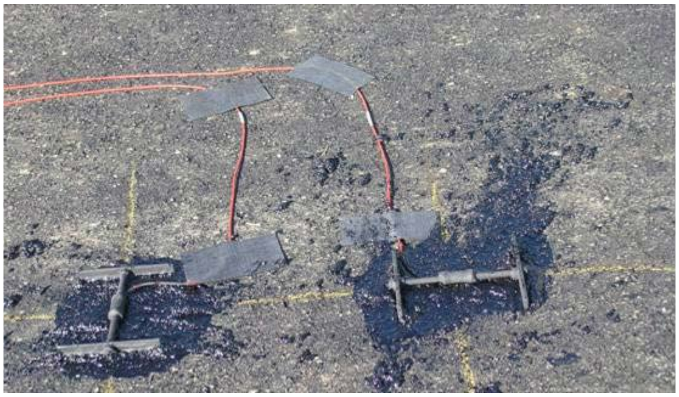

Figure G.44. Sensors placed on bottom lift of PG 64-28PM, glued with mastic of sand and emulsion.

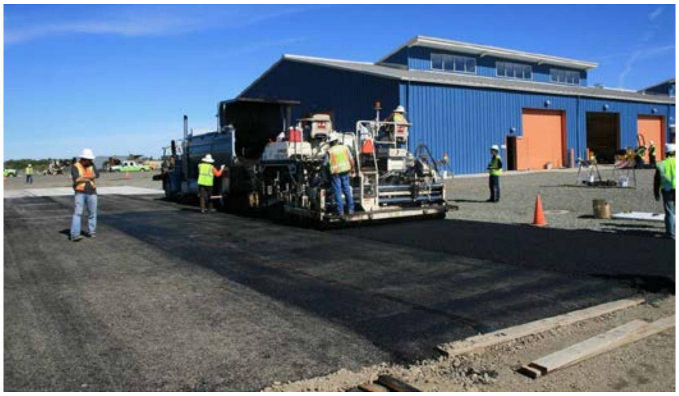

Figure G.45. Paving top lift 2-in. (50-mm) RHMA-G in Lane D, Section 1.

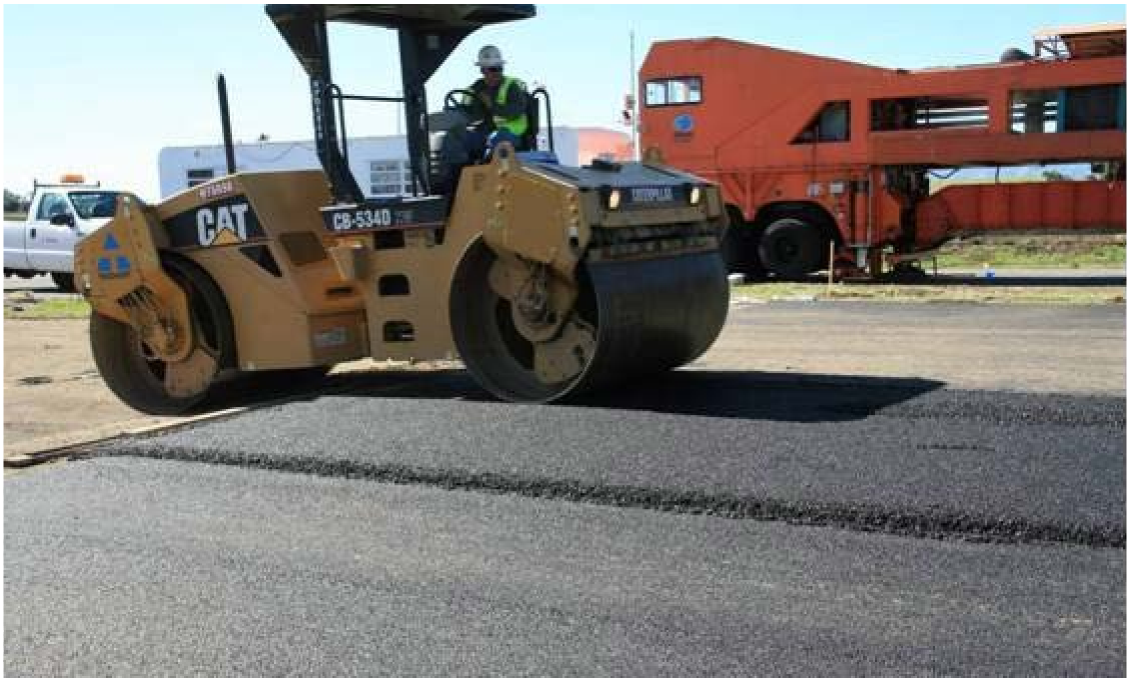

Figure G.46. Compaction of 2.0-in. (50-mm) second lift RHMA-G on Lane C.

determine performance modeling parameters. Figure G.48 shows the compaction mold frame for production of HMA ingots. Figure G.49 shows the hot HMA taken from the paver being weighed for placement in the mold. Figure G.50 shows the final HMA placement and cleaning of the compaction platform before rolling. Ingot mold perimeters and exteriors were swept clean before compaction. Careful movement of material was performed to minimize segregation. Figure G.51 shows the compaction process with the rolling wheel compactor. Ingots were properly compacted when the surface of the HMA was flush with the surface of the mold frame, indicating proper air void content. Figure G.52 shows the removal of the ingot mold from the compaction frame, before placement of the next ingot mold. The process was repeated until sufficient ingots were created to produce the required number of laboratory test specimens.

Initial Slab Response Monitoring

During and after construction, temperature gradients and slab and joint movement monitoring were performed.

The set time of the PCC was first established to provide a baseline "time zero" for this project. Determination of concrete set time was made through analysis of temperature gradients and strain behavior at the top and bottom of the PCC. Figure G.53 shows the temperature and strain gradients for Section A1. Immediately after placement of the wet concrete,

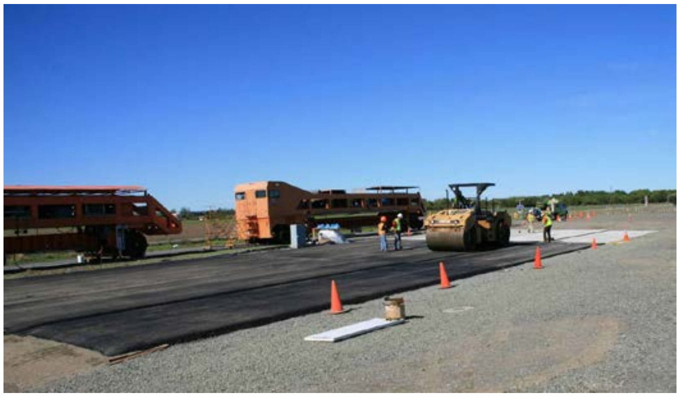

Figure G.47. Completed test track showing two HMA lift thicknesses and PCC sections.

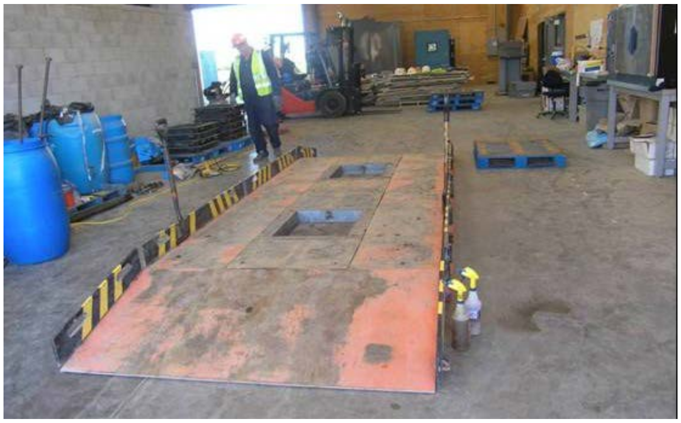

Figure G.48. Assembled compaction frame and ingot molds for field mix–lab compact HMA specimens.

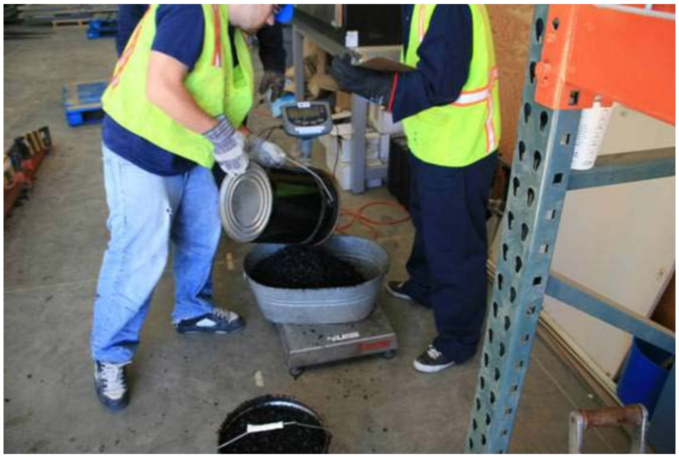

Figure G.49. Weighing of hot HMA for placement into ingot molds.

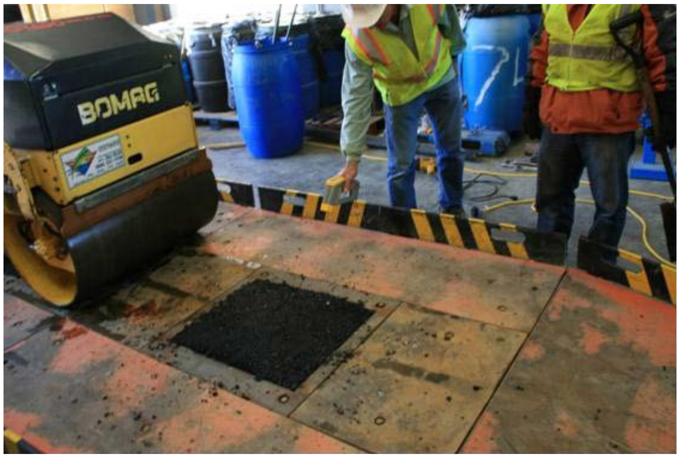

Figure G.51. Compaction of ingots with rolling wheel compactor.

the top and bottom strain gauges trend together because the concrete has not yet solidified. Between approximately 3 p.m. and 4 p.m., the strain sensors start to diverge, indicating solidification of the PCC.

Temperature gradients between the top and bottom of the slabs were calculated from measured temperatures. Figure G.54 shows the temperature differential between top and bottom in Section A1 with 7-in. PCC. Note that the presence of the Burlene curing blanket during the first 3 weeks of curing significantly reduced the temperature gradients compared with the uncovered PCC. Additional slab temperature and temperature gradient data are reported and analyzed in Appendix M.

Temperature Gradients

As an initial look at the effect of HMA thickness on temperature gradients and the reversal of slab curling, Figure G.55, Figure G.56, and Figure G.57 show plots of 7-in. PCC slab temperatures for HMA thicknesses of 4.5, 2.5, and 0 in., respectively. Figure G.58, Figure G.59, and Figure G.60 show plots of 5-in. PCC slab temperatures for HMA thicknesses of 4.5, 2.5, and 0 in. respectively. All these plots were made from data taken on October 27, 2009. Figure G.61 shows the air temperature for October 27, 2009, the day for which these gradients are plotted.

It can be seen that the temperature gradients increase with decreasing PCC and HMA thickness. In addition, the effect of the HMA layer was to increase the overall temperature of the PCC compared with the PCC without an HMA layer.

Slab Movements

Horizontal slab movement measurements were performed using HJDMDs, affixed to joints as described previously.

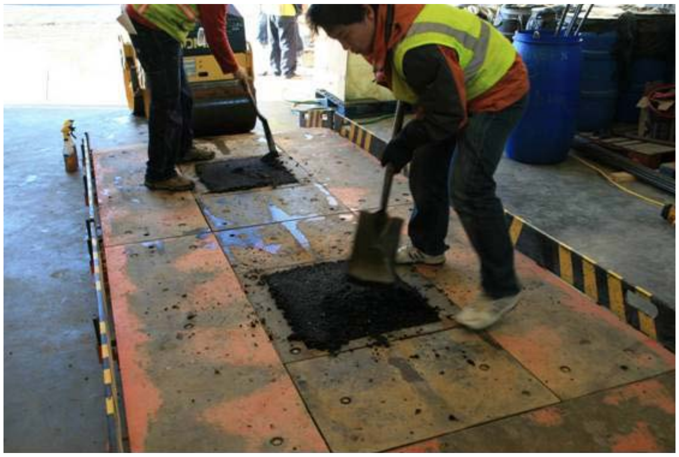

Figure G.50. HMA mix being spread out in the mold.

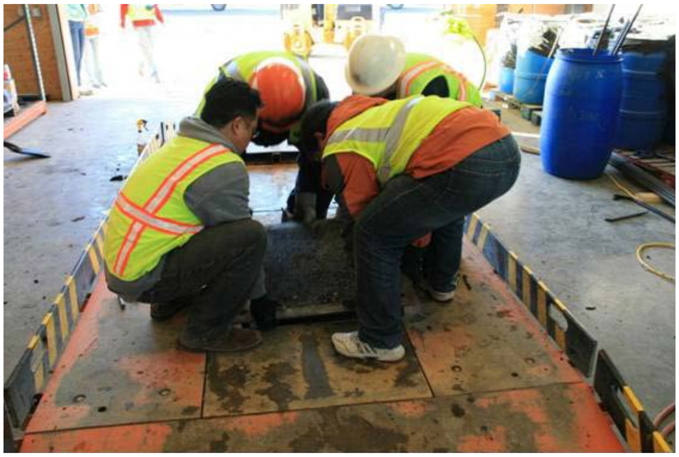

Figure G.52. Removal of compacted HMA ingot, with a weight of approximately 150 lb.

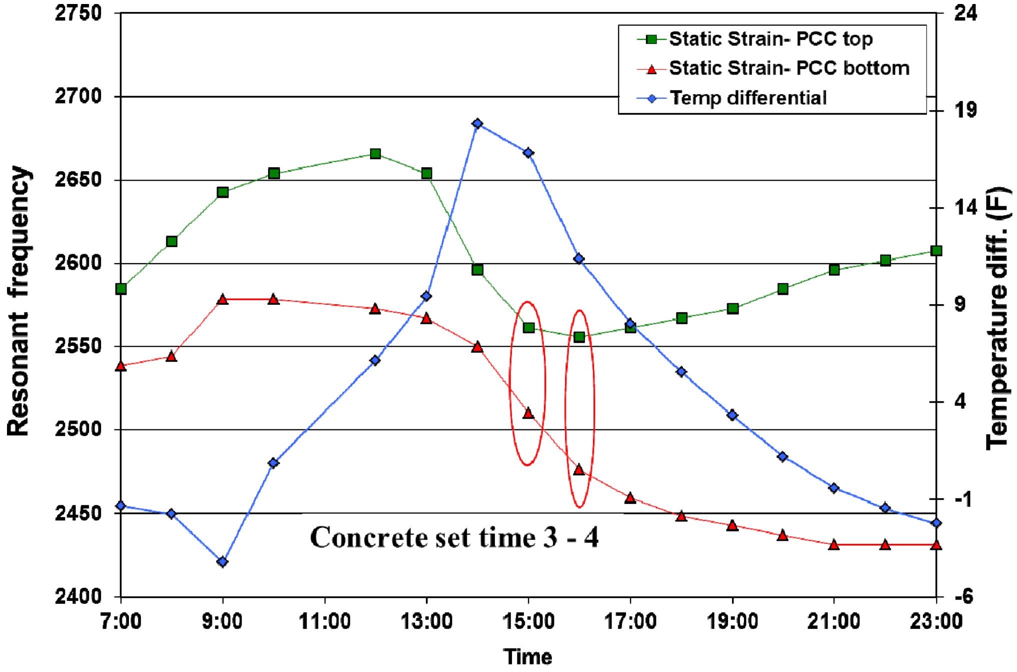

Figure G.53. Concrete set time determination through strain and temperature gradients.

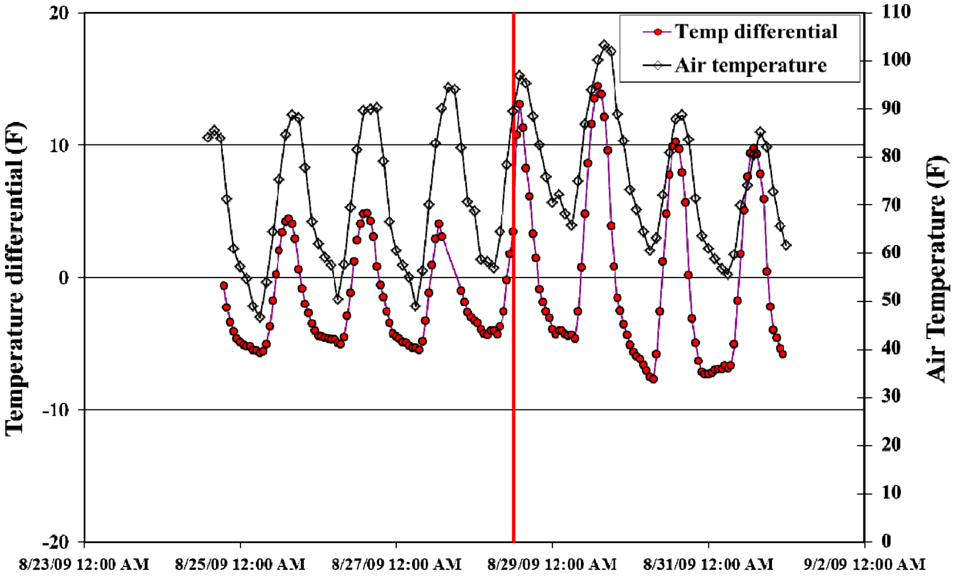

Figure G.54. Temperature difference between top and bottom of slab in Slab A1 (7 in. thick) before and after Burlene removal (red vertical line, 8/29/09).

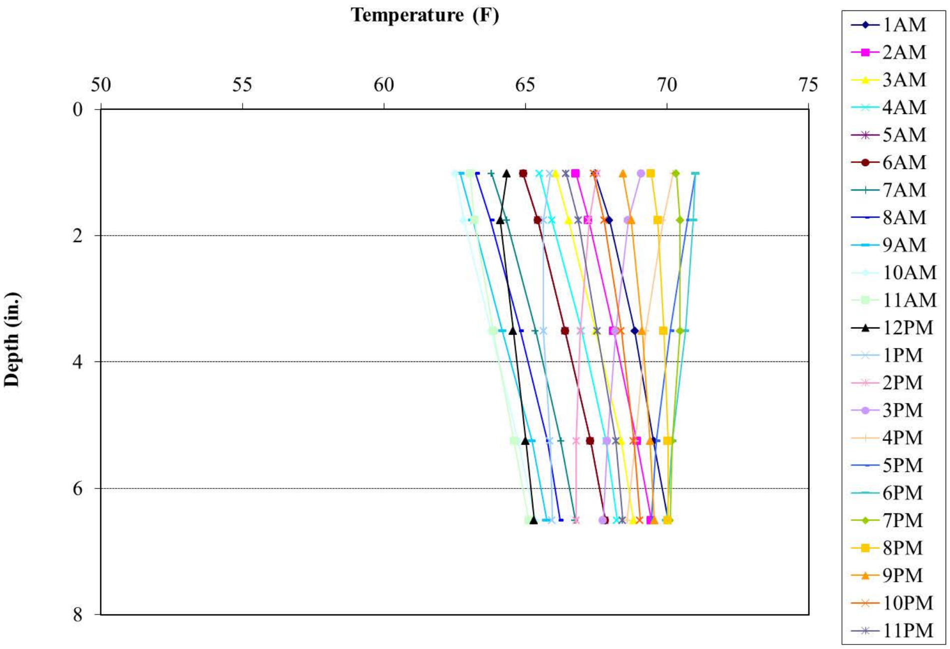

Figure G.55. Temperature gradient for Section A1, 4.5-in. HMA over 7-in. PCC.

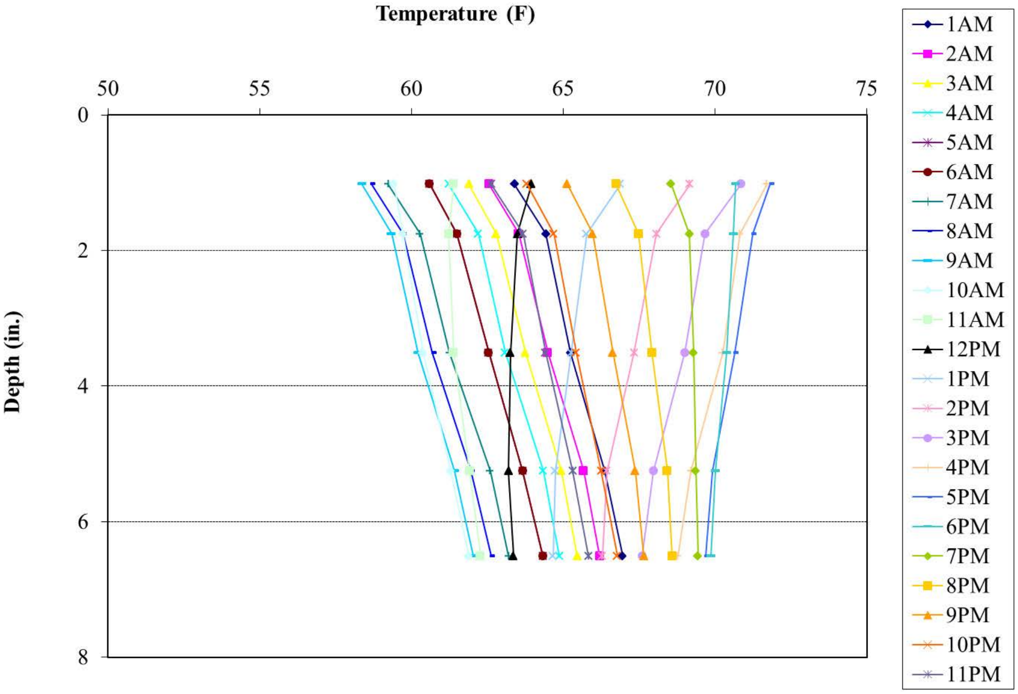

Figure G.56. Temperature gradient for Section A2, 2.5-in. HMA over 7-in. PCC.

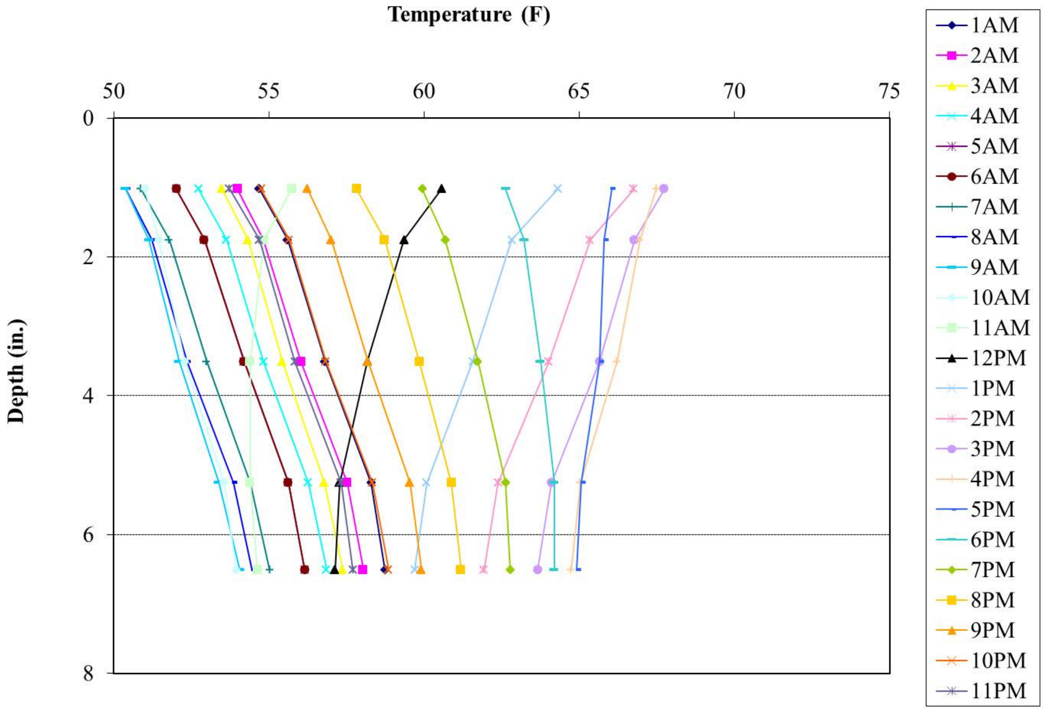

Figure G.57. Temperature gradient for Section A3, 7-in. PCC with no HMA layer.

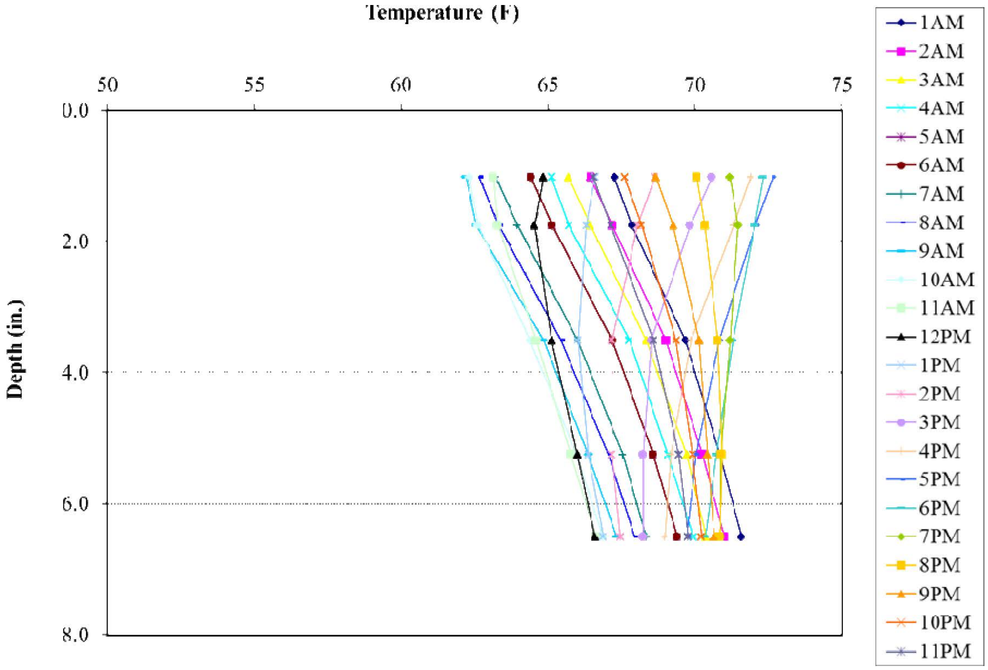

Figure G.58. Temperature gradient for Section D1, 4.5-in. HMA over 5-in. PCC.

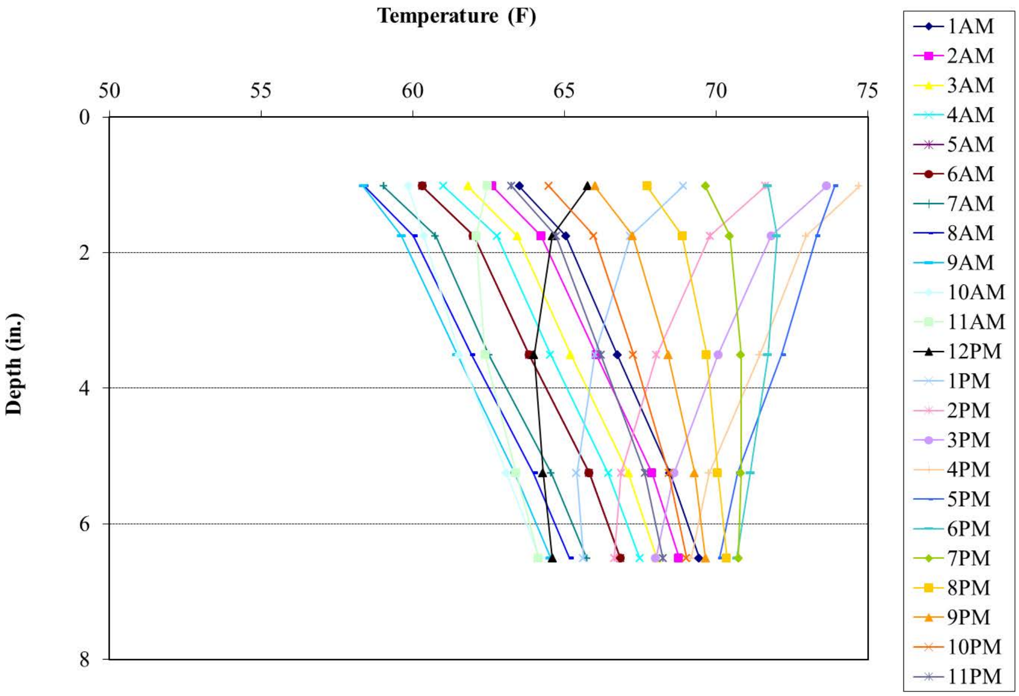

Figure G.59. Temperature gradient for Section D2, 2.5-in. HMA over 5-in. PCC.

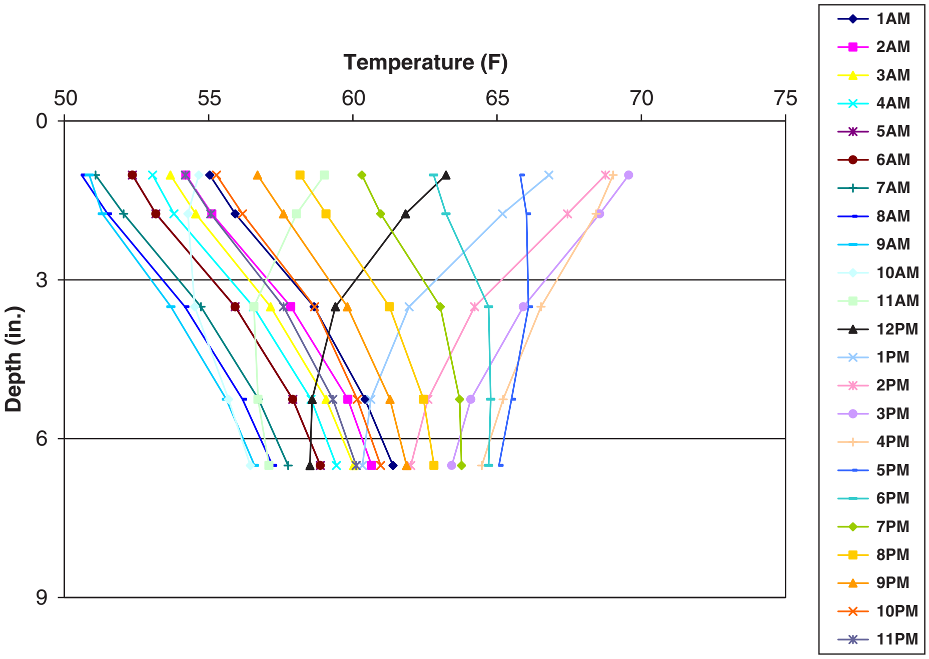

Figure G.60. Temperature gradient for Section D3, 5-in. PCC with no HMA layer.

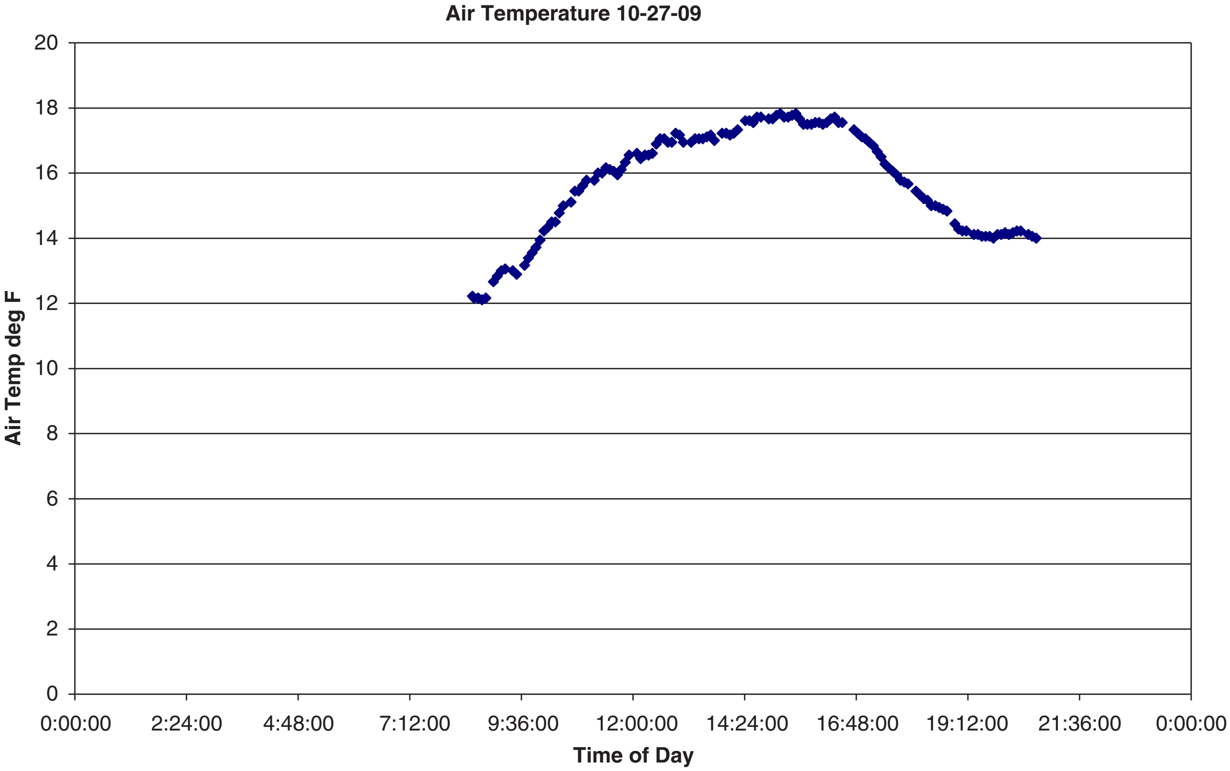

Figure G.61. Air temperature corresponding to PCC temperature gradient charts.

Figure G.62 shows the layout of HJDMDs for monitoring horizontal slab movement. Note that both 7-in. (183-mm) and 5-in. (130-mm) slabs were monitored before HMA paving.

Figure G.63 shows horizontal slab movement for Joints J4 to J8 in Lane B. The total opening amplitude is approximately 0.04 in. (1 mm). Note that the joint opening varies slightly because of day-to-day temperature fluctuations and is at maximum before sunrise.

Vertical joint movement caused by temperature fluctuations was measured on 7-in. (183-mm) and 5-in. (130-mm) slabs using JDMDs, affixed as previously discussed. These readings were taken 1 month after PCC construction. Figure G.64 shows the arrangement of JDMDs on the test track for measuring vertical joint movement. Figure G.65, Figure G.66, and Figure G.67 show the vertical joint and horizontal movements measured in Lanes A (doweled), C (nondoweled), and D (nondoweled), respectively. The relative thermally induced vertical movement for doweled and nondoweled, 7-in. (183-mm) slabs was approximately the same. Thermally induced vertical joint movement for the 5-in. (130-mm) slabs was approximately 20% higher than for the 7-in. (183-mm) slabs.

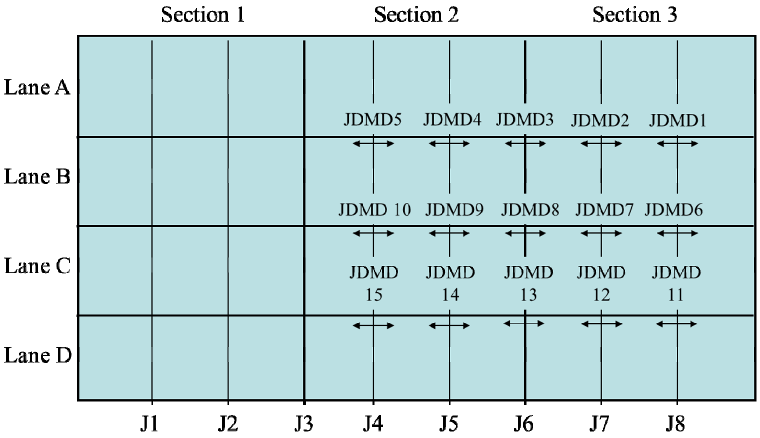
Section 1
Section 2
Section 3
Lane A
Lane B
Lane C
Lane D
JDMD5
JDMD4
JDMD3
JDMD2
JDMD1
JDMD 10
JDMD9
JDMD8
JDMD7
JDMD6
JDMD 15
JDMD 14
JDMD 13
JDMD 12
JDMD 11
J1
J2
J3
J4
J5
J6
J7
J8

Figure G.62. Layout for measuring horizontal joint movement for Lanes B, C, and D.

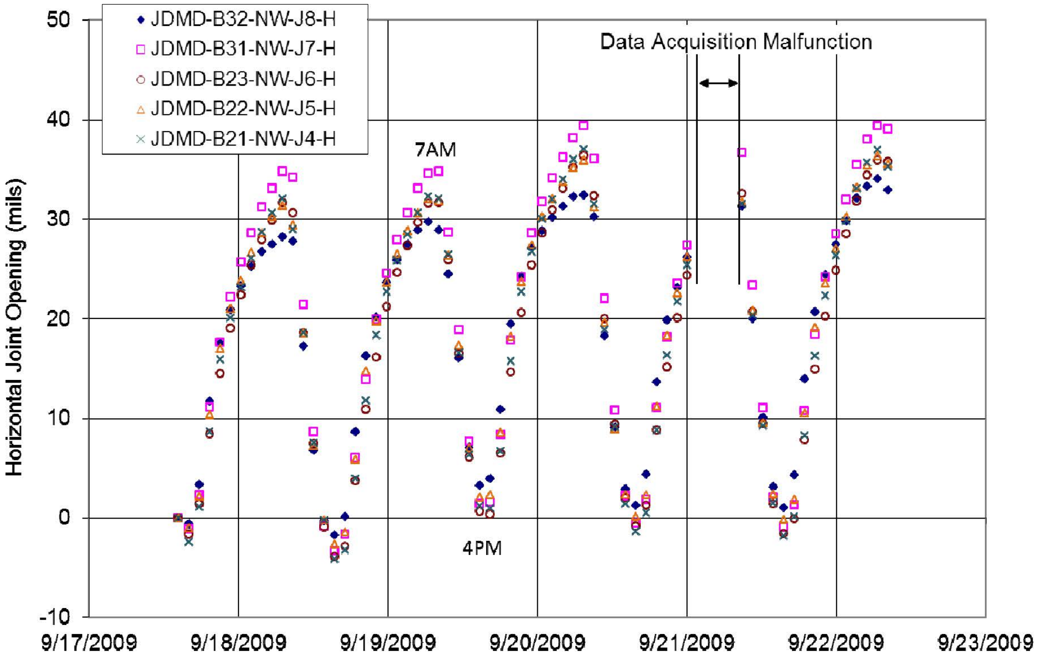

Figure G.63. Horizontal joint movement for Joints J4 to J8, Lane B.

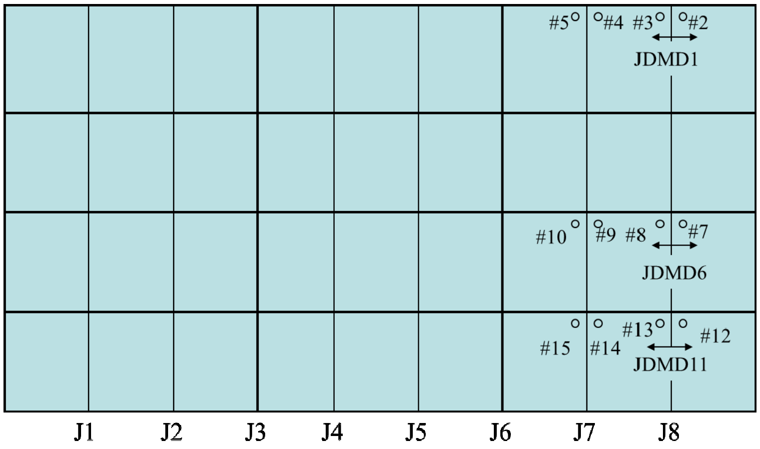
#5
#4
#3
#2
JDMD1
#10
#9
#8
#7
JDMD6
#13
#12
#15
#14
JDMD11
J1
J2
J3
J4
J5
J6
J7
J8

Figure G.64. Layout for measuring vertical joint movement in Joint J8.

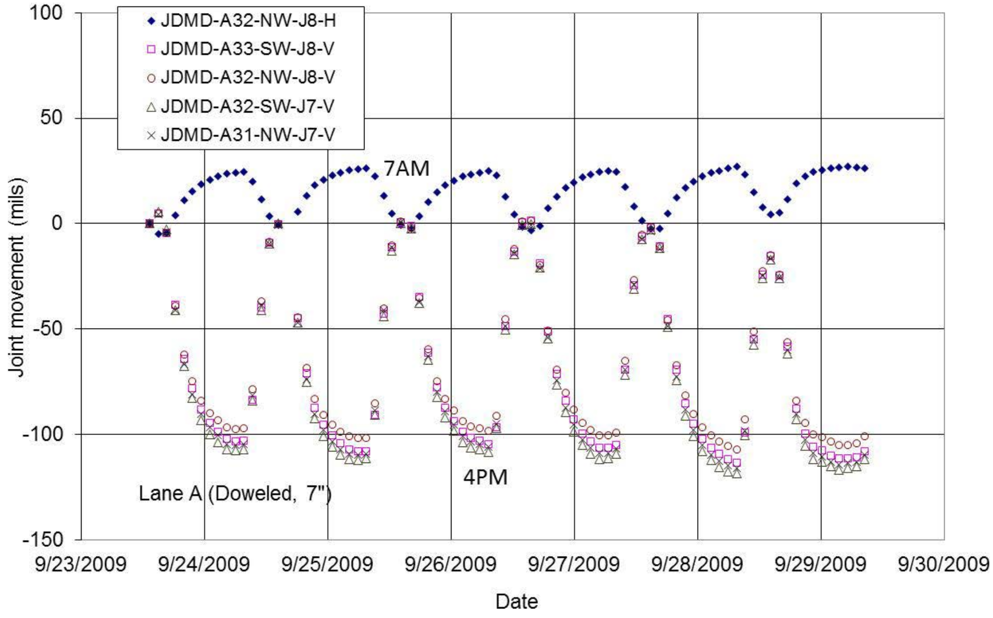

Figure G.65. Joint movement in Lane A (7-in. doweled)—horizontal (*dark solid fill*) and vertical (*no fill*).

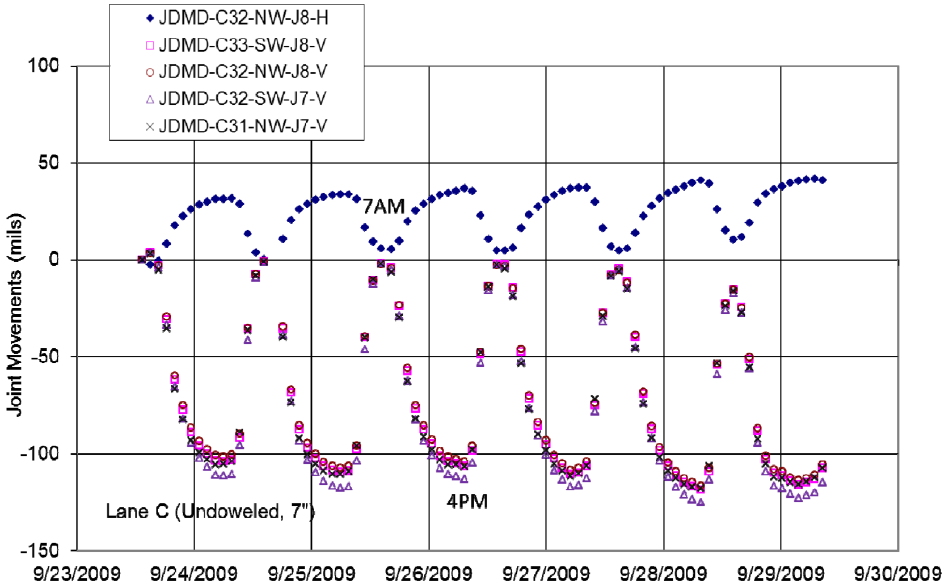

Figure G.66. Joint movement in Lane C (7-in. nondoweled)—horizontal (*dark solid fill*) and vertical (*no fill*).

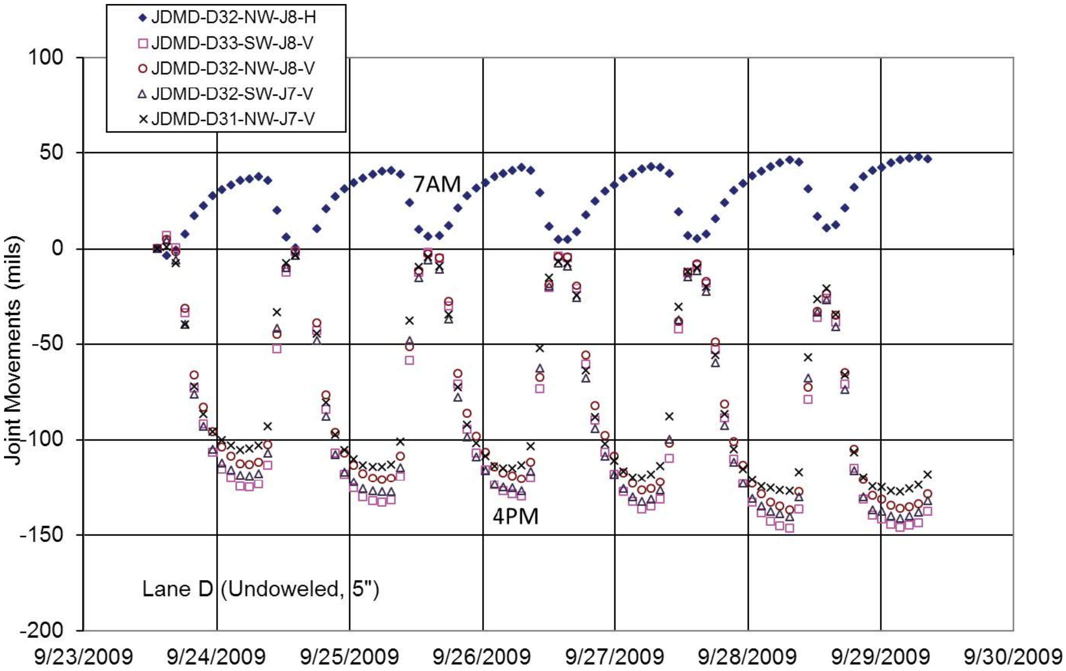

Figure G.67. Joint movement in Lane D (5-in. nondoweled)—horizontal (*dark solid fill*) and vertical (*no fill*).

APPENDIX H

Instrumentation and Analysis of Instrumented Data at MnROAD

Introduction

The three SHRP 2 R21 experimental pavement sections were heavily instrumented with a variety of sensors capable of measuring temperature, relative humidity, and static and dynamic strain at multiple locations and depths within each pavement structure. In addition, a weather station is located on site to capture all primary climate indicators, such as ambient temperature, solar radiation, wind speed and direction, as well as precipitation. The instrumentation installed in the pavement is used to characterize the environmental conditions within the slab for each type of pavement structure. The static strain gauges are then used to characterize the deformation in the slab as a result of these environmental loads and built-in gradients. The data from the instrumentation are essential to a subsequent assessment of the resulting stresses in the slabs through the use of the finite element modeling (FEM) and eventually developing design guidelines for composite pavements.

The instrumentation of the upper exposed aggregate concrete (EAC) layer for Cells 71 and 72 was quite challenging. This is because the sensors in the upper layer needed to be installed after the placement of the first layer and before the placement of the second layer. Any sensors higher than the depth of the first layer would be hit by the pan of the paver as the first layer was being placed. The fact that the amount of time between the placement of the first and second layer is restricted to less than 30 minutes to ensure bonding between the two layers provided further complications. Note that although a 90-minute upper limit was specified, the time between the lifts was desired to be between 15 and 60 minutes, and the instrumentation crew was directed not to delay paving.

The other challenge with the sensor installations in the upper layer was that the each of the sensors had lead wires that needed to be wired into the dataloggers before paving so that data could be collected as the concrete was being placed. The lead wires for the sensors to be installed in both the upper and lower layers need to be buried underground before the passing of the paver to avoid being damaged by the track of the paver. This can be seen in Figure H.1. Therefore, the sensors to be installed in the upper layer had to be temporarily stored in the lower layer as it was being paved.

The easiest way to instrument these pavements would be to install the sensors in the lower layer before paving and then to retrofit sensors in the upper layer after paving. Unfortunately, this would prevent the collection of climatic and static strain data in the upper concrete layer as the concrete hardens, so this was not a viable option for the project. Therefore, innovative installation techniques had to be developed for installing the sensors in the upper layer before the passing of the second paver. A description of each of the sensors used and the innovative installation techniques developed is provided below.

A survey was performed to document the elevations of the top of the base, the sensors, and the top of the pavement so that the thickness of the slab and the depth of each sensor could be established. Unfortunately, the survey crew had difficulties, so for many sensors, only the design depths are known.

Temperature Sensors

Thermocouples (designated as "TC") were installed throughout the depth of the pavement structure so that temperature could be measured. Type T thermocouple wire from Omega Engineering was used. The thermocouple wire contains two dissimilar metals: copper and constantan. When a junction is formed between these two metals, a small but unique voltage is produced. Because the change in voltage is approximately linear with changes in temperature, a relationship can be established. Before installation, the ends of the thermocouple wire were spliced and soldered, creating a junction at the end of the wire. The Omega Type T Special thermocouple was used, so the limit of error is the greater of 0.4% or 0.9°F. Figure H.2 shows a typical thermocouple installation for these composite sections. It can be seen that holes were drilled into a polymerized

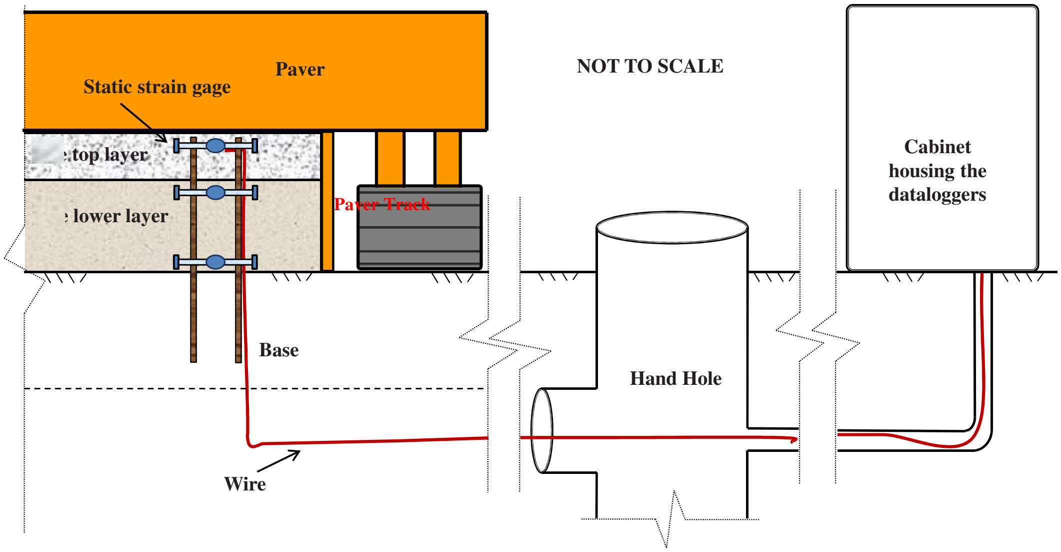

Figure H.1. Sensor wire path to data collection cabinet.

vinyl chloride (PVC) pipe at various depths so that the thermocouple junction could be extended through the pipe wall. After the thermocouple wires were in place, the PVC pipe was filled with epoxy so the wires would not move during the paving process and so that the rigidity of the PVC pipe was more similar to that of the concrete.

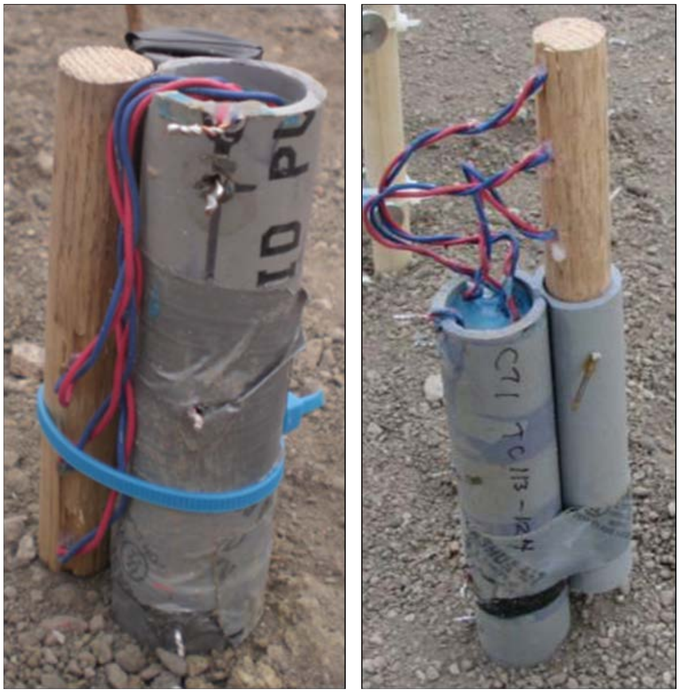
(a) (b)

Figure H.2. Thermocouple installed in Cells 71 and 72. (a) Installation before the passing of the first paver. (b) Position of where the dowel would be when the second paver passed.

Thermocouples installed in the upper concrete layer for Cells 71 and 72 were attached to a wood dowel that eventually was placed in a holder attached to the side of the PVC pipe (Figure H.2b). The holder had a pin driven through it to ensure the dowel would be positioned at the correct depth. Before the passing of the first paver, the dowel was anchored to the PVC pipe with cable ties, as shown in Figure H.2a. A piece of electric tape was placed over the top of the holder to ensure it was not filled with concrete when the first paver passed. After the passing of the first paver, each sensor was located in the first layer of portland cement concrete (PCC) and the cable tie was cut. The wood dowel was then placed in the holder attached to the side of the PVC pipe, as shown in Figure H.2b. A screw was driven through the holder and into the dowel to secure it in place before the second paver passed. Cable ties were attached to each dowel so that the tie extended outward above the elevation of the first layer of concrete. This way the sensor locations were easily identified after the passing of the first paver (Figure H.3).

For Cell 70, the thermocouples to be installed in the hot-mix asphalt (HMA) layer were not attached to a dowel, as seen in Figure H.4. The group of loose wires was pulled to the surface of the PCC layer right after the paver passed. Once the HMA layer was placed, a core was pulled from this layer near these installations so that the group of loose wire could be drawn up through the core hole. They were then installed in the HMA layer at predetermined depths.

Concrete Moisture Sensors

To measure moisture within the concrete, Sensirion SHT75 relative humidity (designated as “MC”) and temperature sensors were installed. The SHT75 sensor is a relatively small

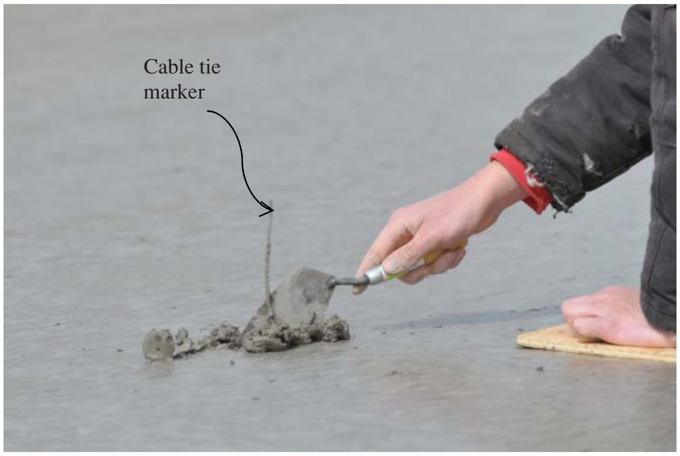

Figure H.3. Cable ties attached to the dowel so that the sensor locations could be easily located.

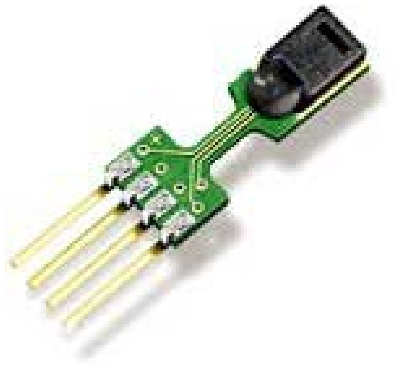

Source: www.sensirion.com, June 2011.

Figure H.5. Sensirion SHT75 relative humidity and temperature sensor.

(approximately 0.75- × 0.25- × 0.125-in.) and cost-effective means of measuring relative humidity in concrete. The sensor, which is shown in Figure H.5, uses a capacitive polymer sensing element to measure relative humidity and a band gap temperature sensor to measure temperature. Communication to and from the sensor was accommodated by four connector pins, which supply power, receive clock instructions, and transmit temperature and relative humidity data.

The error associated with measuring relative humidity and temperature using these sensors is shown in Figures H.6 and H.7, respectively. It should be noted that error in the relative humidity is high at values of relative humidity greater than 90%. This is important because the relative humidity of the concrete is quite high early and maintains a saturated, or near saturated, condition near the bottom portion of the slab throughout the life of the pavement. These sensors do allow for accurate measurements near the upper portion of the slab, where the relative humidity is lower and exhibits greater fluctuations.

Figure H.8 is a photograph of the installation of these relative humidity sensors in Cell 70. Each sensor was fed through a PVC pipe, as was done for the installation of the thermocouples. The sensors were pulled through holes drilled into the wall of the PVC pipe, and protective capsules were then mounted on the outside of the PVC pipe over the sensor. These sensors are easily damaged and thus had to be encapsulated in such a way that water vapor could reach the sensor, but the sensor could not come into contact with the fresh concrete.

In Cell 70, the moisture sensors were installed in the lower PCC layer but not the upper HMA layer, whereas in Cells 71 and 72 the moisture sensors were installed in the upper and lower PCC layers. An example of the installations for Cells 71

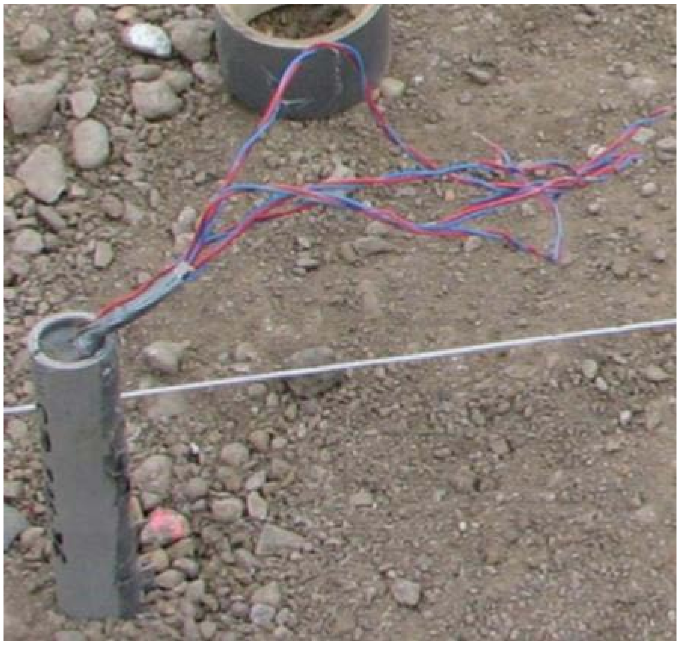

Figure H.4. Thermocouples installed in Cell 70.

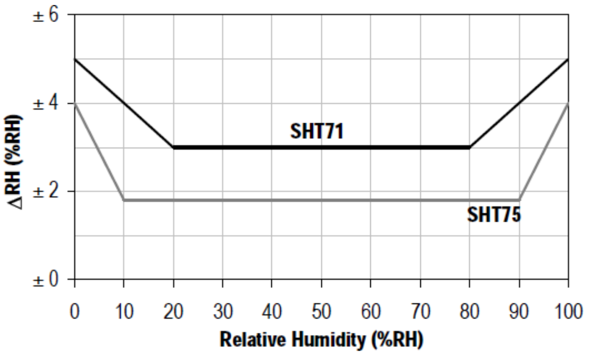

Source: www.sensirion.com, June 2011.

Figure H.6. The error associated with relative humidity measurements made using the SHT75.

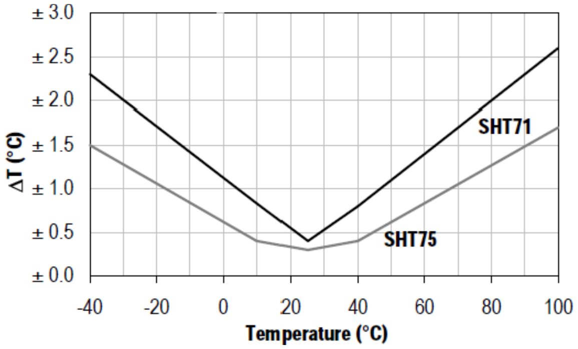

Source: www.sensirion.com, June 2011.

Figure H.7. The error associated with temperature measurements made using the SHT75.

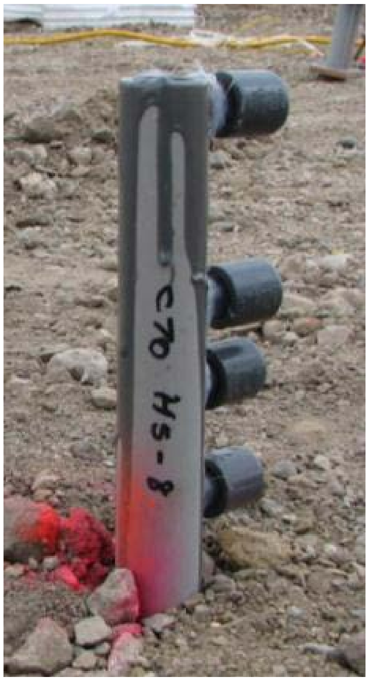

Figure H.8. Concrete relative humidity sensors installed in Cell 70.

and 72 is shown in Figure H.9. The lower portion of the installation for these cells was the same as that used for Cell 70, except three additional sensors were pulled through the PVC pipe and attached to a wood dowel, as seen in Figure H.9a. These three sensors were for installing in the upper PCC layer. Holes were drilled through the dowel, and the sensors were then pulled through these holes. Protective capsules were placed over the sensors and mounted to the dowel. As shown in Figure H.9a, the end of the dowel was cut on an angle so that the depth the dowel was wedged into the PVC pipe could be controlled. A screw was then driven through the PVC pipe and into the dowel to lock it into place before the passing of the second paver.

To protect the sensors mounted to the dowel as the first paver passed over them, the sensors were wrapped in plastic and anchored to the PVC pipe with cable ties, as shown in Figure H.9b. During paving, the sensors were located in the bottom concrete layer after the passing of the first paver. The cable tie was cut, the plastic removed, and the dowel installed in the PVC pipe before the passing of the second paver.

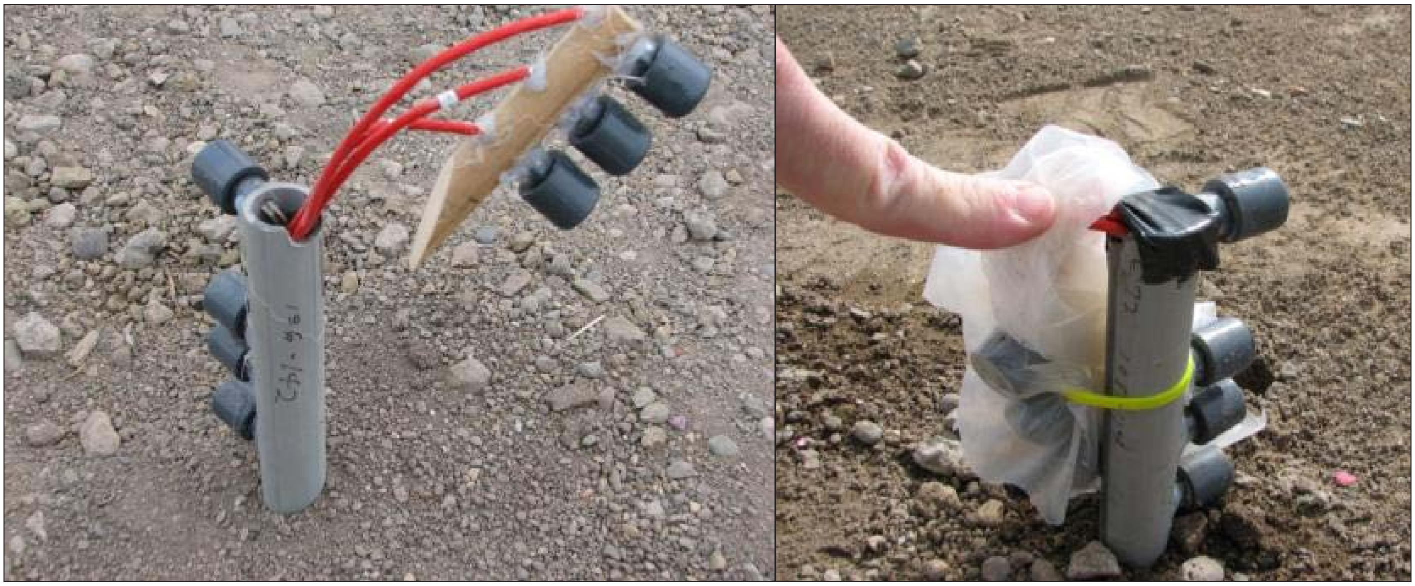

(a) (b)

Figure H.9. Concrete relative humidity sensors installed in Cells 71 and 72. (a) Sensors to be installed in the upper and lower PCC layers and (b) installation just before the passing of the first paver.

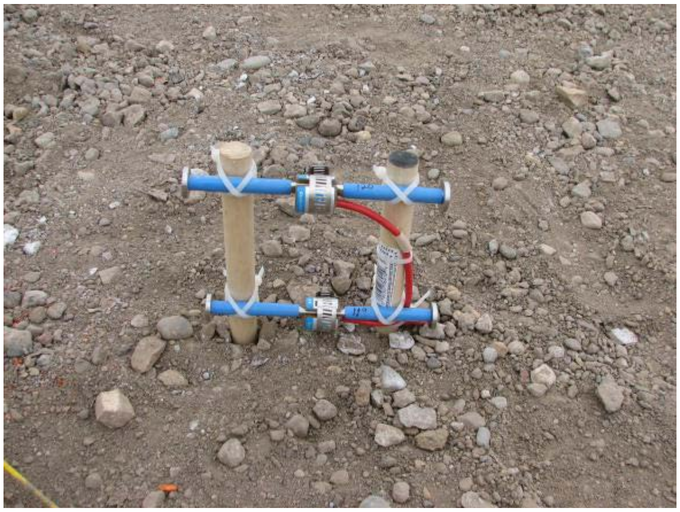

Figure H.10. Static strain gauge installation for Cell 70.

Static Strain Gauges

The PCC response to static environmental loads is measured using vibrating wire (VW) strain gauges. Geokon Model 4200 VW concrete embedment strain gauges, as shown in Figure H.10, were used. In these gauges, a steel cable is tensioned between two metal end blocks. When the gauge is embedded in concrete and concrete deformations occur, these end blocks move relative to one another. The movement of these end blocks influences the degree of tension in the steel cable. This tension in the cable is quantified by an electromagnetic coil, which measures the cable's resonant frequency of vibration upon being plucked. The sensor is also equipped with a thermistor so corrections for temperature can be made. The resolution of the strain gauge is ±1 microstrain, with the accuracy of the thermistor being ±0.75°F.

Figure H.10 shows a typical installation setup for the VW gauges in Cell 70. For Cells 71 and 72, each installation location included two VW gauges in the lower PCC layer, as was done for Cell 70, along with one additional sensor in the upper PCC layer, as shown in Figure H.11. Before the lower layer was paved, the cylindrical housing containing the plucker and thermistor portion of the VW gauge was removed from the hollow tube portion of the gauge. The housing was then covered with plastic and cable tied to the lower wooden dowel rod, as shown in Figure H.12. The hollow tube was attached to two dowels that were used to extend the dowels on which the lower two gauges were hung into the second layer of concrete. Couplings were glued and screwed to the bottoms of the two extensions so the extensions could be easily attached to the existing dowels after the placement of the first layer of concrete. The extensions were customized individually for each installation to be sure the final depth and location of the sensor were correct.

After the first paver passed, the sensors were located within the bottom layer of concrete. The cylindrical housing was cut free from the dowel and the protective plastic sheet removed. The housing was then reattached to the hollow tube/extension assembly using a hose clamp. The couplings on the end of the extension assembly were then fitted on top of the dowels in the lower layer of concrete. A screw was driven through the coupling and into the dowel to lock it into place before the top layer of concrete was placed. The installation of the hollow tube/extension assembly after the passing of the first paver can be seen in Figure H.13.

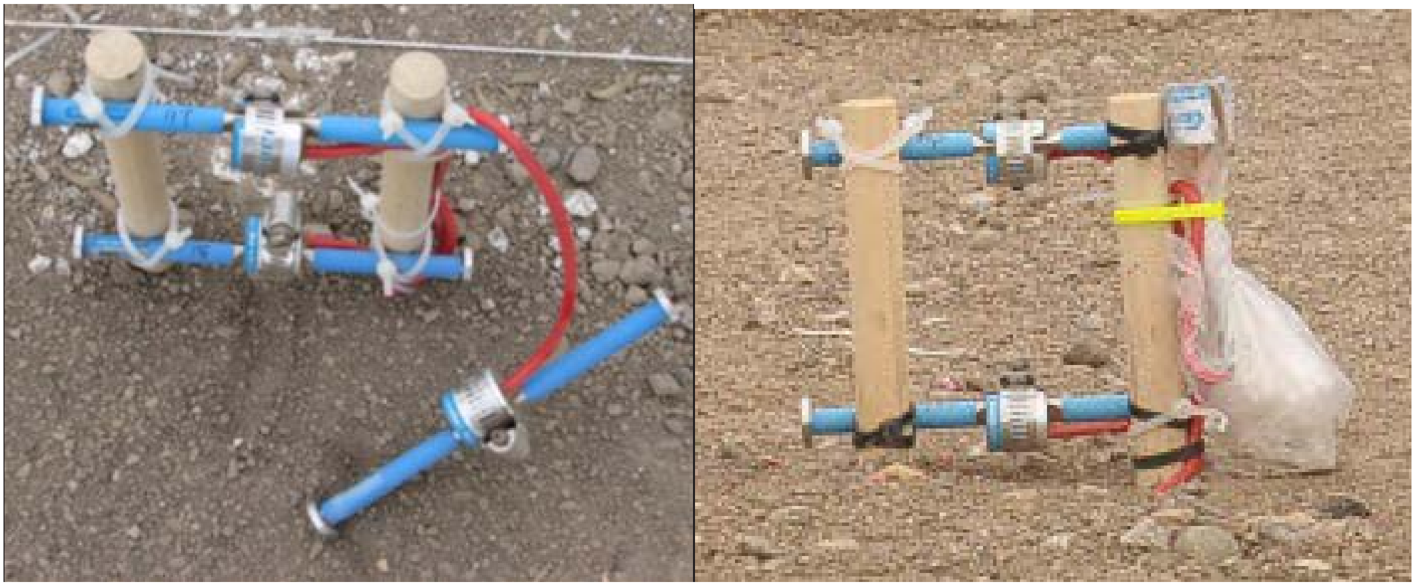

Figure H.11. Static strain gauge installations for Cells 71 and 72.

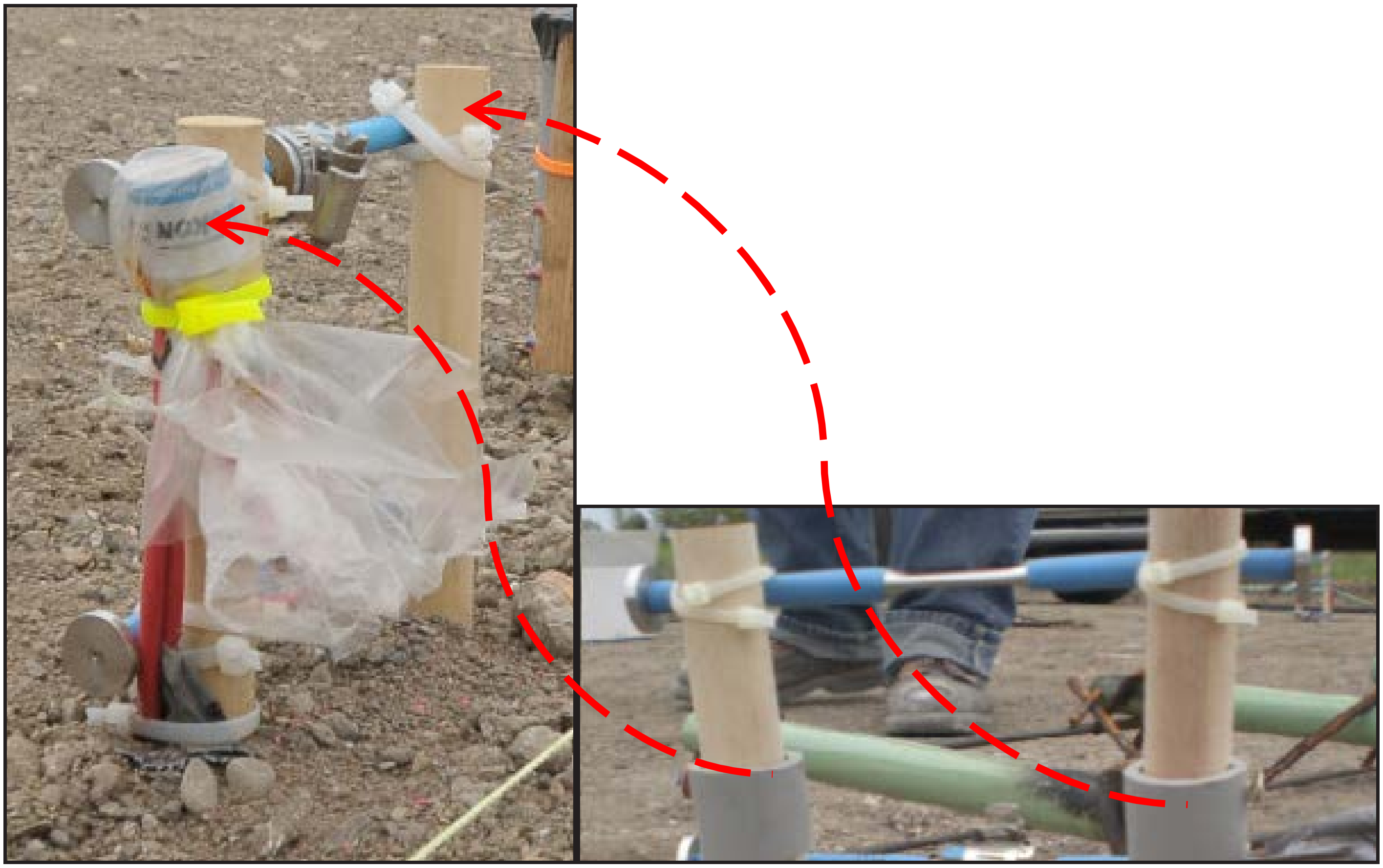

Figure H.12. Technique for installing the static strain gauge in the upper concrete layer for Cells 71 and 72.

Dynamic Strain Gauges

Dynamic strain sensors (designated as “CE” sensors) were installed to measure the slab response to loads applied by truck traffic and the falling weight deflectometer (FWD). Tokyo Sokki PML-60-2L dynamic strain gauges were used. The Tokyo Sokki PML-60-2L consists of a copper/nickel alloy resistance foil gauge attached to two lead wires. The foil is attached to an electrically insulated backing, and with the use of a special adhesive, is attached to one of two thin acrylic plates. The two plates are sealed together to protect the gauge from contamination when installed in the concrete. These acrylic plates are coated with a fine, granular material to improve bonding to the surrounding concrete. The insulated backing expands and contracts with the concrete, causing the resistance in the foil gauge to change. From resistance, strain can be found using the following relationship:

Figure H.13. Installation of the static strain gauge for the upper concrete layer for Cells 71 and 72.

$$\varepsilon = \frac{\Delta L}{L} = \frac{\Delta R/R}{K} \tag{H.1}$$

where

$\Delta L/L$ = change in length (ΔL) per unit length (L)
ε = strain,
R = gauge resistance,
ΔR = resistance change due to strain, and
K = gauge factor.

The dynamic strain gauges are installed in each of the three cells. In Cell 70, the dynamic gauges were installed at the bottom of the PCC slab by pinning them to the granular base using wire and nails, as shown in Figure H.14. In Cells 71 and 72, dynamic

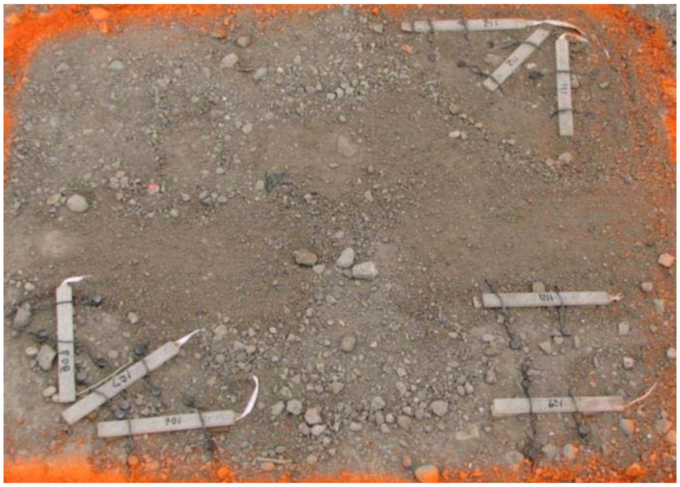

Figure H.14. Dynamic strain gauge installation for Cell 70.

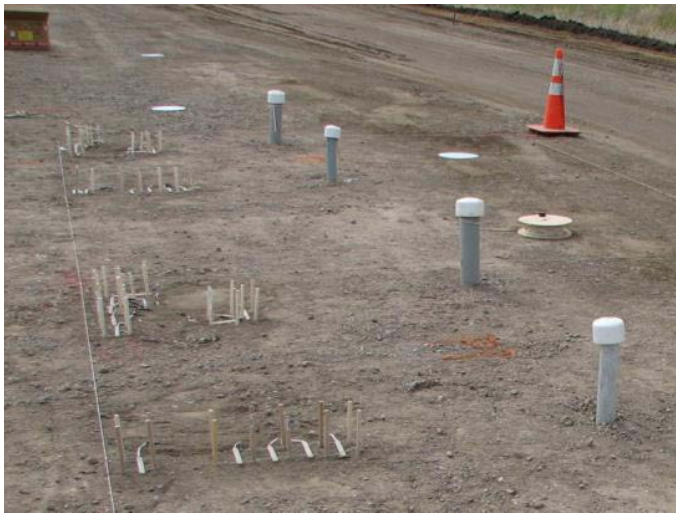

Figure H.16. Example of the vertical PVC pipe where the dynamic strain gauges were stored until after the pass of the first paver for Cells 71 and 72.

strain gauges were installed in both the upper and lower layers of concrete. The sensors were suspended from wood dowels using wire, as shown in Figure H.15. To install the dynamic sensors in the upper concrete layer for Cells 71 and 72, the dowels were extended with couplings, similar to the installation technique used for the static strain gauges.

The dynamic strain gauges to be installed in the upper concrete layer were stored in a PVC pipe extending up from the base until after the first paver passed. This allowed the sensor lead wires to be run along the bottom of the base and out through a hand hole, where they could be run through a piping system in the ground to the cabinets housing the dataloggers. These vertical PVC pipe can be seen in Figure H.16. Once the first paver passed, the PVC pipe and sensor installations were located in the first layer of concrete. Dowel extensions were installed on top of each dowel in the lower layer using couplings; then a screw was driven through the coupling into the dowel to lock it in place. Wire was used to hang the dynamic gauge from the dowels, as shown in Figure H.17.

Weather Station

A weather station is available on site at MnROAD. The weather station provides ambient temperature and relative humidity, solar radiation, wind speed and direction, and precipitation data. The climatic data are collected every 15 minutes.

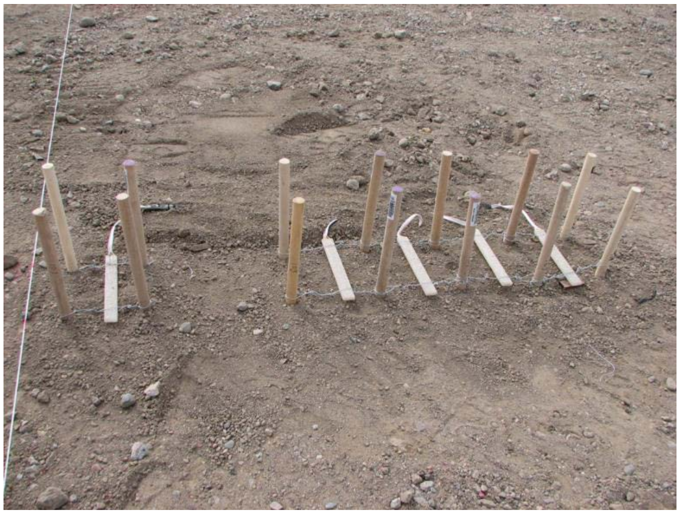

Figure H.15. Dynamic strain gauge installation for Cells 71 and 72.

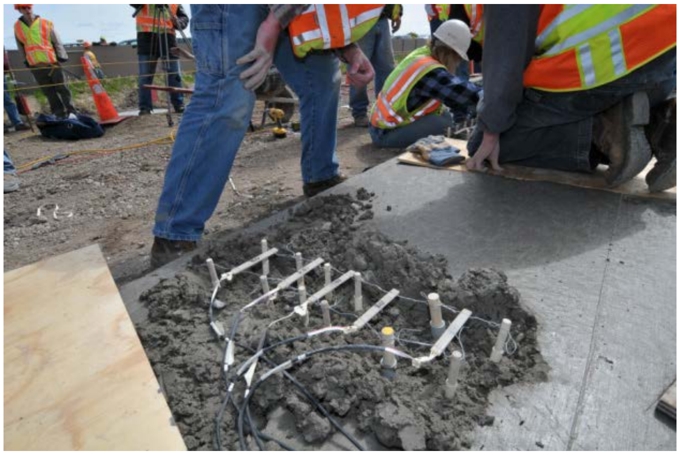

Figure H.17. Example of the installation of the dynamic strain gauges in the upper concrete layer for Cells 71 and 72.

Data Acquisition

Campbell Scientific dataloggers are used to collect all data for the static strain and environmental sensors. These data are collected at 15-minute intervals. The sensors are wired into dataloggers and multiplexers (which increase the number of sensors with which the datalogger can communicate) that are housed in cabinets located adjacent to the roadway. The dataloggers collect the data and provide temporary storage. Periodically, the data are transferred out of this temporary storage and preliminary data quality checks are performed before the data are placed in final storage in the MnROAD database. This data collection system is referred to as online because the dataloggers are in continuous communication with the sensors.

The dynamic strain data are not online. The data acquisition system used for the dynamic strain gauges is housed in a mobile unit that can be taken to each cell for manual data collection. The data are collected at a rate of approximately 1,200 Hz so that the dynamic response of the slab can be characterized accurately. For proper interpretation of the dynamic strains, the loading conditions must be characterized accurately. Therefore, dynamic strain data typically are collected only under controlled loading conditions.

Sensor Layout

The three composite pavement cells are located in the central portion of the mainline section. Each cell contains four instrumented slabs. The instrumented slab furthest west within each cell is labeled Slab 1, and the next four consecutive slabs are labeled Slab 2 through Slab 5, as shown in Figure H.18. All instrumented slabs are in the driving lane in the westbound direction.

More than 540 sensors are installed in the composite pavements constructed at MnROAD. Cell 70 has CE, VW, TC, and relative humidity (RH) sensors in the PCC layer and TC sensors in the HMA layer. Cells 71 and 72 have CE, VW, TC, and RH sensors in both the upper and lower PCC layers. The stationing for each instrumented slab and the number of each sensor type within each cell are summarized in Table H.1.

Table H.1. Summary of the Number of Sensors and Sensor Types for Each Cell

Cell	Slab	Stationing	Sensors
70	1	1,166 + 67 to 1,166 + 82	10 VW, 36 TC, 12 MC
	2	1,166 + 82 to 1,166 + 97	10 VW, 36 TC, 12 MC
	3	1,166 + 97 to 1,167 + 12	None
	4	1,167 + 12 to 1,167 + 27	14 CE
	5	1,167 + 27 to 1,167 + 42	14 CE
71	1	1,170 + 53 to 1,170 + 68	15 VW, 36 TC, 21 MC
	2	1,170 + 68 to 1,170 + 83	15 VW, 36 TC, 21 MC
	3	1,170 + 83 to 1,170 + 98	None
	4	1,170 + 98 to 1,171 + 13	28 CE
	5	1,171 + 13 to 1,171 + 28	28 CE
72	1	1,175 + 63 to 1,175 + 78	15 VW, 36 TC, 21 MC
	2	1,175 + 78 to 1,175 + 93	15 VW, 36 TC, 21 MC
	3	1,175 + 93 to 1,176 + 08	None
	4	1,176 + 08 to 1,176 + 23	28 CE
	5	1,176 + 23 to 1,167 + 38	28 CE

The sensor locations for each slab are provided in Figure H.19. The sensor layout in Slab 1 is replicated in Slab 2, and the sensor layout in Slab 4 is replicated in Slab 5. The distribution of sensors with depth for Cells 70, 71, and 72 can be seen in Figure H.20. Only sensors installed in the upper HMA layer for Cell 70 are thermocouples. The upper EAC layer for Cells 71 and 72 contain TC, MC, VW, and CE gauges. Figure H.21 and Figure H.22 provide the dimensions for each sensor layout.

A photograph of Slabs 1 and 2 before paving is provided in Figure H.23 so that the sensor layout can be observed. As stated, Slabs 1 and 2 contain thermocouples, static strain gauges, and moisture sensors. Figure H.24 provides a photograph of just the sensors installed at midslab. The sensors to

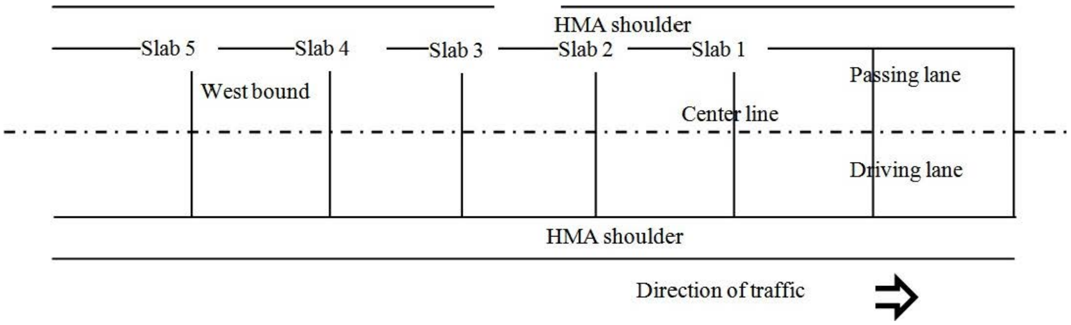

Figure H.18. Layout of the Instrumented Slabs for Cells 70, 71, and 72.

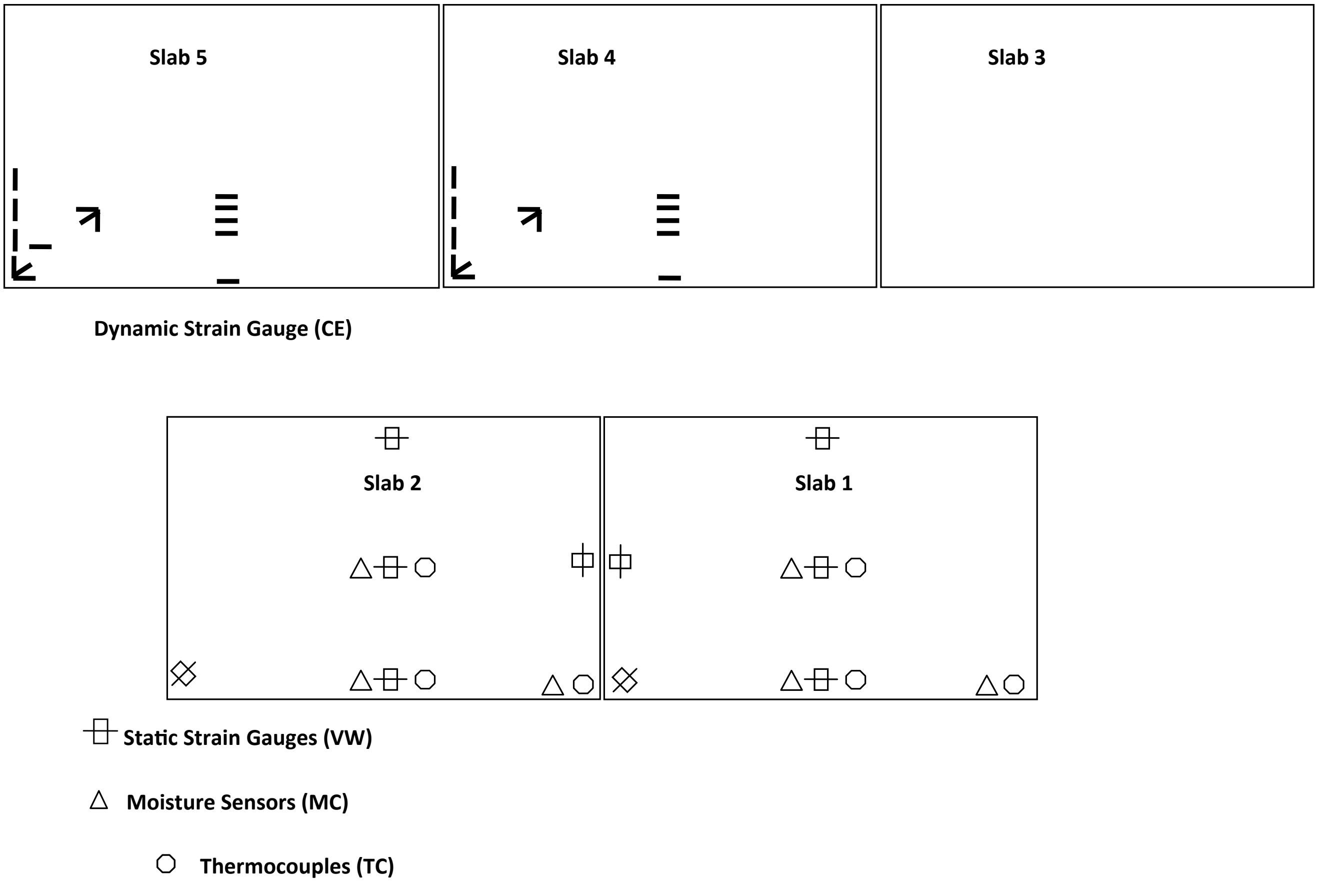
Slab 5
Slab 4
Slab 3
Dynamic Strain Gauge (CE)
Slab 2
Slab 1
Static Strain Gauges (VW)
Moisture Sensors (MC)
Thermocouples (TC)

Figure H.19. Sensor layout for all three cells.

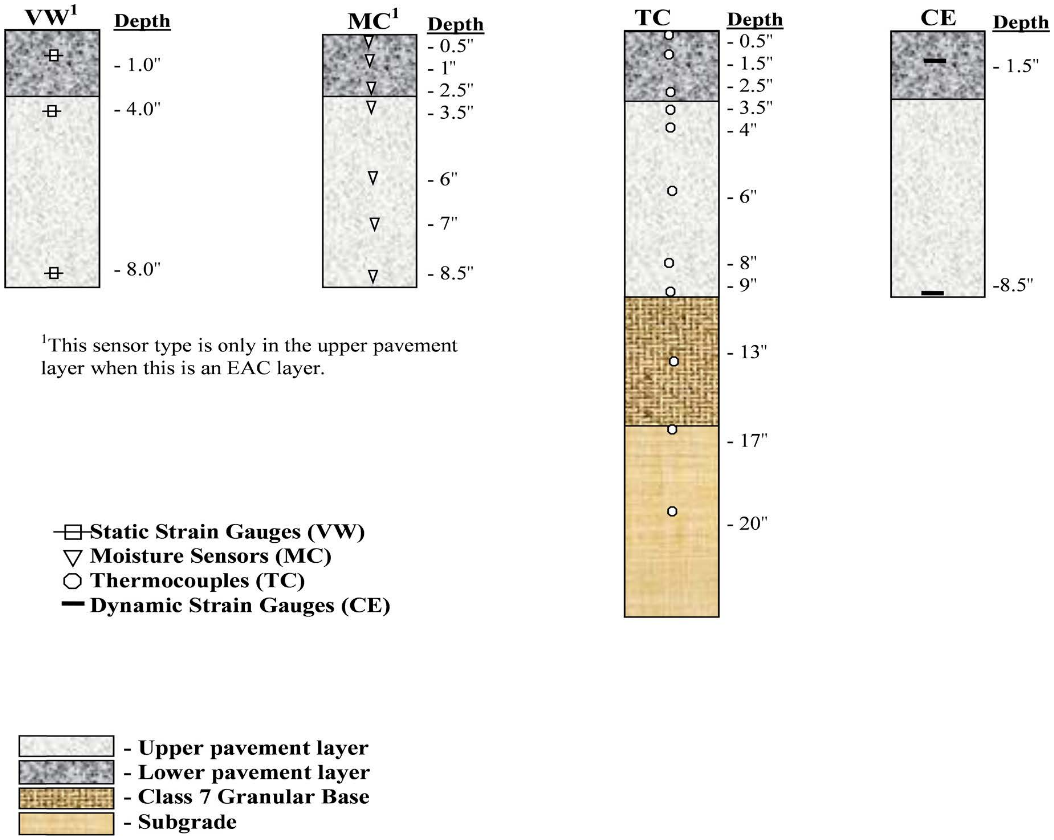
VW¹
Depth
- 1.0"
- 4.0"
- 8.0"
MC¹
Depth
- 0.5"
- 1"
- 2.5"
- 3.5"
- 6"
- 7"
- 8.5"
TC
Depth
- 0.5"
- 1.5"
- 2.5"
- 3.5"
- 4"
- 6"
- 8"
- 9"
- 13"
- 17"
- 20"
CE
Depth
- 1.5"
-8.5"
¹This sensor type is only in the upper pavement layer when this is an EAC layer.
Static Strain Gauges (VW)
Moisture Sensors (MC)
Thermocouples (TC)
Dynamic Strain Gauges (CE)
- Upper pavement layer
- Lower pavement layer
- Class 7 Granular Base
- Subgrade

Figure H.20. Depth of static and dynamic strain gauges and environmental sensors for all cells.

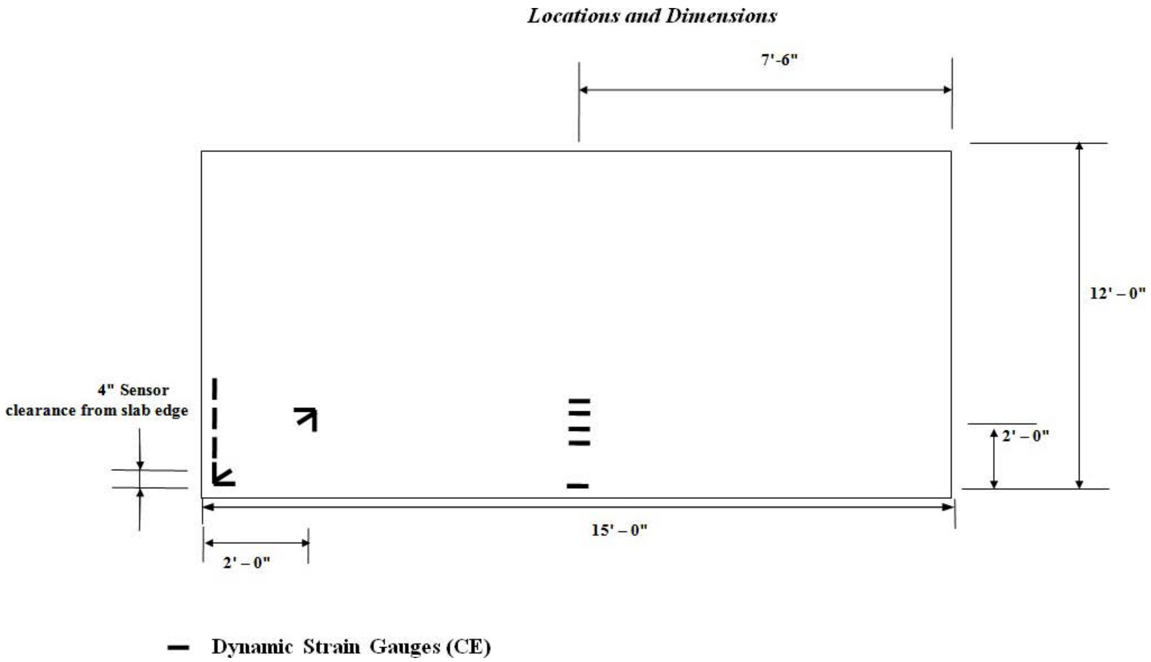
Locations and Dimensions
7'-6"
12' – 0"
4" Sensor clearance from slab edge
2' – 0"
15' – 0"
2' – 0"
Dynamic Strain Gauges (CE)

Figure H.21. Dimensions for dynamic strain gauge locations for all cells.

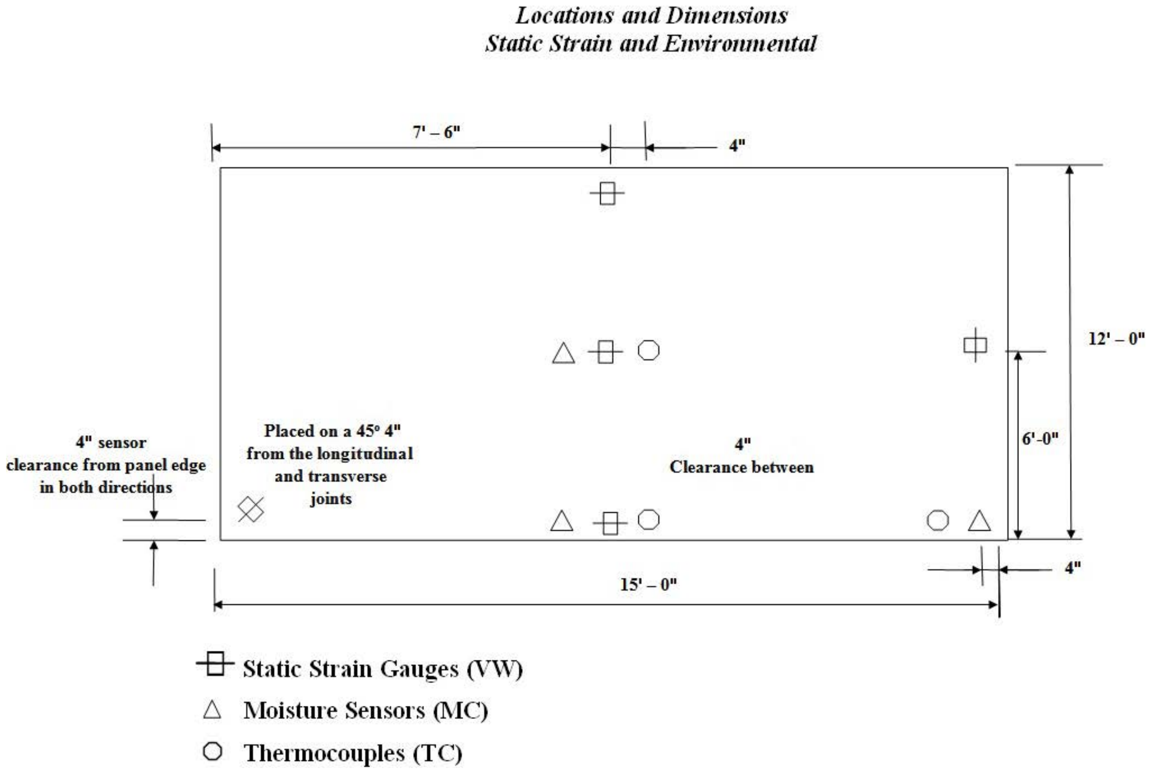
Locations and Dimensions
Static Strain and Environmental
7' – 6"
4"
12' – 0"
6'-0"
4" sensor clearance from panel edge in both directions
Placed on a 45° 4" from the longitudinal and transverse joints
4" Clearance between
15' – 0"
4"
Static Strain Gauges (VW)
Moisture Sensors (MC)
Thermocouples (TC)

Figure H.22. Dimensions for static strain gauge and environmental sensor locations for all cells.

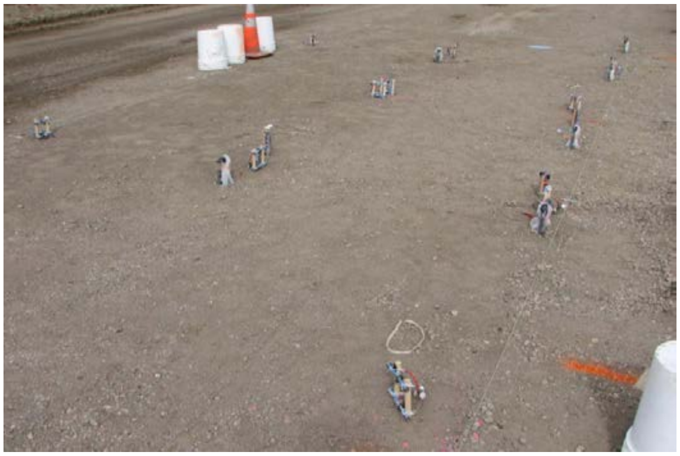

Figure H.23. Photograph of the sensors installed in Slabs 1 and 2 before paving.

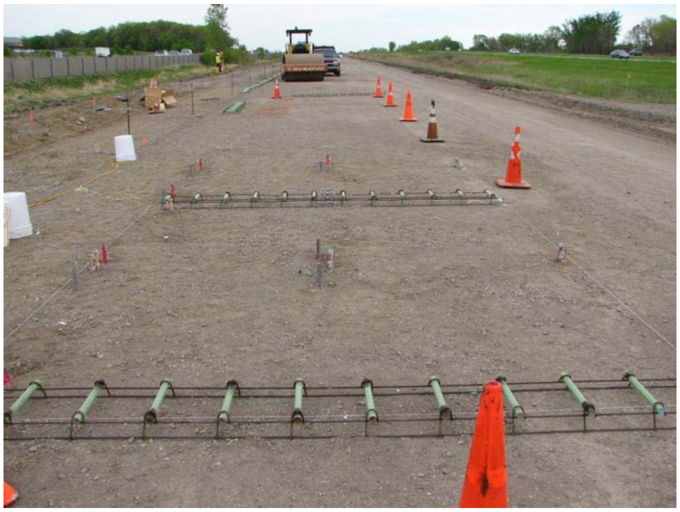

Figure H.25. Photograph of VW, TC, and MC installations in Cell 70 before paving.

be installed in the upper EAC layer can be seen in both of these photographs.

Construction of the Composite Pavements at MnROAD

Cell 70

The lower recycled concrete layer for Cell 70 was paved on May 5, 2010, at approximately 7:30 a.m. A photograph of the sensors before paving is provided in Figure H.25. The paver passed the slabs with sensors at approximately 7:45 a.m. To protect the sensors, fresh concrete was placed by hand around the sensors and consolidated with a shaft vibrator just before the paver passed over the sensors. This can be seen in Figure H.26 and Figure H.27.

After the paver passed, the three thermocouples to eventually be installed in the HMA layer, at each of the six locations, were located, pulled from the lower PCC layer, and left exposed for later installation after the HMA layer was placed. Concrete was placed in the void left by the thermocouples and consolidated by hand. On May 20, 2010, at approximately 7:00 a.m., the upper HMA layer was placed on the lower recycled concrete layer of Cell 70. The thermocouples were then installed in the HMA, as described previously.

Cell 71 and Cell 72

Figure H.28 shows a photograph of the sensors installed in Cell 71 as the paver approaches. Cells 71 and 72 involved the construction of two concrete layers. The maximum time targeted between the placement of the lower and upper layer was 30 minutes to prevent a cold joint from forming between the two layers. The paving of Cell 71 began on the morning of

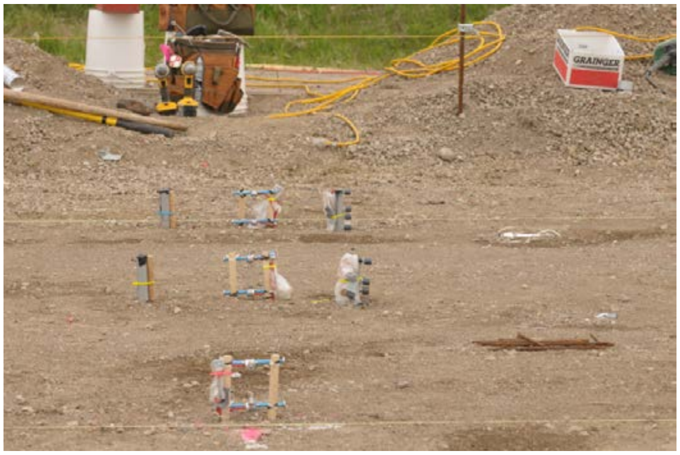

Figure H.24. An example of the sensors installed at midslab for Cells 71 and 72.

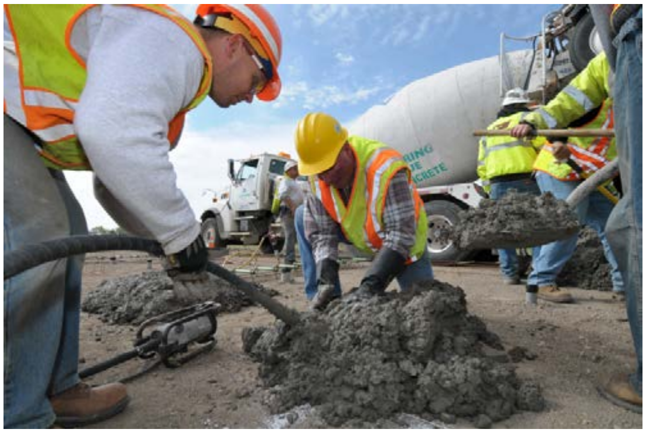

Figure H.26. Concrete was placed around the sensors to protect the sensor before the passing of the paver.

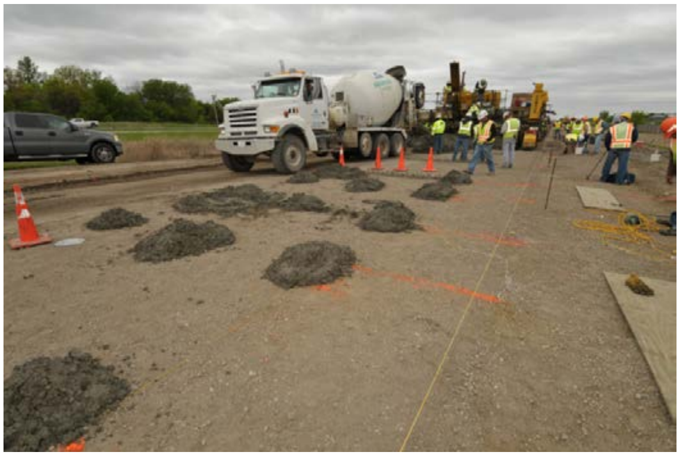

Figure H.27. Mounds of concrete placed around the sensors before the passing of the paver.

May 6, 2010, at approximately 7:30 a.m., with the first paver passing the sensors at approximately 8:00 a.m. The paving of Cell 72 began on May 10, 2010, at approximately 8:00 a.m., with the paver passing the sensors at approximately 8:45 a.m. The paving of Cells 71 and 72 was performed by using a separate paver to pave each lift. As with Cell 70, concrete was packed and vibrated around the sensors before the passing of the paver to protect them from potential damage.

After the first paver passed, the sensors installed in the lower layer were located and the tops of the installation rods exposed (Figure H.29). The rod extensions with the sensors for the upper lift were then installed, as described previously. Once the sensors for the upper lift were installed, concrete was placed in all of the voids created throughout this process and then consolidated by hand. The second paver used for paving the EAC layer passed approximately 45 minutes after the paving of the lower layer for Cells 71 and 72.

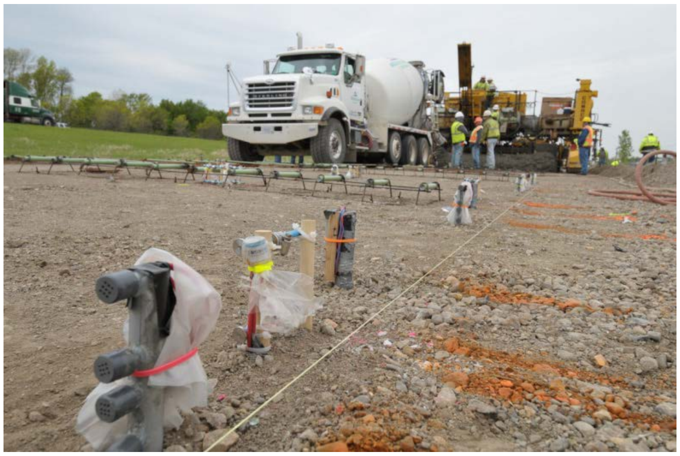

Figure H.28. Photograph of the sensors directly adjacent to the shoulder as the paver approaches.

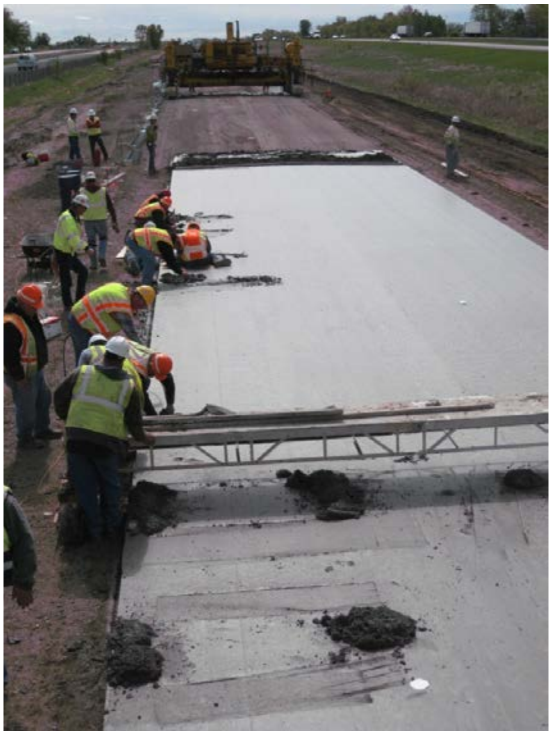

Figure H.29. Installation of sensors for the upper PCC layer after passage of the first paver. Photograph taken from the second paver.

Characterization of Temperature and Moisture Gradients that Developed in Composite Sections at MnROAD

It is common knowledge that PCC slabs do not remain flat but instead curl because of the effects of temperature and moisture gradients. Temperature and moisture gradients result in curling and warping, respectively, of the slab. When this deformation is restrained by its own self-weight, friction with the base, and load transfer with adjacent slabs, stresses develop in the slab. These stresses, when enhanced by repetitive axle loadings, contribute to the fatigue damage and eventual crack development within the slab. To predict the performance life of the pavement structure, the temperature and moisture gradients that develop within the slab must be quantified accurately. Much work has gone into quantifying the magnitude of the temperature and moisture gradients that develop in traditional jointed plain concrete pavements, but the magnitude and resulting stress that develops in these composite structures are not well known. This section of the report focuses on characterizing the temperature and moisture gradients that develop within composite pavements.

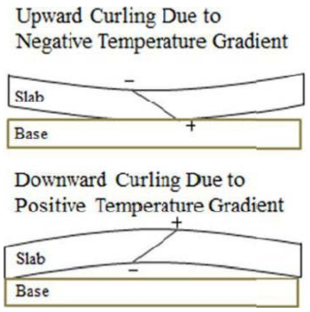
Upward Curling Due to Negative Temperature Gradient
−
Slab
+
Base
Downward Curling Due to Positive Temperature Gradient
+
Slab
−
Base

Figure H.30. Effects of temperature gradients on upward curling and downward curling of the slab.

When a positive gradient is present, the top of the slab is warmer than the bottom and the slab is curled downward. A negative gradient occurs when the bottom of the slab is warmer than the top and the slab is curled upward. This is illustrated in Figure H.30.

The second factor that results in curvature of the slab is moisture gradients. Relative humidity measurements by Janssen (1987) revealed that the majority of the fluctuation in the moisture content in the concrete occurs in approximately the upper 2 in. of the slab. At the bottom, the slab remains almost saturated, even during the dry seasons. This is attributed to the low porosity of the concrete, which limits the diffusion of moisture through the concrete and into the environment. Therefore, the differential deformation caused by moisture gradients results only in the slab warping upward. This is because drying shrinkage always occurs at the top of the slab, so the surface contracts relative to the bottom.

Characterizing the environmental loads (temperature and moisture gradients) in the three different composite pavements constructed at MnROAD is the focus of this section, but the variation in the temperature regimes that develop throughout the different composite pavement structures is first assessed. This analysis is of interest because different temperature regimes induce different stresses in each structure. Finally, the moisture conditions measured in the slab for the different pavement structures are presented.

Variation in Average Temperature Within and Between Cells

The variation in the weighted average temperature (WAT) between the three composite pavements was analyzed before looking at the difference between the temperature gradients that develop. First, the WAT within slabs was investigated to verify repeatability within cells. This analysis will also help to validate the as-designed sensor depths assumed.

Table H.2. Statistics for WAT Estimated for Slabs 1 and 2 in Cell 71 from May 6, 2010, to March 1, 2011

	Temperature, °F	
	Slab 1	Slab 2
Average	53	53
Maximum	104	106
Minimum	0	–1
Standard deviation	26.2	26.3
Median	57	57

Number of observations per slab = 29,884

Variation in WAT Within Cells

The calculation of the WAT is performed using the following equation:

$$\mathrm{WAT} = \sum_{i=1}^{n}\left[\frac{(0.5)(t_i + t_{i+1})(d_i - d_{i+1})}{(d_1 - d_n)}\right] \tag{H.2}$$

where

n = number of sensors,
t_i = temperature at location i, and
d_i = depth at location i.

The first comparison looks at the variation between the WAT for Slabs 1 and 2 in Cell 71. This analysis includes only the temperature sensors located at midslab for Slabs 1 and 2. The summary statistics provided in Table H.2 indicate good repeatability.

A comparison was then made between the WAT for Slabs 1 and 2 in Cell 72. The summary statistics in Table H.3 again indicated good repeatability between the WAT for the two slabs in Cell 72. Note that the number of observations for the

Table H.3. Statistics for WAT Estimated for Slabs 1 and 2 in Cell 72

	Temperature, °F	
	Slab 1	Slab 2
Average	60	60
Maximum	98	96
Minimum	15	16
Standard deviation	19.5	19.1
Median	62	62

Number of observations per slab = 14,366

Table H.4. Statistics for WAT Estimated for Slabs 1 and 2 in Cell 70

	Temperature, °F	
	Slab 1	Slab 2
Average	55	55
Maximum	107	107
Minimum	4	4
Standard deviation	27.1	27.1
Median	58	58

Number of observations per slab = 28,672

Table H.5. Statistics for WAT Estimated for Slab 2 in Cells 71 and 72

	Temperature, °F	
	Cell 71	Cell 72
Average	66	64
Maximum	106	96
Minimum	15	16
Standard deviation	19.1	17.6
Median	69	67

Number of observations per slab = 20,813

comparisons within Cell 72 is less than that for Cell 71 because of the errors in the datalogger program encountered early on for Slab 2 in Cell 72. The two slabs in Cell 70 also showed good repeatability, as can be seen in Table H.4.

Variation in WAT Between Cells

Now that it has been shown that there is good repeatability within cells, a comparison of the WAT between cells is performed. A comparison is made between the WAT for Cell 70, in which the upper layer is HMA, and Cell 71, in which the upper layer is PCC. This comparison is valuable in quantifying the effects of the HMA layer on the temperatures that develop in the lower PCC layer. It should be noted that the comparisons presented are based on the thermocouple sensors located at midslab. While comparing Cells 70 and 71, the average of the WATs measured in two different slabs are considered. The amount of thermocouple data available for Slab 1 in Cell 72 was limited because of problems encountered with the datalogger program. Therefore, only thermocouple data from the midslab location of Slab 2 was used in this analysis.

The comparison of the estimated WAT for the PCC over PCC composite pavements in Cells 71 and 72 is provided in Table H.5. The average and maximum value of WAT for Cell 71 is 2°F and 10°F higher than for Cell 72, respectively, even though both the composite pavements were constructed with a similar type of PCC upper layer. This difference is significant and is evaluated in greater detail below. The interesting observation from the comparison of WAT between Cells 70 and 71 is that it seems the HMA layer contributes to a higher temperature in the lower concrete. This can be attributed to the lower albedo of the HMA resulting in a higher absorption of solar radiation by HMA when compared with that of PCC.

To gain additional insight into the variation in WAT between the three cells, temperature profiles, generated at two different times throughout the day (morning and late afternoon) in different seasons, are compared. Figures H.31 through H.38 present the temperature profiles that are generated at 5 a.m. and 4 p.m. for four different seasons. A notable observation in this analysis is that the variation in the temperature profiles between cells is a function of both season and time of day. During the morning, less variation is observed between the WAT for all of the cells. The WAT is highest in Cell 70 and lowest in Cell 72 in the afternoon. The variation between Cell 71 and Cell 72 is not very large in any of the figures. It is suspected that the variation between the maximum WAT reported for Cells 71 and 72 observed in Table H.6 is the result of a gap in the Cell 72 data during the day when the peak WAT developed. The largest variation was observed in the summer (in late afternoon), and a lower variation is observed in the winter. A smaller range of extreme daily temperatures could be the reason for the lower variation between the temperature profiles during the winter. The other important observation from this analysis is that although the magnitudes of the temperatures between Cells 71 and 72 differ, the temperature gradients behave similarly. This could be verified from the next subsections, where linear temperature and equivalent linear temperature gradients for these two cells are compared. The

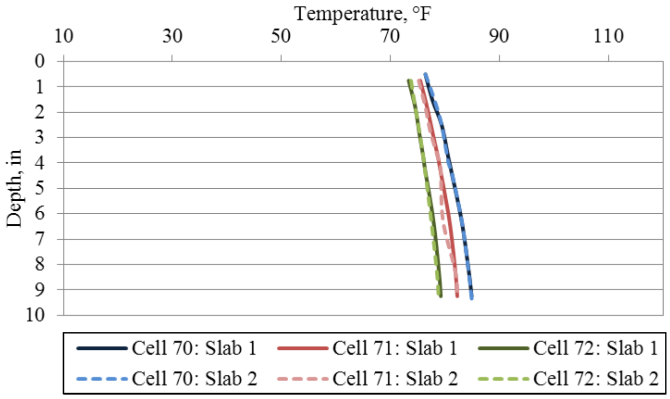

Figure H.31. Temperature profile in morning (5 a.m.) on May 23, 2010.

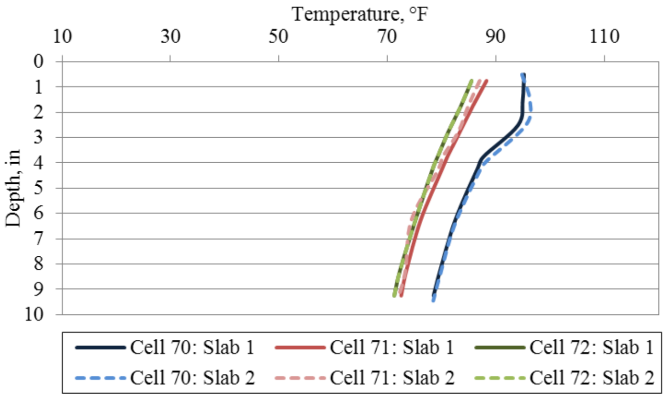

Figure H.32. **Temperature profile in late afternoon (4 p.m.) on May 23, 2010.**

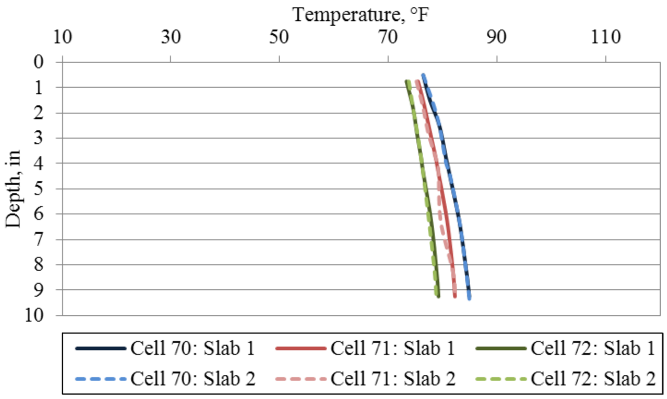

Figure H.33. **Temperature profile in morning (5 a.m.) on July 23, 2010.**

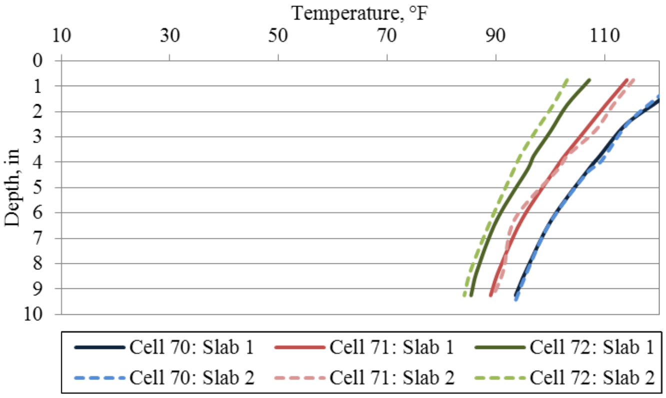

Figure H.34. **Temperature profile in late afternoon (4 p.m.) on July 23, 2010.**

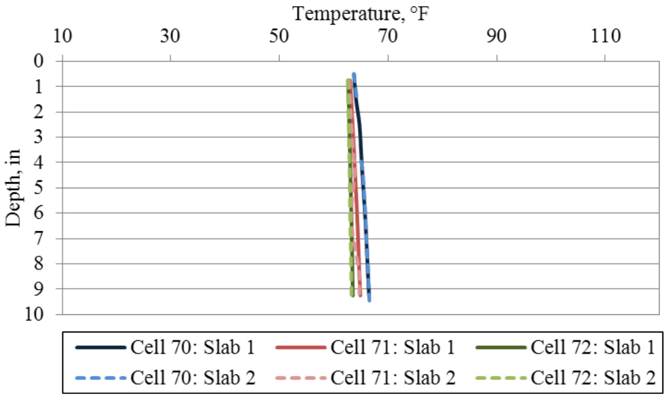

Figure H.35. **Temperature profile in morning (5 a.m.) on September 23, 2010.**

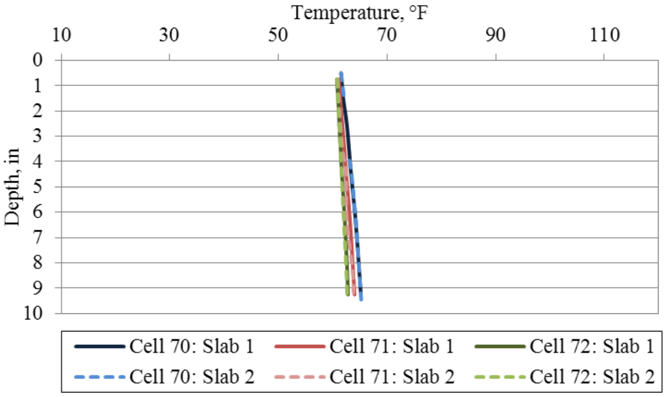

Figure H.36. **Temperature profile in late afternoon (4 p.m.) on September 23, 2010.**

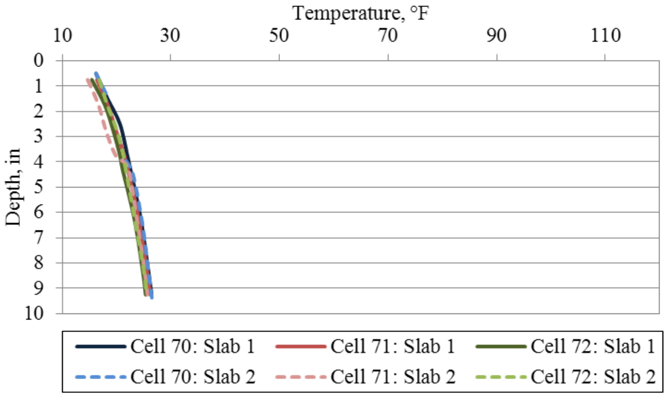

Figure H.37. **Temperature profile in morning (5 a.m.) on December 7, 2010.**

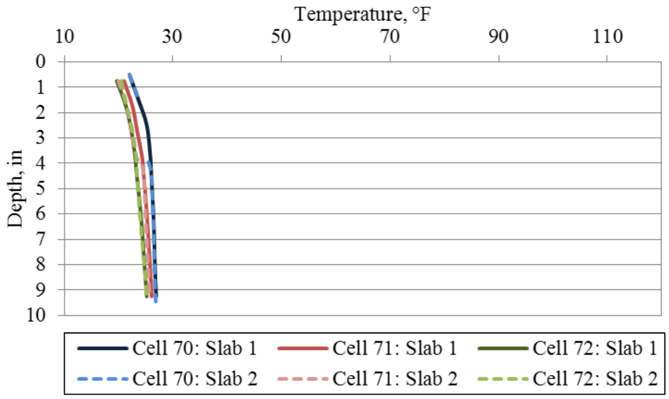

Figure H.38. Temperature profile in late afternoon (4 p.m.) on December 7, 2010.

temperature profiles for Cell 70 also reveal that nonlinearity of the temperature gradient in HMA over PCC composite pavements lies mainly in the HMA layer and becomes more linear in the lower layer.

Characterizing Temperature Gradients in Slabs

The simplest way to characterize the temperature distribution in the slab is by assuming a linear distribution for the temperature throughout the depth of the slab. The linear temperature gradient (LTG) is calculated as the temperature difference between the top and bottom of the slab taken over the distance between the two. Several field studies, however, have shown that the distribution of temperature throughout the slab depth is primarily nonlinear (Armaghani et al. 1987; Yu et al. 1998). To account for the nonlinearity of the temperature distribution in the slab the equivalent temperature gradient concept was developed (Thomlinson 1940; Choubane and Tia 1992; Mohamed and Hansen 1997). The equivalent linear temperature gradient (ELTG) is a gradient that would produce the same curvature in the slab as the original nonlinear temperature gradient. The ELTG concept was later generalized for nonuniform, multilayered slabs (Khazanovich 1994; Ioannides and Khazanovich 1998). The latter methodology in which the ELTG is established for an effective slab, with a thickness and stiffness equivalent to that of a composite multilayer section, is used in this study.

The analysis of temperature distribution throughout the three different composite pavements constructed at MnROAD is carried out in this section using both the LTG and ELTG concepts. For the three composite sections at MnROAD, temperature distribution throughout the slabs is compared at three different locations within the slab. The variation in the temperature gradients within the slab is assessed first in one slab to determine if the temperature gradient was similar throughout the slab at all locations.

Table H.6. Statistics for WAT Estimated for Slabs in Cells 70 and 71

	Temperature, °F	
	Cell 70	Cell 71
Average	55	53
Maximum	107	105
Minimum	4	0
Standard deviation	27.1	26.6
Median	58	56

Number of observations per cell = 28,671

Variation of Temperature Gradients Between Location Within a Slab

In this subsection, an assessment was made for the LTGs between locations within each slab. It is possible that the magnitude of temperature gradients in a slab can differ between locations because of the different boundary conditions at midslab, edge, and corner. This section also investigates the variation in the temperature gradients that develop in these composite pavements.

To assess the variation in the temperature gradients that develop in the slab with location, LTG in the PCC layer for Cell 70 and the composite of the upper and lower layers for Cells 71 and 72 were calculated over a typical day. Temperature data collected on July 19, 2010, was used for this analysis. The ambient temperature and solar radiation for this day are presented in Figure H.39, which shows that overcast conditions were present in the forenoon hours, thus the peak ambient temperature and solar radiation were observed in the late afternoon. It should be mentioned that the maximum ambient

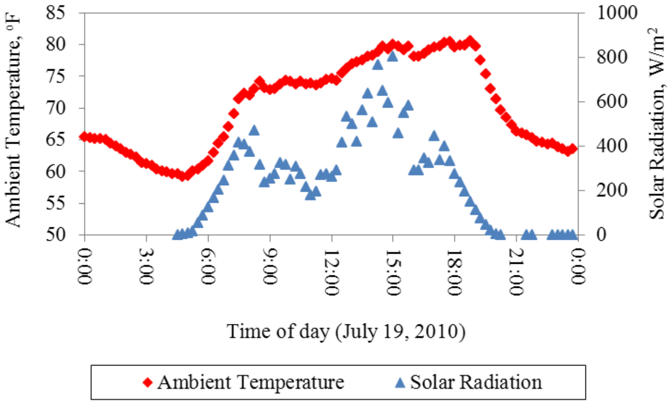

Figure H.39. Ambient temperature and solar radiation for July 19, 2010, measured at the project site.

temperature of 80°F observed on July 19, 2010, is not representative of the extreme conditions observed at MnROAD during the summer. However, because the objective of this analysis is only to determine the variation in temperature gradients with location over a typical day, the LTGs computed for this date from the temperature data at all the available thermocouple locations still serve the purpose.

The variation seen with respect to location for each cell is discussed in the following section.

Cell 70

The LTGs for Cell 70 are shown in Figure H.40. LTGs are calculated at the midslab, edge, and corner for both Slabs 1 and 2 in each cell. For Cell 70, the LTGs for all locations throughout the majority of the day are consistent. The peak LTG for all locations is observed in the late afternoon, when the peak ambient temperature and solar radiation are seen. Based on this figure, the highest LTG was observed at midslab and the smallest in the corner, although the variation is marginal.

The depths of the two thermocouples used at each location to establish the gradients affect the magnitude of the LTGs. The as-built depths for the thermocouples in Slabs 1 and 2 for Cell 70 are given in Table H.7. It should be noted that Cell 70 consists of an HMA layer on top of a PCC layer. The depths of the thermocouples provided in Table H.7 are from the top surface of the HMA layer. It can be seen that the as-built depths for the thermocouples in Slab 1 are the same for all locations. For Slab 2, corner thermocouples are approximately 0.25 in. above the top thermocouples at the edge and midslab locations. Therefore, the depths of the thermocouples reported in Table H.7 can be considered to be approximately the same for all locations. It should be noted that the depth of the sensors throughout the slab was established by subtracting the design depth from the surveyed position of the top sensor. The possible differences between the actual and estimated depths of the sensors most likely contributed to some variation in the magnitude of the LTGs.

Table H.7. Depths (in inches) at the Top and Bottom Thermocouples for the PCC Layer in Cell 70

	Corner	Midslab	Edge
Top	3.75	3.75	3.75
Bottom	9.25	9.25	9.25

Figure H.40 shows there is some variation in the LTG as a function of the location of the thermocouples within the slab. As can be seen, the magnitude of the gradient is slightly larger at midslab for both slabs. The LTGs at the edge are also slightly larger than those at the corner for both slabs.

Cells 71 and 72

The LTGs calculated at different locations within Cells 71 and 72 are shown in Figure H.41 and Figure H.42. Similar to Cell 70, midslab locations in both Slabs 1 and 2 for both cells experience higher magnitudes of LTG than do other locations. The thermocouple depths are summarized in Table H.8 for both cells. The depths available for the sensors, shown in Table H.8, indicate that the sensors were installed at similar depths for each of the locations. More variability was observed within each location for each slab in Cells 71 and 72 than was observed for Cell 70. This could be due to the way the sensor depths were approximated.

Based on the comparative analysis of the variation in the LTG for each location within the slab presented, it can be

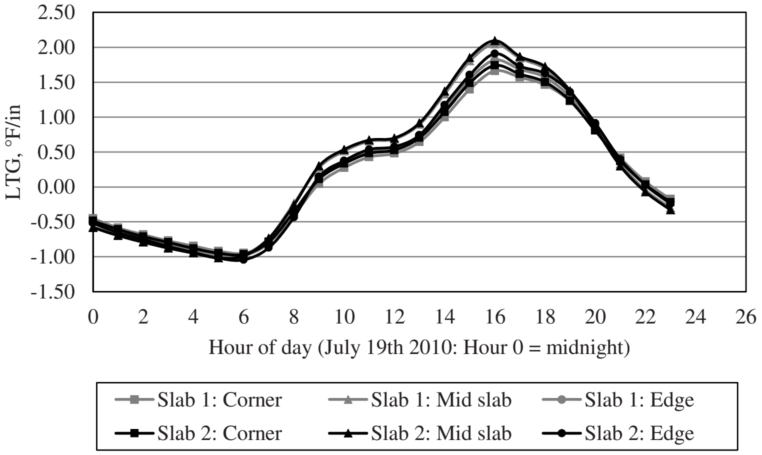

Figure H.40. LTG in the PCC layer for various slab locations in Cell 70 on July 19, 2010.

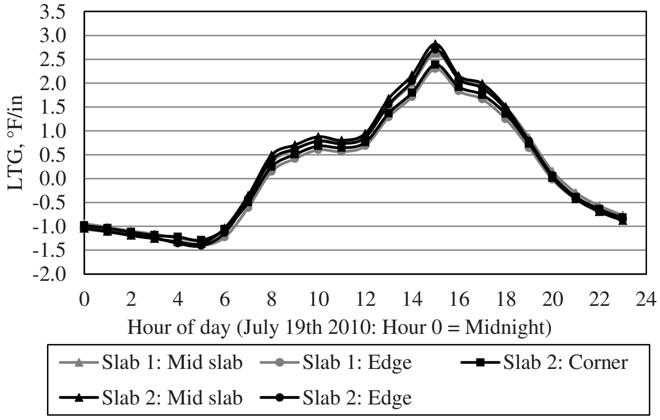

Figure H.41. LTGs for various slab locations in Cell 71 on July 19, 2010.

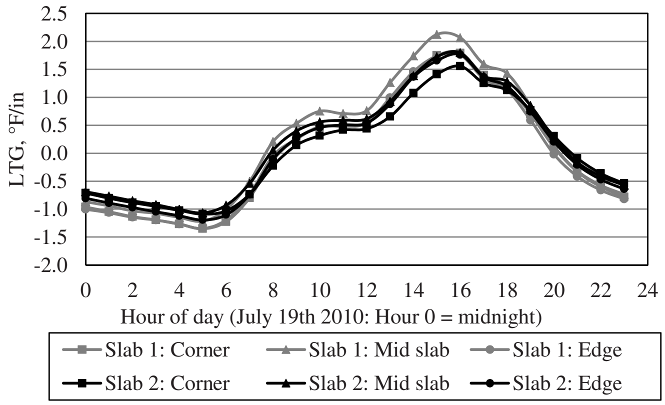

Figure H.42. LTGs at various locations in the slabs in Cell 72 on July 19, 2010.

concluded that the largest positive and negative LTGs occur at the midslab. Therefore, the LTG corresponding to this location will be used for subsequent analyses. It also should be noted that the variation between LTGs for different locations is not significant and is not expected to affect the analysis in the following sections.

Variation in LTGs Between Cells 71 and 72

Figure H.43 and Figure H.44 show histograms of the LTG distribution in the slabs for Cells 71 and 72. Based on these figures, it is apparent that the variation in LTGs between the slabs within the same cell is negligible. To compare the LTGs between Cells 71 and 72, LTGs only for Slab 2 are compared in Table H.9. As previously mentioned, the temperature data for Slab 1 in Cell 72 was not reliable for a considerable period, so the data for Slab 2 in both the cells is considered.

Based on Table H.9 the variation between the two cells is apparent. Cell 71 experiences larger temperature gradients more frequently. It may be recalled that the WAT for Cell 71 was also higher than that for Cell 72. This finding it quite surprising and could be the result of the limited data collected. This analysis should be performed again once a larger database of data is available. The difficulties encountered with the data collections system early on through the summer in Cell 72 could be contributing to these unanticipated results.

Cell 71 Versus Cell 70

For comparison between the temperature gradients that develop in Cells 71 and 72 with respect to Cell 70, only the data for Cell 71 will be used because the data for this cell is complete, unlike that for Cell 72. Unlike in the previous comparisons between Cells 71 and 72, a complete set of data will be used in this analysis because there were no gaps in either data set.

In the case of Cell 70, the curling of the PCC layer covered with HMA is dictated by the temperature gradient in the PCC because of the relatively lower stiffness of the HMA. Therefore, the temperature gradient throughout only the PCC layer for Cell 70 is considered in the analysis. In Cell 71, the curling induced by a temperature gradient is caused by the temperature distribution throughout the entire slab. Therefore, the temperature gradient will be established in Cell 71 based on the composite temperature distribution of the upper EAC layer and the lower PCC layer.

Figure H.45 and Figure H.43 show the distribution of the LTGs in the PCC layer for Cell 70 and the entire slab for Cell 71,

Table H.8. Approximate Depths of the Top and Bottom Thermocouples for Cells 71 and 72

	Thermocouple Depths, in.					
	Cells 71 and 72			**Cells 71 and 72: Slab 2**		
Location	**Corner**	**Midslab**	**Edge**	**Corner**	**Midslab**	**Edge**
Top	0.75	0.75	0.75	0.75	0.75	0.75
Bottom	9.25	9.25	9.25	9.25	9.25	9.25

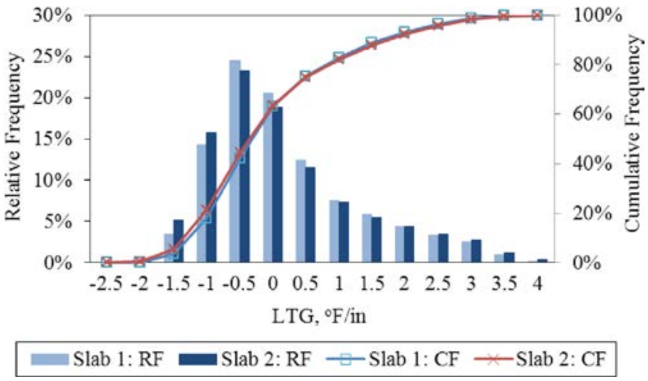

RF = Relative frequency; CF = cumulative frequency.

Figure H.43. LTG distribution for Slabs 1 and 2 in Cell 71.

Table H.9. Statistics for LTG Over the Analysis Period, Comparing Cells 71 and 72

	LTG, °F/in.	
	Cell 71	Cell 72
Average	0.03	0.01
Maximum	4.14	2.93
Minimum	–2.22	–1.91
Standard deviation	1.26	0.93
Median	–0.37	–0.25

Number of observations per slab = 20,814

respectively. Table H.10 summarizes a statistical comparison made between the distributions of LTGs. As can be seen in Table H.10 and by comparing the histograms for the two pavement cells, the LTGs are lower for Cell 70 than for Cell 71. The reason for this is that in Cell 70, the nonlinearity of the temperature gradient decreases because of the HMA layer (see Figures H.31 through H.38).

Figure H.46 provides a direct comparison between the average LTGs for both slabs in Cells 70 and 71. Cell 70 shows a higher frequency of occurrence of gradients near zero and a lower frequency of larger gradients when compared to Cell 71 on the basis of Figure H.46. Again, the upper HMA layer in Cell 70 serves as an insulating layer.

The previous two analyses have shown that although the magnitude of the WAT for Cell 70 was relatively large, the linear temperature gradients that develop were less. It is hypothesized that not only is the magnitude of the gradient lower in Cell 70 than in Cells 71 and 72, but that the nonlinear component of the temperature gradient also is reduced. The upper HMA layer helps to buffer the lower PCC layer from more rapid temperature swings, thereby reducing the potential for highly nonlinear temperature distributions to develop in the upper portion of the PCC layer. Figure H.47 and Figure H.48 illustrate the temperature distributions in the slabs throughout a single summer day for Cells 70 and 71, respectively. As can be seen from these figures, the deviation of the temperature profiles from a linear gradient is more pronounced in Cell 71. Based on this, it can be concluded that the LTG alone is not sufficient in characterizing the actual variation of the temperature throughout the depth. The nonlinearity of the temperature distribution should also be evaluated.

The ELTGs were estimated for Cells 70 and 71, using Equations H.3 to H.5.

$$\Delta T_{\text{eff}} = \frac{12}{h_{\text{eff}}^{2}} * \left\{ \begin{aligned} &\int_{-x}^{h_{\text{top}}-x} (T(z)-T_0)\, z\,dz \\ &+ \frac{\alpha_{\text{bot}} \cdot E_{\text{bot}}}{\alpha_{\text{top}} \cdot E_{\text{top}}} \int_{h_{\text{top}}-x}^{h_{\text{top}}+h_{\text{bot}}-x} (T(z)-T_0)\, z\,dz \end{aligned} \right\} \tag{H.3}$$

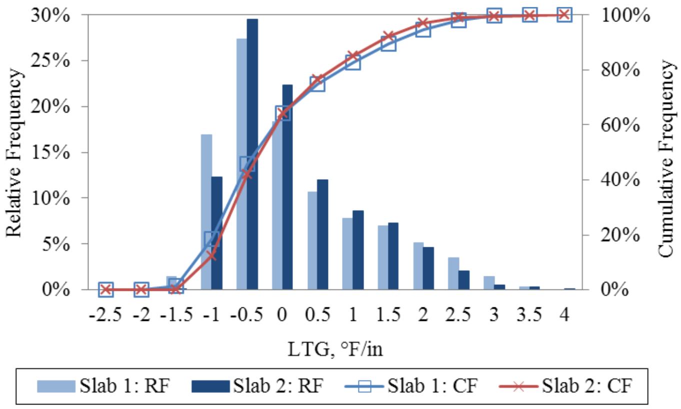

RF = Relative frequency; CF = cumulative frequency.

Figure H.44. LTG distribution for Slabs 1 and 2 in Cell 72.

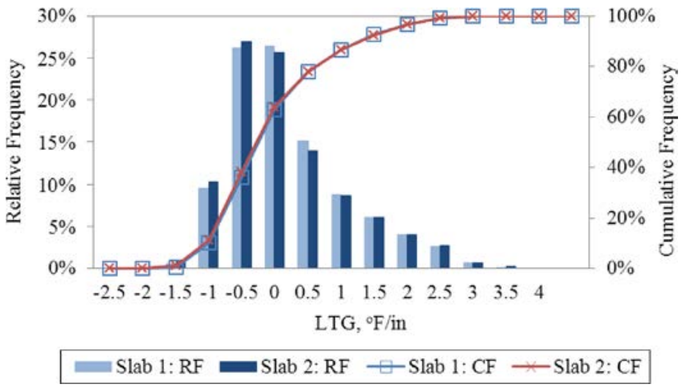

RF = Relative frequency; CF = cumulative frequency.

Figure H.45. LTG distribution for Slabs 1 and 2 for Cell 70. (RF = Relative frequency; CF = cumulative frequency.)

Table H.10. Comparison of LTG Statistics Between Cells 70 and 71

	LTG, °F/in.			
	Cell 70		Cell 71	
	Slab 1	Slab 2	Slab 1	Slab 2
Average	–0.06	–0.08	–0.09	–0.10
Maximum	3.32	3.37	3.94	4.14
Minimum	–1.83	–1.97	–2.20	–2.26
Standard deviation	0.88	0.90	1.14	1.22
Median	–0.27	–0.30	–0.36	–0.38

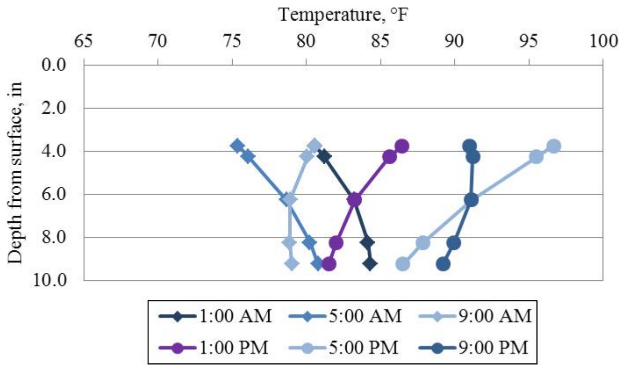

Figure H.47. Temperature distribution in the PCC for Cell 70.

where

ΔT_{eff} = difference between temperatures at the top and bottom surfaces of the effective slab,

$T(z)$ = temperatures distribution through the PCC concrete,

T_0 = zero stress temperature,

z = vertical coordinate measured downward from the neutral axis of the composite pavement,

h_{top} = thickness of the upper layer,

h_{bot} = thickness of the lower layer,

E_{top} = elastic modulus of the upper layer,

E_{bot} = elastic modulus of the lower layer,

α_{top} = coefficient of thermal expansion (CTE) of the upper layer,

α_{bot} = CTE of the lower layer, and

h_{eff} = effective thickness of the pavement, which can be determined from the following equation:

$$h_{\mathrm{eff}} = \sqrt[3]{h_{\mathrm{top}}^3 + \frac{E_{\mathrm{bot}}}{E_{\mathrm{top}}} h_{\mathrm{bot}}^3 + 12 \left(\begin{array}{l} h_{\mathrm{top}} \left(x - \dfrac{h_{\mathrm{top}}}{2} \right)^2 \\ + \dfrac{E_{\mathrm{bot}}}{E_{\mathrm{top}}} \left(h_{\mathrm{top}} + \dfrac{h_{\mathrm{bot}}}{2} - x \right)^2 h_{\mathrm{bot}} \end{array} \right)} \tag{H.4}$$

x = distance between the neutral plane and the top surface of the upper layer, which can be determined from the following equation:

$$x = \frac{\dfrac{h_{\mathrm{top}}^2}{2} + \dfrac{E_{\mathrm{bot}}}{E_{\mathrm{top}}} h_{\mathrm{bot}} \left(h_{\mathrm{top}} + \dfrac{h_{\mathrm{bot}}}{2} \right)}{h_{\mathrm{top}} + \dfrac{E_{\mathrm{bot}}}{E_{\mathrm{top}}} h_{\mathrm{bot}}} \tag{H.5}$$

Figure H.49 shows the variation in the ELTGs between Cells 70 and 71. The inputs used to compute the ELTGs for Cell 71 are provided in Table H.11. The CTE and the elastic modulus of the concrete were measured by the FHWA Mobile Concrete Laboratory. Typical values were assumed for the CTE and the elastic modulus of the HMA. In Cell 70 the temperature gradient was computed only for the lower 6-in. PCC layer so the first portion of Equation H.3 was used. The summary statistics for the ELTGs that developed in both cells are presented in Table H.12 and Table H.13. As was noted, Cell 70 shows a higher frequency of occurrence of ELTGs close to zero, than does Cell 71. It can be seen in Figure H.49 that the shape of the frequency distribution curve of LTGs and ELTGs for Cell 70

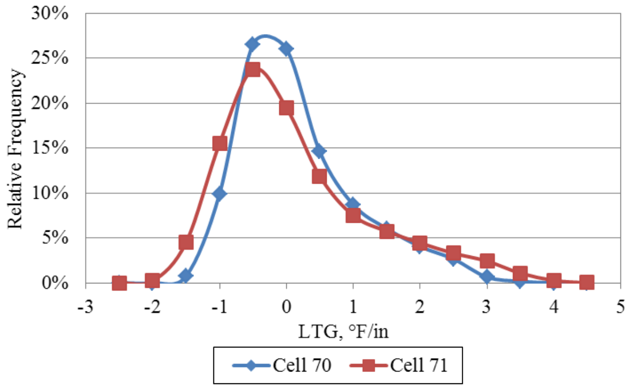

Figure H.46. Comparison of relative frequencies for LTGs in Cells 70 and 71.

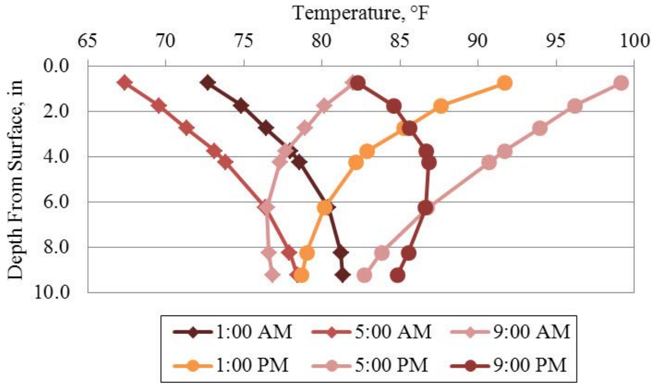

Figure H.48. Temperature distribution in the composite section for Cell 71.

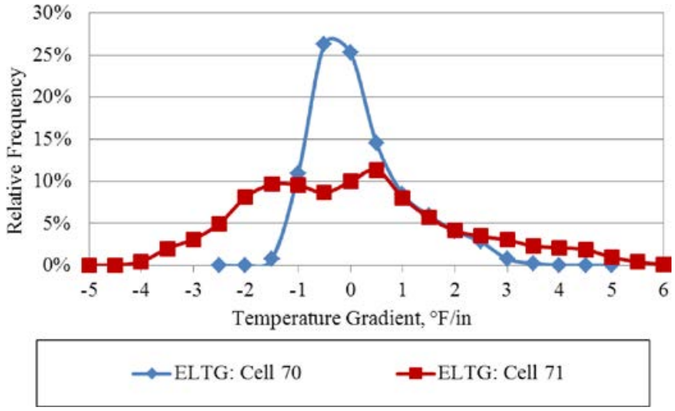

Figure H.49. Comparison of relative frequencies for ELTGs in Cells 70 and 71.

is quite similar, whereas a considerable variation is observed in Cell 71. Unlike the LTGs, the ELTGs for Cell 71 are more evenly distributed over a broader range. To investigate the significance of variation in LTGs and ELTGs within a cell and the variation of each of these gradients between the cells, paired *t* test for two sample means was performed. Results from the *t* tests are also given in Table H.12 and Table H.13. The variation between the LTGs and ELTGs is not significant for Cell 70 but is quite significant for Cell 71. This indicates that the gradients that develop in the HMA over PCC pavements tend to be much more linear than in the PCC over PCC pavements, as is supported by the temperature profiles provided in Figure H.48.

The results of the paired *t* test for the ELTGs between Cells 70 and 71 also conclude the difference in the ELTGs is significant at a 95% confidence level. The ELTGs in Cell 71 are much higher over a lager period of time than are the ELTGs for Cell 70. It can be seen in Figure H.49 that the magnitude of the temperature gradients and the frequency at which these higher gradients develop are significantly greater when a PCC over PCC pavement is constructed than when an HMA over PCC pavement is constructed.

Table H.11. Inputs for Computing ELTGs in Cell 71

Input	Value
h_{top}, in.	3
h_{bot}, in.	6
E_{top}, psi	4.4×10^6
E_{bot}, psi	4.4×10^6
T_0, °F	55
α_{top}/°F	6×10^{-6}
α_{bot}/°F	4×10^{-6}

Table H.12. Comparing the LTG and ELTG Within Each Cell for Cells 70 and 71

	Cell 70		Cell 71	
	LTG	ELTG	LTG	ELTG
Average, °F/in.	–0.07	–0.07	–0.08	–0.20
Variance, °F/in.	0.79	0.829	1.29	3.85
Observations	28,649			
Hypothesized mean difference	0			
Degrees of freedom	28,648			
t statistics	1.43		14.64	
p-value	0.15		0	
t-critical two-tail	1.96		1.96	

An equivalent linear temperature gradient obtained using Equations H.3 through H.5 will result in approximately the same deflection profile of the slab as the actual nonlinear temperature profile. This is because a nonlinear temperature profile is the superposition of three components. These three components are the uniform temperature component, the linear temperature component, and the nonlinear temperature component. The first component is responsible for the uniform expansion and contraction of the slab, whereas the second component results in curling of the slab. The last component, the nonlinear portion of the temperature profile,

Table H.13. Comparing the ELTG Statistics for Cells 70 and 71

	ELTG, °F/in.	
	Cell 70	Cell 71
Average	–0.070	–0.195
Maximum	3.540	5.951
Minimum	–1.864	–4.699
Standard deviation	0.911	1.961
Median	–0.292	–0.336
Paired *t* test results		
Variance, °F/in.	0.829	3.845
Observations	28,649	
Hypothesized mean difference	0	
Degrees of freedom	28,648	
t statistics	15.11	
p-value	0	
t-critical two-tail	1.96	

results in no temperature moment and thus does not influence the deflection profile of the slab. This third component will result in residual stresses across the depth of the concrete, although this stress has been shown by Hiller and Roesler (2010) to be relatively small.

The shape of the profile of the slab attributable to the linear gradient does play a significant role in the development of stress within the pavement because a larger unsupported area increases stress caused by the restraint (slab self weight, dowel, tie bars, and so forth) of deformation and the application of a wheel load on this unsupported area. Based on the analysis performed, the linear gradients that develop in the HMA over PCC pavements are lower than those in the PCC over PCC pavements. This will result in lower environmental stresses. It cannot yet be concluded that these lower stresses will result in an increase in the fatigue life because the flexural stiffness of the HMA over PCC pavement is lower than that of the PCC over PCC pavement when the overall thickness is held constant. Therefore, the effect of both environmental and wheel loads may still be lower for the PCC over PCC pavements. Now that the temperature distributions have been characterized, a stress analysis should be performed to quantify the combined effect of these temperatures gradients and the traffic loads. Then the performance life of these composite pavement structures can be accurately determined.

Characterization of Moisture Gradients in Slabs

In addition to temperature variation within the slab, the moisture variation throughout the depth is important. This is because the moisture variation across the depth of the slab produces an upward warping of the slab. To capture the variation in the moisture content across the depth of the concrete layers, relative humidity was measured at different depths and locations.

In this study, 108 MC sensors were installed in the three cells. Apart from the embedded sensors in the pavement sections, ambient relative humidity, temperature, and solar radiation were measured with the weather station on site. The variation in the daily average ambient relative humidity at the project location over the analysis period (May 2010 to March 2011) can be seen in Figure H.50. The range of the average daily ambient relative humidity is between 50% and 100%. The variation in the relative humidity in the concrete at very shallow depths might show a variation similar to that of the ambient relative humidity with time. Overall though, it is more likely that the variation in the relative humidity in the concrete follows seasonal trends because of a slow diffusion of water through concrete.

To assess the seasonal trends in the ambient relative humidity, the average ambient relative humidity for each month of the analysis period was calculated as shown in Figure H.51. It can be seen that the ambient relative humidity increases in the winter, with the highest values in November and December and the lowest value in September.

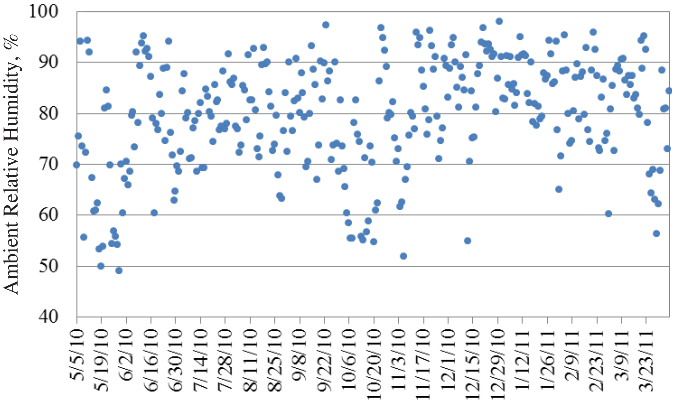

Figure H.50. Daily average ambient relative humidity at MnROAD.

As mentioned, the relative humidity data collected by several sensors were not of an acceptable quality. Therefore, an initial quality check was performed on the data to select sensor locations with a suitable data set. On this basis, the relative humidity data for the edge and corner of Slab 2 for Cell 70, midslab and corner of Slab 2 for Cell 71, and edge of Slabs 1 and 2 for Cell 72 were selected.

Figures H.52 through H.55 present the variation in relative humidity with depth for the locations in Cells 70 and 71 identified above. The common observation for all four figures is that for the first 2 to 3 weeks after paving, there is a significant drop in relative humidity that is uniform for all sensors throughout the depth of the concrete. This may be attributed to hydration of the concrete. Figure H.52 was produced using the relative humidity data from the edge of the slab in Cell 70. It shows a variation in the relative humidity in the concrete during the

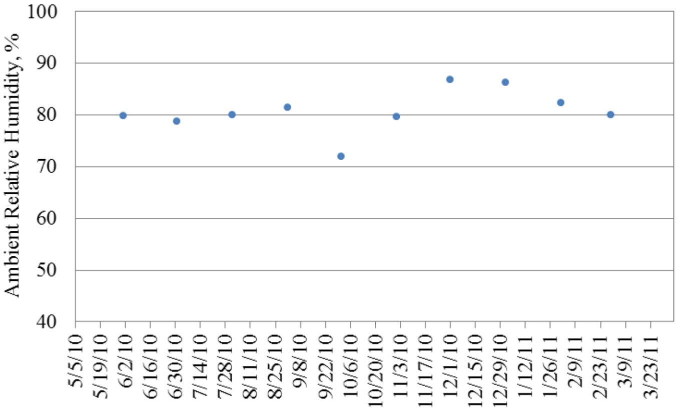

Figure H.51. Monthly average ambient relative humidity at MnROAD.

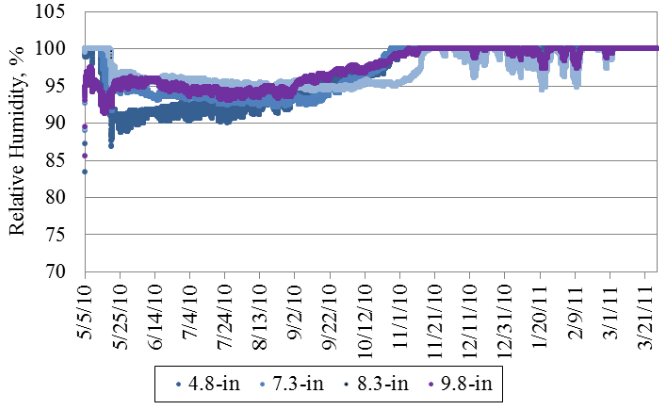

Figure H.52. Relative humidity in the concrete at the edge of Slab 2 in Cell 70.

winter months, but the variation was less than that experienced at the corner location (Figure H.53). It can be seen that in late November, the variation in the relative humidity increases suddenly and continues throughout the winter and early spring. The increase in relative humidity during the winter months is the result of a decrease in the temperature and not a change in the moisture content. Unfortunately, the moisture content in the concrete cannot be measured directly and must be estimated based on the measured relative humidity. Therefore, when interpreting these data, it is important to remember that the relative humidity will increase when the temperature decreases, even when the moisture content remains constant. For this reason, it is important to make comparisons between the concrete relative humidity measurements made at the same time of the year over a period of 5 or 6 years. It typically takes about 5 to 7 years before all of the irrecoverable drying shrinkage develops at the surface of the slab. Unfortunately, the complete interpretation of the moisture data is not possible because less than a year of data was available at the time the analysis for this report was performed.

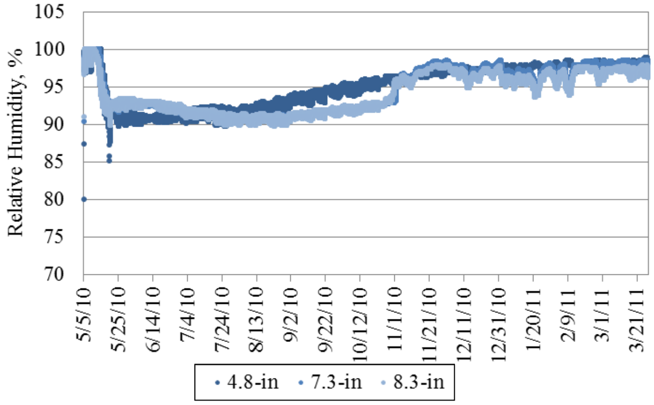

Figure H.53. Relative humidity in the concrete at the corner of Slab 2 in Cell 70.

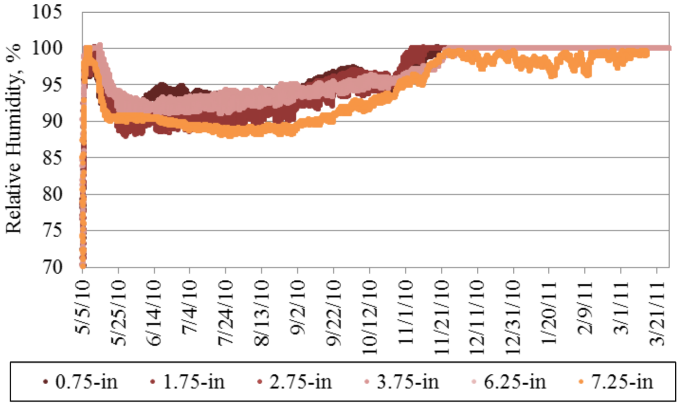

Figure H.54. Relative humidity in the concrete at midslab for Slab 2 in Cell 71.

Another observation in Cell 70, which was constructed with an HMA layer, is that the relative humidity near the surface of the lower PCC layer (4.8 in. from the HMA surface) experienced a sudden drop in relative humidity in the third week of May. This time period coincides with the time when the HMA layer was placed (May 20, 2010). To further investigate the reason for this sudden drop in relative humidity, the daily variation of the relative humidity and temperature in the concrete in Cell 70 can be found in Figure H.56. The time period depicted in the graph represents approximately 4 days before and 3 days after the HMA layer was placed.

The placement of the HMA layer is indicated by a spike in the temperature of the sensor at a depth 4.8 in. from the upper layer surface. The relative humidity drops at the time of the placement of the HMA layer because the high temperature of the asphalt mix accelerates the evaporation of moisture from the surface of the concrete layer. After the HMA layer cools, it acts as an insulation layer to the underlying PCC layer. This is reflected in the flat trend exhibited for the relative humidity measured near the surface of the lower PCC layer after May 20, 2010.

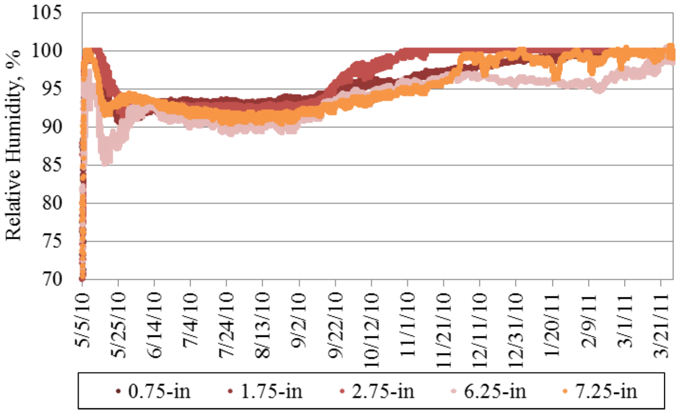

Figure H.55. Relative humidity in the concrete for the corner of Slab 2 in Cell 71.

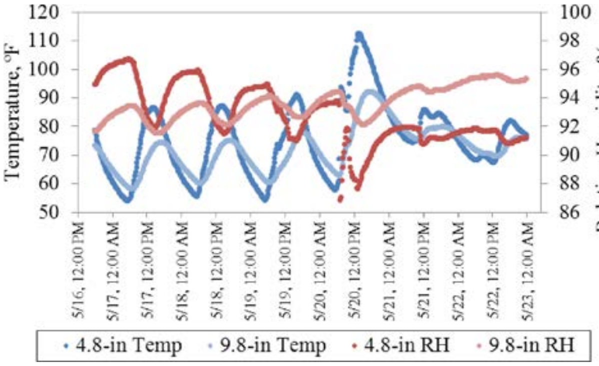

Figure H.56. Daily variation in relative humidity and temperature in the PCC 4 days before and 3 days after the HMA layer was placed in Cell 70.

The most reasonable measurements of the relative humidity in the concrete were obtained from Cell 72. These measurements are shown in Figure H.57 and Figure H.58. The relative humidity measured at the top of Slabs 1 and 2 for this cell show the largest daily variations. This is expected because the sensors close to the surface are most heavily influenced by the ambient conditions. However, the two top sensors in the adjacent slab do not show the same behavior over the analysis period. The variation in the relative humidity between the lower sensors is small and remains constant over the year after initial drying of the concrete. It is possible that this variability is the result of variations in the sensor depth because the exact as-built depths are unknown. A better interpretation will be possible as more data become available over time.

Conclusions

It was found that the magnitude of variation in the temperature gradient between locations within a cell is relatively insignificant, with it being marginally higher at midslab and lower at the corner. This finding led to the use of only midslab temperature data for subsequent analyses. The variation in the temperature measured for different slabs within the same cell and between cells was also evaluated. Significant variation was not observed between the LTG and the WAT between slabs within a cell. This finding suggests that the thermocouple installations have good repeatability.

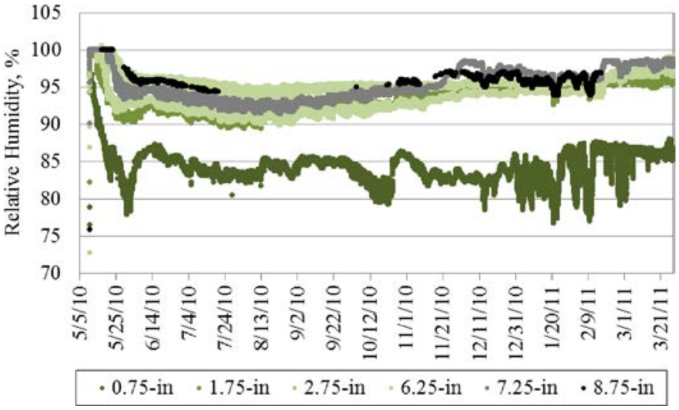

Figure H.57. Relative humidity in the concrete at the edge of Slab 1 in Cell 72.

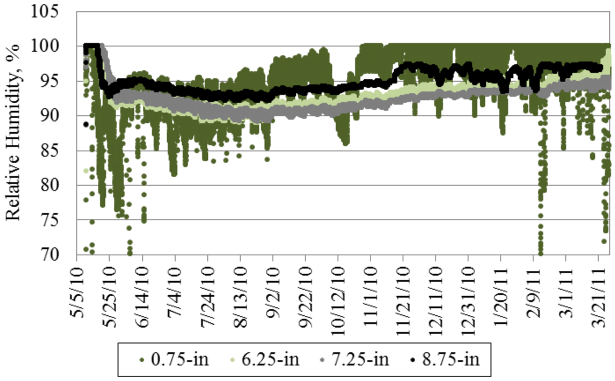

Figure H.58. Relative humidity in the concrete at the edge of Slab 2 in Cell 72.

While comparing the temperature gradient between cells, in terms of LTG and ELTG, it was found that both the severity of the temperature gradients and the frequency with which they develop were different when compared with different upper-layer types. The difference between Cells 71 and 72, which were constructed with similar concrete upper PCC layers, was minor. Based on the *t* test, it was found that there was a significant difference in the trends of the LTG and ELTG between Cells 70 and 71; Cell 70 was covered with HMA whereas Cell 71 was covered with PCC. Cell 70 experiences a higher frequency of occurrence of zero and close-to-zero LTGs compared with Cell 71. This finding suggests that an insulation effect was provided by the HMA layer to the PCC layer underneath. The HMA layer also improved the linearity of the concrete layer temperature gradient.

It was noticed that the RH at the top sensor in Cell 70 continued to decrease for a short while after the upper asphalt layer was placed but eventually started to trend toward the relative humidity measured by the other sensors. This indicates that placement of the HMA layer decreased the moisture content in the upper portion of the concrete layer, but it eventually re-saturated.

Establishing Built-in Temperature Gradient

The shape of the slab at any point in time throughout its service life is dictated by the contribution of transient temperature and moisture gradients, as well as the built-in gradient. Although transient temperature gradients vary daily, moisture gradients tend to exhibit more seasonal changes. The built-in gradient is considered to include the combined effects of the temperature and moisture gradient present at the time the concrete sets and the warping that results from irreversible drying shrinkage that develops in the upper portion of the slab.

The built-in gradient includes the temperature and moisture gradient that lock into the slab at the zero stress time (TZ). TZ occurs after final set and is the point in time when the slab has sufficient strength to respond to temperature changes. Although moisture gradients at TZ have been shown to be close to zero (Wells et al. 2006), temperature gradients at this point in time can have influential values. It is important to acknowledge the built-in temperature gradient in the slab because as a result of this gradient, the slab does not remain flat in the absence of transient temperature and moisture gradients during its service life. Before TZ, the slab is flat regardless of the temperature gradient in the slab. The temperature gradient that is present in the slab at TZ is locked into the slab. This built-in temperature gradient will either increase or decrease the effects of transient temperature gradients. To define the curvature in the slab for a given time, it is critical to quantify this built-in gradient.

The WAT in the slab at TZ also must be defined. This is because tensile stress will develop due to the restraint against expansion when the transient WAT is greater than the WAT at TZ. Similarly, compressive stress will develop due to the restraint against contraction because the transient WAT is smaller than the WAT at TZ.

Two different methodologies are used in this section to establish TZ and consequently the built-in temperature gradient for the instrumented slabs in Cells 70, 71, and 72. Both methodologies make use of the VW strain gauges. The first methodology is based on the strain-temperature relation established for the slab whereas the second methodology is based on the curvature of the slab. The data from Cell 71 is used to describe the two methodologies followed by the analysis for Cells 70 and 72.

Establishing TZ for Cell 71 with Methodology 1

The PCC and EAC layers for Cell 71 were constructed on the morning of May 6, 2010. The first paver, placing the PCC layer, passed over the instrumented cells at approximately 7:15 a.m. Approximately 45 minutes after the first layer was placed, the second paver used for paving the EAC passed over the sensors. As described, VW strain gauges were installed in each cell.

When a VW gauge is embedded in hardened concrete, it measures the actual strain in the concrete as determined using Equation H.6. In this equation, R_0 is the strain reading at the time for which the gauge is zeroed and R_1 is the strain reading at any subsequent time. B is the batch factor provided by the gauge manufacturer. T_1 and T_0 are the temperatures obtained from the thermistor in the VW gauge corresponding to R_1 and R_0, respectively and α_s is the CTE for the steel wire used in the VW gauge.

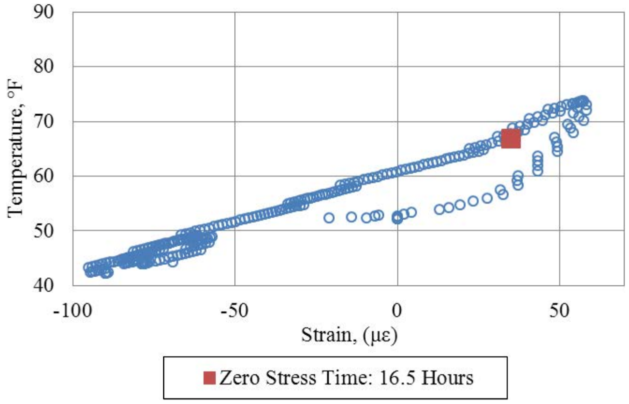

Figure H.59. Establishing TZ for the PCC layer at the centerline of Slab 1 in Cell 71.

$$\varepsilon_{\text{total}} = (R_1 - R_0)B + (T_1 - T_0)\times\alpha_s \qquad \text{(H.6)}$$

Strain defined using Equation H.6 is used to establish TZ based on a methodology developed in a previous study (Wells et al. 2006). In this methodology, TZ is defined as the transition point in the strain-temperature response of the slab, as the concrete gradually transforms from a thixotropic material capable of flow to a hardened, rigid material. At this point, a uniform change in strain with temperature can be observed.

Strain-temperature relationships were established for both layers of Slabs 1 and 2 in Cell 71 using the readings from the VW gauges. The relationship for the PCC and EAC layers is shown in Figures H.59 and H.60, respectively. TZ (represented

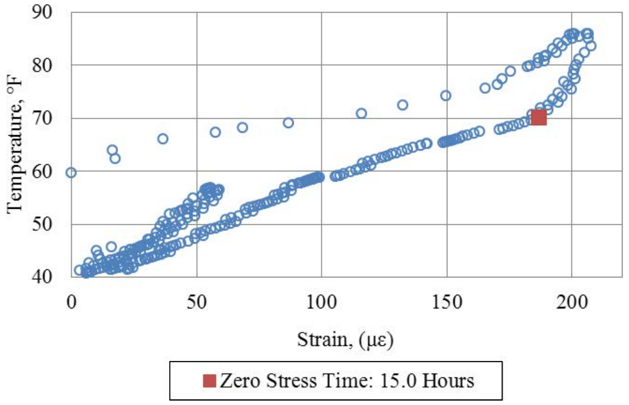

Figure H.60. Establishing TZ for the EAC layer at the centerline of Slab 1 in Cell 71.

Table H.14. TZ Established for Cell 71 Using Methodology 1

	Time after Placement (h)					
	Slab 1			Slab 2		
	Top Gauge	Middle Gauge	Bottom Gauge	Top Gauge	Middle Gauge	Bottom Gauge
Edge	15.25	14.25	16.75	NA	16.50	17.00
Midslab	16.25	15.50	17.25	NA	NA	NA
Centerline	15.00	NA	16.50	NA	NA	NA

Note: NA = not available.

by the red square in Figure H.59) is identified as the point after which the slab deforms at a constant rate with respect to changes in temperature. The slope of the strain-temperature relationship during the period between placement and TZ is different from that after TZ. In this region, less strain is observed with each incremental change in temperature. Therefore, it can be concluded that sufficient stiffness in the concrete has not yet been achieved to sustain the thermal deformation of the slab.

TZ was also established in the same manner using the other sensors with different orientations and locations in Slabs 1 and 2 for Cell 71. The gauges in both the EAC and PCC layers oriented in the longitudinal direction were used for this purpose. The results are summarized in Table H.14. As seen in Table H.14, the early-age data were missing for some locations. This was because of an error in the initial datalogger program. TZ varies between 15 and 16.25 hours for the top layer and between 14.25 and 17 hours for the lower layer at different locations on the basis of data in Table H.14.

Establishing TZ for Cell 71 with Methodology 2

The other methodology used in this study to establish TZ is to monitor the change in curvature of the slab with respect to temperature gradients. In this methodology, the time when the concrete has developed sufficient stiffness to curl in response to temperature gradients is established as TZ. The calculation of the curvature for the composite slabs is carried out using Equation H.7

$$\rho = -\frac{\varepsilon_t - \varepsilon_b}{D(1+\varepsilon_t+\varepsilon_b)} \qquad \text{(H.7)}$$

where

ε_t = strain calculated using Equation H.6 based on the VW strain gauge readings at the top of the EAC layer,
ε_b = strain at the bottom of PCC layer, and
D = distance between the gauges.

Figure H.61 presents the curvature and the LTG in Slab 1 on Cell 71. The VW gauge used to generate Figure H.61 is the same (longitudinal, at the centerline) as that used for Figure H.59. In Figure H.61, the largest gradient develops shortly after paving. However, slab curvature did not start to respond to the LTG until about 16 hours after paving. After this point, it can be seen that the slab starts to curl up because of the increasing negative temperature gradient. Therefore, this point can be recognized as TZ for the slab. Two more figures like Figure H.61 were produced for the edge (Figure H.62) and midslab (Figure H.63) of Slab 1 for Cell 71. Table H.15 presents a summary of the estimated times for the initial development of curling after paving based on Figures H.61 through Figure H.63.

From Table H.15, it can be concluded that TZ is equal to about 15 hours for Cell 71 based on Methodology 2. The TZ established for Cell 71 using Methodology 1 varies between 15 and 16.25 hours for the top layer, with an average value of 15.5 hours. For the lower layer, TZ varies between 14.25 and 17 hours, with an average value of 16.25 hours, based on Methodology 1. The TZs obtained using the two methodologies agree relatively well.

Establishing Built-in Temperature Gradient for Cell 71

TZ was established in the previous sections for Cell 71. The ELTG at TZ is the built-in temperature gradient that locks

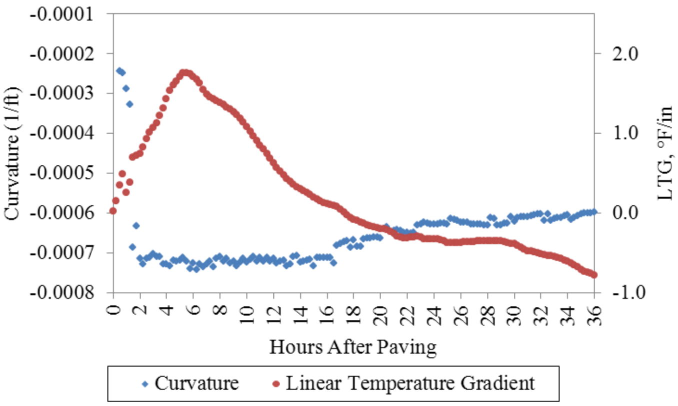

Figure H.61. Relationship between longitudinal curvature and LTG at the centerline of Slab 1 in Cell 71.

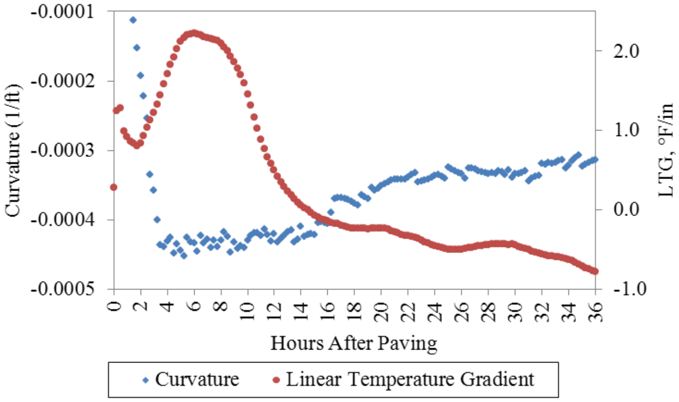

Figure H.62. Relationship between longitudinal curvature and LTG at the edge of Slab 1 in Cell 71.

into the slab and influences its future shape. The average TZ (calculated on the basis of both methodologies) for top and lower layers falls between 15 hours and 16.25 hours. The ELTGs estimated using thermocouple data from Slab 2 over this period of time can be seen in Figure H.64. It should be noted that the thermocouple data from Slab 1 on this cell was not usable for the first 5 days. From Figure H.64, it can be seen that the ELTG is approximately –0.7°F/in. in the period of time under study. Because ELTG within the range of TZs established for the two layers remains constant between hours 15 and 16, hour 15 established using Methodology 2 is selected as TZ for both layers on this cell.

Establishing Zero Stress Temperature for Cell 71

The slab average temperature at TZ is another parameter that needs to be established. As stated, this parameter is significant because it defines the amount of uniform thermal expansion and contraction in the slab. Figure H.65 presents the WAT for the PCC layer in Cell 71 over the range of potential TZs. The WAT at hour 15, selected as the TZ, is approximately 79°F.

Table H.15. TZ Established for Different Locations for Cell 71, Using Methodology 2

Location	Time after Placement (h)
	Slab 1
Edge	15
Midslab	15
Centerline	15

Figure H.66 shows the range of the WAT for the EAC layer in Cell 71 around TZ. For the EAC layer, the WAT at TZ (hour 15) is approximately 75°F.

Establishing TZ for Cell 70 with Methodology 1

Cell 70 consisted of an HMA layer over a PCC layer. The PCC layer in Cell 70 was constructed on the morning of May 5, 2010, with the paver passing the instrumented cells at approximately 7:45 a.m. A typical strain–temperature relationship established using the VW gauges in Cell 70 is presented in Figure H.67. The strain and temperature readings in Figure H.67 were zeroed to the time when the concrete was placed around the sensor installations.

As seen in Figure H.67, the strain readings increased from zero to about 50 microstrains in the first 10 hours (the area labeled by arrow 1 in the figure). The temperature of the concrete did not change significantly within this period. The readings then enter a period between 20 and 30 hours after placement (arrow 2 in the figure), in which the strain oscillates around approximately 50 microstrains. The strain does not change significantly, even though there are significant changes in temperature. During the period labeled with arrow 3, a

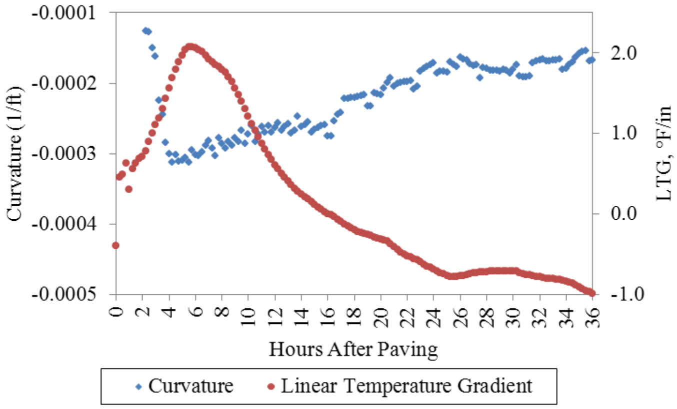

Figure H.63. Relationship between longitudinal curvature and LTG at the midslab of Slab 1 in Cell 71.

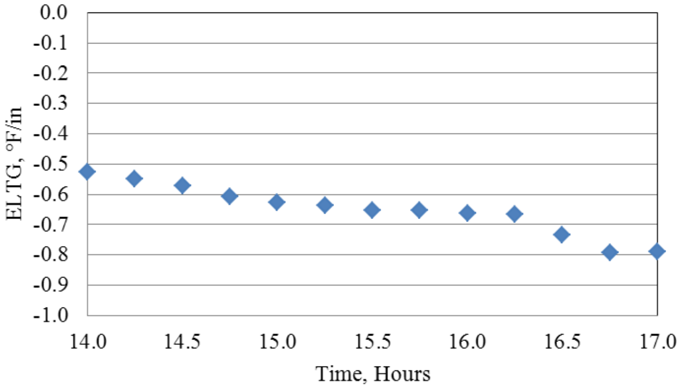

Figure H.64. ELTG over the range of TZs for Slab 2 in Cell 71 using thermocouple data.

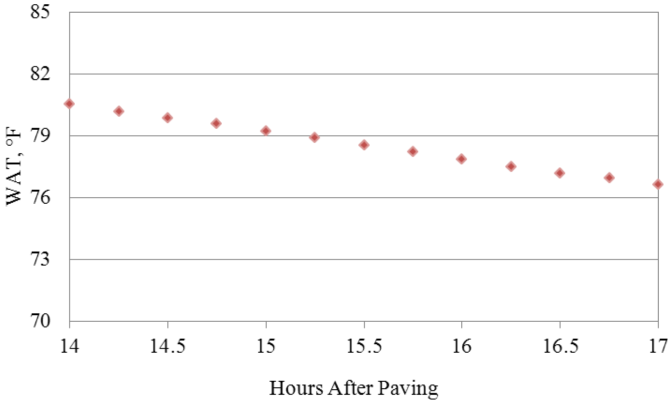

Figure H.65. WAT over the range of TZs for the PCC layer for Slab 2 in Cell 71 using thermocouple data.

relatively fixed relationship between strain and temperature is observed. The same behavior was observed at other locations as well in Cell 70. This behavior could be attributed to the joints in the slabs not cracking during this time period. With these data, it is difficult to use the relationship between strain and temperature to establish TZ. Therefore, the curvature–time relationship was investigated.

Establishing TZ for Cell 70 with Methodology 2

Figures H.68 through H.70 provide the curvatures and corresponding LTGs over the first 36 hours after paving for both slabs in Cell 70. Both curvatures and LTGs are determined for three different locations: namely, centerline, midslab, and edge. When comparing these six figures, the trend in curvature with respect to LTG appears to be quite anomalous. There is no consistent relationship when comparing the sensors within a slab or when comparing the same location between slabs.

As shown, neither Methodology 1 nor Methodology 2 can be used to establish TZ. Therefore, TZ is established for the

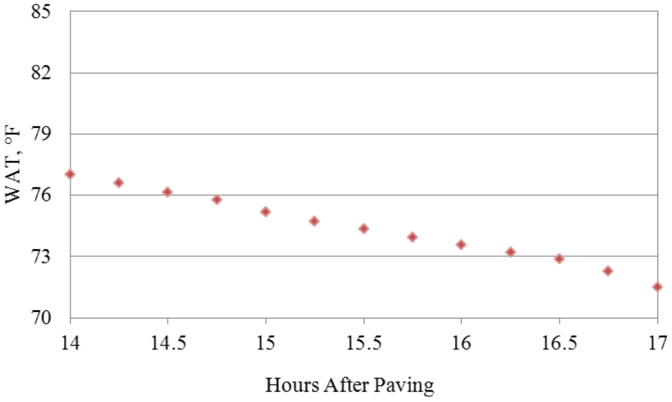

Figure H.66. WAT for the range of TZs for the EAC layer for Slab 2 in Cell 71 using thermocouple data.

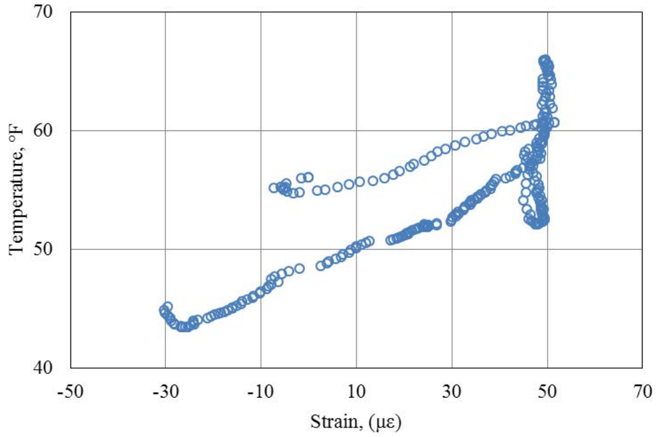

Figure H.67. Typical strain-temperature relationship based on VW gauge data for Cell 70.

PCC layer in Cell 70 using the TZ established for the PCC layer in Cell 70 and maturity concepts.

The lower layer of Cell 71 is a PCC layer that has the same mixture design as the PCC layer for Cell 70. Therefore, the maturity of the concrete in Cell 71 at TZ was used to estimate TZ for Cell 70, assuming that TZ occurs at a constant level of maturity for a given mix when hydrating in nearly the same restraint conditions. Maturity is simply the integral of the time–temperature curve above a datum temperature. The Nurse-Saul relation is commonly used for this purpose and is provided in the following equation:

$$M = \sum (T - T_0)\Delta t \tag{H.8}$$

where

M = maturity in °F-hour,
Δt = time interval in hours,
T = average slab temperature over Δt in °F, and
T_0 = datum temperature assumed as 14°F.

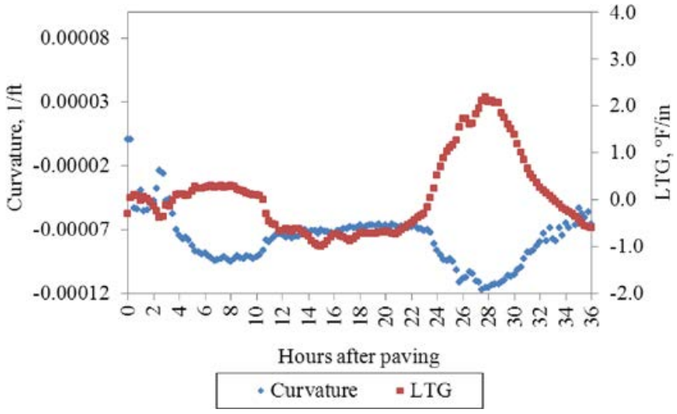

Figure H.68. Relationship between longitudinal curvature and LTG at the edge of Slab 1 in Cell 70.

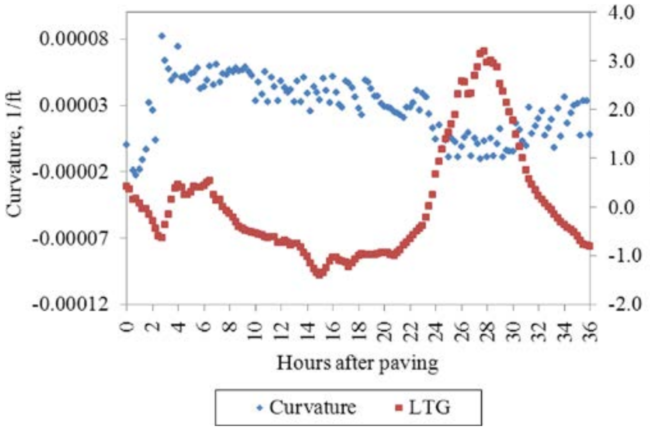

Figure H.69. Relationship between longitudinal curvature and LTG at the edge of Slab 2 in Cell 70.

Figure H.71 shows the maturity development in the PCC layer for Slab 1 of Cells 70 and 71 for the first 24 hours after construction. Slab 1 of Cell 71 was selected over Slab 2 because the majority of gauges installed in Slab 2 of Cell 71 were not active during the period of interest. To estimate maturity, thermistor data from the middepth VW gauges at three different locations, namely the edge, midslab, and centerline, were used. From Figure H.71, it is apparent that the TZ for Cell 70 is between approximately 19 and 20 hours for the three different locations.

Establishing Built-in Temperature Gradient for Cell 70

In the previous section, TZ was established as being between 19 and 20 hours based on the maturity at TZ observed for Cell 71. The ELTG was estimated based on the data from the thermocouples in Slab 1. The data from the thermocouples in Slab 2 were not usable until Day 5. The built-in temperature gradient for Cell 70 can then be determined as approximately −1.1°F/in. based on Figure H.72. Since the ELTG does not vary significantly in the period of 19 to 20 hours, hour 19 is selected as TZ for this cell.

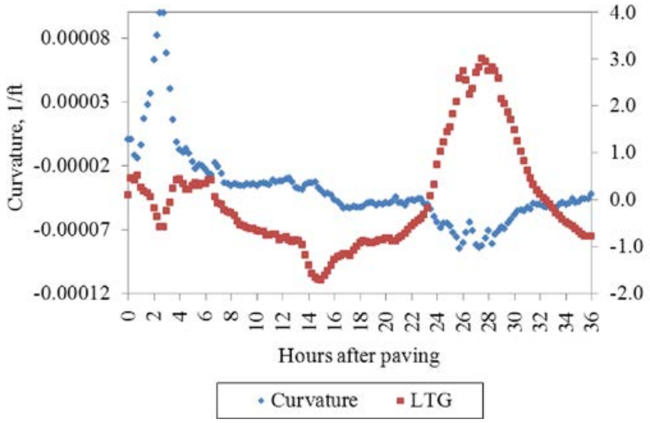

Figure H.70. Relationship between longitudinal curvature and LTG at the centerline of Slab 2, Cell 70.

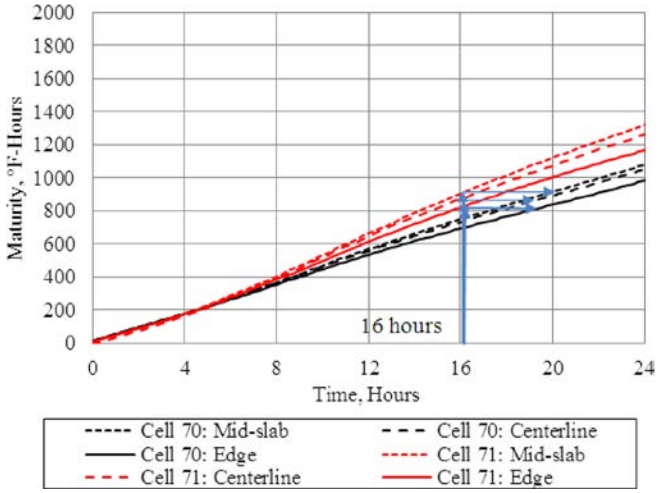

Figure H.71. Comparison of maturity at TZ for the middepth of the PCC layer, Slab 1 of Cells 70 and 71.

Establishing Zero Stress Temperature for Cell 70

Figure H.73 presents the WATs calculated using data from thermocouples in Slab 2 over the same time span used in Figure H.73. At midslab, the WAT at TZ (i.e., about 19 hours after paving), is approximately 53°F.

Establishing TZ for Cell 72

Both layers for Cell 72 were constructed on the morning of May 10, 2010, with the paver passing the instrumented cells at approximately 8:45 a.m. Unfortunately, for this cell, the strain

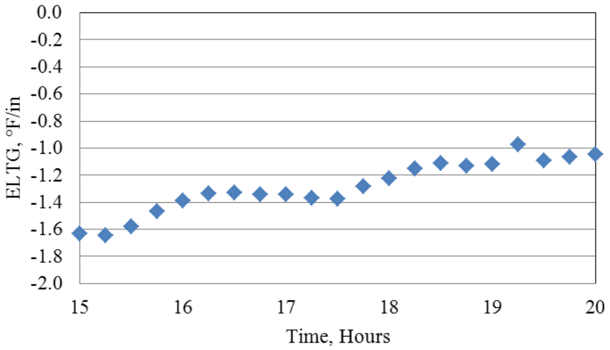

Figure H.72. ELTG over the range of TZs for Slab 2 in Cell 70 using thermocouple data.

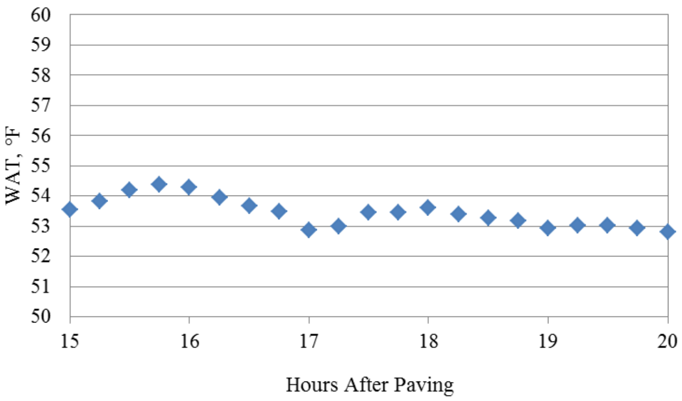

Figure H.73. WAT over the established range of TZs for Cell 70 using the thermocouple data in Slab 2.

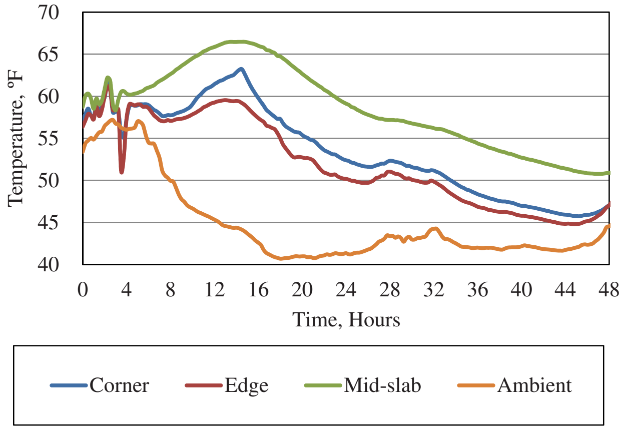

Figure H.75. Thermocouple data at the middepth of the lower layer for Slab 2 in Cell 72.

and thermistor data were not available to establish the TZ. Although the cause of this error is not known, it appears to be related to the datalogger programming for the VW gauges.

The EAC layer in Cell 72 has the same mixture design as the EAC layer in Cell 71. Therefore, the TZ for the EAC layer in Cell 72 can be determined based on the maturity at the TZ for the EAC layer in Cell 71. As shown in Figure H.74, the TZ for the EAC layer ranges between 16 and 20 hours, depending on the location.

Establishing the TZ for the lower layer in Cell 72 without VW gauge data is quite challenging. A rough assumption can be that TZ occurs around 14 to 24 hours after paving, considering the TZs for all other layers in Cells 70 and 71 all fall in this range. One way to check the validity of this assumption is based on the temperature changes in the layer during hydration. It is known that for a hydrating concrete in isothermal conditions, the TZ occurs sometime during the cooling phase, after the hydration peak. Fortunately, temperature has been measured in the lower layer of Slab 2 for Cell 72 since placement. The data are presented, together with the ambient temperature, in Figure H.75 for the first 36 hours after placement of the layer. As can be seen in the figure, when the peak temperature is observed for the lower layer, the ambient temperature is dropping, implying that hydration is in progress. The peak of hydration appears at around hour 14, and the time when the concrete temperature starts to follow the ambient temperature (indicating that hydration has almost ceased) is approximately 24 hours. It is believed that TZ occurred between 16 and 24 hours.

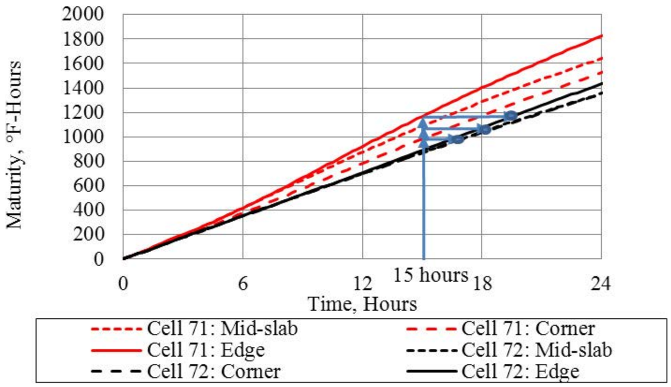

Figure H.74. Comparison of maturity at the TZ for middepth of the EAC layer for Slab 1 in Cells 71 and 72.

Establishing Built-in Temperature Gradient for Cell 72

TZ was established as being between 16 and 20 hours for the top layer and 16 and 24 hours for the lower layer. The ELTG, based on the thermocouple readings over the time period of 16 to 24 hours after paving, is presented in Figure H.76. Because the ELTG in the entire time span shows a significant variation, hour 20, at which the ELTG stabilizes and remains constant thereafter is selected as TZ for both layers in this cell. The ELTG at TZ is approximately –0.8 °F/in.

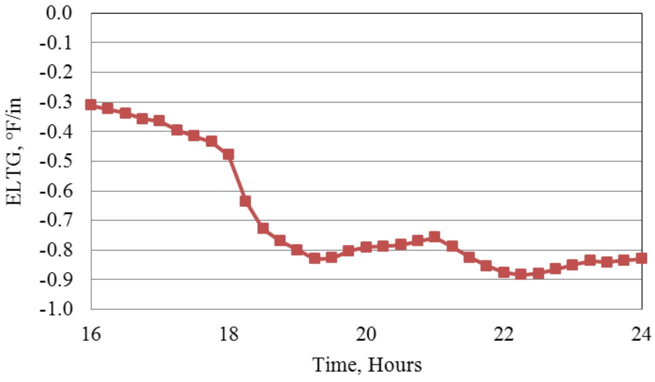

Figure H.76. ELTG estimated using thermocouple data in Slab 2 for the range of the TZs for Cell 72.

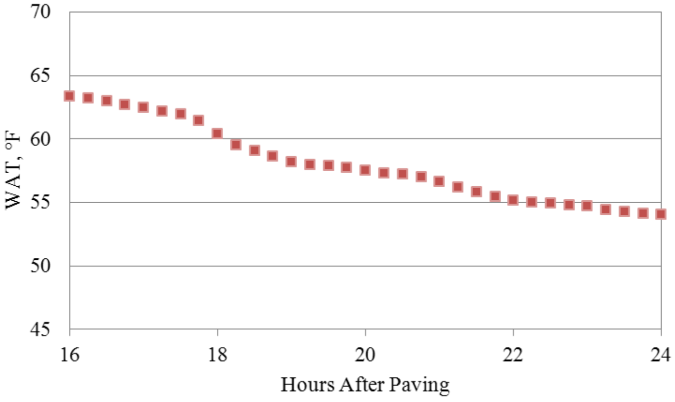

Figure H.77. WAT over the range of TZs for the EAC of Slab 2, Cell 72 using thermocouple data.

Establishing Zero Stress Temperature for Cell 72

The WATs over the same time period shown in Figure H.76 for both layers are shown in Figure H.77 and Figure H.78, respectively. The WAT at the selected TZ (hour 20) is approximately 58°F at midslab for the EAC layer and approximately 62°F at mid-slab for the lower layer.

Establishing Built-in Moisture Gradient

For fresh concrete, the moisture profile throughout the depth of the slab has been shown to be completely saturated at the TZ (Wells et al. 2006).

Conclusions

The TZ, WAT, and built-in temperature gradient were established for each instrumented cell at MnROAD. To establish TZ, two methodologies were used, one based on the variation seen in the measured strain with respect to temperature changes in the slab and the other based on the initiation of curling in the slabs with respect to LTG.

For Cell 71, TZ was established to be between 15 and 17 hours using Methodology 1 and between 14 and 15 hours using Methodology 2. For Cell 70, neither of the two methodologies was able to yield TZs; therefore, the concept of maturity was used to derive the TZ for Cell 70 based on the TZ for Cell 71. Based on an equivalent maturity established between the two cells, it was determined that the TZ for Cell 70 was close to 18 hours. The early-age data was missing for Cell 72. TZ was again determined, based on the maturity concept for the EAC layer in Cell 72, as being between 16 and 20 hours whereas TZ for the lower layer was estimated as being between 16 and 24 hours. Fortunately, overcast conditions at the time of paving resulted in relatively constant temperature conditions in the slab over the first 24 hours after paving. Therefore, the climatic conditions in the slab at the TZ could be established relatively well, even with the limited data available.

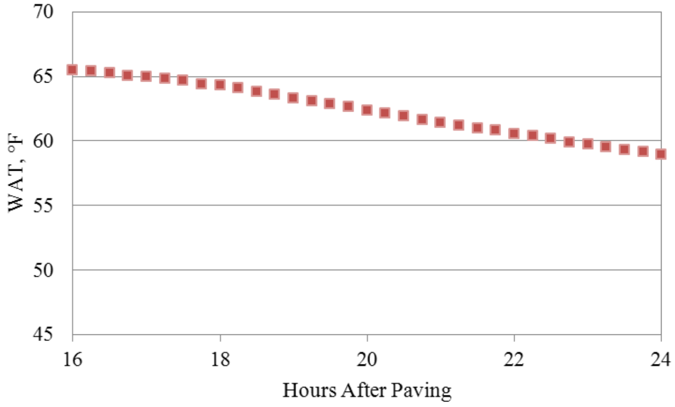

Figure H.78. WAT over the range of TZs for the lower layer of Slab 2 on Cell 72 using thermocouple data.

Composite Pavement Curvature in Response to Environmental Loads

In the previous three sections, the transient temperature, moisture, and built-in gradients were characterized for all three cells over the first 11 months after construction. The response of the slabs, in terms of curvature, to these gradients is analyzed here. The curvature of a slab influences both the location and magnitude of the critical stress in the slab. The location and magnitude of the critical stress relative to the strength of the structure ultimately controls the mode of failure and fatigue life of the pavement.

Static strain gauges were used to measure the strain in the slabs using Equation H.5, previously presented. These strains are then used to estimate the curvature in the slab using Equation H.6, as previously presented. Strain readings are available at different locations in each slab, and there are two slabs within each cell. Therefore, a baseline can be established regarding the variability in the curvature calculation between locations and between slabs with each cell. This baseline can thereafter be used to evaluate the difference in the curvature between cells.

It is worth mentioning that the gauges located at the edge, midslab, and centerline are oriented in the longitudinal direction (parallel to the direction of traffic). The gauge at midslab width and adjacent to the transverse joint is oriented in the transverse direction (perpendicular to the direction of traffic). The last gauge is located in the corner of the slab near the longitudinal lane/shoulder joint. This gauge is oriented on a 45-degree angle from the longitudinal and transverse joints. Hereafter, these gauges will be referred to as the transverse and diagonal gauges, respectively.

To calculate curvature, each strain gauge is first zeroed to the TZ, as established in the previous section, because before this time the strain in the slab is zero. It has been discussed in the previous section that the TZ varies between slabs and between locations. In the forthcoming analyses, the average TZ for the various locations within a cell is used as a single value for the entire cell. This means that the time used to zero the strain readings in the PCC layer for Cell 70 is 18 hours after paving. As presented, the variation of TZ between different locations in Cell 71 is insignificant; because of this, a TZ determined by Methodology 2 of 15 hours after paving was used for this cell. For Cell 72, a range of 16 to 20 hours was estimated for the EAC and 16 to 24 hours for the lower layer. Hour 18 was selected as TZ for zeroing the strains measured for this cell. In the following sections, curvatures will be estimated based on the zeroed strains for the three cells. For each cell, comparisons will be discussed between different locations and slabs.

Cell 70 Slab Curvature

Figures H.79 through H.83 show a comparison of curvatures between the two slabs in Cell 70 at all locations. Based on these figures, almost all locations show a positive upward curvature for the first 11 months after construction.

From the figures, one can conclude that curvatures in all directions are consistent between the two slabs through fall 2010. For the period between the fall and spring, the calculated curvature is quite different between the two slabs in Cell 70, with Slab 1 exhibiting consistently more curvature than Slab 2 at all locations. This disparity is particularly obvious for the gauges oriented in the longitudinal direction. On the other hand, the curvatures in the transverse direction agree well between slabs. The range of disparity in the diagonal direction lies between that for the transverse and the longitudinal directions. The fact that the transverse curvatures are consistent between slabs but the longitudinal curvatures are different could be an indication that both transverse joints for each slab did not crack during the fall. This would result in the effective length of one slab being twice that of the other slab. This additional restraint results in reduced curvature.

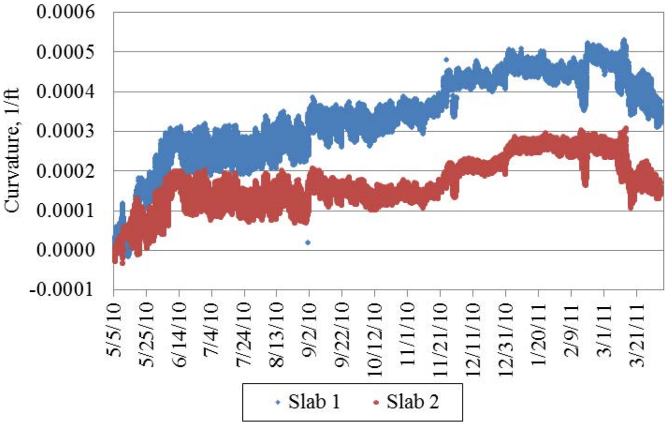

Figure H.80. Comparison between the longitudinal curvature at midslab between the two slabs in Cell 70.

To investigate the effect of temperature gradients in the slabs on the curvature seen in the above figures, Figure H.84 is provided. Figure H.84 presents the variation in the LTG with time. Comparing Figures H.79 through Figure H.83 to Figure H.84, it is noticed that the variation in curvature corresponds with the variation in LTG. A larger daily variation of curvatures corresponds to a larger daily variation of LTGs.

Despite the daily variation, there is a general increase in curvature with time for all locations. This is not only because of temperature gradients because the daily average LTG in Figure H.84 only drops 0.5°F/in. from summer to winter. It is believed that the general increasing trend in curvature is more influenced by drying shrinkage. Nassiri (2011) observed that the duration of drying shrinkage resulting in an increase of

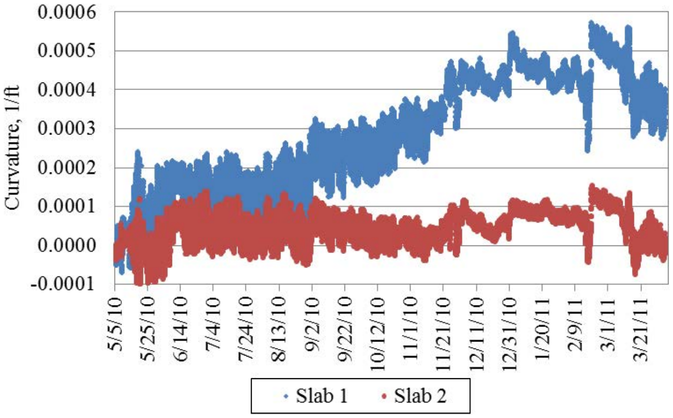

Figure H.79. Comparison between the longitudinal curvature at the edge of the two slabs in Cell 70.

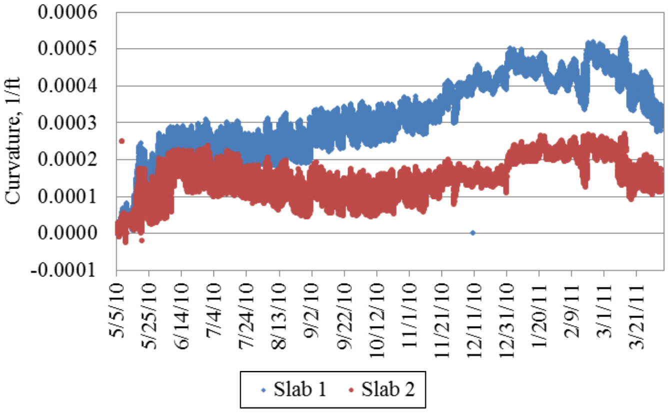

Figure H.81. Comparison between the longitudinal curvature at the centerline of the two slabs in Cell 70.

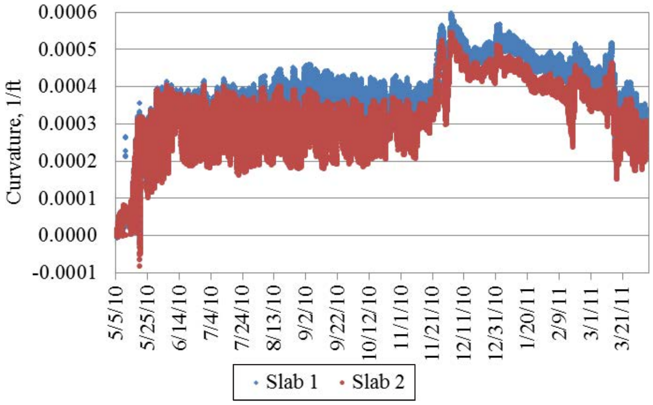

Figure H.82. Comparison between the transverse curvature of the two slabs in Cell 70.

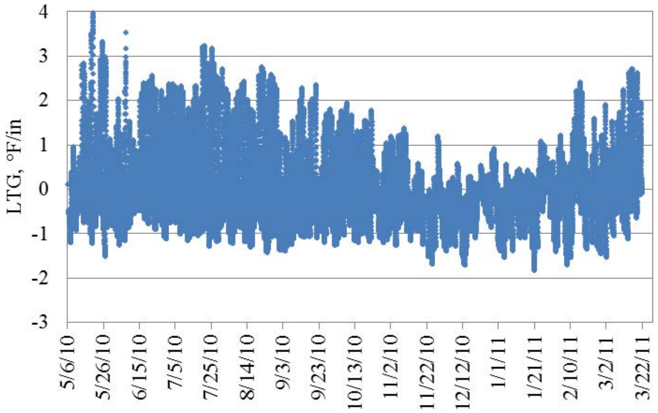

Figure H.84. Variation in the LTG estimated using thermocouple data from midslab of Slab 1 in Cell 70.

curvature could be as long as 5 to 7 years. Figure H.85, extracted from the aforementioned reference, shows the variation in curvature caused by drying shrinkage with time for Cells 37 and 38 at MnROAD. These cells are comprised of 6-in. slabs on granular base layers. It is apparent from the figure that the curvature progressively grows for the first 40 months after construction. For this study, curvature and temperature data are available for only the first 11 months after construction, which makes it impossible to carry out a comprehensive evaluation on the effect of drying shrinkage.

Another interesting finding from Figures H.79 through Figure H.83 is that there is a rapid development in curvature within the first month after construction. The curvature in the transverse and diagonal directions further suggests that the beginning of the rapid increase coincides with the placement of the asphalt layer. After 1 month, the curvature continues to increase but at a slower rate until it starts to decrease during the spring. This observation can be explained by the drying shrinkage of the PCC due to placement of the upper HMA layer. At the time when the upper HMA layer is placed, the moisture at the surface of the PCC layer evaporates and thus a negative moisture gradient is imposed.

The rate of drying shrinkage declines around 1 month after construction because there is ample rainfall available in the summer that rewets the upper portion of the PCC layer. The rewetting and subsequent recovery of curvature are more obvious during the spring. The permeability of the asphalt also plays an important role in the rewetting process. If the upper layer was constructed of PCC and had the same thickness as the HMA upper layer, the recoverable drying shrinkage in the underlying PCC layer most likely would be less.

It is also noticed that in Figures H.79 through Figure H.83, the curvature in the longitudinal and transverse directions remains relatively constant between June and September. During this time period, peak temperatures are reached in the PCC layer. Therefore, it is suspected that joint lockup occurred in the slabs during this period of time. To further investigate the joint lockup, strains measured in the slabs were evaluated with respect to temperature. This is presented in Figure H.86 to Figure H.91. Figure H.86 and Figure H.87 show the strain

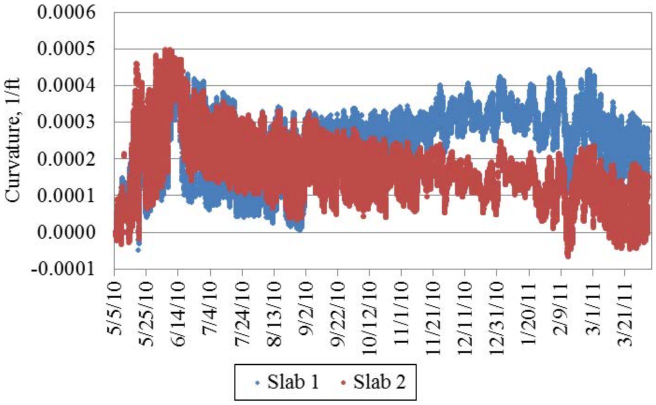

Figure H.83. Comparison between the diagonal curvature of the two slabs in Cell 70.

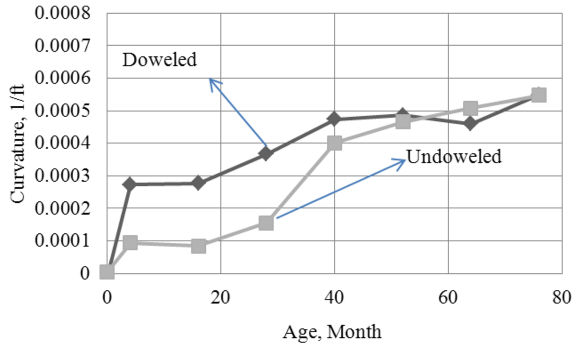

Source: Nassiri 2011.

Figure H.85. Effects of drying shrinkage on the curvature for Cells 37 and 38 at MnROAD. (Undoweled = nondoweled.)

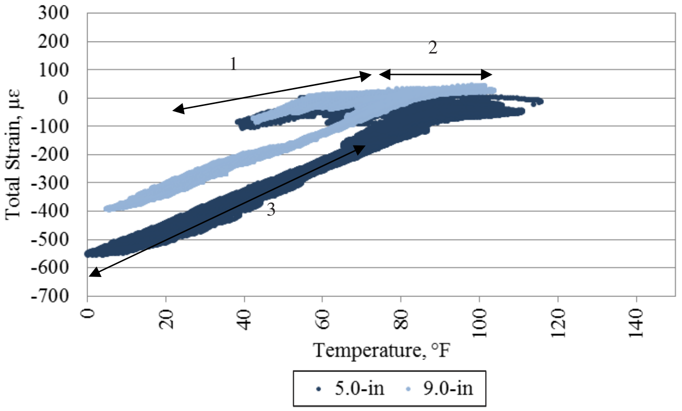

Figure H.86. Longitudinal strain with respect to temperature at the midslab for Slab 1 in Cell 70.

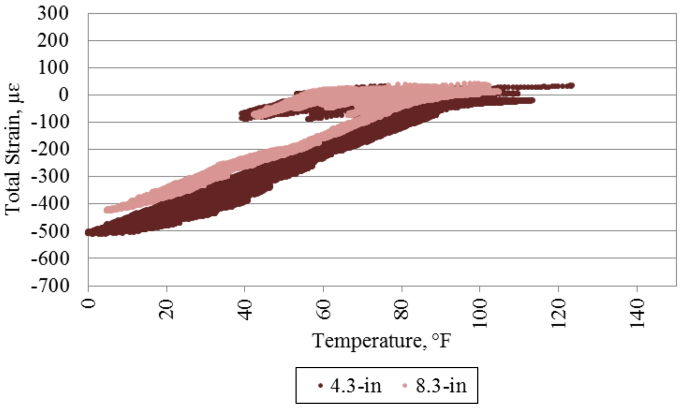

Figure H.87. Longitudinal strain with respect to temperature at the midslab for Slab 2 in Cell 70.

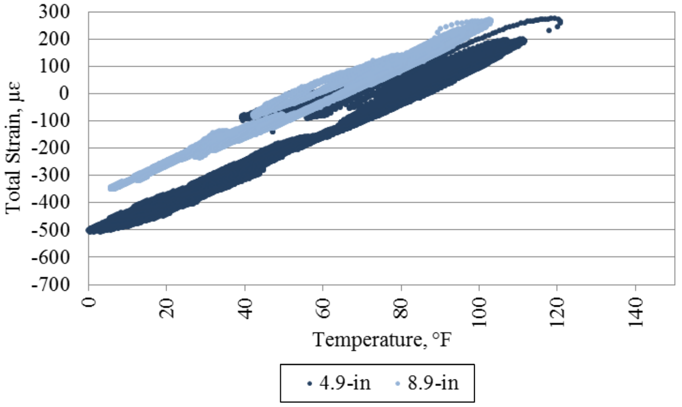

Figure H.88. Transverse strain with respect to temperature at the midslab for Slab 1 in Cell 70.

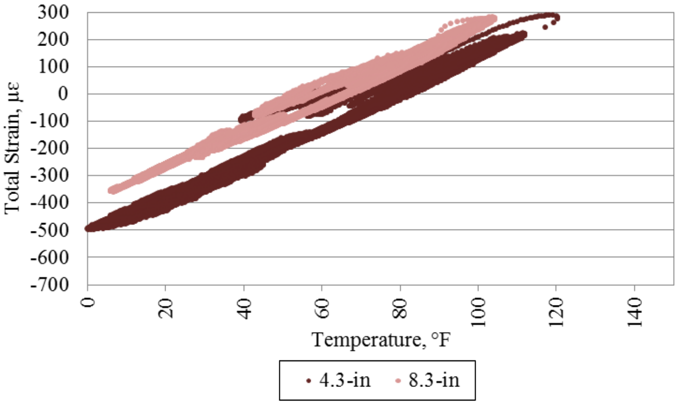

Figure H.89. Transverse strain with respect to temperature at the midslab for Slab 2 in Cell 70.

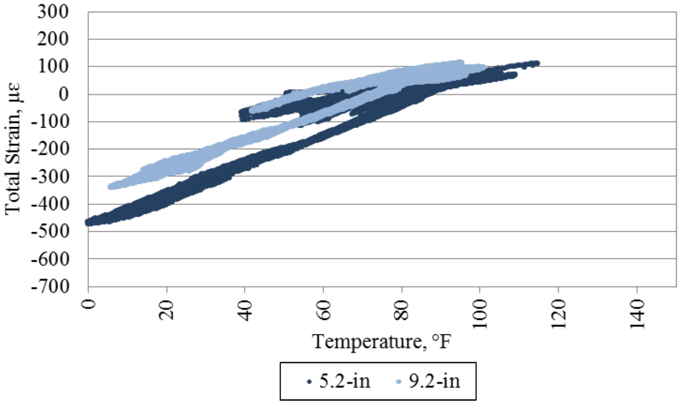

Figure H.90. Diagonal strain with respect to temperature at the midslab for Slab 1 in Cell 70.

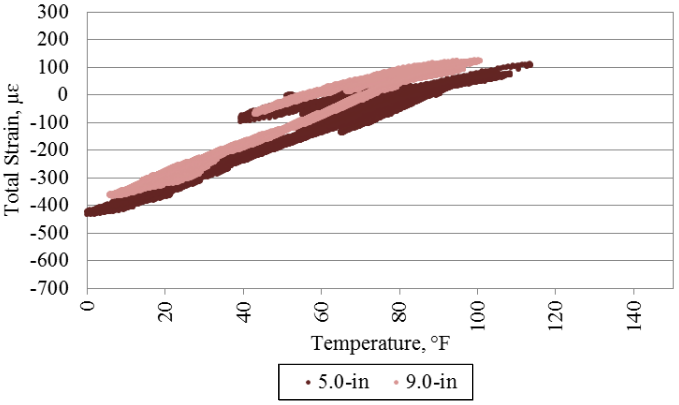

Figure H.91. Diagonal strain with respect to temperature at the midslab for Slab 2 in Cell 70.

with respect to temperature in the longitudinal direction for Slabs 1 and 2, respectively. Figure H.88 and Figure H.89 show the strain in the transverse direction, and Figure H.90 and Figure H.91 correspond to the strain at the corner of the slab in the diagonal direction.

Figure H.86 also shows the sequence of data and the three distinct trends seen in the strain–temperature behavior of the slab. Based on this figure, for the first trend (this trend corresponds to the time period between May and June) the strain is almost zero, whereas the temperature of the slab is increasing. This behavior of the slab can be explained by considering the WAT at the TZ, which was established in the previous section. The WAT at the TZ for this cell ranged between 58°F and 65°F. For the joints of the slab to crack, when the WAT in the slab drop below the WAT at the TZ, the slab contracts. This contraction is restrained by the friction between the slab and the base. The resulting tensile stresses contribute to the development of transverse cracks off the bottom of the saw cut at the transverse joints. Since the WAT at the TZ was very low for this cell, the slabs did not crack until the fall when the WAT of the pavement dropped. The longer slabs provided sufficient restraint to prevent the slab from deforming (almost zero strain) throughout the duration of the summer while the temperatures were higher. For the second trend in the strain–temperature behavior in Figure H.86, it is obvious that there is a ceiling on the amount of total strain exhibited in the slab between June and September. When the transverse joints lock up, the slab no longer expands. The shift seen in the strain at different depths of the slab is due to more drying shrinkage that occurs at the top versus bottom of the slab. Furthermore, as a result of the drying shrinkage, the top of the slab locks up at a higher temperature than does the bottom.

Figure H.88 and Figure H.89 show the slab strain–temperature behavior in the transverse direction. The effects of joint lockup are not observed in the transverse direction because the asphalt shoulders are not sufficiently stiff, especially at high temperatures, to provide restraint against expansion of the slab. The effect of the transverse joints locking up is reflected in the diagonal direction as well, as seen in Figure H.90 and Figure H.91.

Figure shows three distinct strain trends corresponding to different times of the year.

Cell 71 Slab Curvature

Strain and thermistor data were not available before the TZ for 10 of the VW strain gauges in Slab 2 for Cell 71. Therefore, the missing data were filled with the corresponding values from Slab 1. For Cell 71, a comparison of the calculated curvature between the slabs at each location is shown in Figures H.92 through H.96.

Based on these figures, a better agreement is seen between the two slabs in Cell 71 than in Cell 70. The slight variation between the slabs could be caused by inaccuracy in determining the as-built depth of the gauges, as was discussed.

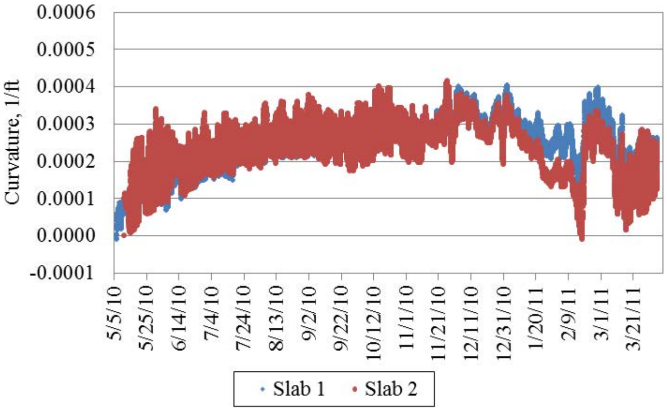

Figure H.92. Comparison of longitudinal curvature at the edge between the two slabs in Cell 71.

Joint lockup also occurred in Cell 71 during the summer. This is seen in Figure H.97 and Figure H.98. These figures show the longitudinal strain variation with respect to temperature at different depths for the two slabs in Cell 71. The remainder of the figures corresponding to the transverse and diagonal directions is not provided here. These graphs exhibited the same as those for Cell 70 in that joint lockup occurs only in the longitudinal direction. In Cell 70, more pronounced drying shrinkage at the top in comparison with the middle and bottom of the slab was noticeable, as seen in Figure H.97.

Cell 72 Slab Curvature

For Cell 72, strain and thermistor data were not available for either of the slabs until 52 hours after paving. Because the strains need to be zeroed based on the strain at TZ, the strain at this time must be estimated. The strain difference measured in Cell 71 starting at TZ and ending at a time when strain data

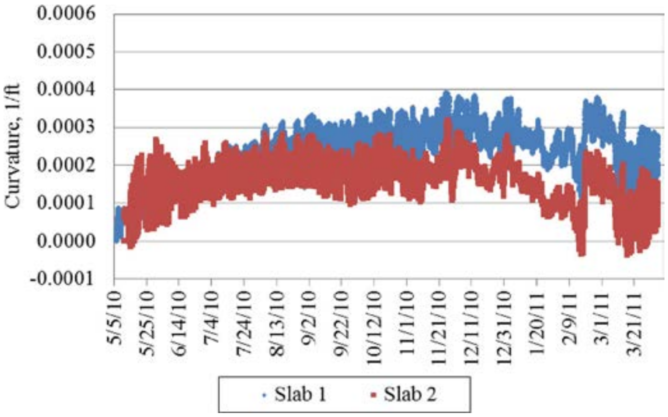

Figure H.93. Comparison of longitudinal curvature at midslab between the two slabs in Cell 71.

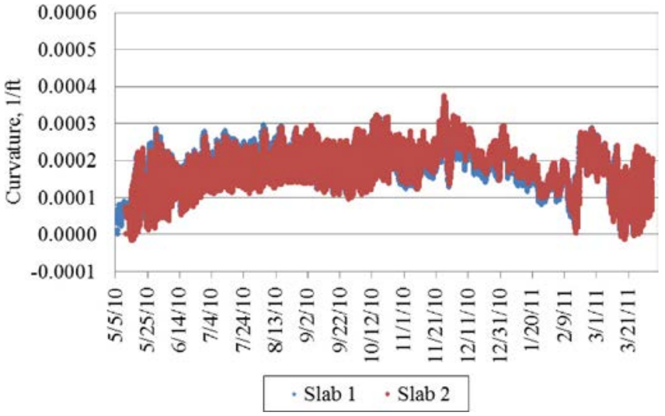

Figure H.94. Comparison of longitudinal curvature at the centerline between the two slabs in Cell 71.

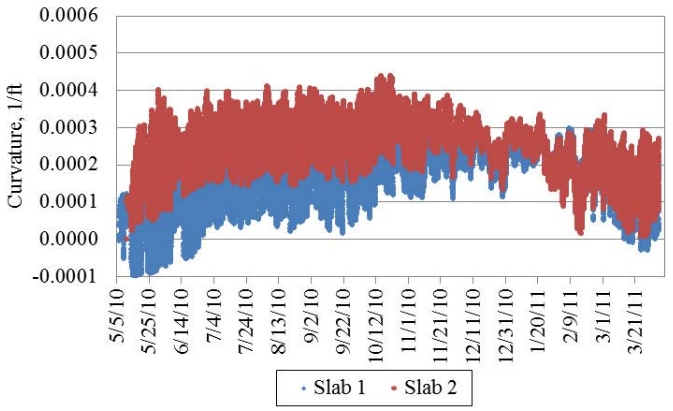

Figure H.96. Comparison of diagonal curvatures between the two slabs in Cell 71.

are available for Cell 72 was used to back-calculate the strain at TZ in Cell 72. The relatively short time interval between TZ and the first reoccurrence of ELTG at TZ was used to calculate the strain difference in Cell 71 to limit the effect of drying shrinkage and ELTG on strain. In addition, the drying shrinkage between Cells 72 and 71 is expected to be the same, because the top EAC layer in both cells is made of the same PCC mixture. With regard to the lower layer, which is different between the two cells, not much drying is expected to occur after placement of the upper layer. Therefore, changes in WAT are then primarily responsible for the difference in strain measured at these two times. Because both cells were paved in the morning, the variations in WAT between cells for a given time interval are comparable. To zero the strain in Cell 72, the calculated strain difference is used to adjust the strain in Cell 72 measured at the same time after paving as the reoccurrence of ELTG at TZ in Cell 71.

Using the estimated strains, curvature was established for the slabs on Cell 72. A comparison of the curvature in Cell 72 between the five locations in each slab is presented in Figures H.99 through H.103. Most locations, with the exception of the centerline and diagonal gauges, show good agreement between the slabs. This small discrepancy might be attributable to inaccuracies in the estimated depth of the VW gauges.

The occurrence of joint lockup during the summer was investigated for this cell as well. The longitudinal strain at midslab for Slabs 1 and 2 can be seen in Figure H.104 and Figure H.105. Based on these figures, the strain remains close to zero after the construction of the slab. Joint lockup occurs during the summer, when the temperature of the slab is higher than approximately 75°F.

Comparison of Curvature Between Cells

The analysis performed in the previous sections established a baseline for the consistency of curvature readings between multiple locations and between the two replicated slabs for each cell. A similar trend in curvature was found between the

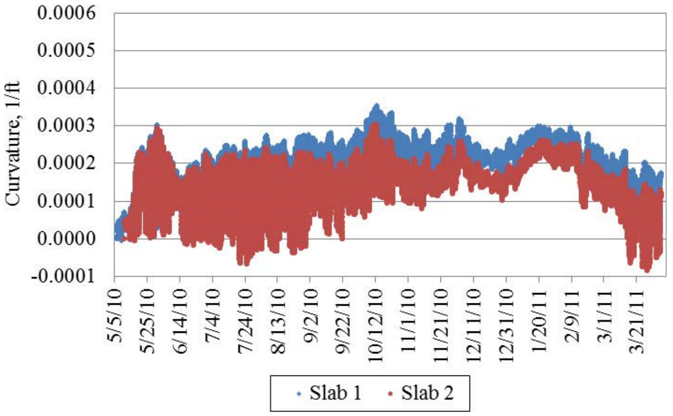

Figure H.95. Comparison of transverse curvature between the two slabs in Cell 71.

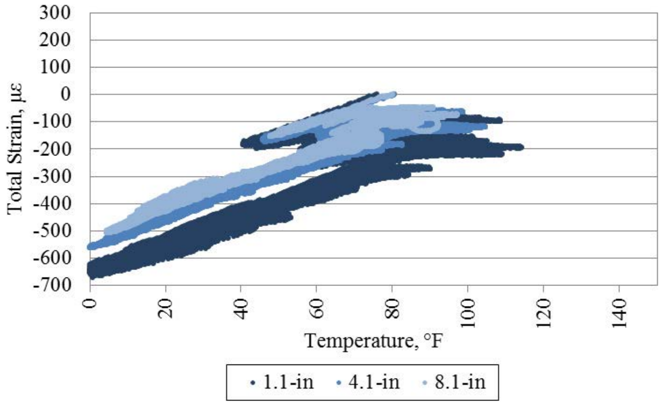

Figure H.97. Longitudinal strain versus temperature at midslab of Slab 1 in Cell 71.

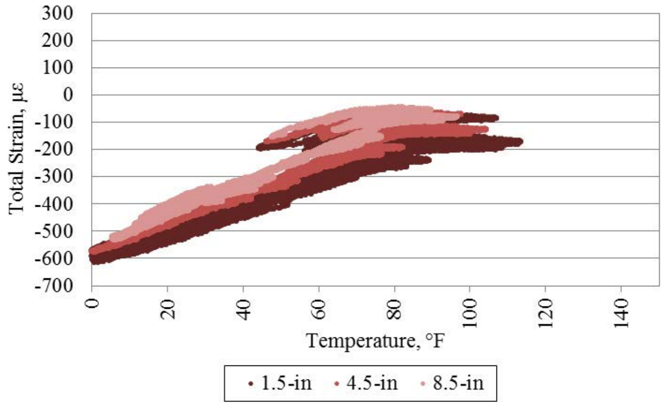

Figure H.98. Longitudinal strain versus temperature at midslab of Slab 2 in Cell 71.

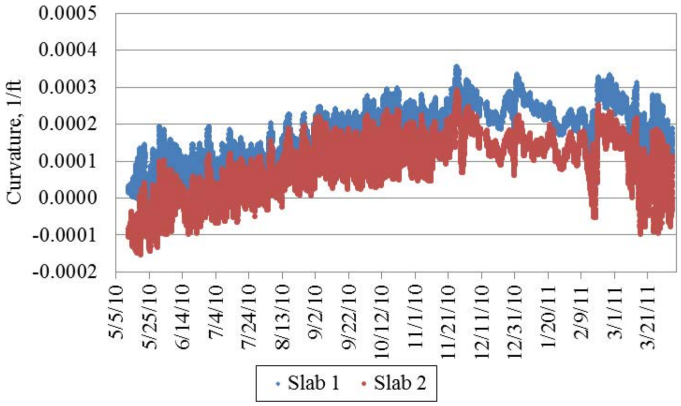

Figure H.99. Comparison of longitudinal curvature at the edge between the two slabs in Cell 72.

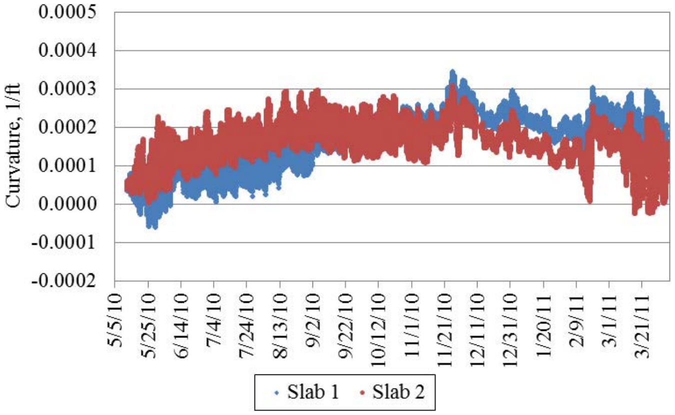

Figure H.100. Comparison of longitudinal curvature at midslab between the two slabs in Cell 72.

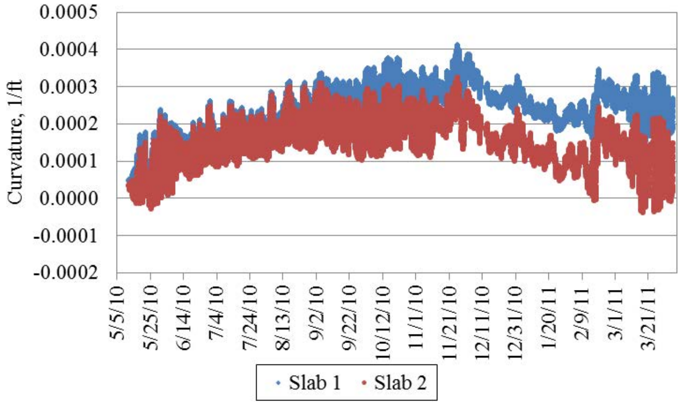

Figure H.101. Comparison of longitudinal curvature at the centerline between the two slabs in Cell 72.

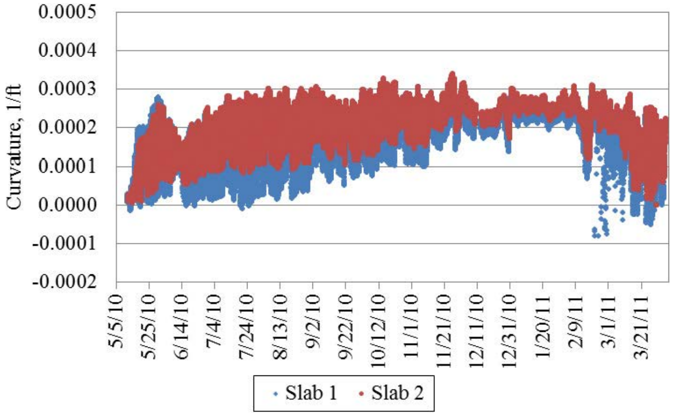

Figure H.102. Comparison of transverse curvature between the two slabs in Cell 72.

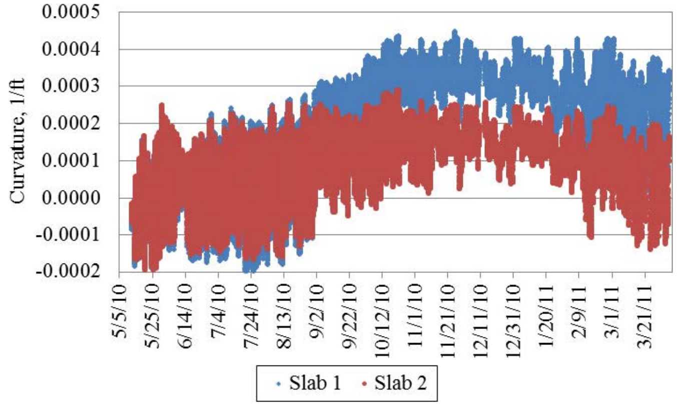

Figure H.103. Comparison of diagonal curvature between the two slabs in Cell 72.

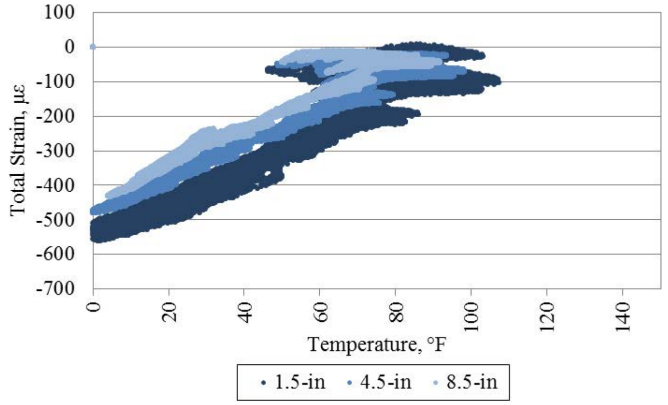

Figure H.104. Longitudinal strain with respect to temperature at midslab for Slab 1 in Cell 72.

locations for Cell 71 (Figure H.92 to Figure H.96) and Cell 72 (Figure H.99 to Figure H.103) but not for Cell 70 (Figure H.79 to Figure H.83).

A large variation in curvature was found between the two replicated slabs for Cell 70, whereas there was good consistency between slabs for the other two cells. It is suspected that not all the joints cracked at the same time, and the different effective slab lengths resulted in inconsistent curvatures between slabs for Cell 70. It is believed that the lockup of the transverse joints between June and September introduced a ceiling to the longitudinal curvatures for all cells. On the other hand, there was no lockup for the longitudinal joints because of the weak restraints provided by the asphalt shoulder.

Considering the large variation between the two slabs for Cell 70, it seems inappropriate to use the average of these values. Therefore, the curvatures for both Slabs 1 and 2 for Cell 70 are compared with the average values of Cells 71 and 72, as shown in Figure H.106.

In Figure H.106, there is no significant difference in curvature between Cells 71 and 72. However, a difference can be found between Cell 70 and Cells 71 and 72. For both slabs in Cell 70, a peak in curvature was reached in the middle of June (i.e., shortly after construction). However, the difference between the two slabs is that Slab 1 presented a decreasing curvature since June, whereas Slab 2 regained some curvature between June and December.

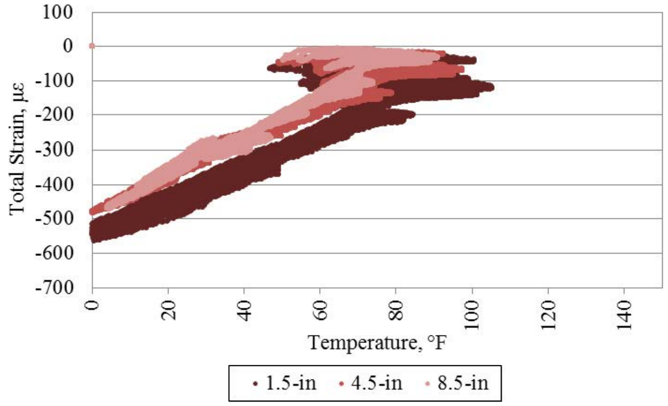

Figure H.105. Longitudinal strain with respect to temperature at midslab for Slab 2 in Cell 72.

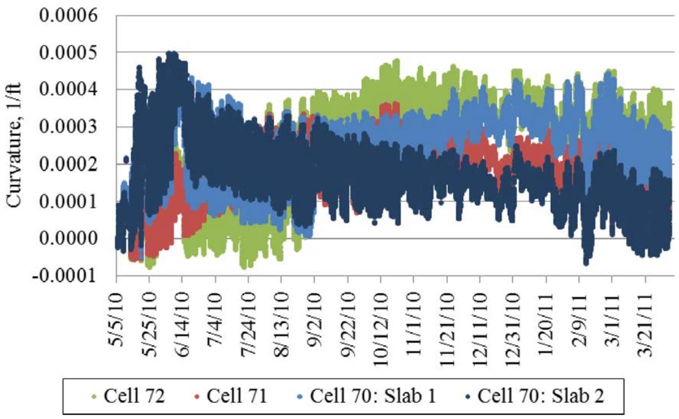

Figure H.106. Comparison of average slab curvature at the diagonal location. Cell 72 and 71 curvatures are averages of two slabs.

The initial peak in curvature is likely caused by the construction of the HMA layer. The high HMA temperatures at placement cause evaporation of the moisture in the upper portion of the lower PCC layer. However, as mentioned, the HMA layer has a higher permeability than does a concrete layer of the same thickness, which makes it possible for rewetting of the concrete to occur more readily. This is most likely why Slab 2 of Cell 70 is the only slab that presents a decreasing trend in curvature during the summer. Regarding Slab 1 of Cell 70, although an increasing curvature was observed between June and December, the magnitude of the increase is smaller (0.0001 × 1/ft) than that for Cells 71 (0.0002 × 1/ft) and 72 (0.00025 × 1/ft). This still implies the effect of the HMA layer in diffusing moisture downward and therefore rewetting the lower PCC layer. The effect of the HMA layer can also be verified with respect to the LTGs in the slab.

Figure H.107 and Figure H.108 present the variation in the LTG during the winter for Cells 70 and 71, respectively. In comparing these figures, it can be seen that the positive temperature gradients in Cell 71 are larger in magnitude than those in Cell 70. This results in larger daily fluctuations in the curvature. This indicates the HMA layer has an insulating effect.

The curvature for Cell 71 is slightly higher than that for Cell 72 during the warmer months (June, July, and August) and less than that for Cell 71 in the colder months (November, December, January, February, and March). This trend can be explained theoretically by considering the relative CTEs of the two pavement layers in these cells, as shown in Figure H.109.

Unlike for plain PCC pavements, the expansion and contraction caused by changes in the WAT for composite pavements are not uniform with depth. Changes in the WAT for composite

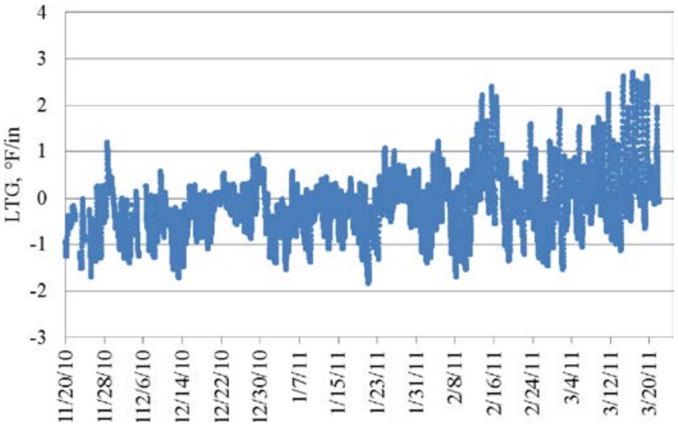

Figure H.107. LTG over the winter at the midslab for Slab 1 in Cell 70.

pavements tend to induce curvature in the slab. The direction (upward or downward) of the additional curvature depends on if the current temperature is higher or lower than the reference temperature and on the relative CTEs between the two layers. The diagonal curvature calculated for Slab 2 in Cells 71 and 72 supports this theory because it can be observed that positive curvature is higher in Cell 71 during the warmest months of the year and lower during the coldest months of the year. This effect likely would be more pronounced if the difference in CTEs of the two layers of the composite concrete pavement was greater.

Conclusions

The strain data obtained from the instrumented composite pavement slabs at MnROAD were used primarily to compare the curvature in the different cells. The analysis of these data consisted of two parts. The first part assessed the variability in the data within a given cell, whereas the second part assessed the differences between cells. It was determined in the first part that the curvatures for the two slabs within Cell 70 varied greatly, whereas Cell 71 and Cell 72 showed agreement between the two slabs at most locations.

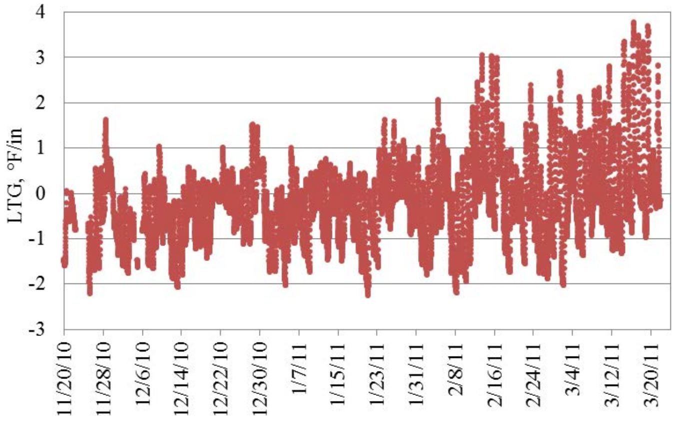

Figure H.108. LTG over the winter at the midslab for Slab 1 in Cell 71.

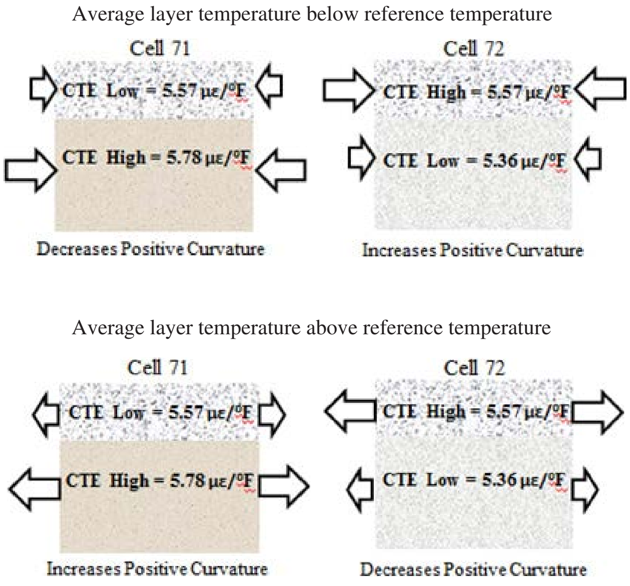
Average layer temperature below reference temperature
Cell 71
CTE Low = 5.57 µε/°F
CTE High = 5.78 µε/°F
Decreases Positive Curvature
Cell 72
CTE High = 5.57 µε/°F
CTE Low = 5.36 µε/°F
Increases Positive Curvature
Average layer temperature above reference temperature
Cell 71
CTE Low = 5.57 µε/°F
CTE High = 5.78 µε/°F
Increases Positive Curvature
Cell 72
CTE High = 5.57 µε/°F
CTE Low = 5.36 µε/°F
Decreases Positive Curvature

Figure H.109. Curvature induced in composite pavements because of uniform changes in the WAT.

For Cell 70, it was found that the placement of the HMA upper layer resulted in a sudden increase in the curvature, which was attributed to the evaporation of moisture from the upper portion of the PCC layer. The HMA surface layer also had long-term effects on the behavior of the PCC layer. For instance, it acted as an insulation layer and reduced the temperature gradients that developed in the underlying PCC layer. Furthermore, the high permeability of the HMA layer resulted in additional rewetting of the PCC layer for Cell 70 in comparison with the other cells during the summer.

It was also hypothesized that the seasonal differences in the relative magnitude of the curvature for Cell 71 relative to Cell 72 were attributable to the variation in the relative CTEs. Differences in the CTEs for the top and bottom layers of the two cells affect the influence of the WAT on curvature for these PCC-over-PCC composite sections.

The analysis performed throughout this body of work has shown that these instrumented pavements can provide great insight into the environmental conditions that develop in these composite structures as well as the response of the pavements to these environmental loads. The information that could be gleaned was limited because these pavements have been in service for only about a year. It is essential that these sections continue to be monitored so the environmental loads that develop throughout the life of these structures can be characterized accurately. This is especially important when characterizing the effects of drying shrinkage, which appears to be the most significant component contributing to the shape of the slab.

APPENDIX I

HMA/PCC Rutting Model

Introduction

Multiple rut depth transfer functions have been developed over time. Most of these transfer functions were reviewed and summarized by Monismith et al. (1994) during the SHRP 2 research work and by Von Quintus et al. (2011) in the conduct of National Cooperative Highway Research Program (NCHRP) Project 9-30. The *Mechanistic–Empirical Pavement Design Guide* (*MEPDG*) software version 1.1, submitted to NCHRP as a product from NCHRP Project 1-37A, included one rut depth transfer function, referred to as the Kaloush-Witczak equation (or the Kaloush equation). This transfer function was based on the use of repeated load uniaxial tests and was calibrated to rut depths measured on more than 100 test sections, most of which were included in the Long-Term Pavement Performance (LTPP) program. This transfer function also was used as the basis for developing the asphalt mixture performance test (AMPT) and for judging the acceptance of hot-mix asphalt (HMA) mixtures under NCHRP Project 9-22. However, the rut depth prediction methodology included in the *MEPDG* has received criticism for multiple reasons. Three of the more common reasons include (1) the use of uniaxial or unconfined repeated load tests, (2) the applicability of the depth function, and (3) the resulting high standard error after the calibration-validation under NCHRP Project 1-40D. None of the pavement structures included in the initial calibration-validation process, however, included new HMA/portland cement concrete (PCC) composite pavement structures.

The objective of NCHRP Project 9-30A was to recommend revisions to the HMA rut depth transfer function in the *MEPDG* software. The recommended revisions were based on the calibration and validation of multiple rut depth transfer functions with measured material properties and performance data from roadways and other full-scale pavement sections that incorporate modified or other specialty mixtures, as well as unmodified asphalt binders. This appendix details the evaluation of the NCHRP 9-30A (Von Quintus et al. 2011) rutting models for HMA/PCC composite pavements.

MEPDG Version 9-30A for Predicting Rut Depths—Enhancements

Multiple rut depth transfer functions are included in *MEPDG* Version 9-30A. Three rut depth transfer functions were used for the calibration process to determine the applicability and accuracy of each for use in composite pavements: (1) the original version of the Kaloush rut depth transfer function, (2) a modified version of the Asphalt Institute vertical elastic strain and deviator stress transfer function, and (3) the WesTrack shear strain and shear stress transfer function.

MEPDG Rut Depth Transfer Function

The plastic strain relationship included in the *MEPDG* to predict rut depth in the HMA layer increments is shown as Equation I.1 and represents the baseline condition for evaluating a mixture's susceptibility to distortion (NCHRP 2008).

$$\varepsilon_p = \varepsilon_r K_Z \beta_{r1} 10^{k_{r1}} (T)^{k_{r2}\beta_{r2}} (N)^{k_{r3}\beta_{r3}} \qquad \text{(I.1)}$$

where

ε_p = incremental plastic strain at the middepth of a thickness increment,

ε_r = resilient strain calculated at the middepth of a thickness increment,

T = temperature at the middepth of a thickness increment, °F,

N = number of axle load applications of a specific axle type and load interval within a specific time period,

β_{r1}, β_{r2}, β_{r3} = local calibration coefficients; all equal to 1.0 for the global calibration effort completed under NCHRP Project 1-40D,

k_{r1} = plastic deformation factor and equal to –3.35412 based on the global calibration effort,

k_{r2} = plastic deformation factor related to the effect of temperature and equal to 1.5606 based on the global calibration effort,

k_{r3} = plastic deformation factor related to the effect of wheel loads and equal to 0.4791 based on the global calibration effort, and

K_Z = depth function and equal to

$$K_Z = (C_1 + C_2 D)(0.328196)^D \tag{I.2}$$

$$C_1 = -0.1039H_{\mathrm{HMA}}^2 + 2.4868H_{\mathrm{HMA}} - 17.342 \tag{I.3}$$

$$C_2 = -0.0172H_{\mathrm{HMA}}^2 - 1.7331H_{\mathrm{HMA}} + 27.428 \tag{I.4}$$

where

D = depth to the middepth of the thickness increment, in., and

H_{HMA} = thickness of the HMA layers, in.

The rationale for the plastic-to-resilient strain ratio transfer functions is to consolidate the effects of stress level. Vertical stress affects the resilient elastic strain, as well as plastic strain. Normalizing the plastic strain to the elastic strain is hypothesized to capture the stress effect without including it in the regression equation or transfer function (Kaloush and Witczak 2000).

The regression coefficients or plastic deformation coefficients (k_{r1}, k_{r2}, k_{r3}) were determined from unconfined, uniaxial repeated load plastic deformation tests conducted in the laboratory and adjusted to field-measured values. The k_{r3} factor is the slope in the steady state or secondary range, whereas the k_{r1} is the intercept of the log-log relationship between the number of load applications and cumulative plastic strain. The k_{r2} factor is the effect of temperature on the intercept.

The *MEPDG* uses an incremental thickness and time approach in calculating total HMA rut depth. The depth function (see Equation I.2) is included to consider the effect of confinement from the upper HMA thickness increments in calculating the incremental rut depths through all of the HMA layers. A time-hardening scheme is included to accumulate plastic deformation over multiple load levels and seasons (NCHRP 2008). There has been some industry criticism of the applicability of the depth function, whereas the time-hardening scheme has been used by others in calculating total HMA rutting with time.

Modified Leahy Rut Depth Transfer Function

A modified form of the Asphalt Institute or original Leahy equation was used in NCHRP Project 1-40B in an attempt to explain the large bias between the predicted and measured rut depths (Von Quintus 2005). This modified form is shown below in Equation I.5; it did not eliminate the bias or reduce the standard error using the selected LTPP experiments Special Pavement Studies (SPS)-1 and SPS-5 test sections.

$$\begin{aligned}\mathrm{Log}\left(\frac{\varepsilon_p}{\varepsilon_r}\right) &= -0.505 + 0.25\mathrm{Log}(N) + 0.110\mathrm{Log}(\sigma_d)\\ &\quad + 0.930\mathrm{Log}(V_{\mathrm{beff}}) + 0.501\mathrm{Log}(V_a)\end{aligned} \tag{I.5}$$

where

V_a = air voids, %,

V_{beff} = effective asphalt content by volume, %, and

σ_d = deviator stress, psi.

Temperature and viscosity terms were included in the original version of the Asphalt Institute transfer function but were removed because dynamic modulus is calculated on an incremental basis with HMA depth and time. It was hypothesized that the influence of temperature and viscosity on the intercept is adequately accounted for through dynamic modulus—smaller computed elastic vertical strains with increasing dynamic modulus values. The average intercept coefficient was determined at the equivalent temperature and calibrated to field-measured values. The effective asphalt content by volume and air void terms were left in the regression equation because of their significance (Von Quintus 2006). The other major difference between the original Asphalt Institute and the Modified Leahy transfer function is that the modified Leahy equation was based on results from repeated load-confined triaxial tests.

WesTrack Rut Depth Transfer Function

The WesTrack plastic shear strain transfer function was developed using data from the WesTrack field experiment (WesTrack Team 2000). The mathematical formulation, shown in Equation I.6, is M-E based for predicting HMA rutting using shear strain and shear stress. This formulation was developed to provide a more realistic simulation through laboratory testing of the horizontal plastic deformations that can occur in the field (Sousa et al. 1994).

$$\gamma_p = a e^{b\tau} \gamma_e N^c \tag{I.6}$$

where

γ_p = permanent shear strain at a depth of 2 in. beneath the tire edge,

τ = corresponding elastic shear stress,

γ_r = corresponding resilient shear strain, and

a, b, c = regression coefficients.

The resilient shear strain measured from the repeated load simple shear tests conducted at constant height was used in the calibration of the plastic deformation coefficients of the HMA mixture. The regression coefficients were determined at multiple temperatures, but temperature was excluded in the final regression equation. For conventional HMA mixtures, the recommended values for the transfer function are $a = 2.114$, $b = 0.04$, and $c = 0.124$. The form of the equation included in *MEPDG* Version 9-30A software uses the intercept measured at the equivalent annual temperature.

The time-hardening principle included in the *MEPDG* is used to estimate the accumulation of plastic shear strains in the HMA under varying site conditions. To implement this transfer function in the *MEPDG* computational framework, the N_{virt} expression in the software was changed as shown in Equation I.7:

$$\ln(N_{\text{virt}}) = (\ln(\gamma_p/\gamma_r) - \ln(a) - b\tau)/c \tag{I.7}$$

The incremental plastic shear strain is computed for a given stress state, load frequency, modulus, and N in accordance with Equation I.7. The rutting that is estimated in the HMA layer due to the plastic deformation is determined from Equation I.8, where K equals a coefficient related to the thickness of the HMA layer, as shown in Table I.1. As a result, the depth function included in the *MEPDG* is "turned off" when using the WesTrack transfer function.

$$PD = K\gamma_p \tag{I.8}$$

HMA Layer Specific Plastic Deformation Model Coefficients

In the *MEPDG* versions released through NCHRP, one set of plastic deformation coefficients is used for all HMA layers. The *MEPDG* computational methodology assumes that the differences in HMA dynamic modulus will correctly account for differences in rutting susceptibility between different mixtures. This assumption has been found to result in a bias and increases the standard error of the predicted rut depths (Von Quintus 2005).

Table I.1. Values of K as a Function of HMA Layer Thickness for the WesTrack Transfer Function

HMA Thickness, in.	*K*-Value
5 to 7	5.5
7 to 9	7.0
9 to 12	8.5
>12	10.0

Under NCHRP Project 9-30A, the *MEPDG* software was revised to permit the user to enter layer-specific plastic deformation coefficients determined from laboratory repeated load tests. Figure I.1 provides a comparison of the total rut depths predicted over time for four conditions using the Wisconsin LTPP SPS-10116 test section: (1) global default plastic

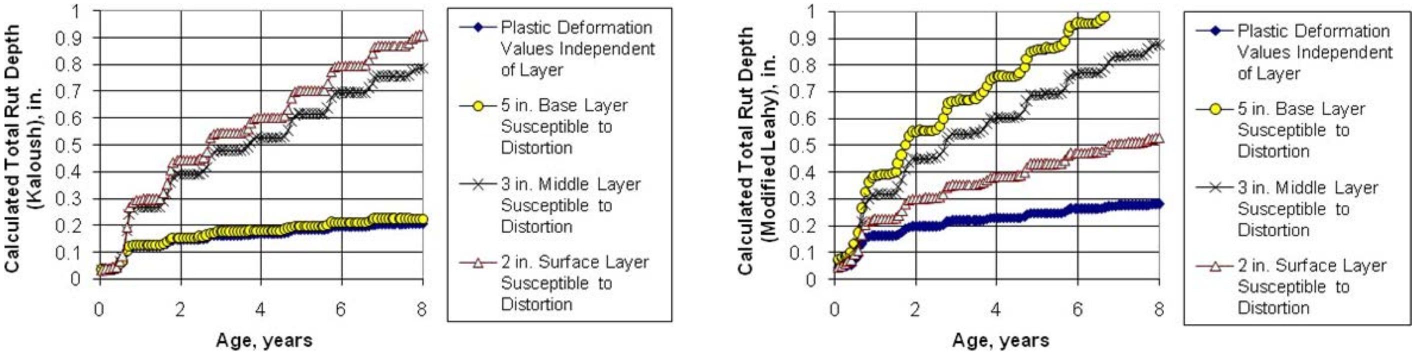

(a) Kaloush Transfer Function.

(b) Modified Leahy Transfer Function.

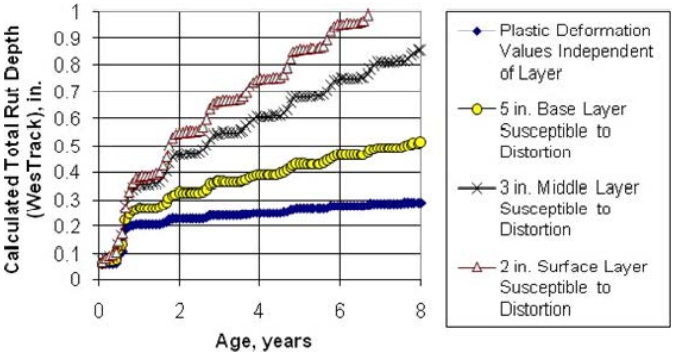

(c) WesTrack Transfer Function.

Source: Von Quintus et al. 2011.

Figure I.1. Predicted rut depths using layer-independent and mixture-dependent plastic deformation coefficients for a deep-strength HMA pavement.

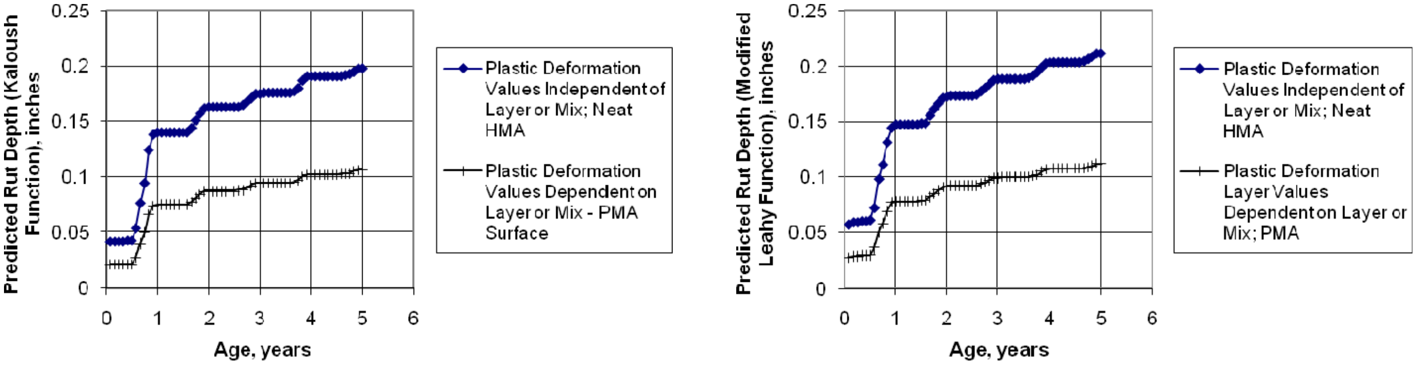

(a) Kaloush Transfer Function.

(b) Modified Leahy Transfer Function.

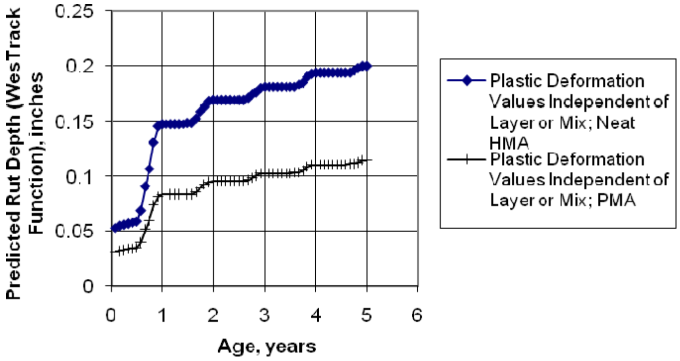

(c) WesTrack Transfer Function.

Figure I.2. Predicted rut depths using layer-independent and mixture-dependent plastic deformation parameters for HMA/PCC composite pavement in South Carolina.

deformation coefficients that are layer independent, (2) the surface layer is susceptible to plastic deformation, (3) the middle layer is susceptible to plastic deformation, and (4) the lower HMA layer is susceptible to plastic deformation.

As shown, the layer- or mixture-dependent plastic deformation coefficients can have a significant impact, which depends on the coefficients of the individual layers and location of the mixture. The deeper the distortion susceptible layer, the rutting decreases for the Kaloush and WesTrack transfer functions. Conversely, the rutting predicted with the Modified Leahy transfer function increases the deeper the distortion susceptible layer. This observation is inconsistent with experience from past forensic investigations and is believed to be related to the depth function in relation to the stress term in the Modified Leahy transfer function.

For composite pavements with one HMA layer, layer specific plastic deformation parameters are not needed. However, some of the composite pavement sections do include two layers or lifts of HMA placed above the PCC slab layer. Figure I.2 shows a similar comparison of the total rut depths predicted over time for two conditions: (1) global default plastic deformation parameters that are mix independent and (2) the lower HMA layer is susceptible to plastic deformation and different from the wearing surface layer. Similar results were found for the composite pavements: dynamic modulus does not accurately account for the plastic deformation potential between layers with different properties.

Lateral Wander Effects

The standard deviation is used to define the practical limits of the width of the lateral distribution of wheel loads. A uniform distribution of wheel or axle loads is used between the limits defined by the standard deviation of wheel loads. A normal distribution is believed to provide a more realistic distribution of wheel loads for computing total rutting. Thus, under NCHRP Project 9-30A, the *MEPDG* was revised to include a normal distribution in the lateral location of the wheel loads for calculating the pavement responses in computing total rut depth.

Predicted Rut Depths—Transfer Function Coefficient Global Values

The three transfer functions and their global coefficients were used to predict the rut depths measured on the Heavy Vehicle Simulator (HVS) test sections and on each of the SHRP 2 R21 composite pavement field survey sections. Figures I.3 through I.5 compare the predicted and measured rut depths. The NCHRP Project 1-40B procedure (Local Calibration Guide) was followed in judging whether any of the

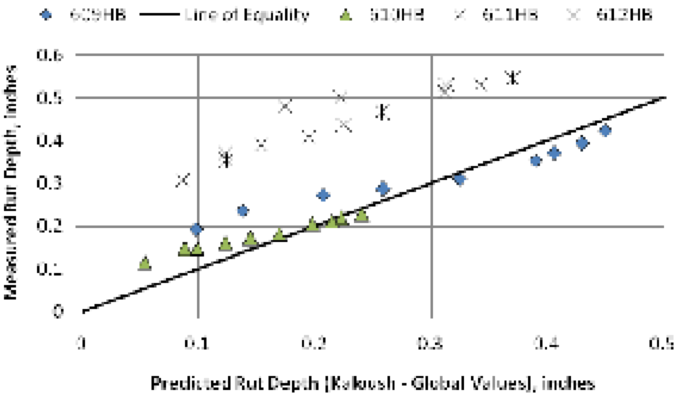

(a) UCPRC Test Sections.

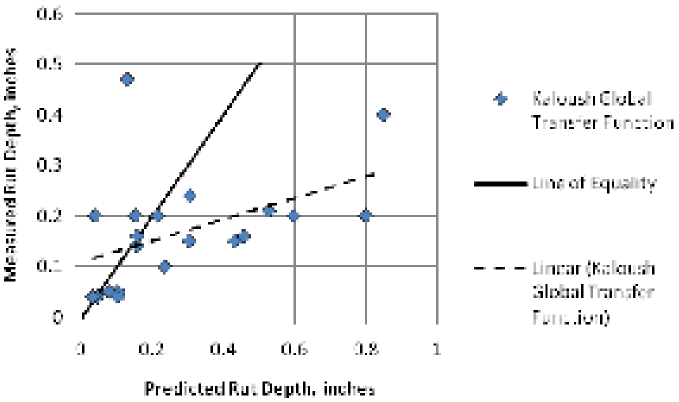

(b) Field Survey Sections.

Figure I.3. Comparison of predicted and measured rut depths using the Kaloush transfer function global coefficients.

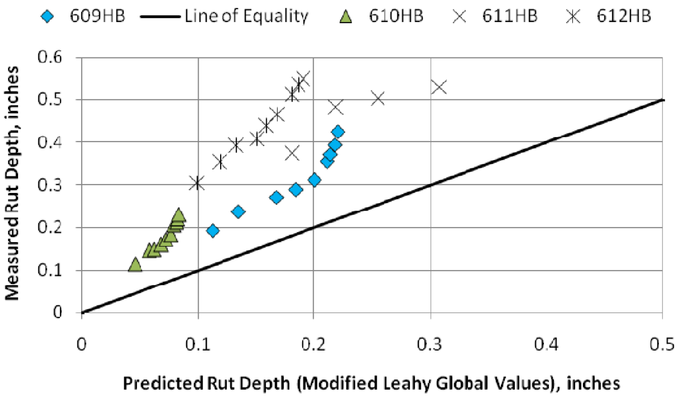

(a) UCPRC Test Sections.

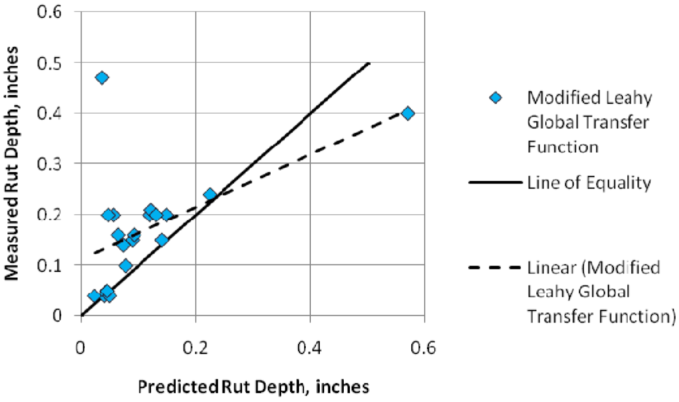

(b) Field Survey Sections.

Figure I.4. Comparison of predicted and measured rut depths using the Modified Leahy transfer function global coefficients: (a) UCPRC test sections and (b) field survey sections.

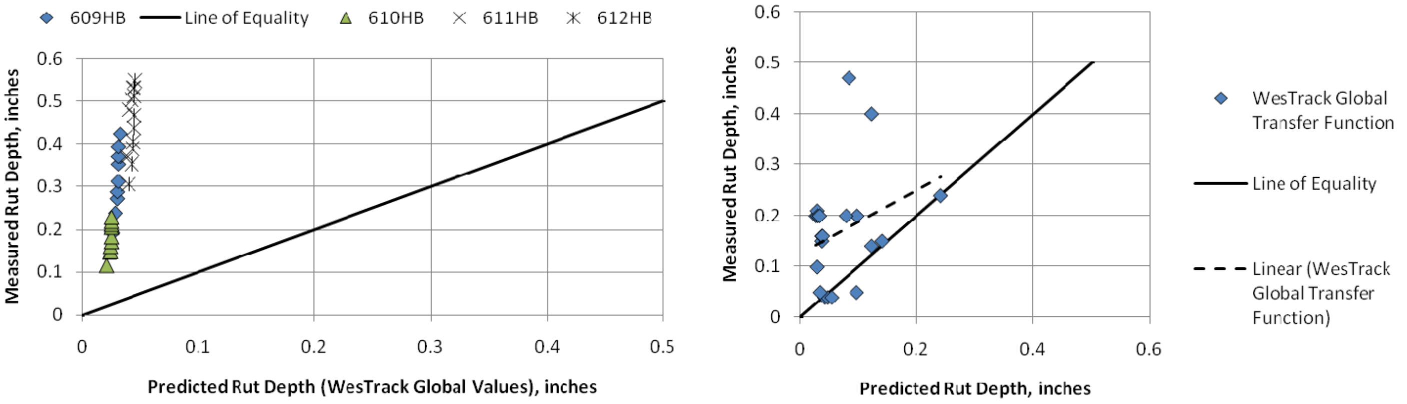

(a) UCPRC Test Sections.

(b) Field Survey Sections.

Figure I.5. Comparison of predicted and measured rut depths using the WesTrack transfer function global coefficients: (a) UCPRC test sections and (b) field survey sections.

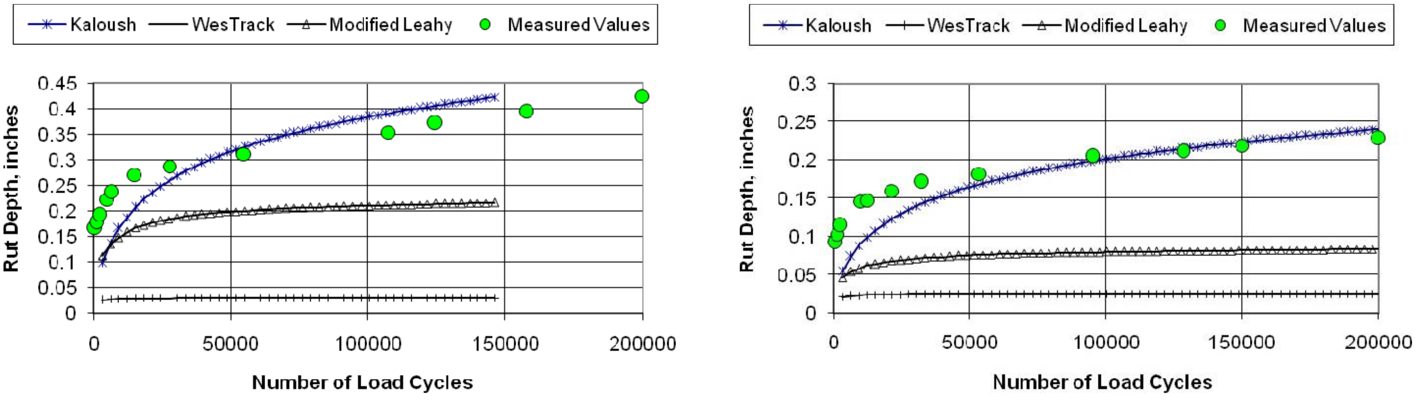

(a) Section 609HB; HMA Thickness = 4.5 inches.

(b) Section 610HB; HMA Thickness = 2.5 inches.

Figure I.6. Comparison of predicted rut depth and measured rut depth for the PG 64-28PM mixture using the global rut depth transfer functions.

transfer functions and their global coefficients is a reasonable simulation of the measured rut depths. Two parameters are used in determining whether the transfer function is adequate or needs to be recalibrated to the specific features under evaluation (in this case, composite pavement structures): the slope and intercept between the predicted and measured values. The following text summarizes the comparisons.

- The Kaloush transfer function using the global coefficients provided a reasonable estimate of the rut depths of the HVS test sections for the PG64-28PM mixture, but it underpredicted the rut depths in the RHMA-G mixture (Figure I.3a). However, the Kaloush transfer function using the global coefficients generally overpredicted the rut depths measured along the field survey sections (Figure I.3b).
- The Modified Leahy transfer function using the global coefficients significantly underpredicted the rut depths measured along all HVS test sections and field survey sections (Figure I.4).
- The WesTrack transfer function using the global coefficients significantly underpredicted the rut depths measured along all HVS test sections and field survey sections (Figure I.5).

Rut depth time or loading series data are available for the HVS test sections, but only a few field survey sections include rut depths measured over time. Most of these include the rut depths measured at one point in time. Figure I.6 and Figure I.7 compare the measured rut depths at varying loading cycles with the rut depths predicted with each transfer function using the global values for the transfer functions. As shown, the magnitudes of the predicted rut depths and relative change of predicted rut depths with number of load cycles deviate from the measured values.

In summary, the slope and intercept of the trend line between the predicted and measured rut depths deviate significantly from 1.0 (equality), and the trend line does not go through the origin for any of the transfer functions, except for the Kaloush transfer function, in predicting the rut depths measured on the HVS PG 64-28PM test sections. None of the rut depth transfer

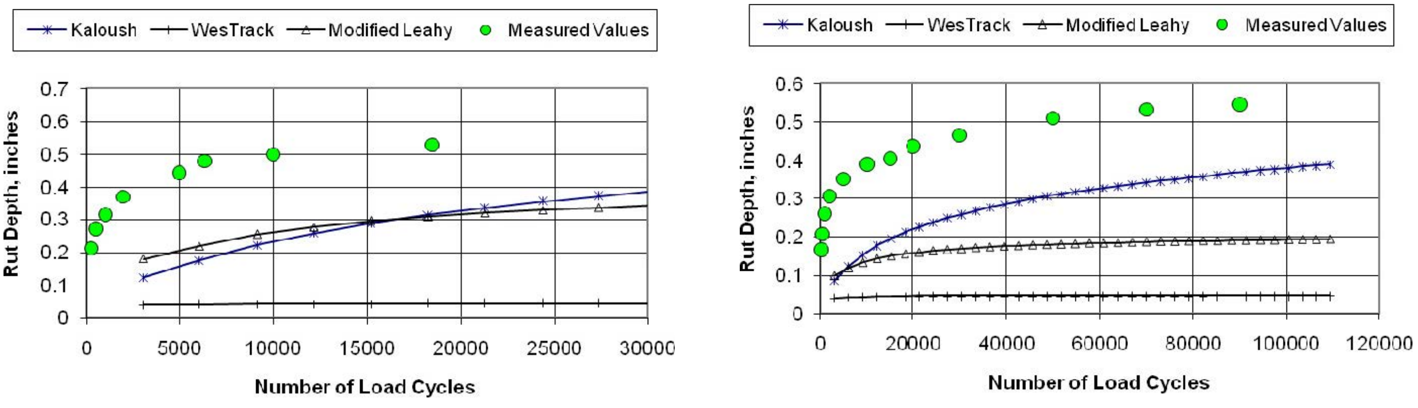

(a) Section 611HB; HMA Thickness = 4.5 inches.

(b) Section 612HB; HMA Thickness = 2.5 inches.

Figure I.7. Comparison of predicted rut depth and measured rut depth for the RHMA mixture using the global rut depth transfer functions.

functions using their global coefficients are believed to provide an accurate simulation of the measured rut depths exhibited on the HVS test sections and field survey sections. As such, all rut depth transfer functions need to be redefined for composite pavement structures.

Laboratory-Derived Plastic Deformation Coefficients

All transfer functions embedded in *MEPDG* Version 9-30A represent the steady state or secondary region from repeated load plastic deformation tests. The laboratory test results from the secondary region of the repeated load confined, triaxial, and constant-height shear tests can be represented by Equation I.9.

$$\varepsilon_p\,(\text{Lab}) \text{ or } \gamma_p\,(\text{Lab}) = I_s\,(N)^m \qquad \text{(I.9)}$$

where

ε_p(Lab) = plastic axial strain accumulated in repeated load triaxial tests, in./in.,
γ_p(Lab) = plastic shear strain accumulated in repeated load shear tests, in./in.,
m = average slope in secondary region of repeated load tests,
I_s = intercept from secondary region of repeated load tests, in./in.

$$I_s = d(T)^n \qquad \text{(I.10)}$$

where

T = test temperature, °F, and
d,n = regression constants from secondary region of repeated load tests.

Repeated load, constant-height shear tests were performed on each of the mixtures placed at UCPRC. The plastic strain parameters for the WesTrack transfer function were estimated from these repeated load shear tests. Repeated load triaxial tests were not performed on any of the mixtures, so the Kaloush transfer function and the Modified Leahy transfer function coefficients for the 64-28PM and RHMA mixtures were estimated based on the comparison of shear and triaxial test results included in the NCHRP 9-30A report. More important, repeated load plastic deformation tests were unavailable for all mixtures of the field survey sections. As a result, the plastic strain parameters for the different mixtures were estimated using HMA layer or lift properties for the three transfer functions based on results from NCHRP Projects 9-30A and 1-40B.

Figure I.8 and Figure I.9 summarize the repeated load shear tests for the PG 64-28PM and RHMA mixtures. The laboratory-derived plastic deformation coefficients for the WesTrack transfer function were determined in accordance with the procedure established under NCHRP Project 9-30A (Von Quintus et al. 2011). Figure I.10 and Figure I.11 provide a summary of the average slope from the repeated-load, constant-height shear strain tests for both mixtures, whereas Table I.2 lists the *a* and *c* values from these tests.

For a high-quality HMA mixture resistant to plastic deformation that was tested under NCHRP 9-30A, the laboratory-derived slope or exponent to the *N*-term varied from 0.25 to 0.35, whereas the laboratory-derived intercept varied from 0.001 to 0.0025 (Figure I.12 and Figure I.13). The *c* value from the repeated-load, constant-height shear tests from this study for the PG 64-28PM and RHMA mixtures (Table I.2) was found to be low in comparison with typical values measured and reported under NCHRP Project 9-30A, whereas the *a* value was found to be high. The reason for the significant difference between the repeated load shear test results from this study and those completed under NCHRP 9-30A is unknown.

The field-derived slopes and intercepts for the UCPRC rut depth data sets were determined for the three transfer functions to minimize the difference between the predicted and measured

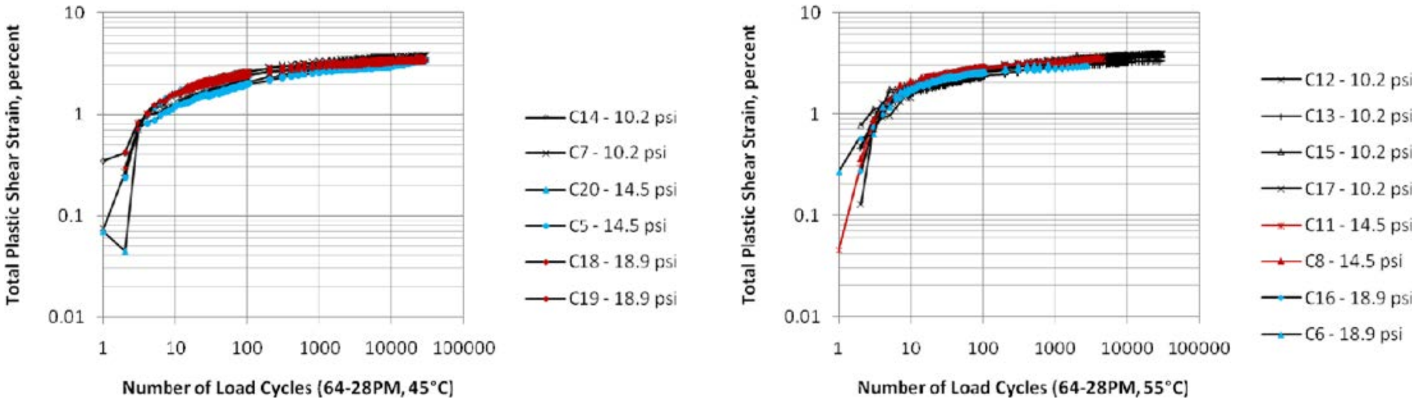

(a) Test Temperature – 45°C.

(b) Test Temperature – 55°C.

Figure I.8. Repeated load plastic shear strain for the PG 64-28PM mixture.

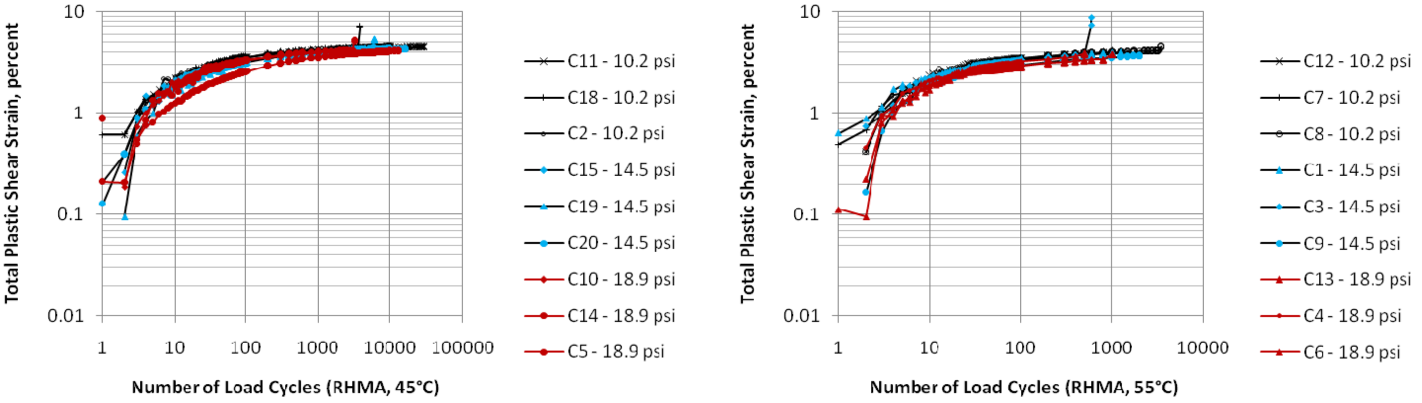

(a) Test Temperature – 45°C.

(b) Test Temperature – 55°C.

Figure I.9. Repeated load plastic shear strain for the RHMA mix.

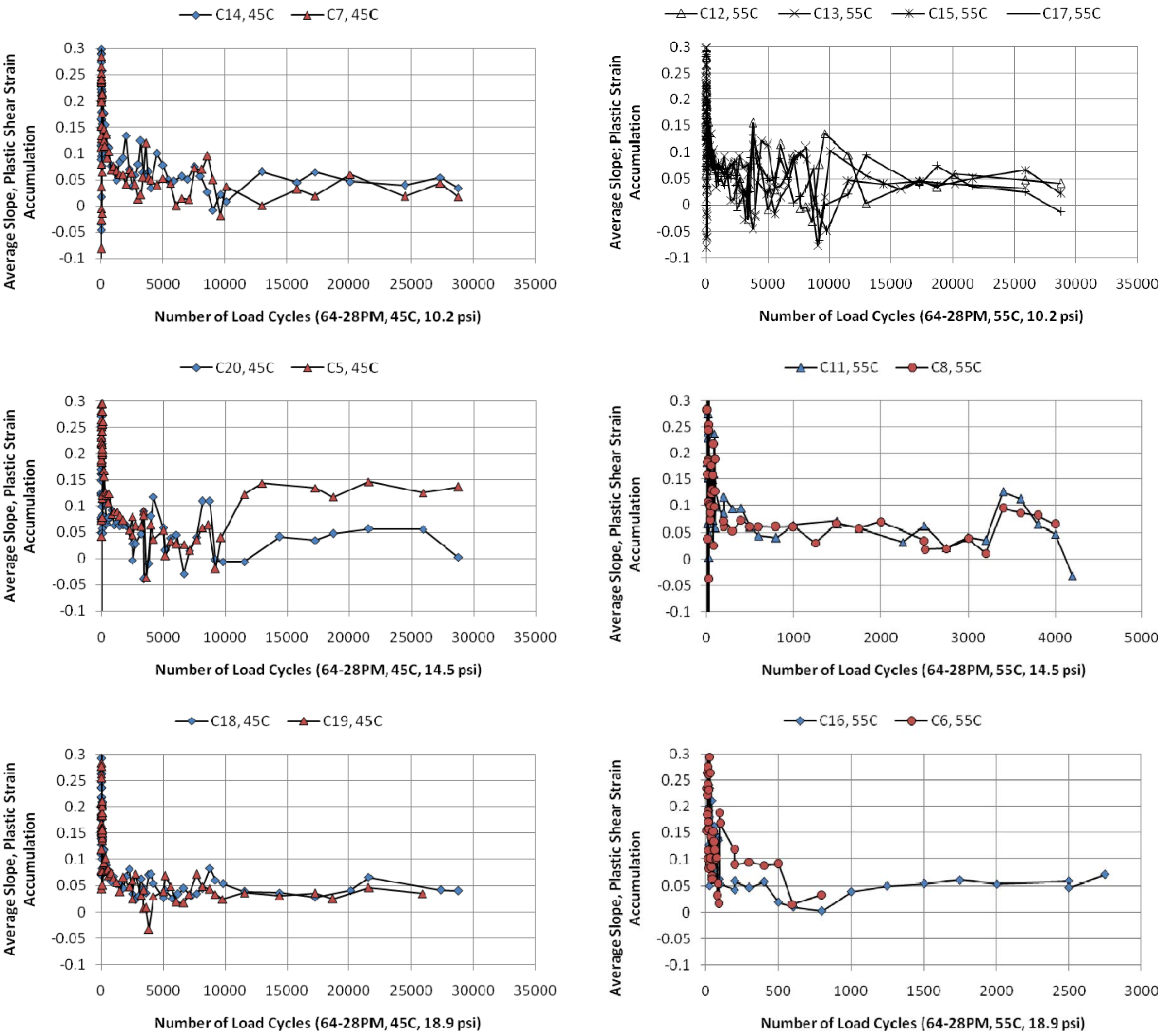

Figure I.10. Average slope from the repeated-load, constant-height shear strain test for the PG 64-28PM mixture.

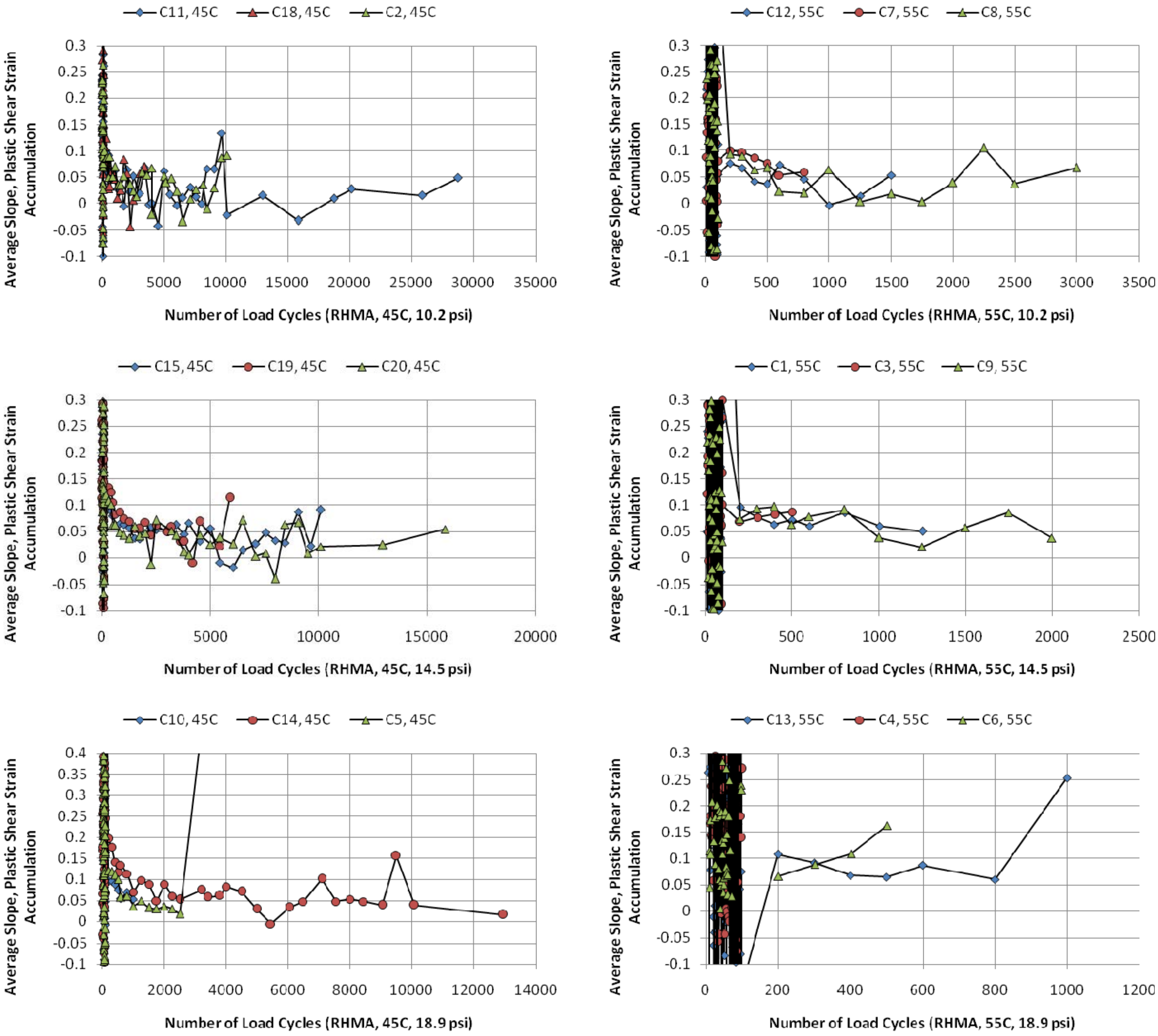

Figure I.11. Average slope from the repeated-load, constant-height shear strain test for the RHMA mixture.

Table I.2. Summary of Plastic Shear Strain Coefficients for the WesTrack Transfer Function

Mixture	Temperature, °C	Transfer Function Coefficients[a]		
		a	*b*	*c*
PG 64-28PM	45	0.0155	0.01	0.0625
PG 64-28PM	55	0.0188	0.01	0.0606
RHMA	45	0.0245	0.01	0.0610
RHMA	55	0.0255	0.01	0.0982

[a] See Equation I.6.

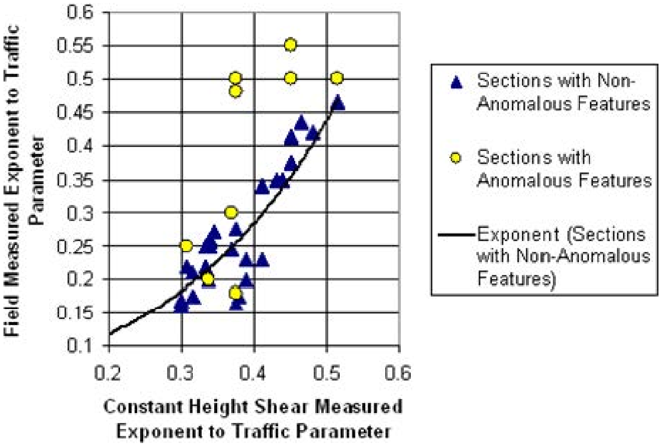

Source: Von Quintus et al. 2011.

Figure I.12. Field-matched slopes to the laboratory-measured values using repeated-load, constant-height shear tests.

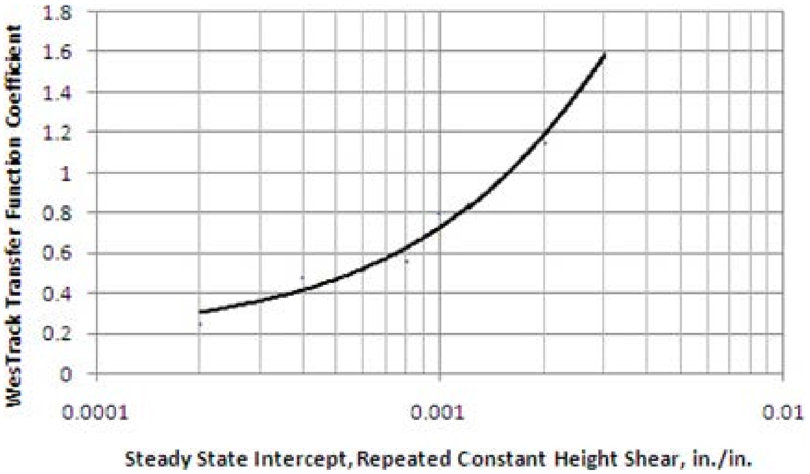

Source: Von Quintus et al. 2011.

Figure I.13. Field-matched intercept of coefficient of the WesTrack transfer function using repeated-load, constant-height shear tests.

rut depths for the thicker HMA layer (4.5 in.). Table I.3 summarizes the field-derived values for the two mixtures and thicker test sections (4.5 in.). The field-matched slopes for the mixtures placed at UCPRC (0.25 for the RHMA and 0.35 for the PG 64-28PM mixtures) are within the same range of values reported in NCHRP 9-30A (Figure I.12). Conversely, the field-matched intercepts for the two mixtures are higher than those reported in NCHRP 9-30A (Figure I.13).

Composite Pavement Calibration Parameters

The results from previous calibration studies were used in determining the coefficients for each of the three rut depth transfer functions, including NCHRP Projects 9-30, 1-40B, and 9-30A. The parameters that have been reported to reduce model bias and the standard error of the rut depth transfer functions include HMA thickness, stress term coefficient, and volumetric properties of the HMA layers (air voids, asphalt content, and gradation). However, it should be understood that the in-place volumetric properties were adequately measured for the mixtures placed at the UCPRC HVS test sections, but the same properties were extracted from construction records for the field survey sections. The reliability of data extracted from construction records is undefined; as a minimum, these data include more error than do the data for the UCPRC HVS test sections.

HMA Stress Effect in Predicting Rut Depths

Two of the three rut depth transfer functions include a stress term: the Modified Leahy (Equation I.5) and WesTrack (Equation I.6) functions. Results from NCHRP Project 9-30A recommended use of the transfer functions that include a stress term, even though the standard error for all three was found to be comparable. In other words, the standard errors between the three transfer functions were found to be indifferent. The

Table I.3. Summary of Field-Derived Plastic Strain Coefficients from the 4.5-in. HMA Layer Test Sections for the Three Transfer Functions

Mixture	Transfer Function	Transfer Function Coefficients		
		Intercept, k_{r1}	Stress or Temperature Term Exponent, k_{r2}	Slope; *N*-Term Exponent, k_{r3}
PG 64-28PM	Kaloush	–2.761	1.5606	0.35
PG 64-28PM	Modified Leahy	–2.163	1.0	0.35
PG 64-28PM	WesTrack	3.619	0.01	0.35
RHMA	Kaloush	–2.20	1.5606	0.25
RHMA	Modified Leahy	–1.735	1.0	0.25
RHMA	WesTrack	13.30	0.01	0.25

primary reason for that recommendation was the Kaloush transfer function required the use of a thickness correction factor, in addition to the depth function, going from thin to thick HMA layers, whereas the stress term was able to account for this thickness effect on rutting for the WesTrack and Modified Leahy transfer functions for flexible pavements and HMA overlays.

Figure I.14a shows the effect of shear stress on rut depth over a range of HMA layer thickness using the WesTrack transfer function for flexible pavements and HMA overlays. Figure I.14b, on the other hand, shows the effect of deviator stress on rut depth for the Modified Leahy function. A combination of values for the intercept and stress term can be used for which the rut depth becomes less dependent on HMA thickness.

At about 6 to 8 in., the coefficients for both deviator stress and shear stress have little effect on rut depth with increasing HMA thickness for flexible pavements. There is an effect, but the effect is small. In other words, there is a combination of deviator and shear stress terms for which the predicted rut depths from the WesTrack and Modified Leahy transfer functions begin to converge, rather than diverge, for the thinner HMA pavements. This observation is consistent with the results from many forensic investigations in measuring plastic deformation with depth in HMA layers.

Pavements with thick HMA layers were used to determine the transfer function coefficients. Those model coefficients were then used to predict the rut depths of thin HMA layers of the same mixture. The value of the stress term was varied to determine its effect on model bias, if any. For conventional flexible and deep-strength flexible pavements, specific values for the stress terms were found to minimize model bias. The appropriate values recommended for use from NCHRP 9-30A are $b = 0.01$ for the WesTrack transfer function and $C_3 = 1.0$ for the Modified Leahy function. These values were determined from NCHRP Project 9-30A and were simply accepted for predicting the HMA rut depths in composite pavements.

The question to be answered for composite pavements is: Are the default values for the coefficients of the stress terms

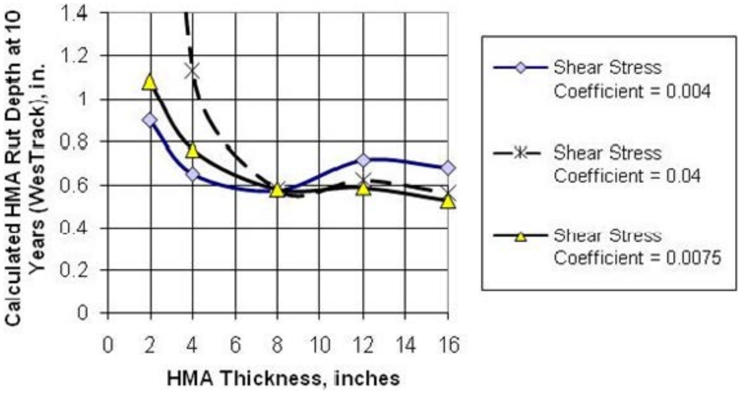

a. Effect of HMA layer thickness and shear stress coefficient value on calculated rutting.

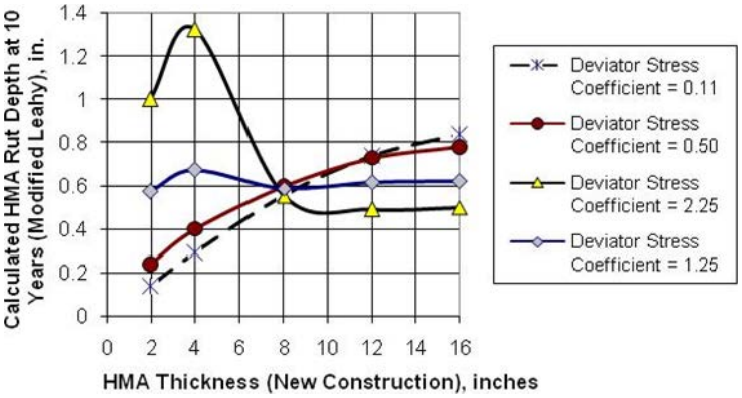

b. Effect of HMA layer thickness and deviator stress coefficient value on calculated rutting.

Note: In (a), the reason the rut depth decreases, increases, and decreases with HMA thickness is a result of the stepped depth correction parameter and the sublayering completed by the *MEPDG* software. In (b), as the deviator stress term increases, the rut depth becomes less dependent on HMA thickness. At about a value of 1.0, the effect of thickness is similar to the WesTrack transfer function for shear stress.

Figure I.14. Effect of stress on rut depth: WesTrack and Modified Leahy transfer functions.

reasonable for the range in thickness where stress is important or has a significant effect on the calculated rut depth? The UCPRC test sections were used to confirm the reasonableness of the stress term coefficient values for composite pavements because two different HMA thicknesses were included in the experiment for the same mixtures (2.5 and 4.5 in.). The field survey sections were not used because none of the projects included varying HMA layer thickness with the same mixture.

The effect of the stress term was investigated to determine the value at which a layer thickness adjustment factor is not needed for the transfer functions that include a stress term (WesTrack and Modified Leahy functions). Using the same mixture properties (PG 64-28PM and RHMA) for the thicker HMA layers (Table I.3), the intercepts of the transfer functions were estimated for different stress term values, and those values were used to predict the rut depth of the thinner HMA layers.

However, for composite pavements, the bias does not approach zero. This implies the stress term value has little impact on the model bias for composite pavements. As such, the values recommended for use from NCHRP 9-30A were used to predict the measured rut depths for both stress-based transfer functions.

HMA Layer Thickness Effect in Predicting Rut Depths

MEPDG Version 9-30A was used to predict the maximum rutting for different pavement structures with varying HMA layer thicknesses. A summary of these results is provided in Figure I.15a, and shows the effect of increasing HMA thickness on rut depth with the different transfer functions. The rut depth predicted with the deviator stress based transfer functions (Modified Leahy) continues to increase with increasing HMA thickness. Conversely, the rut depth decreases with increasing HMA thickness for the pure vertical strain based function (Kaloush). Many local calibration studies completed by individual state agencies have included an HMA thickness adjustment factor for the Kaloush transfer

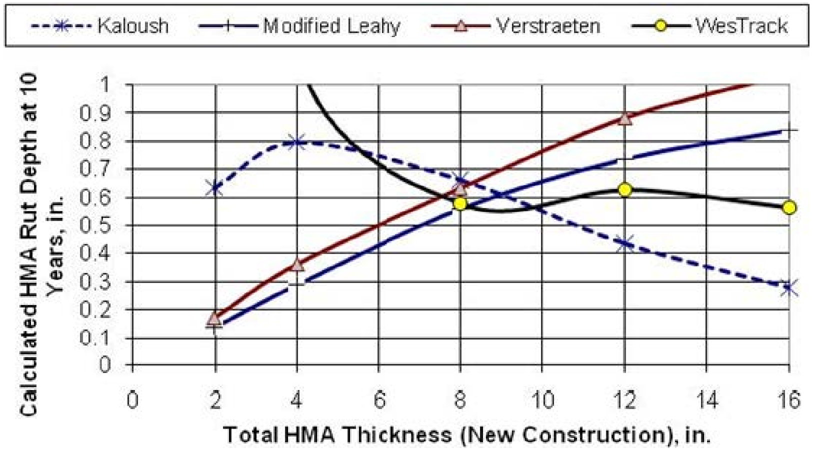

(a) New conventional flexible pavement construction.

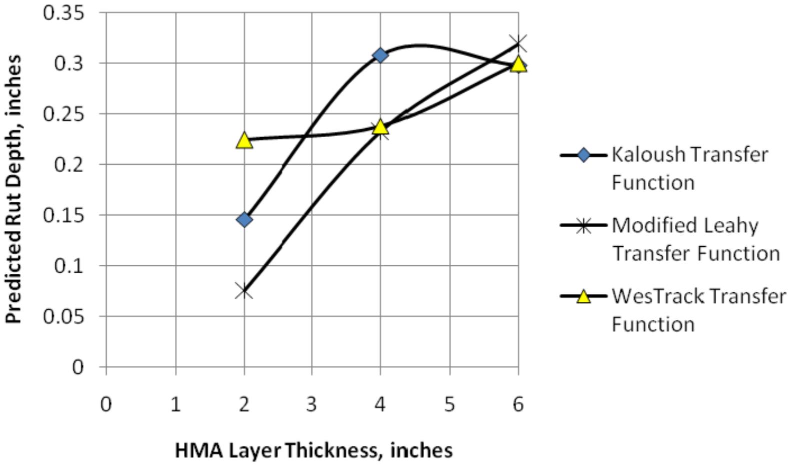

(b) New composite pavement construction.

Figure I.15. HMA layer thickness effect on calculated HMA rut depth for (a) new conventional flexible pavement construction and (b) new composite pavement construction.

function. The shear strain and shear stress based transfer function (WesTrack) is different: the rut depth is relatively constant with increasing HMA thickness, with the exception of thin (less than 5 in.) HMA layers.

For composite pavement structures, the depth function for the Kaloush transfer function becomes less important because the thickness of the HMA layers generally is less than 4 in. Conversely, the depth correction factors become more important for the WesTrack function. *MEPDG* Version 9-30A was used to calculate the rut depth for varying HMA thicknesses of a typical composite pavement structure. Results from these runs are shown in Figure I.15b. As shown, the maximum rut depth calculated with the Kaloush and Modified Leahy transfer functions for increasing HMA layer thickness is similar to that for flexible pavements; rut depth increases with increasing HMA layer thickness for the Modified Leahy function, and rut depth increases with HMA thickness at about 4 in., at which rutting starts to decrease with the Kaloush function. Conversely, the maximum rut depth slightly increases with increasing HMA layer thickness for the WesTrack transfer function. These results are consistent with the measured data from the UCPRC test sections; the test sections with the thicker HMA layers exhibited the higher magnitudes of rutting for both mixtures (Figures I.6 and I.7). This observation suggests the WesTrack shear strain and stress-based transfer function is more consistent with simulating the field-measured values.

HMA Volumetric Properties: Air Voids and Asphalt Content

Under NCHRP Projects 9-30, 1-40B, and 9-30A, the volumetric properties of the in-place mixtures were found to have a significant impact on reducing the standard error and bias of the transfer functions. Previous results have found that increasing air voids and increasing asphalt contents results in higher measured rut depths. The Modified Leahy transfer function includes air voids and asphalt content in the transfer function, which have been found to be reasonable in accounting for the effect of the volumetric properties on the plastic deformation coefficients.

For the field survey sections, there is correspondence between HMA lift thickness and air voids (Figure I.16). This correspondence between two of the parameters that have been used to develop local calibration factors for HMA pavements increases the difficulty in determining specific values with limited data.

Temperature

It should be noted that the k_2 parameter or exponent for the temperature term of the Kaloush transfer function was set at 1.5606 and was not varied between the different mixtures. The reason for setting this value as a constant is based on the findings from NCHRP 9-30A, for which the impact of temperature was found to be similar between significantly different mixtures and pavement structures. Figure I.17 illustrates that finding; the effect on temperature on the plastic deformation appears to be the same for repeated load shear testing of laboratory-prepared and field cores, as well as for laboratory-prepared, repeated-load triaxial tests. The *d* and *n* parameters represent those included in Equation I.10. Thus, the k_2 parameter recommended for use from NCHRP 9-30A was simply assumed and set for all mixtures, including the UCPRC test sections and field-surveyed sections.

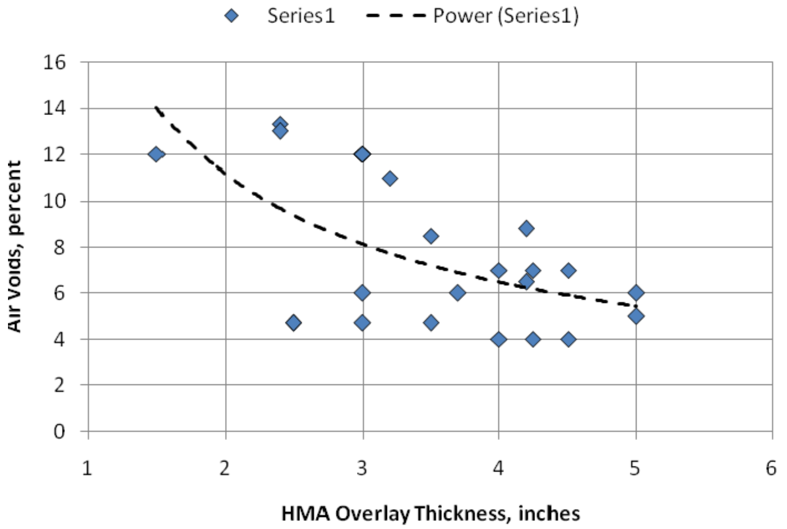

Figure I.16. Relationship between HMA lift thickness and air voids for the field survey sections.

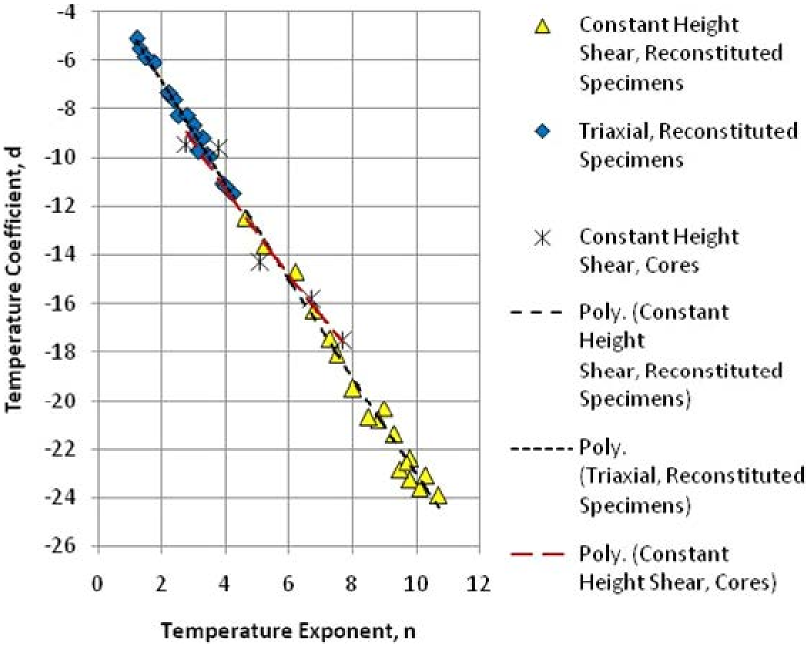

Source: Von Quintus et al. 2011

Figure I.17. Relationship of temperature exponent (*n*-value) and coefficient (*d*-value) for both repeated load tests.

Determinations of Plastic Deformation Coefficients

Figures I.18 through Figure I.21 are examples comparing the predicted and measured rut depths for each transfer function for selected UCPRC, test tracks, and LTPP test sections. As shown, all of the transfer functions can provide an accurate simulation of the measured rut depths (ranging from very low to high) over a diverse range of mixtures, conditions, and pavement structures. The other important observation from these field-derived values is that the *N*-term exponent was found to be the same among all of the transfer functions.

UCPRC Test Sections

The three transfer functions were used to predict the rut depths measured on the test sections built at UCPRC and measured on each of the field-surveyed sections. The difference between the roadway and UCPRC test sections is that repeated-load constant-height shear tests were performed on each of the HMA mixtures placed at UCPRC.

UCPRC test-section–derived plastic deformation coefficients were determined for the thicker composite test sections that minimize the difference between the predicted and measured rut depths. This analysis was completed to determine the

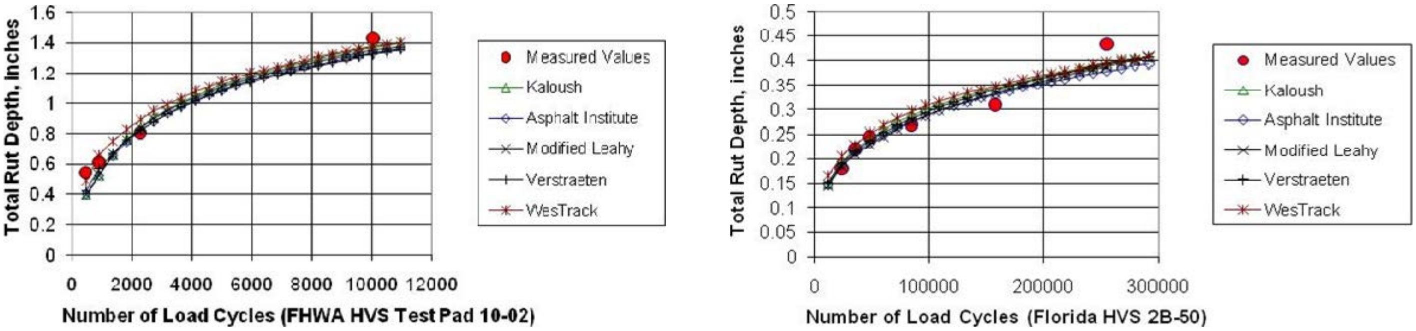

(a) Predicted Rut Depths for the FHWA HVS Test Pad 10-02, Rutting Experiment.

(b) Predicted Rut Depths for Florida HVS Pad 2B-50; Modifier Experiment.

Source: Von Quintus et al. 2011.

Figure I.18. Field-matched plastic deformation coefficients using different transfer functions for FHWA and Florida HVS sections, simulated truck loadings.

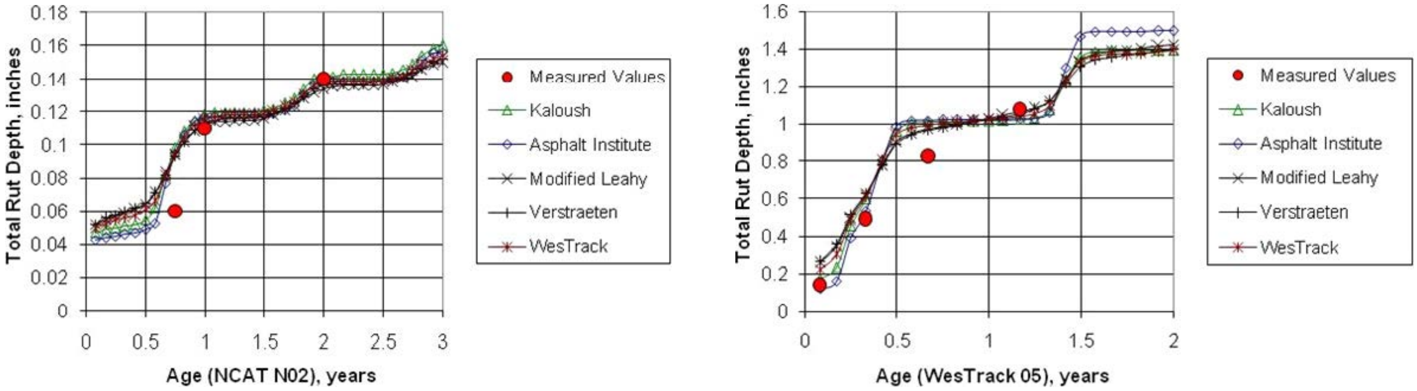

(a) Predicted Rut Depths for NCAT Test Section N02.

(b) Predicted Rut Depths for WesTrack Test Section 05.

Source: Von Quintus et al. 2011.

Figure I.19. Field-matched plastic deformation coefficients using different transfer functions for selected National Center for Asphalt Technology (NCAT) and WesTrack test sections.

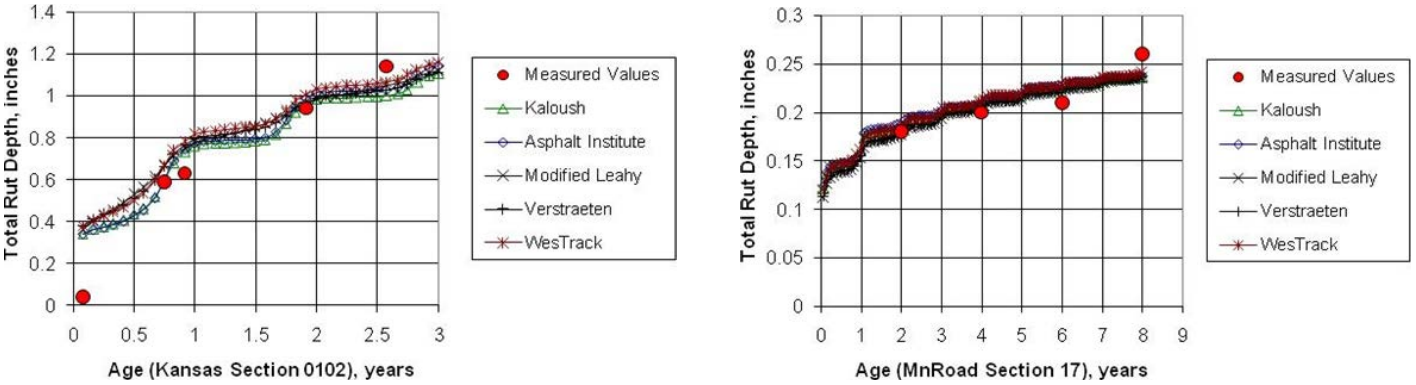

(a) Predicted Rut Depths for the Kansas SPS-0102, New Construction, Thin HMA.

(b) Predicted Rut Depths for MnRoad Section 17, New Construction, Thick HMA.

Source: Von Quintus et al. 2011.

Figure I.20. Field-matched plastic deformation coefficients using different transfer functions for selected new construction test sections.

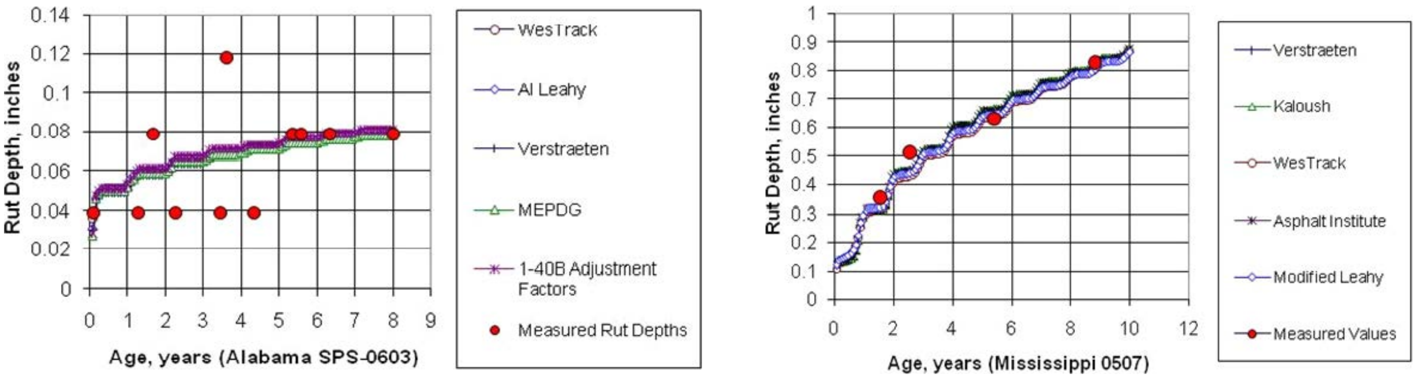

(a) Predicted Rut Depths for the Alabama SPS-0603, Overlay of PCC Pavement.

(b) Predicted Rut Depths for Mississippi SPS-0507, Overlay of HMA Pavements.

Source: Von Quintus et al. 2011.

Figure I.21. Field-matched plastic deformation coefficients using different transfer functions for selected test sections in the LTPP SPS-5 and SPS-6 experiments, rehabilitated pavements.

intercept coefficient for each transfer function that provides an accurate estimate of the rut depths measured over time. These coefficients were also used to determine the transfer functions that would or would not accurately predict the rutting evolution over a diverse range of mixtures.

Figure I.22 compares the predicted and measured rut depths for each transfer function for the UCPRC test sections. As shown, all of the transfer functions can provide an accurate simulation of the measured rut depths (ranging from very low to high). However, the results also suggest that thickness correction factors are needed for all transfer functions, even for the relatively thin HMA layers over PCC layers.

Thickness adjustment factors were estimated from these results to eliminate model bias caused by layer thickness. Table I.4 summarizes the HMA thickness adjustment factors for each transfer function. Figure I.23 provides a comparison between the predicted and measured rut depths after applying the thickness adjustment factor. In summary, all three transfer functions can provide an accurate simulation of the measured rut depths. Results from the UCPRC test sections were used to estimate the thickness correction factors for the field survey sections, which are discussed in the next section.

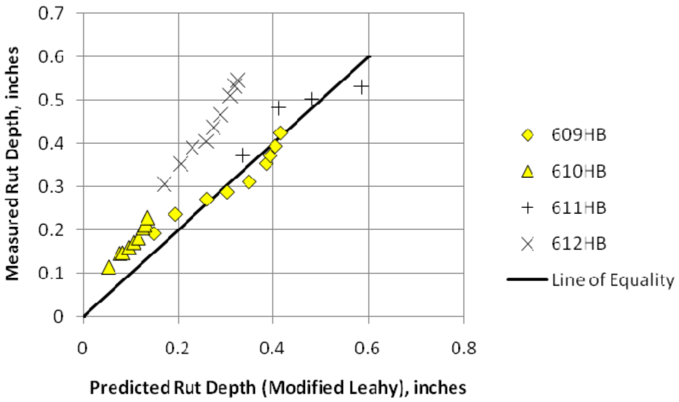

(a) Modified Leahy Transfer Function.

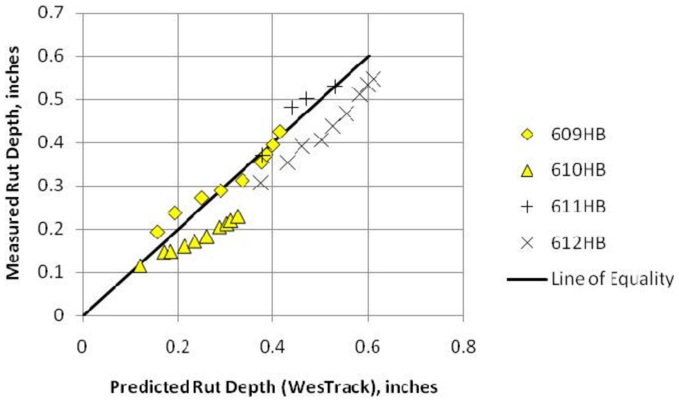

(b) WesTrack Transfer Function.

Figure I.22. Measured and predicted rut depths using the Modified Leahy and WesTrack transfer function for the UCPRC test sections.

Table I.4. Thickness Correction or Adjustment Factors for Composite Pavements

	HMA Layer Thickness	
Transfer Function	**2.5 in.**	**4.5 in.**
Kaloush	1.08	1.0
Modified Leahy	1.35	1.0
WesTrack	0.80	1.0

Composite Pavement Roadway Sections

The exponent for the number of load cycles for the three transfer functions was assumed for all field survey sections because time series data were unavailable for most of these test sections. The rut depths measured on the field survey sections are low and suggest well-designed mixtures that are resistant to deformation. Most of the measured rut depths are less than 0.30 in., with an average value from all field survey sections of approximately 0.17 in. Some of these sections have heavy truck traffic. The slope value assumed for all projects was simply the average value determined for the test sections included in the NCHRP Project 9-30A study representing good quality mixtures, a value of 0.235 (Figure I.12). Plastic deformation coefficients were determined for the composite test sections in the same way as for NCHRP 9-30A.

Table I.5 summarizes the transfer function intercepts or coefficients, which were found to be dependent on HMA layer thickness and air voids. Asphalt content was found to have little to no impact on reducing the model bias and standard error. However, asphalt content is an important parameter based on the results from NCHRP Projects 1-40B and 9-30A. It is believed that the values extracted from the project files include errors in determining the effective asphalt content by volume, which may account for the inconsistent results from other studies. There are other important observations from these results for composite pavements; they are listed below.

- The magnitudes of the intercept for the three transfer functions are higher than reported for conventional and deep strength flexible pavement. Some of this difference probably is related to the stress term values and lower HMA thicknesses in comparison with other test sections used in the calibration process for flexible pavements.
- The effect of HMA thickness is inconsistent for all transfer functions: the coefficients do not consistently increase or decrease with increasing layer thickness. The higher intercept values occur in the range of 3 to 4 in.; thinner and thicker layers result in a decrease in the values for the intercept.

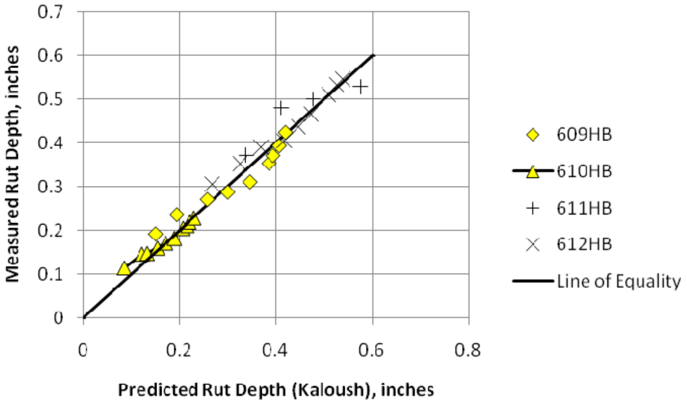

(a) Kaloush Transfer Function.

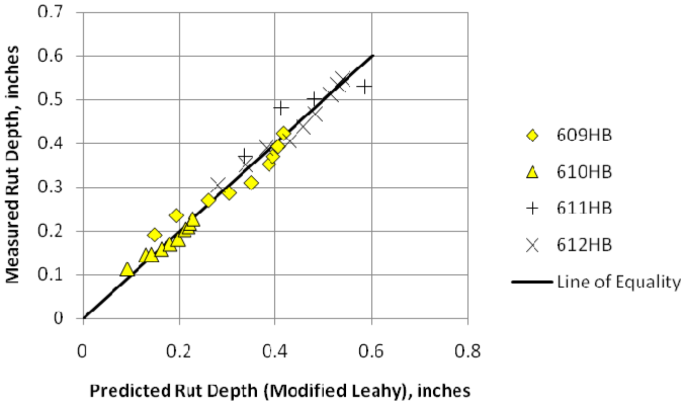

(b) Modified Leahy Transfer Function.

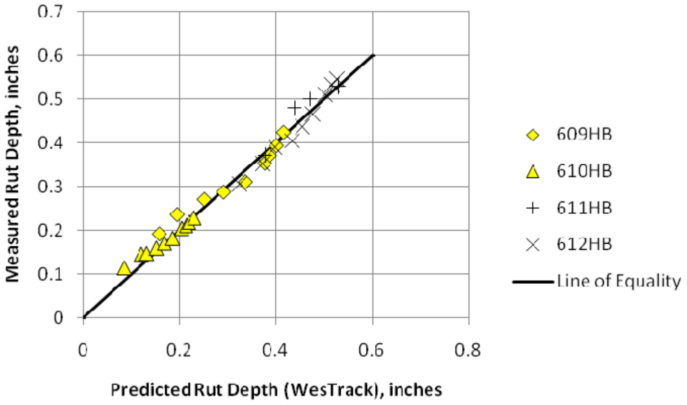

(c) WesTrack Transfer Function.

Figure I.23. Measured and predicted rut depths for the UCPRC test sections.

- Air voids in the typical range of construction specification have little impact on the measured and predicted rut depths. Air voids have an impact on the intercept when they exceed typical construction specifications. Higher air voids result in greater amounts of rutting.

Table I.5. Transfer Function Coefficients Used to Predict the Rut Depths for the Field Survey Sections

Transfer Function	HMA Layer Thickness, in.	HMA Air Voids, %		
		<6.0	6.1–9.0	>9.0
Kaloush; Equation I.1, k_{r1}	< 3	–2.30	–2.30	–2.05
	3–4	–2.15	–2.15	–2.05
	>4	–2.30	–2.30	–1.95
Modified Leahy; Equation I.5, C_1	<3	–1.90	–1.90	–1.4
	3–4	–1.80	–1.80	–1.5
	>4	–2.00	–2.00	–1.3
WesTrack; Equation I.6, *a*	<3	10.5	10.5	10.5
	3–4	14.0	16.0	20.0
	>4	10.5	10.5	16.0

The following lists the transfer functions and their plastic deformation coefficients used to predict the rut depths for all of the field survey sections (Equations I.11, I.12, I.13). It should be understood that the *N*-term exponent of 0.235 for all transfer functions represents well-designed mixtures resistant to plastic deformation.

$$\varepsilon_p = \varepsilon_r K_Z 10^{k_{r1}} (T)^{1.5606} (N)^{0.235} \tag{I.11}$$

$$\text{Log}\left(\frac{\varepsilon_p}{\varepsilon_r}\right) = C_1 + 0.235\text{Log}(N) + 1.0\text{Log}(\sigma_d) + 0.930\text{Log}(V_{\text{beff}}) + 0.501\text{Log}(V_a) \tag{I.12}$$

$$\gamma_p = a e^{0.01\tau} \gamma_e N^{0.235} \tag{I.13}$$

The k_{r1}, C_1, and *a* terms or intercept values are defined in accordance with Table I.5.

Figure I.24a provides a comparison of the predicted and measured rut depths for all field survey sections using the Kaloush function, whereas Figure I.24b provides a comparison of the residual errors and the predicted values. Figure I.25 and Figure I.26 provide a similar comparison for the other two transfer functions. As shown, all three transfer functions provide reasonable estimates of the measured values. However, two of the composite pavement roadway sections are considered outliers for all three transfer functions: sections LTPP 2 and TX1. All three transfer functions overpredict the rutting measured on the TX1 section and underpredict rutting for the LTPP 2 section. Both of these sections are considered outliers.

Figures I.25 through I.27 (composite pavement plastic deformation coefficients) can be compared with Figures I.3 through I.5 (global plastic deformation coefficients) to illustrate the improvement in the model by considering layer thickness and air voids. The statistics resulting from the comparisons between the measured and predicted rut depths

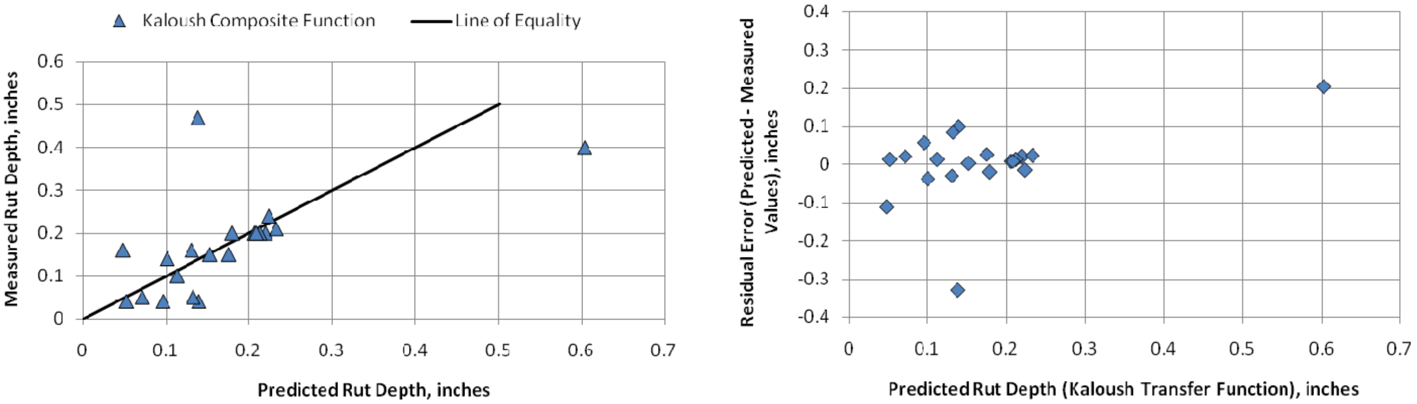

(a) Comparison of Measured and Predicted Rut Depths.

(b) Residual Error Versus Predicted Rut Depths.

Figure I.24. Measured and predicted rut depths using the Kaloush transfer function for the field survey sections.

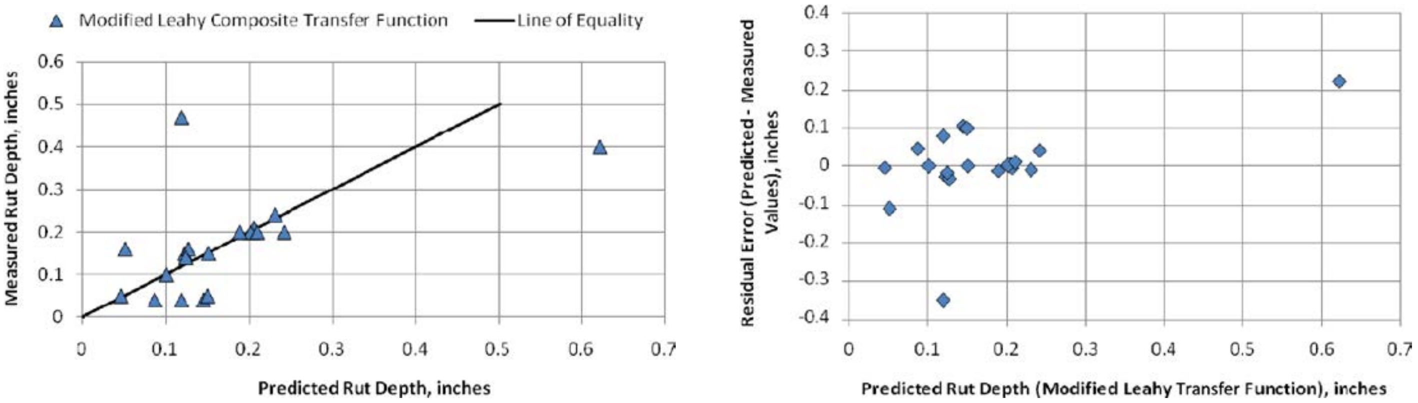

(a) Comparison of Measured and Predicted Rut Depths.

(b) Residual Error Versus Predicted Rut Depths.

Figure I.25. Measured and predicted rut depths using the Modified Leahy transfer function for the field survey sections.

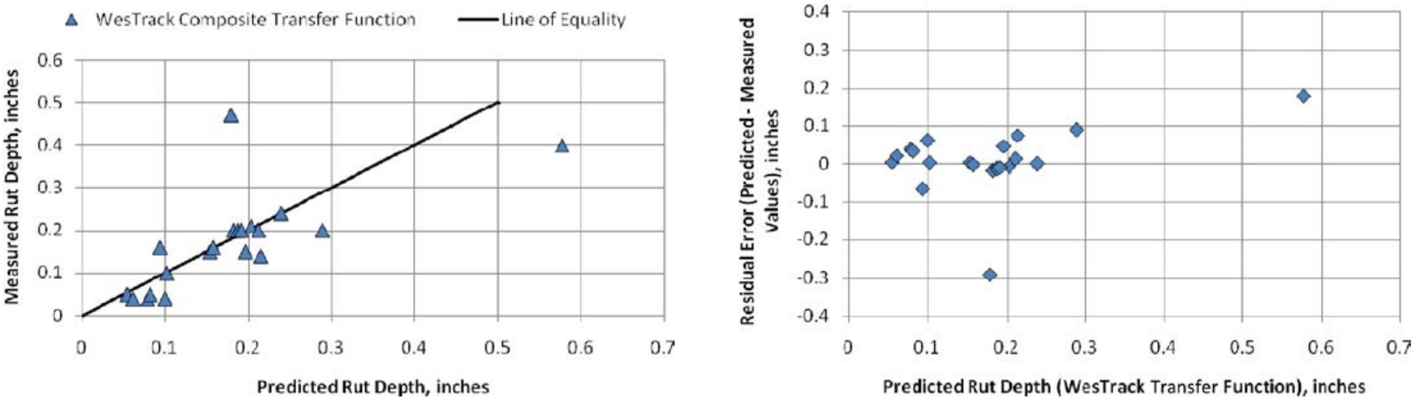

(a) Comparison of Measured and Predicted Rut Depths.

(b) Residual Error Versus Predicted Rut Depths.

Figure I.26. Measured and predicted rut depths using the WesTrack transfer function for the field survey sections.

Table I.6. Summary of Statistical Values for the Three Transfer Functions Resulting from Predicting the Measured Rut Depths of the Field Survey Sections

Statistical Parameters	**Transfer Function**		
	Kaloush	**Modified Leahy**	**WesTrack**
Number of data points	21	21	21
Model bias, in.	0.00221	0.0025	0.0077
Standard error	0.100	0.107	0.087
Standard error ratio, *se/sy*	0.887	0.953	0.770
R squared	0.213	0.092	0.403

are summarized in Table I.6 for each transfer function. All transfer functions are considered adequate for predicting the measured rutting: There is no significant model bias and there are reasonable standard error terms. Some of the model statistics are poor and are indicative of a model that does not explain the variability in the measured values. However, trying to predict low rut depths is difficult at best, especially without project- or mixture-specific test data.

Summary

In summary, all three transfer functions did a fair job of predicting the measured rutting values using mixture properties and other pavement layer properties extracted from project files. Thus, the rut depth transfer functions are believed to be reasonable for composite pavements. The WesTrack transfer function or repeated-load, constant-height shear tests are recommended because cores can be recovered and tested in the laboratory. This feature or capability to test field cores is believed to be a significant benefit over the repeated-load triaxial tests that are required for the Kaloush and Modified Leahy transfer functions.

It is also recommended that the transfer functions that include the stress term parameter also be used because of the relationship between HMA thickness and rut depth. The stress terms appear to account for the effect of thickness on rut depth that the depth functions do not capture.

APPENDIX J

Measurement and Analysis of PCC Slab Temperature Profiles at UCPRC

Objectives

The objectives of collecting portland cement concrete (PCC) slab temperature gradient data are as follows:

1. Compare PCC temperature gradients for sections with thick, thin, and no hot-mix asphalt (HMA) layers to identify the effect of an HMA layer as a thermal insulator.
2. Identify the effect of HMA type (PG 64-28 polymer-modified (PM), rubberized hot-mix asphalt with gap-graded aggregate [RHMA-G]) on the variation of PCC temperature gradients.
3. Determine the effect of PCC layer thickness on the variation of PCC temperature gradients.
4. Determine the effect of aging (change in HMA layer surface color) on the variation of PCC temperature gradients.

Figure J.1 illustrates the temperature changes within the PCC layer for a 5-day period. The figure shows that temperature measured by the thermocouple at the top of the PCC layer is immediately affected by the changes in air temperatures. On the other hand, the measurements show a time lag between the air temperature peak and peak temperature at the bottom of the PCC layer. This time lag creates the PCC temperature gradients between the top and bottom of the PCC layer that cause stresses at the top and bottom of PCC. PCC temperature gradients also are shown in Figure J.1, calculated by using Equation J.1:

$$\nabla T = \frac{(T_{\text{top}} - T_{\text{bottom}})}{(D_{\text{top}} - D_{\text{bottom}})} \tag{J.1}$$

where

∇T = PCC temperature gradient (°C/m),
T_{top} = temperature measured by the top thermocouple (°C),
T_{bottom} = Temperature measured by the bottom thermocouple (°C),
D_{top} = depth for top thermocouple (m), and
D_{bottom} = depth for bottom thermocouple (m).

To identify the effects of HMA and PCC layer thickness and HMA type on the variation of the PCC temperature gradients, 1 year of temperature data (1/1/2010 to 12/31/2010) was analyzed from the thermocouples on located on every section. Lane A has the PG 64-28 PM HMA layer with the thick PCC layer (7 in. [178 mm]). Temperature data for Lane B is assumed to be similar to the data for Lane A and was not considered for the temperature analysis because the only difference between Lane A and Lane B is the dowel bars on the Lane A transverse joints. Lane C has the RHMA-G HMA layer with thick PCC layer (7 in. [178 mm]) underneath, whereas Lane D has the same mix with thin concrete (5 in. [127 mm]) underneath. HMA layer thicknesses also vary along the test sections. Figure J.2 shows the PCC temperature gradients for Lanes A, C, and D by truncated (few outliers excluded) box plots. The figure shows that the inclusion of the HMA layers causes a significant decrease in the PCC temperature gradients, whereas no significant effect of PCC layer thickness on the variation of PCC temperature gradients is observed. In the box plots, the middle line is the median value. The top and bottom of the box are the 25th and 75th percentile values and the bracketed lines above and below the boxes are the minimum and maximum values.

To evaluate the effect of HMA thickness on the variation of PCC temperature gradients, exact distributions of PCC temperature gradients are given in Figure J.3. Figure J.3a shows that the section with the 114-mm thick PG 64-28 PM HMA layer has the lowest level of positive and negative PCC temperature gradients and that the range of gradients increases when the HMA layer thickness is decreased to 64 mm. The corresponding section with no HMA layer has the largest variability in PCC temperature gradients, ranging from –44° to +75°C/m. This result indicates that the HMA layer acts as a thermal insulator that decreases the temperature gradient within the PCC layer, reducing the overall probability of

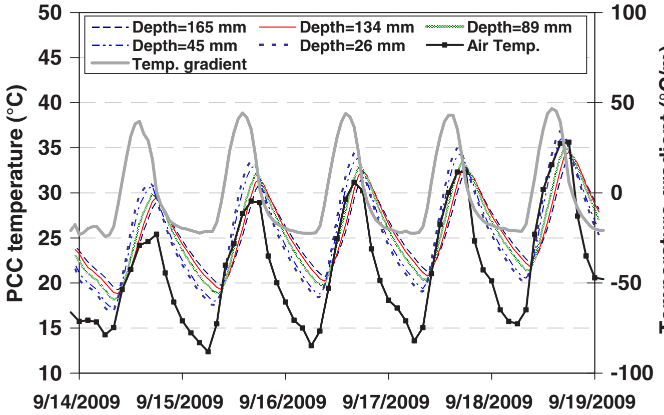

Note: Fahrenheit = Celsius × 9/5 + 32; 25.4 mm = 1 in.

Figure J.1. Changes in temperature within the PCC layer for a 5-day period.

negative temperature gradients and most of the extreme negative temperature gradients, which cause tensile stresses on the top of the slab, and generally increasing the probability of small temperature gradients.

Similar results were observed for Lanes C and D. However, Figure J.3b and Figure J.3c show that thickness of the HMA layer did not significantly affect the variability of PCC temperature gradients with the RHMA-G layer.

To determine the effect of HMA layer mix type on the variation of PCC temperature gradients, distributions for the gradients for sections with thick HMA layers (Lane A and Lane C) were compared. HMA layers on Lane A and Lane C were constructed from PG 64-28 PM and RHMA-G mixes, respectively, as shown in Figure J.4. The figure shows that significantly higher positive PCC temperature gradients occurred on the section with the RHMA-G layer. This result also agrees with the albedo measurements performed on sections with RHMA-G layer, PG 64-28 PM layer, and no HMA layer (PCC). Figure J.5 shows the results for the albedo measurements. The PG 64-28 PM layer is reflecting more solar radiation (higher albedo) than is the RHMA-G layer, which is causing lower positive PCC temperature gradients for the sections with the PG 64-28 PM layer. Thus, the section with the RHMA-G layer will experience larger thermal stresses at the bottom of the PCC layer than will the section with the PG 64-28 PM layer as a result of the larger positive PCC temperature gradients, whereas the maximum values of negative temperature gradients causing stresses at the top of the PCC slabs are similar for both materials.

The effect of PCC layer thickness on the variation of PCC temperature gradients is determined by comparing the gradient distributions of sections without an HMA layer for Lanes C and D. Distributions are given in Figure J.6. The figure shows that there are no significant differences between the distributions. This result suggests that thickness of PCC layer does not have any considerable effect on the variation of the PCC temperature gradients for these slab thicknesses.

PCC temperature gradient distributions were further analyzed by using statistical design and interaction plots. Design

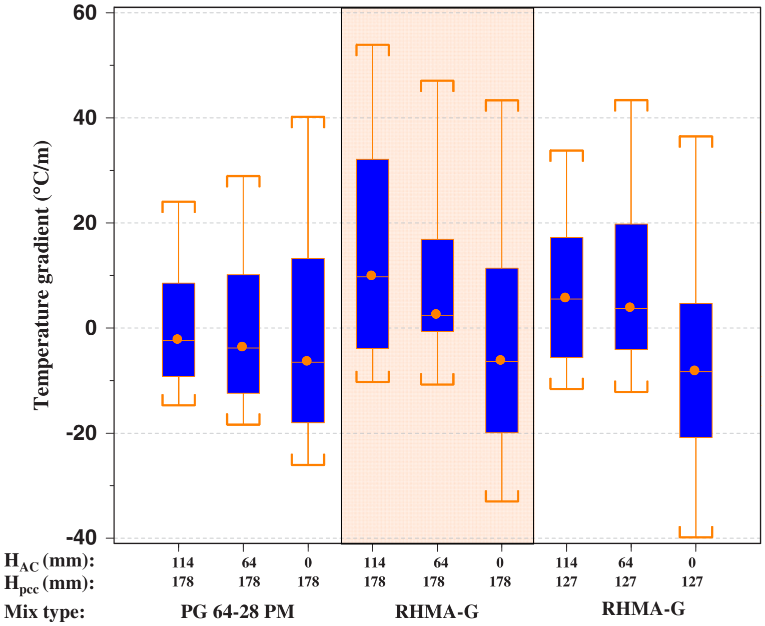

Note: H_{AC} is HMA thickness, H_{PCC} is PCC thickness; Fahrenheit = Celsius × 9/5 + 32; 25.4 mm = 1 in.; 1 m = 39.37 in.

Figure J.2. Distribution of PCC temperature gradients for all sections.

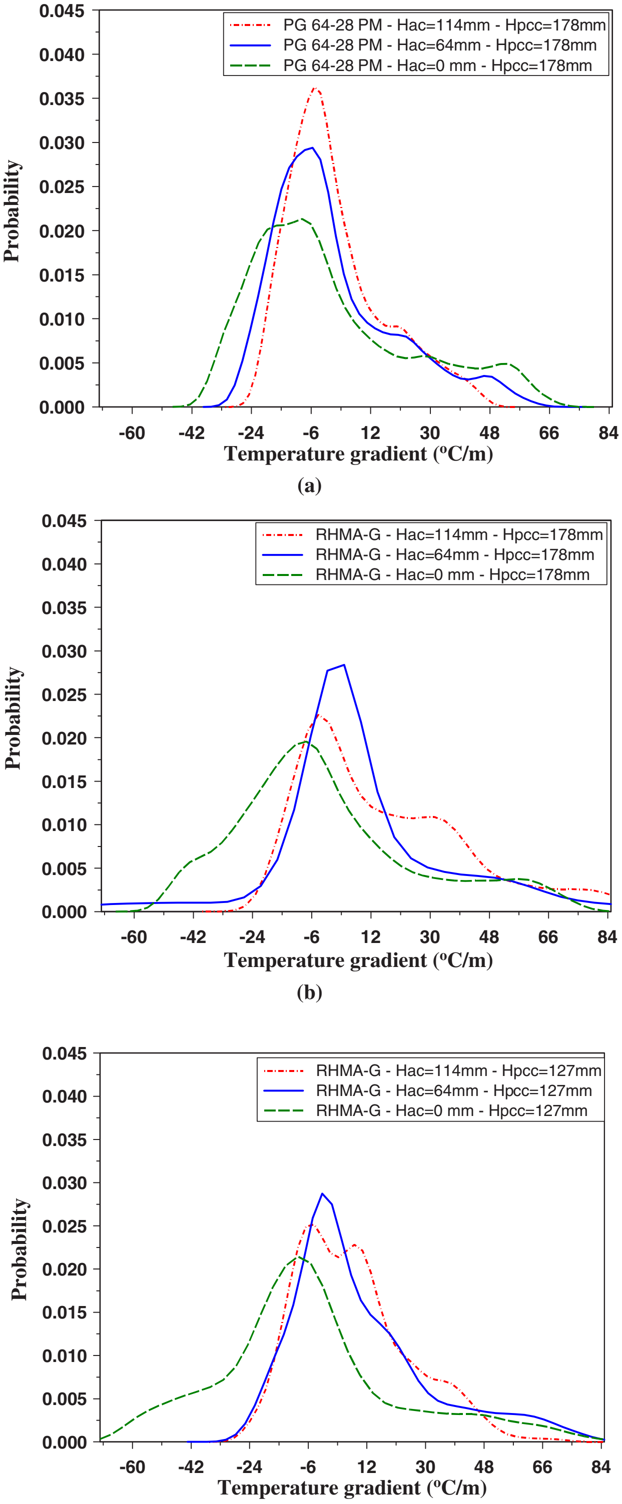

Note: Fahrenheit = Celsius × 9/5 + 32; 25.4 mm = 1 in.

Figure J.3. Probability distributions of PCC temperature gradients for year 2010: (a) Lane A, (b) Lane C, and (c) Lane D.

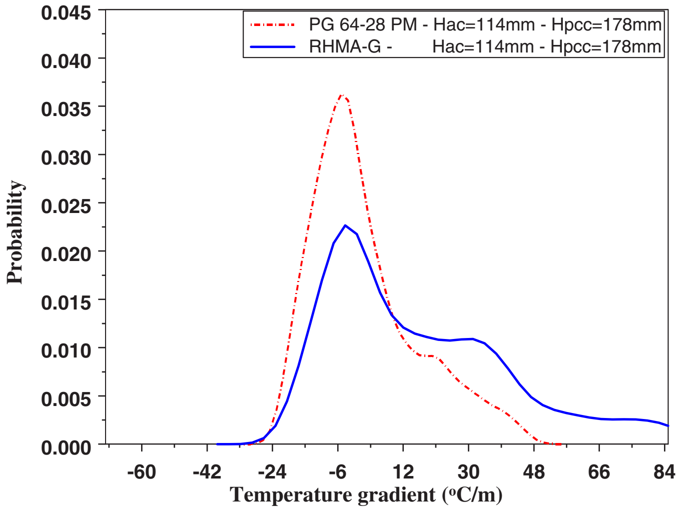

Note: Fahrenheit = Celsius × 9/5 + 32; 1 m = 39.37 in., 25.4 mm = 1 in.

Figure J.4. Probability distribution of PCC temperature gradients for sections constructed from PG 64-28 PM and RHMA-G mixes.

and interaction plots generally are used to compare the influence of a factor on the variation of the dependent variable with respect to other factors. Absolute values of the PCC temperature gradients were used as dependent variables for the analysis because both negative and positive PCC temperature gradients will cause tensile stresses. PCC and HMA thickness and HMA mix type were used as the independent variables for the design and interaction plots. Figure J.7 shows the design plot, with each plot showing the mean for the factor levels for each variable as a short horizontal line, compared with the overall mean of the data shown as a long horizontal line across all variables. The figure shows that PCC thickness does not have any significant effect on the variability of PCC temperature gradients. On the other hand, the HMA layer appears to significantly decrease the PCC temperature gradients within the PCC layer. In addition, the calculated average for thickness of the HMA layer does not have much effect on the PCC temperature gradient. The PG 64-28 PM mix causes considerably lower PCC temperature gradients in the PCC layer than does the RHMA-G mix.

To determine the separate effect of each independent variable on the variability of PCC temperature gradients, interaction plots were used (Figure J.8). Figure J.8a shows that RHMA-G layers cause higher PCC temperature gradients for all thicknesses than do PG 64-28 PM layers. Figure J.8b shows the extent to which the HMA layers reduce the PCC temperature gradients. The use of a thick or thin HMA layer does not cause any significant difference between the gradients for the thicker PCC slabs, whereas HMA layer thickness causes lower PCC temperature gradients for sections with thin PCC slabs (127 mm).

The effect of aging on the variation of the PCC temperature gradients was also investigated. Two 100-hour periods with

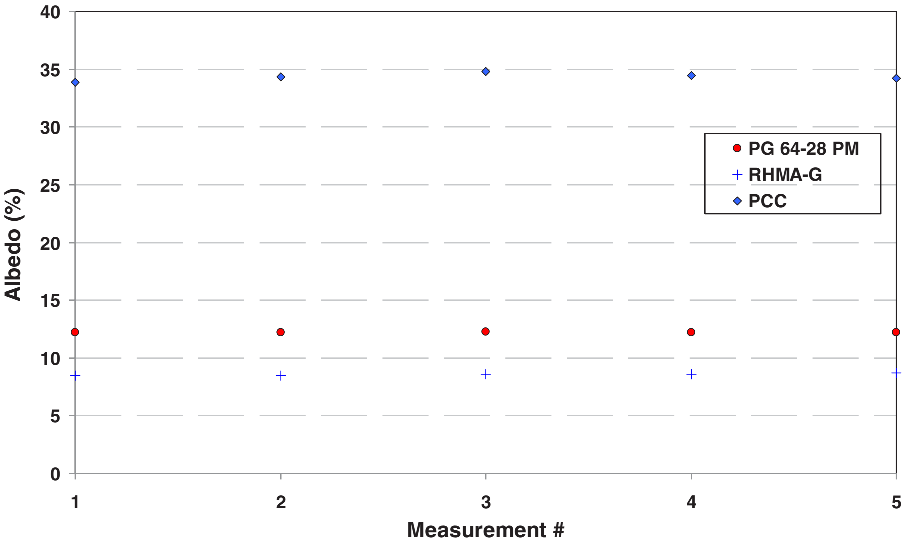

Figure J.5. Measured albedo for the Heavy Vehicle Simulator test sections.

similar air temperatures from 2009 and 2010 were selected to determine the effect of aging on PCC temperature gradients. Figure J.9 shows the air temperatures and PCC temperature gradients for the section with thick PG 64-28 PM and thick PCC layers (Lane A). Absolute values of PCC temperature gradients for the aged HMA case (8/13/2010) appear to be lower than those for the new HMA case (9/7/2009). Although this result indicates that HMA aging resulted in a decrease of the PCC temperature gradients, additional cases should be analyzed considering the measured solar radiation and albedo effects to produce more definitive conclusions. Figure J.10 shows the variation of PCC temperature gradients for the section without an HMA layer. The figure shows that PCC gradients are close to each other because concrete aging did not cause significant changes in the color of the PCC.

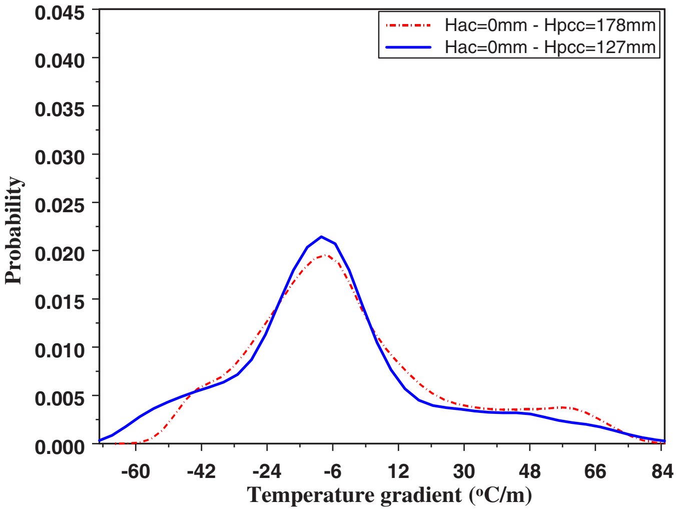

Note: Fahrenheit = Celsius × 9/5 + 32; 1 m = 39.37 in., 25.4 mm = 1 in.

Figure J.6. Probability distribution of PCC temperature gradients for thick and thin PCC layer sections without HMA layer.

Results Summary

The following are key findings from the PCC thermocouple measurements:

- HMA layer significantly decreased the PCC temperature gradients.
- The thickness of the HMA layer (4.5 in. [114 mm] versus 2.5 in. [64 mm]) did not have much effect on the PCC temperature gradient.
- Significantly higher positive PCC temperature gradients can be observed for the section with RHMA-G layer than for the PG 64-28 PM layer. This shows that the PG 64-28 PM layer is reflecting more solar radiation (higher albedo) than is the RHMA-G layer. Thus, the section with the RHMA-G layer will experience larger thermal stresses at the bottom of the PCC layer than will the section with the PG 64-28 PM layer as a result of the larger positive PCC temperature gradients.
- No significant effect of PCC layer thickness on the variation of PCC temperature gradients was observed.
- One year of HMA aging for a period with similar air temperatures, although 1 month apart, appeared to reduce the PCC temperature gradients for the two 100-hour periods investigated in this study. However, additional cases should be analyzed by considering the measured solar radiation and albedo effects to produce more definitive conclusions.

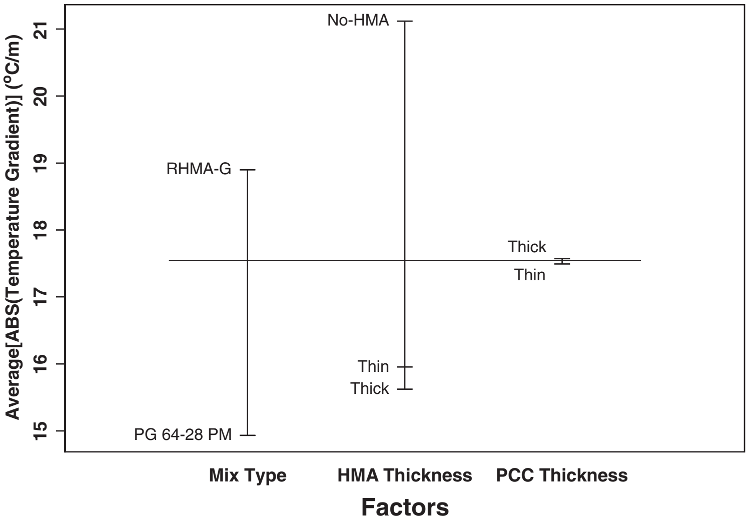

Note: Fahrenheit = Celsius × 9/5 + 32; 1 m = 39.37 in.

Figure J.7. Design plot comparing the influence of variables HMA and PCC thickness and HMA type on the variation of the dependent variable PCC temperature gradient.

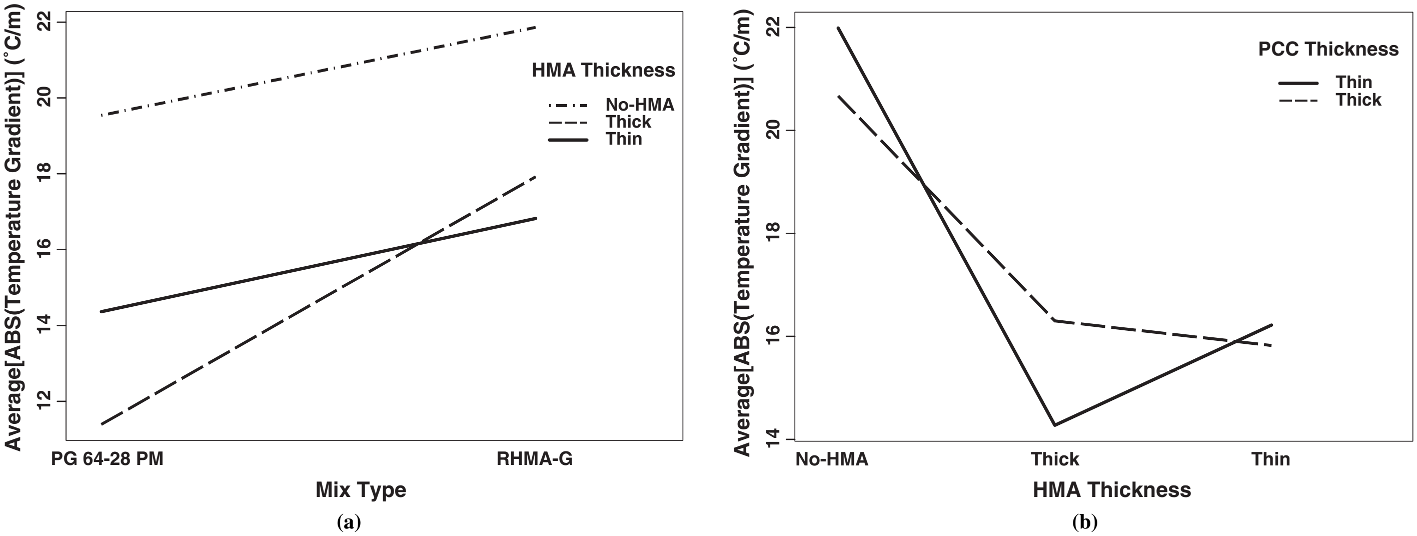

(a) (b)

Note: Fahrenheit = Celsius × 9/5 + 32; 1 m = 39.37 in.

Figure J.8. Interaction plots comparing the influence of variables HMA and PCC thickness and HMA type on the variation of the dependent variable PCC temperature gradient: (a) Mix type evaluation for all PCC thicknesses and (b) HMA thickness evaluation for all mix types.

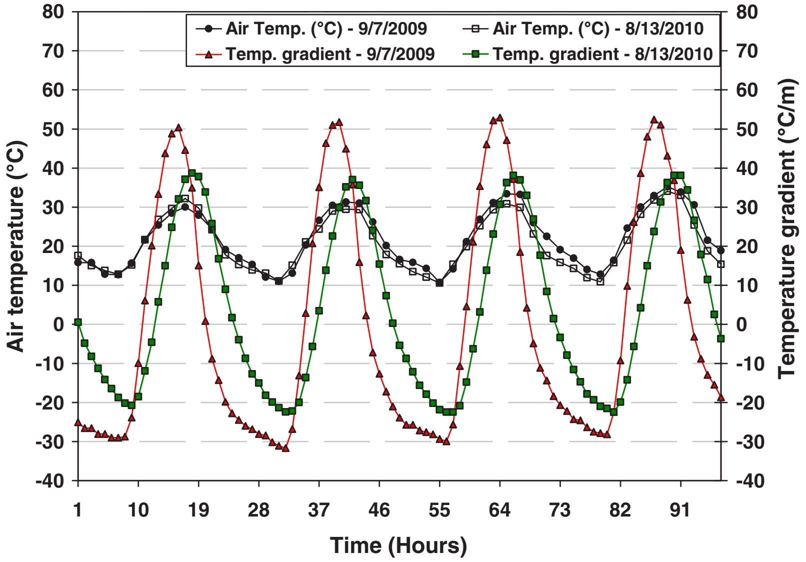

Note: Fahrenheit = Celsius × 9/5 + 32; 1 m = 39.37 in.

Figure J.9. Air temperatures and PCC temperature gradients for the section with thick HMA and thick PCC layers constructed with HMA mix PG 64-28 PM (Lane A) starting from 9/7/2009 and 8/13/2010.

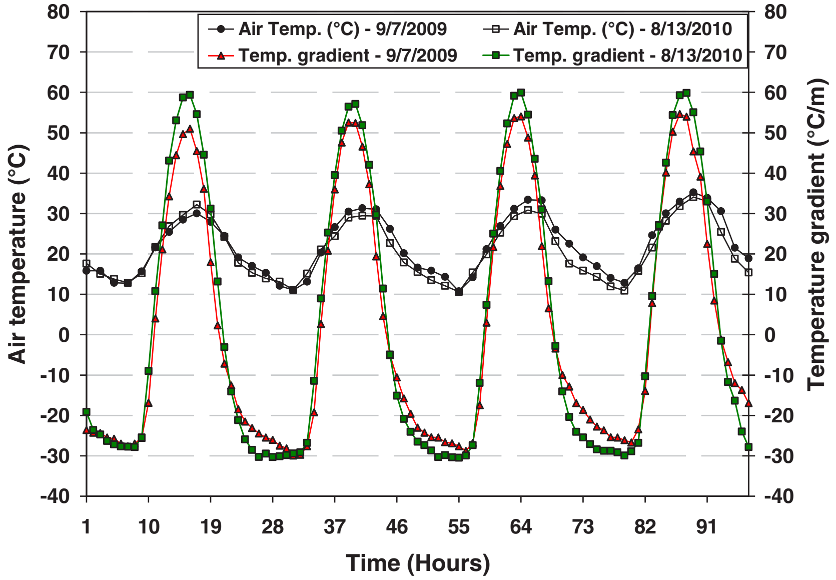

Note: Fahrenheit = Celsius × 9/5 + 32; 1 m = 39.37 in.

Figure J.10. Air temperatures and PCC temperature gradients for the section without HMA layer (only thick PCC) starting from 9/7/2009 and 8/13/2010.

APPENDIX K

HVS Cracking Tests at UCPRC

Description of the HVS Testing Program for Cracking

Objective and Introduction

Cracking tests on hot-mix asphalt/portland cement concrete (HMA/PCC) composite pavements were conducted on the University of California, Pavement Research Center (UCPRC) SHRP 2 R21 test track to evaluate cracking failure mechanisms, which include both reflection cracking near the PCC joints and fatigue cracking in the PCC slabs. The data collected provides insights for designing HMA/PCC composite pavements as well as calibration of related mechanistic-empirical models.

Eight HMA/PCC composite sections were built on the test track. Two of them, coded Sections 613HB and 614HB, respectively, were tested as part of SHRP 2 R21, the results of which are summarized and reported in this appendix.

Section Layout

Figure K.1 shows the overall layout for the Heavy Vehicle Simulator (HVS) test sections. The HVS sections are coded uniquely with three digits and two letters, the latter indicating which HVS was used for the testing. They have been left off for planned sections 615 to 618 because it has not yet been decided which HVS will be used. Figure K.1 also shows the labeling of each transverse joint as J1 to J8, from south to north. Both rutting and cracking test sections at UCPRC are each 0.6 m (2.0 ft) wide and 8 m (26.2 ft) long, including a 1-m (3.3-ft) turnaround zone at each end of the section. Sections 609HB to 612HB are the rutting sections on which testing has been completed. The remaining sections are for cracking tests and have a testing sequence number shown in parentheses. Section 613HB was tested first and completed 3/17/2011 and testing on Section 614HB was completed May 20, 2011.

The detailed pavement structures can be found in Appendix G. The structure for Section 613HB and 614HB are also listed in Table K.1.

Protocols

The general HVS test section layout, test setup, trafficking, and measurements followed standard UCPRC protocols (Jones 2005).

Pavement Instrumentation and Monitoring Methods

Measurements were taken with the instruments listed below. Intervals between measurements, in terms of load repetitions, were selected to enable adequate characterization of the pavement as damage developed.

- Thermocouples measured pavement temperature and ambient temperature.
- Laser Profilometer measured transverse surface profile to allow tracking of profile change.
- PCC dynamic strain gauges measured horizontal strain in the PCC caused by HVS traffic.
- Joint deflection measuring device (JDMD) measured pavement deflections near joints.
- Road surface deflectometer (RSD) measured vertical pavement deflections near the joints and at the middle of the slab.

Thermocouples

Type K thermocouples were used in this project to measure pavement and air temperatures (both inside and outside the temperature chamber). Five thermocouples were bundled together to form a “thermocouple tree” to allow measurement of pavement temperature at multiple depths at each location. The locations of thermocouple trees are shown in Figure K.2. Note that two sets of thermocouples were used: one set for manual measurements using a thermometer and the other set for automatic measurements using the HVS data

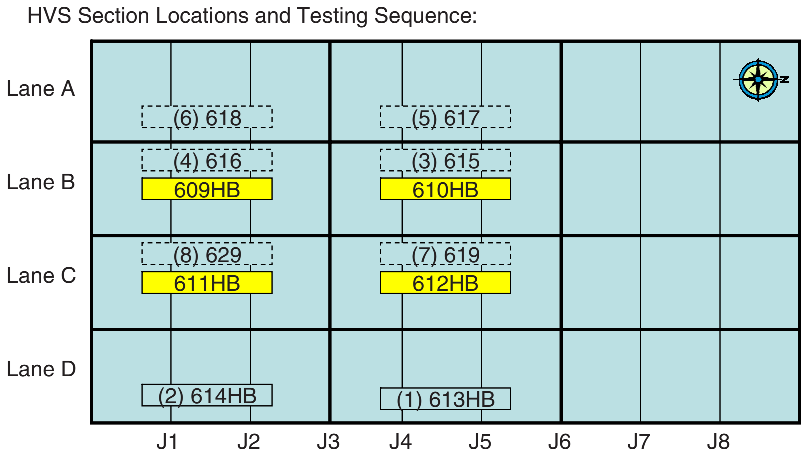
HVS Section Locations and Testing Sequence:
Lane A
Lane B
Lane C
Lane D
(6) 618
(5) 617
(4) 616
609HB
(3) 615
610HB
(8) 629
611HB
(7) 619
612HB
(2) 614HB
(1) 613HB
J1
J2
J3
J4
J5
J6
J7
J8
N

Figure K.1. HVS section layout of the SHRP 2 R21 test track.

Table K.1. Pavement Structure for Sections 613HB and 614HB

Layer No.	Description	Design Thickness
1	Rubberized hot-mix asphalt with gap-graded aggregate (RHMA-G)	2.5 in. for 613HB 4.5 in. for 614HB
2	PCC	5.0 in.
3	Aggregate base	6.0 in.
4	Subgrade	na

Note: na = not applicable.

acquisition system (DAS). The exact locations of the thermocouples may be slightly different. Table K.2 and Table K.3 show the locations of thermocouples in Sections 613HB and 614HB, respectively.

Laser Profilometer

The Laser Profilometer was used to the measure transverse surface profile of the test section at every station (i.e., from Stations 0 to 16). The difference between the surface profile after HVS trafficking and the initial surface profile is the permanent change in surface profile. Based on the change in surface profile, the maximum rut was determined for each station, as illustrated in Figure K.3.

JDMD, RSD, and Strain Gauges in 613HB

The RSD and JDMD are essentially specialized linear variable differential transformers (LVDTs). A schematic of the section showing RSD, JDMD, and dynamic strain gauge layouts is included in Figure K.4 for Section 613HB. The exact locations of the JDMDs, dynamic strain gauges, and RSDs used in Section 613HB are listed in Table K.4, along with the *x*-coordinate of the two joints J4 and J5. A minus symbol (−) or plus symbol (+) after the joint name indicates whether a location is at the south or north of the corresponding joint, respectively. For example, "J5−" means it is located at the south side of joint J5. The two dynamic strain gauges measured longitudinal strain in the horizontal direction, one installed 0.79 in. (20 mm) below the top of the PCC layer and the other 0.79 in. (20 mm) above the bottom of the PCC layer. The locations of Joints J4

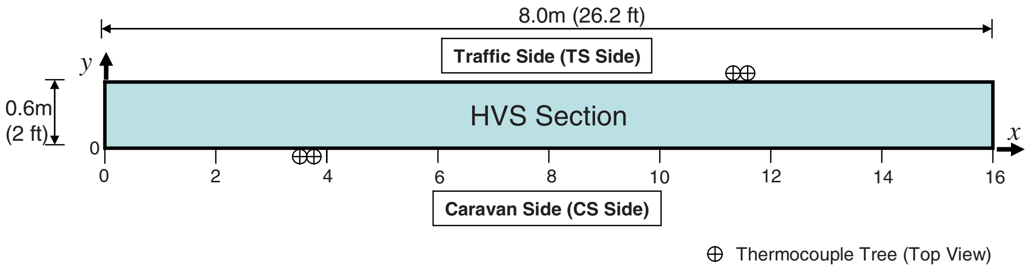
8.0m (26.2 ft)
Traffic Side (TS Side)
y
0.6m
(2 ft)
0
HVS Section
x
0
2
4
6
8
10
12
14
16
Caravan Side (CS Side)
⊕ Thermocouple Tree (Top View)

Figure K.2. Schematic of HVS test section and stationing, thermocouple tree locations, and coordinate system. The y-axis points upward following the right-hand convention with zero at the pavement surface (i.e., top of the HMA layer).

Table K.2. Coordinates of Thermocouples Used in Section 613HB[a]

Label	*X* (mm/in.)	*Y* (mm/in.)	*Z* (mm/in.)
4CS-0	1,900/75	–100/–3.9	0/0
4CS-25	1,900/75	–100/–3.9	–25/–1.0
4CS-50	1,900/75	–100/–3.9	–50/–2.0
4CS-60	1,900/75	–100/–3.9	–60/–2.4
4CS-90	1,900/75	–100/–3.9	–90/–3.5
12TS-0	5,800/228	700/27.6	0/0
12TS-25	5,800/228	700/27.6	–25/–1.0
12TS-50	5,800/228	700/27.6	–50/–2.0
12TS-60	5,800/228	700/27.6	–60/–2.4
12TS-90	5,800/228	700/27.6	–90/–3.5

[a] See Figure K.2 for coordinate system.

Table K.3. Coordinates of Thermocouples Used in Section 614HB[a]

Label	*X* (mm/in.)	*Y* (mm/in.)	*Z* (mm/in.)
4CS-0	1,900/75	–100/–3.9	0/0
4CS-25	1,900/75	–100/–3.9	–25/–1.0
4CS-50	1,900/75	–100/–3.9	–50/–2.0
4CS-90	1,900/75	–100/–3.9	–90/–3.5
4CS-120	1,900/75	–100/–3.9	–120/–4.7
12TS-0	5,800/228	700/27.6	0/0
12TS-25	5,800/228	700/27.6	–25/–1.0
12TS-50	5,800/228	700/27.6	–50/–2.0
12TS-90	5,800/228	700/27.6	–90/–2.4
12TS-120	5,800/228	700/27.6	–120/–4.7

[a] See Figure K.2 for coordinate system.

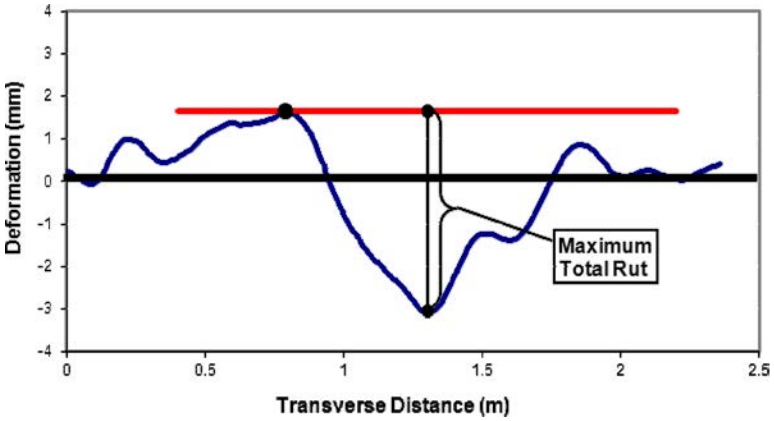

Figure K.3. Illustration of maximum rut depth for a leveled profile. (Red line = highest point on profile. Blue line = transverse surface profile.)

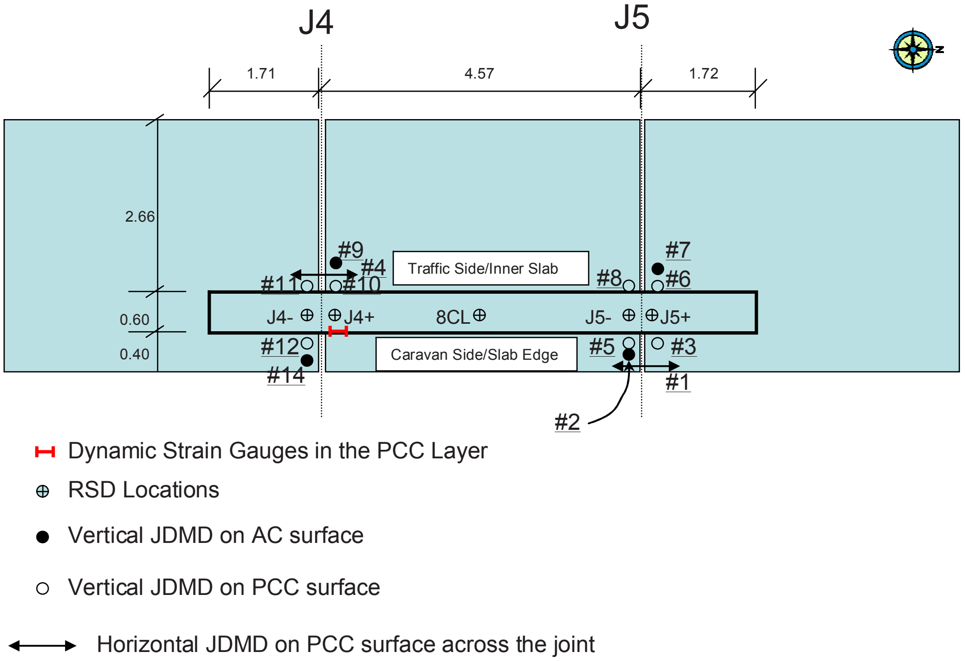
J4
J5
z
1.71
4.57
1.72
2.66
0.60
0.40
#9
#4
#11
#10
Traffic Side/Inner Slab
#8
#7
#6
J4-
J4+
8CL
J5-
J5+
#12
#14
Caravan Side/Slab Edge
#5
#3
#1
#2
⊢⊣ Dynamic Strain Gauges in the PCC Layer
⊕ RSD Locations
● Vertical JDMD on AC surface
○ Vertical JDMD on PCC surface
↔ Horizontal JDMD on PCC surface across the joint

Figure K.4. Section 613HB: Section and instrument layout (JDMD No. 13 did not work properly during the testing). Dimensions are in meters (1 m = 3.3 ft).

Table K.4. Coordinates of Joints, JDMDs, RSDs, and Dynamic Strain Gauges for Section 613HB[a]

Label	Type	*X* (mm/in.)	*Y* (mm/in.)	*Z* (mm/in.)
Joint J4	Joint	1,730/68	na	na
Joint J5	Joint	6,300/248	na	na
JDMD No. 1	JDMD	6,300/248	–340/–13.4	–63/–2.5
JDMD No. 2	JDMD	6,235/245	–230/–9.1	0/0.0
JDMD No. 3	JDMD	6,235/245	–110/–4.3	–63/–2.5
JDMD No. 4	JDMD	1,730/68	840/33.1	–63/–2.5
JDMD No. 5	JDMD	6,365/251	–110/–4.3	–63/–2.5
JDMD No. 6	JDMD	6,370/251	700/27.6	–63/–2.5
JDMD No. 7	JDMD	6,370/251	830/32.7	0/0.0
JDMD No. 8	JDMD	6,230/245	700/27.6	–63/–2.5
JDMD No. 9	JDMD	1,800/71	940/37.0	0/0.0
JDMD No. 10	JDMD	1,800/71	720/28.3	–63/–2.5
JDMD No. 11	JDMD	1,660/65	720/28.3	–63/–2.5
JDMD No. 12	JDMD	1,660/65	–120/–4.7	–63/–2.5
JDMD No. 14	JDMD	1,660/65	–240/–9.4	0/0.0
J4–	RSD	1,640/65	300/11.8	0/0.0
J4+	RSD	1,770/70	300/11.8	0/0.0
8CL	RSD	4,000/157	300/11.8	0/0.0
J5–	RSD	6,200/244	300/11.8	0/0.0
J5+	RSD	6,370/251	300/11.8	0/0.0
SG-613-4-PCC-T	Dynamic strain gauge	1,770/69.7	0/0	–90/–3.5
SG-613-4-PCC-B	Dynamic strain gauge	1,770/69.7	0/0	–170/–6.7

[a] See Figure K.2 for coordinate system.

and J5, RSD, and JDMD for Section 613HB are shown in Figure K.5. Figure K.6 shows JDMDs installed at traffic side (inner slab) near Joint J4.

JDMD nos. 1, 2, 3, 5, 12, and 14 were located on the caravan side (CS) of the test section; they were also at the edge of the underlying PCC slab. All the other JDMDs were on the traffic side (TS) of the test section and were at least 1.0 m (3.3 ft) from the edge of the PCC slab. Their location is therefore referred to as the "inner" slab.

JDMD, RSD, and Strain Gauges in 614HB

A schematic of the section showing RSD, JDMD, and dynamic strain gauge layouts is included in Figure K.7 for Section 614HB. Strain gauges were installed at two locations, one at the middle of Slab D12 and the other near the northeast corner of Slab D12. Strain gauges at the middle of the slab did not work properly. A photograph of the section showing

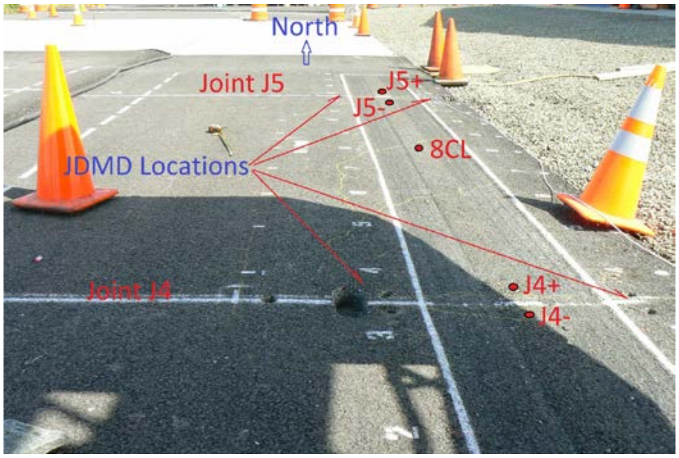

Figure K.5. Section 613HB: Photograph shows joint, RSD, and JDMD locations. Eight (8) CL represents the location of the RSD while J4+, J4–, J5+, and J5– represent locations of the JDMDs.

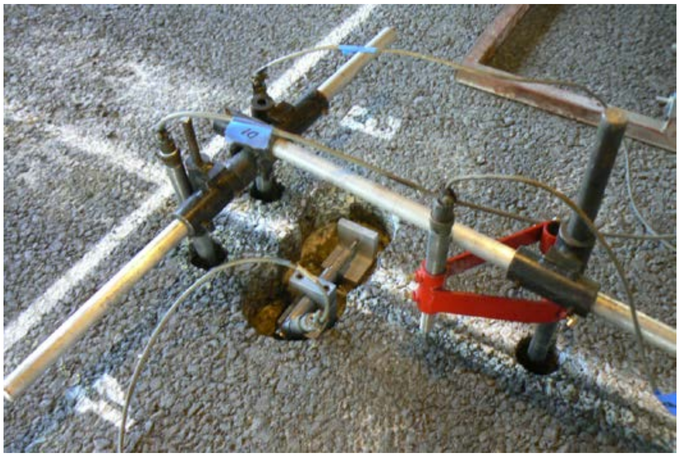

Figure K.6. Photograph shows JDMDs installed at traffic side (inner slab) near Joint J4. There are two vertical JDMDs on PCC, one horizontal JDMD on PCC, and one vertical JDMD on HMA.

locations of the joints, JDMDs, and RSD measurement points is presented in Figure K.8. The exact locations of the JDMDs, dynamic strain gauges, and RSDs used in Section 614HB are listed in Table K.5, along with the *x*-coordinate of the two joints J1 and J2.

JDMD nos. 1, 2, 3, 5, 12, and 14 were located on the CS of the test section, at the edge of the underlying PCC slab. All the other JDMDs were on the TS of the test section and were at least 1.0 m (3.3 ft) from the edge of the PCC slab. The location of the TS JDMDs is therefore referred to as the "inner" slab.

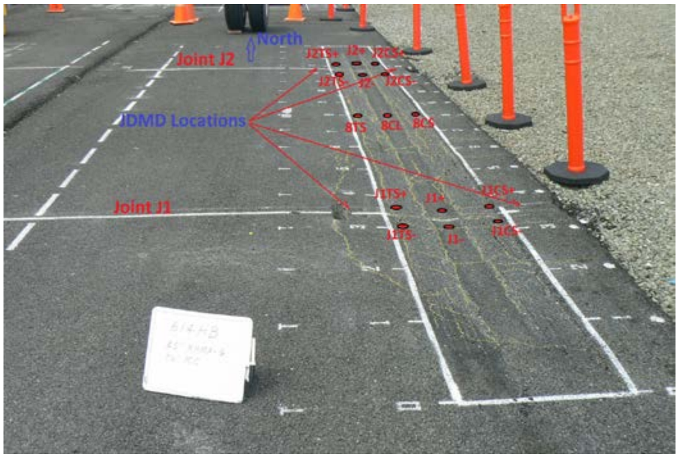
North
Joint J2
JDMD Locations
Joint J1
J2TS+
J2+
J2CS+
J2TS-
J2-
J2CS-
8TS
8CL
8CS
J1TS+
J1+
J1CS+
J1TS-
J1-
J1CS-
614HB

Figure K.8. Section 614HB: Photograph shows joint, RSD, and JDMD locations.

HVS Test Program

Test Section Failure Criteria

Reflection cracking in the HMA layer and fatigue cracking in the PCC slab were set as the failure criteria for the experiment. Reflection cracking failure is defined as the time when cracks

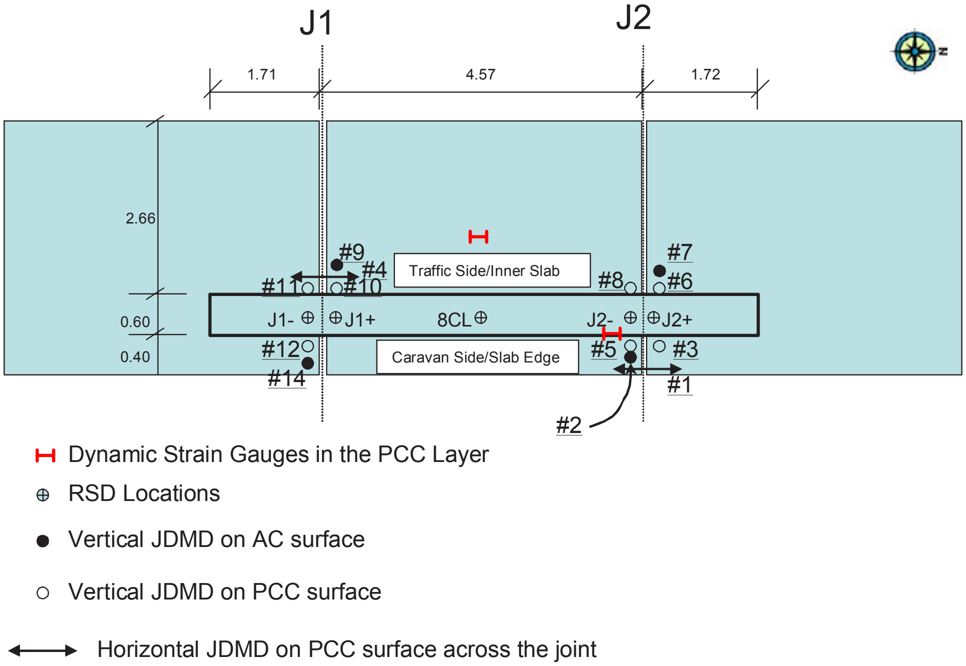
J1
J2
N
1.71
4.57
1.72
2.66
0.60
0.40
#9
#4
#11
#10
Traffic Side/Inner Slab
#8
#7
#6
J1-
J1+
8CL
J2-
J2+
#12
#5
#3
Caravan Side/Slab Edge
#14
#1
#2
Dynamic Strain Gauges in the PCC Layer
RSD Locations
Vertical JDMD on AC surface
Vertical JDMD on PCC surface
Horizontal JDMD on PCC surface across the joint

Note: Dimensions are in meters (1 m = 3.3 ft).

Figure K.7. Section 614HB: Section and instrument layout (JDMD No. 13 did not work properly during the testing).

Table K.5. Coordinates of Joints, JDMDs, RSDs, and Dynamic Strain Gauges for Section 614HB[a]

Label	Type	*X* (mm/in.)	*Y* (mm/in.)	*Z* (mm/in.)
Joint J1	Joint	1,730/68	na	na
Joint J2	Joint	6,300/248	na	na
JDMD No. 1	JDMD	6,300/248	–330/–13.0	–114/–4.5
JDMD No. 2	JDMD	6,220/245	–200/–7.9	0/0
JDMD No. 3	JDMD	6,235/245	–140/–5.5	–114/–4.5
JDMD No. 4	JDMD	1,730/68	840/33.1	–114/–4.5
JDMD No. 5	JDMD	6,365/251	–140/–5.5	–114/–4.5
JDMD No. 6	JDMD	6,390/252	710/28.0	–114/–4.5
JDMD No. 7	JDMD	6,370/251	975/38.4	0/0
JDMD No. 8	JDMD	6,230/245	710/28.0	–114/–4.5
JDMD No. 9	JDMD	1,845/73	1,020/40.2	0/0
JDMD No. 10	JDMD	1,790/70	720/28.3	–114/–4.5
JDMD No. 11	JDMD	1,670/66	720/28.3	–114/–4.5
JDMD No. 12	JDMD	1,670/66	–120/–4.7	–114/–4.5
JDMD No. 14	JDMD	1,670/66	–290/–11.4	0/0
J1–	RSD	1,640/65	300/11.8	0/0
J1+	RSD	1,770/70	300/11.8	0/0
8CL	RSD	4,000/157	300/11.8	0/0
J2+	RSD	6,370/251	300/11.8	0/0
J2–	RSD	6,200/244	300/11.8	0/0
8CL+	RSD	4,001/158	300/11.8	0/0
J1TS–	RSD	1,640/65	570/22.4	0/0
J1TS+	RSD	1,770/70	570/22.4	0/0
8TS	RSD	4,000/157	570/22.4	0/0
8TS+	RSD	4,001/158	570/22.4	0/0
J2TS+	RSD	6,370/251	570/22.4	0/0
J2TS–	RSD	6,200/244	570/22.4	0/0
J2CS–	RSD	6,200/244	50/2.0	0/0
J2CS+	RSD	6,370/251	50/2.0	0/0
J1CS–	RSD	1,640/65	50/2.0	0/0
J1CS+	RSD	1,770/70	50/2.0	0/0
8CS+	RSD	4,001/158	50/2.0	0/0
SG-614HB-12-TP	Dynamic strain gauge	5,930/233	0/.0	–161/–6.3
SG-614HB-12-BP	Dynamic strain gauge	5,930/233	0/.0	–226/–8.9

[a] See Figure K.2 for coordinate system.

appear in the HMA layer above the underlying joints. PCC fatigue cracking failure is defined as the time when one of the underlying slabs has either corner cracking or midslab cracking caused by the HVS traffic. HVS testing was stopped once both cracking failures were confirmed. For PCC fatigue cracking, this means the cracks in the PCC had to be reflected through the HMA surface.

Loading Programs

The testing began with a pavement response evaluation stage (Stage 1) and was followed by a crack-inducing stage (Stage 2). Each stage was further divided into substages based on pavement temperature and wheel load level. Descriptions of the two stages and the substages are listed in Table K.6. Section 613HB included Stages 1.1 to 2.3, whereas Section 614HB included all stages. Equivalent single-axle load (ESAL) was determined using the following conversion in Equation K.1:

$$\text{ESALs} = (\text{HVS repetitions}) \times (\text{Half axle load in kN}/80)^{3.8} \tag{K.1}$$

All trafficking with a wheel load of 23.5 kip (100 kN) or less was carried out with a dual-wheel configuration, using radial truck tires (Firestone FS507 Radial 11R22.5 14PR) inflated to a pressure of 690 kPa (100 psi), in a channelized, unidirectional loading mode. The distance between the two wheels was 365 mm (14.4 in.) on center. Trafficking with the 27 kip (120 kN) load was carried out using a tubeless, single-wheel aircraft tire (BF Goodrich TSO C62C, 46 × 16) inflated to 1,380 kPa (200 psi).

Pavement Temperature Control

The pavement temperature at 50 mm (2.0 in.) depth was maintained at 50°C ± 2°C (122°F ± 4°F) for the first 3 days of testing (Stage 1.1). The HVS section was enclosed with insulation panels to form a temperature control chamber. Heaters controlled by a programmable thermostat inside the chamber were used to maintain the pavement temperature. The pavement surface received no direct rainfall because it was protected by the ceiling of the temperature control chamber.

Measurement Schedule Summary

There were two modes of data collection during HVS testing: trafficking mode and manual mode. In trafficking mode, there was no need for the HVS wheel to stop, and wheel movements were controlled by a predefined schedule stored in the operating computer. In manual mode, normal HVS trafficking had to be stopped before data collection could start, and the wheel movements were controlled using a hand controller. HVS wheels traveled at 8.6 km/hour (5.3 mph) in trafficking mode and 3.1 km/hour (1.9 mph) in manual mode, with the former referred to as the "full speed" and the latter as "creep speed." The wheel load in trafficking mode was determined by the HVS loading program, and therefore could have only one level at any given time. However, in manual mode, the wheel load typically was set to different levels to evaluate the effect of load level on pavement responses. Some instruments could function only under manual mode, whereas others functioned under both modes. The usage of each instrument in both data collection modes is listed in Table K.7.

Data from thermocouples, JDMDs, and dynamic strain gauges were collected throughout the whole HVS testing in trafficking mode. Data were recorded for every load repetition for the Stage 1 testing (i.e., ST_1.1 and ST_1.2; see Table K.6). For Stage 2 testing, only data from the first six repetitions of each 100 were recorded. Table K.8 and Table K.9 list the data collection schedules of manual data measurements.

The measurement schedule for temperatures was different from that of all the other data in that there were two sets of thermocouples. The set of thermocouples connected to the HVS DAQ system provided temperature data for every data item collected using the DAQ system. In addition, a second set of thermocouples read from a hand thermometer was

Table K.6. Description of Testing Stages

Stage Code	Beginning Repetition	Ending Repetition	Ending ESALs (million)	Wheel Load/Half-Axle Load (kip)	Target Pavement Temperature
ST 1.1	0	7,200	0.013	6.7, 9, 13.5[a]	50°C/122°F
ST_1.2	7,201	14,400	0.027	6.7, 9, 13.5[a]	Ambient
ST_2.1	14,401	100,000	0.113	9 (40 kN)	Ambient
ST_2.2	100,001	200,000	0.580	13.5 (60 kN)	Ambient
ST_2.3	200,001	300,000	1.939	18 (80 kN)	Ambient
ST_2.4	300,001	520,000	9.129	23.5 (100 kN)	Ambient
ST_2.5	520,001	522,000	9.259	27 (120 kN) with single aircraft tire	Ambient

[a] Each load level was maintained for 2,400 repetitions, with 100 repetitions applied at the beginning of each hour.

Table K.7. List of Instruments and Their Usage in Each Data Collection Mode

Instrument	Data Measured	Trafficking Mode	Manual Mode
Thermocouple	Temperature	Yes	Yes
JDMD	Vertical and horizontal joint movements	Yes	Yes
Dynamic strain gauge	Longitudinal strain	Yes	Yes
Laser Profilometer	Surface profile	No	Yes
RSD	Vertical surface deflection	No	Yes
Camera	Surface photographs	No	Yes

used to record pavement and air temperatures at 1-hour intervals during HVS operation.

HVS Test Results for Section 613HB

Introduction

This section provides a summary of the data collected from Section 613HB, the first set of HVS cracking tests. Data collected included air temperatures inside and outside the temperature control chamber, pavement temperatures, dynamic strains in the PCC layer, surface deflections from RSD, joint movements from JDMDs, and surface permanent deformation.

Pavement Temperatures

Pavement temperatures were controlled using the temperature control unit for the first 3 days of testing (Stage 1.1, see Table K.6). After that, the pavement was exposed to the outside environment, with the only temperature control coming from shading of the section by the HVS. Both air (inside and outside the temperature box) and pavement temperatures were monitored and recorded hourly during the entire loading period.

Test Summary

Loading commenced on 02/16/2011 and ended on 03/16/2011. A total of 300,000 load repetitions were applied. The HVS

Table K.8. Manual Data Collection Schedule for Section 613HB

Scheduled Repetition	Surface Profile	Wheel Loads[a] (kip)[b]	Photograph	Actual Repetition	Actual Date
0	Yes	None	Yes	0	2/9/2011
14,400	Yes	9	Yes	na	na
20,000	Yes	9	Yes	20,000	2/28/2011
40,000	Yes	9	Yes	40,000	3/1/2011
60,000	Yes	9	Yes	60,000	3/3/2011
80,000	Yes	9	Yes	80,000	3/4/2011
100,000	Yes	9 and 13.5	Yes	100,000	3/5/2011
120,000	Yes	9 and 13.5	Yes	120,000	3/6/2011
140,000	Yes	9 and 13.5	Yes	140,002	3/7/2011
160,000	Yes	9 and 13.5	Yes	156,002	3/8/2011
180,000	Yes	9 and 13.5	Yes	175,015	3/9/2011
200,000	Yes	9, 13.5, and 18	Yes	203,600	3/11/2011
220,000	Yes	9, 13.5, and 18	Yes	220,020	3/12/2011
240,000	Yes	9, 13.5, and 18	Yes	240,000	3/13/2011
260,000	Yes	9, 13.5, and 18	Yes	260,000	3/14/2011
280,000	Yes	9, 13.5, and 18	Yes	na	na
300,000	Yes	9, 13.5, and 18	Yes	300,002	3/16/2011

[a] Wheel loads were applied for taking RSD, JDMD, and dynamic strain gauge data.

[b] 9 kip = 40 kN; 13.5 kip = 60 kN; 18 kip = 80 kN.

Table K.9. Manual Data Collection Schedule for Section 614HB

Scheduled Repetition	Surface Profile	Wheel Loads[a] (kip)[b]	Photograph	Actual Repetition	Actual Date
0	Yes	None	Yes	0	3/23/2011
7,200	No	6.75, 9, and 13.5	No	7,201	4/15/2011
14,400	Yes	9	Yes	14,401	4/20/2011
20,000	Yes	9	Yes	20,000	4/21/2011
40,000	Yes	9	Yes	40,000	4/22/2011
60,000	Yes	9	Yes	60,000	4/23/2011
80,000	Yes	9	Yes	80,000	4/24/2011
100,000	Yes	9 and 13.5	Yes	100,003	4/25/2011
120,000	Yes	9 and 13.5	Yes	120,006	4/26/2011
140,000	Yes	9 and 13.5	Yes	140,001	4/27/2011
160,000	Yes	9 and 13.5	Yes	160,001	4/28/2011
180,000	Yes	9 and 13.5	Yes	180,003	4/29/2011
200,000	Yes	9, 13.5, and 18	Yes	200,005	4/30/2011
220,000	Yes	9, 13.5, and 18	Yes	220,005	5/1/2011
240,000	Yes	9, 13.5, and 18	Yes	239,007	5/2/2011
260,000	Yes	9, 13.5, and 18	Yes	259,011	5/3/2011
280,000	Yes	9, 13.5, and 18	Yes	280,002	5/4/2011
300,000	Yes	9, 13.5, and 18	Yes	298,402	5/5/2011
320,000	Yes	9, 13.5, 18, and 23.5	Yes	320,001	5/8/2011
340,000	Yes	9, 13.5, 18, and 23.5	Yes	340,007	5/9/2011
360,000	Yes	9, 13.5, 18, and 23.5	Yes	360,012	5/10/2011
380,000	Yes	9, 13.5, 18, and 23.5	Yes	380,000	5/11/2011
400,000	Yes	9, 13.5, 18, and 23.5	Yes	400,003	5/12/2011
420,000	Yes	9, 13.5, 18, and 23.5	Yes	419,510	5/13/2011
440,000	Yes	9, 13.5, 18, and 23.5	Yes	440,013	5/14/2011
460,000	Yes	9, 13.5, 18, and 23.5	Yes	460,018	5/15/2011
480,000	Yes	9, 13.5, 18, and 23.5	Yes	480,018	5/16/2011
500,000	Yes	9, 13.5, 18, and 23.5	Yes	500,000	5/17/2011
520,000	Yes	9, 13.5, 18, 23.5, and 27	Yes	520,000	5/18/2011
522,000	Yes	9, 13.5, 18, 23.5, and 27	Yes	522,066	5/20/2011

[a] Wheel loads were applied for taking RSD, JDMD, and dynamic strain gauge data.

[b] 9 kip = 40 kN; 13.5 kip = 60 kN; 18 kip = 80 kN; 23.5 kip = 100 kN; 27 kip = 120 kN.

loading history for Section 613HB is listed in Table K.6. A summary of the pavement and air temperatures for various stages is listed in Table K.10.

Outside Air Temperatures

Outside air temperatures while the HVS was trafficking are summarized in Figure K.9. Vertical error bars on each point on the graph show the daily temperature range. Daily average temperatures ranged from 42°F to 59°F (5°C to 15°C) during the course of HVS testing. Typical daily variation range was 20°F to 35°F (11 to 19°C).

Air Temperatures in the Temperature Control Unit

The daily average air temperatures recorded in the temperature control unit, calculated from the hourly temperatures recorded during HVS operation, are shown in Figure K.10.

Table K.10. Average and Standard Deviation of Temperatures Measured During HVS Testing

Stage	Quantity	Outside Air (°F)	Inside Air (°F)	Thermocouple Depths below HMA Surface (in.)				
				0 (HMA)	1.0 (HMA)	2.0 (HMA)	2.4 (HMA)	3.5 (PCC)
ST_1.1, 122°F target, 6.7 kip	Average standard deviation (SD)	45.5 3.7	116.4 8.0	123.0 6.0	123.9 4.3	122.6 3.0	121.1 2.6	118.5 1.9
ST_1.1, 122°F target, 9 kip	Average SD	44.2 1.8	90.7 5.7	112.9 11.4	110.9 10.3	109.8 9.7	108.2 9.2	105.9 8.3
ST_1.1, 122°F target, 13.5 kip	Average SD	40.5 1.8	87.0 7.3	113.9 7.5	111.6 6.9	110.5 6.7	108.7 6.5	105.8 6.4
ST_1.2, ambient, 6.7 kip	Average SD	50.2 8.4	55.1 4.8	66.4 9.7	67.7 10.9	71.4 13.0	72.6 13.7	74.7 14.4
ST_1.2, ambient, 9 kip	Average SD	47.4 6.5	49.1 7.9	56.3 7.3	56.5 6.2	58.0 4.8	58.5 4.2	59.7 3.3
ST_1.2, ambient, 13.5 kip	Average SD	48.0 2.1	47.9 1.8	51.8 1.5	52.3 1.2	53.8 1.1	54.4 1.1	56.0 1.2
ST_2.1, ambient, 9 kip	Average SD	52.8 8.3	53.9 8.4	57.6 7.1	57.3 6.1	57.7 4.8	57.7 4.3	58.1 3.6
ST_2.2, ambient, 13.5 kip	Average SD	55.0 6.9	55.8 6.9	59.5 5.4	59.4 4.7	60.0 3.6	60.1 3.2	60.7 2.6
ST_2.3, ambient, 18 kip	Average SD	56.1 5.3	57.5 6.0	61.6 5.3	61.5 4.4	62.2 3.5	62.3 3.0	62.9 2.4

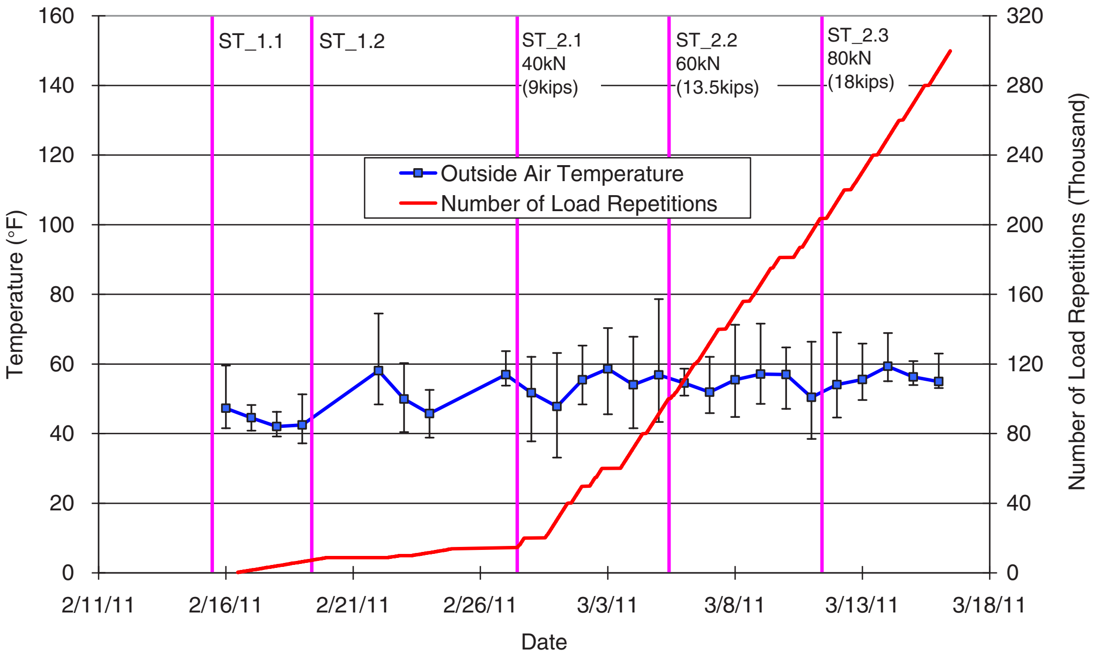

Figure K.9. Section 613HB: Daily average outside air temperatures during HVS trafficking.

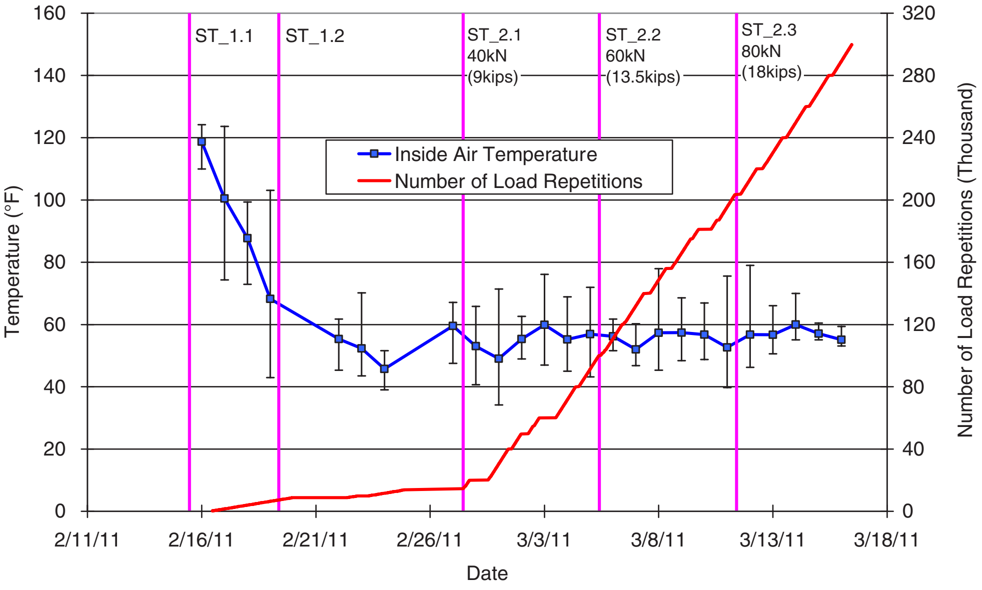

Figure K.10. Section 613HB: Daily average inside air temperatures during HVS trafficking.

Vertical error bars on each point on the graph show the daily temperature range. During the test, air temperatures inside the temperature control unit ranged from 68°F to 119°F (20°C to 48°C) for Stage 1.1 when the target pavement temperature was 122°F (50°C), and ranged from 46°F to 60°F (8°C to 16°C) for the rest of the test when pavement temperature was not controlled (i.e., determined by ambient temperature).

Temperatures in the Pavement

Daily averages of the surface and in-depth pavement temperatures are shown in Figure K.11. Pavement temperatures at different depths were similar.

Visual Inspection

Figure K.12 shows the top view of the section surface at the end of the test for Section 613HB. Fatigue distress in an HMA/PCC composite pavement manifests itself in the form of surface cracks. Crack monitoring was an essential component of the data collection program. This monitoring entailed the following:

- Visual inspections of the test section and marking of visible cracks;
- Photographic documentation of the marked cracks;
- Correction of the photographs for camera angle;
- Digitization of the crack traces; and
- Calculation of the crack length.

The pavement surface was photographed during the test when profilometer data were taken. Each of the photographs covers only 0.5 m (1.6 ft) of the section in the longitudinal direction and includes cracks traced with crayon.

Cracks traced on the HMA surface at selected points of the HVS testing are shown in Figure K.13. Reflection cracking from underlying joints was first observed after 140,000 load repetitions (0.34 million ESALs) over both joints. Slab cracking as evidenced by reflection of the cracked slab to the surface of the HMA was first observed after 260,000 load repetitions (1.72 million ESALs). Although it was not observed, it is believed that all of the surface cracks had reached the edge of the slab.

According to Figure K.13, surface cracks appeared in the following sequence:

1. Cracks that were reflected from the underlying joints.
2. Cracks that were reflected from the first fatigue crack in the PCC, which is located at the southeast corner of the middle slab. The point where this crack intersects the longitudinal centerline of the test section is 4.2 ft (1.27 m) north of Joint J4.
3. Cracks that were reflected from a second fatigue crack in the PCC slab, which intersects the longitudinal centerline of the test section about 6.6 ft (2.0 m) south of Joint J5.

Surface Rut

Figure K.14 shows the average change in transverse cross section measured with the Laser Profilometer at various stages of the test. This plot clearly shows a slight increase in rutting

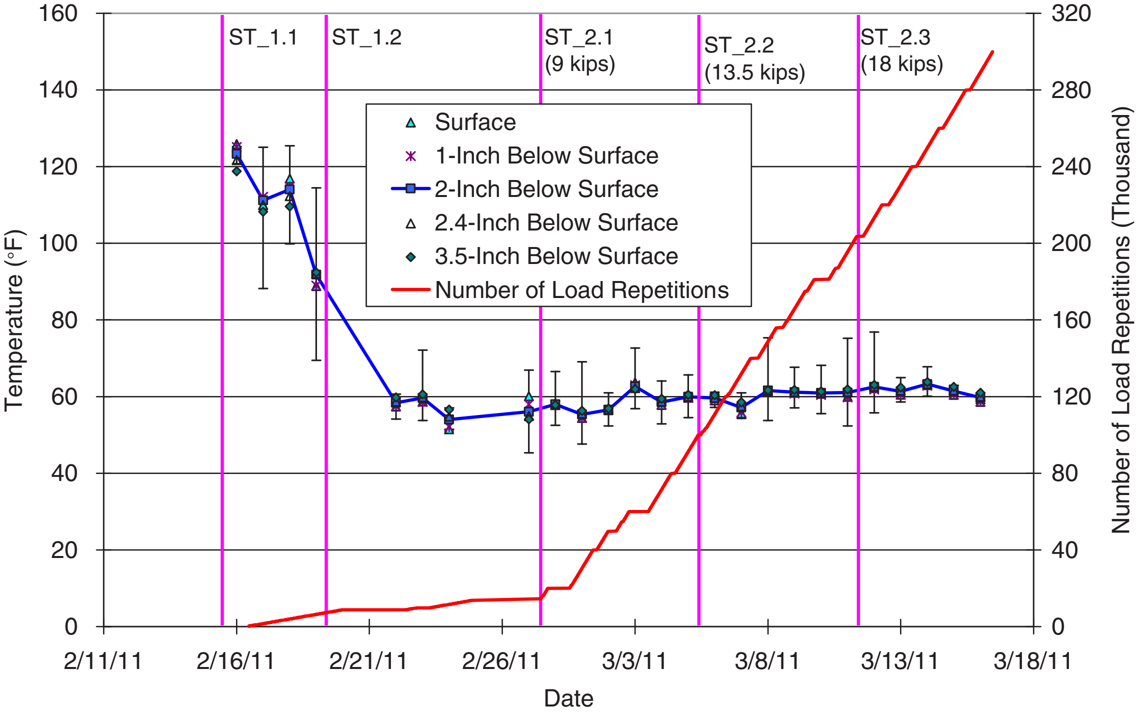

Figure K.11. Section 613HB: Daily average temperatures at pavement surface (i.e., top of HMA layer) and various depths during HVS trafficking. The last thermocouple measures PCC temperature.

after the first 20,000 load repetitions but significant tilting of the underlying slab for the duration of the test. Profile measurements were not symmetric with respect to the wheelpaths because the test section was located at the edge of the slab. The tilting was caused by cracking in the underlying PCC slab. The repetition at which the tilting increased significantly was between 203,600 and 240,000 repetitions.

During HVS testing, rutting usually occurs at a high rate initially, and then it typically diminishes as trafficking progresses until reaching a steady state. This initial phase is referred to as the "embedment" phase. Figure K.15 shows the development of permanent deformation with load repetitions as measured with the Laser Profilometer for the test section, with an embedment phase apparent only at the beginning of the experiment (i.e., first 20,000 repetitions). Error bars on the average reading indicate that there was very little variation along the length of the section until the very end of the test.

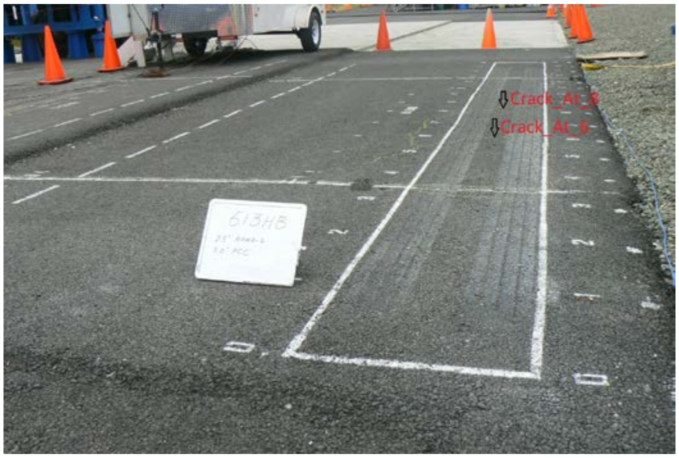

Figure K.12. Section photograph at test completion for Section 613HB, along with labels for cracks.

Figure K.16 and Figure K.17 show contour plots of the pavement surface at the end of the test (300,000 repetitions), indicating that tilting occurred mostly between Stations 2 and 8. After trafficking was completed, the average maximum rut depth was 10.0 mm (0.4 in.). The maximum rut depth measured on the section was 14.1 mm (0.55 in.), recorded at Station 3.

Elastic Response under Manual Mode

Elastic (recoverable) response provides an indication of the overall stiffness of the pavement structure and, therefore, a measure of the load-carrying capacity. As the stiffness of a pavement structure deteriorates, its ability to resist the deformation/deflection/strain caused by a given load and tire pressure decreases. During HVS testing, elastic surface deflections are measured with two instruments: the road surface deflectometer (RSD) and the joint deflection measuring device (JDMD). In

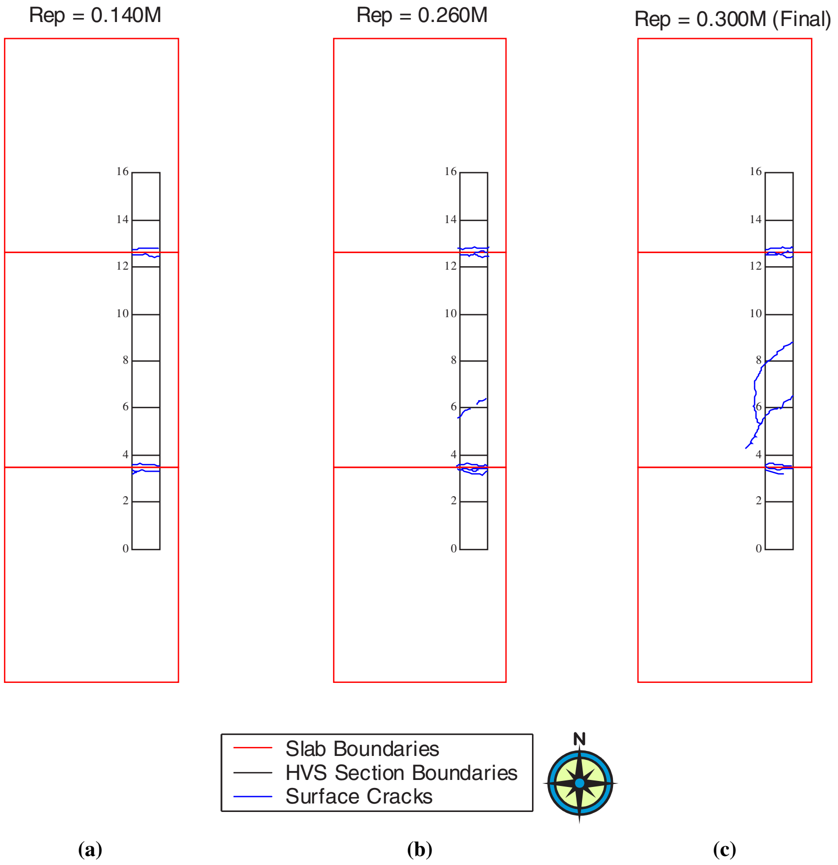
Rep = 0.140M
Rep = 0.260M
Rep = 0.300M (Final)
16
14
12
10
8
6
4
2
0
Slab Boundaries
HVS Section Boundaries
Surface Cracks
N
(a)
(b)
(c)

Figure K.13. Top views of surface cracks after different numbers of load repetitions: (a) Repetition = 0.14 million and crack length = 2.5 m (8.3 ft); (b) repetition = 0.26 million and crack length = 4.4 m (14 ft); and (c) repetition = 0.30 million and crack length = 6.4 m (21 ft).

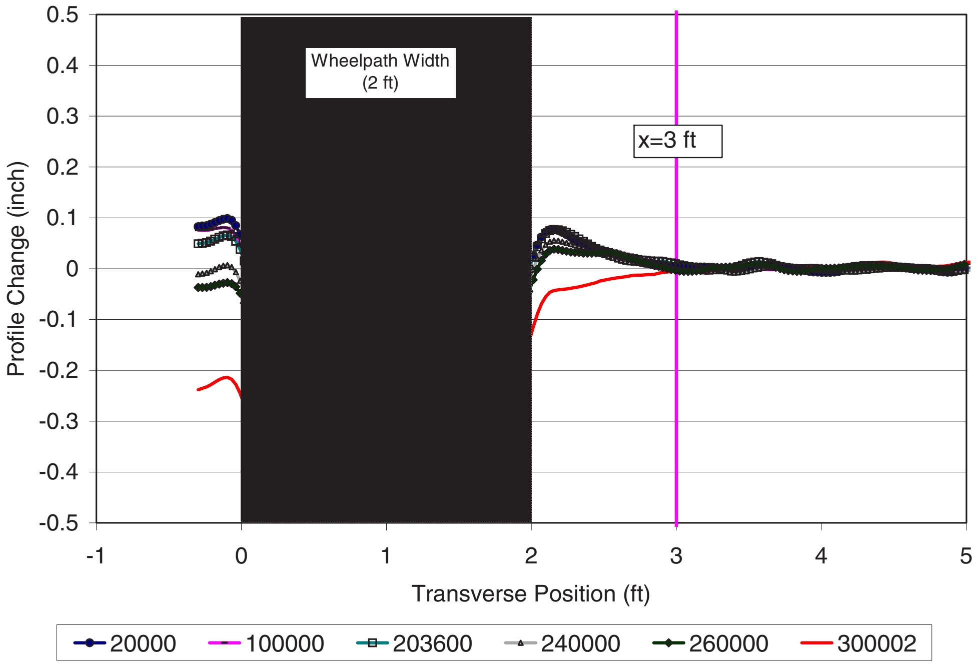

Figure K.14. Average profilometer cross section at various load repetitions for Section 613HB.

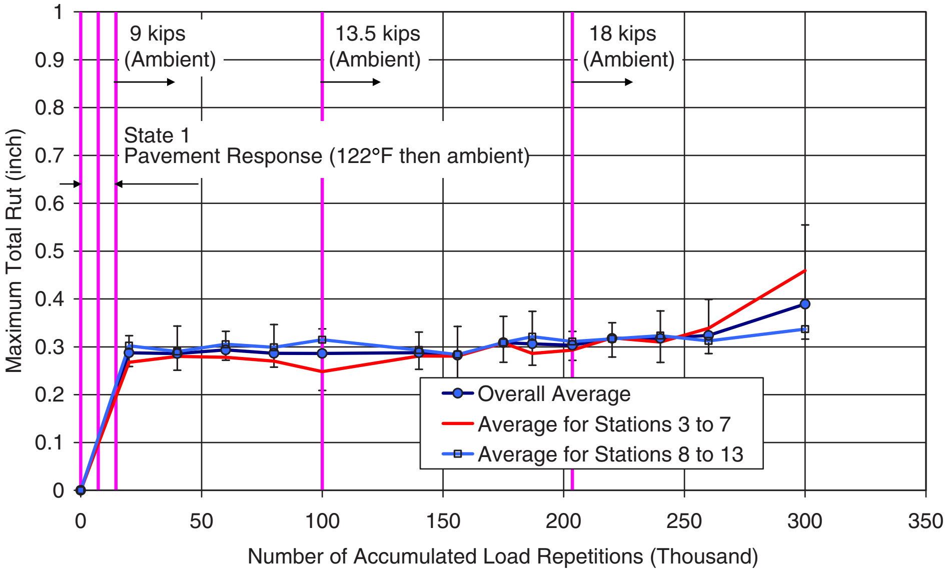

Figure K.15. Development of maximum total rut for Section 613HB.

addition to RSD and JDMD measurements, dynamic strain gauges are used to measure longitudinal strain at the bottom and top of the PCC layer caused by HVS wheel loads.

Surface Elastic Deflection from RSD

In this section, surface deflections as measured by the RSD under a load of 9 kip (40 kN) are summarized. Although the load increased during the test program, deflection measurements were always taken with a 9-kip (40 kN) load.

Table K.11 compares the average 40-kN RSD deflections for locations J4–, J4+, 8CL, J5–, and J5+ before and on completion of testing (see Figure K.4, Figure K.5, and Table K.4 for their locations). Figure K.18 shows the change of RSD peak deflections with accumulated number of load repetitions. RSD deflections were found to increase to a maximum

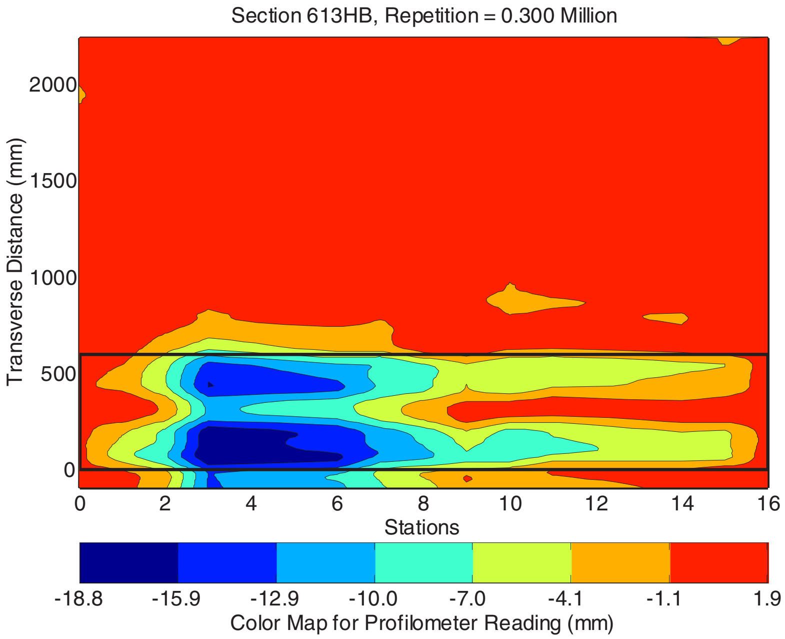

Figure K.16. Two-dimensional contour plot of change in surface elevation relative to untrafficked condition at end of test for Section 613HB (1 in. = 25.4 mm).

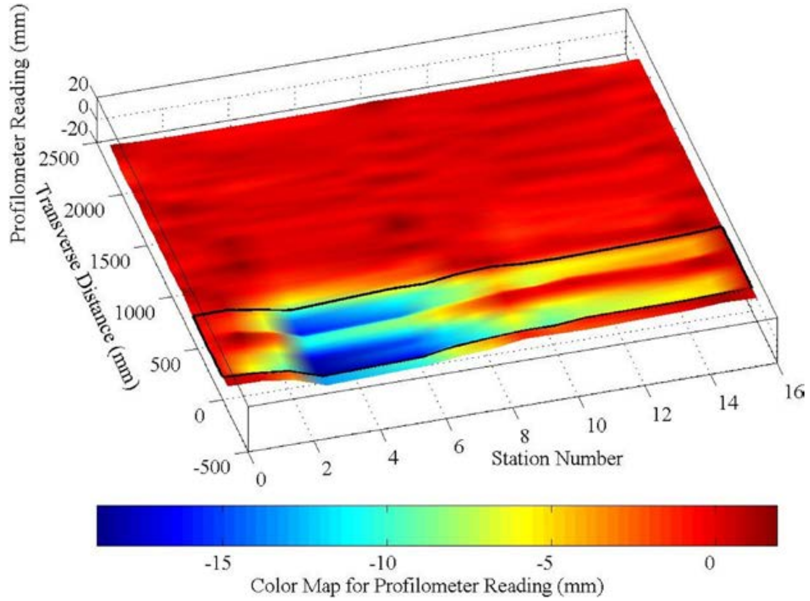

Figure K.17. Three-dimensional contour plot of change in surface elevation relative to the untrafficked condition at the end of the test for Section 613HB (1 in. = 25.4 mm).

value then decrease significantly before increasing again. This is why "maximum during trafficking" is shown in Table K.11.

RSD deflections measured at the center of the slab (location 8CL) generally were less than those measured near the two joints. Deflections near Joint J4 generally were higher than the ones near Joint J5, indicating either weaker structure or weaker aggregate interlock for the PCC layer at Joint J4 compared with Joint J5. During the course of the test, substantial damage occurred on the HMA layer and the PCC slab over the entire section under HVS trafficking. This is confirmed by the ratio of peak-to-initial deflections for all RSD locations, which show that surface deflections increase by two times for locations near joints and four times for the center of slab.

Table K.11. Section 613HB: Average 9-kip RSD Deflections Before and After Testing

Position	Deflection (mil)			
	Before Trafficking	Maximum During Trafficking	After Trafficking	Ratio of Peak/Initial
J4–	27.4	60.5	39.8	2.2
J4+	22.6	44.8	41.8	2.0
8CL	7.4	28.9	28.9	3.9
J5–	18.6	40.2	31.7	2.2
J5+	19.1	42.3	20.3	2.2

Note: Nine (9) kip equal 40 kNK.

During the course of the test, surface deflections measured at the middle of the slab increased monotonically but showed a significant decrease after reaching peak values, compared with those measured near joints. The significant deflection drop signifies structural change near the joints and is discussed further in this section.

The deflection bowls at the different locations at test start, load change intervals, and test completion are shown in Figures K.19 to K.22, all of which use the same scale. The wheel position shown in these figures corresponds to the *x*-coordinate shown in Figure K.2. The deflections generally increase over time. Note that the shape of the RSD deflection bowls as the wheel rolls approaching the RSD location (essentially influence lines) also change over time, which again indicates structural changes that are likely related to cracking in the HMA layer and the underlying PCC slab.

Elastic Deflections from JDMD

The schedule of JDMD measurements with various test loads for Section 613HB is listed in Table K.8. Only limited data were collected at 13.5-kip (60-kN) and 18-kip (80-kN) test loads, so the following discussion focuses on results obtained with the 9-kip (40-kN) load, which were collected throughout the HVS loading. Table K.12 and Figures K.23 through K.29 summarize the elastic deflections measured at each side of each joint by JDMDs. The figures also include RSD measurements taken on the surface at the same side of each joint as the JDMDs. Similar to RSD deflections, JDMD deflections

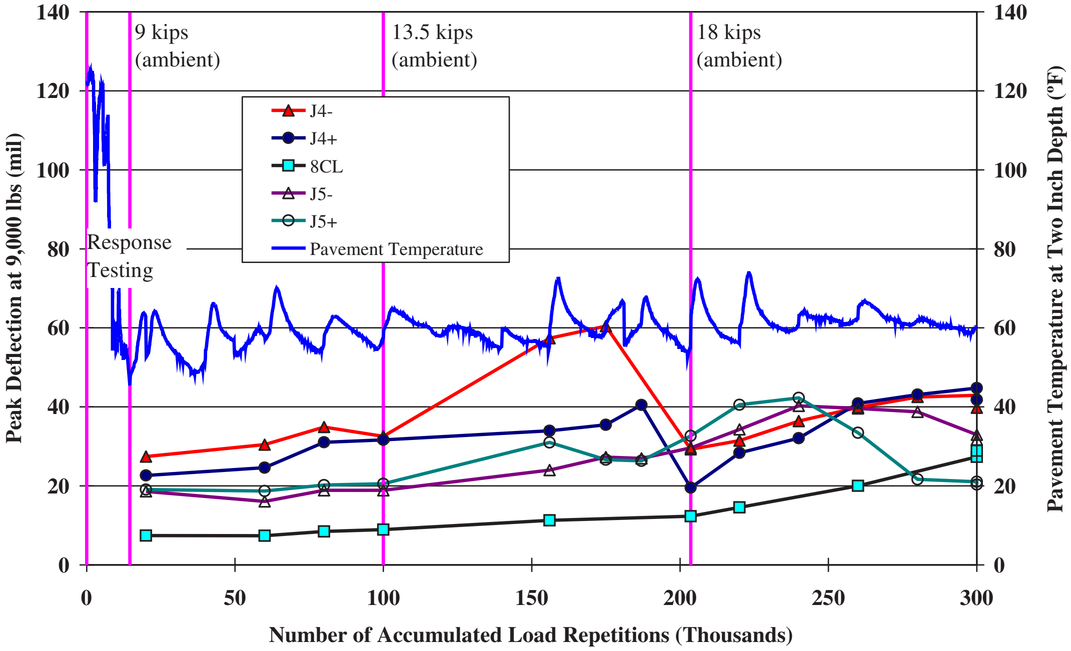

Figure K.18. Section 613HB: RSD surface deflections with 9-kip (40-kN) test load for each location.

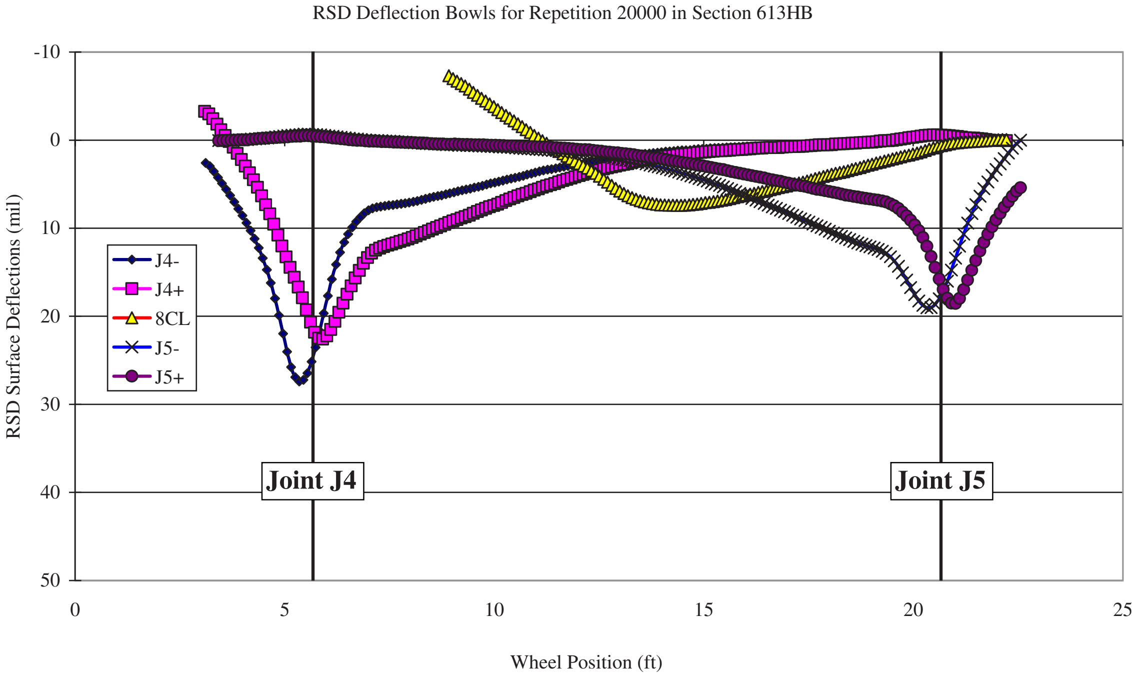

Figure K.19. Section 613HB: RSD deflections at different locations with 9-kip (40-kN) test load at 20,000 repetitions (when the trafficking load changed from 40 to 60 kN).

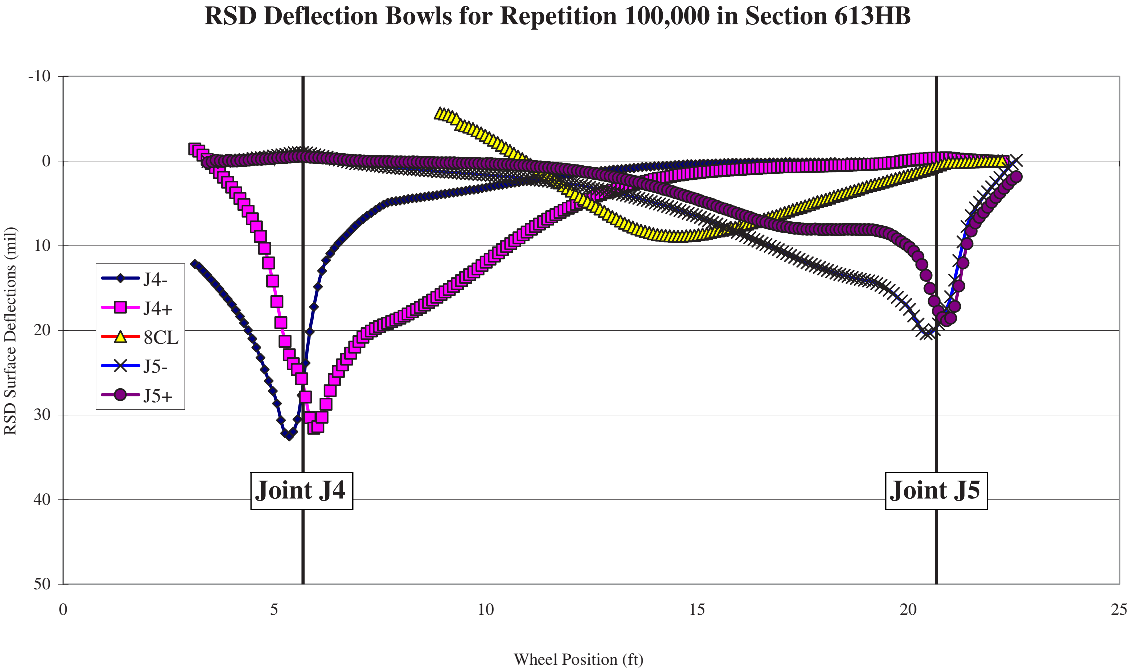

Figure K.20. Section 613HB: RSD deflections at different locations with 9-kip (40-kN) test load after 100,000 repetitions (when the trafficking load changed from 40 to 60 kN).

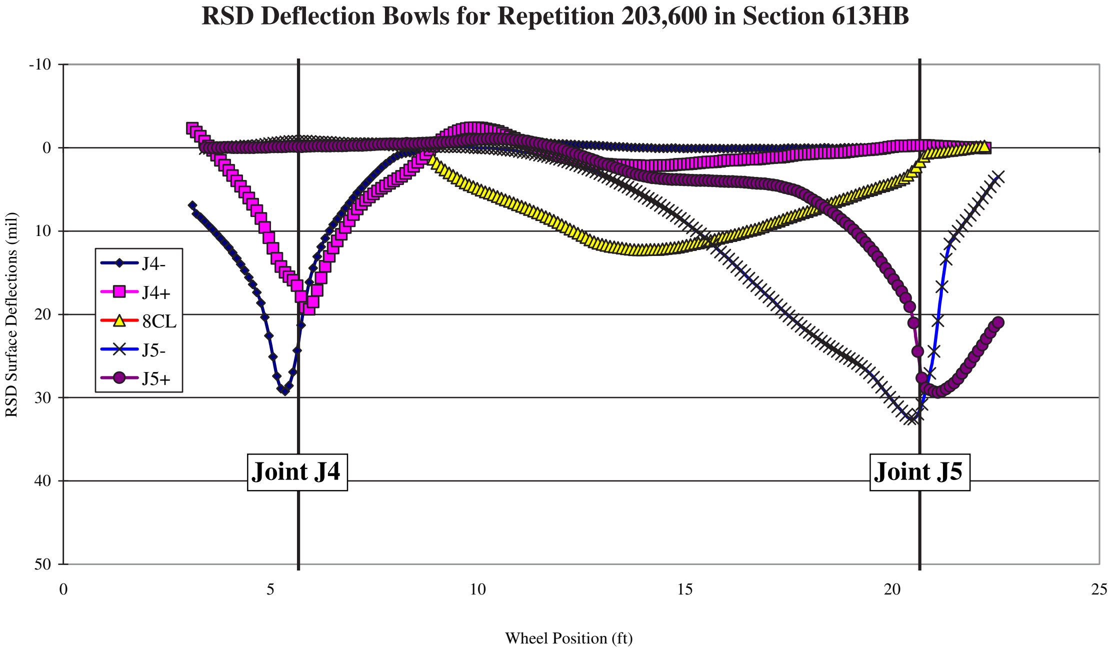

Figure K.21. Section 613HB: RSD deflections at different locations with 9-kip (40-kN) test load after 203,600 repetitions (when the trafficking load changed from 60 to 80 kN).

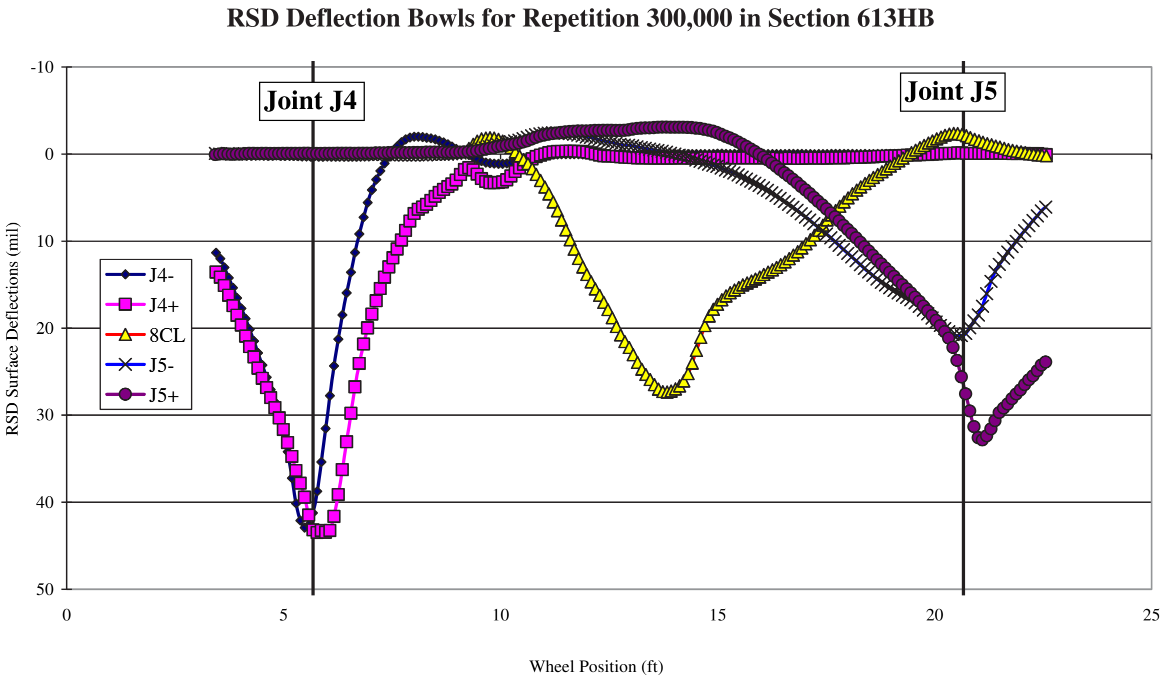

Figure K.22. Section 613HB: RSD deflections at different locations with 9-kip (40-kN) test load at test completion.

Table K.12. Section 613HB: Average 9-kip (40-kN) Elastic Deflections Before and After Testing

Position	Deflection (mil)			
	Before Trafficking	Maximum During Trafficking	After Trafficking	Ratio of Peak/Initial
JDMD No. 1: J5, edge, horizontal	3.0	10.0	6.5	3.3
JDMD No. 2: J5–, edge, vertical, AC	17.7	54.9	20.3	3.1
JDMD No. 3: J5–, edge, vertical	22.8	64.3	18.2	2.8
JDMD No. 4: J4, inner, horizontal	2.5	8.8	8.0	3.5
JDMD No. 5: J5+, edge, vertical	19.5	67.7	38.9	3.5
JDMD No. 6: J5+, inner, vertical	10.1	38.9	27.9	3.8
JDMD No. 7: J5+, inner, vertical, AC	7.6	26.9	15.6	3.5
JDMD No. 8: J5–, inner, vertical	12.9	41.7	20.4	3.2
JDMD No. 9: J4+, inner, vertical, AC	9.1	18.6	2.7	2.0
JDMD No. 10: J4+, inner, vertical	18.9	35.9	26.2	1.9
JDMD No. 11: J4–, inner, vertical	21.2	50.3	34.1	2.4
JDMD No. 12: J4–, edge, vertical	37.5	83.5	38.0	2.2
JDMD No. 14: J4–, edge, vertical, AC	29.4	79.0	20.5	2.7

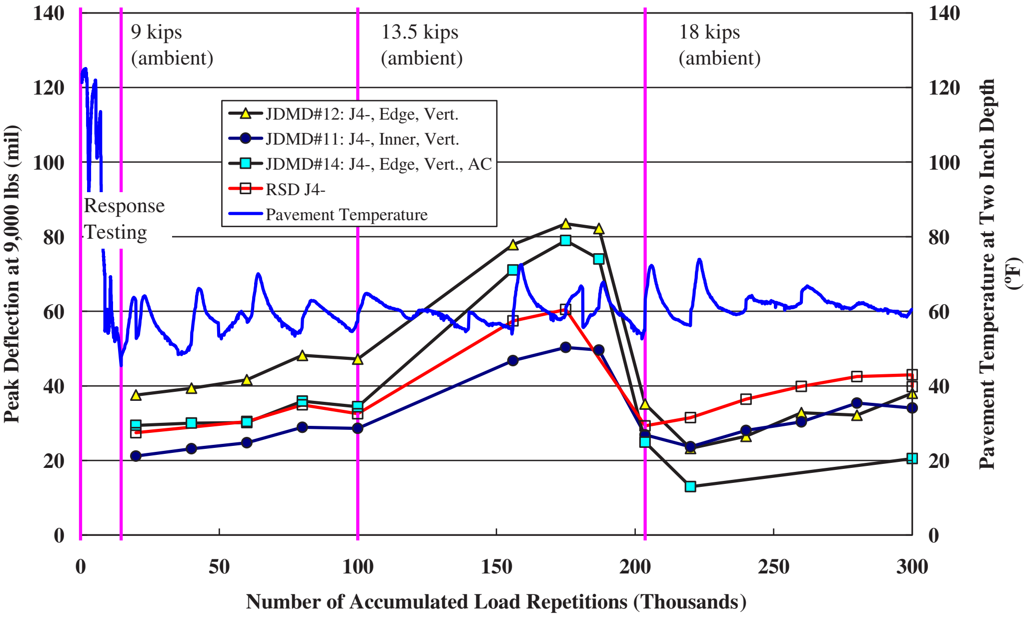

Note: AC indicates that a JDMD is installed on HMA surface.

Figure K.23. Section 613HB: Vertical elastic deflections at south side of Joint J4 with 9-kip (40-kN) test load.

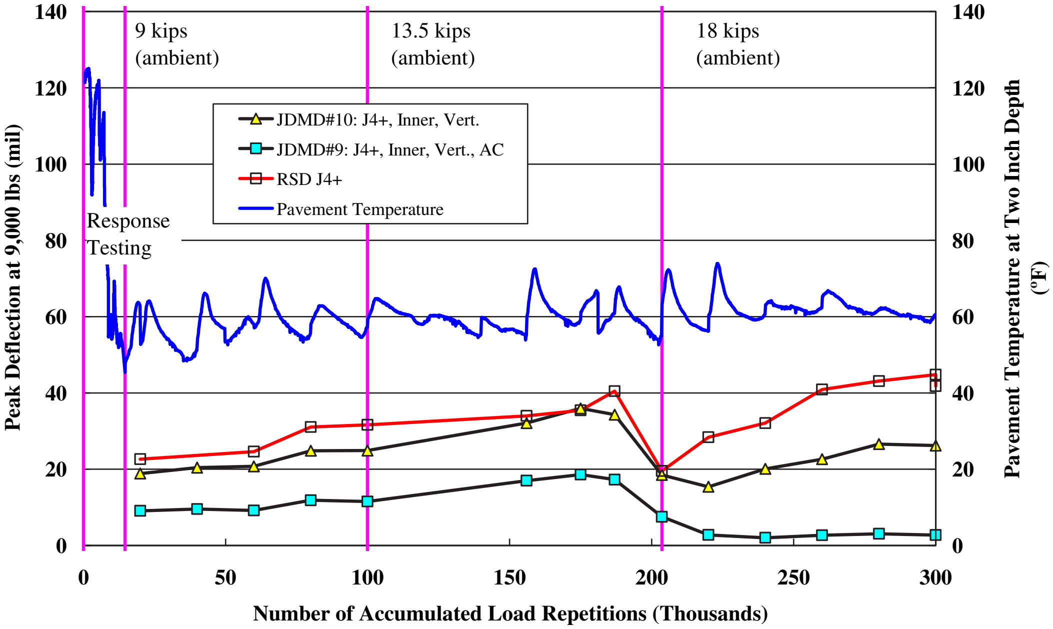

Note: AC indicates that a JDMD is installed on HMA surface.

Figure K.24. Section 613HB: Vertical elastic deflections at north side of Joint J4 with 9-kip (40-kN) test load.

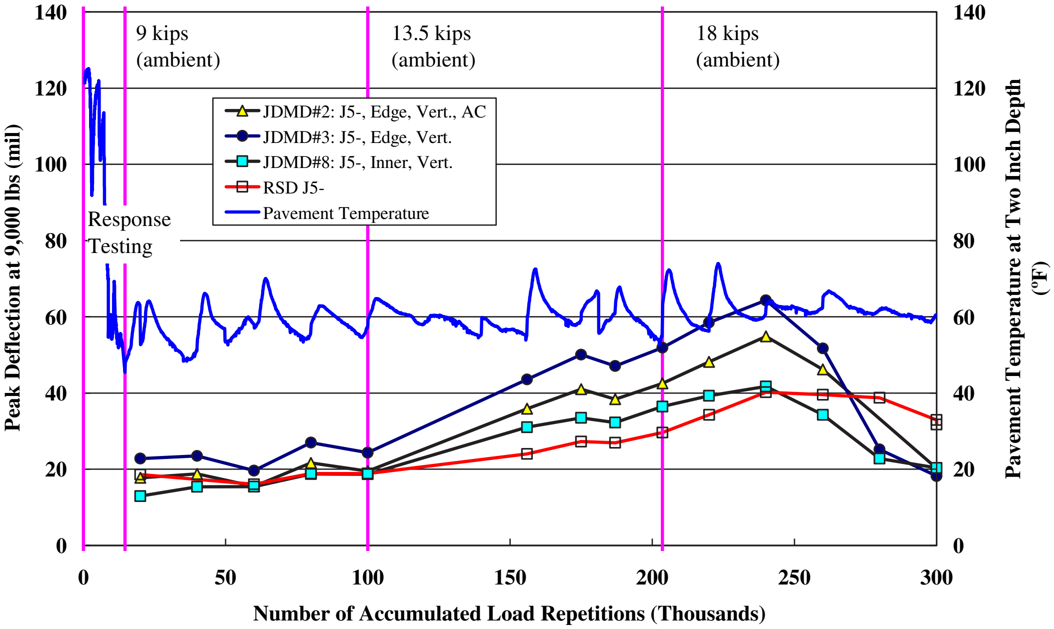

Note: AC indicates that a JDMD is installed on HMA surface.

Figure K.25. Section 613HB: Vertical elastic deflections at south side of Joint J5 with 9-kip (40-kN) test load.

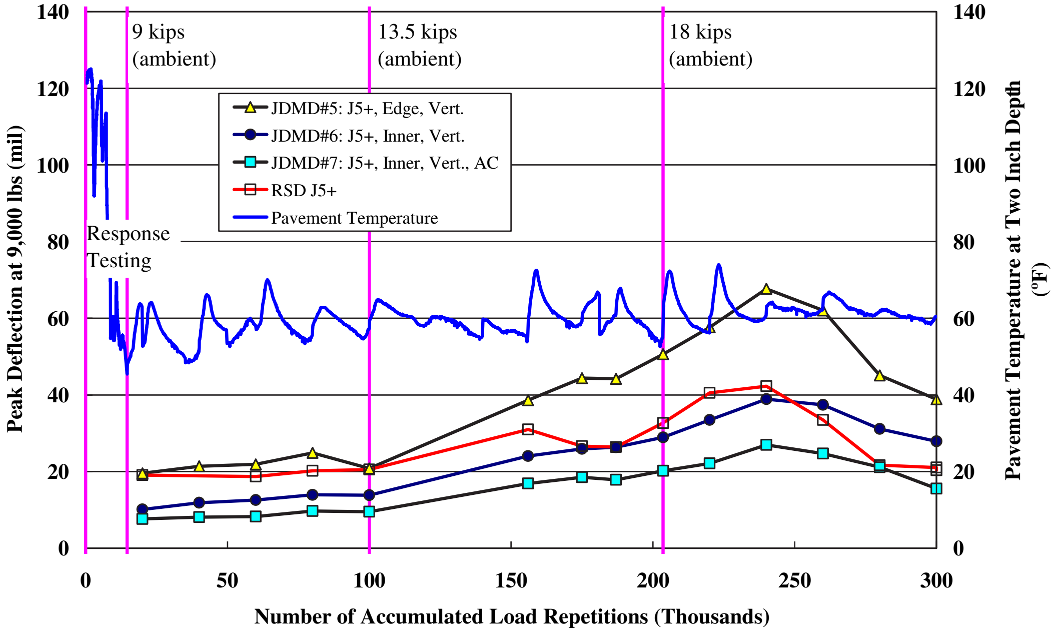

Note: AC indicates that a JDMD is installed on HMA surface.

Figure K.26. Section 613HB: Vertical elastic deflections at north side of Joint J5 with 9-kip (40-kN) test load.

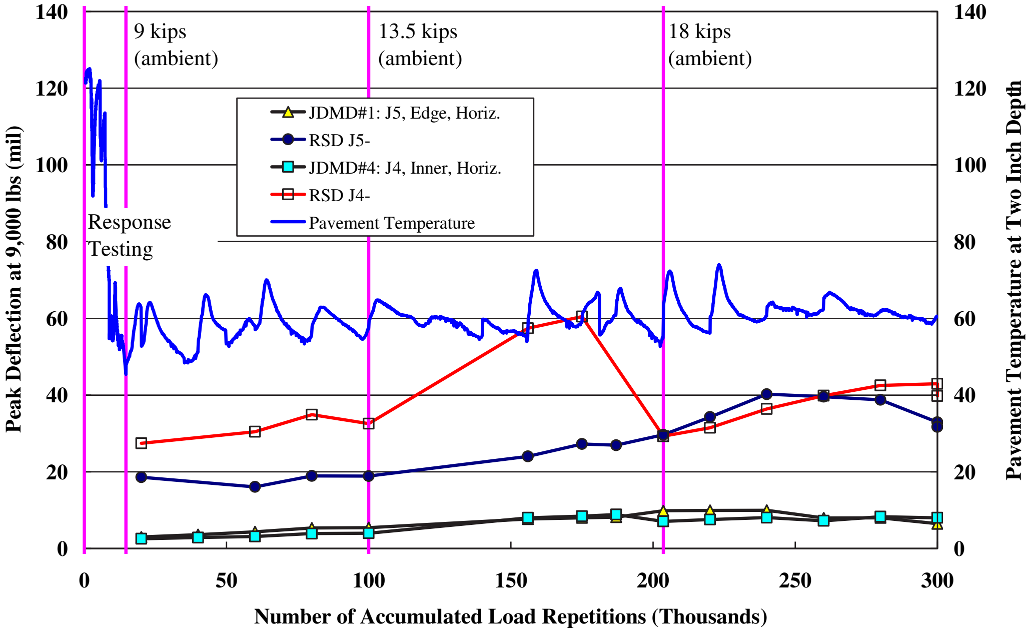

Note: AC indicates that a JDMD is installed on HMA surface.

Figure K.27. Section 613HB: Horizontal elastic deflections at Joints J4 and J5 with 9-kip (40-kN) test load.

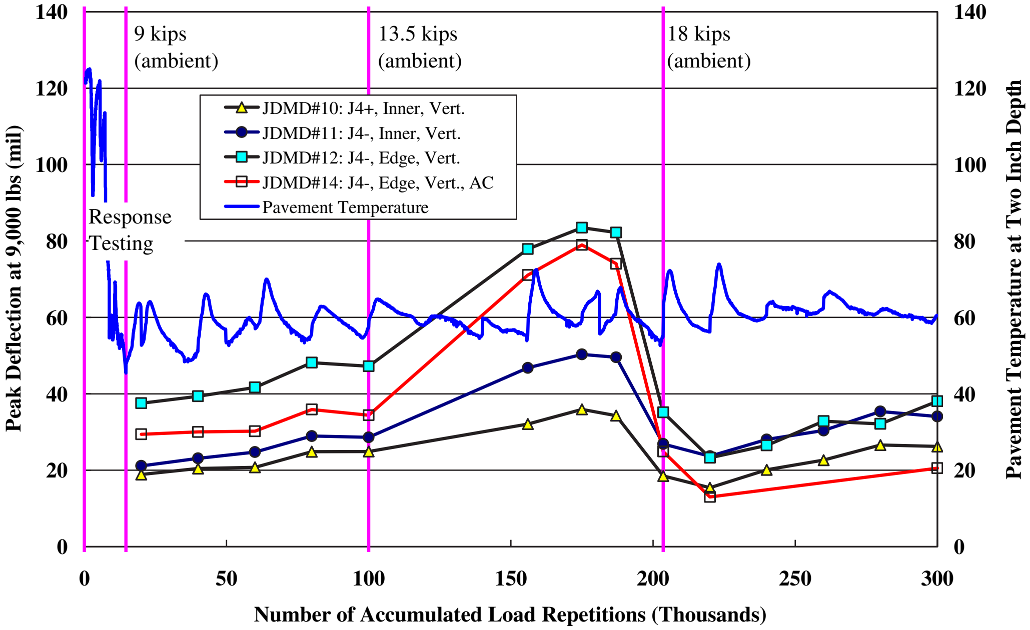

Note: AC indicates that a JDMD is installed on HMA surface.

Figure K.28. Section 613HB: Vertical elastic deflections at Joint J4 with 9-kip (40-kN) test load.

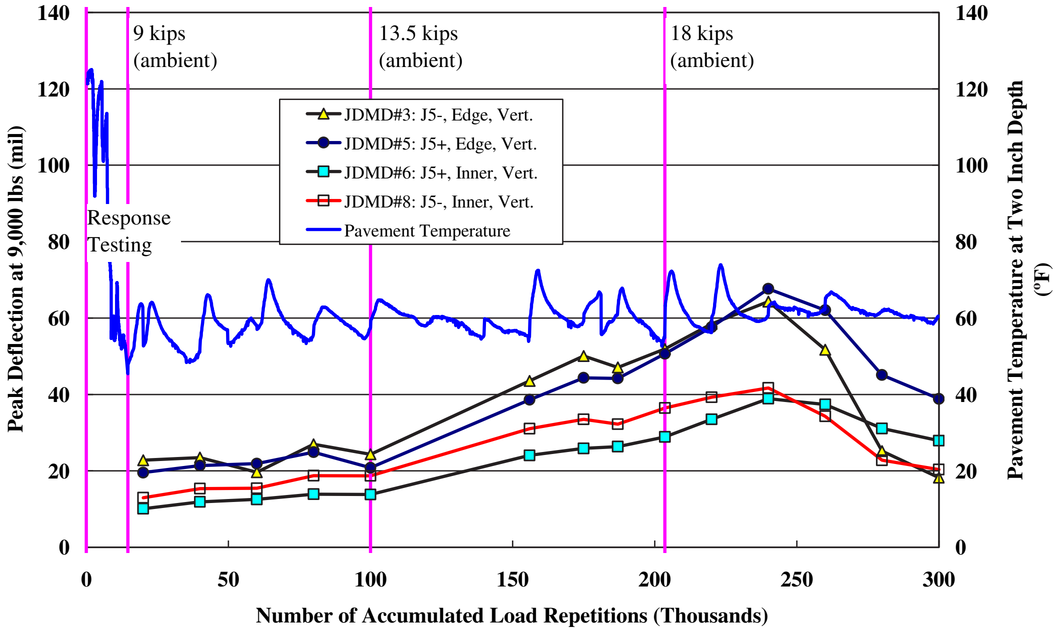

Note: AC indicates that a JDMD is installed on HMA surface.

Figure K.29. Section 613HB: Vertical elastic deflections at Joint J5 with 9-kip (40-kN) test load.

were found to increase to a maximum value then decrease significantly before increasing again. This is why "maximum during trafficking" is shown in Table K.12.

Elastic PCC Strains from Dynamic Strain Gauge

Both dynamic strain gauges in the PCC slabs stopped working at Repetition 131,130, which is before the first pavement response data collection in manual mode. As a result, there are no elastic PCC dynamic strain data available for Section 613HB under manual mode.

Elastic Response Under Trafficking Mode

Similar to the elastic responses under manual mode, elastic responses under trafficking mode reflect pavement structural integrity. Continuous elastic response data from JDMD and dynamic strain gauges under trafficking mode record the pavement structure deterioration process.

Elastic Deflections from JDMD

As mentioned in the section on measurement schedule summaries, JDMD data were recorded for every load repetition in Stage 1 (response testing) and every 100 repetitions afterward. These deflections correspond to the HVS trafficking load, which was increased step by step during Stage 2 of the HVS test.

Figures K.30 through K.36 summarize the elastic deflections measured at each side of each joint by JDMDs in trafficking mode. The figures also include RSD measurements taken on the surface on the same side of each joint as the JDMDs at the same wheel load but at creep speed. Note that in these figures only one data point is plotted for every 1,000 load repetitions to make the plots readable. In addition, there were stoppages in HVS trafficking during the testing, which resulted in jumps in temperature readings.

From the measured JDMD deflections, the following observations can be made:

- Elastic deflections in general increase with the number of load repetitions, indicating deterioration of pavement structure caused by HVS trafficking.
- Elastic deflections increase when pavement temperature decreases. HMA layer stiffness increases with temperature, which indicates that elastic deflections are not controlled by the HMA layer and that PCC slab curling is the main factor that controls JDMD elastic deflections.
- RSD deflections share the same trends as corresponding JDMDs.
- There are multiple occasions when vertical JDMD elastic deflections decrease significantly when there is no change in pavement temperature and HVS trafficking load. A list of these events is shown in Table K.13. These events are most likely caused by cracking in either the HMA layer or in the underlying PCC layer.
- The inner JDMDs show less elastic deflections than do the corresponding edge JDMDs, both in terms of absolute values and daily variations.

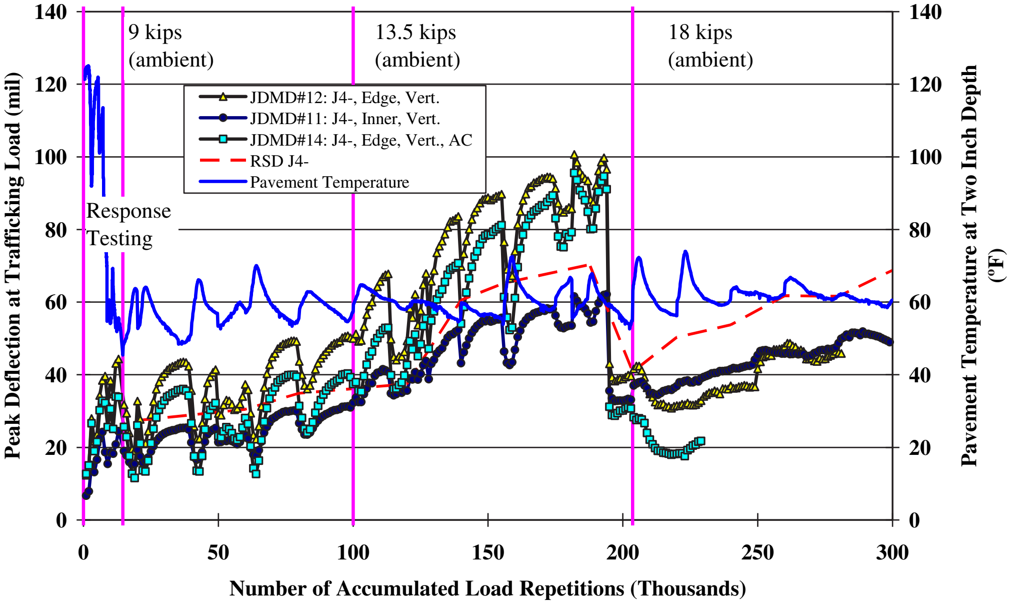

Note: AC indicates that a JDMD is installed on HMA surface.

Figure K.30. Section 613HB: Vertical elastic deflections at south side of Joint J4 with trafficking load.

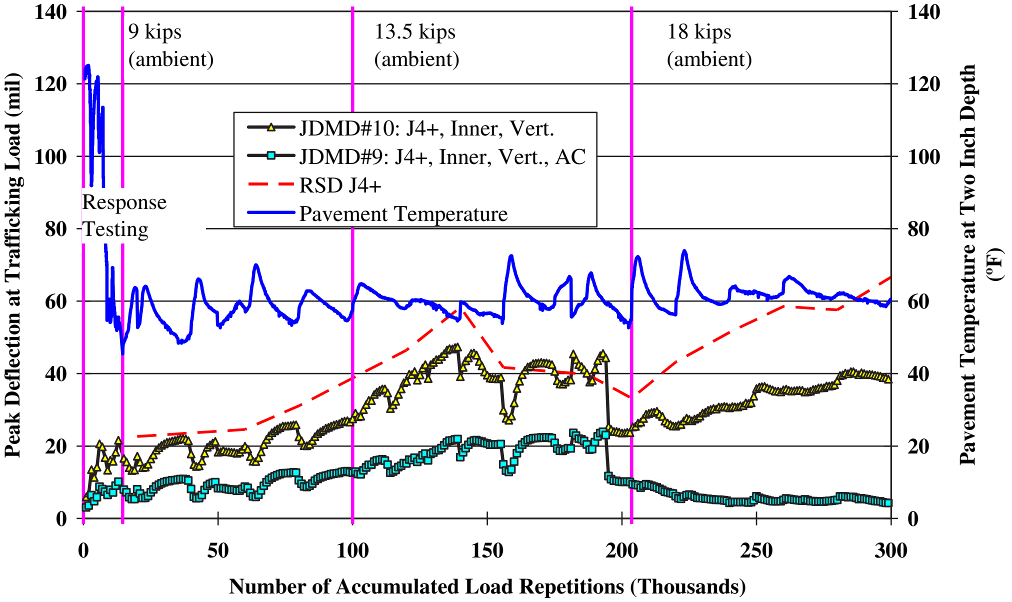

Note: AC indicates that a JDMD is installed on HMA surface.

Figure K.31. Section 613HB: Vertical elastic deflections at north side of Joint J4 with trafficking load.

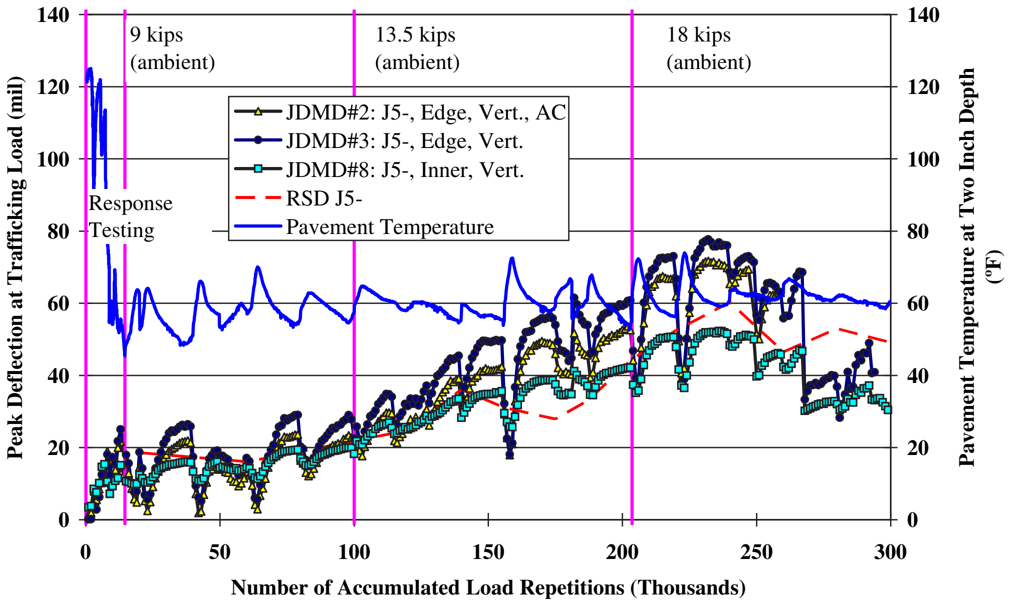

Note: AC indicates that a JDMD is installed on HMA surface.

Figure K.32. Section 613HB: Vertical elastic deflections at south side of Joint J5 with trafficking load.

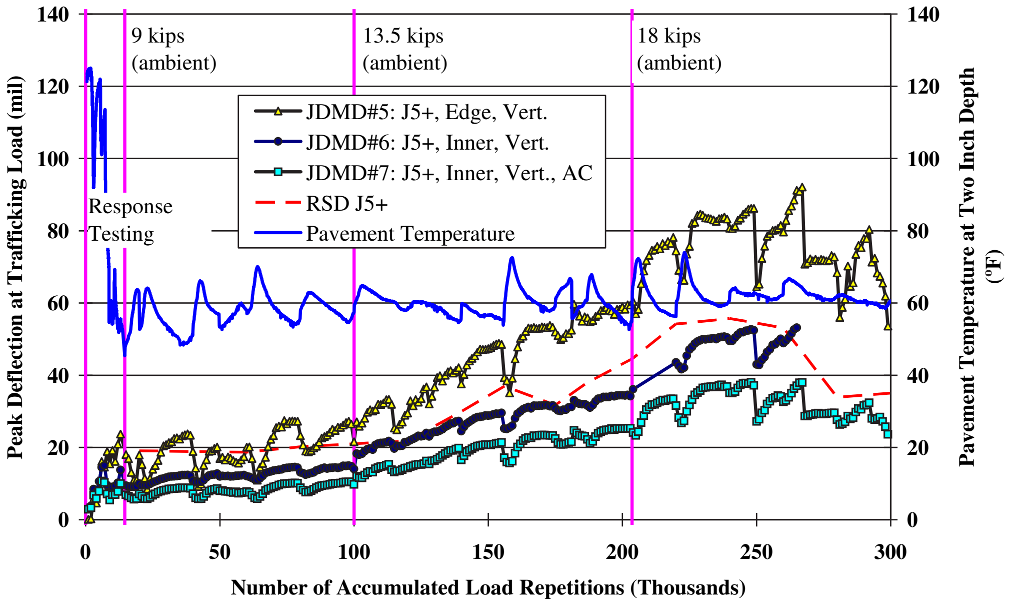

Note: AC indicates that a JDMD is installed on HMA surface.

Figure K.33. Section 613HB: Vertical elastic deflections at north side of Joint J5 with trafficking load.

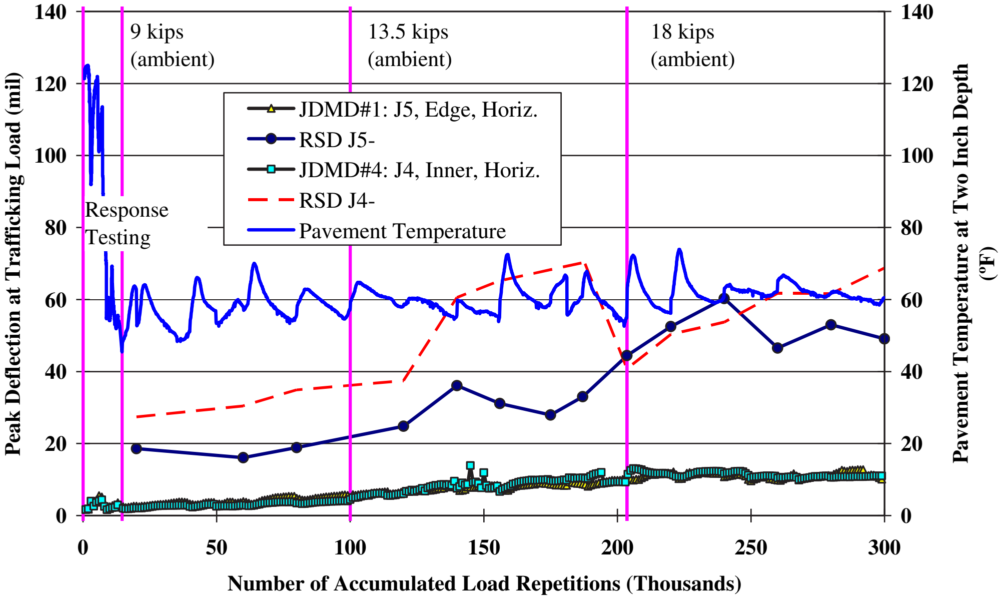

Note: AC indicates that a JDMD is installed on HMA surface.

Figure K.34. Section 613HB: Horizontal elastic deflections at Joints J4 and J5 with trafficking load.

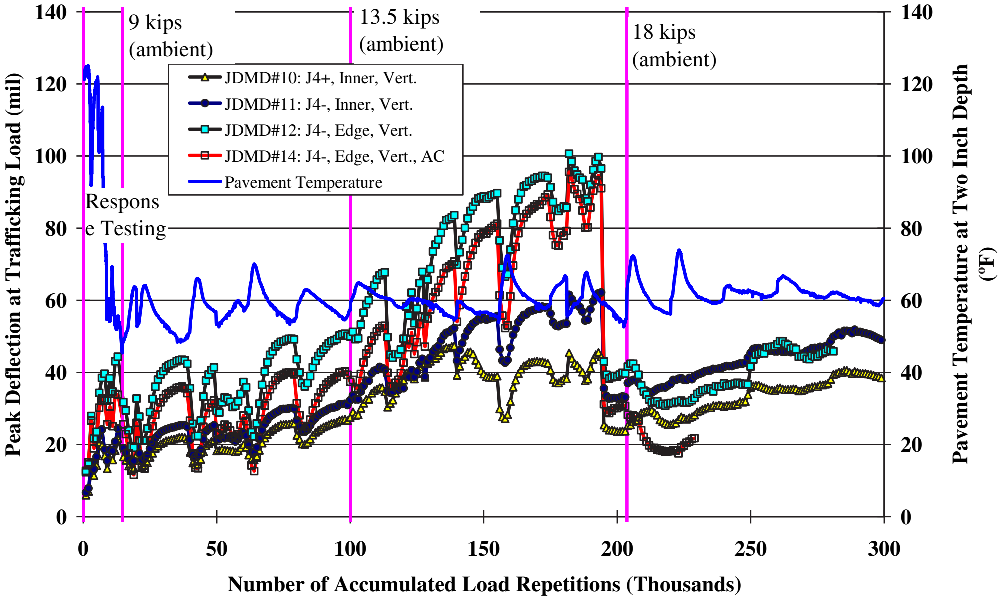

Note: AC indicates that a JDMD is installed on HMA surface.

Figure K.35. Section 613HB: Vertical elastic deflections at both sides of Joint J4 with trafficking load.

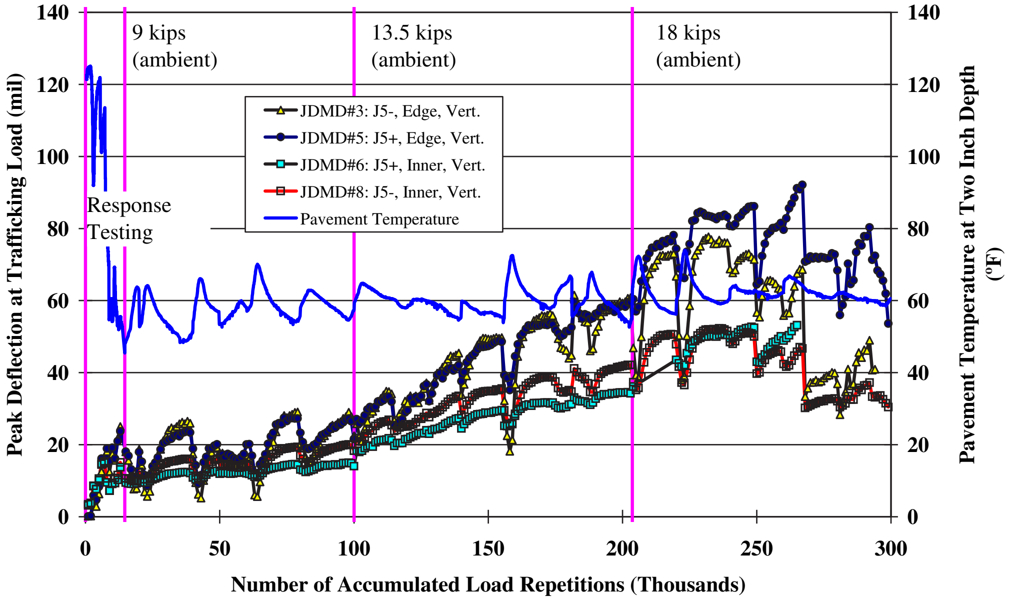

Note: AC indicates that a JDMD is installed on HMA surface.

Figure K.36. Section 613HB: Vertical elastic deflections at both sides of Joint J5 with trafficking load.

Selected deflection bowls for each JDMD are shown in Figures K.37 through K.49. These figures show deflection bowls for the initial reading (after 3,000 repetitions), after the Stage 1 response test, and before and after each of the relevant displacement jump events listed in Table K.13.

Combining the information regarding the appearance of PCC cracks at the surface of the HMA and locations shown in Figure K.13, the displacement jump events listed in Table K.13 are interpreted as:

- Event 1 at Repetition 114,000 should correspond to reflection cracking failure over Joint J4 even though there are no significant changes in deflection bowl shapes, considering that surface cracks are observed over Joint J4 after 140,000 load repetitions.
- Event 2 at Repetition 115,000 should correspond to reflection cracking failure over Joint J5 based for a reason similar to that for Event 1. The fact that reflection cracking life at Joint J5 is longer than at Joint J4 is consistent with the observation that RSD deflections are higher at Joint J4 than at Joint J5 (see the section on surface elastic deflection from RSD).
- Event 3 at Repetition 195,000 should correspond to the first fatigue cracking (i.e., Crack_At_6 in Figure K.12) of the PCC slabs at 195,000 repetitions at the southeast corner of the slab near Joint J4.

Table K.13. Section 613HB: List of Displacement Jump Events for Vertical JDMDs

Event Number	Repetition	JDMDs	Average Peak Deflections		
			Before (mil)	After (mil)	Decrease (%)
1	114,000	All JDMDs near Joint J4[a]	42.2	33.5	21
2	115,000	All JDMDs near Joint J5[b]	26.0	21.8	16
3	195,000	All JDMDs near Joint J4	63.4	29.4	54
4	250,000	All JDMDs near Joint J5	59.4	46.2	22
5	268,000	All JDMDs near Joint J5[c]	61.3	40.7	34

[a] All vertical JDMDs near Joint J4 include JDMDs No. 9, No. 10, No. 11, No. 12, and No. 14.

[b] All vertical JDMDs near Joint J5 include JDMDs No. 2, No. 3, No. 5, No. 6, No. 7, and No. 8.

[c] At the time, only JDMDs No. 3, No. 5, No. 7, and No. 8 were still measuring properly.

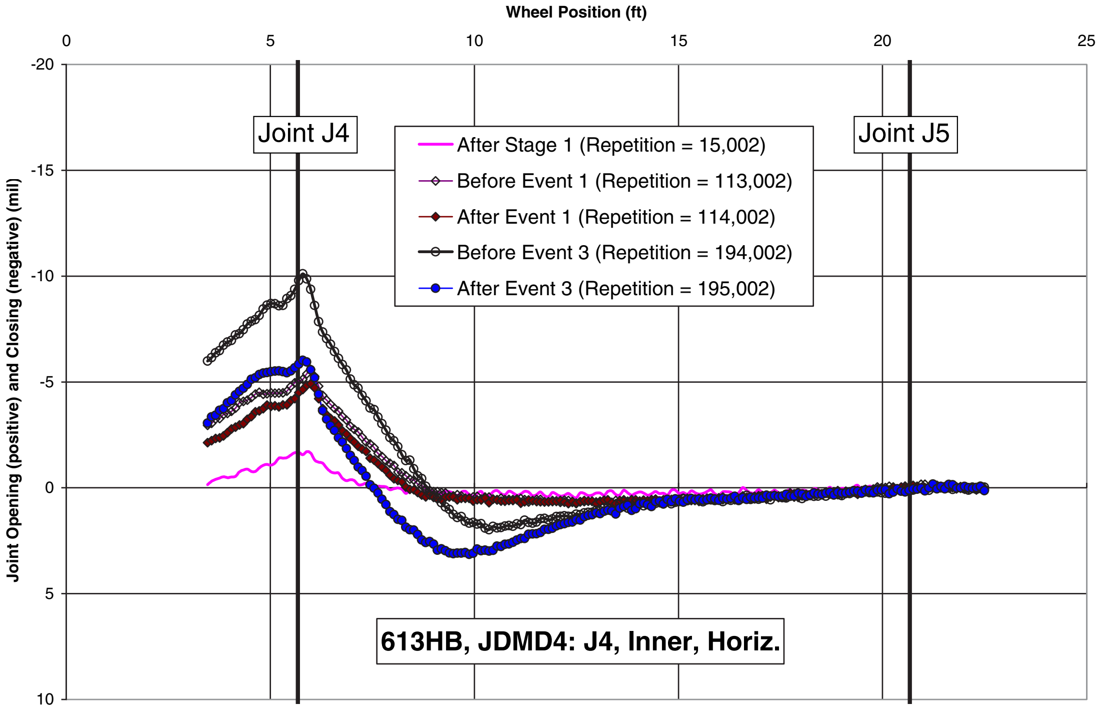

Figure K.37. Selected horizontal deflection (opening/closing) bowls for Joint J4 in Section 613HB.

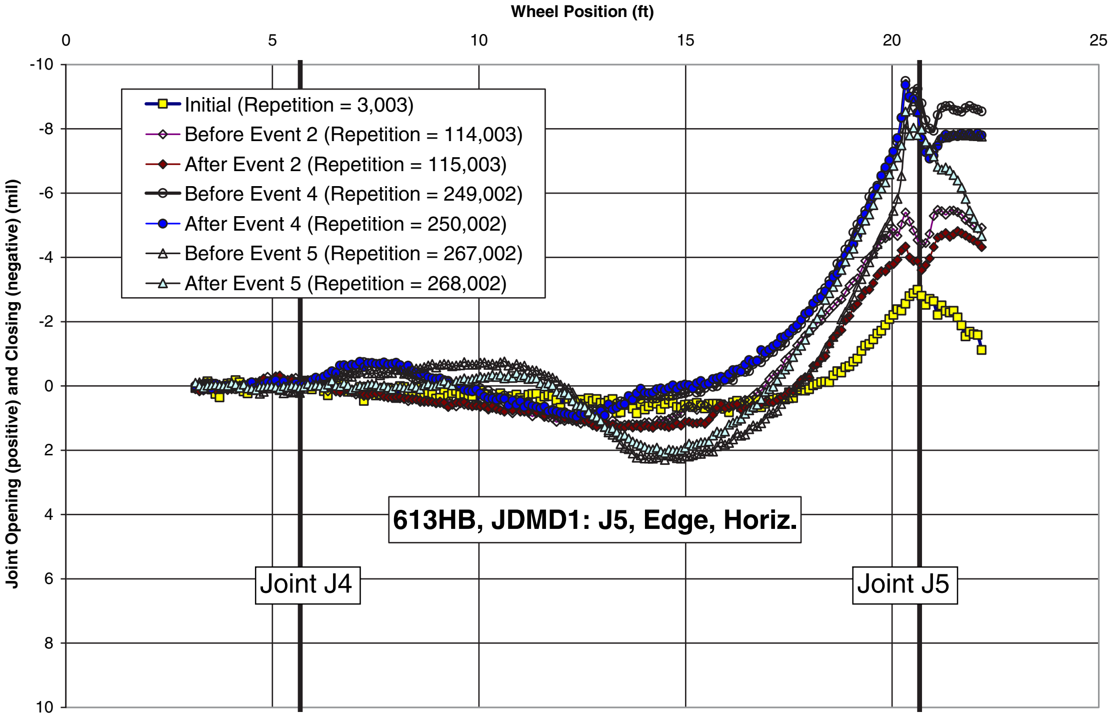

Figure K.38. Selected horizontal deflection (opening/closing) bowls for Joint J5 in Section 613HB.

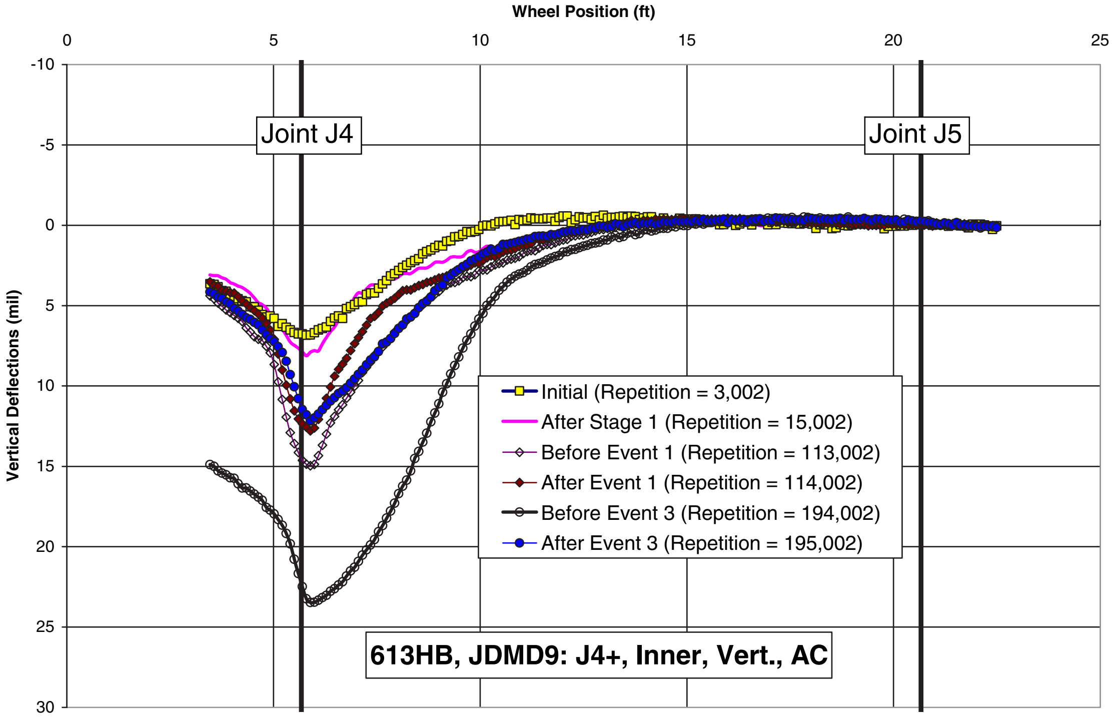

Figure K.39. Selected vertical deflection bowls for JDMD No. 9 in Section 613HB.

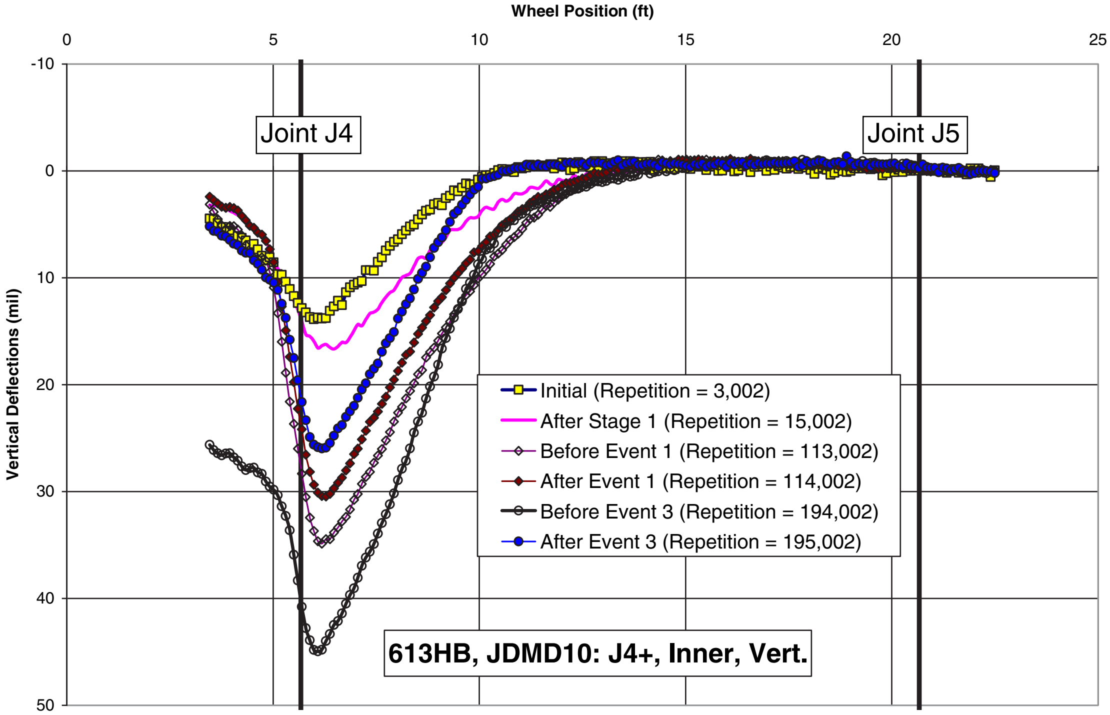

Figure K.40. Selected vertical deflection bowls for JDMD No. 10 in Section 613HB.

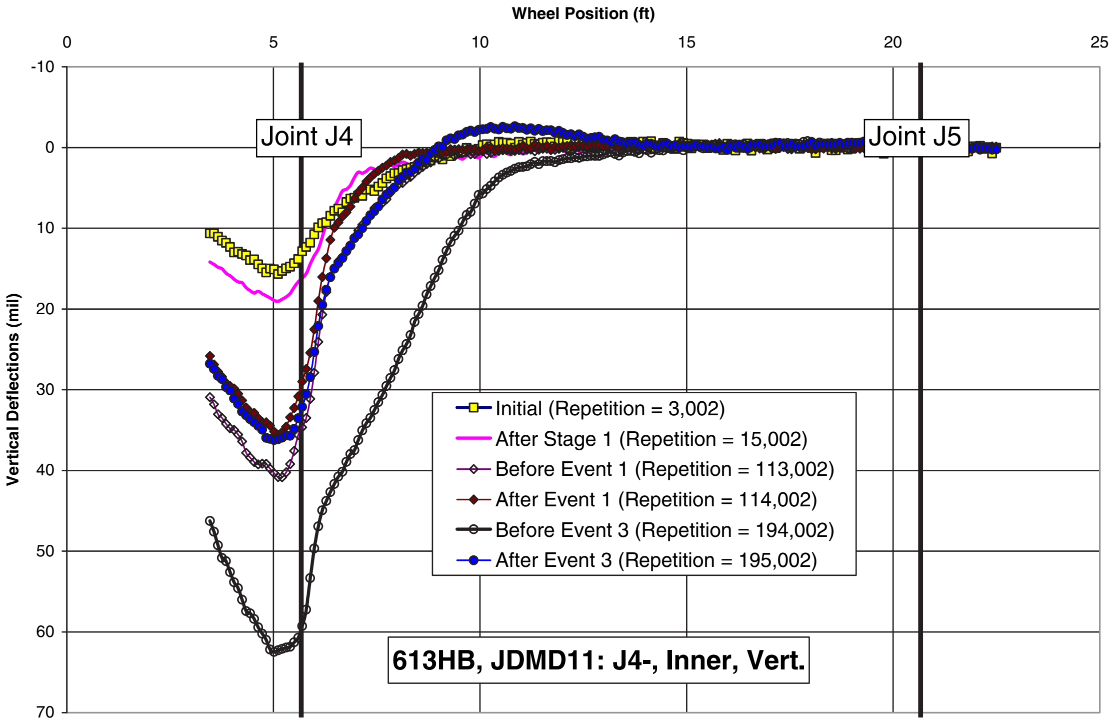

Figure K.41. Selected vertical deflection bowls for JDMD No. 11 in Section 613HB.

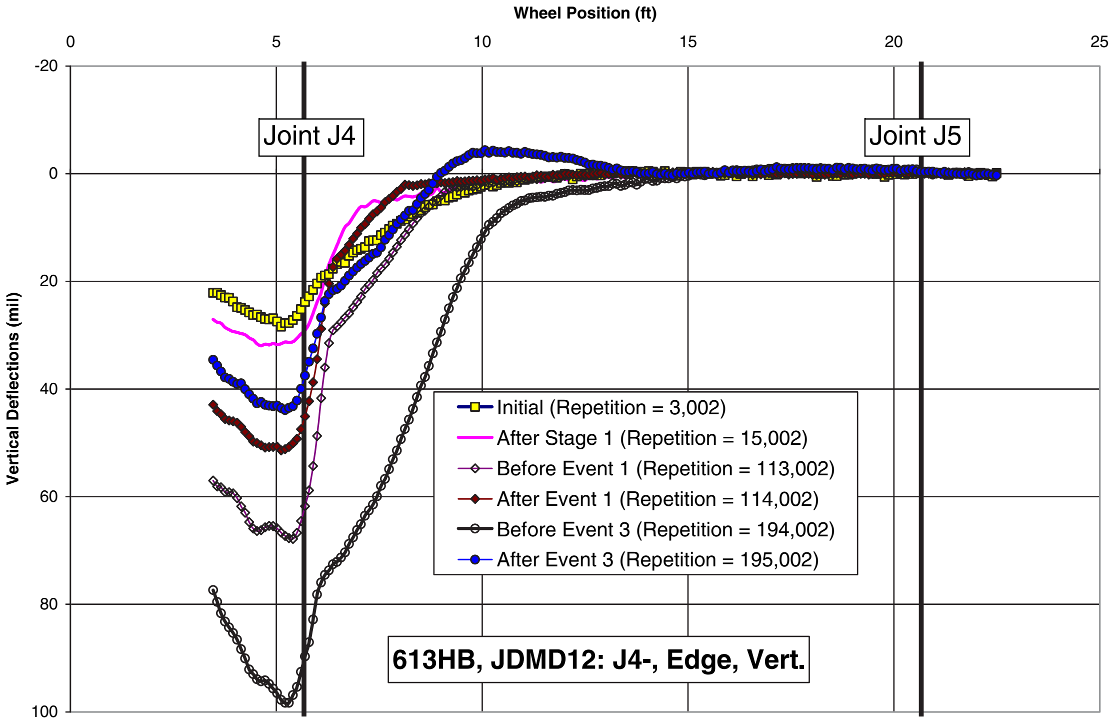

Figure K.42. Selected vertical deflection bowls for JDMD No. 12 in Section 613HB.

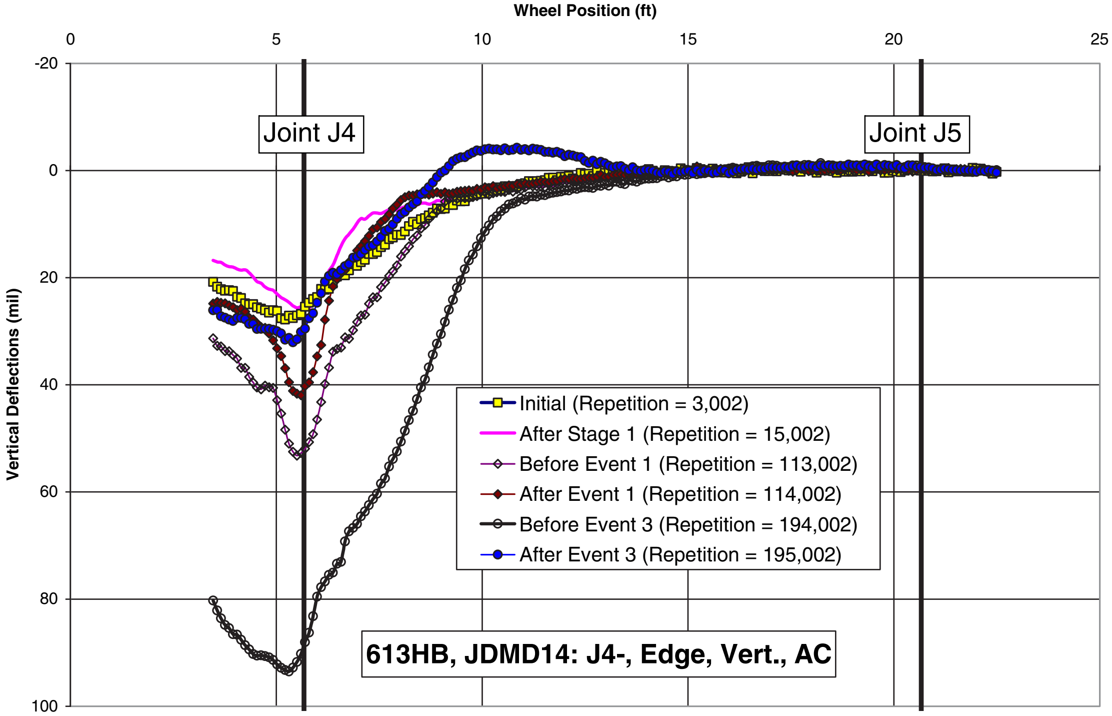

Figure K.43. Selected vertical deflection bowls for JDMD No. 14 in Section 613HB.

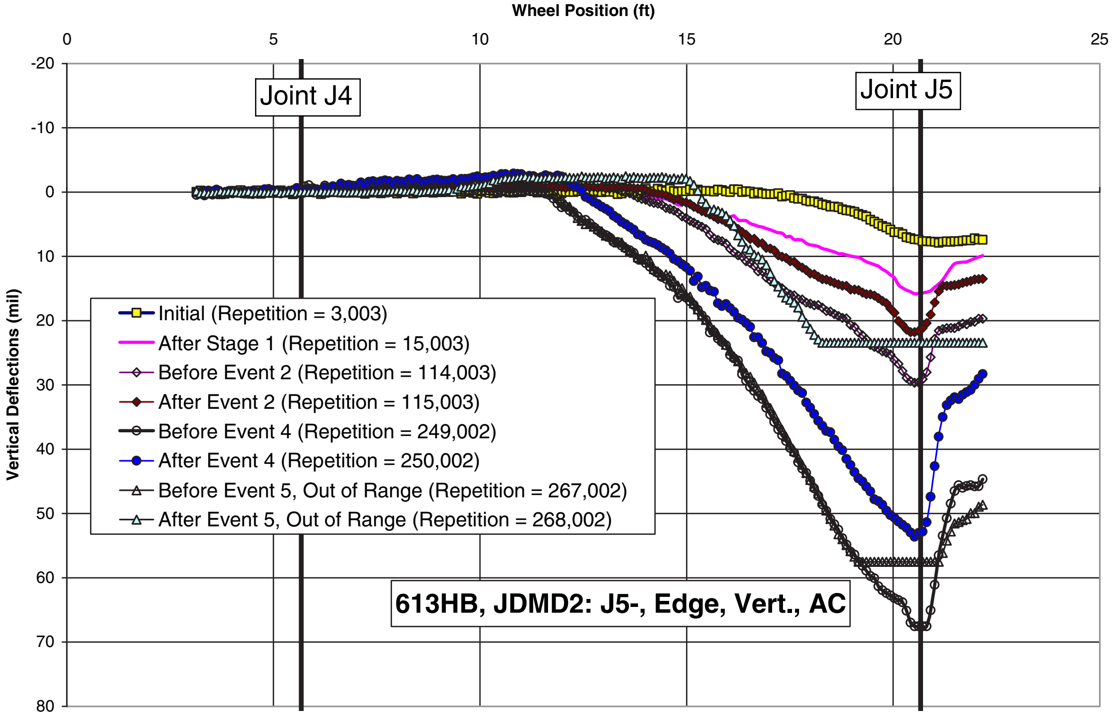

Figure K.44. Selected vertical deflection bowls for JDMD No. 2 in Section 613HB.

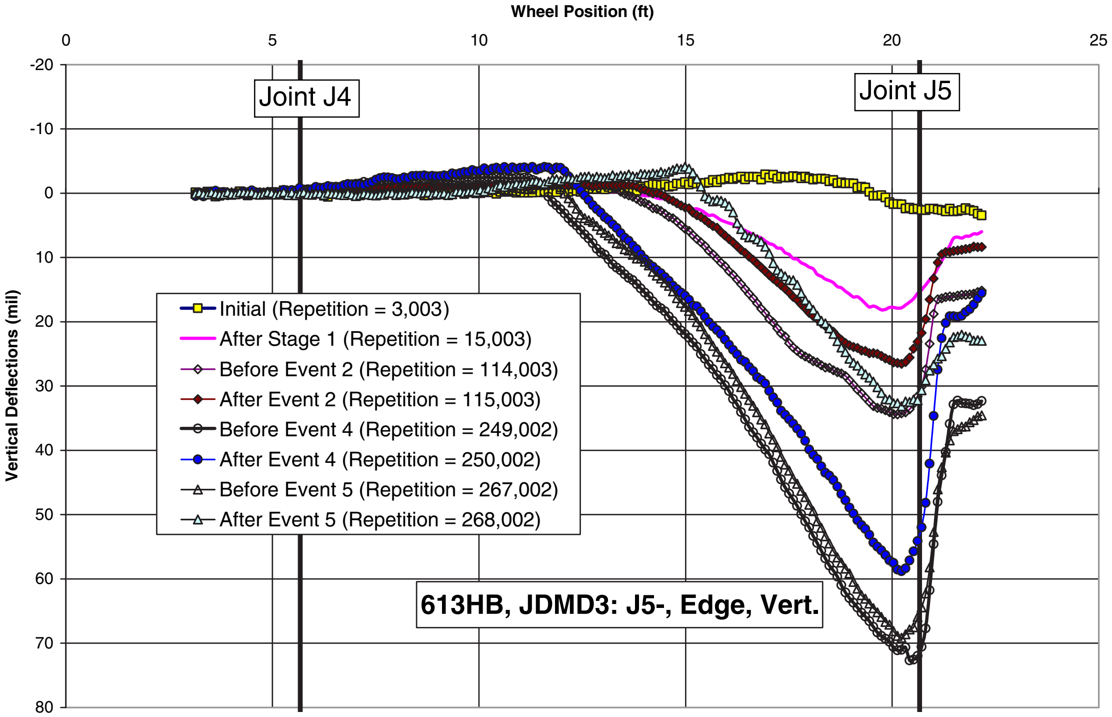

Figure K.45. Selected vertical deflection bowls for JDMD No. 3 in Section 613HB.

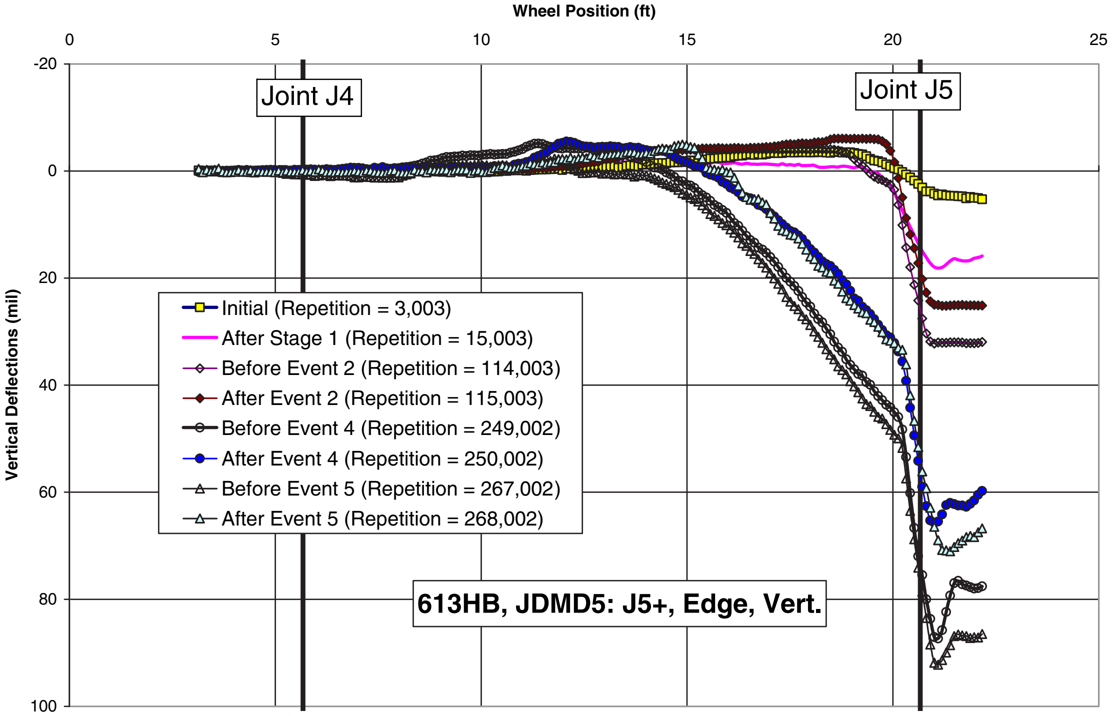

Figure K.46. Selected vertical deflection bowls for JDMD No. 5 in Section 613HB.

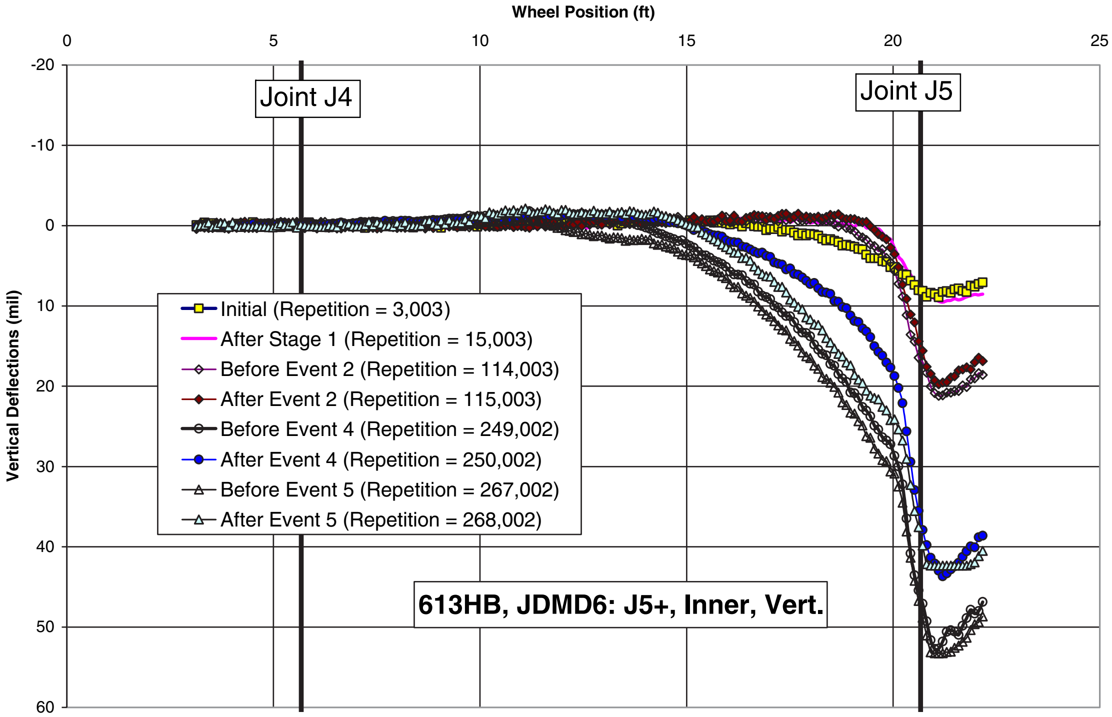

Figure K.47. Selected vertical deflection bowls for JDMD No. 6 in Section 613HB.

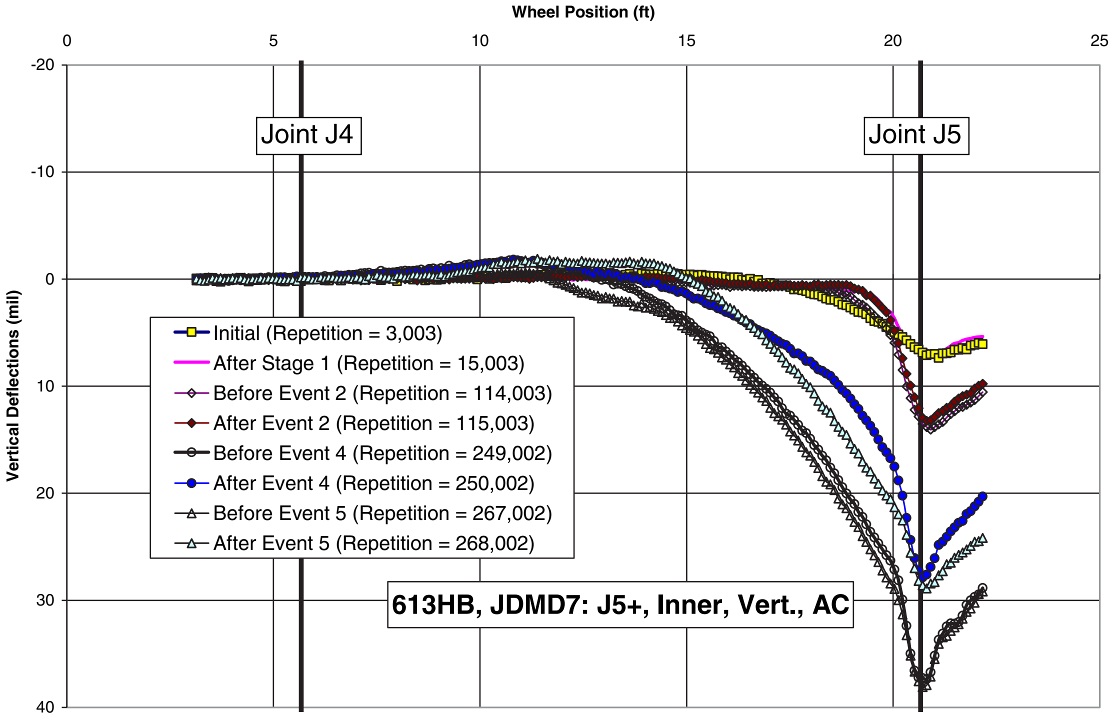

Figure K.48. Selected vertical deflection bowls for JDMD No. 7 in Section 613HB.

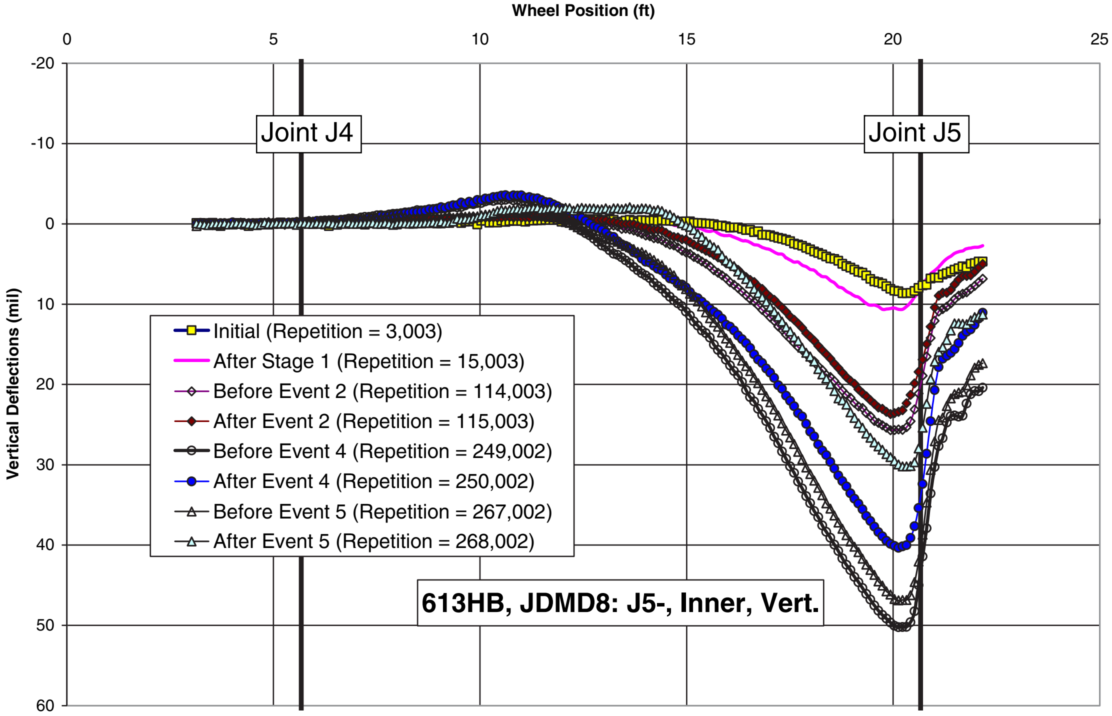

Figure K.49. Selected vertical deflection bowls for JDMD No. 8 in Section 613HB.

- Event 4 at Repetition 250,000 should correspond to the second fatigue cracking (i.e., Crack_At_8 in Figure K.12) of the PCC slab even though no significant changes in the shapes of deflection bowls are observed around it.
- Event 5 at Repetition 268,000 should correspond to further propagation of the second fatigue crack (i.e., Crack_At_8, in the PCC slab).

This means reflection cracking life is 114,000 load repetitions at Joint J4 and 115,000 load repetitions at Joint J5, and fatigue life of the underlying PCC slab is approximately 195,000 load repetitions. Using the 3.8 exponent and a 9-kip (40-kN) reference half-axle load, these load repetition numbers correspond to 0.18 million (for both 114,000 and 115,000) and 0.56 million (for 195,000) ESALs, respectively.

Elastic Strain from Dynamic Strain Gauges

As mentioned in the section on JDMD, RSD, and strain gauges in 613HB, two strain gauges were installed in the PCC layer during construction. They were configured properly only after 2,800 load repetitions and stopped working after 10,000 load repetitions. Even during the period when they were still working, the strain gauges did not always provide stable readings. Figure K.50 shows the initial strain bowls measured at repetition 3,002. Figure K.51 shows the recorded peak-to-peak differences for the first 10,000 load repetitions. Note that the jump in pavement temperatures shown in Figure K.51 is normal because testing in Stage 1 ran for only 6 minutes of each hour. As shown in Figure K.49, the strain bowl for the top of the PCC gauge is almost the mirror image of the bowl for the bottom of the PCC gauge, which indicates that the PCC slab is acting mostly as a cantilever beam at the beginning of the test.

HVS Test Results for Section 614HB

Introduction

This section provides a summary of the data collected from Section 614HB, the second set of HVS cracking tests. Data collected included air temperatures inside and outside the temperature control chamber, pavement temperatures, dynamic strains in the PCC layer, surface deflections from the RSD, joint movements from JDMDs, and surface permanent deformation.

Pavement Temperatures

Pavement temperatures were controlled using the temperature control unit for the first 3 days of testing (Stage 1.1,

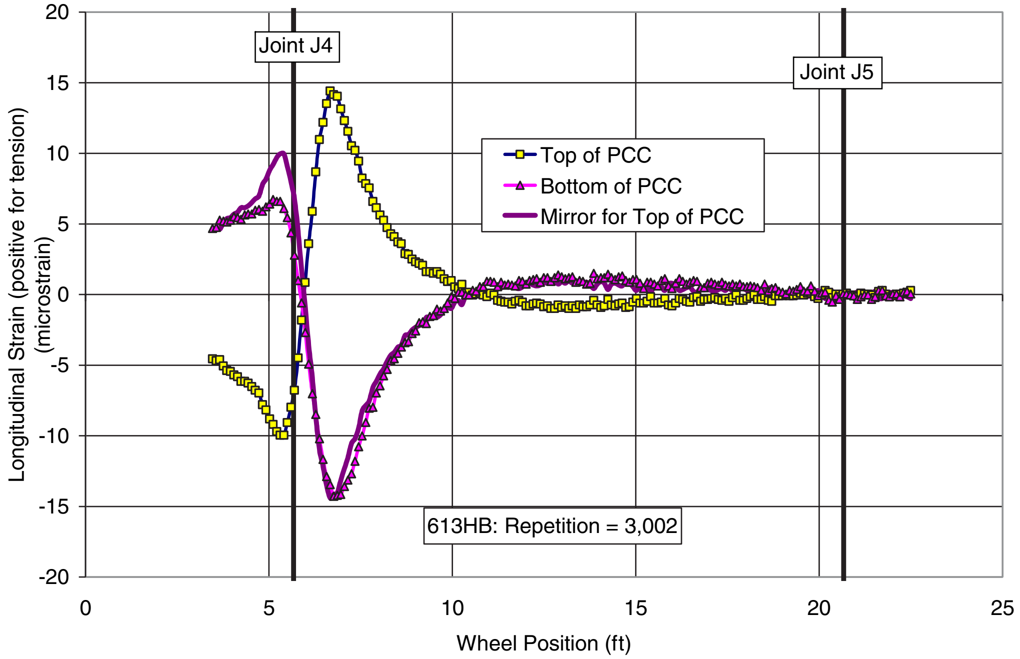

Figure K.50. Section 613HB: Initial strain bowls for dynamic strain gauges in the PCC layer, measuring longitudinal strain in the horizontal direction. The mirror for the strain bowl for the top of the PCC matches almost exactly the bowl for the bottom of the PCC.

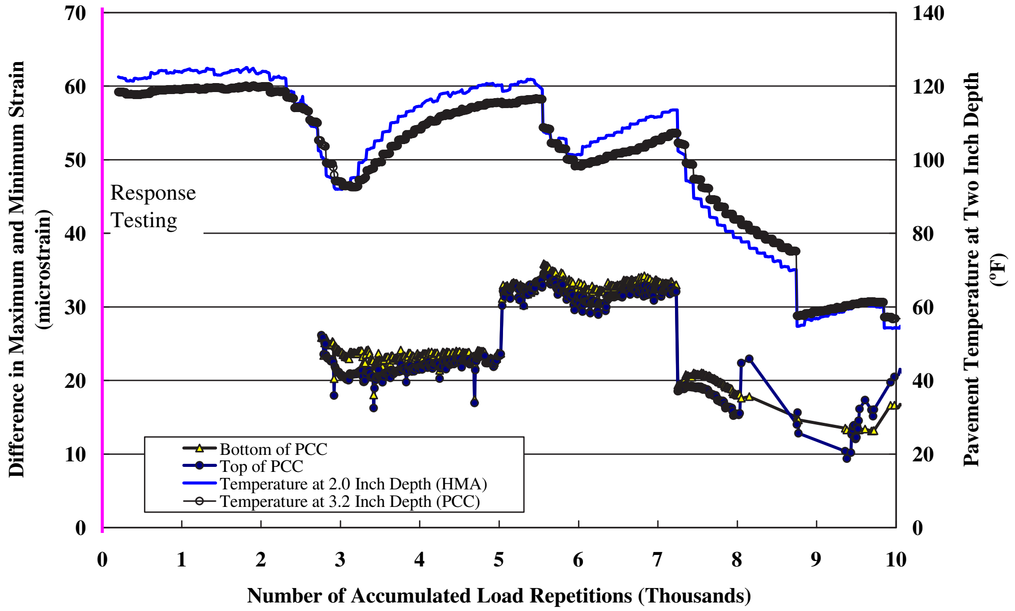

Figure K.51. Section 613HB: Difference between maximum and minimum strain for dynamic longitudinal strain gauges in the PCC. The strain gauges worked for only the first 10,000 load repetitions.

see Table K.6). After that, the pavement was exposed to the outside environment, with the only temperature control coming from shading of the section by the HVS. Both air (inside and outside the temperature box) and pavement temperatures were monitored and recorded hourly during the entire loading period.

Test Summary

Loading commenced on 3/23/2011 and ended on 5/20/2011. A total of 522,000 load repetitions were applied. The HVS loading program for Section 614HB is shown in Table K.6. A summary of the pavement and air temperatures for various stages is provided in Table K.14.

Outside Air Temperatures

Outside air temperatures while the HVS was trafficking are summarized in Figure K.52. Vertical error bars on each point on the graph show the daily temperature range. Daily average temperatures ranged from 51°F to 81°F (10°C to 27°C) during the course of HVS testing. Typical daily variation range was 10°F to 40°F (5°C to 22°C).

Air Temperatures in the Temperature Control Unit

The daily average air temperatures recorded in the temperature control unit, calculated from the hourly temperatures recorded during HVS operation, are shown in Figure K.53. Vertical error bars on each point on the graph show the daily temperature range. During the test, air temperatures inside the temperature control unit ranged from 97°F to 117°F (36°C to 47°C) for Stage 1.1 when the target pavement temperature was 122°F (50°C), and ranged from 52°F to 79°F (11°C to 26°C) for the rest of the test when pavement temperature was not controlled (i.e., determined by ambient temperature).

Temperatures in the Pavement

Daily averages of the surface and in-depth pavement temperatures are shown in Figure K.54. Pavement temperatures at different depths were similar.

Table K.14. Average and Standard Deviation of Temperatures Measured During HVS Testing

				Thermocouple Depths below HMA Surface (in.)				
Stage	**Quantity**	**Outside Air (°F)**	**Inside Air (°F)**	**0 (HMA)**	**1.0 (HMA)**	**2.0 (HMA)**	**2.4 (HMA)**	**3.5 (PCC)**
ST_1.1, 122°F target, 6.7 kip	Average	56.2	98.7	117.1	117.9	118.1	117.3	115.7
	standard deviation (SD)	9.6	10.7	8.1	7.9	6.9	6.3	4.9
ST_1.1, 122°F target, 9 kip	Average	64.3	107.3	122.2	121.5	120.2	119.0	117.0
	SD	8.8	7.1	6.1	6.3	5.4	4.9	4.1
ST_1.1, 122°F target, 13.5 kip	Average	75.6	114.3	127.2	125.4	123.9	123.0	121.0
	SD	5.4	8.5	6.4	3.7	1.6	1.3	0.8
ST_1.2, ambient, 6.7 kip	Average	67.8	68.7	80.4	81.3	84.3	85.5	87.7
	SD	10.8	10.2	10.1	9.0	7.2	6.5	5.3
ST_1.2, ambient, 9 kip	Average	67.3	67.1	73.9	74.6	77.4	78.4	80.4
	SD	8.0	6.6	5.2	4.7	4.0	3.7	3.4
ST_1.2, ambient, 13.5 kip	Average	58.6	59.6	67.7	68.4	71.1	72.1	74.0
	SD	8.1	7.3	5.0	4.4	3.5	3.2	2.9
ST_2.1, ambient, 9 kip	Average	59.1	60.4	66.3	66.5	67.9	68.4	69.5
	SD	7.9	7.6	7.7	6.8	5.3	4.7	3.8
ST_2.2, ambient, 13.5 kip	Average	57.4	59.1	65.9	66.0	67.3	67.8	68.7
	SD	9.9	10.2	10.3	9.0	6.9	6.2	4.8
ST_2.3, ambient, 18 kip	Average	67.0	68.4	73.5	73.3	73.7	73.8	74.0
	SD	12.1	11.9	11.1	10.0	7.8	7.0	5.6
ST_2.4, ambient, 22.5 kip	Average	58.8	60.6	66.8	67.1	68.8	69.1	70.2
	SD	10.7	11.0	10.4	9.5	8.0	7.4	6.3
ST_2.5, ambient, 27 kip	Average	78.4	79.0	75.9	74.9	72.9	72.2	71.3
	SD	1.1	2.7	1.8	1.6	1.0	1.0	0.6

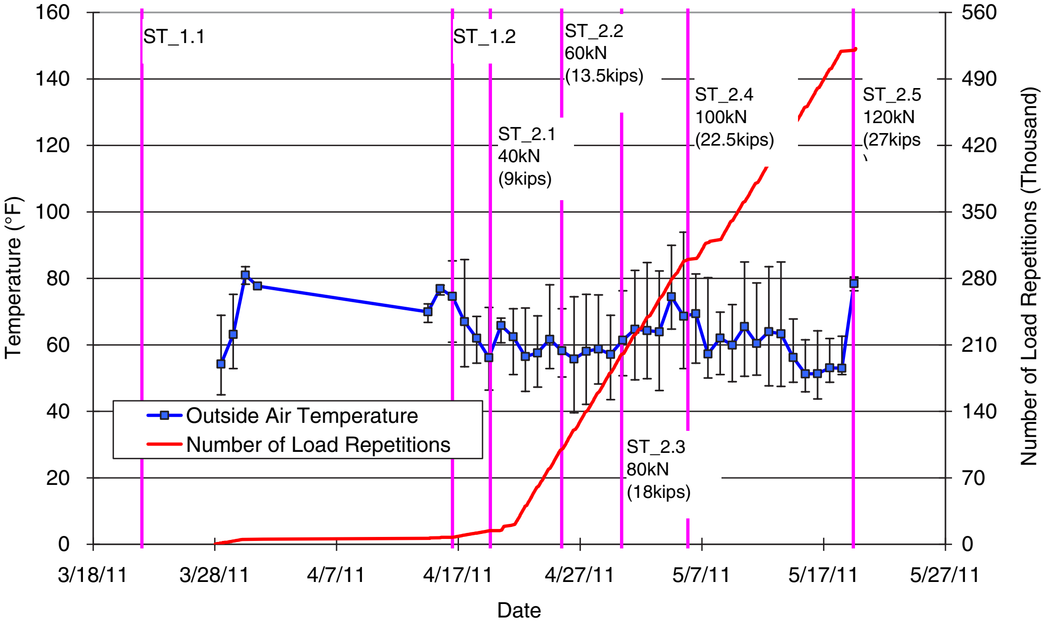

Figure K.52. Section 614HB: Daily average outside air temperatures during HVS trafficking.

Visual Inspection

Figure K.55 shows the top view of the section surface at the end of the test for Section 614HB. Fatigue distress in an HMA/PCC composite pavement manifests itself in the form of surface cracks. Crack monitoring was the same as in Section 613HB.

Cracks traced on the HMA surface at selected points of the HVS testing are shown in Figure K.56. Reflection cracking from underlying joints was first observed after 298,400 load repetitions (2.5 million ESALs) over Joint J1. No additional surface cracking was observed after 520,000 load repetitions (12.8 million ESALs), at which point the dual wheel half-axle was replaced by single-wheel aircraft tire and the wheel load was increased to 120 kN (27 kip) and 1.38 MPa (200 psi). Once the trafficking with the aircraft tire was begun, extensive surface cracking started to develop, and after only 2,000 additional

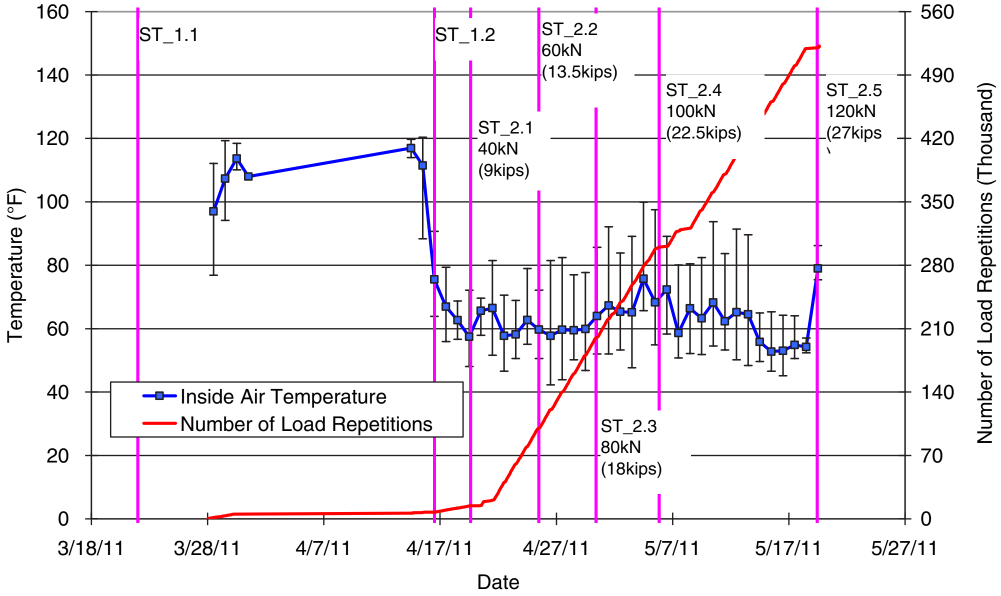

Figure K.53. Section 614HB: Daily average inside air temperatures during HVS trafficking.

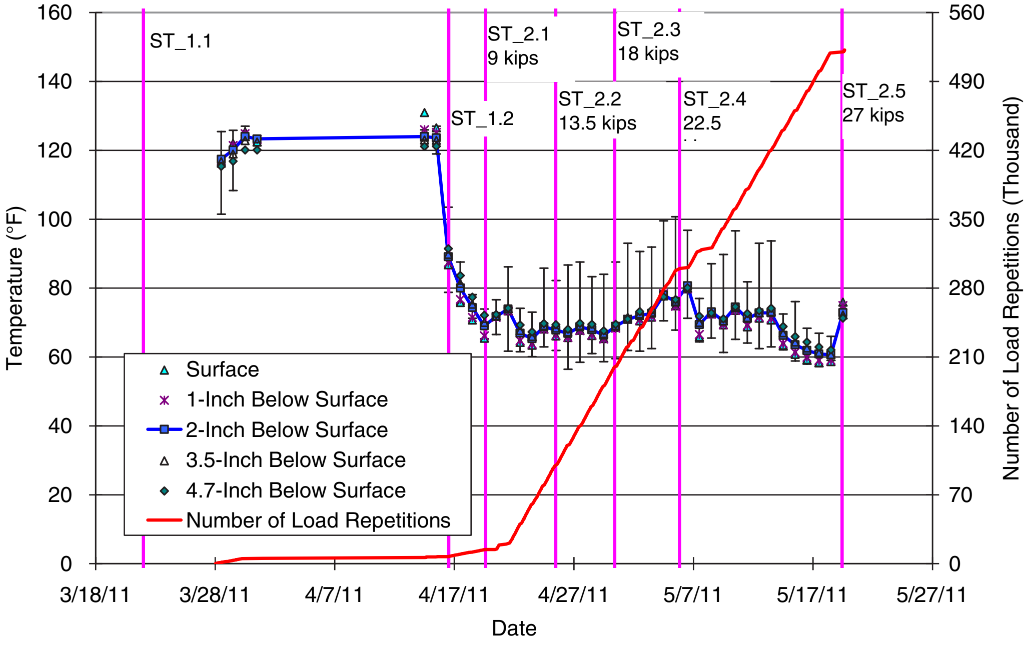

Figure K.54. Section 614HB: Daily average temperatures at pavement surface (i.e., top of HMA layer) and at various depths during HVS trafficking temperature. The last thermocouple measures PCC temperature.

load repetitions (0.13 million ESALs) with the aircraft tire, the total length of the surface crack had increased from 0.8 m (2.5 ft) to 17.8 m (58.5 ft).

As shown in Figure K.55, most of the surface cracks run longitudinally along the edge of the wheelpaths of the dual wheel. They were caused by the change of tire types (i.e., from dual-wheel to single-wheel) and therefore were not a reflection of cracks in the underlying PCC slab. The transverse cracks at Stations 2, 3, 5, and 6 may or may not be reflection cracks because the HMA layer was found sliding horizontally when trafficked by the aircraft tire, meaning that the bond between the RHMA and the PCC had been broken. The crack labeled Crack_1 shown in Figure K.55 is definitely a reflection of underlying slab cracking, as clarified by the photograph shown in Figure K.57.

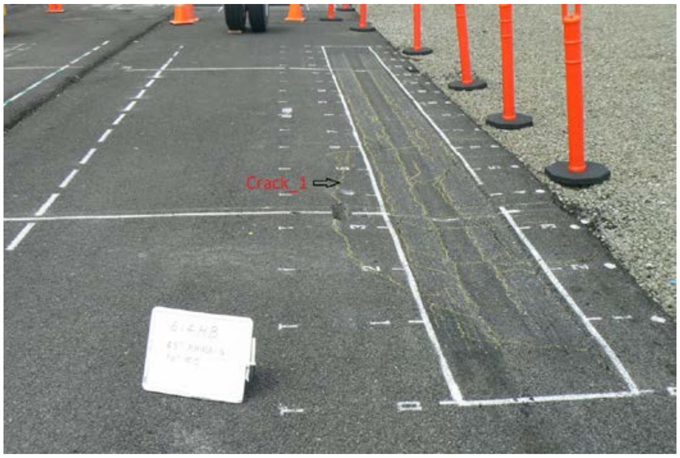

Figure K.55. Section photograph at test completion for Section 614HB.

According to Figure K.56, surface cracks appeared in the following sequence:

1. Cracks reflected from the underlying Joint J1 were observed after 298,400 load repetitions.
2. No additional cracks were observed after 520,000 load repetitions with maximum 23.5-kip (100-kN) half-axle load.
3. After testing switched to the aircraft tire with the 27-kip (120-kN) load and 2,000 additional load repetitions, cracks reflected from both Joint J2 and a fatigue crack in the PCC slab. In addition, longitudinal cracks developed along the edges of the dual-wheel wheelpaths. Transverse cracks also developed because of horizontal sliding of the HMA layer relative to the underlying PCC slab.

Surface Rut

Figure K.58 shows the average change in transverse cross section measured with the Laser Profilometer at various stages of the test. This plot clearly shows a slight increase in rutting after the first 14,400 load repetitions (i.e., the response

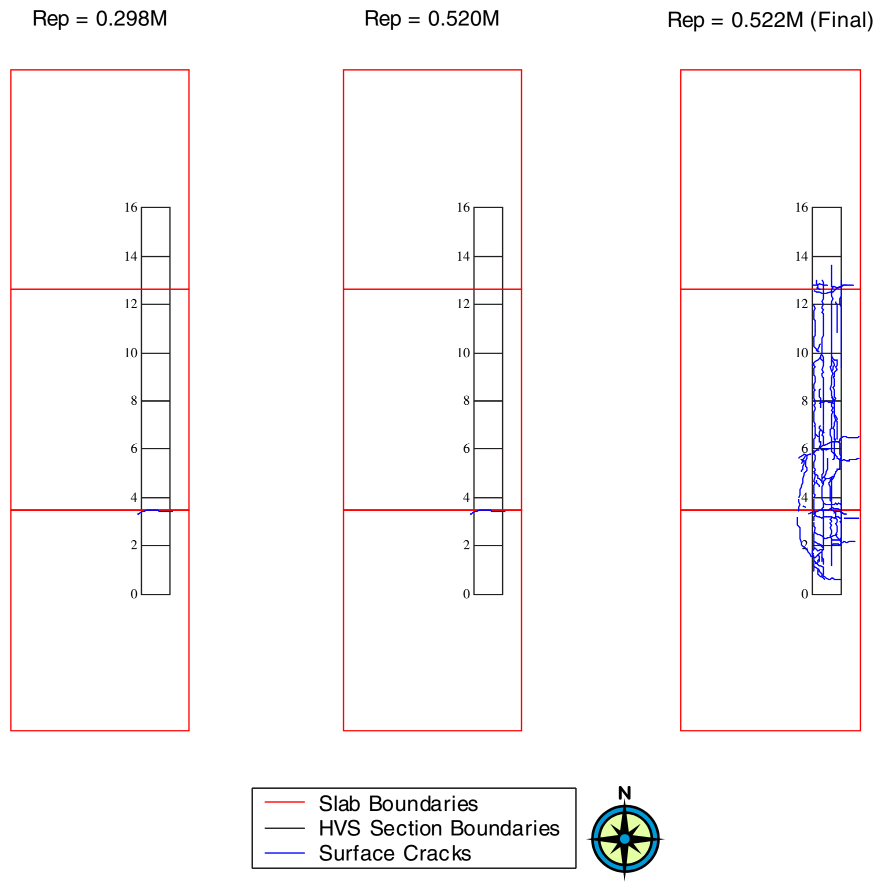

(a) (b) (c)

Figure K.56. Top views of surface cracks after different numbers of load repetitions: (a) Repetition = 0.298 million and crack length = 0.8 m (2.5 ft); (b) repetition = 0.520 million and crack length = 0.8 m (2.5 ft); and (c) repetition = 0.522 million and crack length = 17.8 m (58.5 ft).

testing stage) but significant tilting of the underlying slab. The use of the single aircraft tire to replace the dual truck wheels caused the center hump of the RHMA rutting to be pushed down. Profile measurements were not symmetric with respect to the wheelpaths because the test section was located at the edge of the slab. The tilting was caused by cracking in the underlying PCC slab. The tilting seems to have begun before 520,000 repetitions but increased significantly afterward.

Figure K.59 shows the development of permanent deformation with load repetitions as measured with the Laser Profilometer for the test section, with an embedment phase apparent only at the beginning of the experiment (i.e., the first 14,400 repetitions). Error bars on the average readings indicate that there was roughly ±⅛ in. of variation along the length of the section until the end of the test.

Figure K.60 and Figure K.61 show contour plots of the pavement surface at the end of the test (522,000 repetitions), indicating that tilting occurred mostly between Stations 2

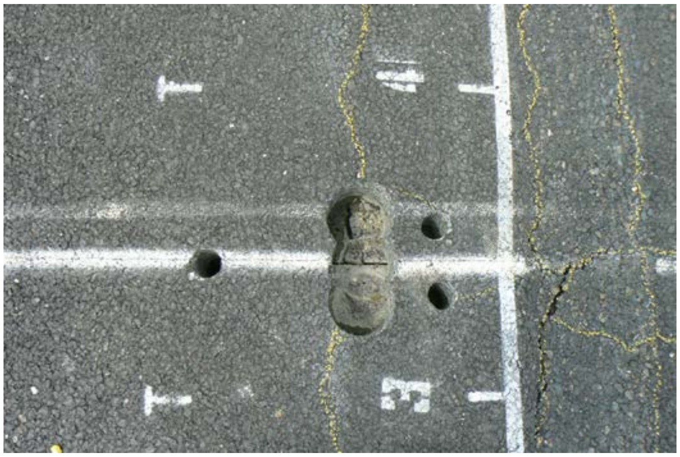

Figure K.57. Top view of Section 614HB taken near Joint J1 showing slab cracking underneath.

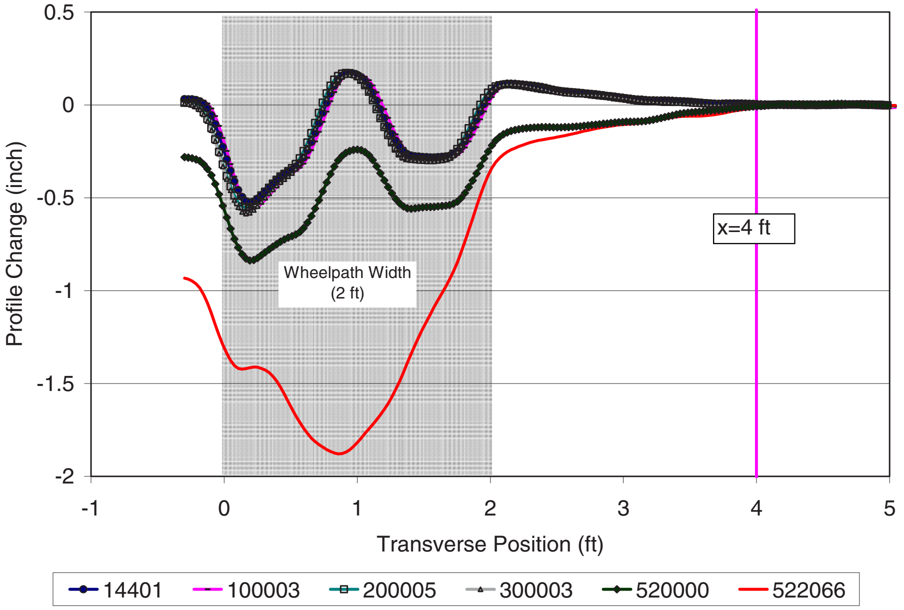

Figure K.58. Average profilometer cross section at various load repetitions for Section 614HB.

and 6. After trafficking was completed, the average maximum rut depth was 1.6 in. (40.6 mm). The maximum rut depth measured on the section was 2.2 in. (55.9 mm), recorded at Station 5.

Elastic Response Under Manual Mode

Elastic responses were measured in the same manner used for Section 613HB. Specifically, RSD, JDMD, and dynamic strain gauges were used to monitor elastic pavement responses.

Surface Elastic Deflection from RSD

In this section, surface deflections as measured by the RSD under a load of 9 kip (40 kN) are summarized. Although the load increased during the test program, deflection measurements were always taken with a 9-kip load.

Table K.15 compares the average 40-kN RSD deflections for locations J1–, J1+, 8CL, J2–, and J2+ before and on completion of testing (see Figure K.7, Figure K.8 and Table K.5 for their locations). Figure K.62 shows the change of RSD peak

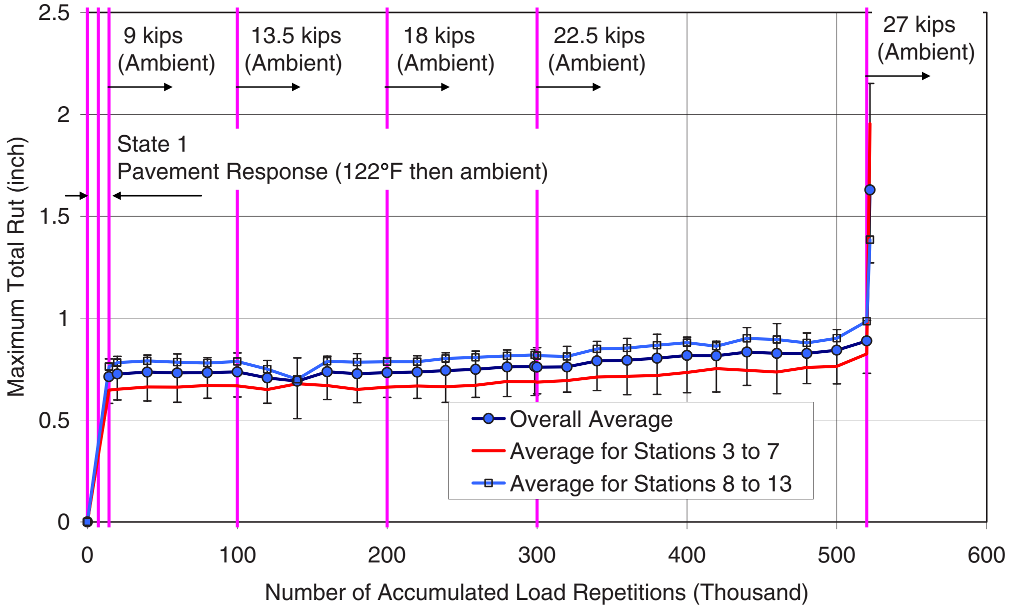

Figure K.59. Development of maximum total rut for Section 614HB.

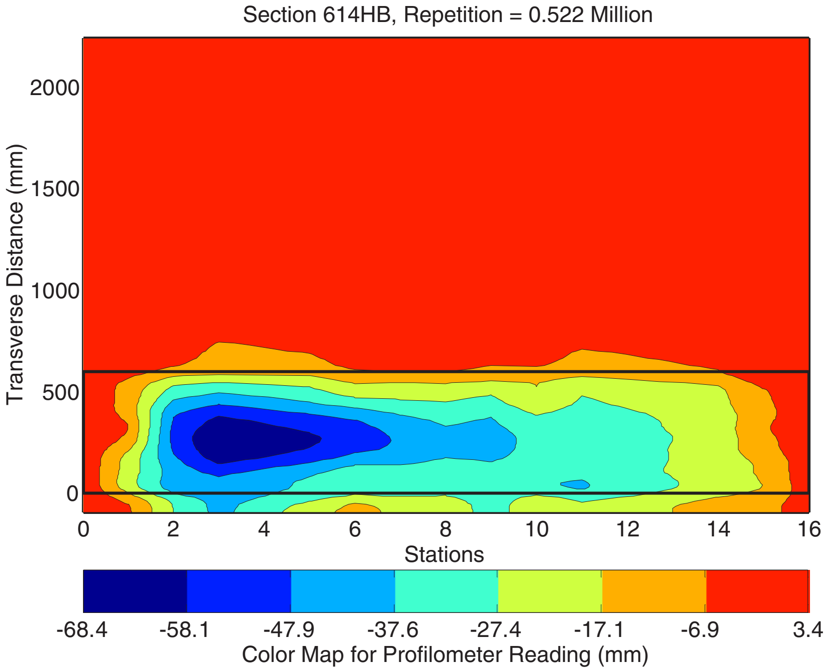

Figure K.60. Two-dimensional contour plot of change in surface elevation relative to the untrafficked condition at the end of test for Section 614HB (1 in. = 25.4 mm).

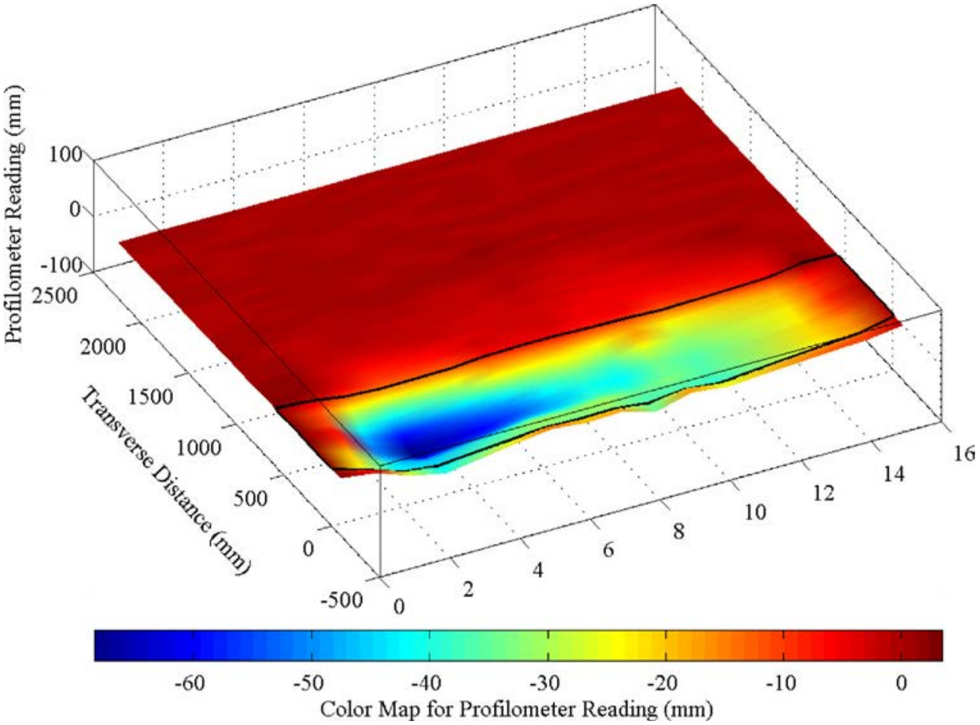

Figure K.61. Three-dimensional contour plot of change in surface elevation relative to the untrafficked condition at the end of the test for Section 614HB (1 in. = 25.4 mm).

Table K.15. Average 9-kip (40-kN) RSD Deflections Before and After Testing for Section 614HB

Position	Deflection (mil)			
	Before Trafficking	Maximum During Trafficking	After Trafficking	Ratio of Peak/Initial
J1–	18.3	61.2	61.2	3.3
J1+	11.2	61.7	61.7	5.5
8CL	6.1	35.4	35.4	5.8
J2–	18.1	55.4	55.4	3.1
J2+	18.2	44.9	44.9	2.5

deflections with accumulated number of load repetitions. RSD deflections were found to increase to a maximum value then decrease significantly before increasing again. This is why "maximum during trafficking" is shown in Table K.15.

RSD deflections measured at the center of the slab (location 8CL) generally were less than those measured near the two joints. Deflections near Joint J2 were higher than those near Joint J1 at the beginning of the test, but HVS trafficking caused deflections near Joint J1 to increase much faster than near Joint J2. Substantial damage occurred on the HMA layer and the PCC slab over the entire section under HVS trafficking. This is confirmed by the ratio of peak-to-initial deflections for all RSD locations, which show that surface deflections increased by 2.5 to 5.5 times for locations near joints and 5.8 times for the center of the slab.

During the course of the test, surface deflections measured at the middle of the slab generally increased monotonically but those measured near joints show a significant decrease after reaching peak values. This significant deflection drop signifies structural changes near the joints that are discussed further in this section.

The deflection bowls at the different locations at test start, load change intervals, and test completion are shown in Figures K.63 through K.71, all of which use the same scale. The wheel position shown in these figures corresponds to the *x*-coordinate shown in Figure K.2. The deflections generally increase over time. Note that the shape of the RSD deflection bowls as the wheel rolls approaching the RSD location (essentially influence lines) also change over time, which again indicates structural changes that likely are related to cracking in the underlying PCC slab and the HMA layer. Specifically, Figure K.67 indicates that the PCC slab crack may have occurred near the area where the wheel position equaled 9.2 ft.

Elastic Deflections from JDMD

The schedule of JDMD measurements with various test loads is listed in Table K.9. Only limited data were collected at 13.5-kip (60-kN) and 18-kip (80-kN) test loads, so the

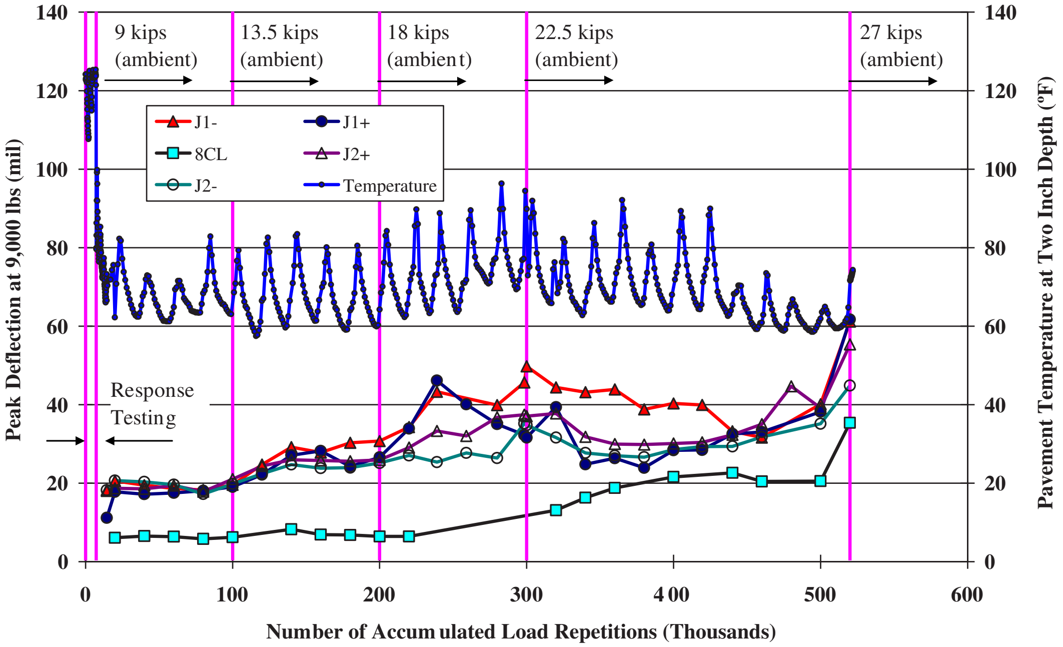

Figure K.62. 614HB: RSD surface deflections with 9-kip (40-kN) test load for each location.

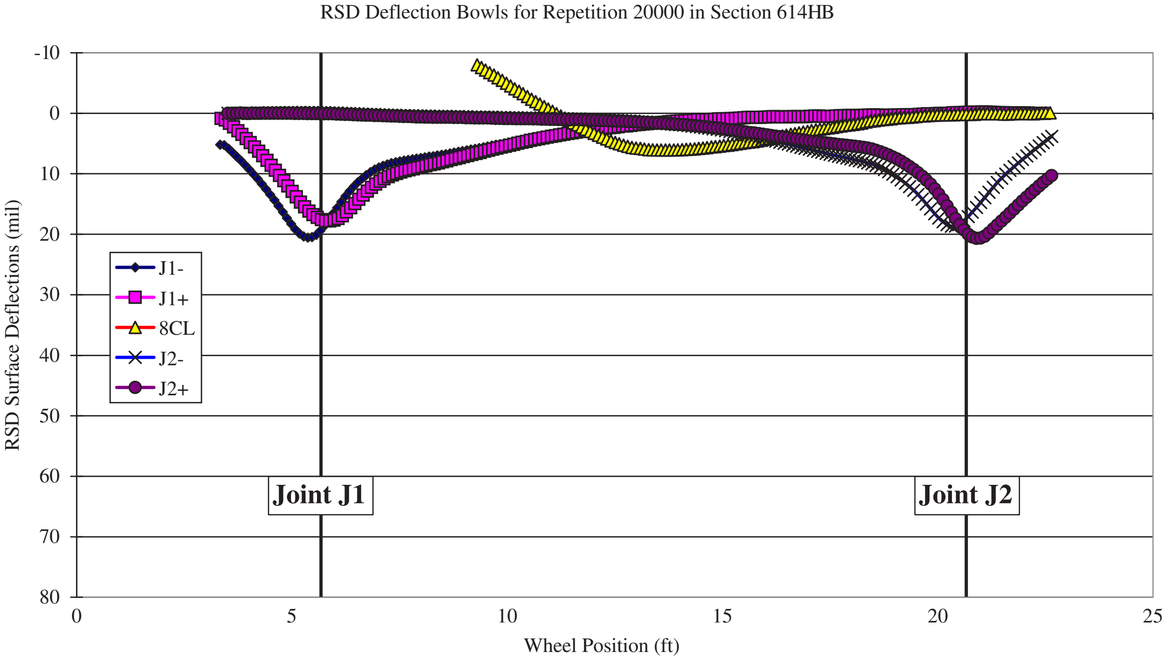

Figure K.63. Section 614HB: RSD deflections at different locations with 9-kip (40-kN) test load at 20,000 repetitions (when the trafficking load changed from 9 kip to 13.5 kip).

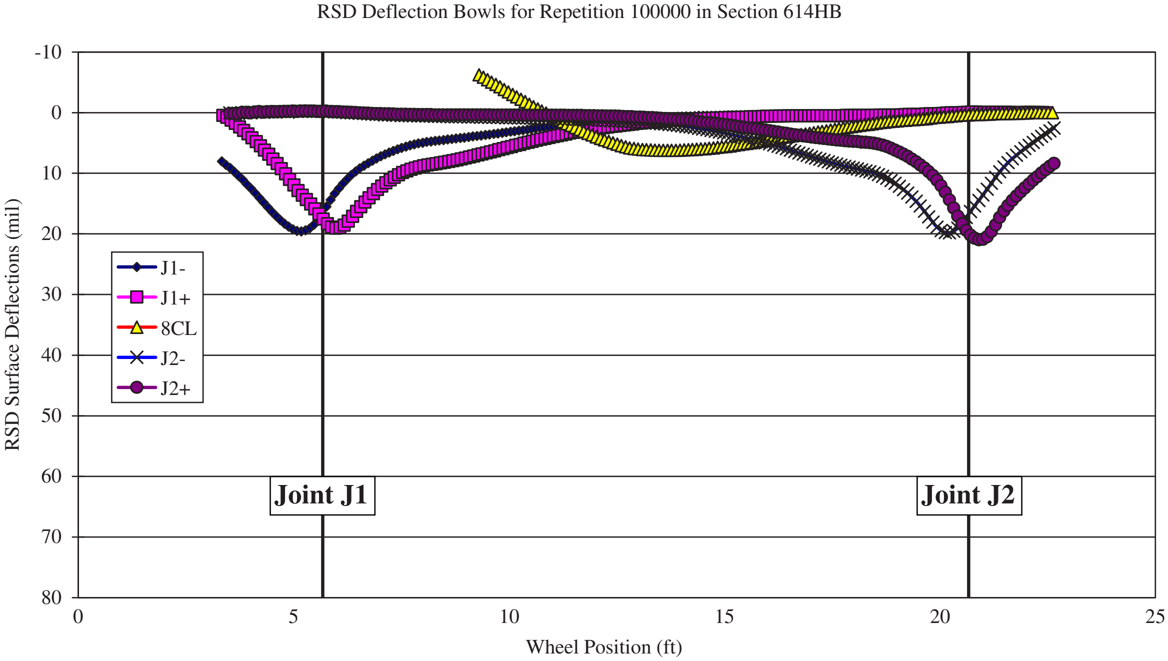

Figure K.64. Section 614HB: RSD deflections at different locations with 9-kip (40-kN) test load after 100,000 repetitions (when the trafficking load changed from 9 kip to 13.5 kip).

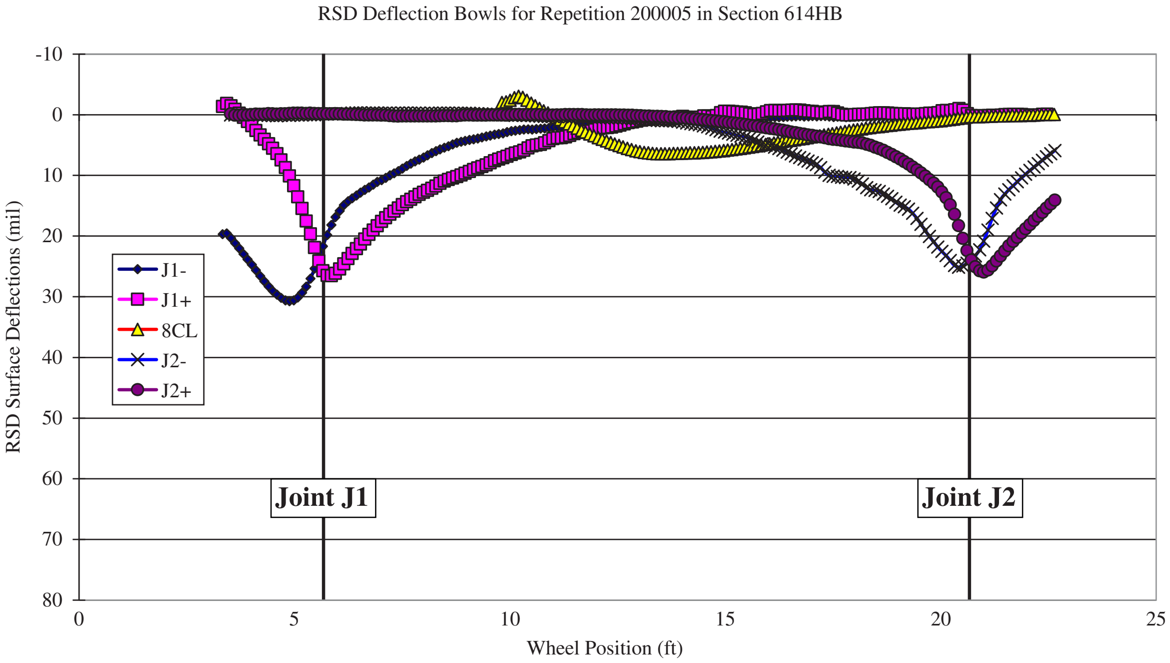

Figure K.65. Section 614HB: RSD deflections at different locations with 9-kip (40-kN) test load after 203,600 repetitions (when the trafficking load changed from 13.5 kip to 18 kip).

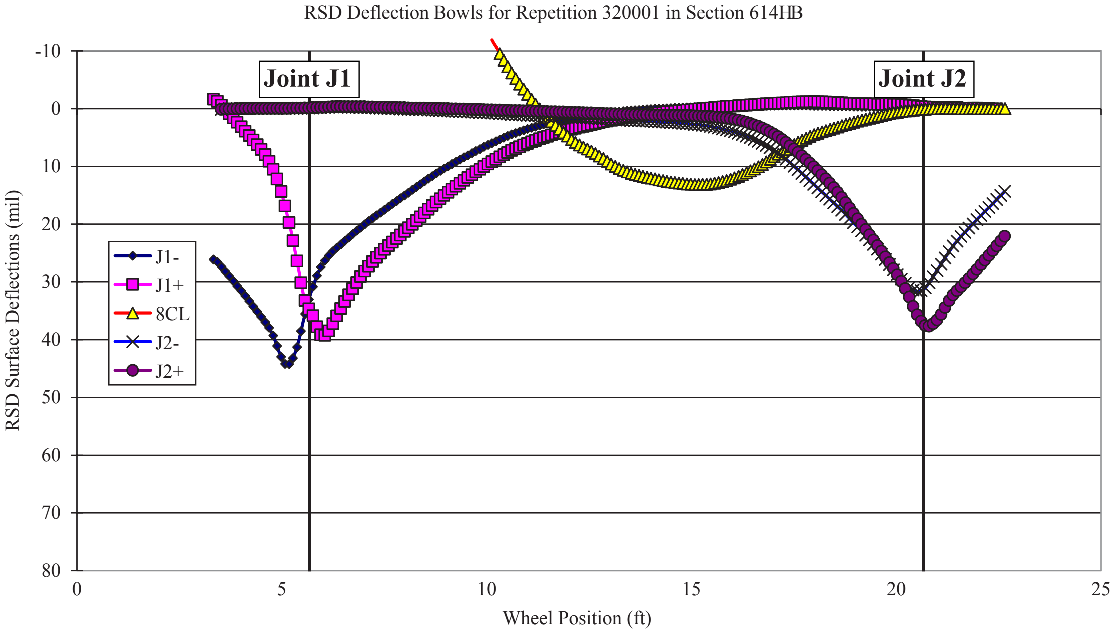

Figure K.66. Section 614HB: RSD deflections at different locations with 9-kip (40-kN) test load after 320,000 load repetitions (HVS trafficking load increased from 18 kip to 23.5 kip after 300,000 repetitions).

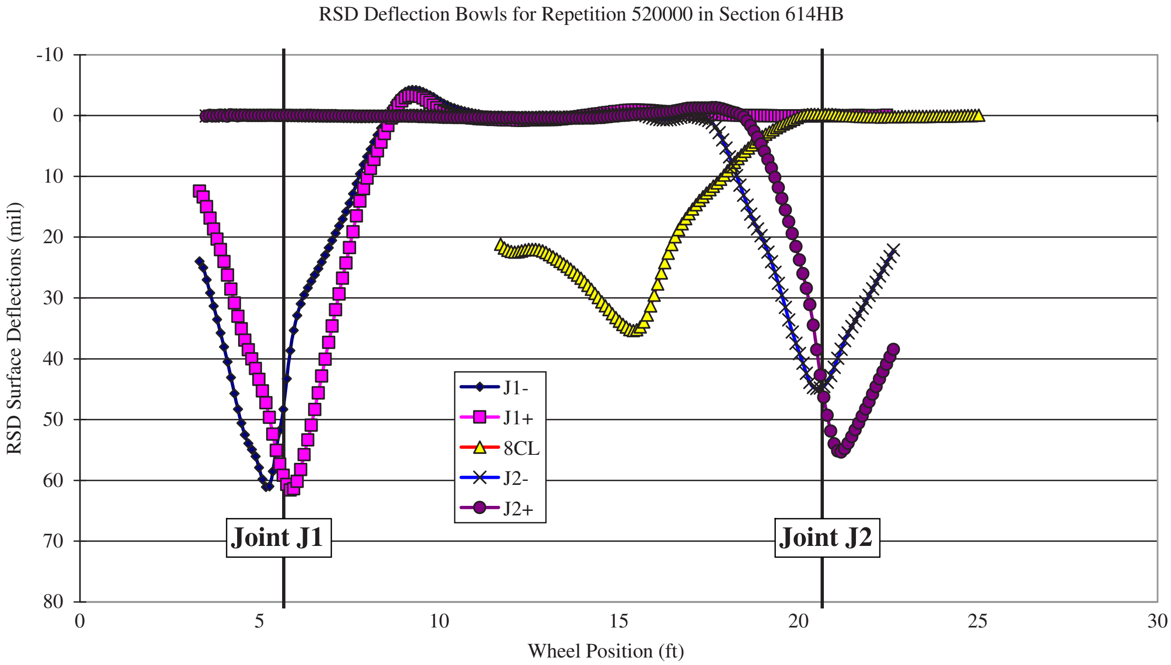

Figure K.67. Section 614HB: RSD deflections at different locations with 9-kip (40-kN) test load after 520,000 load repetitions (when the trafficking load changed from 23.5 kip to single aircraft tire with 27 kip).

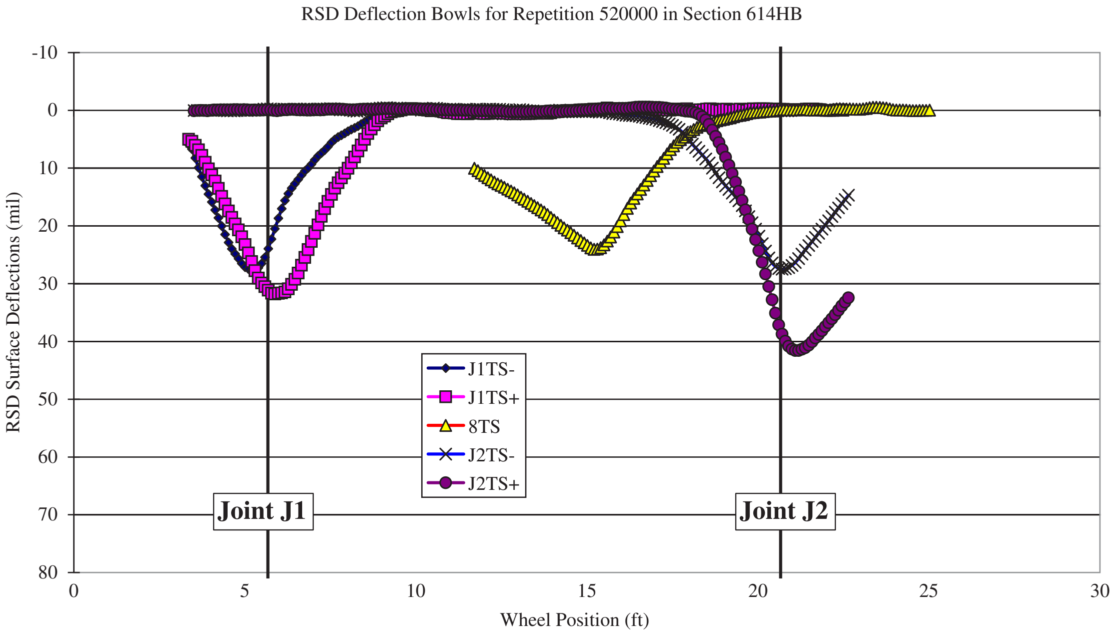

Figure K.68. Section 614HB: RSD deflections at different locations along traffic side with 9-kip (40-kN) test load after 520,000 load repetitions (when the trafficking load changed from 23.5 kip truck tire to aircraft tire with 27 kip).

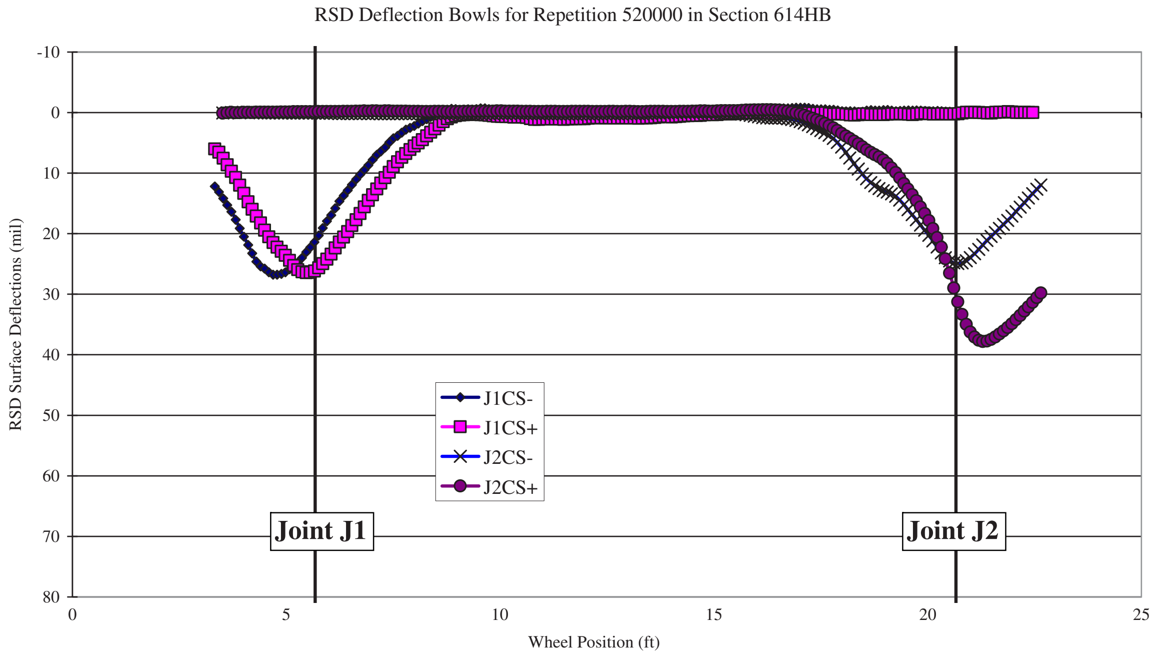

Figure K.69. Section 614HB: RSD deflections at different locations along caravan side with 9-kip (40-kN) test load after 520,000 load repetitions (when the trafficking load changed from 23.5 kip to aircraft tire with 27 kip).

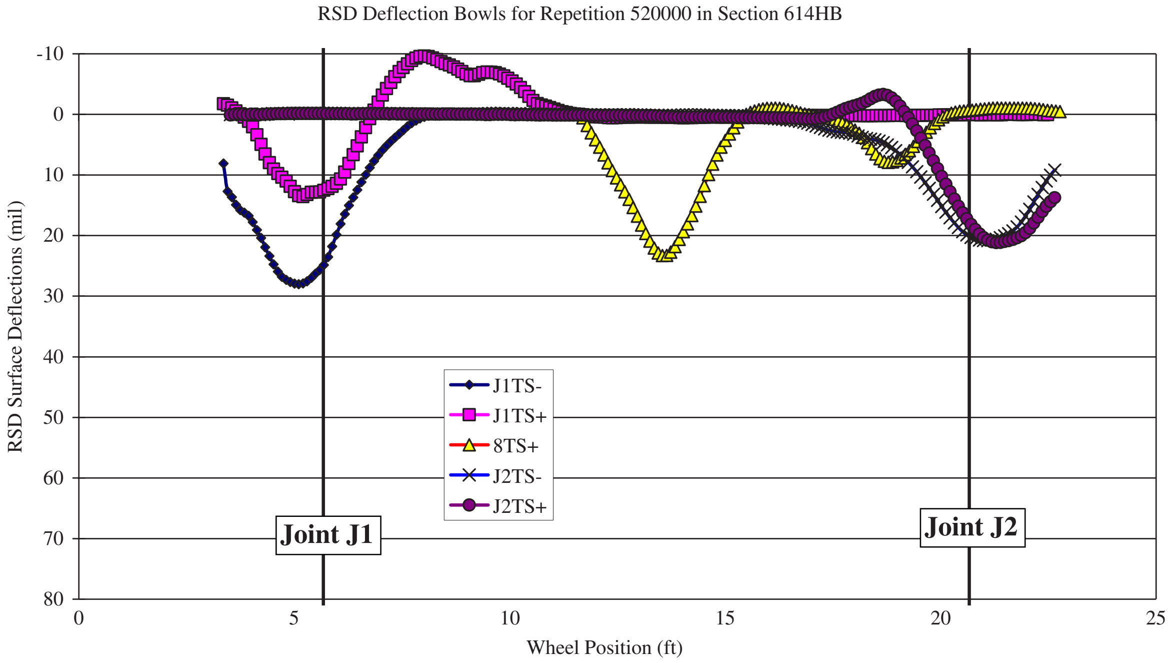

Figure K.70. Section 614HB: RSD deflections at different locations at traffic side with 9-kip (40-kN) test load at test completion.

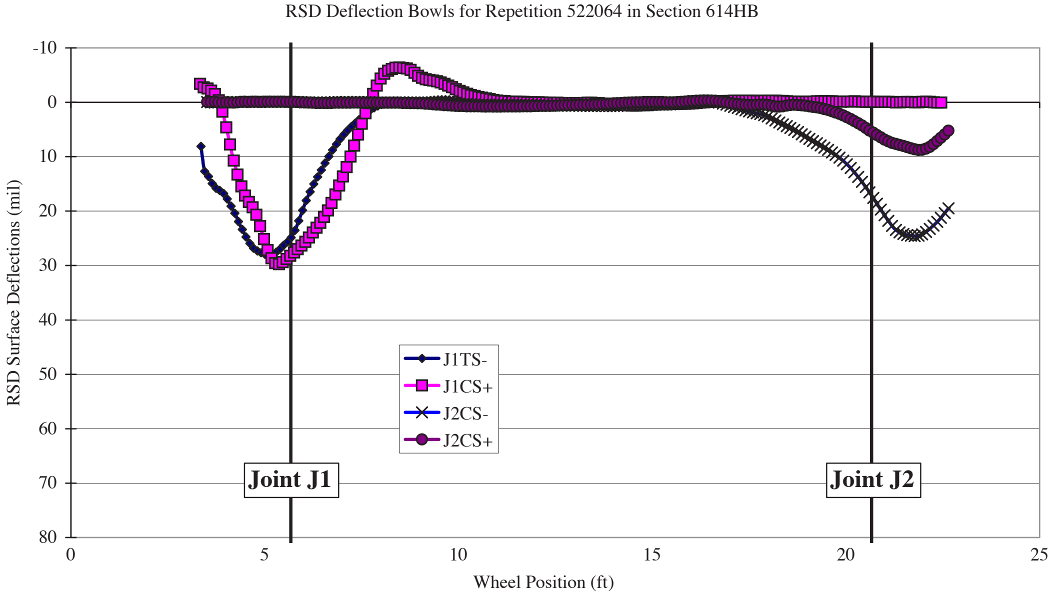

Figure K.71. Section 614HB: RSD deflections at different locations along caravan side with 9-kip (40-kN) test load at test completion.

following discussion focuses on results obtained with the 9-kip (40-kN) load, which were collected throughout the HVS loading. Table K.16 and Figures K.72 through K.78 summarize the elastic deflections measured at each side of each joint by JDMD. The figures also include RSD measurements taken on the surface at the same side of each joint as the JDMDs. Figure K.79 shows the history of differences in maximum and minimum strain with the number of load repetitions.

As with RSD deflections, JDMD deflections in Figures K.72 through K.78 were found to increase to a maximum value and then decrease significantly before increasing again. This is why "maximum during trafficking" is shown in Table K.16.

Table K.16. Section 614HB: Average 9-kip (40-kN) Elastic Deflections Before and After Testing

Position	Deflection (mil)			
	Before Trafficking	Maximum During Trafficking	After Trafficking	Ratio of Peak/Initial
JDMD No. 1: J2, edge, horizontal	4.6	9.6	3.6	2.1
JDMD No. 2: J2–, edge, vertical, AC	14.2	22.4	4.9	1.6
JDMD No. 3: J2–, edge, vertical	11.3	22.8	6.7	2.0
JDMD No. 4: J1, inner, horizontal	0.8	10.8	10.8	13.0
JDMD No. 5: J2+, edge, vertical	18.1	22.3	12.5	1.2
JDMD No. 6: J2+, inner, vertical	8.8	37.6	20.5	4.3
JDMD No. 7: J2+, inner, vertical, AC	4.3	9.2	0.3	2.1
JDMD No. 8: J2–, inner, vertical	8.6	30.3	30.3	3.5
JDMD No. 9: J1+, inner, vertical, AC	3.2	12.1	0.3	3.8
JDMD No. 10: J1+, inner, vertical	6.9	35.8	35.8	5.2
JDMD No. 11: J1–, inner, vertical	3.5	6.5	5.0	1.9
JDMD No. 12: J1–, edge, vertical	2.5	26.5	20.8	10.6
JDMD No. 14: J1–, edge, vertical, AC	4.7	16.4	0.3	3.5

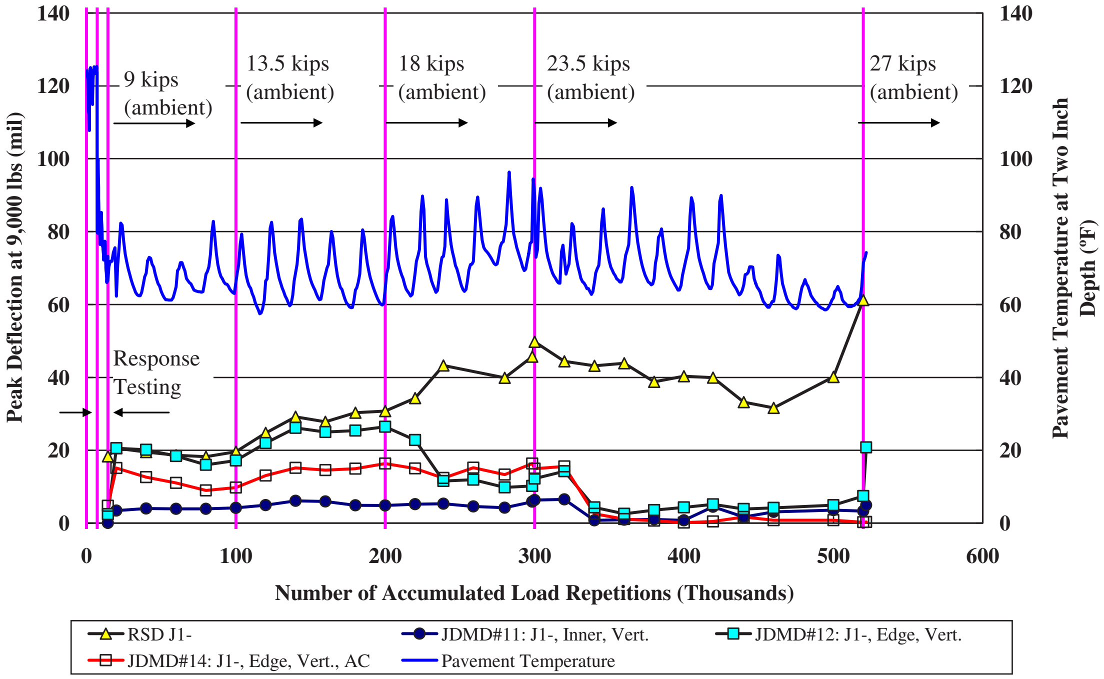

Figure K.72. Section 614HB: Vertical elastic deflections at south side of Joint J1 with 9-kip (40-kN) test load.

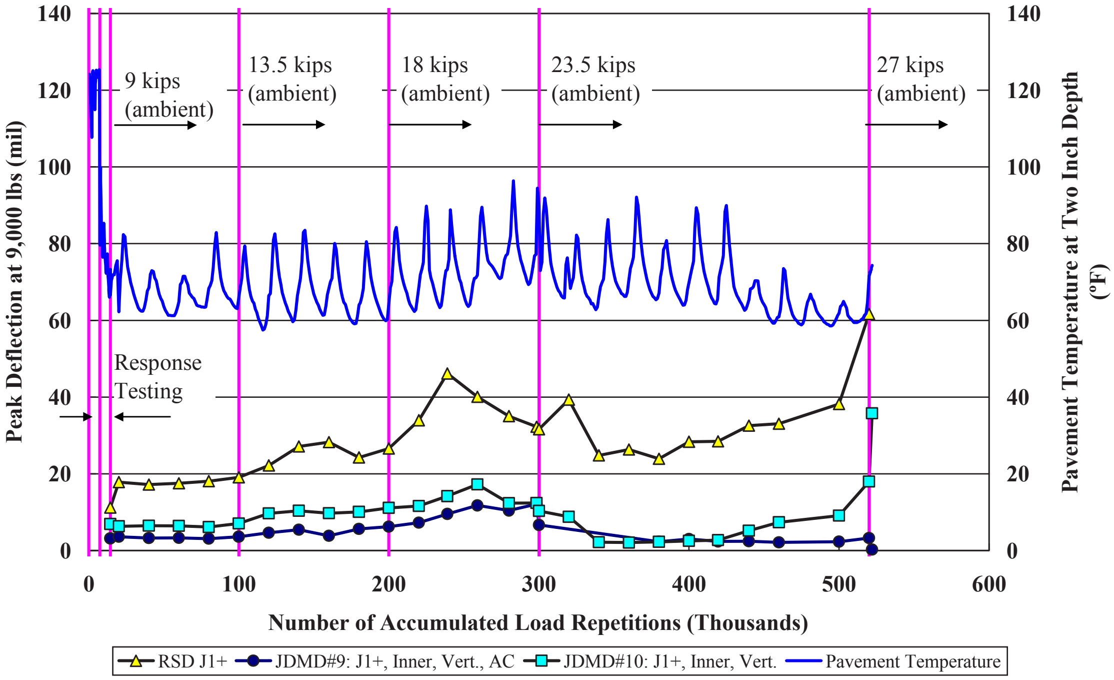

Figure K.73. Section 614HB: Vertical elastic deflections at north side of Joint J4 with 9-kip (40-kN) test load.

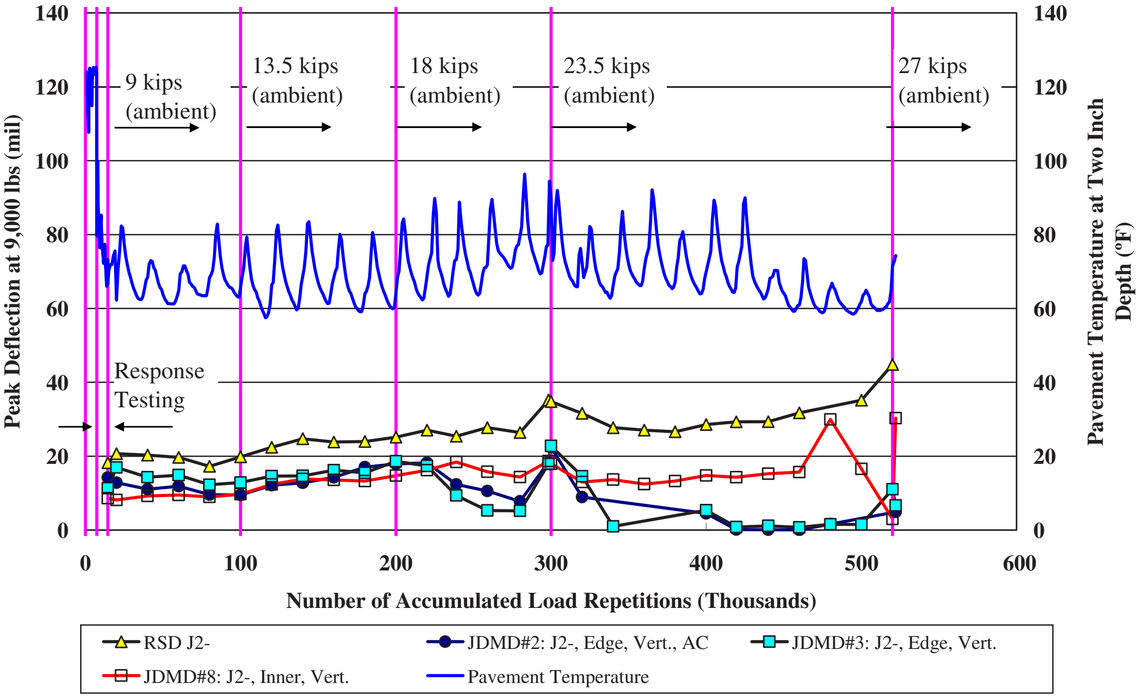

Figure K.74. Section 614HB: Vertical elastic deflections at south side of Joint J2 with 9-kip (40-kN) test load.

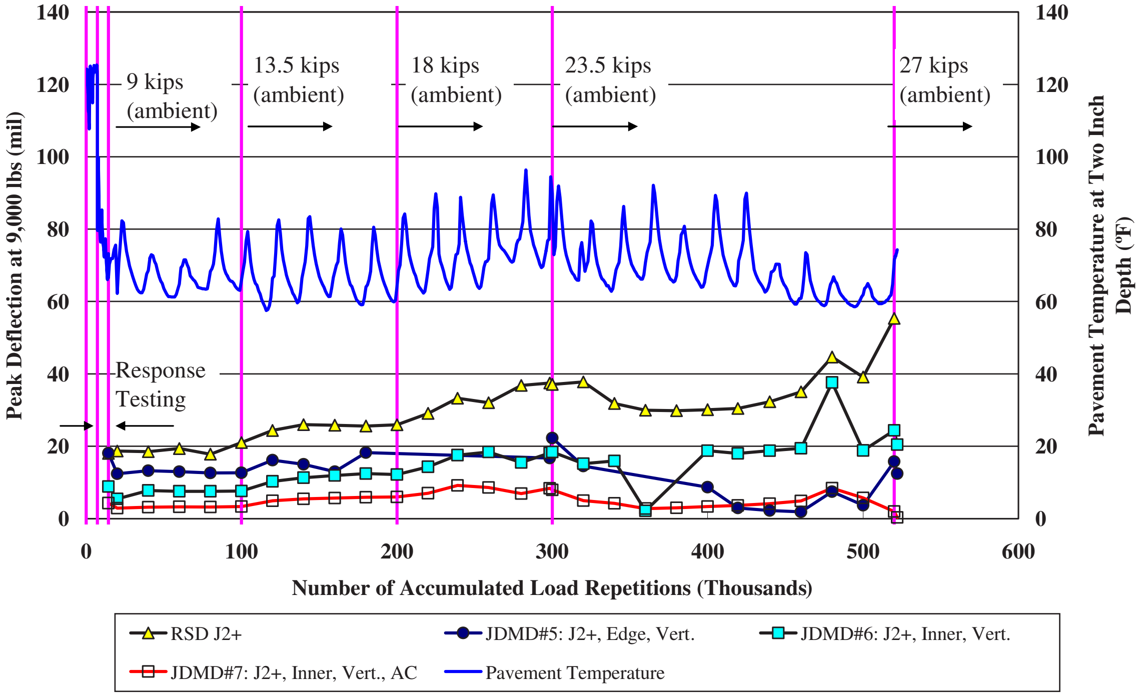

Figure K.75. Section 614HB: Vertical elastic deflections at north side of Joint J2 with 9-kip (40-kN) test load.

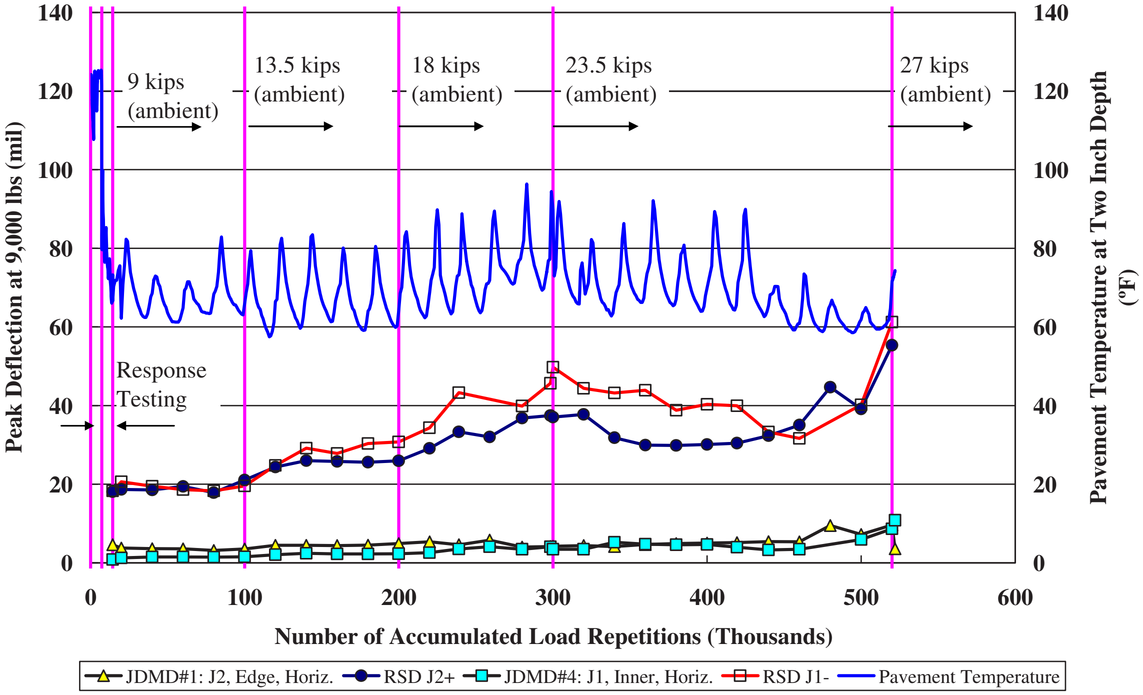

Figure K.76. Section 614HB: Horizontal elastic deflections at Joints J4 and J5 with 9-kip (40-kN) test load.

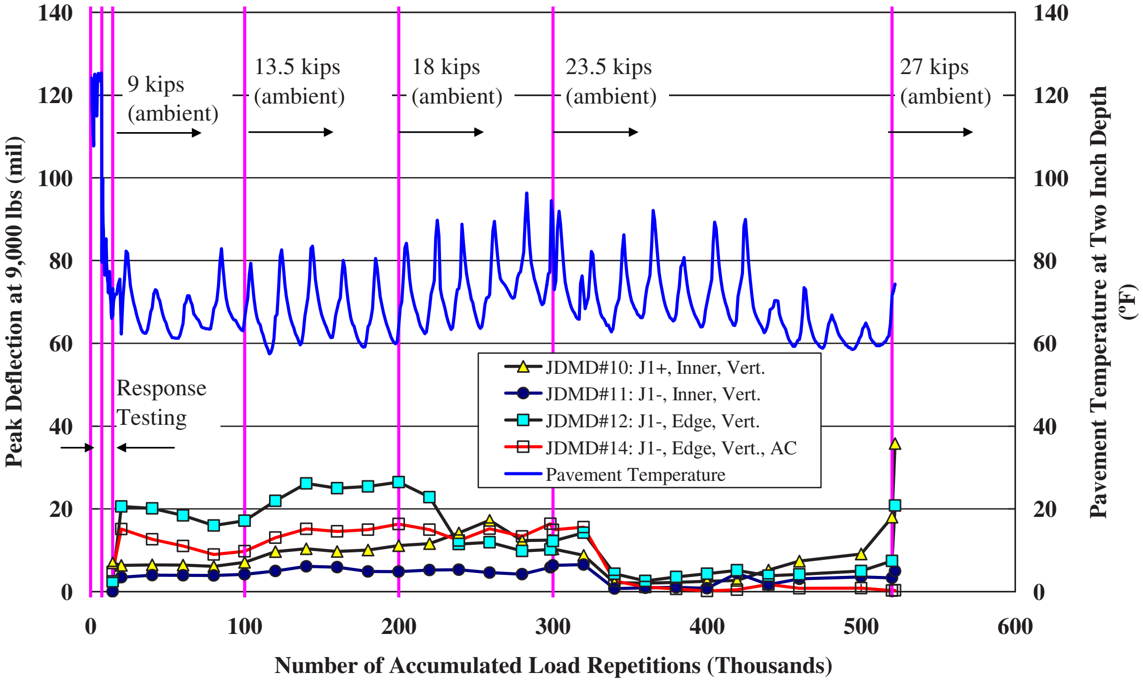

Figure K.77. Section 614HB: Vertical elastic deflections at Joint J1 with 9-kip (40-kN) test load.

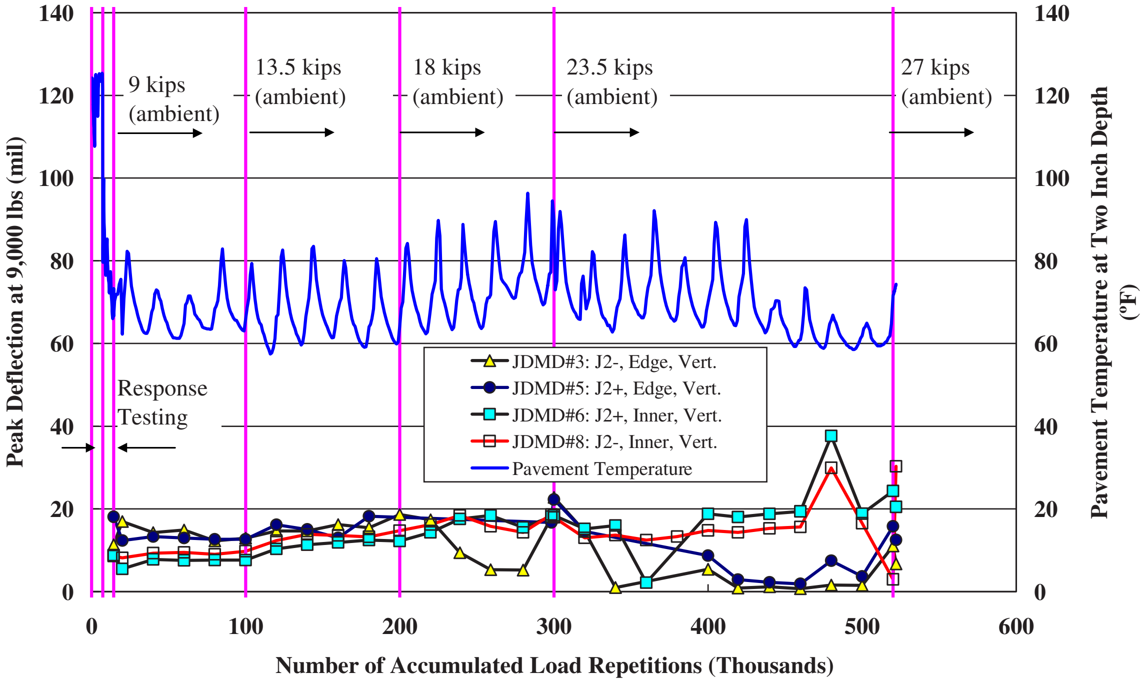

Figure K.78. Section 614HB: Vertical elastic deflections at Joint J2 with 9-kip (40-kN) test load.

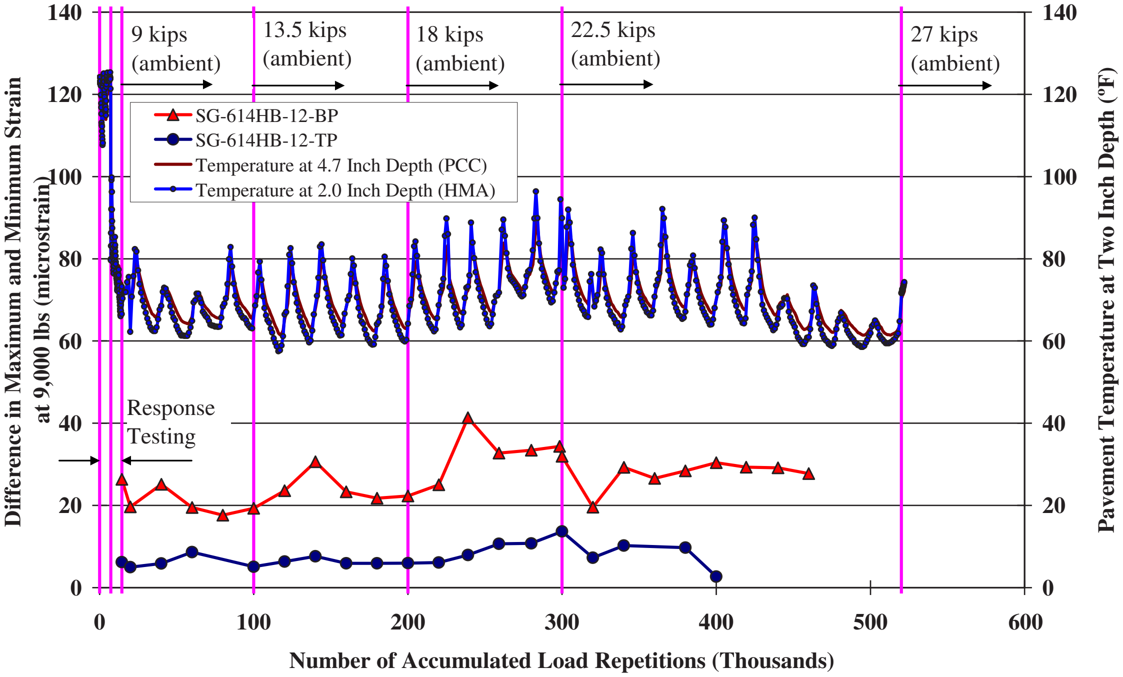

Figure K.79. Section 614HB: History of differences in maximum and minimum strain with number of load repetitions.

Elastic PCC Strains from Dynamic Strain Gauge

Only two dynamic strain gauges in the PCC slabs functioned properly during the HVS testing. They were both located near Station 12 at the same horizontal location, with one at the top of the PCC slab and the other at the bottom. They stopped working during the later stages of HVS testing. Different branches of the Wheatstone bridge-based strain gauge showed infinite resistance, which is a sign of a broken wire, possibly caused by cracking in the PCC slab.

The initial strain bowls measured at 14,400 load repetition are shown in Figure K.80. The strains for the top and bottom of the PCC slab show opposite signs with the bottom strain gauge recording much larger absolute values. This indicates a neutral axis between the two strain gauges but much closer to the top of the PCC than the bottom of the PCC. This is expected for a composite pavement with 4.5-in. RHMA-G layer on a 5.0-in. PCC slab.

Elastic Response under Trafficking Mode

Similar to the elastic responses under manual mode, elastic responses under trafficking mode reflect pavement structural integrity. Continuous elastic response data from JDMD and dynamic strain gauges under trafficking mode record the pavement structure deterioration process.

Elastic Deflections from JDMD

As mentioned in the section on measurement schedule summaries, JDMD data were recorded for every load repetition in Stage 1 (response testing) and every 100 repetitions afterward. These deflections correspond to the HVS trafficking load, which was increased step by step during Stage 2 of the HVS test.

Figures K.81 through K.87 summarize the elastic deflections measured at each side of each joint by JDMDs in trafficking mode. The figures also include RSD measurements taken on the surface on the same side of each joint as the JDMDs at the same wheel load but at creep speed. Note that in these figures only one data point is plotted for every 2,000 load repetitions to make the plots readable. In addition, there were stoppages in HVS trafficking during the testing, which resulted in jumps in temperature readings.

From the measured JDMD deflections, the following observations can be made:

- In general, elastic deflections at joints increase with the number of load repetitions, indicating deterioration of pavement structure caused by HVS trafficking.

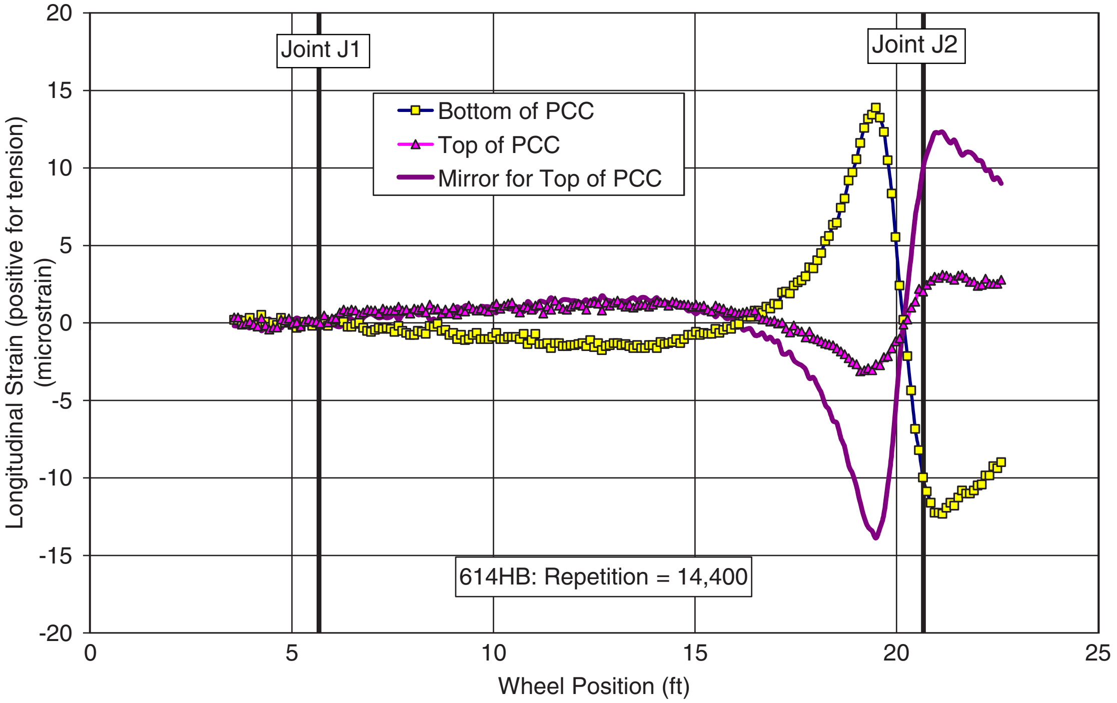

Figure K.80. Section 614HB: Initial strain bowls for dynamic strain gauges in the PCC layer, measuring longitudinal strain in the horizontal direction. The mirror for the strain bowl for the top of PCC matches almost exactly the bowl for the bottom of PCC in shape but not in strain value.

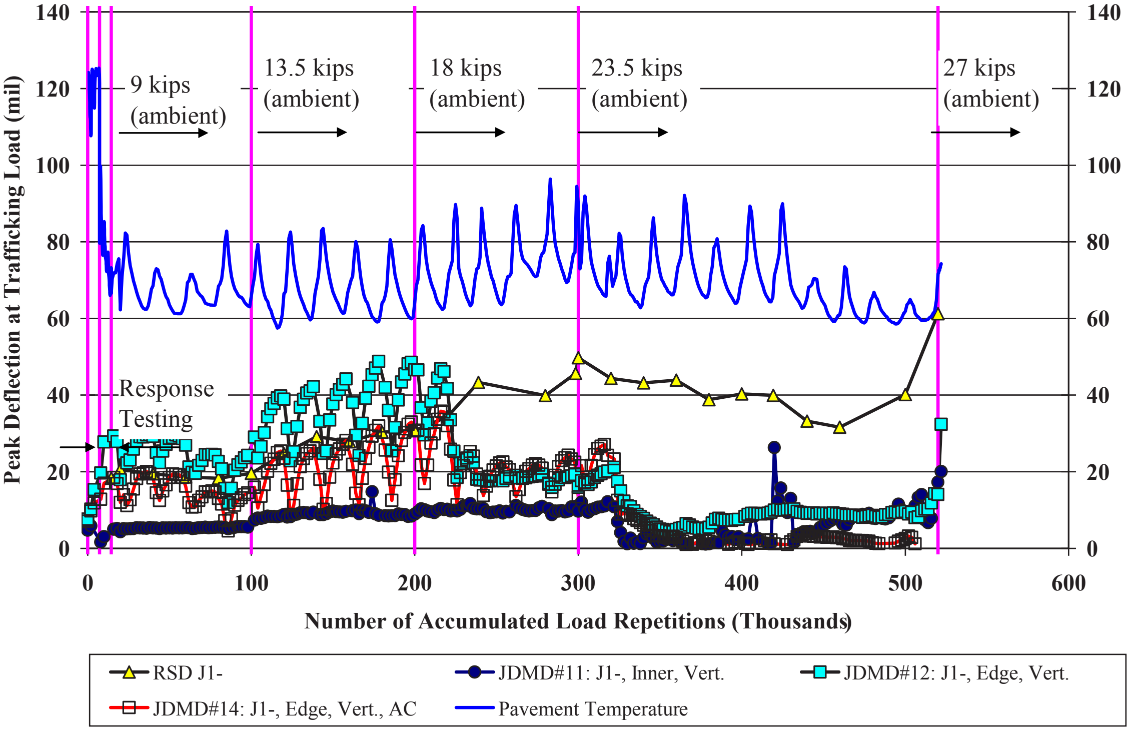

Figure K.81. Section 614HB: Vertical elastic deflections at south side of Joint J1 with trafficking load. "AC" in legend indicates that a JDMD is installed on the HMA surface.

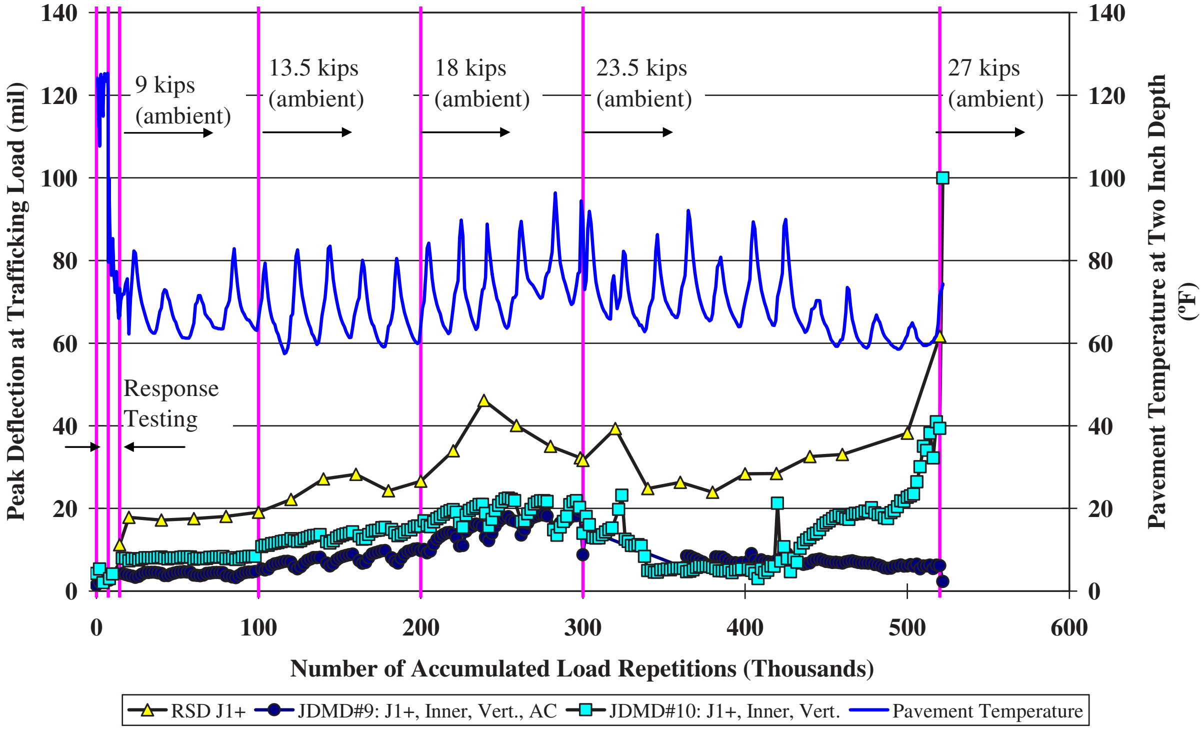

Figure K.82. Section 614HB: Vertical elastic deflections at north side of Joint J1 with trafficking load.

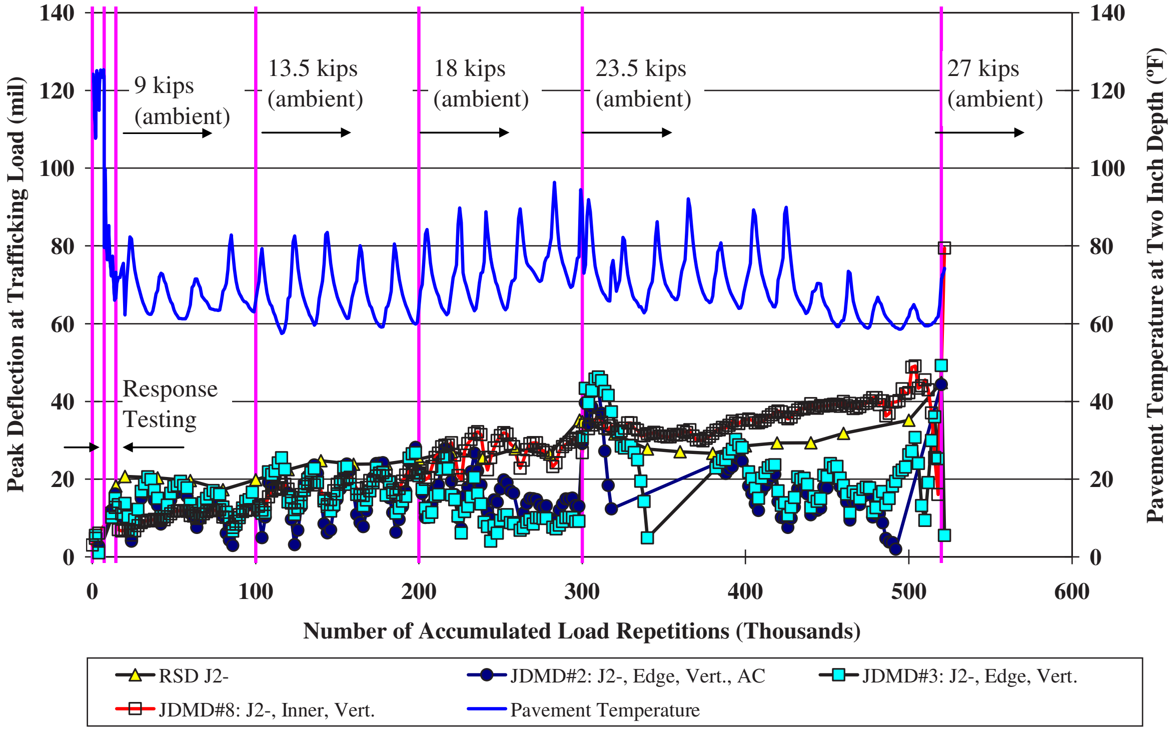

Figure K.83. Section 614HB: Vertical elastic deflections at south side of Joint J2 with trafficking load.

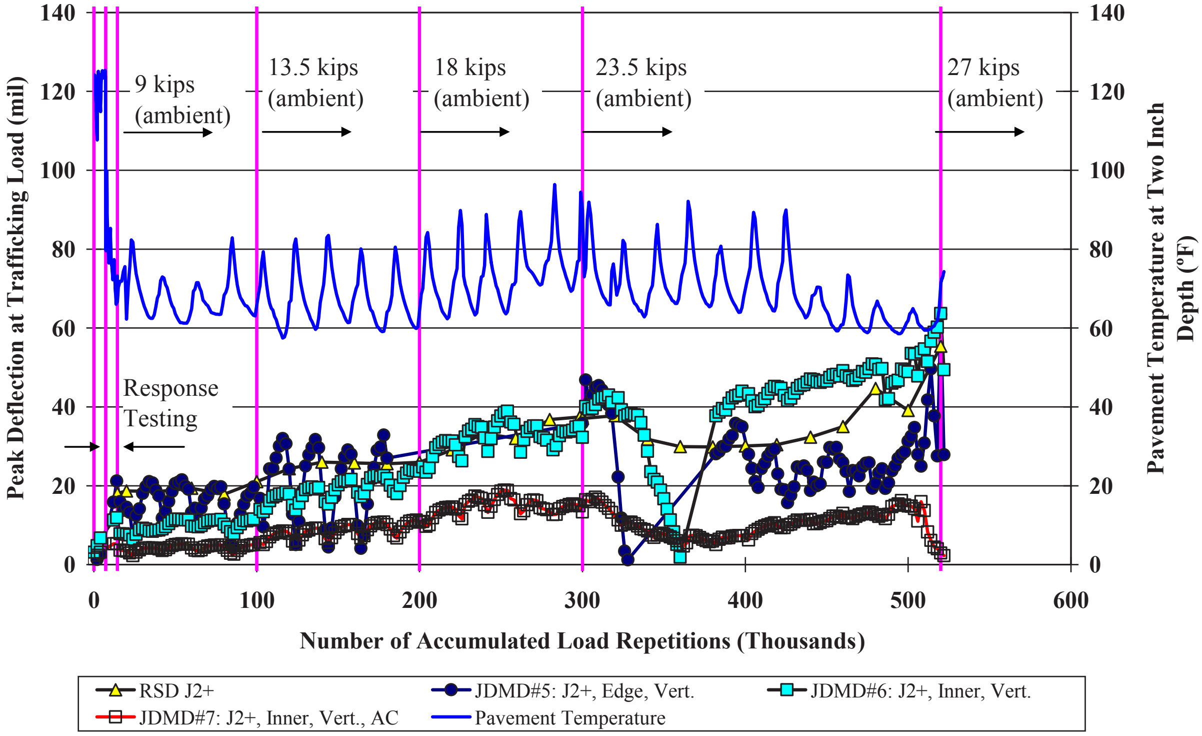

Figure K.84. Section 614HB: Vertical elastic deflections at north side of Joint J2 with trafficking load.

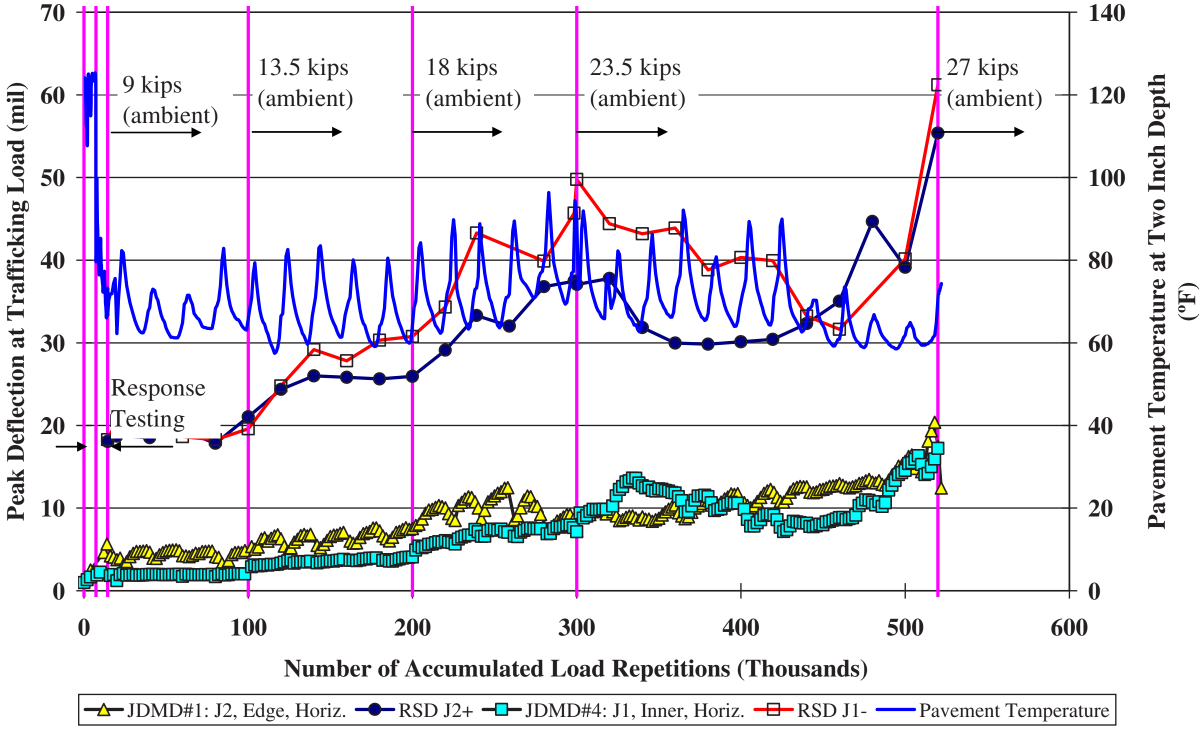

Figure K.85. Section 614HB: Horizontal elastic deflections at Joints J1 and J2 with trafficking load.

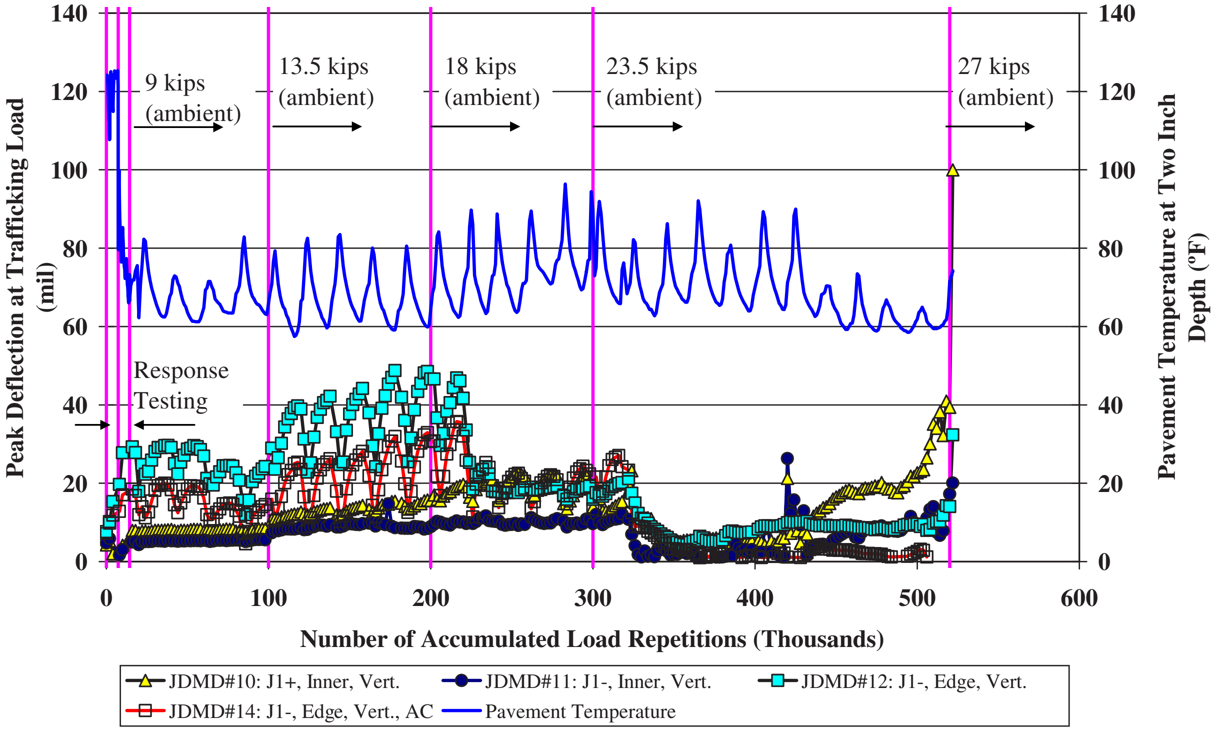

Figure K.86. Section 614HB: Vertical elastic deflections at both sides of Joint J1 with trafficking load.

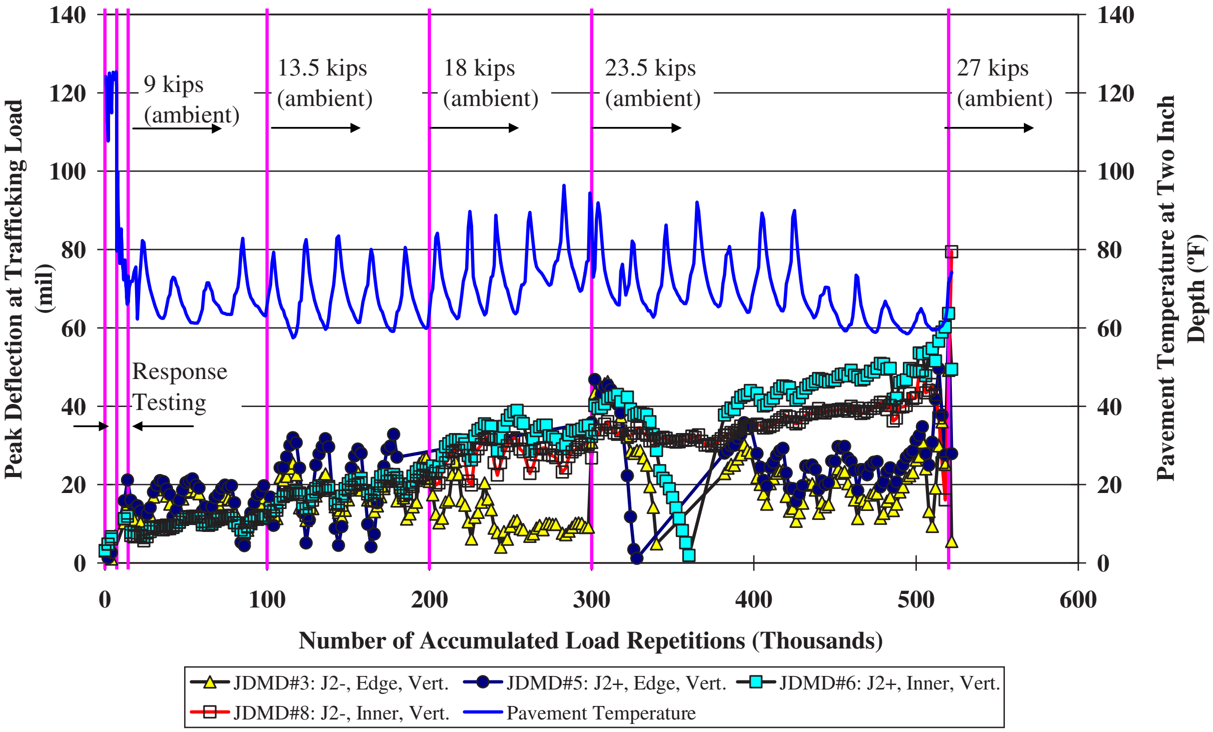

Figure K.87. Section 614HB: Vertical elastic deflections at both sides of Joint J2 with trafficking load.

- Elastic deflections at joints increase when pavement temperature decreases. The HMA layer stiffness increases with temperature, which indicates that elastic deflections are not controlled by the HMA layer and that PCC slab curling is the main factor that controls JDMD elastic deflections.
- In general, RSD deflections share the same trends as corresponding JDMDs.
- There are multiple occasions when vertical JDMD elastic deflections decrease significantly when there are no changes to pavement temperature or HVS trafficking load. A list of these events is shown in Table K.17. These events are most likely caused by cracking in either the HMA layer or the underlying PCC layer.
- The inner JDMDs show less elastic deflections than do the corresponding edge JDMDs, both in terms of absolute values and daily variations.

Elastic Strain from Dynamic Strain Gauges

As mentioned in the section on JDMD, RSD, and Strain gauges in 613HB, two strain gauges were installed in the PCC layer during construction. Figure K.88 shows the recorded peak-to-peak differences for the two strain gauges before they stopped working. Note that the jump in pavement temperatures shown in Figure K.88 is normal because HVS trafficking is not always continuous. Figure K.89 and Figure K.90 show the strain bowls for the two dynamic strain gauges measured under trafficking loads. The shape of the strain bowls did not change until after 310,000 load repetitions. The change in strain bowl shapes is believed to be caused by cracking in the underlying PCC slab.

Note that during each daily pavement temperature variation cycle, the strain amplitudes (defined as the difference

Table K.17. Section 614HB: List of Displacement Jump Events for Vertical JDMDs

Event Number	Repetitions (Thousand)	JDMDs Affected
1	218 to 224	All edge vertical JDMDs near Joint J1 (No. 12 and No. 14)
2	316 to 354	All vertical JDMDs near Joint J1[a]
3	234 to 248	All edge vertical JDMDs near Joint J2 (No. 2 and No. 3 only; No. 5 has no valid data)
4	312 to 364	All JDMDs near Joint J2[b] except No. 8
5	398 to 408	All edge vertical JDMDs near Joint J2
6	484 to 486	No. 6 (J2+, inner, vertical)
7	504 to 520	No. 7 (J2+, inner, vertical, AC) and No. 8 (J2–, inner, vertical)

[a] All vertical JDMDs near Joint J1 include JDMDs No. 9, No. 10, No. 11, No. 12, and No. 14.

[b] All vertical JDMDs near Joint J2 include JDMDs No. 2, No. 3, No. 5, No. 6, No. 7, and No. 8.

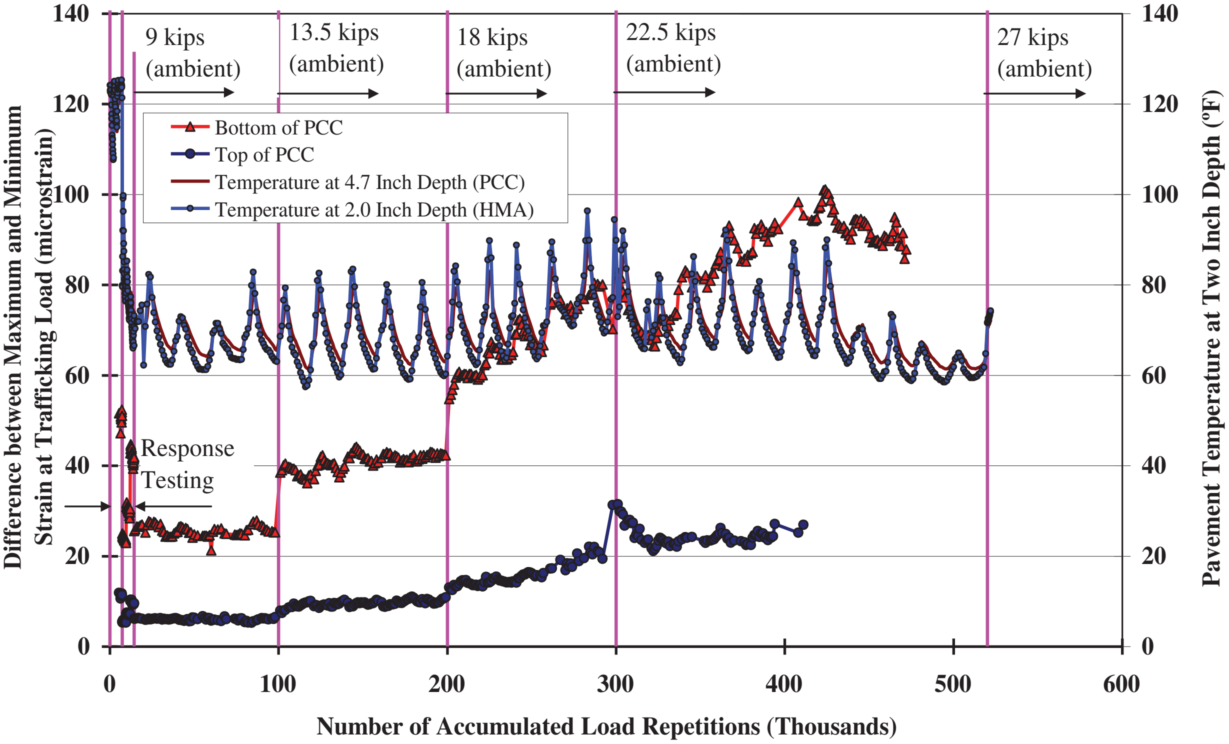

Figure K.88. Section 614HB: Difference between maximum and minimum strain for dynamic longitudinal strain gauges in the PCC.

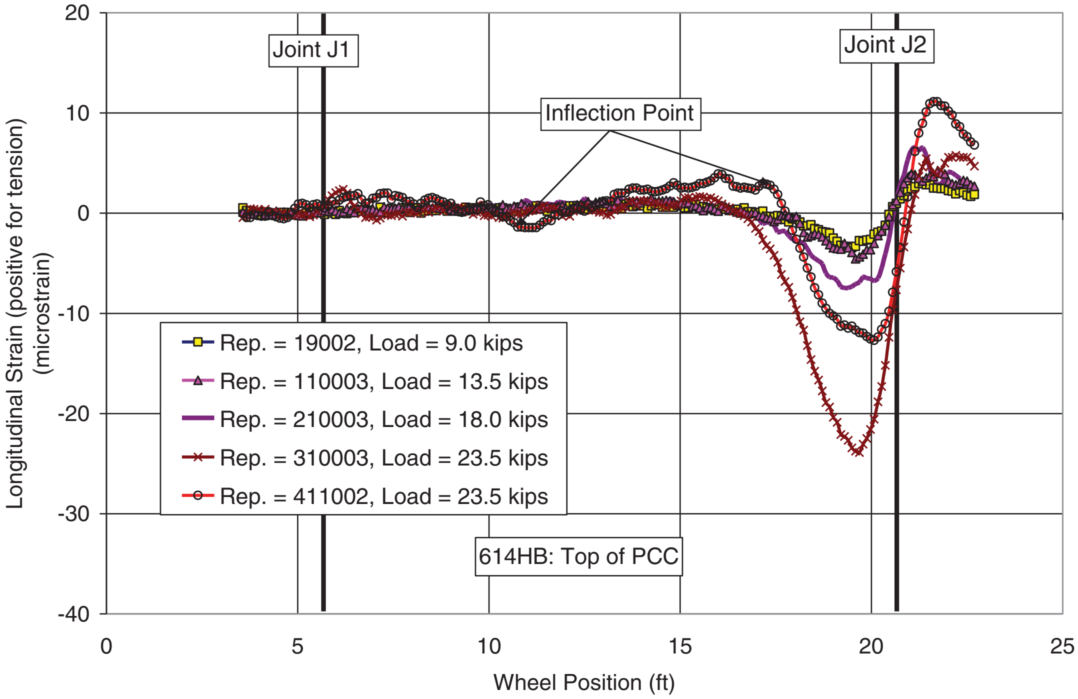

Figure K.89. Section 614HB: Strain bowls for dynamic strain gauges at the top of the PCC layer, measuring longitudinal strain in the horizontal direction under trafficking load.

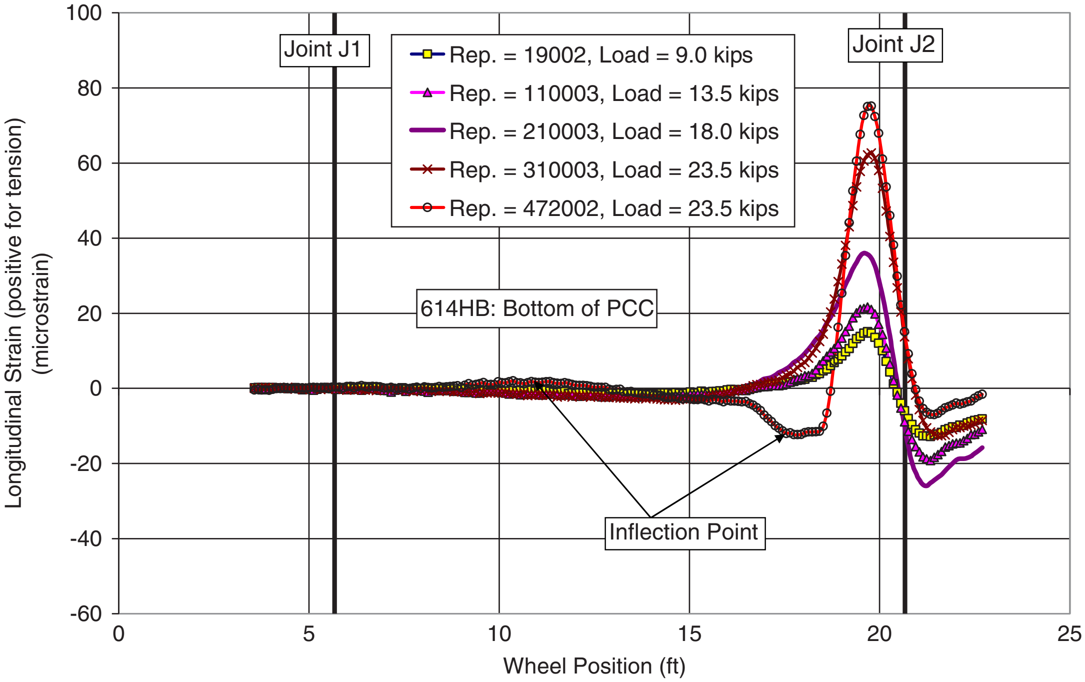

Figure K.90. Section 614HB: Strain bowls for dynamic strain gauges at the bottom of the PCC layer, measuring longitudinal strain in the horizontal direction under trafficking load.

between maximum and minimum strain for each given strain bowl) in the PCC increase with increasing pavement temperature, whereas peak JDMD deflections decrease with pavement temperature (see the section on elastic deflections from JDMD). This indicates that HMA layer stiffness does not affect pavement deflections but has an effect on traffic-induced strains in the PCC layer.

Determination of Timing for Cracking Events

As shown in Figure K.56, HVS traffic induced various cracks in the pavement for Section 614HB. In this section, data measured during HVS testing are used to determine the timing of two types of cracking events: (1) reflection cracking over the underlying joints and (2) slab cracking in the PCC caused by fatigue.

Based on visual inspection, reflection cracking over Joint J1 was first observed in the surface after 298,400 load repetitions, whereas reflection cracking over Joint J2 was not observed until the end of the HVS testing, when the section was extensively cracked by the aircraft tire. Slab cracking, evident by its reflection in the surface, also was not observed until the end of the HVS testing.

Based on the surface rut (i.e., change in surface elevation) measurement, tilting of the slab started after 300,000 load repetitions (i.e., after switching to a 100-kN [23.5-kip] wheel load) but accelerated after the aircraft tire was used at 520,000 load repetitions. The tilting is most severe near Station 5.

Based on RSD peak deflection histories and deflection bowls, some cracking in the PCC slab must have occurred between 320,000 and 520,000 load repetitions to cause deflection bowls to change, as was observed. Specifically, an inflection point appears when the wheel position equals 9.2 ft (2.8 m, Station 5.6) in the deflection bowls for repetition 520,000. After reviewing more RSD deflection bowls during this period, it was found that the inflection point in the deflection bowls first appeared after 340,000 load repetitions (see Figure K.91). This indicates that the PCC cracking event occurred between 320,000 and 340,000 load repetitions. A final top view of the test section between Station 5 and 6 is shown in Figure K.92. The transverse cracks shown in Figure K.92 are a reflection of the cracking in the underlying PCC slab.

Based on the changes in strain bowls over the course of the HVS testing (see Figure K.89 and Figure K.90), there must have been slab cracking near wheel positions 10.9 ft (3.3 m, Station 6.6) and 17.4 ft (5.3 m, Station 10.6) between 310,000 and 411,000 load repetitions for the strain bowls to have inflection points at those locations. The conclusion that the slab cracking at Station 6.6 was reflected through the surface at the end of the test is based in part on the presence of the transverse crack shown in Figure K.93. However, the crack at Station 10.6 was not reflected through at the end of the test. Note that slab cracking at Station 5.6 did not affect the strain bowls because the strain gauges were installed near Station 12 and were too far away from the crack to be affected. After reviewing more strain bowls between 310,000 and 411,000 repetitions, it was found

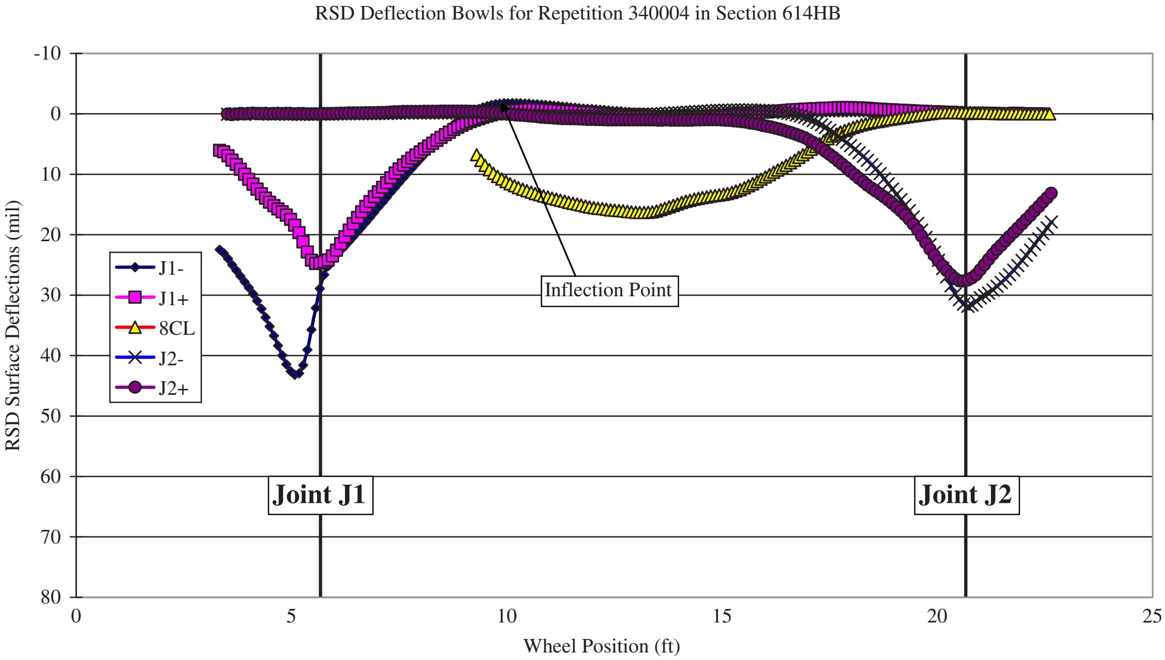

Figure K.91. Section 614HB: RSD deflection bowls after 340,004 load repetitions under 9-kip (40-kN) load in manual mode.

that inflection points at wheel position 17.4 ft first appeared in strain bowls for repetition 320,000.

After considering the above observations, the peak JDMD displacement jump events listed in Table K.17 can be interpreted as:

- Event 1 (218,000 to 224,000 load repetitions): reflection cracking of Joint J1;
- Event 2 (316,000 to 354,000 load repetitions): slab cracking near Station 5.6;
- Event 3 (234,000 to 248,000 load repetitions): reflection cracking of Joint J2;
- Event 4 (312,000 to 364,000 load repetitions): slab cracking near Station 10.6; and
- Events 5, 6, and 7: further propagation of cracks near Joint J2.

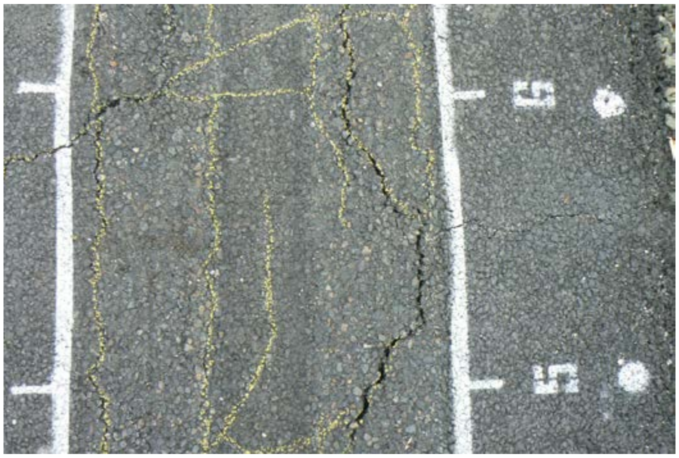

Figure K.92. Section 614HB: Top view of the section between Stations 5 and 6 after completion of HVS testing. Transverse cracks (i.e., running left to right) can be seen. Chalk lines indicate hairline cracks visible at the pavement surface.

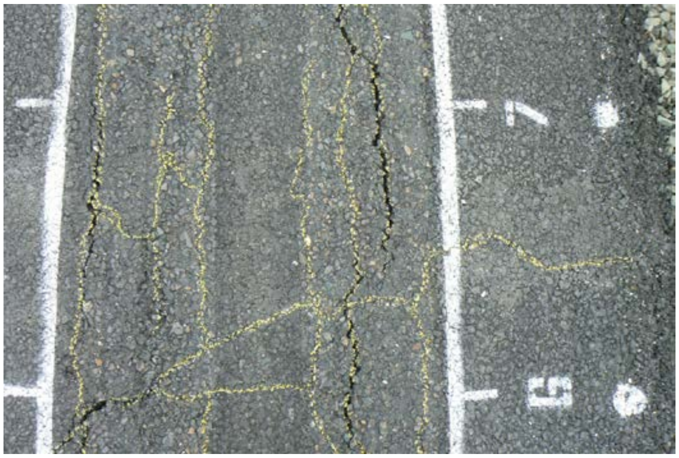

Figure K.93. Section 614HB: Top view of the section between Stations 6 and 7 after completion of HVS testing. Transverse cracks (i.e., running left to right) can be seen. Chalk lines indicate hairline cracks visible at the pavement surface.

This means that the reflection cracking life is 218,000 load repetitions at Joint J1 and 234,000 load repetitions at Joint J2, and the fatigue life of the underlying PCC slab is approximately 320,000 load repetitions. Using the 3.8 exponent and a 9-kip (40-kN) reference half-axle load, these load repetition numbers correspond to 1.0 million (for 218,000), 1.3 million (for 234,000), and 3.4 million (for 320,000) ESALs, respectively.

Summary and Conclusions

Sections 613HB and 614HB are the first two of eight planned cracking sections on the UCPRC track at its ATIRC facility. Testing on Section 613HB was conducted between mid-February and mid-March 2011, whereas testing on Section 614HB was conducted right after that of Section 613HB and was completed on May 20, 2011.

Section 613HB and Section 614HB are HMA/PCC composite pavement with an RHMA-G (rubberized hot-mix asphalt with gap-graded aggregates) layer on top of 5.0-in. (125-mm) newly placed PCC. Section 613HB has a 2.5-in. (63-mm) HMA layer, whereas Section 614HB has a 4.5-in. (114-mm) HMA layer.

A total of 300,000 load repetitions were applied on Section 613HB at increasing wheel loads, which is equivalent to a total of 1.9 million ESALs. Most of the testing was done under ambient temperatures with daily average air temperatures that ranged from 42°F to 59°F (5°C to 15°C) during the course of HVS testing. The typical daily variation range in air temperature was 20°F to 35°F (11°C to 19°C).

A total of 522,000 load repetitions were applied on Section 614HB at increasing wheel loads, which is equivalent to a total of 9.3 million ESALs. Most of the testing was done under ambient temperatures with daily average air temperatures that ranged from 51°F to 81°F (10°C to 27°C) during the course of HVS testing. The typical daily variation range in air temperature was 10°F to 40°F (5°C to 22°C).

During the HVS testing, various instruments were used to monitor and record pavement temperature, deflection, strain, surface cracking, and permanent surface profile change. Based on the measured data, the following observations are made:

- For both sections, the pavement failed by reflection cracking over the joints first, followed by fatigue cracking in the underlying PCC slab that also reflected through the HMA layer.
- For cracking failure in Section 613HB: Reflection cracking at the joints developed after 114,000 load repetitions (0.18 million ESALs) over Joint J4 and 115,000 repetitions (0.18 million ESALs) over Joint J5, but was first observed in the surface after 140,000 load repetitions (0.30 million ESALs) over both joints. Fatigue cracking in the PCC first developed after 195,000 load repetitions (0.56 million ESALs), and its reflection on the HMA surface was not observed until after 260,000 load repetitions (1.38 million ESALs).
- For cracking failure in Section 614HB: Reflection cracking at the joints developed after 218,000 load repetitions (1.0 million ESALs) over Joint J1 and 234,000 repetitions (1.3 million ESALs) over Joint J2 but was first observed in the surface after 298,400 load repetitions (1.95 million ESALs) over Joint J1 only. Fatigue cracking in the PCC first developed after 320,000 load repetitions (3.4 million ESALs), and its reflection on the HMA surface was not observed until after 522,000 load repetitions (9.3 million ESALs).
- For rutting in Section 613HB: The average total rut at the end of the test was 0.4 in. (10 mm), but reached 0.3 in. (7.5 mm) after only 20,000 load repetitions (0.04 million ESALs). It should be noted that the first 7,200 load repetitions were applied with a 122°F (50°C) target temperature for 2-in. (50-mm) depth, whereas the remainder of the test was conducted under ambient temperature.
- For rutting in Section 614HB: The average total rut at the end of the test was 1.6 in. (40.6 mm) but reached 0.71 in. (18.0 mm) after only 14,400 load repetitions (0.029 million ESALs). The average total rut before the switch to the aircraft tire was 0.89 in. (22.6 mm). It should be noted that the first 7,200 load repetitions were applied with a 122°F (50°C) target temperature for 2-in. (50-mm) depth, whereas the remainder of the test was conducted under ambient temperature.
- Joint movements decrease with increasing pavement temperature, indicating that these movements are controlled by curling in the underlying PCC and not the stiffness of the HMA.
- Traffic-induced PCC strain amplitudes increase with increasing pavement temperature, indicating that these strains are affected by the stiffness of the HMA layer.
- Joint movements measured by both JDMD and RSD increased with the number of load repetitions applied but decreased after fatigue cracks occurred in the PCC slab.
- Surface deflections measured by RSD at the middle of the slab increased consistently with increasing number of load repetitions.
- In Section 613HB, longitudinal strain gauges installed horizontally near the top and bottom of the PCC layer recorded almost exactly the same strain bowl but with the sign opposite the one at the beginning of the HVS test. This implies that the PCC layer is acting as a cantilever beam with a neutral axis at midthickness of the layer (i.e., the PCC slab is not in solid contact with the underlying base at the edge of the slab).
- In Section 614HB, longitudinal strain gauges installed horizontally near the top and bottom of the PCC layer recorded strain bowls that are similar in shape but with the sign opposite the one at the beginning of the HVS test. In addition, the peak strain at the top (in compression) is only

Table K.18. Summary Comparison of Performance for 2.5- and 4.5-in. HMA Sections

Performance Parameter	ESALs (millions)		Ratio of ESALs for Thick HMA Layer versus Thin HMA Layer
	Section 613HB 2.5-in. HMA	Section 614HB 4.5-in. HMA	
Reflection cracking of first joint	0.18	1.0	5.6
Reflection cracking of second joint	0.18	1.3	7.2
Reflection at surface	0.30	2.0	6.5
Initial PCC cracking	0.56	3.4	6.1
Reflection of PCC cracking	1.38	9.3	6.7
Rut depth of RHMA (in.) after 300,000 repetitions (2.0 million ESALs)	0.40	0.76 (Rut depth increase from thicker HMA layer)	90%

about one-fourth of the peak strain at the bottom (in tension). This implies that the PCC layer is acting as a cantilever beam with a neutral axis at the upper half of the PCC layer between the two strain gauges.

The two test sections were essentially the same, except for the HMA thickness. The general conclusions regarding the effects of the thicker HMA layer are summarized in Table K.18. The results indicate that the thicker HMA layer had a very large effect on the cracking life of the composite pavement, both for reflection cracking of the joints and for cracking of the PCC slab, and subsequent reflection of those cracks to the surface. At the same time, rutting increased with the thicker HMA layer.

APPENDIX L

HVS Rutting Tests at UCPRC

This appendix details the HVS rutting tests conducted at the University of California, Pavement Research Center (UCPRC). The objective was to determine the rutting performance of hot-mix asphalt (HMA) layers on top of portland cement concrete (PCC) layers at critical temperatures and traffic loads.

Preliminary Analysis for the HVS Test Sections

Analyses Performed for Performance Evaluation of HVS Test Sections

A sensitivity analysis of pavement designs was performed using the EverFE, three-dimensional finite-element analysis tool for simulating the response of jointed plain concrete pavement (JPCP) to axle loads and environmental effects. Inputs were based on measurements obtained during the site investigation and estimates of the moduli of an aggregate base-course, concrete, and asphalt concrete layers based on previous experience. The purpose of the analyses was to avoid premature cracking failures on concrete layers during the Heavy Vehicle Simulator (HVS) tests. Temperature differentials (difference in temperature) or gradients (temperature difference divided by thickness) between the top and bottom of concrete were calculated by using the enhanced integrated climatic model (EICM), a program that simulates climate effects on temperature distributions in pavements. EICM simulations were performed for the climate at Davis. Results of the EICM simulations for the HVS test sections are given in Figure L.1. The 5th and 95th percentile values from the given temperature gradient distributions were used to simulate the effects of temperature gradients with EverFE. For sections with HMA surface layer, −3°C and 5°C were used as critical extreme temperature differentials, whereas −10°C and 14°C, and −8°C and 11°C were used for sections with thick (7-in.) and thin (5-in.) HMA layers, respectively.

All slabs analyzed (and constructed) for this study were 3.7 m (12 ft) wide and 4.5 m (15 ft) long, and were bare jointed concrete pavement. The effect of nonlinear temperature gradients on curling stresses was determined for all sections by EverFE. It was observed that only the section with the thinner concrete layer (5 in.) will be exposed to relatively high levels of tensile curling stresses whereas the effect of the temperature gradient on other sections will be insignificant. Figure L.2 illustrates the distribution of tensile stresses for critical positive and negative temperature differentials for the section with thin concrete layer (5 in.).

Critical tensile stresses that may occur at the HVS test sections under trafficking were also determined by EverFE. The effects of the HVS loading (60-kN wheel load for a tire with 720-kPa pressure) was simulated for all HVS test sections at the corner and midslab edge locations for four critical temperature differentials. The factorial for the sensitivity analyses is given in Table L.1.

Results of the analyses indicated that midslab edge loading will be more critical than corner loading for all sections. Because of the reduced temperature gradient, tensile stresses at the sections with HMA layers will be less than those for the sections without an HMA layer. For the section with 5-in. PCC layer, early cracking failure may be observed because of high tensile stresses (approximately 10 MPa).

HVS traffic conditions were also simulated by using the *Mechanistic–Empirical Pavement Design Guide* (*MEPDG*) for the corresponding Davis climate. Results of the analysis indicated that during the initial 4 days (loading at 20 kN [4,500 lb], 40 kN [9,000 lb], 60 kN [13,500 lb], and 100 kN [22,500 lb] for 24 hours each), none of the sections would fail. However, when loading was continued with 60 kN (13,500 lb), sections without an HMA surface layer started to show slight transverse cracking and faulting after 1,000,000 repetitions. In other words, *MEPDG* results suggested that there would not be a premature failure for the HVS test sections.

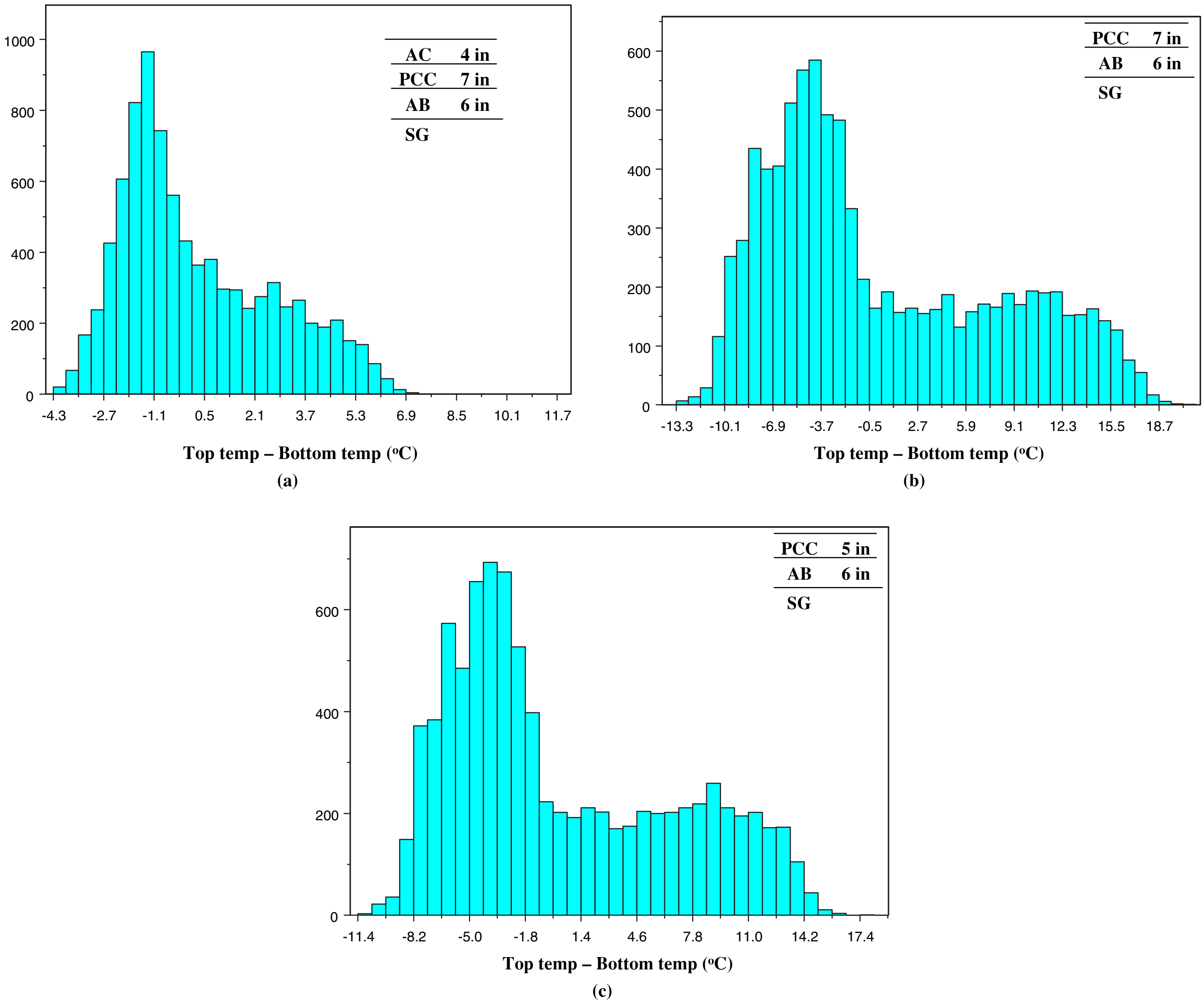

Figure L.1. The calculated temperature gradient distributions from EICM for the HVS test sections for Davis climate: (a) section with thick HMA layer (4 in.), (b) section with thick concrete layer (7 in.) without HMA layer, and (c) section with thin concrete layer (5 in.) without HMA layer.

HVS Test Criteria

Protocols

HVS test section layout, test setup, trafficking, and measurements followed standard UCPRC protocols (Jones 2005).

Pavement Instrumentation and Monitoring Methods

Instrumentation for the HVS rutting tests is shown in Figure L.3 and included the following types and collection intervals:

- Laser Profilometer, a portable beam with a traveling laser collecting 260 points across its 2.3-m length, was used to measure the transverse surface profile across the wheelpath, with measurements taken at each 0.5-m station and at load repetition intervals selected to provide characterization of the rut development.
- Thermocouples measured ambient and pavement temperatures, with measurements taken at Stations 4 and 12 and for ambient temperature at 1-hour intervals during HVS operation.
- AC strain gauges took measurements at the locations shown in Figure L.3 and at load repetition intervals selected to provide characterization of the rut development.

Surface and in-depth deflections were not measured during the HVS rutting tests. As can be seen in Figure L.3, HMA

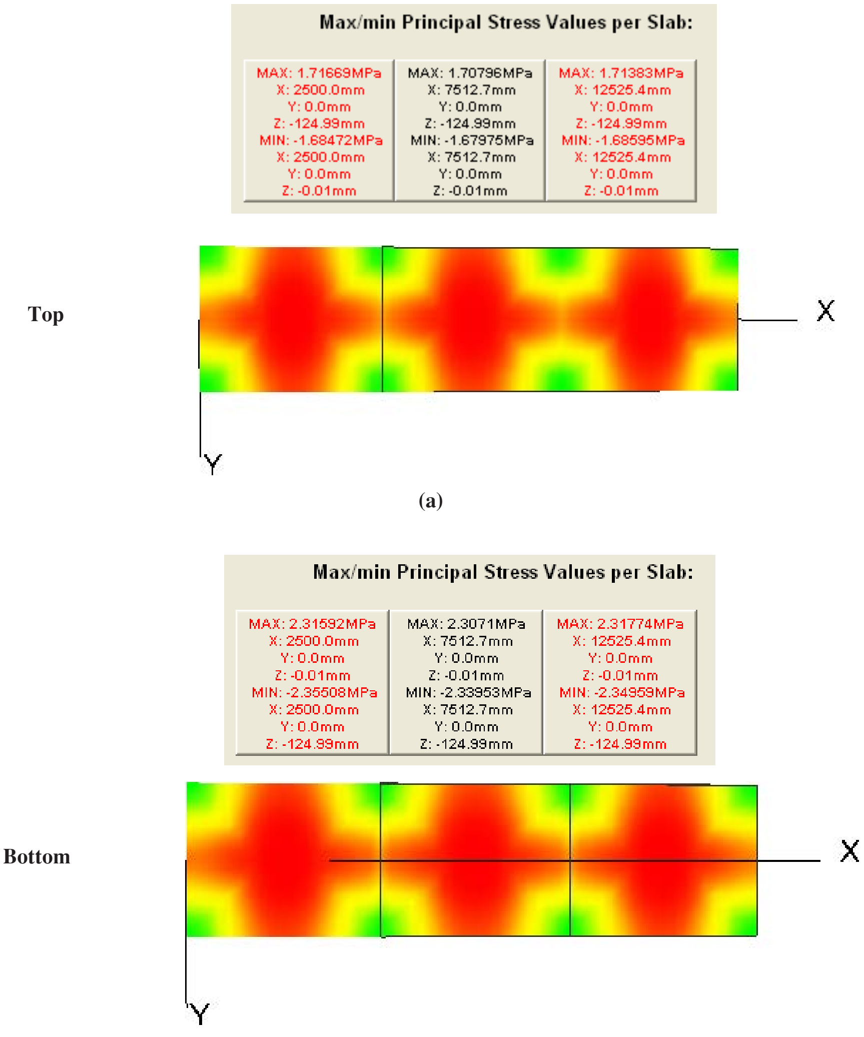

Max/min Principal Stress Values per Slab:

MAX: 1.71669MPa X: 2500.0mm Y: 0.0mm Z: -124.99mm MIN: -1.68472MPa X: 2500.0mm Y: 0.0mm Z: -0.01mm	MAX: 1.70796MPa X: 7512.7mm Y: 0.0mm Z: -124.99mm MIN: -1.67975MPa X: 7512.7mm Y: 0.0mm Z: -0.01mm	MAX: 1.71383MPa X: 12525.4mm Y: 0.0mm Z: -124.99mm MIN: -1.68595MPa X: 12525.4mm Y: 0.0mm Z: -0.01mm

(a)

Max/min Principal Stress Values per Slab:

MAX: 2.31592MPa X: 2500.0mm Y: 0.0mm Z: -0.01mm MIN: -2.35508MPa X: 2500.0mm Y: 0.0mm Z: -124.99mm	MAX: 2.3071MPa X: 7512.7mm Y: 0.0mm Z: -0.01mm MIN: -2.33953MPa X: 7512.7mm Y: 0.0mm Z: -124.99mm	MAX: 2.31774MPa X: 12525.4mm Y: 0.0mm Z: -0.01mm MIN: -2.34959MPa X: 12525.4mm Y: 0.0mm Z: -124.99mm

(b)

Figure L.2. Critical curling stresses for the HVS section with thin concrete layer (5 in.). (a) Results of the analysis for negative critical temperature differential (−8°C). (b) Results of the analysis for positive critical temperature differential (11°C).

strain gauges at 50-mm depth were used to collect pavement response in the asphalt layers throughout the HVS tests. These strain gauges were located under the wheelpath and at the edge of the wheelpath to provide information about the response of the HMA layer to the shearing action of the tires. Results for the strain gauge measurements are given in "Asphalt Strain Gauge Results". Pavement cells on which HVS rutting test sections were performed are shown in Figure L.4. The purpose of the HVS rutting tests was to evaluate the effects of HMA thickness on rutting performance for thin HMA layers on PCC slabs. For this reason, two HMA thicknesses were tested for each of the two mix types placed on the UCPRC test sections.

Table L.1. Factorial for EverFE Sensitivity Analyses

Load Location	Section–Dowel	TD (°C)	CTE (per °C)
Corner	H_{PCC} = 5 in.–no dowel	–3	0.9×10^{-5}
		5	
	H_{PCC} = 7 in.–no dowel	–10	
Midslab edge	H_{PCC} = 7 in.–dowelled	14	1.17×10^{-5}

Note: CTE = Coefficient of thermal expansion; TD = temperature differential; H_{PCC} = thickness of PCC layer.

Description of HVS at UCPRC

The HVS is a mobile load frame that uses a full-scale wheel (dual or single) to traffic the pavement test section. The trafficked test section is 8 m (26.4 ft) long, of which 1 m (3.3 ft) on each end is used for turnaround of the wheel and generally is not included in analysis and reporting of results. This wheelpath length permits the testing of one slab of jointed PCC of up to approximately 6 m (19.8 ft) with the trafficking

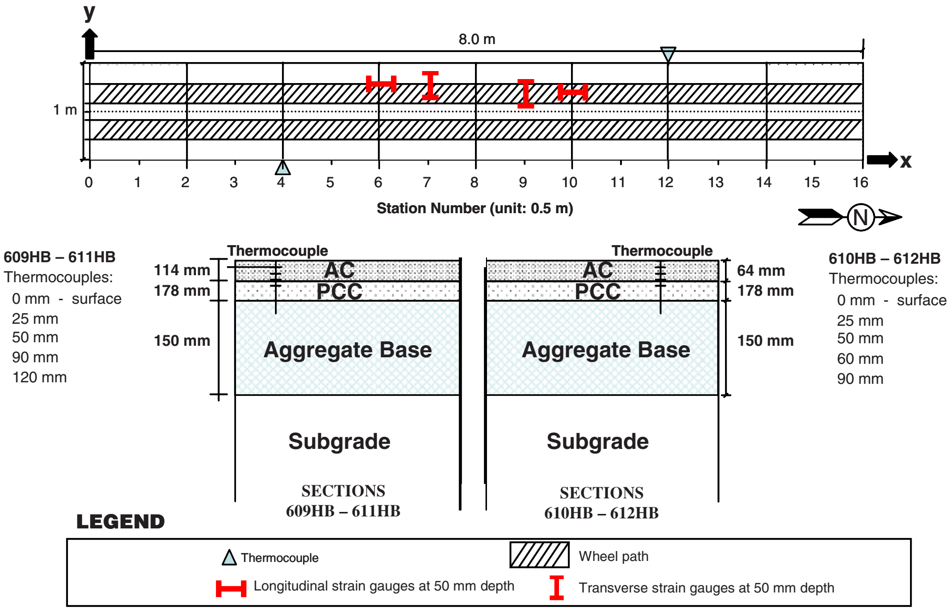
y
8.0 m
1 m
x
0
1
2
3
4
5
6
7
8
9
10
11
12
13
14
15
16
Station Number (unit: 0.5 m)
N
609HB – 611HB
Thermocouples:
0 mm - surface
25 mm
50 mm
90 mm
120 mm
Thermocouple
114 mm
178 mm
150 mm
AC
PCC
Aggregate Base
Subgrade
SECTIONS
609HB – 611HB
Thermocouple
64 mm
178 mm
150 mm
AC
PCC
Aggregate Base
Subgrade
SECTIONS
610HB – 612HB
610HB – 612HB
Thermocouples:
0 mm - surface
25 mm
50 mm
60 mm
90 mm
LEGEND
Thermocouple
Wheel path
Longitudinal strain gauges at 50 mm depth
Transverse strain gauges at 50 mm depth

Figure L.3. HVS rutting test section layout and location of thermocouples.

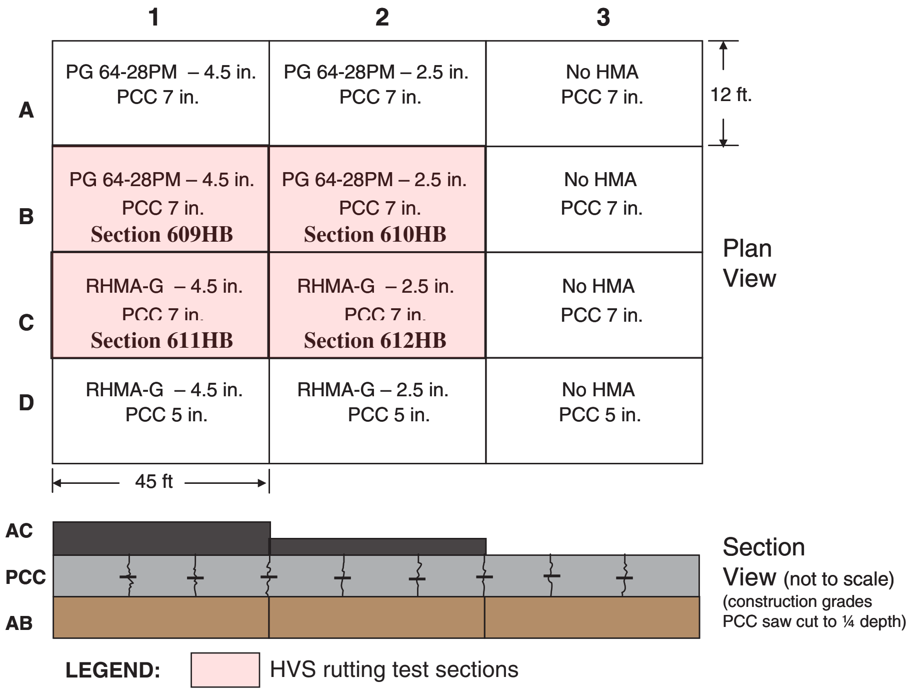
1
2
3
A
PG 64-28PM – 4.5 in.
PCC 7 in.
PG 64-28PM – 2.5 in.
PCC 7 in.
No HMA
PCC 7 in.
12 ft.
B
PG 64-28PM – 4.5 in.
PCC 7 in.
Section 609HB
PG 64-28PM – 2.5 in.
PCC 7 in.
Section 610HB
No HMA
PCC 7 in.
Plan View
C
RHMA-G – 4.5 in.
PCC 7 in.
Section 611HB
RHMA-G – 2.5 in.
PCC 7 in.
Section 612HB
No HMA
PCC 7 in.
D
RHMA-G – 4.5 in.
PCC 5 in.
RHMA-G – 2.5 in.
PCC 5 in.
No HMA
PCC 5 in.
45 ft
AC
PCC
AB
Section View (not to scale)
(construction grades
PCC saw cut to ¼ depth)
LEGEND:
HVS rutting test sections

Figure L.4. Pavement cells with HVS rutting tests.

Overall weight		59,646 kg
Load weight of the test wheel tire		20-100 kN with truck tire 20-200 kN with aircraft tire
Dimensions of tested area of pavement		1.5 m × 8 m maximum
Velocity of the test wheel		10 km/hr maximum
Maximum trafficking rate		1000 repetitions/hr
Average trafficking rate		750 repetitions/hr
Average daily repetitions		16,000
Dimensions:	Length	22.56 m
	Width, overall	3.73 m
	Height	3.7 m
	Wheel base	16.7m
Number of axles		3 (1 in rear, 2 in front)

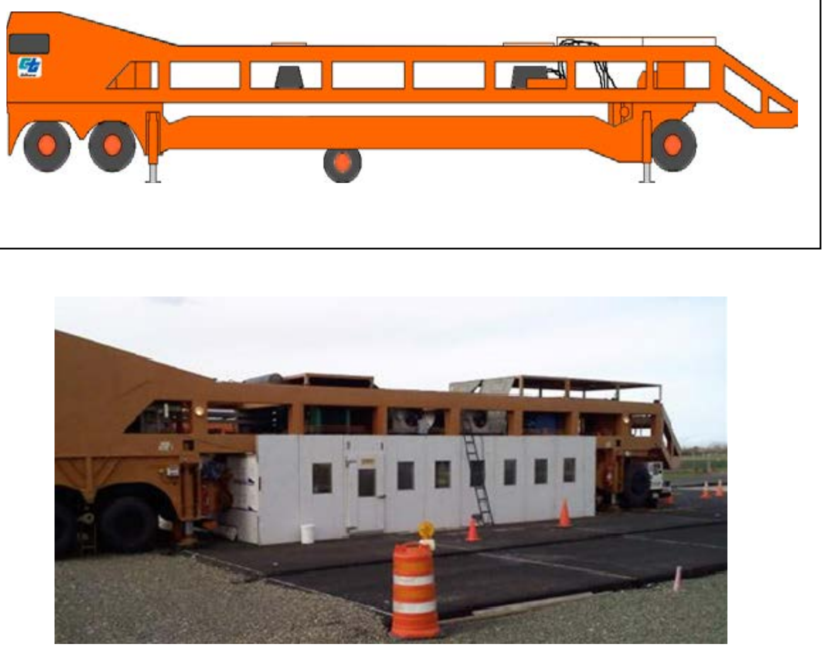

Figure L.5. Specifications and photograph of HVS on SHRP 2 R21 test section at UCPRC.

including both joints and the entire slab. The specifications and a photograph of the HVS are shown in Figure L.5.

HVS Test Criteria and Conditions

Test Section Failure Criterion

The failure criterion was defined as an average maximum rut of 12.5 mm (0.5 in.) over the full monitored section (Station 3 to Station 13). Testing was continued past a 12.5-mm average rut depth until the rutting accumulation rate stabilized.

Environmental Conditions

The pavement temperature at 50 mm (2.0 in.) depth was maintained at 50°C ± 4°C (122°F ± 7°F) to assess rutting potential under typical pavement conditions. Heaters were operated inside the temperature control box to maintain the pavement temperature. The pavement surface received no direct rainfall because it was protected by the temperature control unit. The sections were tested predominantly during the wet season; however, measures were taken to keep water from entering the pavement structure inside the temperature control box, and there was an extensive drainage system placed around the entire set of pavement test sections. In addition, plastic sheets were placed on the surface to keep water out of the pavement.

Test Schedule

The schedule of HVS trafficking and number of loads on each section are shown in Table L.2.

Table L.2. Test Duration for HVS Rutting Tests

Section	Mix Type	Design Thickness (mm)	As-built Thickness (mm)	As-built Air Void (%)	Start Date	Finish Date	Total Repetitions
609HB	PG 64-28 PM	114	116	9.8	1/28/2010	2/26/2010	200,000
610HB	PG 64-28 PM	64	72	10.0	3/4/2010	3/23/2010	201,200
611HB	RHMA-G	114	118	13.8	3/29/2010	4/2/2010	18,503
612HB	RHMA-G	64	74	13.4	4/13/2010	4/27/2010	90,000

Loading Program

The HVS loading program for each section is summarized in Table L.3. All trafficking was carried out with a dual-wheel configuration with the centerlines of the two tires spaced 360 mm (14.2 in.) apart, using radial truck tires (Goodyear G159-11R22.5 steel belt radial) inflated to a pressure of 690 kPa (100 psi), in a channelized (no wander), unidirectional loading mode in which the wheel travels one direction loaded and is lifted off the pavement for the return pass. Channelized trafficking is used to simulate the tracking of radial tires in the wheelpath once a small rut forms and is more aggressive than field conditions in the initial stages of rutting before tires begin to track in the ruts. Wheel speed for all tests was 8.7 km/hour (5.4 mph).

Air Void Content Distribution in HMA Layers from Image Analysis

Prism-shaped blocks were cut from the asphalt layers in Cells B1, B2, C1, and C2 for air void evaluation using image analysis. Figure L.6 shows the locations for the asphalt concrete samples that were sawn from the constructed HMA layers for the image analysis. Air voids were determined by the CoreLok (AASHTO T331) method. Air voids for the rubberized hot-mix asphalt with gap-graded aggregates (RHMA-G) mix averaged 13.4%, and for the PG 64-28 polymer-modified (PM) mix averaged 10.2%, both of which are higher than the average air void contents for these mixes (approximately 11% and 7%, respectively) in practice on the state highway network.

Air void contents and distributions for the field blocks were also evaluated using computerized tomography (CT) scanning performed at the University of California, Davis Medical Center. Figure L.7 shows the three-dimensional distribution of air voids from CT scanning for two prismatic samples sawn from HVS test sections. The top two images are for PG 64-28 PM mix from HVS Test Section 609HB (B1) and the bottom two images are for RHMA-G from HVS Test Section 611HB (C1). Figure L.8 shows the distribution of air voids with depth for the thick asphalt sections; the figure also shows the two lifts. It can be observed that the air void content in the middle depth of each lift is lower than that in the bottom and top of the lift, most likely the result of greater temperatures being retained longer in the middle of the lift. It can also be seen that the bottom lift is better compacted than the top lift. This is a result of the reheating and additional compaction of the bottom lift occurring during the compaction of the top lift.

Changes in the distribution of air voids in HMA blocks were also determined by analyzing the CT images before and

Table L.3. Summary of HVS Loading Program

Section	Mix Type	As-built Thickness (mm)	Wheel Load[a] (kN)	Temperatures at 50 mm (2 in.) Average (°C)	Temperatures at 50 mm (2 in.) SD (°C)	Total Repetitions
609HB	PG 64-28 PM	116	40 60	49.5	1.1	63,750 136,250
610HB	PG 64-28 PM	72	40 60	49.8	1.0	64,000 137,200
611HB	RHMA-G	118	40	48.7	1.1	18,503
612HB	RHMA-G	74	40	49.7	1.3	90,000
Total						509,703

[a] 40 kN = 9,000 lb; 60 kN = 13,500 lb; 25.4 mm = 1 in. Fahrenheit = Celsius × 9/5 + 32.

Note: SD = standard deviation.

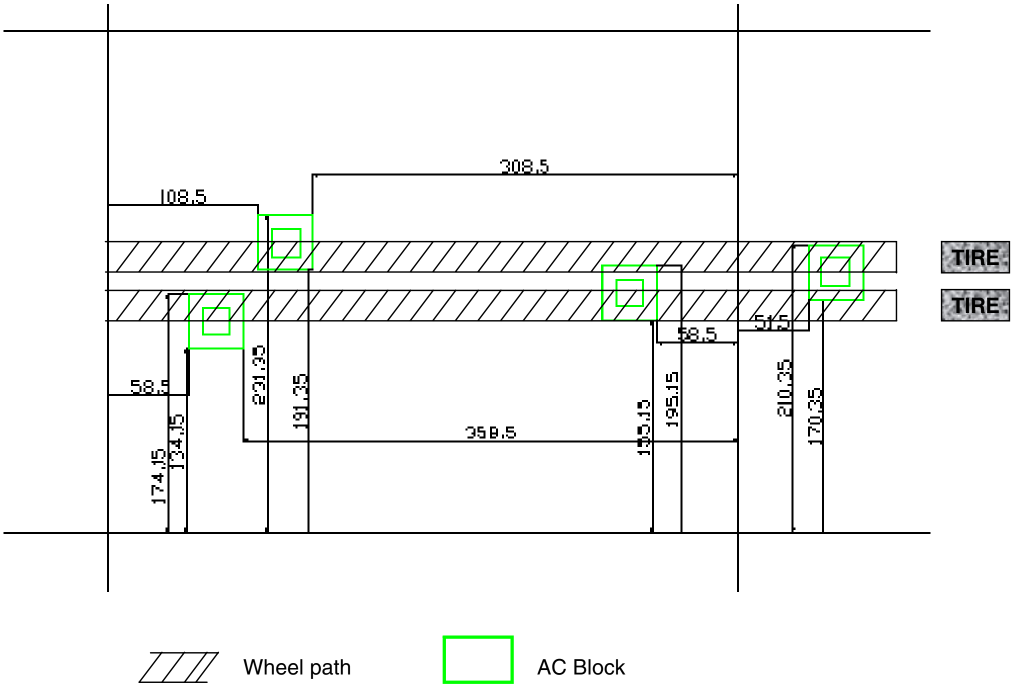
308.5
108.5
TIRE
TIRE
58.5
51.5
58.5
231.35
191.35
358.5
155.15
195.15
210.35
170.35
174.15
134.15
Wheel path
AC Block

Note: scaled, dimensions in centimeters: 2.54 cm = 1 in.

Figure L.6. Locations of asphalt concrete samples sawed from HMA layers for image analysis.

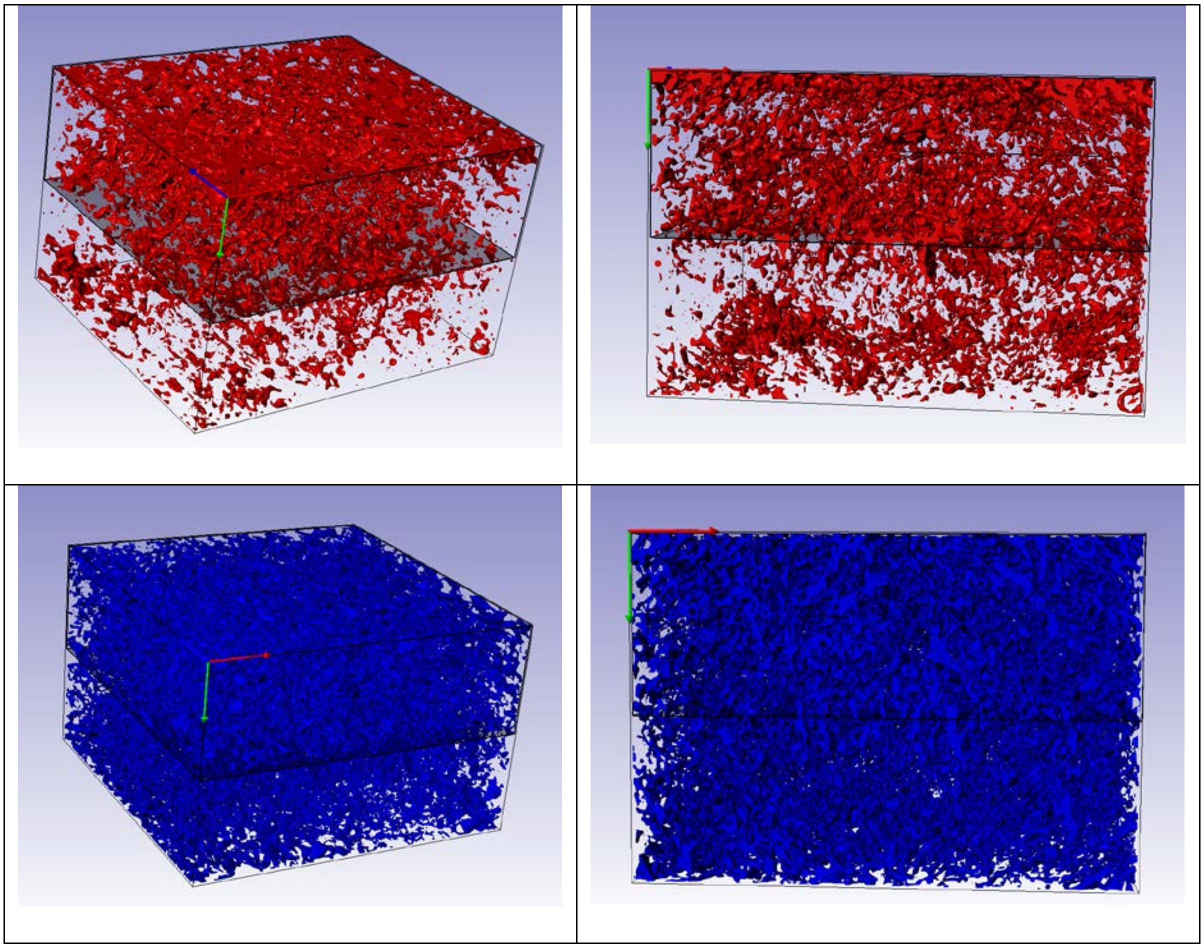

Note: Two lifts of asphalt are shown in each figure part.

Figure L.7. Air void distributions (colored volumes are air voids) from CT images.

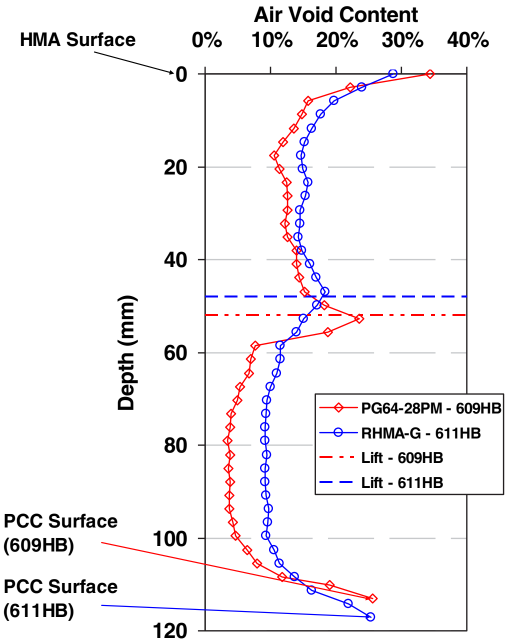

Note: 25.4 mm = 1 in.

Figure L.8. Air void content distribution for samples from HVS Test Sections 609HB and 611HB.

after the HVS tests. Four asphalt concrete specimens were sawn from each HVS rutting test section (16 specimens from 4 sections). Figure L.9 illustrates the changes in air void distribution caused by HVS testing. The two images on the top are for PG 64-28 PM mix from HVS Test Section 609HB (B1) for "before" (left) and "after" (right) HVS testing. The two images on the bottom are for RHMA-G from HVS Test Section 611HB (C1) for "before" (left) and "after" (right) HVS testing. Trafficked area is the right side of each prism, and the left side is untrafficked, including the "hump" caused by shear deformation. Table L.4 shows the changes in air void content of the HMA blocks caused by HVS loading. More densification is observed for the sections with PG 64-28 PM mix (609HB and 610HB) than for those with RHMA-G mix.

HVS Test Data Summary

Introduction

The results of the HVS rut tests were summarized, and a first-level analysis was performed. In assessing rutting performance, the temperature at 50-mm depth of the asphalt concrete and the temperature gradient are two important temperature

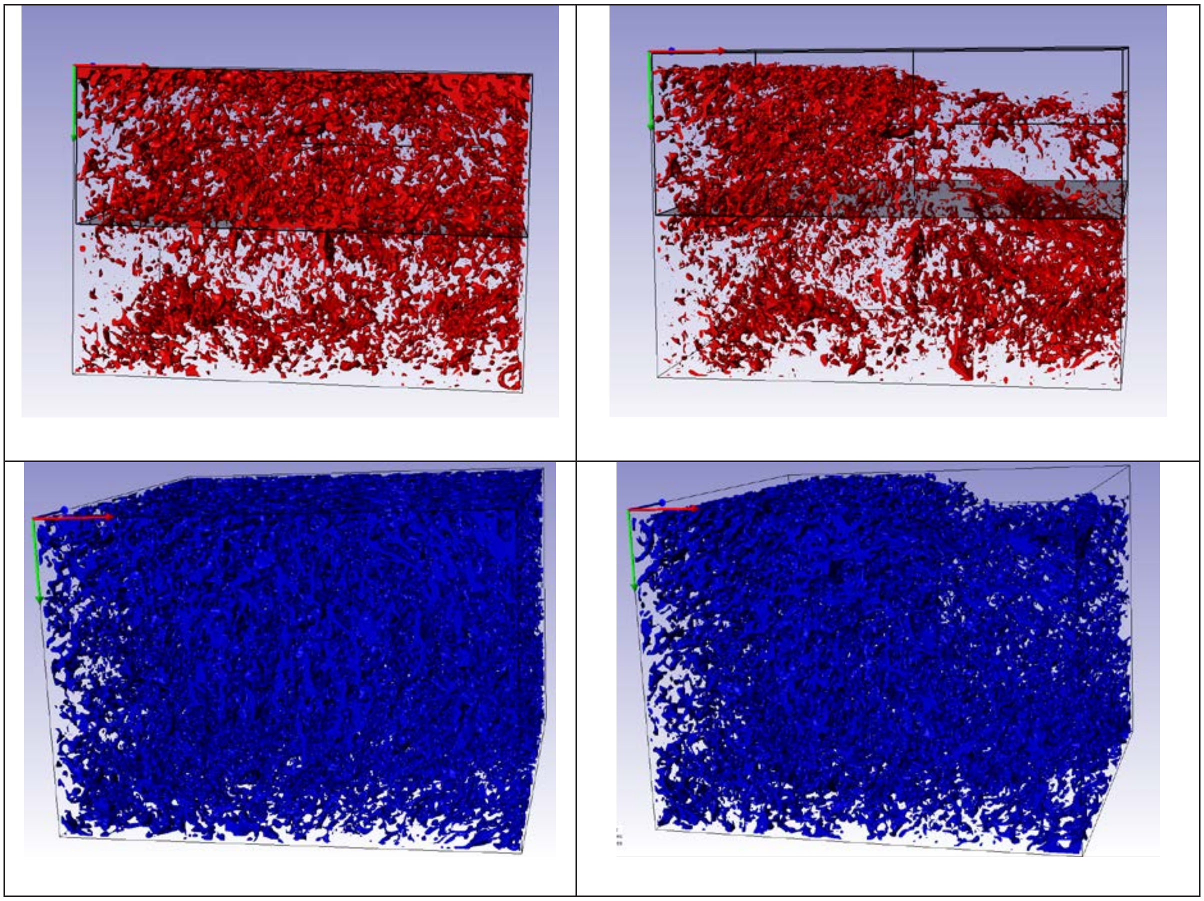

Figure L.9. Distribution of air voids shown as colored volume.

Table L.4. Average Distribution of Air Voids in the HVS Test Sections

Section	Mix Type	As-built Thickness (mm)	B[1]-AV (%)	A[2]-AV[3] (%)	B-AV Hump (%)	A-AV Hump (%)	B-AV WP (%)	A-AV WP[4] (%)	AV Red.[5] WP (%)	AV Red. Total (%)
609HB	PG 64-28	116	9.8	8.1	10.5	10.0	9.1	6.0	33	17
610HB	PG 64-28	72	10.0	7.9	9.6	9.8	10.4	6.0	42	21
611HB	RHMA-G	118	13.8	11.4	14.5	13.2	13.1	9.3	29	17
612HB	RHMA-G	74	13.4	11.7	13.2	13.6	13.6	9.7	29	12

Note: [1] Before HVS testing; [2] After HVS testing; [3] Air void content; [4] Wheelpath; [5] Reduction, 25.4 mm = 1 in.

parameters controlling the stiffness of the asphalt concrete, which was used to compute plastic strain. Permanent deformation at the pavement surface (rutting) was monitored with the Laser Profilometer at the surface and strain gauges at 50-mm depth in the asphalt in the sections with thicker HMA layers (strain gauges placed between the two lifts of HMA used to construct the surface layer). The Laser Profilometer is a stand-alone moveable beam with a traveling downward-shooting vertical laser, which is used to take surface profiles transverse to the direction of the HVS wheel track. Transverse profiles are taken at 0.5-m (1.15-ft) intervals along the test section. The following rut parameters were determined from the surface profile measurements taken with the Laser Profilometer, as illustrated in Figure L.10:

- Average maximum rut depth;
- Average deformation;
- Location and magnitude of the maximum rut depth; and
- Rate of rut development.

The Laser Profilometer provides sufficient information to evaluate the evolution of permanent surface deformation of the entire test section at various loading stages. The rut depth figures show the average values over the entire section (Stations 3 through 13) as well as values for half-meter interval locations between Stations 3 and 8 and Stations 9 and 13. These two additional data series were plotted to illustrate any differences along the length of the section. The permanent deformation will be further characterized after a forensic investigation (test pits and cores) on each section when all testing on the test track has been completed, which will occur after the end of the SHRP 2 R21 project, and is expected to be completed with Caltrans funding. Tire pressure was constant at 690 kPa (100 psi) for all test sections.

The data from each HVS test is presented separately, with the presentation of each test following the same format. Data plots are presented on the same scale to facilitate comparisons of performance.

Section 609HB: PG 64-28 PM Mix, HMA thickness 114 mm

Test Summary

Loading commenced on January 28, 2010, and ended on February 26, 2010. A total of 200,000 load repetitions were applied, and 36 data sets were collected across the duration of the testing. Testing was interrupted for 6 days (February 13, 2010, through February 19, 2010) because of an oil leak caused

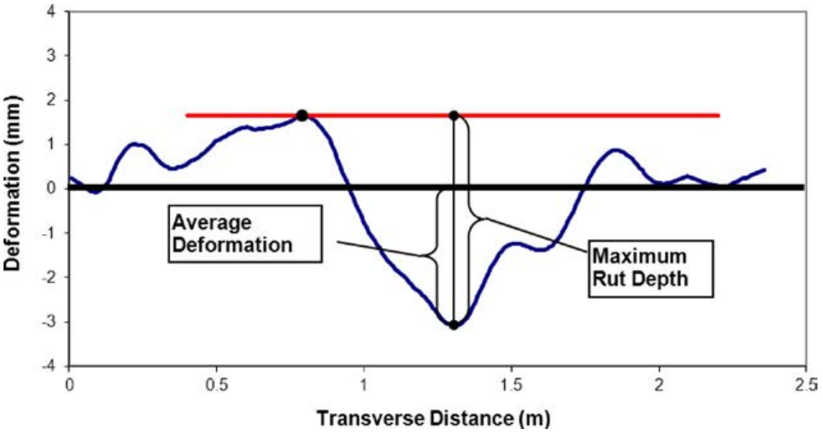

Figure L.10. Illustration of maximum rut depth and average deformation of a leveled profile.

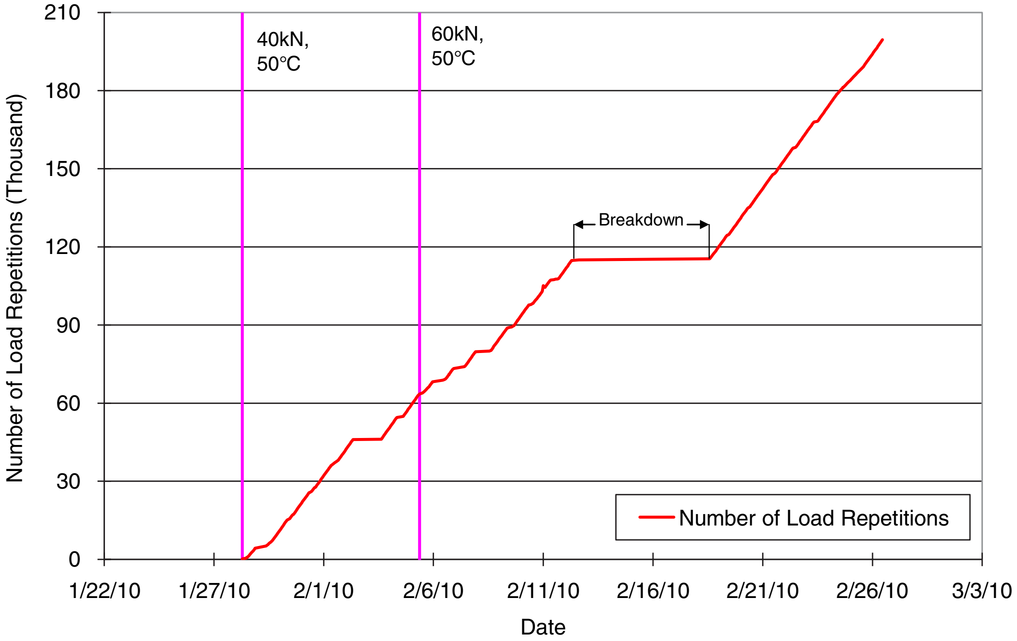

Figure L.11. Load history for Section 609HB, PG 64-28 PM, 114 mm.

by a broken O-ring in the carriage. The HVS loading history for Section 609HB is shown in Figure L.11.

Outside Air Temperatures

Outside air temperatures are summarized in Figure L.12. Vertical error bars on each point on the graph show daily temperature range. Temperatures ranged from 1.4°C to 20.9°C (34.5°F to 69.6°F) during the course of HVS testing, with a daily average of 10.6°C (51.1°F), an average minimum of 6.7°C (44.1°F), and an average maximum of 15.5°C (59.9°F).

Air Temperatures in the Temperature Control Unit

During the test, air temperatures inside the temperature control unit ranged from 15.6°C to 52.9°C (60.1°F to 127.2°F)

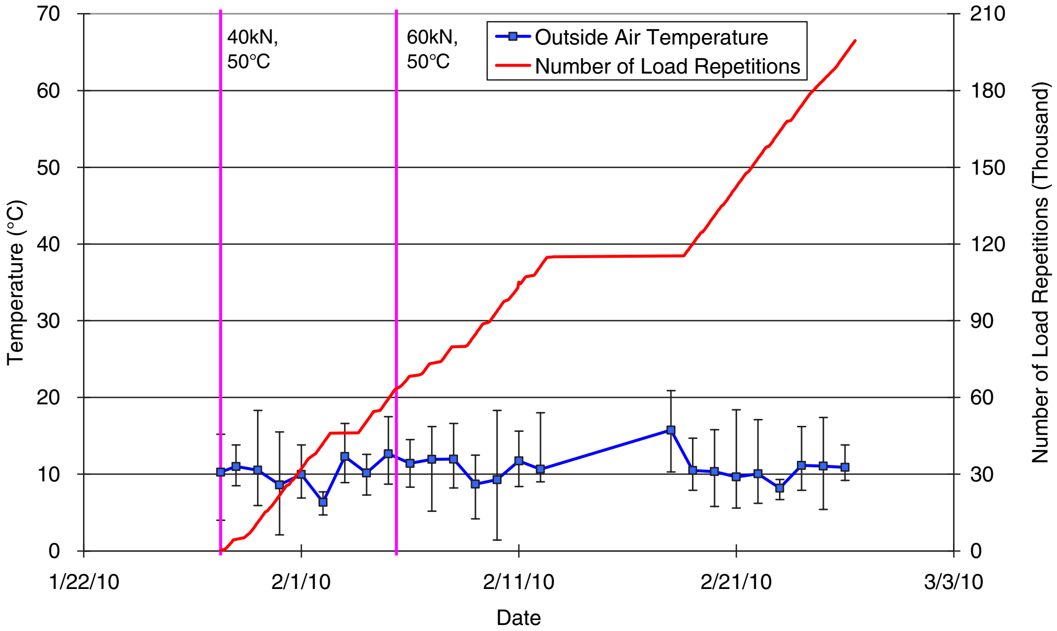

Figure L.12. Daily average outside air temperatures for Section 609HB, PG 64-28 PM, 114 mm.

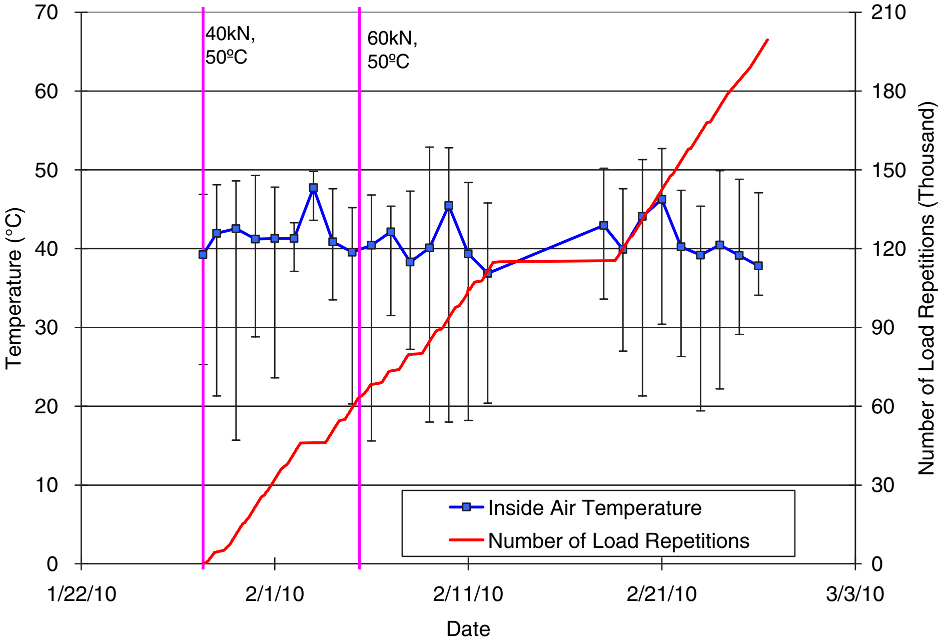

Figure L.13. Daily average inside air temperatures for Section 609HB, PG 64-28 PM, 114 mm.

with an average of 41.1°C (106°F) and standard deviation of 2.6°C (4.7°F). The daily average air temperatures recorded in the temperature control unit, calculated from the hourly temperatures recorded during HVS operation, are shown in Figure L.13. Vertical error bars on each point on the graph show daily temperature range.

Temperatures in the Asphalt Concrete Layers

Daily averages of the surface and in-depth temperatures of the asphalt concrete layers are listed in Table L.5 and shown in Figure L.14. Pavement temperatures decreased slightly with increasing depth in the pavement, which was expected because there usually is a thermal gradient between the top and bottom of the asphalt concrete pavement layers.

Table L.5. Section 609HB, PG 64-28 PM, 114 mm: Temperature Summary for Air and Pavement

Temperature	Average (°C)	SD (°C)	Average (°F)	SD (°F)
Outside air	10.6	1.8	51.1	3.2
Inside air	41.1	2.6	106.0	4.7
Pavement surface	47.8	2.0	118.0	3.6
25 mm below surface	49.7	1.3	121.4	2.4
50 mm below surface	49.5	1.1	121.1	2.0
90 mm below surface	48.6	0.9	119.5	1.7
120 mm below surface	47.5	0.9	117.4	1.7

Note: SD = standard deviation.

Permanent Surface Deformation (Rutting)

Figure L.15 shows the average transverse cross section measured with the Laser Profilometer at various stages of the test.

During HVS testing, rutting usually accumulates at a faster rate initially because of fast reduction of air voids (densification), and then it typically diminishes as trafficking progresses until reaching a steady state. This initial phase is referred to as the "embedment" phase. Figure L.16 and Figure L.17 show the development of permanent deformation (average maximum rut and average deformation, respectively) with load repetitions as measured with the Laser Profilometer for the test section, with an embedment phase apparent only at the beginning of the experiment (i.e., first 15,000 repetitions). Error bars on the average reading indicate that there was high variation along the length of the section, which was a result of the HMA blocks removed for CT image evaluation. (For details see "Air Void Content Distribution in HMA layers from Image Analysis.") Figure L.18 shows the distribution of rutting along the test section after data for Stations 4, 10, 11, and 13, which are close to CT blocks, were excluded from the data set. It can be observed that variability significantly decreases after excluding data for those four biased stations. Figure L.19 shows a contour plot of the pavement surface at the end of

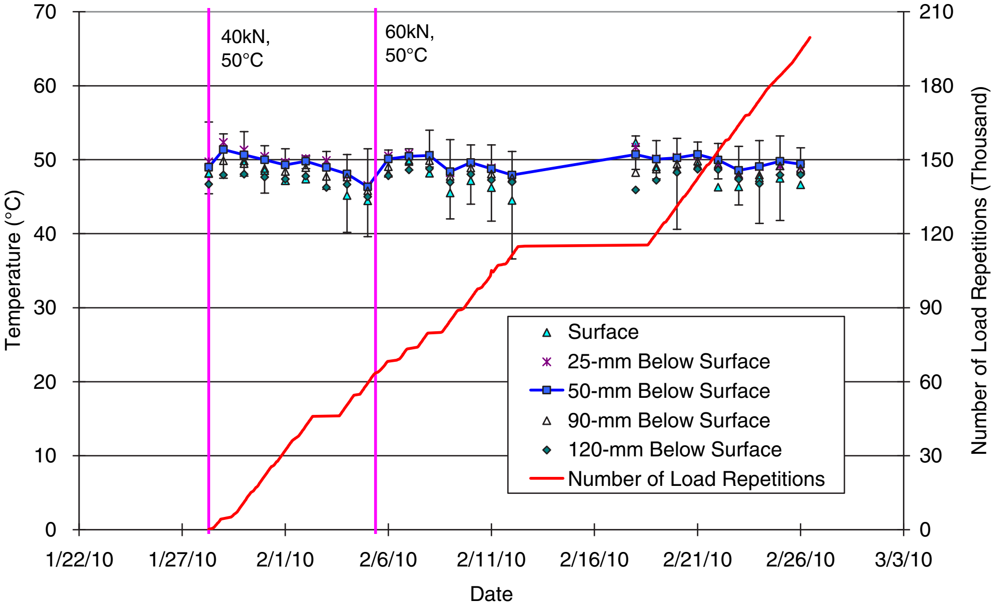

Figure L.14. Daily average temperatures at pavement surface and various depths for Section 609HB, PG 64-28 PM, 114 mm.

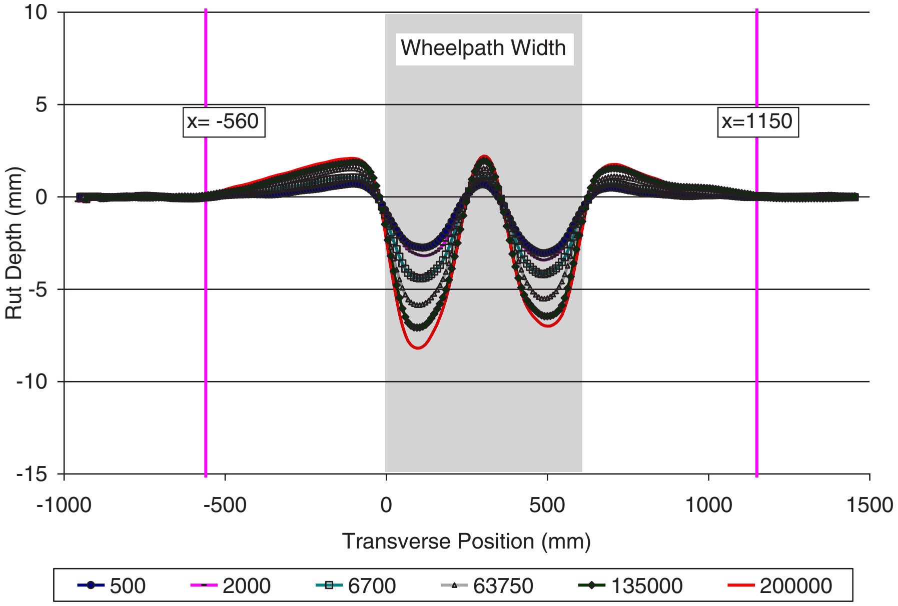

Figure L.15. Laser Profilometer cross section at various load repetitions for Section 609HB, PG 64-28 PM, 114 mm.

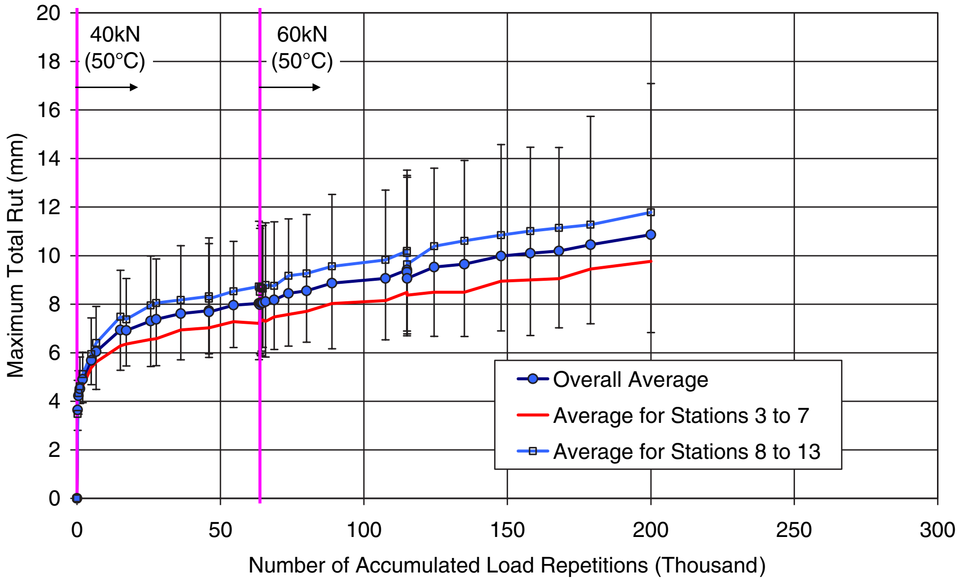

Figure L.16. Average maximum total rut for Section 609HB, PG 64-28 PM, 114 mm.

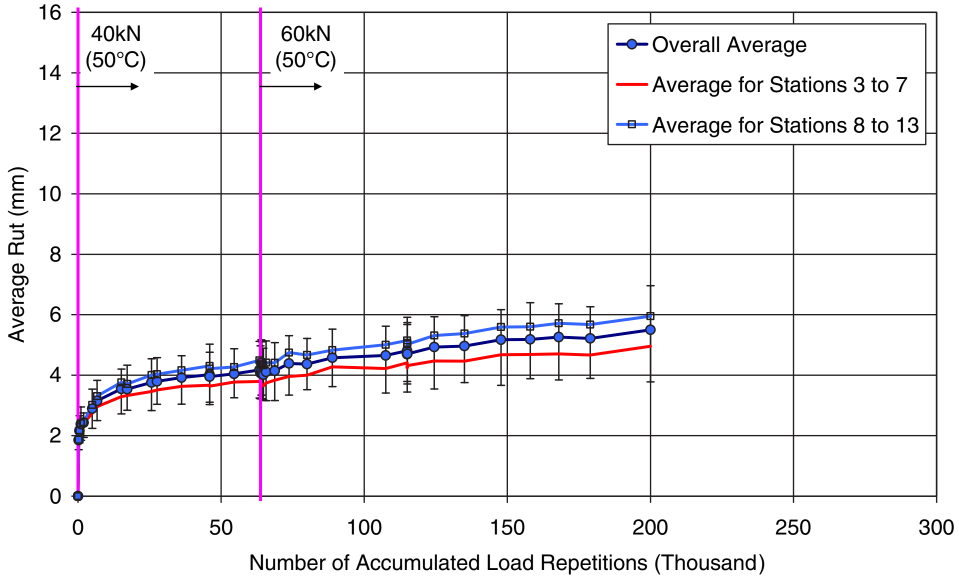

Figure L.17. Average deformation for Section 609HB, PG 64-28 PM, 114 mm.

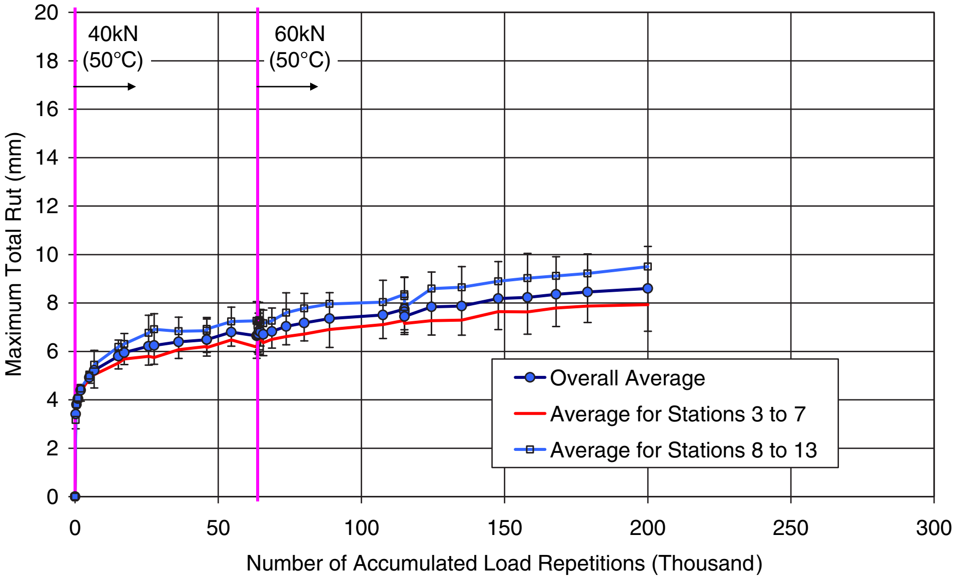

Figure L.18. Average maximum total rut after excluding data for Stations 4, 10, 11, and 13, which are close to CT blocks, for Section 609HB, PG 64-28 PM, 114 mm.

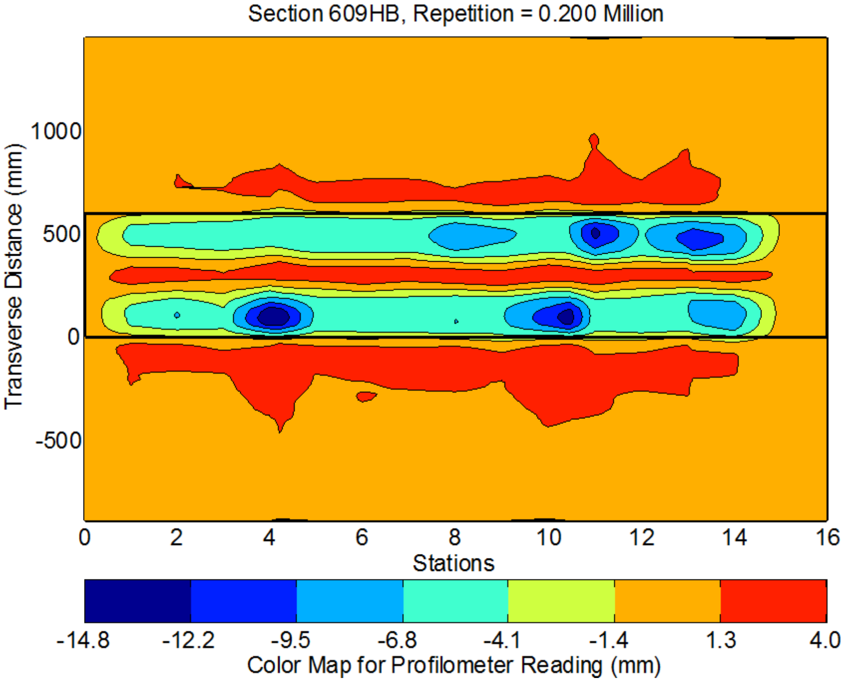

Figure L.19. Contour plot of permanent surface deformation at end of test for Section 609HB, PG 64-28 PM, 114 mm.

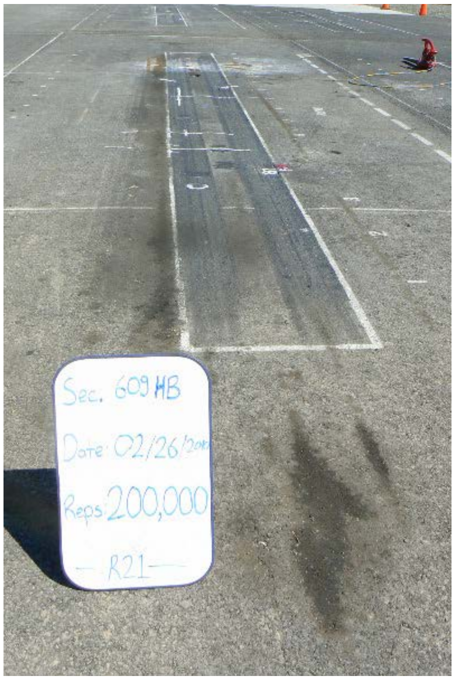

Figure L.20. Photograph at test completion of Section 609HB, PG 64-28 PM, 114 mm.

the test (200,000 repetitions), also indicating localized permanent deformation near the block locations. In addition, a slightly deeper rut was recorded in one of the wheel tracks, which was attributed to the positioning of the HVS on the cross-fall on the section. After trafficking was completed, the average maximum rut depth and average deformation were 10.9 mm (0.43 in.) and 5.5 mm (0.22 in.), respectively. The maximum rut depth measured on the section was 17.1 mm (0.67 in.), recorded at Station 4, which is close to one of the CT blocks.

Visual Inspection

Apart from rutting, no other distress was recorded on the section. Figure L.20 is a photograph taken of the surface at the end of the test.

Section 610HB: PG 64-28 PM Mix, HMA thickness 64 mm

Test Summary

Loading commenced on March 4, 2010, and ended on March 23, 2010. A total of 201,200 load repetitions were applied, and 31 data sets were collected. The HVS loading history for Section 610HB is shown in Figure L.21. No breakdowns occurred during this test.

Outside Air Temperatures

Outside air temperatures are summarized in Figure L.22. Vertical error bars on each point on the graph show daily temperature range. Temperatures ranged from 1.0°C to 28.5°C (33.8°F to 83.3°F) during the course of HVS testing, with a daily average of 12.0°C (53.6°F), an average minimum of 5.4°C (41.7°F), and an average maximum of 20.1°C (68.1°F).

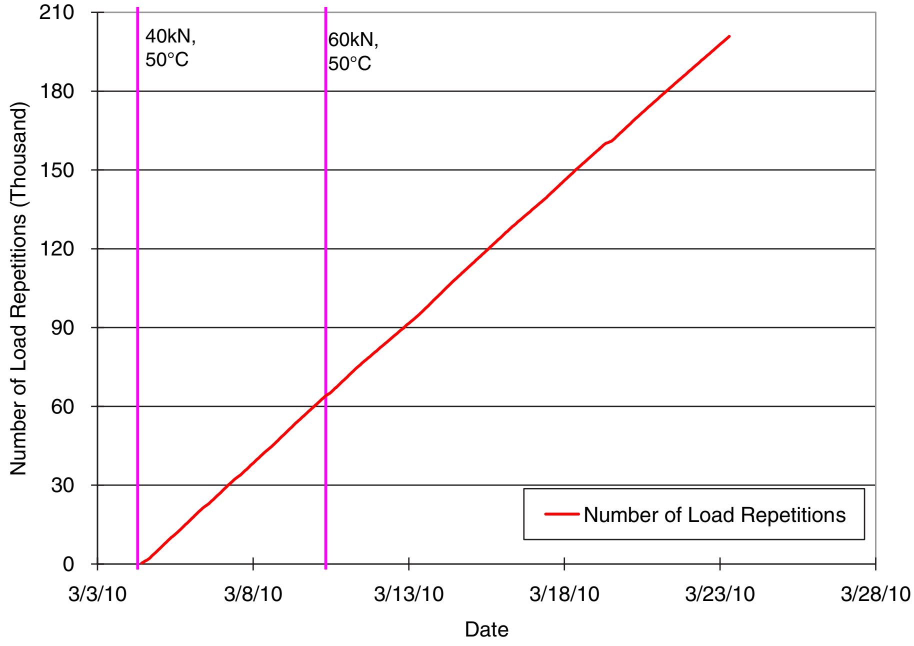

Figure L.21. Load history for Section 610HB, PG 64-28 PM, 64 mm.

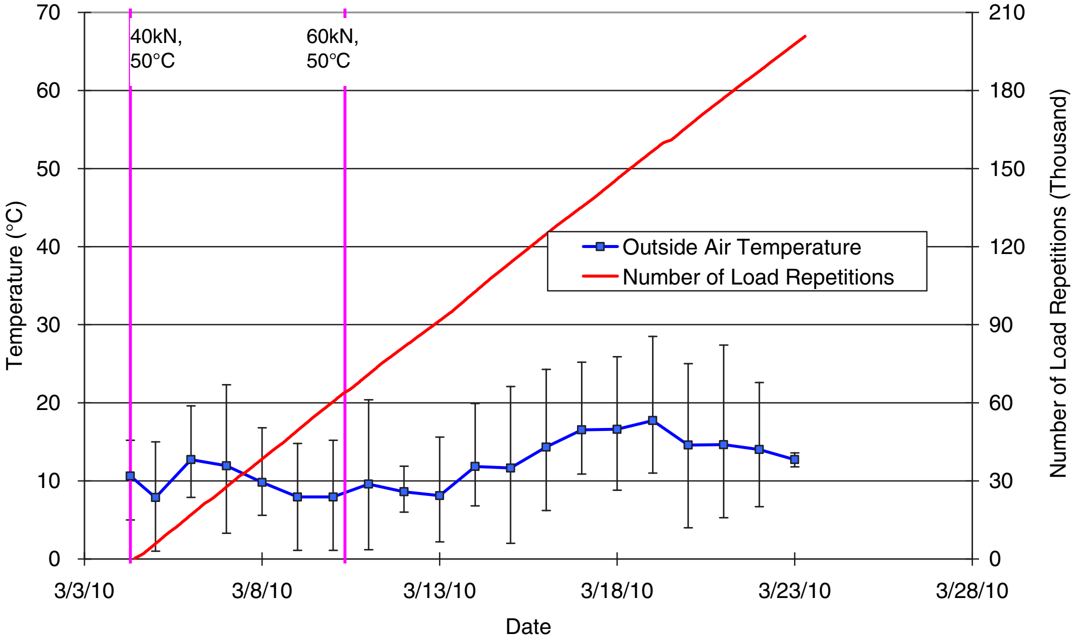

Figure L.22. Daily average outside air temperatures for Section 610HB, PG 64-28 PM, 64 mm.

Air Temperatures in the Temperature Control Unit

During the test, the measured air temperatures inside the temperature control unit ranged from 16.3°C to 52.3°C (61.3°F to 126.1°F) with an average of 40.4°C (104.8°F) and standard deviation of 1.9°C (3.5°F). The daily average air temperatures recorded in the temperature control unit, calculated from the hourly temperatures recorded during HVS operation, are shown in Figure L.23. Vertical error bars on each point on the graph show daily temperature range.

Temperatures in the Asphalt Concrete Layers

Daily averages of the surface and in-depth temperatures of the asphalt concrete layers are listed in Table L.6 and shown in Figure L.24. Pavement temperatures decreased slightly

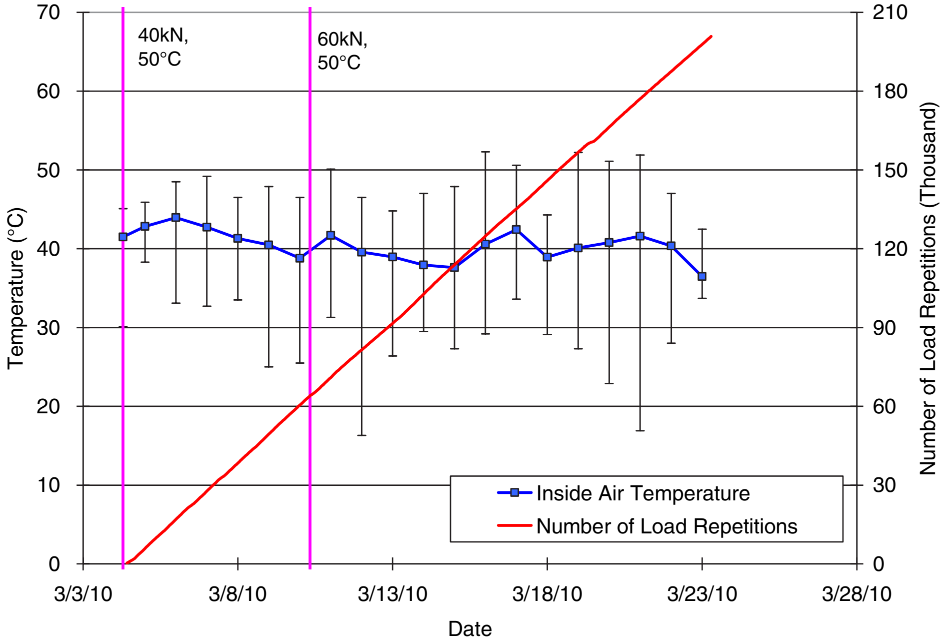

Figure L.23. Daily average inside air temperatures for Section 610HB, PG 64-28 PM, 64 mm.

Table L.6. 610HB, PG 64-28 PM, 64 mm: Temperature Summary for Air and Pavement

Temperature	Section 610HB			
	Average (°C)	SD (°C)	Average (°F)	SD (°F)
Outside air	12.0	3.1	53.6	5.7
Inside air	40.4	1.9	104.8	3.5
Pavement surface	50.5	1.2	122.9	2.2
25 mm below surface	50.4	1.1	122.8	1.9
50 mm below surface	49.8	1.0	121.7	1.9
60 mm below surface	49.5	1.1	121.0	1.9
90 mm below surface	48.4	1.3	119.2	2.3

Note: SD = standard deviation.

with increasing depth in the pavement, as expected. Average pavement temperatures at all depths of Section 610HB were similar to those recorded on the section 609HB.

Permanent Surface Deformation (Rutting)

Figure L.25 shows the average transverse cross section measured with the Laser Profilometer at various stages of the test.

Figure L.26 and Figure L.27 show the development of permanent deformation (average maximum rut and average deformation, respectively) with load repetitions as measured with the Laser Profilometer for the test section. Error bars on the average reading indicate that the level of variability caused by the CT blocks is less than the variability for Section 609HB. This is a result of the epoxy material used on Section 610HB to glue CT blocks to pavement. Figure L.28 shows the distribution of rutting along the test section after data for Stations 4, 5, 11, and 13, which are close to CT blocks, are excluded from the data set. It can be observed that excluding data for those four biased stations does not cause any significant change in variability and average accumulated rutting.

Results for Section 609HB are also shown for comparative purposes in Figure L.26 and Figure L.27. It can be observed that rutting accumulation rates after the embedment phase are similar for both sections. However, a high level of densification at the embedment stage resulted in higher rutting for Section 609HB. Because both pavements are constructed from the same mix type, the only reason for higher rutting can be the differences in HMA layer thicknesses. To identify the effect of thickness on accumulated rutting, rutting measurements were converted to permanent shear strain (PSS) by dividing the measured rutting by the HMA layer thickness of each section. Figure L.29 shows that PSS curves for Sections 609HB and 610HB are close to each other. This result indicates that accumulated rutting for these two sections is a function of thickness. It should be noted that this result is most likely to be a result of the underlying concrete layer, which minimizes permanent deformation at the unbound layers. A similar result may not be observed when the section does not have any concrete layer under the HMA.

Figure L.30 shows a contour plot of the pavement surface at the end of the test (201,200 repetitions). After trafficking was completed, the average maximum rut depth and the average deformation were 5.8 mm (0.23 in.) and 2.9 mm

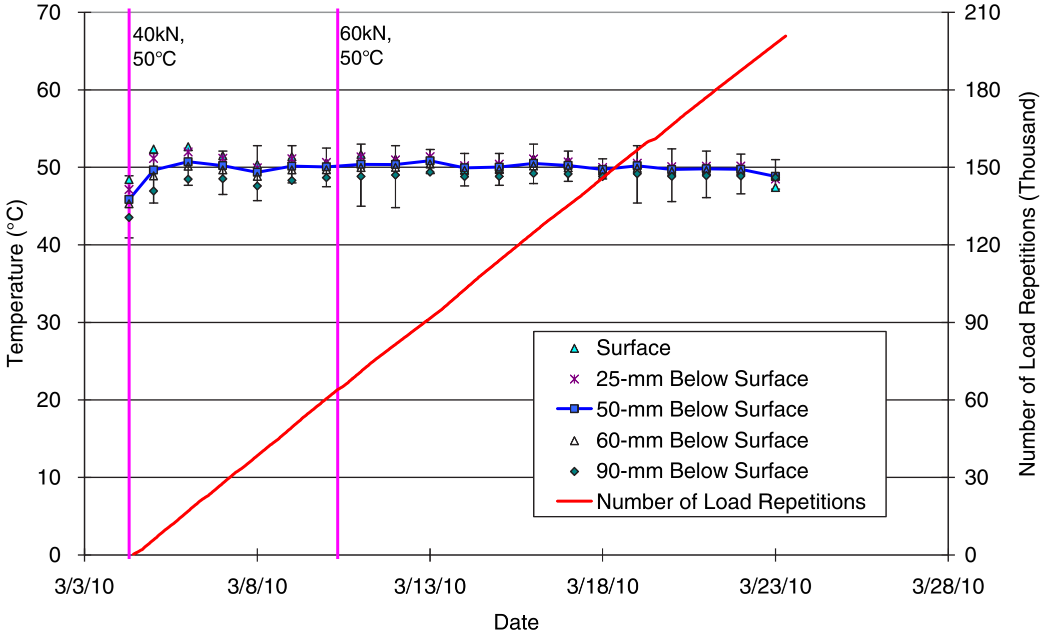

Figure L.24. Daily average temperatures at pavement surface and various depths for Section 610HB, PG 64-28 PM, 64 mm.

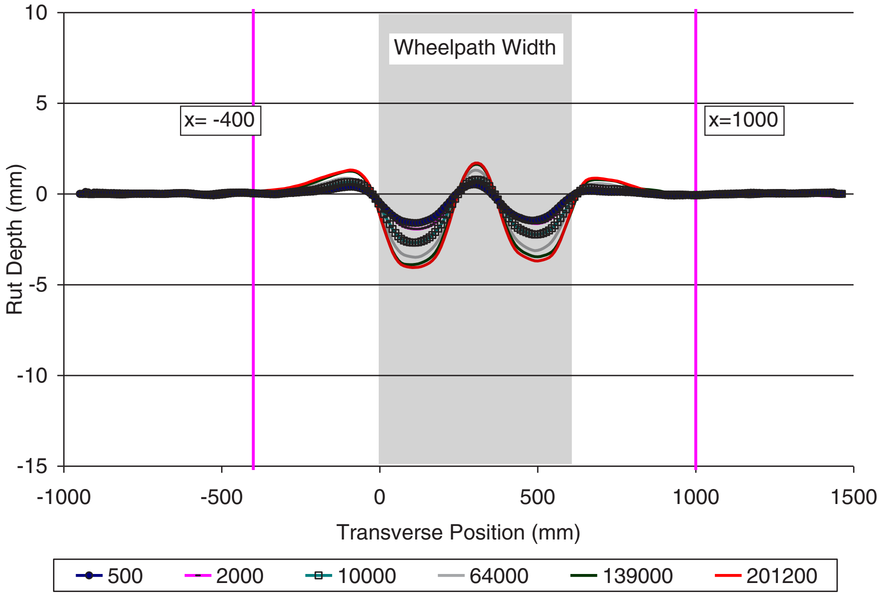

Figure L.25. Laser Profilometer cross section at various load repetitions for Section 610HB, PG 64-28 PM, 64 mm.

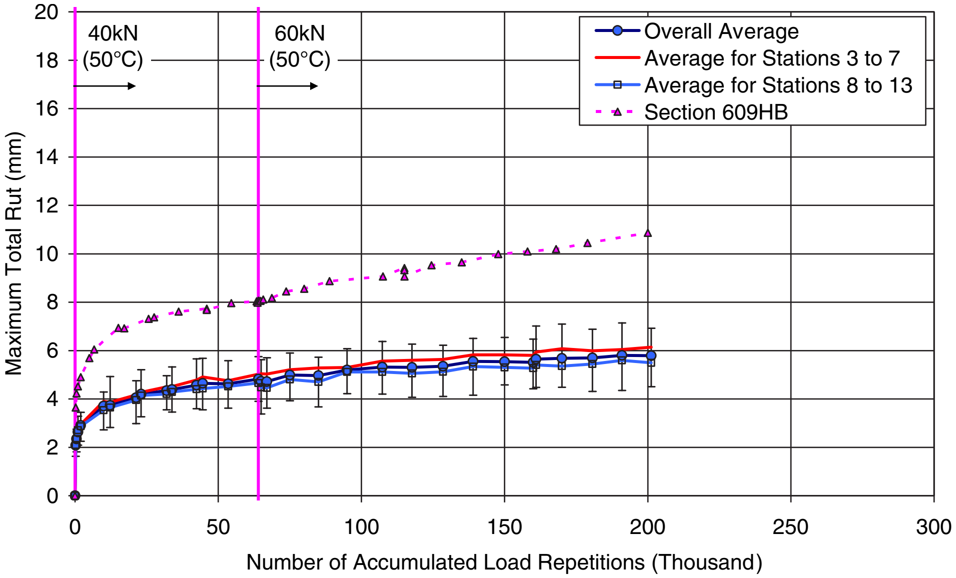

Figure L.26. Average maximum total rut for Section 610HB, PG 64-28 PM, 64 mm.

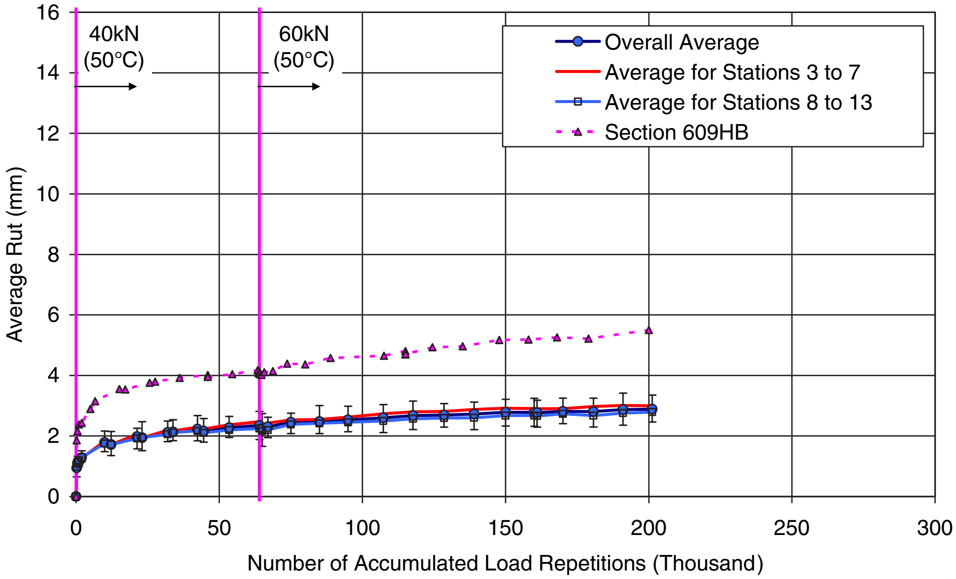

Figure L.27. Average deformation for Section 610HB, PG 64-28 PM, 64 mm.

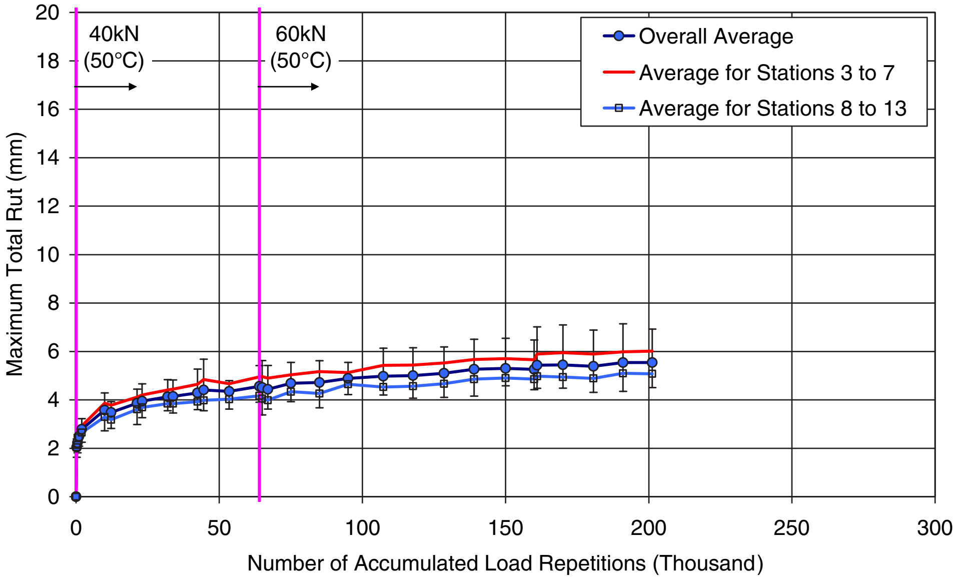

Figure L.28. Average maximum rut after excluding data for Stations 4, 5, 11, and 13, which are close to CT blocks, for Section 610HB, PG 64-28 PM, 64 mm.

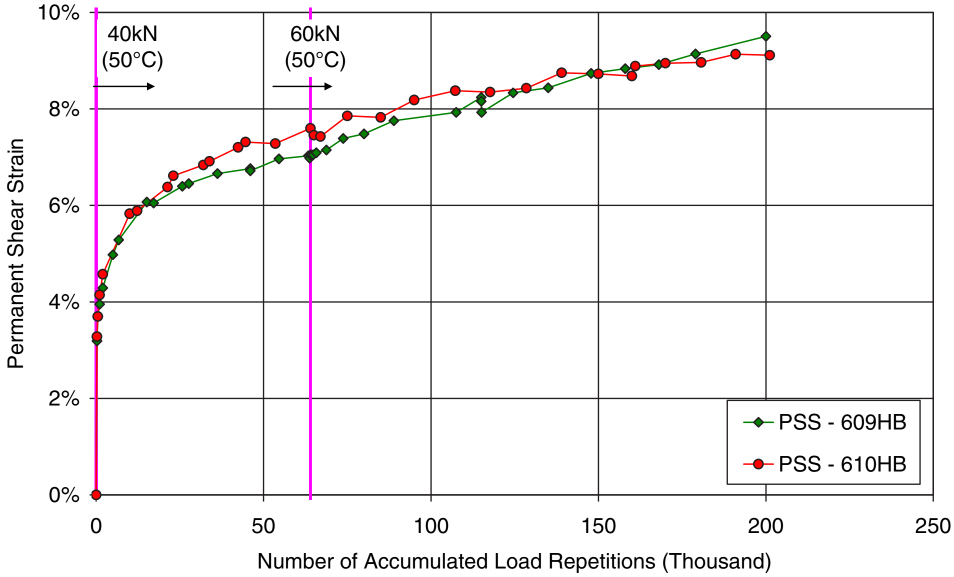

Figure L.29. Comparison of PSS for Section 609HB, PG 64-28 PM, 114 mm, and Section 610HB, PG 64-28 PM, 64 mm.

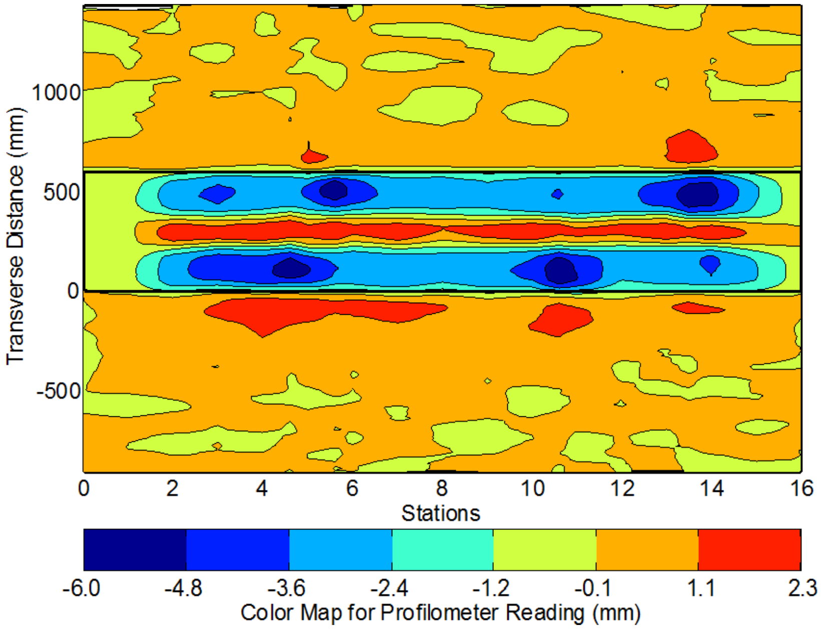

Figure L.30. Contour plot of permanent surface deformation at end of test for Section 610HB, PG 64-28 PM, 64 mm.

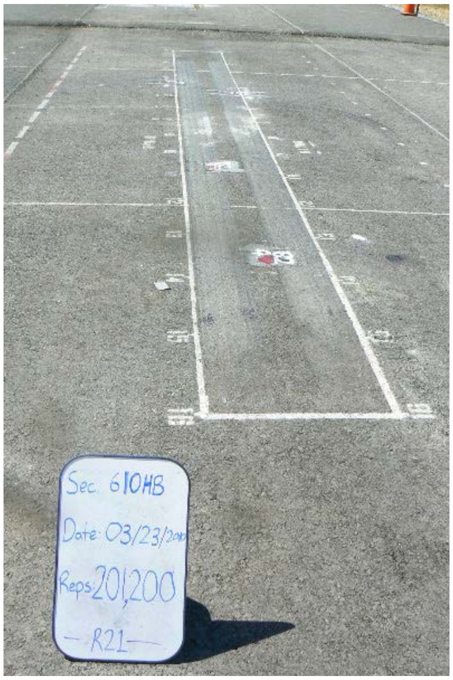

Figure L.31. Photograph at test completion of Section 610HB, PG 64-28 PM, 64 mm.

(0.11 in.), respectively. The maximum rut depth measured on the section was 6.9 mm (0.27 in.), recorded at Station 4.

Visual Inspection

Apart from rutting, no other distress was recorded on the section at the end of testing. Figure L.31 is a photograph taken of the surface at the end of the test.

Section 611HB: RHMA-G Mix, HMA thickness 114 mm

Test Summary

Loading commenced on March 29, 2010, and ended on April 2, 2010. A total of 18,503 load repetitions were applied and 10 data sets were collected. Early failure was observed for the section when compared with Sections 609HB and 610HB. The HVS loading history for Section 611HB is shown in Figure L.32. Although the failure criterion (12.5 mm rut depth) was reached after 6,400 repetitions, testing was continued until the rutting accumulation rate stabilized.

Outside Air Temperatures

Outside air temperatures are summarized in Figure L.33. Vertical error bars on each point on the graph show daily temperature range. Temperatures ranged from 5.2°C to 21.5°C (41.4°F to 70.7°F) during the course of HVS testing, with a daily average of 13.0°C (55.4°F), an average minimum of 9.4°C (49°F), and an average maximum of 16.2°C (61.2°F).

Air Temperatures in the Temperature Control Unit

During the test, air temperatures inside the temperature control unit ranged from 16.1°C to 45.1°C (61°F to 113.2°F) with an average of 35.2°C (95.4°F) and standard deviation of 3.6°C (6.5°F). The air temperature was adjusted to maintain a pavement temperature of 50°C ± 4°C (122°F ± 7°F). The daily average air temperatures recorded in the temperature control unit, calculated from the hourly temperatures recorded during HVS operation, are shown in Figure L.34.

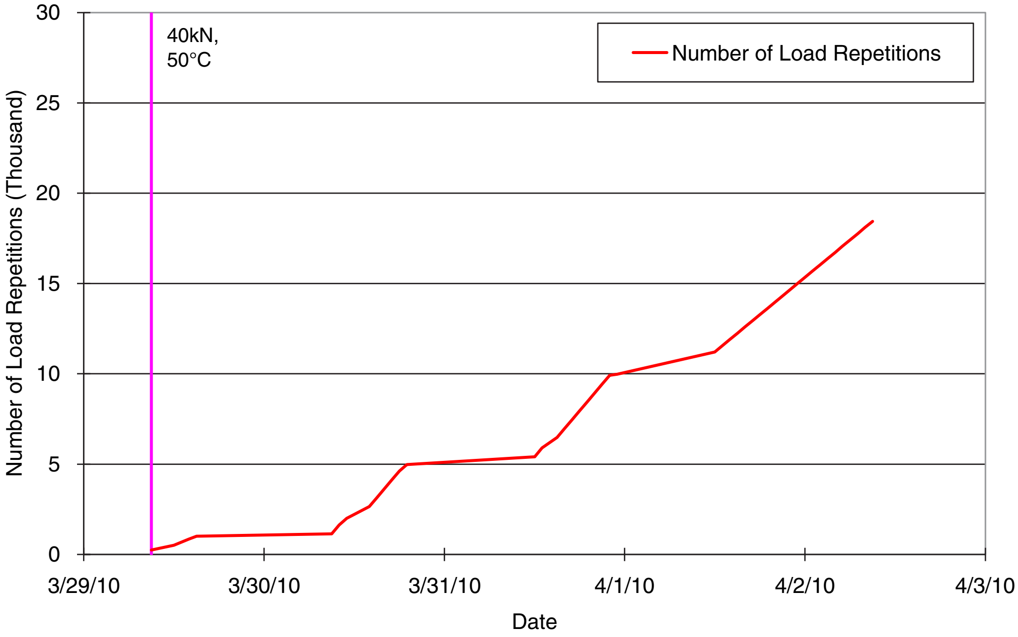

Figure L.32. Load history for Section 611HB, RHMA-G, 114 mm.

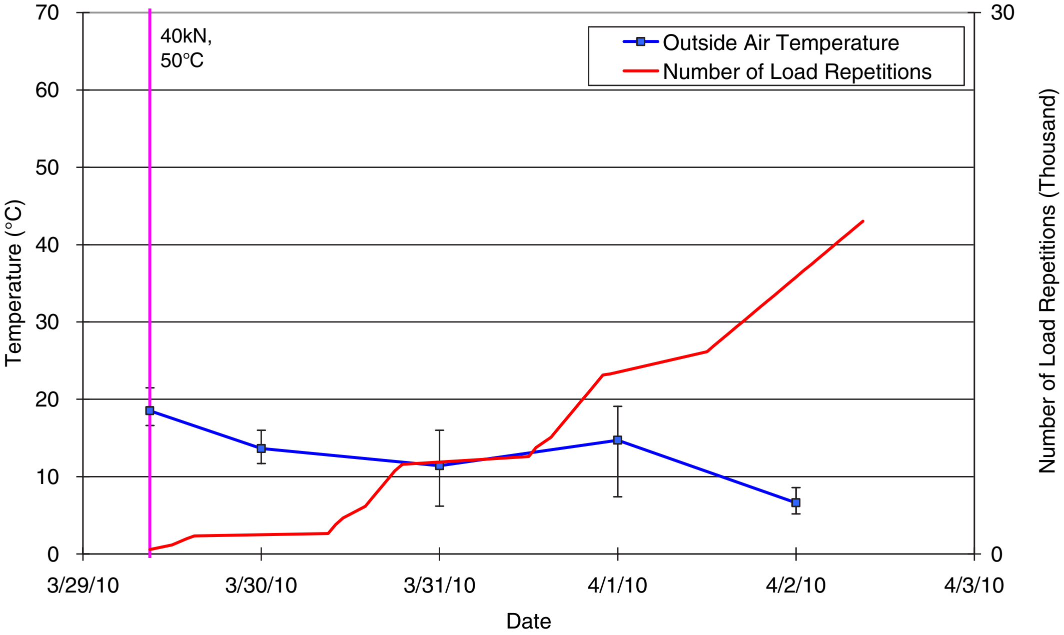

Figure L.33. Daily average outside air temperatures for Section 611HB, RHMA-G, 114 mm.

Vertical error bars on each point on the graph show daily temperature range.

Temperatures in the Asphalt Concrete Layers

Daily averages of the surface and in-depth temperatures of the asphalt concrete layers are listed in Table L.7 and shown in Figure L.35. Pavement temperatures decreased slightly with increasing depth in the pavement, as expected. Average pavement temperatures at all depths of Section 611HB were similar to those recorded for Sections 609HB and 610HB.

Permanent Surface Deformation (Rutting)

Figure L.36 shows the average transverse cross section measured with the Laser Profilometer at various stages of the test.

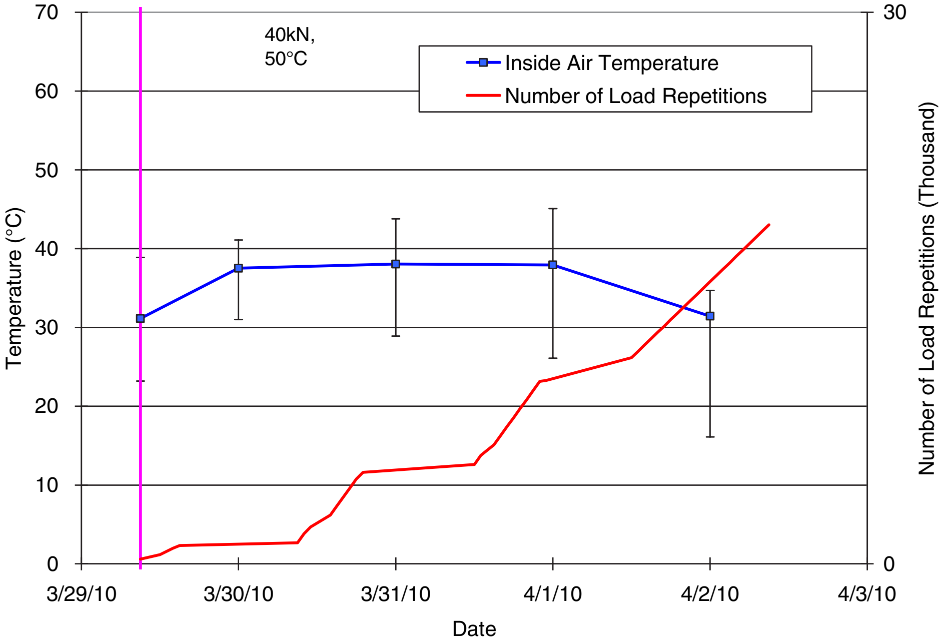

Figure L.34. Daily average inside air temperatures for Section 611HB, RHMA-G, 114 mm.

Table L.7. 611HB, RHMA-G, 114 mm: Temperature Summary for Air and Pavement

Temperature	611HB			
	Average (°C)	SD (°C)	Average (°F)	SD (°F)
Outside air	13.0	4.4	55.4	7.9
Inside air	35.2	3.6	95.4	6.5
Pavement surface	48.8	1.5	119.8	2.8
25 mm below surface	49.4	1.4	120.9	2.4
50 mm below surface	48.7	1.1	119.6	1.9
90 mm below surface	47.1	1.0	116.8	1.7
120 mm below surface	45.9	0.9	114.6	1.5

Note: SD = standard deviation.

This plot clearly shows the increase in rutting and deformation over the duration of the test.

Figure L.37 and Figure L.38 show the development of permanent deformation (average maximum rut and average deformation, respectively) with load repetitions as measured with the Laser Profilometer for the test section. It can be observed that early failure occurred after 18,503 repetitions. Error bars on the average reading indicate that the level of variability caused by the CT blocks is less than the variability for Section 609HB. This is a result of the epoxy material used on Section 611HB to glue CT blocks to pavement. Figure L.39 shows the distribution of rutting along the test section after data for Stations 4, 10, 11, and 12, which are close to CT blocks, were excluded from the data set. It can be observed that excluding data for those four biased stations did not cause any significant change in variability and average accumulated rutting.

Figure L.40 shows a contour plot of the pavement surface at the end of the test (18,503 repetitions). After trafficking was completed, the average maximum rut depth and the average deformation were 13.5 mm (0.53 in.) and 5.5 mm (0.22 in.), respectively. The maximum rut depth measured on the section was 16.2 mm (0.64 in.) recorded at Station 12.

Visual Inspection

Apart from rutting, no other distress was recorded on the section. Figure L.41 shows a photograph taken of the surface at the end of the test.

Section 612HB: Mix RHMA-G, HMA thickness 64 mm

Test Summary

Loading commenced on April 13, 2010, and ended on April 27, 2010. A total of 90,000 load repetitions were applied, and 19 data sets were collected. Considerably more load repetitions (90,000) were applied to Section 612HB than to Section 611HB. Although the failure criterion (12.5 mm rut depth) was reached after 40,000 repetitions, testing was continued until the rutting accumulation rate stabilized. The HVS loading history for Section 612HB is shown in Figure L.42.

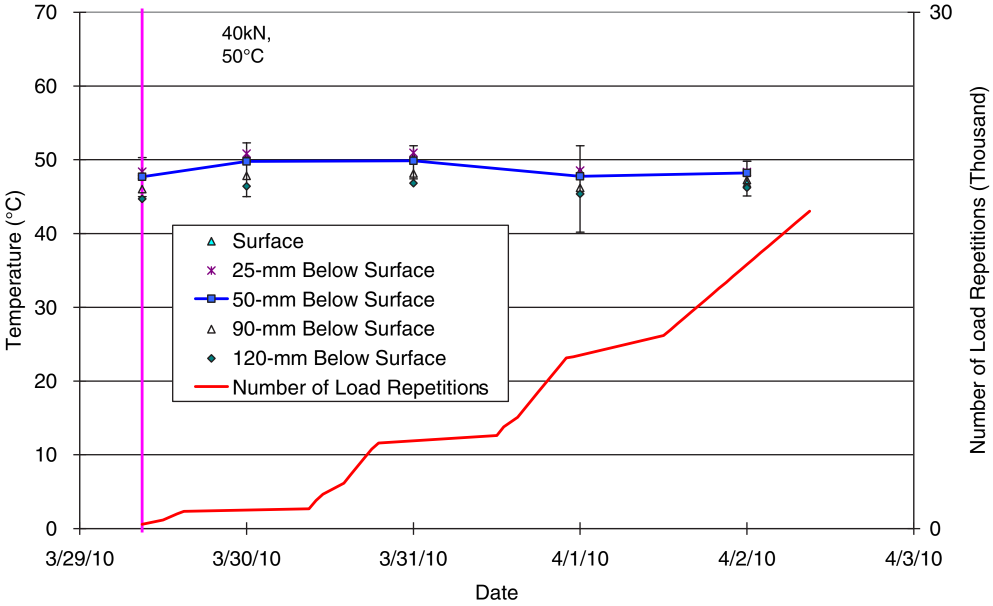

Figure L.35. Daily average temperatures at pavement surface and various depths for Section 611HB, RHMA-G, 114 mm.

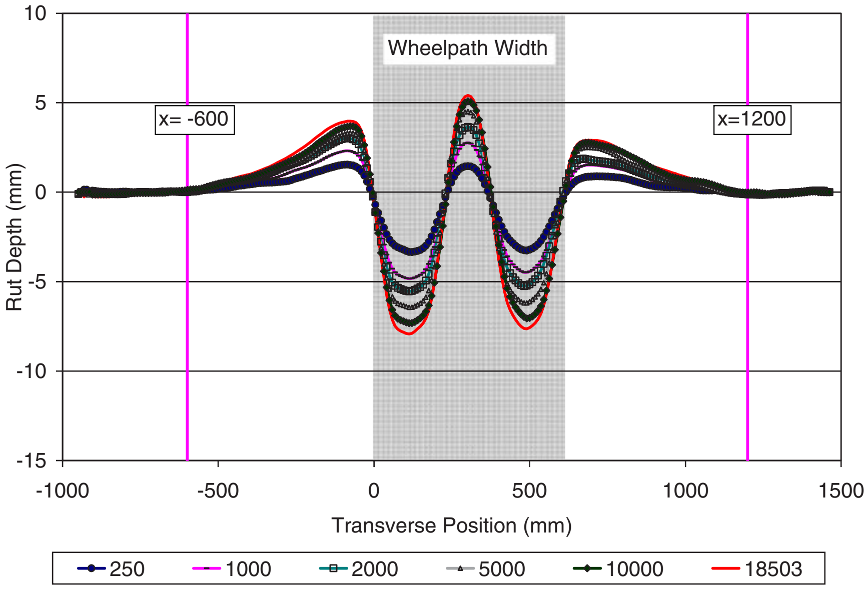

Figure L.36. Laser Profilometer cross section at various load repetitions for Section 611HB, RHMA-G, 114 mm.

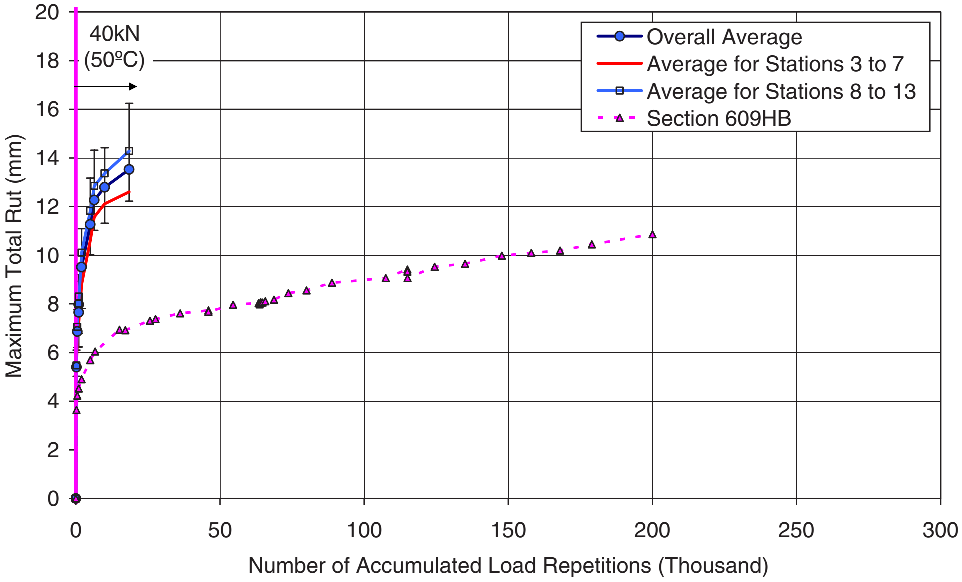

Figure L.37. Average maximum total rut for Section 611HB, RHMA-G, 114 mm. Note that data for Section 609HB, PG 64-28 PM, 114 mm, also are shown.

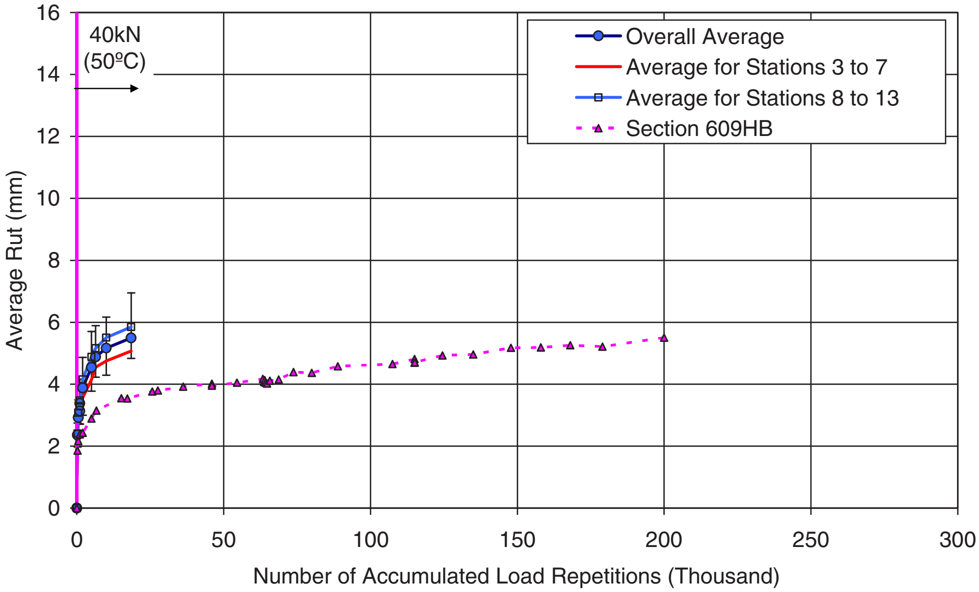

Figure L.38. Average deformation for Section 611HB, RHMA-G, 114 mm. Note that data for Section 609HB, PG 64-28 PM, 114 mm, also are shown.

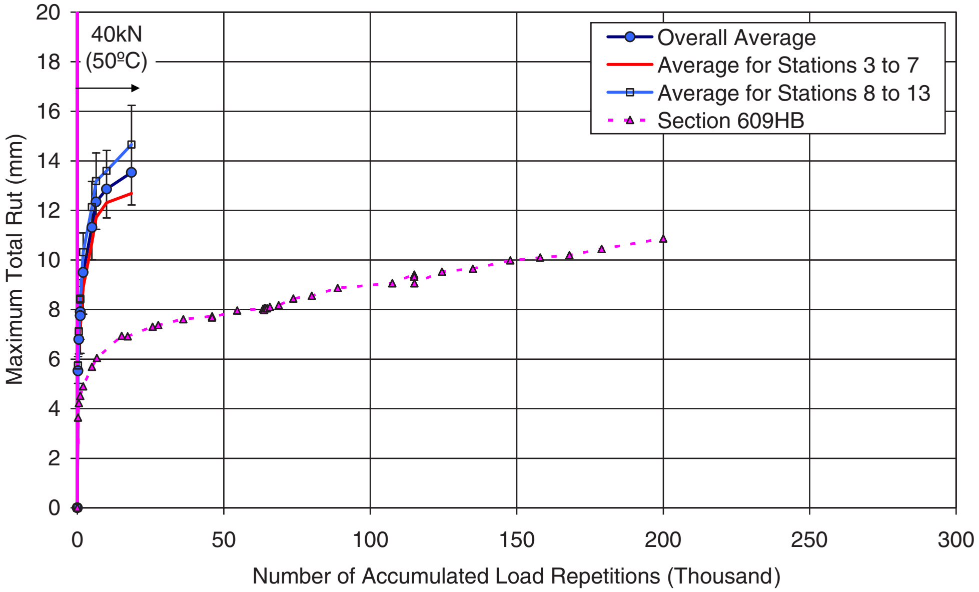

Figure L.39. Average maximum total rut after excluding data for Stations 4, 10, 11, and 12, which are close to CT blocks, for Section 611HB, RHMA-G, 114 mm. Note that data for Section 609HB, PG 64-28 PM, 114 mm, also are shown.

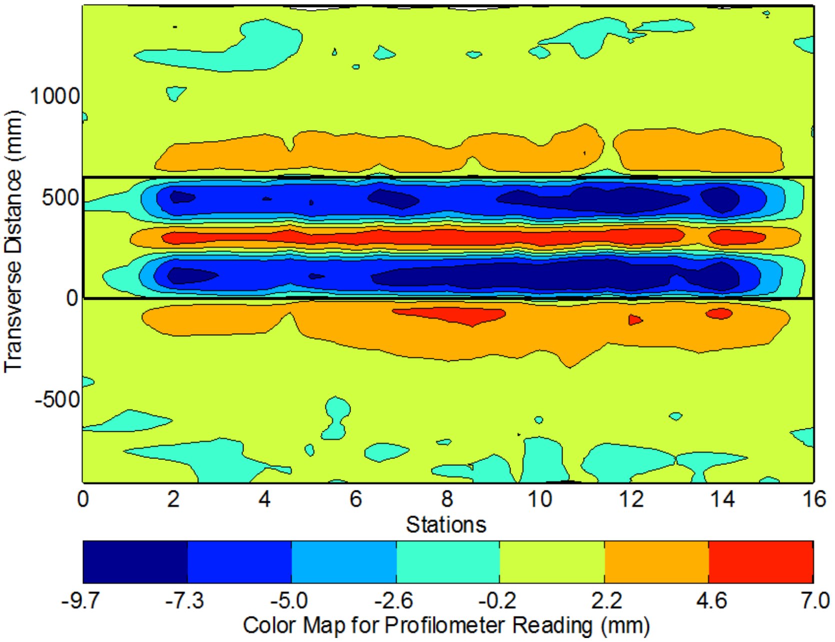

Figure L.40. Contour plot of permanent surface deformation at end of test for Section 611HB, RHMA-G, 114 mm.

Outside Air Temperatures

Outside air temperatures are summarized in Figure L.43. Vertical error bars on each point on the graph show daily temperature range. Temperatures ranged from 5.4°C to 30.7°C (41.7°F to 87.3°F) during the course of HVS testing, with a daily average of 15.0°C (59.1°F), an average minimum of 8.4°C (47.1°F), and an average maximum of 23.4°C (74.1°F).

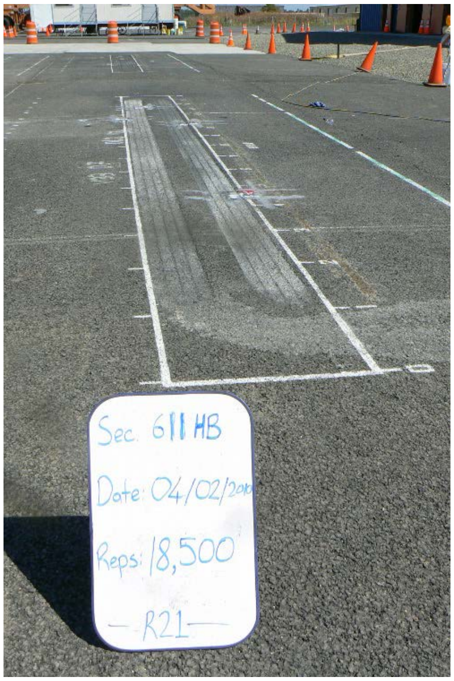

Figure L.41. Photograph at test completion of Section 611HB, RHMA-G, 114 mm.

Air Temperatures in the Temperature Control Unit

During the test, air temperatures inside the temperature control unit ranged from 14.7°C to 51.6°C (58.5°F to 124.9°F) with an average of 37.0°C (98.5°F) and standard deviation of 3.2°C (5.8°F). The air temperature was adjusted to maintain a pavement temperature of 50°C ± 4°C (122°F ± 7°F) at 50-mm depth throughout the test. The daily average air temperatures recorded in the temperature control unit, calculated from the hourly temperatures recorded during HVS operation, are shown in Figure L.44. Vertical error bars on each point on the graph show daily temperature range.

Temperatures in the Asphalt Concrete Layers

Daily averages of the surface and in-depth temperatures of the asphalt concrete layers are listed in Table L.8 and shown in Figure L.45. Pavement temperatures decreased slightly with increasing depth in the pavement, as expected. Average pavement temperatures at all depths on Section 612HB were similar to those recorded for the other sections.

Permanent Surface Deformation (Rutting)

Figure L.46 shows the average transverse cross section measured with the Laser Profilometer at various stages of the test.

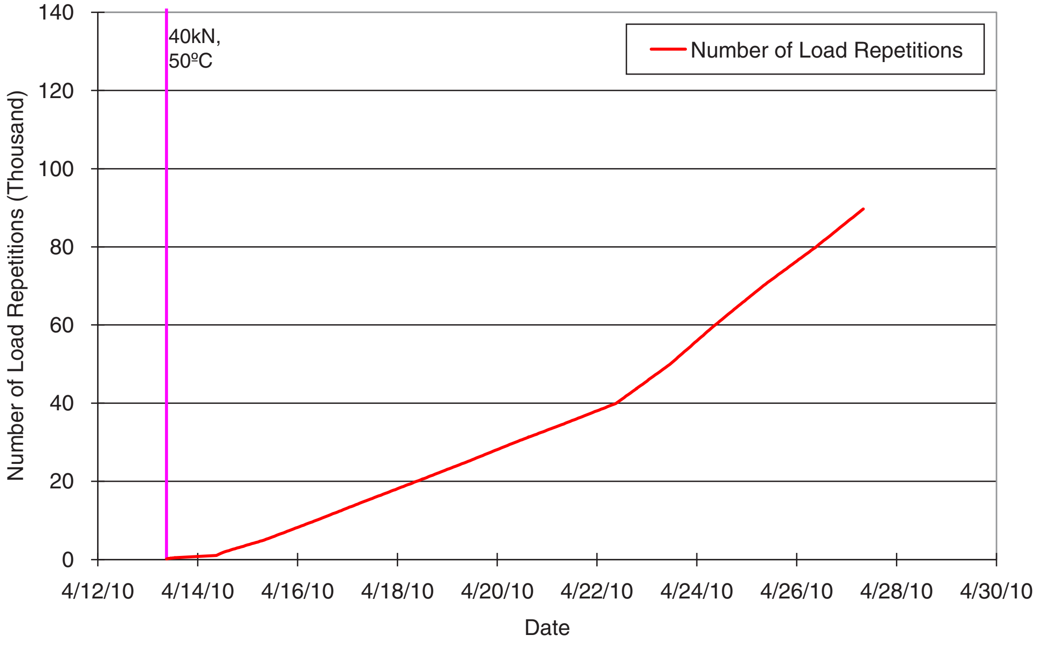

Figure L.42. Load history for Section 612HB, RHMA-G, 64 mm.

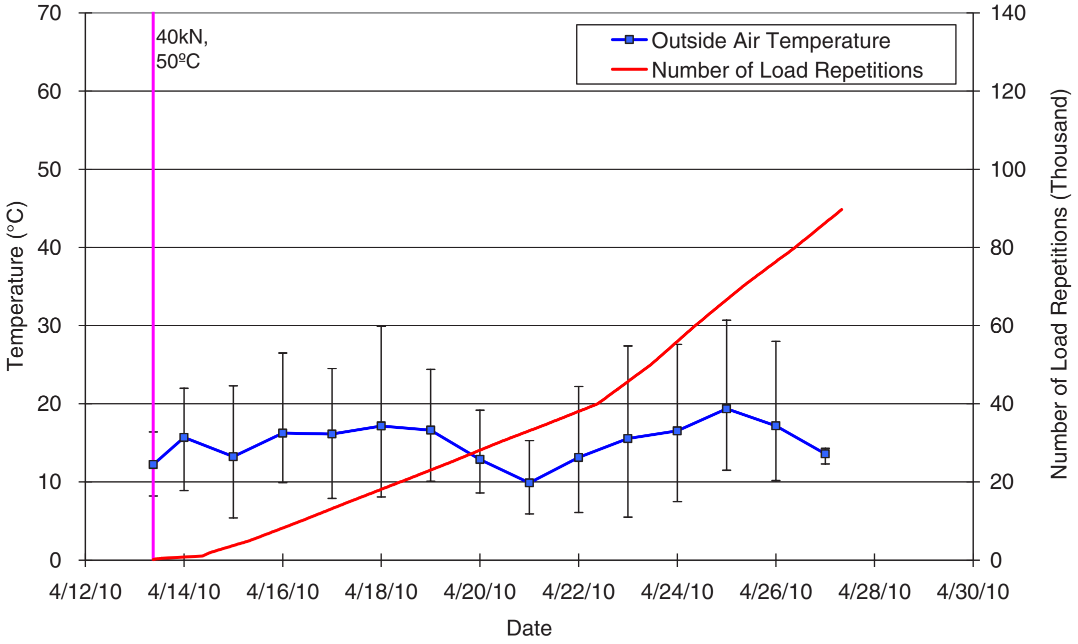

Figure L.43. Daily average outside air temperatures for Section 612HB, RHMA-G, 64 mm.

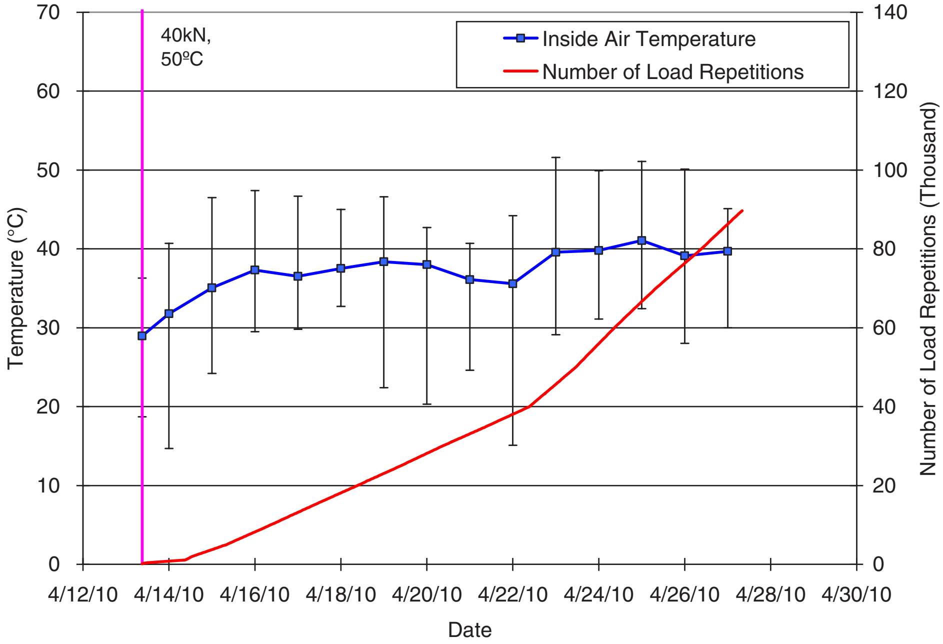

Figure L.44. Daily average inside air temperatures for Section 612HB, RHMA-G, 64 mm.

This plot clearly shows the increase in rutting and deformation over the duration of the test.

Figure L.47 and Figure L.48 show the development of permanent deformation (average maximum rut and average deformation, respectively) with load repetitions as measured with the Laser Profilometer for the test section. Error bars on the average reading indicate that the level of variability caused by the CT blocks is less than the variability for Section 609HB. This is a result of the epoxy material used on Section 612HB to glue CT blocks to pavement. Figure L.49 shows the distribution of rutting along the test section after data for Stations 4, 5, 11, and 13, which are close to CT blocks, were excluded from the data set. It can be observed that excluding data for those four biased stations did not cause any significant change in variability and average accumulated rutting.

Results for Section 611HB are also shown for comparative purposes in Figure L.47 and Figure L.48. It can be observed that rutting accumulation rates after the embedment phase are similar for both sections. However, the high level of densification at the embedment stage resulted in higher rutting for Section 611HB. Because both pavements were constructed from the same mix type, the only reason for higher rutting can be the differences in HMA layer thicknesses. To identify the effect of thickness on accumulated rutting, rutting measurements were converted to permanent shear strain (PSS) by dividing the measured rutting by the HMA layer thickness of each section. Figure L.50 shows that PSS accumulation rate for Section 612HB was faster than was the rate for Section 611HB.

Figure L.51 shows a contour plot of the pavement surface at the end of the test (90,000 repetitions). After trafficking was completed, the average maximum rut depth and the average deformation were 13.9 mm (0.55 in.) and 4.4 mm (0.17 in.), respectively. The maximum rut depth measured on the section was 19.9 mm (0.78 in.), recorded at Station 13.

Table L.8. 612HB, RHMA-G, 64 mm: Temperature Summary for Air and Pavement

	Section 612HB			
Temperature	**Average (°C)**	**SD (°C)**	**Average (°F)**	**SD (°F)**
Outside air	15.0	2.4	59.1	4.4
Inside air	37.0	3.2	98.5	5.8
Pavement surface	51.3	1.3	124.4	2.3
25 mm below surface	50.7	1.2	123.3	2.2
50 mm below surface	49.7	1.3	121.4	2.4
60 mm below surface	49.3	1.4	120.7	2.5
90 mm below surface	48.1	1.6	118.6	2.8

Note: SD = standard deviation.

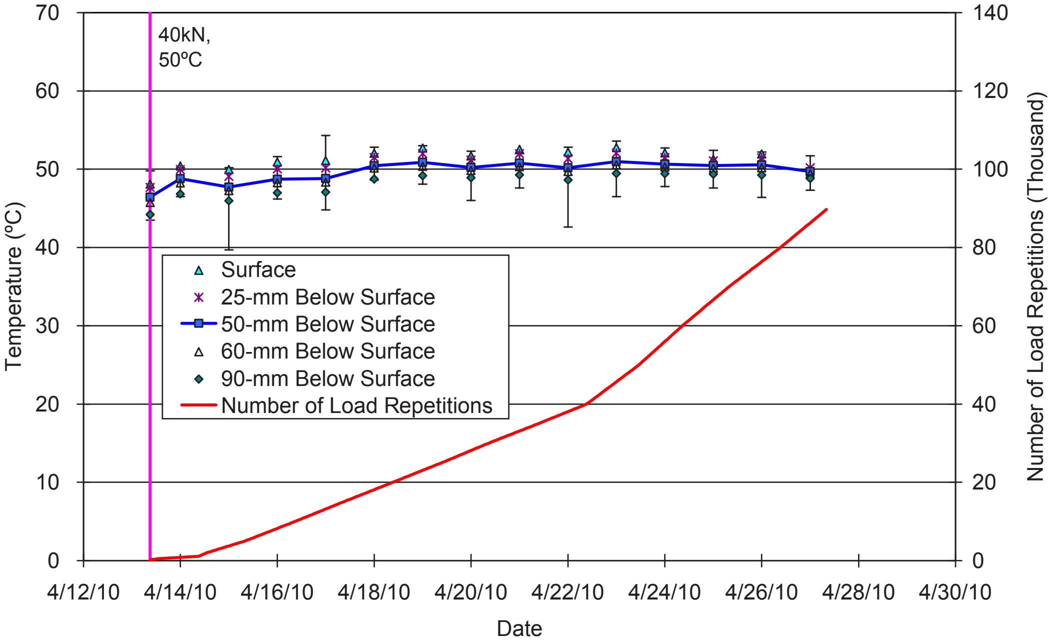

Figure L.45. Daily average temperatures at pavement surface and various depths for Section 612HB, RHMA-G, 64 mm.

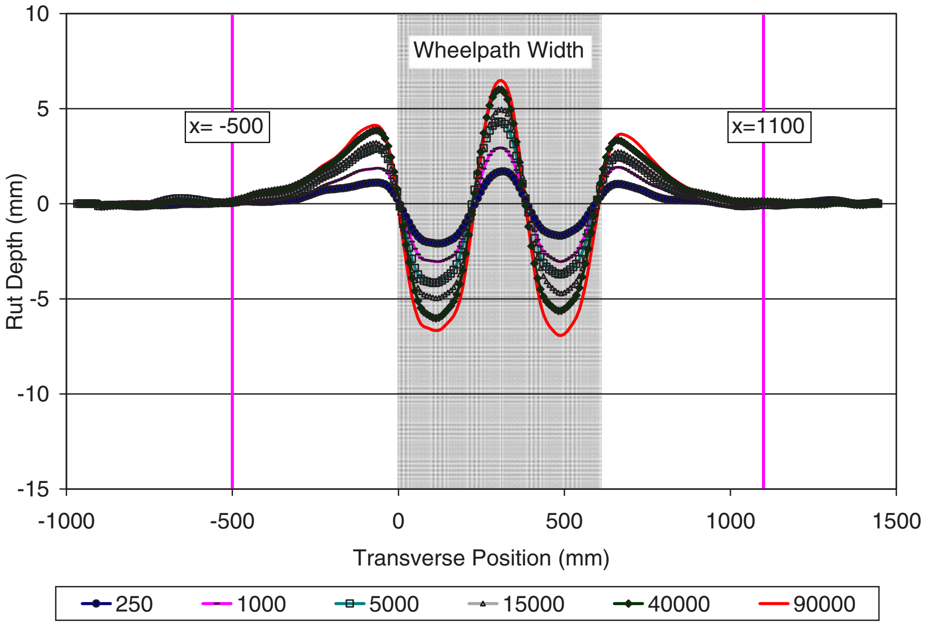

Figure L.46. Laser Profilometer cross section at various load repetitions for 612HB, RHMA-G, 64 mm.

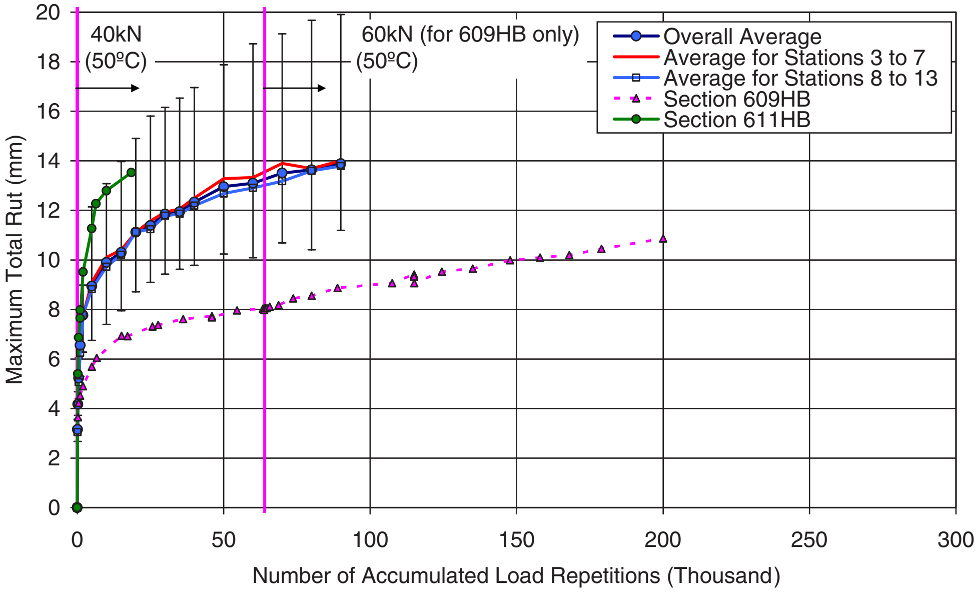

Figure L.47. Average maximum rut for Section 612HB, RHMA-G, 64 mm. Note that data for Section 609HB, PG 64-28 PM, 114 mm, and Section 611HB, RHMA-G, 114 mm, also are shown.

Visual Inspection

Apart from rutting, no other distress was recorded on the section. Figure L.52 is a photograph taken of the surface at the end of the test.

Test Results Summary

Rutting performance of the four sections is shown in Figure L.53 (average maximum rut) and Figure L.54 (average deformation). It can be seen that larger rut depths were measured for sections with thicker HMA layers for both mix types (Sections 609HB and 611HB) and that there was a greater difference between mix types than thicknesses for the two mixes included in the experiment. The wheel load for the two sections with the PG 64-28 PM mix (Sections 609HB and 610HB) was increased from 40 kN to 60 kN at approximately 64,000 repetitions. However, increasing the load did not have any significant effect on the rutting accumulation rate. Early

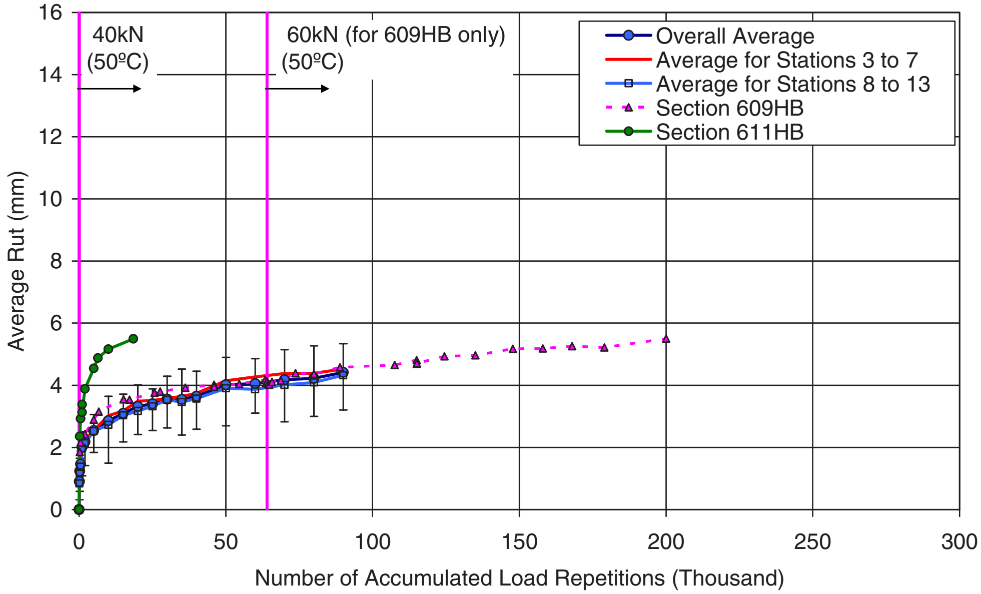

Figure L.48. Average deformation for Section 612HB, RHMA-G, 64 mm. Note that data for Section 609HB, PG 64-28 PM, 114 mm, and Section 611HB, RHMA-G, 114 mm, also are shown.

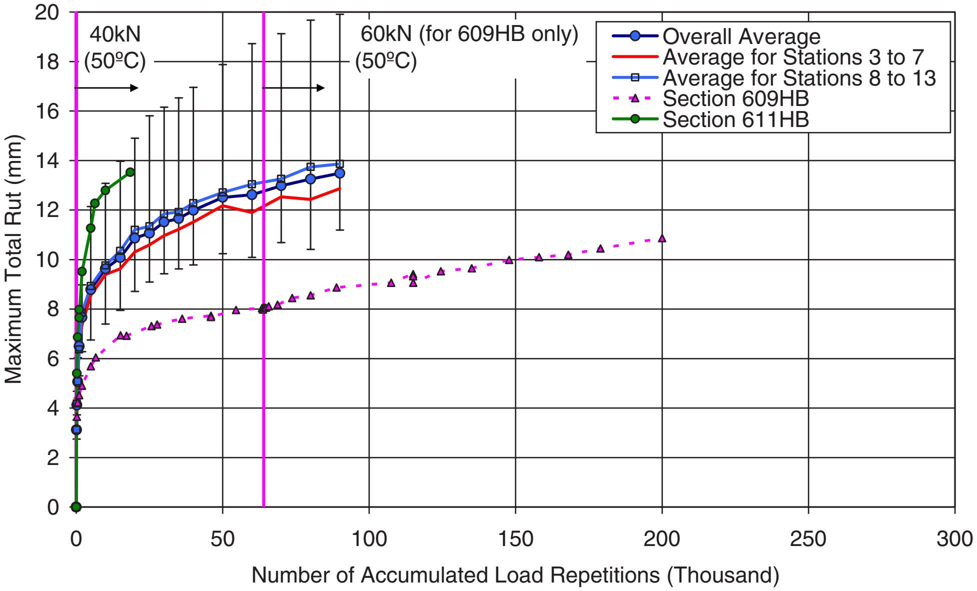

Figure L.49. Average maximum total rut after excluding data for Stations 4, 5, 11, and 13, which are close to CT blocks, for Section 612HB, RHMA-G, 64 mm. Note that data for Section 609HB, PG 64-28 PM, 114 mm, and Section 611HB, RHMA-G, 114 mm, also are shown.

failure was observed for the thick RHMA-G section (Section 611HB).

The results shown in Figure L.55 for average deformation, which is the measure of the downward rut compared with the original pavement surface, indicate that there was less than 6 mm (0.25 in.) of downward deformation of material under the wheels. The maximum rut depth, which considers both downward deformation and "humping" of material sheared to the sides of the wheelpath, is approximately two times greater than the average rut depth for both of the PG 64-28 PM sections, and nearly three times greater for both of the RHMA-G sections, indicating that shearing of material to the side of the wheelpath is as important (or more important) a contributor as the downward rut.

To identify the effect of thickness on accumulated rutting, rutting measurements were converted to permanent shear strain (PSS), similar to the PSS determined in the laboratory repeated shear test, by dividing the measured average

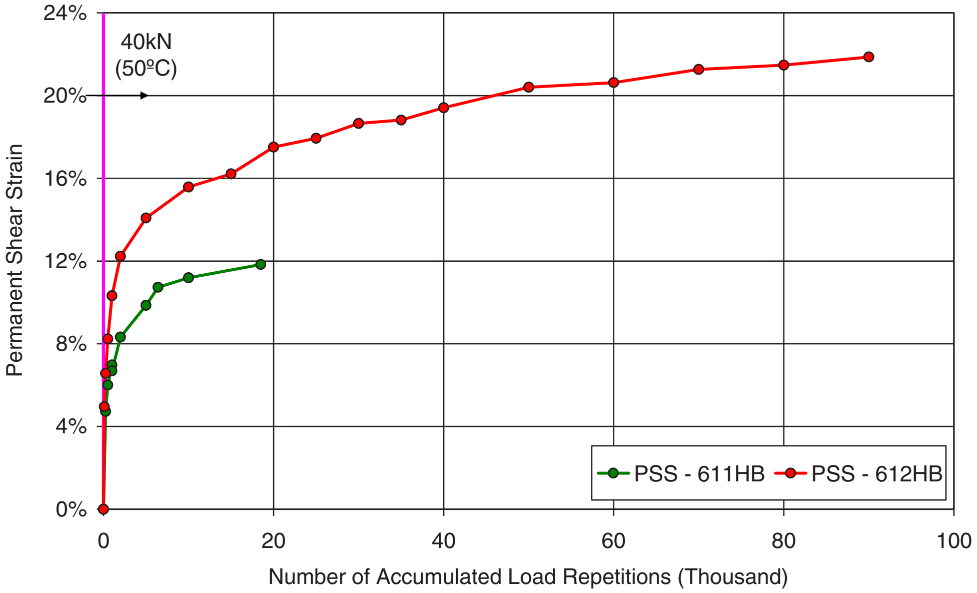

Figure L.50. Comparison of PSS for Section 611HB, RHMA-G, 114 mm, and Section 612HB, RHMA-G, 64 mm.

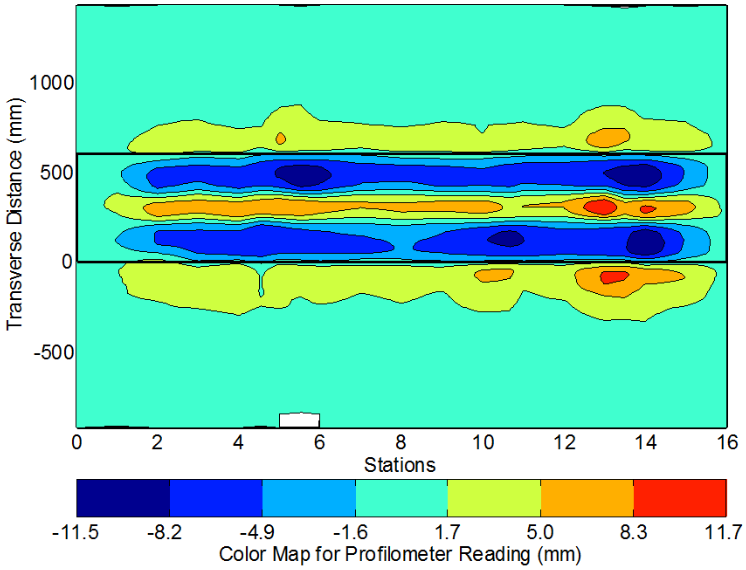

Figure L.51. Contour plot of permanent surface deformation at the end of the test for Section 612HB, RHMA-G, 64 mm.

maximum rut by the HMA layer thickness of each section. Figure L.55 shows the PSS curves for all sections. It can be observed that the PSS curves for the two thicknesses of the PG 64-28 PM mix (Sections 609HB and 610HB) are very close. This result indicates that accumulated rutting for these two sections is approximately a linear function of thickness for the thickness range in this experiment in which the HMA thicknesses are less than 125 mm (5 in.). This result is compatible with results of visco-elastoplastic finite element simulations of rut depth for different HMA thicknesses on concrete pavement performed during the future Strategic Highway Research Program (F-SHRP) A-003A project (Sousa et al. 1994). The simulation showed a typical increase in rut depth with increasing asphalt thickness at an approximately 1:1 ratio to a thickness of approximately 200 mm (8 in.) for a given asphalt response to repeated shear loading and a diminishing effect of asphalt thickness at greater thicknesses, assuming uniform temperature and properties through the full depth of the asphalt and full bonding with the concrete. This result is most likely attributable to the effects of the underlying concrete layer on shear stress distributions at the edges of the tires, which reduce permanent deformation in the asphalt. A similar result may not occur when the section does not have a concrete layer under the HMA. A less consistent result was observed for the RHMA-G sections (Sections 611HB and 612HB), where the thinner section rutted at a faster rate relative to thickness than did the thicker section.

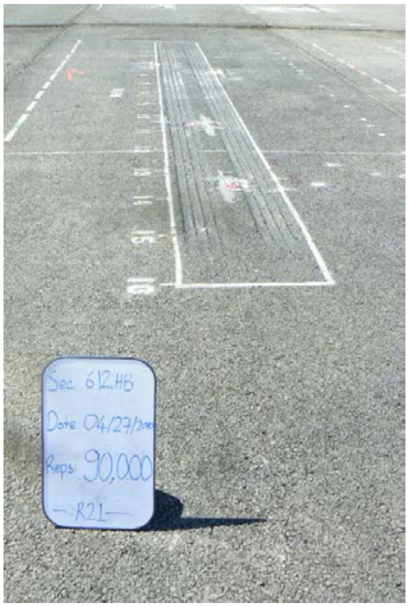

Figure L.52. Photograph at test completion of Section 612HB, RHMA-G, 64 mm.

Key findings from the HVS rutting study include

- Maximum rut depths for same trafficking were observed to increase for thicker HMA layers for both mix types, with the PG 64-28 PM mix showing an approximately 1:1 relationship between rut depth development and thickness and a greater than 1:1 relationship, although less consistent, for the RHMA-G mix.
- The downward deformation in the wheelpath was approximately equal to the upward deformation of material at the sides of the wheelpath for the PG 64-28 PM mix. For the RHMA-G mix, the upward deformations at the sides of the wheelpath were greater than the downward wheelpath deformation.
- Increasing the wheel load for Sections 609HB and 610HB from 40 kN to 60 kN at approximately 64,000 repetitions did not appear to have any significant effect on the rutting accumulation rate.

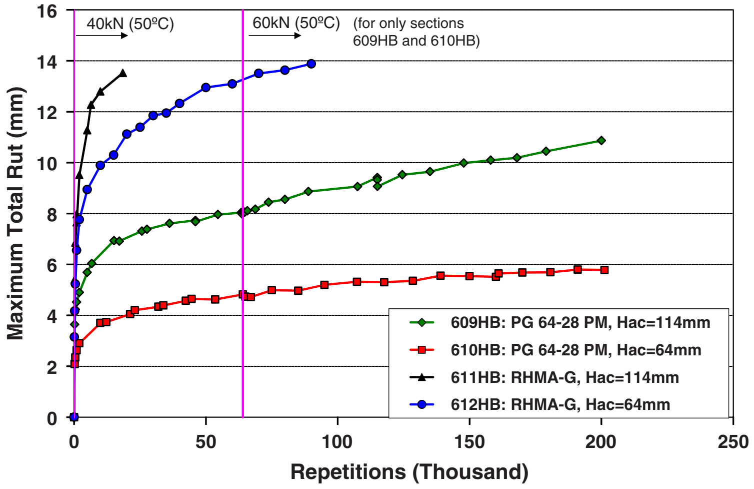

Figure L.53. Comparison of average maximum total rut.

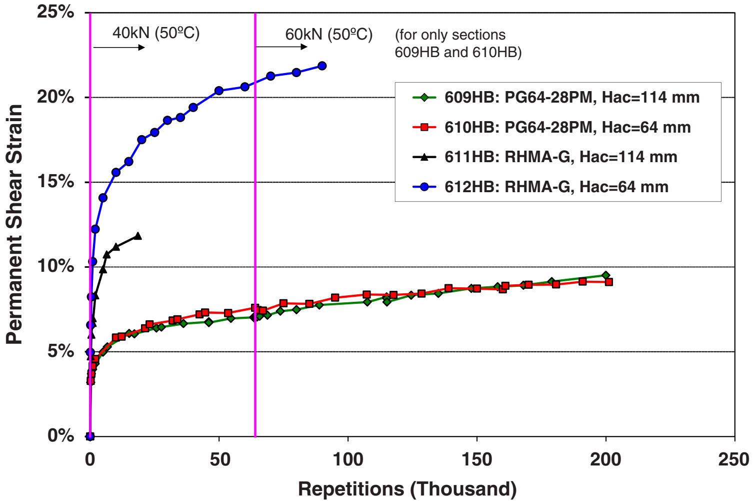

Figure L.54. Comparison of average deformation.

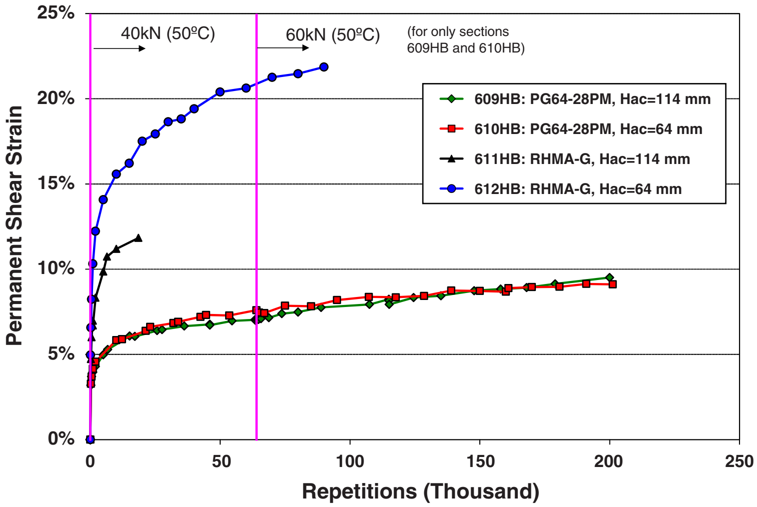

Figure L.55. Comparison of PSS for all HVS rut test sections.

Asphalt Strain Gauge Results

Four asphalt strain gauges manufactured by the CTL group were located at 2 in. (50 mm) depth (between the first and second lifts) of the HMA layers at two different longitudinal locations for each section with 4.5-in. (113-mm) HMA layer thickness (Sections 609HB and 611HB). One of the strain gauge couples (transverse and longitudinal) was placed under the centerline of the tire, whereas the other one was located at the edge of the tire. Details about the strain gauge locations and specifications are given in "HVS Test Criteria" and in Appendix G, respectively.

Strain data collected during the HVS tests were used to assess the densification rate of the HMA layer based on the general trend of the collected data. After the HVS test, a sensitivity study was performed on the same sections to identify the relative importance of load, temperature, and wheel speed on measured elastic strain.

Figure L.56 shows the measured elastic strain values throughout the HVS test for Section 609HB. The strain gauge located under the center of the tire (CT) in the transverse direction reached its limit at the initial repetitions of the test because of excessive densification. The strain in the longitudinal direction under the center of the tire is higher than the strain in the longitudinal direction at the edge of the tire (ET) during the first 60,000 repetitions. Because densification directly affected the CT gauge, strain at both locations started to converge after 60,000 repetitions due to the reduced densification rate. Measurements also indicated that all three gauges started to measure similar strain values after the HMA layer was densified.

Figure L.57 shows the measured strain values throughout the HVS test for Section 611HB. The strain gauge located under the center of the tire in the transverse direction was broken during construction. Trafficking was stopped at specific intervals to collect profilometer data. Jumps in strain occurred after the trafficking was restarted as a result of the higher loads that were applied during the first 15 repetitions due to proportional integral derivative (PID) adjustments performed by the wheel load system. However, it can be observed that these jumps were larger than the ones observed for Section 609HB (Figure L.56), which may point to a relaxation stage for the RHMA-G mix after the trafficking was stopped. It can be observed that strain in the longitudinal direction under the center of the tire was higher than the strain in the longitudinal direction at the edge of the tire throughout the test. Reduction in strain with increasing repetitions was not observed for that section. This might be a result of the low level of densification at that depth.

Sensitivity Study with Strain Gauges

A sensitivity study was performed using the HVS to determine the sensitivity of strain at 50-mm depth in the asphalt to temperature, speed, and load.

The experimental plan for the sensitivity study is given in Table L.9. A total of 72 tests were run. For each test, 100 repetitions were applied (7,200 repetitions for the complete test). Data for the initial 15 repetitions for each test were excluded from the data set because higher loads were applied during that stage due to PID adjustments performed by the system. Figure L.58 and Figure L.59 show the comparisons for the target and measured temperatures at 50-mm depth for Section 609HB and Section 611HB, respectively. It can be observed that temperature error was always at acceptable levels except for the 20°C tests run for Section 609HB. Because of the high outside air temperatures, the temperature at 50-mm depth was only

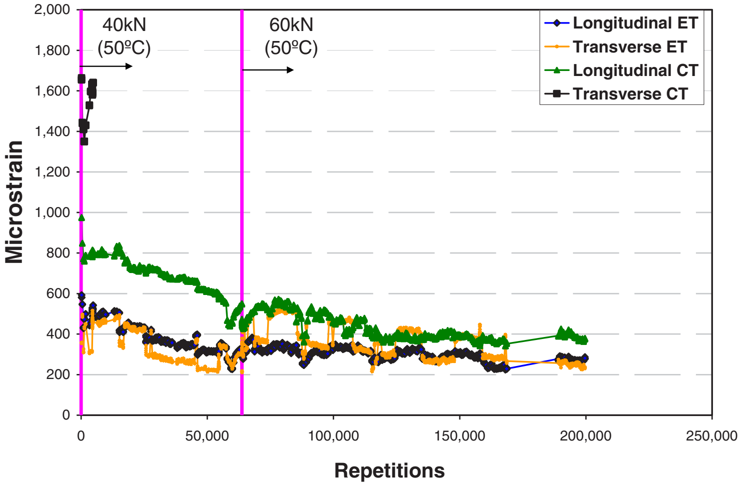

Figure L.56. Section 609HB: Measured strain values throughout the HVS test (1 kN = 225 lb). Note that ET is the gauge at the edge of the tire; CT is the gauge at the center of tire.

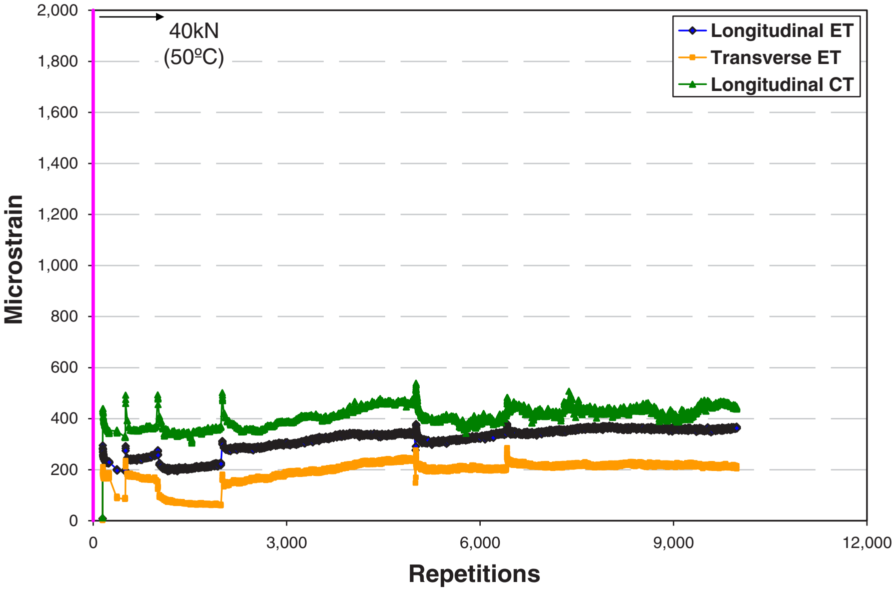

Figure L.57. Section 611HB: Measured strain values throughout the HVS test (1 kN = 225 lb).

decreased to 22.5°C whereas the target temperature was 20°C. Air temperatures inside the temperature control unit are shown in Figure L.60 and Figure L.61 for Section 609HB and Section 611HB, respectively.

Results for the sensitivity study for Section 609HB are given in Figure L.62 and Figure L.63 for the strain gauge at the ET and CT locations, respectively. Both strain gauges were located longitudinally to the direction of traffic at 50-mm depth during construction. Vertical error bars on each point on the graph show the strain range for that particular test. It can be observed that variability in measured strain for all tests was negligible. For all temperatures, measured strains at the edge of tire were lower than strains measured at the center of tire. Temperature appears to be the most significant parameter that affected the strain for both gauges. Strain levels increased drastically when temperature was increased from 40°C to 50°C. In addition, it was observed that changes in speed and load also affected the measured strain for both gauges.

Table L.9. Experimental Plan for Sensitivity Study[a]

Section	Load (kN)	Speed (km/h)	Temperature (°C)
609HB, PG 64-28 PM, 114 mm thick	40 60	3.1 5.9	20 30
611HB, RHMA-G, 114 mm thick	80 80	8.7 8.7	40 50

[a] 1 kN = 225 lb (Fahrenheit = Celsius × 9/5 + 32); 1 km/h = 0.62 mph.

Results for the sensitivity study for Section 611HB are given in Figure L.64 and Figure L.65 for the strain gauge located longitudinally and transversely to the direction of traffic, respectively. Both strain gauges were located at the edge of tire at 50-mm depth during construction. Vertical error bars on each point on the graph show the strain range for that particular test. It can be observed that variability in measured strain for all tests is negligible. For all temperatures, measured transverse strains at the edge of the tire were higher than longitudinal strains measured at the center of

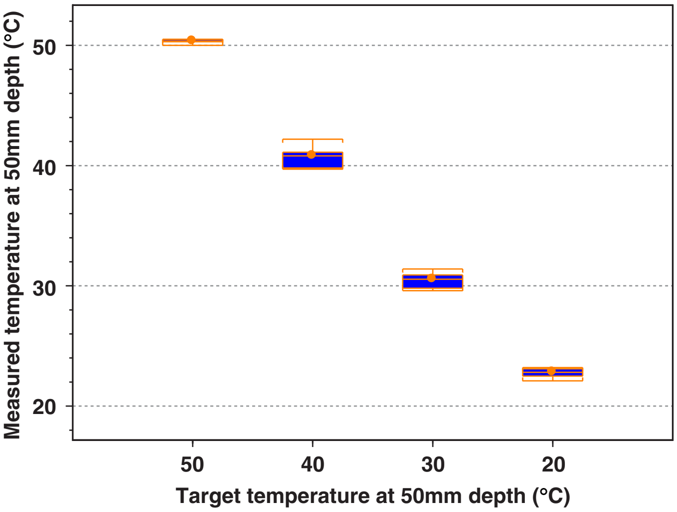

Figure L.58. Comparison of target and measured temperatures at 50-mm (2-in.) depth for Section 609HB. Fahrenheit = Celsius × 9/5 + 32. (For key, see Figure N.1.)

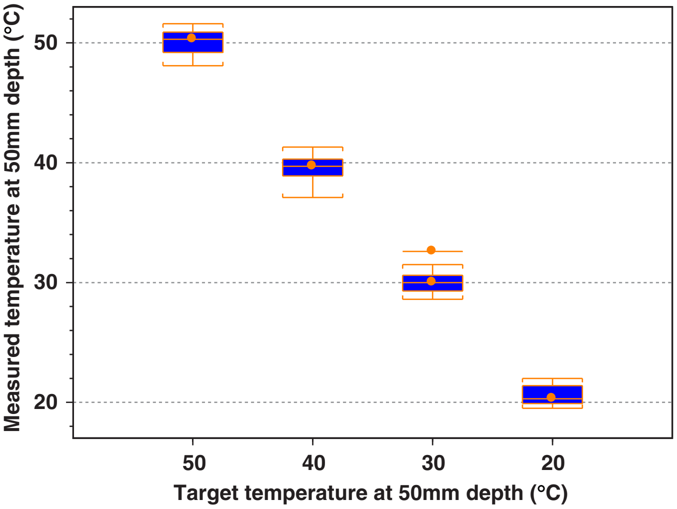

Figure L.59. Comparison of target and measured temperatures at 50-mm (2-in.) depth for Section 611HB. Fahrenheit = Celsius × 9/5 + 32.

the tire. Temperature appeared to be the most significant parameter that affected the strain for both gauges. Strain levels increased drastically when temperature was increased from 40°C to 50°C for the gauge in transverse direction while increasing temperature was linearly increasing the strains for the gauge in longitudinal direction. In addition, it was observed that changes in speed and load also affected the measured strain for both gauges. The effect of load increase on strain appeared to be more significant for the gauge in the transverse direction. Strain slightly decreased with increasing load for some tests run with strain gauges located in the longitudinal direction. This was a result of the constant tire pressure used for tests. Increasing load with constant tire pressure increases the loading area while maintaining constant pressure. However, increasing load always increases the transverse strain gauge measurements.

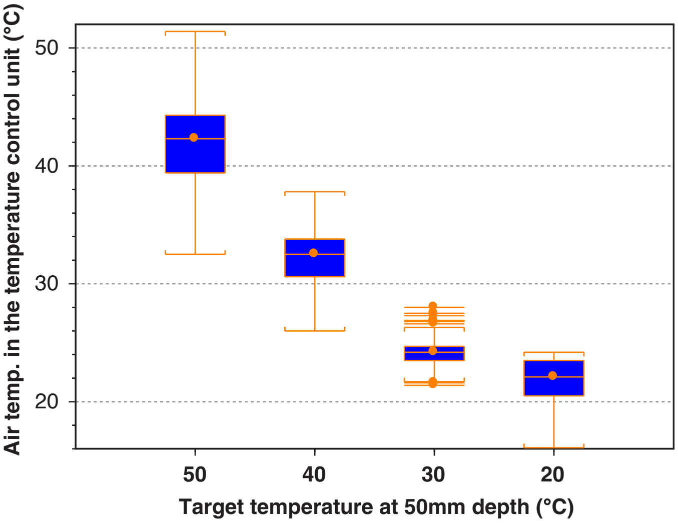

Figure L.60. Air temperatures in the temperature control unit for the corresponding target 50-mm (2-in.) depth temperatures for Section 609HB. Fahrenheit = Celsius × 9/5 + 32.

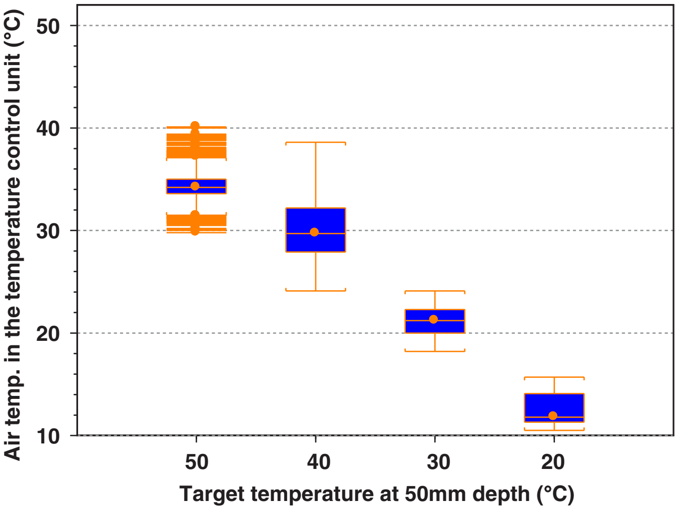

Figure L.61. Air temperatures in the temperature control unit for the corresponding target 50-mm (2-in.) depth temperatures for Section 611HB. Fahrenheit = Celsius × 9/5 + 32.

The effect of temperature, load, and speed parameters on measured strain was quantified and evaluated by using the analysis of variance (ANOVA) method. ANOVA *p*-values for each strain gauge measurement are given in Table L.10. Results of the ANOVA analysis indicated that temperature is the most significant variable that affects the measured strain values with *p*-values equal to zero for all strain gauge measurements. In addition, speed appears to be an important parameter affecting the measured strain values with *p*-values smaller than 0.05 for all strain gauge measurements. On the other hand, load does not have a significant effect on measured strain for the gauges located in longitudinal direction whereas changes in load significantly affect the transverse strain gauge measurements.

The strain values given in Figure L.62 and Figure L.64 can be compared to identify the effect of mix difference on strain because location and direction of both gauges were identical. It can be observed that strain measured at 50°C for Section 609HB (PG 64-28 PM) is 25% greater than the strain measured for Section 611HB (RHMA-G). However, the results of the HVS rutting tests indicated that the rutting resistance of Section 609HB was considerably higher than that for Section 611HB (see "HVS Test Data Summary"). The reason behind this unexpected result will be investigated based on the CT image analyses of HVS samples.

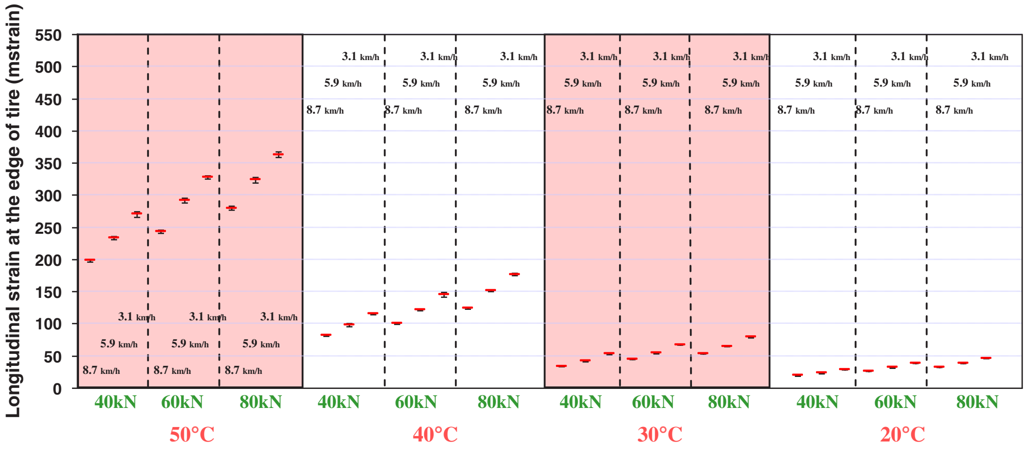

Figure L.62. Results for the sensitivity study for Section 609HB, longitudinal strain at the edge of the tire. Fahrenheit = Celsius × 9/5 + 32; 1 kN = 225 lb; 1 km/h = 0.62 mph.

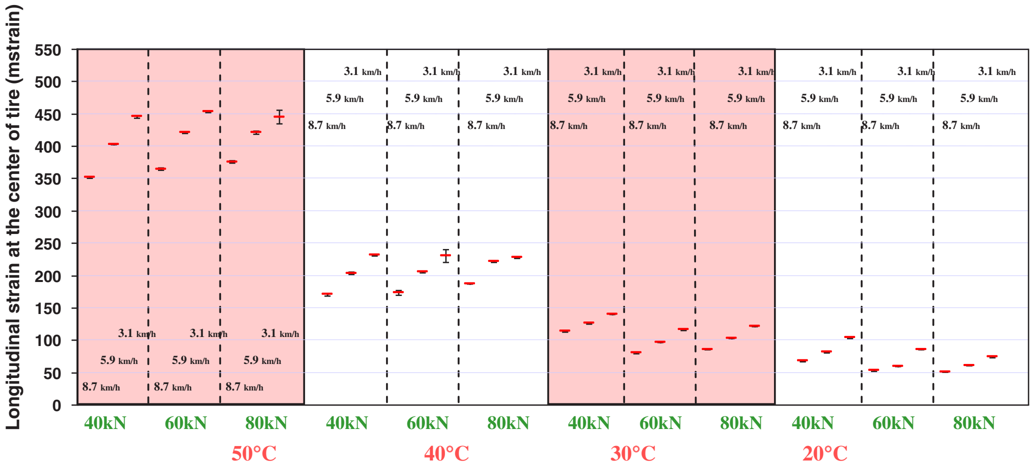

Figure L.63. Results for the sensitivity study for Section 609HB, longitudinal strain at the center of the tire. Fahrenheit = Celsius × 9/5 + 32; 1 kN = 225 lb; 1 km/h = 0.62 mph.

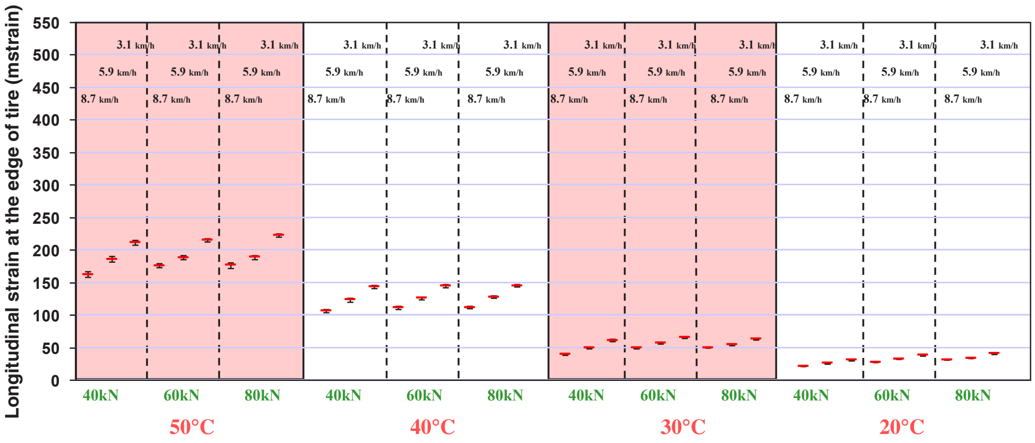

Figure L.64. Results for the sensitivity study for Section 611HB, longitudinal strain at the edge of the tire. Fahrenheit = Celsius × 9/5 + 32; 1 kN = 225 lb; 1 km/h = 0.62 mph.

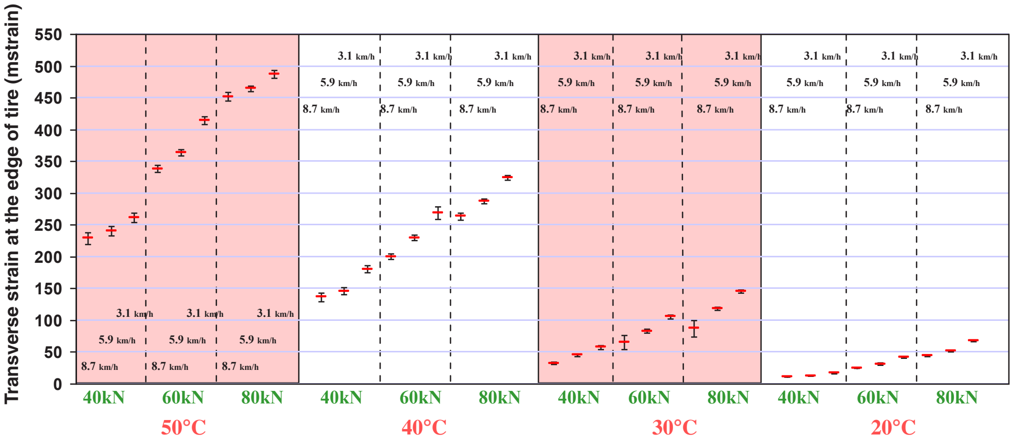

Figure L.65. Results for the sensitivity study for Section 611HB, transverse strain at the edge of the tire. Fahrenheit = Celsius × 9/5 + 32; 1 kN = 225 lb; 1 km/h = 0.62 mph.

Table L.10. ANOVA Fvalues *for Strains*

	Section 609HB		Section 611HB	
	Longitudinal ET	**Longitudinal CT**	**Longitudinal ET**	**Transverse ET**
Temperature (°C)	0.000	0.000	0.000	0.000
Speed (km/h)	0.021	0.012	0.000	0.022
Load (kN)	0.010	0.773	0.926	0.000

Note: CT = center of the tire; ET = edge of the tire.

Conclusions

The key findings of the HVS rutting tests conducted at UCPRC include the following:

- Sensitivity analyses performed with EverFE and EICM for the 3.7 × 4.5 m (12 × 15 ft) bare jointed concrete slabs that were 125- and 175-mm (5- and 7-in.) thick show that midslab edge loading will be more critical than corner loading for all sections. Because of the reduced temperature gradient, tensile stresses at the sections with HMA layers will be less than the sections without an HMA layer.
- Sensitivity analyses performed with *MEPDG* suggest that there will not be a rapid early concrete cracking failure for the HVS test sections.
- HMA densities in the range of 92% to 93% relative to theoretical maximum density (7% to 8% air voids) were achieved, which resembles typical field construction.
- Computerized tomography image analyses performed with blocks cut from the HVS test sections showed that air void contents were higher in the top lift than in the bottom lift for Section 609HB, indicating poorer compaction in the top lift. This is expected in multilift construction because the bottom lift is reheated during placement of the next lift and receives additional compaction while the next lift is being compacted.
- Thick RHMA-G layers appeared to have more uniform air void content distributions than did the thick PG 64-28 PM layers. High volumes of air voids were observed at the bottom of each lift for sections with a PG 64-28 PM layer. This compaction problem is a result of the larger nominal maximum aggregate size for PG 64-28 PM mixes (19 mm) than the RHMA-G mixes (12.5 mm).
- Higher rut depths were observed for sections with thick HMA layers (Sections 609HB and 611HB).
- Increasing the wheel load for Sections 609HB and 610HB with PG 64-28 PM mix from 40 kN to 60 kN at approximately 64,000 repetitions did not appear to have any significant effect on the rutting accumulation rate.
- To identify the effect of thickness on accumulated rutting, rutting measurements were converted to PSS by dividing the measured rutting by the HMA layer thickness of each section. It was observed that PSS curves for Sections 609HB and 610HB, thick and thin PG 64-28 PM layers, are very close. This result indicated that accumulated rutting for these two sections is a function of thickness. It should be noted that this result is most likely to be a result of the underlying concrete layer, which minimizes permanent deformation at the unbound layers. A similar result may not be observed when the section does not have any concrete layer under the HMA.
- Early failure was observed for Section 611HB, which is a result of mix type (RHMA-G) and thick HMA layer. However, although early failure was observed for Section 611HB, it was observed that the PSS accumulation rate for that section was slower than for Section 612HB.

APPENDIX M

Joint Movement Monitoring at UCPRC

Introduction

At the Heavy Vehicle Simulator (HVS) test track at the University of California, Pavement Research Center (UCPRC), joint deflection measurement devices (JDMDs) were used to monitor the horizontal opening and closing of the slab joints and the vertical movements of the slab corners caused by daily temperature variation, and without traffic loading, on numerous slab corners. Data were collected before and after HMA construction. The data were used to establish the effects of portland cement concrete (PCC) layer thickness, existence of dowels, HMA thickness, and HMA material type on joint movements.

Monitoring Program

Site Layout and Slab Labeling

A detailed description of the test track can be found in Appendix G. Figure M.1 shows the section layout and labeling system for individual PCC slabs.

JDMD Locations and Labeling

When monitoring joint movements, JDMDs are deployed at the corners of the slabs. A vertical JDMD monitors the upward and downward curling of one PCC slab corner, whereas a horizontal JDMD monitors relative horizontal displacements between two adjacent corners. A JDMD is identified by its location, orientation, nearby joint, and the surface type (HMA or PCC) it is measuring. More specifics of the naming scheme include

- A slab has four corners: NW (northwest), NE (northeast), SW (southwest), and SE (southeast).
- There are two orientations: H (horizontal) and V (vertical).
- There are eight joints: J1 to J8, as shown in Figure M.1.
- There are two surface types: A (HMA) and P (PCC).

For example, JDMD-B22-SE-J4-V-P, shown in Figure M.1, indicates that the JDMD is located at the southeast (SE) corner of slab B22, near Joint J4, is measuring vertical movements, and is installed on the PCC surface (P).

Instrumentation and Monitoring Methods

For this study, two types of data were collected: ambient air temperature and joint movements. Ambient air temperature is recorded continuously by an automatic weather station at the project site (Figure M.2) that recorded hourly temperature, wind speed, sun radiation, and precipitation. Joint movements were recorded with JDMDs, which are essentially linear voltage differential transducers (LVDTs). Figure M.3 shows the configuration for measuring vertical and horizontal joint movements. The anchoring rods are each 5 ft (1.5 m) long.

Albedo values were also measured for the three kinds of surface at the test track: polymer-modified (PM) mix, rubberized hot-mix asphalt with gap-graded aggregates (RHMA-G), and bare PCC. A picture of the albedometer is shown in Figure M.4. Measurement was done on 4/8/2011.

The HVS data acquisition system (DAS) recorded joint movements at 1-minute intervals. Because of the channel number limit of the HVS DAS, a maximum of 15 JDMDs could be deployed at a time. Joint movements were monitored in batches, with each batch consisting of about 1 week of data.

Monitoring Program

The timeline of JDMD monitoring batches is listed in Table M.1. Batch numbers one to five were conducted before HMA placement while batches six to 10 were conducted after HMA placement. The longitudinal joints between adjacent lanes were sawn to remove the interference between lanes. The objective of each batch is also shown in Table M.1.

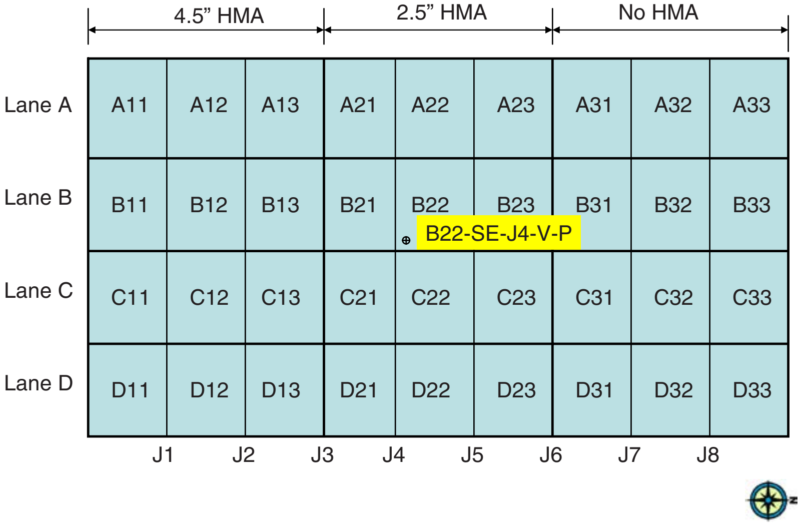

Lane A	A11	A12	A13	A21	A22	A23	A31	A32	A33
Lane B	B11	B12	B13	B21	B22	B23	B31	B32	B33
Lane C	C11	C12	C13	C21	C22	C23	C31	C32	C33
Lane D	D11	D12	D13	D21	D22	D23	D31	D32	D33

Figure M.1. Section layout and slab labeling system: Each slab is named with one letter indicating the lane and two digits indicating the location within each lane. The first digit indicates the structure type, whereas the second digit indicates the slab sequence from south to north within each structure.

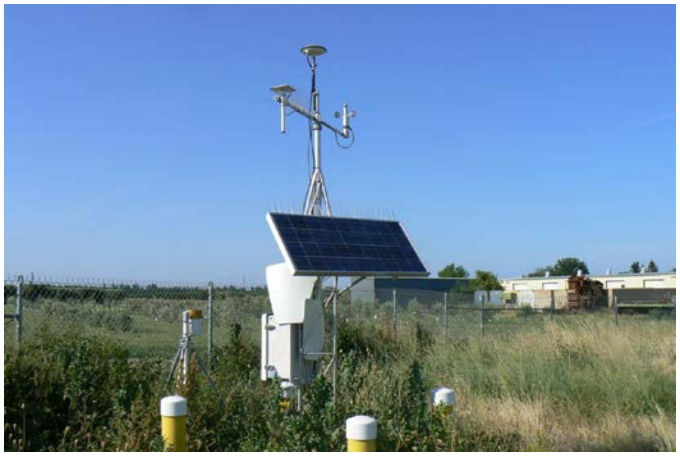

Figure M.2. Photograph of the automatic datalogging weather station at the project site.

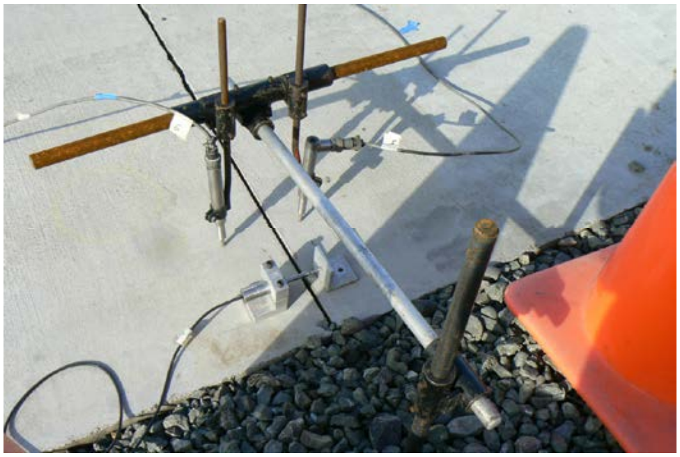

Figure M.3. Photograph showing the JDMD configuration for monitoring both horizontal and vertical movements at a joint. The horizontal JDMD shown is model DSD800SE5 made by Daytronic, and the vertical JDMDs are model GHSD/GHSDR 750 made by Macro Sensors.

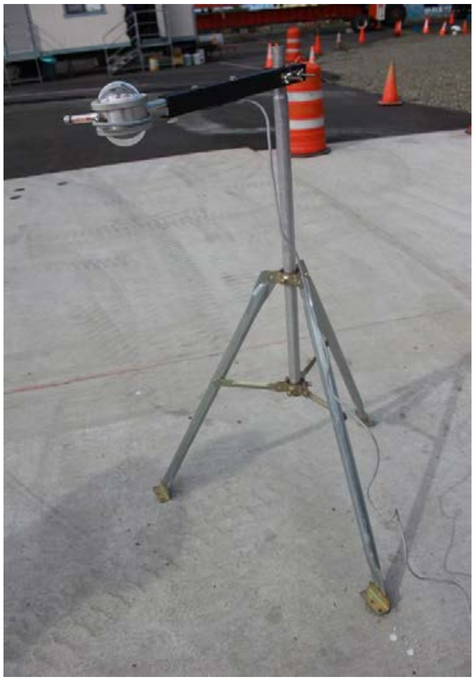

Figure M.4. Photograph of NovaLynx 240-8104 Albedometer (Dual Pyranometer) used for albedo measurement.

The JDMD layouts for the batches are shown in Figures M.5 through M.14, with the JDMD label indicating the HVS DAQ channel to which it was attached. Each batch was given a unique code to indicate its objective and location. A circle or arrow on each figure shows the location of each vertical JDMD, and an arrow indicates each horizontal JDMD. Note that the northwest corner of Slab C32 was monitored as part of every batch to provide reference joint movements. This is important because average ambient temperature changed among different batches, and as a result, the shape of PCC slabs changed and caused joint movement characteristics to change. In addition, some of the JDMDs did not function properly, and their labels are enclosed in parentheses.

Results Summary

This section presents the raw deflection readings recorded in each batch along with the ambient temperature. The variations of deflection and ambient temperature with time for the batches are shown in Figures M.15 through M.44. Note that an increase in deflection reading implies downward movements for vertical JDMDs and opening movements for horizontal JDMDs. In the figures, the legends include the JDMD number as well as its label, and these numbers correspond to those shown in Figure M.5 through Figure M.14.

The reference JDMDs shown in each figure are always the ones located at the northwest corner of Slab C32 (for instance, C32-NW-J8-V-P for vertical movements and C32-NW-J8-H-P for horizontal movements). As pointed out earlier, these two JDMDs are part of every batch and thus provide a consistent reference for all the other measurements.

Note that the data from Batch 1 show more noise than do the data from all the other batches. The noise is high-frequency (around 1,000 Hz but not consistent) measurement noise associated with the JDMDs manufactured by Daytronic. In later batches, the noise was removed by changing the way readings were taken. In the first batch, only one reading was taken and recorded every minute. In all the later batches, there was still only one reading recorded for every minute, but each

Table M.1. JDMD Monitoring Timeline for Each Batch

Batch and Layout No.	Description of Objective	Begin	End
1	Evaluate horizontal movements of joints on west side of Lane A and Lane C	9/11/2009	9/17/2009
2	Evaluate horizontal movements of joints on west side of Lanes B, C, and D	9/17/2009	9/22/2009
3	Compare vertical and horizontal movements of joints on west side of Lanes A, C, and D on Slabs A32, C32, and D32	9/23/2009	9/29/2009
4	Evaluate symmetry of four corners on nondoweled Slab C32, along with NW corner of B32	9/29/2009	10/5/2009
5	Evaluate symmetry of four corners on doweled Slab A32, along with NW corner of C32	10/5/2009	10/13/2009
6	Evaluate movements of joints on Lane D on east edge, with Slab C32 as reference	1/11/2011	1/18/2011
7	Evaluate movements of joints on Lane B, with Slab C32 as reference after HMA placement	1/21/2011	1/28/2011
8	Evaluate movements of joints along J5, with Slab C32 as reference after HMA placement	1/28/2011	2/7/2011
9	Evaluate movements of joints on Lane A, with Slab C32 as reference	4/27/2011	5/11/2011
10	Evaluate movements of joints on west edge of Lane C, with Slab C32 as reference	5/11/2011	5/23/2011

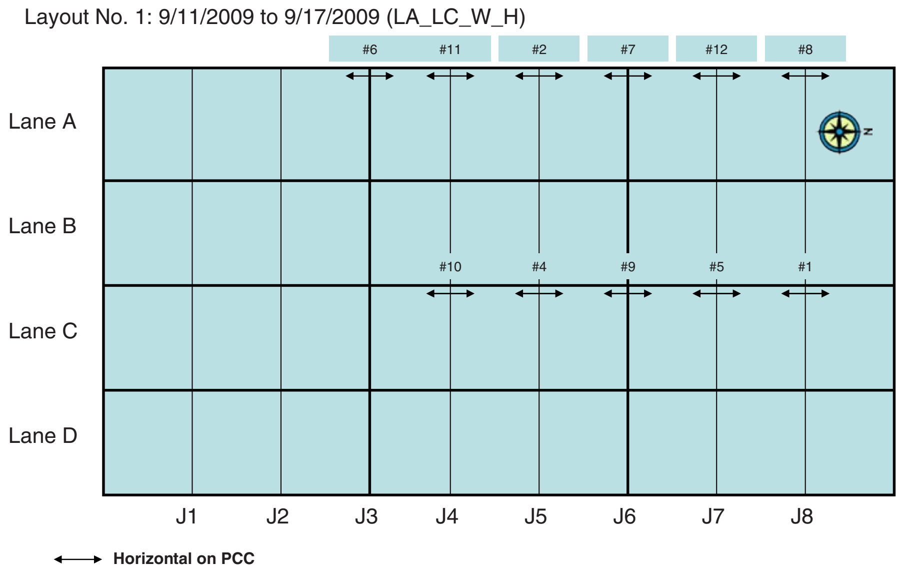
Layout No. 1: 9/11/2009 to 9/17/2009 (LA_LC_W_H)
#6
#11
#2
#7
#12
#8
Lane A
Lane B
Lane C
Lane D
#10
#4
#9
#5
#1
N
J1
J2
J3
J4
J5
J6
J7
J8
Horizontal on PCC

Figure M.5. JDMD monitoring layout for Batch 1, coded LA_LC_W_H, monitored the horizontal movements of joints on west side of Lanes A and C. The JDMD label, for Example #6, indicates the HVS DAS channel number used.

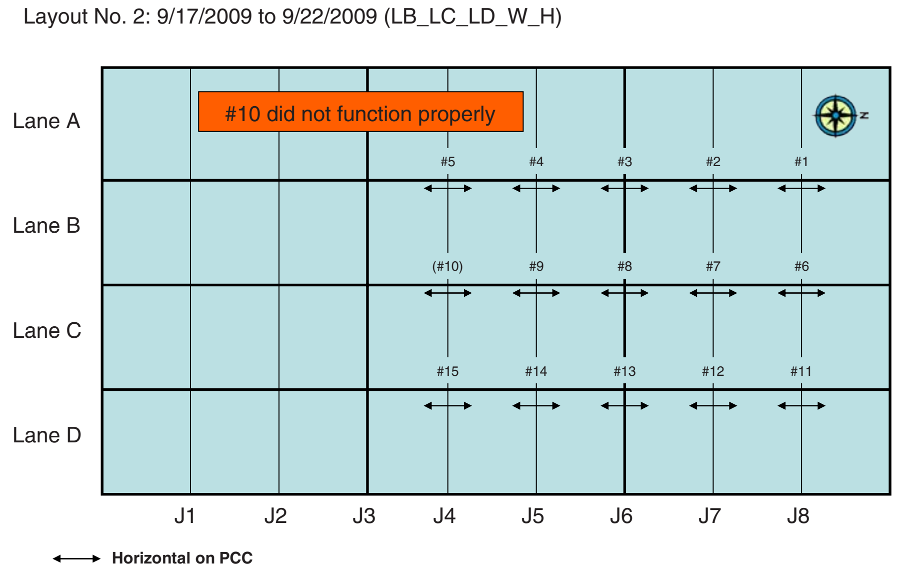
Layout No. 2: 9/17/2009 to 9/22/2009 (LB_LC_LD_W_H)
Lane A
Lane B
Lane C
Lane D
#10 did not function properly
N
#5
#4
#3
#2
#1
(#10)
#9
#8
#7
#6
#15
#14
#13
#12
#11
J1
J2
J3
J4
J5
J6
J7
J8
Horizontal on PCC

Figure M.6. JDMD monitoring layout for Batch 2, coded LB_LC_LD_W_H, monitored the horizontal movements of joints on west side of Lanes B, C, and D. Label for Channel #10 in parentheses indicates that it did not function properly.

Layout No. 3: 9/23/2009 to 9/29/2009 (LA_LC_LD_W_HV)

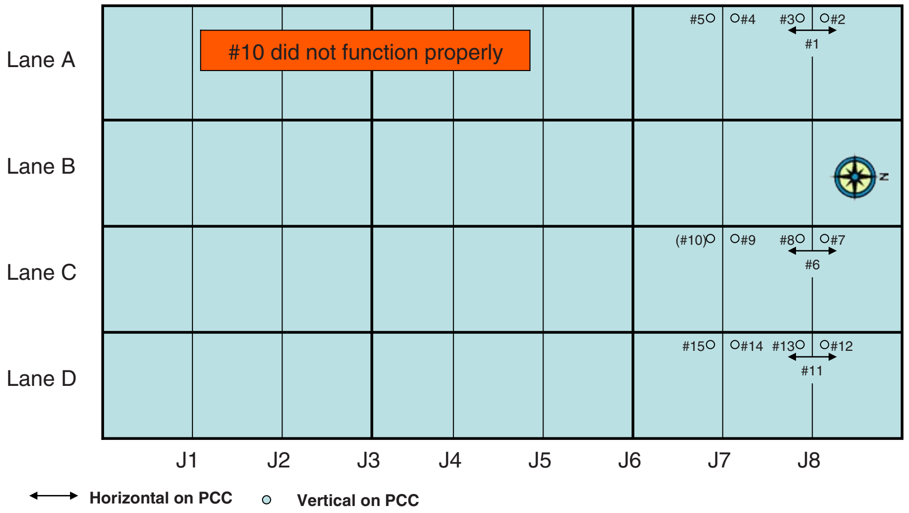
Lane A
Lane B
Lane C
Lane D
#10 did not function properly
#5
#4
#3
#2
#1
(#10)
#9
#8
#7
#6
#15
#14
#13
#12
#11
N
J1
J2
J3
J4
J5
J6
J7
J8
Horizontal on PCC
Vertical on PCC

Figure M.7. JDMD monitoring layout for Batch 3, coded LA_LC_LD_W_HV, compared the vertical and horizontal movements of joints on west side of Lanes A, C, and D.

Layout No. 4: 9/29/2009 to 10/05/2009 (C32_Asym_And_B32_HV)

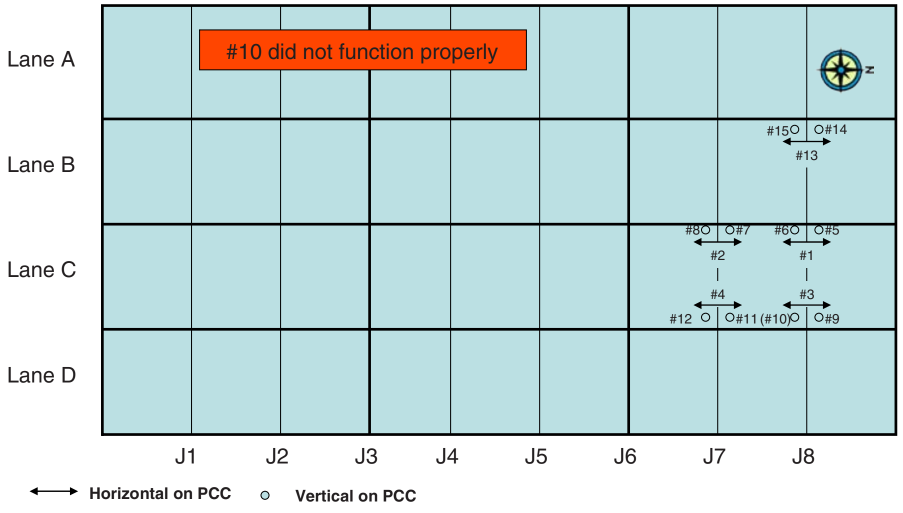
Lane A
Lane B
Lane C
Lane D
#10 did not function properly
N
#15
#14
#13
#8
#7
#6
#5
#2
#1
#4
#3
#12
#11
(#10)
#9
J1
J2
J3
J4
J5
J6
J7
J8
Horizontal on PCC
Vertical on PCC

Figure M.8. JDMD monitoring layout for Batch 4, coded C32_Asym_And_B32_HV, evaluated the symmetry of four corners on nondoweled Slab C32, along with NW corner of B32.

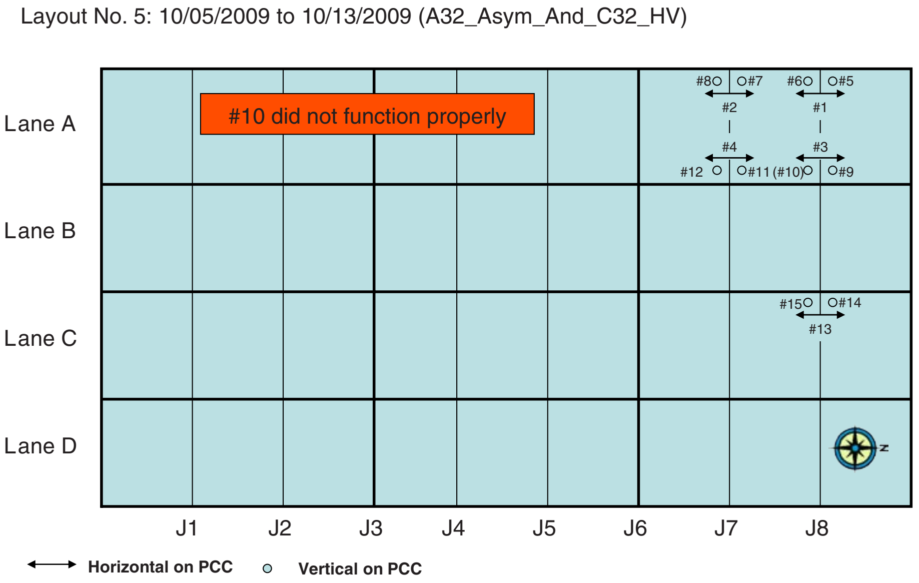
Layout No. 5: 10/05/2009 to 10/13/2009 (A32_Asym_And_C32_HV)
#10 did not function properly
Lane A
Lane B
Lane C
Lane D
#8
#7
#6
#5
#2
#1
#4
#3
#12
#11
(#10)
#9
#15
#14
#13
J1
J2
J3
J4
J5
J6
J7
J8
Horizontal on PCC
Vertical on PCC

Figure M.9. JDMD monitoring layout for Batch 5, coded A32_Asym_And_C32_HV, evaluated the symmetry of four corners on doweled Slab A32, along with the NW corner of C32.

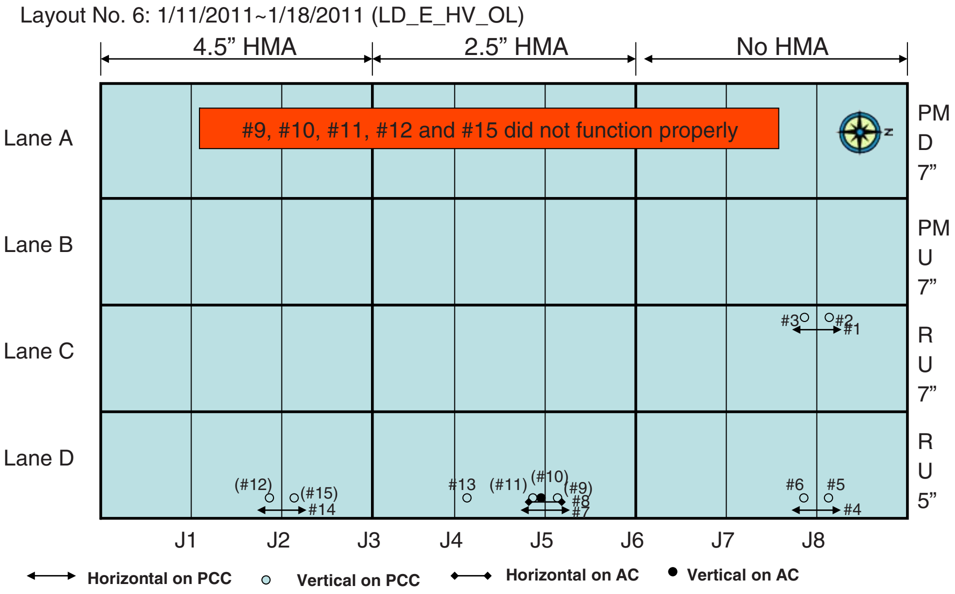
Layout No. 6: 1/11/2011~1/18/2011 (LD_E_HV_OL)
4.5" HMA
2.5" HMA
No HMA
#9, #10, #11, #12 and #15 did not function properly
Lane A
Lane B
Lane C
Lane D
PM D 7"
PM U 7"
R U 7"
R U 5"
#3
#2
#1
(#12)
(#15)
#14
#13
(#11)
(#10)
(#9)
#8
#7
#6
#5
#4
J1
J2
J3
J4
J5
J6
J7
J8
Horizontal on PCC
Vertical on PCC
Horizontal on AC
Vertical on AC

Figure M.10. JDMD monitoring layout for Batch 6, coded LD_E_HV_OL, monitored the movements of joints on Lane D on the east edge after HMA placement, with Slab C32 as a reference.

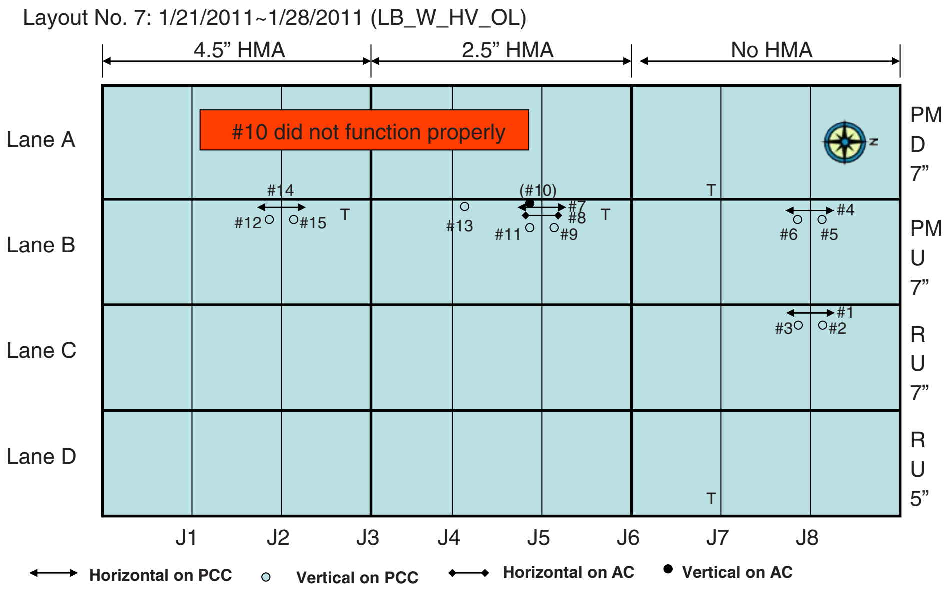
Layout No. 7: 1/21/2011~1/28/2011 (LB_W_HV_OL)

4.5" HMA
2.5" HMA
No HMA
Lane A
Lane B
Lane C
Lane D
#10 did not function properly
PM D 7"
PM U 7"
R U 7"
R U 5"
#14
#12
#15
T
#13
(#10)
#7
#8
#11
#9
#4
#6
#5
#1
#3
#2
J1
J2
J3
J4
J5
J6
J7
J8
Horizontal on PCC
Vertical on PCC
Horizontal on AC
Vertical on AC

Figure M.11. JDMD monitoring layout for Batch 7, coded LB_W_HV_OL, monitored the movements of joints on Lane B after HMA placement, with Slab C32 as a reference.

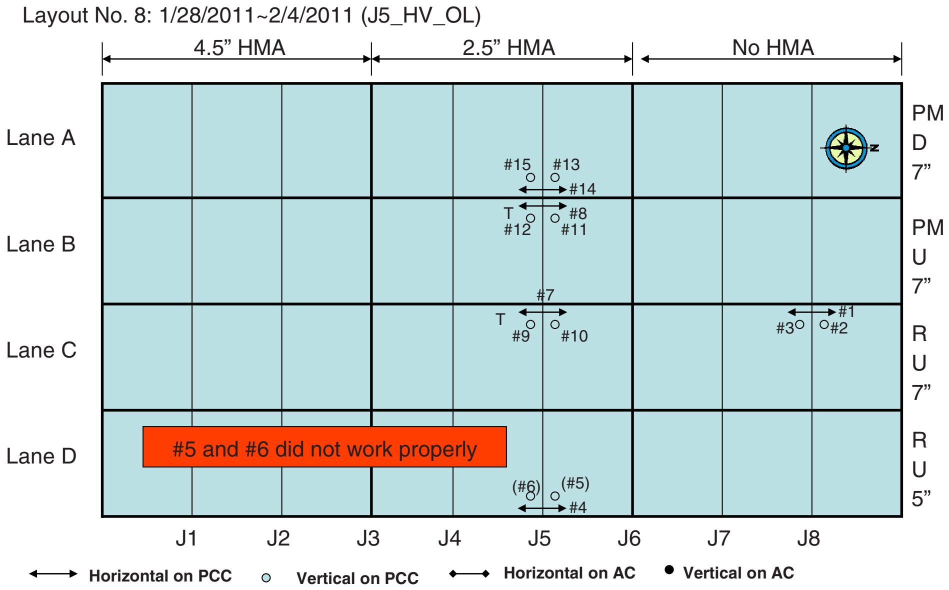
Layout No. 8: 1/28/2011~2/4/2011 (J5_HV_OL)

4.5" HMA
2.5" HMA
No HMA
Lane A
Lane B
Lane C
Lane D
PM D 7"
PM U 7"
R U 7"
R U 5"
#15
#13
#14
T
#8
#12
#11
#7
#9
#10
#1
#3
#2
#5 and #6 did not work properly
(#6)
(#5)
#4
J1
J2
J3
J4
J5
J6
J7
J8
Horizontal on PCC
Vertical on PCC
Horizontal on AC
Vertical on AC

Figure M.12. JDMD monitoring layout for Batch 8, coded J5_HV_OL, monitored the movements of joints along J5 after HMA placement, with Slab C32 as a reference.

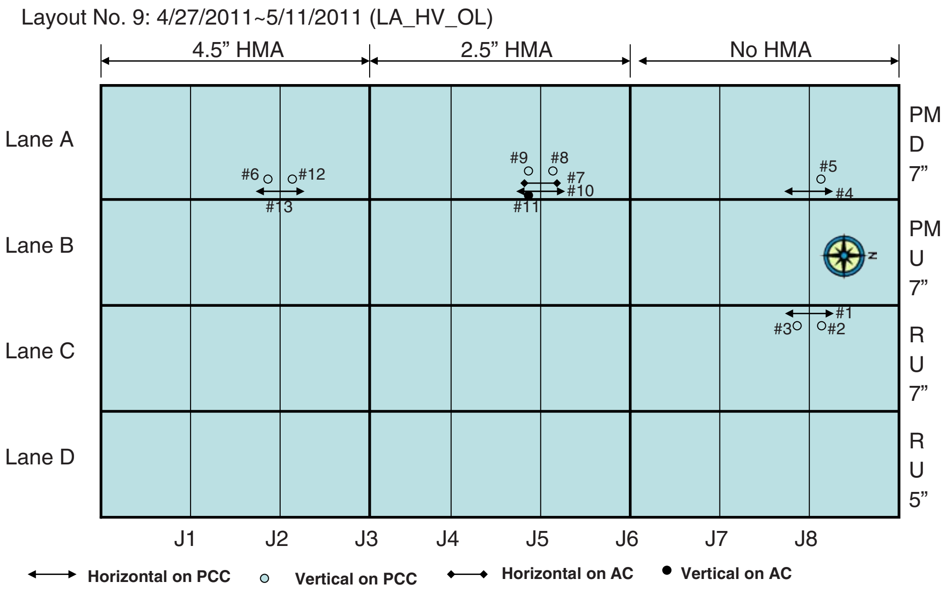
Layout No. 9: 4/27/2011~5/11/2011 (LA_HV_OL)
4.5" HMA
2.5" HMA
No HMA
Lane A
Lane B
Lane C
Lane D
#6
#12
#13
#9
#8
#7
#10
#11
#5
#4
#1
#3
#2
PM D 7"
PM U 7"
R U 7"
R U 5"
J1
J2
J3
J4
J5
J6
J7
J8
Horizontal on PCC
Vertical on PCC
Horizontal on AC
Vertical on AC

Figure M.13. JDMD monitoring layout for Batch 9, coded LA_HV_OL, monitored the movements of joints on Lane A after HMA placement, with Slab C32 as a reference.

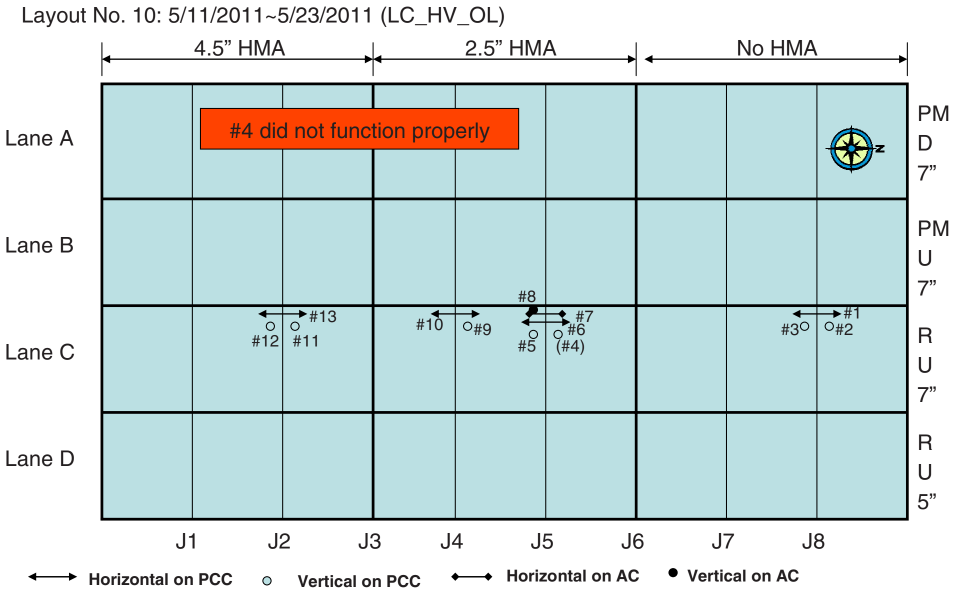
Layout No. 10: 5/11/2011~5/23/2011 (LC_HV_OL)
4.5" HMA
2.5" HMA
No HMA
#4 did not function properly
Lane A
Lane B
Lane C
Lane D
#13
#12
#11
#10
#9
#8
#7
#6
#5
(#4)
#1
#3
#2
PM D 7"
PM U 7"
R U 7"
R U 5"
J1
J2
J3
J4
J5
J6
J7
J8
Horizontal on PCC
Vertical on PCC
Horizontal on AC
Vertical on AC

Figure M.14. JDMD monitoring layout for Batch 10, coded LC_HV_OL, monitored the movements of joints on west edge of Lane C after HMA placement, with Slab C32 as a reference.

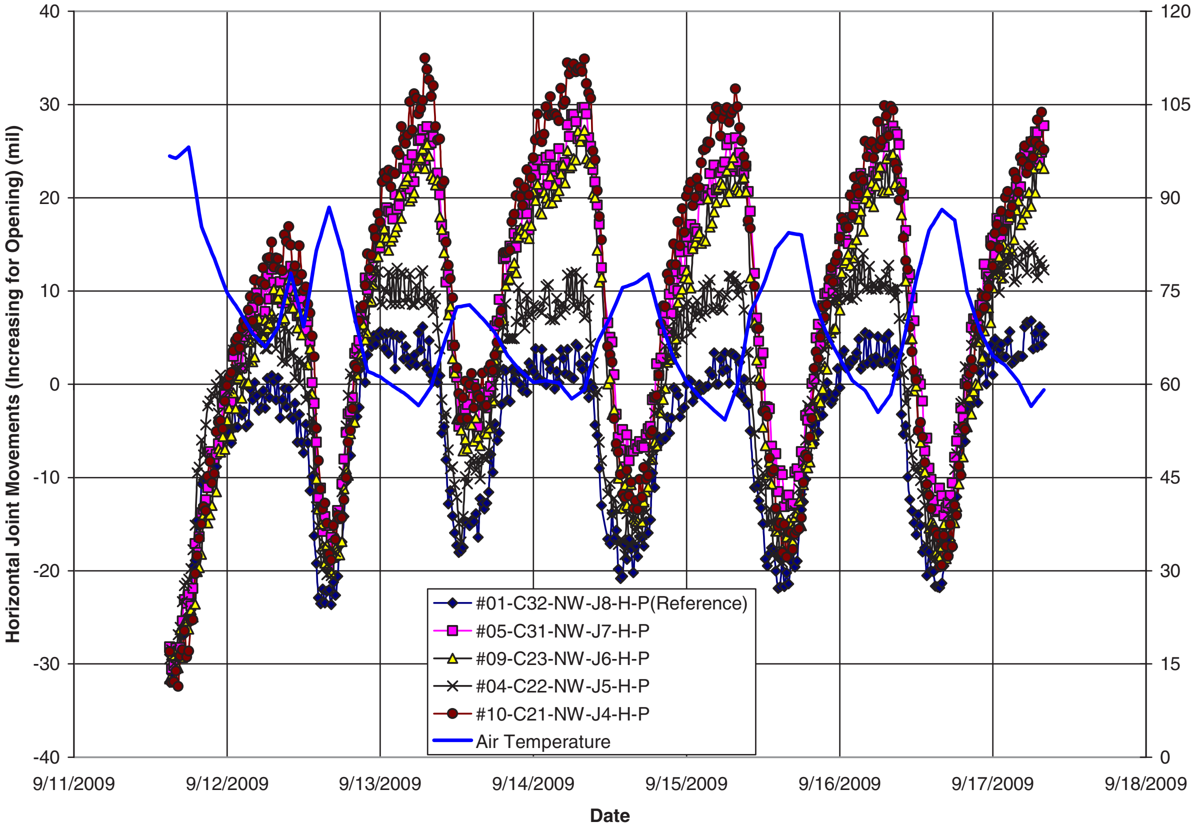

Figure M.15. Batch 1: Horizontal joint movements along Lane C (nondoweled) before HMA placement. See Figure M.5 for JDMD layout.

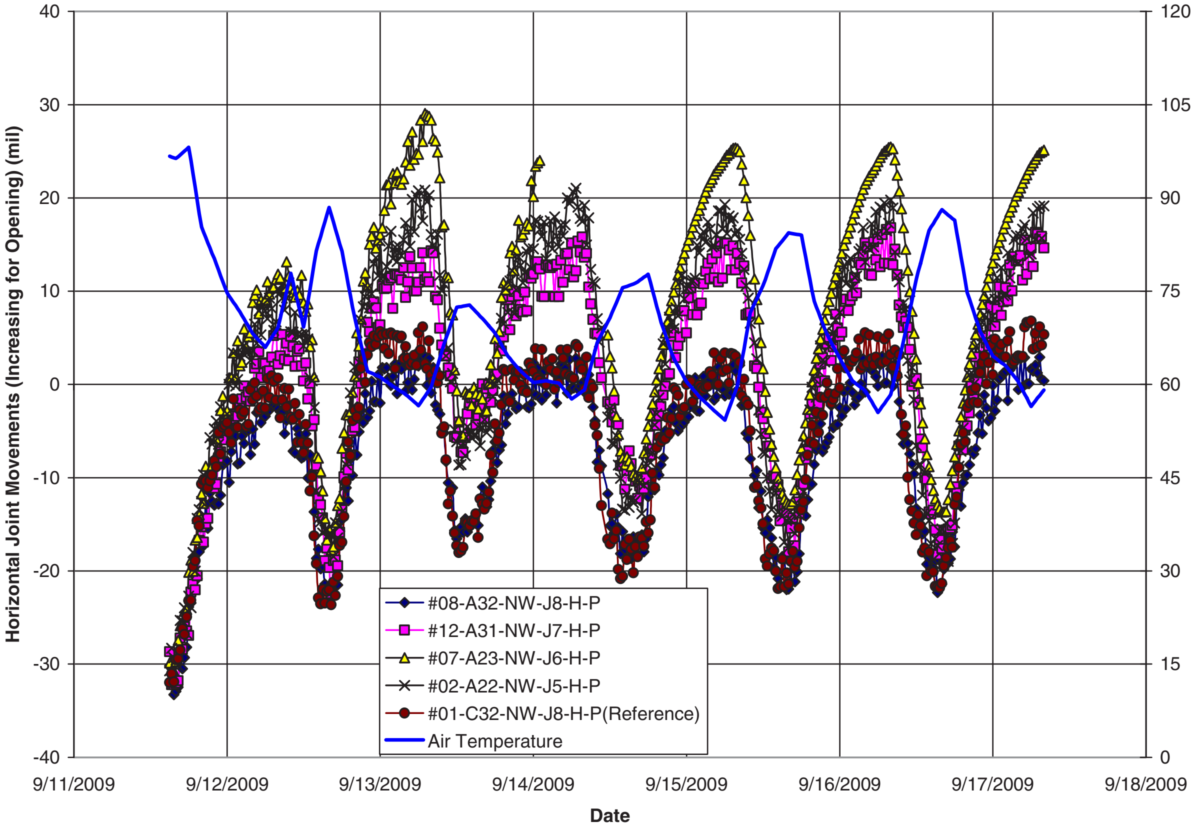

Figure M.16. Batch 1: Horizontal joint movements along Lane A (doweled) before HMA placement. See Figure M.5 for JDMD layout; JDMD #7 was first measured by Daytronic LVDT and later by Macro Sensor LVDT.

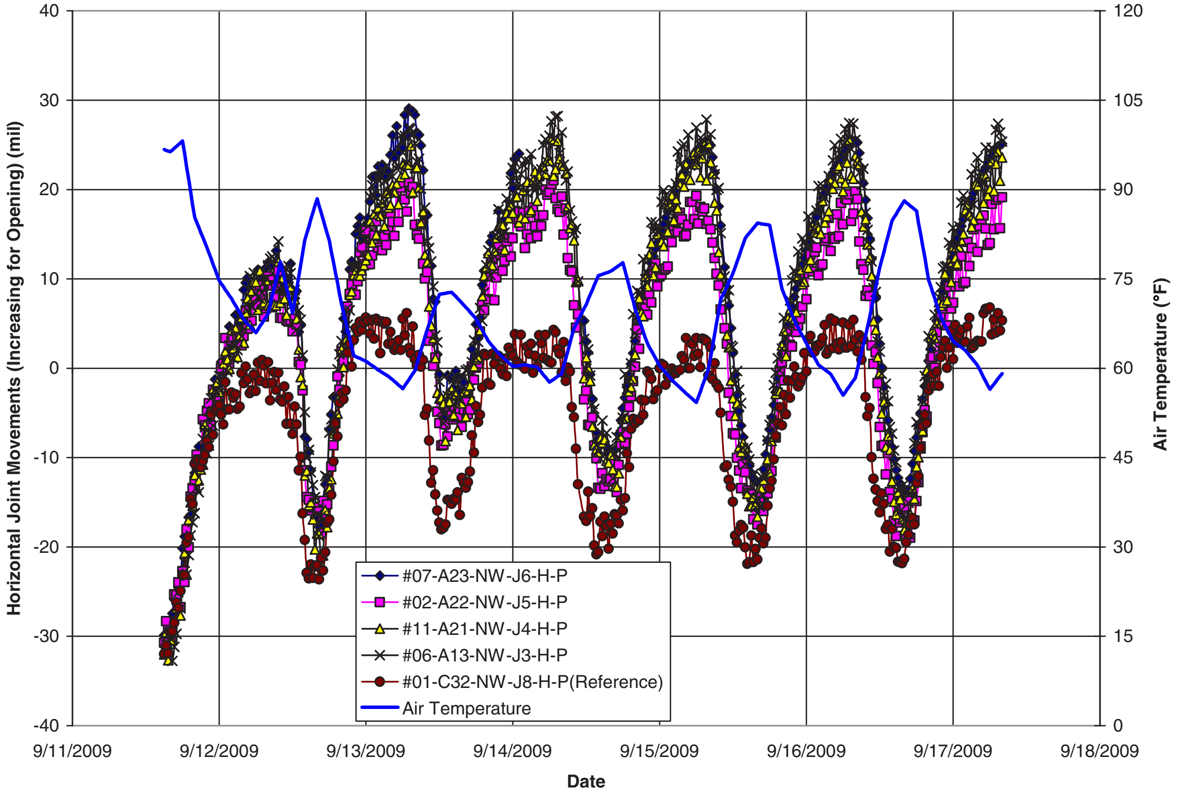

Figure M.17. Batch 1: Additional horizontal joint movements along Lane A (doweled) before placement. See Figure M.5 for JDMD layout.

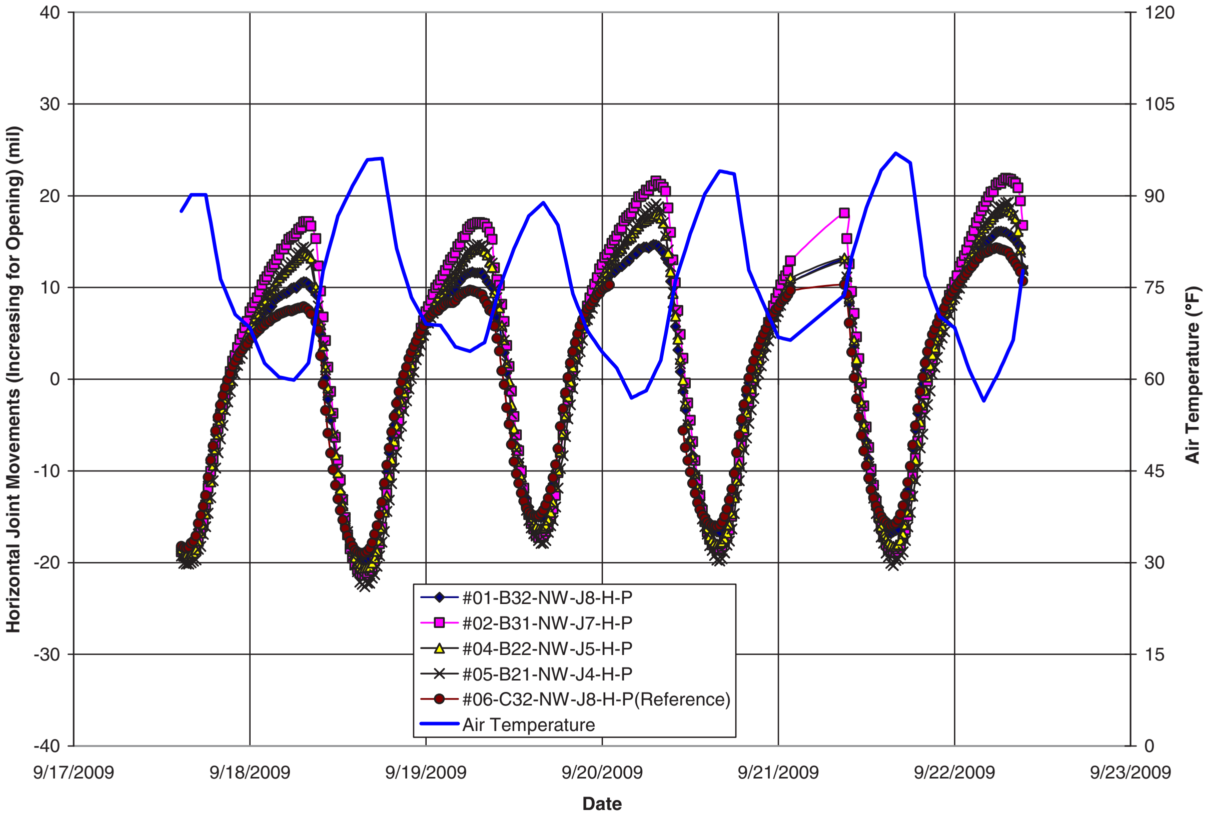

Figure M.18. Batch 2: Horizontal joint movements along Lane B before HMA placement. See Figure M.6 for JDMD layout.

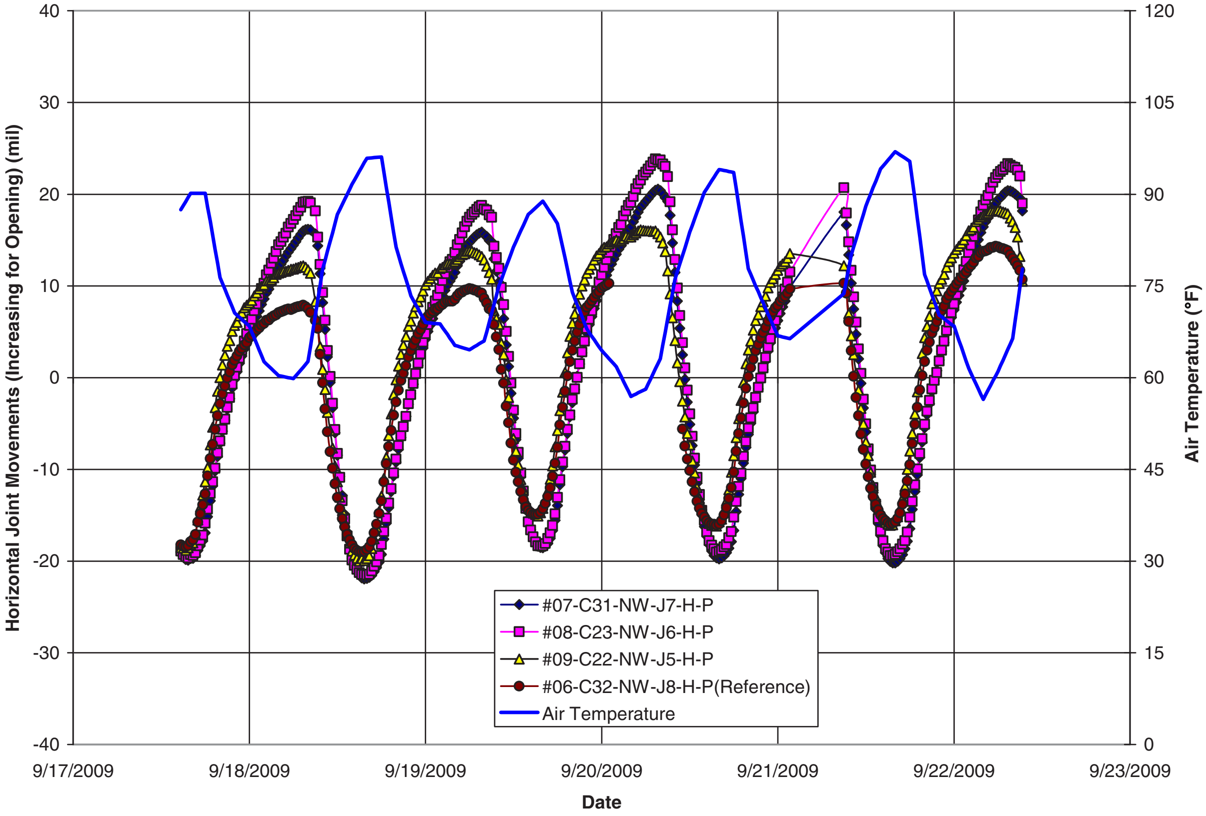

Figure M.19. Batch 2: Horizontal joint movements along Lane C before HMA placement. See Figure M.6 for JDMD layout.

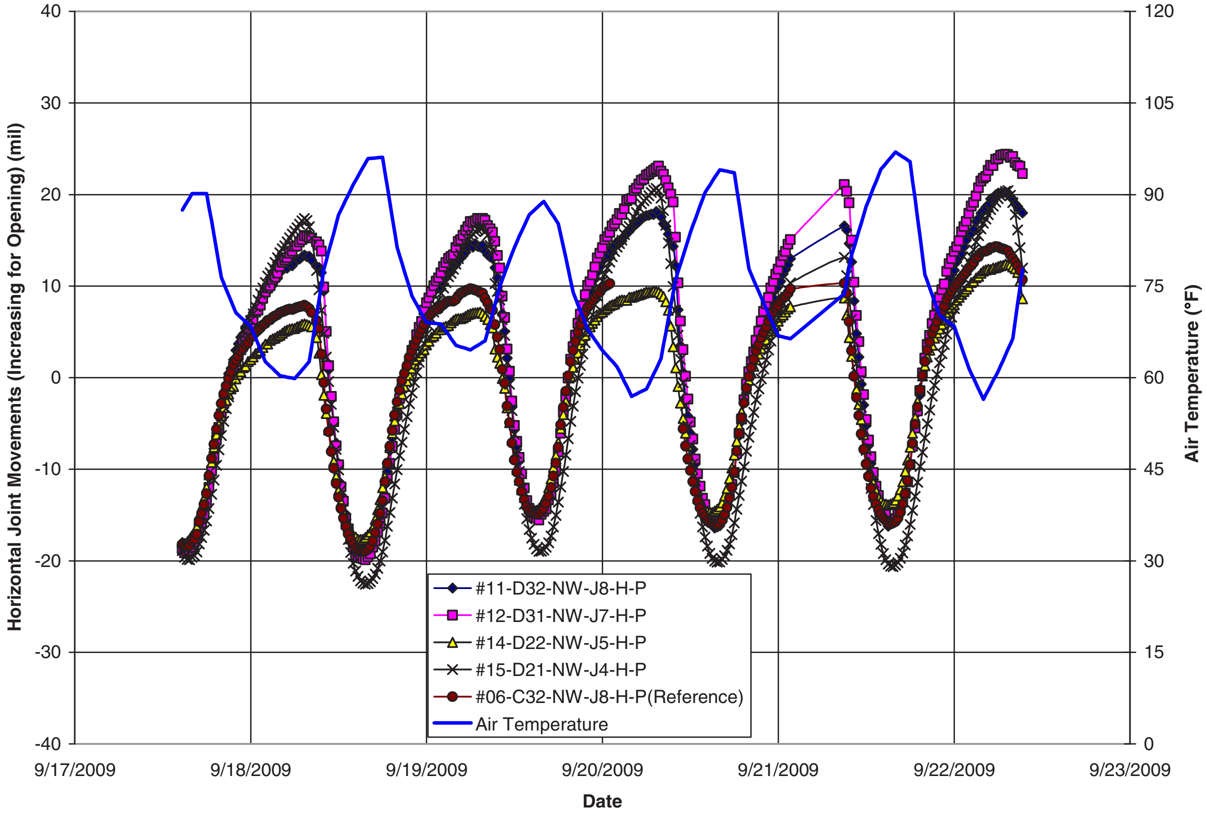

Figure M.20. Batch 2: Horizontal joint movements along Lane D before HMA placement. See Figure M.6 for JDMD layout.

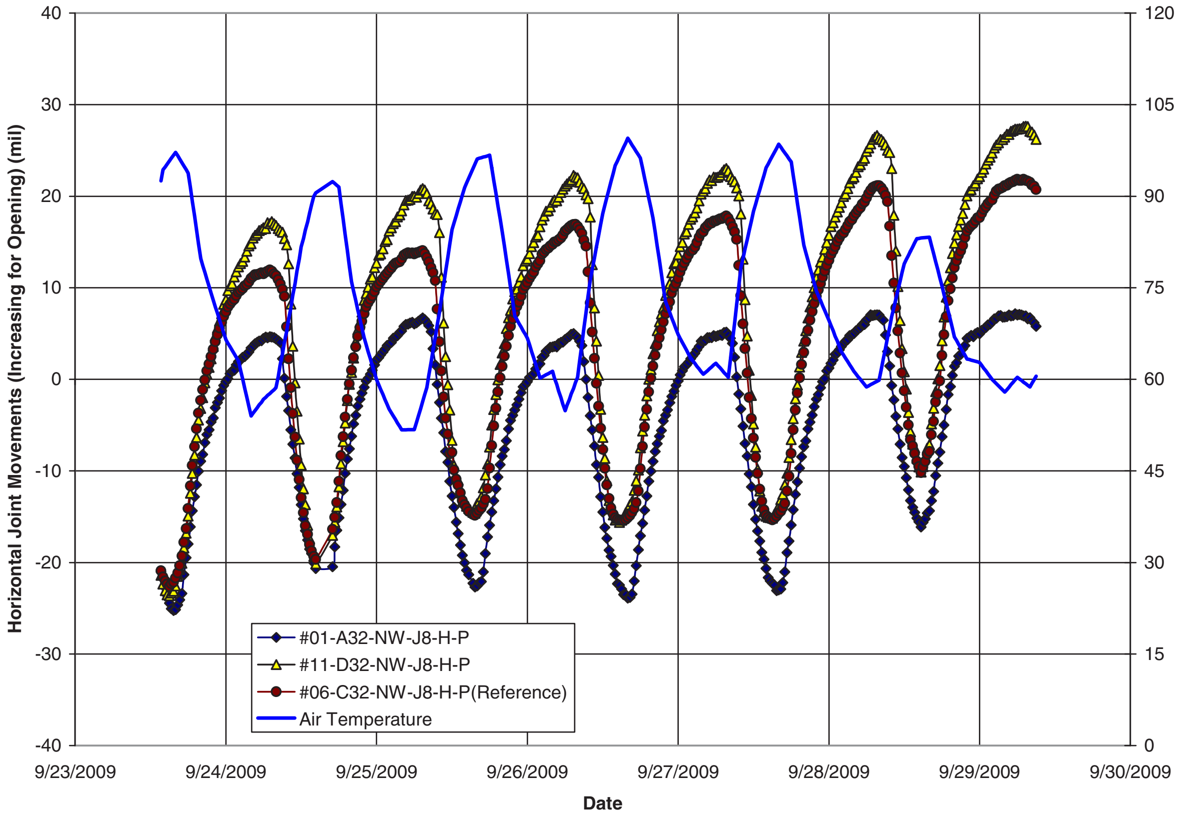

Figure M.21. Batch 3: Horizontal joint movements along Joint J8 before HMA placement. See Figure M.7 for JDMD layout.

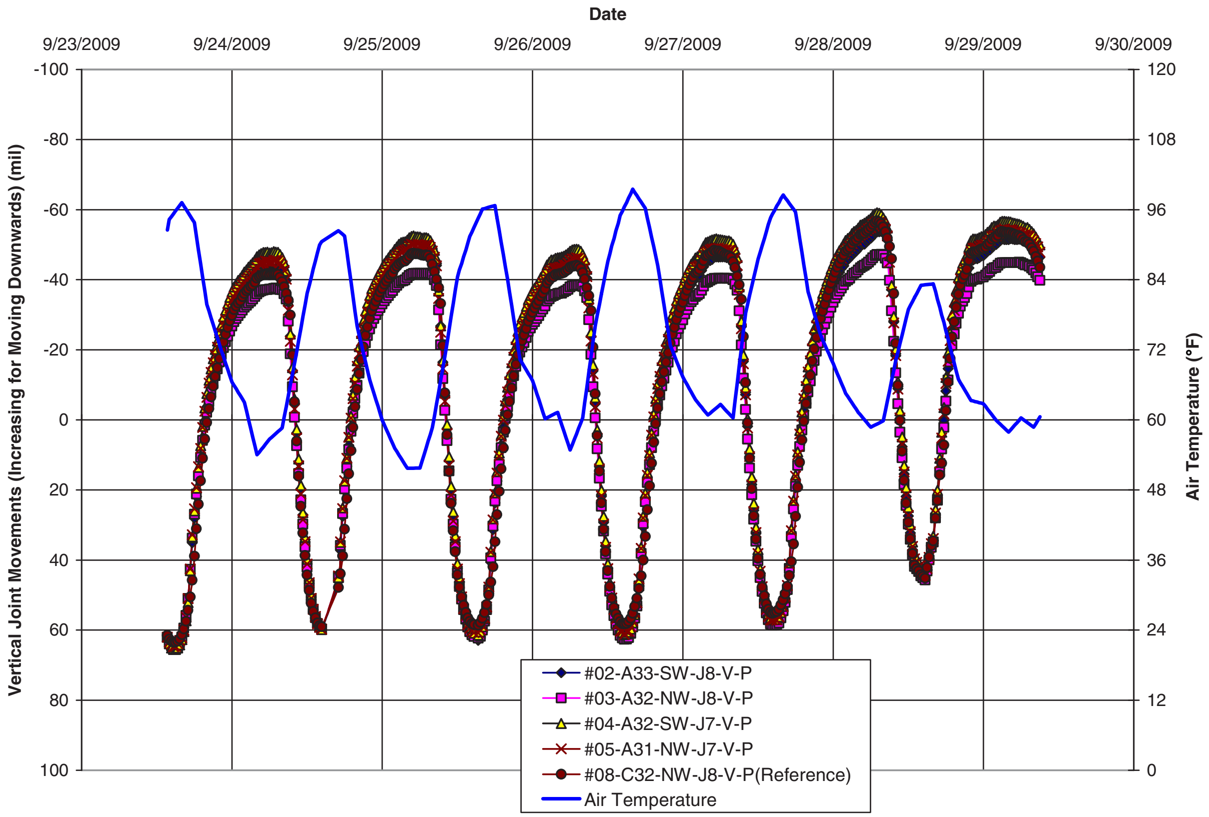

Figure M.22. Batch 3: Vertical joint movements along Lane A before HMA placement. See Figure M.7 for JDMD layout.

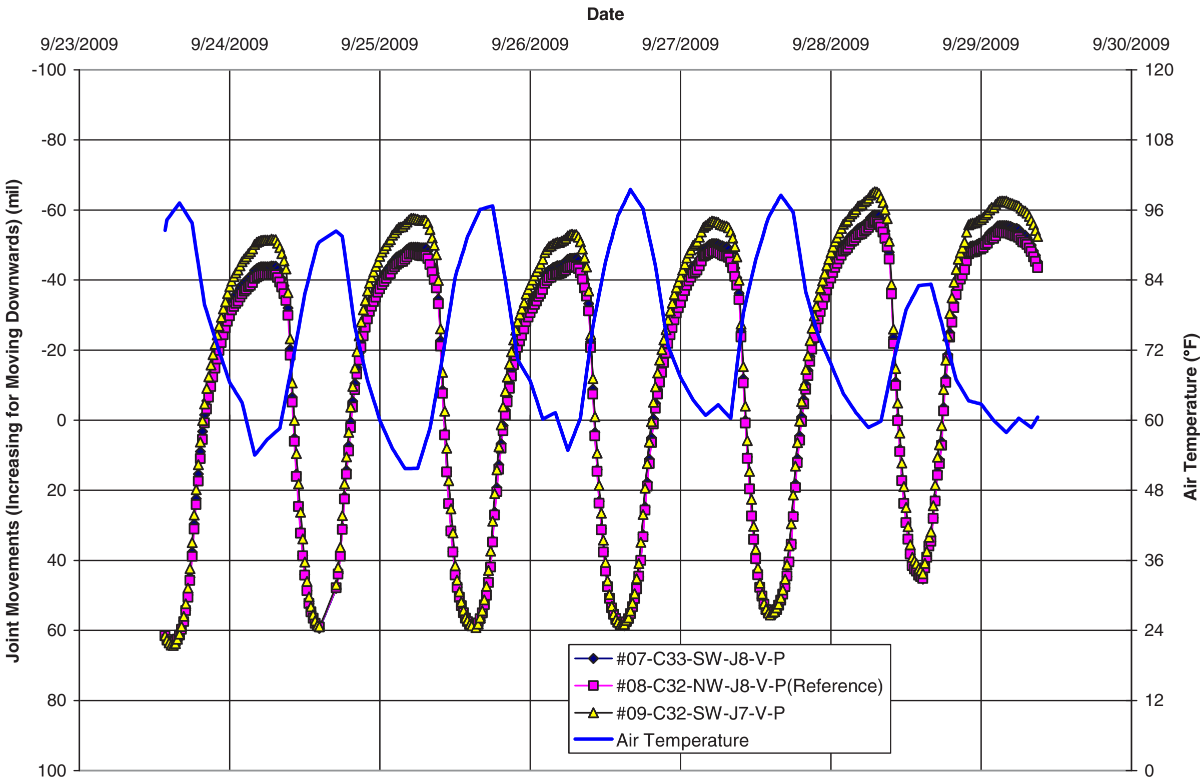

Figure M.23. Batch 3: Horizontal joint movements along Lane C before HMA placement. See Figure M.7 for JDMD layout.

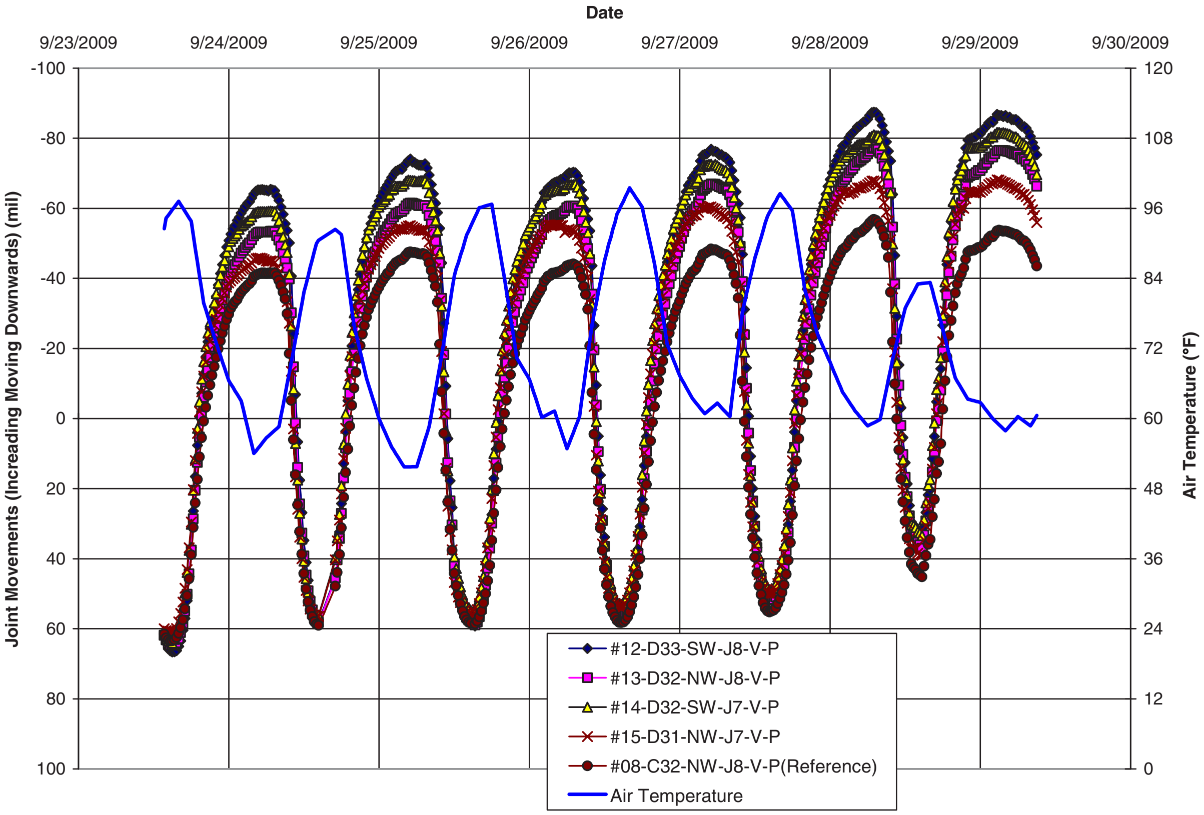

Figure M.24. Batch 3: Vertical joint movements along Lane D before HMA placement. See Figure M.7 for JDMD layout.

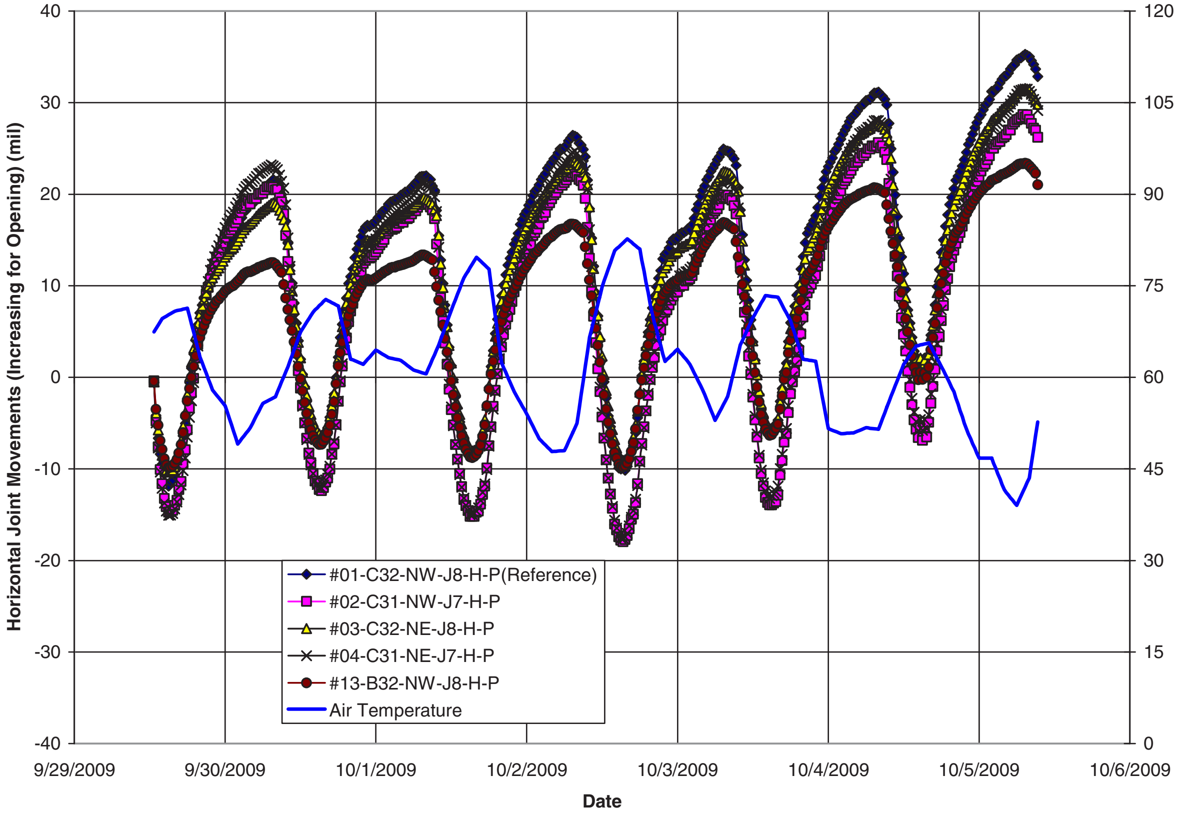

Figure M.25. Batch 4: Horizontal joint movements along Lane C before HMA placement. See Figure M.8 for JDMD layout.

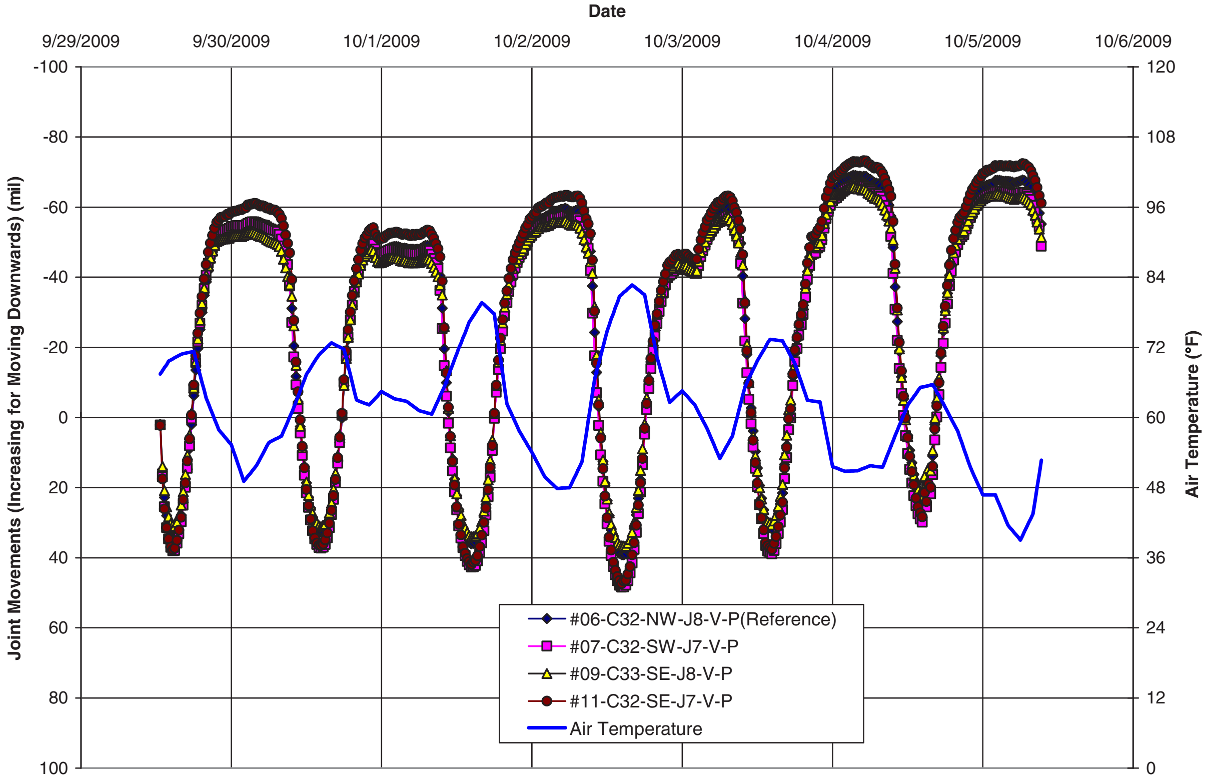

Figure M.26. Batch 4: Vertical joint movements at four corners of Slab C32 before HMA placement. See Figure M.8 for JDMD layout. JDMD #10 did not function properly, so neighboring JDMD #9 is shown instead.

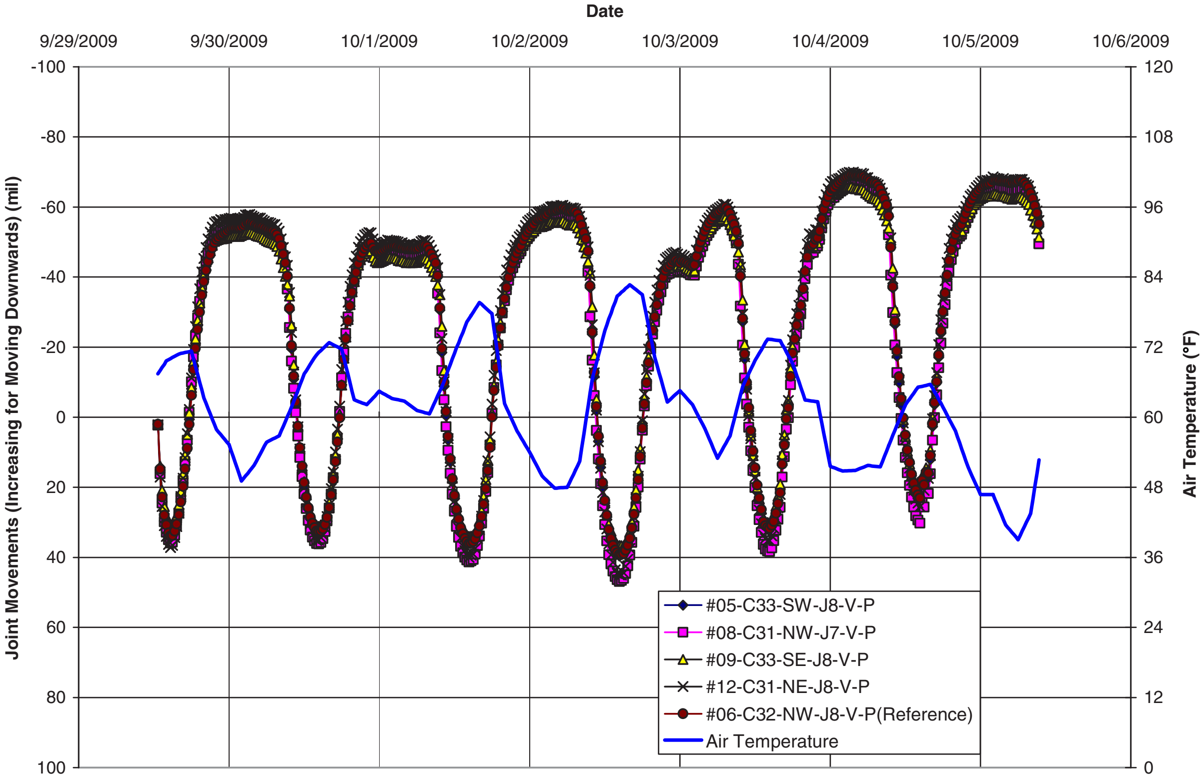

Figure M.27. **Batch 4: Additional vertical joint movements next to Slab C32 on Lane C before HMA placement. See Figure M.8 for JDMD layout.**

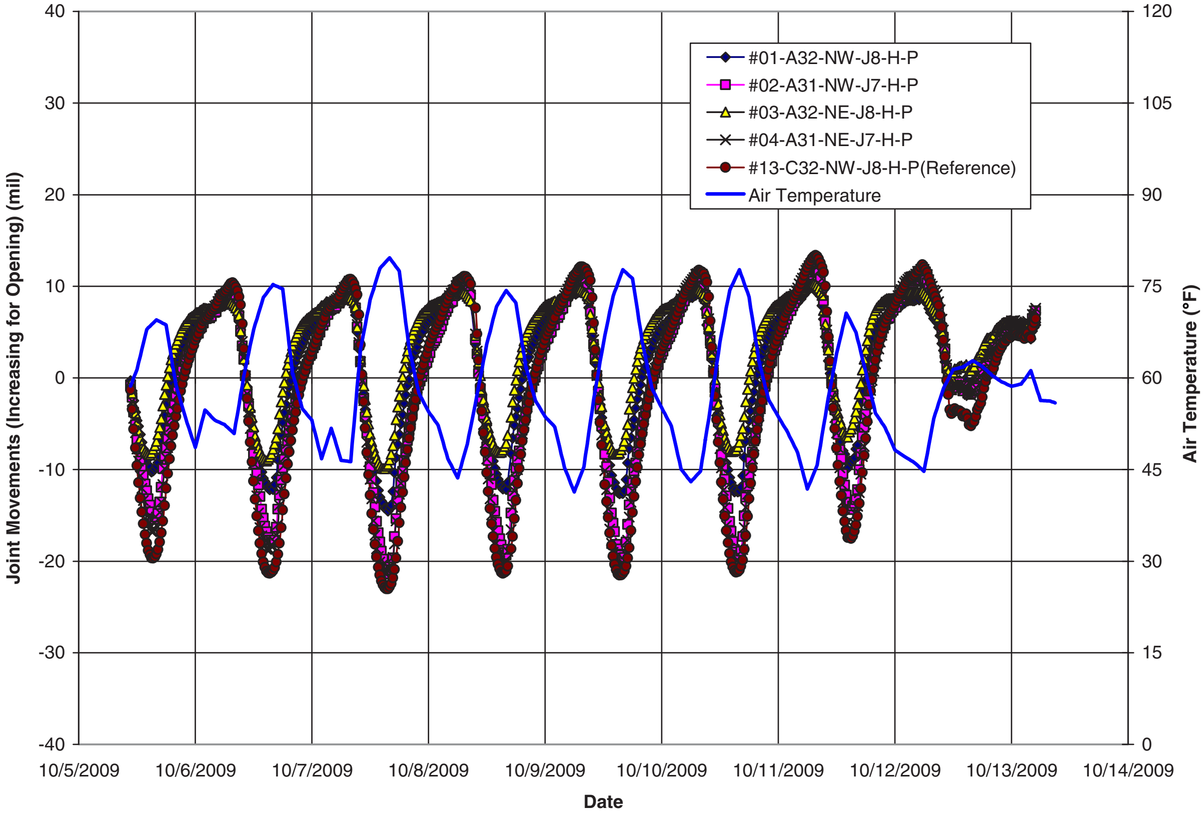

Figure M.28. **Batch 5: Horizontal joint movements along Lane A (doweled) before HMA placement. See Figure M.9 for JDMD layout.**

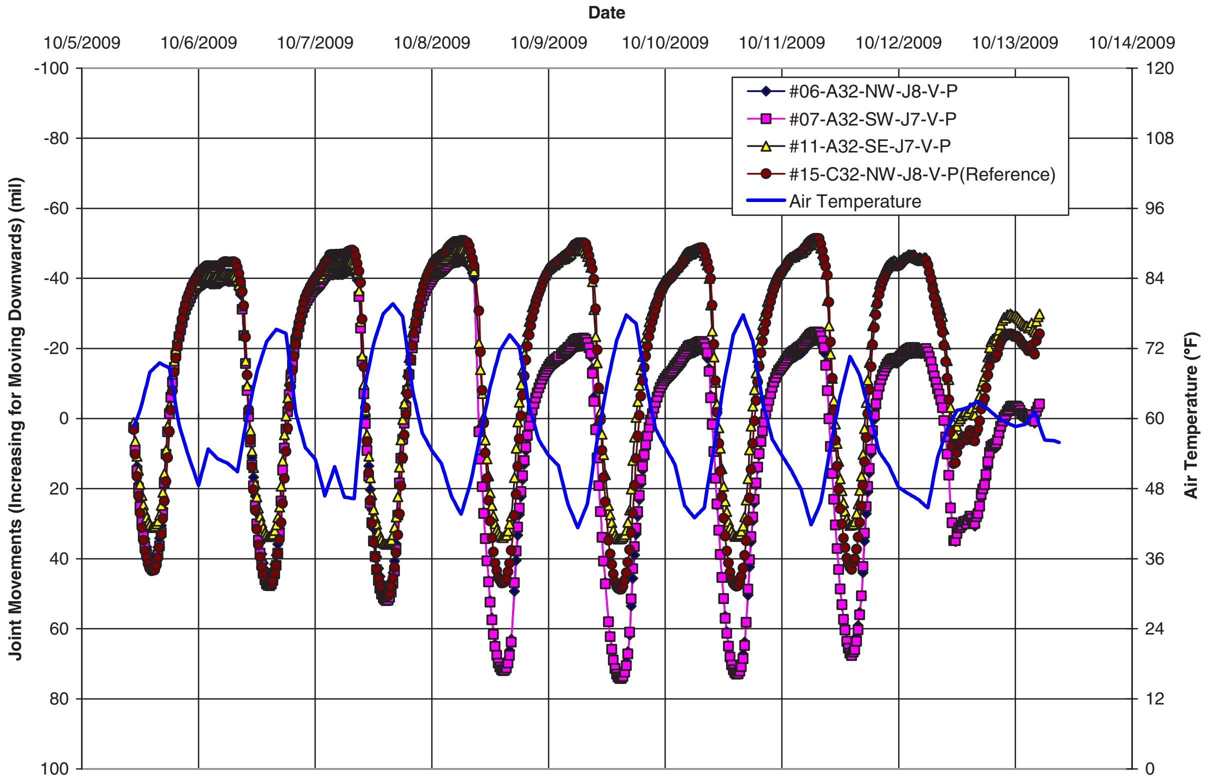

Figure M.29. Batch 5: Vertical joint movements at corners of Slab A32 (doweled) before HMA placement. See Figure M.9 for JDMD layout; JDMD #10 did not function properly.

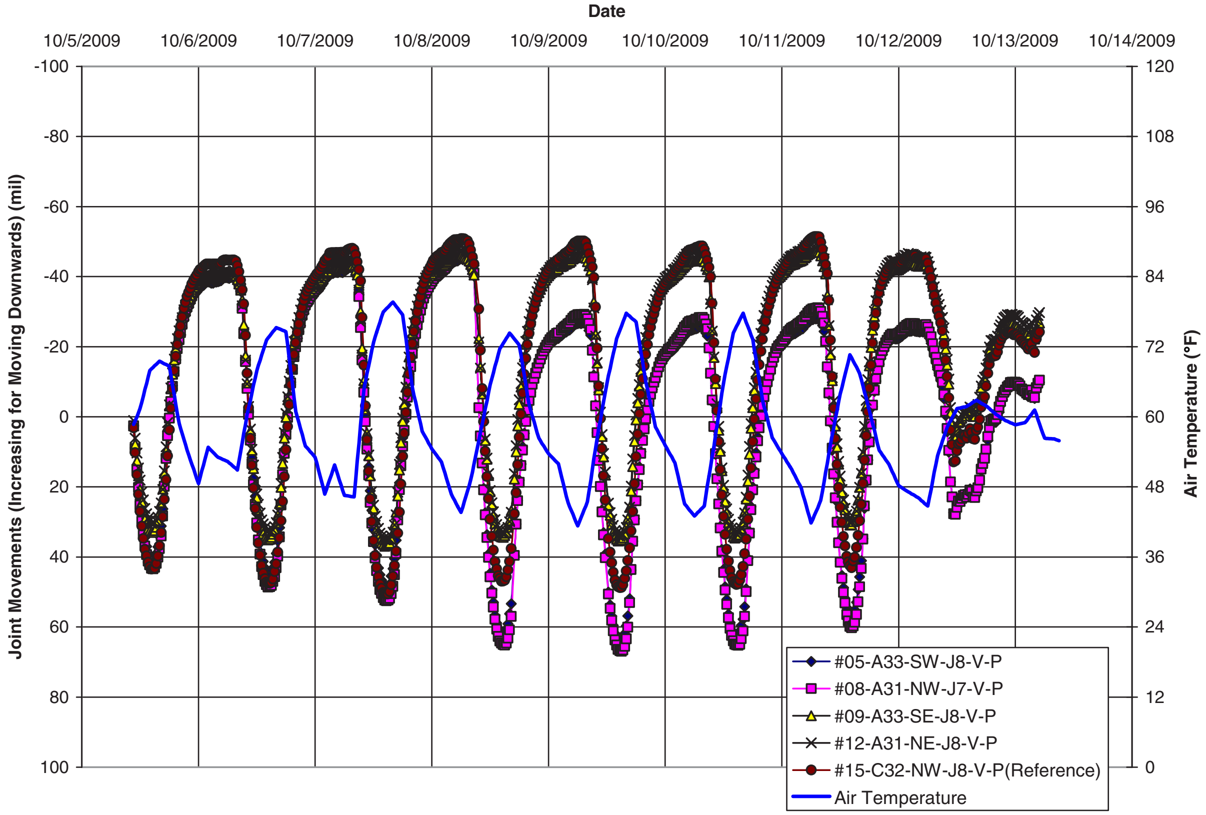

Figure M.30. Batch 5: Vertical joint movements at corners adjacent to Slab A32 (doweled) along Lane A before HMA placement. See Figure M.9 for JDMD layout.

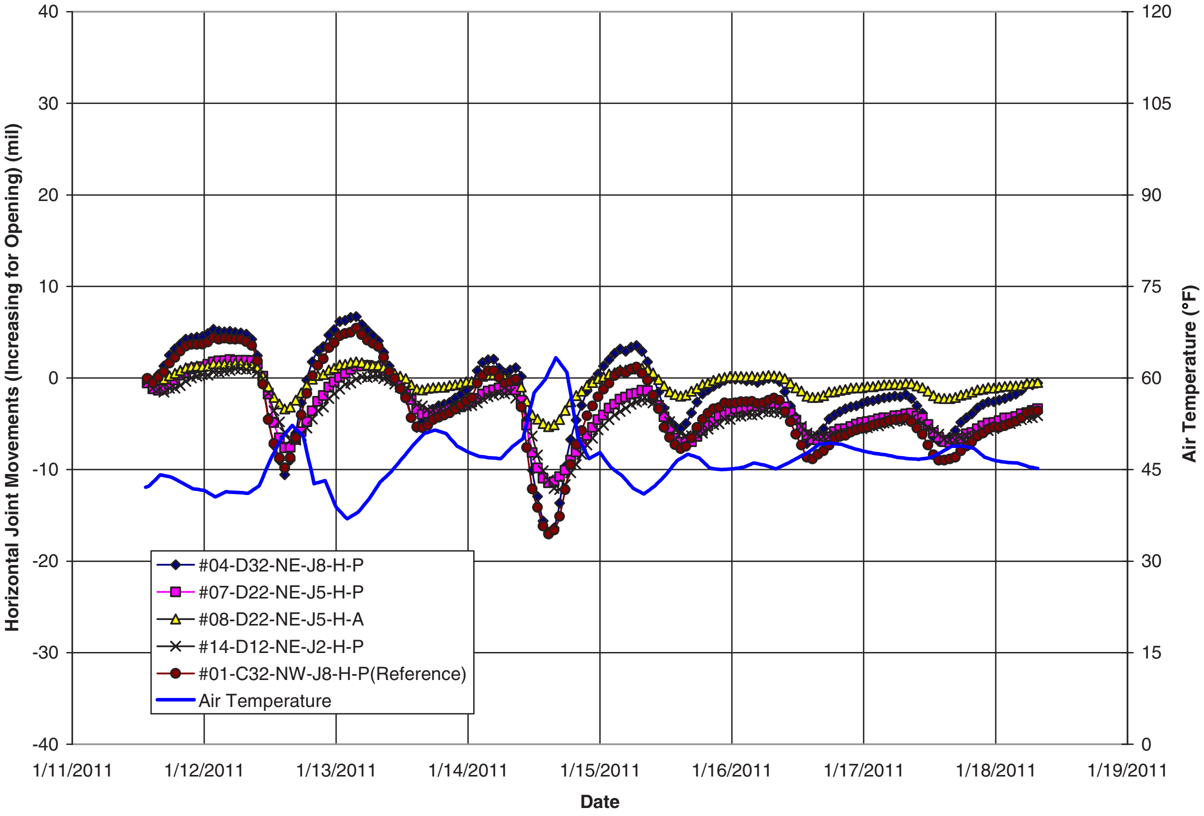

Figure M.31. Batch 6: Horizontal joint movements along Lanes C and D after HMA placement. See Figure M.10 for JDMD layout.

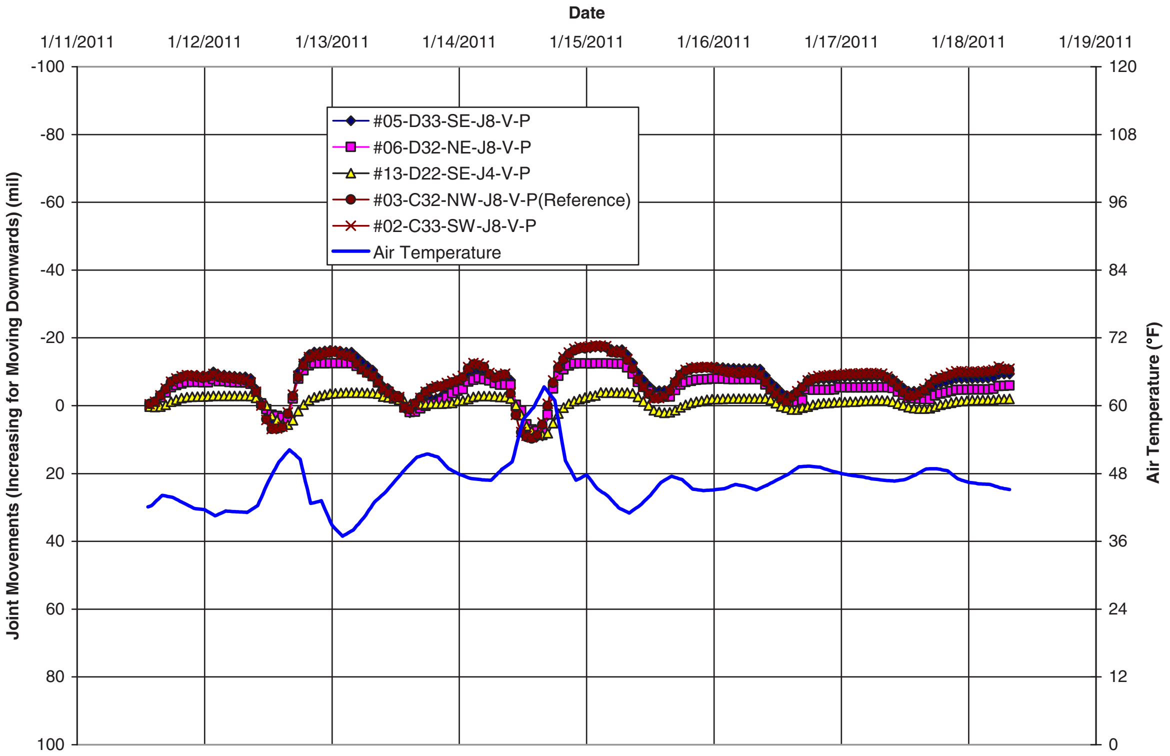

Figure M.32. Batch 6: Vertical joint movements along Lanes C and D after HMA placement. See Figure M.10 for JDMD layout.

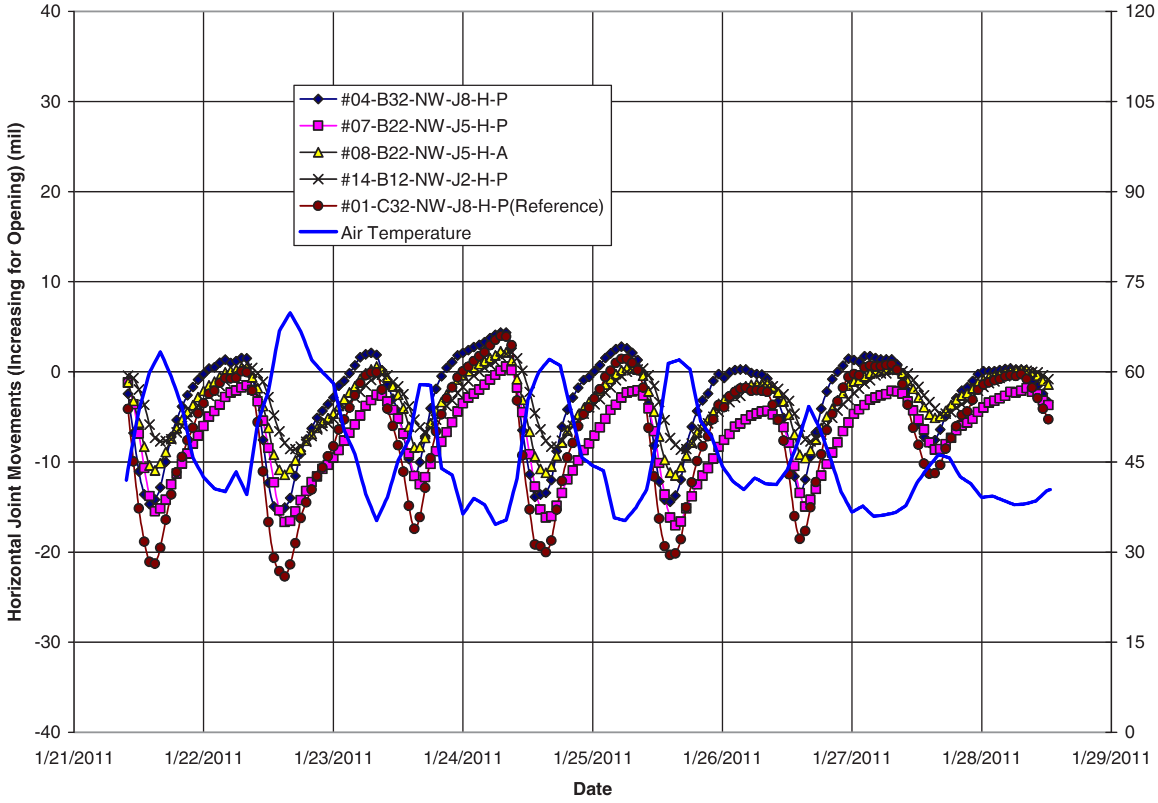

Figure M.33. Batch 7: Horizontal joint movements along Lane B after HMA placement. See Figure M.11 for JDMD layout.

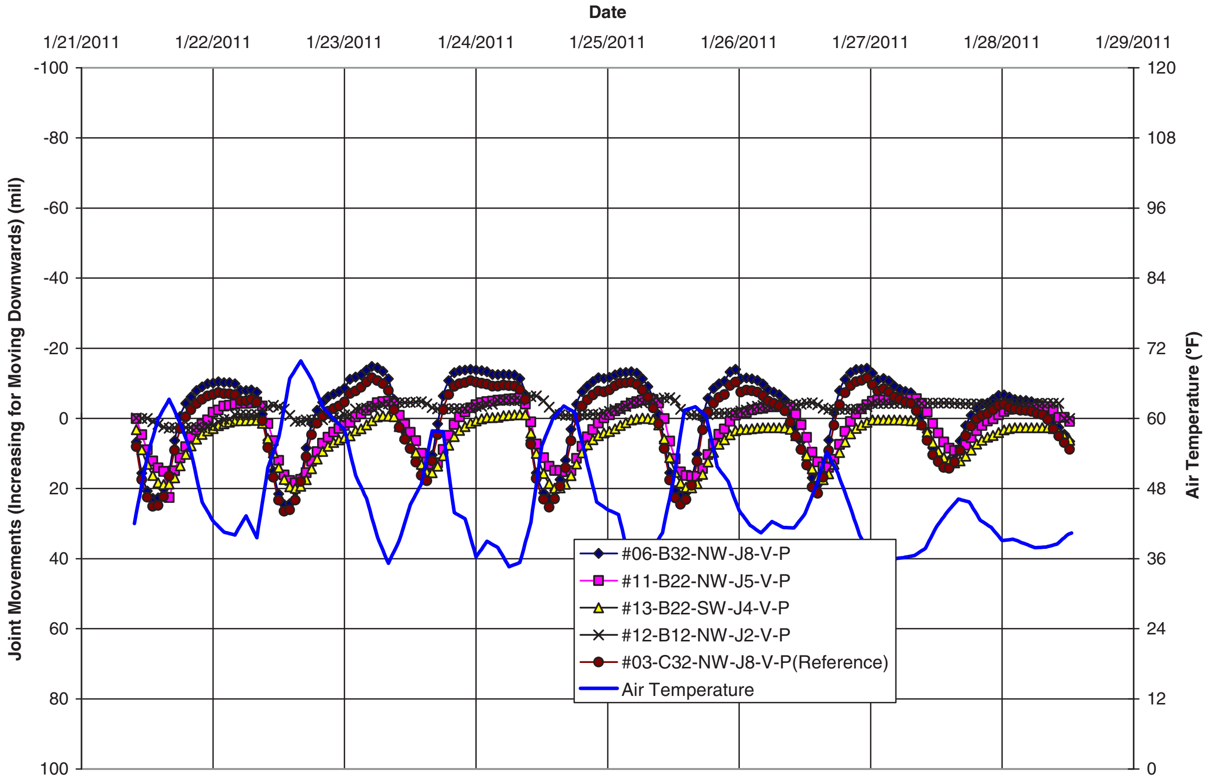

Figure M.34. Batch 7: Vertical joint movements along Lane B after HMA placement. See Figure M.11 for JDMD layout.

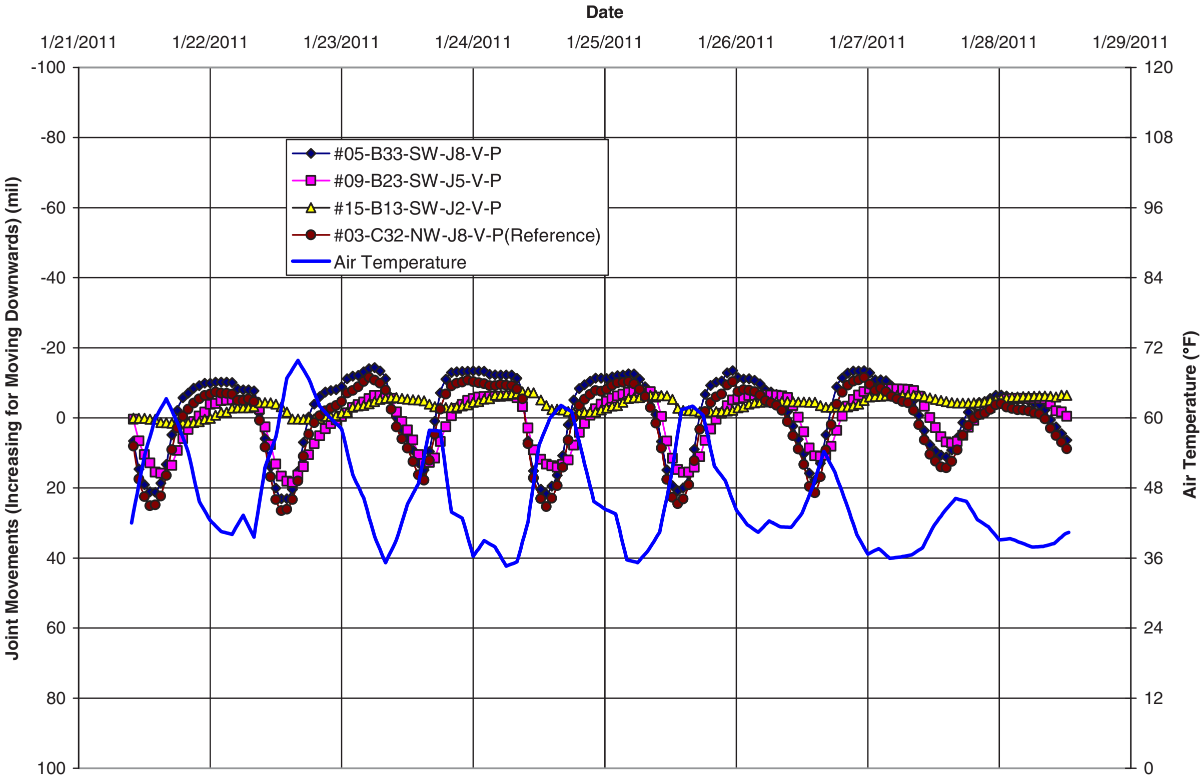

Figure M.35. Batch 7: Vertical joint movements along Lanes B and C after HMA placement. See Figure M.11 for JDMD layout.

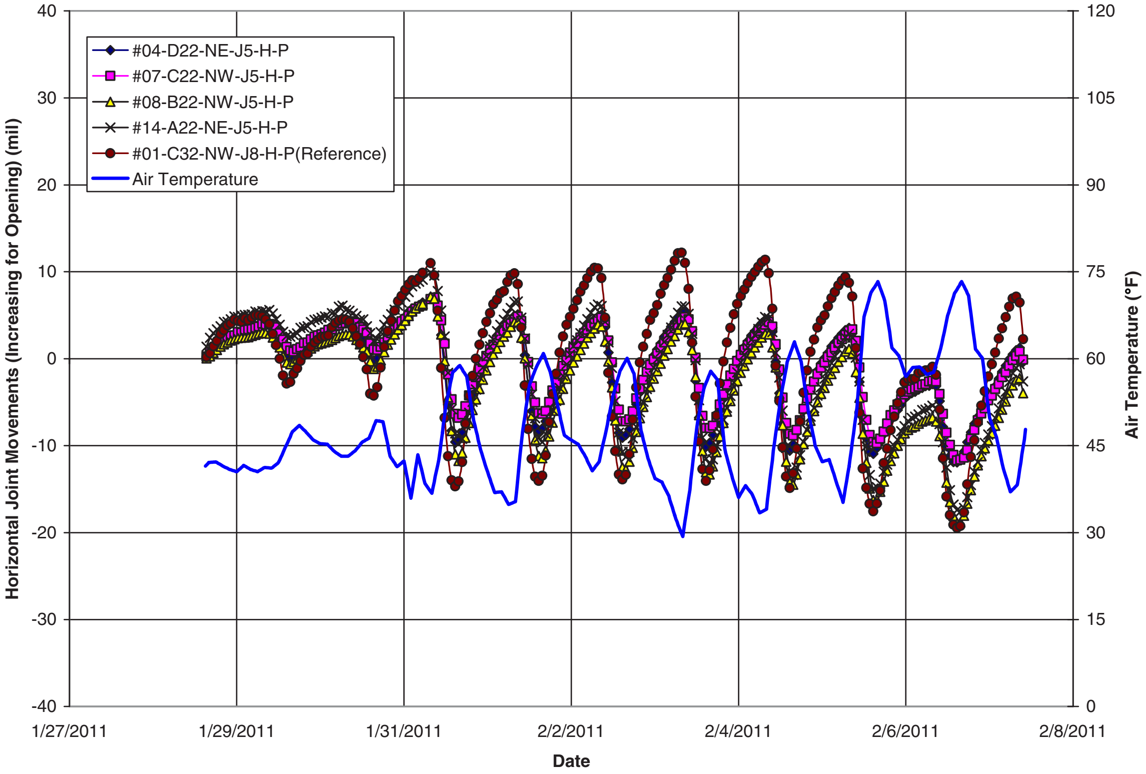

Figure M.36. Batch 8: Horizontal joint movements along Joint J5 after HMA placement. See Figure M.12 for JDMD layout.

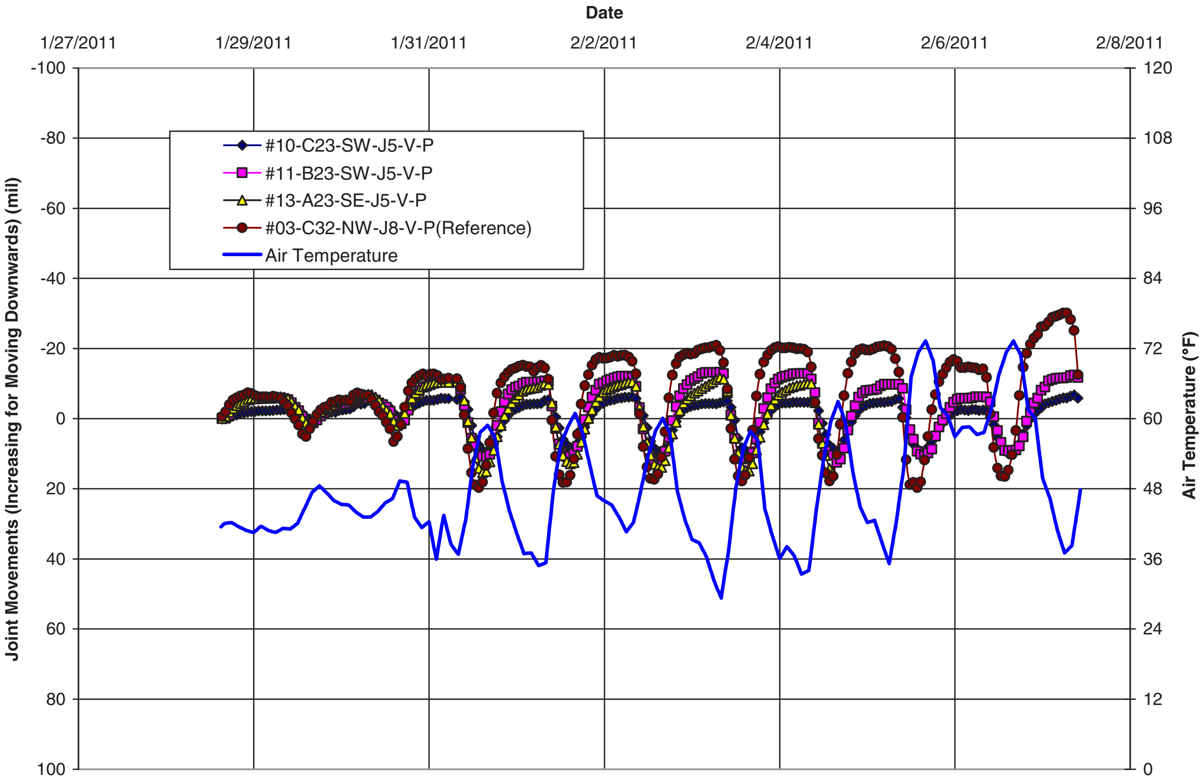

Figure M.37. Batch 8: Vertical joint movements along north side of Joint J5 after HMA placement. See Figure M.12 for JDMD layout.

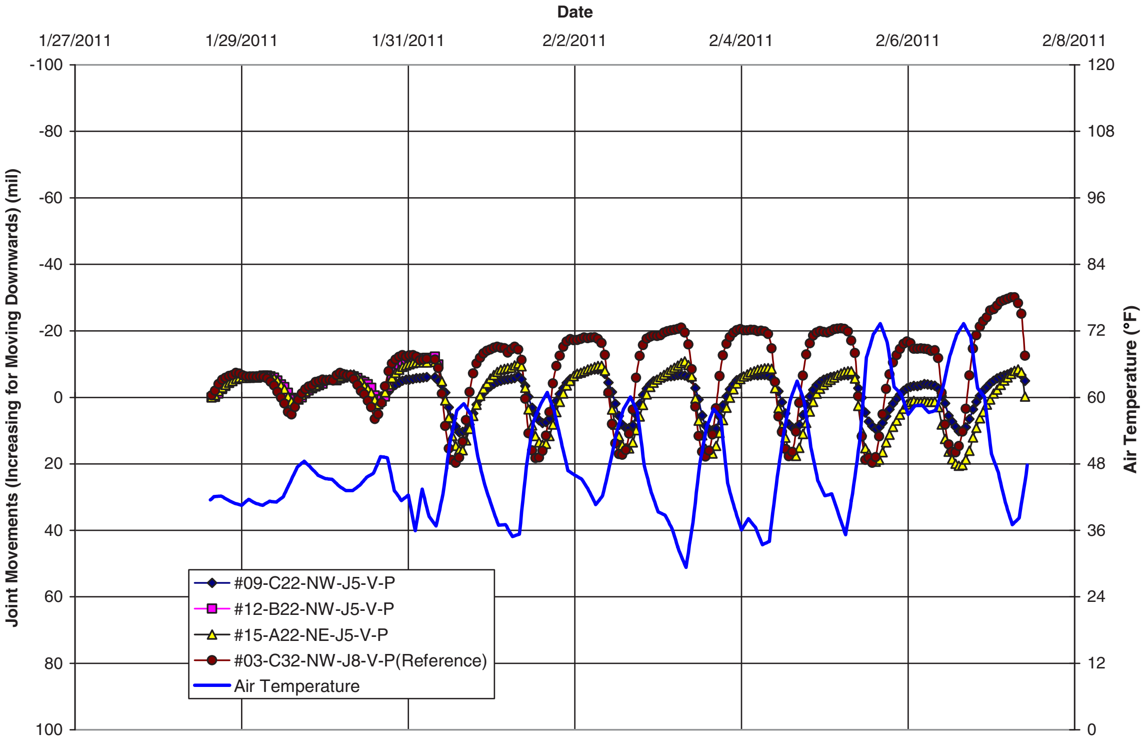

Figure M.38. Batch 8: Vertical joint movements along south side of Joint J5 after HMA placement. See Figure M.12 for JDMD layout.

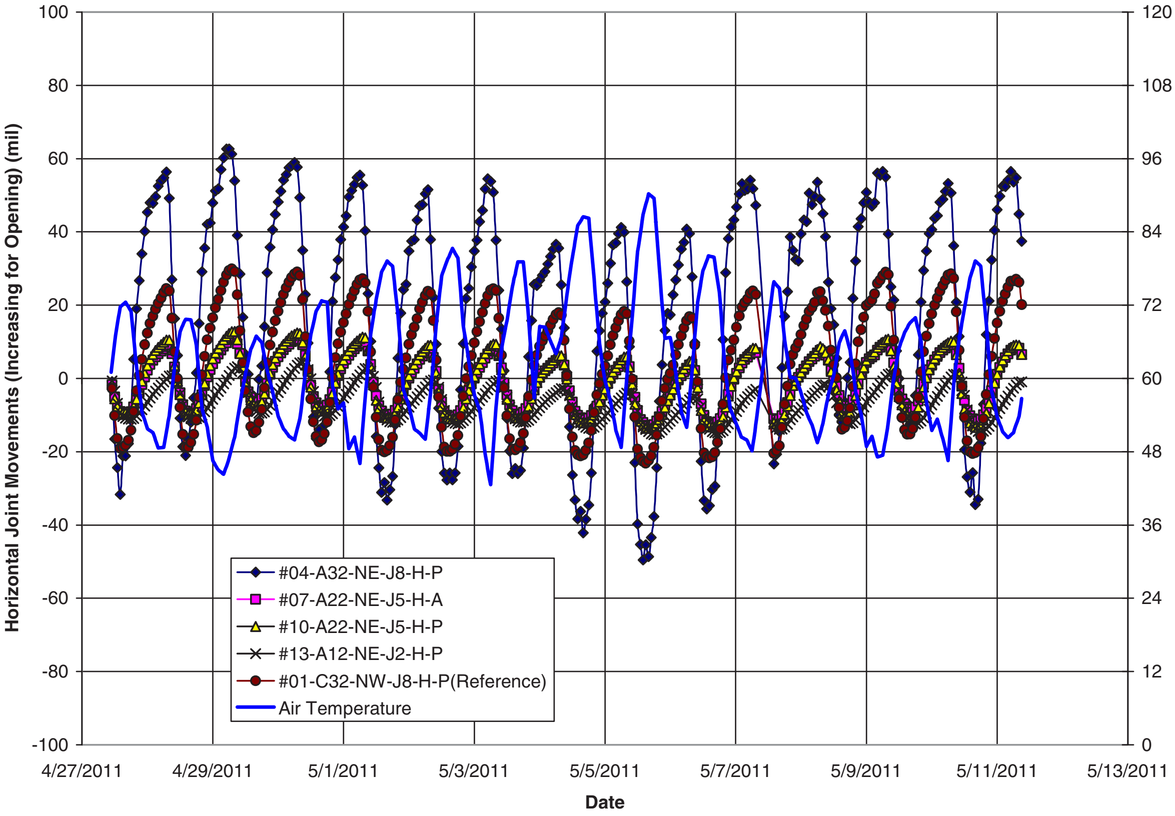

Figure M.39. Batch 9: Horizontal joint movements along Lane A after HMA placement. See Figure M.13 for JDMD layout.

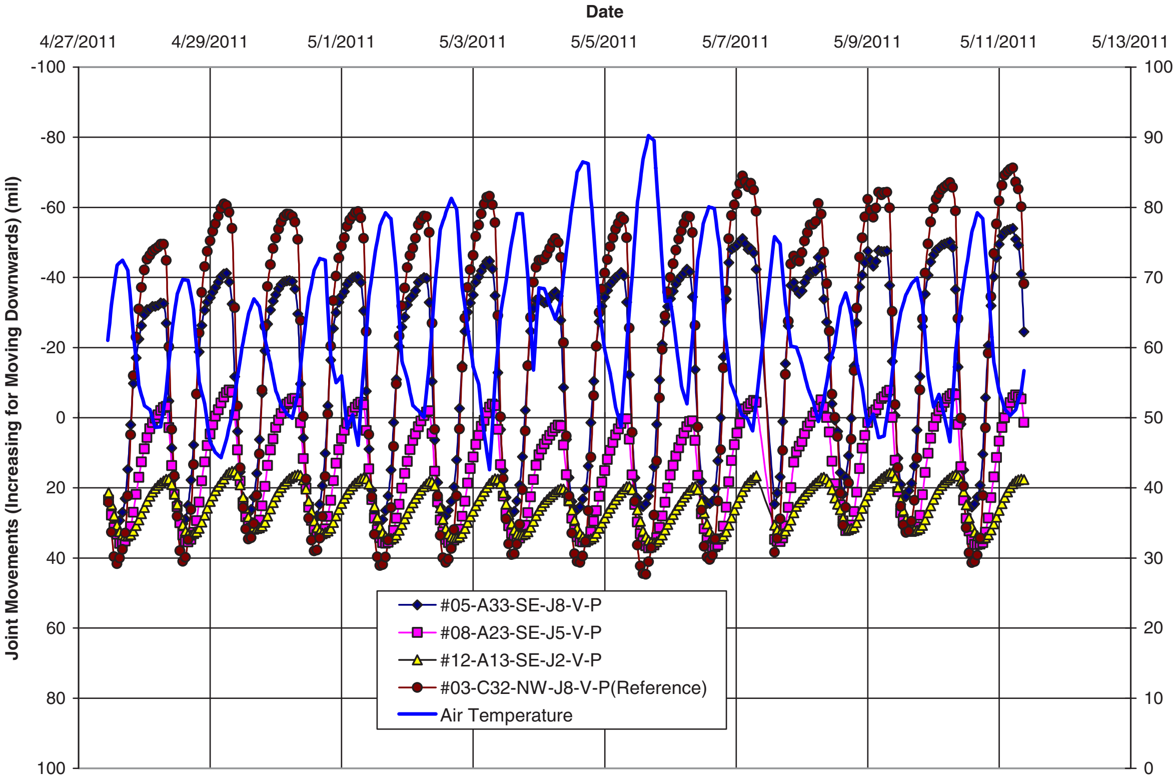

Figure M.40. Batch 9: Vertical joint movements along Lane A after HMA placement. See Figure M.13 for JDMD layout.

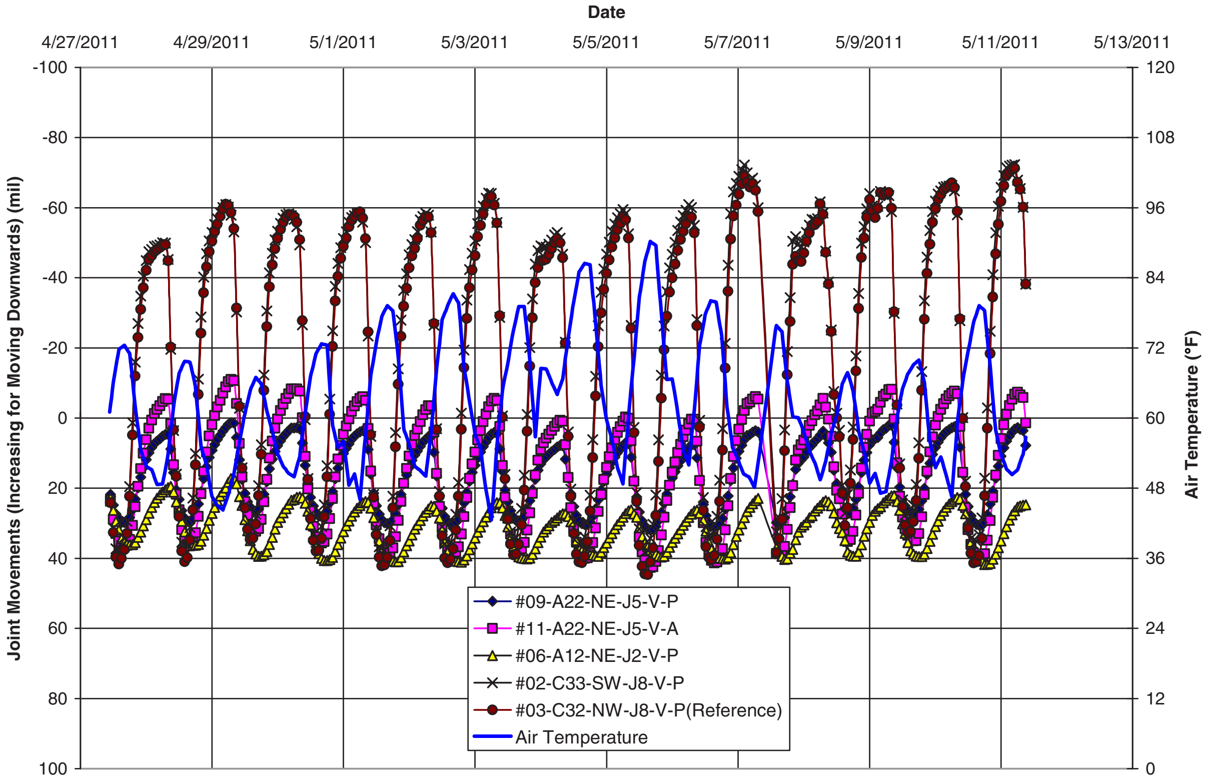

Figure M.41. Batch 9: Additional vertical joint movements along Lane A after HMA placement. See Figure M.13 for JDMD layout.

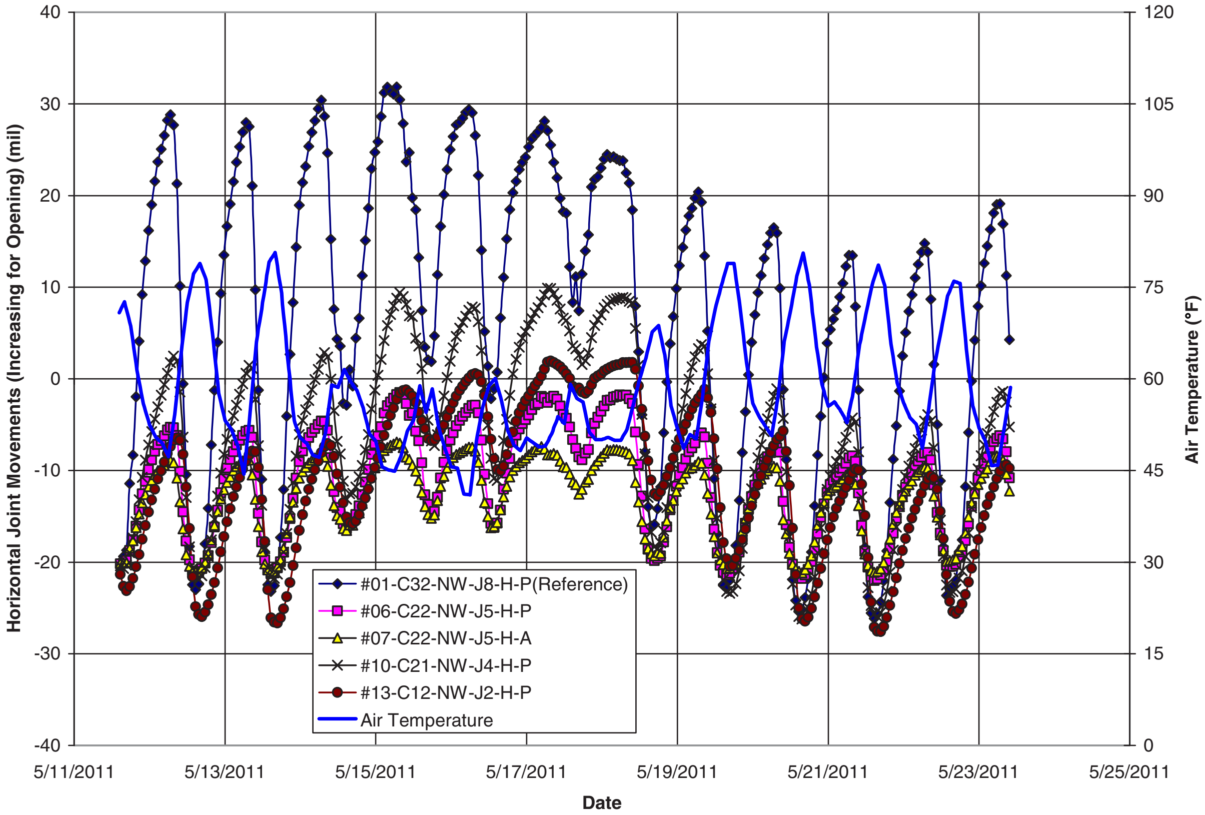

Figure M.42. Batch 10: Horizontal joint movements along Lane C after HMA placement. See Figure M.14 for JDMD layout.

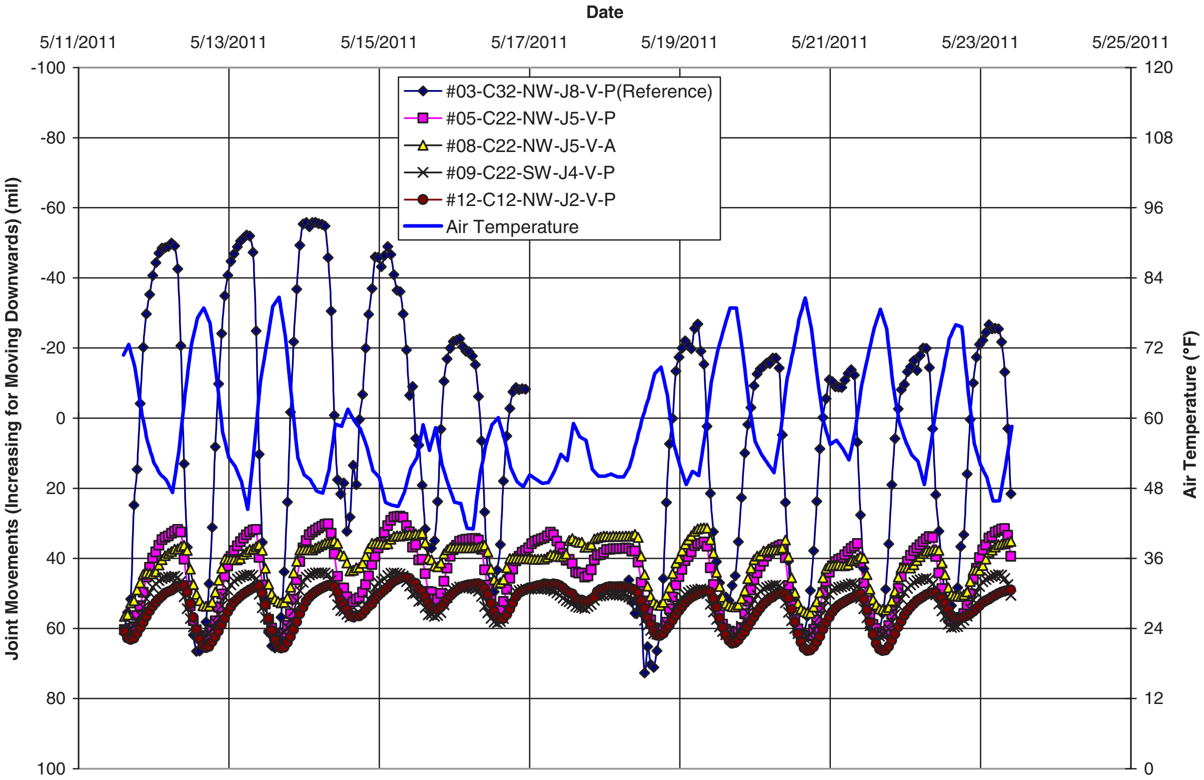

Figure M.43. Batch 10: Vertical joint movements along Lane C after HMA placement. See Figure M.14 for JDMD layout.

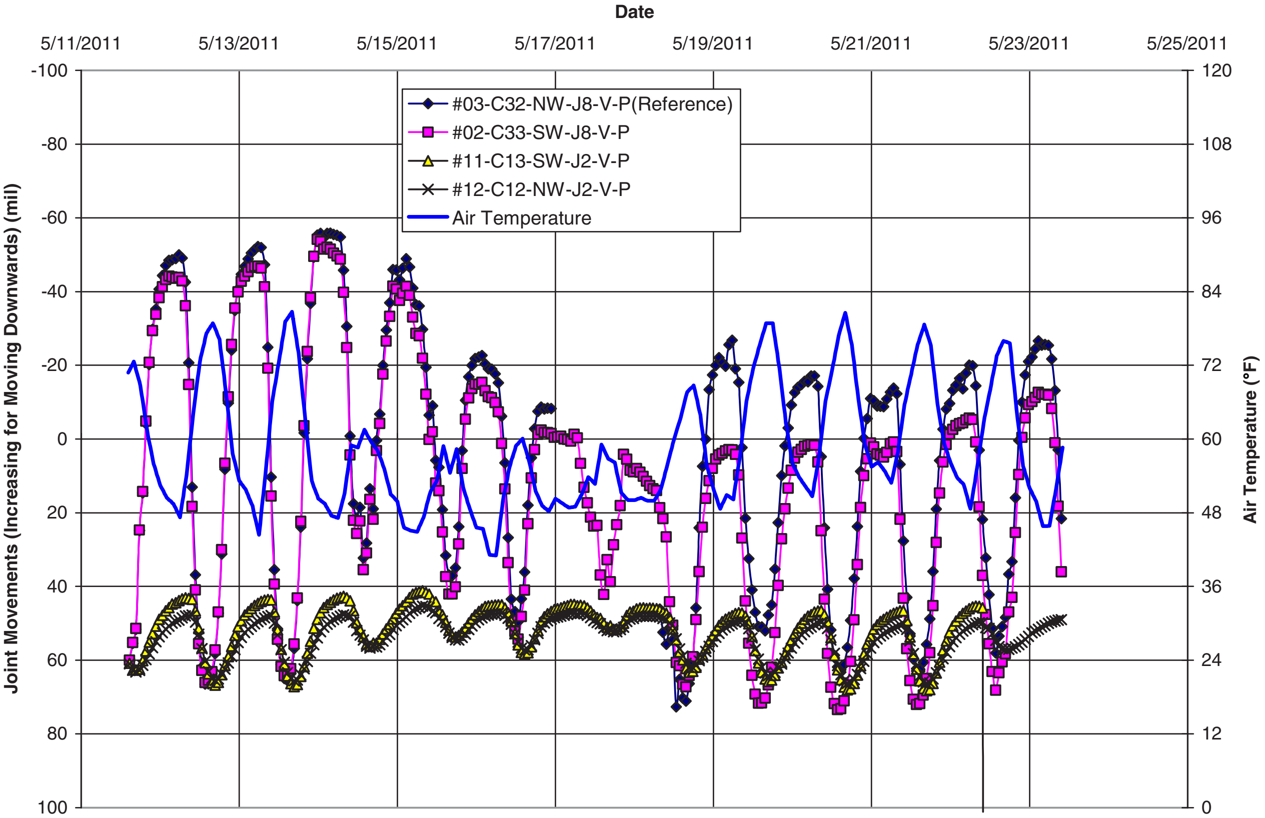

Figure M.44. Batch 10: Additional vertical joint movements along Lane C after HMA placement. See Figure M.14 for JDMD layout.

reading was the result of averaging 100 measurements taken over 0.1 second (i.e., at a sampling rate of 1,000 Hz).

Note that the starting value for JDMD measurements is arbitrary. The starting values were set to be exactly the same for each type of JDMD (i.e., horizontal or vertical) within each batch to show clearer trends.

Some basic observations can be made based on the raw results of the data from each batch:

- Batches 1 and 2 (before HMA placement): Horizontal movements can be different by about 30% among joints in the same lane (i.e., same structure).
- Batch 3 (before HMA placement): Dowels can reduce horizontal joint movement by 30%, and joints between 5-in. PCC slabs have about 20% more horizontal joint movement than do joints between 7-in. PCC slabs.
- Batches 4 and 5 (before HMA placement): Vertical movements at the four corners of each slab are roughly the same, indicating symmetric temperature-induced deformation in both doweled and nondoweled PCC slabs.
- Batches 6, 7, 9, and 10 (after HMA placement): HMA layers reduce horizontal and vertical joint movements.
- Batch 8 (after HMA placement): The differences between different lanes are relatively small.

Albedo values for different materials at the test track are listed in Table M.2. Both HMA materials have significantly lower albedo values than does PCC, indicating that more solar radiation is absorbed by the pavement as a result of the HMA layer. Furthermore, the RHMA-G mix has a smaller albedo value than does the PM mix used.

Data Analysis and Observations

The joint movement rate (JMR) defined as the amount of horizontal or vertical displacement caused by a unit increase in ambient air temperature, was calculated as the slope of the straight line fitted through the joint displacement-versus-air temperature data for each individual JDMD. Figure M.45 and Figure M.46 show example variations of horizontal and vertical joint displacements with ambient air temperature. The JMR for horizontal JDMDs is negative, indicating that joints close as air temperature increases. The JMR for vertical JDMDs is positive, which indicates slab corners curl downward as air temperature increases.

Table M.2. Albedo Values for Different Materials at UCPRC Test Track

Material	Average (%)	SD	Number of Samples
PCC	32.3	2.8	2
PM mix	12.2	0.6	3
RHMA-G	8.5	0.1	3
Aggregate	11.4	na	1
Grass	18.2	na	1

Note: SD = standard deviation.

Figure M.47 shows the variation of JMR with average ambient air temperature for the two reference JDMDs. It is apparent that JMR is not a constant, but rather that it varies with ambient air temperature when the joint movements are measured. This is reasonable because ambient air temperature affects the shape of a PCC slab, which in turn affects the amount it would deform with a unit temperature change.

Figure M.47 also indicates that JMRs for both vertical and horizontal movements peak at approximately 60°F, which may indicate that the shape of that particular slab allows maximum freedom of movement at around that temperature.

Because joint movement is affected by ambient temperature, it is important to only compare results measured within the same batch or among batches with similar ambient temperature. In the following two sections, the joint movements before and after HMA placement are examined. The data collected before HMA placement provide information about the effects of dowels and PCC thickness on joint movements in bare PCC pavements, as well as variability in JMR. The data collected after HMA placement provide information on the effects of dowels, HMA thickness, and HMA mix type on joint movements in composite pavements.

Joint Movements Before HMA Construction

Horizontal JMR variations for different joints and different lanes on bare PCC pavements are evaluated in Batch 1 and 2. The JMR plots are shown in Figure M.48 and Figure M.49. Figure M.48 shows that dowel joints have slightly lower absolute JMR values than do nondoweled joints. Figure M.49 indicates that joints in 5-in. PCC slabs generally have the same JMR values as 7-in. PCC slabs. The average value of horizontal JMR is approximately −1.0 mil/°F. This implies a coefficient of thermal expansion of approximately 5.6 microstrain/°F because the slab length is 15 ft.

The vertical JMR values for different slabs and different lanes are evaluated in Batch 3, 4, and 5. The results are plotted in Figures M.50 through M.52. Figure M.50 indicates that 5-in. PCC slabs have higher JMRs than do 7-in. PCC slabs and that slabs with doweled joints have lower JMR values. Figure M.51 indicates that vertical JMR values vary slightly. Figure M.52 again indicates that slabs with doweled joints have lower vertical JMR values.

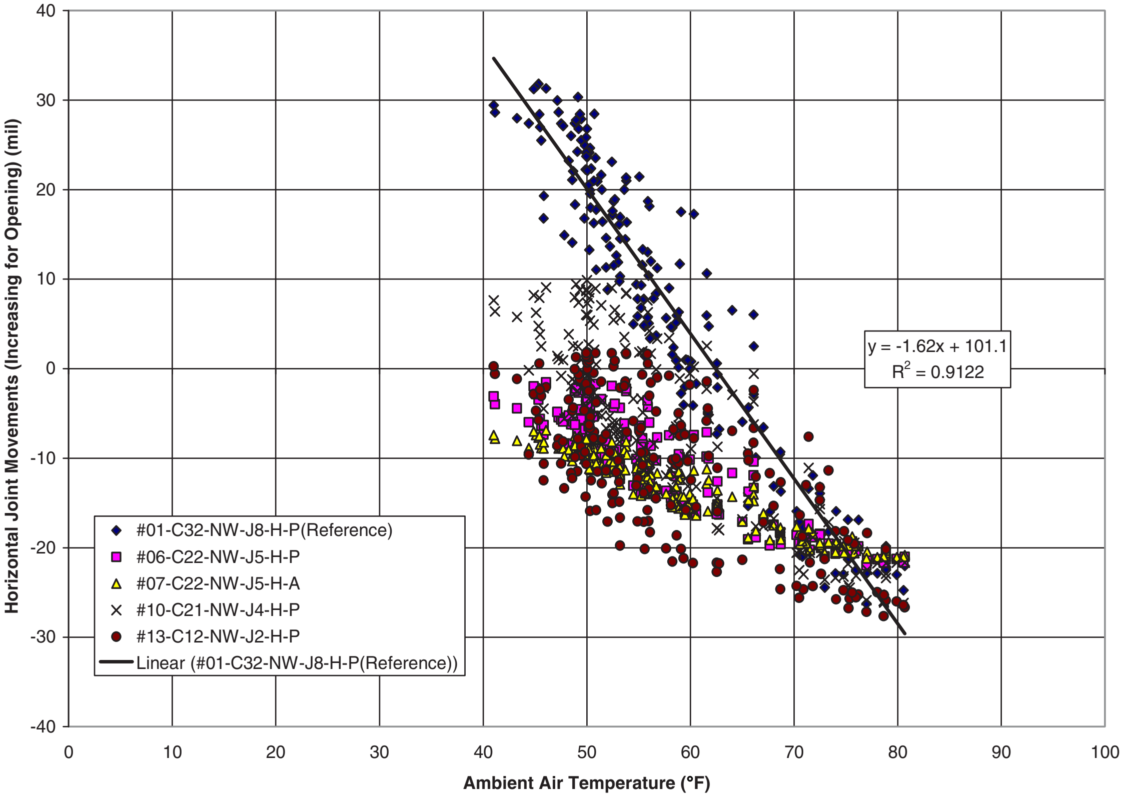

Figure M.45. Example variation of horizontal joint movement with ambient air temperature for Batch 10, Lane C, after HMA placement. A linear regression line is shown for the reference JDMD. The joint movement rate (JMR) is defined as the slope of each individual linear regression line. JMR = −1.62 mil/°F for the reference case in this batch.

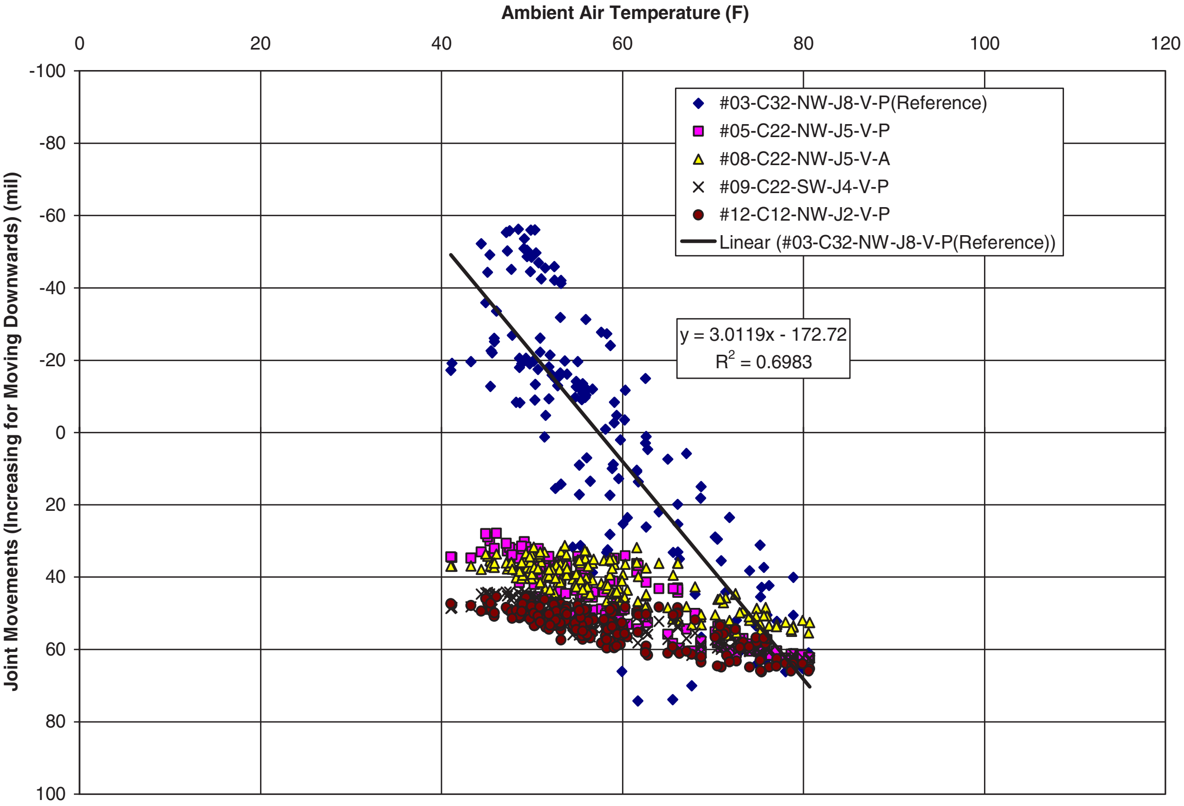

Figure M.46. Example variation of vertical joint movement with ambient air temperature for Batch 10, Lane C, after HMA placement. A linear regression line is shown for the reference JDMD. The joint movement rate (JMR) is defined as the slope of each individual linear regression line. JMR = 3.01 mil/°F for the reference case in this batch.

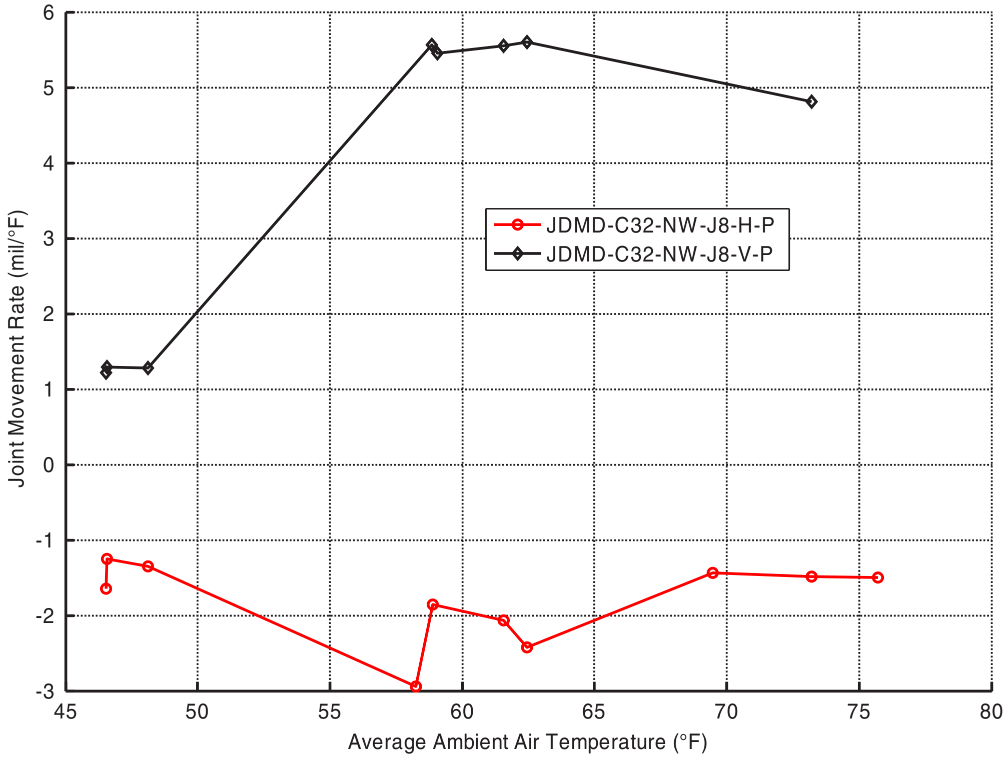

Figure M.47. Variation of JMR versus average ambient temperature for the reference JDMDs.

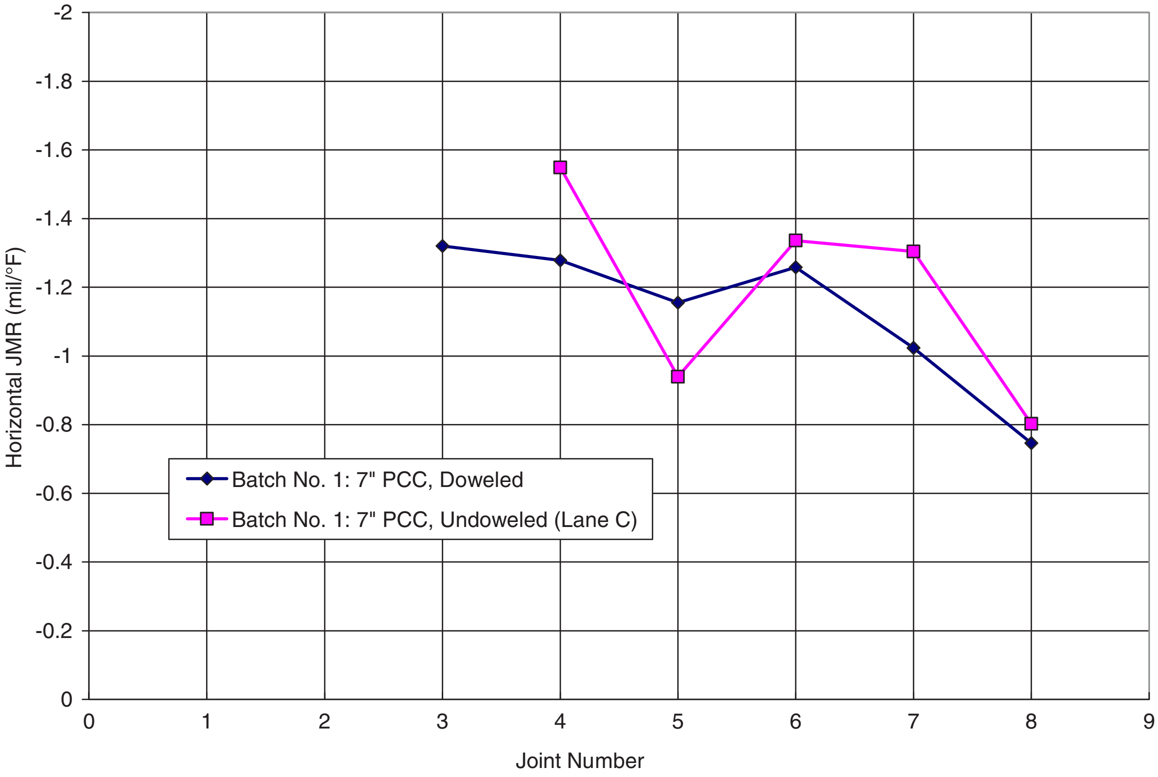

Figure M.48. Horizontal JMRs measured in Batch 1 before HMA placement. (Undoweled = nondoweled.)

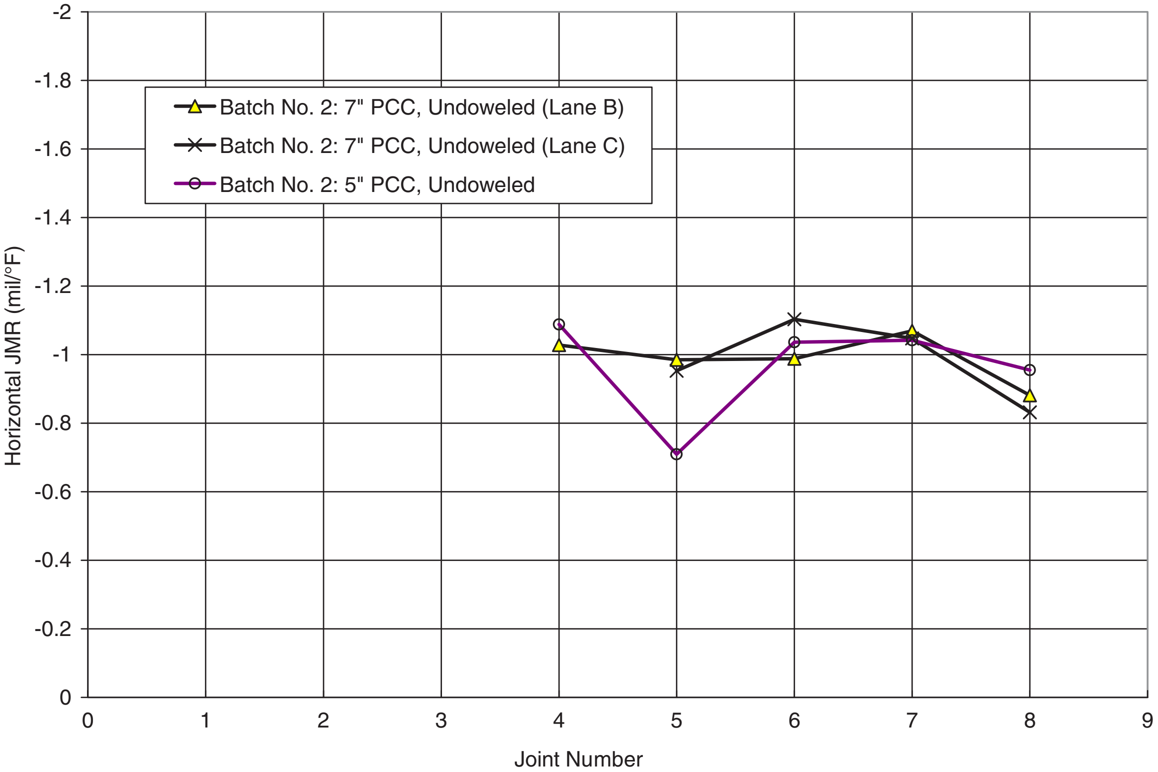

Figure M.49. Horizontal JMRs measured in Batch 2 (before HMA placement). (Undoweled = nondoweled.)

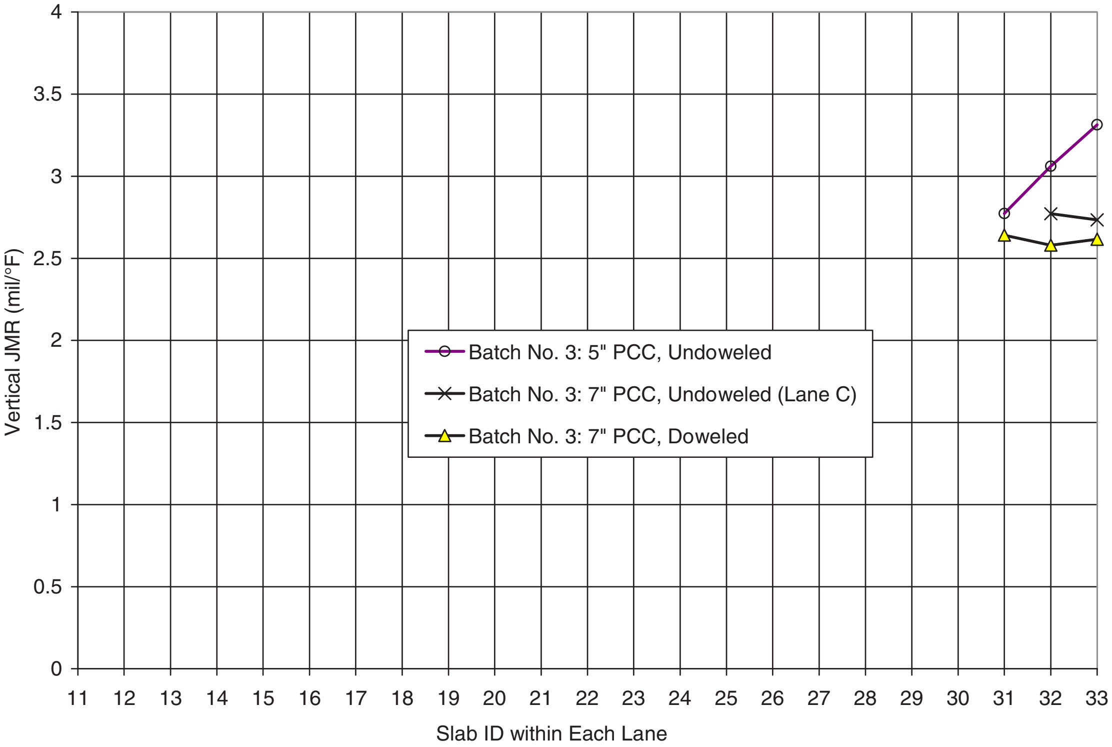

Figure M.50. Vertical JMRs measured in Batch 3 before HMA placement. (Undoweled = nondoweled.)

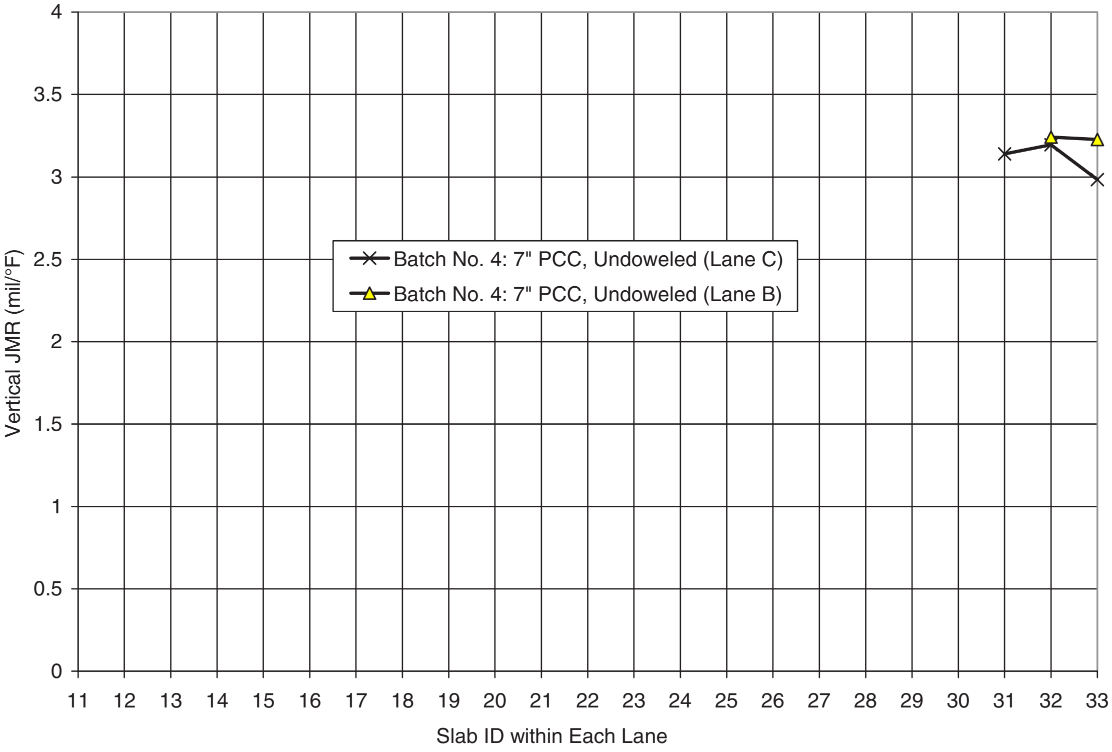

Figure M.51. Vertical JMRs measured in Batch 4 before HMA placement. (Undoweled = nondoweled.)

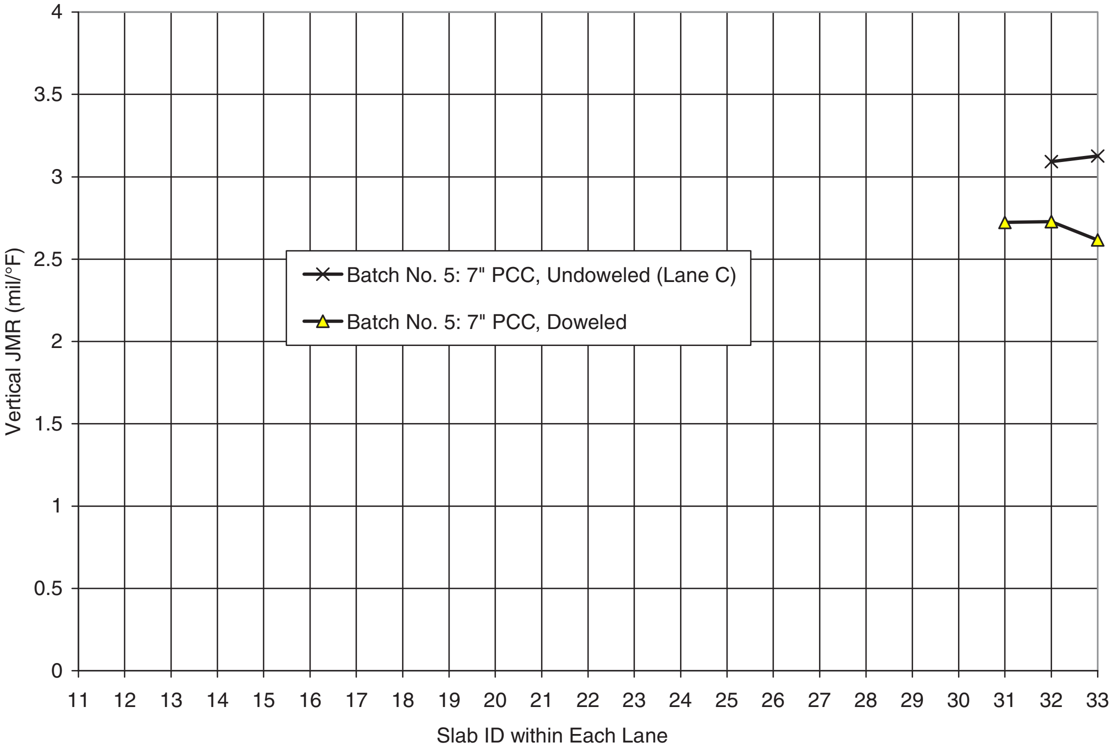

Figure M.52. Vertical JMRs measured in Batch 5 before HMA placement. (Undoweled = nondoweled.)

Note that although the effects of dowels and slab thickness on both horizontal and vertical JMRs are clear, the difference is roughly comparable with the variation in JMR values within each lane (i.e., construction variability).

Joint Movements After HMA Construction

Figures M.53 through M.62 show the joint movement versus ambient air temperature plots for each of the five batches measured after HMA placement. The plots show the effects of HMA thickness and structure type on joint movements. In addition, Figures M.63 through M.66 show the comparison of JMRs for different locations.

Table M.3 and Table M.4 show the effect of HMA thickness on horizontal and vertical JMRs, respectively.

Based on these plots, the following observations are made with regard to the vertical and horizontal JMR:

- Placement of HMA layers on PCC pavements lowers the values for both horizontal and vertical JMR compared with those of bare PCC pavement. The thicker the HMA layer, the greater the decrease in JMR (see Figure M.63 and Figure M.64).
- On the reduction effect of HMA thickness on horizontal JMR (Figure M.63 and Table M.3) and vertical JMR (Figure M.64 and Table M.4):
    - ○ All 2.5-in. HMA thickness showed significant reduction in JMR except for PM mix on 7-in. nondoweled PCC.
    - ○ 4.5-in. PM mix showed a significant further reduction in JMR compared with that of 2.5-in. HMA thickness.
    - ○ 4.5-in. thickness RHMA-G mix showed only a slight further reduction or even a slight increase in JMR compared with that of 2.5-in. thickness.
- On JMR for composite pavements with 2.5-in. HMA thickness (see Figure M.65 and Figure M.66):
    - ○ 2.5-in. thickness PM mix on 7-in. doweled PCC has roughly the same vertical and horizontal JMR as does 2.5-in. thickness PM mix on 7-in. nondoweled PCC (i.e., the effect of dowel is minimal).
    - ○ Vertical and horizontal JMR for 2.5-in. thickness RHMA-G on 7-in. nondoweled PCC is ½ to ⅔ of the values for 2.5-in. thickness PM mix on 7-in. nondoweled PCC (i.e., RHMA-G is more efficient than PM mix in reducing JMR when used in a 2.5-in. thickness layer).
    - ○ Horizontal JMR values are roughly the same for 2.5-in. thickness RHMA-G on 7-in. and 5-in. PCC.

Summary of Findings

Some key findings observed in this study are summarized:

- JMR is not a constant for a given joint or slab corner, and in general the higher the average daily ambient temperature, the higher the values for JMR.

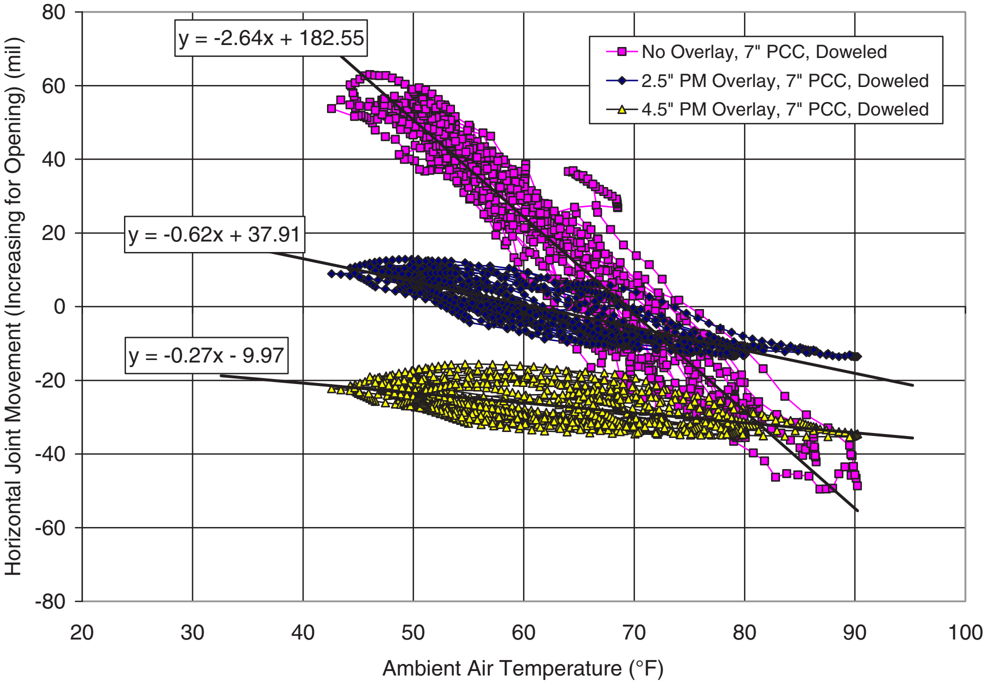

Figure M.53. Horizontal joint movement versus air temperature plots for Lane A after HMA placement.

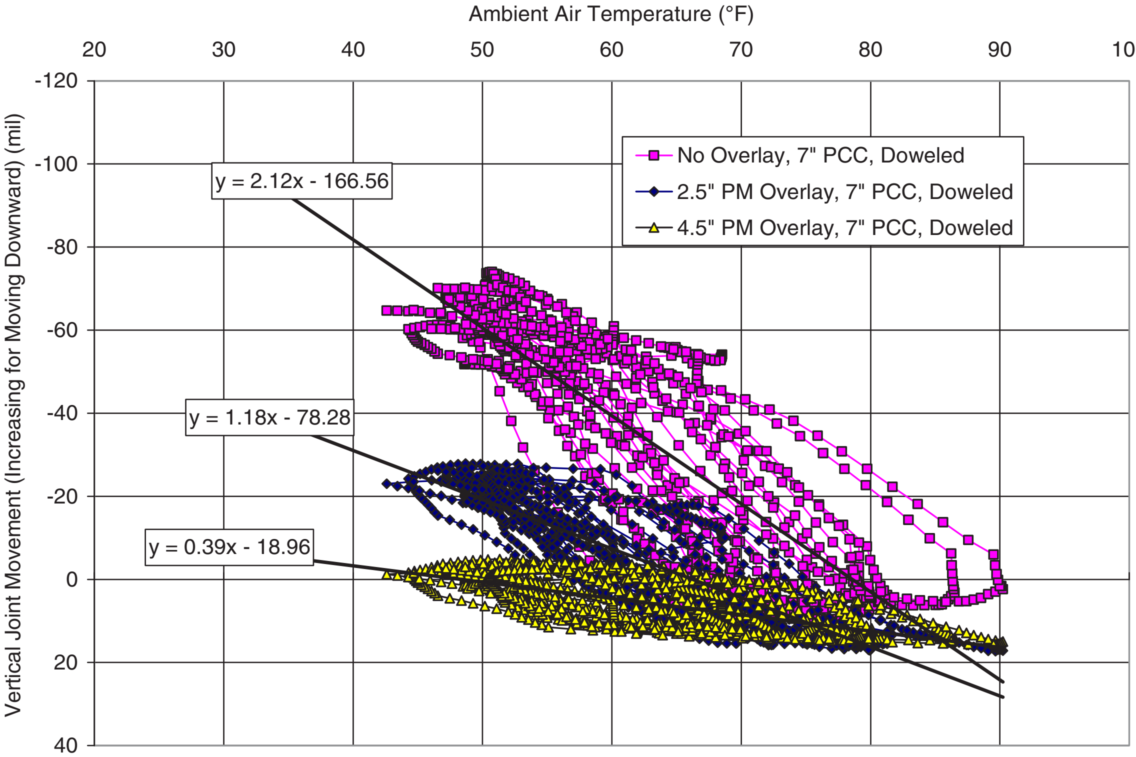

Figure M.54. Vertical joint movement versus air temperature plots for Lane A after HMA placement.

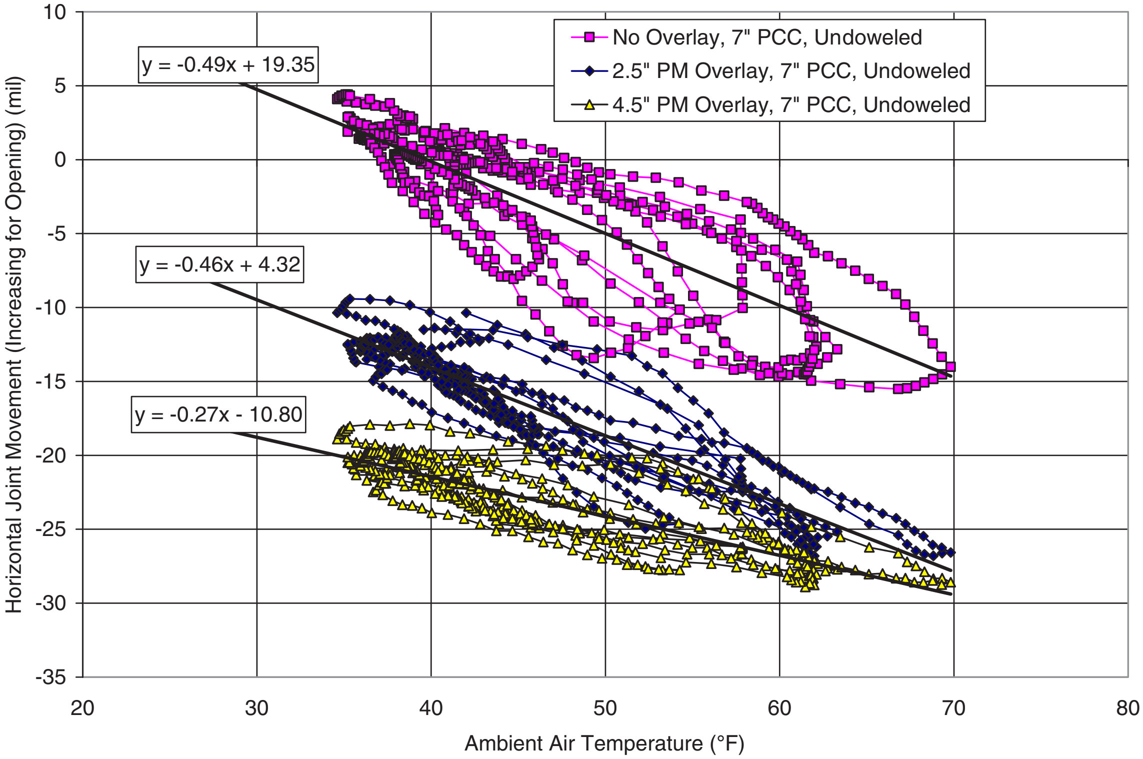

Figure M.55. Horizontal joint movement versus air temperature plots for Lane B after HMA placement. (Undoweled = nondoweled.)

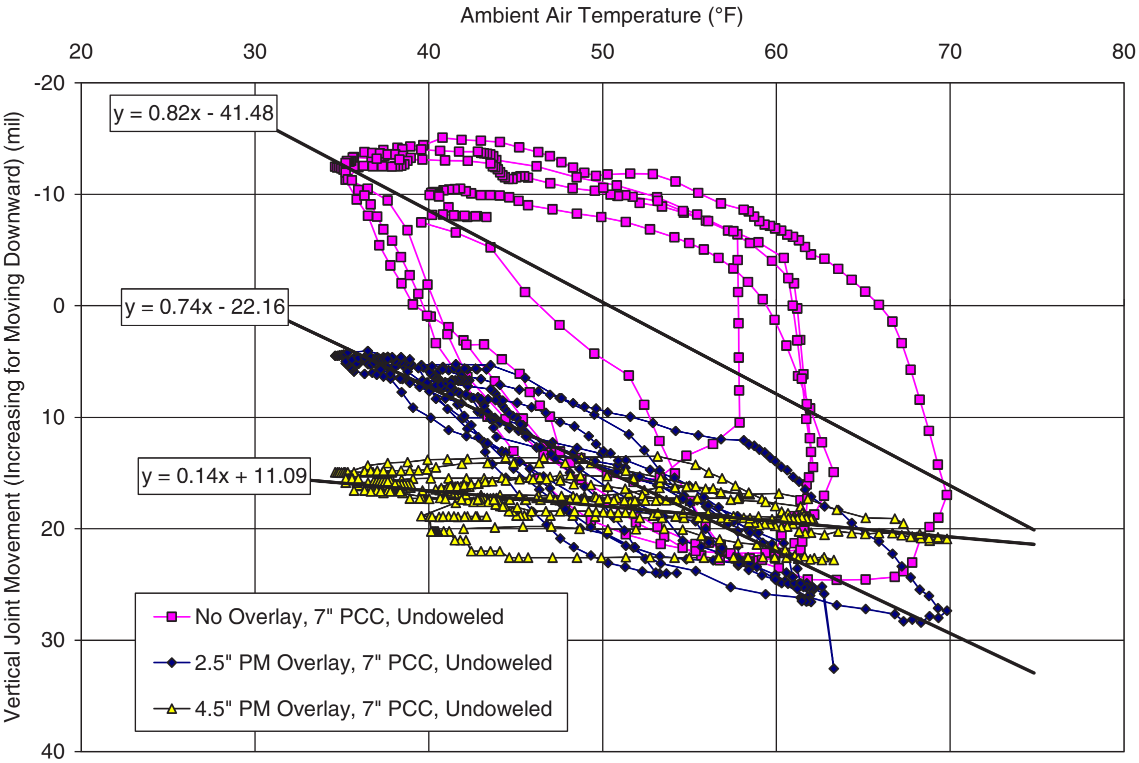

Figure M.56. Vertical joint movement versus air temperature plots for Lane B after HMA placement. (Undoweled = nondoweled.)

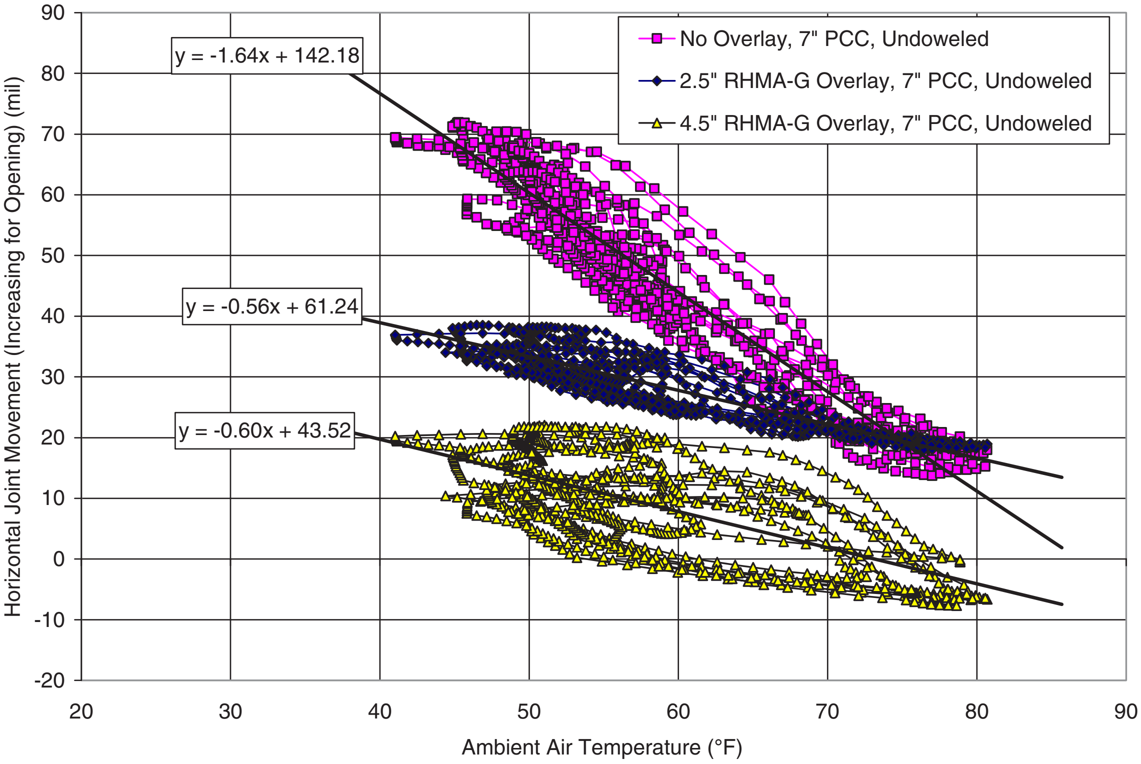

Figure M.57. Horizontal joint movement versus air temperature plots for Lane C after HMA placement. (Undoweled = nondoweled.)

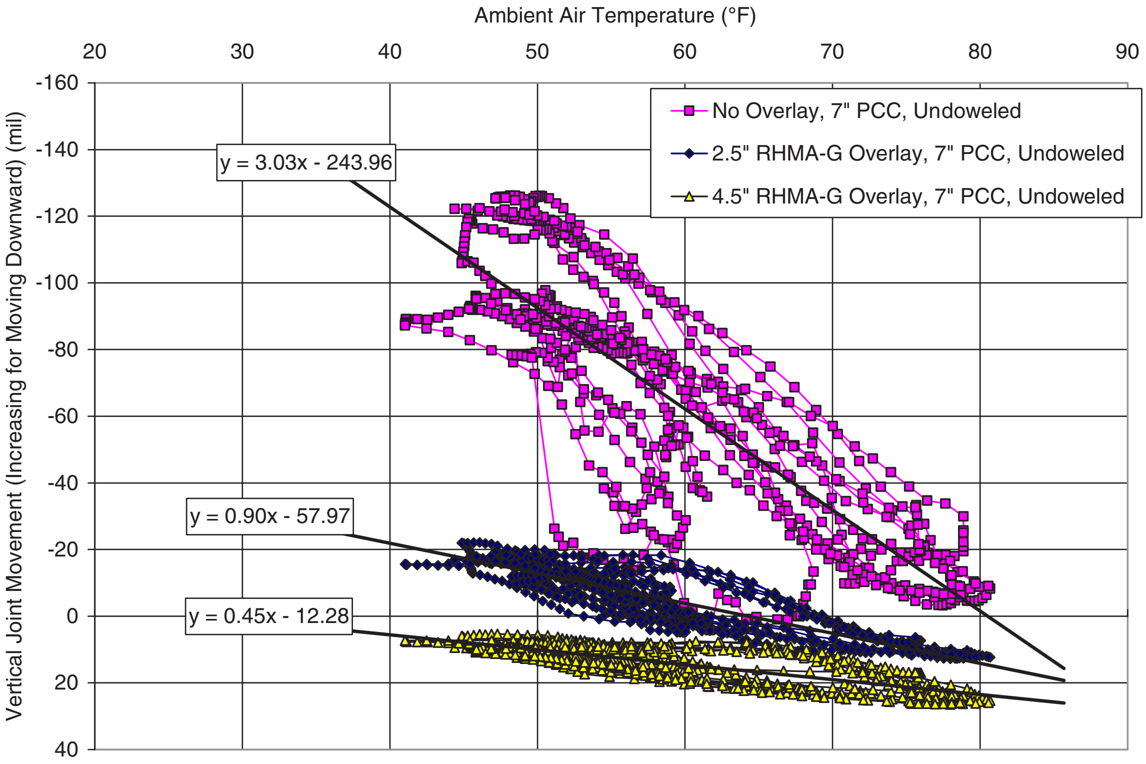

Figure M.58. Vertical joint movement versus air temperature plots for Lane C after HMA placement. (Undoweled = nondoweled.)

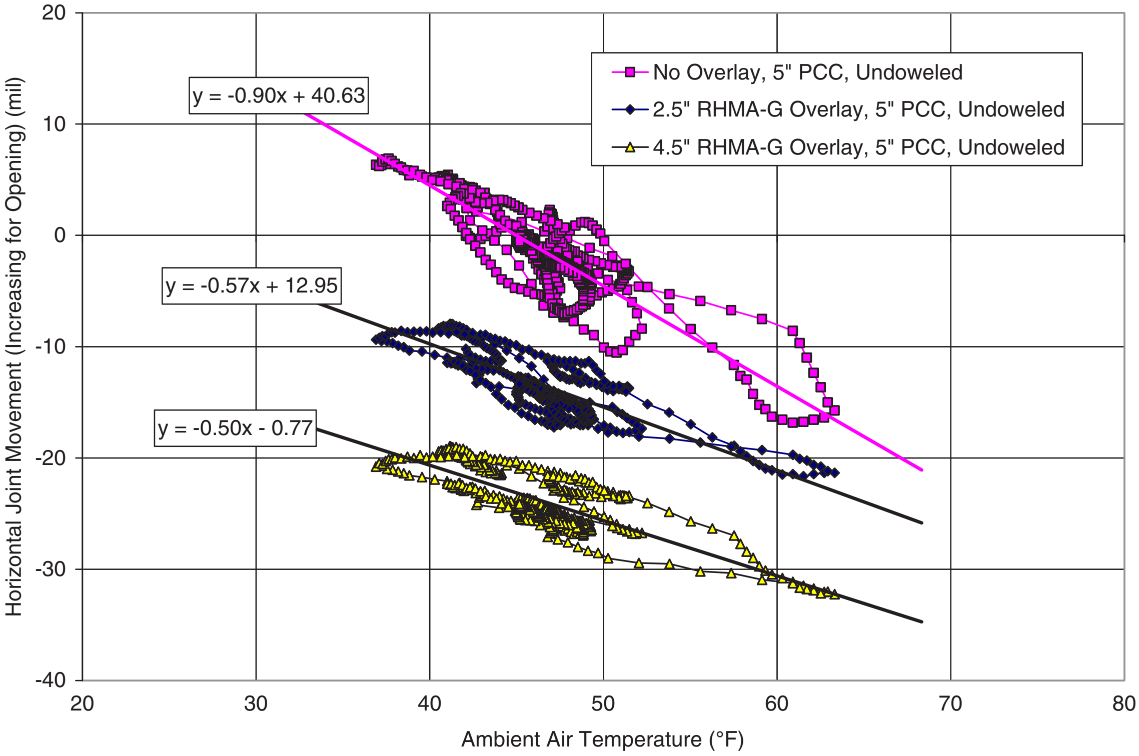

Figure M.59. Horizontal joint movement versus air temperature plots for Lane D after HMA placement. (Undoweled = nondoweled.)

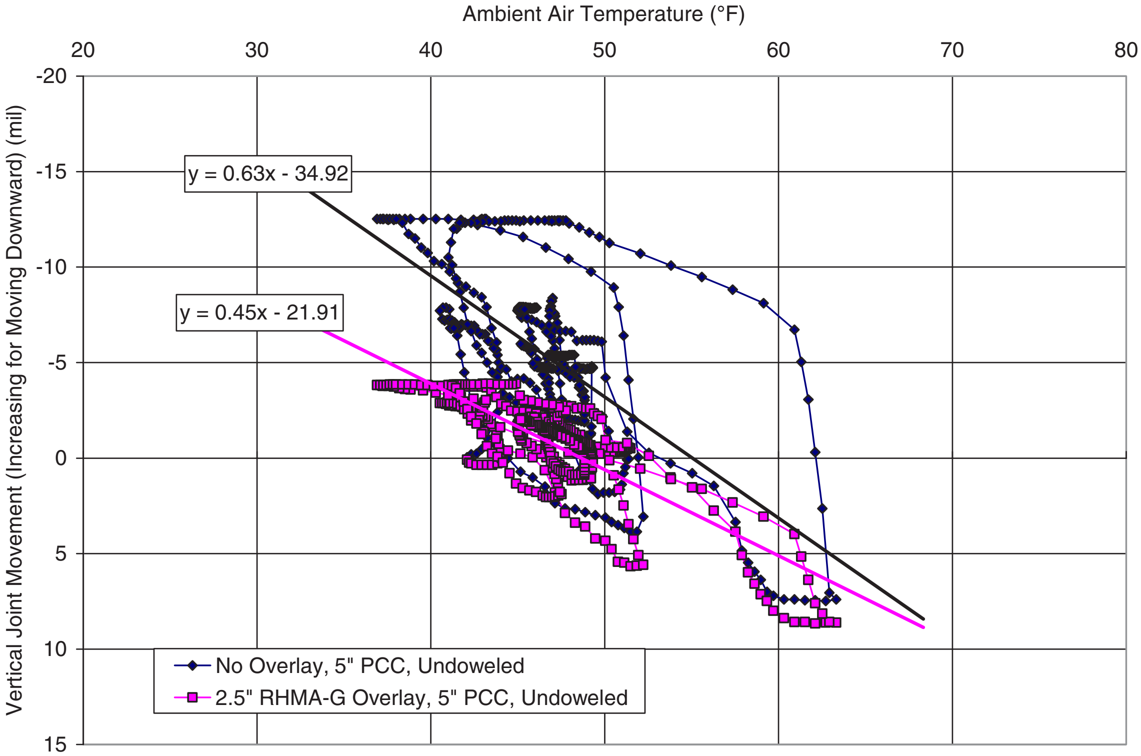

Figure M.60. Vertical joint movement versus air temperature plots for Lane D after HMA placement. (Undoweled = nondoweled.)

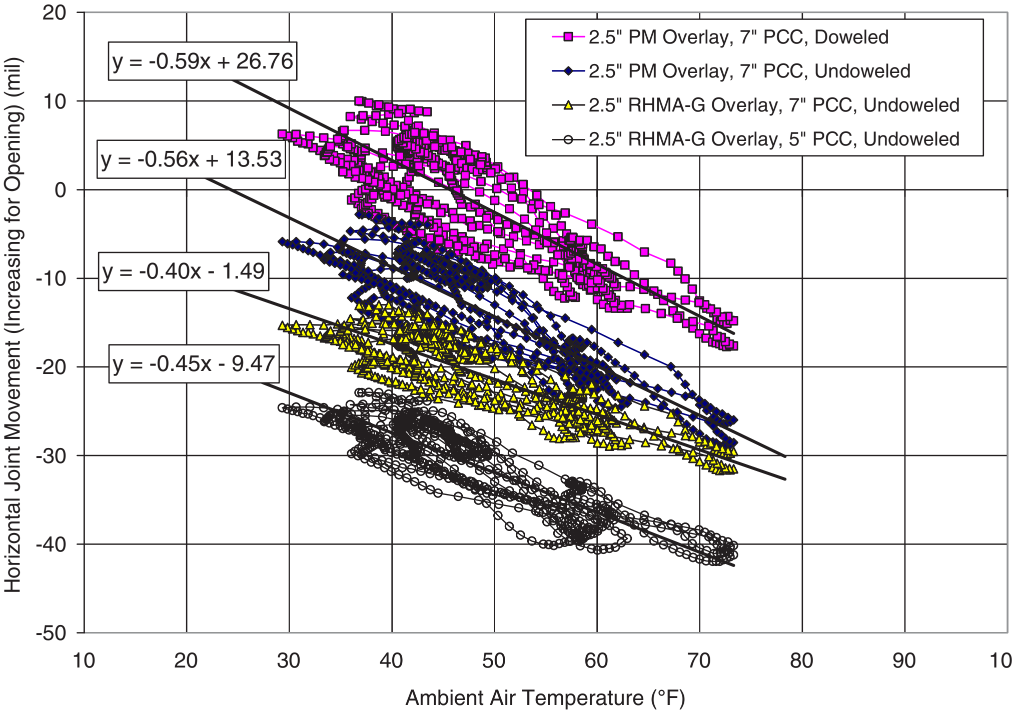

Figure M.61. Horizontal joint movement versus air temperature plots for Joint J5 after HMA placement. (Undoweled = nondoweled.)

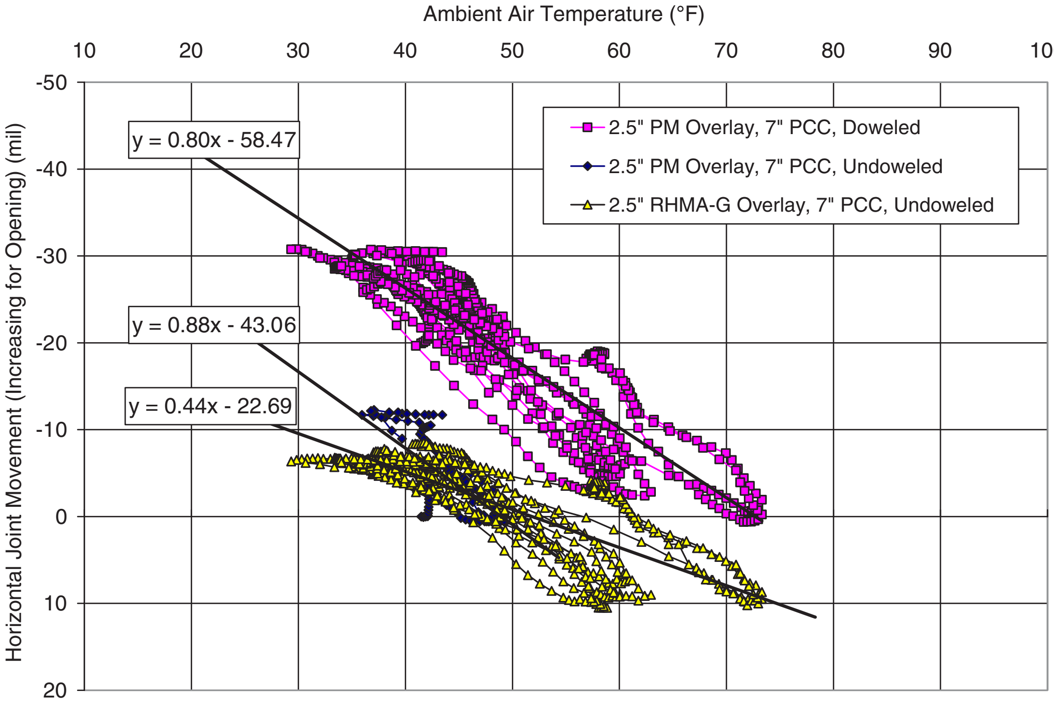

Figure M.62. Horizontal joint movement versus air temperature plots for Joint J5 after HMA placement. (Undoweled = nondoweled.)

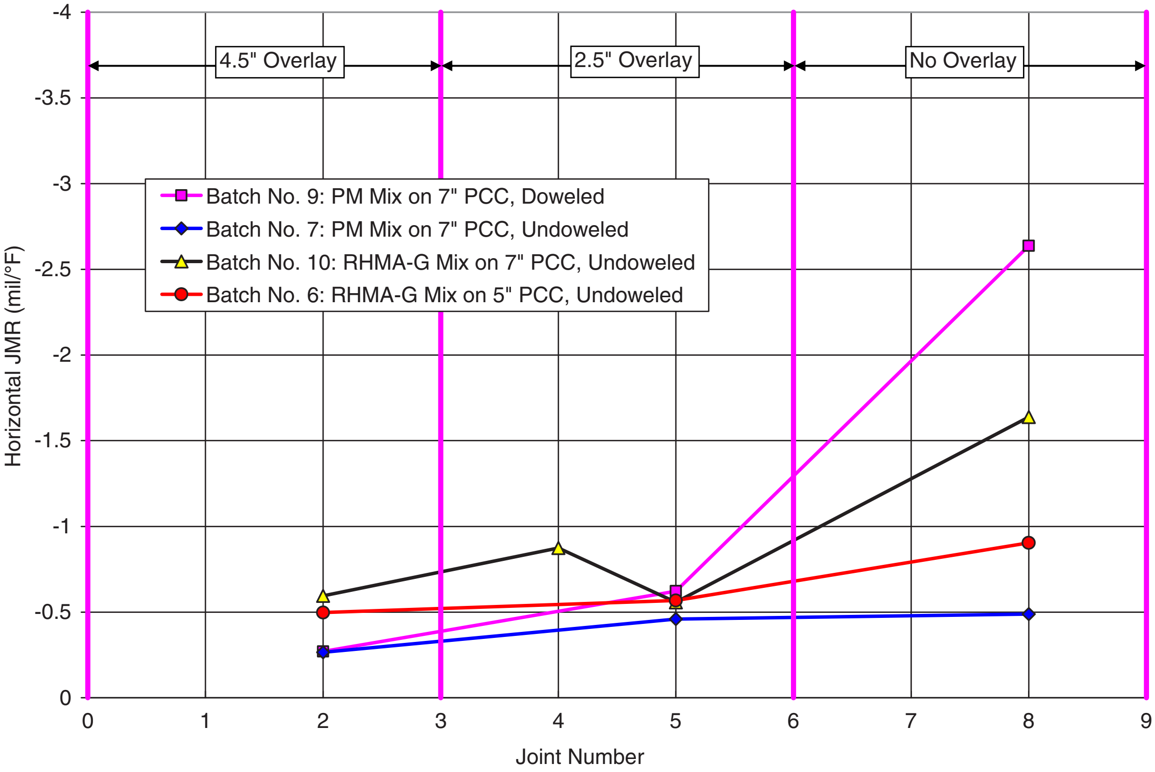

Figure M.63. Horizontal JMRs for different lanes and joints after HMA placement. (Undoweled = nondoweled.)

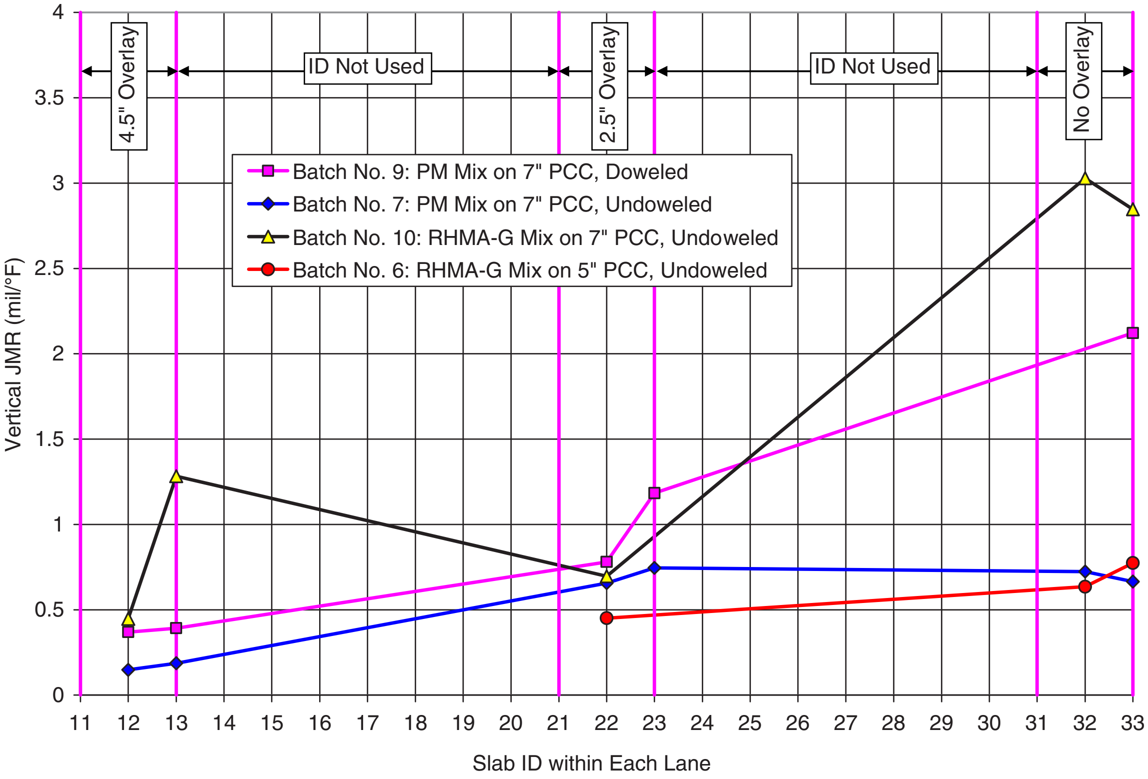

Figure M.64. Vertical JMRs for different lanes and joints after HMA placement. (Undoweled = nondoweled.)

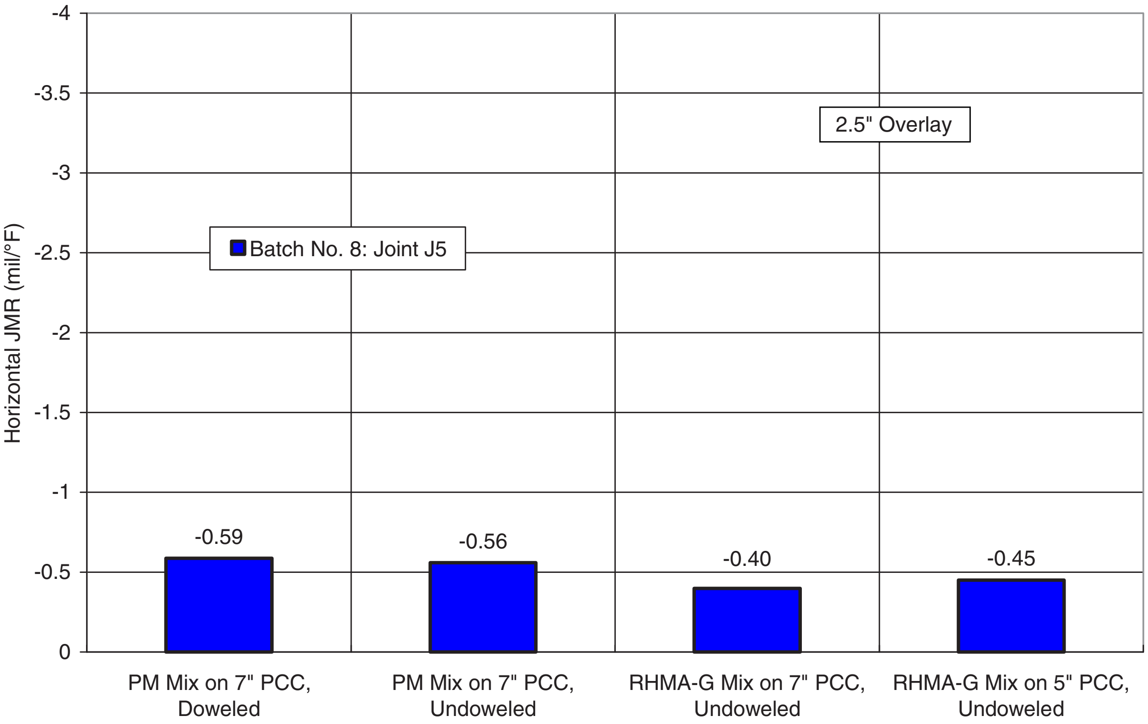

Figure M.65. Horizontal JMR for different lanes at Joint J5 after HMA placement. (Undoweled = nondoweled.)

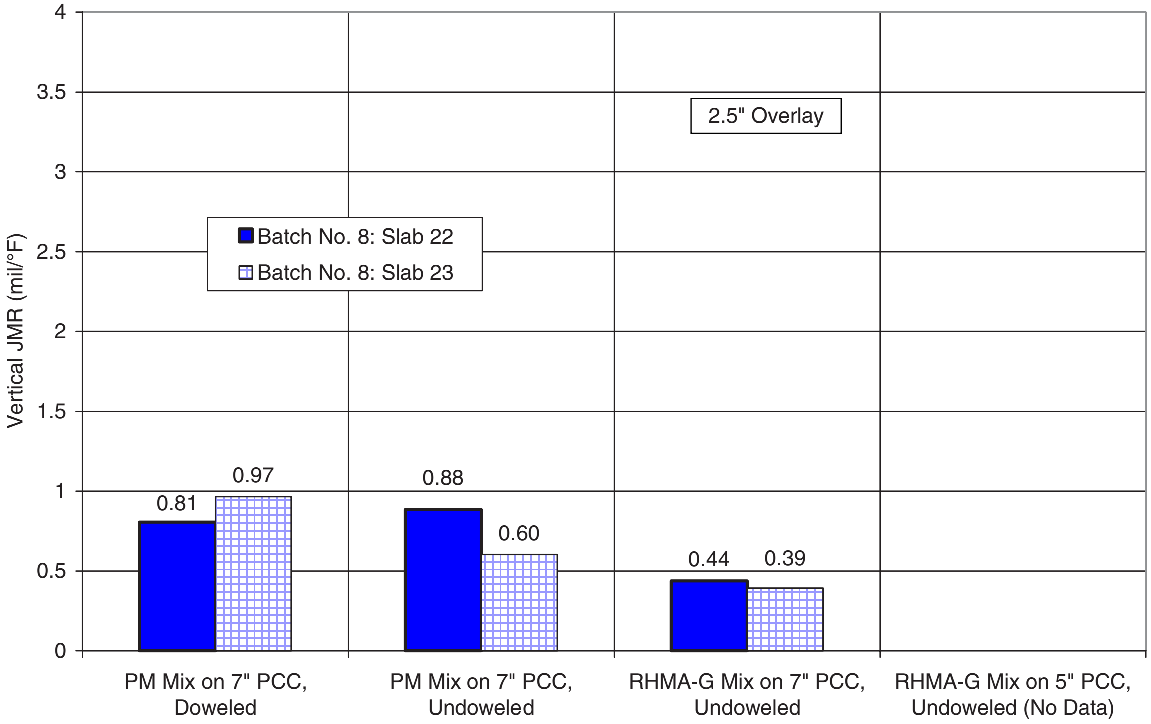

Figure M.66. Vertical JMRs for slabs adjacent to Joint J5 in different lanes after HMA placement. Joint J5 is located between Slab 22 and Slab 23 in each lane. (Undoweled = nondoweled.)

Table M.3. Effect of HMA Thickness on Horizontal JMR

Mix Type	Doweled?	PCC Thickness (in.)	JMR Values (mil/°F)			% JMR Reduction		
			0 in.	2.5 in.	4.5 in.	0 in.	2.5 in.	4.5 in.
PM mix	Yes	7	–2.64	–0.62	–0.27	0	76	90
PM mix	No	7	–0.49	–0.46	–0.27	0	6	46
RHMA-G	No	7	–1.64	–0.72	–0.60	0	56	64
RHMA-G	No	5	–0.90	–0.57	–0.50	0	37	45

Table M.4. Effect of HMA Thickness on Vertical JMR

Mix Type	Doweled?	PCC Thickness (in.)	JMR Values (mil/°F)			% JMR Reduction		
			0 in.	2.5 in.	4.5 in.	0 in.	2.5 in.	4.5 in.
PM mix	Yes	7	2.12	0.98	0.38	0	54	82
PM mix	No	7	0.69	0.70	0.17	0	–1	76
RHMA-G	No	7	2.94	0.70	0.86	0	76	71
RHMA-G	No	5	0.70	0.45	(No data)	0	36	(No data)

- The four corners of each slab were found to show similar movements before HMA placement, indicating symmetric temperature-induced shape change of PCC slabs.
- For joints in bare PCC pavement:
  - Doweled joints have lower vertical and horizontal JMR values than do nondoweled joints.
  - Joints in 5-in. PCC slabs have roughly the same horizontal JMR but higher vertical JMR than do joints in 7-in. PCC slabs.
  - The construction variability in JMR is comparable with the observed effects of both dowel and PCC thickness on JMR.
- For the effects of HMA layer on JMR:
  - HMA layers reduce both horizontal and vertical JMR.
  - The thicker the HMA, the more significant the JMR reduction effect.
  - 2.5-in. HMA thickness can effectively reduce JMR, except when PM mix is used and placed on 7-in. nondoweled slabs.
  - When PM mix is used, the 4.5-in. HMA thickness shows significant improvement compared with the 2.5-in. HMA thickness in reducing JMR.
  - When RHMA-G mix is used, 4.5-in. thickness shows only small improvement over the 2.5-in. thickness.
  - When 2.5-in. HMA thickness is used, the effect of dowels is minimal, and RHMA-G is more efficient than PM mix in reducing JMR.
- On the significance of albedo value:
  - Albedo values for both HMA materials are significantly lower than the value for bare PCC. This indicates that more solar radiation is absorbed by the composite pavements than bare PCC pavements, even though composite pavements have lower JMR values than do bare PCC pavements. The albedo value for RHMA-G mix is lower than the value for PM mix, which is believed to lead to more efficient JMR reduction by the RHMA-G mix than the PM mix when both are used in 2.5-in. thickness.

APPENDIX N

Laboratory Testing of HMA Mixes at UCPRC

Laboratory testing of hot-mix asphalt (HMA) materials from the Heavy Vehicle Simulator (HVS) and MnROAD test sections included repeated shear, flexural fatigue, and stiffness frequency sweep tests. The materials tested from the HVS test sections were dense-graded HMA with PG 64-28 polymer-modified (PM) binder (referred to as PG 64-28 PM) and gap-graded hot mix with rubberized asphalt binder (referred to as RHMA-G). The mix from MnROAD Cell 70 was dense-graded HMA with PG 64-34 binder.

Tests on HMA mixes were performed on field-mixed, laboratory-compacted beams and cores sawed from ingots that were compacted during the test section construction (see Appendix G). During construction, loose mix was taken from the trucks with a skip loader immediately before it was tipped into the paver and dumped next to the preparation area. The required volume of material, based on the theoretical maximum densities determined earlier in the contractor's laboratory, was weighed and compacted, using a rolling wheel, into molds at the same temperatures as those recorded on the test track. Specimens were cut into 15- × 2.5- × 2-in. (380- × 62.5- × 50-mm) beams or cored and then cut into 6- × 2-in. (150- × 50-mm) shear specimens. The experimental designs for stress or strain, temperature, and number of replicates used in previous studies were also used for this study to facilitate later comparison of results.

Experiment Design

Shear Testing

The AASHTO T-320 Permanent Shear Strain and Stiffness Test was used for shear testing in this study. In the standard test methodology, cylindrical test specimens 150 mm in diameter and 50 mm thick (6.0 × 2.0 in.) are subjected to repeated loading in shear using a 0.1-second haversine waveform followed by a 0.6-second rest period while the permanent (unrecoverable) and recoverable shear strains are measured. The permanent shear strain (PSS) versus applied repetitions normally is recorded until a 5% strain is reached, although T-320 calls for loading to only 5,000 repetitions. A constant temperature is maintained during the test.

Twelve shear tests were performed for PG 64-28 PM mix and 18 shear tests for RHMA-G and PG 64-34 mixes, the difference being the number of replicates. The number of replicate tests differed based on the number of specimens available and the variability in test results for each mix. The full factorial experiment design was as follows:

- Two temperatures: 45°C and 55°C (113°F and 131°F);
- Three stresses: 70 kPa, 100 kPa, and 130 kPa (10.2, 14.5, and 18.9 psi); and
- Three replicates for RHMA-G and PG 64-34 mixes and two replicates for PG 64-28 PM mix.

Fatigue Beam Tests

The AASHTO T-321 Flexural Controlled-Deformation Fatigue Test method was used. In this test, beam test specimens that are 50 mm thick × 63 mm wide × 380 mm long (2.0- × 2.5- × 15-in.) are subjected to four-point bending using a sinusoidal controlled deformation waveform at a loading frequency of 10 Hz. Flexural Controlled-Deformation Frequency Sweep Test methods were used to establish the relationship between complex modulus, temperature, and load frequency. The same sinusoidal waveform was used in a controlled deformation mode and at frequencies of 15, 10, 5, 2, 1, 0.5, 0.2, 0.1, 0.05, 0.02, and 0.01 Hz. The upper limit of 15 Hz is a constraint imposed by the capabilities of the test machine. To ensure that the specimen was tested in a nondestructive manner, the frequency sweep test was conducted at a small strain amplitude level, proceeding from the highest frequency to the lowest in the sequence noted above.

A total of 16 fatigue and 6 frequency sweep tests were carried out on mixes PG 64-28 PM and RHMA-G, whereas

18 fatigue and 6 frequency sweep tests were conducted on PG 64-34 mix (total of 68 tests for the three mixes), with full factorial experiment designs as follows:

Flexural Fatigue Test: Mixes PG 64-28 PM and RHMA-G

- Two temperatures: 10°C and 20°C (50°F and 68°F);
- Four strains: 200 microstrain, 400 microstrain, 600 microstrain, and 800 microstrain; and
- Two replicates for each mix.

Flexural Fatigue Test: Mix PG 64-34

- Two temperatures: 10°C and 20°C (50°F and 68°F);
- Two strains: 400 microstrain and 700 microstrain; and
- Three replicates.

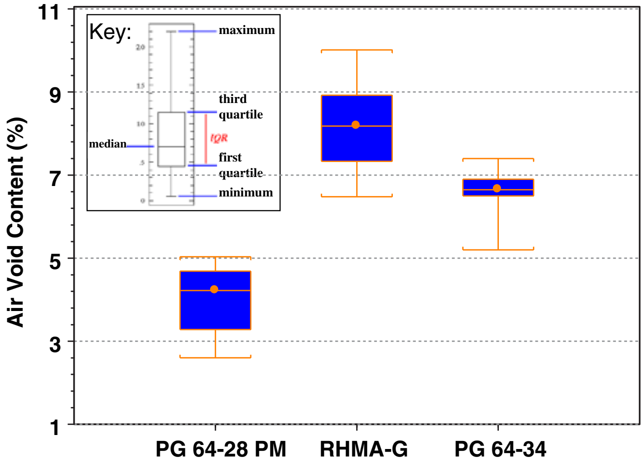

Figure N.1. Air void contents of shear specimens. (IQR = interquartile range.)

Frequency Sweep Test: Mixes PG 64-28 PM and RHMA-G

- Three temperatures: 10°C, 20°C, and 30°C (50°F, 68°F, and 86°F);
- One strain: 100 microstrain; and
- Two replicates for mixes PG 64-28 PM and RHMA-G, and one replicate for PG 64-34 mix.

Test Results

Shear Testing

Air Void Content

Air void contents were measured using the CoreLok method (AASHTO T-331). Table N.1 summarizes the air void distribution categorized by mix type, test temperature, and test shear stress level. Figure N.1 presents the summary box plots of air void content based on mix type. The differences in air void content distributions between the three mixes are clearly apparent. The mean difference for the mean air void content of mix RHMA-G and the mean air void content of mix PG 64-28 PM is as high as 4.2%.

Repetitive Simple Shear Test at Constant Height (RSST-CH) results for PG 64-28 PM, RHMA-G, and PG 64-34 mixes are given in Figures N.2, N.3, and N.4, respectively.

The figures show that the permanent deformation accumulation rate is extremely fast for mix PG 64-34. This result indicates that early rutting failure is likely to be observed for that mix if exposed to pavement temperatures at 50-mm depth (2-in.) of 45°C to 55°C (115°F to 122°F). On the other hand, PG 64-28 PM mix shows the best performance with slowest deformation accumulation. In the following section, test results were further analyzed based on the conventional RSST-CH performance prediction parameters, resilient shear modulus, number of required cycles to 2% and 5% deformation, and PSS at

Table N.1. Summary of Air Void Contents of Shear Test Specimens

Temperature			PG 64-28 PM		RHMA-G		PG 64-34	
°C	°F	Stress Level (kPa)	Mean	SD	Mean	SD	Mean	SD
45	113	70 100 130	4.1 4.1 3.9	0.4 0.9 1.2	8.5 9.4 8.5	0.6 0.6 0.4	6.9 6.3 6.7	0.4 1.0 0.1
55	131	70 100 130	4.9 4.2 2.9	0.3 0.2 0.4	7.8 7.5 7.5	1.2 1.3 0.3	6.5 6.9 6.7	0.1 0.4 0.4
Overall			4.0	0.8	8.2	1.0	6.7	0.5

Note: SD = standard deviation.

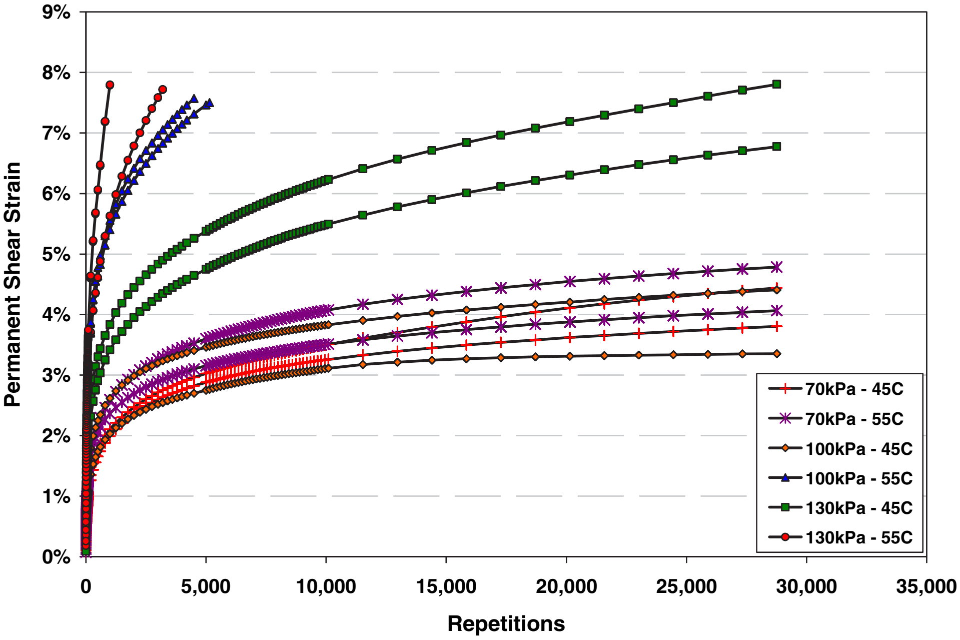

Figure N.2. RSST-CH test results for mix PG 64-28 PM.

repetition 5,000. Definitions for each parameter are given as follows:

- *Resilient shear modulus.* The ratio of applied peak shear stress to the measured elastic (recoverable) shear strain at the 100th repetition of the test.
- *Number of required cycles to 2% and 5% deformation.* The number of cycles to 2% and 5% PSS provides an indication of the rut resistance of an asphalt mix, with higher numbers of cycles implying better rut resistance. Cycles to 2% PSS give an indication of the early rutting behavior, and cycles to 5% PSS give information about the rutting behavior after further trafficking.
- *PSS at repetition 5,000.* The measurement of PSS accumulated after 5,000 cycles provides an alternative indication of the rut resistance capacity of an asphalt mix. This parameter

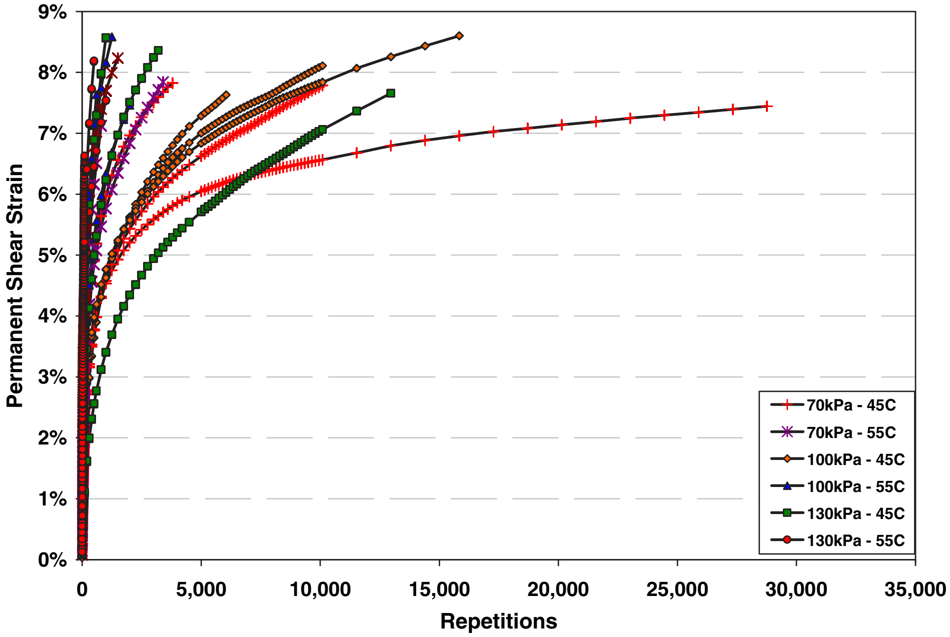

Figure N.3. RSST-CH test results for mix RHMA-G.

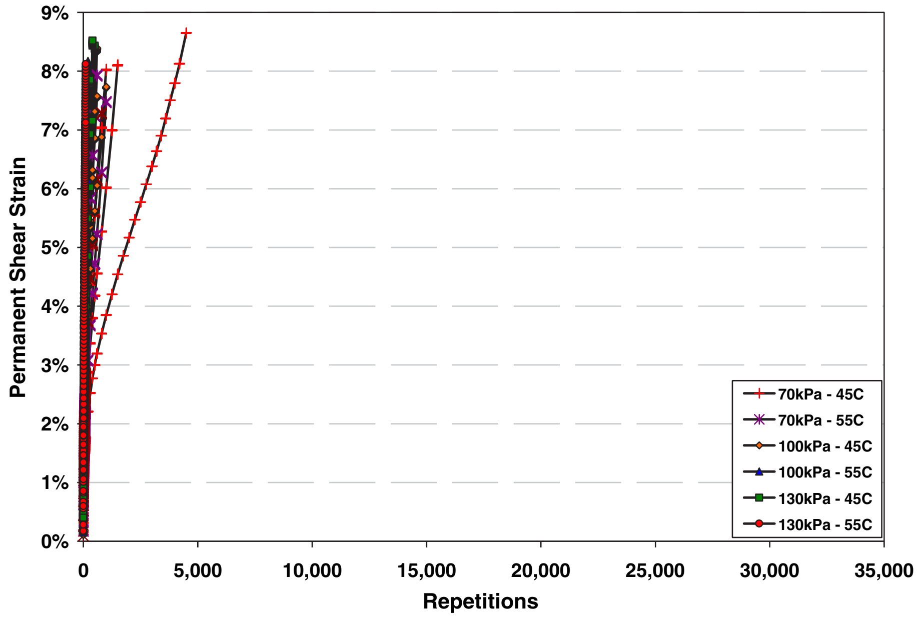

Figure N.4. RSST-CH test results for mix PG 64-34.

is simply the measured or extrapolated PSS at the 5,000th test repetition. The smaller the PSS, the better the mixture's rut resistance capacity.

Resilient Shear Modulus (G)

The resilient shear modulus results for the three mixes are summarized in Figure N.5. The resilient shear modulus is influenced by temperature, with the modulus increasing with decreasing temperature. Resilient shear modulus was not significantly influenced by stress. The variation of resilient shear moduli at 45°C was considerable compared with the results at 55°C for mixes PG 64-28 PM and RHMA-G. However, coefficient of variation should be checked to get a better assessment for variability. The RHMA-G mix has higher resilient shear modulus values at 45°C, whereas PG 64-28 PM and RHMA-G mixes have similar modulus values at 55°C. It can be observed that the resilient shear modulus of the PG 64-28 PM is less susceptible to temperature changes than is that of the other two mixes. The PG 64-34 mix has lower shear modulus than the other two mixes and does not show much effect of shear stress or temperature.

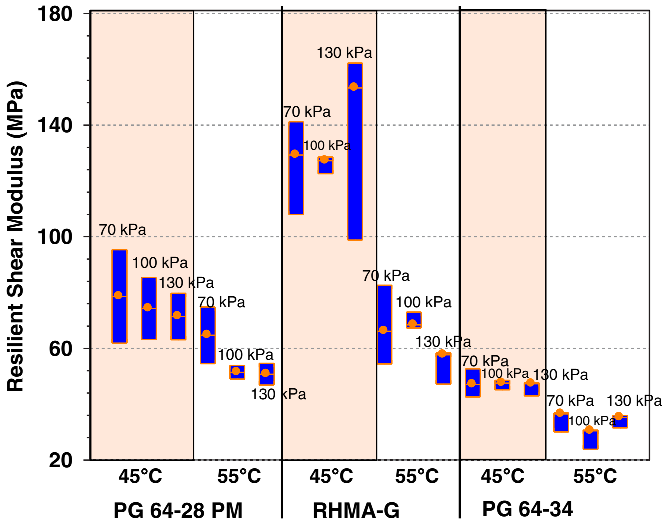

Figure N.5. Summary box plots of resilient shear modulus.

Cycles to 2% and 5% PSS

The number of cycles to 2% and 5% PSS provides an indication of the rut resistance of an asphalt mix, with higher numbers of cycles implying better rut resistance. Figures N.6 and N.7 summarize the shear test results in terms of the natural logarithm of these parameters for mixes PG 64-28 PM, RHMA-G, and PG 64-34. Results show similar trends for both parameters, although less variability is observed for the parameter number of cycles to 5% PSS. As expected, the rut resistance capacity decreased with increasing temperature and stress level. However, these parameters do not appear to be significantly affected by stress level for the RHMA-G mix. The PG 64-28 PM mix specimens had the highest number of cycles to 2% and 5% PSS for both temperatures, as expected, although the shear stiffnesses are similar for the two mixes at 55°C, and the PG 64-28 PM mix has lower stiffness than the RHMA-G at 45°C. These results show that stiffness often is not a good

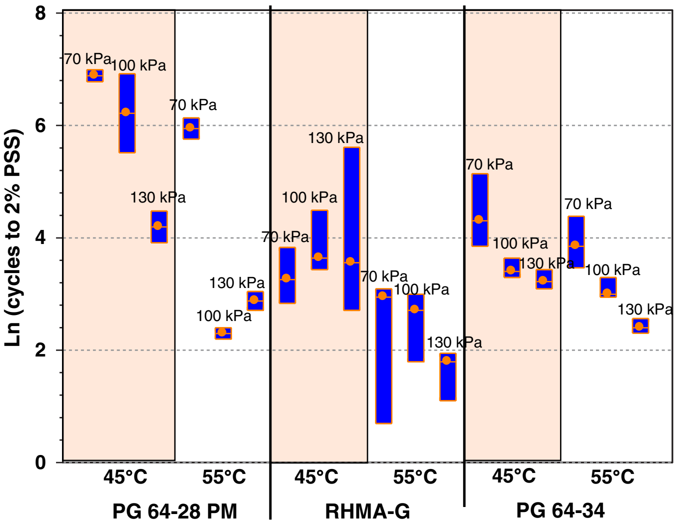

Figure N.6. Summary box plots of cycles to 2% PSS.

predictor of rutting performance for mixes with modified binders. This result is also similar to measured rutting performance for HVS test sections. The changes in the number of cycles to 2% and 5% PSS with increasing temperature from 45°C to 55°C for the mix PG 64-28 PM are higher than the change observed for the mixes RHMA-G and PG 64-34.

PSS at 5,000 Cycles

The measurement of PSS accumulated after 5,000 cycles provides an alternative indication of the rut resistance capacity of an asphalt mix. The smaller the PSS, the better the mixture's rut resistance capacity. Figure N.8 summarizes the rutting performance of the two mixes in terms of the natural logarithm of this parameter (i.e., increasingly negative values represent smaller cumulative PSS). The results indicate that

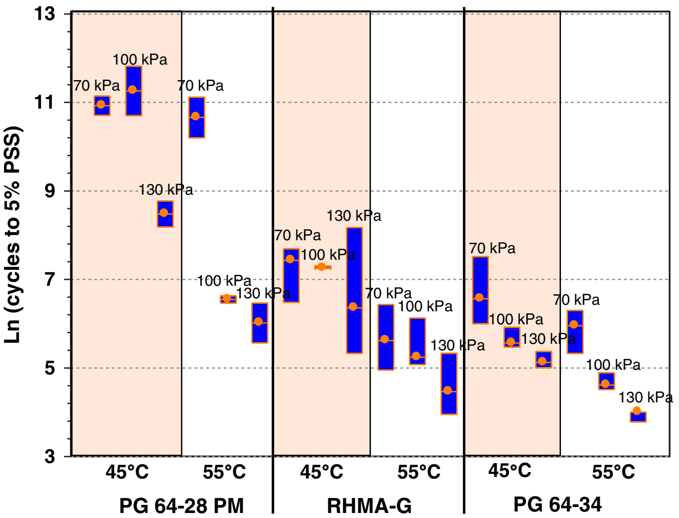

Figure N.7. Summary box plots of cycles to 5% PSS.

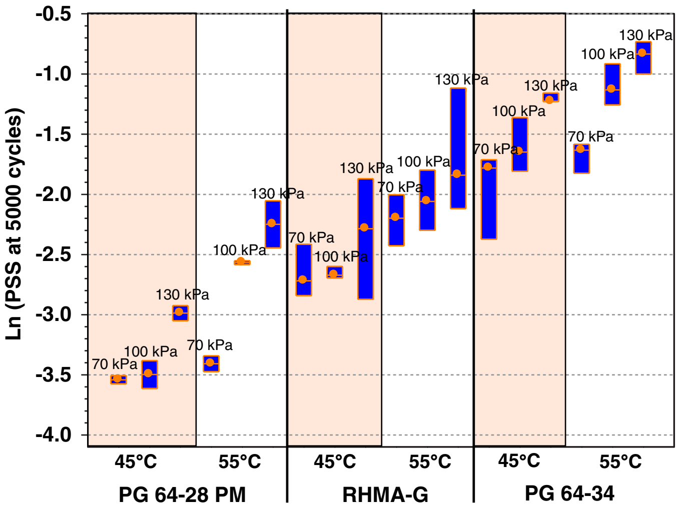

Figure N.8. Summary box plots of cumulative PSS at 5,000 cycles.

- The effect of shear stress level and temperature is more significant for PG 64-28 PM and PG 64-34 mixes.
- Mix PG 64-28 PM always has higher rut resistance.
- The higher the temperature and stress level, the larger the cumulative PSS.
- In general, mix PG 64-28 PM accumulated less PSS than did the mixes RHMA-G and PG 64-34 at the same stress level and temperature, as expected.
- Mix PG 64-34 shows the worst performance, with extremely high PSS at 5,000 cycles at 55°C.
- Variability is higher for the RHMA-G mix.

Fatigue Beam Tests

Air Void Content

Air void contents of the fatigue beams were measured using the CoreLok method (AASHTO T-331). Tables N.2, N.3, and N.4 summarize the air void distribution categorized by mix type, test temperature, and test tensile strain level for the fatigue beam and frequency sweep specimens. Figure N.9 and Figure N.10 present the summary box plots of air void content for the fatigue beam and flexural frequency sweep specimens, respectively. There was no significant difference in air void content between the specimens tested at different temperatures for the same mix type, but significant differences exist among the three mixes.

Table N.2. Summary of Air Void Contents of Fatigue Beam Specimens for Mixes PG 64-28 PM and RHMA-G

Strain (μstrain)	Temperature		PG 64-28 PM		RHMA-G	
	°C	°F	Mean	SD	Mean	SD
200	10	50	3.6	0.3	8.6	0.6
	20	68	3.7	0.2	8.9	0.4
400	10	50	4.0	0.1	9.7	0.1
	20	68	3.6	0.8	9.2	1.6
600	10	50	4.2	0.4	9.8	0.8
	20	68	4.2	1.1	9.5	0.7
800	10	50	4.2	0.7	9.6	1.2
	20	68	4.5	0.1	10.1	0.1
Overall			4.0	0.5	9.4	0.8

Note: SD = standard deviation.

Table N.3. Summary of Air Void Contents of Fatigue Beam Specimens for Mix PG 64-34

Strain (μstrain)	Temperature		PG 64-34	
	°C	°F	Mean	SD
400	10	50	6.6	0.5
	20	68	6.3	0.2
700	10	50	6.2	0.1
	20	68	6.6	0.2
Overall			6.4	0.3

Note: SD = standard deviation.

Table N.4. Summary of Air Void Contents of Flexural Frequency Sweep Specimens

Temperature		PG 64-28 PM		RHMA-G		PG 64-34	
°C	°F	Mean	SD	Mean	SD	Mean	SD
10	50	4.1	0.9	9.2	1.5	6.4	0.0[a]
20	68	4.2	0.3	8.7	0.8	6.2	0.0[a]
30	86	3.7	0.4	9.7	1.0	6.3	0.0[a]

[a] Only one specimen in tests.

Note: SD = standard deviation.

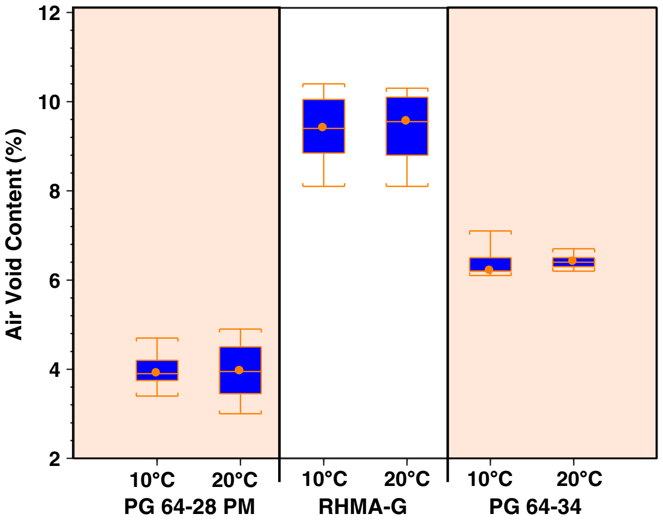

Figure N.9. Air void contents of fatigue beam specimens.

Initial Stiffness

Figure N.11 illustrates the initial stiffness comparison at different strain levels and temperatures for the three mix types of this study from the flexural fatigue tests (10 Hz). The following observations were made:

- Initial stiffness generally was strain-independent for all the mixes.
- Temperature has a significant effect on initial stiffnesses for all mix types.

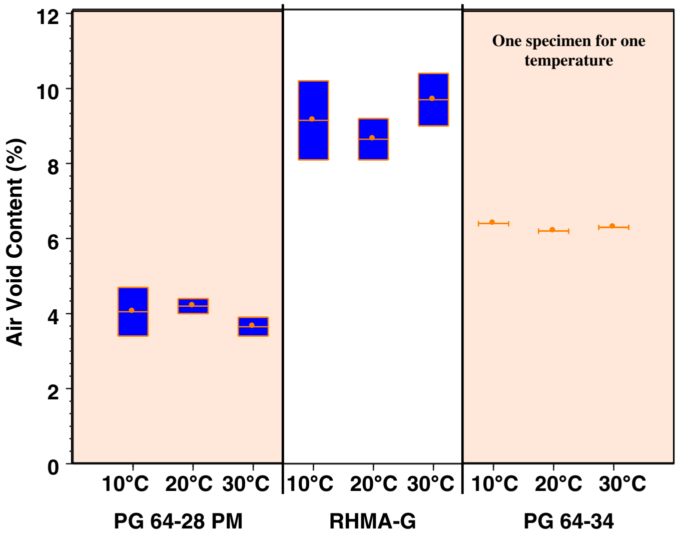

Figure N.10. Air void contents of flexural frequency sweep specimens.

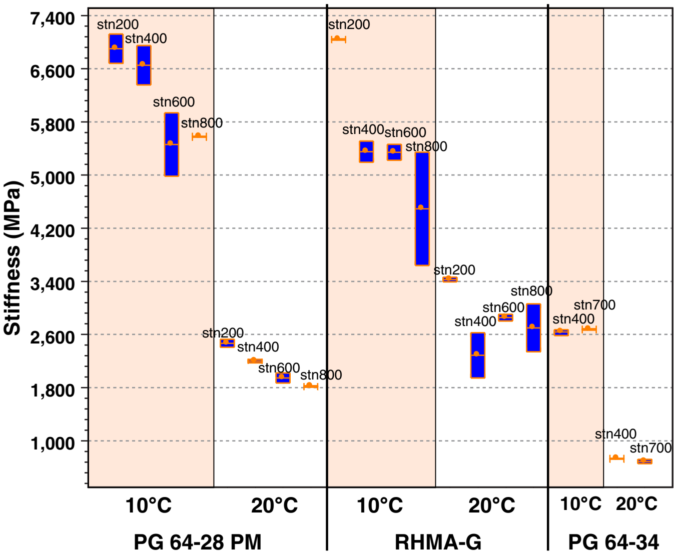

Figure N.11. Summary box plots of initial stiffness. (Stn = strain.)

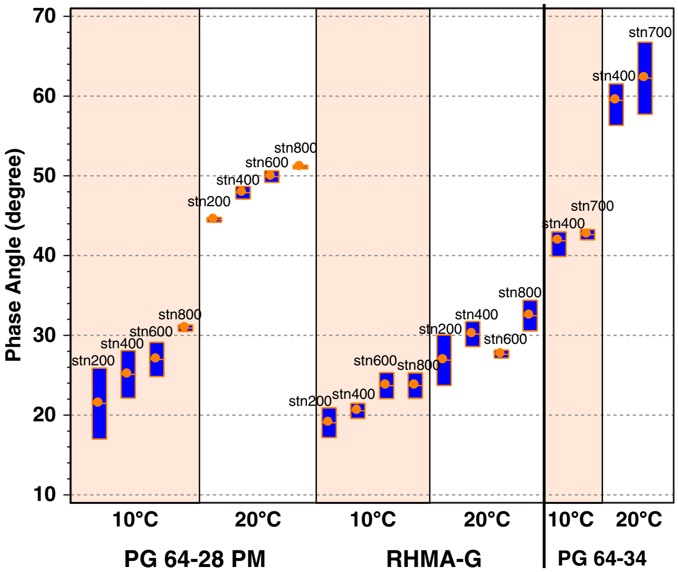

Figure N.12. Summary box plots of initial phase angle. (Stn = strain.)

- Initial stiffness values for mixes PG 64-28 PM and RHMA-G are similar for temperatures 10°C and 20°C. The PG 64-34 is considerably softer than the other two mixes at both temperatures.

Initial Phase Angle

The initial phase angle can be used as an index of mix viscoelastic properties, with higher phase angles corresponding to more viscous and less elastic behavior. Figure N.12 illustrates the side-by-side phase angle comparison of mixes PG 64-28 PM, RHMA-G, and PG 64-34. The following observations were made:

- The initial phase angle increased with increasing temperature, as expected.
- Temperature sensitivity of the initial phase angle was higher for mixes PG 64-28 PM and PG 64-34 than for RHMA-G.
- The initial phase angle appeared to be strain-dependent for all mixes.
- The initial phase angle was highly negatively correlated with the initial stiffness for PG 64-28 PM and PG 64-34 mixes, whereas the correlation was weaker for mix RHMA-G.
- There was no significant difference between the PG 64-28 PM and RHMA-G mixes in terms of initial phase angle at 10°C, whereas higher initial phase angles were measured for the PG 64-28 PM mix at 20°C.
- Phase angles are highest for the PG 64-34 mix at both temperatures, indicating a great ability to relax constant or near-constant stresses at these temperatures.

Fatigue Life at 50% Stiffness Reduction

Damage in the flexural fatigue test appears as a decrease in mix stiffness with increasing repetitions. Conventional fatigue life is defined as the number of load repetitions when 50% stiffness reduction has been reached. A high fatigue life implies a slow fatigue damage rate and consequently higher fatigue resistance for a given strain or deformation. The side-by-side fatigue life comparison of mixes PG 64-28 PM, RHMA-G, and PG 64-34 is plotted in Figure N.13. The following observations were made:

- Fatigue life was strain-dependent. In general, lower strains resulted in higher fatigue life and vice versa, as expected.
- Fatigue life was also temperature-dependent, although it is not as significant as strain dependency. Higher fatigue life was observed at 20°C.
- PG 64-34 mix appeared to have a longer fatigue life at both test temperatures than did the RHMA-G and PG 64-28 PM mixes, which is typical of softer mixes compared with stiffer mixes for a given deformation or strain.
- Fatigue life at constant strain (or deformation) generally is a good indicator of fatigue life under reflective cracking conditions because strains and deformations are not controlled by the mix stiffness unless the material is in a thick layer over the cracks or joints, and generally softer mixes such as the PG 64-34 will have longer fatigue lives under these conditions.

Flexural Frequency Sweep

The average stiffness values of the two replicates tested at the three temperatures were used to develop the flexural complex

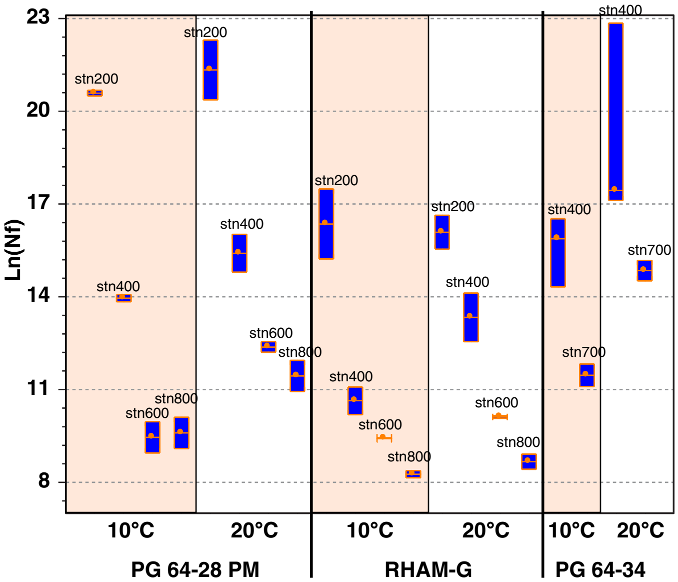

Figure N.13. Summary box plots of fatigue life. (Stn = strain.)

modulus (E*) master curve for the PG 64-28 PM and RHMA-G mixes, whereas only one mix (no replicates) was used for the PG 64-34 mix. This is considered a useful tool for characterizing the effects of loading frequency (or vehicle speed) and temperature on the initial stiffness of an asphalt mix (i.e., before any fatigue damage has occurred). Measured E* values are given in Figures N.14, N.15, and N.16 for mixes PG 64-28 PM, RHMA-G, and PG 64-34, respectively. It can be observed that variability in test results is very small. Phase angles are also given in Figures N.17, N.18, and N.19 for mixes PG 64-28 PM, RHMA-G, and PG 64-34, respectively. The shifted master curve with minimized residual-sum-of-squares derived using the Excel solver routine can be fitted with the modified gamma function shown in Equation N.1:

$$E^* = D + A\cdot\left(1-\exp\left(-\frac{(x-C)}{B}\right)\cdot\sum_{m}^{n-1}\frac{(x-C)^m}{B^m m!}\right) \qquad \text{(N.1)}$$

where

E^* is the flexural complex modulus (MPa),

$x = \ln \text{freq} + \ln aT$ is the loading frequency in Hz and $\ln aT$ can be obtained from the temperature-shifting relationship (Equation N.2), and

A, B, C, D, and n are the experimentally determined parameters.

$$\ln aT = A\cdot\left(1-\exp\left(-\frac{T-T_{\text{ref}}}{B}\right)\right) \qquad \text{(N.2)}$$

where

$\ln aT$ is a horizontal shift to correct the temperature effect with the same unit as ln freq;

T is the temperature in °C;

T_{ref} is the reference temperature, in this case, $T_{\text{ref}} = 20°\text{C}$; and

A and B are the experimentally determined parameters.

The experimentally determined parameters of the modified gamma function for each mix type are listed in Table N.5, together with the parameters in the temperature-shifting relationship.

Figures N.20 and N.21 show the shifted master curves with gamma-fitted lines and the temperature-shifting relationships, respectively. The temperature-shifting relationships were obtained during the construction of the complex modulus master curve and can be used to correct the temperature effect

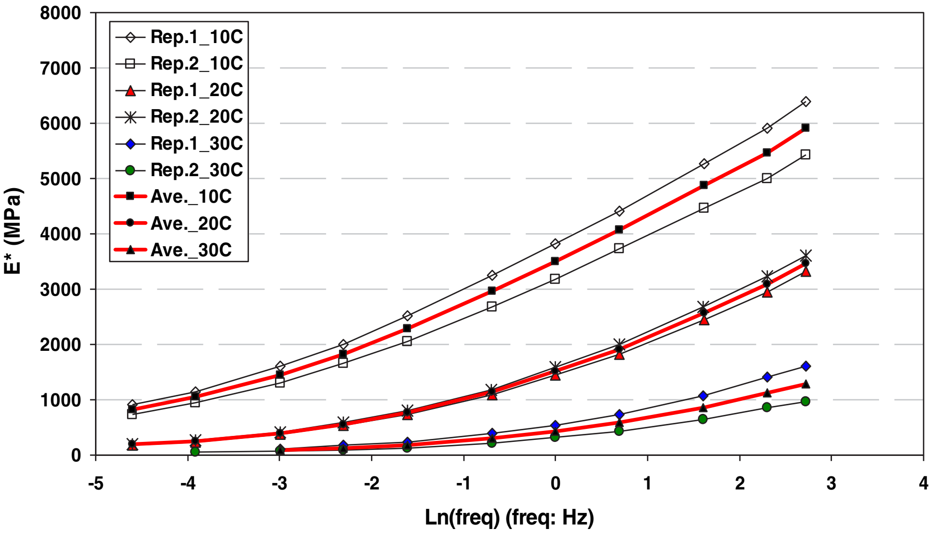

Figure N.14. Measured E* values for mix PG 64-28 PM.

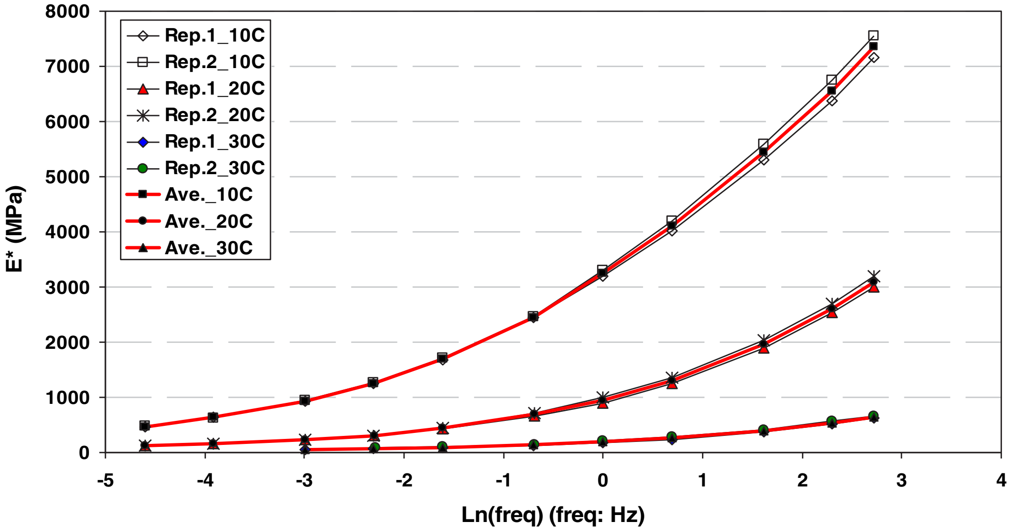

Figure N.15. Measured E values for mix RHMA-G.*

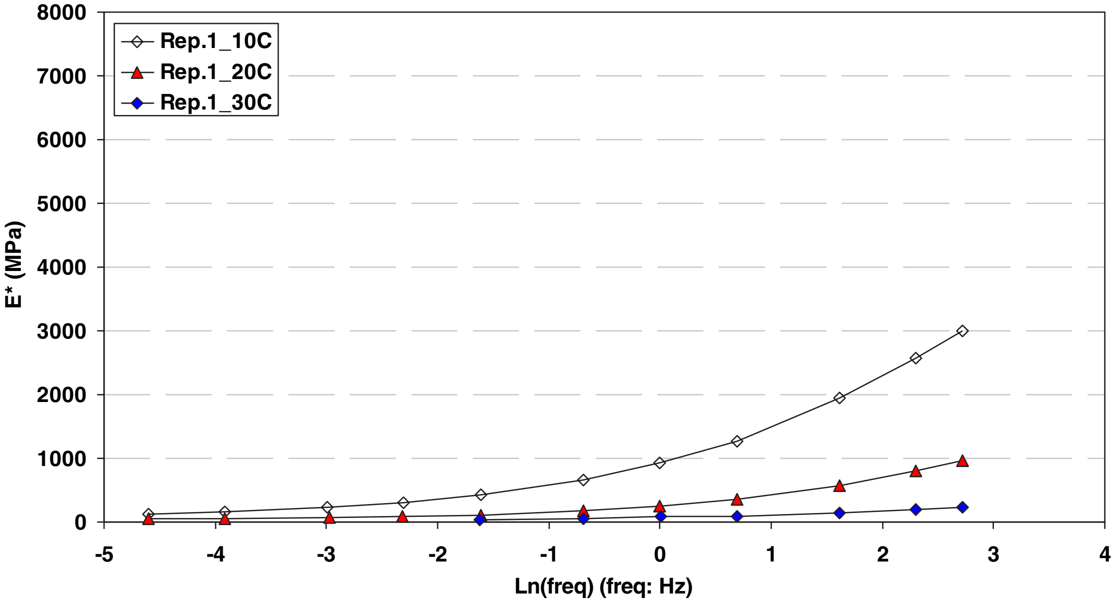

Figure N.16. Measured E values for mix PG 64-34.*

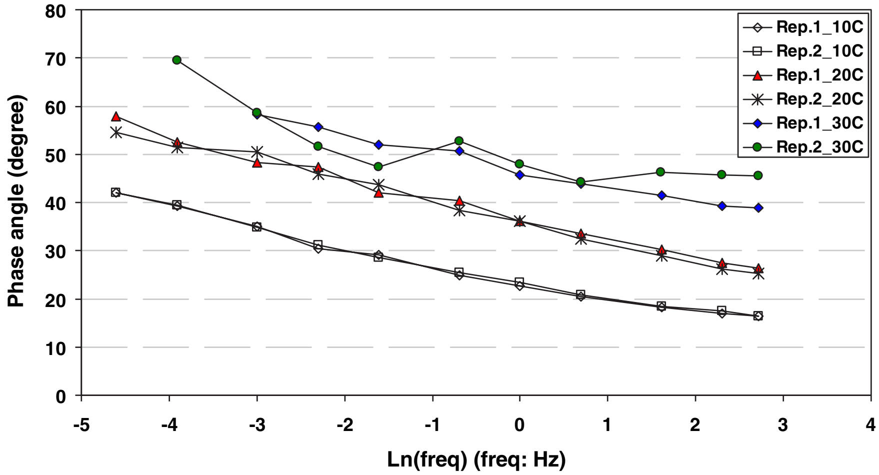

Figure N.17. Measured phase angles for mix PG 64-28 PM.

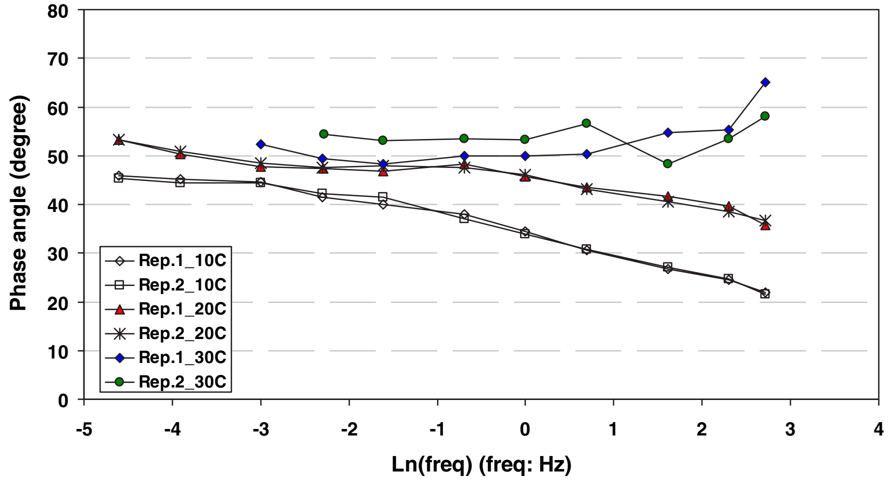

Figure N.18. Measured phase angles for mix RHMA-G.

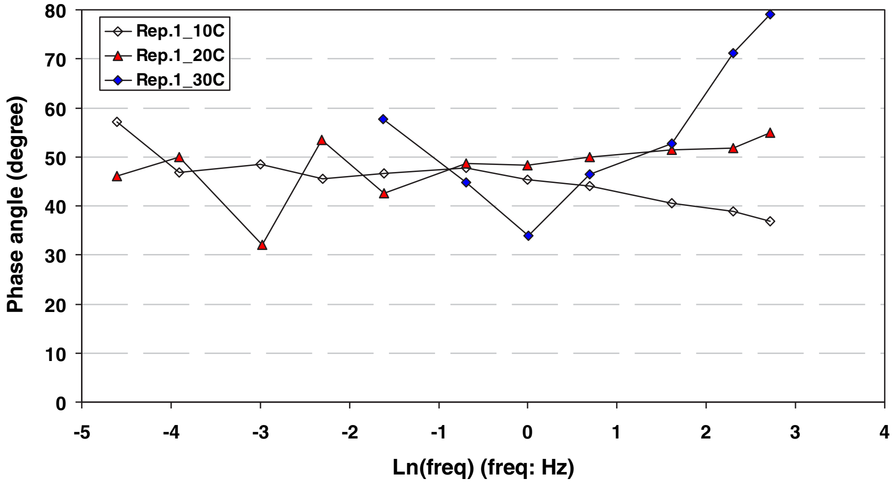

Figure N.19. Measured phase angles for mix PG 64-34.

Table N.5. Summary of Master Curves and Time-Temperature Relationships

	Master Curve					Time-Temperature Relationship	
Mix	**N**	**A**	**B**	**C**	**D**	**A**	**B**
PG 64-28PM	4	18,079.41	4.530603	–7.133406	134.1760	–1,275.0121	4,226.596
RHMA-G	4	186,792.79	9.344232	–6.032686	115.2986	–4,467.6430	15,040.775
PG 64-34	4	10,211.74	9.885365	–7.096904	52.10614	46.3571	–172.28

Note: The reference temperature is 20°C. Master curve gamma-fitted equations: $n = 4$,

$$E^* = D + A \cdot \left(1 - \exp\left(-\frac{(x-C)}{B}\right) \cdot \left(1 + \frac{x-C}{B} + \frac{(x-C)^2}{2B^2} + \frac{(x-C)^3}{6B^3}\right)\right),$$ where $x = \ln \text{freq} + \ln aT$. Time-temperature

relationship: $\ln aT = A \cdot \left(1 - \exp\left(-\frac{T - T_{\text{ref}}}{B}\right)\right)$.

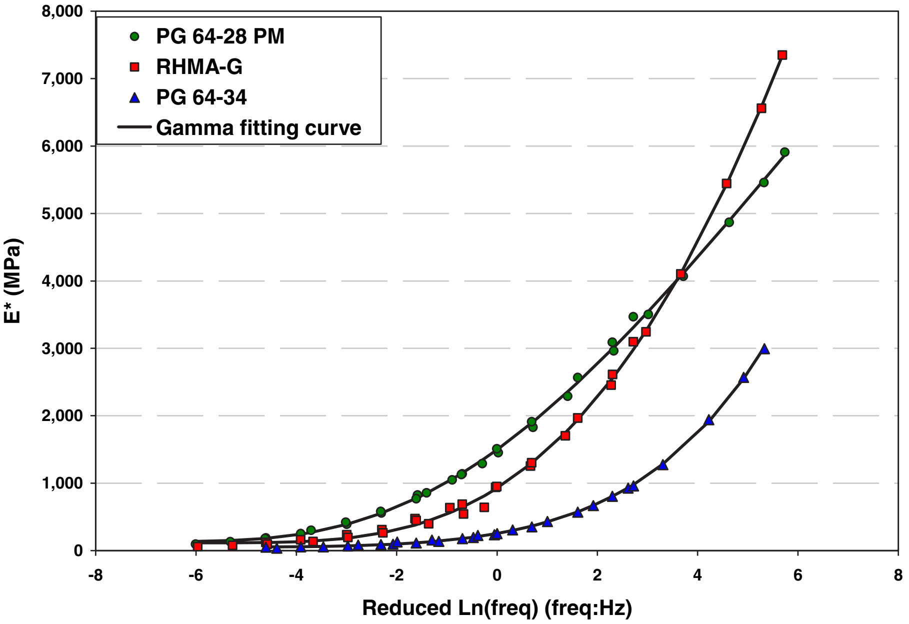

Figure N.20. Complex modulus (E) master curves.*

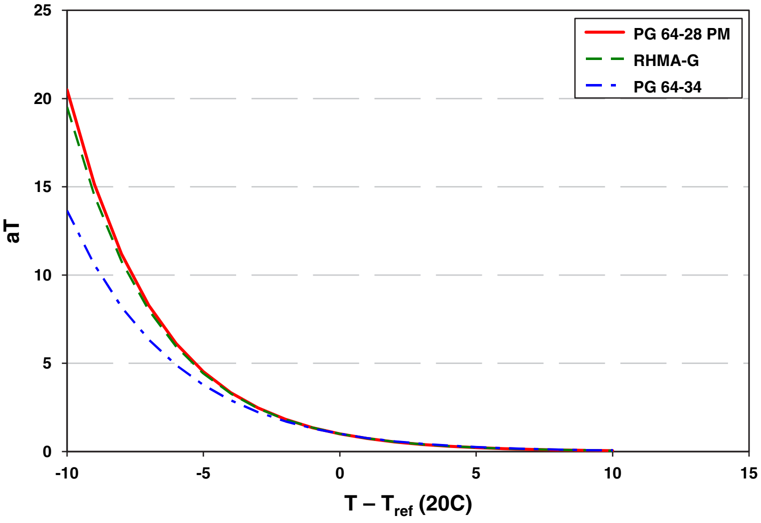

Figure N.21. Temperature-shifting relationship.

on initial stiffness. Note that a positive lnaT value needs to be applied when the temperature is lower than the reference temperature, whereas a negative lnaT value needs to be used when the temperature is higher than the reference temperature.

The following observations were made from the frequency sweep test results:

- Similar to the stiffnesses measured in fatigue test, significantly lower stiffnesses were measured for PG 64-34 mix.
- The complex modulus curves of the mixes showed that PG 64-28 PM and PG 64-34 mixes are less susceptible to loading frequencies than is the RHMA-G mix (Figure N.20).
- The temperature-shifting relationships indicated that there were no apparent temperature-sensitivity differences between the mixes PG 64-28 PM and RHMA-G, whereas mix PG 64-34 appeared to be less susceptible to temperature changes.

APPENDIX O

HMA/PCC Bonding and Friction Literature

Introduction

Bonding, in terms of pavement design and construction, is the adherence of different pavement layers to one another. Friction between the layers relates specifically to horizontal slippage between two layers, not necessarily vertical adhesion. In this appendix, the word "bond" is used, but this implies full horizontal friction with zero slippage between layers. Typical construction of asphalt pavements consists of laying thin lifts of hot-mix asphalt (HMA) on top of one another to a desired total height, allowing for easy and uniform compaction of the pavement surface. For composite pavements, an asphalt layer is placed directly on a new (hardened) portland cement concrete (PCC) surface. To ensure a good bond and friction between layers, tack coats are used as an adhesive to bond layers together. Materials used for tack coats include asphalt binder, cutbacks, and emulsions. The use of cutbacks has been banned in many places because of the evaporation of volatile petroleum solvents, which are considered harmful to the environment.

Tack coats are applied to a clean, broomed paving surface before paving. The amount of time before the HMA lift is laid down depends on the type of tack used. If an emulsion is used, the water must be allowed to evaporate from the solution before paving. The speed of the paving operation must also be considered to reduce the amount of construction equipment tracking through applied tack coats. Tack coats are applied from a spray bar at the rear of a tanker. Nozzles used to distribute tack should overlap material to ensure uniform coverage. They should be applied as uniformly as possible, covering about 90% of the surface. The application rate of the tack depends on many factors, including surface condition of the lower pavement surface, tack material, and weather. Many studies have been conducted to determine the optimal application rate of specific tack materials. Only as much tack coat as is needed to achieve an optimal bond should be applied. Excess tack can act as a lubricant that decreases bond and can cause bleeding in thin overlays from changes in mix properties (Flexible Pavements of Ohio 2001). For HMA overlays over PCC pavements, additional tack coat is recommended because achieving bond is more difficult (Collop et al. 2003). Romanoschi and Metcalf (2001) also documented a situation in which a Tennessee asphalt overlay was applied without tack coat on a surface that had small loose milling. Paving the overlay melted the millings, yielding an unintended bonding layer between HMA courses.

In current construction practices, it is assumed that the tack coat adhesive fully bonds the pavement layers into one integral unit. However, this assumption may not be true. Deviation from good bond usually originates from nonoptimal use of tack coats and choosing aggregates with little aggregate interlock (Mejía et al. 2008). Poor bond can result in many different pavement distresses that decrease the pavement structural strength and life, including top-down cracking, potholes, and fatigue failure (Wheat 2007). However, poor bond is most commonly associated with slippage failure. Slippage failure can be seen as curved surface grooves or crescent shaped cracking opposite to the direction of traffic (Mejía et al. 2008). It is believed that high horizontal stresses and dynamic normal loads in areas where vehicles accelerate, break, and turn are the main cause of slippage failure (West et al. 2005; Mejía et al. 2008).

Objective

The influence of bond condition on pavement life has been investigated. For example, Kruntcheva et al. (2004) completed a theoretical study on the effect of poor bonding on asphalt pavement performance. The study consisted of a BISAR analysis with varying pavement interface horizontal shear compliance (horizontal displacement/shear stress) conditions. These values were applied to University of Nottingham pavement performance regression models for fatigue and rutting life. Fatigue and rutting life data, normalized to the full bond condition at failure, were plotted against horizontal shear stiffness. For the full bond condition, failure depended on subgrade stiffness. For subgrades of less than 80 kPa, the pavement failed in rutting.

For those greater than 80 kPa, the pavement failed in fatigue. Additional analysis showed that decreased bond strength between the binder base HMA courses result in as much as 80% reduction in life, which was similar to the findings of other studies. Pavement performance was not significantly increased by increasing the subgrade stiffness past 40 kPa for poor to no bond between the asphalt layers (Kruntcheva et al. 2005). A similar study was done by Roffe and Chaignon (2002) using the French layered elastic program ALIZE. Their results showed about a 12-year loss of life from a lack of bond on a 20-year design life pavement (West et al. 2005).

However, most of the studies are limited in scope, and there is no agreement with respect to the role played by bonding, how to model its behavior in the context of pavement design, and how to experimentally determine relevant properties that can be used in pavement design and construction. The objective of the current literature search is to summarize the relevant research efforts dealing with bonding and to identify the areas that need to be further developed to fully understand the role played by the bond between the different pavement surface layers. The *Mechanistic–Empirical Pavement Design Guide* (*MEPDG*) allows only for full bond/friction or for zero bond/friction. Certainly zero bond/friction never exists in composite pavements, but partial bond/friction (with slippage) exists in more situations than is probably known. However, full bond/friction is always assumed in design, or the pavement would require unrealistically thick layers.

Interface Modeling

Originally, bond could be described only as either full bond or full slip (no bond). Uzan et al. (1978) presented the first solutions for multilayered pavement layers with partially bonded interfaces, where the Goodman constitutive model was used to describe interface performance to loading, as shown in Equation O.1.

$$\tau = K \cdot \Delta u \tag{O.1}$$

where τ is the interface shear stress, K is the horizontal interface reaction modulus, and Δu is the relative change in displacement of the two interface faces.

Romanoschi and Metcalf (2001) introduced a new constitutive model for HMA layer interface. Previous models assumed full bond between layers when it is likely not the case. Some other models allow for a bonding coefficient that is difficult to choose because there is not a standardized testing procedure to measure it. The new model consists of two phases. The first phase models the shear displacement linearly increasing with shear stress (interface reaction modulus) to the maximum shear strength of the interface. This is the Goodman constitutive model. The second phase models postfailure behavior at the interface, where surface friction between the layers provides the only resistance to slippage (Romanoschi and Metcalf 2001).

Direct shear tests were conducted at different loadings and temperatures, with and without tack coating. Stress versus displacement measurements were used to develop the mechanical model. Shear fatigue tests were also completed to find interface shear fatigue resistance. The results of the direct shear test show that the interface model can be described by the interface reaction modulus, the max shear strength, and surface friction coefficient. These parameters are temperature dependent. The friction coefficient used in the second phase is not affected by the normal loading. The interface reaction modulus and interface shear strength do not change with normal loading when a tack coat is used but do change without tack coat use. The interface can fail in fatigue, where there is a linear increase in permanent shear displacement to number of load repetitions (Romanoschi and Metcalf 2001).

Kruntcheva et al. (2006) provided a technical note for the experimental investigation of factors affecting bond between pavement layers using the Nottingham shear box apparatus. Only application rate and temperature were considered as experimental factors, not type of bonding material. Displacements to multiple magnitudes of cyclic horizontal loadings were measured with linear voltage differential transducers (LVDTs) in the vertical and horizontal directions. Samples that did not fail under dynamic testing were tested again under displacement controlled conditions to failure. Three-dimensional FE models of bonded and weakly bonded specimens were created to yield a shear stress distribution along the interface to aid in the analysis of the test results. The experimental results showed that the interface properties depend more on the type of materials in contact rather than the tack coat application rate and the interface condition. It was shown that a dry and clean interface with no tack coat performs in a manner similar to that of an interface with a (British) standard quantity of tack coat. No tack coat would be needed in this situation. The results of the shear box test must be analyzed with care because of the complex behavior at the interface under a horizontal load. Models show that the failure mode of a weak interface is not purely in shear but has an additional vertical bending-like movement at the surface course, between the points of normal load application that causes larger normal strains at the interface and failure. It was suggested that the interface bond should be described by introducing a vertical shear reaction modulus, as well as using the horizontal shear reaction modulus that describes the interface stiffness in the vertical direction from horizontal loads (Kruntcheva et al. 2006).

Interface Testing Methods

Shear Test

From the research conducted, shear testing is the most popular method for determining interface bond shear strength in the laboratory. The generic test setup is shown in Figure O.1

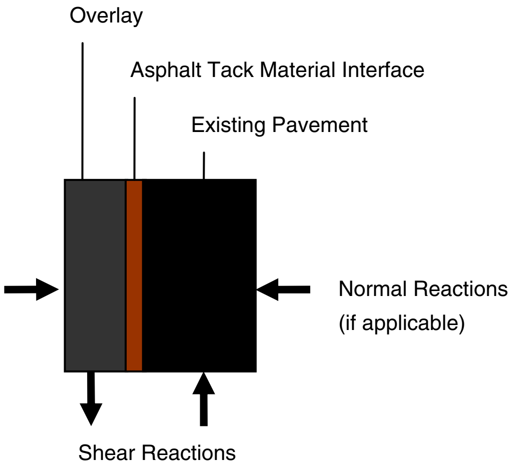

Figure O.1. Typical shear testing schematic.

and consists of loading one pavement layer to create a shear failure at the bond interface.

Leutner Test

The Leutner test is a German standardized direct shear test used since 1979 to measure the bond between two asphalt layers (Kruntcheva et al. 2004). Testing specimens consist of 150-mm cylinders with a minimum of two bonded layers. Specimens can be either laboratory made or field cores. The testing is run under displacement control in the apparatus at a rate of 50 mm/minute. There is only one test temperature, 20°C, for this test. No normal force is applied to the specimen, only a shear force. The shear force on the specimen is measured and plotted against the shear displacement. The plot can yield a maximum shear stress and shear displacement. Typical plot curves are nonlinear, which makes finding a tangential derivate (shear modulus reaction) difficult (Collop et al. 2003).

Swiss Standard SN 671 961 is a standardized testing method and criteria used for evaluating the bond strength of HMA layers. The standard uses a layer-parallel direct shear (LPDS) tester apparatus developed for the Leutner test. Cores are loaded at 2.0-in./minute. Swiss interlayers require a minimum shear force of 3,372 lbf for wearing-binder course bonds and 2,698 lbf for other bonds (West et al. 2005).

FDOT Test

The Florida Department of Transportation (FDOT) designed a simple test apparatus that conducts direct shear test for tack coat. Six-inch road cores or laboratory specimens are used for analysis. The machine is run in displacement control at a rate of 2-in./minute. Samples are tested where the shear direction matches the vehicle traffic direction. Samples are tested at 77°F inside an environmental chamber. The horizontal gap between the shear rings is set at 3/16 in. and accommodates for interface skewness for cores not drilled parallel to the roadway, bending stresses in the cores, and irregular core surfaces. The shear strength at the interface is calculated by Equation O.2 (Sholar et al. 2002):

$$\tau = \frac{4 \cdot P}{\pi \cdot D^2} \tag{O.2}$$

where τ is the interface bond strength in pounds per square inch (psi), P is the maximum load at failure in poundforce (lbf), and D is the specimen diameter in in.

NCAT Bond Strength Device

The National Center for Asphalt Technology (NCAT) conducted a two-phase study to develop a new test and testing procedure for asphalt bond properties for the Alabama Department of Transportation. The first phase consisted of a statistical factorial designed experiment to investigate the major factors that affect asphalt bond tested with the NCAT Bond Strength Device, pictured in Figure O.2.

Test temperature, normal loading on the specimen, tack coat material, aggregate gradation and application rate had the greatest effects in the laboratory shearing experiment. From the results of the first phase, NCAT developed an "easy" bond strength testing procedure for different asphalt layers. The procedure and device were assessed with a field experiment in the second phase of the study. Test sections with varying amounts of tack material were created from seven separate pavement construction projects. Cores were taken from the test sections to test the developed procedure and compared with measured tack material application. The second phase showed that the ASTM standard procedure for measuring the application rate of asphalt material works very well, milled asphalt concrete surfaces produce higher bond strength values, and the performance grade (PG) asphalt binder used in the study works just as well as the asphalt emulsions used (West et al. 2005).

ASTRA

Canestrari et al. (2005) studied interface behavior by developing a testing device to measure shear stress resistance. The Italian Ancona Shear Testing Research and Analysis device (ASTRA) resembles the direct shear test used in soil mechanics. Different parameters were taken into account in the exploratory study, including type of emulsion, sample preparation method, and curing time. Mohr-Coulomb failure criteria is a theory used in reporting results of bond strength. The peak shear stress is the parameter that expresses the effectiveness of the interface bonding. The results of the ASTRA device were compared with results of similar tests conducted by the LPDS test. Results from the different testing methods are different but

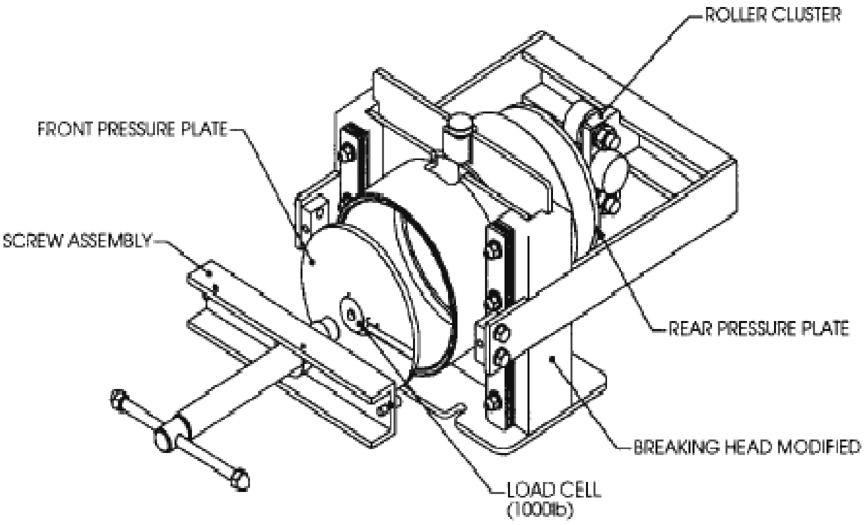

Figure O.2. Diagram of NCAT bond strength device.

comparable. A correction factor of 3 is needed to convert an ASTRA to the LPDS peak shear stress value.

Torsion Testing

Torque Bond

The torque bond test originally was developed in Sweden as a field test and currently is used to measure bond strength of ultrathin surface courses in the United Kingdom. A 100-mm core is drilled into the pavement to a depth of 20 mm below the desired bonded layer for testing but not removed from the pavement. A circular metal plate is bonded to the top of the core, parallel to the surface. When the adhesive has cured, a torque meter is attached to the metal plate. A constant torque is applied to the metal plate at a rate of 3 degrees per second to create a twisting shear stress in the specimen. The test is conducted until 300 N-m is reached or the specimen fails. A study by Tashman et al. (2006) used a failure criteria of 400 N-m.

$$\tau = \frac{12 \cdot T \times 10^6}{\pi \cdot D^3} \tag{O.3}$$

where τ is the interface bond strength in kilopascals (kPa), T is the maximum torque at failure in newton meters (N-m), and D is the core diameter in millimeters (mm). Typically, six samples are used to report the average bond strength (Tashman et al. 2006).

There is also a laboratory torque bond test that is similar to the field test but provides a more controlled testing location. Instead of the core remaining in the pavement, the core is made to a minimum depth of 80 mm past the surface course. The core is removed and placed in an apparatus, where the core is exposed at least 20 mm above the apparatus clamp. Unlike the field test, for which the temperature after failure is recorded, the laboratory torque test is done at 20°C (Tashman et al. 2006).

Tension Testing

ATACKer

ATACKer was developed by InstroTek Inc. for evaluating the tensile and shear strength of tack coat applications and patented in January 2007. The device, which is similar to that described in ASTM D4541, determines adhesive strength of tack coat applications by applying normal pressure to a test plate with tack coat and recording the tensile force or torque required to break the tack coat bond between the two test plates.

The test begins by compressing a circular aluminum plate onto a specimen of cured tack coat to standard normal force of 40 lbf for 60 seconds. Then the force needed to completely remove the contact plate from the testing surface by either tension or torque-shear is recorded. The equations for tensile strength (σ_t) and shear strength (τ) are given in Equation O.4.

$$\sigma_t = \frac{P}{A} = \frac{4P_u}{\pi d^2}$$
$$\tau = \frac{Tr}{J} = \frac{2T_u r}{\pi r^4} = \frac{2T_u}{\pi r^3} \tag{O.4}$$

where P_u is the ultimate tensile load, J is the polar moment of inertia, d is the diameter of the contact plate, T_u is the ultimate torque, and r is the distance from the turning axis (radius of contact plate).

Because of a variation in the tensile and shear strength of the tack coat materials and limitations of the load gauges, different contact plate diameters were tested and selected to test PG binder grades, nondiluted emulsions, and diluted emulsions. Both 0.5- and 1-in plates were used to test PG binders. Nondiluted emulsions were tested with a 2-in. plate, and diluted emulsions were tested with a 5-in. diameter plate (Buchanan and Woods 2004).

UTEP Pull-off Apparatus

The UTEP test was developed in 2004 at the University of Texas–El Paso and used to measure in-situ tack coat tensile strength. A circular piece of "moisture bearing foam" is attached to a metal plate by double-sided tape. After the tack coat is applied and allowed to set for 30 minutes, the metal plate is lowered to the pavement. A surcharge weight of 40 pounds is applied to the apparatus, to allow the bearing foam to properly adhere to the tack coat. After 10 minutes of surcharge loading, the surcharge is removed and a torque is applied to the loading screw. The screw lifts the central rod that is connected to the metal plate. The maximum torque needed to remove the plate from the tack coat is converted to a tensile strength by using a calibration factor. The calibration factor is predetermined and obtained from fitting a linear trend line through data from testing multiple loads and corresponding removal torque values (Tashman et al. 2006).

Wedge Splitting Test

Tschegg et al. (1995) developed a procedure for measuring the fracture mechanics behavior of layer bonding. A wedge splitting test, is essentially a tension test because debonding results from the wedge pushing the substrates apart at the interface. The test is used to record load-displacement curves of notched asphalt samples under stable crack propagation along the interface until failure (separation). Integrating the curve and dividing by the fractured area yields the specific fracture energy, a material property measuring resistance to crack growth. This parameter is independent of specimen shape if specimen size effect is minimized. This value is used to characterize the bond strength. Experimental results of fracture experiments with a finite element model were presented in a simple example using measured material values and the concept of "damage simulation," for which "damage" means the material modulus decreases to zero during fracture. The model produces details on deformation, and fracture behavior of pavements can be made from repeating the simulation with different bonding and material behaviors.

Other Test Methods

RSD

The rock strength device (RSD) was designed by the University of Minnesota for measuring strength parameters (internal friction angle and cohesion) of sedimentary rocks. The device is based on other industry scratch based tests used to measure adhesion of coatings on various surfaces. This test is based on the rock cutting model that involves a combination of "pure" cutting and the cutter head contact friction. Uniaxial compressive strength is directly related to the intrinsic specific energy and the ratio of vertical to horizontal force on the cutting face (Zofka et al. 2004).

The RSD machine consists of a frame that holds the sample and a moving cart that holds the vertical positioning system, load cell to measure vertical and horizontal force, and a diamond cutting head to cut the rock. Cutting velocity and depth are variable with precise fine adjustments. A sample is tested by scratching the specimen at a constant cutting depth with sharp and/or dull cutters, whereas the load cell measures the cutting forces. Dull cutters measure the internal friction angle, and sharp cutters measure the cohesive properties of the sample (Zofka et al. 2004).

LCB Test

The Laboratorio de Caminos de Barcelona developed a bond interface test that was better suited for the testing equipment and procedures used in Spain. Cylindrical samples or field cores are simply supported on the testing apparatus and loaded under three-point bending to generating shear stresses at the interface bond. The bond area is slightly offset from one of the supports to minimize bending moments but still allowed to generate shear. The test measures resistance to tangential stress produced between the bond and the deformation/displacement of the layers with respect to each other (Recasens et al. 2005).

Impulse Hammer

Kruntcheva et al. (2006) performed an exploratory study on the use of a nondestructive impulse hammer test method to measure bond condition beneath thin asphalt surfaces. Several interface conditions were quantified and compared. These conditions ranged from bonded to debonded interfaces with varying thicknesses. Responses to the instrumented impulse hammer loading were measured by accelerometers close to the impact location. Cores from specific test points were taken and tested using the Leutner method to compare the results of the impulse hammer. Leutner test results are similar to the predicted condition determined by the impulse hammer testing. A finite-element analysis was used to give a greater understanding of thin surface course response of various amount of bond. The models showed that impulse loading caused completely different responses in the samples for the differences in bonding. The response differences seen were determined to result from vibration of the upper pavement layer, rather than wave reflective from the sample.

The results of the impulse hammer testing indicate this method could be an efficient and relatively economic way to predict localized debonding. Bond information can be taken from a thin surface of approximately 10 to 50 mm thick, over an area of radius of 300 mm. Visual inspection of the impulse loading could give qualitative information about the interface bond. Layer thickness can be measured using the device from the frequency of the maximum transfer function estimate. Larger wave frequencies indicate thicker lifts. The benefits of not destroying the pavement to test for bond also make this test very attractive in the field. Additional research is needed to develop a consistent procedure for different materials (Kruntcheva et al. 2004).

Indirect Test

Freund and Suresh (2004) describe an indirect test for testing interface fracture properties used in materials joined by diffusion bonding, welding, explosive cladding, and brazing. The test resembles the Brazilian rock test that is used to test mixed-mode fracture mechanics properties of brittle solids. A thin film is applied to a thick substrate, as shown in Figure O.3, with an initial precrack, typically made by adding a small layer of carbon to prevent the film from bonding. Testing consists of applying a compressive load to the specimen and rotating the interface to some orientation θ. Pure tension fracture (mode I failure) occurs at $\theta = 0$ degrees. If θ is not 0 degrees, the phase angle is not 0 at the edge of the delamination zone. By varying θ between 0 and 90 degrees for a homogeneous material, the crack edge opening and shear stress intensity factor (K_{I} and K_{II}) can be found using Equation O.5.

$$K_{\mathrm{I}} = \frac{P \cdot p_{\mathrm{I}}}{R}\sqrt{\frac{a}{\pi}} \qquad K_{\mathrm{II}} = \frac{P \cdot p_{\mathrm{II}}}{R}\sqrt{\frac{a}{\pi}} \tag{O.5}$$

where P is the compressive load, t_f is the film thickness, R is the specimen radius, θ is the angle of inclination, a is the crack length, K_I is the stress intensity factor for a particular failure mode, and p_i is the nondimensional function of relative crack size a/R and loading angle θ.

Double Cleavage Drilled Compression Indirect Test

Freund and Suresh (2004) describe a compression test that evaluates interface fracture toughness. The testing specimen is a rectangular block of material (substrate) with a thin layer of adhesive at the central interface of the block (Figure O.4). Typically, at least one of the substrates is made of a transparent material, such as sapphire single crystal or glass, to measure the crack with a microscope during testing. A circular hole is drilled in the center to create a stress concentration in the specimen. When loaded, the specimen will fracture there under controlled conditions. Under compressive loading parallel to the interface, tensile stresses develop at the poles of the hole, where cracking initiates and propagates along the interface.

For a homogeneous brittle solid, the energy release rate (ς) for fracture is estimated using Equation O.6, obtained from the results of a finite element calculation of specimen deformation. The crack growth will be stable in this test configuration because of the energy release rate decreasing with crack propagation and a fixed load. Specimens made with two different substrate materials will not have an energy release rate given by Equation O.6. The modeling equation is more complicated because the stress field is not symmetric with respect to the cracking plane and yields a mixed failure mode.

$$\varsigma = \frac{\pi \cdot \sigma^2 \cdot R}{E_s}\left[\frac{h_s}{R} + \left(0.235\frac{h_s}{R} - 0.259\right)\frac{a}{R}\right]^{-2}$$

$$\sigma = \frac{P}{2h_s}$$

$$\text{when } \frac{h_s}{R} \le \frac{a}{R} \le 15 \quad \text{and} \quad 2 \le \frac{h_s}{R} \le 4 \tag{O.6}$$

where h_s is half the thickness of the specimen, R is the radius of the hole, a is the crack/debonded length, σ is the nominal compressive stress from applied load P, and E_s is Young's

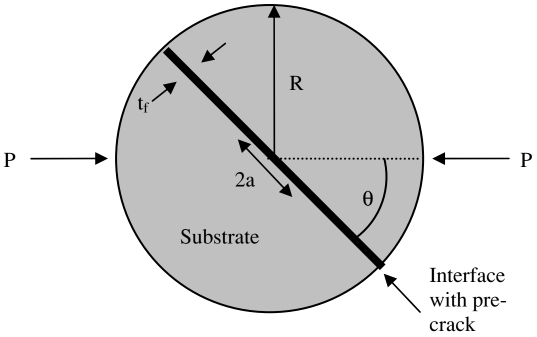

Figure O.3. Schematic of indirect test.

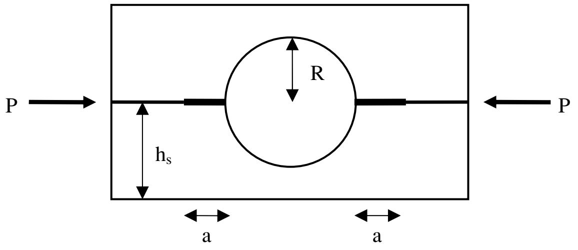

Figure O.4. Diagram of double cleavage drilled compression test specimen.

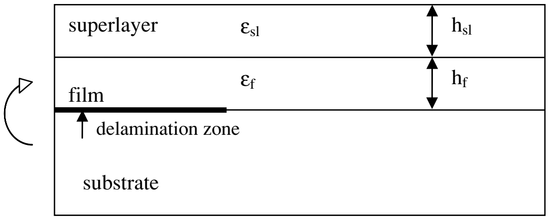

Figure O.5. Schematic of a bilayer superlayer test.

modulus of the substrate. The coefficient values were statistically fit from the results of a finite element analysis.

Superlayer Testing

Freund and Suresh (2004) also describe a test for which there is no external loading to drive delamination. This is accomplished by the use of a strained superlayer (Figure O.5). A second film is deposited on top of the first film on a thick substrate, for which the elastic energy stored in the superlayer is enough to start delamination at the interface between the underlying film and substrate. It is especially useful when energy stored in the thin bonded film is not enough to start delamination spontaneously and an additional driving force is needed.

Most interfaces require an initial work of separation that is substantially greater than the available driving force, requiring that the delamination driving force be increased from that of processing without altering the properties of the film or interface. Correct design of the superlayer is very important to increasing the driving force.

HMA on PCC Field or Laboratory Studies

Donovan et al. (2000) developed a laboratory testing procedure for geocomposite membranes bonded between to concrete bridge decks and asphalt overlays. This system is designed to prevent water and chloride infiltration through the concrete deck that would corrode steel reinforcement. A direct shear test with a dynamic loading was used to determine the optimum tack coat application rate needed to prevent slippage of the geocomposite membrane. Tack coat rates ranged from 0.5 to 3.0 kg/m^{-2} for the concrete bond, following current design practices used in the United States and Italy, respectively. Application rates for the asphalt bond were much less, and ranged from 0.22 to 0.45 kg/m^{-2}. Two different PG graded binders, PG 64-22 and 76-22, were tested, but it was later determined that the lower grade of binder was sufficient for the study. The results show that 1.75 and 1.5 kg/m^{-2} of asphalt binder achieves the optimal bond for the concrete and asphalt overlay, respectively. The use of the geocomposite membrane system increases the life (number of cycles) of the bond better than does a system without the membrane. However, the derivate of the shear stress versus ultimate number of load cycles decreases with the use of the membrane.

Yildirim et al. (2005) investigated the factors that contribute to the performance of thin HMA overlays on PCC pavements. A tack coat laboratory testing procedure was developed to optimize interlayer design options. The Hamburg wheel and shear tests were used to evaluate the performance of gyratory compacted HMA laboratory samples on concrete disks under controlled conditions. A statistical analysis of the shear test results show the main factors that significantly influence tack coat performance are mix type, application rate, and Hamburg tracking. Five thousand Hamburg tracking cycles was not enough to cause failure. Of the four response variables investigated, the area beneath the stress-displacement curve was found to be a better discriminating factor to determine the significance of main effects and interactions because this factor considers the maximum shear strength of the interface and the energy required for the bond to fail.

Al-Qadi et al. (2008) performed a direct shear test to evaluate interface bond strength of asphalt overlays on PCC pavements. The research team performed an initial trial study to determine the potential failure criteria: maximum shear stress from a less rigorous monotonic loading or maximum number of load repetitions from a more realistic cyclic loading. The monotonic loading was found to better measure the interface bond properties and was used in the laboratory testing phase. The shear testing apparatus used in the laboratory was similar to the one used by Donovan et al. in 2000. Samples varied by overlay gradation, tack material type and application rate, concrete surface texture, temperature, and sample moisture condition. Because of the quantity of differing factors used, a partial factorial experiment design consisting of four subexperiments was used. The results from testing suggest that finer overlays are stronger than coarser overlays, shear strength and optimum application rate are independent of tack material type, rougher concrete surfaces provide better bond than do tined or smooth surfaces, and moisture condition significantly decreases interface bond. A field study of 25 test sections under accelerated loading is under way in conjunction with this study.

Leng et al. (2008) investigated interface bonding of HMA overlays on PCC. Direct monotonic shear testing without normal load application was done to investigate characteristics of the HMA/PCC interface and to determine the interface shear strength. Several variables affecting the interface performance were considered, including HMA mix, tack coat type, and application to PCC surface texture. The significance of the tests was statistically validated. This study found that finer HMA mixtures had greater interface shear strength than did coarse mixtures. The asphalt emulsion (SS-1hP) at an application rate of 0.08 gal/yd^2 provided the greatest interface shear strength. Of the three surface textures investigated, the tining direction had no effect on the interface shear strength at 20°C. However, tined surfaces provided higher interface shear strength than did smooth surfaces at a low application rate of tack, and smooth surfaces provided better bonding potential at the optimum tack application for intermediate temperatures. Lower temperatures produced better bonding, but this may not be true as the temperature approaches the glassy temperature of the HMA or tack coat because the HMA is more brittle and can debond more easily.

HMA on HMA Field or Laboratory Studies

Uzan et al. (1978) performed laboratory experiments to determine the strength at failure (Mohr envelope), horizontal interface modulus, and condition of interface adhesion for asphalt interfaces at various temperatures, tack coat application rates, and normal stresses. The group's tests showed that interface shear resistance is highly dependent on temperature and vertical pressure. The amount of tack coat used (application rate) on fresh asphalt has an optimal value when compared to ultimate shear resistance. For the constant 0.25 cm/minute shear rate used in the tests, the horizontal reaction modulus is low. This value decreases with increases in temperature and increases with increasing vertical pressure. If higher shear rates were used, closer to those of passing vehicles, a more correct horizontal interface modulus would be found (estimated at 1,000 kg/cm^3). The literature reviewed suggests that horizontal interface modulus values determined in laboratory tests are considered intermediate friction condition.

Hachiya and Sato (1997) conducted a study on the effect of tack coat and surface cleanliness on the bond between HMA layers, following a Japanese investigation of several airfield surface course problems at locations where large tire shear stresses were loading the pavement, namely where aircraft brake and turn at high speeds. They modeled the pavement stresses at the bonding interface under a Boeing 747 loading. Results from their study showed that the surface course failed after debonding from the binder course from high horizontal forces exerted on the pavement. They recommended either (1) increasing the surface course thickness to decrease the shear stresses acting on interlayer or (2) increasing the bond strength to handle the loading forces as solutions to the issue. Laboratory testing for this study consisted of a shear test, tested at different temperatures, loading rates, tack coat type and application rates, and amount of curing time. The results showed the tack coat bond was stronger at 40°C than at 20°C. Loading rate was a significant factor in bond strength. The faster loading rate (4 in./minute) yielded much higher strengths than did the slower rate of 0.04 in./minute. Most interestingly, cleanliness of the bonding surface had a negligible effect on bond strength if the tack coat had been properly cured. If not properly cured, neither emulsion used in the study was effective in bonding the layers. Samples with the rubberized asphalt emulsion, applied at a rate of 0.044 gal/yd^2, produced the highest bond strength.

Hanson (2001) investigated the use of a HMA layer placed on a heavy asphalt emulsion as a new technology for a cost-effective maintenance strategy to increase surface durability and surface friction. The use of the heavy asphalt emulsion allows for proper adhesion between the two asphalt layers by compensating for losses caused by filling of small cracks and surface voids. A proper and strong bond between HMA layers is assumed achieved when the free asphalt binder rises to about one third of the height of the new surface course. The ultra-thin-bonded surface course (UTBWC) procedure was developed in France in 1986 and introduced to the United States in 1992. Case studies from 1992–1993 in Pennsylvania and Alabama showed very good results with this construction technique, with no raveling seen years after construction (indicates good bonding). An additional round of case studies was investigated in 2000. Test sections in Alabama, Missouri, Iowa, and Colorado produced good results with respect to bonding. Minnesota test sections had minor raveling problems caused by improper emulsion application. Overall, the UTBWC procedure provides excellent bonding between HMA and existing HMA or PCC pavements with little delamination problems.

Mohammad et al. (2002) investigated the need for tack coat and an optimum application rate in the laboratory by testing different tack coat materials, application rates, and test temperatures. A shear test was performed on samples using the Superpave® shear test to find shear strength at the interface under a constant load. The statistical analysis showed that the cationic rapid set polymer modified emulsion provided significantly higher interface shear strength and was the best overall performer. It was generally shown that increasing the application rate decreased the shear strength at the lower temperature (25°C), but shear strength was not affected by application rate at the higher temperature (55°C). The shear strength results of the best performing tack coat compared with a monolithic specimen suggest that current construction practices of constructing asphalt pavements in multiple lifts weakens the interfaces.

Collop et al. (2003) performed a laboratory study to determine bond condition with the Leutner shear test. Three different tack coat applications were considered for both stone matrix and HMA binder courses at different levels of cleanliness: clean with optimal amount of tack, dirty without tack, and very dirty with excessive tack. The results of the experiment showed all the material combinations have an approximately linear trend between shear strength and shear displacement. This shows that shear strength is not completely dependent on the bond condition for the conditions imposed. This linearity can be used to find a secant shear reaction modulus for all bonding conditions, resulting from the relationship between shear stress and shear displacement at the interface, depending on dilation as shear displacements increase across the interface and contact stiffness from the tack coat bonding to the asphalt layers. This is similar to the frictional resistance seen in direct shear testing of sands. Ideally, different bond conditions result in different shear strengths and corresponding shear displacements values, showing that bond adhesion/shear strength varies with bonding conditions (i.e., a higher shear contact strength achieved with an optimal amount of tack coat would provide a better bond than would a dirty interface or no tack coat).

Recasens et al. (2005) assessed the use of heat-activated emulsions as a tack coat material. Conventional emulsion tack costs can be removed by passing construction vehicles during paving, leading to poor layer bond in these areas. New low-penetration asphalt emulsions, known as heat-adhesive emulsions, have been developed to resist construction traffic. The study by Recasens et al. compared the performance of different heat-adhesive emulsions to a conventional emulsion by testing Marshall compacted laboratory specimens and test-section field cores using the Spanish Laboratorio de Caminos de Barcelona test. The modified heat-adhesive emulsion generally performed better. The conventional heat-adhesive emulsion performed better at medium temperatures, but at low temperatures its shear resistance is not very high. The conventional emulsion has higher shear resistance at low temperatures, similar to the modified heat-adhesive emulsion. At medium and high temperatures, it has less resistance. The bond strengths for immersed and dry samples are very similar. The field core results confirm the laboratory trends, although the shear resistances of the cores were much lower than those of the laboratory specimens.

Raab and Partl (2007) conducted a follow-up study on the long-term shear performance of interlayer bond. The original study tested cores from new pavement sections (constructed in 1999) using the LPDS test. The follow-up study used cores taken from the original pavement sections that had experienced at least 10 years of service. Results from the study show that compaction and settlement from traffic increase the shear resistance of the bond in most cases; shear stiffness (and forces) in and outside of the wheelpath are similar in binder courses; and many heavy loadings over time can cause bonding problems.

Diakhate et al. (2006) investigated asphalt tack coat shear behavior under cyclic loadings. Asphalt slab specimens with dual asphalt bond interfaces were tested under repeated shear loading. Interface failures were measured with resistors, where bond failure was defined as breaking the resistor wire. Shear displacement and force were also measured. Major findings from the study show that the behavior of interlayers has two distinct stages: a progressive failure of the bond where the shear force decreases linearly, followed by dramatic decreases in shear loading by crack propagation. The decrease in load taken by the tack material indicates that the shear stiffness decreases over time, and aggregate interlock (friction) between the layers resists the shear loading.

Mrawira and Damude (1999) performed a direct shear test to evaluate interface strength. Their test results were different from other previous research. Test specimens consisted of asphalt cores of varying pavement age and aggregate sources. Bonding to asphalt surfaces also was examined by comparing saw-cutting (smooth) to traffic-worn textures. Tack was applied at two different application rates and temperatures and left to cure for less than 1 hour. Once the curing time ended, an overlay was compacted on top of the core using two Marshall compacted lifts. The specimens tested under displacement control at a rate of 1 mm/minute with the shear apparatus. Test results showed higher ultimate shear strengths without tack coat. The tack coat weakened the interface bond strength, a finding in opposition to the results of other research. Specimens with smooth saw-cut surfaces exhibited lower ultimate shear strengths than did traffic-worn specimens with and without tack coat.

APPENDIX P

CalME Model

Procedure for Rutting Performance Prediction and Calibration

The mechanistic-empirical approach to pavement design makes use of fundamental physical properties and a theoretical model to predict stresses, strains, and deflections (i.e., the pavement response) caused by a load on the pavement.

CalME uses a modified version of the shear-based procedure developed by Deacon et al. (2002) to predict accumulated rut depth in hot-mix asphalt (HMA) layers by considering the effects of temperature, material properties, load levels, and speed. It is a mechanistic-empirical approach to pavement design that makes use of fundamental physical properties and a theoretical model to predict pavement response caused by a load on the pavement. CalME follows an increment-recursive procedure when simulating pavement performance, where material properties are updated for each time increment by considering the changes in environmental conditions, traffic characteristics, and HMA stiffness. Calculated damage (permanent deformation for rutting, stiffness change otherwise) for each time increment is recursively accumulated to be able to predict the pavement condition at any point in time. The increment-recursive mechanism has been found to be an effective approach for considering damage accumulation and has been implemented in CalME (Ullidtz et al. 2008) and, to a partial extent, in the *MEPDG* (NCHRP 2004). The general framework followed for rutting performance model calibration is given in Figure P.1.

The gamma function used to calculate permanent shear strain by using elastic shear strain, number of repetitions, and shear strain as the independent variables is given as follows in equation P.1 (Ullidtz et al. 2008):

$$\gamma^{i} = \exp\left(A + \alpha \times \left[1 - \exp\left(\frac{-\ln(N)}{\gamma} \right) \times \left(\frac{1 + \ln(N)}{\gamma} \right) \right] \right) \times \exp\left(\frac{\beta \times \tau}{\tau_{\text{ref}}} \right) \times (\gamma^{e})^{\delta} \qquad \text{(P.1)}$$

where

γ^{i} is permanent shear strain,
γ^{e} is elastic shear strain,
τ is shear stress,
N is number of load repetitions,
τ_{ref} is reference shear stress (0.1 MPa = atmospheric pressure), and
A, α, and β are model coefficients determined from the repeated load simple shear test at constant height (RSST-CH) results.

Model coefficients for Equation P.1 for this study were calculated based on laboratory RSST-CH data for the HMA mixes of the Heavy Vehicle Simulator (HVS) (PG 64-28 polymer-modified [PM] and rubberized hot-mix asphalt with gap-graded aggregates [RHMA-G]) and MnROAD (PG 64-34) test sections by using nonlinear regression. Results for the tests are given in Appendix N. Calculated model coefficients are given in Table P.1. Figures P.2, P.3, and P.4 compare the RSST-CH permanent shear strains (PSS) measured in the laboratory with those calculated using the calibrated Equation P.1 models for the PG 64-28 PM, RHMA-G, and PG 64-34 mixes, respectively.

Shear stresses at 50-mm (2-in.) depth at the edge of the tire are calculated by using the calculated stiffnesses, traffic-vehicle characteristics, and material properties as inputs to a layered elastic program. Elastic shear strain values for each repetition interval are calculated by using Equation P.2 (Ullidtz et al. 2008):

$$\gamma^{e} = \frac{\tau}{E_i/(1+\nu_i)} \qquad \text{(P.2)}$$

where

τ = shear strain calculated from layer elastic theory,
E_i = modulus of layer i, and
ν_i = Poisson's ratio for layer i (assumed to be 0.35 for all layers).

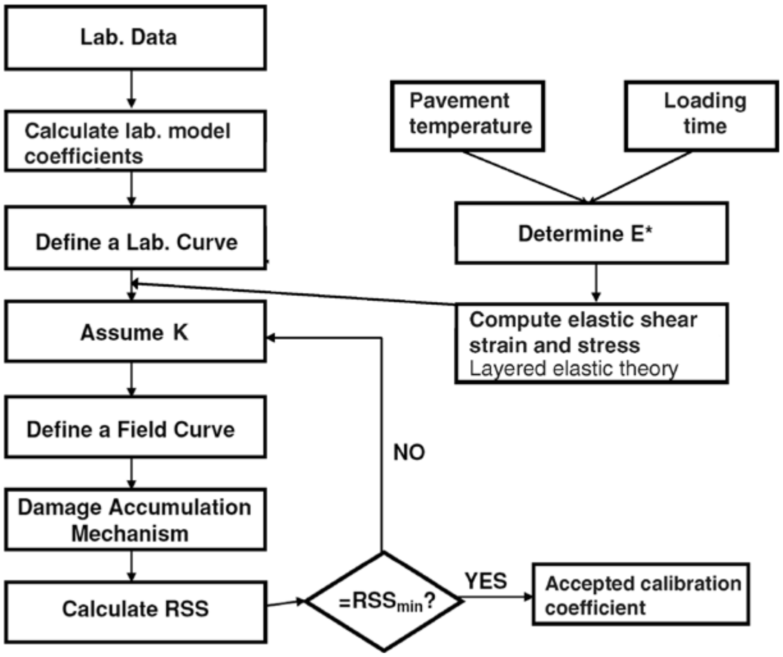
Lab. Data
Calculate lab. model coefficients
Define a Lab. Curve
Assume K
Define a Field Curve
Damage Accumulation Mechanism
Calculate RSS
=RSS$_{min}$?
NO
YES
Accepted calibration coefficient
Pavement temperature
Loading time
Determine E*
Compute elastic shear strain and stress
Layered elastic theory

Figure P.1. General framework for rutting model calibration. (Coleri et al. 2008). Note that* K *= calibration coefficient (described in Equation P.3);* E* *= elastic modulus;* RSS *= residual sum of squares (described in Equation P.4).

Calculated elastic strain values for the corresponding repetition interval are used in Equation P.1 to calculate plastic shear strain. For the calibration of the HVS and MnROAD sections, the coefficient for the shear stress variable (β) is assumed to be equal to zero for all material types because the effect of shear stress on accumulated permanent shear strain is simulated using the elastic shear strain variable. CalME assumes that rutting is confined to the upper 100 mm of the asphalt layers (Ullidtz et al. 2008), therefore calculated plastic shear strains (from Equation P.1) for each repetition interval are multiplied by 100 mm to calculate corresponding rutting deformation. Calculated rut depths for each repetition interval are accumulated based on the IR procedure to develop the final rutting curve.

The optimum calibration coefficient (K) is calculated by relating calculated permanent shear strain values to measured downward rut depths using Equation P.3 and optimization:

$$dpi = K \times h_i \times \gamma^i \tag{P.3}$$

where

K = calibration coefficient,
h_i = thickness of layer i (to 100 mm, assumed to be 100 mm for thicker asphalt layers), and
dp_i = rut depth.

The procedure given in Figure P.1 can be repeated several times to develop rutting deformation curves for several calibration coefficients (K). The optimum calibration coefficient between the laboratory regression equations and the measured rutting can be determined on the basis of a fitness function, given as follows in equation P.4:

$$RSS = \sum_{i=1}^{n} (\text{Predicted Rut Depth} - \text{Measured Rut Depth})^2 \tag{P.4}$$

where

n = number of rut depth measurements, and
RSS = residual sum of squares.

The plot for calibration coefficient versus RSS can be fitted by a second-order polynomial curve whose minimum RSS will correspond to an optimum calibration coefficient that can be used for design.

Table P.1. Model Coefficients for CalME Rutting Model (Equation P.1) for Mixes PG 64-28 PM, RHMA-G, and PG 64-24

Mixes	***A***	α	τ_{ref}	β	γ	δ
PG 64-28 PM	1.9166	2.6490	0.1	0	4.2084	1
RHMA-G	0.3593	3.9425	0.1	0	1.7189	1
PG 64-34	0.7546	3.3804	0.1	0	2.2463	1

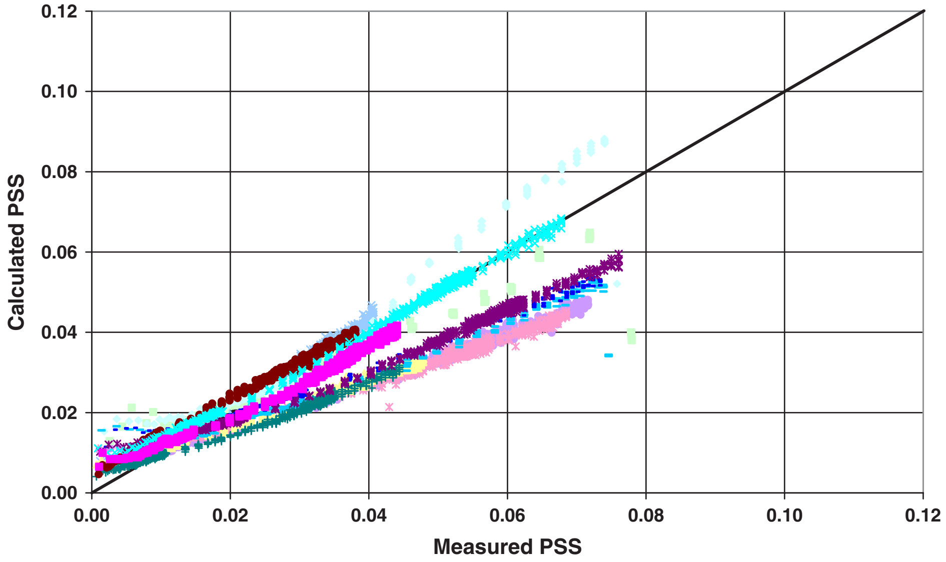

Figure P.2. Laboratory-measured and calculated PSS of the mix PG 64-28 PM.

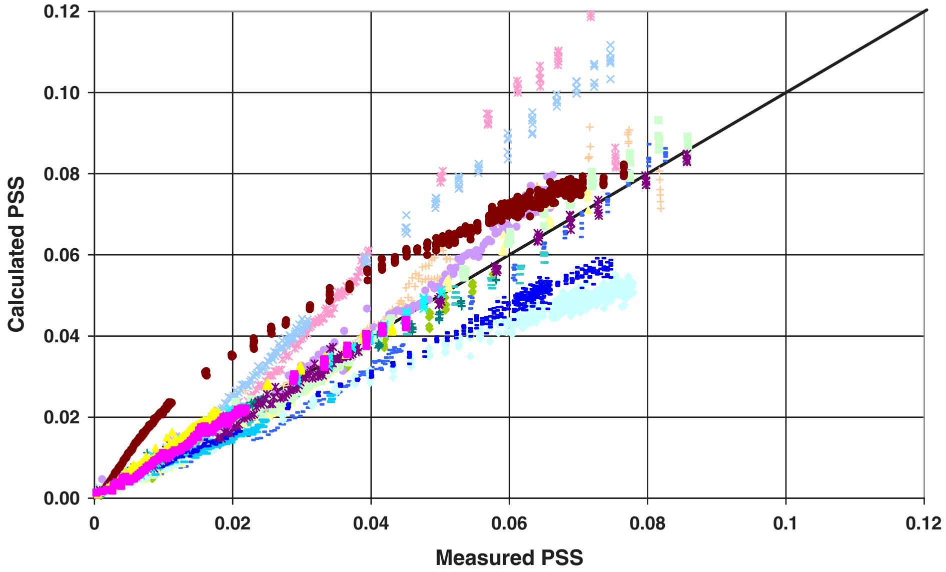

Figure P.3. Laboratory-measured and calculated PSS of the mix RHMA-G.

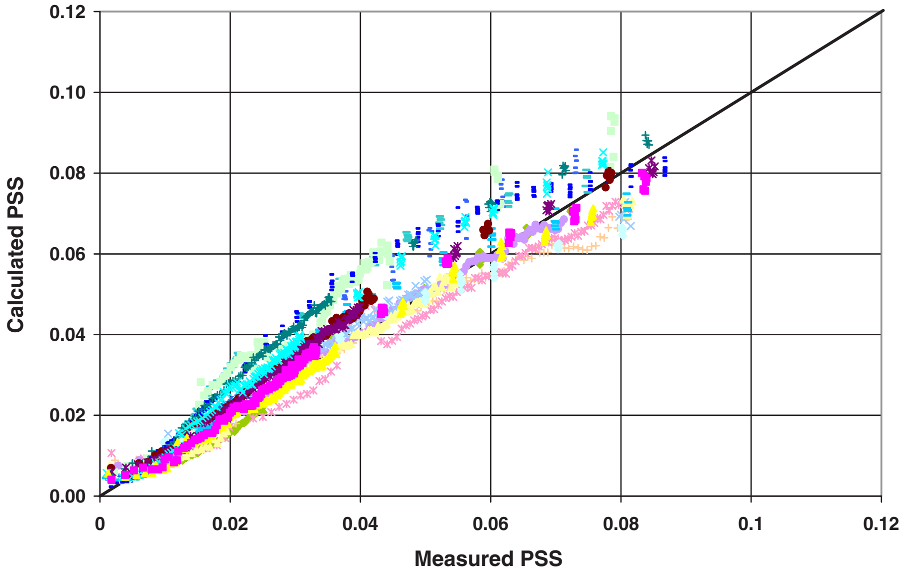

Figure P.4. Laboratory-measured and calculated PSS of the mix PG 64-34.

Table P.2. Model Coefficients for CalME HMA Modulus Model (Equations P. 5 and P.6) for Mixes PG 64-28 PM, RHMA-G, and PG 64-34

Mixes	δ	β	γ	aT	E_{ref}	T_{ref}	α
PG 64-28 PM	2.3010	1.4305	1.0982	1.0251	2,579	20	1.7367
RHMA-G	2.3010	0.6478	1.0118	1.0318	3,148	20	1.5583
PG 64-34	2.3010	2.8411	0.9748	1.0690	652	20	2.000

Note: In Equation P.6, lt = 0.015 for all mixes. In Equation P.7, $A = 9.6307$ and $VTS = -3.5047$.

Stiffness Model for Asphalt-Bound Materials

The asphalt-bound material modulus is modeled in CalME as a function of temperature and loading time, using the NCHRP 1-37A Design Guide model (ARA, Inc. 2004), as shown in Equation P.5:

$$\log(E) = \delta + \frac{\alpha}{1 + \exp(\beta + \gamma \log(\text{tr}))} \tag{P.5}$$

where

E is the modulus (in MPa),
tr is reduced time (in sec), and
α, β, γ, and δ are constants and logarithms are to base 10.

Reduced loading time *tr* is found from Equation P.6

$$\text{tr} = \text{lt} \times \left[\frac{\eta(T_{\text{ref}})}{\eta(T)}\right]^{aT} \tag{P.6}$$

where

lt = loading time (in sec),
$\eta(T_{\text{ref}})$ = the binder viscosity at the reference temperature,
$\eta(T)$ = the binder viscosity at the actual temperature, and
aT = a constant.

The viscosity (cPoise) is found from Equation P.7

$$\log(\log(\text{visccPoise})) = A + VTS \times \log(t_k) \tag{P.7}$$

where

t_k is the temperature in degrees Kelvin and A and VTS are constants.

The master curves for the different asphalt materials were determined in the laboratory from frequency sweep tests on beams. Results for the tests are given in Appendix N. Calculated model coefficients are given in Table P.2. Figures P.5, P.6, and P.7 compare the laboratory-measured and calculated modulus values of the PG 64-28 PM, RHMA-G, and PG 64-34 mixes, respectively.

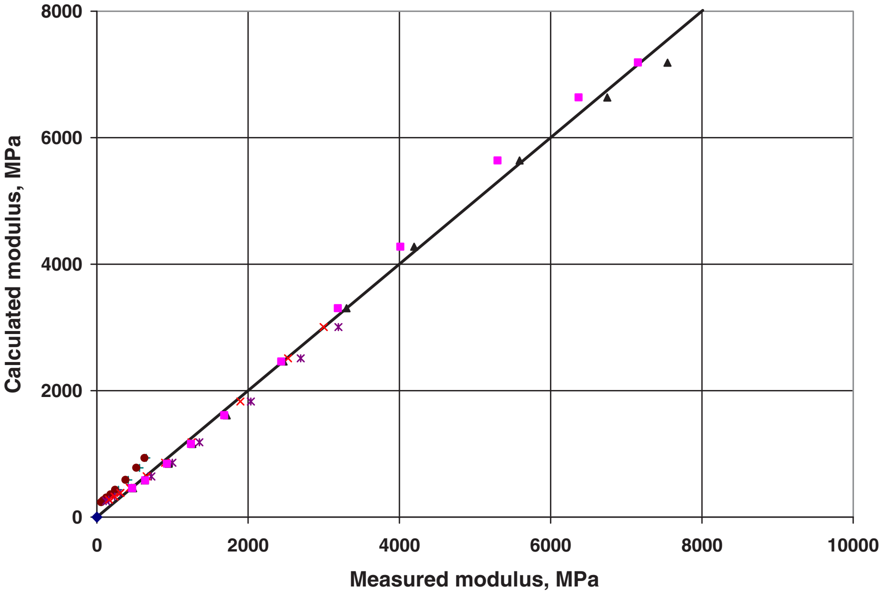

Figure P.5. Laboratory-measured and calculated modulus of the mix PG 64-28 PM (1 MPa = 145 psi).

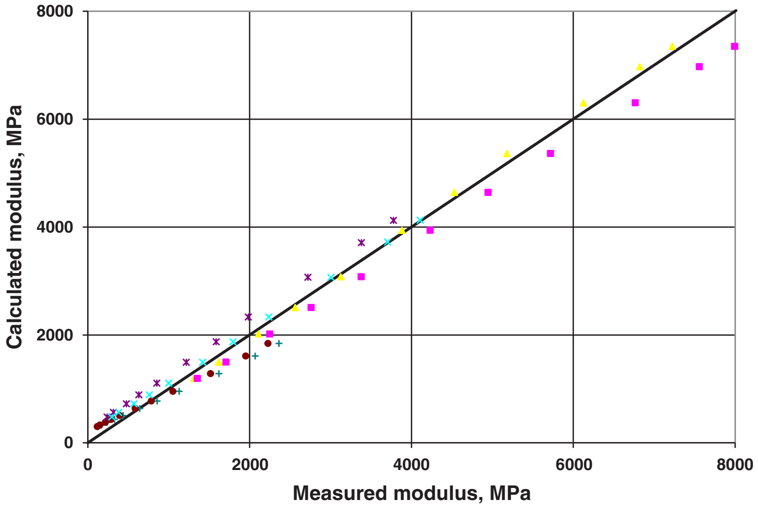

Figure P.6. Laboratory-measured and calculated modulus of the mix RHMA-G (1 MPa = 145 psi).

Fatigue Cracking Model

Fatigue causes damage in asphalt-bound materials and appears at the surface as reflection cracking in composite pavement. In CalME, the density of surface cracking caused by fatigue is a function of the damage in an asphalt-bound layer. The fatigue damage, in turn, is accumulated at a rate that is determined by the tensile strain caused by traffic loading. Fatigue damage determines the residual stiffness of asphalt-bound materials. Specifically, the modulus for asphalt-bound material with damage ω becomes Equation P.8:

$$\log(E) = \delta + \frac{\alpha \times (1-\omega)}{1+\exp(\beta+\gamma\log(tr))} \qquad \text{(P.8)}$$

where the variables are defined in Equation P.5 and the damage ω is calculated from Equation P.9

$$\omega = \left(\frac{MN}{FSF \cdot MN_p}\right)^{\alpha} \qquad \text{(P.9)}$$

where

MN = number of load applications in millions,

MN_p = allowable number of load repetitions in millions,

FSF = fatigue shift factor, and

α = a material-dependent exponent. α is calculated using Equation P.10:

$$\alpha = \exp\left(\alpha_0 + \alpha_1 \times \frac{t}{1°\text{C}}\right) \qquad \text{(P.10)}$$

where

t is the material temperature (in °C), and α_0 and α_1 are material constants

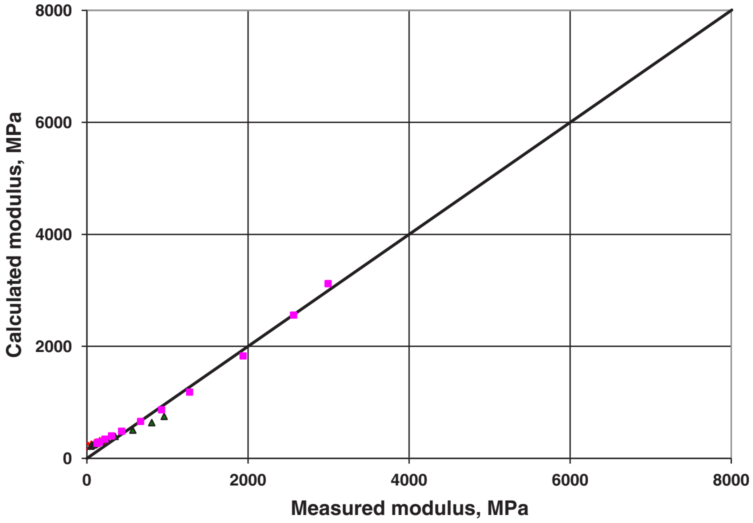

Figure P.7. Laboratory-measured and calculated modulus of the mix PG 64-34 (1 MPa = 145 psi).

Table P.3. Model Coefficients for CalME HMA Cracking Model (Equations P.9, P.10, and P.11) for Mixes, PG 64-28 PM, RHMA-G, and PG 64-34

Mixes	A	α_0	ε_{ref}	β	E_{ref}	γ
PG 64-28 PM	1,565.32	–1.4141	200	–6.0073	3,000	–3.0037
RHMA-G	17.28	–0.2919	200	–5.4939	3,000	–2.7470
PG 64-34	366.61	–1.3835	200	–4.6388	3,000	–2.3194

while MN_p is calculated using Equation P.11:

$$MN_P = A \times \left(\frac{\varepsilon}{\varepsilon_{\text{ref}}}\right)^{\beta} \times \left(\frac{E}{E_{\text{ref}}}\right)^{\gamma} \times \left(\frac{E_i}{E_{\text{ref}}}\right)^{\delta} \qquad \text{(P.11)}$$

where

ε = bending strain at the bottom of the asphalt layer, $\mu\varepsilon$

ε_{ref} = reference bending strain, $\mu\varepsilon$,

E_i = intact modulus for the current temperature and loading time,

E_{ref} = reference modulus, and

A, β, γ, and δ = material constants.

The model parameters for Equations P.9, P.10, and P.11 are determined by fitting the stiffness reduction curves from beam bending fatigue tests conducted at 20°C. If all of the parameters are allowed to vary, the resulting damage model leads to unreasonable predictions of field performance. Specifically, that model would indicate that nearly all the damage occurs in hot weather and most of the damage will occur in the summer. It was decided to apply the following restrictions to the parameters in Equation P.11 while this issue is being investigated: $\alpha_1 = 0$, $\delta = 0$. It was further decided to set $\gamma = \beta/2$ to be consistent with the concept of damage driven by strain energy.

It should be noted that fatigue damage is not evaluated solely on the relative decrease in modulus. In fact, as shown in Equation P.12,

$$\omega = \frac{\ln(E/E_i)}{\ln(E_{\min}/E_i)} = \frac{\ln(SR)}{\ln(E_{\min}/E_i)} \qquad \text{(P.12)}$$

where

SR is the residual stiffness ratio, and

$E_{\min} = \exp(\delta)$ is the minimum modulus (δ is the one defined in Equation P.5).

As shown in Equation P.12, the actual relative decrease in modulus will depend on the minimum modulus, $E_{\min}$, and on the intact modulus, E_i, which again is a function of temperature and loading time. For example, a decrease in modulus by 50% would correspond to a damage between 0.15 and 0.30 if $E_{\min} = 100$ MPa, depending on the initial modulus.

Model coefficients for Equations P.9, P.10, and P.11 were calculated based on laboratory fatigue test results for the HMA mixes of HVS test sections (PG 64-28 PM and RHMA-G) and MnROAD (PG 64-34) by using nonlinear regression. Results for the tests are given in Appendix N. Calculated model coefficients are given in Table P.3. Figures P.8, P.9, and P.10 compare flexural fatigue stiffness ratios measured in the laboratory with those calculated using the calibrated Equation P.9 through

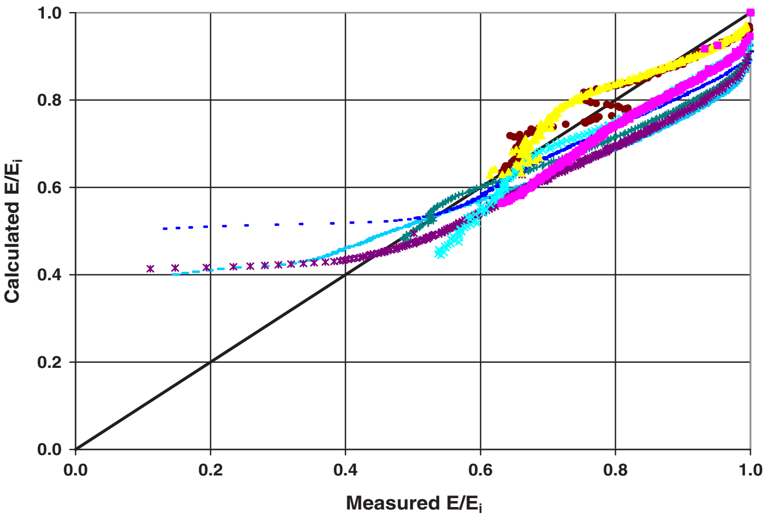

Figure P.8. Laboratory-measured and calculated stiffness ratio (E/E$_i$) of the mix PG 64-28 PM.

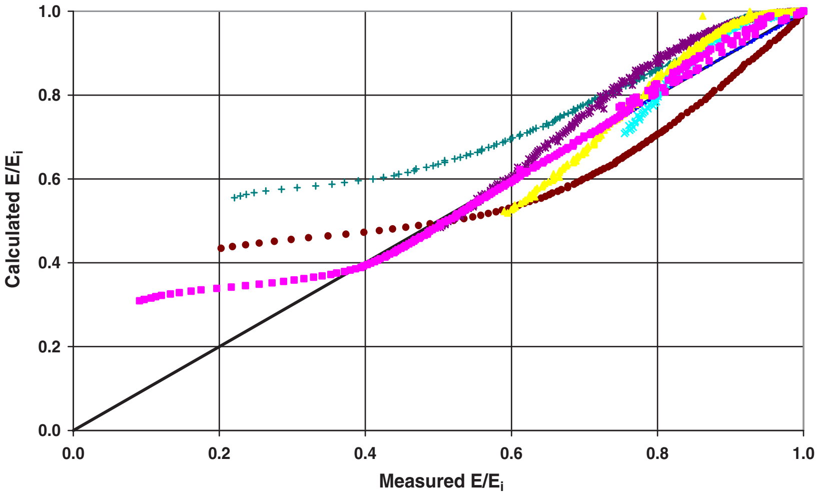

Figure P.9. Laboratory-measured and calculated stiffness ratio (E/E$_i$) of the mix RHMA-G.

Equation P.12 models for the PG 64-28 PM, RHMA-G, and PG 64-34 mixes, respectively.

The fatigue shift factor, *FSF*, is determined from a reference factor accounting for the difference between laboratory fatigue tests and full-scale testing denoted as FSF_{ref}, and the effects of rest periods (Equation P.13):

$$FSF = \left\{1 + \left[\frac{RP}{RP_{\text{ref}}} \times \left(\frac{\eta(T_{\text{ref}})}{\eta(T)}\right)^{aT}\right]^{\varphi}\right\} \times FSF_{\text{ref}} \qquad \text{(P.13)}$$

where

RP = rest period for traffic loading,
$\eta(T_{\text{ref}}), \eta(T)$ = stiffness master curve parameters, and aT
RP_{ref} = 10 seconds is the reference rest period, and
$\varphi = 0.4$ is a constant model parameter.

Once the fatigue damage for the asphalt surface layer has been determined, the surface crack density, with the unit m/m^2, can be calculated. The amount of cracking at crack initiation must be assumed (in calibration studies, values of 5% of the wheelpath or 0.5 m/m^2 have been used) as shown in Equation P.14.

$$CR = \frac{CR_{\max} \times (\omega^{\alpha}_{initiation} - 1)}{\omega^{\alpha}_{initiation} - \dfrac{CR_{\max}}{CR_i} + \left(\dfrac{CR_{\max}}{CR_i} - 1\right) \cdot \omega^{\alpha}} \qquad \text{(P.14)}$$

where

$CR_{\max}$ = 100% or 10 m/m^2 is the maximum surface crack density,
CR_i = 5% or 0.5 m/m^2 is the surface crack density corresponding to crack initiation,
ω = damage in asphalt bound material,

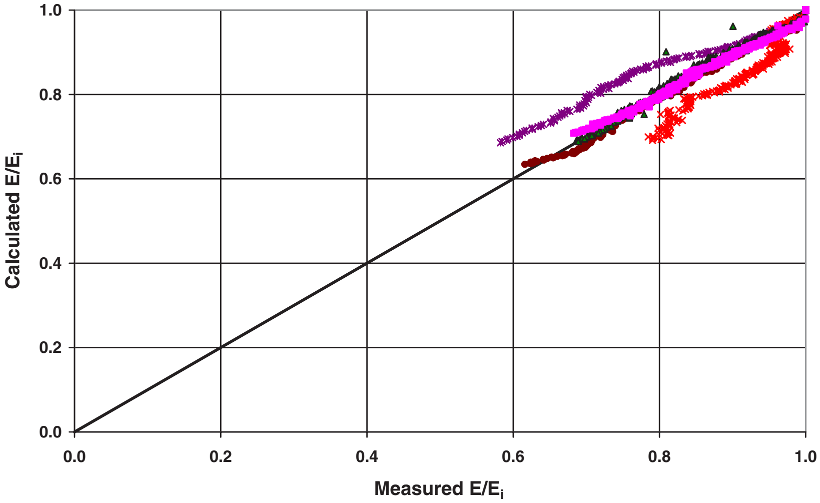

Figure P.10. Laboratory-measured and calculated stiffness ratio (E/E$_i$) of the mix PG 64-34.

$\omega_{initiation}$ = damage corresponding to crack initiation, which is calculated separately, and

α = a model constant determined from field calibration.

The crack initiation damage $\omega_{initiation}$ is calculated using Equation P.15:

$$\omega_{initiation} = \frac{A_i}{1+\left(\frac{h_{AC}}{h_{ref}}\right)^{a_i}} \tag{P.15}$$

where

h_{AC} = combined HMA thickness,

h_{ref} = 250 mm is the reference HMA thickness,

a_i = −2.0 is a model parameter determined from field calibration, and

A_i = 1.0 is a another model parameter determined from field calibration.

Reflection Cracking Model

Reflection cracking damage was calculated the same way as fatigue cracking damage (i.e., using Equation P.9 to Equation P.11). The difference is that the strain in Equation P.11 for reflection cracking strain is calculated differently, based on a method developed by Wu (2005). Once reflection cracking damage is calculated, surface crack density is calculated using Equation P.14 and Equation P.15 but with different values for A_i and a_i. Specifically, $A_i = 0.54$ and $a_i = -0.90$.

To use Equation P.11, one needs to provide the crack tip strain (CTS) attributable to the existence of the underlying crack or joint, which can not be calculated with multilayer elastic theory. In CalME, CTSs are calculated using regression equations that were developed based on thousands of finite element runs. CTS is a function of structural characteristics and loading conditions. A schematic of finite element idealization for composite pavement with an HMA surface layer is shown in Figure P.11. Note that the cracks or joints in the underlying portland cement concrete (PCC) layer are assumed to be in the transverse direction. The supporting layers are simplified as Winkler foundation.

Based on HVS studies and finite element analysis, it is believed that debonding occurs quickly after a composite pavement is opened to traffic. The debonding causes the HMA layer to act as a flexural beam, as shown in the bending strain contour in Figure P.12.

Accordingly, CTS is defined as the maximum bending strain at the bottom of the HMA layer caused by a passing truck axle. The critical wheel position that leads to maximum CTS may be the shear loading or the normal loading position (Figure P.13). The factors found to significantly affect CTS are listed in Table P.4, along with the range of their values used in developing the regression equations.

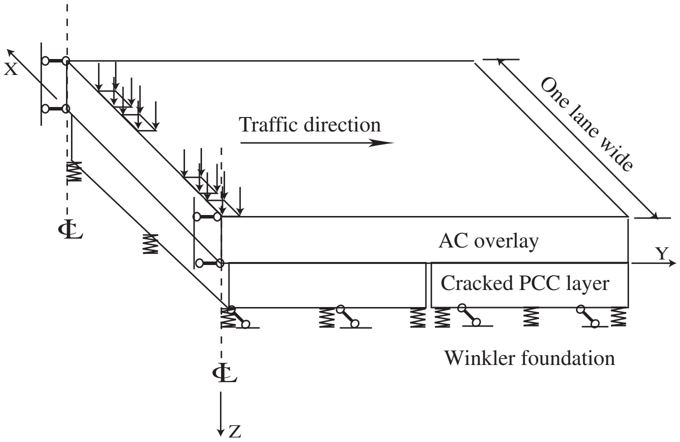

Figure P.11. Finite element idealization of the composite pavement with HMA surface.

The regression equation for tensile strain at the bottom of the HMA layer is demonstrated below in Figure P.14.

To use the regression equation, one needs to know the subgrade reaction modulus K_y. Subgrade reaction modulus is determined by simulating the plate load test that is used in the field for measuring K_y. Specifically, surface deflection caused by a circular load of 381 mm (15 in.) in radius applied on the surface layer is calculated using layer elastic theory. The reason for placing the plate on top of the surface course, rather than on top of the layers supporting the PCC layer, is to account for the load-spreading effect of PCC slabs when the pavement is loaded in actual highway traffic.

Model Capabilities and Limitations

The CalME reflection cracking model considers traffic loading only. This is based on the original assumptions that temperate and hot climates do not experience temperatures that are extremely low compared with construction temperatures, and that joints are not farther apart than 15 ft (4.5 m), as is the case in California, so that thermal strains induced by temperature variation in the HMA layer are not significant.

Thermal cracking in HMA surface layers is more likely for certain parts of the United States, either because the temperature variation is very large or because the crack/joint spacing in the underlying PCC layer is long enough. The CalME model needs to be complemented by an appropriate thermal cracking model, particularly for locations with very low temperatures.

The CalME reflection cracking model currently does not explicitly account for any structural treatments that might exist, such as dowel bars placed across an underlying joint or reinforcing steel nets placed in the HMA layer. The effect of these treatments can be considered by applying an adjustment factor to the calculated CTS.

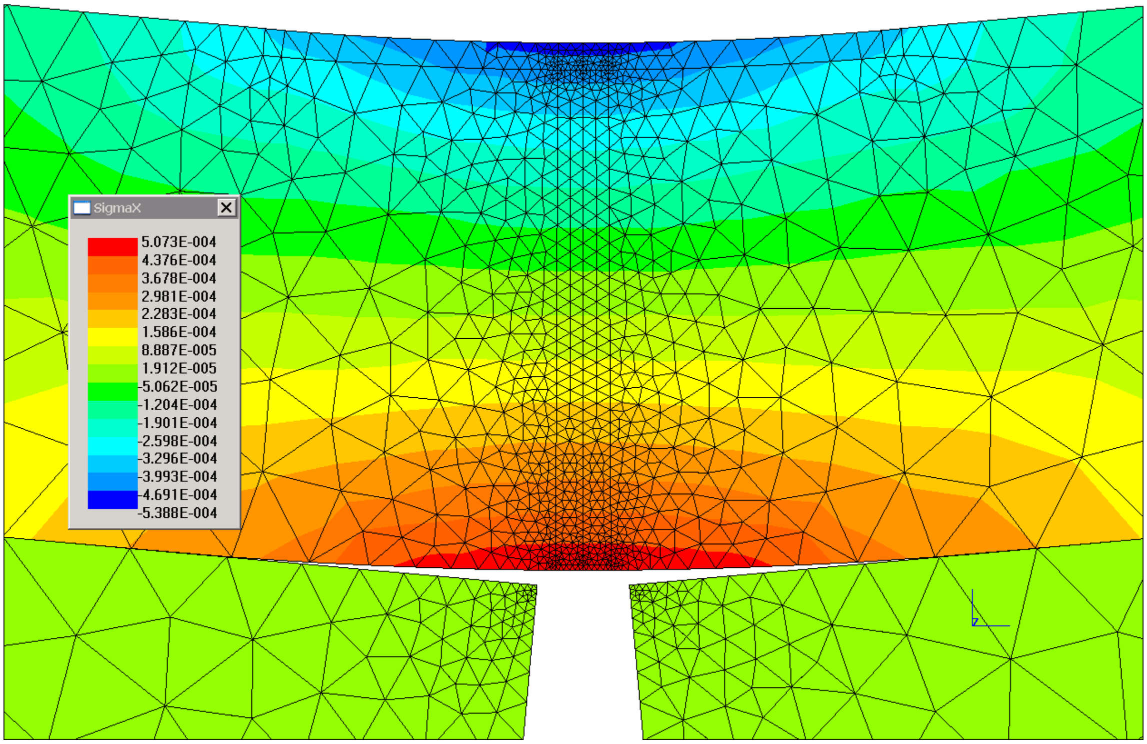

Figure P.12. Bending strain contour around the tip of the joint, axle load applied right over the joint, HMA layer debonded from the underlying PCC slab around the joint.

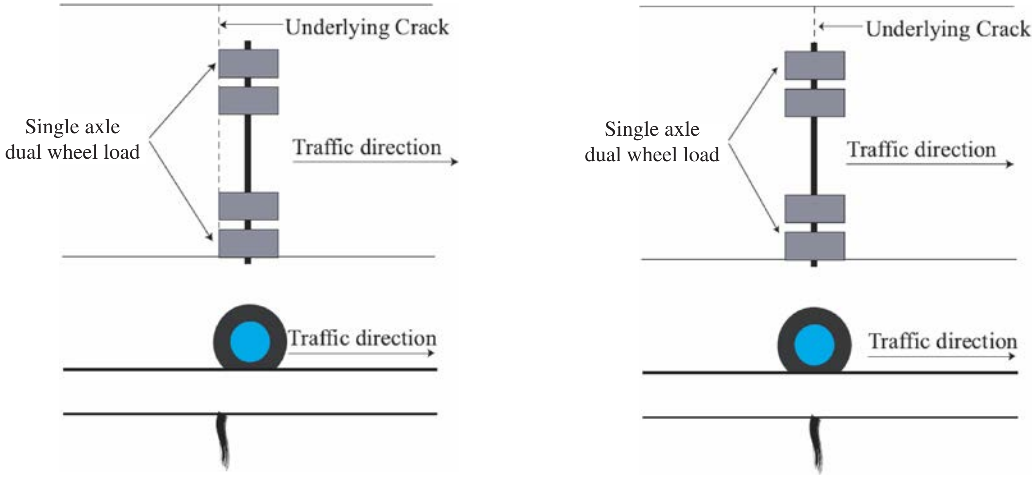
Underlying Crack
Single axle
dual wheel load
Traffic direction
Traffic direction
Underlying Crack
Single axle
dual wheel load
Traffic direction
Traffic direction

(a)

(b)

Figure P.13. Different loading positions relative to the underlying joint: (a) shear loading, wheel load on one side of the underlying joint, and (b) normal loading, wheel load symmetric about the underlying joint.

Table P.4. Significant Factors for Calculating Crack Tip Strain and the Ranges of Their Value

Description	Name	Unit	Normalizer	Minimum	Maximum
HMA stiffness	Ea	MPa	10,000	1,000	12,000
HMA thickness	Ha	Mm	100	50	250
PCC thickness	Hu	Mm	200	100	300
SG reaction modulus	Ky	MPa/mm	0.09	0.03	0.12
Axle load	Fx	kN	80	40	80
Joint spacing	LS	mm	1,000	500	4,000

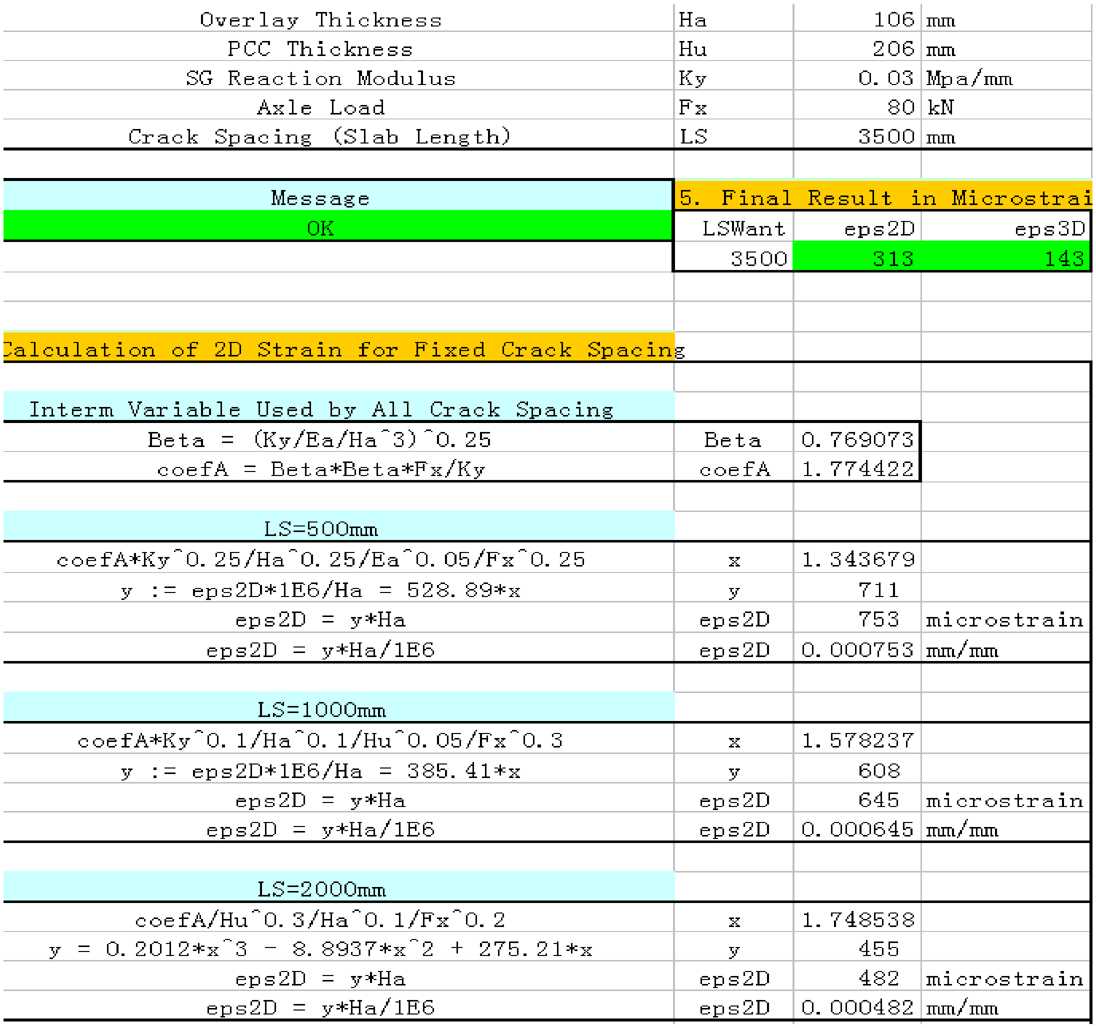

Overlay Thickness	Ha	106	mm
PCC Thickness	Hu	206	mm
SG Reaction Modulus	Ky	0.03	Mpa/mm
Axle Load	Fx	80	kN
Crack Spacing (Slab Length)	LS	3500	mm
Message	5. Final Result in Microstrai		
OK	LSWant	eps2D	eps3D
	3500	313	143
Calculation of 2D Strain for Fixed Crack Spacing			
Interm Variable Used by All Crack Spacing			
Beta = (Ky/Ea/Ha^3)^0.25	Beta	0.769073	
coefA = Beta*Beta*Fx/Ky	coefA	1.774422	
LS=500mm			
coefA*Ky^0.25/Ha^0.25/Ea^0.05/Fx^0.25	x	1.343679	
y := eps2D*1E6/Ha = 528.89*x	y	711	
eps2D = y*Ha	eps2D	753	microstrain
eps2D = y*Ha/1E6	eps2D	0.000753	mm/mm
LS=1000mm			
coefA*Ky^0.1/Ha^0.1/Hu^0.05/Fx^0.3	x	1.578237	
y := eps2D*1E6/Ha = 385.41*x	y	608	
eps2D = y*Ha	eps2D	645	microstrain
eps2D = y*Ha/1E6	eps2D	0.000645	mm/mm
LS=2000mm			
coefA/Hu^0.3/Ha^0.1/Fx^0.2	x	1.748538	
y = 0.2012*x^3 - 8.8937*x^2 + 275.21*x	y	455	
eps2D = y*Ha	eps2D	482	microstrain
eps2D = y*Ha/1E6	eps2D	0.000482	mm/mm

Figure P.14. Regression equations for calculating crack tip strains for traffic-induced reflection cracking in CalME; eps3D shown in the graph is used for calculating reflection cracking damage.

Calibration of Incremental-Recursive Rutting Prediction Models in CalME Using HVS and MnROAD Experiments

CalME rutting prediction models were calibrated using the results of the HVS and MnROAD experiments by following the procedure described and using the rutting model coefficients.

Calibration of Rutting Prediction Models in CalME Using HVS Experiments

HVS rutting experiments were performed on four sections making up a full factorial of mix type (PG 64-28PM dense graded and RHMA-G) and thickness (2.5 and 4.5 in. [64 and 114 mm]), which were described in Appendix L. CalME model parameters were determined based on the laboratory test results (Appendix N) using nonlinear regression. Model parameters given earlier in this appendix were used with HVS test results to calibrate the CalME rutting model for composite pavements.

Thermocouple measurements were used for the prediction of stiffnesses based on the *MEPDG* procedure. Shear stresses at 50-mm depth at the edge of the tire were calculated by using the calculated stiffnesses, traffic-vehicle characteristics, and material properties as inputs to a layered elastic program. Calculated elastic strain values for the corresponding repetition interval were used to calculate plastic shear strain. In CalME, rut depths are calculated for the upper 100 mm of the asphalt layers (Ullidtz et al. 2008), so the calculated plastic shear strains for each repetition interval have been multiplied by 100 mm to calculate the corresponding rutting deformation. Calculated rut depths for each repetition interval were accumulated based on the IR procedure to develop the final rutting curve.

In this study, measured downward rut depths (layer compression compared with the original surface of the pavement, referred to as average rut depth) were used for model calibration.

HVS repetitions were converted to continuous time (year) for calibrations. Figures P.15 through P.18 show the results of the calibrations. The Kcalib. rutting curve in each figure is the calibrated rutting prediction curve, whereas the Kavg curve is the predicted rutting curve using the calibration coefficient obtained by averaging the calibration coefficients of all four HVS test sections. Kavg was assumed to be the calibration factor for composite pavements used for the CalME rutting model sensitivity analysis. It can be observed that Kavg gives reasonable predictions for all sections. Although the 114-mm thick RHMA-G section (Section 611HB) showed early failure, it can be observed that measured performance can be effectively predicted with CalME models without having extreme differences in calibration coefficients. In other words, CalME was able to predict the early failure for that section with the same calibration coefficient used for the other sections.

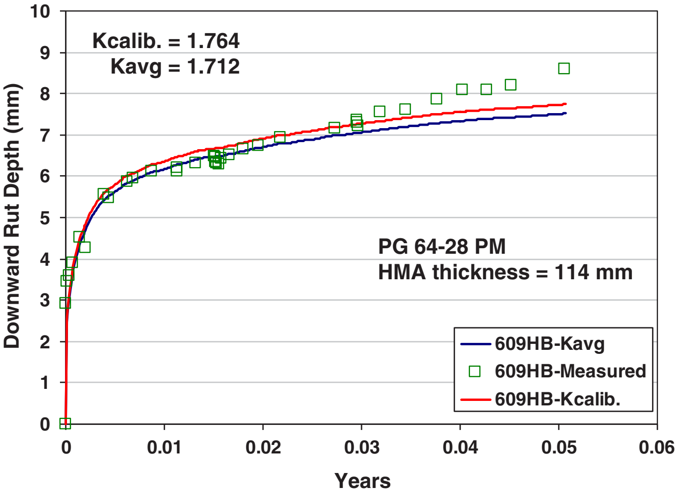

Figure P.15. Section 609HB: HVS test results compared with calibrated CalME rutting model predictions (25.4 mm = 1 in.).

Calibration of Rutting Prediction Models in CalME Using MnROAD Experiments

Data for MnROAD Cell 70 were also used to calibrate CalME rutting models. The pavement structure for Cell 70 was as follows:

- 75-mm (3-in.) thick, PG 64-34 dense-graded asphalt concrete layer;
- 150-mm (6-in.) recycled PCC;

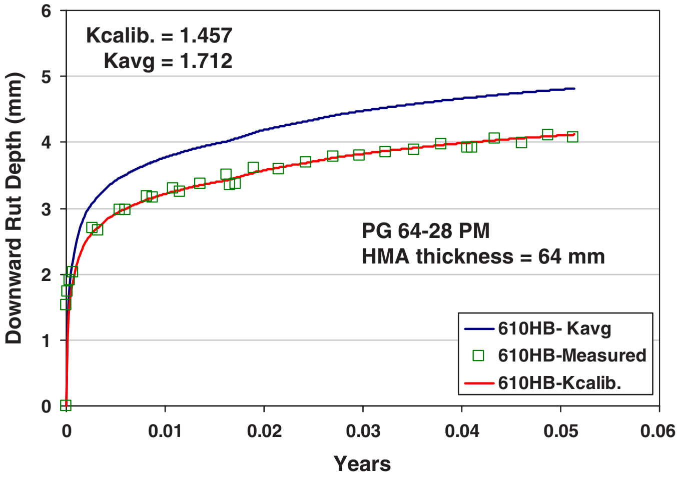

Figure P.16. Section 610HB: HVS test results compared with calibrated CalME rutting model predictions (25.4 mm = 1 in.).

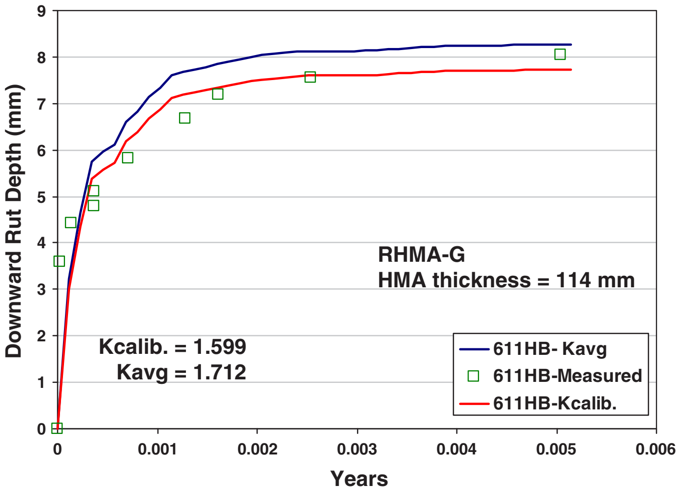

Figure P.17. Section 611HB: HVS test results compared with calibrated CalME rutting model predictions (25.4 mm = 1 in.).

- 200-mm (8-in.) Class 7 aggregate base; and
- Clay subgrade.

Measured pavement surface and air temperatures for Cell 70 during the analysis period are given in Figure P.19. Traffic data from the corresponding WIM station used for the analyses are summarized in Figure P.20 and Figure P.21. Figure P.20 shows the distribution of equivalent single-axle loads (ESALs) by class and lane. It can be seen that Class 9 vehicles make up a significant percentage of the traffic. Gross vehicle weights for vehicle Class 9 for the passing lane are given in Figure P.21.

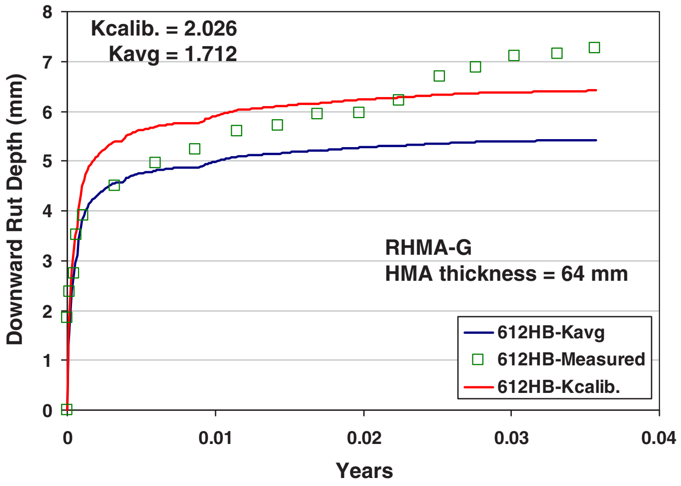

Figure P.18. Section 612HB: HVS test results compared with calibrated CalME rutting model predictions (25.4 mm = 1 in.).

Falling weight deflectometer (FWD) data from Cell 70 was processed with *CalBack* software to back-calculate the stiffness values for the aggregate base and subgrade layers. Distributions for the back-calculated stiffness values are given in Figure P.22. Average aggregate base and subgrade stiffness values used for the calibration were 29,753 psi (205 MPa) and 11,466 psi (79 MPa), respectively.

CalME model parameters for the MnROAD Cell 70 asphalt mix (PG 64-34) were determined by nonlinear regression and used for rutting model calibrations. The procedure followed for HVS rutting model calibration was also applied to MnROAD calibration. However, at the time of the analysis only one

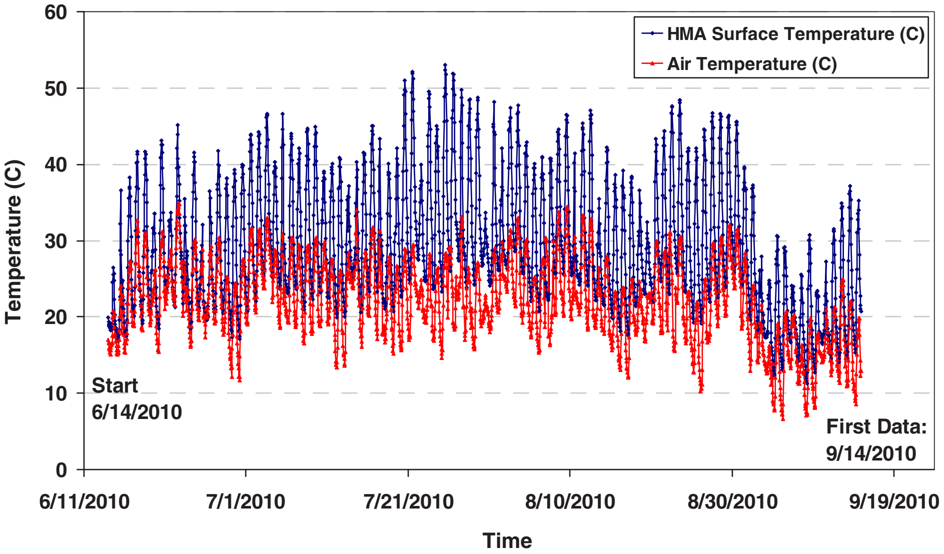

Figure P.19. Variation of HMA surface and air temperatures for Cell 70 of MnROAD for the analysis period. Note that Fahrenheit = Celsius × 9/5 + 32.

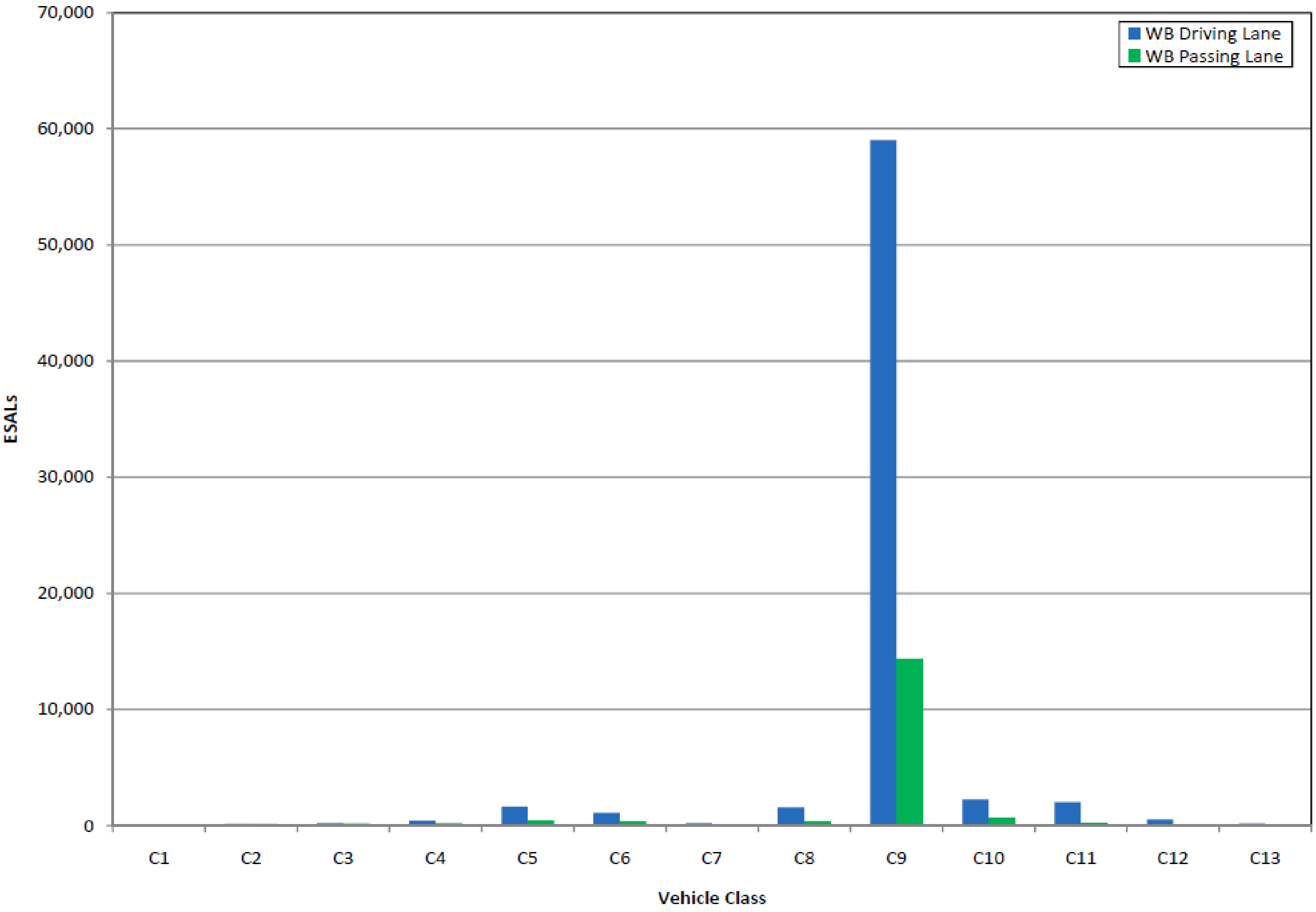

Figure P.20. Total ESALs by vehicle class and lane.

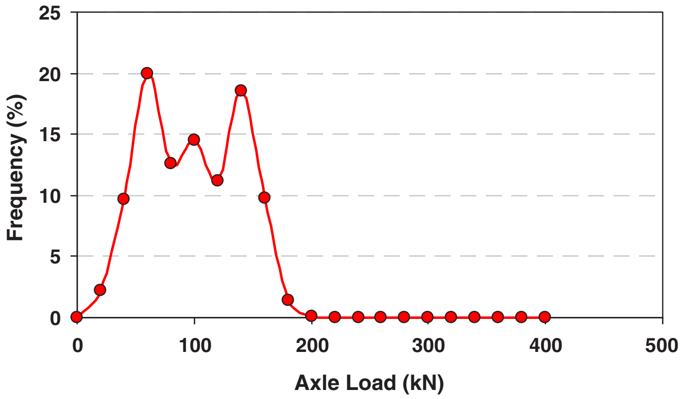

Figure P.21. Tandem axle load distribution (1 kN = 225 lb).

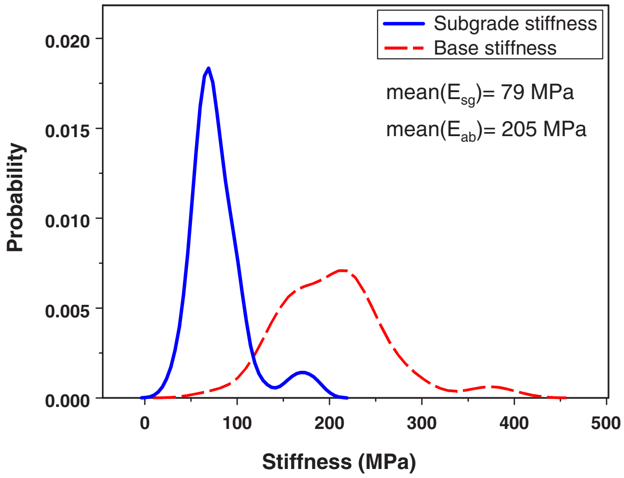

Figure P.22. Distributions for the back-calculated stiffness values (1 MPa = 145 psi).

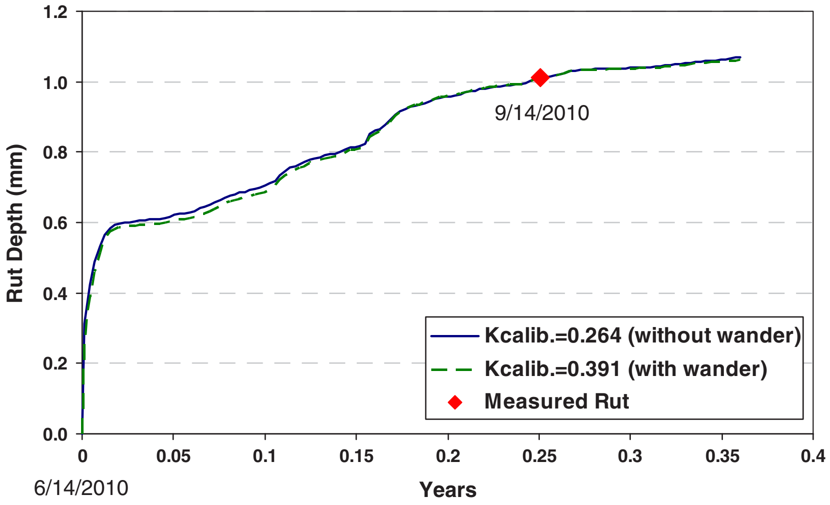

Figure P.23. MnROAD-measured rutting compared with calibrated CalME rutting model predictions (25.4 mm = 1 in.).

rutting performance data point, collected on September 14, 2010, was available for the calibration, which significantly decreases the reliability of the predicted calibration coefficient. However, calibration coefficients can be modified using the data from future collections.

Rut depths were calculated by averaging the measured data from the inside and outside wheelpaths and using the maximum for calibration. The average of maximum rut depths was used for the calibration. Data collected on June 7, 2010, was subtracted from the data collected on September 14, 2010, to determine the accumulated rut depth after the start date of the trafficking, which was June 14, 2010. CalME simulations were performed with and without traffic wander. Figure P.23 shows the calibration results. The calibration coefficient for Cell 70 appears to be lower than the coefficients calculated for the HVS test sections. The low calibration coefficients appear to be a result of the worse performance of the asphalt concrete laboratory samples under RSST-CH testing, and having only one very early performance point to calibrate against. In addition, the mix was tested at 45°C and 55°C in the laboratory, before temperature history was obtained from MnROAD. It appears that it would have been more appropriate to perform the RSST-CH results at 35°C and 45°C, which are temperatures more typical of those that occur at 50-mm depth at MnROAD.

Composite structures similar to those in the HVS test sections were subjected to a sensitivity analysis using the CalME rutting and reflection cracking models. The purpose of the sensitivity analysis was to determine the effect of asphalt thickness under several traffic and climate scenarios on rutting and reflection cracking performance for a factorial of composite pavement structures. The effects of HMA thickness on concrete cracking are considered in this appendix. Variables considered in this study were climate, traffic, mix type, aggregate base stiffness, crack spacing, and asphalt concrete layer thickness.

Factor Levels for Sensitivity Study Variables

Climate

Data from five climate regions were used for the analysis: Denton, Texas; the MnROAD site in Minnesota; Sacramento and Los Angeles in California; and Kenansville, Florida. Air temperatures were converted to pavement surface temperatures using the stand-alone Enhanced Integrated Climatic Model (EICM) software for the thin HMA (64-mm) structure of the HVS test sections. Distributions of pavement surface temperatures for the given climate regions from EICM are shown in Figure P.24.

Traffic

Internal CalME traffic groups classified by Lu et al. (2009) were used for the sensitivity analysis. Lu et al. processed Caltrans WIM data collected during the period 1991 to 2003 from all 108 California WIM stations and classified truck traffic from the stations into a small number of groups on the basis of cluster analysis of axle load spectra. In this sensitivity study, four different axle load spectra groups were used: WIM 1A, WIM 2AA, WIM 2BA, and WIM 3B. The axle load spectra in each group, averaged to give the group-level default load spectra, are plotted in Figure P.25. Trucks at WIM sites in Group 1 have more light axles than heavy axles, and trucks at the other WIM sites have more heavy axles. Trucks at WIM sites in Group 3 have the highest percentage of heavy axles

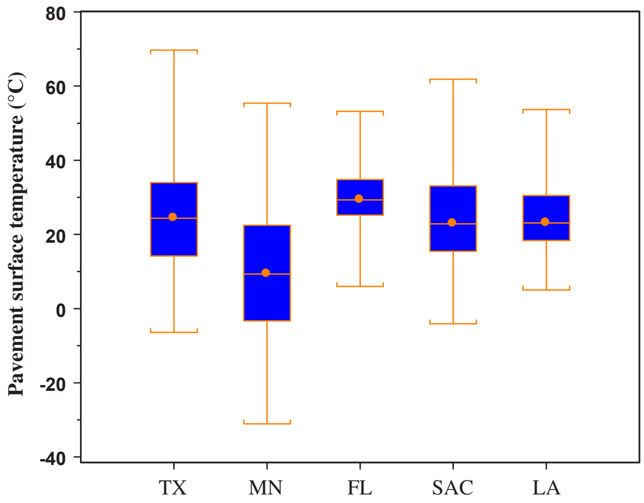

Figure P.24. Distribution of pavement surface temperatures for the five climate regions: Texas (TX), Minnesota (MN), Florida (FL), and Sacramento (SAC) and Los Angeles (LA) in California. Note: Fahrenheit = Celsius × 9/5 + 32.

and represent the typical long-haul traffic on rural Interstates. Trucks at WIM sites in Groups 2A and 2B have similar percentages of heavy axles, but trucks at Group 2B WIM sites have higher percentages of intermediate load axles and lower percentages of light axles than do trucks at Group 2A WIM sites (Lu et al. 2009).

California state highway axle load spectra generally have less than approximately 10% of tandem axles that are over the California legal limit (34 kip [151 kN]). Previous comparisons with WIM data from some midwestern stations indicate that those states may have as much as 20% overloaded vehicles, an axle load spectrum group that was not considered in this study.

Mix Type

Three mix types were considered: PG 64-28 PM dense-graded, RHMA-G, and PG 64-16 dense-graded. Rutting and cracking model coefficients for each material type were determined based on the laboratory tests results described in Appendix N, except for the PG 64-16 mix, for which the coefficients were taken from a previous laboratory study. It should be noted that the aggregate source is the same for the PG 64-28 PM and RHMA-G mixes and different for the PG 64-16 mix. The rutting model calibration coefficient (*K*) calculated by using the result of the HVS tests (Appendix L) was used for the sensitivity analysis.

Structure Type

Two composite structure sections, one with 2.5 in. (64 mm) of asphalt and the other with 4.5 in. (114 mm) of asphalt, on top of a 7-in. (178-mm) PCC layer and 6-in. (150-mm) aggregate base were used for the sensitivity analysis. These structures are the same as those of one of the HVS test sections. PCC layers were assumed to be nondoweled for the analysis.

Aggregate Base Stiffness

Two different aggregate base stiffness values (29,028 psi [200 MPa] and 58,055 psi [400 MPa]) were used to identify

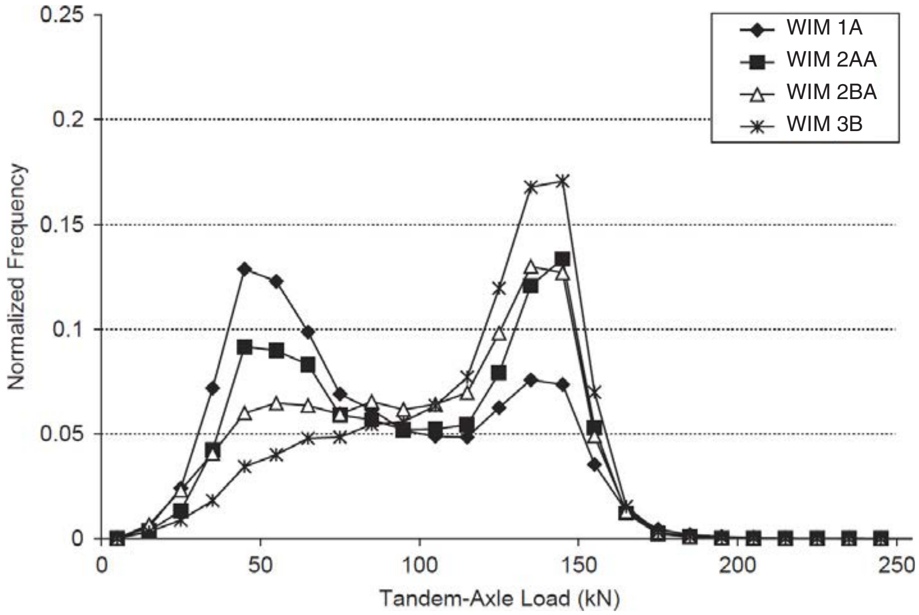

Figure P.25. Tandem axle load spectra averaged by group (Lu et al. 2009) (1 kN = 225 lb).

the effect of this parameter on rutting and cracking performance. The 200 MPa stiffness is similar to the aggregate base stiffness of the MnROAD and HVS test sections. The subgrade stiffness was assumed to be 14,514 psi (100 MPa) and was not varied in the sensitivity study.

Crack Spacing

The effect of crack spacing on cracking performance was also analyzed. Two crack spacing values were used for the analysis, 3.28 ft (1 m) and 15.1 ft (4.6 m), the latter being the joint spacing for the HVS test sections.

Results of the Sensitivity Study

The factorial of 5 climates × 4 traffic spectra × 3 mixes × 2 asphalt thicknesses × 2 base stiffnesses (included for the cracking study) resulted in 240 cases for rutting sensitivity analysis. Addition of the crack spacing parameter (1 m and 4.6 m) resulted in 480 cases for the analysis of reflection cracking performance. Design plots were used to identify the effects of all variables on rutting and reflection cracking. Design plots generally are used to compare the influence of different variables and factor levels on the variation of the dependent variable.

Rutting and cracking at 5, 10, 15, and 20 years were used as dependent variables for the analysis. However, most of the rutting is accumulated at the initial stages of the design life, so the trend in the design plots does not appear to change with increasing years. Similarly, the order and the level of influence for each parameter in the cracking sensitivity analysis do not change with increasing traffic. For this reason, the design plot for only the 5th year is shown for rutting and the design plots for only the 5th and 20th years for cracking analyses.

It can be seen in Figure P.26 that for the rutting analysis, mix type has the largest effect on accumulated rutting, which is a result of the good rutting performance of mix PG 64-16. Climate and layer thickness also appear to significantly affect the predicted rutting values. As expected, higher rut depths were observed for the structure with the thicker asphalt layer. By comparing Figure P.24 and Figure P.26, it can be concluded that there is strong correlation between the peak pavement surface temperatures and predicted rutting values. For this reason, predicted mean rutting for Minnesota (MnROAD), Florida (Kenansville), and Los Angeles appear to be close to each other.

Design plots for the 5th and 20th years predicted reflection cracking, as shown in Figure P.27 and Figure P.28, respectively. Results are given in surface crack density (m/m^2). One hundred percent of the joints are cracked when the surface crack density reaches the value of 1/(crack spacing) under the assumption that all surface cracks are reflection. In this sensitivity study, two crack spacing values were used for the analysis, 3.28 ft (1 m) and 15.1 ft (4.6 m), the latter being the joint spacing for the HVS test sections. It can be observed that mix type has the largest influence on simulated cracking. Crack spacing and asphalt layer thickness also appear to significantly affect the predicted cracking values. On the other hand, the effects of traffic and climate appear to be masked by the significant influence of thickness, mix type, and crack spacing variables. The longer crack spacing predicts less reflection cracking for load-related strains, whereas it would

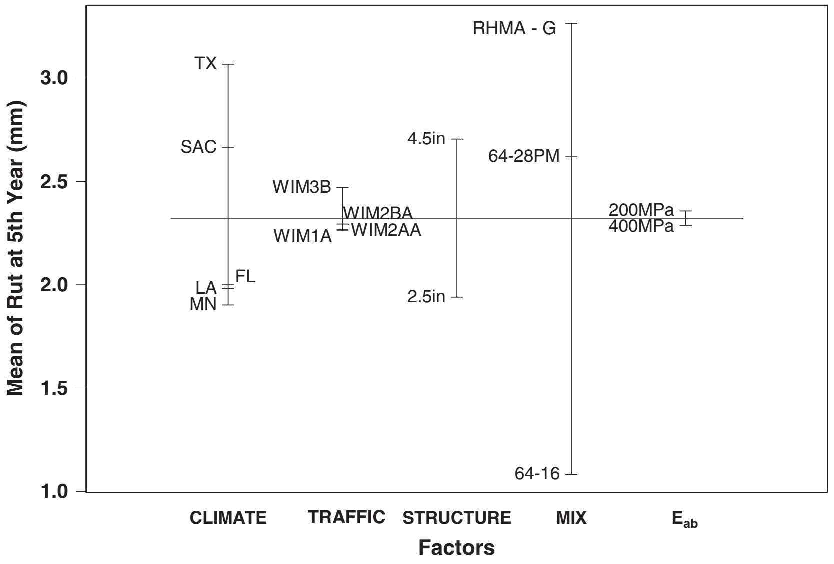

Figure P.26. Design plot of 5th year rutting (downward rut) showing effects of climate, traffic, structure, mix type, and aggregate base stiffness (E_{ab}) (25.4 mm = 1 in.).

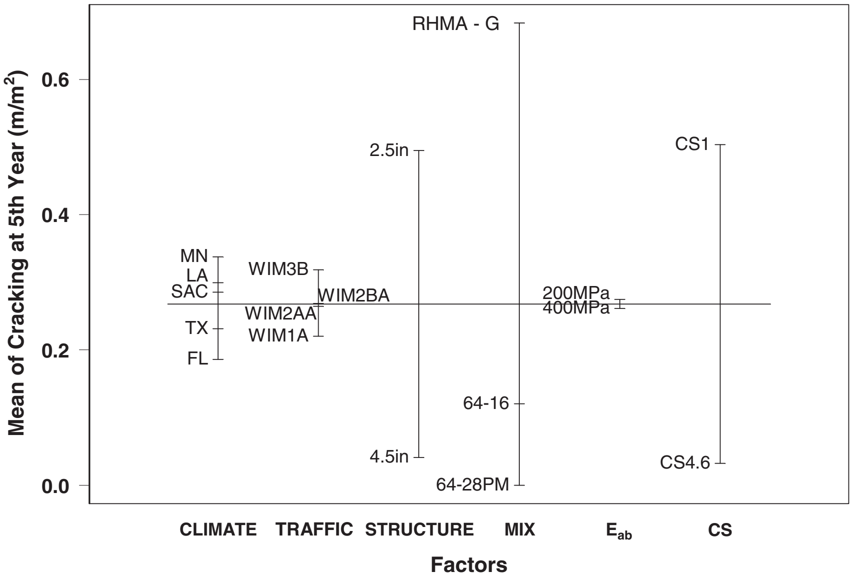

Figure P.27. Design plot of 5th year cracking showing effects of climate, traffic, structure, mix type, aggregate base stiffness, and crack spacing (1 m = 39.37 in.).

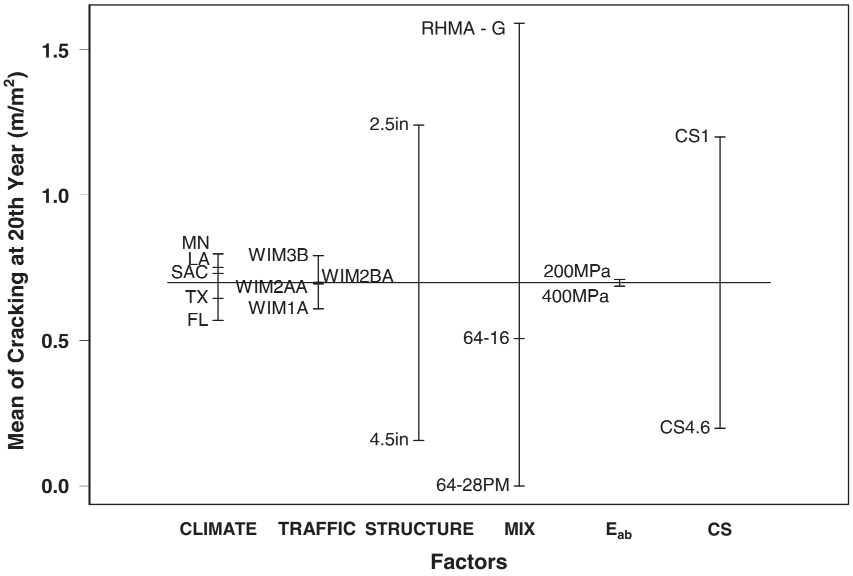

Figure P.28. Design plot of 20th year cracking showing effects of climate, traffic, structure, mix type, aggregate base stiffness, and crack spacing (1 m = 39.37 in.).

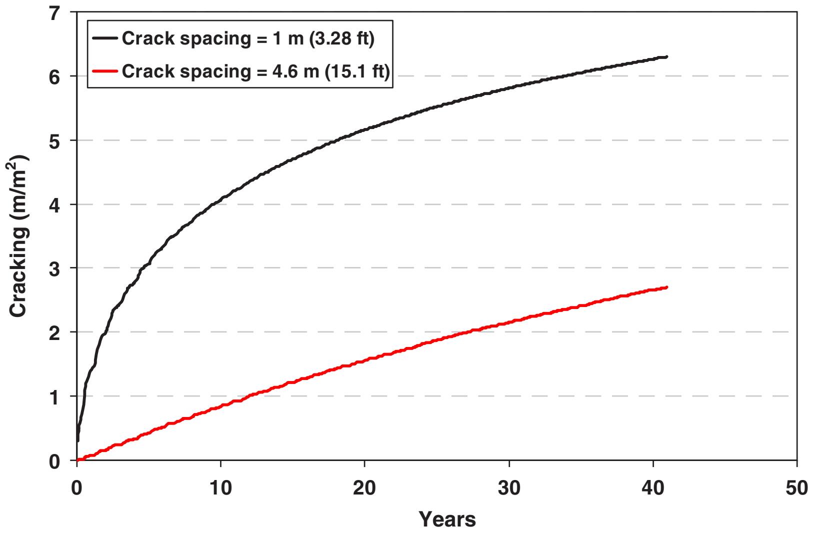

Figure P.29. The effect of crack spacing on predicted cracking for the Minnesota climate case: (a) structure: HMA thickness is 2.5 in., PCC thickness is 7 in.; (b) mix type: RHMA-G; and (c) aggregate base stiffness is 200 MPa (the only difference between the two cases is the crack spacing).

be expected to potentially produce more cracking for low-temperature–induced strains, which are not considered in CalME at this time. It can be seen that cracking generally doubles between the 5th and 20th years.

By comparing Figure P.24 and Figure P.27, it can be concluded that predicted cracking values are correlated with the median pavement surface temperatures, but this correlation is not as strong as was observed for rutting. PG 64-28 PM mix does not show any cracking for any of the cases analyzed in this sensitivity study. As expected from the laboratory test results, mean predicted cracking for the highway with PG 64-28 PM mix is significantly lower than that for the RHMA-G mix. The effect of crack spacing over time is illustrated in Figure P.29. It can be observed that decreasing crack spacing from 15.1 ft (4.6 m) to 3.28 ft (1 m) nearly doubles the surface cracking for a 40-year design period.

APPENDIX Q

Laboratory Testing of PCC Mixes

Introduction

Laboratory work to measure plastic and hardened concrete properties was a part of the SHRP 2 R21 Composite Pavements project. This appendix reports on the properties of recycled concrete aggregate (RCA) and all aggregates used in the composite pavement concretes, concrete mixture design development for the portland cement concrete (PCC)/PCC composite pavements, and plastic and hardened concrete properties to use in software modeling the composite pavements. As a review, the concrete mixture designs consisted of an exposed aggregate concrete (EAC) mixture that served as the top layer of the PCC/PCC composite pavements and RCA and a high fly ash (low cost [LC]) concrete mixture that served as concrete for the lower lifts of the PCC/PCC composite pavements.

To understand the scope of these tests and estimate the time and equipment necessary to accomplish these tasks, a preliminary laboratory plan was assembled with a timeline. This preliminary laboratory plan is featured. Although the plan does not capture all of the laboratory work that was done, it is included in this report because it provided a framework with which to develop a work plan that helped the team move forward.

Following the preliminary laboratory plan, the following sections are included in this appendix:

- Aggregates: summary of adopting an aggregate gradation for the exposed aggregate concrete and summary of finding a substitute source of recycled concrete aggregates for RCA mix design development; and
- Results from third party independent laboratory tests of the proposed concrete mix designs to be used for composite pavement construction.

SHRP 2 R21 Preliminary Laboratory Plan

Tables Q.1 through Q.3 explain some of the tasks in the preliminary laboratory plan.

Aggregates

Exposed Aggregate Concrete

The exposed aggregate concrete required a gradation of both coarse and fine aggregates that allowed a certain number of exposed aggregate peaks once the paste was brushed away. The range of percent by mass of aggregate particles passing each sieve was determined based on the recommendations of a German contractor with experience building EAC-surfaced pavements. The ideal EAC gradation range, which includes coarse and fine aggregates, is noted in Figure Q.1 with dotted lines. The x-axis shows the sieve size and the y-axis represents that percentage by mass of aggregates passing through each sieve size. The accepted EAC gradation range is denoted on Figure Q.1 with dashed lines. The actual gradation of coarse and fine aggregates used to build the SHRP 2 R21 exposed aggregate concrete surface is indicated by a smooth line. Although the gradation is not ideal since it does not meet the originally-specified gap gradation, the R21 contractor had access to aggregates that fit within the upper and lower bounds of the relaxed (final) target gradation.

Recycled Concrete Aggregates

The SHRP 2 R21 research team and the ready mix concrete provider encountered a challenge during preparations for construction of the composite pavement lower lifts that contained RCA. The RCA that was going to be used in construction would not be available for tests or mix design development until a few days before construction began, and the research team needed to find an acceptable substitute. From an extensive literature review of RCA use in concrete, the research team knew that the substitute RCA needed to

- Have a similar gradation.
- Come from an existing concrete with a similar maximum size aggregate.

Table Q.1. Aggregate Gradation and Absorption Analysis

ASTM	Estimated No. of People and Amount of Time	Sample Size	Equipment
C702—Reducing large field aggregate samples	1 person 1.5 h (first time)	15 kg (33 lb) (for maximum 1.5-in. aggregate)	• Clean area on floor • Flat shovel • Push broom • Hand broom • Dust pan • Aggregate receptacle
C117—Grading of materials finer than No. 200 sieve by washing	1 person Time dependent on time it takes sample to dry in oven	Based on the amount of fines gleaned from sample obtained in C702	• Pan (for drying aggregate) • Scale • Nos. 200 and 16 sieves • Water receptacle • Container that can be agitated without losing water • Oven
C136—Sieve analysis of fine and coarse aggregates	2 or more persons (if the automatic sieve shaker in the laboratory is not working), 1–2 persons if it is working Time dependent on time it takes sample to dry in oven	15 kg (33 lb) (for maximum 1.5-in. aggregate)	• Pan (for drying aggregate) • Scale • Coarse aggregate sieves—1.5-, 1-, ¾-, ½-, ⅜-in. • Fine aggregate sieves—Nos. 4, 8, 16, 30, 50, 100 • Clean, preweighed receptacles for sieved aggregate • Oven (230°F ± 9°F)
C127—Density, specific gravity, and absorption of coarse aggregate	1 Person Time (Day 1) dependent on time it takes sample to dry in oven +30 min Time (Day 2) dependent on time it takes sample to dry in oven +2.5 h	Coarse aggregate from sieve analysis	• Scale • Scale that can measure hanging basket • Hanging wire basket • Water tank • Oven • Sieve
C29—Unit weight and voids in aggregate	1 Person Time is immediately following final drying for absorption test—1 h	125%–200% of the quantity required to fill the measure (use coarse and fine aggregate from sieve analysis)	• Scale • Tamping rod • Measure (bottom of air pressure test apparatus) • Shovel or scoop

Table Q.2. Mixing Concrete and Filling Molds

ASTM	Estimated No. of People and Amount of Time	Sample Size	Equipment
Finish cleaning laboratory Clean out floor water drain Clean out large concrete mixer Clean pans and bowls Prepare volumetric air meter	2 people Time is 3 hours	na	• Hammer, screwdriver, chisel • CPC concrete remover
Label cylinders, beams, and cube molds, prep beam molds with release agent, make modulus of elasticity sample holders with gauge studs	2 people Time is 4 h	na	• Permanent markers • Beam molds • Cylinder molds • Cube molds • Masking tape/duct tape • Gloves
Soak coarse RCA for at least 24 h before batching. Prepare to apply saturated surface dry condition for batching.	1 person Time is 15 min	na	• Coarse aggregate • Tub to soak aggregate

(continued on next page)

Table Q.2. Mixing Concrete and Filling Molds (continued)

ASTM	Estimated No. of People and Amount of Time	Sample Size	Equipment
C566—Moisture content of fine/coarse aggregate	1 person Time is 15 min	Depends on the size of the hot plate/pan	• Sample of aggregate • Frying pan (old) • Hot plate
Adjust water requirement of mix based on C566	1 person Time is unknown	na	• Computer
C192—Making and curing concrete test specimens in the laboratory	2 or more People Time depends on how many batches need to be done Estimate 2 h/batch with cleanup in between	1 batch (⅓ yd^3)	• Mixer • Materials for making concrete • Scale • Internal vibrator (must use for low slump) • Graduated cylinder • Clean pans to hold mix constituents • Tamping rods • Rubber mallet • Cylinder molds • Beam molds • Cube molds
C143—Slump	1 person at 5, 10, and 15 min after batching Time is 5 min	Glean from mixer	• Slump apparatus • Rod • Shovel • Gloves
C173—Air content, volumetric method	1 person Time is 30 min	Glean from mixer	• Volumetric air meter • Funnel • Tamping rod • Strike-off bar • Graduated cylinder • Isopropyl alcohol • Measuring device for alcohol • Rubber syringe • Scoop • Rubber mallet • Gloves
C138—Density and yield	1 person Time is 15 min	Glean from mixer	• Scale • Tamping rod • Internal vibrator • Measure (bottom of pressure-based air test apparatus) • Strike-off plate • Rubber mallet
C1064—Temperature of freshly mixed concrete	1 person Time is 5 min	Use a cast cylinder	• Digital thermometer
Curing	na	na	• Curing bath • Curing environment: 73.5°F ± 3.5°F
Cleanup	2 or more people Time is 2 h	na	• Towels • Water

Note: NA = not available.

Table Q.3. Strength and Freeze-Thaw Testing

Time after Batching	ASTM/Test	Estimated No. of People and Amount of Time	Type/No. of Samples	Equipment
24 ± 8 h	Demold cylinders	2 People Time is 4 h	All	• Hole poker • Hammer • Air nozzle • Carts for transport
24 ± 2 h	RILEM 117—demold cubes and place in tap water bath	1 Person Time is 1.5 h	6 prisms/mix	• Tub for bath
Day 2	C617—Capping cylindrical concrete specimens	1 Person Time is setup plus 30 min	3 cylinders/mix	• Capping compound • Capping equipment in hood
Day 3	C39—Compressive strength of cylindrical concrete specimens	1 person Time is 1 h	3 cylinders	• Forney machine • Camera
Day 6	C617—Capping cylindrical concrete specimens	1 person Time is set up plus 30 min	3 cylinders	• Capping compound • Capping equipment in hood
Day 7	C39—Compressive strength of cylindrical concrete specimens	1 person Time is 1 h	3 cylinders	• Forney machine • Camera
Day 7	RILEM 117—Remove prisms from tap water and store in 68°F, 65% relative humidity dry environment	1 person Time is 1.5 h	6 prisms	• Temperature/humidity control room
Day 13	C617—Capping cylindrical concrete specimens	1 person Time is set up plus 30 min	3 cylinders	• Capping compound • Capping equipment in hood
Day 14	C39—Compressive strength of cylindrical concrete specimens	1 person Time is 1 h	3 cylinders	• Forney machine • Camera
Day 14	RILEM 117—Seal lateral sides of prism specimens	1 person Time is 2 h	6 prisms	• Aluminum foil with butyl rubber
Day 21	RILEM 117—Weigh specimens and place specimens in holders	1 person Time is 2 h	6 prisms	• 3% Sodium chloride solution at 68°C • Scale • Plastic syringe
Day 22	RILEM 117—Check fluid level in specimen containers and weigh specimens	1–2 people Time is 2 h	6 prisms	• 3% Sodium chloride solution at 68°C • Container for sodium, chloride solution • Scale • Plastic syringe
Day 24	RILEM 117—Check fluid level in specimen containers and weigh specimens	1–2 people Time is 2 h	6 prisms	• 3% Sodium chloride solution at 68°C • Container for sodium chloride solution • Scale • Plastic syringe
Day 27	RILEM 117—Check fluid level in specimen containers and weigh specimens	1–2 people Time is 2 h	6 prisms	• 3% Sodium chloride solution at 68°C • Container for sodium chloride solution • Scale • Plastic syringe
Day 27	C617—Capping cylindrical concrete specimens	1 Person Time is set up plus 30 min	3 cylinders	• Capping compound • Capping equipment in hood
Day 28	RILEM 117—Clean specimens in ultrasonic bath—discard particles	1 Person Time is 1 h	6 prisms	• Ultrasonic bath
Day 28	C39—Compressive strength of cylindrical concrete specimens	1 person Time is 1 h	3 cylinders	• Forney machine • Camera
Day 31 (after 6 cycles)	RILEM 117—Measure scaling Dry filtered material	2 people Time is 2.5 h	6 prisms	• Scale • Ultrasonic bath • Filter • Filter paper—weighed • Drying oven

(continued on next page)

Table Q.3. Strength and Freeze-Thaw Testing (continued)

Time after Batching	ASTM/Test	Estimated No. of People and Amount of Time	Type/No. of Samples	Equipment
Day 32	RILEM 117—After 24 h drying and 2 h at 20°C, 65% relative humidity, weigh filter plus scaled material	1 Person Time is 2 h	6 filters	• Scale
Day 35 (after 14 cycles)	RILEM 117—Measure scaling Dry filtered material	2 people Time is 2.5 h	6 prisms	• Scale • Ultrasonic bath • Filter • Filter paper—weighed • Drying oven
Day 36	RILEM 117—After 24 h drying and 2 h at 20°C, 65% relative humidity, weigh filter plus scaled material	1 Person Time is 2 h	6 filters	• Scale
Day 42 (after 28 cycles)	RILEM 117—Measure scaling Dry filtered material	2 people Time is 2.5 h	6 prisms	• Scale • Ultrasonic bath • Filter • Filter paper—weighed • Drying oven
Day 43	RILEM 117—After 24 h drying and 2 h at 20°C, 65% relative humidity, weigh filter plus scaled material	1 Person Time is 2 h	6 filters	• Scale
Day 55	C617—Capping cylindrical concrete specimens	1 Person Time is set up plus 30 min	3 cylinders	• Capping compound • Capping equipment in hood
Day 56	C39—Compressive strength of cylindrical concrete specimens	1 person Time is 1 h	3 cylinders	• Forney machine • Camera

- Come from an existing pavement that failed because of fatigue or structural inadequacies and not because of material failure.
- Have a similar absorption capacity, implying that the quantity of mortar attached to the aggregates was similar.
- Come from a concrete mix with approximately the same strength requirements (similar quantity of cement, w/c ratio).
- Be crushed with similar equipment (industrial jaw crusher with a secondary cone crusher).

The following options were explored:

- Minneapolis had a large stockpile of RCA that was produced from multiple sources of existing concrete, such as street, curb, and drainage infrastructure. The existing concrete was crushed by a large industrial crushing contractor, similar to the crushing process that would be used for the R21 RCA, for use as a road base. Because of the variable sources from which the RCA was made, the research team decided against using this as a substitute test aggregate

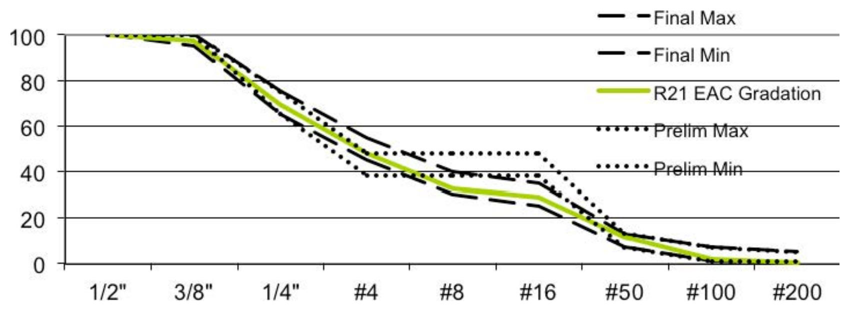

Figure Q.1. Exposed aggregate concrete aggregate gradation, indicated by percentage passing each sieve, and limits.

because, given the variable source material, it would have been difficult to obtain a final product with a consistent absorption and gradation.

- MnROAD had a small quantity of existing concrete pavement that contained similar aggregates and was made with a similar mix design as the concrete pavement that would be removed and crushed to produce RCA for the R21 project. Consultation with three large crushing operators resulted in the same conclusion: there was not enough material to produce any RCA with a large-scale crusher. Instead, the material was crushed in a laboratory that had a small concrete crusher. The result was an RCA that looked much different from any RCA the research team had seen before. Instead of the typical aggregate covered with mortar, the particles appeared to be primarily mortar embedded with pieces of broken aggregate. The particles were more angular and rough than even a typical crushed aggregate.
- The Minneapolis–St. Paul International Airport was reconstructing a runway, and an industrial crushing contractor was stationed on site to crush the existing concrete pavement. The original aggregate was limestone aggregate, different from the crushed gravel that would be used for R21 construction. The R21 research team obtained a dump-truck full of this material.

Ultimately, the choice was between an RCA made from a similar source material but crushed with a different technique and an RCA made from a source material with a different aggregate but crushed with similar equipment that would be used to make the RCA for the concrete used in the composite pavement construction. Visual inspection, gradation, and absorption were the parameters employed to help the R21 research team make a decision. The following figures show the results of inspection, gradation, and absorption of the potential substitute RCAs.

Inspection

The following photographs show the visual differences between the Minneapolis, laboratory-crushed, and airport RCAs. Figure Q.2 shows the Minneapolis RCA variability of aggregate color and shape as it was processed from many different original concrete sources. Figure Q.3 shows that many of the laboratory-crushed RCA particles appear as aggregate particles embedded in mortar. Figure Q.4 shows a sample of the limestone-based airport RCA. The particles appear mostly intact, with small quantities of mortar on the original aggregate particles.

Gradation

The research team was limited by the project specifications to using RCA particles in the size range that passed the 1-in.

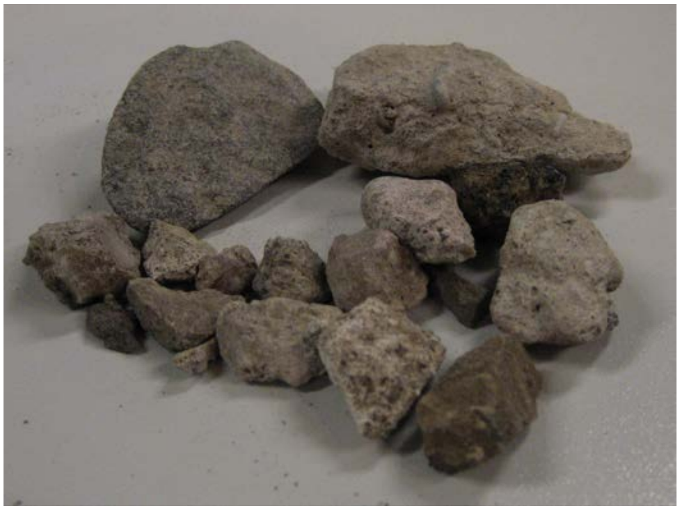

Figure Q.2. Minneapolis RCA that originated from multiple sources.

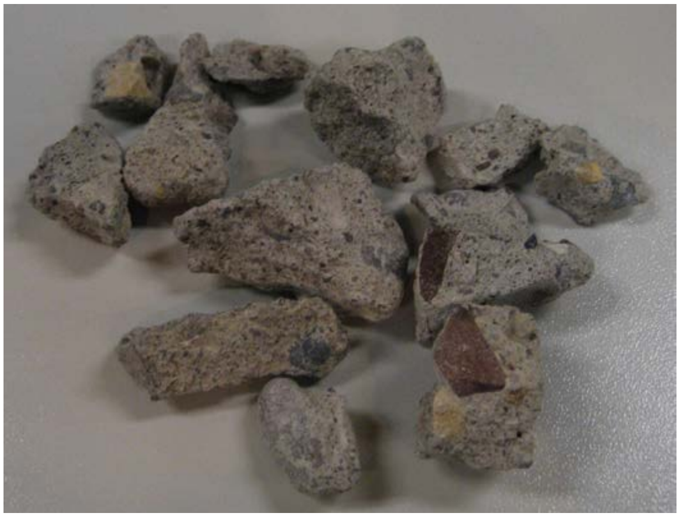

Figure Q.3. Laboratory-crushed RCA.

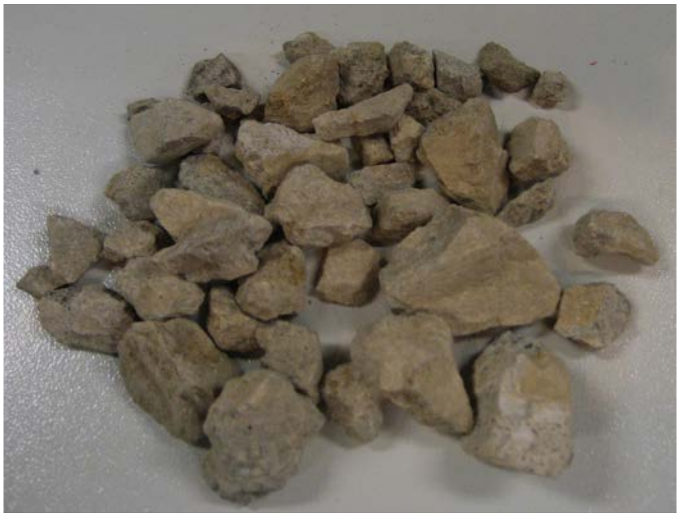

Figure Q.4. Airport RCA.

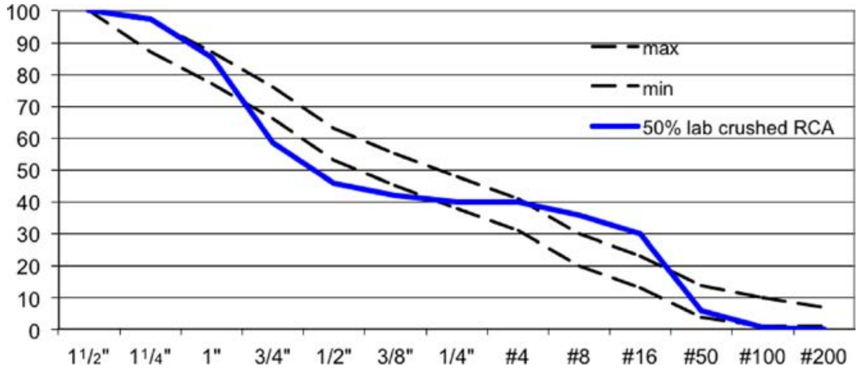

Figure Q.5. Gradation indicated by percentage passing each sieve with 50% of coarse aggregate replaced with laboratory-crushed RCA.

sieve and remained on the No. 4 sieve. In total, 50% of the coarse aggregate could consist of RCA. The RCA was combined with a No. 4 coarse conventional gravel aggregate source that contained particles between 1 in. and 1½ in. and a fine conventional aggregate source. As a guide, limits were established for the complete gradation because neither the contractor nor the research team knew what the gradation of the RCA—from any source—would look like. The following figures show how the aggregate gradations looked with both the laboratory-crushed RCA and the airport RCA. After observing the variability in the Minneapolis RCA, it was decided not to use it as alternate source.

Sieve analyses were conducted on the laboratory-crushed and airport RCA according to ASTM C136 (Sieve Analysis for Fine and Coarse Aggregates) (see Figure Q.5 and Figure Q.6). Airport RCA fines—aggregates that did not pass the No. 4 sieve—were separated from the coarse RCA by sieving and washing, because recycled fines were not used for this project.

Absorption

In addition to the aggregate gradation, a regimen of tests were conducted on the lab-crushed and airport RCA according to ASTM C127 (Density, Relative Density [Specific Gravity], and Absorption of Coarse Aggregate) and ASTM C29 (Bulk Density [Unit Weight] and Voids in Aggregate). The following aggregate properties and corresponding values determined from these tests are presented in Tables Q.4 and Q.5.

As a follow-up to this battery of tests, the University of Minnesota conducted three additional absorption tests on the airport RCA. These absorption values in addition to an average absorption, including the value taken from Table Q.5, are shown in Table Q.6.

Based on observation (most uniform), gradation (mostly within limits), and absorption (airport = 2.42% versus laboratory-crushed = 3.3%), the R21 research team made the recommendation that the airport RCA would be the best RCA to use for mix design development.

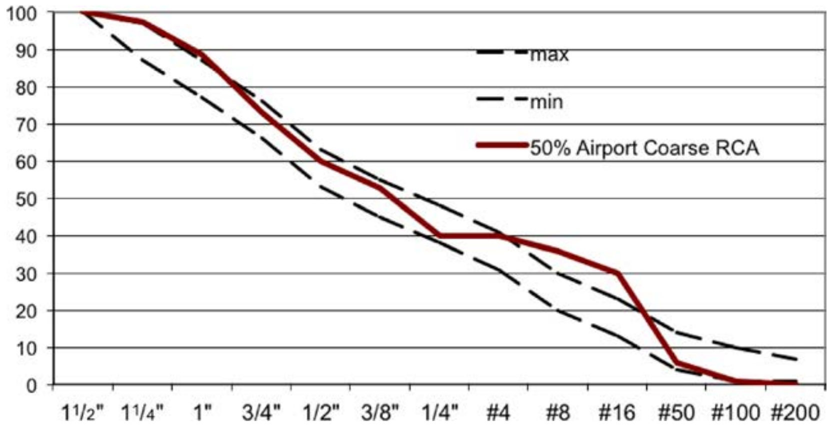

Figure Q.6. Gradation indicated by percentage passing each sieve with 50% of coarse aggregate replaced with airport RCA.

Table Q.4. Assessment of Laboratory-Crushed Coarse RCA Properties

Property Name	Value
Saturated surface dry (SSD) specific gravity	2.54
Absorption	3.2%

Table Q.5. Assessment of Airport Coarse RCA Properties

Property Name	Value
Oven dry (OD) specific gravity	2.34
SSD specific gravity	2.38
Density (OD)	146 lb/ft^3
Density (SSD)	149 lb/ft^3
Absorption	1.9%
Bulk density (of dry rodded sample)	96.62 lb/ft^3
Percentage of voids (of dry rodded sample)	33.73%

It was noted that when the contractor preliminarily batched the RCA mix using 2.5% for the absorption of the RCA to adjust the mixture water requirements, the contractor reported that the mix required more water than was calculated (approximately 2% to 5% more than anticipated). The research team suspected that the primary reason for the additional water requirement was the failure to wash the RCA of fine material (i.e., for the airport RCA, 2% by weight of particles passed the No. 200 sieve). As part of its preparatory research in the R21 project use of RCA, the research team found that a majority of the literature on large-scale use of RCA identified recycled fines as a major problem. In the future, it was recommended that all RCA be washed and kept saturated (e.g., through the use of a continuous sprinkler) before batching.

Table Q.6. Reported Absorption for RCA Recovered from Minneapolis–St. Paul Airport

	Absorption (Percent Water Retained)
Trial 1	1.90
Trial 2	2.78
Trial 3	2.83
Trial 4	2.16
Average	2.42

RCA Used for Construction of R21 Composite Pavements

The RCA used in the concrete for construction of the R21 composite pavements came from existing concrete pavement that was removed from the existing I-94 roadway, delivered to the contractor, crushed, washed, and delivered to the ready-mix concrete plant. Figure Q.7 shows the gradation, indicated by percentage aggregate particles passing each sieve, of the 50% RCA aggregate created with industrial crushed concrete pavement, conventional No. 4 aggregate, and conventional fine aggregate.

As indicated by Figure Q.7, this gradation was mostly between the limits and more smooth than either of the gradations that contained the lab-crushed and airport RCA. It should be noted that the crushing process was specifically tailored to create aggregate particles smaller than 1 in. and to limit the amount of fines, which may be one of the reasons for the particular shape of the gradation curve. In contrast, the existing airport concrete was crushed for the purpose of being road base. It is beyond the expertise of the research team or the R21 concrete crushing contractor to know if the airport RCA would have had a different gradation had it been crushed specifically for the R21 project. Similarly, it is likely that the

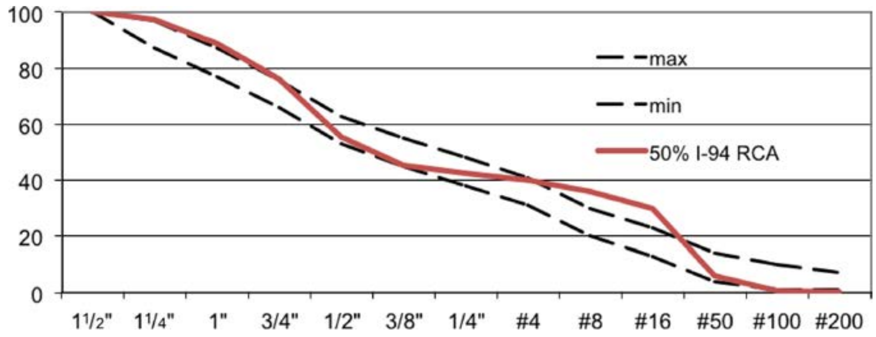

Figure Q.7. Percentage of washed industrial-crushed I-94 concrete pavement passing each sieve.

laboratory-crushed RCA would have had a similar appearance and gradation as the I-94 RCA if it had been crushed with industrial crushing machines and to the specifications of the R21 project.

Verifying Mix Designs

For construction of a typical concrete pavement in Minnesota, the contractor typically uses a preapproved MnDOT concrete mix design. Because of the unique two-layer system of PCC/PCC composite pavements, the project had the opportunity to innovate with the pavement concrete because three new mix designs were required. The following bullets outline the items that guided the contractor regarding development of each of the three mix designs. These items were included in the project's special specifications:

- A top layer concrete that would have an exposed aggregate finish. The R21 project team required the contractor to use a crushed granite polish-resistant aggregate and the team provided the contractor with an aggregate gradation that would be necessary to achieve the exposed aggregate finish. This mixture will be referred to as EAC.
- A bottom layer concrete that allowed up to 50% of the coarse aggregate between the sizes of No. 4 and 1 in. The RCA specification allowed as much as 10% of the recycled aggregate particles to be asphalt particles. This mixture will be referred to as RCA.
- A bottom layer concrete that allowed as much as 60% fly ash or ground granulated blast furnace slag substitution of cement and allowed relaxed restrictions on the aggregate used. This mixture will be referred to as low cost (LC).

All concretes were required to meet a compressive strength of 4,000 psi at 28 days, to have a 7% ± 1.5% entrained air bubble volume, and to maintain a w/c ratio below 0.4. In addition to developing the concrete mixtures, it was the responsibility of the contractor to have them verified by a third-party, independent testing agency. Table Q.7 shows the mix design constituents and Table Q.8 shows the plastic concrete properties. Table Q.9 shows the compressive strengths. Table Q.10 shows the flexural strengths of these concrete mix designs as reported by the third-party independent testing agency.

The materials used by the independent testing agency were the same materials used by the contractor:

Cement:	Holcim St. Genevieve Portland Cement (ASTM C150) Type ½
Fly Ash:	Headwaters Coal Creek (ASTM C618 Class F)
Fine Aggregate:	Elk River Concrete Sand (ASTM C33)

Table Q.7. Mix Design Constituents of the Concrete Mixtures Designed for PCC/PCC Composite Pavement Construction

Quantity (per yd^3)	**EAC**	**RCA**	**LC**
Type 1 cement (lb)	616	360	240
Fly ash (lb)	109	240	360
Sand (lb)	843	1,200	1,263
⅜-in. Washed granite chips (lb)	843	na	na
½-in. Washed granite chips (lb)	1,133	na	na
¾-in. Rock (lb)	na	na	1,102
1½-in. rock (lb)	na	na	787
No. 4 (1½-in.) Rock (lb)	na	825	na
Recycled concrete aggregate No. 4 (1 in.)	na	920	na
Water reducer (oz)	14.5	10	6
Accelerator (oz)	na	180	180
Hydration stabilizer (oz)	18.1	na	na
Air entrainer (oz)	10.5	2.8	6.5
Water (lb)	283	234	173
Water/Cementitious ratio	0.39	0.39	0.29

Table Q.8. Plastic Concrete Properties

	EAC	**RCA**	**LC**
Slump, initial (in.) After 15 min (in.) After 30 min (in.)	2.0 1.75 1.75	3.0 2.5 2.25	2.0 2.0 1.75
Air content, initial (%) After 15 min (%) After 30 min (%)	6.1 6.0 5.7	7.2 6.8 6.5	6.8 6.0 5.8
Unit weight (lb/ft^3)	143.2	142.6	147.2
Temperature (°F)	67	75	67
Initial set time (h:min) Final set time (h:min)	6:09 7:55	4:30 5:55	5:08 7:11

Table Q.9. Compressive Strength

Compressive Strength (psi)[a]	**EAC**	**RCA**	**LC**
1 day	3,310	1,070	1,520
3 days	5,000	3,310	2,360
7 days	5,660	3,690	3,110
28 days	6,590	5,260	4,110
56 days	7,280	na	5,150

[a] Average of two tests.

Table Q.10. Flexural Strength

Flexural Strength (psi)[a]	EAC	RCA	LC
1 day	505	410	250
3 days	760	730	350
7 days	855	585	600
28 days	1,150	990	640
56 days	1,175	na	810

[a] Average of two tests.

Coarse Aggregate (EAC):	⅜ in. Washed Granite Chips Martin Marietta (ASTM C33) and ½ in. Washed Granite Chips Martin Marietta (ASTM C33)
Coarse Aggregate (RCA):	Recycle Concrete Aggregate McCrossan Maple Grove (ASTM C33) and No. 4 (1½ in.) Gravel Elk River (ASTM C33)
Coarse Aggregate (LC):	No. 67 ¾ in. Gravel Elk River (ASTM C33) and No. 4 (1½ in.) Gravel Elk River (ASTM C33)
Water Reducer:	Sika 686 (ASTM C494, Type A)
Accelerator:	Sika Set NC (ASTM C494, Type C)
Hydration Stabilizer:	BASF Delvo (ASTM C494, Type S)
Air Entrainment:	Sika Multi-Air 25 (ASTM C260)

Plastic concrete tests were performed according to the following ASTM standards:

Slump:	C143: Standard Test Method for Slump of Portland Cement Concrete
Air:	C231: Standard Test Method for Air Content of Freshly Mixed Concrete by the Pressure Method
Unit Weight:	C138: Standard Test Method for Unit Weight, Yield and Air Content (Gravimetric) of Concrete
Time of Setting:	C430: Standard Test Method for Time of Setting Concrete Mixtures by Penetration Resistance

Compressive strength tests were performed on 4- × 8-in. cylinders according to ASTM C39: Standard Test Method for Compressive Strength of Cylindrical Concrete Specimens.

Flexural strength tests were performed on 6- × 6- × 24-in. beams according to ASTM C78: Standard Test Method for Flexural Strength of Concrete.

APPENDIX R

MEPDG Modifications for PCC/PCC Pavements

MEPDG EICM Modifications for SHRP 2 R21

In adopting the *Mechanistic–Empirical Pavement Design Guide* (*MEPDG*) for the design and analysis of newly constructed composite portland cement concrete (PCC)/PCC pavements, an initial modeling simplification made was to treat a newly constructed PCC/PCC composite pavement as a bonded PCC-over-jointed plain concrete pavement (JPCP) project. This change was implemented in *MEPDG* (beta versions 1.014:9030A and 1.206:R21), and research for the composite PCC/PCC portion of the SHRP 2 R21 project that used the *MEPDG* simulated new PCC/PCC construction using a bonded PCC-over-JPCP project in the *MEPDG*. However, the decision to use a bonded PCC overlay project to mirror new PCC/PCC construction introduced numerous challenges. An important goal of the research was the desire to overcome these challenges in a way that was compatible with the Enhanced Integrated Climatic Model (EICM) and the *MEPDG*. The following sections describe the research that uncovered and addressed the challenges in using *MEPDG* to design and predict the performance of newly constructed PCC/PCC by detailing:

1. How the *MEPDG* challenges addressed by the R21 research were first encountered.
2. The relevant sensitivity studies conducted to understand the models at work in *MEPDG* and the EICM used by *MEPDG*.
3. A brief overview of the *MEPDG* calculation of stresses for rigid pavements, with particular emphasis on temperature curling stresses.
4. A few modeling simplifications made by EICM for bonded PCC overlay projects and suggested revisions to EICM to adjust the models for the benefit of composite PCC pavements.
5. The implementation of these suggested revisions and a brief sensitivity study to examine the effect of these revisions on the *MEPDG*.

Problem Formulation

Several experimental batch runs were conducted to gauge the fundamentals of the *MEPDG* for performance predictions of PCC/PCC composite pavements. One simple test of the *MEPDG* modeling was to create two projects describing the same PCC pavement. The only difference in the two projects was that one project was a bonded PCC-over-JPCP project (*MEPDG*'s analog to new PCC/PCC, as discussed above) and the other project was a single-layer JPCP. The input parameters defining these two cases, and the layer properties themselves, were identical except for the layer thicknesses. The project inputs are briefly summarized in Table R.1, where PCC properties listed are for a single-layer project and both layers of a two-lift project.

These structurally identical projects were run through the *MEPDG* for identical traffic levels, climate, and design life. Table R.2 reports results for this pair of pavements for *MEPDG* 1.014:9030A.

This simple comparison of PCC/PCC and its single-layer PCC equivalent revealed notable discrepancies in the predicted performance (particularly in damage caused by top-down cracking). Again, these two pavements are structurally equivalent and should perform identically from a mechanistic point of view. Although the empirical nature of the *MEPDG* prevents the predicted performance from being identical, it is reasonable to assume that performance of these pavements should have very small discrepancies. Table R.2 illustrates that this is not the case. As a result of this early observation, a more extensive sensitivity analysis was conducted to better understand the differences in predicted performance for structurally equivalent two-lift and single-layer PCC pavements in the *MEPDG*.

MEPDG EICM Sensitivity Analysis

An extensive sensitivity analysis was conducted using two beta versions of the *MEPDG* (1.013:9030A and 1.206:R21) to differentiate between the modeling of composite PCC/PCC

Table R.1. **MEPDG** *Inputs for Basic Sensitivity Analysis Project for R21 PCC/PCC Investigation*

Input Parameter	Value	Input Parameter	Value
Design life	20	PCC composite thickness	9
Location	Florida, US-41	PCC modulus of rupture	650
Initial international roughness index (IRI)	63	PCC Poisson's ratio	0.2
Traffic	800	PCC coefficient of thermal expansion	5.5×10^{-6}
Permanent curl/warp	–10	PCC thermal conductivity	1.25
Dowel spacing	1.25 in.	PCC heat capacity	0.28
Dowel diameter	12 in.	PCC unit weight	150
Base	6 in., lime stabilized	PCC cement content	600
Subbase	12 in., A-3	PCC w/c ratio	0.42

pavements (bonded PCC overlay) with their structurally equivalent single-layer JPCP counterparts. The factorials composing the sensitivity analysis focused on variables, including

- Composite PCC layer thicknesses;
- Upper lift PCC (overlay) flexural strength;
- Lower lift PCC flexural strength;
- Upper lift PCC coefficient of thermal expansion; and
- Upper lift PCC modulus of elasticity.

Although the two versions produced different results, this is not because of changes in the EICM modeling, which was consistent for both versions and which was the focus of the research detailed here. The most interesting of the sensitivity analysis cases were those in which only the thicknesses of the PCC/PCC composite layers were adjusted. These cases are compared with one another in Table R.3.

Both bottom-up cracking and top-down cracking vary unreasonably for such small changes to PCC lift thickness. Although a statistical analysis of these data might be revealing, simple observation reveals inherent modeling contradictions. According to the initial modeling used for *MEPDG* R21, a reduction in top layer thickness from 3 in. to 2.5 in. increased bottom-up cracking by 205%; however, a reduction in top layer thickness from 3 in. to 1.5 in. increased bottom-up cracking only by 13%.

In addition, the cases depicted in Table R.2 yielded interesting results on the calculated subgrade response, or *k*-value, for the two systems. Figure R.1 illustrates these results. Note that *MEPDG* calculates the subgrade *k*-value on a monthly basis, and the values for 1 year are representative of those in the pavement 20-year design life.

It is apparent in Figure R.1 that the *k*-values of the PCC/PCC project (in blue) and those of its single-layer equivalent (in red) are not similar; these values differ by as much as 7.5%. Even at the most similar, the two *k*-values diverge by 3.5%. These results suggested that the EICM subgrade reaction calculation was deserving of additional attention.

The sensitivity analysis presented above clearly indicates that an analysis of identical structures performed by the *MEPDG* leads to different characterizations of the structures and, subsequently, performance predictions. A detailed analysis of the *MEPDG* temporary project files identified problems in the interaction of the EICM with the stress analysis routines. To address this issue, the stress analysis of the multilayered JPCP in the *MEPDG* was first reconsidered, after which modifications

Table R.2. **MEPDG** *1.014:9030A Predictions for Performance of Composite PCC/PCC and Its Single-Layer Structural Equivalent*

H (in.)	IRI (in./mi)	% Slabs Cracked	Faulting (in.)	Bottom-up Cracking	Top-down Cracking
9	67	0.4	0.006	0.0421	0.0431
3 over 6	68.9	0.8	0.006	0.0223	0.0846
Absolute % differential in predicted performance	2.8%	100%	0.0%	47.0%	96.3%

Note: H = PCC thickness.

Table R.3. Top-Lift (PCC Overlay) Thickness and Bottom-Up Cracking in **MEPDG** *Version 1.014:9030A*

H (in.)	IRI (in./mi)	% Slabs Cracked	Faulting (in.)	Bottom-up Cracking	Top-down Cracking
3 over 6	68.9	0.8	0.006	0.0223	0.0846
3.1 over 5.9	69.1	0.6	0.005	0.0136	0.0740
2.9 over 6.1	69.4	0.7	0.006	0.0404	0.0722
2.8 over 6.2	69.4	0.8	0.006	0.0488	0.0715
2.5 over 6.5	69.4	0.9	0.006	0.0681	0.0624
2 over 7	69.3	0.8	0.006	0.0434	0.0750
1.5 over 7.5	68.8	0.8	0.006	0.0252	0.0808

Note: H = PCC thickness.

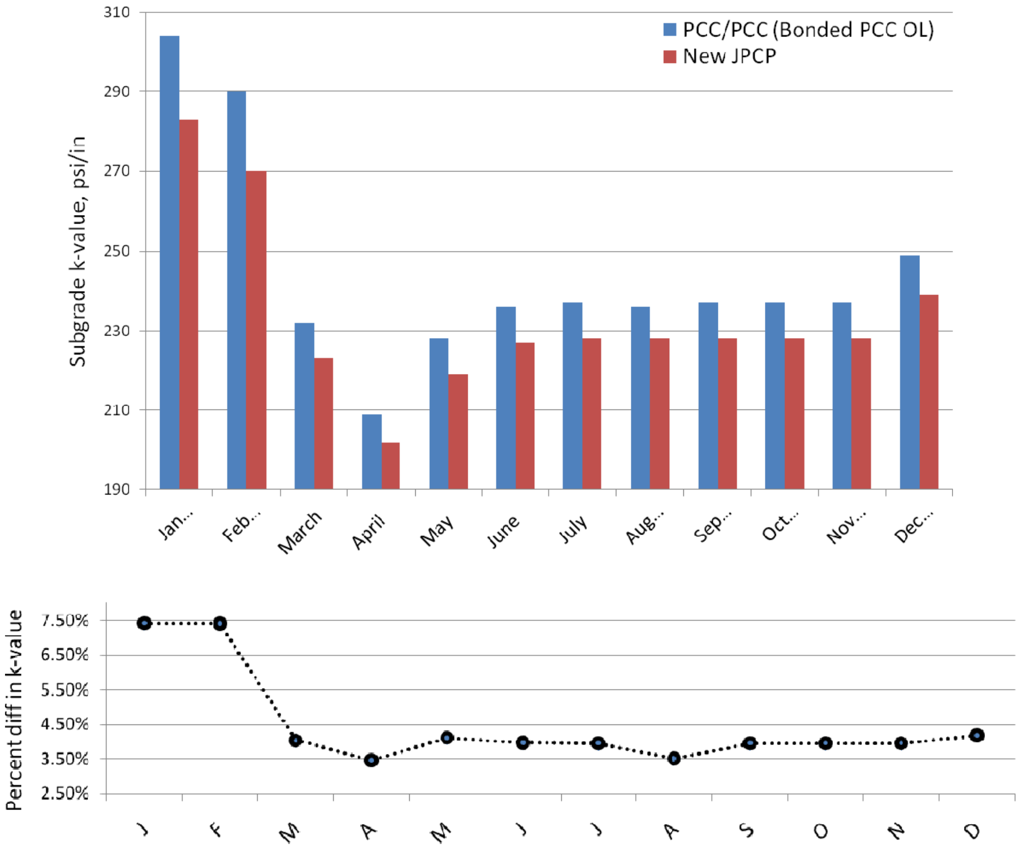

Figure R.1. Subgrade **k***-value calculation for a PCC/PCC pavement and its JPCP single-layer structural analog* **(MEPDG** *versus 1.206:R21). (OL = Overlay.)*

to the EICM to better interact with the *MEPDG* stress analysis routines were developed. The following sections detail the relevant *MEPDG* stress calculation routines and the relevant EICM routines.

MEPDG Stress Calculation

The *MEPDG* stress analysis of rigid pavements is based on the slab equivalency concept and the use of artificial neural networks. The following subsections describe the slab equivalency concept, which was adopted by the *MEPDG* to reduce the number of independent parameters affecting PCC stresses without introducing any additional error. A main component of the stresses in a rigid system is temperature curling, and given that suggested EICM revisions later detailed in this appendix deal with the distribution of temperature through a single-layer or two-layer PCC slab, thermal stresses in rigid systems are briefly reviewed.

Stresses Caused by Temperature Curling

Rigid and composite pavements are subjected to bending stresses under temperature gradients and traffic loads. Khazanovich (1994) demonstrated the existence of an additional stress attributed to the nonlinear temperature distribution through a PCC layer that acts on single or multilayered pavement systems so as to produce stresses that are self-equilibrating in nature. Consider a slab on an elastic foundation subjected to an arbitrary temperature distribution. The arbitrary temperature distribution may be linear or nonlinear through the thickness of the slab but does not vary in the plane of the slab, and the slab is free to contract or expand in the horizontal directions. According to Thomlinson (1940) any arbitrary temperature distribution, $T(z)$, can be divided into a constant-strain-causing temperature component, T_C, a linear-strain-causing temperature component, T_L, and a nonlinear-strain-causing temperature component, T_{NL}. Each of these three components may vary through the depth of the slab, z, along with the temperature $T(z)$.

The constant-strain-causing temperature component, T_C, produces horizontal strains that are constant through the depth of the slab. These strains do not produce stress when the slab is unrestrained in the horizontal direction. The linear-strain-causing temperature component, T_L, produces horizontal strains that are linearly distributed along the depth of the slab. T_L produces bending stresses that can be solved by using any finite element-based method. Given the constant and linear strain-causing temperature components, T_L and T_C, the nonlinear-strain-causing temperature component, T_{NL}, can be written as seen in Equation R.1:

$$T_{NL}(z)-T_o = T(z)-[T_C(z)-T_o]-[T_L(z)-T_o]-T_o \qquad \text{(R.1)}$$

where T_o is a given reference temperature and z is the depth through the slab. For slabs modeled using linear elastic material models, the corresponding stress at any depth z according to Hooke's law is given in Equation R.2:

$$\sigma_{NL}(z) = -\frac{E(z)\alpha(z)}{(1-\mu)}(T_{NL}(z)-T_o) \qquad \text{(R.2)}$$

where μ is the Poisson's ratio of the layer. The total stress at any point in the slab caused by combined traffic loading and temperature curling is given in Equation R.3:

$$\sigma_{\text{Total}}(z) = \sigma_{\text{bending}}(z)+\sigma_{NL}(z) \qquad \text{(R.3)}$$

where bending stresses caused by traffic loads and linear-strain-causing temperature component T_L should be added to the self-equilibrating stresses caused by the nonlinear-strain-causing temperature component T_{NL}.

Slab Equivalency Concept

In the *MEPDG* calculation of stresses for rigid pavements, the number of independent parameters affecting stresses in a multilayered system can be reduced by using an equivalent single layer slab and equivalent linear temperature gradient. Once the stresses in the equivalent system are solved for, the stresses in the multilayered system can be computed using Korenev's equivalent slab method (detailed below). According to this concept, a multilayered pavement system could be simplified by using an equivalent transformed section in the form of a single layer slab (AASHTO 2008). The solution of a multilayered system could be developed from the solution for the equivalent single-layer slab.

The equivalent single-layer slab must exhibit the same deflection profile as the multilayered slab if the load and the foundation properties (k-value) are the same. This concept employs three equivalency conditions: (1) equivalent thickness, (2) equivalent temperature gradient, and (3) equivalent slab. The *MEPDG* documents application of this theory for the analysis of a JPCP with a base layer. Equations R.4 to R.12 demonstrate the equivalency concept for a bonded PCC-base composite system. Similar equations are provided in the *MEPDG* documentation for an unbonded PCC-base system.

Equivalent Thickness

Ioannides et al. (1992) presented an equivalent thickness solution for a multilayered pavement system. The transformation involved flexural stiffness D, with an assumption that the Poisson's ratio of all the layers and that of the equivalent layer were equal:

$$D_{\text{eqn}} = D_{\text{PCC}} + D_{\text{Base}} \qquad \text{(R.4)}$$

$$\mu_{\mathrm{eqn}} = \mu_{\mathrm{PCC}} = \mu_{\mathrm{Base}} \tag{R.5}$$

where the flexural stiffness D is given as

$$D = \frac{E\,h^3}{12(1-\mu^2)} \tag{R.6}$$

where

E, h, μ = Young's modulus, layer thickness, and Poisson's ratio (respectively).

According to Khazanovich (1994), the governing equation of the transformation (Equation R.4) can also be written in terms of moment in each plate M, as follows:

$$M_{\mathrm{eqn}} = M_{\mathrm{PCC}} + M_{\mathrm{Base}} \tag{R.7}$$

For a fully bonded PCC-base system, the neutral axis of the bonded system, assuming the origin is at the top of the PCC layer, is given as follows:

$$x = \frac{\int_0^h E(z)\,z\,dz}{\int_0^h E(z)\,dz} = \frac{E_{\mathrm{PCC}}h_{\mathrm{PCC}}\left(\dfrac{h_{\mathrm{PCC}}}{2}\right) + E_{\mathrm{Base}}h_{\mathrm{Base}}\left(h_{\mathrm{PCC}} + \dfrac{h_{\mathrm{Base}}}{2}\right)}{E_{\mathrm{PCC}}h_{\mathrm{PCC}} + E_{\mathrm{Base}}h_{\mathrm{Base}}} \tag{R.8}$$

where x = location of the neutral axis from the top of PCC layer.

The thickness and modulus of the equivalent single-layer slab can be established in terms of the thicknesses and moduli of the corresponding multilayered slab by combining Equations R.4 to R.8 as follows:

$$E_{\mathrm{eff}}h_{\mathrm{eff}}^3 = E_{\mathrm{PCC}}h_{\mathrm{PCC}}^3 + E_{\mathrm{Base}}h_{\mathrm{Base}}^3 + 12\left[\begin{array}{l} E_{\mathrm{PCC}}h_{\mathrm{PCC}}\left(\dfrac{h_{\mathrm{PCC}}}{2} - x\right)^2 \\ + E_{\mathrm{Base}}h_{\mathrm{Base}}\left(h_{\mathrm{PCC}} + \dfrac{h_{\mathrm{Base}}}{2} - x\right)^2 \end{array}\right] \tag{R.9}$$

For a fully bonded PCC/PCC-base system, the neutral axis x is located as follows, assuming the origin is located at the surface of the upper lift PCC layer:

$$x = \frac{\dfrac{E_{\mathrm{PCC1}}}{E_{\mathrm{PCC2}}}\dfrac{h_{\mathrm{PCC1}}^2}{2} + h_{\mathrm{PCC2}}\left(h_{\mathrm{PCC1}} + \dfrac{h_{\mathrm{PCC2}}}{2}\right) + \dfrac{E_{\mathrm{Base}}}{E_{\mathrm{PCC2}}}h_{\mathrm{Base}}\left(h_{\mathrm{PCC1}} + h_{\mathrm{PCC2}} + \dfrac{h_{\mathrm{Base}}}{2}\right)}{\dfrac{E_{\mathrm{PCC1}}}{E_{\mathrm{PCC2}}}h_{\mathrm{PCC1}} + h_{\mathrm{PCC2}} + \dfrac{E_{\mathrm{Base}}}{E_{\mathrm{PCC2}}}h_{\mathrm{Base}}} \tag{R.10}$$

where E_{eff}, E_{PCC1}, E_{PCC2}, and E_{Base} are the Young's moduli of the effective composite system, upper-lift PCC, lower-lift PCC, and base layers, respectively, and h_{eqn}, h_{PCC1}, h_{PCC2}, and h_{Base} are the thicknesses of the effective composite slab, upper-lift PCC, lower-lift PCC, and base layers, respectively.

One check of the solution for the neutral axis in the three-layer PCC system is to consider that if $E_{\mathrm{PCC1}} = E_{\mathrm{PCC2}}$, Equation R.10 will reduce to Equation R.8, which represents the location of the neutral axis in a single-layer PCC over base layer system. The thickness and modulus of the equivalent single-layer slab for the three-layer system can be established, as in Equation R.9, where

$$E_{\mathrm{eff}}h_{\mathrm{eff}}^3 = E_{\mathrm{PCC1}}h_{\mathrm{PCC1}}^3 + E_{\mathrm{PCC2}}h_{\mathrm{PCC2}}^3 + E_{\mathrm{Base}}h_{\mathrm{Base}}^3 + 12\left[\begin{array}{l} E_{\mathrm{PCC1}}h_{\mathrm{PCC1}}\left(x - \dfrac{h_{\mathrm{PCC1}}}{2}\right)^2 \\ + E_{\mathrm{PCC2}}h_{\mathrm{PCC2}}\left(h_{\mathrm{PCC1}} + \dfrac{h_{\mathrm{PCC2}}}{2} - x\right)^2 \\ + E_{\mathrm{Base}}h_{\mathrm{Base}}\left(h_{\mathrm{PCC1}} + h_{\mathrm{PCC2}} + \dfrac{h_{\mathrm{Base}}}{2} - x\right)^2 \end{array}\right] \tag{R.11}$$

Equivalent Linear Temperature Gradient

Thomlinson (1940) introduced the concept of equivalent temperature gradient for a single-layer slab. Khazanovich (1994) and Ioannides and Khazanovich (1998) later generalized the concept for a nonuniform, multilayered slab. The *MEPDG* documentation states that "if two slabs have the same plane-view geometry, flexural stiffness, self-weight, boundary conditions, and applied pressure, and rest on the same foundation, then these slabs have the same deflection and bending moment distributions if their through-the-thickness temperature distributions satisfy the following condition" (Khazanovich et al. 2001):

$$\int_{h_A} E_A(z)\alpha_A(z)(T_A(z) - T_{0,A})\,z\,dz = \int_{h_B} E_B(z)\alpha_B(z)(T_B(z) - T_{0,B})\,z\,dz \tag{R.12}$$

where

A and B = subscripts denoting the two slabs,
z = distance from the neutral axis,
T_0 = temperature at which these slabs are assumed to be flat,
α = coefficient of thermal expansion,
E = modulus of elasticity, and
h = slab thickness.

Khazanovich (1994) also states that "[A]s a corollary, two temperature distributions are equivalent only if their respective linear strain components are identical." Therefore, Equation R.12 can be employed for the curling analysis of a multilayered slab in terms of the curling analysis of a single-layer equivalent slab. The temperature distribution in the single-layer equivalent slab is chosen to be a linear function of depth and can be expressed in terms of temperature distributions of the PCC and base layers as follows in Equation R.13:

$$\Delta T_{L,\text{eff}} = \frac{-12}{h_{\text{eff}}^2}\left(\begin{array}{l} \displaystyle\int_{-x}^{h_{\text{PCC}}-x} [T(z)-T_o]\,z\,dz \\ \displaystyle +\frac{\alpha_{\text{Base}}E_{\text{Base}}}{\alpha_{\text{PCC}}E_{\text{PCC}}} \int_{h_{\text{PCC}}-x}^{h_{\text{PCC}}+h_{\text{Base}}-x} [T(z)-T_o]\,z\,dz \end{array}\right) \tag{R.13}$$

where

$\Delta T_{L,\text{eff}}$ = difference between the top and bottom surface temperatures of the equivalent slab;

$T(z)$ and T_o = temperature distributions and reference temperature, respectively; and

α_{PCC} and α_{Base} = coefficients of thermal expansion of the PCC and base layers, respectively.

For a fully bonded PCC/PCC-base system, the temperature distribution in the single-layer equivalent slab is chosen to be a linear function of depth and can be expressed in terms of temperature distributions of the PCC and base layers as follows in Equation R.14:

$$\Delta T_{L,\text{eff}} = \frac{-12}{h_{\text{eff}}^2}\left(\begin{array}{l} \displaystyle\int_{-x}^{h_{\text{PCC1}}-x} \frac{\alpha_{\text{PCC1}}E_{\text{PCC1}}}{\alpha_{\text{PCC2}}E_{\text{PCC2}}}[T(z)-T_{o\text{PCC1}}]\,z\,dz \\ \displaystyle +\int_{h_{\text{PCC1}}-x}^{h_{\text{PCC1}}+h_{\text{PCC2}}-x} [T(z)-T_{o\text{PCC2}}]\,z\,dz \\ \displaystyle +\int_{h_{\text{PCC1}}+h_{\text{PCC2}}-x}^{h_{\text{PCC1}}+h_{\text{PCC2}}+h_{\text{Base}}-x} \frac{\alpha_{\text{Base}}E_{\text{Base}}}{\alpha_{\text{PCC2}}E_{\text{PCC2}}}[T(z)-T_{o\text{Base}}]\,z\,dz \end{array}\right) \tag{R.14}$$

where

$\Delta T_{L,\text{eff}}$ = difference between the top and bottom surface temperatures of the equivalent slab;

$T(z)$, $T_{o\text{PCC1}}$, $T_{o\text{PCC2}}$, $T_{o\text{BASE}}$ = temperature distribution and reference temperatures for respective PCC and base layers;

α_{PCC1}, α_{PCC2}, and α_{Base} = coefficients of thermal expansion of the PCC and base layers, respectively;

E_{PCC1}, E_{PCC2}, and E_{Base} = Young's moduli of the PCC and base layers, respectively;

h_{PCC1}, h_{PCC2}, and h_{Base} = thicknesses PCC and base layers, respectively; and

h_{eff} = effective thickness of equivalent single-layer system.

One can observe that if $E_{\text{PCC1}} = E_{\text{PCC2}}$, then the solution for the three-layered system in Equation R.14 should coincide with the solution for a single-layer system in Equation R.13.

Equivalent Slab According to Korenev

Korenev and Chernigovskaya (1962) proposed an equivalency concept for circular slabs resting on a Winkler foundation and subjected to traffic loads and temperature curling. According to this concept, the stress distribution in a slab of known dimensions, properties, loading conditions, and temperature gradients is related to the stress distribution in another slab by Equation R.15, if the following are the same (AASHTO 2008):

- Ratio of the slab characteristic dimension to the radius of relative stiffness (L/l);
- The total applied load to the slab self-weight (P/Q); and
- Korenev's nondimensional temperature gradient ϕ.

$$\sigma_1 = \frac{h_2\gamma_1 l_1^2}{h_1\gamma_2 l_2^2}\sigma_2 \tag{R.15}$$

where σ, h, γ, and l = temperature stress, thickness, unit-weight, and radius of relative stiffness of a given slab, respectively.

The *MEPDG* adopts the Korenev's nondimensional temperature gradient to combine many factors that affect curling stresses into one parameter (Khazanovich et al. 2001; AASHTO 2008). It is defined as shown in Equation R.16:

$$\phi = \frac{2\alpha(1+\mu)l^2}{h^2}\frac{k}{\gamma}\Delta T_L \tag{R.16}$$

where

α, μ, l, γ, h = coefficient of thermal expansion, Poisson's ratio, radius of relative stiffness, unit-weight, and thickness of the slab, respectively;

k = modulus of subgrade reaction; and

ΔT_L = linear temperature difference between the top and bottom surface of the slab.

Korenev's slab equivalency concept was modified for the analysis of rectangular slabs. It was found that if the following conditions are fulfilled, then the concept holds true for rectangular slab as well (AASHTO 2008) (Equation R.17):

$$\begin{gathered} l_1 = l_2 \\ L_1 = L_2 \\ \phi_1 = \phi_2 \\ \frac{\text{AGG}_1}{k_1 l_1} = \frac{\text{AGG}_2}{k_2 l_2} \\ \frac{P_1}{\gamma_1 h_1} = \frac{P_2}{\gamma_2 h_2} \\ s_1 = s_2 \end{gathered} \tag{R.17}$$

where

$l = \sqrt[4]{\dfrac{Eh^3}{12(1-\mu^2)k}}$, the stiffness of the slab relative to the foundation stiffness;

E, h, μ = PCC modulus of elasticity, thickness, Poisson's ratio;

L = joint spacing;

ϕ = Korenev's nondimensional temperature gradient;

AGG = aggregate interlock between the main lane and the shoulder;

P = axle weight;

γ = PCC slab unit weight; and

s = distance between slab edge and outer wheel edge.

EICM Temperature Distribution Characterization

EICM Representation of a Thermal Gradient Through a Composite Pavement System

In the original EICM thermal analysis (Version 1.003 and versions before 1.014:9030A), 10 nodes were distributed through the PCC slab with an additional node at the bottom of the base layer, resulting in a total of 11 nodes used to represent the temperature through the PCC slab and base with respect to a reference temperature (NCHRP 2004, Larson and Dempsey 1997, Lytton et al. 1989). This distribution of nodes was then used to calculate the nonlinear stresses at the top and bottom of the slabs for damage calculations, as detailed in "*MEPDG* Stress Calculation."

In the revised EICM thermal analysis in Versions 1.014:9030A and 1.206:R21 for SHRP 2 R21, rather than the 10 nodes being applied to the entire composite slab (approximated by the bonded PCC overlay project), each layer of the slab was assigned 10 nodes, which results in the use of a minimum of 20 temperature nodes for the entire slab and base. These additional nodes present two key challenges. The first challenge is that their inclusion dramatically increases the run-time for the damage calculation in the PCC/PCC pavement. The second, and more important, challenge is that the system with additional nodes threatens the self-consistency of the *MEPDG*, as evidenced by the results in Table R.2. As noted, for a single-layer PCC pavement, EICM uses only 10 nodes. For a new PCC/PCC pavement, the thermal gradient is approximated by EICM using 20 or more nodes through the composite slab. This modeling difference ripples through the project runs and provides results for structurally equivalent systems that are significantly different, when they should instead be nearly identical.

To adjust for this difference, the thermal gradient for a bonded PCC overlay was modified to use PCC layer thicknesses and the base layer thickness to develop 11 equally spaced nodes through the composite slab and a 12th node at the bottom of the base layer, thereby creating 10 intervals in the composite slab and 1 for the base layer. The thermal node arrangement used in *MEPDG* Versions 1.014:9030A and 1.206:R21 is described in Figure R.2a. The R21 recommended thermal node arrangement (used in *MEPDG* versus 1.3000:R21) is described in Figure R.2b.

The recommended modification ensures that PCC/PCC projects and their structurally equivalent single-layer JPCP projects will have the same number of intervals through the PCC slab, be it single-lift or two-lift. This recommendation was implemented in *MEPDG* Version 1.3000:R21.

Implementation of EICM Thermal Node Revisions and Results

To test the effectiveness of the revised thermal nodes of EICM, as implemented in *MEPDG* Version 1.3000:R21, a follow-on sensitivity analysis along the lines of Table R.3 was conducted. Figure R.3 displays the results for this analysis.

In Figure R.3, the reduction in variability in the cracking prediction in the revised EICM used by *MEPDG* Version 1.3000:R21 is immediately apparent. Previous versions that used the original EICM (top of Figure R.3) display erratic behavior, with standard deviation of 0.01472, as the thickness of the upper-lift PCC is decreased in a homogeneous two-lift project. Table R.3 also referred to this behavior, where reductions in upper-lift thickness from 3 to 2.5 in. increased bottom-up cracking by 205%, whereas a reduction in the top layer thickness from 3 to 1.5 in. increased bottom-up cracking only by 13%.

Figure R.3 at bottom illustrates that the revised EICM handles the layer thicknesses in a homogeneous system much more responsibly. Given that both PCC layers are identical, ideally the cracking prediction should not differ no matter the layer thickness. The revised EICM holds to this expectation, displaying a standard deviation of 0.00016, which is 92 times lower than the distribution experienced for the cracking prediction using the original EICM.

EICM Calculation of Subgrade Response for Single-layer and Composite Two-layer Rigid Pavement Systems

After the EICM adjusts the subgrade properties for seasonal variation in the moisture content, a special routine in the *MEPDG* converts the resilient modulus into the subgrade *k*-value to enable the stress analysis.

In adapting the *MEPDG* and EICM to model newly constructed PCC/PCC composite pavements as bonded PCC overlays of existing pavements, a major consideration was the effect of this modeling choice on the calculation of the subgrade response, or *k*-value. For a typical single-layer PCC pavement, the effective dynamic *k*-value is obtained by first

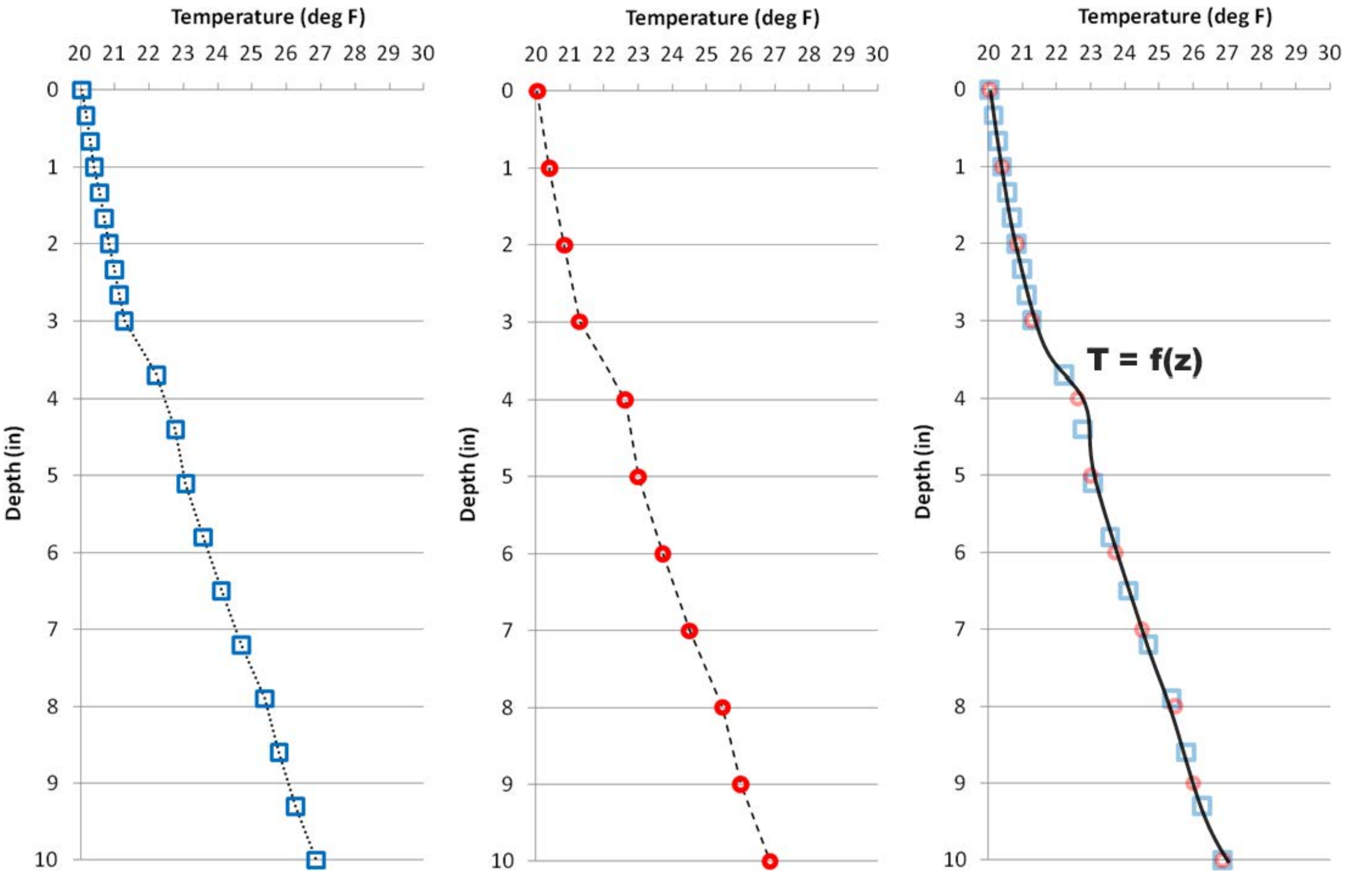

(a) (b) (c)

Figure R.2. Modified thermal nodes through slab thickness in MEPDG *for (a)* MEPDG *1, (b) recommended by R21, and (c) both approximations relative to nonlinear thermal gradient.*

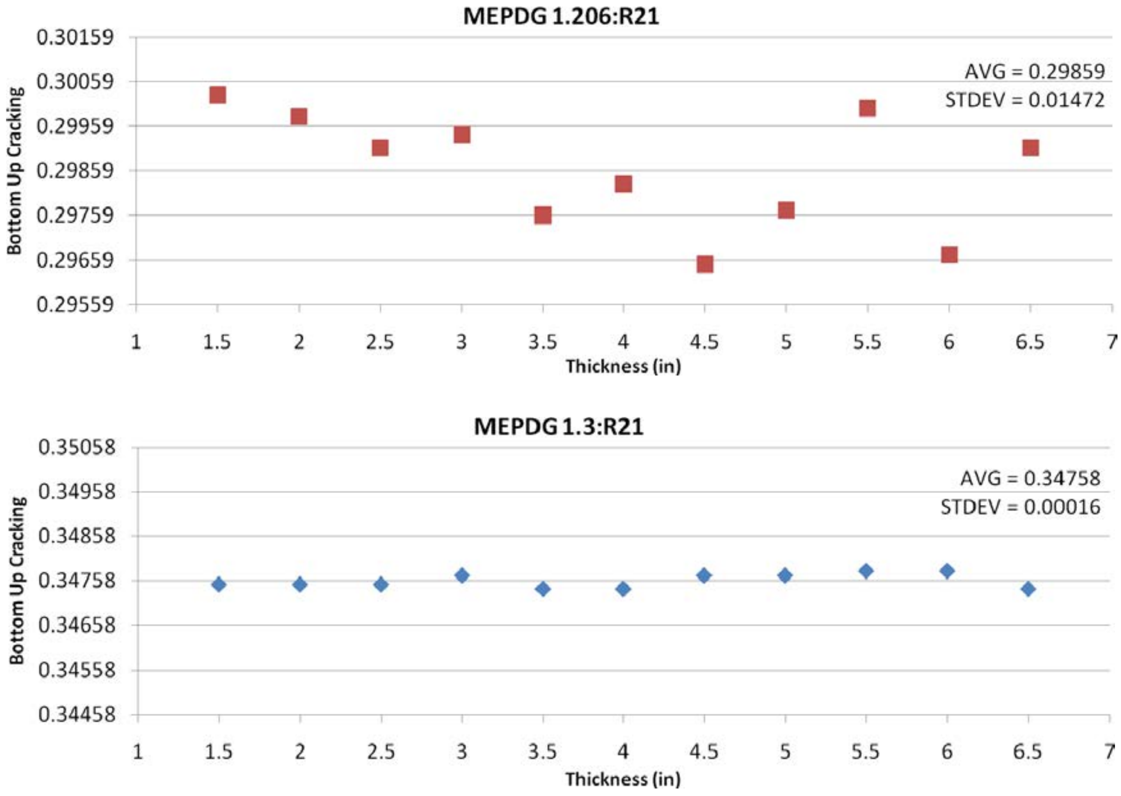

Figure R.3. MEPDG *sensitivity to top-lift (PCC overlay) thickness in terms of bottom-up cracking for* MEPDG *using original EICM (*top*) and revised EICM (*bottom*).*

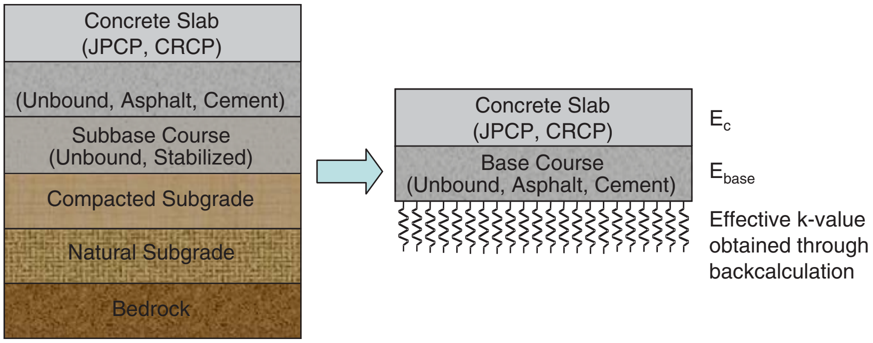

Concrete Slab (JPCP, CRCP)
(Unbound, Asphalt, Cement)
Subbase Course (Unbound, Stabilized)
Compacted Subgrade
Natural Subgrade
Bedrock
Concrete Slab (JPCP, CRCP)
Base Course (Unbound, Asphalt, Cement)
E_c
E_{base}
Effective k-value obtained through backcalculation

Figure R.4. Model illustrating rigid pavement structural response computations.

determining the deflection profile of the PCC surface using an elastic layer program, modeling all layers specified for the design (Figure R.4). The subgrade resilient modulus is adjusted to reflect the lower deviator stresses that typically exist under a concrete slab and base course as compared with the deviator stress used in laboratory resilient modulus testing. Next, the computed deflection profile is used to back-calculate the effective dynamic *k*-value. Thus, the effective dynamic *k*-value is a computed value, not a direct input to the *MEPDG* design procedure (except in rehabilitation).

The effective *k*-value used in the *MEPDG* is a dynamic *k*-value, as opposed to traditional static *k*-values used in previous design procedures. The effective dynamic *k*-value of the subgrade is calculated for each month of the year and used directly to compute critical stresses and deflections in the incremental damage accumulation over the design life of the pavement. Factors such as water table depth, depth to bedrock, and frost penetration depth (frozen material) can significantly affect effective dynamic *k*-value. All of these factors are considered in the EICM (AASHTO 2008).

However, this procedure is different for bonded PCC overlay projects. For a bonded PCC overlay, only the existing PCC layer is used to determine the deflection profile of the PCC using an elastic layer program. Thus, the stiffness contribution of the overlay is discounted. Figure R.5 shows the monthly difference in *k*-values between structurally identical bonded

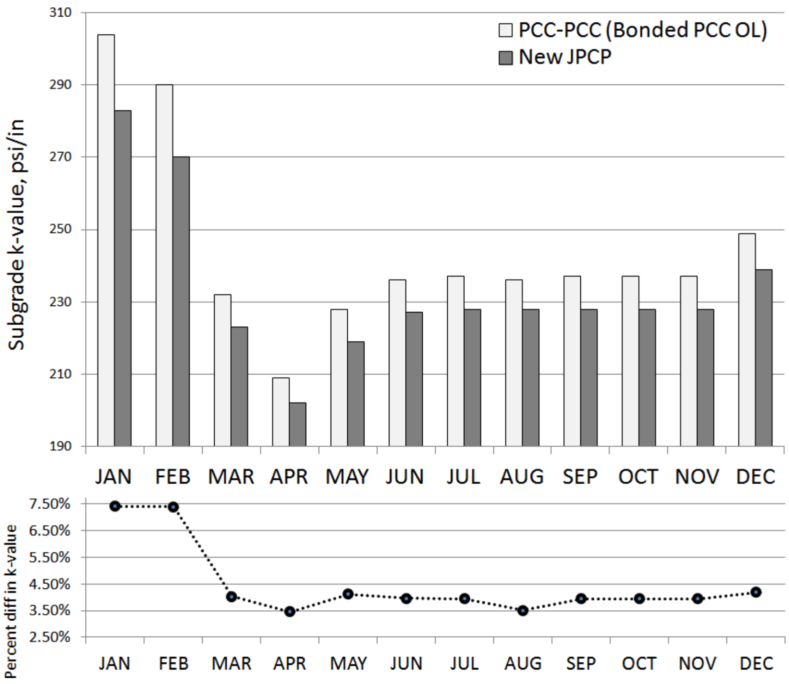

Figure R.5. Subgrade k-value calculation for a PCC/PCC pavement and its JPCP single-layer structural analog (previous versions of MEPDG). (OL = Overlay.)

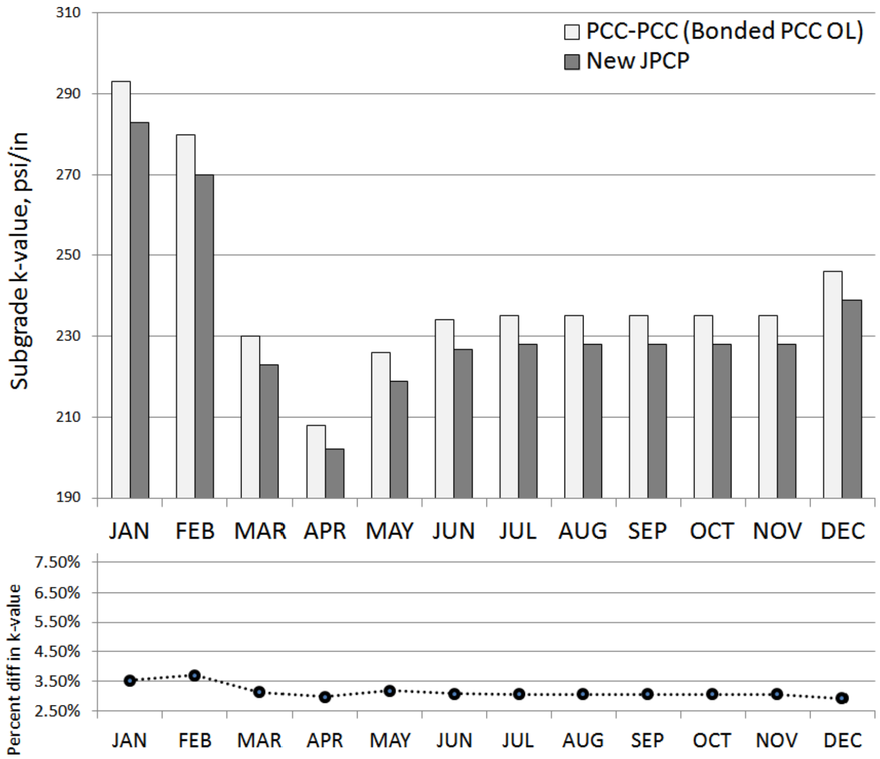

Figure R.6. Subgrade* k*-value calculation for a PCC/PCC pavement and its JPCP single-layer structural analog (*MEPDG *Version 1.3000:R21). (OL = Overlay.)

PCC overlay of JPCP and new JPCP using a previous version of *MEPDG*. The bonded PCC overlay of JPCP (the proxy for PCC/PCC composite pavement) is 3 in. over 6 in. and the JPCP is 9 in., with all material properties for all PCC layers being identical. As described above, this difference arises because the *k*-value is back-calculated using the elastic layer deflection profile and 9-in. PCC for the JPCP but only 6-in. PCC for bonded PCC overlay of JPCP and consequently for PCC/JPCP. For *MEPDG* (Version 1.3000:R21), the bonded PCC overlay of PCC pavement was modified to include the overlay. Or, in terms of composite PCC/PCC, the subgrade response calculation included both lifts of the two-layer PCC slab.

Figure R.6 illustrates that modifications to calculation of the subgrade *k*-value for the bonded PCC overlay project have reduced the extreme differences in the *k*-value for the structurally equivalent systems. However, it may be valuable for future research to note that small differences (approximately 3%) still remain in the monthly calculation of the subgrade reaction, suggesting that additional modifications to the EICM calculation would be needed to make the two designs identical.

APPENDIX S

Lattice 3D Model Background

Lattice Models

A lattice model consists of a triangular grid of points connected by one-dimensional spring elements. This network of springs represents the discretized medium. The lattice can be deformed by internal strains resulting from diffusive, thermal, or hygral processes and/or by external displacements or forces. Lattice models can differ in the representations of the constitutive relations used for individual springs (or, instead, the minimization of the stored elastic energy) (Schlangen and van Mier 1992). The varying properties of springs allow the lattice to simulate the behavior of heterogeneous media, such as concrete.

The characterization of fracture, the essence of the debonding problem, often is simulated in pavement engineering using finite element methods (FEM) that begin with continuum equations. Although FEM can be successfully applied to a fracture problem, the success of the application depends largely on the homogeneity of the medium and the lack of disorder in crack propagation. Modeling of crack propagation in FEM requires the use of special elements in the crack path that must be specified a priori. Thus, if the medium is relatively homogeneous and the crack path can be anticipated, then FEM is more than adequate to simulate cracking. In cases exhibiting heterogeneity or nontrivial crack paths, the placement of the specialized elements for fracture becomes a nontrivial problem. This problem is commonly solved using trial-and-error methods with computationally expensive and cumbersome re-meshing during the fracture process.

In light of these challenges, lattice models are a viable alternative to and/or a candidate to be coupled with FEM. In the lattice model, the simulation of cohesive cracking involves a reduction of stiffness and strength and the removal of individual springs. The lattice model does not require a priori knowledge of the crack path. The application of a specific lattice model—that is, a random network of spring elements—to the portland cement concrete (PCC)/PCC debonding problem is prefaced with a summary of the model formulation and its simulation of fracture.

Lattice Model Formulation and Refinement for Fracture

As discussed in the introduction, FEM is a common approach when one is faced with a numerical problem in engineering research. However, when the fracture occurs in a heterogeneous medium or in a location not easily anticipated, lattice models offer an interesting alternative. Lattice models can be more flexible in predicting cracking through the medium, and the material properties of elements in the lattice can be assigned to replicate a heterogeneous medium—that is, no complications are introduced by neighboring elements possessing vastly different material properties. The formulation of a lattice network of spring elements and the fracture rules assigned to the body are detailed below.

Basic Model Formulation

The lattice model applied to the relevant SHRP 2 R21 project work is a rigid-body-spring network (Bolander and Saito 1998). Beginning with a region containing randomly distributed points, a Delaunay tessellation is used to define a network through the connection of these random points. The model then uses Voronoi diagrams to establish facets surrounding random points (to create nodes) and define nodal/facet volumes for later stress calculations. For each pair of neighboring nodes, we define an element *ij* connecting these nodes (Figure S.1).

Element *ij* can be more easily characterized by the shared facet between the two nodes. Each facet is associated with a total of six spring constants as shown in equations S.1 and S.2 corresponding to displacements in the *x*, *y*, and *z* directions and rotations about each of these axes.

$$k_x = k_y = k_z = E\frac{A_{ij}}{h_{ij}} \tag{S.1}$$

$$k_{\varphi x} = E\frac{J_p}{h_{ij}}, \qquad k_{\varphi y} = E\frac{I_{zz}}{h_{ij}}, \qquad k_{\varphi z} = E\frac{I_{I1}}{h_{ij}} \tag{S.2}$$

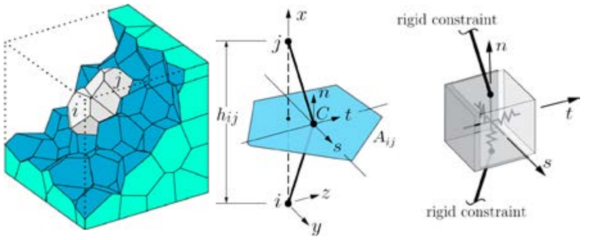

Figure S.1. Element* ij *within network at left; facet and springs associated with* ij *at right (Bolander 2008).

The basis of the elastic equations for the lattice model then is, for representative element *ij*, $F = Kd$, where F is a load vector, K is a 12×12 stiffness matrix, and d is a vector of displacements. Taken for all elements in the lattice, this model represents a linear elastic system of equations. (Other factors not included in this formulation are those accounting for thermal and hygral diffusive processes, which can be and have been incorporated into lattice models.) More detail on the formulation and solution of these problems can be found in Schlangen and Garbocki (1996).

This formulation can be applied to any arrangement of elements in the lattice. The model described here uses a random geometry network to define the desired domain. The geometry is based on a Voronoi diagram for a given number of randomly generated points within the region. A major advantage to the use of random geometry networks is that these networks as implemented in this model are such that the model preserves elastic uniformity under loading. That is, for the strain for each element in the random geometry network agrees with the global strain for the body under consideration (Schlangen and Garbocki 1996; Bolander and Sukumar 2005). Figure S.2 illustrates the issue of elastic uniformity with histograms for elemental strains in a random geometry network and elemental strains in a regular lattice network for a cube under uniform tensile loading. The quantities A_{ij} and H_{ij} describe the area and length of element *ij*, respectively. In the instance of a regular or ordinary lattice, elemental area A_{ij} is described as uniform area $\bar{A}$ for all elements.

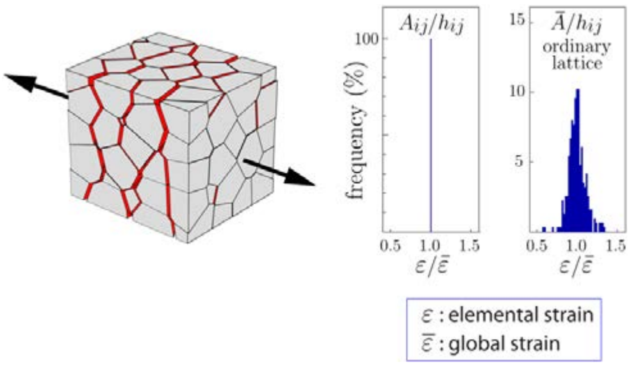

Figure S.2. Random geometry networks are implemented in such a way that the model describes uniform elastic behavior under loading (Bolander 2008).

Furthermore, it should be noted that although regular, symmetric networks also ensure elastic uniformity, regular networks create bias in crack propagation. Random geometry networks eliminate this bias.

Mixed-mode Fracture Criteria

A key feature of this model, as alluded to earlier, is that it does not adopt a continuum approach for fracture. Rather, its discrete representation allows for the development of parameters governing fracture in the body, as suggested by Jagota and Bennison (1994). These parameters are rules based on element response to critical stresses that are applied to the body after the constitutive equation has been solved for a given load-step.

In this model, crack initiation and propagation are governed by the tensile and shearing stresses at the facet defining element *ij*. These stresses are considered in terms of a Mohr-Coulomb fracture criterion, in which both the tensile and resultant shear stresses acting on element *ij* are held against critical strength values for the element to determine if breaking occurs. For this model, after the solution of a given load-step, for each element the criterion $R = r/r_f$ is calculated, where $r = \sqrt{\sigma_{ij}^2 + \tau_{ij}^2}$, σ_{ij} is the normal stress for the facet, τ_{ij} is the resultant shear stress for the facet, and r_f is the distance to the fracture criterion curve in Figure S.3.

Other important parameters in Figure S.3 are the tensile strength f_t, pure shear failure criterion $\tau_c = \rho f_t$, approximate shear strength under critical tensile stress $\tau^* = \rho_2 f_t$, and the angle $\gamma = \tan^{-1}(\rho\text{-}\rho_2)$ to further specify the slope of the fracture criterion curve, where ρ and ρ_2 are specified material parameters through τ_c and τ^*.

When $R > 1$, an element is defined as having undergone a fracture event; for instances in which more than one element has a value of R in excess of 1, only the element with the largest value of R is considered. More detail on the Mohr-Coulomb criterion and rules governing fracture for this model can be found in Bolander and Saito (1998). Later figures will refer back to the mixed-mode fracture curve of Figure S.3 to define fracture events in simulations. Furthermore, the fracture rules assigned by this model include the degradation of spring stiffnesses to simulate softening. The model described here uses a bilinear softening relationship. For every successive fracture event according to the rules above, both the modulus of elasticity E and the tensile strength f_t are reduced according to a bilinear softening relation such as that of Figure S.3.

Thus, there is a recursive effect between the softening relation and the mixed-mode fracture criterion itself. As fracture

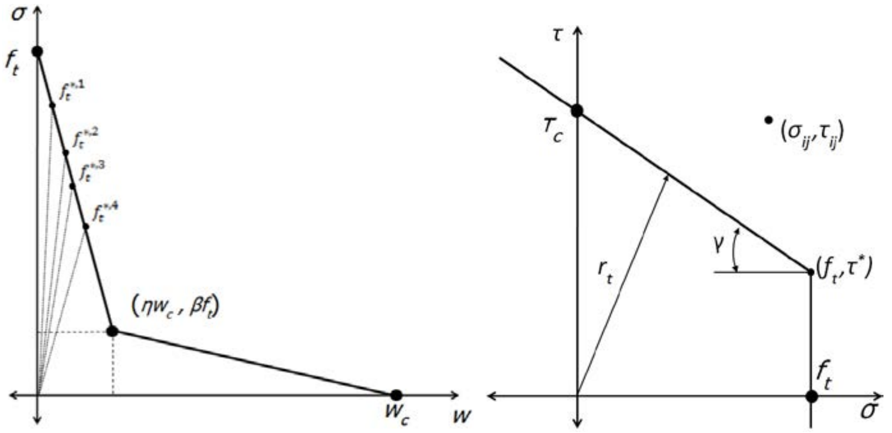

Figure S.3. At left, bilinear softening to describe degradation of stiffnesses of elements under breaking; at right, Mohr-Coulomb fracture criterion defines breaking in the described lattice model.

events are characterized for an element *ij* according to the Mohr-Coulomb criterion, both *E* and f_t for the element are consequently reduced. The softening in f_t then causes the σ and τ intercepts of the Mohr-Coulomb criterion, as represented in the curve in Figure S.3 by f_t and τ_c, respectively, to become reduced as well. When extensive fracturing occurs, the mixed-mode fracture criterion will "collapse" gradually toward the origin as a result of the bilinear softening. This effect is summarized in Figure S.4.

Later figures will depict simulations that involve mixed-mode fracture and characterizing these events, and the visibility of reduced criterion curves, as in Figure S.4, will be visible in the simulations. Once the strength has been reduced to zero, the spring is removed from the lattice and its contributions to the global stiffness matrix are consequently negated.

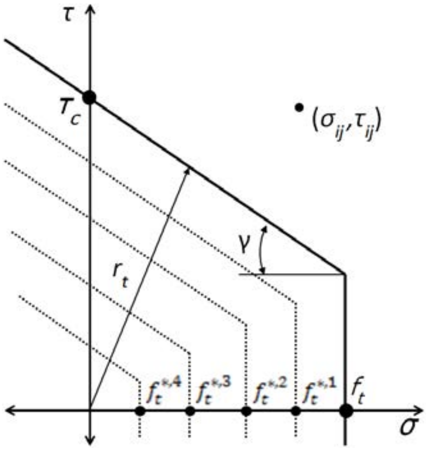

Figure S.4. So-called collapse of mixed-mode fracture criterion curve toward origin in the event of extensive fracture for a given element ij.

Model Simulations of PCC/PCC Interface

Laboratorio de Caminos de Barcelona Beam Test in Bending

To better develop models for debonding in concrete composites, the research reviewed laboratory tests for bond interface integrity. Of the many available tests, the test developed at the Road Laboratory of Barcelona (Laboratorio de Caminos de Barcelona) appealed to the project researchers in its simple and direct experiment to induce the loss of bond integrity in a layered asphalt field core or laboratory sample. In the Laboratorio de Caminos de Barcelona procedure, cylindrical asphalt cores are clamped into the testing apparatus and subjected to loading under modified three-point bending. The intention is to generate shear stresses at the interface and avoid a bending moment by placing the interface very near the support. This procedure measures resistance to tangential stress at the interface and the displacement of the layers with respect to one another (Recasens et al. 2006).

Although the procedure is designed for asphalt composite cores or samples only, the test could be used for concrete composites. The specimens would be cast using wet-on-wet techniques to mirror the techniques used in the field. The Laboratorio de Caminos de Barcelona test was adopted for this research as the physical analog for the debonding simulations.

Idealized Beam Specimen for Simulation

For the investigation of debonding, all simulated beams feature a refined interface oriented in the manner of the Laboratorio de Caminos de Barcelona beam test.

Multiple random geometry networks were generated to locate the interface at different locations measured from the roller support, as illustrated by l_1 and corresponding hashed lines in Figure S.5. The random point generators used to develop all specimens were oriented such that more points were distributed in the region surrounding the beam. Furthermore, each simulated beam was developed to accommodate nodes expressly to act as sites of forcing to accommodate three-point loading.

Although some simulated beams use arbitrary properties and dimensions, others use properties or dimensions based on similar laboratory studies for fracture in concrete beams (for instance, those of Roesler et al. 2007). Based on the information in Figure S.6, beams discussed below have dimensions $L = 1{,}000$ mm, $b = 80$ mm, and $h = 250$ mm, with vertical displacement control applied at midspan ($L/2 = 500$ mm). Locations of the interface vary and are reported based on their distance from the right-most (roller) support. The two layers in the composite beam are kept homogeneous (and referred to as PCC1 and PCC2) to isolate the performance of the interface, whose properties vary from case to case. The baseline properties for the PCC1 and PCC2 layers are modulus of elasticity $E = 32$ GPa and tensile strength $f_t = 4$ MPa.

Beam Simulation Results and Discussion

The simulations presented in this section are studies of (1) the effects of interface properties on the ultimate load magnitude and location of fracture and (2) the effects interface location on the beam behavior. These simulations are conducted to determine if the model characterizes mixed-mode fracture according to expectations. Furthermore, the simulations provide an idea of the extent to which an interface would have to be weakened for debonding to occur in these composite beams.

Interface Strength and Beam Response

The first problem involves a comparison of the behavior of a beam with varying material properties for an interface near the right roller support (as in the Laboratorio de Caminos de Barcelona test). Multiple factorials were conducted for this problem to evaluate the sensitivity of the model to parameters, and all factorials use the same random geometry with the interface near the roller support at $l_6 = 25$ mm (the designation l_6 is explained later in this appendix).

The first factorial examined the tensile strength f_t at the interface and its effect on the performance of the beam for constant $\rho = 1.5$ and $\rho_2 = 0.7$. A vertical displacement (through the depth of the beam) was applied at midspan ($L/2 = 500$ mm) until simulated failure occurred according to the breaking rules described later in this appendix. The vertical displacement was prescribed to be 0.01 mm until 0.1 mm of total displacement is reached, then 0.001 mm until beam failure. The problems use a random geometry lattice for a domain of $80 \times 1{,}100 \times 250$ mm, where supports are placed 50 mm from the end to yield an effective span of $L = 1{,}000$ mm. For the interface strength problems, the interface is located near the support at $l_6 = 25$ mm.

Two-layered beam properties are described in Table S.1, where layers PCC1 and PCC2 are equivalent to isolate the effects of the interface.

In Table S.1, E is the modulus of elasticity in MPa, f_t is the critical tensile strength (in MPa), pure shear failure criterion $\tau_c = \rho f_t$ (in MPa), approximate shear strength under critical tensile stress $\tau^* = \rho_2 f_t$ (in MPa), *NFE* is the number of fracture events for a given element *ij* required to break the element, *COBP* is the crack opening at the break point (in mm), and *TFCO* is the traction-free crack opening (in mm). Note that ρ and ρ_2 are unitless parameters implied from τ_c and τ^* to develop the mixed-mode breaking rules (Figure S.3), and that $\rho = 1.5$ and $\rho_2 = 0.7$ for all values of f_t.

The factorial contained 40 cases in which the tensile strength of the interface was adjusted, which led to a corresponding collapse of the fracture criterion to the origin (see Figure S.1 and Figure S.5). Observe in Figure S.6 that because the shape of the fracture criterion is held constant from case to case in the factorial, changes to f_t correspond to changes in both τ_c and τ^*.

Results from the factorial are summarized in Figure S.6. Ultimate load values are reported in the figure, and the inset figure describes the location of failure in the beam for cases in the factorial. Ultimate load values for cases when $f_t > 1.46$ MPa are excluded from the figure to improve resolution on the reduction in ultimate load. For all cases in the factorial not reported in Figure S.6 (i.e., cases for which $f_t > 1.46$ MPa), the ultimate load is equal to 17,234 N.

***Table S.1. Beam Properties for Weakened Interface Using Factorial of* f$_t$**

	E (MPa)	f_t (MPa)	τ_c (MPa)	τ^* (MPa)	NFE	COBP (mm)	TFCO (mm)
PCC1	32,000	4.0	6.0	2.8	100	0.002	0.008
PCC2	32,000	4.0	6.0	2.8	100	0.002	0.008
Interface	32,000	0.1–4.0	0.15–6.0	0.07–2.8	100	0.002	0.008

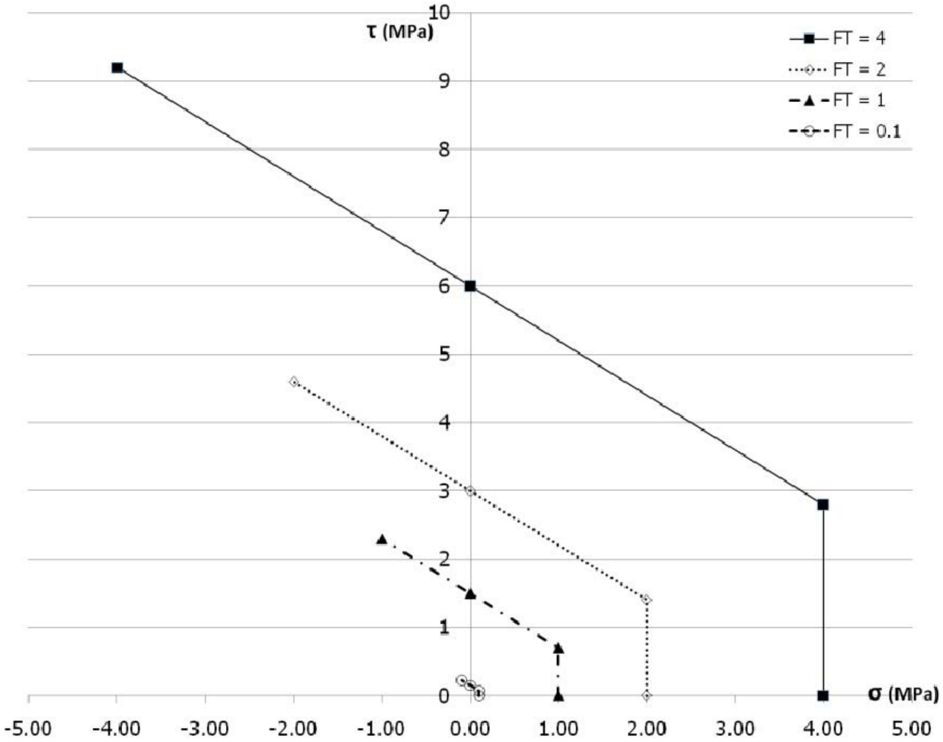

Figure S.5. Selected fracture criterion curves representing factorial of 40 cases investigating variable f_t with constant fracture criterion $\rho = 1.5$ and $\rho 2 = 0.7$.

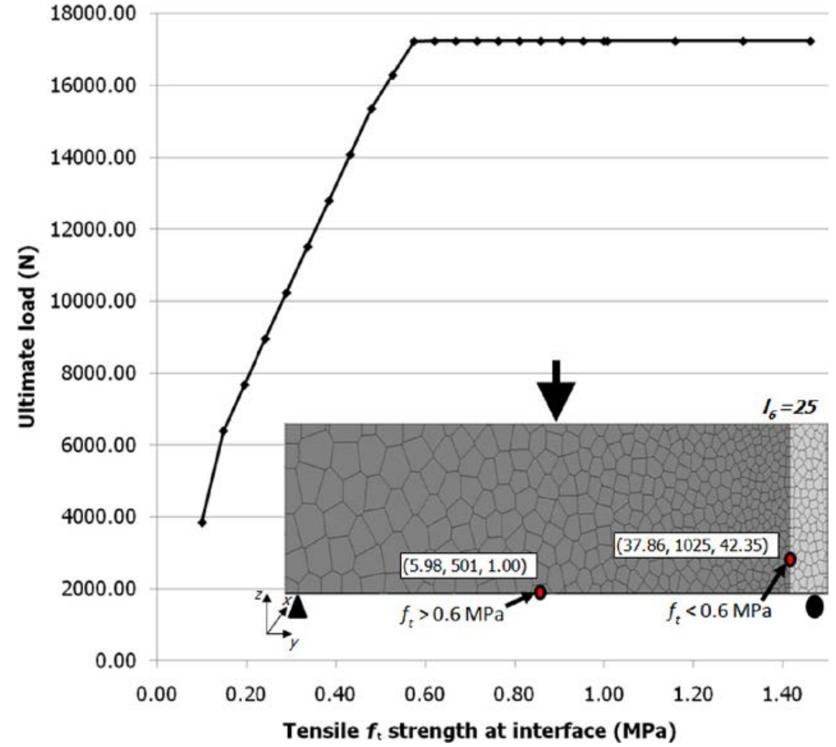

Figure S.6. Relationship between ultimate load and tensile strength f_t at interface for cases with interface nearest support (l_6 = 25 mm) and location of fracture initiations in red (*inset*).

Table S.2. Beam Properties for Weakened Interface Using Factorial of τ_c and τ^*

	E (MPa)	f_t (MPa)	τ_c (MPa)	τ^* (MPa)	NFE	COBP (mm)	TFCO (mm)
PCC1	32,000	4.0	6.0	2.8	100	0.002	0.008
PCC2	32,000	4.0	6.0	2.8	100	0.002	0.008
Interface	32,000	0.4	0.36–0.6	0.28–0.04	100	0.002	0.008

Figure S.6 summarizes two key results. First, for cases where f_t for the interface is greater than 0.6 MPa, the beam failed near midspan under a load of 17.2 kN. This ultimate load induces a bending stress of roughly 5 MPa at midspan, according to elastic beam theory. Thus, failure at midspan is reasonable given $f_t = 4.0$ MPa outside of the interface. Second, for interfaces where f_t is less than 0.6 MPa, failure occurred at the interface near the support, with ultimate loads indicated in Figure S.6. The bending stress at the location where failure occurs in all cases never exceeds the tensile strength, which is to say that failure in pure tension cannot occur. Thus, the model accounts for the resultant shear stress in determining failure at $l_6 = 25$ mm for $f_t < 0.6$ MPa.

The second factorial more closely examines beam failure for $f_t < 0.6$ MPa, specifically failure in shear. Here, a constant value of $f_t = 0.4$ MPa is selected given that it is in the region of failure for the beam (from Figure S.6). The factorial instead focuses on varying τ_c and τ^*. The hypothesis is that if the shear strength does contribute to failure at $l_6 = 25$ mm, which is expected, then a reduction in τ_c while f_t is held constant should have a significant effect. Prescribed vertical displacements were 0.01 mm until 0.06 mm of total displacement was reached, after which 0.001 mm was displaced vertically until beam failure. Composite beam properties are described in Table S.2, where layers PCC1 and PCC2 are equivalent to isolate the effects of the interface; the reader is referred to the description of Table S.1 for further details on material parameters.

Twenty-one cases were conducted in this factorial. Each case varied only in the τ intercept on the fracture criterion curve. The slope of the curve remained the same, as it was in the first factorial of cases (that is, $\rho_2 - \rho = -0.8$ or $\tau_c - \tau^* = 0.32$ for all cases), and the σ intercept (f_t) also remained the same as in the first factorial. The fracture criterion curves for four of the 21 cases, including the two extremes, are presented in Figure S.7.

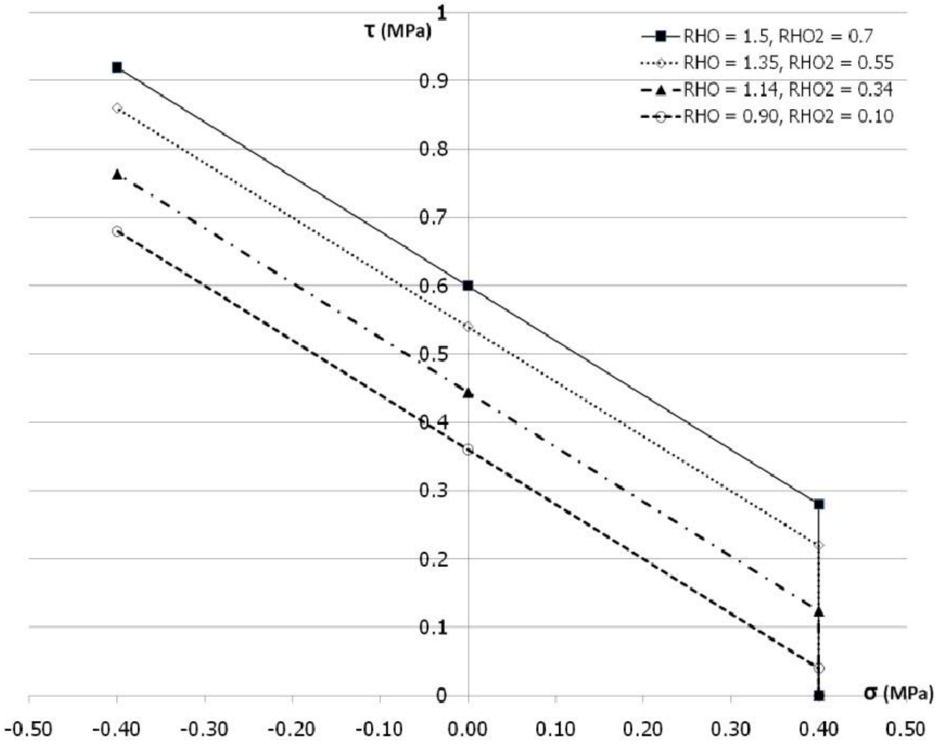

Figure S.7. Selected fracture criterion curves representing factorial of 21 cases investigating influence of τ_c and τ^*. Note that RHO (ρ) = τ_c/f_t and RHO2 ($\rho 2$) = τ^*/f_t.

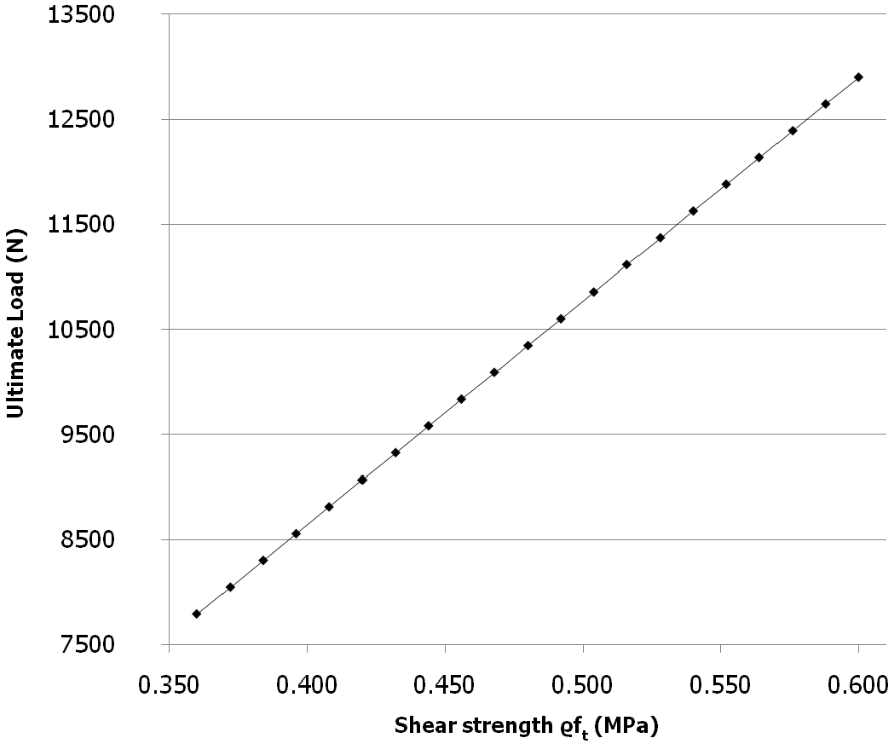

Figure S.8. Relationship between ultimate load and shear strength τ_c at interface for cases with interface nearest support (l6 = 25 mm) and tensile strength f_t = 0.4 MPa.

Results of the reduction in the fracture criterion curve for $f_t = 0.4$ MPa under controlled displacement at the midspan are presented in Figure S.8.

The results support the notion that the shear strength is a contributor to the resiliency of the interface. However, because the lower bound of τ_c is limited by the desire to retain the shape of the criterion curve, another factorial is desirable. Furthermore, the relatively small value of $f_t = 0.4$ MPa confounds the factorial somewhat.

Thus, the third factorial examined beam failure when f_t is sufficiently strong in tension (here, when $f_t = 4.0$ MPa) yet compromised considerably in shear strength. In this factorial, τ_c is variable, as indicated in Table S.3 and $\tau^* = 0$. The effect of holding $\tau^* = 0$ is to change the fracture criterion curve so that it can be reduced closer to zero for values of τ_c. Extremely small values for shear strength will make their influence on beam failure more apparent. Sixty cases were conducted for this factorial. Prescribed vertical displacements were 0.001 mm until beam failure. Composite beam properties are described in Table S.3, where layers PCC1 and PCC2 are equivalent to isolate the effects of the interface; the reader is referred to the description of Table S.1 for further details on material parameters.

For the third factorial, the fracture criterion has changed. The geometric effect of $\tau^* = 0$, or $\rho_2 = 0$, is that the slope of the criterion curve is dictated explicitly by τ_c (in that the slope is equal to ρ, which varies with τ_c). When values for τ_c are sufficiently small, the overall slope of the criterion is consequently flat; when τ_c is large, the slope is more steep. An excessively steep slope on the fracture criterion curve can be problematic

Table S.3. Beam Properties for Interface Using Factorial of τ_c When $\tau^* = 0$ and f_t = 4.0 MPa

	E (MPa)	f_t (MPa)	τ_c (MPa)	τ^* (MPa)	NFE	COBP (mm)	TFCO (mm)
PCC1	32,000	4.0	6.0	2.8	100	0.002	0.008
PCC2	32,000	4.0	6.0	2.8	100	0.002	0.008
Interface	32,000	4.0	6.0–0.05	0	100	0.002	0.008

in that it may exclude legitimate fracture events in the second quadrant (where the normal stress is in compression). However, for a maximum value of $\rho = 1.5$, the researchers though this was not sufficient to exclude events. The fracture criterion curves for four of the 60 cases, including the two extremes, are presented in Figure S.9.

Results of the third factorial for $\tau_c < 1.20$ MPa are reported in Figure S.10. Note that cases where $\tau_c > 1.20$ MPa are not reported to reduce redundancy in the figure and improve resolution in the region where a reduction in shear strength τ_c contributes to a reduction in the ultimate load. For those cases where $\tau_c > 1.20$ MPa failed at a loading of 17,233 N, as in the first factorial, the location of failure was near midspan, not in the interface (consult Figure S.7).

The dramatic reduction in ultimate load capacity with a reduction in τ_c further supports the criticality of the shear strength at the interface for the cases near $l_6 = 25$ mm. Note that all failure reported in Figure S.10 occurs at the interface, in a manner as reported in Figure S.6. The final question is to determine, for an interface sufficiently strong in shear, the sensitivity of beam failure to tensile strength.

A final subset of cases for this problem attempted to further resolve the contributions of tensile strength to the integrity of the interface. In this factorial both τ_c and τ^* are held to constant values of 0.9 MPa and 0, respectively, whereas f_t is restricted to relatively low values (< 1.0 MPa). Prescribed vertical displacements were 0.001 mm until beam failure, and the interface is again located near the support at $l_6 = 25$ mm. Composite beam properties are described in Table S.4, where layers PCC1 and PCC2 are equivalent to isolate the effects of the interface. The reader is referred to the previous description of Table S.1 for further details on material parameters.

In the final factorial, the fracture criterion has changed dramatically once again. The geometric effect of $\tau^* = 0$, or $\rho_2 = 0$, is that the slope of the criterion curve is inversely proportional to values of f_t (in this case, the slope has value ρ, which varies with $\tau_c = \rho f_t$). When values for f_t are sufficiently small, the overall slope of the criterion is steep. As in the third factorial, concerns over excluding legitimate fracture events, and thereby inaccurately predicting failure, are overlooked for the sake of investigating model sensitivity to parameters. The fracture criterion curves for the five cases are presented in Figure S.11.

Given the similarity in results for these final cases, the results are presented in Table S.5 rather than in a figure.

For a reduction of f_t by five times, the ultimate load is decreased by less than 5%. Thus, when the interface is near the support at $l_6 = 25$ mm, the criticality of the shear strength is a far greater contributor to the interface integrity than is the shear strength. However, the factorials run for this problem

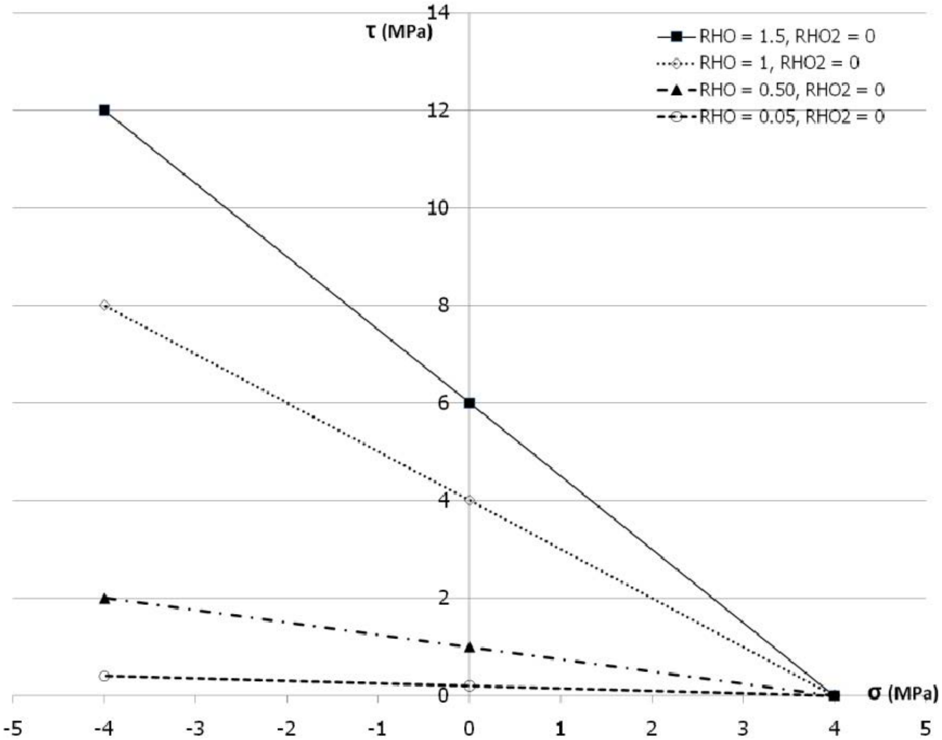

Figure S.9. ***Selected fracture criterion curves representing factorial of 40 cases investigating influence of τ_c when $\tau^* = 0$ and $f_t = 4.0$ MPa.***

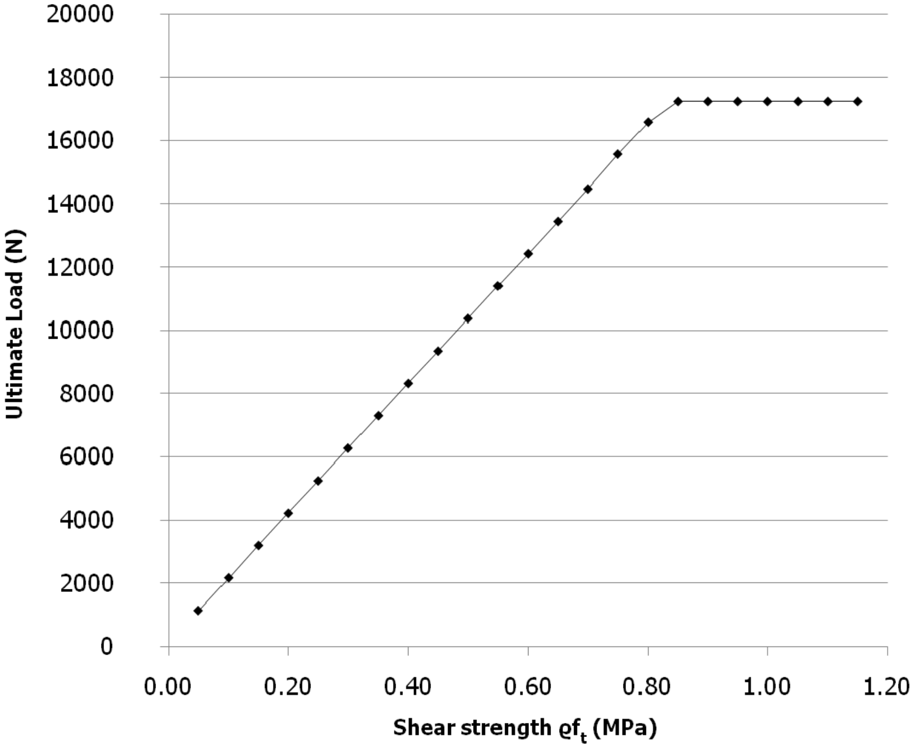

Figure S.10. Relationship between ultimate load and shear strength τ_c at interface for cases with interface nearest support (l6 = 25 mm) and tensile strength f_t = 4.0 MPa.

are testing the beam under a mechanism that can be considered pure tension, a condition that will rarely occur in practice. To examine mixed modes of failure, a moving interface is also considered.

Moving Interface in Beam and Characterization of Fracture

The next cases allow a closer examination of mixed-mode failure at a given interface. That is accomplished by loading a beam at midspan and gradually moving the interface away from the load toward a support; it was hypothesized that as the interface was moved away from midspan, the nature of fracture would shift from one that is tensile to one that is mixed. In the interface strength problems, a controlled displacement of 0.01 mm until 0.1 mm is reached, and a controlled displacement of 0.001 mm thereafter. The controlled displacement is applied at midspan ($L/2$ = 500 mm) until simulated failure occurs according to the breaking rules.

The problems use six distinct random geometry lattices for a domain of 80 × 1,100 × 250 mm, where supports are placed 50 mm from the end to yield an effective span of $L = 1{,}000$ mm. The six lattices differ in the location of the interface, which is near the load at l_1 = 490 mm, near the support at l_6 = 25 mm, and at four locations in between the load at midspan and the support ($l_2 = 330$ mm, $l_3 = 190$ mm, $l_4 = 110$ mm, $l_5 = 50$ mm). Beam properties are indicated in Table S.6, where parameters are those of Table S.1. Note again that layers PCC1 and PCC2 are equivalent to isolate the effects of the interface.

The value of f_t = 0.2 MPa was selected, based on earlier experience, to provide a sufficiently weak interface. For the six cases described here, specimen failures in the two extremes of this problem are illustrated in Figure S.12.

Table S.4. Beam Properties for Variable f_t with τ_c = 0.9 MPa and τ^* = 0

	E (MPa)	f_t (MPa)	τ_c (MPa)	τ^* (MPa)	NFE	COBP (mm)	TFCO (mm)
PCC1	32,000	4.0	6.0	2.8	100	0.002	0.008
PCC2	32,000	4.0	6.0	2.8	100	0.002	0.008
Interface	32,000	0.2–1.0	0.9	0	100	0.002	0.008

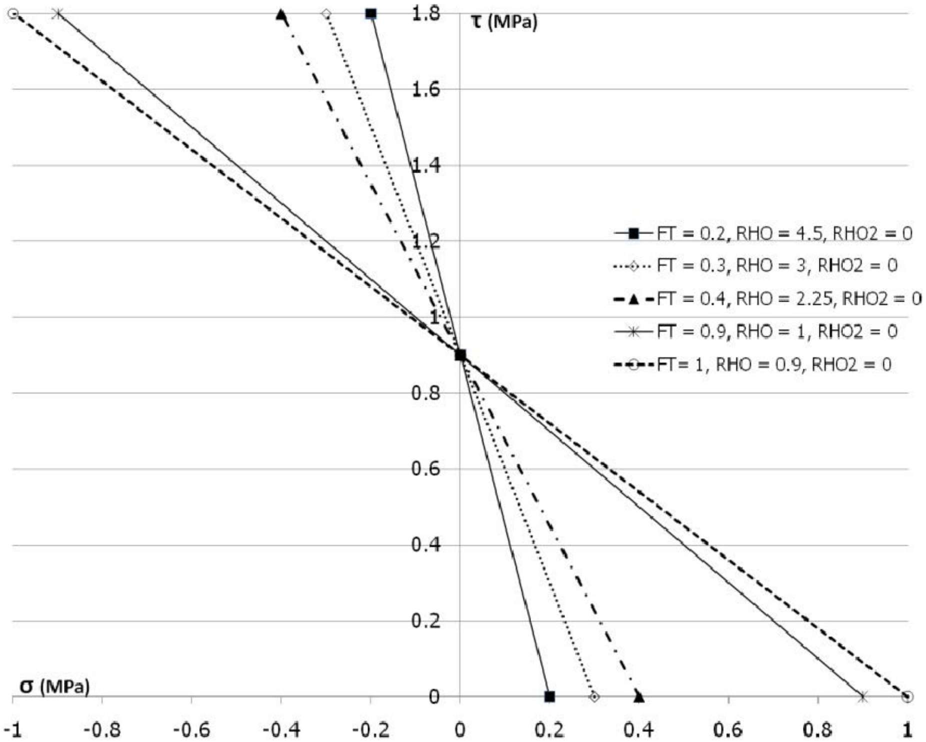

Figure S.11. Fracture criterion curves for f_t ***< 1.0 MPa with*** $\tau_c = 0.9$ ***MPa and*** $\tau^* = 0$.

One would expect that the location of the weak interface has an influence on the load capacity and failure of the beam. Figure S.13 illustrates the reduction in the ultimate load as the interface is moved from the support toward midspan. Note again that span length $L = 1{,}000$ mm.

Again, the hypothesis being tested by the six cases of this problem is the expectation that as the interface was moved within the span, the nature of the initial fracture would shift from being largely tensile under midspan (as is commonly observed in three-point bending tests) to a mixed-mode. The analysis, then, begins with $l_1 = 490$ mm, when the interface is almost directly beneath the controlled displacement at midspan. In this instance, we would expect the failure to be classical Mode I fracture. The first 1,000 fracture events are plotted against the fracture criterion curve in Figure S.14.

Table S.5. Change in Ultimate Load for Cases f_t ***< 1.0 MPa with*** $\tau_c = 0.9$ ***MPa and*** $\tau^* = 0$

Case	f_t (MPa)	Ultimate Load (N)
A	1.0	17,234
B	0.9	17,234
C	0.4	17,234
D	0.3	17,227
E	0.2	16,583

Fracture events in Figure S.14 are represented by a single black dot. The aggregate of these dots into one large mass cleanly illustrates that the initial fracture events are purely tensile in nature and in the neighborhood of 0.25 MPa, which exceeds the interface critical strength of $f_t = 0.2$ MPa. In this regard, the model simulation confirms our initial hypothesis. It is important to note that only the initial (for these purposes, the first 1,000) events are plotted. This is done to make plots more legible and to further distinguish the separate cases, whose most striking differences in fracture are in initiation.

The problem then examines cases as the interface is moved gradually toward the roller support, the beam is loaded, and the nature of the fracture is recorded. The first 1,000 fracture events in each of the following four cases (where $l_2 = 330$ mm, $l_3 = 190$ mm, $l_4 = 110$ mm, and $l_5 = 50$ mm) are presented together in Figure S.15.

Beginning with the case when $l_2 = 330$ mm, we observe that the nature of the fracture is mostly tensile; however, some events feature a shear component as high as ~0.1 MPa. As we continue clockwise through the subfigures of Figure S.16, the shear component becomes more pronounced and reaches values as high as ~0.3 MPa at $l_1 = 950$ mm. The final case then is the placement of the interface at $l_6 = 25$ mm. The first 1,000 fracture events for the final case are presented in Figure S.16.

Table S.6. Beam Properties for Multiple Interface Locations

	E (MPa)	f_t (MPa)	τ_c (MPa)	τ^* (MPa)	NFE	COBP (mm)	TFCO (mm)
PCC1	32,000	4.0	6.0	2.8	100	0.002	0.008
PCC2	32,000	4.0	6.0	2.8	100	0.002	0.008
Interface	32,000	0.2	0.3	0.14	100	0.002	0.008

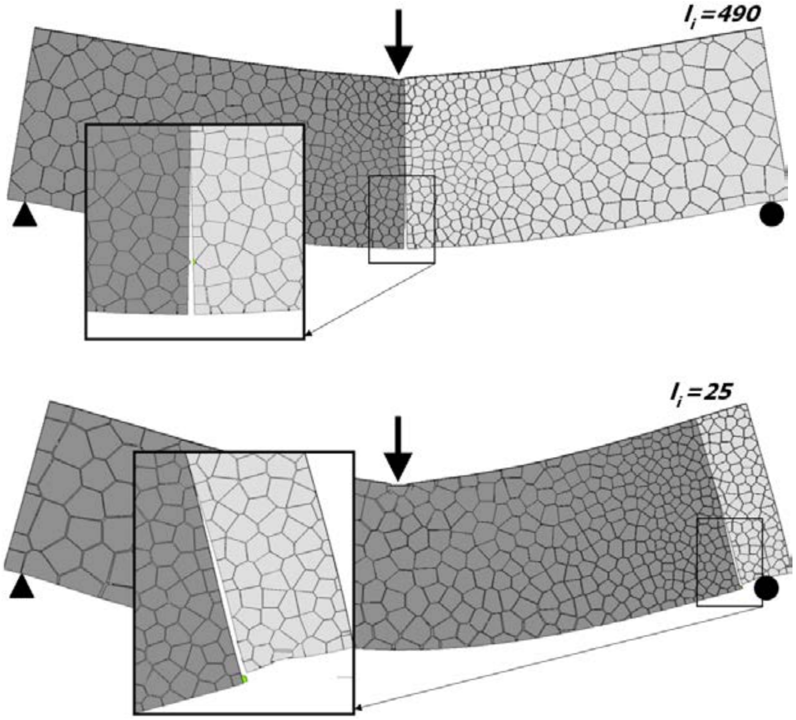

Figure S.12. Failure in composite beams with weakened interface near midspan and near support under loading.

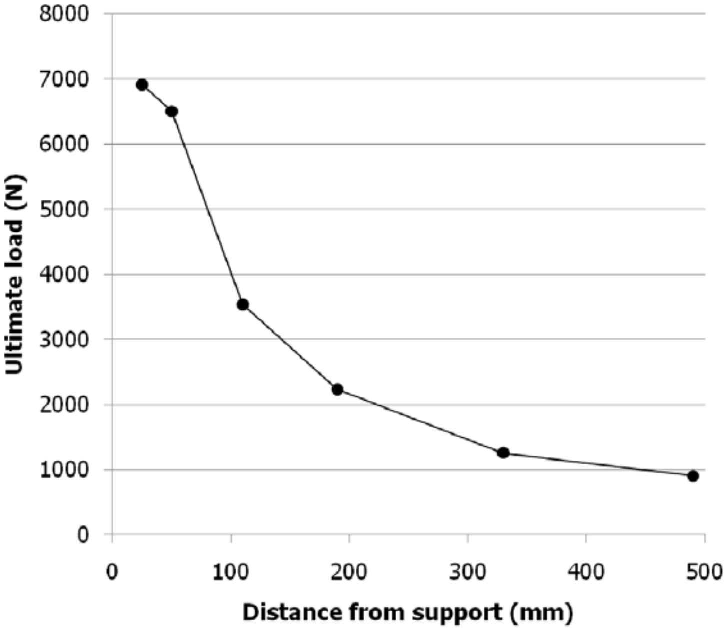

Figure S.13. Reduction of ultimate load as weak interface is moved toward midspan.

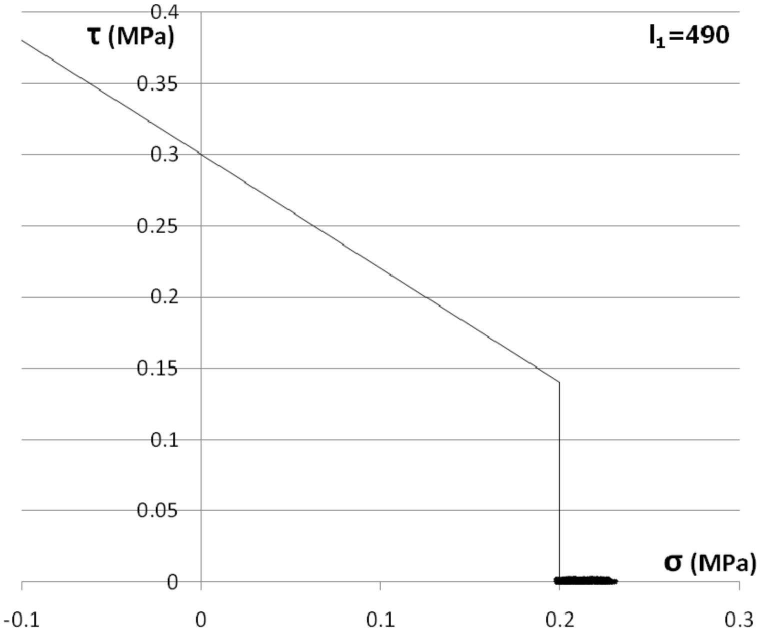

Figure S.14. Failure in tension predominates at a weakened interface near midspan (l_1 = 490 mm).

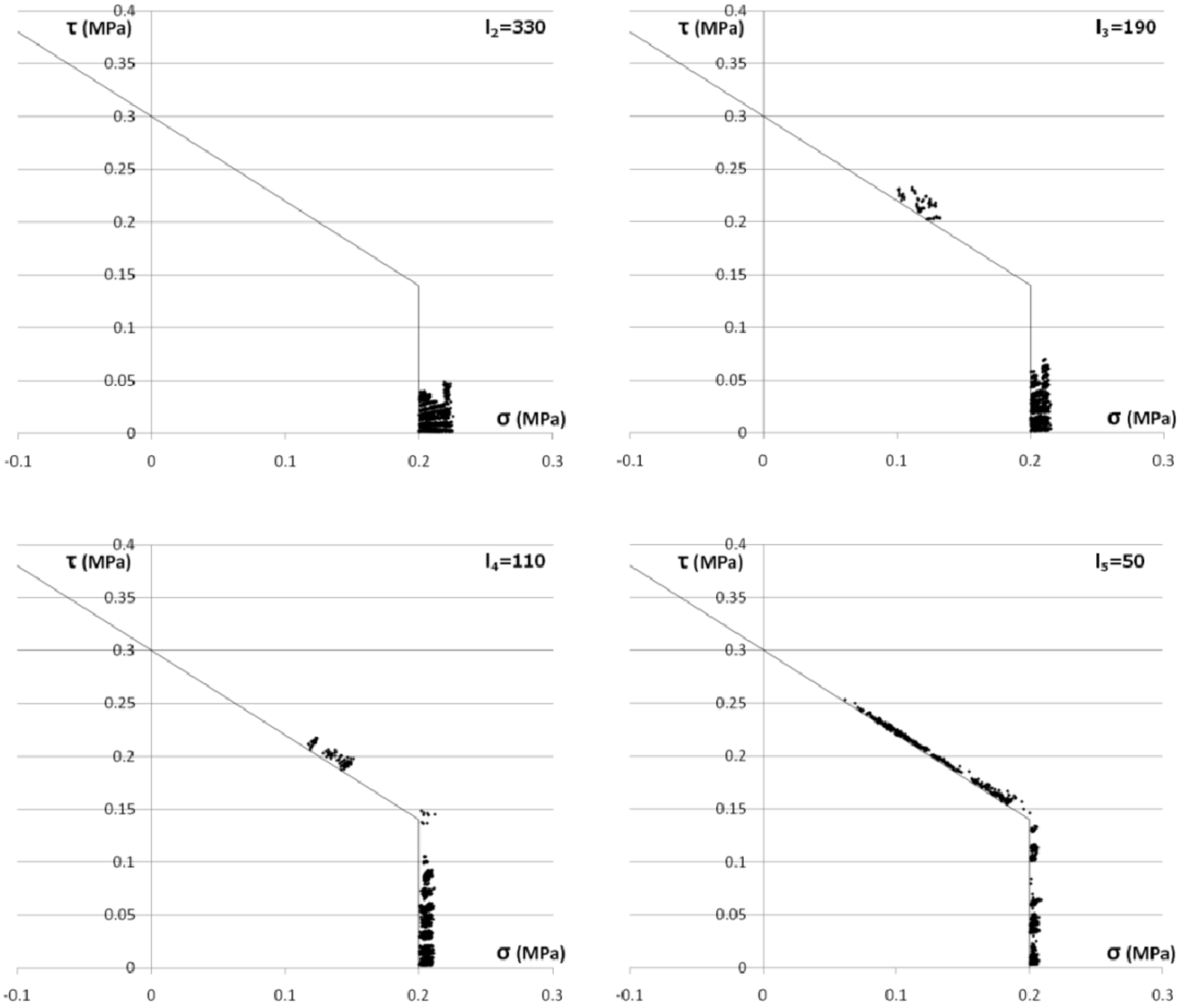

Figure S.15. Evolution of mixed-mode fracture as interface is moved from midspan toward support (beginning top left with l_2 = 330 mm, finishing bottom left at l_5 = 50 mm).

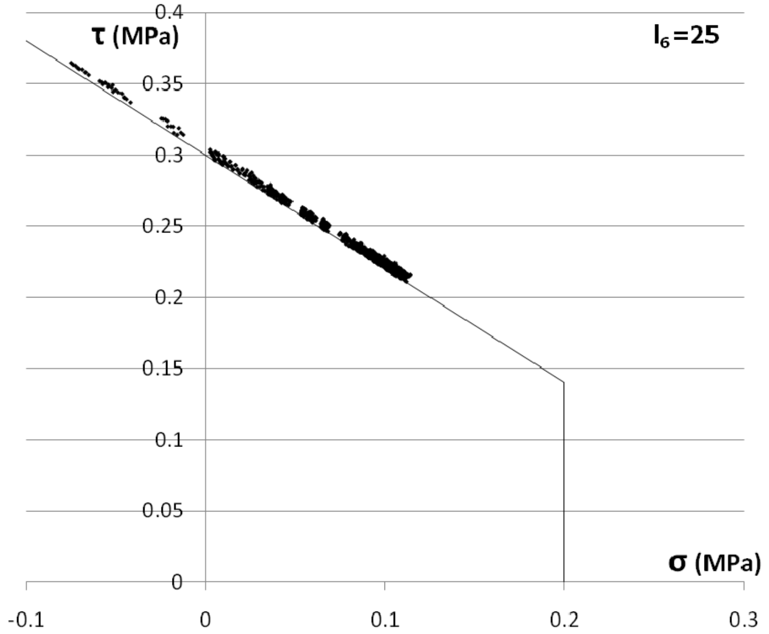

Figure S.16. Shear events characterize mixed-mode failure at a weakened interface near support (l_6 = 25 mm).

Figure S.16 illustrates the observation that near the support, the shear component of fracture events is larger than the tensile events; shear stresses are nearly 0.4 MPa in this case. It is not until later events (only a few of which occur within the first 1,000) that normal (tensile) stresses exceed those of shear. Furthermore, it is worth noting that the normal stresses for the first of the fracture events are compressive in nature. This phenomenon is most likely attributable to the proximity of the support, which acts to both compress and shear elements in the vicinity to instigate fracture.

The six cases that constitute this problem, taken in concert with the earlier results, support the concept of mixed-mode fracture. Although the idea is not novel given that the model determines the criterion, the simulations satisfy expectations of fracture behavior in particular situations: in Mode I (opening) fracture situations, the tensile strength contributes more to the determination of failure, whereas in predominately Mode II (in-plane shearing) fracture situations, the shear strength weighs more heavily in predicting failure.

Conclusions from Beam Simulations

This brief analysis established the lattice model as a basis for simulating the effects at the interface of a composite concrete beam. As noted, the model is desirable in that it requires no a priori knowledge of the crack location and any complicated remeshing or "special" elements (as in the case of FEM). This presentation of the lattice model was not intended to be a comprehensive fundamental basis for the model but rather an overview with useful resources in the act of introducing the research project and a recent effort in debonding analysis.

The analysis above illustrates that the lattice model applied to composite concrete pavements has great promise. The model is able to accommodate mixed-mode fracture, including both extremes of pure tension and pure shear, and the parameters dictating the fracture criterion are easily adjusted and allow for flexible modeling.

In the case of composite concrete pavements, there are two situations in which the model has possibilities that incorporate both shear and tensile stresses that may lead to fracture. The first is the possible case of differential strains in the layers, such as in the case of shrinkage strains. These strains may create shearing stresses in the layers; the model is capable of simulating the interface in this situation. Although early U.S. designs for PCC/PCC used the shear strength as a design parameter, this was a reaction to debonding concerns relative to bonded PCC, and shear strength was a measure of bond integrity. In the event of newly constructed PCC/PCC, however, the bond can assumed to be full. Moving forward, it will be worthwhile to apply the lattice model to this situation to determine if the shear stresses that result from differential shrinkage are a cause for concern. This is discussed in detail in Composite Pavement Systems Volume 2: PCC/PCC Composite Pavements.

The second possible case involves tensile stresses at the edge of a slab caused by curling stresses. Here the lower lift of the composite pavement restrains the upper lift, and given that the interface is the site of this restraint, there is the possibility of debonding if the stresses are severe enough and/or the

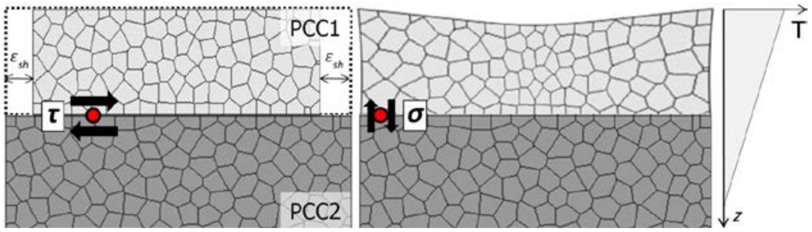

Figure S.17. At left, pure shear induced through differential shrinkage strain; at right, pure tension initiated through thermal gradient and associated curling stress.

interface strength is compromised. This situation involves mixed-mode fracture and, as described above, the lattice model can meet these demands. This is discussed in detail in Composite Pavement Systems Volume 2: PCC/PCC Composite Pavements.

The possible applications described here cannot be met without additional modifications and improvements to the lattice model. The fracture criterion can be made more comprehensive through a calibration using experimental results. Furthermore, the model is capable of modeling diffusion, and thus hygral and thermal gradients can be coupled to the elastic and fracture analysis. Both of these modifications are natural improvements to meet the challenge presented by the two example applications in Figure S.17. Finally, although the method has its advantages in simulating fracture, given that it requires no a priori knowledge of fracture, it does have its computation expense if it is to be applied to a large specimen, such as a full-scale PCC/PCC slab. Coupling the lattice model with FEM, so that FEM is responsible for the far-field slab behavior and the lattice model is responsible for relatively localized (joint and interface) behavior, is a direction the research will take in further addressing the issue of debonding and other phenomena for PCC/PCC as discussed in Composite Pavement Systems Volume 2: PCC/PCC Composite Pavements.

APPENDIX T

Recycled Concrete Aggregates in PCC

History of RCA Use in PCC and Relevant Issues

Introduction

State departments of transportation began using recycled concrete aggregates (RCA) in the structural layers of portland cement concrete (PCC) pavement in the United States around the late 1970s. Although RCA is rarely used as a structural component in PCC pavement in the United States, the impetus for its continued use is the same as it was then: a lack of landfill space and a shortage of quality, natural aggregates. However, as American pavement engineers and researchers continue to place a greater emphasis on sustainable, renewable roadways, the conventional uses for RCA in American roadways should be reconsidered along with these new priorities.

After the early 1990s, the same states that were using recycled concrete as a coarse aggregate in rigid pavements began finding alternative uses for it. In the United States, RCA is often used in a base layer or its fines are used to stabilize a subbase or frost protection layer. It has also been incorporated into concrete mixes for curbs and gutters, sidewalks, concrete barriers, driveways, shoulders, rip rap, fill, and as coarse aggregate in hot-mix asphalt. Although an ideal use of RCA would be as a component of a structural layer for new concrete pavements, that application is rarely pursued in the United States. At the time of a 2004 Federal Highway Administration (FHWA) national review of RCA applications in the United States, no states were using RCA as a structural component of rigid pavements (FHWA 2004).

However, if our nation's aggregate piles are depleting as fast as we contend and new landfills become more difficult to zone, the United States may not be able to continue its current practices with RCA much longer. In addition, recent sustainability initiatives could be the impetus needed to once again look at RCA as a resource, rather than a waste product. The Green Roads Initiative, a recent project from the University of Washington, aims to create a national standard for constructing and labeling sustainably built roads. This standard mirrors the form of the United States Green Building Council's (USGBC's) Leadership in Environmental Energy and Design (LEED) rating standard. Interestingly, Green Roads Initiative's rating points can be earned for using RCA in the subbase only if the RCA is used primarily in the pavement's structural layer. In other words, no points can be earned if RCA is used solely in the pavement's subbase or frost layer (Söderlund et al. 2008).

Although an insufficient attention to sustainability in the past is in part to blame for the relegation of RCA to the base layers of American rigid pavements, one of the main obstacles to its use in a rigid pavement slab is the stigma from a few bad experiences. The Michigan Department of Transportation's experience with RCA in rigid pavement slabs officially ended in 1991, when Michigan Department of Transportation (MDOT) issued a moratorium on the use of RCA in PCC pavements (Harrington 2008). While not being as explicit, other states, especially those that were the early pioneers of using RCA in PCC pavements, have followed MDOT's example. These actions have closed off many pavement engineers to the notion of RCA as a constituent of rigid pavements and restricted uses of RCA to unbound base layers. However, recent interest in composite pavements challenges these long-standing attitudes in pavement engineering. The SHRP 2 R21 Composite Pavement project and the TPF(5)-149 pooled-fund study present new opportunities for unconventional uses of recycled materials, including RCA.

This appendix proposes to revisit the use of recycled concrete as an aggregate in the concrete slab of rigid pavements by using overlooked research to address the concerns that prevented the wide-scale adoption of RCA as a structural component of pavements by state departments of transportation. As this study was in part motivated by FHWA and SHRP 2 tours of European pavements, the literature reviewed is mainly European studies that have received little attention in the United States. Furthermore, this appendix will describe challenges encountered in countries (mostly restricted to Europe) where the use of RCA in the concrete slab is more common. The appendix will briefly detail the past American research of RCA in rigid pavements. The sections that follow will then review the properties of concrete containing RCA, salvage issues for existing pavement, optimizing RCA use in rigid pavements, processing RCA for rigid pavement use, and the review of selected case studies on the performance of PCC pavements containing RCA.

RCA in Rigid Pavements: Past Research in the United States

In the 1980s through the early 1990s, state departments of transportation (DOTs) and university researchers teamed together to study RCA in PCC pavements in both lab and field settings. In 1989, an NCHRP study reported some of the first field observations of pavements containing RCA that were placed in Minnesota, Iowa, Michigan, and Wisconsin between 1981 and 1986 (Yrjanson 1989). In 1997, researchers at the University of Minnesota surveyed the condition of rigid pavements containing RCA that were designed and constructed in the early to late 1980s in Connecticut, Kansas, Minnesota, Wisconsin, and Wyoming (Cuttell 1996; Cuttell et al. 1997). Subsequently, the Recycled Materials Resource Center (RMRC) at the University of New Hampshire published a follow-up study in 2006 (Sturtevant et al. 2006). After the early 1990s, no documented studies indicate that RCA was used as an aggregate in a structural layer of rigid pavement.

As the use of RCA in the structural layer of PCC pavement declined, the topics of American research switched from a focus on implementation to a focus on lab testing concrete mixes with RCA for such properties as strength, freeze-thaw durability, and chloride infiltration, economic advantages of RCA, and case studies of alternative RCA use. For instance, the American Concrete Institute (ACI) sponsored a comprehensive special report reviewing government agency roles in using RCA, the economics of RCA, and the reasons the U.S. pavement community remains skeptical of RCA's durability and performance (Melton 2004). The conclusions of these publications are that practitioners have found other ways to use RCA, particularly as a pavement base material.

In other examples of this trend, four FHWA-sponsored papers published this decade either discuss or mention RCA but do not include a case study of its use in a rigid pavement slab in the United States. A 2000 case study on Recycled Materials in European Highway Environment favors recycled asphalt pavement (RAP) and reviews implementation policy (Schimmoller et al. 2000). A 2003 study concludes that RCA PCC can be used for secondary structures such as curb and gutter or sidewalk, but is not suitable—for strength reasons—for use in pavement structures (Ansari et al. 2000). A 2004 review on the state of RCA use in the United States reports on the implementation of RCA by selected states and reviews environmental policy decisions (FHWA 2004). Surprisingly, this report also found that only 32 of the 50 states recycle concrete rubble in any kind of application. The other 18 states still find it acceptable to landfill a majority of their concrete construction debris. The recent increase in attention to sustainable practices may steer the pavement community toward aggressive use of RCA in the concrete layer of rigid pavements.

Properties of Concretes Containing RCA

Challenges to RCA Use in PCC Pavements

Using recycled materials in new construction requires that the user understand the variations found in recycled materials that are not present in the more conventional materials they replace. RCA's primary difference from natural aggregate is its porosity due to the existing mortar surrounding the original aggregate. Concrete mixes using the more porous RCA require more water than does a conventional concrete mix. If this water is not supplied, the workability of the concrete is reduced, which complicates placement. As crushing processes and virgin aggregate characteristics vary by region, one solution cannot be prescribed for this problem. Rather, many contractors find that familiarity with the RCA in a PCC mix makes the material much easier to work with (Franke 1994). Another challenge of using RCA in PCC pavement is the fines. Although studies have confirmed that the use of coarse RCA in PCC yields durable and strong pavements, incorporating RCA fines into mix designs often results in unpredictable pavement behavior. A third challenge of incorporating RCA into a pavement's structural layer is a historical fear that RCA has a proclivity for alkali-silica reaction (ASR) and D-cracking.

Porosity

Because RCA is more porous than natural aggregate, due to its recycled mortar content, it differs from natural aggregate in two consequential ways. First, it is less dense (Cuttell et al. 1997). Second, it requires attention to mix design because each batch of recycled aggregate requires a unique adjustment to satisfy the water absorption of the aggregate (Yrjanson 1989). Researchers have discovered methods to decrease the negative effects of porosity on concrete performance. One such discovery indicates that fly ash is an agent that reduces hardened concrete's overall permeability (Sani et al. 2005). The other is accommodating the increased water demand of the RCA. The absorption of both natural aggregate and sand is around 1.0% or less. According to lab studies, the absorption of coarse RCA is around 2% to 5% greater and that of the fine RCA between 6% and 12% greater than that of natural aggregates (Shayan and Xu 2003, Yang et al. 2008). If the increased water demand of RCA is not accommodated, either not enough water will cause a decrease in workability that prohibits placement or a high water-cement ratio will compromise future strength.

Absorption is especially important given that a key difference between RCA and natural aggregate is the variability in the absorption capacity of different RCAs, due in part to the existing mortar surrounding the original aggregate (Figure T.1).

Concrete mixes that incorporate the more porous RCA can require more water than a conventional concrete mix, depending on the saturation state of the RCA. If this water is not supplied, the workability of the concrete is reduced, which complicates placement and early-age performance.

Researchers and practitioners have uncovered different means to add this water to the concrete mix. One method is to lab-test the RCA's absorption parameter to determine the amount of water necessary above that required for the water-cement ratio (Cristofoletti et al. 1994). However, this is time-consuming, not easily done at a remote construction site, and not practical for mass production. Some take a more relaxed approach and suggest simply wetting the aggregate or adding a little more water to the concrete mix (Franke 1994). Ultimately, sprinkling the RCA for 48 hours before incorporating it into a concrete mix ensures that each aggregate batch is fully saturated without guessing or testing for its water requirements while the intended water-cement ratio of the mix design remains relevant (Werner 1994).

RCA Fines

Unless stated otherwise, when researchers claim 100% of existing concrete is used, the fines (0/4) are incorporated into the subbase or frost blanket, not into the concrete mix (Krenn and Stinglhammer 1994; Sommer 1994). The reason for this is that recycled concrete fines are generally unwelcome concrete mix constituents. Recycled concrete fines are primarily small particles of mortar, not durable aggregates. Their absorption levels alone (6% to 12%) cause unpredictability in the behavior of the wet concrete (Hendricks 2002). Other research indicates that recycled fines decrease workability, demand more water, increase porosity, and decrease strength compared with mixes made with natural fines (Sani et al. 2005; Krenn and Stinglhammer 1994; Zachlehner and Ullmann 1994).

As an exception to the conventional wisdom of RCA fines, a project in Switzerland successfully incorporated 100% recycled fine and coarse aggregates into a concrete pavement. After 2 years, the high-volume road sections that were constructed with this 100% RCA were still performing well. Most notably, this pavement resisted infiltrations from winter applications of salt. This success was attributed to splitting the aggregate into four sizes (0/4, 4/8, 8/16, 16/32) before incorporating it into the new concrete mix and to assuring that the old concrete cement paste was 100% saturated before the RCA was incorporated into the concrete mix (Werner 1994).

Others have found a balance by exploring the limit of natural fine replacement with recycled concrete fines. Shayan and Xu (2003) found a mix design including coarse RCA, silica fume, air-entraining admixture (AEA), and high-range water-reducing admixture (HRWRA) that could accommodate as much as 50% recycled fines and still achieve 53 MPa compressive, 6.9 MPa flexural, and 4.0 MPa splitting tensile strengths after 28 days. The slump (60 mm) was also acceptable.

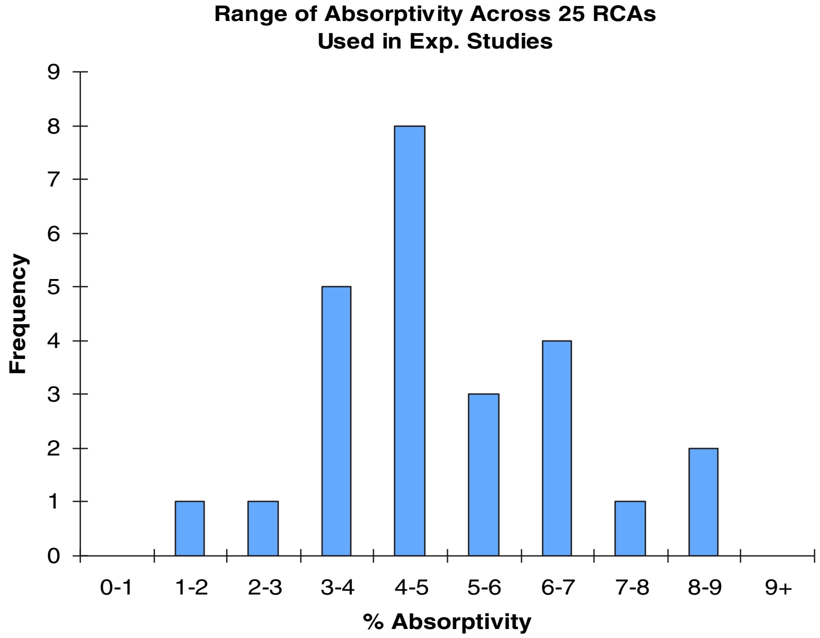

Figure T.1. Range of absorptive capacities of RCA encountered across 17 studies in the R21 Interim Report on RCA.

However, it is important to mention that other research indicated that a concrete mix including coarse RCA and 50% RCA fines did not adequately resist attack of frost and deicing chemicals (Sommer 1994). This concrete mix contained plasticizer but not a supplementary cementitious material (SCM) such as fly ash or silica fume.

ASR and D-cracking

Previous concerns with RCA in pavement applications were often restricted to alkali-silica reaction (ASR) and D-cracking. However, current efforts in research surrounding RCA no longer focus on these issues, or if ASR or D-cracking is mentioned, it is in conjunction with a larger research concern. This is mainly because of the use of RCA originating from D-cracked or ASR concretes being discouraged by the pavement community at large. Furthermore, processes on incorporating RCA originating from D-cracked or ASR concretes have been well documented in the United States and will not be reproduced here.

Strength Properties of PCC with RCA

Although the porous layer of existing mortar around the original aggregate makes PCC pavement mix design more complicated, this feature of RCA facilitates good bonds between the old mortar and the new cement. In turn, the compression, tensile, and flexural strengths do not decrease on account of the interlock failure between the aggregates and new cement (Sommer 1994). However, other research hypothesizes that the microstructure of the weak surface layer of porous motor surrounding the aggregate was the cause of low ultimate strength values. This work found that treating RCA with a sodium silicate solution in an attempt to consolidate and improve the surface features of the aggregate did not improve strength or durability. Instead, the addition of an SCM, specifically silica fume, and limiting the amount of recycled concrete fines (0/4 mm) to 50% of total fines were the important factors in achieving 50 MPa compressive strength in RCA concrete (Shayan and Xu 2003).

Both lab tests and strength tests of cores taken from RCA PCC pavement sections confirm that with the addition of an SCM such as silica fume or fly ash (Franke 1994; Shayan and Xu 2003; Werner 1994), the compressive strength is equal to or slightly less than PCC pavements made with natural aggregates (Cuttell et al. 1997; Franke 1994; Cristofoletti et al. 1994; Krenn and Stinglhammer 1994; Sommer 1994; Zachlehner and Ullmann 1994; Gomez-Soberon 2002). Although the compressive strengths of some PCC made with coarse RCA decreased slightly, most of these compressive strengths are still equal to or comfortably above 35 MPa (5,076 psi). This implies that even if the substitution of RCA for natural coarse aggregate decreases the compressive strength slightly, the pavement's compressive strength is still equal to or greater than the required minimum, which in turn, places an emphasis on the flexural and tensile strengths of RCA PCC.

A majority of lab and field reports indicated a similar value or an increase in value for the tensile and flexural strengths as a result of substituting coarse RCA for coarse natural aggregate (Franke 1994; Cristofoletti et al. 1994; Krenn and Stinglhammer 1994; Sommer 1994; Zachlehner and Ullmann 1994; Springenschmid and Sodeikat 1998; Smith and Tighe 2008). Few studies reported a decrease in tensile strength due to the use of RCA, but in reviewing the concrete mix constituents used in these studies, an SCM was not included in either mix, and in one of them, neither was an HRWRA agent (Shayan and Xu 2003; Gomez-Soberon 2002; Ahmad et al. 1996).

The addition of plasticizing agents to RCA concrete can also improve the strength properties of a mix and contribute to its use in structural applications. The use of admixtures in RCA concretes can allow for a workable mix with high initial strength, thereby alleviating two common complaints of RCA concretes. In the best case scenario, absorption is compensated for by presaturation of RCA, and plasticizing agents reduce the total required water-cement ratio to maintain both strength and workability (Springenschmid and Sodeikat 1998).

Although strength is not the only characteristic of a durable and long-lasting pavement, these discoveries—the addition of SCMs and plasticizing agents and limiting the addition of recycled concrete fines to the concrete mix design—are the keys to high-strength RCA concrete and indicate a solution to one perceived limitation to RCA use in structural PCC pavements.

Shrinkage, Creep, and Warping

It has been observed that RCA concrete offers less restraint to volumetric expansion in response to temperature and moisture fluctuation (humidity and infiltration), primarily because its modulus of elasticity, so its stiffness is consistently found to be less than that of conventional concrete (Cuttell et al. 1997; Yang et al. 2008; Springenschmid and Sodeikat 1998; Huber et al. 2004).

On a similar note, strain caused by shrinkage and creep has been found to increase as the percentage of RCA increases (Yang et al. 2008; Gomez-Soberon 2002; Kou et al. 2007). Yang took this concept one step further and found that shrinkage was dependent on the amount of mortar left on the original aggregate. As water absorption increases and specific gravity decreases—meaning a greater percentage of leftover mortar—the aggregate stiffness also decreases and offers less restraint to shrinkage (Yang et al. 2008). Although the initial shrinkage rate of conventional concrete exceeds that of RCA concrete, after 10 days, the difference in shrinkage becomes especially noticeable as the shrinkage rate of conventional concrete slows at a quicker rate than does that of RCA concrete (Yang et al. 2008). Besides decreasing the amount of mortar attached to the recycled aggregate, both a partial substitution of fly ash for cement and a decrease in the water-cement ratio reduced the drying shrinkage and creep of RCA (Kou et al. 2007). A third factor in decreasing creep and shrinkage is time. The total porosity of concrete with coarse RCA decreases over a period of 90 days because of the crystallization of products that reduce both the number and size of the pores (Gomez-Soberon 2002).

It is interesting to note that the concrete mix designs behind the research vary in the absorption and specific gravity values of the recycled aggregate, the use of fly ash, and the use of HRWRA. For example, some mix designs contain HRWRA but not fly ash or other SCMs. In another example, the absorption and specific gravities of coarse RCA represented in a cement mix will range from low to high (1.5% to 8%). Finally, a concrete mix containing neither HRWRA—resulting in a high water-cement ratio—nor fly ash could represent RCA with high absorption and a low specific gravity. From these three examples, it is possible to conclude that a concrete mix that included recycled aggregate with a limited amount of old mortar, HRWRA, and fly ash or another SCM could be almost as resistant to shrinkage and creep as conventional concrete.

Although both moisture and thermal gradients are responsible for volume changes in PCC, research indicates that the temperature gradient is the primary cause of shrinkage and swelling in PCC containing RCA. Both laboratory and field work indicated that the hygral gradient in PCC RCA pavement is negligible compared to the temperature gradient (Huber et al. 2004). Another source of shrinkage—carbonation—was found to cause negligible shrinkage in RCA concrete (Shayan and Xu 2003).

The importance of limiting shrinkage, creep, and warping is more apparent when considering the structural elements of pavements. Because of the larger strains, due to thermal gradients, cracks and joints can contract more given the appropriate conditions. The result is decreased load transferability across the joint or crack leading to early degradation of the pavement. An example of this is portrayed by a case study from a stretch of RCA PCC pavement in Minnesota. The RCA pavement section and a natural aggregate control pavement section were placed about the same time on US-52 near Zumbrota. A sample of the RCA pavement indicated an 83.6% mortar content and the conventional sample revealed a 51.5% mortar content. After only 10 years of service, the RCA section was 88% cracked versus 22% cracked for the control section. After 22 years, the RCA section was 92% cracked and the control section was 24% cracked. Although the control section was significantly cracked, the performance of the RCA may have been attributable, in part, to the high mortar content of the recycled aggregate.

Recycling of Old PCC Pavements

RCA in Base Material and Leaching

Although many states avoid using RCA as a coarse aggregate in PCC, RCA is commonly used in unbound pavement base layers. Water that passes through unbound RCA leaves with a high pH and possibly carries other nutrients, such as calcium. Research on this topic is conflicting and neither fully supports nor strongly cautions against this practice (FHWA 2004; Schimmoller et al. 2000; Sani et al. 2005). Other concerns are that metal culverts could be sensitive to the effluent's pH and formation of Tufa on the ground surface in the form of a white mineral stain (Melton 2004). There are two primary justifications for continued use of RCA in the United States. The first justification is that the effluent is sufficiently diluted a short time after it leaves the contaminant source. The second justification is that the potential environmental degradation resulting from the effluent is outweighed by the problem of filling landfills (FHWA 2004).

Usability Issues in Recycling Old Concrete

A majority of current and past research in RCA addresses issues related to the condition of concretes prior to becoming RCA. This review will not speak to all of these issues but will detail some of the more well-known issues.

D-cracked and ASR Pavement as New RCA

One of the primary differences between the European and American experience with RCA is that Europeans refuse to use an existing pavement as RCA in a new structural pavement layer if it is distressed because of D-cracking or ASR. European researchers praise existing concrete pavements for their strength and durability and frequently indicate that the old concrete pavement being recycled into coarse aggregate must be in good condition (Krenn and Stinglhammer 1994; Sommer 1994; Zachlehner and Ullmann 1994; Springenschmid and Sodeikat 1998; Hall et al. 2007). Practitioners in the United States have, because of successful lab experiments, used D-cracked and ASR-damaged existing pavements as coarse aggregate for new concrete pavements. For example, in Minnesota, a 16-mile rehabilitation project on US-59 between Worthington and Fulda was the first known project to recycle concrete pavement that failed extensively because of D-cracking (Yrjanson 1989). Lab research identified that the original virgin coarse aggregate had shown poor durability, and subsequently, the concrete pavements containing this aggregate were D-cracked. In response, the Minnesota Department of Transportation (MnDOT) limited the size of the recycled coarse aggregate to 19 mm (¾ in.) for dilation reduction (Cuttell 1996). Again, research showed that fly ash could be used to ameliorate the chances of D-cracking. In laboratory studies, concrete pavement mixes with fly ash substituted for cement by 0%, 10%, and 20% by weight of cement were tested by ASTM C666 Method B modified to observe freeze-thaw durability. The mixture with 20% fly ash replacement showed a greatly reduced potential for D-cracking (Yrjanson 1989).

A 1994 FHWA report and a 2006 follow-up study described pavement sections, two in Minnesota and one in Kansas, that were constructed with previously D-cracked pavement (FHWA 2004; Sturtevant et al. 2006). The Minnesota (MN-2) section that contained less than 10% recycled mortar content showed no signs of recurrent D-cracking after 22 years. The other Minnesota (MN-3) section showed no signs of recurrent D-cracking after 26 years. The coarse RCA used for these projects was limited to maximum size of 19 mm (¾ in.). The Kansas section (KS-1), which in addition to coarse RCA incorporated 25% recycled fines into its mix and allowed a minimum coarse RCA size of 38 mm (1.5 in.) had a different outcome. After 9 years, no recurrent D-cracking was observed. However, in 2002, a bituminous overlay was placed over the RCA PCC pavement because recurrent D-cracking had occurred.

The same reports also detail the recycling of an existing PCC pavement with ASR problems in Wyoming (WY-1) into RCA for new PCC pavement. The two unique qualities of the RCA concrete mix are that (1) the coarse RCA contained less than 10% mortar content and (2) 25% of natural fines in the mix were replaced with recycled concrete fines. Also important in the mix design was the use of ASR mitigation techniques of using a low alkali cement and using Class F fly ash. The original 1994 study reported that uranyl acetate testing found a moderate amount of silica gel in the mortar around aggregate particles of the RCA section and minimal amounts of silica gel in the control section. By 2006, there was visual evidence of localized ASR surface cracking, indicating minor ASR activity after more than 20 years. The possible conclusions from this case study are that the ASR mitigation techniques prevented more severe recurrent ASR and that using 100% natural fines may have prevented or lessened the reoccurrence. Although it is only one example, it may also be safe to conclude—especially considering the European practices of only recycling good PCC pavement—that recycling PCC pavement with ASR problems is not an acceptable practice or, at best, one that should be undertaken with caution.

Existing Pavement with a Thin Bituminous Overlay

Many of the European motorways that required reconstruction had been in service for many years. As a result, many of these pavements were repaired with a thin, bituminous overlay. In the United States, the bituminous overlays are typically scraped away before the concrete pavement is salvaged, but this practice is time consuming, inefficient, and not in accordance with the ideal of sustainable, rapid renewal. European researchers established limits of bituminous fractions in coarse RCA (4/32) that would be used in new PCC pavements (Krenn and Stinglhammer 1994; Sommer 1994). Although asphalt contents of as much as 20% did not significantly reduce the pavement's flexural strength and asphalt contents as great as 33% did not compromise shrinkage and swelling behavior, asphalt contents of more than 20% impaired the pavement's frost resistance (Sommer 1994). Ultimately, Austria limited to 10% the amount of 4/32 asphalt particles in the recycled aggregate used in PCC pavement mixes (Sommer 1994). As a comparison, Minnesota allows as much as 3% of the coarse RCA to be asphalt (FHWA 2004).

Methods to Optimize Use of RCA

The percentage of the existing concrete pavement that can be recycled into coarse aggregate is not uniform across experiences. A Wisconsin recycling project was able to salvage 70% of the original material for coarse aggregate. Of the remaining existing concrete, 20% was fines and 10% was lost to construction practices (Yrjanson 1989). Other projects reported lower salvage values of between 60% and 65% (Franke 1994; Krenn and Stinglhammer 1994). Austrian specifications require a minimum 65% reclamation (Sommer 1994).

Methods for recycling existing concrete pavement into aggregates for new concrete pavement are not governed by a single methodology, and certain methods allow workers to recapture more of the existing concrete into aggregate sizes greater than 4 mm. An account of one experience suggests that impact-type crushers operating at less than maximum output allow the maximum coarse aggregate particles to be reclaimed (Sommer 1994). Size specifications for coarse RCA also affect the percentage of recycled material that is usable. A greater portion of the existing pavement can be recycled as the maximum recycled aggregate size increases. For example, a 25-mm (1-in.) maximum aggregate size corresponds to reclaiming 55% to 65% of the original concrete pavement for coarse aggregate use, whereas 80% of the existing pavement could be recovered if the maximum aggregate size of the new concrete pavement mix increased to 38 mm (1.5 in.) (Cuttell et al. 1997). Although increasing the maximum coarse aggregate size will result in more recyclable material, a larger aggregate size could, depending on the nature of the old mortar, potentially compromise workability, durability, and strength.

Field Performance of Rigid Pavements Containing RCA as a Structural Component

United States

The approach of this review is not to replicate the information widely disseminated in the United States, but the American case studies that are highlighted for this appendix are interwoven with the text to emphasize an RCA topic or design suggestion. For more information on placements of RCA PCC single-layer pavements, the reader can refer to the 1989 NCHRP study (Yrjanson 1989) and the 1997 FHWA study (Cuttell et al. 1997).

A few high-profile PCC RCA pavement failures in the early 1990s may have made state departments of transportation hesitant to continue using RCA in the structural layers of its PCC pavements. Experiences by the Michigan Department of Transportation (MDOT), Texas Department of Transportation (TxDOT), and Minnesota Department of Transportation (MnDOT) provide some insight into this hesitancy. After paving approximately 650 lane miles with RCA rigid pavement, MDOT issued a moratorium on new PCC RCA pavements in 1988 and then again, permanently, in 1991. The moratorium was instated after rigid pavements containing RCA on I-94 and I-75 experienced premature transverse cracking, faulting, and spalling. The moratorium continued despite results from a University of Michigan study that suggested these problems were the result not only of the RCA but also of problems with base design, uniformity of the foundation layers, stiffness of the subgrade material, thickness of the pavement slab, and the temperature when the concrete was placed (Harrington 2008). Although TxDOT is researching the use of RCA in PCC structural pavement, it restricts RCA from PCC pavement structural layers because it has experienced creep and shrinkage problems when using RCA in pavements (FHWA 2004; TxDOT 2008).

An FHWA report highlighted four PCC RCA pavement sections in Minnesota that were constructed during the 1980s. One of the four, labeled MN-1, was on a stretch of I-94 near Brandon and proved to be the most underperforming section of the four. After 6 years, this dowel-reinforced pavement showed virtually no cracking despite 8.2-m (27-ft) joint spacing and generally was performing better than conventional pavement constructed in the same region at the same time. Unlike most RCA sections that are compared with conventional sections, its coefficient of thermal expansion was equal. However, by 2006 the MN-1 section was 31% cracked, compared with 0% for the control section. Although the RCA section contained less than the recommended amount of cement plus cementitious materials recommended by the FHWA for durability, it displayed no visible freeze-thaw distress, and petrographic evaluation revealed no signs of poor freeze-thaw resistance. Two causes for the cracking could be the low cement content and the relatively high water-cement ratio (0.56) and water-cement to fly ash ratio (0.47) compared with the water-cement ratios of other well-performing RCA pavement sections (Cuttell 1996). Although the MnDOT was a pioneer in replacing aging highways with RCA PCC, contractors have not adopted these practices in recent times. Perhaps this is in response to the cracking of the MN-1 section or due to an MnDOT change to a 60-year design life for all high-volume freeways and a 35-year design life for other highways associated with warranties (FHWA 2004).

Europe

In some European countries, most notably Austria and Germany, RCA is used as the coarse aggregate for the bottom layer of composite concrete-on-concrete pavement. In 1989, Austria pioneered the practice by developing a system to recycle the existing concrete pavement along the A1 motorway between Vienna and Salzburg because more than 50% required replacement. Today, Austria requires the use of recycled concrete in the lower layer of its two-course PCC pavements (Hall et al. 2007). This system entails using the 4/32 crushed coarse aggregates for the new roadway and the 0/4 fines to stabilize the frost layer (Krenn and Stinglhammer 1994). A second review of the reconstruction of the A1 motorway specifically studied 60 km of the existing roadway with a thin, bituminous overlay. Crushing resulted in no more than 10% of bituminous particles in the total recycled coarse aggregate fraction (4/32).

Based on the Austrian experience of repaving the A1 motorway, German engineers replaced a 6-km section of the A9 motorway near Dessau. RCA was used as coarse aggregate (2/32 mm) in the bottom lift of two-lift PCC pavement. The specific experience that persuaded the Germans to experiment with RCA despite not having standard specifications for its use was Austria's suggestion to eliminate recycled concrete fines from the mix for the lower lifts because of the fines' negative effect on workability (Zachlehner and Ullmann 1994).

Another Austrian-inspired RCA PCC project was constructed on the A27 motorway in Lower Saxony, Germany. Coarse RCA was used in the lower lift of two-lift pavement in 6-km sections (Franke 1994). Later in the 1990s, German researchers confirmed the resistance of RCA PCC pavement to deicing salt penetration through observation of the in-field performance of the pavement along the A93 motorway in Bavaria. A single-layer concrete pavement with 100% coarse RCA (no recycled fines) survived the particularly hard winter of 1995–1996 and showed no deterioration (Springenschmid and Sodeikat 1998). In a final example from Germany, sections of the A9 Motorway constructed with RCA PCC were observed to have a higher resistance to cracking than its conventional counterpart undergoing similar environmental conditions. The others proposed two hypotheses for this phenomenon. The first is that recycled aggregate's rough surface has the ability to create a better bond with the new mortar than does natural aggregate. The second explanation is that there may be a local reduction in the water-cement ratio near the bond area because of the porosity of the recycled cement paste (Springenschmid and Sodeikat 1998).

A case study from Switzerland determined that cracking failure in RCA PCC that was initially attributed to low strength (and indirectly to the use of RCA) was, instead, a result of premature aggregate demixing and the contractor's inability to accommodate RCA's increased demand for water. Although the RCA concrete stockpile indicated a desirable aggregate gradation at the storage site, en route to the mixing cite, the aggregate supply became severely demixed. The ensuing difficulties were irregular consistency for placement, and ultimately, the hardened cores did not meet strength requirements (Werner 1994).

New Opportunities for the Adoption of RCA PCC in Rigid Pavements

The development of this review is due in part to the 2006 FHWA scanning tour of European concrete pavements, which detailed the uses of RCA in European pavements (Hall et al. 2007). In addition, the desire to better understand unconventional uses of RCA was inspired by several recent projects in the study of composite pavements that might incorporate RCA in a more involved manner.

The Iowa State University Center for Transportation Research and Education, under FHWA sponsorship, conducted an investigation into two-lift PCC pavements (Cable and Frentress 2004). This study also provided recommendations and guidelines for the adoption of these pavements into the United States. One of the caveats of this review was the additional expense of the construction of two-layer PCC pavements in the United States, given the need for equipment and expertise that are not familiar to American pavement engineers and contractors. One immediate cost-saving measure would be the use of RCA in the lower of the two PCC lifts.

The California, Washington, and Minnesota DOTs are involved in the transportation pooled-fund study TPF(5)-149 Design and Construction Guidelines for Thermally Insulated Concrete Pavements. This study, under the guidance of the FHWA, investigates composite pavements that consist of a jointed or continuously reinforced concrete layer covered by an asphalt layer during or shortly after construction. This asphalt layer is considered to be a kind of thermal insulation for the concrete lower lift. Although the main objective of this study refers to new construction, the study will also investigate the use of asphalt overlays as thermal insulators for existing concrete pavements. These existing pavements might include single-layer PCC pavements that have RCA as a structural component. A recent tour of European pavements for the SHRP 2 R21 project found that in Europe RCA has been used in these lower PCC lifts in composite pavements with great success.

The use of RCA in the lower PCC lift of a composite pavement, as detailed in the projects above, allows for numerous opportunities for the pavement system:

- The economy and sustainability of reusing reclaimed materials;
- The ability to take advantage of RCA's structural contributions without experiencing the drawbacks (polishing, smoothness, and so forth) of RCA as an aggregate in an equivalent single-layer pavement; and
- The ability to take advantage of environmental incentives for road construction.

Preliminary Testing of RCA Delivered for R21 MnROAD Use

A few months before the MnROAD SHRP 2 R21 construction, a sieve analysis on the airport RCA was conducted according to ASTM C136 (Sieve Analysis for Fine and Coarse Aggregates) (see Figure T.2). Airport RCA fines—aggregates that did not pass the No. 4 sieve—were separated from the coarse RCA because recycled fines will not be used for this project. The coarse RCA aggregate gradation was substituted for the RCA gradation that the contractor assumed for its preliminary mix design. The airport RCA and conventional fine aggregates produced a combined gradation that was almost identical to the contractor's estimated RCA gradation.

In addition to the aggregate gradation, a regimen of tests were conducted on the airport RCA according to ASTM C127 (Density, Relative Density [Specific Gravity], and Absorption of Coarse Aggregate) and ASTM C29 (Bulk Density [Unit Weight] and Voids in Aggregate). The following aggregate properties and corresponding values determined from these tests are presented in Table T.1.

As a follow-up to the above battery of tests, additional absorption tests on airport RCA were conducted. Results from these tests are presented in Table T.2 below.

When the contractor preliminarily batched the RCA mix using 2.5% for the absorption of the RCA to adjust the mixture water requirements, the contractor reported that the mix required much more water than was calculated (approximately 2% to 5% more than had been anticipated). The research team suspects that the primary reason for the additional water requirement is the failure to wash the RCA of fine material (i.e., for the Minneapolis–St. Paul Airport RCA, 2% by weight of particles passed the No. 200 sieve).

Crushing Methods and Properties of RCA for R21 MnROAD Construction

Introduction

The majority of previous studies used recycled aggregates produced from concrete created and crushed in the laboratory (Fathifazl 2008). These estimates do not account for properties of recycled aggregate produced from field concrete crushed commercially. The few studies to use field concrete crushed in

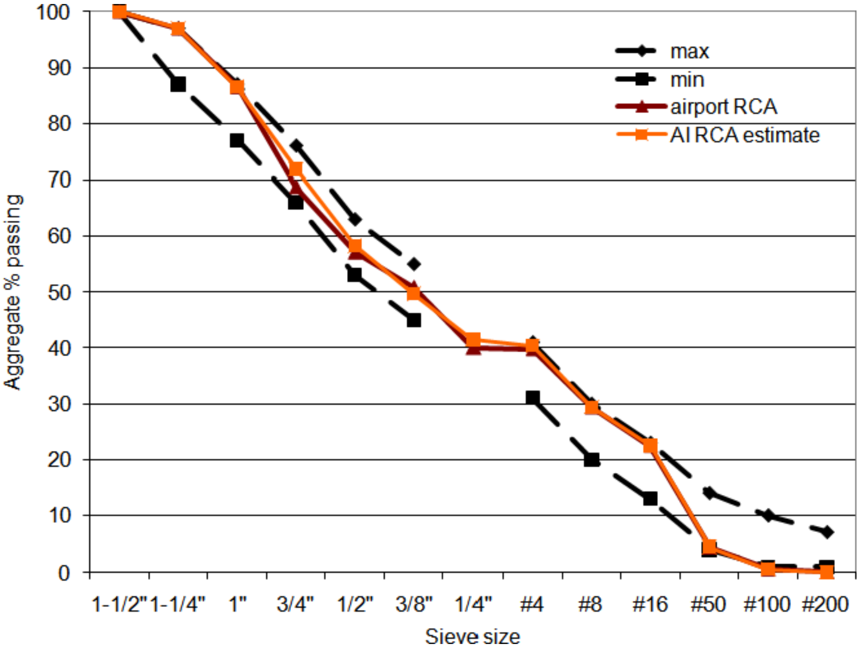

Figure T.2. Gradation of airport RCA relative to contractor estimate. (AI RCA = Aggregate Industries.)

an industrial crushing system generally shows results comparable to conventional aggregate concretes, so long as the crushing process removes sufficient mortar content (Gress et al. 2009; Cuttell 1996; Vancura et al. 2009). However, almost no studies compare differing original aggregate and crushing process.

Recycled Coarse Aggregate Production

Crushing and Crushing Methods

The RCA classified for this study was crushed by two different systems. The first type of crusher was an industrial crushing operation that included a primary jaw crusher (Figure T.3) and a secondary cone crusher (Figure T.4). The second type of crusher was a small laboratory jaw crusher (Figure T.5).

Industrial Crushing System

Concrete pieces about 12 to 16 in. are fed into the jaw crusher as the primary crusher (ACI Committee 555 2001). The jaw crusher jaws are distanced to adjust the maximum aggregate size produced (Hansen 1992). The jaw crusher produces good recycled aggregate size and a predictable gradation for concrete production (ACI Committee 555 2001; Hansen 1986; Hansen and Narud 1983).

A cone crusher is used as secondary crusher to further remove the mortar from the natural aggregates. The cone crusher

Table T.1. Initial Assessment of Coarse RCA (Airport) Properties

Property Name	Value
Oven dry (OD) specific gravity	2.34
Saturated surface dry (SSD) specific gravity	2.38
Density (OD)	146 lb/ft^3
Density (SSD)	149 lb/ft^3
Absorption	1.9%
Bulk density (of dry rodded sample)	96.62 lb/ft^3
% Voids (of dry rodded sample)	33.73%

Table T.2. Reported Absorption for RCA Recovered from the Minneapolis–St. Paul Airport

	Absorption (Percent Water Retained)
Trial 1	1.90
Trial 2	2.78
Trial 3	2.83
Trial 4	2.16
Average	2.42

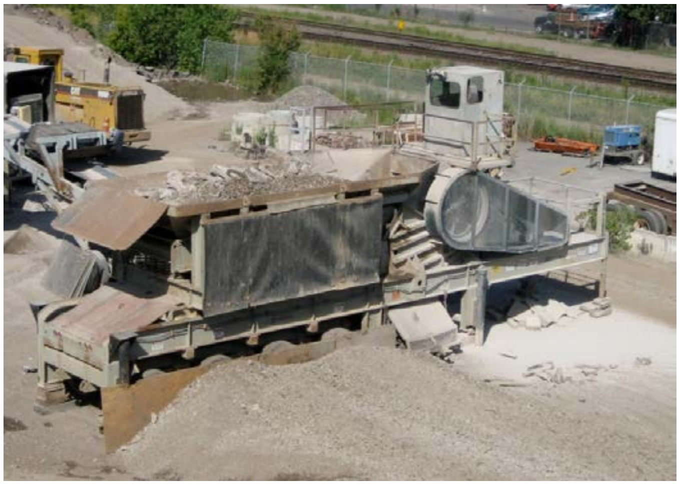

Figure T.3. Jaw crusher used in the production of limestone industrial and I-94 industrial RCA.

must be used as a secondary crusher because it cannot handle materials greater than 200 mm (Hansen 1992). A cone crusher squeezes material between an eccentrically gyrating spindle and a bowl below. As the pieces are broken, they fall to the lower, more closely spaced, part of the crusher and are further crushed until small enough to fall through the bottom opening (Kivikyto-Reponen et al. 2009).

The additional removal of mortar from the aggregates produces less angular or oddly shaped pieces and aggregate with lower absorption capacity. Although higher costs are incurred, the additional crushing removes attached mortar and thereby produces a higher quality of recycled aggregate (Sanchez de Juan and Gutierrez 2009). This suggests that the mortar content on the recycled aggregates determines the overall qualities of that aggregate.

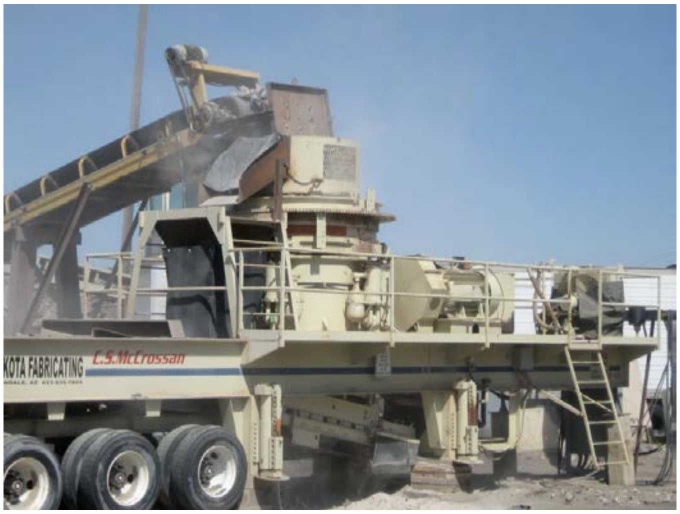

Figure T.4. Cone crusher used in the production of limestone industrial and I-94 industrial RCA.

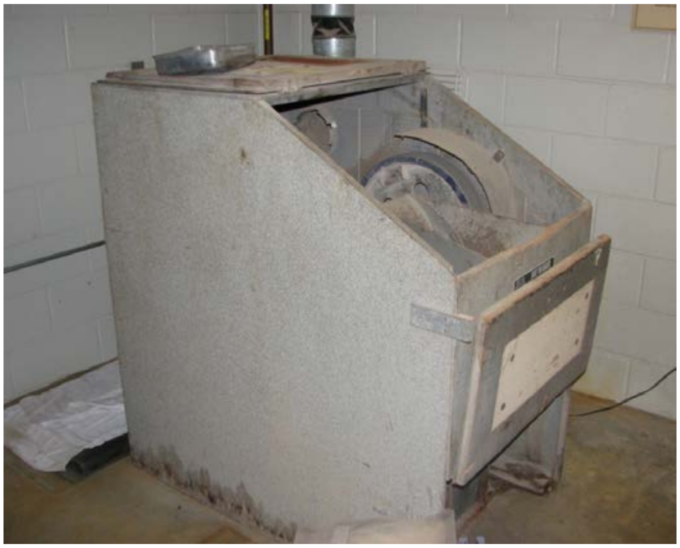

Figure T.5. Jaw crusher used to produce I-94 laboratory-crushed RCA.

Impact crushers are another common industrial crusher used in concrete demolition. German pavements use an impact crusher as the last crushing operation in the crushing sequence. Impact crushers are specifically used when reinforcement is present in general demolition (Hansen 1992). However, the crusher does not distinguish between aggregate and mortar. (Hansen 1992; ACI Committee 555 2001). This type of crusher was not used in this experiment.

Laboratory Crushing System

The smaller laboratory crusher is more commonly used in the study of RCA. It can crush smaller quantities of material and can fit in a laboratory.

The crusher is a jaw crusher and uses the same mechanism as the jaw crusher described. However, because of the closeness of the jaws and smaller quantity of material, the crusher tends to break both the mortar and aggregate. This produces more angular pieces with a higher percent of attached mortar (Hiller et al. 2010).

Aggregate-Mortar Separation

The resulting RCA is also a product of the natural aggregate type and original aggregate strength. An aggregate with a rough surface, such as crushed aggregate, will have a stronger bond than a sawn or smooth surface aggregate. However, this difference is twofold. The crushed rock has a higher bond strength and therefore is less likely to initiate cracking at the interface. The crushed rock tends to be weaker and thus is more likely to fracture through the aggregate rather than at the interface if the matrix is sufficiently strong. RCA production generally uses concrete in a structure at the end of its effective life. Thus, the concrete is close to its maximum strength at the time of crushing. In concrete produced with smoother aggregates, the interface generally is the weakest point. When the concrete is crushed to produce RCA, the smoother surface should allow better separation of the mortar and natural aggregate (Giacco and Zerbino 1998). This indicates that smooth natural aggregate concrete may be more suitable for RCA production.

A higher attached mortar content was found for an original higher strength concrete (Hansen 1992). The original lower strength concrete had more cracking in the attached mortar. This made the overall aggregate weaker because of a secondary weak interface surface.

Good mortar-aggregate separation is needed through the aggregate properties and crushing method. The removal of this mortar improves the concrete properties and thus should be considered when determining the cost of additional processing and aggregate choice (Cuttell et al. 1997).

Sieving

After the concrete is crushed, it is sieved to remove finer particles and grade the final product. Sieving equipment is already part of an industrial crushing system, so no additional costs are incurred.

The fine aggregate resulting from concrete crushing and RCA production must be removed from the coarse aggregate pieces. The fine aggregate portion of crushed concrete generally is taken as particles passing the No. 4 sieve. Coarse aggregates are most efficiently sorted with inclined, low-frequency, vibrating screens (Hansen 1986). ACI advises that material smaller than 2 mm be removed because most of the strength loss comes from these particles (ACI Committee 555 2001).

Additional Preparation

The aggregate may also have additional preparation before its addition to the concrete. Washing the aggregate generally is the most common for RCA and natural aggregate. Presoaking has been used in lightweight and RCA aggregate to improve other properties.

Washing the RCA

Eliminating the fine fraction of RCA that is used in concrete is a common practice. However, there is not a consensus on the necessity of washing coarse aggregates before using them in concrete. Fine particles increase cohesion among cement and fine aggregate particles, which influences the ability of the cement paste to cling to itself and the aggregates (Hansen and Narud 1983).

A recently published paper on the treatment of RCA indicates that for RCA to be used in concrete, the RCA must be washed (Cuperus and Boone 2003). Another study concluded that washing RCA increased the strength and permeability, while having no effect on the drying shrinkage (Yanagi et al. 1993). ASTM C33 allows for 1.5% of the coarse aggregate fraction to be smaller than the No. 200 sieve with exceptions that could apply to coarse RCA. Technically, this implies that some coarse RCA could be used without washing. Ultimately, the decision to wash or not to wash will be decided by the impact that the residual fines have on the workability of the concrete.

Presoaking the RCA

The RCA attached mortar causes a high and varied absorption capacity (Schulz 1994). The high absorption also increases the water demand. It is often suggested that one way to mitigate the affect of RCA on a concrete's water demand in concrete is to presoak the RCA to accommodate the RCA's absorption (Schulz 1994; Hansen 1986).

According to Schulz, presoaking to the point of saturation is the best method because it ensures consistent moisture content and makes the absorption capacity irrelevant. This method is only viable if storage capacity exists and aggregates can be added quickly to prevent drying (Schulz 1994). Hansen also pointed out that through literature soaking recycled aggregate is suggested to "maintain uniform quality during concrete production" because of the high absorption capacity (Hansen 1992). Thus, testing of the RCA's moisture content is imperative before mixing and averaging the absorption capacity of multiple RCA samples to manage water content in concrete made with RCA.

The suggested length of presoaking time varies between researchers. Morlion et al. concluded that 15 minutes was sufficient to saturate 4 to 28 mm RCA with a 5% absorption capacity. Hansen (1992) also observed that air-dry coarse aggregates became saturated in the concrete mix after 15 minutes. This would explain the faster drying phenomenon observed by Hansen. Hansen suggested that an hour of soaking should be sufficient. Kaga et al., however, found that more than 24 hours of immersion in water were necessary for complete saturation of RCA (Hansen 1992).

Properties of Crushed RCA and Concretes Containing RCA

Development of Mixes for Laboratory Testing

Mix design development for the RCA lift of the SHRP 2 R21 project was imperative because the ready-mix supplier had no experience manufacturing concrete with RCA. However, the pavement that was going to be crushed into RCA for the new pavement construction could not be processed into RCA until 2 weeks before construction. Therefore, the mix design development needed to proceed with an alternative but similar RCA. This appendix investigates the properties of RCA (recycled aggregate size larger than the No. 4 sieve) that result from different original source material and crushing processes.

There were two RCAs available for mix design development, and initially, it was not clear what RCA would most resemble the RCA that would be used for actual construction. One of the recycled aggregates was made from a pavement that was similar in aggregate (river gravel), age (17 years), and cement content to the pavement that was going to be used for the composite pavement construction. Because there was only a small quantity of this pavement available, it was crushed with a laboratory jaw crusher. This RCA will be referred to as I-94 laboratory crushed RCA. The other RCA option was a pavement that incorporated limestone aggregate and an unknown cement content but was crushed with a similar industrial process as would be used to crush the pavement into RCA for the R21 project. This RCA will be referred to as limestone RCA. To determine what RCA to use for mix development, the aggregates were classified by absorption and specific gravity and then 1-ft^3 trial batches of concrete were made with each of the aggregates to assess workability and strength. In addition, once the RCA used for SHRP 2 R21 construction became available, similar tests were conducted on that RCA. This RCA will be referred to as I-94 industrial crushed RCA.

Laboratory Methods

ASTM 127 was used to test the absorption of the three RCAs. In general, RCA has higher absorption capacity than conventional aggregate because of the attached mortar (ACI Committee 555 2001; Sanchez and Gutierrez 2009). The typical absorption of RCA quoted in literature was 3% to 6%, and sometimes as high as 10% (Bairagi et al. 1990; Hansen 1986; Sanchez and Gutierrez 2009). Conventional aggregate absorption capacity typically is 1% to 3% (Bairagi et al. 1990). High aggregate absorption is detrimental to concrete because aggregate with a high absorption capacity results in a highly variable moisture content throughout the stockpile. Variable moisture of a stockpiled aggregate can result in unpredictable workability (Schulz 1994). Because of the effect of absorption, the RILEM specifications for RCA recommend that RCA with an asphalt content greater than 10% not be used (Henrichsen 1994).

The bulk specific gravity of the RCAs was determined according to ASTM 127. In general, the density of RCA is slightly less than the original aggregates because the attached mortar is less dense than aggregate (Hansen 1986). It has also been observed that the specific gravity of RCA reduces with decreasing RCA size because of increasing mortar content (Hiller et al. 2010).

ASTM C136 was followed to determine the RCA gradations. All RCAs were washed to remove the leftover fine material and oven dried before gradations were taken. The industrial crushing process influences RCA aggregate gradation because the machines can be adjusted to accommodate the desired top size aggregate. In addition, screens, which can be compared to large aggregate sieves, are also used during the industrial crushing process to screen out or capture aggregates within a certain size range.

The top size aggregate for the limestone RCA was ¾ in. This RCA was originally crushed to be used for road base. Further screening of particles passing the No. 4 sieve was done before the RCA was classified and mixed into concrete. The top sized aggregate for the I-94 laboratory crushed RCA was 1 in. The laboratory crushing process does not afford the same opportunities for sorting and sieving as the industrial crushing process. The maximum size I-94 industrial crushed RCA was ¾ in. The aggregate particles smaller than the No. 4 sieve were removed from the I-94 industrial crushed RCA during processing.

To test gradation's effect on mortar content, the percentage of No. 4 and ⅜-in. particles of the industrial crushed RCAs were lowered to those of the I-94 laboratory-crushed RCA. The samples were then tested for absorption capacity and SSD bulk specific gravity.

For the purposes of making concrete for testing the plastic and strength properties of concrete made with different sources of RCA, the coarse RCA was augmented with conventional coarse aggregates between ¾ and 1.5 in. and conventional fine aggregate. Although the coarse limestone, I-94 laboratory crushed, and I-94 industrial crushed RCA had different gradations, for purposes of comparison of plastic and strength properties of concrete, concrete for testing RCA was made with an equal amount of each supplementary coarse and fine aggregate based on weight. The amounts of supplementary fine and coarse aggregates were established by adjusting their amounts around an arbitrary, assumed RCA gradation so that the total gradation would fit within gradation limits established by the SHRP 2 R21 project specifications.

Two steps that are sometimes required to prepare RCA for use in concrete that are not required of conventional coarse aggregate are washing the aggregate after crushing to remove the fracture dust and presoaking the RCA. All RCA used in mix design development and the R21 construction was washed. One-half batch of concrete was produced with presoaked I-94 lab crushed RCA to compare plastic properties and strength. All other RCA was used in an air-dry condition.

Eliminating the fine fraction of RCA that is used in concrete is a common practice. However, there is not a consensus on the necessity of washing coarse aggregates before using them in concrete. Fine particles increase cohesion among cement and fine aggregate particles, which influences the ability of the cement paste to cling to itself and the aggregates (Hansen and Narud 1983).

Cuperus and Boone (2003) indicate that for RCA to be used in concrete, the RCA must be washed. Another study concluded that washing RCA increased the strength and permeability, while having no effect on the drying shrinkage (Yanagi 1992). ASTM C33 allows for 1.5% of the coarse aggregate fraction to be smaller than the No. 200 sieve with exceptions that could apply to coarse RCA. Technically, this implies that some coarse RCA could be used without washing. Ultimately, the decision to wash or not to wash will be decided by the impact that the residual fines have on the workability of the concrete.

The RCA attached mortar causes a high and varied absorption capacity (Schulz 1994). The high absorption also increases the water demand. It is often suggested that one way to mitigate the effect of RCA on a concrete's water demand in concrete is to presoak the RCA to accommodate the RCA's absorption (Schulz 1994; Hansen 1986). In addition, testing the RCA's moisture content before mixing and averaging the absorption of multiple RCA samples are other ways to manage water in concrete made with RCA. A recent study used presoaked RCA and accounted for additional water by simply subtracting the known RCA SSD mass (Fathifazl 2008).

Making Concrete with RCA

Concrete made with the limestone, I-94 laboratory crushed, and I-94 industrial crushed RCA were made according to ASTM C192. In addition to the type of RCA, the quantity of all other mix constituents—cement, fly ash, supplementary fine and coarse aggregates—was held constant. Water was varied based on the moisture and absorption of all aggregate in the mix to hold the free-water-to-cementitious ratio relatively constant (0.36 to 0.38). The air entrainment admixture was varied with subsequent batches to meet the 6.5% air content.

The workability of the plastic concrete was measured by the slump test according to ASTM C143 and by its cohesiveness, which was measured by inspection. To test cohesion, a palm size portion of concrete was moved in a circular pattern to observe if concrete forms a ball or spreads. The more the concrete clings to itself, allowing a ball to form, the higher the cohesion. The air content of the plastic concrete was measured according to ASTM C231. Two 8- × 4-in. cylinder specimens were made for compressive strength tests at 3, 7, and 28 days and cured in a water bath. The presoaked I-94 laboratory had no 3-day specimens.

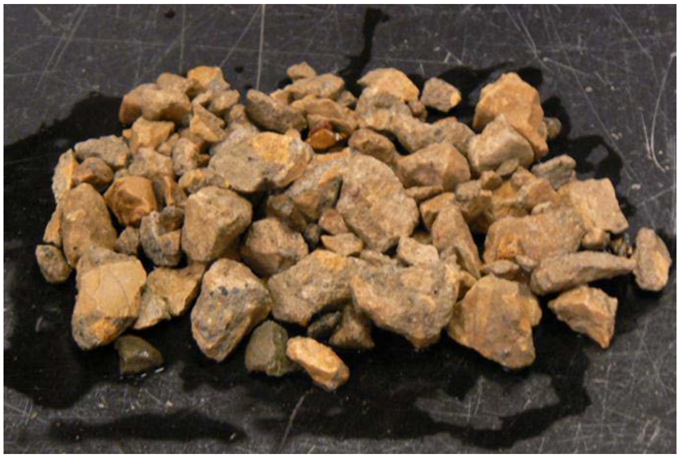

Figure T.6. Limestone industrial crushed RCA wetted to distinguish natural aggregate from residual mortar.

Laboratory Results

A sample of the limestone RCA is shown in Figure T.6. The sample was wetted for the picture to show the contrasting colors of the natural aggregate and the residual mortar.

Some of the RCA particles resembled the natural limestone aggregate particles whereas other RCA particles had the appearance of natural limestone aggregate covered with residual mortar. In addition, some of the RCA particles appeared to be comprised primarily of mortar embedded with fractured pieces of limestone.

A sample of the I-94 laboratory crushed RCA is shown in Figure T.7. The sample was wetted for the picture to show the contrasting colors of the natural aggregate and the residual mortar. The RCA does not resemble the original gravel coarse aggregate. Instead, the RCA appears as mortar embedded with fractured natural gravel aggregate. Visually, it appears as though

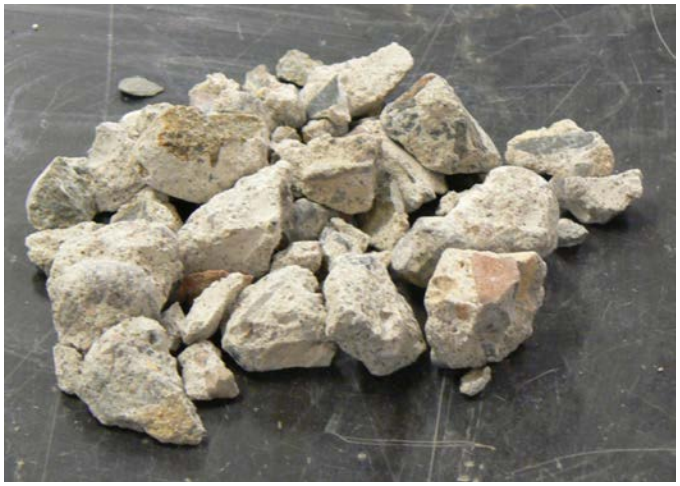

Figure T.7. I-94 laboratory-crushed RCA.

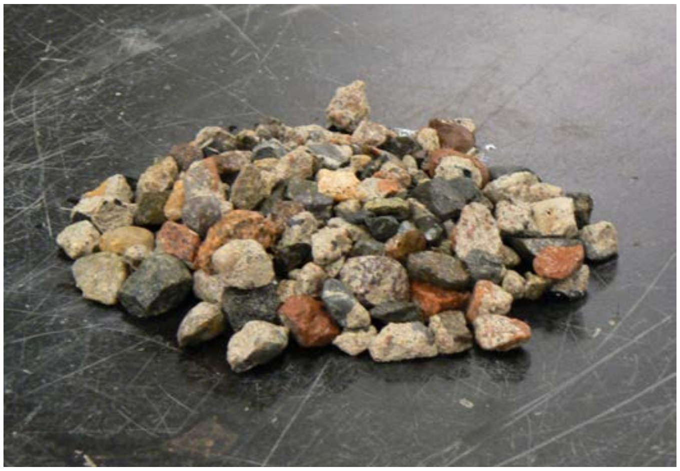

Figure T.8. I-94 industrial crushed RCA wetted to distinguish natural aggregate from residual mortar.

this RCA retained much of its mortar as compared with the other RCAs. A sample of the I-94 industrial crushed RCA is shown in Figure T.8. The sample was wetted for the picture to show the contrasting colors of the natural aggregate and the residual mortar. Most of the RCA particles consisted of the original aggregate with or without some residual mortar attached. In general, there were few particles that consisted primarily of mortar with embedded fractured aggregate as described for the other two samples.

Table T.3. RCA Oven Dry Unit Weight, Absorption Capacity, and Bulk SSD Specific Gravity

	Limestone Industrial	I-94 Laboratory	I-94 Industrial
Oven dry unit weight lb/yd^3 (kg/m^3)	2,492 (1,500)	2,257 (1,359)	2,419 (1,456)
Absorption capacity	4.03%	3.18%	3.02%
Bulk SSD specific gravity	2.38	2.54	2.55

RCA Unit Weight, Absorption, and Specific Gravity

The oven dry unit weight, absorption capacity, and bulk saturated surface dry (SSD) specific gravity of the RCAs are recorded in Table T.3. The values shown are an average of four trials.

RCA Gradation

Figure T.9 shows the gradations of the limestone, I-94 laboratory crushed, and I-94 industrial crushed RCA after particles smaller than No. 4 have been removed. The gradations highlight that the two industrial crushed RCAs had similar gradations and that the I-94 laboratory-crushed RCA

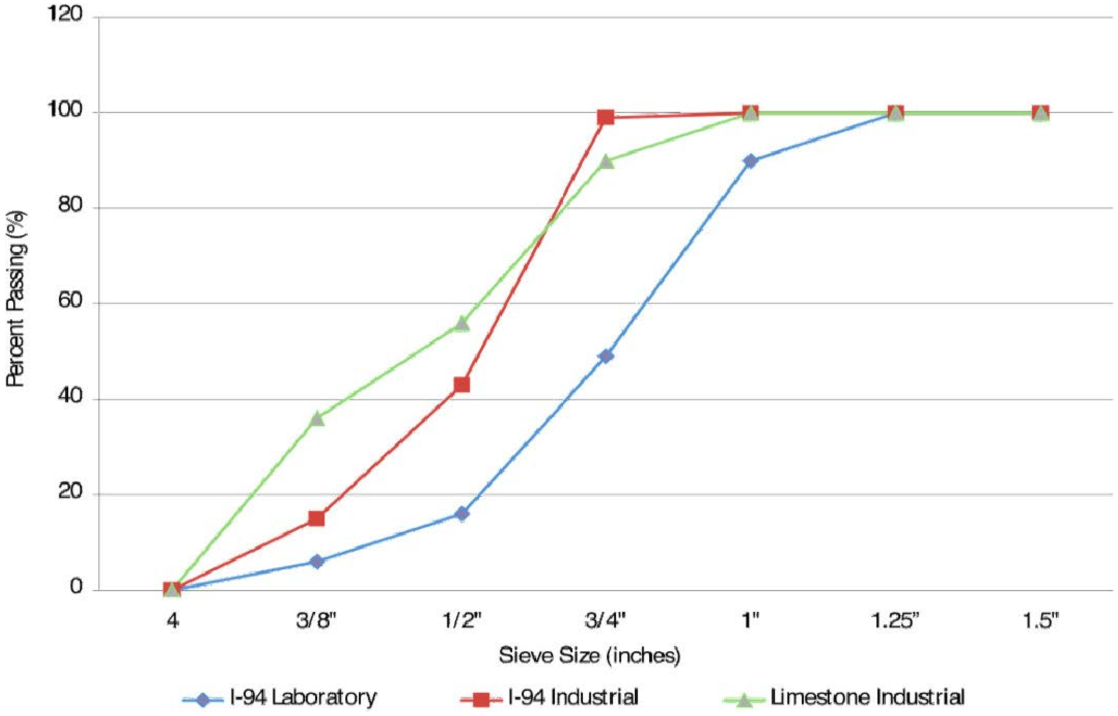

Figure T.9. Percent passing gradation of washed recycled coarse aggregate after particles smaller than No. 4 removed.

Table T.4. Cohesiveness, Slump, Air, and Unit Weight of Plastic Concrete Made with Limestone Industrial Crushed, I-94 Laboratory Crushed, and I-94 Industrial Crushed RCA

	Limestone Industrial Crushed, psi (MPa)	I-94 Laboratory Crushed, psi (MPa)	I-94 Laboratory Presoaked, psi (MPa)	I-94 Industrial Crushed RCA, psi (MPa)
Cohesiveness	Weak	None	Moderate	Weak
Slump, in. (mm)	9.0 (228)	10.25 (260)	6.5 (165)	8.0 (230)
Air content (%)	4.9	4.6	3.7	8.0
Unit weight lb/yd^3 (kg/m^3)	3,925 (2,364)	3,804 (2,291)	3,868 (2,330)	NA

Table T.5. Strength of Limestone Industrial Crushed, I-94 Laboratory Crushed, and I-94 Industrial Crushed RCA

Age (day)	Limestone Industrial Crushed, psi (MPa)	I-94 Laboratory Crushed, psi (MPa)	I-94 Laboratory Presoaked, psi (MPa)	I-94 Industrial Crushed RCA, psi (MPa)
3	1,134 (7.82)	1,290 (8.89)	na	1,155 (7.96)
7	1,644 (11.33)	1,744 (12.02)	1,375 (9.48)	1,235 (8.52)
28	2,982 (20.56)	2,517 (17.35)	2,566	2,050 (14.13)

gradation included a large percentage of particles in the ½- to 1-in. (12.5- to 25-mm) range.

Plastic RCA Concrete Properties

The plastic properties, including cohesiveness, slump, air content, and unit weight, measured for the concretes made with limestone industrial crushed, I-94 laboratory crushed, and I-94 industrial crushed RCA are shown Table T.4.

Compressive Strengths of RCA Concrete

The 3-, 7-, and 28-day compressive strengths of concrete made with limestone industrial crushed, I-94 laboratory crushed, and I-94 industrial crushed RCA are shown in Table T.5. In addition, compressive strengths are shown for concrete that was made with presoaked I-94 laboratory-crushed RCA. The compressive strengths listed are an average of two samples.

APPENDIX U

Freeze-Thaw Durability Testing of PCC Mixes

Introduction

There are high standards for portland cement concrete (PCC) mixture constituents that are used for PCC pavements because most pavements are expected to withstand physical and environmental loads for 30 years or more without needing substantial maintenance. Although the composite pavement itself provides the structural integrity to resist environmental and traffic loading, much of the durability of PCC pavements relies on the wear and tear of the upper lift surface concrete.

The SHRP 2 R21 project explored the concept of PCC/PCC composite pavement through material investigation, mechanical modeling, and two full-scale, instrumented pavement test sections built at the Minnesota Road Research Center in 2010. PCC/PCC composite pavement is designed with a thin (2- to 3-in.) upper layer of high cementitious content and durable aggregate concrete over a thicker (6- to 9-in.) layer of concrete that has at least 4,000 psi compressive strength but does not need to meet the durability requirements of a typical pavement concrete, which relaxes some of the standards and potentially reduces the cost of the pavement. Some possible cost reductions are the replacement of cement with supplementary cementitious materials, such as fly ash or limestone, the replacement of coarse aggregate with aggregate that does not meet standards for conventional concrete pavement or replacement of some of the coarse aggregate with recycled concrete aggregate (RCA).

Despite a relaxation in constituent standards, it is still important for the lower layer pavement concrete to be freeze-thaw durable because the surface concrete layer will act as an insulator in reducing temperature extremes but will not prevent the lower layer from experiencing regular freeze-thaw cycles. To test the freeze-thaw durability of the proposed concrete mixtures, the SHRP 2 R21 project chose to implement the RILEM CIF concrete freeze-thaw standard (Setzer 1997; Auberg 2002) instead of the ASTM C666 A and ASTM C672 standards. RILEM is an international union of laboratories and experts in construction materials, systems, and structures. The CIF test evaluates the capillary suction, surface scaling resistance, and internal damage, of concrete samples exposed to 3% by volume sodium chloride solution, whereas ASTM C666 A evaluates concrete submerged in water for internal damage caused by rapid freeze-thaw cycles, and ASTM C672 evaluates the scaling resistance of concrete exposed to 4% sodium chloride solution and freeze-thaw cycles. The main goals of this appendix are to describe the differences between the RILEM and ASTM standards and to report on RILEM CIF testing conducted as a part of SHRP 2 R21. Furthermore, this appendix will briefly investigate the importance of prescribing the test liquid as 3% sodium chloride solution (as in RILEM CIF and ASTM C672) versus pure water (as in ASTM C666 A).

RILEM and ASTM Freeze-Thaw Standards

The decision to use the RILEM CIF freeze-thaw standard rather than the ASTM C666 A and C672 standards was made because the SHRP 2 R21 research team collaborated with consultants from Europe who preferred the RILEM CIF standard.

Comparison of RILEM and ASTM Standards

Table U.1 compares the RILEM CIF test to the ASTM C666 A and ASTM C672 standards.

Explanation of RILEM CIF Measurements

The RILEM CIF freeze-thaw test assesses the freeze-thaw resistance of concrete subjected to 3% sodium chloride solution by measuring

- Capillary suction both during a 7-day preconditioning phase and during freeze/thaw cycles;

Table U.1. Comparison of the RILEM CIF Freeze-Thaw Test to the ASTM C666 A and ASTM C672 Standards

Parameter	ASTM C666 A	ASTM C672	RILEM 176 CIF
Typical sample size	3 × 4 × 16 in. (76 × 102 × 406 mm)	Surface Area (SA) >72 in^2 (0.045 m^2) Depth >3 in. (75 mm)	2.75 × 4.33 × 5.9 in (70 × 110 × 150 mm)
Days curing before freeze/thaw cycles	14	28	35
Curing environment	• 1 day covered in mold • 14 days lime water storage 23°C ± 2°	• 1 day covered in mold • 14 days moist storage 23°C ± 2°C/95% relative humidity (RH) • 14 days dry storage at 23°C ± 2°C/45%–55% RH	• 1 day covered in mold • 7 days tap water 20°C ± 2°C • 21 days dry storage 20°C/65% RH • 7 days capillary suction 20°C ± 2°C
Sample preparation	None	After bleeding, test surface is finished with a wood strike-off board followed by brushing with a medium-stiff brush Build a 25-mm (1-in.) wide × 20 mm (¾-in.) high dike around perimeter of test surface	Sides are sealed with an epoxy resin or aluminum foil with butyl rubber
Separation distance from bottom of sample container	3 mm (0.1181 in.)	None	5 mm (0.1969 in.)
Freezing and thawing medium in contact with sample surface	Water	4% sodium chloride and water solution by volume	3% sodium chloride and water solution by volume
Depth of sample immersed in liquid	1–3 mm (0.0394 to 0.1181 in.)	6 mm (¼ in.)	5 mm (0.1969 in.)
Cycle time	2–5 h	22–26 h	12 h
Time spent at the lowest temperature during each cycle	10 minutes	16–18 h	3 h
Maximum number of cycles	300	25–50	28 or 56
Failure criteria	Relative dynamic modulus reaches 60% of initial modulus or >0.10% length change	None specifically stated in standard	Relative modulus reaches 80% of the initial modulus at 56 cycles Mass of scaled material >1,500 g/m^2 after 56 cycles
Measurements	Transverse frequency to determine the relative dynamic modulus of elasticity and durability factor	Visual rating from 0 = no scaling to 5 = severe scaling (coarse aggregate visible over entire surface)	Moisture uptake by capillary pores Mass of scaled material Transit time through specimens (ultrasonic pulse velocity)

- Surface scaling through measurement of the mass of scaled-off particles; and
- Internal damage through nondestructive ultrasonic pulse velocity measurements.

The following paragraphs give a brief overview of why each of these measurements is important for predicting the freeze-thaw durability of concrete.

Capillary Suction

Capillary pore size is especially relevant to the freeze-thaw durability of concrete. There is not an equivalent ASTM standard that measures capillary suction as a means for evaluating the freeze-thaw durability of concrete. Capillary pores are the remnants of the space occupied by water that surrounded the cement grains in plastic concrete (Pigeon and Pleau 1995; Mindess et al. 2002). The size of the capillary pores is controlled by both the water/cement (w/c) ratio of concrete and the degree of hydration of a concrete paste (Pigeon and Pleau 1995). As the w/c ratio is reduced, there is less available water to surround cement particles, which results in smaller capillary pores. Similarly, as the percent of cement volume that hydrates increases, the size of the capillary pore decreases.

For the CIF test, capillary suction, measured by the increase in mass of the specimen, is used as an indicator of the size and volume of capillary pores in the concrete paste. The size of capillary pores in concrete affects the freeze-thaw durability of concrete because the smaller the ore, the colder it must be for the water inside of the pore to freeze. As shown in Pigeon and Pleau 1995, the water in a capillary pore that is 10 nm in diameter will freeze at −20°C, whereas the water in a capillary pore that is 40 nm in diameter will freeze at a temperature just below the freezing point of 0°C (Pigeon and Pleau 1995). Furthermore, as the average capillary pore size and pore volume decrease, there is less continuity of the pore system, which protects the concrete as water uptake increases during freezing and thawing cycles and is redistributed to smaller capillaries and gel pores (Setzer 2009). Finally, pore size is significant for freeze-thaw durability of concrete because as the volume and size of capillary pore structure increases, more of the paste is saturated and concrete paste must be saturated to be susceptible to freeze-thaw distress (Setzer 2009).

Deicing Salt Scaling

Scaling is one of two major distresses observed in concrete that has been subjected to freezing and thawing. Scaling is typically a concrete surface phenomenon that affects only the top 1 to 4 mm of concrete. Concrete that is distressed by salt scaling becomes rough and pitted from spalling of small pieces of mortar.

While deicing salt application to concrete receives a majority of the blame for scaling, experimental evidence suggests that most scaling is the result of an inadequate quantity and spacing of entrained air bubbles in the surface concrete and on over finishing the concrete's surface, which effectively increases the w/c ratio of the surface concrete. An increased w/c ratio effectively decreases the concrete's strength and increases the size and volume of its capillary pores (Jana 2004). However, even if a surface concrete has been sufficiently air entrained and finished, the presence of deicing salt has the potential to cause scaling, and the CIF test assesses this effect. The primary mechanisms of salt scaling have been theorized (Mindess et al. 2002):

- Salt solutions have a lower vapor pressure than pure water, so there is a lower rate of evaporation and a higher degree of saturation.
- Salt consumes heat and causes a rapid decrease in temperature at the concrete surface. This may cause damage because of the rapid freezing or stress caused by differential thermal strains.
- The addition of salt to an alkaline pore solution will increase the effects of osmotic pressure.

Internal Damage

Internal damage caused by cracking is the second of two major distresses observed in concrete that has been subjected to freezing and thawing. Internal damage of the concrete specimens can be attributed to the many mechanisms of frost action within the bulk matrix of concrete. More information on the frost action mechanisms in concrete can be found in (Pigeon and Pleau 1995). Once critical saturation of the concrete sample's capillary pore system is reached, internal cracking begins as concrete is subjected to freezing and thawing cycles (Heine and Setzer 2002).

Methodology

This study, which evaluates SHRP 2 R21 composite concrete pavement concrete, had two experimental goals. The first goal was to develop a better understanding of the concretes' durability. Because the ASTM and RILEM freeze-thaw standards were to be compared, it was decided to investigate the influence of the test liquid on the samples during freeze-thaw cycles as a second goal. This goal was accomplished by using both pure water and 3% sodium chloride solution while following the RILEM CIF standard. The use of pure water deviates from the RILEM standard, which prescribes using a 3% sodium chloride solution. In the remainder of this appendix, the concrete samples that are labeled as "field" samples were tested in pure water and the samples that are labeled as "lab" samples were tested in 3% sodium chloride solution.

The following sections describe the mixture designs for the SHRP 2 R21 concretes and some of their field and hardened properties and the RILEM sample preparation requirements. There is also an overview of the RILEM CIF test procedures.

SHRP 2 R21 Concretes

For the SHRP 2 R21 project, three new concrete mixtures were developed. These mixtures included a high cementitious content, granite aggregate mixture for an exposed aggregate concrete (EAC) upper layer and two lower cost concretes for the lower layer. In one of the lower layer concretes, 50% of the course aggregates were replaced with coarse RCA that came from crushing the existing concrete pavement that the SHRP 2 R21 composite pavement construction replaced. In the other lower layer concrete, 60% of the cementitious content was replaced with fly ash. This high fly ash replacement concrete is referred to as low cost (LC) in the remainder of the study. Also included in a part of this study was a control concrete mixture that was modeled after a standard Minnesota Department of Transportation (MnDOT) concrete pavement mixture. Table U.2 shows the concrete mixture constituents for the RCA, LC, EAC, and control concretes.

Table U.3 shows some of the plastic and hardened properties of both the field and laboratory concrete samples. The plastic properties include slump, air, and unit weight, which were measured according to ASTM Standards C143, C138,

Table U.2. Concrete Mixture Compositions of the RCA, LC, EAC, and Control Concretes

	RCA	LC	EAC	Control
Type 1/2 cement (lb/yd^3)	360	240	616	420
Class C/Class F fly ash (lb/yd^3)	240	360	109	140
Coarse aggregate (lb/yd^3)	1,745	1,889	1,976	1,860
Fine aggregate (lb/yd^3)	1,200	1,263	843	1,255
Water (lb/yd^3)	234	173	283	224
Accelerator (oz/yd^3)	180 (48)	180	0	0
Water reducer (oz/yd^3)	10 (18)	6 (30)	14.5 (18)	17
Air entrainer (oz/yd^3)	2.8 (6)	6.5 (8)	10.5 (6)	4
Target w/c ratio	0.39	0.29	0.39	0.4

Note: Numbers in parentheses indicate quantity of admixtures in field samples.

and C231, respectively. The hardened properties include the 7-day and 28-day compressive strengths, which are an average of two cylinders (4 × 8 in.) tested according to ASTM C39.

RILEM Sample Preparation

The freeze-thaw machine used to control the temperature and environment for the CIF test has a 10-sample capacity, and the CIF test procedure recommends that five samples of each concrete mixture be tested at a time. The first round of concrete samples tested by the RILEM CIF standard consisted of five RCA and five EAC samples. These samples were made from concrete collected from concrete trucks delivering concrete for construction of SHRP 2 R21 composite pavements. The RCA samples were molded into three 150-mm cubes, and the EAC sample was molded into a 152- × 152- × 610-mm beam. The concrete samples were consolidated on a vibrating table and allowed to cure for 24 hours next to the new pavement. After 24 hours, the samples were transported to the laboratory and stored in the environment prescribed for the CIF test.

The second round of concrete samples tested by the RILEM CIF standard consisted of one control, three RCA, three LC, and three EAC samples. These samples were made from concrete produced in the laboratory with the same materials, admixtures, and concrete mixture designs that were used to build the composite pavements. The EAC, RCA, and control samples were molded in 150-mm cubes, and the EAC sample was molded into a 152- × 152- × 610-mm beam. The samples were consolidated by rodding the concrete in three lifts and were cured according the CIF test.

The targeted sample size for the CIF test is 150- × 110- × 50-mm (±2 mm in each dimension). All concrete samples were cut to this size with a diamond blade wet saw. The average length and width and the mass of all samples without foil are listed on Table U.4. The test surface of each sample was designated as one of the cut surfaces. Two of the samples were 1 mm outside of RILEM's allowable deviance for specimen dimensions. However, it was necessary to use these samples because there were no available materials to recast specimens.

In accordance with the CIF test procedures, 3 days before the beginning of the presaturation phase, the side surfaces of

Table U.3. Plastic and Hardened Properties of Field and Laboratory Samples

	Field RCA	Field EAC	Lab RCA	Lab LC	Lab EAC	Lab Control
Plastic properties						
Slump (in.)	1.75	2.25	4.5	2	1	4.75
Air (%)	6.5	4.5	7.5	6.2	4.7	8
Unit weight (lb/ft^3)	145	145	140	140	151	141
Hardened properties						
7-day compression strength (psi)	3,599	5,314	1,738	2,950	3,836	1,769
28-day compression strength (psi)	4,305	5,855	2,365	4,185	4,404	2,294

Table U.4. Average Length of the Concrete Samples' Short and Long Sides and the Mass of the Concrete Samples Without Foil Before the Capillary Suction Phase

Concrete Sample	Average Short Side Length (mm)	Average Long Side Length (mm)	Sample Mass without Foil (g)
Field samples			
RCA 1f	108	150	2,640.0
RCA 2f	108	151	2,680.0
RCA 3f	108	152	2,620.0
RCA 4f	109	152	2,650.0
RCA 5f	109	151	2,670.0
EAC 1f	109	150	2,635.0
EAC 2f	109	150	2,720.0
EAC 3f	107	150	2,600.0
EAC 4f	108	150	2,685.0
EAC 5f	110	150	2,655.0
Laboratory samples			
RCA 1	112	149	2,479.4
RCA 2	109	151	2,500.0
RCA 3	108	155	2,461.3
LC 1	110	152	2,823.3
LC 2	110	152	2,796.9
LC 3	108	152	2,838.4
EAC 1	111	150	2,551.0
EAC 2	114	147	2,527.2
EAC 3	112	148	2,522.2
Control	110	150	2,574.7

each sample were wrapped with aluminum foil with a butyl rubber backing.

RILEM Test Procedure

This section will highlight some of the important steps of the CIF standard. Repeatable instructions can be found in the RILEM CIF standard (Setzer 2009).

Capillary Suction

The CIF test considers capillary pore water uptake in two stages. The first stage, or preconditioning stage, was designed to mimic field saturation conditions (Setzer 1997). Beginning with the preconditioning phase and continuing through the freeze-thaw cycles, the test surface of each sample is submerged in 3% sodium chloride solution to a depth of 5 mm. The preconditioning stage lasts 7 days and follows 21 days of drying at 65% relative humidity. During the preconditioning stage, samples are kept at 20°C. The second stage of capillary suction begins with the freeze-thaw cycles. During the freeze-thaw cycles, the samples' uptake of water increases as water redistributes to smaller capillary pores and gel pores within the concrete matrix. The reader is reminded that the test surfaces of the field RCA and EAC samples were submerged in pure water, rather than 3% sodium chloride solution.

Deicing Salt Scaling

For the CIF test, salt-scaling susceptibility of concrete samples is assessed by collecting, drying, and weighing the scaled material at regular freeze-thaw intervals. The RILEM CIF method suggests that a concrete is resistant to salt scaling if it has a cumulative mass of scaled material less than 1,500 g/m^2 after 56 freeze-thaw cycles. To observe the scaling resistance of the field and laboratory SHRP 2 R21 concrete mixtures, the number of freeze-thaw cycles was extended to 106 for the field samples and 98 for the laboratory samples.

Internal Damage

The CIF test nondestructively measures internal damage by measuring the ultrasonic pulse velocity (UPV) through the specimen at regular freeze-thaw cycle intervals. Figure U.1 shows the UPV test setup with one of the CIF test concrete samples. The sensors on either side of the sample are connected to a UPV reader.

The UPV time measurements are converted into a value that is called the relative modulus of elasticity of ultrasonic transit time and is reported as a percentage of the modulus before the sample was subjected to freezing and thawing. RILEM requires the use of Equations U.1 through U.3 to determine the relative modulus for each concrete specimen:

$$tc = \frac{lc}{vc} \tag{U.1}$$

where

tc = transit time in coupling,
lc = transit length in coupling medium (for calibration sample = 15 mm), and
vc = velocity of ultrasonic signal in coupling medium, which can be assumed to be water.

$$\tau_n = \frac{tcs - tc}{tn - tc} \tag{U.2}$$

where

τ_n = relative transit time,
tcs = total transit time at end of capillary suction (in milliseconds) before the first freeze-thaw cycle, and
tn = total transit time after n freeze-thaw cycles.

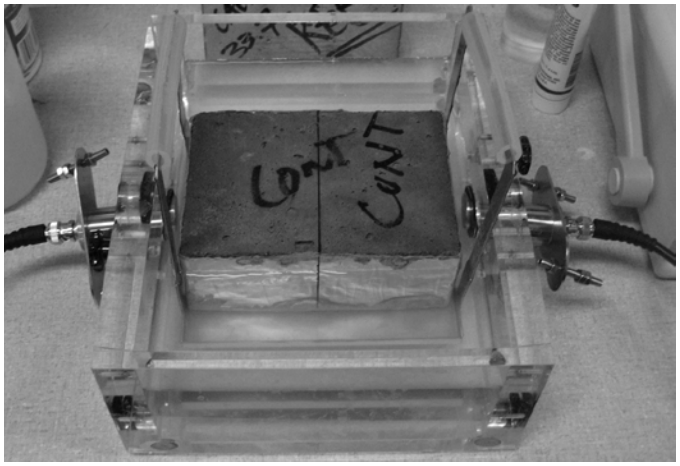

Figure U.1. Concrete sample in UPV test setup.

$$R_{u,n} = \tau_n^2 \tag{U.3}$$

where

$R_{u,n}$ = relative modulus of elasticity of ultrasonic transit time.

The sample is considered not freeze-thaw durable if its relative modulus decreases below 80% before 56 complete freeze-thaw cycles. The fall of the modulus is an indicator of internal cracking, and internal cracking results in the reduction of the sample's tensile strength, which is of particular importance to pavements (Auberg 2002). Compressive strength also decreases as internal cracking becomes more severe but not as dramatically as the tensile strength.

Results and Discussion

The RILEM CIF standard has three primary measures of freeze-thaw durability. They are (1) capillary suction, (2) deicing salt scaling, and (3) internal damage.

The following sections present the response of the SHRP 2 R21 concrete samples to the RILEM CIF test in the presence of both pure water and 3% sodium chloride solution.

Capillary Suction

Figure U.2 shows the mass of water or solution absorbed per unit sample area during the capillary suction period (cycle 0) and during freeze-thaw cycles. The test surfaces of the field RCA and EAC samples were submerged in pure water, and the test surfaces of the laboratory RCA, LC, EAC, and control samples were submerged in 3% sodium chloride solution. The dotted line on Figure U.2 indicates the moisture uptake of the concrete samples at 56 freeze-thaw cycles.

Table U.5 and Table U.6 show the mean and standard deviations of mass increase after the capillary suction phase and before freeze-thaw cycles began (0), at the critical freeze-thaw cycle (56), and at the end of the test. There were 106 cycles for the field samples and 98 cycles for the laboratory samples.

During the 7-day preconditioning period, the field RCA and EAC samples averaged a 0.49% mass gain because of capillary suction of pure water. Comparatively, the laboratory RCA and EAC samples averaged mass gains of 1.58% and 1.03%, respectively, because of capillary suction of 3% sodium chloride solution. After the preconditioning period and during the freeze-thaw cycles, the rate of mass increase was approximately equal for all field and laboratory samples. At approximately 30 freeze-thaw cycles, the rate of mass increase for all field and laboratory samples decreased to almost zero.

At first glance, it seems that the disparity in the initial uptake of test liquid between the field and laboratory samples is a function of the test liquid—pure water for the field samples and 3% sodium chloride solution for the lab samples.

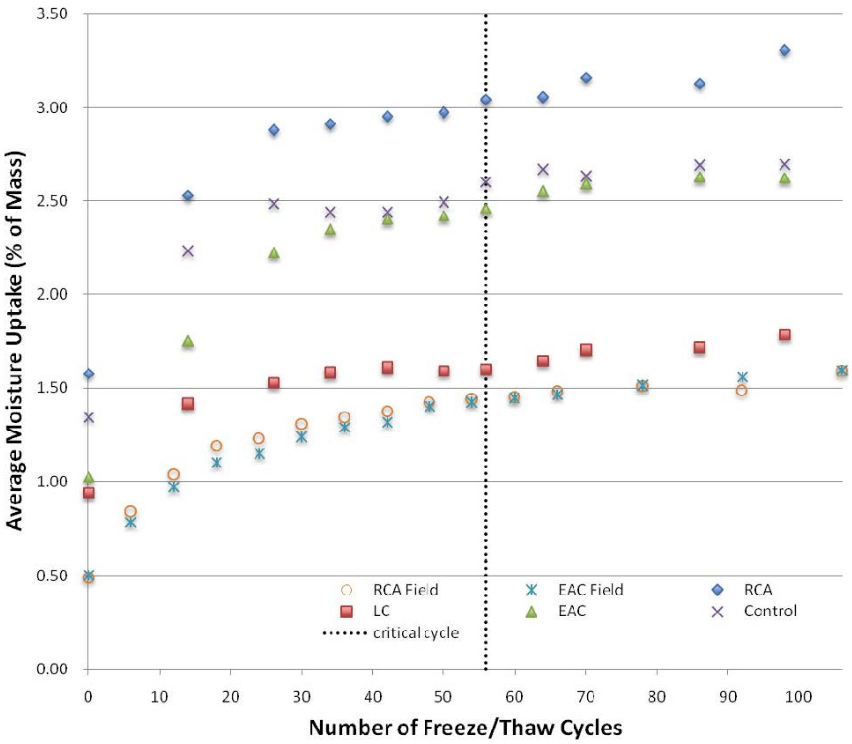

Figure U.2. Field and laboratory sample average moisture uptake as a percentage of sample mass during freeze-thaw cycles.

Table U.5. Field Sample Relative Increase in Mass Mean and Standard Deviation

Cycle	Field RCA Mean Mass Increase (%)	Field RCA SD Mass Increase (%)	Field EAC Mean Mass Increase (%)	Field EAC SD Mass Increase (%)
0	0.49	0.0012	0.50	0.001
66	1.48	0.0016	1.47	0.0016
106	1.59	0.0024	1.60	0.0022

Note: SD = standard deviation.

Table U.6. Laboratory Sample Relative Increase in Mass Mean and Standard Deviation

Cycle	Laboratory Mean RCA Mass Increase (%)	RCA SD Mass Increase (%)	Laboratory Mean LC Mass Increase (%)	LC SD Mass Increase (%)	Laboratory Mean EAC Mass Increase (%)	EAC SD Mass Increase (%)	Laboratory Mean Control Mass Increase (%)	Control SD Mass Increase (%)
0	1.58	0.17	0.94	0.07	1.03	0.16	1.34	na
64	3.06	0.20	1.65	0.11	2.55	0.06	2.67	na
98	3.31	0.18	1.78	0.06	2.63	0.07	2.70	na

However, consideration of the compressive strengths (Table U.3) and the delineation of moisture uptake between the field and the laboratory samples (Figure U.2) suggest that the disparity in moisture uptake has more to do with the samples' capillary porosity than with the test liquid. In other words, despite being made with identical mix designs and concrete constituents, the laboratory samples had a greater volume and average capillary pore size than did the field samples, as evidenced by the lower 7- and 28-day strengths. The average RCA lab sample 28-day compressive strength was 50% that of the average RCA field samples. Similarly, the average EAC lab sample 28-day compressive strength was 75% that of the average EAC field samples.

The reason for the strength, and thus capillary suction, disparity between the field and laboratory samples remains unknown. Two production disparities between the field and lab samples may have contributed to the disparity in moisture uptake. One production disparity was that the concrete used to make the field samples was batched at a ready-mix concrete plant and the concrete used to make the laboratory samples was batched in a 1-yd³ mixer. Second, the field samples were consolidated on a vibrating table and the lab samples were consolidated by rodding. It is interesting to note that the laboratory samples were prepared twice because the first samples failed to gain the expected strength. The compressive strength of the second batch of laboratory samples also did not gain the expected strength.

In a RILEM CIF test study of high performance concrete mixtures with w/c ratios around 0.30 and average cement contents of 742 lb/yd³, the moisture uptake was between 1.5% and 3.0% of the samples' mass (Palecki and Setzer 2002). In another study that used the CIF test on concrete samples with 0.5 w/c ratios and with between 50% and 100% coarse RCA substitution, the moisture uptake was between 3% and 4.5% (Heine and Setzer 2002). For the current study, because the moisture uptake ranged from 0.5% to 3%, it is reasonable to conclude that the water uptake by all of the field and laboratory samples was within an acceptable range.

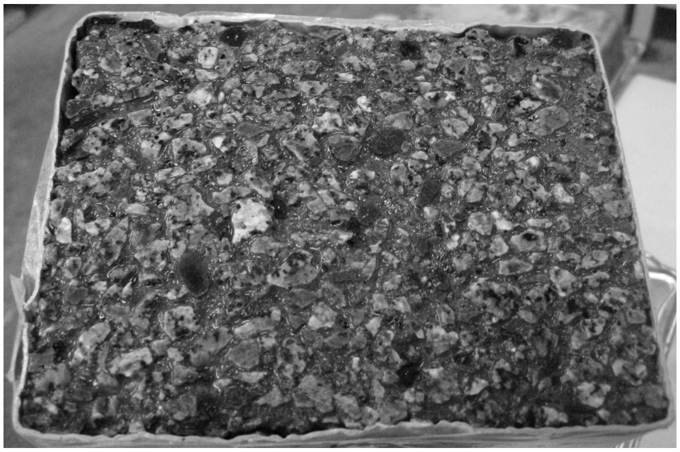

Figure U.3. Scaled test surfaces of an EAC concrete sample after 56 freeze-thaw cycles.

Deicing Salt Scaling

Figure U.3 shows the scaled test surfaces of an EAC sample after 56 freeze-thaw cycles.

Figure U.4 shows the cumulative mass of scaled material per unit area for both field and laboratory concrete samples as the number of freeze-thaw cycles increases. It is important

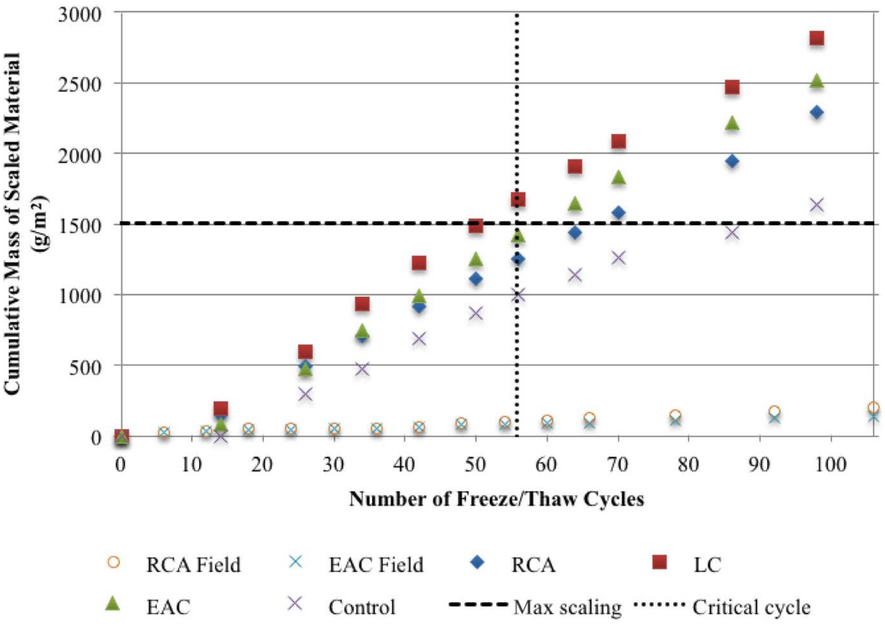

Figure U.4. Cumulative mass of scaled material per unit area subjected to freeze-thaw cycles.

Table U.7. Mean and Standard Deviation of Field Sample Scaled Material per Surface Area

Cycle	Field RCA Mean Scaled Material (g/m²)	Field RCA SD (g/m²)	Field EAC Mean Scaled Material (g/m²)	Field EAC SD (g/m²)
66	126	19	95	19
106	204	30	143	25

to reiterate here that the test surfaces of the field RCA and EAC samples were submerged in pure water and the test surfaces of the laboratory RCA, LC, EAC, and control samples were submerged in 3% sodium chloride solution. The horizontal dashed line on Figure U.4 indicates the maximum recommended scaling mass after 56 freeze-thaw cycles. The vertical dotted line indicates mass of scaled material at the 56th freeze-thaw cycle.

Table U.7 and Table U.8 show the mean value and the standard deviation of scaled material at the 56th freeze-thaw cycle and after termination of the CIF test for the field and laboratory concrete samples, respectively.

As shown by Figure U.4, all field and laboratory samples, except the lab LC sample, averaged less than 1,500 g/m^2 of scaled material at 56 freeze-thaw cycles. The lab LC sample average was 1,913 g/m^2, which is within 2 SD of the limit and thus can cautiously be accepted as adequately able to resist surface scaling.

The field RCA and EAC samples scaled significantly less than the lab RCA and EAC samples. This disparity was expected and is attributable primarily to the difference in test liquid (pure water for field samples and 3% sodium chloride solution for lab samples). The disparity was not caused by capillary suction (Palecki and Setzer 2002) and likely was not caused by a lack of entrained air in the surface concrete. The entrained air measurements of the plastic concretes were sufficient for all field and laboratory samples (between 4.5% and 8%, see Table U.3).

For the SHRP 2 R21 project, the EAC concrete was the only concrete that would have been subjected to deicing salt, and it proved to be an adequate concrete mixture for resisting deicing salt scaling.

It is interesting to note that two studies were found that compared the quantities of deicing salt scaling material produced by the RILEM CIF test and the ASTM C672 standard, but they present conflicting correlations. In one study, authors found that concretes with a higher w/c ratio produce more scaling by the CIF test than do concretes with a lower w/c ratio. Conversely, ASTM C672 causes more scaling on the low w/c ratio sample than on the high w/c ratio samples (Petersson and Utgenannt 1999). In another study, authors found that for concretes with w/c ratios of 0.45, 0.55, and 0.65 the ASTM C672 test produced approximately twice the quantity of scaled material did as the RILEM CIF test (Gondai et al. 2009).

Internal Damage

Figure U.5 shows the relative modulus of elasticity of ultrasonic transit time (relative modulus) for field and laboratory samples. The vertical dotted line indicates the relative modulus at 56 freeze-thaw cycles. The horizontal dashed line indicates the modulus below which the sample is considered distressed. Table U.9 and Table U.10 show the mean and standard deviation relative modulus values at 0, 56, and either 106 or 98 freeze-thaw cycles for the field and laboratory CIF test samples, respectively.

After 56 freeze-thaw cycles, the relative moduli of the field RCA and EAC samples were approximately 94% and 98%, respectively, indicating very little internal damage. As confirmed by the low uptake of moisture, the capillary porosity of the field samples was low and the capillaries were likely disconnected, which are indicators of a freeze-thaw damage-resistant concrete paste. In addition, these samples were adequately air entrained. CIF experiments by others have shown that internal damage is not a function of test liquid (sodium chloride solution), surface texture, or carbonation but rather depends mostly on the sample's w/c ratio and the quantity and spacing of entrained air bubbles (Heine and Setzer 2002).

Table U.8. Mean and Standard Deviation of Laboratory Sample Scaled Material per Surface Area

Cycle	Laboratory Mean RCA Scaled Material (g/m²)	RCA SD (g/m²)	Laboratory Mean LC Scaled Material (g/m²)	LC SD (g/m²)	Laboratory Mean EAC Scaled Material (g/m²)	EAC SD (g/m²)	Laboratory Mean Control Scaled Material (g/m²)	Control SD (g/m²)
64	1,438	71	1,913	225	1,651	342	1,139	na
98	2,296	251	2,816	270	2,520	348	1,642	na

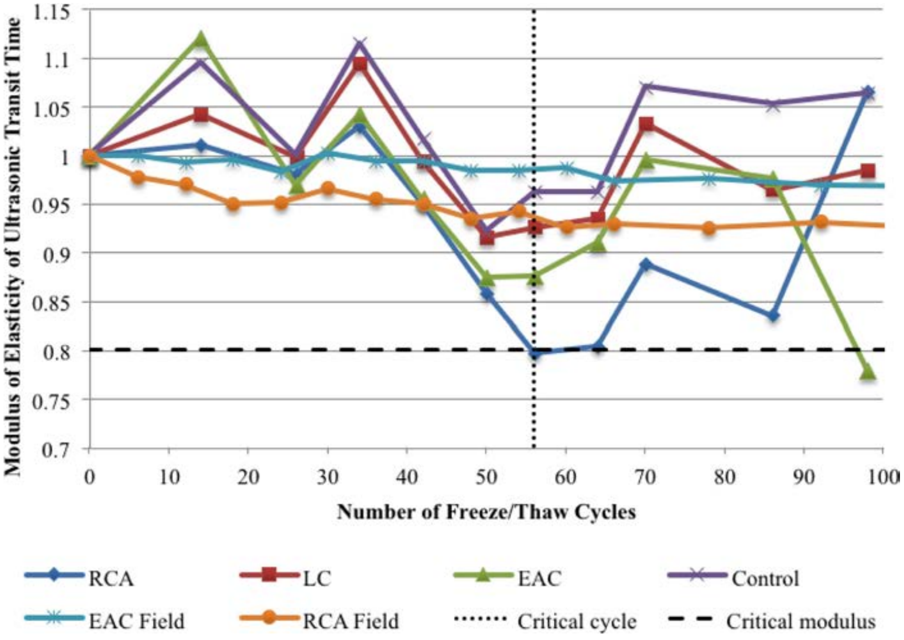

Figure U.5. Modulus of elasticity of ultrasonic pulse velocity.

As indicated by the erratic peaks and valleys of the laboratory sample modulus measurements, the data did not follow a neat downward line, and sometimes the modulus values exceeded 100%. Despite the fluctuations, the data trended toward a decreasing modulus as the number of freeze-thaw cycles increased. The relative moduli of the samples also remained at or above the 80% after 56 cycles, which indicates that the samples adequately resisted internal damage caused by frost action. As stated, it is the strength of the concrete matrix, rather than the test liquid, that influences the resistance of a sample to internal damage.

Compared with the decrease in relative modulus of other concrete samples studied with the RILEM CIF procedure, the decrease in relative moduli of all of the field and lab samples were relatively small (Heine and Setzer 2002; Palecki and Setzer 2002). The difference between the concretes used for this study and those in the referenced studies is that all of this study's samples were air entrained. One study evaluated 0.5 w/c ratio concrete without entrained air, and the relative modulus values decreased below 80% after between 10 and 30 freeze-thaw cycles (Heine and Setzer 2002). Another study showed that even in a CIF experiment that evaluated 0.3 w/c ratio and high cement content samples, only those concrete mixtures that contained entrained air were able to adequately resist internal cracking according to the RILEM CIF standard.

For the SHRP 2 R21 composite pavement project, the lack of internal damage in both the RCA and LC concrete mixtures after 56 freeze-thaw cycles indicates that these mixtures are suitable for use in long-life concrete pavements, despite containing RCA or having a 60% cement replacement with fly ash, respectively. It was expected that the EAC concrete samples would experience minimal internal damage caused by frost action because of its superior granite aggregates and high cement content paste.

Table U.9. Average Relative Modulus of Elasticity of Ultrasonic Transit Time for Field RCA and EAC Samples

Cycle	Field RCA Average $R_{u,n}$ (%)	Field RCA SD (%)	Field EAC Average $R_{u,n}$ (%)	Field EAC SD (%)
0	100	0	100	0
54	94	4	98	2
60	93	3	99	2
106	93	3	97	2

Note: The values shown represent an average from five samples.

Conclusions

A key conclusion to be taken from the testing is the value of the RILEM CIF standard. Although many of the same results could have been achieved through a combination of ASTM C666 A and C672, the SHRP 2 R21 research shows that the RILEM CIF experience is worthwhile and beneficial. Specifically, the freeze-thaw machines used for the RILEM test method provide a stable temperature cycle, the CIF method does not rely on visual ratings for assessing the freeze-thaw durability of concrete, the CIF method is especially relevant in

Table U.10. Average Relative Modulus of Elasticity of Ultrasonic Transit Time for Laboratory RCA, LC, EAC, and Control Samples

Cycle	Laboratory Average RCA $R_{u,n}$	RCA SD	Laboratory Average LC $R_{u,n}$	LC SD	Laboratory Average EAC $R_{u,n}$	EAC SD	Laboratory Average Control $R_{u,n}$	Control SD
0	100	0	100	0	100	0	100	na
56	80	17	93	2	88	3	96	na
98	84	3	98	12	78	26	106	na

cold climates where deicing salts are prevalent and cause damage to concrete, and the RILEM technical committees have been diligent about crafting a test that is repeatable.

The experience also provided several insights that may be useful to other institutions, agencies, and consultancies as they apply the standard to their own concrete materials work. Testing was continued beyond the prescribed 56 cycles, and it was found that some samples that technically failed or almost failed (reached 80% modulus after 56 cycles) recovered to a modulus of 100% in the ensuing 15 to 40 cycles. The recovered modulus could be the result of not measuring the same path through the concrete sample each time. However, there could also be a problem with repeatability of the UPV test for concretes with low w/c ratios, or self-healing of the microstructure could have occurred. These items are topics for future research in this area.

Although the experience was generally positive, there were some difficulties in the testing. The first and most glaring of these had nothing to do with RILEM but rather a dearth of materials for concrete batching. As a result of this, the testing suffered from not having enough samples for testing. The RILEM-ready test apparatus also held only 10 samples, which limited the breadth of samples that could be examined for any given round of testing. As for the RILEM standard itself, the expectation of specimen dimensions was especially demanding. Given the difficulty of obtaining materials, the R21 testing had to use two specimens that technically were outside of the RILEM specifications.

In conclusion, as PCC materials expand to include a variety of nontraditional materials, more thorough and exacting test standards for durability, such as that of RILEM CIF, will prove to be of great benefit to materials and engineering researchers in the United States. To that end, this application of RILEM CIF to pavement research proved to be very beneficial.

APPENDIX V

Brushing and Exposed Aggregate Concrete

Introduction

In preparation for the exposed aggregate concrete (EAC) brushing on MnROAD Cells 71 and 72, five experiments were performed. The purpose of the five experiments was to better understand the timing of the brushing relative to the placement of the concrete. The experiments also allowed the SHRP 2 R21 research team to develop a familiarity with the characteristics of the concrete in anticipation of brushing and construction.

Exposed Aggregate Concrete Brushing: Laboratory Experience

Test 1: Initial EAC Brush Testing

EAC concrete was made in the laboratory according to the original EAC mixture design (Table V.1). Two concrete specimens were made from this concrete, and each was treated with one of two compounds: the BASF MBT Reveal curing/retarding compound or the Sika Rugasol-S retarding compound.

Specimen dimensions were approximately 13.5 × 10 × 2.5 in. The respective compounds were sprayed onto the specimen surfaces immediately after the surfaces were finished with a wood trowel (Figure V.1 and Figure V.2). Specimens were allowed to cure in a 68°F to 72°F environment. Curing progress was observed hourly for the first 3 hours then every 2 hours thereafter (i.e., at 1, 2, 3, 5, 7 hours and so forth). At each observation, brushing readiness was evaluated by the ease with which the aggregates separated from the paste when prodded with a fork (Figure V.3).

After 7 hours, the aggregates were firmly set in the concrete matrix. At this time the concrete samples were brushed with a metal-bristled brush to simulate the rotating wire brush that was going to be used to expose aggregate in the field. The samples were brushed until there was a negligible amount of concrete powder removed by the brush. The depth to which the mortar was removed is referred to as the depth of etch.

Although the depth of etch is difficult to quantify for an entire specimen, it was generally observed to be approximately 3 to 5 mm for both specimens (Figure V.4). The depth of etch for the BASF MBT Reveal specimen was observed to be more uniform and less deep than that of the Sika Rugasol-S (Figure V.5). However, given that only one specimen was cast to examine each compound, the observed results are anecdotal. This initial brushing test provided the R21 research team with a "hands on" experience, and a feel for the EAC concrete mixture and brushing process. In addition, it was decided that MBT Reveal would be used as the curing/retarding compound in further laboratory and field experiments.

Test 2: Examining EAC Setting Time and Brushing

Attempting to more precisely target the setting time ahead of brushing, the R21 research team conducted an experiment with an adjusted quantity of air entrainer and plasticizer admixtures in the EAC mix. The concrete specimen cast for this experiment shared dimensions with the initial brushing test specimen, and only the BASF MBT Reveal was used. The additional air entrainer and plasticizer were required to achieve the desired slump and air voids of the EAC mixture, which lacked entrained air and slump in Test 1. It was suspected that the additional air and slump could have influenced the texturing, so the specimen was subjected to the procedure indicated for the initial brushing test.

Figure V.6 illustrates the curing progress at 2 hours (scratched area at far right) and 3 hours (scratched area second from right). The aggregate was unable to be pushed out of the concrete after 6 hours (Figure V.7).

Test 2 confirmed that between 6 and 7 hours the concrete had cured enough to allow brushing. When the specimen was brushed, the depth of etch of 2 to 3 mm exceeded the specifications, and the aggregate spacing appeared too large.

Table V.1. Proposed Mix Designs for MnROAD R21 EAC Layer

	Estimated Yield (CY)	Cement (lb/CY)	Fly Ash (lb/CY)	½″ Washed Granite Chips (lb/CY)	⅜″ Washed Granite Chips (lb/CY)	Elk River Mason Sand (lb/CY)	Slump (in.)	Air (%)	w/c
EACMIX (original)	1	553	98	1,774	0	1,183	1	6.5–7.0	< 0.4
EACMIX (revised)	1	616	109	1,140	850	850	1	6.5–7.0	< 0.4

Note: CY = cubic yards.

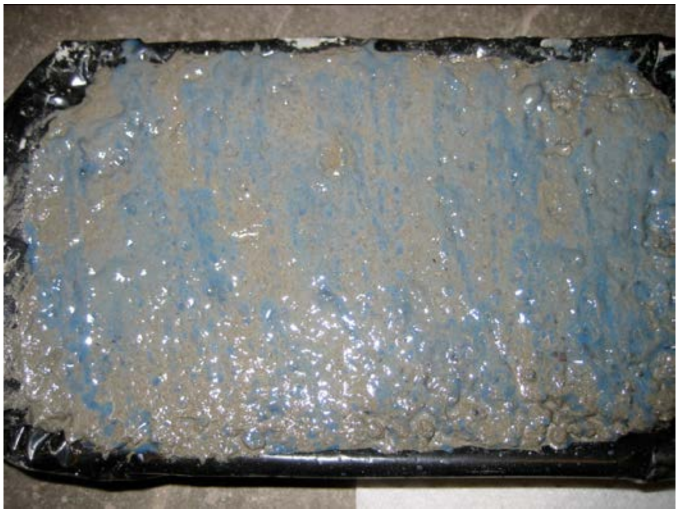

Figure V.1. Specimen with BASF MBT Reveal surface treatment.

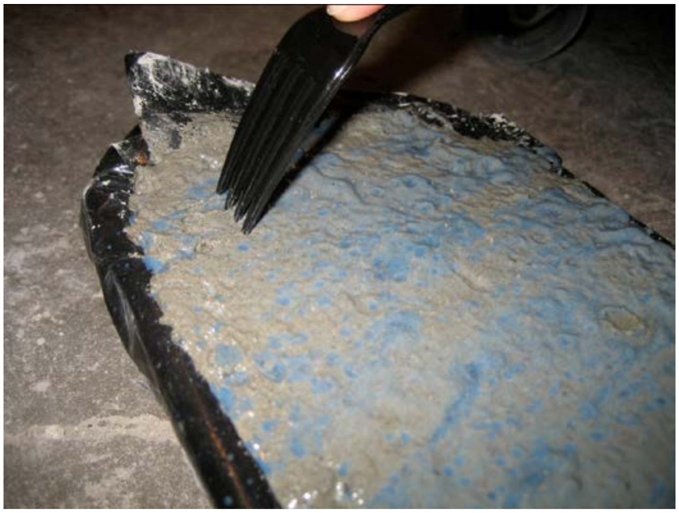

Figure V.3. Brushing readiness test at 5 hours.

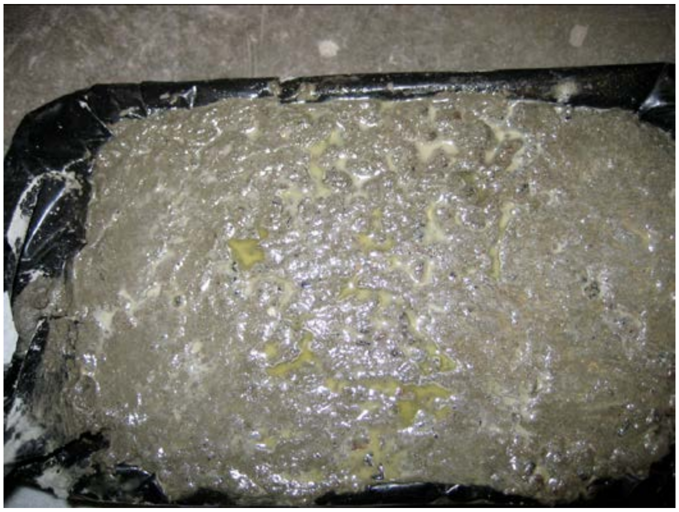

Figure V.2. Specimen with Sika Rugasol-S surface treatment.

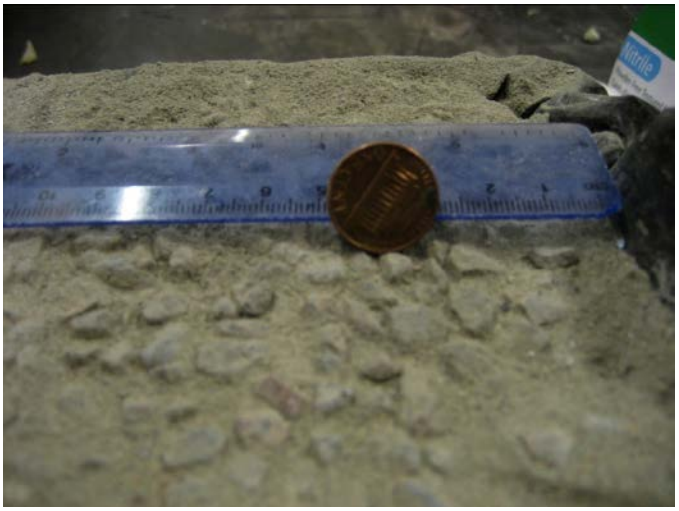

Figure V.4. Shows approximate depth of etch between 3 and 5 mm.

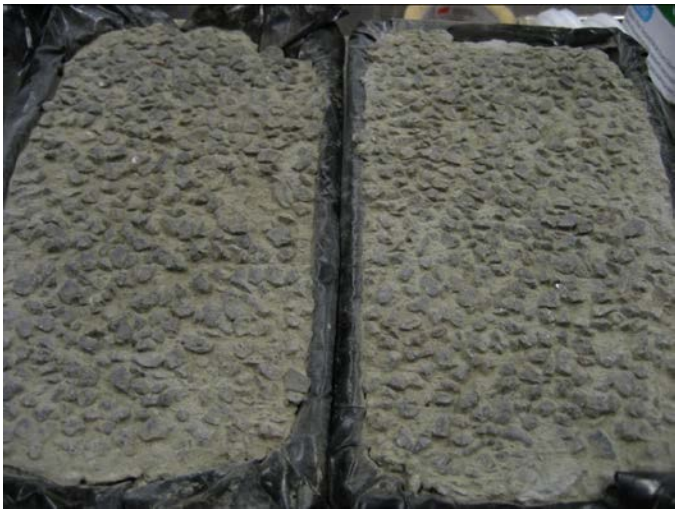

*Figure V.5. Specimens with Sika Rugasol-S (*at left*) and BASF MBT Reveal (*at right*) after brushing.*

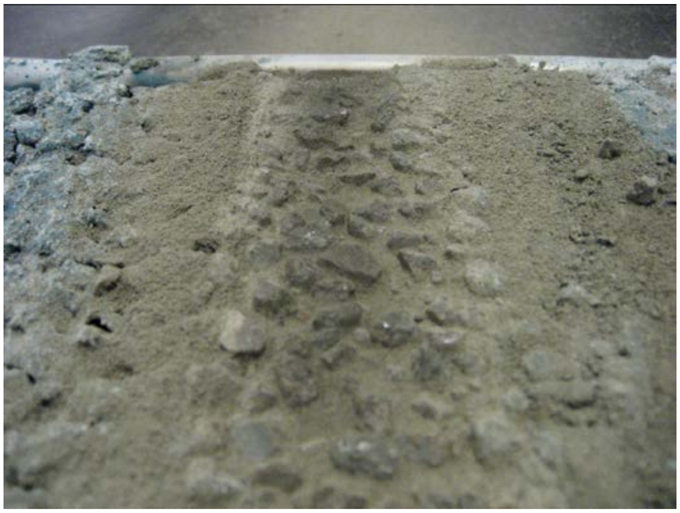

Figure V.7. At 6 hours, the mix could be brushed and aggregates exposed without dislodging from the paste.

Test 3: Batching and Brushing of Contractor Revisions to EAC Mix

After Test 2, the R21 project contractor modified the gradations of the aggregates in the EAC mix design to incorporate both ⅜-in. chip and ½-in. chip granite coarse aggregates. These revisions occurred because the contractor had difficulty with paste coverage of aggregates in the original EAC mix. Revisions are shown as EACMIX (revised) in Table V.1.

Once provided with the revised EAC mix, the research team conducted trial batching, surface treatment, and brush testing in the manners described above. Observations of the specimen were conducted according to the procedure of the original initial brush testing. For this single specimen, the surface treatment used only the BASF MBT Reveal compound.

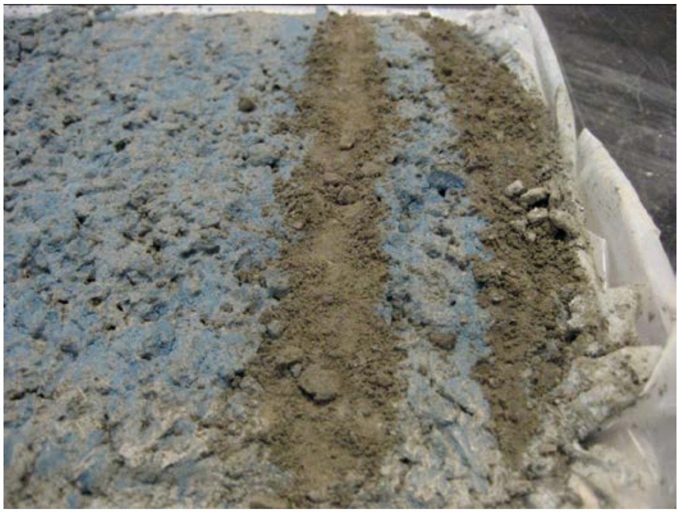

Figure V.6. EAC-2 concrete specimen with curing/retarder BASF MBT Reveal. Scratches at 2 and 3 hours show that aggregate is easily removed from paste.

The surface of the EAC specimen was more easily finished than the surfaces of the previous two specimens and the depth of etch after 6 to 7 hours of curing was between 1 and 2 mm. The exposed surface of the specimen is shown in Figure V.8.

Test 4: Determining Time to Brush by the Maturity Method

A maturity test was used to estimate the brushing readiness of the EAC concrete by correlating concrete temperature with setting time data and compressive strength measurements

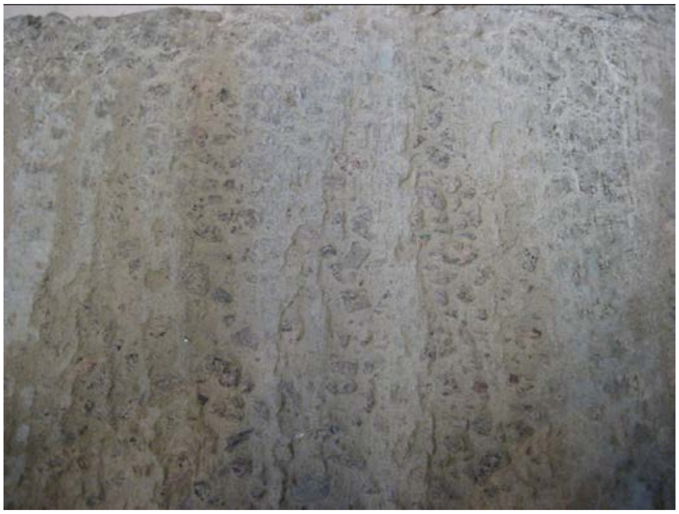

Figure V.8. Surface of revised EAC concrete specimen at 7 hours.

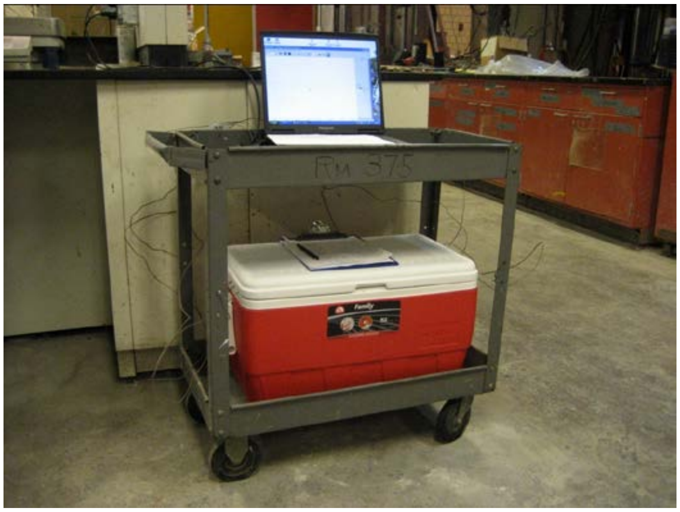

Figure V.9. Concrete temperature data acquisition system.

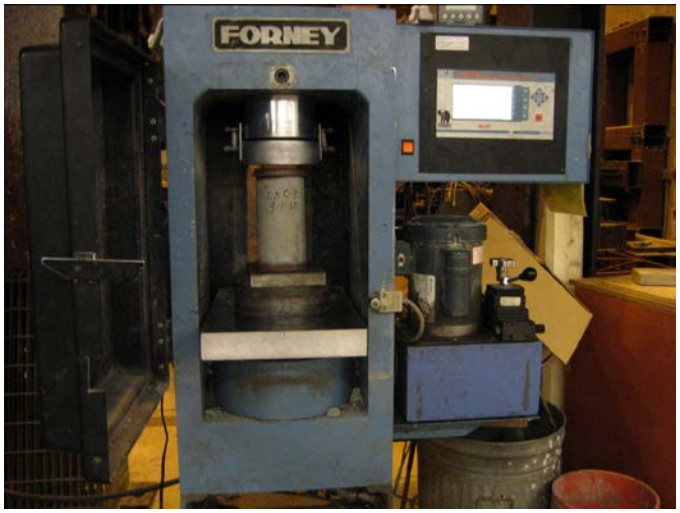

Figure V.10. EAC-3 cylinders were broken every hour from 5 to 10 hours, at 24 hours, and at 72 hours.

with the ability of the brush to dislodge aggregates from the matrix.

To begin, the revised EAC concrete mixture was batched in a laboratory and consolidated into 25 4- × 8-in. cylinder molds. Immediately after the casting, three concrete cylinders and a cylinder of warm water (to act as a temperature control) were placed in a cooler. Thermocouples were inserted into the cylinders at a depth just below the concrete surface. Thermocouples were connected to a temperature data acquisition console (Figure V.9). Simultaneously, a concrete specimen was cast and finished, as described for Test 1, and MBT Reveal was applied to its surface.

At 6.5 hours after batching, the brushing test showed that the concrete specimen covered with MBT Reveal no longer released aggregates when the aggregates were prodded. Therefore, cylinders were demolded and three cylinders were compression tested on the hour according to ASTM C39 until the tenth hour after batching (Figure V.10 and Figure V.11). Because of a communication error between the temperature data acquisition system and the software, the temperature data were not recorded. Without the temperature data, the compression strength data are nothing more than collected data.

Test 5: Determining Time to Brush by The Maturity Method: Laboratory and Small Field Trial

A second attempt was made at correlating the EAC brushing time with concrete maturity. EAC concrete was batched in the laboratory. Fourteen 4- × 8-in. cylinders were cast for compression testing and obtaining time/temperature data in the laboratory, and a 30- × 30- × 3-in. slab was constructed in the field to observe any differences in brushing time when the concrete surface was exposed to nonuniform temperature and moving air.

The field slab was divided into six sections, and different thicknesses, ranging from light to heavy, of MBT Reveal were applied to each section. Figure V.12 shows the test slab. A thermocouple was inserted into the slab just below the surface, and temperature readings were taken intermittently with a handheld electronic temperature reader. At the same time, three 4- × 8-in. concrete cylinders that were still in their molds, were outfitted with thermocouples just below the surface. They were placed in a temperature controlled space, and temperature data were collected by a data acquisition console. The compressive strength of the EAC concrete was tested on two, 4- × 8-in. cylinder samples at 5, 7, 8, 9.5, and 20 hours.

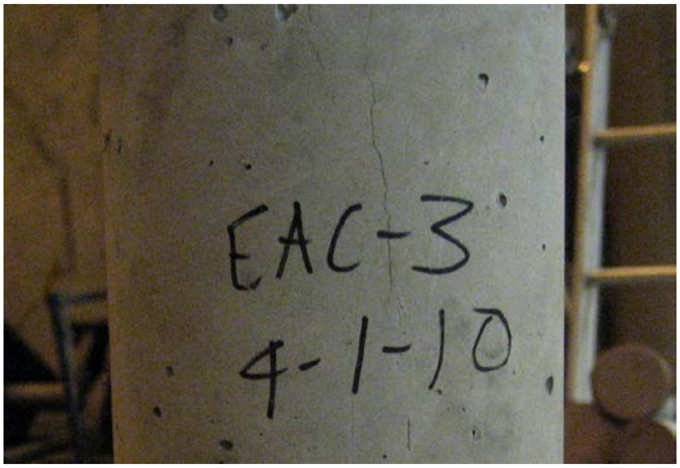

Figure V.11. An EAC-3 cylinder specimen showing shear cracks after failing in the compression machine.

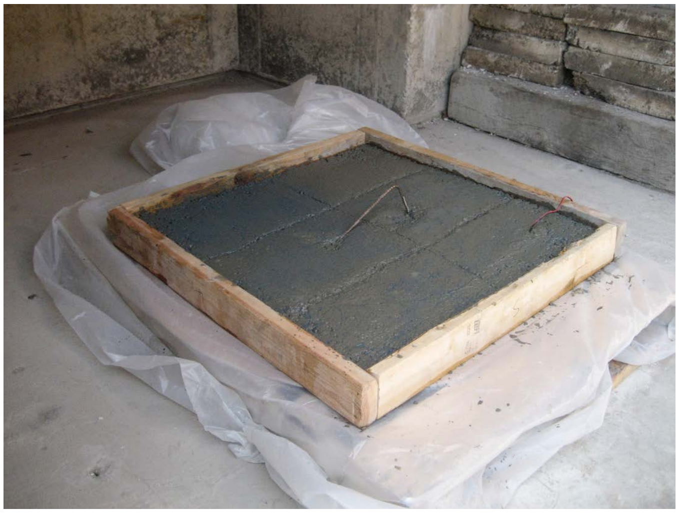

Figure V.12. Field trial of MBT Reveal application.

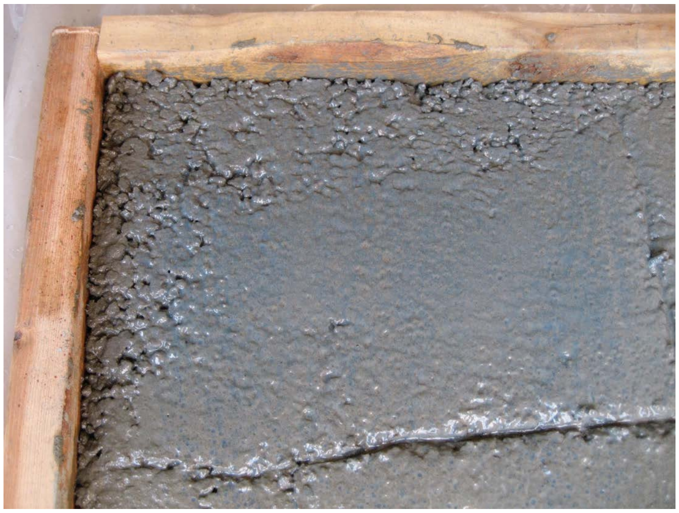

Figure V.13. There is not enough paste available to close the surface of the EAC field sample.

In the field, the six surfaces were observed to determine brushing time. Figure V.14 summarizes the temperature, time, and compressive strength data of the EAC laboratory and field samples. Note the following definitions:

- Slab is the temperature data of the EAC concrete placed in the small field slab.
- Cooler is the temperature data of the EAC concrete placed in 4- × 8-in. cylinders and immediately placed in a temperature controlled space.
- Outside is outside air temperature near the field slab.
- Compression is average compressive strength of two 4- × 8-in. cylinders cured in the laboratory.

All of the sections could have been brushed at 7 hours. This is consistent with the laboratory experiments. Although the quantity of curing/retarding compound did not make a difference in the brushing time, the research team learned that the finishing of the surface and application thickness of the MBT Reveal affected the depth of etch. When the research team finished the field sample's surface with a wooden trowel, it was noted that there was not enough paste to close the surface. This was especially noticeable near the edges, as shown by the nonuniform surface near the north and west borders of one of the field sections (see Figure V.13). Both the surfaces that were not closed and the thickness of MBT Reveal affected the depth of etch. When the surface was not closed, the depth of etch was greater than that in the closed areas. The greater the thickness of MBT Reveal, the more paste was able to be removed and greater the depth of etch. The greater quantity of MBT Reveal also prolonged the time that the researchers could brush and still remove paste. On the two sections with the most curing/retarder compound, it was possible to remove paste after 20 hours, whereas it was not possible to remove paste from the section without curing/retarder compound or from the three sections with less compound.

The information on Figure V.14 suggested that brushing could begin before the concrete reached its maximum temperature when the compression strength was greater than 400 psi. It was the intent of the research team to use this information during construction of the R21 composite pavements with an exposed aggregate finish. Unfortunately, the thermocouples placed in the EAC layer of the demonstration slab were not activated properly, so the research team relied on laboratory experience to initiate brushing in the field.

Exposed Aggregate Concrete Brushing: Field Experience

Although the R21 research team experimented in the laboratory, the construction of the 200-ft demonstration slab before mainline paving was valuable for practicing the finishing of

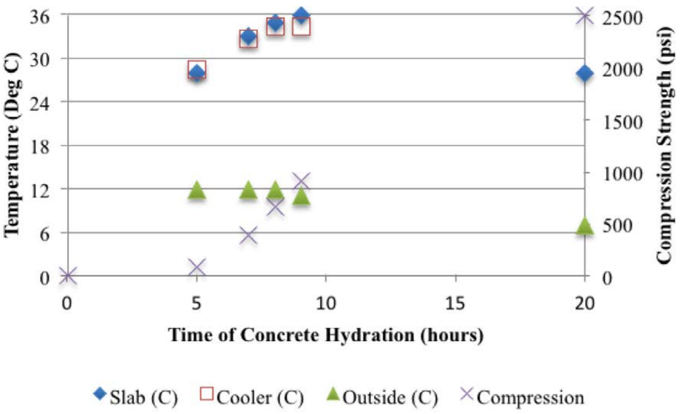

Figure V.14. Time versus temperature and compression strength for EAC laboratory and field samples.

the EAC surface. Lessons were learned regarding the application of the curing/retarder compound, the appropriate method to determine the time to brush, and the number of passes required to remove the required quantity of paste. Despite learning much from constructing the EAC surface on the demonstration slab, the research team and contractor learned that the time of brushing is affected by temperature, cloud cover, wind speed, and rain during EAC surface construction on I-94.

MBT Reveal Application

The application of MBT Reveal, the proprietary product name of the curing/retarder compound used to achieve the exposed aggregate finish of the portland cement concrete (PCC)/PCC composite pavements, required adjusting after the contractor and the research team discovered problems with the way the curing/retarding compound was initially applied to the demonstration slab. Figure V.15 shows the uneven application of MBT Reveal on the demonstration slab. The nozzles of the spray apparatus permitted overlap of the compound in some areas and a paucity of compound in adjacent areas. As a result, portions of the exposed aggregate finish appeared to have a greater depth of etch. The contractor corrected the problem by purchasing spray nozzles with a smaller diameter opening and adjusting the pressure on the line that delivered the curing/retarder compound to the nozzles. During construction of the demonstration slab, a hand sprayer was used to increase the application thickness of MBT Reveal in the first 20 ft because the spray cart's application rate was uneven. However, the hand sprayer's drops were large and lefts small pockmarks in the concrete's surface. For this reason, the use of the hand sprayer was discontinued after the first 20 ft. After brushing, the first 20 feet had the most even aggregate exposure, and there were no immediate signs of differential curing or retarding caused by the pockmarks left by the hand sprayer.

Beyond the first 20 feet, the variation in application rate of the curing/retarder compound was visible after brushing. Areas of lighter MBT Reveal application had less surface paste removed than did areas with the heavier application. The paste in the surface areas that did not receive the adequate amount of curing/retarder compound set more quickly than did the paste areas with thicker coverage. This field experience was similar to the laboratory experience although the lesson learned from the field experience was that the curing/retarder compound must be sufficiently thick to achieve a uniform depth of etch. Once the compound is sufficiently thick, an increase in its thickness does not affect the depth of etch.

Determining Time to Brush

The demonstration slab gave the research team and the contractor practice in determining the appropriate time to initiate brushing to create the EAC surface. At first, a dowel basket stake was used to try and dislodge aggregate from the rest of the concrete matrix. Aggregate was dislodged. However, when a broom was used to sweep away the surface paste, it was difficult to remove enough of the paste to achieve the targeted 0.8 to 1 mm of aggregate exposure. This was different from the experience with laboratory tests. In the laboratory test, if aggregates dislodged with concentrated force, they also dislodged with the brush.

After that initial field experience, a push broom was used to evaluate the readiness of the surface paste for brushing at approximately 20-ft intervals (Figure V.16). Two things

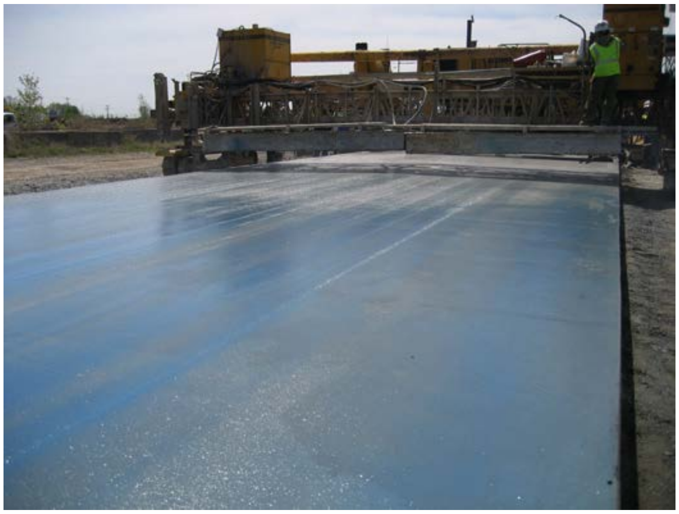

Figure V.15. Streaked application of MBT Reveal on the demonstration slab.

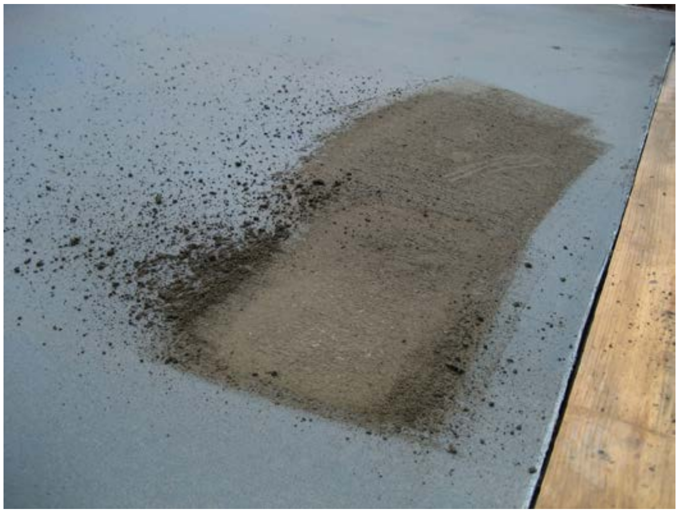

Figure V.16. Evaluating brushing readiness of the EAC surface with a push broom.

occur if the surface needs more curing time before brushing. First, the surface paste and curing/retarder compound clump together when brushed with the hand broom instead of coming off as individual particles. Second, the shear force created by the sweeping action of the broom dislodges aggregates.

Exposing the Aggregate

To determine if the brush was removing the appropriate depth of paste, sand patch tests were performed according to ASTM E965 (Standard Test Method for Measuring Pavement Macrotexture Depth Using a Volumetric Technique) at randomized locations across the demonstration slab. The first sand patch tests yielded an average diameter of 8⅜ in., which indicated a 0.7-mm depth of etch, which meant there was not enough aggregate exposure. The contractor had some control over the pressure exerted by the rotating brush on the concrete surface because he was able to raise and lower the broom by turning a crank (Figure V.17). During the first brushing pass on the demonstration slab, the pressure on the brush was minimal. After the first pass, the pressure that the brush exerted on the ground was increased by decreasing the weight of the brush buoyed by the mechanical arm as the brush was dropped by five cranks (each crank equaled 3⁄32 in.). The second and third passes were made with the brush at this height and more sand patch tests yielded an average diameter of 7 in., which is equivalent to 1 mm of aggregate exposure and was within the target depth of etch (0.8 to 1 mm). When the I-94 mainline sections were brushed, the operator did not use the mechanical arm to buoy the brush. A finished EAC surface from the I-94 construction is shown in Figure V.18.

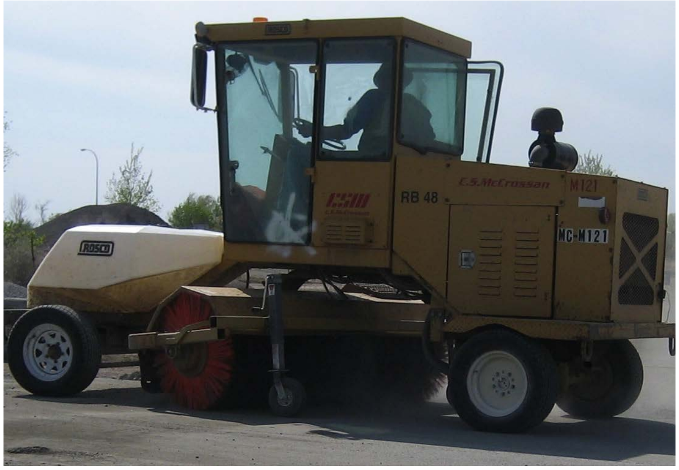

Figure V.17. Rotating sweeper brush with mechanical arm extended to relieve pressure on the brush.

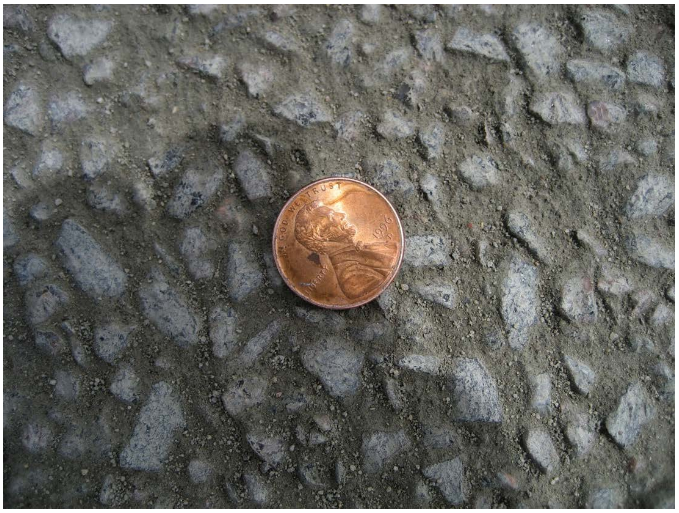

Figure V.18. Properly brushed EAC surface.

More Lessons Learned

Although the demonstration slab gave the contractor and the research team enough confidence to proceed with constructing the composite pavements with EAC surfaces on I-94, more lessons were learned during construction. The first lesson was that if the surface of the pavement is not closed (not enough paste to seal the surface), the brushing will create a rough area in the surface that will likely be deeper than the targeted etch. Figure V.19 shows an EAC surface after brushing in an area where the paste was not closed during paving. This experience was similar to the experience with the small outdoor field trial, where the edges of the small slab were not

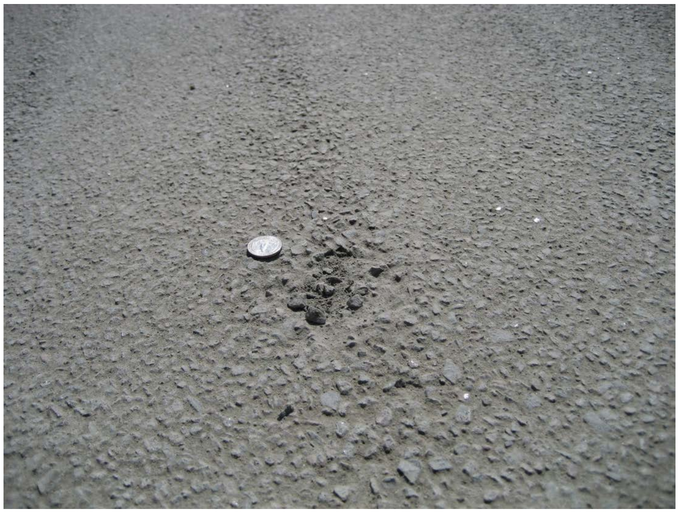

Figure V.19. Area of EAC surface that was not closed before brushing.

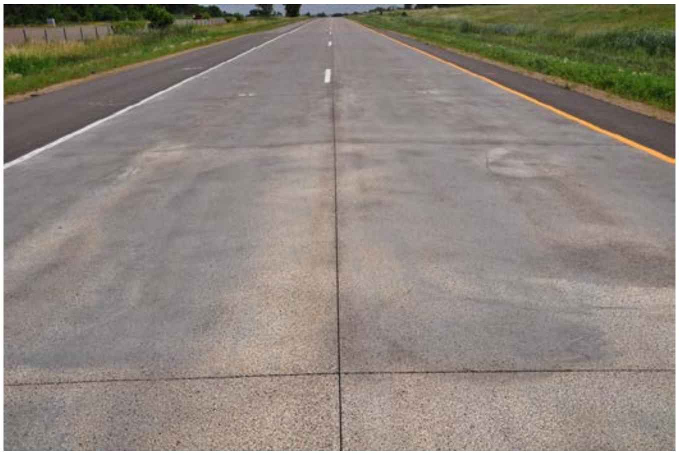

Figure V.20. Streaked appearance of EAC surface caused by caking of paste by brush machine wheels.

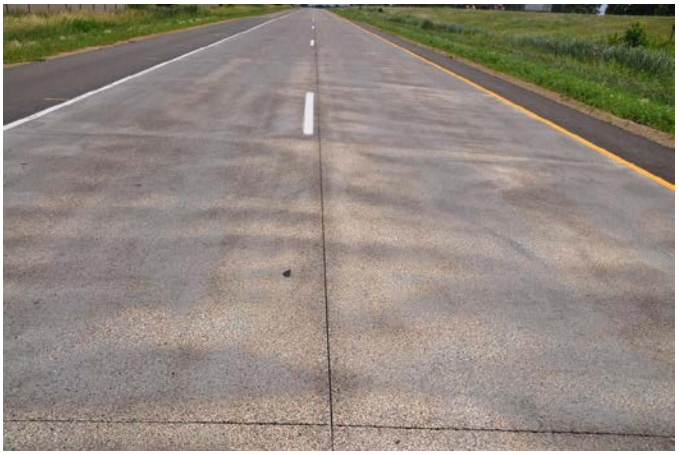

Figure V.21. Marbled EAC surface resulting from saturation during construction.

closed and appeared more susceptible to dislodging of aggregates even after the concrete had appeared to set.

Another lesson was that having the tires preceding the brush also caused an uneven appearance of the surface. On the second day of PCC/PCC composite pavement construction on I-94, it was humid and cloudy, and the concrete beneath the curing retarder compound took longer to set than it had the previous day. While attempts were made to brush a length of surface approximately 50 ft long, it was observed that the front tires of the brushing machine were picking up pieces of the surface concrete in the wheelpath from the first 25 ft and depositing them in the wheelpath of the second 25 ft. As can be seen in Figure V.20, the lighter wheelpath concrete represents the areas where the concrete was deposited. There are few visible exposed aggregates in these paths, and in some cases, the surface concrete is cracking and eventually may be eroded away by enough use. The solution to this problem is to use a front-mounted broom.

Finally, it is important to note that attempting an exposed aggregate concrete finish is not advisable if there is any threat of precipitation. Approximately 250 ft of MnROAD mainline exposed aggregate concrete finish appeared marbled and lacked a uniform depth of etch because the surface, covered with curing/retarder compound, was saturated with rain. The contractor attempted to cover the 250-ft length of pavement with plastic sheeting, but the rain came too fast and was too heavy to avoid damages. The water mixed with the curing/retarder compound and cement paste at the surface. As a result, the slabs had to be saw-cut before the surface was ready to be brushed—approximately 15 hours after the curing/retarder compound had been applied. The water from the saw cutting removed some of the curing/retarder compound at the joints. When the contractor and research team finally agreed that the surface could be brushed, it was difficult to determine if the appropriate amount of paste had been removed because the paste that remained was sticky and formed small peaks. The paste that was removed was in slurry form, and the quantity could not be estimated. Sand patch tests could not be performed because of the wetness of the remaining paste. When the concrete fully cured and the surface eventually dried, the appearance of the surface was marbled, as shown in Figure V.21. Similar to Figure V.20, the lighter areas indicate places with less depth of etch.

References

ACI Committee 555. Removal and Reuse of Hardened Concrete. ACI 555R-01, October 2001, pp. 1–26.

Ahmad, S. H., D. Fisher, and K. Sackett. Mechanical Properties of Concretes with North Carolina Recycled Aggregates. Integrated Design and Environmental Issues in Concrete Technology (K. Sakai, ed.). E & FN Spon, London, 1996.

Ajudkiewicz, A. B., and A. T. Kliszczewicz. *Properties and Usability of HPC with Recycled Aggregates.* Symposium Proceedings: PCI/FHWA/FIB Internationals Symposium on High Strength Performance Concrete. Orlando: Precast/Prestressed Concrete Institute, September 25–27, 2000. Print.

Akkari, A., and B. Izevbekhai. *2010 MnROAD Construction Report.* Report MN/RC 2011-19. Minnesota Department of Transportation, Saint Paul, 2011.

Akkari, A., and B. Izevbekhai. *Composite Pavements at MnROAD: Cells 70, 71, and 72 Construction Report and Early Performance Evaluation.* Minnesota Department of Transportation, 2011.

Allen, H. Proposed Experimental Composite Pavements. *Highway Research Record 434,* HRB, National Research Council, Washington, D.C., 1973, pp. 11–13.

Al-Qadi, I. L., S. H. Carpenter, Z. Leng, and H. Ozer. *Tack Coat Optimization for HMA Overlays: Laboratory Testing.* Report number FHWA-ICT-08-023. Illinois Center for Transportation, University of Illinois, Sept. 2008.

American Association of State Highway and Transportation Officials. *Mechanistic–Empirical Pavement Design Guide, Interim Edition: A Manual of Practice.* Washington, D.C., 2008.

American Concrete Pavement Association. *Concrete Pavement Progress,* Vol. 42, No. 1, 2006, Web. 5 July 2011.

Ansari, F., A. Maher, A. Luke, G. Y. Xhang, and P. Szary. *Recycled Materials in Portland Cement Concrete.* FHWA NJ 2000-03. June 2000.

ARA Inc., ERES Consultants Division. *Guide for Mechanistic–Empirical Design of New and Rehabilitated Pavement Structures.* National Cooperative Highway Research Program, Transportation Research Board, National Research Council, 2004.

Armaghani, J. M., T. J. Larsen, and L. L. Smith. Temperature Response of Concrete Pavement. In *Transportation Research Record 1121,* TRB, National Research Council, Washington, D.C., 1987, pp. 23–33.

Atis, C. D. Strength Properties of High-Volume Fly Ash Roller Compacted and Workable Concrete and Influence of Curing Condition. *Cement and Concrete Research,* Vol. 35, No. 6, 2005, pp. 1112–1121.

Auberg, R. Application of CIF Test in Practice for Reliable Evaluation of Frost Resistance of Concrete. *RILEM PRO 24: Frost Resistance of Concrete from Nano-Structure and Pore Solution to Macroscopic Behaviour and Testing* (M. J. Setzer, R. Auberg, and H.-J. Keck, eds.), Essen, Germany, 2002, pp. 255–267.

Bairagi, N. K., H. S. Vidyadhara, and K. Ravande. Mix Design Procedures for Recycled Aggregate Concrete. *Construction and Building Materials,* Vol. 4, No. 4, 1990, pp. 188–193.

Baker, R. F. New Jersey Composite Pavement Project. In *Highway Research Record, 434,* HRB, National Research Council, Washington, D.C., 1992, pp. 11–19.

Barbhuiya, S. A., J. K. Gbagbo, M. I. Russell, and P. A. M. Basheer. Properties of Fly Ash Concrete with Hydrated Lime and Silica Fume. *Construction and Building Materials,* Vol. 23, 2009, pp. 3233–3239.

Belshe, M., K. Kaloush, and J. Golden. *The Urban Heat Island Effect and Impact of AR-ACFC Overlays on PCC Pavements.* Asphalt Rubber International Conference, Palm Springs, California, 2006.

Bentz, D. P., C. F. Ferraris, I. De la Varga, M. A. Peltz, and J. A. Winpigler. Mixture Proportioning Options for Improving High Volume Fly Ash Concretes. *International Journal of Pavement Research and Technology,* Vol. 3, No. 5, 2010, pp. 234–240.

Bentz, D. P., E. F. Irassar, B. Bucher, and W. J. Weiss. Limestone Fillers to Conserve Cement in Low w/cm Concretes: An Analysis Based on Powers' Model. *Concrete International,* Vol. 31, No. 11, 2009, pp. 35–39.

Berry, E. E., and V. M. Malhotra. Fly Ash in Concrete. *Supplementary Cementing Materials for Concrete,* 1987, pp. 35–163.

Bolander, J. E. *Development of Rigid-Body-Spring Networks for Analyzing Concrete Materials and Structures.* Seminar presented 28 July 2008, Nihon University, Japan, 2008.

Bolander, J. E., and S. Berton. Simulation of Shrinkage Induced Cracking in Cement Composite Overlays. *Cement & Concrete Composites,* Vol. 26, No. 7, Elsevier, 2004.

Bolander, J. E., Z. Li, and M. Yip. Restraint and Cracking during Nonuniform Drying of Cement Composites. *Proceedings of the Transport Properties and Concrete Quality,* 2007, in press.

Bolander, J. E., and S. Saito. Fracture Analyses Using Spring Networks with Random Geometry. *Engineering Fracture Mechanics,* Vol. 61, 1998, pp. 569–591.

Bolander, J. E., and N. Sukumar. Irregular Lattice Model for Quasistatic Crack Propagation. *Physical Review B,* Vol. 71, American Physical Society, 2005.

Bonavetti, V., H. Donza, G. Menedez, O. Cabrera, E. F. Irassar. Limestone Filler Cement in Low w/c Concrete: A Rational Use of Energy. *Cement and Concrete Research 33,* 2003, pp. 865–871.

Buch, N., R. Lyles, and L. Becker. *Cost Effectiveness of European Demonstration Project: I-75 Detroit.* Report No. RC-1381. Michigan Department of Transportation, Lansing, 2000.

Buchanan, M. S., and M. E. Woods. *Field Tack Coat Evaluator (ATACKer™).* Report FHWA/MS-DOT-RD-04-168. Mississippi Transportation Research Center, Mississippi Department of Transportation, Jackson, MS, 2004.

Cable, J. K., and D. P. Frentress. *Two Lift Portland Cement Concrete Pavements to Meet Public Needs.* Publication No. DTF61-01-X-00042 (Project 8). Federal Highway Administration, Washington, D.C., 2004.

Canestrari, F., G. Ferrotti, M. N. Partl, and E. Santagata. Advanced Testing and Characterization of Interlayer Shear Resistance. In *Transportation Research Record: Journal of the Transportation Research Board, No. 1929,* Transportation Research Board of the National Academies, Washington, D.C., 2005, pp. 69–78.

Cement Association of Canada, 2005. www.cement.ca/cement.nsf/e/0832664B1C8588BA8525717A004A20D7?opendocument. Accessed April 20, 2008.

Cho, Y.-H., C. Liu, T. Dossey, and B. F. McCullough. *Asphalt Overlay Design Methods for Rigid Pavements Considering Rutting, Reflection Cracking and Fatigue Cracking.* Center for Transportation Research, The University of Texas at Austin, 1998.

Cho, Y.-H., J. Weissmann, and B. F. McCullough. *Initial Performance of Asphalt Overlays on Overlaid Jointed Concrete Pavement (JCP) and on Flexible Pavements in Field Test Sections in Lufkin.* Center for Transportation Research, Bureau of Engineering Research, The University of Texas at Austin, 1995.

Choubane, B., and M. Tia. Nonlinear Temperature Gradient Effect on Maximum Warping Stresses in Rigid Pavements. In *Transportation Research Record 1370,* TRB, National Research Council, Washington, D.C., 1992, pp. 11–19.

Christory, J. P., D. Grob, Y. Guidoux, and A. Sainton. Composite Pavements: An Example of a 'Shared Technique' for Better Public Spaces and Road Infrastructures. Presented at 7th International Conference on Concrete Pavements, Orlando, FL, Sept. 9–13, 2001.

Cleary, J., and N. Delatte. Implementation of Internal Curing in Transportation Concrete. In *Transportation Research Record: Journal of the Transportation Research Board, No. 2070,* Transportation Research Board of the National Academies, Washington, D.C., 2008, pp. 1–7.

Coleri, E., B.-W. Tsai, and C. L. Monismith. Pavement Rutting Performance Prediction by Integrated Weibull Approach. In *Transportation Research Record: Journal of the Transportation Research Board, No. 2087,* Transportation Research Board of the National Academies, Washington, D.C., 2008, pp. 120–130.

Collop, A. C., N. H. Thom, and C. Sangiorgi. Assessment of Bond Condition using the Leutner Shear Test. *Institution of Civil Engineers Transport,* Vol. 156, TR4, 2003, pp. 211–217.

Cristofoletti, U., M. Cupo-Pagano, A. D'Andrea, E. De Luca, A. Mirabelli, F. Moschettini, and A. M. Tazzi. Concrete Made of Building Demolition Waste (CIMEUROPE s.a.r.l., ed.). Presented at 7th International Symposium on Concrete Roads, Session 3. Reconstruction: Recycling, Stabilization. Vienna, October 3–5, 1994.

Crittenden, J. C., R. R. Trussel, D. W. Hand, K. J. Howe, and G. Tchoban. *Water Treatment: Principles and Design,* 2nd ed. John Wiley and Sons, Inc., New Jersey, 2005.

Cuperus, J. G., and J. Boone. *International Experiences in the Use of Recycled Aggregates.* Recycling and Reuse of Waste Materials: Proceedings of International Symposium Held at the University of Dundee, Scotland, U.K. on 9–11 September 2, 2003, pp. 383–387.

Cuttell, G. D. *Development of Guidelines for Design and Construction of Rigid Pavements Containing Recycled Concrete Aggregates.* MS thesis. University of Minnesota, 1996.

Cuttell, G. D., M. B. Snyder, J. M. Vandenbossche, and M. J. Wade. Performance of Rigid Pavements Containing Recycled Concrete Aggregates. In *Transportation Research Record 1574, No. 971071,* TRB, National Research Council, Washington, D.C., 1997, pp. 89–98.

Dalati, R. E., E. Youssef, S. Yotte, F. Homsi, and S. Haykai. Recommendations for Recycling, Processing and Reuse of Concrete. *2007 ASME Mechanical Engineering Congress and Exposition,* Vol. 13, 2007, pp. 51–55.

Darter, M. I. Report on the 1992 U.S. Tour of European Concrete Highways. Publication No. FHWA-SA-93-012. Federal Highway Administration, Washington, D.C., 1993.

Darter, M. I., and E. J. Barenberg. *Zero-Maintenance Pavement: Field Studies on the Performance Requirements and Capabilities of Conventional Pavement Systems.* Report FHWA-RD-76-105. FHWA, 1976.

Deacon, J. A., J. Harvey, I. Guada, L. Popescu, and C. L. Monismith. Analytically Based Approach to Rutting Prediction. In *Transportation Research Record: Journal of the Transportation Research Board, No. 1806,* Transportation Research Board of the National Academies, Washington, D.C., 2002.

Delatte, N. Simplified Design of Roller-Compacted Concrete Composite Pavement. In *Transportation Research Record: Journal of the Transportation Research Board, No. 1896,* Transportation Research Board of the National Academies, Washington, D.C., 2004, pp. 57–65.

Diakhate, M., A. Phelipot, A. Millien, and C. Petit. Shear Fatigue Behaviour of Tack Coats in Pavements. *Road Materials and Pavement Design: An International Journal,* Vol. 7, No. 2, 2006, pp. 201–222.

Donovan, E. P., I. L. Al-Qadi, and A. Loulizi. Optimization of Tack Coat Application Rate for Geocomposite Membrane on Bridge Decks. In *Transportation Research Record: Journal of the Transportation Research Board, No. 1740,* TRB, National Research Council, Washington, D.C., 2000, pp. 143–150.

Duran-Herrera, A., C. A. Juarez, P. Valdez, and D. P. Bentz. Evaluation of Sustainable High-Volume Fly Ash Concretes. *Cement and Concrete Composites,* Vol. 33, No. 1, 2010, pp. 39–45.

Environmental Protection Agency. National Emission Standards for Hazardous Air Pollutants from the Portland Cement Manufacturing Industry and Standards of Performance for Portland Cement Plants. *Federal Register,* Vol. 75, No. 174, September 2010, Web. 20 July 2011.

ERES Consultants, Inc. *Performance of Concrete Pavements, Volume II—Evaluation of In-Service Concrete Pavements.* Publication No. FHWA-RD-95-110. Federal Highway Administration, Washington, D.C., 1998.

Fathifazl, G. *Structural Performance of Steel Reinforced Recycled Concrete Members.* Diss. U of Ottawa, 2008.

Federal Highway Administration. *Report on the 1992 U.S. Tour of European Concrete Highways.* Publication No. FHWA-SA-93-012. FHWA, U.S. Department of Transportation, Washington, D.C., 1992.

Federal Highway Administration. *Transportation Applications of Recycled Concrete Aggregate: FHWA State of the Practice National Review.* September 2004.

Federal Highway Administration. *High Performance Concrete Pavements, Project Summary.* Publication No. FHWA-IF-06-031. Federal Highway Administration, Washington, D.C., 2006.

Flexible Pavements of Ohio (FPOO). *Technical Bulletin: Proper Tack Coat Application.* Flexible Pavements of Ohio. Columbus, Ohio, May 2001.

Franke, H.-J. Recycling Concrete Pavements in Motorway Construction (CIMEUROPE s.a.r.l., ed.). Presented at 7th International Symposium on Concrete Roads, Session 3. Reconstruction: Recycling, Stabilization. Vienna, October 3–5, 1994.

Freund, L. B., and S. Suresh. *Thin Film Materials.* Cambridge University Press, 2004.

Fults, K. Quiet Pavement Systems in Europe. Publication No. FHWA-PL-05-011. Federal Highway Administration, Washington, D.C., 2005.

Geokon. Instruction Manual-Model 4200/4202/4204/4210 Vibrating Wire Strain Gages. 2010.

Giacco, G., and R. Zerbino. Failure Mechanism of Concrete: Combined Effects of Coarse Aggregates and Strength Level. *Advanced Cement Based Materials,* Vol. 7, 1998, pp. 41–48.

Gomez-Soberon, J. M. V. Porosity of Recycled Concrete With Substitution of Recycled Concrete Aggregate: An Experimental Study. *Cement and Concrete Research,* Vol. 32, March 5, 2002, pp. 1301–1311.

Gondai, Y., Y. Tsukinaga, M. Shoya, M. Aba, and Y. Sakoi. Study on the Test Method for Scaling Resistance of Concrete Exposed to Deicing Chemicals. *Creep, Shrinkage, and Durability Mechanics of Concrete and Concrete Structures* (Tanabe et al., eds.), Taylor & Francis Group, London, 2009.

Gress, D. L., M. B. Snyder, and J. R. Sturtevant. Performance of Rigid Pavements Containing Recycled Concrete Aggregate: Update for 2006. In *Transportation Research Record: Journal of the Transportation Research Board, No. 2113,* Transportation Research Board of the National Academies, Washington, D.C., 2009, pp. 99–107.

Griffith, J. M. Discussion of Experimental Composite Pavements. *Highway Research Record 37,* HRB, National Research Council, Washington, D.C., 1963.

Hachiya, Y., and K. Sato. Effect of Tack Coat on Bonding Characteristics at Interface Between Asphalt Concrete Layers. *Proceedings of the 8th International Conference on Asphalt Pavements.* 1997.

Haider, M. Lärmemission von Fahrbahnoberflächen–Betonstraßen: Concrete Pavements TODAY and TOMORROW. *Austrian Conference on Concrete Roads,* Vienna, Austria, 2007.

Haider, M., J. Steigenberger, and H. Piber. Long-term Performance of Low-noise Concrete Pavements. *Proc., 10th International Symposium on Concrete Roads,* Brussels, Belgium, September 18–22, 2006.

Hall, K. *Long-Life Concrete Pavements in Europe and Canada.* Publication No. FHWA-PL-07-027. Federal Highway Administration, Washington, D.C., 2007.

Hall, K., D. Dawood, S. Vanikar, R. Tally, Jr., T. Cackler, A. Correa, P. Deem, J. Duit, G. Geary, A. Gisi, A. Hanna, S. Kosmatka, R. Rasmussen, S. Tayabji, and G. Voight. *Long-Life Concrete Pavements in Europe and Canada.* FHWA-PL-07-027. August 2007.

Hansen, T. C. Recycled Aggregates and Recycled Aggregate Concrete: Second State-of-the-Art Report 1945–1985. *Materials and Structures,* Vol. 111, 1986, pp. 201–246.

Hansen, T. C. Recycled Aggregates and Recycled Aggregate Concrete: Third State-of-the-Art Report 1945–1989. Recycling of Demolished Concrete and Masonry: Report of Technical Committee 37-DRC Demolition and Reuse of Concrete. *RILEM Report 6,* 1992, pp. 1–159.

Hansen, T. C., and H. Narud. Strength of Recycled Concrete Made from Crushed Concrete Coarse Aggregate. *Concrete International,* Vol. 5, No. 1, 1983, pp. 21–26.

Hanson, D. I. Construction and Performance of an Ultrathin Bonded Hot-Mix Asphalt Wearing Course. In *Transportation Research Record: Journal of the Transportation Research Board, No. 1749,* TRB, National Research Council, Washington, D.C., 2001, pp. 53–59.

Harrington, J. Summary of Michigan Recycled Concrete Aggregate Review. Michigan Department of Transportation, Office of Pavement Technology, August 19–23, 2003. http://www.fhwa.dot.gov/pavement/recycling/rcami.cfm. Retrieved July 27, 2008.

Heine, P., and M. J. Setzer. The Role of Aggregates in the CIF-Test. *RILEM PRO 24: Frost Resistance of Concrete from Nano-Structure and Pore Solution to Macroscopic Behaviour and Testing* (M. J. Setzer, R. Auberg, and H.-J. Keck, eds.). Essen, Germany, 2002, pp. 269–276.

Hendricks, C. F. Certification System for Aggregates Produced from Building Waste and Demolished Buildings. *Environmental Aspects of Construction with Waste Materials,* Elsevier science B.V., March 5, 2002, pp. 821–834.

Hendriks, Ch. F., G. M. T. Janssen, and J. Vogtlander. *Assessment of Recycled Materials with the Eco-Costs/Value Ratio Model.* Recycling and Reuse of Waste Materials: Proceedings of the International Symposium Held at the University of Scotland, U.K. on 9–11 September 2, 2003, pp. 801–814.

Henrichsen, A. Report on Unified Specifications for Recycled Coarse Aggregates for Concrete. *Materials and Structures,* Vol. 27, No. 9, 1994, pp. 557–559.

Hiller, J. *Development of Mechanistic–Empirical Principles for Jointed Plain Concrete Pavement Fatigue Design.* PhD thesis. University of Illinois at Urbana-Champaign, Urbana, 2007.

Hiller, J. E., Y. S. Deshpande, Y. Qin, and C. J. Shorkey. *Efficient Use of Recycled Concrete in Transportation Infrastructure.* 2010.

Hiller, J. E., and J. R. Roesler. Simplified Nonlinear Temperature Curling Analysis for Jointed Concrete Pavements. *Journal of Transportation Engineering,* Vol. 136, No. 7, 2010, pp. 654–663.

Huber, J., K. Beckhaus, K. H. Weigrink, and P. Schiel. Influence of Moisture on the Deformation (Warping and Curling) of Concrete Road Pavements Consisting of One or Two Layers With and Without Recycled Aggregate. Presented at 9th International Symposium on Concrete Roads, Theme 2, Istanbul, Turkey, 2004.

Indiana Department of Transportation. Aggregate Production. *Certified Aggregate Technician,* 2010, pp. 5-1–5-37.

Ioannides, A. M., L. Khazanovich, and J. L. Becque. Structural Evaluation of Base Layers in Concrete Pavement Systems. In *Transportation Research Record 1370,* TRB, National Research Council, Washington, D.C., 1992.

Ioannides, A. M., and L. Khazanovich. Nonlinear Temperature Effects in Multi-Layered Concrete Pavements. *ASCE Journal of Transportation Engineering,* Vol. 124, No. 2, 1998.

Iowa Department of Transportation. *HR-355: The Role of Magnesium in Concrete Deterioration.* 2000.

Jagota, A., and S. J. Bennison. Spring-Network and Finite Element Models for Elasticity and Fracture (K. K. Bardhan, B. K. Chakrabarti, A. Hansen, eds.). Nonlinearity and Breakdown in Soft Condensed Matter. *Springer Lecture Notes in Physics 437,* Springer, Berlin, 1994, 186 pp.

Jana, D. Concrete, Construction, or Salt—Which Causes Scaling? Part I: Importance of Air-Void System in Concrete. *Concrete International,* Nov. 2004, pp. 31–38.

Janssen, D. J. Moisture in Portland Cement Concrete. In *Transportation Research Record 1211,* TRB, National Research Council, Washington, D.C., 1987, pp. 40–44.

Jones, D. *Quality Management System for Site Establishment, Daily Operations, Instrumentation, Data Collection and Data Storage for APT Experiments.* CSIR Transportek: Pretoria, South Africa, 2005.

Kaloush, K. E., and M. W. Witczak. *Development of a Permanent to Elastic Strain Ratio Model for Asphalt Mixtures, Development of the 2002 Guide for the Design of New and Rehabilitated Pavement Structures.* NCHRP 1-37A, Inter-Team Technical Report. September 2000.

Khazanovich, L. *Structural Analysis of Multi-Layered Concrete Pavement Systems.* PhD dissertation. University of Illinois, Urbana, 1994.

Khazanovich, L., O. I. Selezneva, H. T. Yu, and M. I. Darter. Development of Rapid Solutions for Prediction of Critical Continuously Reinforced Concrete Pavement Stresses. In *Transportation Research Record: Journal of the Transportation Research Board, No. 1778,* TRB, National Research Council, Washington, D.C., 2001, pp. 64–72.

Kivikyto-Reponen, P., S. Ala-Kleme, J. Hellman, J. Liimatainen, and S.-P. Hannula. The Correlation of Material Characteristics and Wear in a Laboratory Scale Cone Crusher. *Wear,* Vol. 267, 2009, pp. 568–575.

Kohler, E., V. Kannekanti, and J. Harvey. California Efforts Towards Mechanistic-Empirical Pavement Design. In *Proceedings of the 2006 Airfield and Highway Pavement Specialty Conference,* American Society of Civil Engineers (ASCE), Reston, Va., 2006.

Kohn, S., and M. I. Darter. Structural Design of Composite Concrete Pavements. *Proceedings of the 2nd International Conference of Concrete Pavement Design,* Purdue University, West Lafayette, Indiana, April 14–16, 1981, pp. 107–117.

Korenev, B. G., and E. I. Chernigovskaya. *Analysis of Plates on Elastic Foundation.* Gosstroiizdat, Moscow (in Russian), 1962.

Kou, S. C., C. S. Poon, and D. Chan. Influence of Fly Ash as Cement Replacement on the Properties of Recycled Aggregate Concrete. *ASCE Journal of Materials in Civil Engineering,* September 2007, pp. 709–717.

Krenn, H., and H. Stinglhammer. New From Old Recycling Concrete Pavements (CIMEUROPE s.a.r.l., ed.). Presented at 7th International Symposium on Concrete Roads, Session 3. Reconstruction: Recycling, Stabilization. Vienna, October 3–5, 1994.

Kruntcheva, M. R., A. C. Collop, and N. H. Thom. Feasibility of Assessing Bond Condition of Asphalt Concrete Layers with Dynamic Nondestructive Testing. *ASCE Journal of Transportation Engineering,* Vol. 130, No. 4, 2004, pp. 510–518.

Kruntcheva, M. R., A. C. Collop, and N. H. Thom. Effect of Bond Condition on Flexible Pavement Performance. *ASCE Journal of Transportation Engineering,* Vol. 131, No. 11, 2005, pp. 880–888.

Kruntcheva, M. R., A. C. Collop, and N. H. Thom. Properties of Asphalt Concrete Layer Interfaces. *ASCE Journal of Materials in Civil Engineering,* Vol. 18, No. 3, 2006, pp. 467–471.

Kumar, B., G. K. Tike, and P. K. Nanda. Evaluation of Properties of High-Volume Fly Ash Concrete for Pavements. *Journal of Materials in Civil Engineering,* 2007, pp. 906–911.

Larsen, T. J. A Composite Pavement Design Procedure. *Proceedings of the 2nd International Conference of Concrete Pavement Design,* Purdue University, West Lafayette, Indiana, April 14–16, 1981, pp. 99–105.

Larson, G., and B. J. Dempsey. *Enhanced Integrated Climatic Model.* Version 2.0, Final Report. Contract DTFA MN/DOT 72114. Available at: Department of Civil Engineering, University of Illinois at Urbana-Champaign, Urbana, 1997.

Leng, Z., I. L. Al-Qadi, S. H. Carpenter, and H. Ozer, Interface Bonding Between Hot-Mix Asphalt and Various Portland Cement Concrete Surfaces, *Transportation Research Record: Journal of the Transportation Research Board, No. 2127,* Transportation Research Board of the National Academies, Washington, D.C., 2009, pp. 20–28.

Leng, Z., H. Ozer, I. L. Al-Qadi, and S. H. Carpenter. Interface Bonding between HMA and Various PCC Surfaces: Laboratory Assessment. Presented at Annual Meeting of the Transportation Research Board, Washington, D.C., 2008.

Liu, X., and M.-H. Zhang. Permeability of High-Performance Concrete Incorporating Presoaked Lightweight Aggregates for Internal Curing. *Magazine of Concrete Research,* Vol. 62, No. 2, 2010, pp. 79–89.

Lu, Q., Y. Zhang, and J. T. Harvey. Estimation of Truck Traffic Inputs for Mechanistic–Empirical Pavement Design in California. In *Transportation Research Record: Journal of the Transportation Research Board, No. 2095,* Transportation Research Board of the National Academies, Washington, D.C., 2009, pp. 62–72.

Lytton, R. L., D. E. Pufahl, C. H. Michalak, H. S. Lang, and B. J. Dempsey. *An Integrated Model of the Climatic Effects on Pavements.* Publication No. FHWA-RD-90-033. Available at: U.S. Department of Transportation, Federal Highway Administration, McLean, VA, 1989.

Mehta, P. K. Natural Pozzolans. In *Supplementary Cementing Materials for Concrete,* Canadian Government Publishing Center, Ottawa, 1987, pp. 1–33.

Mejía, D., S. Iyer, C. Rao, P. Shokouhi, and S. Nazarian. *A Work Plan toward Evaluation of Technologies to Assess Presence and Extent of Delamination of HMA Airfield Pavements.* Draft report number 06-04. Center for Transportation Infrastructure Systems, University of Texas, El Paso, 2008.

Melton, J. S. Guidance for Recycled Concrete Aggregate Use in the Highway Environment. *Recycling Concrete and Other Materials for Sustainable Development.* American Concrete Institute, 2004, pp. 47–60.

Merlet, J. D., and P. Pimienta. *Mechanical and Physico-Chemical Properties of Concrete Produced with Coarse and Fine Recycled Concrete Aggregates.* Demolition and Reuse of Concrete and Masonry: Guidelines for Demolition and Reuse of Concrete and Masonry: Proceedings of the Third International RI, 1994, pp. 343–353.

Mindess, S., J. F. Young, and D. Darwin. *Concrete,* 2nd ed. Prentice Hall, 2002.

Mining Engineering Department of the Faculty of Engineering. A Visit to Our Laboratory. Mons, Belgium. www.mecaroc.fpms.ac.be/en/visit_e.htm. Accessed February 4, 2013.

Minnesota Department of Natural Resources Division of Lands and Minerals. *Environmental Regulations for Aggregate Mining.* Fact Sheet 1. 2001a. http://files.dnr.state.mn.us/lands_minerals/aggregate1_mar01.pdf.

Minnesota Department of Natural Resources Division of Lands and Minerals. *Reclamation at Aggregate Mining Sites.* Fact Sheet 3. 2001b. http://files.dnr.state.mn.us/lands_minerals/aggregate3_mar01.pdf.

Minnesota Department of Transportation. *Standard Specifications for Construction 3138.2 C.* 2005.

Minnesota Department of Transportation. *Plant Mixed Asphalt Pavement Combined 2360/2350.* Gyratory/Marshall Design Specification, 2008.

Mohamed, A. R., and W. Hansen. Effect of Nonlinear Temperature Gradient on Curling Stresses in Concrete Pavements. In *Transportation Research Record 1568,* TRB, National Research Council, Washington, D.C., 1997, pp. 65–71.

Mohammad, L. N., M. A. Raqib, and B. Huang. Influence of Asphalt Tack Coat Materials on Interface Shear Strength. In *Transportation Research Record: Journal of the Transportation Research Board, No. 1789,* Transportation Research Board of the National Academies, Washington, D.C., 2002, pp. 56–65.

Monismith, C. L., R. G. Hicks, and F. N. Finn. *SHRP-A-417: Accelerated Performance-Related Tests for Asphalt-Aggregate Mixes and Their Use in Mix Design and Analysis Systems.* Strategic Highway Research Program, National Research Council, Washington, D.C., 1994.

Morbi, A., S. Cangiano, and E. Borgarello. Cement Based Materials for Sustainable Development. *Proceedings of the Second International Conference on Sustainable Construction Materials and Technologies,* University of Wisconsin, Milwaukee, June 28–30, 2010.

Morlion, D., J. Venstermans and J. Vyncke, "Demolition Waste of the Zandvliet Lock as Aggregates for Concrete", Proceedings of the Second International RILEM Symposium, Tokyo, Japan, 1988.

Mrawira, D., and D. J. Damude. Revisiting the Effectiveness of Tack Coats in HMA Overlays: The Shear Strength of Tack Coats in Young Overlays. *Proceedings of the 14th Annual Conference, Canadian Technical Asphalt Association Proceedings,* 1999, pp. 116–129.

Mun, K. J., S. Y. So, and Y. S. Soh. The Effect of Slaked Lime, Anhydrous Gypsum and Limestone Powder on Properties of Blast Furnace Slag Mortar and Concrete. *Construction and Building Materials 21,* 2007, pp. 1576–1582.

Mymrin, V., and S. M. Correa. New Construction Material from Concrete Production and Demolition Waste and Lime Production Waste. *Construction and Building Materials,* 2007, pp. 578–582.

National Concrete Pavement Technology Center. Concrete Pavement Surface Characteristics Program Site Evaluation Report, I-70 Two-Lift Paving. October 6, 2008.

NCHRP. Jackknife Testing–An Experimental Approach to Refine Model Calibration and Validation, *NCHRP Results Digest Number 283,* National Cooperative Highway Research Program, Transportation Research Board of the National Academies, Washington, D.C., 2003a.

NCHRP. Refining the Calibration and Validation of Hot Mix Asphalt Performance Models: An Experimental Plan and Database. *NCHRP Results Digest Number 284,* National Cooperative Highway Research Program, Transportation Research Board of the National Academies, Washington, D.C., 2003b.

NCHRP. *Guide for Mechanistic–Empirical Design of New and Rehabilitated Pavement Structures.* National Cooperative Highway Research Program, Report 1-37A. 2004.

NCHRP. *Recommended Practice for Local Calibration of the M-E Pavement Design Guide.* NCHRP Project 1-40B, Transportation Research Board, Washington, D.C., 2008.

Nassiri, S. *Establishing Permanent Curl/Warp Temperature Gradient for Jointed Plain Concrete Pavements.* PhD dissertation. University of Pittsburgh, PA, 2011.

Norwegian Public Roads Administration. Roller-Compacted Concrete Pavements in Norway, 20 Years Experience. Presented at 7th International Conference on the Bearing Capacity of Roads, Railways and Airfields. Norwegian University of Science and Technology, Trondheim, Norway, 2005.

Packard, R. G. Structural Design of Concrete Pavements with Lean Concrete Lower Course. *Proceedings of the 2nd International Conference of Concrete Pavement Design,* Purdue University, West Lafayette, Indiana, April 14–16, 1981, pp. 119–131.

Palecki, S., and M. J. Setzer. Investigation of High-Performance Concrete Under Frost Attack—Internal Damage and Water Uptake. *RILEM PRO 24: Frost Resistance of Concrete from Nano-Structure and Pore Solution to Macroscopic Behaviour and Testing* (M. J. Setzer, R. Auberg, and H.-J. Keck eds.). Essen, Germany, 2002, pp. 317–325.

Petersson, P. E., and P. Utgenannt. Parameters Influencing the Results When Testing the Scaling Resistance of Concrete. *International RILEM Workshop on Frost Damage in Concrete Minneapolis* (D. Janssen, M. J. Setzer, and M. B. Snyder, eds.). 1999.

Pigeon, M., and R. Pleau. *Durability of Concrete in Cold Climates.* E & FN Spon, 1995.

Raab, C., and M. N. Partl. *Long Term Interlayer Shear Performance of Base Subbase Layers of Asphalt Pavements.* 2007.

Recasens, R. M., A. Martínez, and F. P. Jiménez. Assessing Heat-Adhesive Emulsions for Tack Coats. *Institution of Civil Engineers,* Transport 158, TR1, 2005, pp. 45–51.

Recasens, R. M., A. Martinez, and F. P. Jimenez. Evaluation of Effect of Heat-Adhesive Emulsions for Tack Coats with Shear Test. In *Transportation Research Record: Journal of the Transportation Research Board, No. 1970,* Transportation Research Board of the National Academies, Washington, D.C., 2006, pp. 64–70.

Roesler, J., G. H. Paulino, K. Park, and C. Gaedicke. Concrete Fracture Prediction Using Bilinear Softening. *Cement and Concrete Composites,* Vol. 29, No. 1, 2007, pp. 300–312.

Roffe, J. C., and F. Chaignon. Characterisation Tests on Bond Coats: Worldwide Study, Impact, Tests, and Recommendations. Presented at 3rd International Conference Bituminous Mixtures and Pavements, Thessaloniki, 2002.

Romanoschi, S. A., and J. B. Metcalf. Characterization of Asphalt Concrete Layer Interfaces. In *Transportation Research Record: Journal of the Transportation Research Board, No. 1778,* TRB, National Research Council, Washington, D.C., 2001, pp. 132–139.

Rukavina, Tom. *Aggregate Resources Task Force: Final Report to the Minnesota Legislature.* 2000.

Ryell, J., and J. T. Corkill. Long-Term Performance of an Experimental Composite Pavement. *Highway Research Record 434,* HRB, National Research Council, Washington, D.C., 1973, pp. 1–15.

Sagoe-Crentsil, K. K., T. Brown, and A. H. Taylor. Performance of Concrete Made with Commercially Produced Recycled Concrete Aggregate. *Cement and Concrete Research 31,* 2001, pp. 707–712.

Salem, R. M., E. G. Burdette, and M. Jackson. Resistance to Freezing and Thawing of Recycled Aggregate Concrete. *ACI Material Journal,* May–June 2000, pp. 216–221.

Sales, A., and F. R. de Souza. Concretes and Mortars Recycled with Water Treatment Sludge and Construction and Demolition Sludge. *Construction and Building Materials,* 2009, pp. 2362–2370.

Sanchez de Juan, M., and P. A. Gutierrez. Study on the Influence of Attached Mortar Content on the Properties of Recycled Concrete Aggregate. *Construction and Building Materials,* Vol. 23, No. 2, 2009, pp. 872–877.

Sani, D., G. Moriconi, G. Fava, and V. Corinaldesi. Leaching and Mechanical Behaviour of Concrete Manufactured with Recycled Aggregates. *Waste Management,* Vol. 25, 2005, pp. 177–182.

Schimmoller, V. E., K. Holtz, T. T. Eighmy, C. Wiles, M. Smith, G. Malasheskie, G. J. Rohrbach, S. Schaftlein, G. Helms, R. D. Campbell, C. H. Van Deusen, B. Ford, and J. A. Almborg. *Recycled Materials in European Highway Environments: Uses, Technologies, and Policies.* FHWA-PL-00-025. October 2000.

Schlangen, E., and E. J. Garbocki. New Method for Simulating Fracture Using an Elastically Uniform Random Geometry Lattice. *International Journal of Engineering Science,* Vol. 34, No. 10, 1996, pp. 1131–1144.

Schlangen, E., and J. G. M. van Mier. Simple Lattice Model for Numerical Simulation of Concrete Materials and Structures. *Materials and Structures,* Vol. 25, 1992, pp. 534–542.

Schulz, R. R. The Processing of Building Rubble as Concrete Aggregate in Germany. Demolition and Reuse of Concrete and Masonry: Guidelines for Demolitions and Reuse of Concrete and Masonry. *Proceedings of the Third International RILEM Symposium on Demolition and Reuse of Concrete and Masonry,* held in Odense, Denmark, organized by RILEM 1994, pp. 105–115.

Setzer, M. J. RILEM TC 117-FDC: Freeze-Thaw Ad Deicing Resistance of Concrete. *Materials and Structures,* Supplement March 1997, pp. 3–6.

Setzer, M. J. Frost-Attack on Concrete-Modeling by the Micro-Ice-Les Model—Evaluating by RILEM CIF Test. *Creep, Shrinkage and Durability Mechanics of Concrete and Concrete Structures* (Tanabe et al., eds.), Taylor & Francis Group, London, 2009, pp. 971–977.

Setzer, M. J., P. Heine, S. Kasparek, S. Palecki, R. Auberg, V. Feldrappe, and E. Siebel. Recommendations of RILEM TC 176: Test Methods of Frost Resistance of Concrete. CIF Test: Capillary Suction, Internal Damage, and Freeze-Thaw Test—Reference Method and Alternative Methods A and B. *Materials and Structures,* Vol. 37, 2004, pp. 743–753.

Shayan, A., and A. Xu. Performance and Properties of Structural Concrete Made with Recycled Concrete Aggregate. *ACI Materials Journal,* 100-M42, September–October 2003, pp. 371–380.

Sholar, G. A., G. C. Page, J. A. Musselman, P. B. Upshaw, and H. L. Moseley. *Preliminary Investigation of a Test Method to Evaluate*

Bond Strength of Bituminous Tack Coats. Report number FL/DOT/SMO/02-459. Florida Department of Transportation, State Materials Office, 2002.

Smiley, D. L. *First Year Performance of the European Concrete Pavement on Northbound I-75–Detroit, Michigan.* Research Report No. R-1338. Michigan Department of Transportation, Lansing, 1995.

Smiley, D. L. *Second Year Performance of the European Concrete Pavement on Northbound I-75–Detroit, Michigan.* Research Report No. R-1343. Michigan Department of Transportation, Lansing, 1996.

Smith, J. T., and S. L. Tighe. Recycled Concrete Aggregate—A Viable Aggregate Source for Concrete Pavements. Presented at 87th Annual Meeting of the Transportation Research Board, Washington, D.C., 2008.

Smith, P. Past Performance of Composite Pavements. *Highway Research Record 37,* HRB, National Research Council, Washington, D.C., 1963, pp. 14–30.

Snell, L. M., and B. G. Snell. Oldest Concrete Street in the United States. *Concrete International,* American Concrete Institute, March 2002, pp. 72–74.

Söderlund, M., S. T. Muench, K. Willoughby, J. Uhlmeyer, and J. Weston. Green Roads: A Sustainability Rating System for Roadways. Presented at 87th Annual Meeting of the Transportation Research Board, Washington, D.C., 2008.

Sommer, H. Recycling of Concrete for the Reconstruction of the Concrete Pavement of the Motorway Vienna-Salzburg (CIMEUROPE s.a.r.l., ed.). Presented at 7th International Symposium on Concrete Roads, Session 3, Reconstruction: Recycling, Stabilization, Vienna, October 3–5, 1994.

Sousa, J. B., J. A. Deacon, S. L. Weissman, R. B. Leahy, J. T. Harvey, G. Paulsen, J. S. Coplantz, and C. L. Monismith. *Permanent Deformation Response of Asphalt Aggregate Mixes.* Report SHRP-A-415. Strategic Highway Research Program, National Research Council, Washington, D.C., 1994, 437 pp.

Sousa, J. B., J. C. Pais, R. Saim, G. B. Way, and R. N. Stubstad. Mechanistic–Empirical Overlay Design Method for Reflective Cracking. In *Transportation Research Record: Journal of the Transportation Research Board, No. 1809,* Transportation Research Board of the National Academies, Washington, D.C., 2002, pp. 209–217.

Southwick, D. L., M. Jouseau, G. N. Meyer, J. H. Mossler, and T. E. Wahl. Aggregate Resources Inventory of the Seven-County Metropolitan Area, Minnesota. *Minnesota Geological Survey Information Circular 46,* 2000.

Springenschmid, R., and W. Fleischer. Recent Developments in the Design and Construction of Concrete Pavements for German Expressways. *The Indian Concrete Journal,* Vol. 76, No. 2, 2002, pp. 81–89.

Springenschmid, R., and C. Sodeikat. High-Quality Concrete with Recycled Aggregates. Presented at 8th International Symposium on Concrete Roads, Theme V, Safety and Environment. Lisbon, Portugal, September 13–16, 1998, pp. 191–194.

Sturtevant, J. R., D. L. Gress, and M. B. Snyder. *Performance of Rigid Pavements Containing Recycled Concrete Aggregates—2006 Update.* Recycled Materials Resource Center, University of New Hampshire, 2006.

Tashman, L., K. Nam, and T. Papagiannakis. *Evaluation of the Influence of Tack Coat Construction Factors on the Bond Strength between Pavement Layers.* 2006.

TecEco Inc. 2008. http://www.tececo.com/products.porecocrete.php. Accessed April 20, 2008.

Thomlinson, J. Temperature Variations and Consequent Stresses Produced by Daily and Seasonal Temperature Cycles in Concrete Slabs. *Concrete Constructional Engineering,* Vol. 36, No. 6, pp. 298–307 and Vol. 36, No. 7, pp. 352–360, 1940.

Trevino, M., T. Dossey, B. F. McCullough, and Y. Yildirim. *Applicability of Asphalt Concrete Overlays on Continuously Reinforced Concrete Pavements.* FHWA/TX-05/0-4398-1. Center for Transportation Research, The University of Texas at Austin, 2004.

Tschegg, E. K., G. Kroyer, D.-M. Tan, S. E. Stanzl-Tschegg, and J. Litzka. Investigation of Bonding between Asphalt Layers on Road Construction. *ASCE Journal of Transportation Engineering,* Vol. 121, No. 4, 1995, pp. 309–316.

TxDOT. *Crushed Concrete: Year of the Recycled Roadway Materials.* Publication date not specified. Home: Publications: General Services Publications: Roadway Recycled Materials. www.dot.state.tx.us/publications/general_services.htm. Retrieved June 25, 2008.

Ullidtz, P., J. Harvey, B. W. Tsai, and C. L. Monismith. *Calibration of Incremental-Recursive Flexible Damage Models in CalME Using HVS Experiments.* UCPRC-RR-2005-06. Report Prepared for the California Department of Transportation (Caltrans) Division of Research and Innovation by the University of California Pavement Research Center, Davis and Berkeley, 2006.

Ullidtz, P., J. Harvey, B. W. Tsai, and C. L. Monismith. Calibration of Mechanistic-Empirical Models for Flexible Pavements Using the California Heavy Vehicle Simulators. In *Transportation Research Record: Journal of the Transportation Research Board, No. 2087,* Transportation Research Board of the National Academies, Washington, D.C., 2008, pp. 20–28.

Uzan, J., L. Moshe, and E. Yehuda. Investigation of Adhesion Properties between Asphaltic-Concrete Layers. *Asphalt Paving Technology: Proc., Association of Asphalt Paving Technologists, Technical Sessions,* Vol. 47, 1978, pp. 495–521.

Van Breemen, W. Discussion of Possible Designs of Composite Pavements. *Highway Research Record 37,* HRB, National Research Council, 1963, pp. 5–10.

Vancura, M., D. Tompkins, and L. Khazanovich. Reappraisal of Recycled Concrete Aggregate as a Coarse Aggregate in Concretes for Rigid Pavements. In *Transportation Research Record: Journal of the Transportation Research Board, No. 2113,* TRB, National Research Council, Washington, D.C., 2009, pp. 149–155.

Velosa, A. L., and P. B. Cachim. Hydraulic-Lime Based Concrete: Strength Development Using a Pozzolanic Addition and Different Curing Conditions. *Construction and Building Materials,* Vol. 23, No. 5, 2009, pp. 2107–2111.

Von Quintus, H. L. *Local Calibration Adjustments for the HMA Distress Prediction Models.* Preliminary Draft Final Report, NCHRP 1-40B. National Cooperative Highway Research Program, Transportation Research Board, Washington, D.C., November 2005.

Von Quintus, H. L. *History and Hypothesis Behind the HMA Mixture Adjustment Factors for Rutting and Area Fatigue Cracking Predictions.* White Paper prepared for NCHRP Project 1-40B. Local Calibration Guidance for the Recommended Guide for Mechanistic–Empirical Design of New and Rehabilitated Pavement Structures. February 2006.

Von Quintus, H. L., F. Finn, R. Hudson, and F. Roberts. *Flexible and Composite Structures for Premium Pavements.* FHWA RD-80-154 and 155. Federal Highway Administration, Washington, D.C., 1980.

Von Quintus, H. L., J. Mallela, R. Bonaquist, C. Schwartz, and R. Carvalho. *Calibration of Rutting Models for HMA Structural and Mix Design.* Draft Final Report. NCHRP 9-30A. 2011.

Von Quintus, H. L., and J. S. Moulthrop. *Mechanistic–Empirical Pavement Design Guide Flexible Pavement Performance Prediction Models for Montana: Volume I—Executive Research Summary.* Report Number FHWA/MT-07-008/8158-1. Montana Department of Transportation, Research Programs, Helena, August 2007.

Von Quintus, H. L., J. A. Scherocman, C. S. Hughes, and T. W. Kennedy. *Asphalt-Aggregate Mixture Analysis System: AAMAS*. NCHRP Report No. 338. National Cooperative Highway Research Program, National Research Council, Washington, D.C., March 1991.

Weinfurter, J. A., D. L. Smiley, and R. D. Till. *Construction of European Concrete Pavement on Northbound I-75—Detroit, Michigan.* Research Report R-1333. Michigan Department of Transportation, Lansing, 1994.

Wells, S. A., B. M. Phillips, and J. M. Vandenbossche. Quantifying Built-In Construction Gradients and Early-Age Slab Deformation Caused by Environmental Loads in a Jointed Plain Concrete Pavement. *International Journal of Pavement Eng.,* Vol. 7, No. 4, 2006.

Werner, R. Roadway Pavements of Recycled Concrete (CIMEUROPE s.a.r.l., ed.). Presented at 7th International Symposium on Concrete Roads, Session 3, Reconstruction: Recycling, Stabilization. Vienna, October 3–5, 1994.

West, R. C., J. Zhang, and J. Moore. *Evaluation of Bond Strength between Pavement Layers.* Report Number 05-08. National Center for Asphalt Technology, Auburn University, 2005.

WesTrack Team. *Part II: Performance-Related Specification.* Draft Final Report. Sept. 2000.

Wheat, M. *Evaluation of Bond Strength at Asphalt Interfaces.* M.S. thesis. Kansas State University, Manhattan, 2007.

Wojakowski, J. B. *High Performance Concrete Pavement.* Report No. FHWA–KS–98/2. Kansas Department of Transportation, Topeka, 1998.

Wu, R. *Finite Element Analyses of Reflection Cracking in Asphalt Concrete Overlays.* PhD diss. University of California, Berkeley, 2005.

Yanagi, K., M. Hisaka, and Y. Kasai. Physical Properties of Recycled Concrete Using Recycled Coarse Aggregate Made of Concrete with Finishing Materials. In *Demolition and Reuse of Concrete and Masonry, Guidelines for Demolition and Reuse of Concrete and Masonry: Proceedings of the Third International RILEM Symposium on Demolition and Reuse of Concrete Masonry* (E. K. Lauritzen, ed.), London, E&FN Spon, 1993, pp. 379–390.

Yang, K.-H., H.-S. Chung, and A. F. Ashour. Influence of Type and Replacement Level of Recycled Aggregates on Concrete Properties. *ACI Materials Journal,* Title No. 105-M34, May–June 2008, pp. 289–296.

Yildirim, Y., A. de Fortier Smit, and A. Korkmaz. Development of a Laboratory Test Procedure to Evaluate Tack Coat Performance. *Turkish Journal of Engineering and Environmental Sciences,* Vol. 29, 2005, pp. 195–205.

Yrjanson, W. A. Recycling of Portland Cement Concrete Pavement. *National Cooperative Highway Research Program Synthesis of Highway Practice* # 154. Transportation Research Board, National Research Council, Washington, D.C., December 1989.

Yu, H. T., K. D. Smith, M. I. Darter, J. Jiang, and L. Khazanovich. *Performance of Concrete Pavements Volume III—Improving Concrete Pavement Performance.* Final Report, FHWA-RD-95-111. Federal Highway Administration, McLean, VA, 1998.

Zachlehner, A., and R. Ullmann. Reconstruction of a Section of the A9 Motorway Using Recycled Aggregate Concrete (CIMEUROPE s.a.r.l., ed.). Presented at 7th International Symposium on Concrete Roads, Session 3, Reconstruction: Recycling, Stabilization. Vienna, October 3–5, 1994.

Zaghloul, S. M., T. D. White, and T. Kuczek. Use of Three-Dimensional, Dynamic, Nonlinear Analysis to Develop Load Equivalency Factors for Composite Pavements. In *Transportation Research Record 1449,* TRB, National Research Council, Washington, D.C., 1994, pp. 199–208.

Zareh, A., G. Way, and K. Kaloush. Asphalt-Rubber Open Graded Mix Reduces Tire Pavement Noise. *Proceedings of the Asphalt Rubber Conference,* Palm Springs, CA, 2006, pp. 385–398.

Zofka, A., M. O. Marasteanu, T. R. Clyne, X. Li, and O. Hoffmann. *Development of Simple Asphalt Test for Determination of RAP Blending Charts.* Report Number MN/RC-2004-44. Minnesota Department of Transportation, 2004.

TRB OVERSIGHT COMMITTEE FOR THE STRATEGIC HIGHWAY RESEARCH PROGRAM 2*

Chair: **Kirk T. Steudle,** *Director, Michigan Department of Transportation*

MEMBERS

H. Norman Abramson, *Executive Vice President (retired), Southwest Research Institute*
Alan C. Clark, *MPO Director, Houston–Galveston Area Council*
Frank L. Danchetz, *Vice President, ARCADIS-US, Inc.*
Malcolm Dougherty, *Director, California Department of Transportation*
Stanley Gee, *Executive Deputy Commissioner, New York State Department of Transportation*
Mary L. Klein, *President and CEO, NatureServe*
Michael P. Lewis, *Director, Rhode Island Department of Transportation*
John R. Njord, *Executive Director (retired), Utah Department of Transportation*
Charles F. Potts, *Chief Executive Officer, Heritage Construction and Materials*
Ananth K. Prasad, *Secretary, Florida Department of Transportation*
Gerald M. Ross, *Chief Engineer (retired), Georgia Department of Transportation*
George E. Schoener, *Executive Director, I-95 Corridor Coalition*
Kumares C. Sinha, *Olson Distinguished Professor of Civil Engineering, Purdue University*
Paul Trombino III, *Director, Iowa Department of Transportation*

EX OFFICIO MEMBERS

Victor M. Mendez, *Administrator, Federal Highway Administration*
David L. Strickland, *Administrator, National Highway Transportation Safety Administration*
Frederick "Bud" Wright, *Executive Director, American Association of State Highway and Transportation Officials*

LIAISONS

Ken Jacoby, *Communications and Outreach Team Director, Office of Corporate Research, Technology, and Innovation Management, Federal Highway Administration*
Tony Kane, *Director, Engineering and Technical Services, American Association of State Highway and Transportation Officials*
Jeffrey F. Paniati, *Executive Director, Federal Highway Administration*
John Pearson, *Program Director, Council of Deputy Ministers Responsible for Transportation and Highway Safety, Canada*
Michael F. Trentacoste, *Associate Administrator, Research, Development, and Technology, Federal Highway Administration*

RENEWAL TECHNICAL COORDINATING COMMITTEE*

Chair: **Daniel D'Angelo,** *Recovery Acting Manager, Director and Deputy Chief Engineer, Office of Design, New York State Department of Transportation*

MEMBERS

Rachel Arulraj, *Director of Virtual Design & Construction, Parsons Brinckerhoff*
Michael E. Ayers, *Consultant, Technology Services, American Concrete Pavement Association*
Thomas E. Baker, *State Materials Engineer, Washington State Department of Transportation*
John E. Breen, *Al-Rashid Chair in Civil Engineering Emeritus, University of Texas at Austin*
Steven D. DeWitt, *Chief Engineer (retired), North Carolina Turnpike Authority*
Tom W. Donovan, *Senior Right of Way Agent (retired), California Department of Transportation*
Alan D. Fisher, *Manager, Construction Structures Group, Cianbro Corporation*
Michael Hemmingsen, *Davison Transportation Service Center Manager (retired), Michigan Department of Transportation*
Bruce Johnson, *State Bridge Engineer, Oregon Department of Transportation, Bridge Engineering Section*
Leonnie Kavanagh, *PhD Candidate, Seasonal Lecturer, Civil Engineering Department, University of Manitoba*
Cathy Nelson, *Technical Services Manager/Chief Engineer (retired), Oregon Department of Transportation*
John J. Robinson, Jr., *Assistant Chief Counsel, Pennsylvania Department of Transportation, Governor's Office of General Counsel*
Ted M. Scott II, *Director, Engineering, American Trucking Associations, Inc.*
Gary D. Taylor, *Professional Engineer*
Gary C. Whited, *Program Manager, Construction and Materials Support Center, University of Wisconsin–Madison*

AASHTO LIAISON

James T. McDonnell, *Program Director for Engineering, American Association of State Highway and Transportation Officials*

FHWA LIAISONS

Steve Gaj, *Leader, System Management and Monitoring Team, Office of Asset Management, Federal Highway Administration*
Cheryl Allen Richter, *Assistant Director, Pavement Research and Development, Office of Infrastructure Research and Development, Federal Highway Administration*
J. B. "Butch" Wlaschin, *Director, Office of Asset Management, Federal Highway Administration*

CANADA LIAISONS

Lance Vigfusson, *Assistant Deputy Minister of Engineering & Operations, Manitoba Infrastructure and Transportation*

---

*Membership as of November 2013.

Related SHRP 2 Research

Geotechnical Solutions for Soil Improvement, Rapid Embankment Construction, and Stabilization of the Pavement Working Platform (R02)

Modular Pavement Technology (R05)

Real-Time Smoothness Measurements on Portland Cement Concrete Pavements During Construction (R06E)

Using Existing Pavement In Place and Achieving Long Life (R23)